29th International
Free Electron Laser
Conference
FEL07

Budker INP, Novosibirsk
Aug 26-31, 2007
http://ssrc.inp.nsk.su/FEL07/





Welcome

Dear colleagues,

I am happy to open the 29th International Free Electron Laser Conference here, in Budker Institute of Nuclear Physics.

During 30 years from the first operation of FEL this activity has grown to a big international branch of accelerator physics and technology. Looking at our conference programme one can see a lot of very prospective directions of the FEL development. X-ray FEL projects are close to the final stage, and the German soft x-ray facility has realized first user experiments. Terahertz radiation sources allow new research approaches. Numerous technology achievements provide good prospects for further increase of FEL power and improvement of radiation quality. Due to good theoretical understanding of FEL physics, several novel schemes are under examination.

Our Institute has a long history of participation in the FEL and synchrotron radiation activity, but it is the first time when we hold the International FEL conference. It is a great pleasure for us to be the hosts of this extraordinary meeting of world best experts. I wish us a good conference with fruitful exchange of ideas and discussions.

Gennady N. Kulipanov

Contents

Conference Committees

Conference Chair

G.N. Kulipanov (BINP)

International Executive Committee

I. Ben-Zvi (BNL)
W.B. Colson (NPGS)
M.E. Couprie (CEA/DSM)
J. Galayda (SLAC)
A. Gover (Tel Aviv University)
H. Hama (Tohoku University)
E. Jaeschke (BESSY)
K.-J. Kim (ANL & University of Chicago)
V. N. Litvinenko (BNL & Duke Uni.)
G. R. Neil (TJNAF)
C. Pellegrini (UCLA)
M.W. Poole (ASTEC)
A. Renieri (ENEA)
C.W. Roberson (ONR)
J. Rossbach (DESY & Hamburg Uni.)
T. Smith (Stanford University)
A.F.G. van der Meer (FOM)
N.A. Vinokurov (BINP)
R. Walker (DLS)

Scientific Programme Committee Chair

N.A. Vinokurov (BINP)

Scientific Programme Committee

R. Bakker (SLS)
C. Bochetta (Elettra)
M.E. Couprie (Soleil)
J. Dai (IHEP-Bejing)
J. Feldhaus (DESY)
M. Ferrario (INFN-LNF)
L. Giannessi (ENEA)
W. Graves (MIT)
R. Hajima (JAEA)
J. Hastings (SLAC)
I. Lindau (Stanford University)
V. Litvinenko (BNL)
A. Lumpkin (APS)
B. McNeil (Strathclyde)
L. Merminga (TJNAF)
A. Meseck (BESSY)
P. Michel (FZR)
E. J. Minehara (JAEA)
J. S. Oh (PAL)
J. Pflüger (DESY)
M. Poole (ASTeC)
A. Renieri (ENEA)
J. Rossbach (DESY & Hamburg Univ.)
J. Schmerge (SLAC)
L. Serafini (INFN)
T. Smith (Stanford University)
F. Stephan (DESY)
T. Tanaka (RIKEN)
S. Werin (MAXLAB)
Y. Wu (Duke University)
L. H. Yu (BNL)
A. Zholents (LBL)

Local Organizing Committee Chair

M.V. Kuzin (BINP)

Proceedings Editors

B.Goldenberg (BINP)
V.Eliseev (BINP)
A.Zhirkova (BINP)
P.Budz (BESSY)


FEL-07
29TH INTERNATIONAL FREE ELECTRON LASER CONFERENCE «FEL-2007
26–31 AUGUST, 2007

SELF-FORCE-DERIVED MASS OF AN ELECTRON BUNCH

E. Saldin, DESY, Hamburg, Germany

Abstract

We study an electron bunch together with its self-fields from the viewpoint of basic dynamical quantities. This leads to a methodological discussion about the definition of energy and momentum for fully electromagnetic systems and about the relation between covariance of the energy-momentum pair and stability. We show here that, in the case of unstable systems, there is no mean to define, in a physically meaningful way, a total energy-momentum four-vector: covariance of the energy-momentum pair follows from the stability of the system and viceversa, as originally pointed out by Henry Poincaré. Another version of this paper by G. Geloni and the author can be found in [1].

INTRODUCTION

Nearly one hundred years have passed since Abraham and Lorentz calculated their famous expressions for the energy and momentum of a purely electromagnetic, spherically symmetrical distribution of charges [2], [3]. This distribution constitutes an attempt to build a classical model of the electron: according to Lorentz's initial idea, mass, energy and momentum of the electron could, indeed, be of completely elecromagnetic nature.

Nevertheless, the energy (divided by the speed of light in vacuum, as we will understand through this paper) and momentum of such an electromagnetic electron do not constitute a four-vector. In fact (as Abraham [4] pointed out already in 1904 probably, at that time, without a clear understanding of what a four-vector is), in a frame moving with velocity $\vec{v}$ with respect to the system rest frame, we have

$$E_e = \gamma U'(1 + 1/3\beta^2) \tag{1}$$

and

$$\vec{P}_e = 4/3\gamma\vec{v}U'/c^2, \tag{2}$$

where the index e indicates the electromagnetic nature of the energy E_e and momentum $\vec{P}_e$, γ is the usual Lorentz factor, β is the velocity v/c (normalized to the speed of light in vacuum c), and U' indicates the electromagnetic energy in the electron rest frame [5],

$$U' = \epsilon_0/2 \int \vec{E'}^2 dV', \tag{3}$$

where ϵ_0 is the free space permittivity. U' is purely an electrostatic quantity (in this paper the prime will always indicate quantities calculated in the rest frame; therefore $\vec{E'}$ and dV' are, respectively, the electric field and the volume element in the rest frame of the system).

It is worth to mention here that the factor $4/3$ in Eq. (2) and the term proportional to $1/3\beta^2$ in Eq. (1) depend on the choice of spherical symmetry made on the charge distribution: had we chosen, for instance, an infinitely long line distribution in the direction of $\vec{v}$, we would have found

$$E_{e2} = \gamma U'(1 + \beta^2) \tag{4}$$

and

$$\vec{P}_{e2} = 2\gamma\vec{v}U'/c^2, \tag{5}$$

while, in the case of a line charge oriented perpendicularly to the direction of $\vec{v}$,

$$E_{e3} = \gamma U' \tag{6}$$

and

$$\vec{P}_{e3} = \gamma\vec{v}U'/c^2, \tag{7}$$

which only incidentally, due to the particular choice of the distribution, behaves as a four-vector.

Henry Poincaré solved the problem of the lack of covariance shown in Eq. (1) and Eq. (2) by introducing, in the electron model, energies and momenta of non-electromagnetic nature [6]. These are actually due to non-electomagnetic interactions which keep the electron together. By doing so he strongly related the covariance of energy and momentum with the stability of the system: the electomagnetic energy-momentum pair alone is not a four-vector, but the total energy-momenum pair, accounting for the non-electromagnetic interaction, is a regular four-quantity.

In 1922, Enrico Fermi developed an original, early relativistic approach to the $4/3$ problem [7]; about forty years later a redefinition of the energy-momentum pair related to Fermi's work was proposed by Rohrlich [8], which leaves untouched the total energy-momentum vector, but splits it into electromagnetic and non-electromagnetic contribution in such a way that covariance is granted for both the electromagnetic and the non-electromagnetic part of the energy-momentum pair.

It is possible to show [9], [10] that the treatments by Poincaré and Rohrlich are not in contradiction.

Nevertheless, the approach by Rohrlich [8] was sometimes taken (see e.g. [11]) as the proof that stability and covariance are unrelated matters since, upon redefinition, the electromagnetic part alone is a four-vector.

We will show here, that such a conclusion is incorrect. The stability of the system is related to the covariance of

the total energy-momentum vector, according to the original work by Poincaré: the redefinition procedure mentioned above is indeed acceptable only in the case one is interested in the total energy-momentum vector of a stable system (i.e. a system whose constituents are and stay at rest in a particularly chosen frame), and not in the separate electromagnetic and non-electromagnetic part. Only in that case the arbitrariness included in the recombination of these two contributions does not affect the equation of motion for the system (which deals, in fact, with the total energy-momentum vector).

Some time ago, we were addressing the problem of describing the transverse self-fields originating within an ultrarelativistic electron bunch moving in a fixed trajectory [12].

This is a particularly relevant problem in modern particle accelerator physics, in view of the need for very high-peak current, low emittance beams to be used, for example, in self-amplified spontaneous emission (SASE)-free-electron lasers operating in the x-ray regime (see for example [13], [14]): in fact, the good quality of the beam may be spoiled by self-interaction occurring within the bunch.

Besides practical relevance (which stresses how, after one hundred years, pure academical problems become relevant also to applied physics), an electron bunch is also a very good example of an unstable system subject to purely electromagnetic interactions. For such a system, the total energy and the total momentum in any frame, are just of electrodynamical nature. We will show that (according to our previous statement about the relation between stability and covariance) there is no way, in this case, to define the total energy-momentum pair in a covariant way. In fact, in contrast to what happens for stable systems, there is no way to describe the evolution of an unstable system without the knowledge of the (electromagnetic) field theory governing the (self-)interactions between its constituents.

A PARADOX AND ITS SOLUTION

Let us consider a short electron bunch moving, in a given laboratory frame, in a circular orbit. We can simplify the description of this system accounting only for two electrons which will represent the head and the tail of our bunch.

Imagine that the two particles are moving, initially with the same Lorentz factor $\gamma \gg 1$, in a circular orbit of radius R, and separated by a (curvilinear) distance $\Delta s \ll R/\gamma^3$.

In this situation the two electrons are near enough to be considered travelling with the same velocity vector: indeed it can be shown [15], that they radiate as a single particle of charge $2e$ (e being the electron charge) up to frequencies much above the synchrotron radiation critical frequency (note that, from a quantitative viewpoint, the expression "much above" is trivially connected to "how much" $\Delta s \ll R/\gamma^3$). The requirements specified before consist, from a geometrical viewpoint, in assuming that, at the beginning of the evolution, the two particles world-lines are very close: actually, considering our resolution in space equal to R/γ^3, they initially coincide.

This assumption justifies the presence of an inertial frame in which both particles are, with good approximation, at rest during the initial part of their evolution. We will refer to it simply as the rest frame. A quantitative definition of the initial part of the evolution may be given when a choice is made about close to zero are the velocities of the particles in the rest frame. Note that the existence of the rest frame is central for our study because, referring to it, one can easily analyze the energy and momentum of the system constituted by the two particles together with their electromagnetic fields.

By means of a Lorentz transformation, then, we can recover the same quantities in the laboratory frame.

Starting with the study in the rest frame we will refer, separately, to mechanical and electromagnetic quantities.

Obviously, in the rest frame, the mechanical momentum of the system, $\vec{P'}_{ne}$, is zero, and the mechanical energy, E'_{ne}, is just equal to $2mc^2$, where m is the electron rest mass.

The study of the electromagnetic contributions to energy and momentum is also trivial. Since the electrons are at rest they produce electric field only. Therefore the Poynting vector vanishes and $\vec{P'}_e = 0$. On the other hand, E_e is given, simply, by the work U' done against the field to bring the two particles together (quasistatically) from a situation in which they are separated by an infinite distance.

By doing so, of course, we are neglecting, in both $\vec{P'}_e$ and E'_e, the contributions from the acceleration (self-)fields generated by the system.

This approximation is justified by the fact that we are discussing the asymptotic behavior for the two particles separated by a very small distance: then, as it will be clear from Eq. (16) and Eq. (25), we may assume that the acceleration field contribution are unimportant, when compared with the Coulomb one. In fact acceleration effects saturate in the asymptotic limit of small distance between the two particles [15], while Coulomb ones are singular; once again it must be clear that we are discussing the asymptotic case for small distance between the two particles. Therefore we have:

$$E'_e = U' = e^2/(4\pi\epsilon_0\gamma\Delta s) \tag{8}$$

and

$$\vec{P'}_e = 0. \tag{9}$$

Summing up the electromagnetic and mechanical contributions one gets the total energy and momentum for the system:

$$E'_{tot} = E'_{ne} + E'_e = 2mc^2 + U' \tag{10}$$

and

$$\vec{P'}_{tot} = \vec{P'}_{ne} + \vec{P'}_e = 0. \tag{11}$$

As already said one may, now, use a Lorentz transformation in order to calculate these quantities in the laboratory frame. Again, since we are interested at the beginning of the evolution, it follows from our assumptions that the two particles evolve with the same four-velocity vector. Therefore a direction of motion (which we will designate with z) is well defined for the system in the laboratory frame and the Lorentz transformation from the rest frame is, indeed, a simple boost in the $-z$ direction (note that a good definition of the z direction is equivalent to a good definition of the rest frame). We will represent this boost with a matrix with components $\Lambda^{\mu}_{\ \nu}$ with $\mu, \nu = 0...3$ (where the third component corresponds to the z direction):

$$\Lambda^{\mu}_{\ \nu} = \begin{pmatrix} \gamma & 0 & 0 & \beta\gamma \\ 0 & 1 & 0 & 0 \\ 0 & 0 & 1 & 0 \\ \beta\gamma & 0 & 0 & \gamma \end{pmatrix} . \tag{12}$$

The use one makes of $\Lambda^{\mu}_{\ \nu}$ is a critical point in our derivation. If one (erroneously) assumes that energy and momentum constitute a four-vector, then he gets, straightforwardly:

$$(E_{tot}/c, \vec{P}_{tot})^{\mu} = \Lambda^{\mu}_{\ \nu}(E'_{tot}/c, \vec{P'}_{tot})^{\nu} \tag{13}$$

and, therefore,

$$E_{tot}/c = \gamma \left(2mc^2 + U'\right) , \tag{14}$$

and

$$P_{tot} = \gamma \left(2m + U'/c^2\right) \beta c , \tag{15}$$

where P_{tot} is a scalar quantity, since we understand that $\vec{P}_{tot}$ is oriented along the z direction.

We can now project the equation of motion, $\vec{F}_{syst} = d\vec{P}_{tot}/dt$, onto the transverse direction (perpendicular to z and lying on the orbital plane) thus getting, within our approximations:

$$F_{\perp \mathrm{syst}} = 2eB\beta c + \frac{e^2}{4\pi\varepsilon_0 R\Delta s} \tag{16}$$

As already mentioned in the Introduction (with in mind the applications in the physics of particle accelerators and the one of SASE-FELs, see [13], [14]) we addressed the description of the transverse self-fields originating within an electron bunch moving in a circle in [12]. In that paper an approach has been proposed which involves purely electrodynamical considerations, based on the retarded Green function solution of Maxwell equations.

In particular, in part of [12] we treated the case of two particles separated by a distance Δs (non necessarily much smaller than R/γ^3), moving rigidly in a circle (see Fig. 1) of radius R. Our results disagree with Eq. (16).

Let us briefly justify the latter statement. The total transverse force (orthogonal to its velocity and lying on the orbital plane) felt by the head electron and due to the tail electron source turned out to be (see, again [12]):

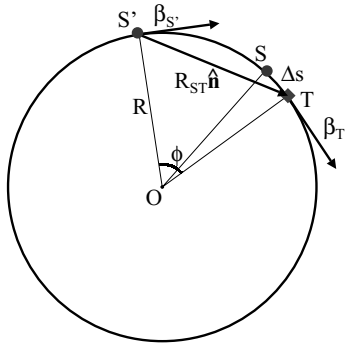

Figure 1: Geometry for the two-particle system in the steady state situation, with the test particle ahead of the source. Here T is the present position of the test particle, S is the present position of the source, while S' indicates the retarded position of the source.

$$F_{\perp} \simeq \frac{e^2\gamma^3}{4\pi\varepsilon_0 R^2}\Phi(\hat{\phi}) , \tag{17}$$

where Φ is defined by

$$\Phi(\hat{\phi}) = \frac{2 + \hat{\phi}^4/8}{\hat{\phi}(1 + \hat{\phi}^2/4)^3} , \tag{18}$$

Here $\hat{\phi}$ is the retarded angle ϕ (which expresses the angular distance between the retarded position of the source the present position of the test electron, see Fig. 1, normalized to the synchrotron radiation formation angle at the critical frequency, $1/\gamma$, i.e. $\hat{\phi} = \gamma\phi$. Eq. (18) is completely independent of the parameters of the system.

It is straightforward to study the asymptotic behaviors of Φ. In order to do so, just remember that the retardation condition linking Δs and ϕ is given by (see [12], [15]):

$$\Delta s = R\phi - 2\beta R \sin\frac{\phi}{2} , \tag{19}$$

or by its approximated form

$$\Delta s = (1 - \beta)R\phi + \frac{R\phi^3}{24} . \tag{20}$$

It is now evident that $\Phi(\Delta\hat{s}) \to 1/(3\Delta\hat{s})$ when $\hat{\phi} \gg 1$ and $\Phi(\Delta\hat{s}) \to 1/(\Delta\hat{s})$ when $\hat{\phi} \ll 1$, having introduced the normalized quantity $\Delta\hat{s} = (\gamma^3/R)\Delta s$. This normalization choice is, again, linked with the fact that the critical synchrotron radiation wavelength, R/γ^3, is also the minimal characteristic distance of our system: as we said before, two particles nearer than such a distance can be considered as a single one radiating, up to the critical frequency, with charge $2e$ (see [12], [15]).

The asymptotic behavior above suggests to study the function $\Phi(\Delta\hat{s})\Delta\hat{s}$. We plotted such a function in Fig. 2 (and the contribution from the acceleration field alone) for values of $\Delta\hat{s}$ running from 0 to 5.

As it is seen from the figure, the contribution from the velocity field is not important in the asymptotic limit for

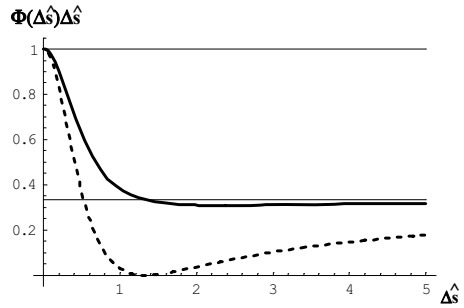

Figure 2: Plot of $\Phi(\Delta\hat{s})\Delta\hat{s}$ (solid line) and comparison with the asymptotic values, 1 and $1/3$. The dashed line shows the contribution from the acceleration field, $\Phi_{\rm R}(\Delta\hat{s})\Delta\hat{s}$, alone.

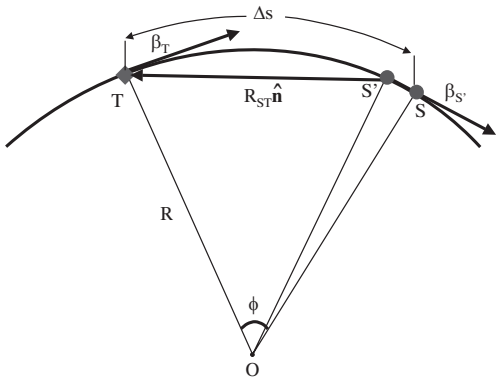

Figure 3: Geometry for the two-particle system in the steady state situation, with the source particle ahead of the test one. Here T is the present position of the test particle, S is the present position of the source, while S' indicates the retarded position of the source.

particles very nearby (our case) or very far away. When, in particular, $\Delta s \ll R\gamma^3$ we can approximate Eq. (17) by

$$F_\perp \simeq \frac{e^2}{4\pi\varepsilon_0 R\Delta s}\,. \tag{21}$$

On the other hand, as regards the force felt by the tail particle (see Fig. 3), it is easily seen that (see [12], [15]) the test electron, which now is the tail particle, "runs against" the electromagnetic signal emitted by the source (while in the previous case it just "runs away" from it). Therefore the relative velocity between the signal and the test electron is equal to $(1+\beta)c$ (instead of $(1-\beta)c$ in the other situation). Hence the retardation condition reads

$$\Delta s = R\phi + 2\beta R\sin\frac{\phi}{2}, \tag{22}$$

or, solved for ϕ in its approximated form,

$$\phi \simeq \frac{\Delta s}{R(1+\beta)}\,. \tag{23}$$

In this situation, $\vec{\beta}_{\rm S}$ is almost parallel (and equal) to $\vec{\beta}_{\rm T}$ and antiparallel to $\vec{n}$ (which is the unit vector oriented as the line connecting the retarded source to the present test particle): it turns out that the only important contribution to the transverse force results from the acceleration field and reads:

$$F_\perp \simeq \frac{e^2}{4\pi\varepsilon_0 R\Delta s}\,. \tag{24}$$

In the case under study, since $\Delta s \ll R/\gamma^3$, the total self-force acting on the system is given by the sum of Eq. (21) and Eq. (24):

$$F_\perp \simeq 2\frac{e^2}{4\pi\varepsilon_0 R\Delta s}\,, \tag{25}$$

which is in disagreement of a factor 2 with respect to the self-force term in Eq. (16). In other words, had we erroneously assumed covariance, we would have encountered a paradox. Again, note that we are treating the asymptotic limit of a small distance between the two electrons: in this limit we can neglect the contribution from the acceleration field in the equation of motion Eq. (16). In fact this contribution saturates for small distance between the two particles (see [15]), while the term missing by comparison between Eq. (16) and Eq. (25) is singular (and, therefore, dominating) in the limit when Δs goes to zero.

This situation should not be too much surprising for the reader familiar with the works [2]... [4] which led to Eq. (1) and (2): the derivation of Eq. (16) is, in fact, performed under the explicit assumption that energy and momentum constitute a four-vector.

As we will immediately see, in the case of unstable systems (like the one we deal with), the use of correct transformation laws for the electromagnetic stress tensor solves the problem but spoils the covariance of the energy-momentum pair.

The energy and momentum of an electromagnetic system in the laboratory frame is given by

$$E = \int T'^{\mu\nu}\Lambda^0{}_\mu\Lambda^0_\nu\frac{dV'}{\gamma} \tag{26}$$

$$P^i = \frac{1}{c}\int T'^{\mu\nu}\Lambda^i{}_\mu\Lambda^0{}_\nu\frac{dV'}{\gamma}, \tag{27}$$

where $T^{\mu\nu}$ are the components (in the rest frame) of the electromagnetic stress tensor of the system, which contains all the information about the (electromagnetic) field theory governing the interactions between the particles. The process of lowering and raising indexes is governed in the usual way by the metric tensor. Here the latin index i runs from 1 to 3 and, as already said, the quantities with prime refer to the rest frame. In our case we will consider the only important component, i.e. the third (along z).

Note that the integrals in Eq. (26) and Eq. (27) include both a single-particle term and an interaction term (compare also [10]). Here we are interested in the interaction term alone: in fact we will treat the (trivial) mechanical

contributions to the energy-momentum pair separately and, once again, we will neglect the acceleration-field contributions. Therefore, in the following, we will understand that T' refers to the interaction term alone.

Then, since the mechanical energy-momentum pair of a single particle is a 4-vector, one gets:

$$(E_{ne}/c, P_{ne})^{\mu} = \Lambda^{\mu}_{\nu}(E'_{ne}/c, P'_{ne})^{\nu} \ , \qquad (28)$$

hence

$$E_{ne} = 2\gamma mc^2 \qquad (29)$$

and

$$P_{ne} = 2\beta\gamma mc. \qquad (30)$$

while

$$E_e = \beta^2\gamma \int T'^{33} dV' + \gamma U', \qquad (31)$$

$$P_e = \gamma\beta U'/c + \gamma\beta/c \int T'^{33} dV', \qquad (32)$$

We should note, here (but this is a valid methodological remark also as regards the previous, incorrect approach), that the particles are subject to a long-range interaction (the electromagnetic interaction) and, therefore, a covariant definition of the total energy and momentum is not straightforward even when one is considering the two particles alone, without including (as we did, instead) the electromagnetic fields in the system. Therefore, strictly speaking, one may object that Eq. (28) does not make any sense at all.

Indeed, if the interaction occurred at a single point in space-time (short-range scattering case), the particle velocities would have been constant, in the view of any inertial observer, before and after the scattering took place. Then if two observers related by a Lorentz boost compared their judgments about the particles velocities, they would have found that these are linked by a Lorentz transformation, the same which transforms from one observer to the other. Nevertheless, this is a particular case. We must remember that, in general, according to the Theory of Relativity, the concept of simultaneity depends on the observer. Therefore, when (as in the situation under study) one deals with a long-range interaction, the velocities of the particles, in the judgment of the two observers above, are not related by a Lorentz transformation anymore (see [16]): the objection about the correct definition of the mechanical energy-momentum vector follows directly from this observation. A good definition of the energy-momentum vector of the two-particle system alone (without their fields!) can, in fact, be recovered using more subtle geometrical methods only, like a regular correlated representation of the world lines (see [16]).

However this objection does not concern us, here, since, as already implicit in the definition of the z direction, we discuss about that region of space-time in which the two particles world lines are very close and are roughly characterized by the same Lorentz factor, that is, once again, at the beginning of the evolution.

Then we can use Eq. (28)... Eq. (32) to get, by summation, the total energy and momentum of the system in the laboratory frame and in the direction of motion (see also [5] and [17]):

$$E_{tot} = \gamma \left(2mc^2 + U' + \beta^2 \int T'^{33} \, dV' \right), \qquad (33)$$

and

$$P_{tot} = \gamma \left(2m + U'/c^2 + \frac{1}{c^2} \int T'^{33} \, dV' \right) \beta c \, . \qquad (34)$$

Note that Eq. (33) and Eq. (34) can be used to obtain Eq. (1) and Eq. (2), as well as Eq. (4)... Eq. (7): different distributions of charge give different expressions for the electromagnetic stress tensor and for the electromagnetic energy.

In our case of two electrons we already know the explicit expression for U'. In fact we remind that, as has already been said, the electromagnetic interaction energy is simply given by the work done against the field to bring the two particles together, quasistatically, from a situation in which they are separated by an infinite distance:

$$U' \simeq \frac{e^2}{4\pi\varepsilon_0\gamma\Delta s} \, . \qquad (35)$$

On the other hand it is easy to calculate $T'33$ (in the rest frame, since we need to integrate over V'). To this purpose we remind that, in the rest frame (and at short distance $\gamma\Delta s \ll R/\gamma^2$, so that the acceleration field contributions are unimportant), the space-space components of the total (comprehensive of both single particle and interaction part) symmetric energy-momentum tensor read (see [5]):

$$T'^{ij}_{tot} = -\varepsilon_0 (E'_i E'_j - \delta_{ij} E'^2/2) \, , \qquad (36)$$

where, here, *i, j* = 1.. 3. The discussion above shows that, for us, the only interesting component is T'_{33}. It can be proven that the interaction part alone is just

$$\int T'^{33} \, dV' = U' \, . \qquad (37)$$

Note that Eq. (37) describes also the case of a charged line distribution oriented in the direction of motion (in the case of a charged line, of course, the single-particle term is not present at all).

The equations for the energy and momentum of the system in the laboratory frame now read:

$$E_{tot} = \gamma \left[2mc^2 + U'(1 + \beta^2) \right] \qquad (38)$$

and

$$P_{tot} = \gamma \left(2m + 2U'/c^2 \right) \beta c \, , \qquad (39)$$

whose electromagnetic parts are the same of Eq. (4) and Eq. (5).

From the transverse component of the equation of motion for the system one gets

$$F_{\perp \mathrm{syst}} \simeq 2eB\beta c + 2\frac{e^2}{4\pi\varepsilon_0 R\Delta s} \tag{40}$$

Eq. (40) is now in perfect agreement with our result in Eq. (25).

Both the terms on the right hand side of Eq. (40) are centripetal as well as in Eq. (16) (although, of course, Eq. (16) and Eq. (40) are in disagreement as concerns the magnitude of the self-interaction term); the first describes the motion of the system under a magnetic field, while the second is linked with the presence, in the system, of electromagnetic fields: an extra centripetal (external) force is needed, if one wants to keep the system moving in a circle of radius R, compensating for the centrifugal self-field contributions calculated in [12].

DISCUSSION

In order to reach the agreement between Eq. (40) and Eq. (25), one has to give up the covariance of the energy-momentum pair of our system, as it is seen directly from Eq. (38) and Eq. (39).

We can sum up the discussion in the previous Section by saying that the assumption of covariance for the transformation of the energy-momentum pair of an unstable system leads to a paradox. Such a paradox can be solved introducing the correct transformation laws for the energy-momentum tensor. In this way, it is seen that the energy-momentum pair for an unstable system (particles and electromagnetic field) is not a four-vector. We already mentioned in the Introduction that the non-covariant character of energy and momentum is also present when one discusses some classical problems which involve the relativistic dynamics of a charged particles stable system. Nevertheless, in these cases, covariance can be always restored by introducing non-electromagnetic stresses which keep the system together or, equivalently, by redefinition (see [8]) of the energy-momentum pair. In particular we can refer to the $4/3$ problem in the classical electron model (as done above in the Introduction) but also to other problems like, for example, the explanation of the Trouton-Noble paradox, which has been treated extensively in literature (see [9], [18].. [21]) all over the last century.

As we already said in the Introduction, there is one major difference with respect to our case, though: our system, in contrast with the latter ones, is, by nature, unstable; there is no reference frame such that its components are and stay at rest. This fact leads to a major difference in the treatment of the total energy and momentum.

In the case of a stable system, the total energy and momentum of the system (including non-electromagnetic binding forces) constitute a four-vector, a well-defined geometrical entity.

On the contrary, in the case of an unstable system, this pair of quantities has no geometrical meaning, although it is possible to give, of course, separate definitions of total energy and momentum in the judgment of any observer.

In the situation discussed in the previous Section this is a direct consequence of the fact that we deal with a fully electrodynamical system and there is no way to introduce, in a straightforward way, an analogue of Poincaré stresses. As a result we must conclude that stability of the system and covariance of the energy-momentum pair are bound together.

Let us discuss the latter statements in detail, starting with a review of well-known arguments for stable systems.

Stable systems are characterized by a zero (total self-) four-force density. When the four-force density can be derived from an energy-momentum tensor $T^{\mu\nu}$, the latter property is equivalent to:

$$T^{\mu\nu}_{\ \ ;\mu} = 0\,, \tag{41}$$

which is the requirement for a zero-divergency energy-momentum tensor.

However, Eq. (41) refers to the total energy-momentum tensor, while the electromagnetic part of it is not divergenceless at all (its divergence is, simply, the Lorentz four-force density).

On the other hand, since stability is characterized by a zero total four-force density, non-electromagnetic stresses must be present (Poincaré stresses), which balance the Lorentz four-force density, thus insuring stability for the system. Poincaré stresses also insure covariance for the energy-momentum pair which is, therefore, a well-defined four-vector: to prove this, one can remember the definition of the total energy-momentum pair (see [5], [9]):

$$P^{\mu} = \frac{1}{c}\int_{\sigma} T^{\mu\nu} d\sigma_{\nu} \tag{42}$$

where the integration is carried out over any hypersurface at $t = constant$ (actually σ may be, more generally, any spacelike surface, see [9]) for any inertial observer.

It can be easily proved (see [9]) that Eq. (42) is independent from the choice of the integration hypesurface. Such a proof is based on Eq. (41).

The choice of different inertial observers is equivalent to the choice, on the space-time manifold, of different time-like unit vectors. The different families of hypersurfaces orthogonal to these vectors represent the physical space at a certain time in the judgement of different observers. From the independence of the definition in Eq. (42) of the choice of the integration hypersurface follows, therefore, the independence of P^{μ} on the reference frame used to evaluate it, and this constitutes the proof that P^{μ} is a well-defined four-vector.

Since P^{μ} is independent from the choice of the integration hypersurface, one is free to choose the one which helps better in solving problems. Historically, two choices have been used in explaining, for example, the Trouton-Noble

paradox. The first (see [9]) consists in considering the surface at $t = constant$ for any observer. This leads to the usual expressions for the electromagnetic energy and momentum in a given frame:

$$\frac{E_e}{c} = P_e^0 = \frac{1}{2c}\int\left(\epsilon_0\vec{E}^2 + \frac{\vec{B}^2}{\mu_0}\right)dV \qquad (43)$$

and

$$\vec{P}_e = \frac{1}{\mu_0 c^2}\int\left(\vec{E}\times\vec{B}\right)dV, \qquad (44)$$

where μ_0 is the free space permeability.

While Eq. (43) and Eq. (44) do not constitute a four-vector, one can straightforwardly solve the problem of the lack of covariance by introducing Poincaré stresses.

The second choice consists in selecting $t = constant$ in the rest frame of the system:

$$\frac{E_e}{c} = P_e^0 = \frac{1}{c}\int\left[\frac{1}{2}\left(\epsilon_0\vec{E}^2 + \frac{\vec{B}^2}{\mu_0}\right) - \vec{v}\cdot\frac{\vec{E}\times\vec{B}}{\mu_0 c^2}\right]dV \qquad (45)$$

and

$$\vec{P}_e = \frac{\gamma}{c}\int\Big[\frac{\vec{E}\times\vec{B}}{\mu_0 c} - \frac{\vec{v}}{2}\cdot\left(\epsilon_0\vec{E}^2 + \frac{\vec{B}^2}{\mu_0}\right) + \\ +\epsilon_0(\vec{v}\cdot\vec{E})\vec{E} + (\vec{v}\cdot\vec{B})\frac{\vec{B}}{\mu_0}\Big]dV \qquad (46)$$

In this case it can be easily shown (see [8], [9]) that the electromagnetic part of the total energy-momentum pair is, actually, a four-vector. This is, in fact, the same redefinition of the four-momentum that Rohrlich used to deal with the electron problem [8]. One can easily check (see [9]) that, in this case, the non-electromagnetic part of the total energy-momentum pair is zero.

All this illustrates the well-known fact that the introduction of Poincaré stresses or the Rohrlich redefinition of energy and momentum are, in fact, equivalent in essence. The choice of the integration hypersurface is a matter of taste for stable systems, since the only important quantity from a geometrical viewpoint is the total energy-momentum four-vector, given by the sum of the electromagnetic and the non-electromagnetic part; this sum, by definition, is independent from such a choice. In other words, different choices of the hypersurface just split the same, total quantity onto two parts (electromagnetic and non-electromagnetic) in two distinct ways but, as quoted from [9] : "The split into electromagnetic and non-electromagnetic parts is quite arbitrary".

Our point is that this situation is completely different in the case of unstable systems, where only electromagnetic forces are present and Poincaré stresses are not.

In the case of unstable systems there is no way one can define the total energy-momentum four-vector. This statement is justified, from a mathematical viewpoint, by the fact that

$$T^{\mu\nu}_{tot\ ;\mu} = T^{\mu\nu}_{e\ ;\mu} \neq 0\ ; \qquad (47)$$

in fact, from the previous discussion, we know that divergenceless is an essential ingredient for the independence of the total energy-momentum pair from the choice of the integration hypersurface.

Note that Eq. (47) means that there is a non-vanishing four-force density field over the space-time. In the case discussed in the previous Section we gave a practical example of the latter statements.

Of course, also for unstable systems, we may consider an observer and find out the energy and momentum of the system with respect to that observer, but this quantities will not be covariant, nor we can recover covariance by integrating the energy-momentum tensor over a suitable hypersurface (as done with stable systems), since the electromagnetic energy-momentum pair (which coincides now with the total energy-momentum pair) would change Eq. (38) and Eq. (39), thus giving an unphysical result on the second term of Eq. (40), when compared with Eq. (25). The latter discrepancy, to the authors view, is similar to the one encountered in [10]. In that paper a system composed by two electron is studied too and a comparison is proposed between energy-derived mass m_u (electrostatic energy divided by c^2), momentum derived mass m_p (momentum divided by γv, being v the system velocity) and self-force-derived mass m_s (self-force divided by $\gamma^3 a$, a being the system acceleration). The authors of [10] point out that $m_s = m_p \neq m_u$ and that the inequality between m_p and m_u can be solved by redefining, following Rohrlich (see [8]) the energy-momentum pair. Nevertheless, in this case, one is left with a discrepancy between m_s and m_u. This fact is perceived by the authors of [10] as an unsolved paradox. Actually the derivation of Eq. (16) (or equivalently, of m_u, treated with Rohrlich's method) is performed under the explicit assumption that energy and momentum constitute a four-vector which is true only in the case of a stable system. As a result, by comparing Eq. (16) and Eq. (25) or, which is the same, m_u (treated by Rohrlich's method or, equivalently, by introducing Poincaré stresses) with m_s, one is comparing quantities which refer to a stable system with quantities which refer to an unstable one, thus giving a paradoxical result.

Consider, as a last example, an unstable system formed by different subsystems initially at rest in a certain frame (as in the case discussed in the previous Section). In general, while dealing with unstable systems, the knowledge of dynamical quantities for the subsystems cannot bring any information about the behavior of the system as a whole, unless we have knowledge of the (electromagnetic) field theory governing the interactions (which make the system unstable).

In our example of the previous Section, even if we can measure, in a certain frame, the particle velocities when they are far away from each other (thus no more interacting) and if we know their rest masses, we cannot say anything about energy and momentum of the total system without the knowledge of the stress tensor, and the reason for that is the presence of a non-zero four-force density field (which we can account for only knowing the stress tensor, i.e. the interaction theory) on that part of the four-dimensional manifold on which we want to have information.

Suppose our system was stable (think about an ideal "rope" responsible for Poincaré stresses, or think, instead of the case of two electrons, about a nuclear fission process in which electromagnetic fields are, before the fission event, balanced by the strong interaction). Put ourselves in the laboratory frame, and imagine that, at a certain moment, for a certain reason (a collision with a neutron, for example) the Poincaré stresses are not present anymore. Thus the system becomes unstable, it breaks in two subsystems and the electromagnetic interaction (if you're thinking about the nucleus imagine we are talking about a charged ion) takes over. If we wait for enough time the two particles will get far away from each other and we can consider them no more interacting.

At this point, the kinetic energy of the particles is equal to the energy previously stored in the electromagnetic field when the system was stable: thus we are able to get information about the total energy-momentum vector of the stable system even if we do not know anything about the stress tensor and the theory of the interaction between the subsystems. In fact, the sum of the momenta of the two free particles and the sum of their energies will give us, respectively, the energy and the momentum of the stable system, which form a four-vector again.

The reason is, simply, that there is no four-force density field in that part of the space time on which we want to have information: from a general viewpoint we can conclude that the presence of a four-force density, which characterizes unstable systems, spoils without remedy the covariance of the energy-momentum pair. The only way to recover such covariance would be to introduce a balancing four-force density, i.e. to make the system stable.

In other words, in agreement with Poincaré, from the stability of the system follows the covariance of the system and, vice versa, from covariance follows stability: the energy-momentum pair of an unstable system does not constitute a four-vector. This conclusion may seem, at first glance, of academical importance only. It has, indeed, very practical consequences in modern electron beam physics. Energy and momentum of an electron bunch are physically measurable quantities and an electron bunch itself is a practical example of an unstable system. Nowadays, technology allows the production of ultra high-brightness, intense electron beams (to be used, for example, in self-amplified spontaneous emission (SASE)-free-electron lasers operating in the x-ray regime). The production of such bunches is one of the most challenging activities for particle accelerators physicists. The description of these systems would be completely incorrect without accounting for self-interactions in the right way. We can conclude that, for example, simulation codes (as well as analytical considerations: actually, as already reminded, we wrote this paper after studying the self-interactions within an electron bunch) which rely on the covariance of the energy-momentum pair would give, $a\ priori$, wrong results which may be immediately confuted by experimental control. Technological developments often transform, as in this case, purely methodological issues into very practical ones.

REFERENCES

[1] G. Geloni and E. Saldin, On energy and momentum of an ultrarelativistic unstable system, DESY 02-201, ISSN 0418-9833, online available at http://arxiv.org/abs/physics/0211093 .

[2] M. Abraham, Theorie der Elektrizitat, vol II: Elektromagnetische Theorie der Stralung, Teubner, Leipzig, 1905

[3] H.A. Lorentz, The Theory of electrons, Leipzig, Teubner, 1909

[4] M. Abraham, Phys. Z., 5, 1904

[5] J. D. Jackson, Classical Electrodynamics, Wiley, N.Y.

[6] H. Poincaré, On the dynamics of the electron, Rendiconti del Circolo Matematico di Palerma 21, 129, 1906

[7] E. Fermi, Il Nuovo Cimento, 25, 159-170, 1923

[8] F. Rohrlich, Classical Charged Particles (Addison-Wesley, Reading, Mass., 1965), Sec. 6-3

[9] S. A. Teukolsky, Am. J. Phys. 64 (9), 1104, 1996

[10] D. J. Griffiths and R. E. Owen, Am. J. Phys. 51 (12), 1120, 1983

[11] M. H. Mac Gregor, The enigmatic electron (Kluwer Academic Publishers, Dordrecht /Boston/London, edited by Alwyn van der Merwe), pp. 19-24

[12] G. Geloni et al., DESY 02-048, May 2002; also, to be submitted to Phys. Rev. E

[13] TESLA Technical Design Report, DESY 2001-011, edited by F. Richard et al. and http://tesla.desy.de/

[14] The LCLS Design Study Group, LCLS Design Study Report, SLAC reports SLAC -R521, Stanford (1998) and http://www-ssrl.slac.stanford.edu/lcls/CDR

[15] E. L. Saldin, E. A. Schneidmiller and M. V. Yurkov, Nucl. Instr. Methods A 398, 373 (1997)

[16] M.A. Trump at al., Classical Relativistic Many-Body Dynamics, Kluwer Academic Publishers, Dordrecht, 1999

[17] C. Möller, The theory of relativity, second edition, Chapter 7, Clarendon press, Oxford (1972)

[18] M. v. Laue, Ann. Phys. 35, 524, 1911

[19] W. Pauli, The thory of relativity, (Pergamon, New York, 1958)

[20] A. K. Singal, Am. J. Phys. 61, 428, 1993

[21] J. W. Butler, Am. J. Phys. 36, 936, 1968

TECHNOLOGY CHALLENGES TOWARDS SHORT-WAVELENGTH FELS

J. Rossbach, Universität Hamburg and DESY, 22603 Hamburg, Germany

Abstract

The paper sheds some light on achievements in accelerator technology that paved the way towards short-wavelength FELs, specifically the FLASH facility at DESY. Also, a few of the technical challenges are discussed which we are facing in view of future X-ray FELs.

INTRODUCTION

Free-electron lasers (FEL) operating in the SASE mode (self-amplified spontaneous emission) at wavelengths far below the visible are now with us since several years, and more, and even more ambitious, projects are ahead of us. Although most of the basic theory is known since the early eighties, it took more than twenty years until FEL saturation was demonstrated experimentally at wavelengths below the visible. Even more, it took almost 30 years until a user facility was put in operation in the VUV regime, although it was clear from the very beginning, that such a radiation source would open up an entirely new world of possibilities for experimenters.

The major reason for this long time span was related to the unprecedented electron beam quality needed to achieve saturation within a reasonable undulator length. Considerable R&D on accelerator physics and technology was indispensable to come to a credible and reliable design of a (soft) X-ray FEL. In particular, it was not only necessary to develop technologies for producing ultra-relativistic electron bunches with high charge (typically 1 nC), small normalized emittance (typically 1 mrad mm) small energy spread (order of 100 keV after compression) and very short bunch length (10 fs range, thus achieving both the kA peak current needed for the FEL and the short radiation pulses desired by users), but it was as important to invent novel beam diagnostics tools to verify and control the beam properties at a micrometer precision level – in all three dimensions. This broad scope of tasks could only be accomplished by big accelerator centres, being able to initiate and conduct a coordinated effort of the full spectrum of accelerator scientists and engineers. This broad spectrum of expertise was traditionally cultivated at big labs dedicated to high-energy particle physics (HEP), for their permanent demand of more powerful and more sophisticated accelerators. It is thus not by accident that the first X-ray FEL programs were initiated mainly by such labs like DESY and SLAC. It will be a most awarding science management task (and, in view of the more and more project oriented funding policies, a very challenging one) to keep alive and even extend the fruitful collaboration of accelerator scientists from both HEP and FEL communities.

The present paper is not considered a review article on this extremely broad subject. It is rather a personal review, mainly referring to the almost 14 years of R&D effort conducted at DESY, Germany towards the FLASH user facility. To a large extent, this effort was based on, and conducted by, the international TESLA collaboration, with the superconducting accelerator called "TESLA Test Facility" still being the backbone hardware. In the spirit mentioned above, part of the accelerator beam time is still allocated to HEP-related accelerator R&D towards the International Linear Collider (ILC), being based on the same TESLA superconducting accelerator technology.

The list of technology issues mentioned in the following is by far not complete. It represents a personal, partly arbitrary selection of topics that are FEL specific, where considerable progress has been made, but which should keep us busy for another while.

TRANSVERSE SPACE CHARGE

In linear 1D theory [1], the power e-folding length L_g of the high-gain FEL can be expressed by

$$L_g = \frac{1}{\sqrt{3}}\left[\frac{2m}{\pi\mu_0 e^2}\frac{\gamma^3\lambda_u}{K^2 n_e}\right]^{1/3} \propto n_e^{-\frac{1}{3}} \qquad (1),$$

where λ_u is the undulator period, K the undulator parameter, γ the electron energy in units of its rest energy, and n_e is the electron density in the lab frame. In order to achieve a sufficiently short power gain length L_g, there is little alternative to calling for very high charge density. Taking into account that particles with large betatron amplitudes fall out of FEL resonance, large n_e must be realized in a combination of small radial beam emittance ε_r and large peak current $\hat{I}$. Such an electron beam is subject to considerable space charge forces, even though such forces are largely suppressed at ultrarelativistic energies. The impact on transverse electron focusing can be estimated from the focal length f generated by the linear defocusing forces on a beam drifting along the accelerator over a distance z ($f > z$ assumed):

$$f \approx \frac{ec}{r_e}\frac{\overline{\beta}\varepsilon_{norm}}{z}\frac{\gamma^2}{\hat{I}} \qquad (2)$$

With typical numbers for the normalized emittance $\varepsilon_{norm} = \beta\gamma\varepsilon_r \approx 1$ mrad mm, the average beta function $\overline{\beta} \approx 10$ m, the peak current $\hat{I} \approx 1$ kA, and the beam energy $\gamma \approx 200$, we get a focal length as small as $f \approx 10$ m already after a few meters of passage length z.

As a consequence, the electron beam carries its own focusing system, i.e. it is difficult to control the transverse beam size just by external quadrupole magnets. This is illustrated in Fig. 1, where the beta functions at FLASH are calculated for different assumptions on the peak current [2]. Note that the peak current inside the bunch is by far not constant (see below) such that different parts of the bunch acquire different focusing. It is then difficult to tell whether the lasing part of the beam has the desired focusing inside the undulator.

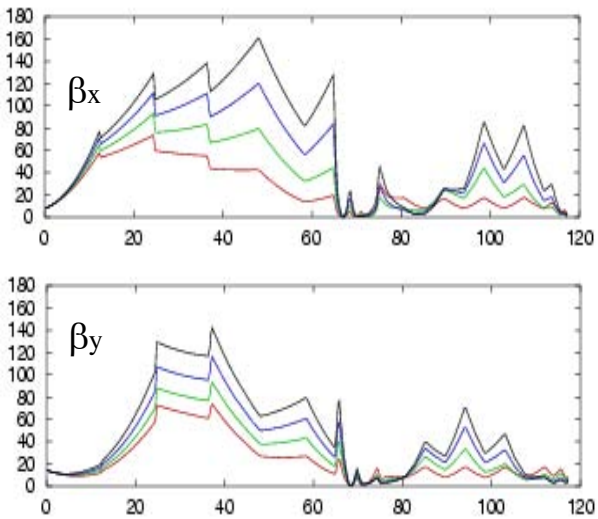

Figure 1: Optics beta functions at FLASH for the beamline after the final bunch compression at 380 MeV, calculated for different peak currents: $\hat{I}$ = 0 kA (red), 1 kA (green), 2 kA (blue), 3 kA (black). It is assumed here that space charge forces are negligible before the compression where the peak current is much lower.

Generation of low emittance electron beams

The reliable generation of electron beams with the desired small emittance is of outmost importance for the over-all design and for the performance of an X-ray FEL. In particular, the requirement that the emittance should fulfil (at least approximately) the condition $\varepsilon_r \le \lambda_{Light}/4\pi$ is extremely demanding if radiation wavelengths (first harmonics) around $\lambda_{Light} \approx 1$ Angstrom are to be achieved. Generally this is the major reason for choosing a rather high electron beam energy beyond 10 GeV at LCLS and at the European XFEL. The electron source is thus the single component where improvements would have the largest impact on the overall design, performance and costs of an X-ray FEL. An overview of this subject is beyond the scope of this paper and can be found in Ref. [3].

At present, most of the FEL projects are based on a RF gun [4]. Through appropriate choice of cathode material and RF frequency, RF guns have been developed both for superconducting and normal conducting linacs, i.e. serving for a wide range of duty cycles and bunch repetition rates. It is of particular importance, that very recently both R&D lines have reported success in achieving the design emittance of approx. 1.0 mrad mm (normalized) for 1 nC charge [5,6]. In order to reduce the nonlinear part of space charge forces, it is beneficial in these guns that the drive laser pulses are shaped towards flat transverse and longitudinal profiles.

It was pointed out before that the lower the beam emittance the better. It is thus exciting that there are alternative concepts potentially performing even better than RF guns:

- A thermionic gun based on a single crystal CeB_6 cathode is used at SCSS [7] and has already demonstrated promising results.
- An array of nanometer size field emitters immediately followed by a high voltage pulsed diode is under study at PSI in order to significantly reduce the thermal emittance and to suppress emittance growth due to space charge forces directly after the emission process [8].
- A dramatic progress might be achieved by plasma-based laser-wakefield acceleration on which a real break-through was demonstrated recently by demonstrating an electron beam of up to 1 GeV and only a few % momentum width [9] with a tabletop setup. Momentum spread, stability, and the transport of the beam into an FEL undulator remain critical issues.

Whatever the electron gun is, precise measurement of the emittance is very critical, in particular since the phase space distribution will be everything else but trivial. Thus, measurements of phase space distribution at resolution in the 10 μm range (in all three dimensions!) are desired. But even if the measurement is restricted to the longitudinal projection of the bunch, it is not trivial to find a parametrization of the distribution adequate for the FEL physics, the reason being that the phase space distributions are generally by far not Gaussian. The general approach is to describe the beam quality in terms of the rms-emittance $\varepsilon_x = \sqrt{\langle x \rangle^2 \langle x' \rangle^2 - \langle x \cdot x' \rangle^2}$. Fig. 2 illustrates a few phase space distributions measured at FLASH with almost the same rms emittances. The question remains whether all these distributions are really equivalent in terms of FEL performance, or whether more appropriate figures of merit should be developed.

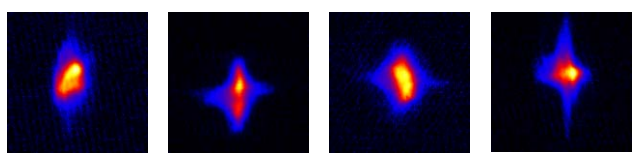

Figure 2: Various phase space distributions measure at FLASH. Are they all equivalent in terms of FEL performance?

SHORT BUNCH ISSUES

From FEL point of view

As mentioned before, in terms of emittance preservation a high peak current in the kA range is only tolerable at ultrarelativistic beam energies. As a consequence, the kA peak current is generated by magnetic bunch compression at some 200 MeV beam energy. In practice it is an unavoidable consequence that this leads to a very short bunch length in the 0.1 mm range. Very strong coherent fields are generated which have a large and detrimental effect on the beam dynamics. As an example, Figure 3 illustrates the longitudinal phase space distribution 1 m after the exit of the first bunch compressor of FLASH as predicted by numerical simulation. It is seen that the phase space distribution is distorted at the head of the bunch due to combined interaction of the electrons with space charge Coulomb forces and coherent synchrotron radiation (csr) generated in the bending magnets of the chicane. For details on beam dynamics simulation in presence of csr, see Ref. [10].

This interaction becomes even more pronounced during final compression. Figure 4 shows the calculated longitudinal phase space distribution in front of the undulator. csr effects are very pronounced in the head of the bunch, which is the only part of the bunch achieving high enough peak current as to expect FEL gain saturation.

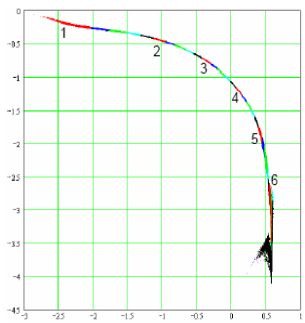

Figure 3: Longitudinal momentum distribution 1 m after the first bunch compressor of FLASH. The head of the bunch is to the right.

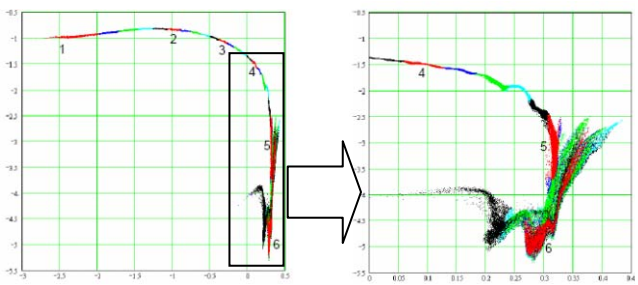

Figure 4: Longitudinal momentum distribution in front of the undulator. The plot on the r.h.s. shows the head of the bunch zoomed.

Csr effects do not only distort the momentum distribution but also the transverse phase space. As a consequence, not all the particles within the head of the bunch have an emittance sufficiently small for lasing. Figure 5 indicates the current distribution resulting from Figure 4 (colours representing the respective particles in Figure 4). The black curve indicates *that* fraction of the particles located within an emittance smaller than the tolerable one ($\varepsilon^{n}_{x,y} \leq 3 \cdot 10^{-6}\,\pi\mathrm{m}$). This part of the bunch achieves a peak current of 1400 A and is only approx. 60 fs (FWHM) long. According to FEL simulation [11], such a beam would generate a radiation pulse approx. 30 fs (FWHM) in length, which agrees nicely with the pulse length measured at FLASH.

Various techniques have been established at DESY to determine the longitudinal bunch current profile experimentally. One of the most powerful ones makes use of a transverse deflecting mode cavity resonator ("LOLA")[12,13]. LOLA's capability of resolving very detailed longitudinal features of the bunch is illustrated in Figure 6.

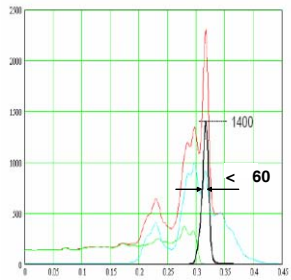

Figure 5: Predicted current distribution in front of the undulator according to beam dynamics calculations.

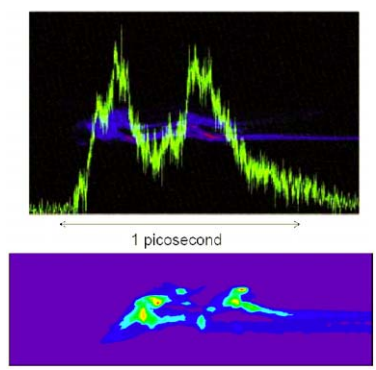

Figure 6: Longitudinal charge distribution within a single electron bunch of FLASH at DESY. Upper part: Image of the bunch on an observation screen, located downstream of the transverse mode cavity LOLA streaking the bunch transversely by a time dependent electro-magnetic field. The horizontal direction corresponds to the time. Only the part containing the spike at the head of the bunch is shown. The (green) solid curve shows the charge density profile projected onto the longitudinal position, i.e. the current profile. In this particular setting of bunch compression parameters, the spike is actually split into two parts approx. 300 fs apart, each part being shorter than 120 fs /(FWHM). The lower part of the figure shows the prediction of numerical beam dynamics simulation.

Due to the pronounced beam dynamics effects in the vicinity of the high peak current spike, not only the distribution of electron not only in the longitudinal, but also the transverse phase space can be heavily distorted. The transverse phase space distribution thus varies considerably along the internal bunch coordinate at FLASH, see Figs. 7,8 [14] illustrating that a capability of measuring properties of bunch slices is essential at an X-ray FEL.

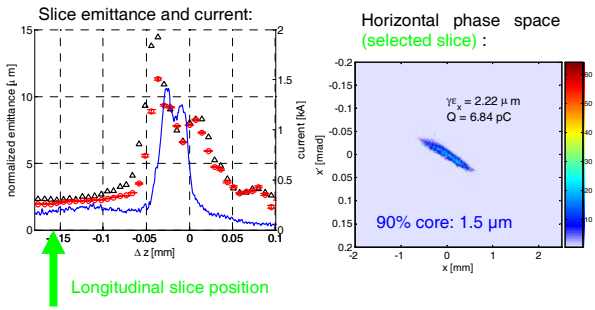

Figure 7: Horizontal phase space distribution of those electrons in the bunch located at the longitudinal position indicated by the green arrow, measured with LOLA at FLASH. Since this a position with relatively small current (blue solid line), the emittance is undistorted.

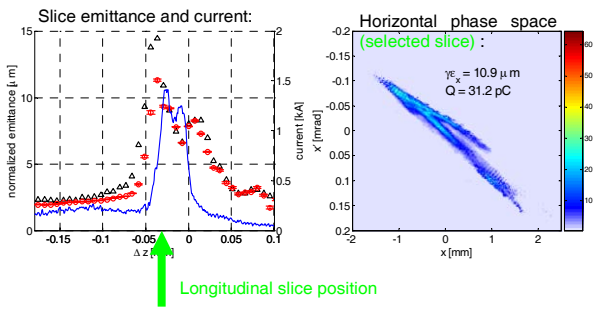

Figure 8: Same conditions as Fig. 7, but now a slice is sampled where the bunch current is high. The distribution of particles within this slice is heavily distorted.

In principle, we should know the bunch properties at a longitudinal resolution smaller than the cooperation length, i.e. for X-ray FELs in the sub-fs range. This is presently not accessible with time-domain beam diagnostics techniques. As an alternative, the coherent part of the infrared (IR) spectrum $dU/d\lambda$ radiated by the electron bunch when traversing magnetic fields or discontinuities like metallic foils contains information about the longitudinal structure function $F(\lambda)$ [15]:

$$\frac{dU}{d\lambda} = \left(\frac{dU}{d\lambda}\right)_1 \left(N + N(N-1)\left|F(\lambda)\right|^2\right) \qquad (3)$$

Here, $(dU/d\lambda)_1$ is the spectral density of a single electron, and N is the total number of electrons radiating. Such measurements should cover the spectral range down to 1 μm wavelength, and they should be, preferably, single shot measurements since some effects taking place at the micrometer-scale are likely to fluctuate considerable from bunch to bunch. As an example, Fig. 9 shows the single bunch spectrum at FLASH taken under SASE conditions. While a unique reconstruction of the longitudinal charge profile is hardly possible due to the loss of phase information, it is easy to identify evidence for substructure inside the bunch occurring at length scales well below the size of the lasing spike.

The coherent IR signal seems to be a good candidate for providing input signal for a SASE feedback loop. In principle, one might think that the maximum total IR power should be correlated with optimum compression and thus maximum SASE. It is, however, not so simple as seen from Fig. 10 [16]. While there is indeed a clear correlation between SASE and IR power within some range, maximum IR power is observed with only little SASE left, most like due to over-compression.

Achieving ultrashort bunches in a reliable way requires not only precise understanding of beam dynamics and lots of advanced diagnostics. In the first place, high stability of rf phase regulation in the 0.1° is needed which is very challenging ti achieve, see. Fig. 11.

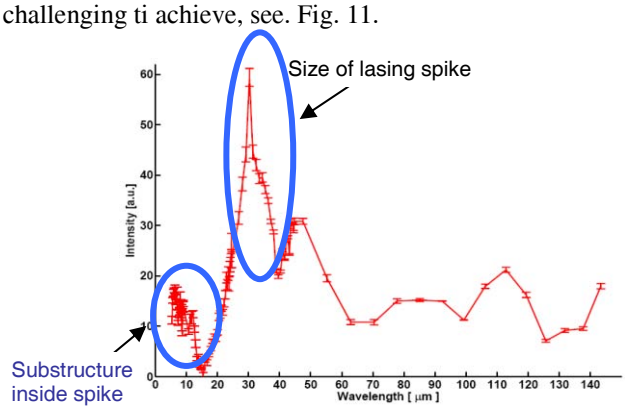

Figure 9: Single shot infrared spectrum taken at FLASH.

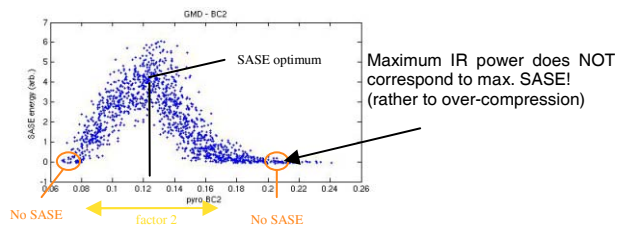

Figure 10: SASE power (vertical axis) versus total IR power measured at FLASH with a pyro detector [16].

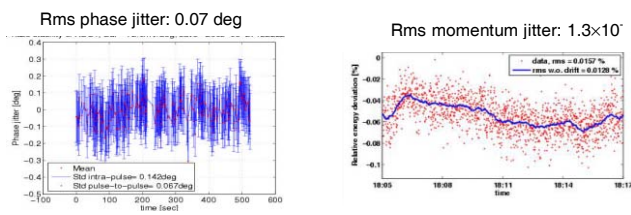

Figure 11: RF phase jitter and rms momentum jitter after first bunch compression at FLASH.

From FEL User point of view

What has been said so far results from requirements of the SASE process – almost independent of user needs. For many users, it is the capability of generating ultra-short, powerful X-ray pulses what makes FELs so attractive. They are thus interested in pulses as short as possible. The lower limit is obviously determined by the cooperation length l_c. At FLASH, with $l_c \approx 1.3\ \mu$m at 13 nm, this limit has been almost achieved with a pulse length $l_{pulse} \approx 3\ \mu$m, i.e. the radiation puls length is almost Fourier limited. At Angstrom FELs, l_c will be as short as $0.03\ \mu$m. This opens up the possibility to generate attosecond pulses [17,18], and calls for electron bunch diagnostics at sub-femtosecond resolution, both big challenges not yet met.

Synchronization Issues

The radiation pulses length being in the 20 fs range, it is important for users to have the pulses arriving at a time jitter well below 100 fs with respect to a reference clock that can be used for a pump-probe set-up. The underlying problem is that a state-of-the-art rf microwave oscillator represents an excellent master clock, but it is impossible to distribute rf signals by rf cables over long distances at fs stability. Techniques are under development to overcome this limitation [19-21], involving electro-optical detection of bunch arrival time, a stabilized optical fibre transmission line and an optical-only master clock system. Presently, a bunch–to-bunch time arrival stability of 200 fs rms has been verified [19, see Fig. 11. It is worth noting that the bunch arrival time is measured at ~10 fs resolution. With the help of an all-optical synchronization system it should become possible to stabilize many accelerator subsystems and lasers with respect to each other at <50 fs precision, even over distances some 1 km apart.

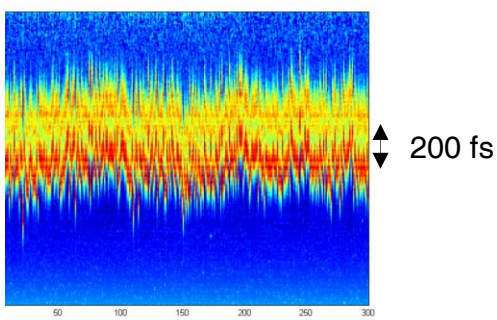

Figure 11: Fluctuation of bunch arrival time of 300 consecutive, compressed bunches at FLASH, measured by electro-optic modulation [19].

CONCLUSION

Impressive progress in accelerator technology made over the past 10-20 year was the backbone of the successful implementation of FELs in the VUV-and soft X-ray regime. Still it is not yet possible to measure the electron beam properties at the undulator entrance at such precision and resolution that the FEL radiation could be inferred from this information at sufficient precision. In particular in view of X-ray FELs being under way, there is thus good reason to support even more refined beam dynamics investigations as well as precise beam diagnostics with micrometer and femtosecond resolution.

ACKNOWLEDGEMENT

The author. wishes to thank the entire FLASH team and numerous colleagues from the TESLA collaboration for their dedication, enthusiasm and hard work which was the basis for the success of FLASH. He also profited a lot from the supportive and friendly spirit within the worldwide FEL community. In particular, he wants to thank his colleagues E.L. Saldin, E.A. Schneidmiller, and M.V. Yurkov for numerous and always inspiring discussions.

REFERENCES

[1] R. Bonifacio, C. Pellegrini, L.M. Narducci, Opt. Commun. **50**, 373 (1984).
[2] V. Balandin, N. Golubeva,
[3] M. Ferrario, Proc. 2006 EPAC Conf. (2006)
[4] J.Fraser, R. Sheffield, Nucl. Instr. Meth. **A250**, 71 (1986).
[5] F. Stephan, et al, this conference
[6] D. Dowell, et al., this conference
[7] T. Shintake, this conference
[8] A. Oppelt, this conference
[9] W P Leemans et al., Nature Physics 2, 699 (2006)
[10] M. Dohlus, Proc. 2006 EPAC Conf. (2006)
[11] E.L. Saldin et al., DESY Print TESLA-FEL 2004-06 (2004)
[12] P. Krejcik, et al., Proc. 2003 Part. Acc. Conf, 423 (2003)
[13] R. Akre et al., Proc. 2002 EPAC Conf. (2002)
[14] M. Roehrs, Proc. 2006 Part. Acc. Conf. (2006)
[15] O. Grimm, Proc. 2006 Part. Acc. Conf. (2006)
[16] H. Delsim-Hashemi, unpublished data (2007)
[17] E.L. Saldin, et al., Opt. Commun. **212**, 377 (2002)
[18] A.A. Zholents, W.M Fawley, PRL **92**, 22, 224801 (2004)
[19] B. Steffen, et al., this conference, WEBAU04
[20] A. Winter, et al., Proc. 2006 Part. Acc. Conf. (2006)
[21] F. Löhl, Proc. 2006 Part. Acc. Conf. (2006)
[22] H. Schlarb, this conference, TUBAU01

VOLC: VOLUME FREE ELECTRON LASER SIMULATION CODE

S. Sytova*, Research Institute for Nuclear Problems, Belarusian State University

Abstract

First lasing of Volume Free Electron Laser (VFEL) in mm wavelength range was obtained recently [1]. Multi-wave volume distributed feedback (VDFB) where electromagnetic waves and electron beam spread angularly one to other in a spatially-periodic structure (resonator) is the VFEL distinctive feature [2]. Mathematical model and numerical methods for VFEL nonlinear stage simulation were proposed [3] and implemented in computer code VOLC that allows to simulate different geometries of two- and three-wave VFEL in amplifier and oscillator regimes. Electron beam is modelled by averaging over initial phases of electrons. VOLC dimensionality is 2D (one spatial coordinate and one phase space coordinate) plus time. A description of VOLC possibilities and representative numerical results are presented.

INTRODUCTION

Principles and theoretical foundations of VFEL operation based on VDFB [4] put the beginning of experimental developing of new type of electronic generators. Creation of VFEL solves the problem of current threshold reduction, frequency tuning in a wide range, miniaturization of resonators. All these problems present some difficulties for widely used schemes of free electron lasers (FEL), backward wave tubes (BWT), travelling wave tube (TWT) and other electronic devices. As a rule, these high efficient devices have optimally specified parameters (electron beam, waveguides, resonators and undulators periods etc.). Changing of one of these parameters to tune frequency leads to abrupt reduction of efficiency of the system. VFEL design features allow to move and rotate diffracting gratings, change the distance between gratings and the gap between gratings and electron beam as well as orientation of grating grooves with respect to electron beam velocity. These aspects provide possibility to tune conditions of diffraction. VFEL threshold current for an electron beam passing through a spatially-periodic structure in degeneration points decreases essentially in comparison with single-wave systems [4]. This is valid for all wavelength ranges regardless the spontaneous radiation mechanism and as a consequence this means the possibility to reduce significantly system sizes.

In VFEL operation the linear stage investigated analytically [5]-[7] quickly changes into the nonlinear one where the most part of the electron beam kinetic energy is transformed into electromagnetic radiation. Nonlinear regime of VFEL operation can be investigated only using methods of mathematical modelling. Experiments on VFEL go on [8]–[9] and need optimal geometry determination and result processing.

MATHEMATICAL FORMULATION OF VFEL PHYSICAL MODEL

The scheme of VFEL resonator of the experimental installation [1] formed by two diffraction gratings with different periods and two smooth side walls the same as the scheme of the volume resonator (so-called "grid" volume resonator) built from the metallic threads inside a rectangular waveguide of the installation [8]–[9] can be considered as the following scheme of VFEL. Here an electron beam with electron velocity u passes through a spatially periodic structure. Under diffraction conditions some strong coupled waves can be excited in the system. If simultaneously electrons of the beam are under synchronism condition, they emit electromagnetic radiation in directions depending on diffraction conditions in oscillator regime. In [10]–[12] different two-wave and three-wave schemes of VFEL were considered in amplifier and oscillator regimes. System of equations for all cases of VFEL is obtained from Maxwell equations in the slowly-varying envelope approximation. For two-wave VFEL it has the following form:

$$\frac{\partial E}{\partial t}+\gamma_0 c\frac{\partial E}{\partial z}+0.5i\omega lE-0.5i\omega\chi_\tau E_\tau=$$

$$=2\pi j\Phi\int_0^{2\pi}\frac{2\pi-p}{8\pi^2}(\exp(-i\Theta(t,z,p)+$$

$$+\exp(-i\Theta(t,z,-p)))dp,$$

$$\frac{\partial E_\tau}{\partial t}+\gamma_1 c\frac{\partial E_\tau}{\partial z}+0.5i\omega\chi_{-\tau}E-0.5i\omega l_1E_\tau=0. \quad (1)$$

Here $E(t,z)$ and $E_\tau(t,z)$ are amplitudes of transmitted and diffracted waves with wave vectors $\mathbf{k}$ and $\mathbf{k}_\tau$ respectively. $l_0=\left(k^2c^2-\omega^2\varepsilon_0\right)/\omega^2$ and $l_1=\left(k_\tau^2c^2-\omega^2\varepsilon_0\right)/\omega^2$ are system parameters. $l=l_0+\delta$. δ is a detuning from synchronism condition. γ_0, γ_1 are VDFB cosines. $\beta=\gamma_0/\gamma_1$ is an asymmetry factor. $\Phi=\sqrt{l_0+\chi_0-1/(u/c\gamma)^2}$. γ is the Lorenz factor. χ_0, $\chi_{\pm\tau}$ are Fourier components of the dielectric susceptibility of the target.

System (1) must be supplemented with proper initial and boundary conditions which can contain conditions for external reflectors. Equations for the phase dynamics of elec-

* sytova@inp.minsk.by

tron beam are written with respect to electron phase:

$$\frac{d^2\Theta(t,z,p)}{dz^2} = \frac{e\Phi}{m\gamma^3\omega^2}\left(k_z - \frac{d\Theta(t,z,p)}{dz}\right)^3 \cdot$$
$$\cdot \mathrm{Re}\left(E\exp(i\Theta(t,z,p))\right), \qquad (2)$$
$$\frac{d\Theta(t,0,p)}{dz} = k_z - \omega/u, \quad \Theta(t,0,p) = p.$$

It was proposed in (2) that the electron beam is synchronous with the transmitted wave E only. The integral form of beam current in the right-hand side of the first equation of (1) is obtained by averaging over the following initial phases of electrons in the beam: entrance time of electron in interaction zone and transverse coordinate of its entrance point. Method of averaging over initial phases of electrons is well-known and widely used in simulation of BWT, TWB, FEL etc. Equations (1)-(2) are more complicated than usually used (see e.g. [14]). System (1)-(2) takes into account two-dimensional distributions with respect to spatial coordinate and electron phase p. So, these equations allow to simulate electron beam dynamics more precisely. This is very important when electron beam moves angularly to electromagnetic waves.

NUMERICAL METHODS AND DESCRIPTION OF VOLC POSSIBILITIES

At present time there are a wide number of different computer codes for FEL simulation. A comparison of existing FEL codes on dimensionality, time-dependent simulation, models of particle beam [15] shows that beam description by collective variables allows the faster calculation in time than by method of the Particle-in-Cell. We used the beam description by collective variables in VFEL simulation too.

Numerical algorithms proposed for solving (1)-(2) allow to use parallel processing and can be started up on standard symmetric multi-processor (SMP) computing systems with some parallel processors based on common memory. The big volume of processor work takes the computation of grid values of Θ in (2). In algorithm proposed their calculation is not locked-in with respect to spatial coordinate z, so it can be executed parallel. Finite difference system in the algorithm has the form AE = F. Matrix A is inverted once before the main computation and then it is multiplied to the vector of right-hand sides F recalculated in each point in time.

Numerical methods for all possible two-wave and three-wave geometries including external reflectors are implemented in computer code VOLC, version 1.0 [10], [11]. VOLC means "VOLume Code". It was developed on the basis of multiple Fortran codes, created in 1991—2005 years. Dimensionality is 2D (one spatial coordinate and one phase space coordinate) plus time. Theree-wave geometries were considered to confirm all main VFEL physical laws and mechanisms.

New version 2.0 of VOLC allows for two-wave VFEL geometries to obtain distributions of VFEL intensities with respect to current density j, resonator length L, diffraction asymmetry factor β, system parameters l_0 or l_1, detuning from Cherenkov condition δ, as well as dynamical regimes recognition and intensity Fourier transforms. Reduction of VOLC possibilities to two-wave case is connected with geometry of experimental installation [8] for which VOLC simulation was designed. Interface of VOLC, version 2.0 is presented in Fig.1. Its block-scheme is depicted in Fig.2.

Interface of VOLC is a standalone program written in Borland C++ Builder 6.0 for use in the Windows Operating environment. Interface allows to define input parameters, check their validity with corresponding messages, call the main routine for VFEL simulation and output some results in the window including 2D plots and summary table of results. The main routine for VFEL simulation was elaborated in Compaq Visual Fortran and can operate without VOLC interface. In this case only the file with input parameters should be filled. Numerical results are written in specified files.

VOLC interface uses the standard MS Windows dialog and are supplied by screen tips. All wrong user actions are stopped with corresponding messages. Computation of distributions of intensities with respect to some parameters can take much of computer time, so at any moment user can stop computation without losses of calculated data.

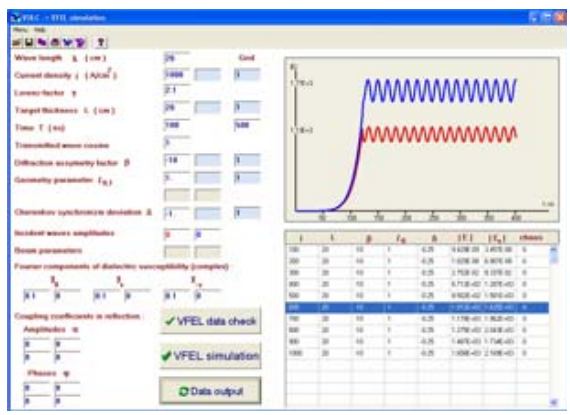

Figure 1: Interface of computer code VOLC

VOLC was tested with carping. Numerical results obtained were reported in [3], [10]–[13]. There were investigated different regimes such as oscillator and amplifier regimes, SASE (Self-Amplified Spontaneous Emission), VFEL as BWT, TWT, BWT-TWT and others. All results correspond to physical theory predictions. Some results of numerical experiments are presented below.

NUMERICAL RESULTS

One of the main VFEL physical laws [4] is the following dependence of threshold current in degeneration points: $j_{th} \sim 1/((kL)^3(k\chi_\tau L)^{2s})$, where s is a number of surplus

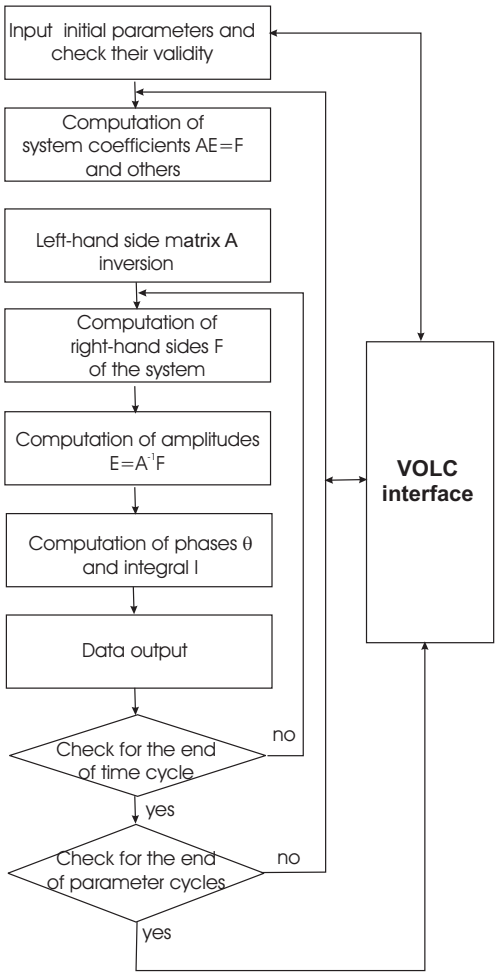

Figure 2: Block-scheme of VOLC

waves in diffraction. So, threshold current can be significantly decreased when modes are degenerated in multi-wave diffraction geometry if $k|\chi_\tau|L \gg 1$. On the other hand interaction length L can be reduced at given current value j. This was confirmed in numerical experiments and demonstrated in [11].

In [13] theoretically derived dependence of the threshold current on asymmetry factor of VDFB was presented. This relation confirms that VDFB allows to control the threshold beam current. Numerical results presented in [11] are in close agreement with the theory. Example of successful simulation with help of code VOLC of VFEL experiment with "grid" volume resonator was proposed in [9].

In electronic devices such as FEL, TWT, BWT etc. self-oscillations are due to interaction of electron beam and electromagnetic field under distributed feedback. Investigation of chaos in such devices is of great interest in modern physics [14], [16]–[18]. In VFEL simulation we faced with chaotic behaviour of electromagnetic field intensities too. Here chaotic dynamics is induced by complicated interaction of electron beam bunches with electromagnetic field under VDFB. Investigation of chaos in VFEL is important in the light of its experimental development.

Two points of beam current threshold exist in VFEL theory. First threshold point corresponds to beginning of electron beam instability. Here regenerative amplification starts while the radiation gain of generating mode is less than radiation losses of the coupled feedback mode. Parameters at which radiation gain becomes equal to absorption correspond to the second threshold point. When electron current exceeds the second threshold value, generation progresses actively. In simulations carried out an important VFEL feature due to VDFB was shown. This is the initiation of quasiperiodic regimes at relatively small current near first and second threshold points that are bifurcation points. This is depicted via intensity plots in Fig.3 with corresponding intensity Fourier transforms in Fig.4. Curve 1 depicts regime under regenerative amplification. Current j is less than the value of the first threshold point. Value j for curve 2 is a little larger than this threshold. Lines 3 and 4 depict 1T periodic regimes that pass to quasiperiodic ones (lines 5-7).

Numerical investigations of chaotic lasing in VFEL show the possibility of complicated transitions between following chaotic regimes: stationary generation, self-modulation and periodicity, quasiperiodicity, intermittency, chaotic self-modulation or "weak" chaos and chaotic self-oscillations or "developed" chaos. Two-parameter analysis of VFEL chaotic lasing was carried out with respect to beam current density j and (1) diffraction asymmetry factor β, (2) detuning from synchronism condition δ, (3) length of the resonator L. One of possible roots to chaos in VFEL is presented in Fig.5 and Fig.6. Windows of periodicity and quasi-periodicity exist between chaos. Larger number of principle frequencies for transmitted wave can be explained by the fact that simultaneous generation at several frequencies is possible in VFEL. In the case considered electrons emit radiation namely in the direction of transmitted wave.

As we have more than ten control parameters (see explanations for (1)-(2)) it seams to be very difficult to investigate the full picture of possible chaotic behavior in VFEL. The aim of this investigation is to show the possibility to choose more precisely domains with periodic self-modulation instead of chaotic one.

CONCLUSION

The original software for VFEL simulation is released and allows to obtain all main VFEL physical laws and dependencies. VOLC overriding goal is to investigate the nonlinear stage of its operation. In simulation VFEL was considered as a dynamical system. Two-parameter analysis shows the complicated root to chaos. Author is grateful to Prof. V.Baryshevsky for permanent attention to her work.

REFERENCES

[1] V.Baryshevsky, K.Batrakov et al., Nucl. Instr. Meth. 483A (2002) 21.

[2] V.Baryshevsky, Nucl. Instr. Meth. 445A (2000) 281.

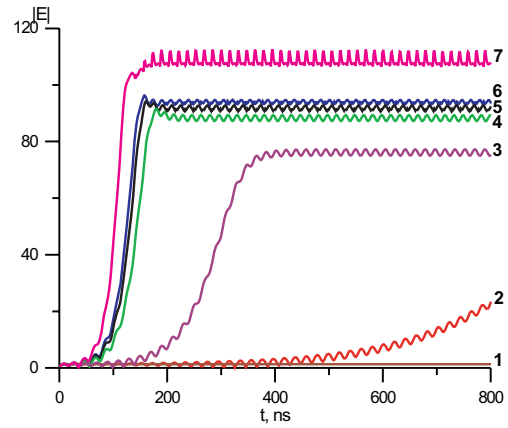

Figure 3: Transition from periodicity to quasiperiodicity for transmitted wave in amplification regime. j is equal to: 1) 350 A/cm^2, 2) 450 A/cm^2, 3) 470 A/cm^2, 4) 515 A/cm^2, 5) 525 A/cm^2, 6) 528 A/cm^2, 7) 550 A/cm^2.

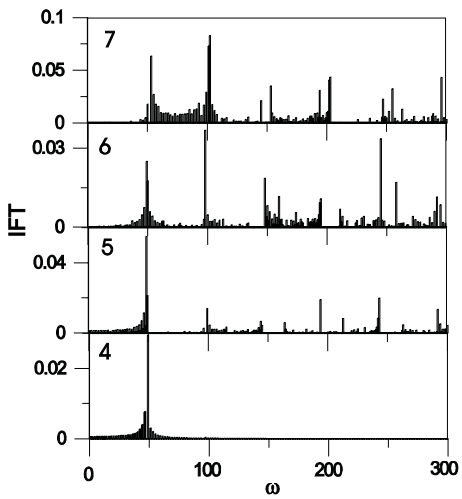

Figure 4: Intensity Fourier transform for curves 4-7 from Fig.3

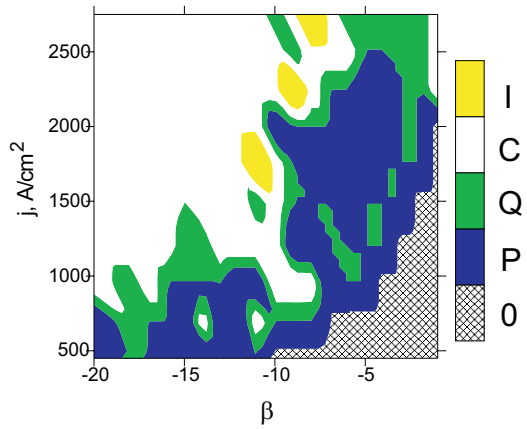

Figure 5: Dependence of the threshold current on asymmetry factor of VDFB for transmitted wave. 0 depicts a domain under beam current threshold. P, Q, C, I correspond to periodic regimes, quasiperiodicity, chaos and intermittency, respectively.

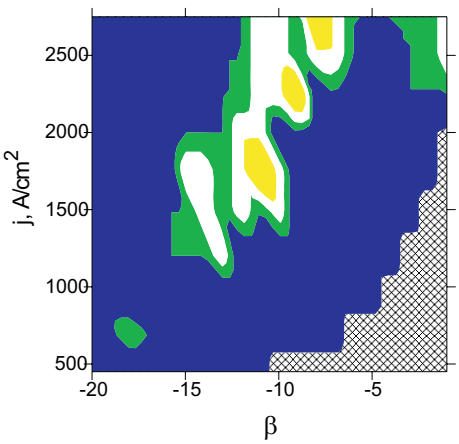

Figure 6: Dependence of the threshold current on asymmetry factor of VDFB for diffracted wave.

[3] K.Batrakov and S.Sytova, Computational Mathematics and Mathematical Physics, 45 (2005) 666.

[4] V.Baryshevsky and I.Feranchuk, Phys. Lett. 102A (1984) 141.

[5] V.Baryshevsky, K.Batrakov, I.Dubovskaya, J. Phys. D. 24 (1991) 1250.

[6] V.Baryshevsky, K.Batrakov, I.Dubovskaya, Phys. Stat. Sol. B169 (1992) 235.

[7] V.Baryshevsky, K.Batrakov, I.Dubovskaya, Nucl. Instr. Meth. 358A (1995) 493.

[8] V.Baryshevsky, K.Batrakov et al., Nucl. Instr. Meth. B252 (2006) 86

[9] V.Baryshevsky et al., "Experimental study of a Volume Free Electron Laser with a "grid" resonator", FEL2006, August 2006, Berlin, p.3311, http://www.JACoW.org

[10] K.Batrakov and S.Sytova, Mathematical modelling and analysis, 11 (2006) 13; 10 (2005) 1.

[11] K.Batrakov and S.Sytova, "Numerical simulation of nonlinear effects in Volume Free Electron Laser (VFEL)", RUPAC2006, September 2006, Novosibirsk, p.141, http://www.JACoW.org

[12] K.Batrakov and S.Sytova, Nonlinear Phenomena in Complex Systems, 8 (2005) 359; 8 (2005) 42.

[13] K. Batrakov K. and S. Sytova, "Generation regimes of FEL with volume distributed feedback", FEL2006, August 2006, Berlin, p.41, http://www.JACoW.org

[14] N.S.Ginzburg, R.M.Rosental, A.S.Sergeev, Tech. Phys. Lett., 29 (2003) 71

[15] S. Reiche, "Computation of FEL processes", PAC2003, May 2003, Portland, Oregon, p.203, http://www.JACoW.org

[16] M.E.Couprie, Nucl. Instr. Meth. A507 (2003) 1

[17] R.Bachelard et al., "Control of the intensity of a wave interacting with charged particles", FEL2006, August 2006, Berlin, p.83, http://www.JACoW.org

[18] M.S.Hur, H.J. Lee, J.K.Lee., Phys. Rev. E58 (1998) 936

MEASUREMENT AND ANALYSIS OF CSR EFFECTS AT FLASH

Bolko Beutner, Winfried Decking, Torsten Limberg, and Michael Röhrs
DESY, Hamburg, Germany

Abstract

The vacuum-ultra-violet free electron laser in Hamburg (FLASH) is a linac driven FEL. High peak currents are produced using magnetic bunch compression chicanes. Such peak currents are required for the SASE process in the undulators. In these magnetic chicanes, the energy distribution along an electron bunch is changed by effects of Coherent Synchrotron Radiation (CSR). Energy changes in dispersive bunch compressor chicanes lead to transverse displacements. These CSR induced displacements are measured using a transverse deflecting RF-structure. Recent experiments and simulations concerning the charge dependence of such transverse displacements are presented and analysed.

INTRODUCTION

Electron bunches in magnetic bunch compressor chicanes are subject to CSR self-forces. CSR induced energy changes along the bunch give rise to different trajectories for different longitudinal slices. Measurements of such effects were done at FLASH in 2006 [1][6]. We present results of CSR induced centroid shift measurements, in the first chicane, as a function of bunch charge.

For an undisturbed measurement of CSR effects, space charge fields are reduced by over-compressing the bunch. The longitudinal energy correlation (chirp) introduced in the accelerating module upstream of the first bunch compressor chicane is chosen to reach minimum bunch length and a peak current of about 1.2 kA toward the end of the second magnet in the chicane. Due to over-compression, the bunch will exit the chicane with a length comparable to its incoming length of about 2 mm RMS, corresponding to about 50 A peak current (see Fig. 1). The integrated effect of space-charge from the exit of the chicane to the observation point ≈ 60 m downstream is then small compared to the CSR effects.

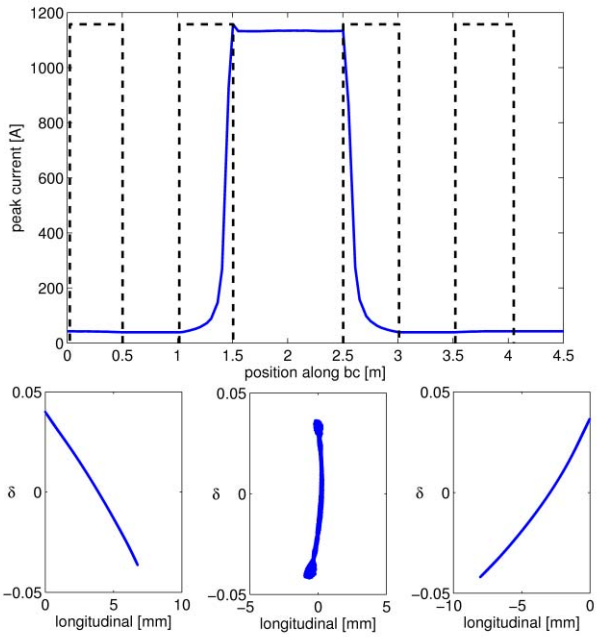

Figure 1: Top: Beam current along the bunch compressor chicane in over-compression mode. Dipoles are indicated as dashed boxes. Bottom: longitudinal phase space at the entrance, the middle, and the end of the bunch compressor.

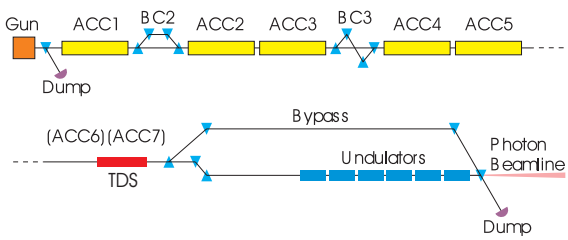

Figure 2: Sketch of FLASH. The blue triangles indicate dipole magnets, the yellow boxes symbolise TESLA accelerator modules.

MEASUREMENTS

A layout of FLASH is given in Fig. 2. We vary the phase offset of acceleration module ACC1 and keep the beam on crest in the modules ACC2/3 and ACC4/5. The expected CSR effects are created in BC2. Downstream, the transverse deflecting RF-structure (TDS) is used to analyse the longitudinal-horizontal beam profile. The experimental setup is as in [1][6].

Starting from a stable SASE working point, we achieved good transmission of the beam in the over-compression range ($\varphi_{ACC1} = 23^\circ - 26^\circ$), while keeping the beam energy constant by adjusting the RF-amplitude.

To optimise the resolution of the measurements, a special beam optics between BC2, the transverse deflecting cavity and the screen is used.

To ensure a proper optics set-up, the emittance and Twiss parameters of the beam were measured in the diagnostic section downstream the first bunch compressor [7]. The measured Twiss parameters are used to determine correc-

tions to the five quadrupoles upstream of this diagnostic section, after BC2, to achieve a matched beam optics in the diagnostic section FODO lattice.

Due to space charge effects in the injector, the beam optics depends on the bunch charge. To ensure a good transmission up to the transverse deflecting cavity, the matching in the DBC2 section was redone for every bunch charge.

IMAGE ANALYSIS

The measured longitudinal-horizontal beam profiles are analysed to obtain information about the general beam dynamics and CSR effects in BC2. We observe a horizontal deformation of the beam profile (see Fig. 3).

In the first step of the analysis, we determine the maximal horizontal displacement of the centroid curve along the bunch and use it as a measure for the strength of the CSR interactions. This maximal centroid displacement is related to the maximal energy loss per longitudinal bunch slice due to CSR in BC2.

Each picture is divided into slices along the longitudinal axis. Only the central part of the picture is analysed. The head and tail sections are omitted because of the noise in these low charge regions.

The horizontal charge profiles of these slices are calculated. Within these horizontal charge profiles the centre position has to be determined. The maximum or the centre of mass can be used for such a definition. The centre of mass within such a slice is strongly influenced by noise in the empty regions of the picture, drawing this value to the geometrical centre of the slice. The maximum of a profile does not underestimate the centroid shifts but is unstable due to noise in the charge profiles. A Gaussian fit to the charge profile is also not completely appropriate to our situation. The horizontal charge profiles are not Gaussian but asymmetric in the regions of the picture with strong centroid shifts which lead to an underestimation of the centre.

A double Gaussian

$$f(x) = a_1 e^{-\left(\frac{x-a_2}{2a_3}\right)^2} + a_4 + a_5 e^{-\left(\frac{x-a_6}{2a_7}\right)^2} \qquad (1)$$

is used to fit the data. As initial values for the fit of a_2 and a_6 we use the maximum and the mean of the transverse charge profile. a_2 is then a good choice for the centre position. It is close to the maximum but more stable than the position of the maximum value.

The centre position of each slice together with the mean of its longitudinal position defines the centroid curve. The centroid curves corresponding to different fit methods are shown in Fig. 3.

In general, the bunch does not line up exactly parallel to the screen axis (see next section). The linear correlation of the different centroid curves, as indicated by the green line in Fig. 3, is subtracted.

After subtraction of the tilt the horizontal peak to peak shifts of the centroid curves are calculated. A summary of these data is shown in Fig. 4.

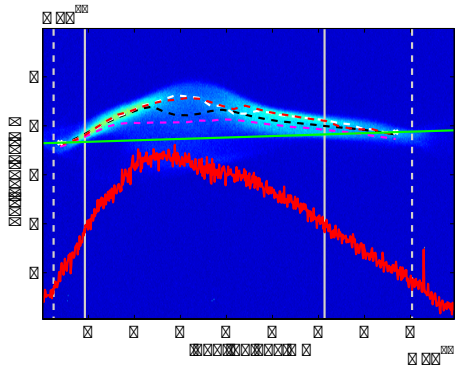

Figure 3: An example of a TDS measurement with bunch charge $q = 0.65$ nC. Longitudinal charge profile (red line), FWHM lines (white solid) and the lines corresponding to "full width of 1/6 maximum" (white dashed) are shown, indicating the omitted head and tail parts of the bunch. Different centroid curves (black - Gaussian fit; white - maximum value; magenta - mean value; red - double Gaussian fit) are plotted as dashed lines. The green line represent an overall linear slope determined from the edge points of the centroid curves. Bunch head is to the left.

SIMULATIONS

Tracking calculations were done to simulate longitudinal-horizontal beam projections at the TDS. Photo emission and beam transport through ACC1 was calculated with the space charge tracking code ASTRA [2]. After ACC1, wake fields are applied as a discrete effective kick [4]. The tracking code CSRTrack [3] is used to simulate CSR effects in BC2. Downstream of ACC1 linear transport theory is used. The actual currents of the quadrupoles were used to calculate the transport matrices. Transverse and longitudinal wake fields are added as perturbations [4]. From the resulting particle distributions at the TDS beam images are obtained by representing each particle with a 2D Gaussian.

The simulated images are analysed with the same methods as the measured ones. In Fig. 4 simulated maximal centroid shifts vs. bunch charge for different threshold intensities are compared with measured data.

To simulate the minimum intensity observable with the camera system, a lower threshold of charge density is used in the image calculation. An image intensity threshold is chosen as a charge density $\rho(T)$ for a given charge T. The intensity of each pixel is reduced by $\rho(T) = T/(\text{total number of pixels})$, while negative values are set to zero.

Considering the space charge effects on bunch length and uncorrelated energy spread, one can predict the behaviour of peak current, and thus the centroid shift, with increasing charge. The peak current is not increasing linearly with charge, it saturates beyond 1 nC and for higher total bunch charges, the peak current is decreasing.

Two effects play a role here. First the bunch length

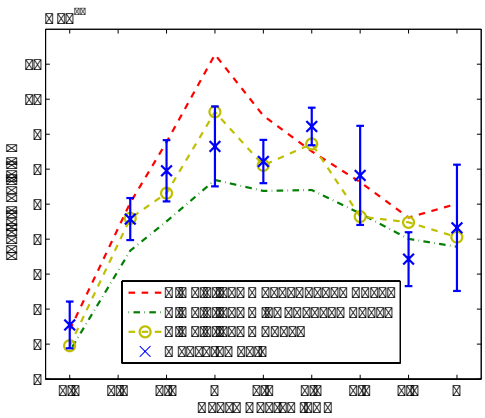

Figure 4: CSR induced centroid shifts as a function of bunch charge. The measured centroid shift is plotted and compared with the simulated obtained from the image analysis for three different image intensity cutoffs.

increases with higher bunch charge due to space charge forces in the RF-Gun, which reduces the charge density and thus the peak current. Second, the space charge interaction in the injector increases the uncorrelated slice energy spread towards higher bunch charges. Due to this increase of the energy spread the width of the charge spike after the chicane is increased. As a result the peak current is reduced even further. While the maximum centroid shift is an important property to identify the strength of the CSR effects, it is not sufficient for the analysis of the beam dynamics. Hence, in a second step of this analysis, the whole centroid curves are compared with simulated data.

The comparison of the measured and simulated centroid curves is summarised in Fig. 5. The measured curves are determined using the Gaussian method described earlier. Error bars are calculated as the standard deviation using the set of 20 pictures taken at each machine setting and a systematic error of the image analysis algorithm.

Different self-field effects act on the beam and cause additional distortions downstream of BC2. A model of transverse wake fields in the acceleration modules ACC2 and ACC3 is included to simulate the observed beam tilt. Together with the spurious dispersion [5] this has an important impact on the centroid curve tilt.

Cavity misalignment and cavity tilts inside an acceleration module yield similar transverse wake fields as a beam offset. On the other hand, the effect of the transverse wake fields and of horizontal dispersion is similar. Images from the TDS can not distinguish between transverse deformations caused by transverse wakes induced by an orbit offset and horizontal dispersion.

Vertical dispersion leads to changes in the longitudinal profile observed at the screen after the TDS because the TDS streaks the longitudinal beam axis in vertical direction. Therefore, one can not distinguish between vertical dispersion at the TDS and errors in the longitudinal dispersion of the transport matrices or phase errors in ACC2-ACC5.

In this sense, the vertical dispersion and the horizontal beam position offset assumed in these simulations are effective parameters, which can not be directly be identified with the real properties of the beam orbit during the measurements.

Other studies on orbit errors and spurious dispersion give a reasonable upper limit estimate of these effects. Orbit errors up to 10 mm and spurious dispersion up to 200 mm have been measured in 2006 [5]. With assumptions of this order the simulated centroid curves can be matched to the measured ones (Fig. 5).

SUMMARY AND OUTLOOK

We did extensive studies on the beam dynamics of FLASH using both numerical simulations and experiments. In normal SASE operation the overall effects on the beam are complicated due to a commingling of different self-field effects, like space charge, CSR, and wake fields. Studies on CSR effects are done in an special over-compression mode. In this compression scheme CSR interactions are the dominant self-field effect.

A quantitative comparison of CSR simulations and measurements was done with a dedicated experiment. CSR induced energy loss throughout the bunch can be observed as a horizontal sag on the TDS screen. The measurement was performed for different bunch charges to compare parameter dependencies with those predicted by simulations. The magnitude of the effect is expected to be up to 130 keV, leading to a trajectory offset of up to 1 mm after the bunch compressor chicane. With proper settings of the optics between the chicane and the TDS (involving 4 more accelerating modules, the 2nd bunch compressor, diagnostic and matching sections) the sag in the longitudinal-horizontal beam profile is of the same order. The sag (i.e. the largest offset of the slices from the nominal position) is derived for different bunch charges. The sag gets smaller for large bunch charges because the bunch length and the uncorrelated energy spread at the entrance of the bunch compressor increases, resulting in a smaller maximal peak current inside the chicane.

A numerical model of the FLASH linac with the same conditions as the real machine was constructed. Despite the limited knowledge of all machine parameters, a good agreement between numerical results and experimental data was achieved. We demonstrated that the numerical tools as well as the beam diagnostics at FLASH are suitable for quantitative studies on CSR.

REFERENCES

[1] B. Beutner and W. Decking and M. Dohlus and T. Limberg and M. Roehrs: Beam Dynamics Experiments and Analysis on CSR Effects at FLASH, FEL 2006 - Proceedings BESSY, Berlin, Germany.

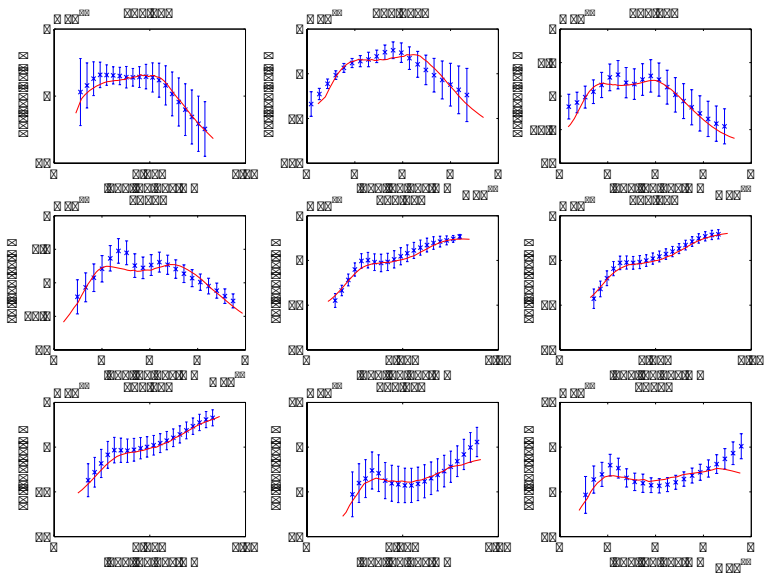

Figure 5: Comparison of centroid curves obtained from measurements (blue) and simulations (red). ACC1 phase offset is $\varphi = 24.9°$. The centroid curves obtained by the image analysis of measured profiles are shown. Bunch heads are to the left.

[2] K. Flöttmann: ASTRA user manual, http://www.desy.de/mpyflo/Astra_dokumentation.

[3] M. Dohlus, T. Limberg: CSRtrack: Faster Calculation of 3D CSR effects, FEL 2004, 2004

[4] T. Weiland and I. Zagorodnov: The Short-Range Transverse Wake Function For TESLA Accelerating Structure, TESLA Report 2003-19

[5] E. Prat and W. Decking and T. Limberg: Measurement and Correction of Dispersion in the VUV-FEL, Proceedings of EPAC 2006, Edinburgh, Scotland

[6] B. Beutner: Measurement and Analysis of Coherent Syn chrotron Radiation Effects at FLASH, PhD Thesis, University Hamburg 2007, to be published

[7] F. Löhl et al.: Measurements of the Transverse Emittance at the FLASH Injector at DESY, Phys. Rev. ST Accel. Beams 9, 092802 (2006)

IMPROVEMENTS OF THE TRACKING CODE ASTRA FOR DARK CURRENT STUDIES AT FLASH

L. Fröhlich*, University of Hamburg and DESY, Hamburg, Germany,
S. Meykopff, DESY, Hamburg, Germany

Abstract

At the Free Electron Laser in Hamburg (FLASH), the activation of components due to dark current emitted by the gun has become a serious problem. To improve the understanding of dark current transport in the linac, we have used extensive tracking simulations. To reduce the required amount of computing time, we have used a novel parallelized version of the Astra tracking code. We present the main parallelization scheme and investigations on the scalability of the code. We also introduce a new library for the description of complex three-dimensional aperture models. Finally, a brief overview of the simulation results and an evaluation of possible remedies of the activation problem are given.

INTRODUCTION

The FLASH linac accelerates electron bunches from a photoinjector to beam energies of up to 700 MeV [1]. The bunch length is reduced in two magnetic chicanes, BC2 and BC3, at energies of 127 MeV and 380 MeV. In front of the undulator, a four-stage collimation system consisting of two transverse and two energy collimators removes particles deviating excessively from the designated reference orbit and momentum (Fig. 1).

Because it is operated at a high electric field amplitude of 40–44 MV/m, the normal conducting RF gun is a major source of dark current. Measurements with a Faraday cup have shown an average current of 200–300 µA exiting the structure during the RF pulse. A substantial part of it is picked up by the first superconducting acceleration module ACC1 and transported through the linac, leading to increased losses and activation of components along the machine. This has become a problem especially near the first dipole magnets of bunch compressor BC2, where the narrow vacuum chamber intercepts a major fraction of the incoming dark current. Equivalent dose rates above 16 mSv/h due to activated material have been measured in this place, requiring an increased radiation protection effort [2].

To investigate possible remedies for this problem, the transport of dark current through the linac has been studied with particle tracking simulations. The space charge tracking code *Astra* [3] was the natural choice for this task because a good model of the FLASH injector was already available for it [4]. Originally covering only the initial 14 m of the machine, this model has been extended to include the complete beamline of about 250 m length. The scope of these simulations required substantial changes to the code in order to reduce execution times as well as the development of a new aperture modelling language capable of describing the complex geometries found in the accelerator.

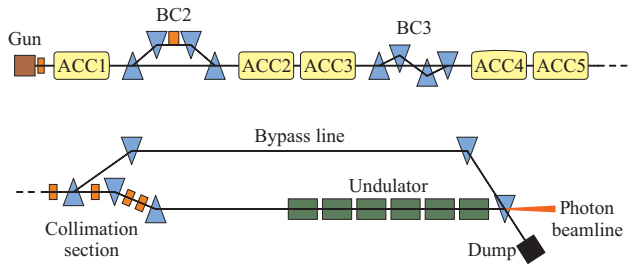

Figure 1: Schematic of the FLASH linac. The five acceleration modules ACC1-5 are shown in yellow, dipole magnets in blue, and collimators in orange color.

In this paper, we provide only a rough outline of simulation setup and results; details are found in [5]. Instead, we focus on the computational aspects of the work.

SIMULATION SETUP

The main simulation is divided into three steps:

1. Beam tracking: A bunch of 10^5 macroparticles is extracted from the cathode by photoemission and tracked to the dump. The step is iterated several times to match the beta function to the design optics.
2. Dark current tracking: 10^6 macroparticles are extracted from the cathode by field emission according to the Fowler-Nordheim model [6] and tracked to the dump. The phase space is saved in intervals of 8 cm, resulting in about 100 GB of data.
3. Aperture check: The saved phase space data are compared against a three-dimensional aperture model of the machine with a separate tool.

While space charge effects have to be included in the tracking of the beam in step 1, they are negligible in step 2 due to the low charge density of the dark current. The number of macroparticles required in step 2 is determined by the desired precision of the results. With a million macroparticles, relative dark current losses down to the level of 10^{-5} – 10^{-4} can be simulated.

We found the conventional single-processor version of *Astra* to be ill-suited for a work load of this magnitude; a single run would take several days to complete on the

* lars.froehlich@desy.de

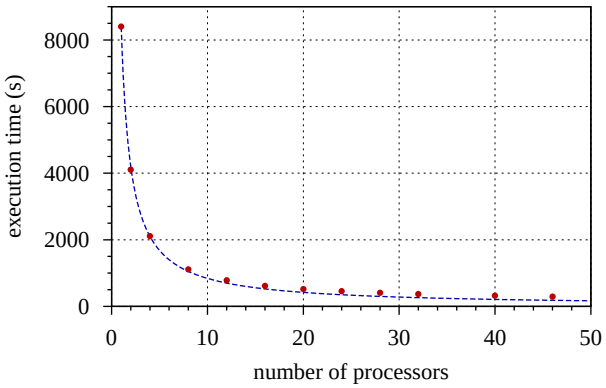

Figure 2: Parallel performance benchmark. The dotted line indicates the best theoretically possible execution time based on the measurement for a single processor, i.e. with assumed full scalability.

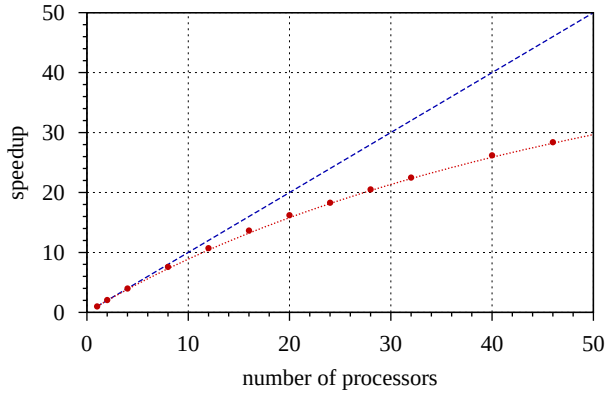

Figure 3: Speedup achieved by running Astra on multiple processors. The dashed line indicates the ideal case of full scalability, the dotted line corresponds to Amdahl's law with a sequential code fraction of $\alpha = 1.4\,\%$.

fastest available computer. Instead, we decided to make use of parallel computing with a new version of the code.

PARALLELIZATION OF THE ASTRA TRACKING CODE

Astra provides several particle-in-cell (PIC) algorithms to calculate the space charge field generated by the macroparticles. The most frequently used one employs a cylindrically symmetric grid in which the single cells are addressed by a radial and a longitudinal bin number, r and l. The code iterates over all N macroparticles to determine the charge present in each cell, Q_{rl}. Afterwards, the main tracking loop iterates over all particles again, for each one summing up the contributions of all partial charges Q_{rl} to the local space charge field as well as external electric and magnetic fields. The forces exerted on each particle are integrated with a fourth-order Runge-Kutta algorithm [7].

Many parallel PIC codes divide the computation work by distributing the grid cells among the available processors, which is especially advantageous in the case of grids with high resolution and with computationally demanding field calculations. However, Astra's cylindrically symmetric algorithm is frequently used with coarse grids (under 1000 cells), and the field calculation is comparatively simple due to the absence of complicated boundary conditions. Investigations with a code profiler also confirm that only a minor part of the execution time is spent in the space charge routines.

On the basis of these considerations, it was decided to achieve parallelization by distributing the macroparticles among the processors. In a run with N particles and P processors, the initial assignment would follow the pattern:

process 0:	particles	$0 \ldots N/P - 1$
process 1:	particles	$N/P \ldots 2N/P - 1$
...		
process N:	particles	$(P-1)N/P \ldots N - 1$

To exploit this form of data parallelism, we have chosen a classical "single program multiple data" (SPMD) approach; the existing serial source code has been extended by calls to the MPICH2 message passing interface library [8]. It is therefore possible to run the executable on a single processor as usual, or to spawn multiple processes within the framework of an existing MPICH2 installation.

Parallel Performance

Figure 2 shows the measured execution times on a cluster with 23 nodes of two CPUs each. Shared memory is used for communication between the twin CPUs, gigabit ethernet for communication between the nodes. The input file used for benchmarking contains the complete model of the FLASH linac, but simulates only the first 20 m of the machine with 10^5 macroparticles including space charge effects. There are no emittance calculations or file outputs except for the saving of one phase space file at the end of tracking.

The speedup ξ achieved by using P processors is defined as the ratio of parallel to sequential execution time, $\xi(P) = \Delta t(P)/\Delta t(1)$. Figure 3 shows that the measured speedup increasingly deviates from ideal behavior with increasing number of processors—the maximum achieved on the cluster is $\xi(46) = 28.4$. This behavior is described well by *Amdahl's law* [9] which states that if a program can be separated into a parallelizable part and a sequential part that takes a fraction α of the total execution time, the speedup by running it on P processors is given by

$$\xi(P) = \left(\alpha + \frac{1-\alpha}{P}\right)^{-1} .$$

By fitting to the data, we obtain a sequential fraction of $\alpha = 1.4\,\%$ for this benchmark case. The maximum possible speedup is then given by

$$\lim_{P\to\infty} \xi(P) \approx 71 .$$

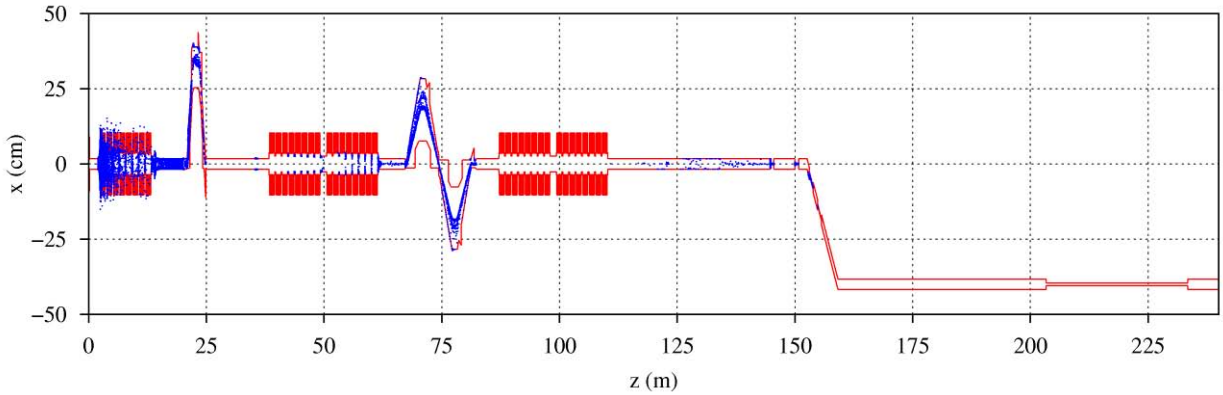

Figure 4: Horizontal section of the FLASH aperture model. The blue dots mark the positions of lost dark current particles. Losses in the gun region are not shown.

However, it is obvious that these figures depend strongly on the specific application—generally, a higher number of macroparticles will increase the speedup, and a higher number of sequential operations like file saving or emittance calculations will decrease it.

APERTURE MODELLING

To obtain reliable information about dark current losses from a tracking simulation, a good knowledge of the apertures along the machine is required. It is also necessary to have tools that can reproduce this geometry in an adequate way. Unfortunately, the built-in capabilities for modelling apertures in Astra and in most tracking codes are limited to basic shapes like circular openings or parallel plates.

To facilitate a coherent and exact description of aperture models, we have developed the portable *ApertureLib* library. It is written in C++ and allows integration to C and Fortran projects by a set of wrapper functions. The library allows to read aperture models from XML files like the following:

```
<aperture-list>
  <circle z="0" name="drift">
    <r>0.017</r>
  </circle>
  <include z="2.4" name="acc. module">
    <filename>acc_module.xml</filename>
  </include>
</aperture-list>
```

In this example, two aperture elements are specified along with their longitudinal positions in the machine. The first one describes a circular aperture with a radius of 1.7 cm, the second one includes another XML file that defines the geometry of cavities and vacuum chambers inside a cryomodule.

A wide variety of element types is available, allowing to model even complicated geometries:

- Primitive profiles (circle, ellipse, rectangle, ...), rotatable to any direction in space
- Elements delimited by an arbitrary number of planes, specified by position and normal vectors
- Combination of other apertures by a logical AND or OR, e.g. to model alternative beamlines or new shapes like semicircles
- Inclusion of other XML files as “building blocks” for repetitive structures
- Inclusion of existing Astra aperture files
- Import of 2-dimensional CAD drawings in DXF format for complex planar geometries

In addition to the library, a set of tools has been created that allows validation and inspection of aperture models as well as generation of plots and checking of phase space files against the model.

With this toolkit, the geometry of the FLASH vacuum chambers shown in Fig. 4 was set up and compared against the phase space files from the previous Astra simulations.

SIMULATION RESULTS

The simulation shows that about 70 % of the emitted dark current are lost in the region from the gun cavity to the first cavity of module ACC1. Many particles arrive there on the wrong phase of the RF wave and are reflected or lost in the module. By scaling to the measured value of ∼250 µA at a Faraday cup behind the gun, we can conclude that roughly 100 µA of dark current are transported through ACC1 (Fig. 5).

After passing the acceleration module, the dark current has reached an energy of about 127 MeV. Since this is well above the giant nuclear resonance threshold, losses may lead to activation of accelerator beamline and components. As expected, the entrance of bunch compressor BC2 with its low vacuum chamber of only 8 mm height intercepts the biggest part of the remaining current, more than 50 µA. The simulation predicts other hot spots at the exit of ACC1, at the entrance and exit of BC3, and at the collimators, which is qualitatively confirmed by the measured radiation levels in these locations [2].

We can also estimate the remaining amount of dark cur-

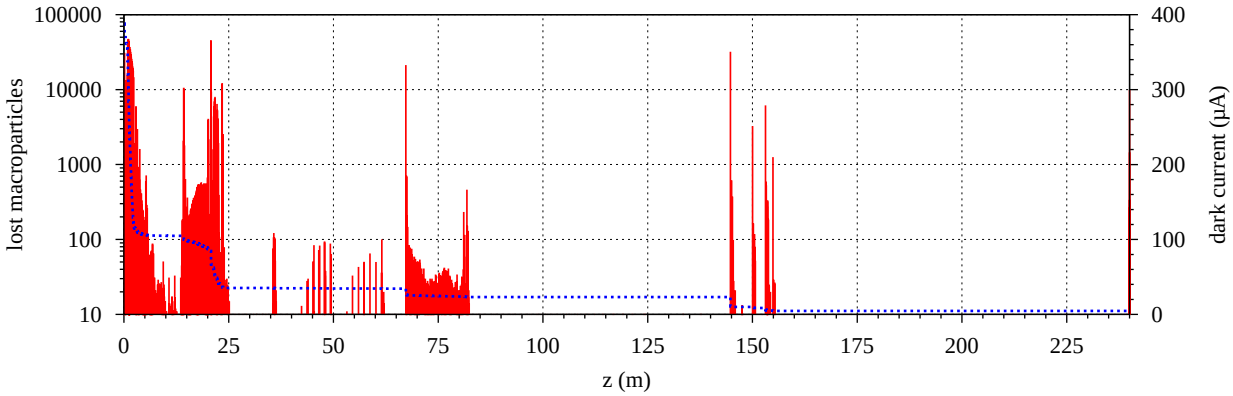

Figure 5: Simulated dark current losses along the FLASH linac. *Red (logarithmic scale):* lost number of macroparticles per phase space file. *Blue (linear scale):* remaining gun dark current.

rent traversing the FEL undulator to be about 5 µA. With the machine set to default optics, it oscillates between rms beam sizes of 250 µm and 1.5 mm in both planes while the beam is smaller than 100 µm. Therefore it is easy to lose some dark current in the undulator chamber by wrong beam steering. Calculations with the particle transport code Fluka [10, 11] have shown that a complete loss of the dark current would deposit a local dose rate of 30 Gy/minute in the permanent magnets.

To reduce the amount of gun dark current that is transported through module ACC1, it has been proposed to increase the drift length between gun and module by 30 cm [12], and to insert a collimator with a circular aperture of 8 mm diameter behind the gun. From simulations with our model, we expect a reduction of transported dark current by about two thirds.

CONCLUSION

The investigation of dark current transport and losses with detailed tracking simulations is computationally demanding. We found the parallelized version of the Astra code well suited for this task. It has been demonstrated that simulation times can be reduced drastically by distributing the work load over several processors. The scalability of the code makes it well suited for multicore-/multiprocessor machines or small clusters with up to 64 processors.

In order to set up a detailed three-dimensional aperture model of the FLASH linac, we have developed the portable C++ library *ApertureLib* and a set of necessary tools. We have used this toolkit to compare phase space files generated by the Astra runs against the aperture model. This allowed us to check variations of the model quickly without having to repeat the tracking. However, the library has also been integrated into Astra as an optional component and can be used directly during the tracking run.

The simulation has provided an insight to the beam dynamics of dark current transport in the linac and allowed to evaluate possible counter measures for the problem of beamline activation. Based on these data, we can predict a reduction of dark current losses at bunch compressor BC2 to about one third of their former amount by the proposed relocation of the gun and the use of a transverse collimator.

ACKNOWLEDGEMENTS

We highly appreciate K. Flöttmann's assistance with the original Astra source code. We also wish to thank him, B. Beutner, and J.-H. Han for many helpful discussions.

REFERENCES

[1] The TESLA Test Facility FEL team, "SASE FEL at the TESLA Facility, Phase 2", TESLA-FEL 2002-01, June 2002, Hamburg.

[2] A. Leuschner, DESY, private communication.

[3] K. Flöttmann, "Astra—A Space Charge Tracking Algorithm", available at http://www.desy.de/~mpyflo/.

[4] K. Flöttmann, E. Schneidmiller, Y. Kim, private communication.

[5] L. Fröhlich, "Dark Current Transport in the FLASH Linac", PAC'07, June 2007, Albuquerque, USA, pp. 956–958.

[6] R. H. Fowler, L. Nordheim, "Electron Emission in Intense Electric Fields", Proc. R. Soc. A, 119, May 1928, London, pp. 173–181.

[7] K. Atkinson, "An Introduction to Numerical Analysis", 2nd ed., Wiley, 1989.

[8] MPICH2, an implementation of the message-passing interface, http://www-unix.mcs.anl.gov/mpi/mpich2/.

[9] G. Amdahl, "Validity of the Single Processor Approach to Achieving Large-Scale Computing Capabilities", Proc. AFIPS, (30), pp. 483–485, 1967.

[10] A. Ferrari, P. R. Sala, A. Fassò, et al., "Fluka: A Multi-Particle Transport Code", CERN-2005-00X, August 2005, Geneva.

[11] A. Fassò, A. Ferrari, S. Roesler, et al., "The Physics Models of FLUKA: Status and Recent Developments", CHEP'03, March 2003, La Jolla.

[12] J.-H. Han, K. Flöttmann, "Dark Current Collimation and Modified Gun Geometry for the European X-Ray FEL Project", FEL'06, August 2006, Berlin, pp. 579-582.

LONGITUDINAL WAKE FIELD FOR AN ELECTRON BEAM ACCELERATED THROUGH A ULTRA-HIGH FIELD GRADIENT

G. Geloni, E. Saldin, E. Schneidmiller and M. Yurkov
Deutsches Elektronen-Synchrotron (DESY), Hamburg, Germany

Abstract

The impact of longitudinal wake fields on an electron beam accelerated through a ultra-high field gradient is discussed, based on solution of Maxwell's equations for the longitudinal field. We consider an acceleration distance much smaller than the overtaking length, as for laser-plasma devices. We give expressions for impedance and wake function that may be evaluated numerically. A limiting expression is found for a large distance of the electron beam from the accelerator compared with the overtaking length. We derive analytical solutions for a Gaussian transverse and longitudinal bunch shape. We apply our analytical asymptote by studying the feasibility of a Table-Top VUV FEL (TT-VUV-FEL) based on laser-plasma driver. Numerical estimations indicate a serious threat to the operation of this device. **A detailed report with relevant references is given in [1]**.

INTRODUCTION

In this paper we study longitudinal wake fields produced within electron beams accelerated with high-gradient fields. We assume that the acceleration distance d_a is much smaller than the the overtaking length. This is the distance travelled by the electrons as a light signal from the tail of the bunch overtakes the head of the bunch. Given a bunch of rms length σ_z, the overtaking length is $2\gamma^2\sigma_z$, and corresponds to the radiation formation length $2\gamma^2\lambda\!\!\!^{-}$ calculated at $\lambda\!\!\!^{-} = \sigma_z$, $\lambda\!\!\!^{-} = \lambda/(2\pi)$ being the reduced radiation wavelength. When $d_a \ll 2\gamma^2\sigma_z$, electrons can be assumed to be accelerated at position z_A down the beamline. This is the case for laser-plasma devices, since acceleration in the GeV range takes place within a few millimeter, but not for conventional accelerators. The assumption $d_a \ll 2\gamma^2\sigma_z$ simplifies wake calculations. When this condition is verified, the wake generated along the part of the trajectory following the acceleration point z_A is independent of any detail of the accelerator. Thus our study is valid independently of the particle accelerator technology chosen, provided that $d_a \ll 2\gamma^2\sigma_z$. One may also have contributions to the wake generated before z_A. These depend on the physical nature of the accelerator, can be separately calculated, and will be neglected here because they do not affect the bunch in the case of a laser-plasma accelerator. We base our study on solution of Maxwell's equations for the longitudinal field. Our consideration is valid in free-space. This approach gives accurate results if the typical dimension of the vacuum pipe a is larger than $\gamma\lambda\!\!\!^{-} = \gamma\sigma_z$, that is the typical transverse size related with the longitudinal electric field. Paraxial approximation can be applied to describe electromagnetic sources up to the observation point, while sources after the observation point in the beam propagation direction can be neglected. We make use of the paraxial approximation to calculate the Fourier transform of the longitudinal field produced by fixed electromagnetic sources (current and charge densities) at a certain observation plane down the beamline. This constitutes the basis of our treatment, because it allows to calculate the longitudinal impedance and the wake function. Impedance and wake function yield an analytical expression in the asymptotic limit of a large distance of the electron beam from the accelerator compared with the overtaking length, i.e. in the far-field zone for all wavelengths of interest (up to $\lambda\!\!\!^{-} \sim \sigma_z$). This asymptotic limit allows simple estimations of the impact of the longitudinal wake on the electron beam energy change. We apply our theory by studying the feasibility of TT-VUV-FELs based on parameters described in [2], and finding a serious threat.

FIELD IN SPACE-FREQUENCY

Let z_A be the exit of the accelerator. After z_A, the nominal Lorentz factor of electrons is γ. Acceleration happens on a scale $d_a \ll 2\gamma^2\lambda\!\!\!^{-}$. Significant emission is present for wavelengths longer than the longitudinal bunch length σ_z, up to transverse beam sizes $\sigma_\perp \lesssim \gamma\sigma_z$. For typical ultra-relativistic beams, condition $d_a \ll 2\gamma^2\lambda\!\!\!^{-}$ can be read as $d_a \ll 2\gamma^2\sigma_z$. We picture the fast acceleration process as a sudden "switch-on" of both harmonics of the electromagnetic sources and of the field. When the switching distance (the acceleration distance) $d_a \ll 2\gamma^2\sigma_z$, the description of the wake generated after the switching point (the acceleration point) z_A, is independent of the nature of the switcher. As long as sources are rapidly switched-on, it does not matter whether we are considering a fast longitudinal acceleration or other switching mechanisms. We first calculate $\bar{E}_z(z_o, \vec{r}_{\perp o}, \omega)$, that is the longitudinal electric field at frequency ω from given electromagnetic sources in vacuum. It is detected at longitudinal position $z_o > z_A$ and transverse position $\vec{r}_{\perp o}$. We define the Fourier transform of a function $f(t)$ as $\bar{f}(\omega) = \int_{-\infty}^{\infty} dt\, f(t) \exp[i\omega t]$, and we follow analogous conven-

tion in the definition of the Fourier transform in two dimensions. The field in the space-frequency domain $\vec{\tilde{E}}(z_o, \vec{r}_{\perp o}, \omega)$ is the Fourier transform of the field in the space-time domain, $\vec{E}(z_o, \vec{r}_{\perp o}, t)$. As is well-known, one may use the field in the space-frequency domain for a given frequency and yet think of the amplitude of a monochromatic field or viceversa. We should solve the paraxial equation for sources located in $[z_A, z_o]$: $c^2 \exp[i\omega z/c] \cdot [\nabla_\perp^2 + 2i\omega/c\partial/(\partial z)]\vec{\tilde{E}} = 4\pi c^2 \vec{\nabla}\bar{\rho} - 4\pi i\omega \vec{j}$. Since electrons are moving along the z-axis, we write the harmonic components of the charge density as $\bar{\rho}(z', \vec{r}'_\perp, \omega) = \rho_o(\vec{r}'_\perp)\bar{f}(\omega)\exp[i\omega z'/v]u(z' - z_A)$, while $\bar{j}_z(z', \vec{r}'_\perp, \omega) = \beta c\bar{\rho}$. Notation $u(z' - z_A)$ indicates a Heaviside step function centered at position z_A, whose presence signifies that there are no sources before the plasma accelerator. Functions ρ_o and $\bar{f}$ are specified once a model for the beam is chosen. The quantity ρ_o has the meaning of transverse electron beam distribution. It may depend on the harmonic ω, but we will assume it does not. Thus, all information about the longitudinal electron density distribution $f(t)$ is included in its Fourier transform $\bar{f}(\omega)$. A typical Gaussian beam model is defined by $\rho_o(\vec{r}'_\perp) = 1/(2\pi\sigma_\perp^2 c)\exp[-r'^2_\perp/(2\sigma_\perp^2)]$, and $f(t) = (-e)N/(\sqrt{2\pi}\sigma_t)\exp[-t^2/(2\sigma_t^2)]$, whose Fourier transform is given by $\bar{f}(\omega) = (-e)N\exp[-\omega^2\sigma_t^2/2]$, N being the number of electrons in the beam and $(-e)$ the electron beam charge. Here σ_t is the *rms* bunch duration, connected σ_z by $\sigma_z = \beta c\sigma_t$, so that in terms of lengths $f(s) = (-e)N/(\sqrt{2\pi}\sigma_z)\exp[-s^2/(2\sigma_z^2)]$. The wake generated along the part of the trajectory following z_A, is independent of the nature of the switcher. However, the above expressions for $\bar{\rho}$ and $\bar{j}_z$ violate the continuity equation, and should be completed by extra-contributions depending on the switcher. For example, if one thinks of an acceleration process where a low energy bunch with Lorentz factor γ_o is accelerated on a distance d_a up to a Lorentz factor γ, one should add to $\bar{\rho}$ and $\bar{j}_z$ the contribution of the harmonic at frequency ω associated with the beam with Lorentz factor γ_o. In that way, the continuity equation can be satisfied. However, these extra-contributions depend on the switching process. Here we will not consider them. We will focus, instead, on the switch-independent part of the problem. Moreover, in the case of a plasma accelerator, the switch-dependent contributions have no effect on the longitudinal wake field acting on the electron beam. For $z_A \to -\infty$, corresponding to the steady state solution, we obtain the following expression:

$$\widetilde{E}_z = -\frac{2i\omega}{\gamma^2 c}\exp\left[\frac{i\omega z_o}{2\gamma^2 c}\right]\bar{f}(\omega) \times \int d\vec{r}'_\perp\, \rho_o(\vec{r}'_\perp) K_o\left(\frac{|\omega|\,|\,\vec{r}_{\perp o} - \vec{r}'_\perp\,|}{\gamma c}\right). \quad (1)$$

$\widetilde{E}_z$ depends on z_o through a phase factor only. When $z_A = 0$, corresponding without loss of generality to the switch-on case, we have:

$$\widetilde{E}_z(z_o, \vec{r}_{\perp o}, \omega) = -\frac{\omega\bar{f}(\omega)}{\gamma^2 c}\int d\vec{r}'_\perp \rho_o\left(\vec{r}'_\perp\right) \times \left\{ i\int_0^{z_o}\frac{dz'}{(z_o - z')}\exp\left[\frac{i\omega z'}{2\gamma^2 c} + i\omega\frac{|\,\vec{r}_{\perp o} - \vec{r}'_\perp\,|^2}{2c(z_o - z')}\right] + \frac{\gamma^2 c}{\omega z_o}\exp\left[i\omega\frac{|\,\vec{r}_{\perp o} - \vec{r}'_\perp\,|^2}{2cz_o}\right]\right\}. \quad (2)$$

Eq. (1) and Eq. (2) can be used to estimate the impact of the field generated by the electron beam on any particle in the beam. We do so with the help of the concepts of wake fields and impedances. By definition of impedance $Z(\omega, z)$ we have $Z(\omega, z) = 1/|\bar{f}(\omega)|^2 \int_V \bar{j}_z^* \bar{E}_z\, dV$, where $|\bar{f}(\omega)|^{-2}$ accounts for the fact that test and source disks have total charge (-e), while $\bar{j}_z^* \propto \bar{f}^*$ and $\bar{E}_z \propto \bar{f}$. Here the volume V encloses the beam up to position z. Relation between impedance Z and wake G is given by $Z = \int_{-\infty}^{\infty} d(\Delta s)/(\beta c)\; G(\Delta s)\exp[i\omega\Delta s/(\beta c)]$. An explicit expression for $Z(\omega, z)$ is

$$Z = -\frac{\omega}{\gamma^2}\int d\vec{r}'_\perp \int d\vec{r}''_\perp \rho_o^*(\vec{r}'_\perp)\rho_o(\vec{r}''_\perp)\int_0^z dz' \left\{ i\int_0^{z'}\frac{dz''}{(z' - z'')}\exp\left[\frac{i\omega}{2c}\left(\frac{z'' - z'}{\gamma^2} + \frac{|\,\vec{r}_{\perp o} - \vec{r}'_\perp\,|^2}{z' - z''}\right)\right] + \frac{\gamma^2 c}{\omega z'}\exp\left[i\omega\frac{|\,\vec{r}_{\perp o} - \vec{r}'_\perp\,|^2}{2cz'}\right]\exp\left[-\frac{i\omega z'}{2\gamma^2 c}\right]\right\}. \quad (3)$$

Eq. (3) constitutes a practical algorithm to compute both real and imaginary parts of the impedance (and, subsequently, of the wake).

Since ρ_o is a real quantity, $Z(\omega)$ has the property $Z(\omega) = Z^*(-\omega)$. Then, Re$[Z](\omega)$ is an even function of ω, while Im$[Z](\omega)$ is odd. The property $Z(\omega) = Z^*(-\omega)$ follows, more in general, from the fact that $G(\Delta s, z)$ is a real function. If we split the wake function in the sum $G = G_S + G_A$ of a symmetric and antisymmetric part, the Fourier transform of G_S gives back Re$[Z]$, while the Fourier Transform of G_A yields Im$[Z]$. The symmetric part of the wake, G_S, is also known as active part and is related with the energy lost by the bunch through radiation. The antisymmetric part G_A is known as reactive part and is related with energy redistribution within the bunch.

ANALYTICAL ASYMPTOTES

Impedance

With the help of Eq. (3) we calculate asymptotes of the real and imaginary parts of the impedance for $z \gg 2\gamma^2\lambda$ (see [1]). The real part is:

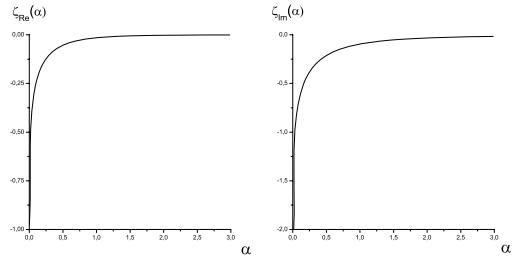

Figure 1: Plot of $\zeta_{\rm Re}$ (left) and plot of $\zeta_{\rm Im}$ (right).

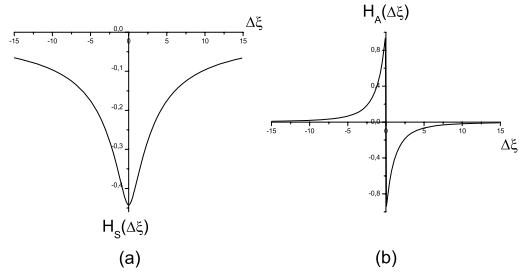

Figure 2: (a) Plot of H_S and (b) plot of H_A.

$$\mathrm{Re}[Z](\omega) = -\frac{c}{\pi}\int d\vec{\theta}\left|\tilde{\rho}_o(\vec{\theta},\omega)\right|^2 \frac{\gamma^4\theta^2}{\left(1+\gamma^2\theta^2\right)^2}\,. \qquad (4)$$

We now choose a Gaussian model for ρ_o, substituting $\tilde{\rho}_o(\vec{\theta},\omega) = 1/c\cdot\exp[-\theta^2\omega^2\sigma_\perp^2/(2c^2)]$ in Eq. (4). This gives $\mathrm{Re}[Z] = Z_o\zeta_{\rm Re}(\alpha)$, where

$$\zeta_{\rm Re}(\alpha) = \frac{1}{4\pi}\left\{1-(1+\alpha^2)\exp[\alpha^2]\Gamma(0,\alpha^2)\right\}\,, \qquad (5)$$

$\Gamma(0,x)$ being the incomplete gamma function, $Z_o = 4\pi/c$ the free-space impedance and $\alpha = \omega\sigma_\perp/(\gamma c)$. A plot of the universal function $\zeta_{\rm Re}(\alpha)$ is given in Fig. 1 (left plot). Re[Z] exhibits a singular behavior for $\sigma_\perp \longrightarrow 0$ (i.e. for $\alpha \longrightarrow 0$ in Fig. 1 (left plot)). This is linked with our particular model, where we chose $d_a \longrightarrow 0$. The imaginary part is:

$$\mathrm{Im}[Z](\omega) = -\frac{1}{\pi}\omega z\int d\vec{\theta}\left|\tilde{\rho}_o(\vec{\theta},\omega)\right|^2 \frac{1}{\left(1+\gamma^2\theta^2\right)}\,. \qquad (6)$$

Similarly as for the real part, use of a Gaussian beam model allows to give an explicit expression for Im[Z]. Namely, $\mathrm{Im}[Z] = (Z_o\hat{z})\,\zeta_{\rm Im}(\alpha)$, where

$$\zeta_{\rm Im}(\alpha) = -\frac{1}{2\pi}\exp[\alpha^2]\,\Gamma(0,\alpha^2)\,, \qquad (7)$$

where and $\hat{z} = z/(2\gamma^2\lambda\!\!\!^{-})$. A plot of the universal function $\zeta_{\rm Im}(\alpha)$ is given in Fig. 1 (right plot).

Wake function

Analytical results given for $z \gg \gamma^2\lambda\!\!\!^{-}$. $G_S(\Delta s)$ can be found calculating the inverse Fourier transform of Re[Z](ω) with respect to $\Delta s/\beta c$. Using notation $\Delta\xi = \gamma(\Delta s)/\sigma_\perp$, one obtains $G_S(\Delta\xi) = \gamma/\sigma_\perp\cdot H_S(\Delta\xi)$ where $H_S(\Delta\xi) = -1/(4\sqrt{\pi})\{\sqrt{\pi}\,|\Delta\xi| + \pi[1-(\Delta\xi)^2/2]\exp[(\Delta\xi)^2/4]\cdot\mathrm{erfc}[|\Delta\xi|/2]\}$. A plot of the universal function H_S as a function of $\Delta\xi$ is given in the left plot of Fig. 2 (a). The energy gained or lost by a single particle at position s within the bunch due to the active (symmetric) part of the wake, averaged over transverse coordinates is given by the convolution $\Delta\mathcal{E}_S(s) = (-e)\int_{-\infty}^{\infty} G_S(\Delta s)f(s-\Delta s)d(\Delta s)$. An explicit expression for $\Delta\mathcal{E}_S/\mathcal{E}_o$ as a function of $\xi = \gamma s/\sigma_\perp$, $\mathcal{E}_o = \gamma m_e c^2$ being the nominal energy of an electron (with rest mass m_e) is

$$\frac{\Delta\mathcal{E}_S}{\mathcal{E}_o} = \frac{I_{\max}}{\gamma I_A}\int_{-\infty}^{\infty} d(\Delta\xi)H_S(\xi-\Delta\xi)\exp\left[-\frac{(\Delta\xi)^2}{2\eta^2}\right]\,, \qquad (8)$$

where we introduced the new parameter $\eta = \gamma\sigma_z/\sigma_\perp$, and we called the Alfven current $I_A = e/(mc^3) \simeq 17$ kA and the beam current $I_{\max} = eNc/(\sqrt{2\pi}\,\sigma_z)$.

G_A can be found calculating the inverse Fourier transform of $i\mathrm{Im}[Z](\omega)$ with respect to $\Delta s/\beta c$. One obtains $G_A(\Delta\xi) = \gamma\eta\hat{z}/\sigma_\perp\cdot H_A(\Delta\xi)$, where $H_A(\Delta\xi) = -\Delta\xi/(2\sqrt{\pi})\,\{2\sqrt{\pi}/|\Delta\xi| - \pi\exp[(\Delta\xi)^2/4]\cdot\mathrm{erfc}[|\Delta\xi|/2]\}$ and we redefined $\hat{z} = z/(2\gamma^2\sigma_z)$. A plot of the universal function H_A is reported in Fig. 2 (b). The energy gained or lost by a single particle at position s within the bunch due to the reactive part of the wake (averaged over transverse coordinates) is given by the convolution $\Delta\mathcal{E}_A(s) = (-e)\int_{-\infty}^{\infty} G_A(\Delta s)f(s-\Delta s)d(\Delta s)$. $\Delta\mathcal{E}_A/\mathcal{E}_o$ as a function of $\xi = \gamma s/\sigma_\perp$ is given by :

$$\frac{\Delta\mathcal{E}_A}{\mathcal{E}_o}\left(\frac{s}{\sigma_z};\eta\right) = \frac{I_{\max}\hat{z}}{\gamma I_A}F\left(\frac{s}{\sigma_z};\eta\right)\,. \qquad (9)$$

where $\mathcal{E}_o = \gamma m_e c^2$, and

$$F\left(\frac{s}{\sigma_z};\eta\right) = \int_{-\infty}^{\infty} d(\Delta\xi)\,\eta\,H_A\left(\eta\frac{s}{\sigma_z}-\Delta\xi\right)\exp\left[-\frac{(\Delta\xi)^2}{2\eta^2}\right]\,. \qquad (10)$$

A plot of F is given as a function of s/σ_z in Fig. 3 for different values of η.

Plots for $\Delta\mathcal{E}_S/\mathcal{E}_o$ and $\Delta\mathcal{E}_A/\mathcal{E}_o$ as a function of ξ can be computed with the help of numerical techniques.

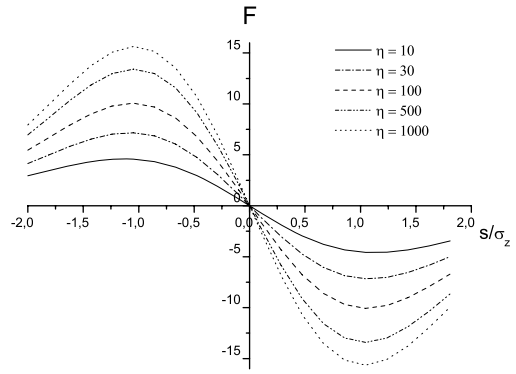

Figure 3: Plot of F at different η.

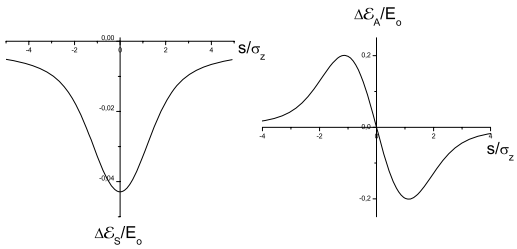

Figure 4: $\Delta\mathcal{E}_s/\mathcal{E}_o$ (left) and $\Delta\mathcal{E}_A/\mathcal{E}_o$ (right) for the TT-VUV-FEL at $z = 0.8$ m.

IMPACT ON TT-VUV-FEL

One of the applications envisaged for next-generation plasma accelerators is as drivers for table-top FELs [2]. Here we will apply our theory to the VUV case in Table I of reference [2]. The undulator parameter K is smaller than unity. Thus, wake field calculations in vacuum can still be used inside the undulator. In the TT-VUV-FEL case $2\gamma^2\lambda\!\!\!^{-} \simeq 18$ cm, several times smaller than the size of the planned undulator, that is about 0.8 m. Therefore we are well-within the applicability region of the our asymptotic expressions. Needed parameters are $\gamma = 300$, $\eta = 10$ and $I = 50$ kA. Also, we need to fix a position along the longitudinal axis. Here we set $z \simeq 0.8$ m, corresponding to the foreseen undulator length. The relative energy change $\Delta\mathcal{E}_{S,A}/\mathcal{E}_o$ are presented respectively on the left and on the right plot in Fig. 4 as a function of the longitudinal coordinate inside the bunch. While travelling down the undulator, a correlated energy change develops along the electron beam. For estimations of the effect on the FEL gain we can use the linear energy chirp parameter $\hat{\alpha} = -(\gamma\omega\rho_{1D}^2)^{-1} \cdot d\gamma/dt$. The effect of linear energy chirp starts to play a significant role on the FEL gain when $\hat{\alpha} \gtrsim 1$. One finds $\hat{\alpha} \simeq 10$, that indicates a very large effect. Note that the energy chirp in Fig. 4 (right plot) depends on the electron beam profile but also on time, because it develops along the undulator. This effect is fundamental, and is directly linked with the feasibility of the proposed FEL scheme. Radiation generated in one part of the undulator cannot interact in resonance in another part of the undulator, and the amplification process is destroyed.

CONCLUSIONS

We studied the impact of longitudinal wake fields on the quality of electron beams produced with high field-gradient accelerators. Our consideration does not depend on the particular realization of the accelerator. However, given present technological developments, one of the most relevant applications of our study should come from the realm of laser-plasma accelerators. We calculated longitudinally symmetric and anti-symmetric parts of the wake function as well as real and imaginary part of the impedance with the help of paraxial approximation within a space-frequency domain formulation of Maxwell's equation. While the general expressions for wakes and impedances need numerical techniques to be evaluated, it is possible to present analytical expressions for the asymptotic limit when the electron bunch has reached a position, down the beamline, that is far from the acceleration point with respect to the overtaking distance. Then, the wake and the impedance are proportional to universal functions. Our results can be used as analytical benchmarks for computer codes. Taking advantage of similarity techniques we presented such result in terms of a complex dependent on the problem parameters ($\gamma\eta\hat{z}/\sigma_\perp$) multiplied by a universal function H_A. Our expression for G_A can further be used to calculate the relative energy change of a particle within a given bunch. In case of a Gaussian longitudinal profile the relative energy spread reduces to Eq. (9). Plots presented in Fig. 3 will help the reader to perform a fast estimation of the influence of the space-charge wake at the stage of planning of experiments. As a particular example, we used our results to estimate the impact of the longitudinal wake fields on the energy change of the electron beam for the TT-VUV-FEL setup in [2]. The total energy deviation is found to be critical.

For details on our work we refer the interested reader to [1].

REFERENCES

[1] G. Geloni, E. Saldin, E. Schneidmiller and M. Yurkov, Nucl. Instrum. and Methods in Phys. Research A 578 (2007) 3446, preprint version DESY 06-222 at http://arxiv.org/abs/physics/0612077

[2] F. Gruener et al., Appl. Phys. B 86, 431 (2007)

THEORY OF NONLINEAR HARMONIC GENERATION IN FELS WITH HELICAL WIGGLERS

G. Geloni, E. Saldin, E. Schneidmiller and M. Yurkov
Deutsches Elektronen-Synchrotron (DESY), Hamburg, Germany

Abstract

Nonlinear Harmonic Generation (NHG) is of importance for both short wavelength FELs, in relation with the achievement of shorter wavelengths with a fixed electron-beam energy, and high-average power FEL resonators, in relation with destructive effects of higher harmonics radiation on mirrors. We present a treatment of NHG from helical wigglers with particular emphasis on the second harmonic. Our study is based on an analytical solution of Maxwell's equations, derived with the help of a Green's function method. We demonstrate that NHG from helical wigglers vanishes on axis. Our conclusion is in contrast with literature, that includes a kinematical mistake in the description of the electron motion. **A detailed report with relevant references is given in [1]**.

INTRODUCTION

NHG is of undisputed relevance in the field of FELs. It is generated by bunching of the electron beam at higher harmonics, driven by interaction with the fundamental. In general, NHG can be treated in terms of an electrodynamical problem where Maxwell's equations are solved with given macroscopic sources in the space-frequency domain. These sources are obtained through the solution of self-consistent equations for electrons and fields. Further on, solution of Maxwell's equations characterizes harmonic radiation in the space-frequency domain. The dependence of sources in the space-frequency domain on transverse and longitudinal coordinates is complicated because is the result of the above-mentioned self-consistent process. However, here we deal with an FEL setup where an ultrarelativistic electron beam is sent, in free space, through an undulator with many periods. Then, paraxial and resonance approximation can be applied. In particular, for a fixed transverse position, the longitudinal dependence is always slow on the scale of an undulator period. NHG has been dealt with in the case of a planar wiggler, both theoretically and experimentally. Odd harmonics have maximal power on axis[1] and are linearly polarized. Even harmonics have been shown to have vanishing on-axis power and to exhibit both horizontal and vertical polarization components. Here we present the first theory of NHG from helical wigglers, based on a solution of Maxwell's equations in the space-frequency domain, obtained with a Green's function technique.

NHG IN HELICAL WIGGLERS

Analysis of the harmonic generation mechanism

We use paraxial Maxwell's equations in the space-frequency domain to describe radiation from ultra-relativistic electrons. Let us call the transverse electric field in the space-frequency domain $\vec{E}_\perp(z,\vec{r}_\perp,\omega)$, where $\vec{r}_\perp = x\vec{e}_x + y\vec{e}_y$ and z identify a point in space. From the paraxial approximation follows that the electric field envelope $\vec{\tilde{E}}_\perp = \vec{E}_\perp \exp[-i\omega z/c]$ does not vary much along z on the scale of the reduced wavelength $\lambda\!\!\!^{-} = \lambda/(2\pi)$. Maxwell's equation in paraxial approximation reads: $\mathcal{D}\left[\vec{\tilde{E}}_\perp(z,\vec{r}_\perp,\omega)\right] = \vec{f}(z,\vec{r}_\perp,\omega)$, where $\mathcal{D} \equiv {\nabla_\perp}^2 + (2i\omega/c)\partial/\partial z$, ${\nabla_\perp}^2$ being the Laplacian operator over transverse cartesian coordinates. The source-term vector $\vec{f}(z,\vec{r}_\perp)$ is specified by the trajectory of the source electrons, and can be written in terms of the Fourier transform of the transverse current density, $\vec{j}_\perp(z,\vec{r}_\perp,\omega)$, and of the charge density, $\bar{\rho}(z,\vec{r}_\perp,\omega)$, as $\vec{f} = -4\pi[(i\omega/c^2)\vec{j}_\perp - \vec{\nabla}_\perp\bar{\rho}]\exp[-i\omega z/c]$. In this paper we will treat $\vec{j}_\perp$ and $\bar{\rho}$ as macroscopic quantities, without investigating individual electron contributions. $\vec{j}_\perp$ and $\bar{\rho}$ are regarded as given data, that can be obtained from any FEL code. Codes actually provide the charge density of the modulated electron beam in the time domain $\rho(z,\vec{r}_\perp,t)$. A post-processor can be used in order to perform the Fourier transform of ρ that can always be presented as $\bar{\rho} = -\widetilde{\rho}(z,\vec{r}_\perp - \vec{r}'_{o\perp}(z),\omega)\exp[i\omega s_o(z)/v_o]$, where the minus sign on the right hand side is introduced for notational convenience only. Quantities $\vec{r}'_{o\perp}(z)$, $s_o(z)$ and v_o pertain a reference electron with nominal Lorentz factor γ_o that is injected on axis with no deflection and is guided by the helical undulator field. Such electron follows a helical trajectory $\vec{r}'_{o\perp}(z) = r'_{ox}\vec{e}_x + r'_{oy}\vec{e}_y$. We assume that $r'_{ox}(z) = K/(\gamma_o k_w)[\cos(k_w z) - 1]$ and $r'_{oy}(z) = K/(\gamma_o k_w)\sin(k_w z)$, where $K = \lambda_w e H_w/(2\pi m_e c^2)$ is the undulator parameter, $\lambda_w = 2\pi/k_w$ being the undulator period, $(-e)$ the negative electron charge, H_w the maximal modulus of the undulator magnetic field on-axis, and m_e the rest mass of the electron. The correspondent velocity is described by $\vec{v}_{o\perp}(z) = v_{ox}\vec{e}_x + v_{oy}\vec{e}_y$. Finally, $s_o(z)$ is the curvi-

[1] Here we assume that the bunching wavefront is perpendicular to the (longitudinal) FEL axis.

linear abscissa measured along the trajectory of the reference particle. Introduction of $\widetilde{\rho}$ is useful when $\widetilde{\rho}$ is a slowly varying function of z on the wavelength scale. This property is granted by the fact that the charge density distribution under study originates from an FEL process. From this fact it also follows that $\widetilde{\rho}$ is slowly varying on the scale of the undulator period λ_w and is peaked around each harmonic of the fundamental $\omega_r = 2k_w c\bar{\gamma}_z^2$, that is fixed imposing resonance condition between electric field and reference particle. The word "peaked" means that the bandwidth of each harmonic component obeys $\Delta\omega/(h\omega_r) \ll 1$ for each positive integer value h. Here $\bar{\gamma}_z = 1/\sqrt{1 - v_{oz}^2/c^2}$ is the longitudinal Lorentz factor. Finally, the relative deviation of the particles energy from $\gamma_o m_e c^2$ is small, i.e. $\delta\gamma/\gamma_o \ll 1$. It follows that for a generic motion we have $\vec{f} = 4\pi \exp\left[i\int_0^z d\bar{z}\omega/(2\bar{\gamma}_z^2 c)\right]\left[i\omega/(c^2)\vec{v}_{o\perp}(z) - \vec{\nabla}_\perp\right]\widetilde{\rho}[z; \vec{r}_\perp - \vec{r}'_{o\perp}(z)]$. We account for a possible deflection angle $\vec{\eta}^{(c)}$ in the the trajectory of the reference electron. Therefore $\vec{r}'_{o\perp}(z) \longrightarrow \vec{r}_\perp^{(c)}(z, \vec{\eta}^{(c)}) = \vec{r}'_{o\perp}(z) + \vec{\eta}^{(c)} z$ and $\vec{v}_{o\perp}(z) \longrightarrow \vec{v}_\perp(z, \vec{\eta}^{(c)}) = \vec{v}_{o\perp}(z) + c\vec{\eta}^{(c)}$. Using $\vec{v}_\perp(z, \vec{\eta}^{(c)})$ in place of $\vec{v}_{o\perp}(z)$ implies that $\gamma_z(z, \vec{\eta}^{(c)})$ is now a function of both z and $\vec{\eta}^{(c)}$. In particular, $1/\gamma_z^2(z, \vec{\eta}^{(c)}) = 1 - v_z^2(z, \vec{\eta}^{(c)})/c^2$, where $v_z^2 = v^2 - v_\perp^2$ is the square of the electron longitudinal velocity. It follows that $1/\bar{\gamma}_z^2$ in $\vec{f}$ should also be substituted by $1/\gamma_z^2(z, \vec{\eta}^{(c)})$. With these prescriptions, we find a solution to paraxial Maxwell's equation with the help of a Green's function technique, without any other assumption about the parameters of the problem. We are interested in the total power emitted and in the directivity diagram of the radiation in the far zone. Thus, we introduce the observation angle $\vec{\theta} = \vec{r}_{\perp o}/z_o$, setting $\theta \equiv |\vec{\theta}|$, taking the limit for $z_o \gg L_w$, where $L_w = N_w\lambda_w$ is the undulator length. Moreover, we are interested in studying frequency near the fundamental harmonic $\omega_r = 2k_w c\bar{\gamma}_z^2$ or its h-th integer multiple. We specify "how near" the frequency ω is to the h-th harmonic by defining a detuning parameter $C_h = \omega/(2\bar{\gamma}_z^2 c) - hk_w = \Delta\omega/\omega_r k_w$. Here $\omega = h\omega_r + \Delta\omega$. Altogether, using Anger-Jacobi expansion, we find

$$\begin{aligned}
\vec{\tilde{E}}_\perp &= \frac{i\omega}{cz_o}\int_{-\infty}^{\infty} dl'_x \int_{-\infty}^{\infty} dl'_y \int_{-L_w/2}^{L_w/2} dz' \widetilde{\rho}\left(z', l'_x, l'_y\right) \\
&\times \exp\left\{ i\frac{\omega}{c}\left[\frac{z_o\left(\theta_x^2 + \theta_y^2\right)}{2} + \frac{K(\theta_x - \eta_x^{(c)})}{k_w\gamma} - (\theta_x l'_x + \theta_y l'_y)\right]\right\} \\
&\times \sum_{m,n=-\infty}^{\infty} J_m(u)J_n(v)\exp\left[\frac{i\pi n}{2}\right]\exp\left[i(n+m+h)k_w z'\right] \\
&\times \exp\left\{ i\left[C_h + \frac{\omega}{2c}\left(\theta_x - \eta_x^{(c)}\right)^2 + \frac{\omega}{2c}\left(\theta_y - \eta_y^{(c)}\right)^2\right] z'\right\} \\
&\times \left\{ \left[\frac{K}{2i\gamma}\left(\exp[ik_w z'] - \exp[-ik_w z']\right) + \left(\theta_x - \eta_x^{(c)}\right)\right]\vec{e}_x \right. \\
&\left. - \left[\frac{K}{2\gamma}\left(\exp[ik_w z'] + \exp[-ik_w z']\right) - \left(\theta_y - \eta_y^{(c)}\right)\right]\vec{e}_y \right\} \quad (1)
\end{aligned}$$

with $u = -K\omega(\theta_y - \eta_y^{(c)})/(c\gamma k_w)$ and $v = -K\omega(\theta_x - \eta_x^{(c)})/(c\gamma k_w)$. Whenever $C_h + \omega/(2c)[(\theta_x - \eta_x^{(c)})^2 + (\theta_y - \eta_y^{(c)})^2] \ll k_w$, the second phase factor in z' in Eq. (1) (the one containing C_h) is varying slowly on the scale of the undulator period λ_w. As a result, simplifications arise when $N_w \gg 1$, because fast oscillating terms in powers of $\exp[ik_w z']$ effectively average to zero. We further select frequencies such that $|\Delta\omega|/\omega_r \ll 1$, i.e. $|C_h| \ll k_w$. Note that this condition on frequencies automatically selects observation angles of interest $h(\vec{\theta} - \vec{\eta}^{(c)})^2 \ll 1/\bar{\gamma}_z^2$. Independently of the value of K and for observation angles of interest we have $|v| \ll 1$ and $|u| \ll 1$, and we can expand $J_n(v)$ and $J_m(u)$ in Eq. (1).

From now on we consider the case $h = 2$. Performing expansion, and accounting for terms giving a non-zero contribution after integration in dz' we obtain

$$\begin{aligned}
\vec{\tilde{E}}_\perp &= \frac{i\omega^2\left(\vec{e}_x + i\vec{e}_y\right)K^2}{2cz_o\omega_r(1+K^2)}\left[\left(\theta_x - \eta_x^{(c)}\right) + i\left(\theta_y - \eta_y^{(c)}\right)\right] \\
&\times \int_{-\infty}^{\infty} dl'_x \int_{-\infty}^{\infty} dl'_y \int_{-L_w/2}^{L_w/2} dz' \widetilde{\rho}\left(z', l'_x, l'_y\right)\exp\left[iC_2 z'\right] \\
&\times \exp\left\{ i\frac{\omega}{c}\left[\frac{z_o\left(\theta_x^2 + \theta_y^2\right)}{2} - \left(\theta_x l'_x + \theta_y l'_y\right)\right]\right\} \\
&\times \exp\left\{ i\frac{\omega}{2c}\left[\left(\theta_x - \eta_x^{(c)}\right)^2 + \left(\theta_y - \eta_y^{(c)}\right)^2\right] z'\right\}. \quad (2)
\end{aligned}$$

The electric field is left circularly polarized and vanishes at $\vec{\theta} = \vec{\eta}^{(c)}$. Polarization characteristics are the same as for the fundamental harmonic, although the fundamental does not vanish at $\vec{\theta} = \vec{\eta}^{(c)}$.

We conclude our analysis of NHG in helical wigglers studying on-axis harmonic generation. We can do so in all generality, i.e. for any harmonic number, with the help of Eq. (1). We set $\vec{\theta} - \vec{\eta}^{(c)} = 0$. It follows that Eq. (1) can be rewritten as

$$\begin{aligned}
\vec{\tilde{E}}_\perp &= \frac{i\omega}{cz_o}\int d\vec{l'} \int_{-L_w/2}^{L_w/2} dz' \widetilde{\rho}\left(z', \vec{l'}\right)\exp\left[iC_h z'\right] \\
&\times \left\{ \left[\frac{K}{2i\gamma}\Big(\exp[i(h+1)k_w z'] - \exp[i(h-1)k_w z']\Big)\right]\vec{e}_x \right. \\
&\left. + \left[-\frac{K}{2\gamma}\Big(\exp[i(h+1)k_w z'] + \exp[i(h-1)k_w z']\Big)\right]\vec{e}_y \right\}. \quad (3)
\end{aligned}$$

Since $\widetilde{\rho}$ is a slowly function of z' on the scale of the undulator period and $C_h \ll k_w$, we see by inspection that, after integration in dz', one obtains non-zero on-axis field only for $h = 1$. This result is in open contrast with what reported in reference [2]: we will address this fact in the discussion section.

Analysis of a simple model

We treat a particular case to exemplify our results. We consider the case when $C_2 = 0$ (i.e. $\omega = 2\omega_r$) and $\widetilde{\rho} = I_o a_2/(2\pi c\sigma_\perp^2)\exp[-l'^2_x + l'^2_y/(2\sigma_\perp^2)]\exp[i2\omega_r/c \cdot (\eta_x^{(c)} l'_x + \eta_y^{(c)} l'_y)]H_{L_w}(z)$, with H_{L_w} a window function equal unity inside the undulator and zero everywhere else. Here I_o is the bunch current, a_2 is a constant determining the strength of the bunching and $\sigma_\perp$ the rms transverse size of the electron beam. This corresponds to a modulation wavefront perpendicular to the direction of motion of the beam. Direct substitution in Eq. (2) and calculations yield

$$\begin{aligned}\vec{\vec{E}}_\perp &= \frac{2iI_o a_2 L_w \omega_r \left(\vec{e}_x + i\vec{e}_y\right)}{c^2 z_o}\left(\frac{K^2}{1+K^2}\right)\\ &\times\left[\left(\theta_x - \eta_x^{(c)}\right) + i\left(\theta_y - \eta_y^{(c)}\right)\right]\exp\left[i\frac{\omega_r}{c}z_o(\theta_x^2+\theta_y^2)\right]\\ &\times\exp\left\{-\frac{2\sigma_\perp^2\omega_r^2}{c^2}\left[\left(\theta_x-\eta_x^{(c)}\right)^2+\left(\theta_y-\eta_y^{(c)}\right)^2\right]\right\}\\ &\times\mathrm{sinc}\left\{\frac{L_w\omega_r}{2c}\left[\left(\theta_x-\eta_x^{(c)}\right)^2+\left(\theta_y-\eta_y^{(c)}\right)^2\right]\right\}. \qquad (4)\end{aligned}$$

Going back to our particular case in Eq. (4), a subject of particular interest is the angular distribution of the radiation intensity, which will be denoted with I_2. Upon introduction of normalized quantities $\hat{\theta}_{x,y} = \sqrt{2\omega_r L_w/c}\ \theta_{x,y} = \sqrt{8\pi N_w}\ \bar{\gamma}_z\theta_{x,y}$, $\hat{\eta}_{x,y}^{(c)} = \sqrt{2\omega_r L_w/c}\ \eta_{x,y}^{(c)} = \sqrt{8\pi N_w}\ \bar{\gamma}_z\ \eta_{x,y}^{(c)}$ and of the Fresnel number $N = 2\omega_r\sigma_\perp^2/(cL_w)$, one obtains

$$I_2 \propto \left|\vec{\hat{\theta}} - \vec{\hat{\eta}}^{(c)}\right|^2 \exp\left\{-N\left|\vec{\hat{\theta}} - \vec{\hat{\eta}}^{(c)}\right|^2\right\}\mathrm{sinc}^2\left\{\frac{1}{4}\left|\vec{\hat{\theta}} - \vec{\hat{\eta}}^{(c)}\right|^2\right\} \qquad (5)$$

In the limit for $N \ll 1$, Eq. (5) gives back the directivity diagram for the second harmonic radiation from a single particle. The directivity diagram in Eq. (5) is plotted in Fig. 1 for different values of N as a function of $|\vec{\hat{\theta}} - \vec{\hat{\eta}}^{(c)}|$, normalized to the maximal intensity $I_2^{\max}$ at each value of N. The next step is the calculation of the second harmonic power that is given by $W_2 = c/(2\pi)\int_{-\infty}^{\infty}dx_o\int_{-\infty}^{\infty}dy_o|\vec{\vec{E}}_\perp(z_o, x_o, y_o)|^2$. It is convenient to present the expressions for W_2 in a dimensionless form. After appropriate normalization it is a function of one dimensionless parameter only, that is $\hat{W}_2 = F_2(N) = \ln[1 + 1/(4N^2)]$. Here $\hat{W}_2 = W_2/W_o^{(2)}$ is the normalized power, while the normalization constant $W_o^{(2)}$ is given by $W_o^{(2)} = (2K^2/1+K^2)^2(I_o^2/c)a_2^2$. The function $F_2(N)$ is plotted in Fig. 2. The logarithmic divergence in $F_2(N)$ in the limit for $N \ll 1$ imposes a limit on the meaningful values of N. However, in the case $N < N_w^{-1}$ we deal with a situation where the dimensionless problem parameter N is smaller than the accuracy of the resonance approximation $\sim N_w^{-1}$, and for estimations we should replace $\ln(N)$ with $\ln(N_w^{-1})$.

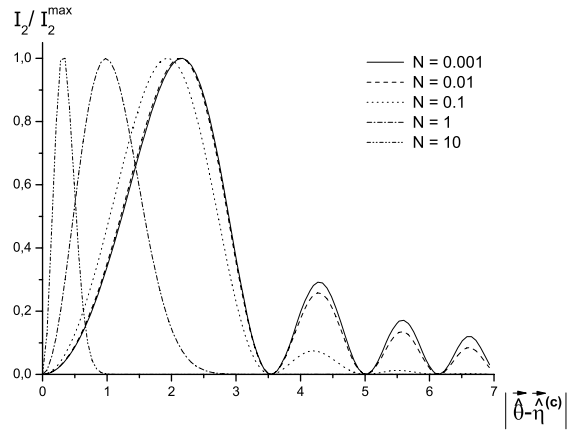

Figure 1: Directivity diagram for the intensity.

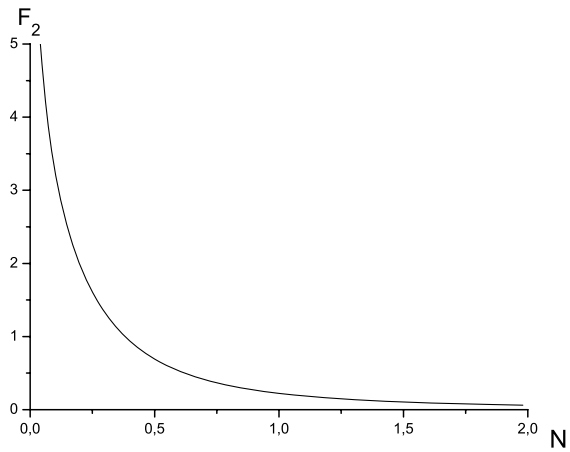

Figure 2: Illustration of the behavior of $F_2(N)$.

DISCUSSION

NHG in a helical wiggler has been addressed in [2], where a numerical study-case guarantees that paraxial and resonance approximation can be applied. The main result of [2] is that characteristics of helical undulator radiation from an extended source, i.e. a bunched electron beam, are drastically different compared to those from a single electron. In particular, NHG does not vanish on-axis, in open contrast with our conclusions. In our understanding, results in [2] are incorrect. Any linear superposition of a given field harmonic from single electrons conserves single-particle characteristics like parametric dependence on undulator parameters and polarization. In particular, since field harmonics from a single electron vanishes on-axis, they must vanish on-axis for the linear superposition as well. This also applies in the case of NHG, because the dependence of charge and current density distributions of the bunched beam on the longitudinal coordinate is slow on the scale of the undulator

period. This argument suggests that results in reference [2] are incorrect. A flaw can be pinpointed in the azimuthal resonance condition proposed in [2]: "The azimuthal electron motion in helical wigglers is $\theta = k_w z$ (k_w is the wave number for the wiggler period λ_w), which couples to circularly polarized waves that vary as $\exp(i\phi_h)$, where $\phi_h = kz + h\theta - \omega t$ is the wave phase. Hence, the phase along the particle trajectories varies as $\phi_h = (k + hk_w)z - \omega t$, and the hth order azimuthal mode corresponds to the hth harmonic resonance [i.e., $\omega \approx (k + hk_w)v_z$]". There θ indicates an azimuthal position as in Fig. 3. Note that the phase $\phi_h = kz + h\theta - \omega t$ pertains a circularly polarized wave whose electric field is written in terms of unit vectors $\vec{e}_\rho$ and $\vec{e}_\theta$ and not of $\vec{e}_x$ and $\vec{e}_y$ ($\vec{e}_\rho$, $\vec{e}_\theta$, $\vec{e}_x$ and $\vec{e}_y$ are shown in Fig. 3). In fact one may write the electric field of a (e.g. left) circularly polarized plane wave at position $\vec{r}$ and time t as $E_o(\vec{e}_r + i\,\vec{e}_\theta)\exp[i\phi_h]$, E_o being a constant field strength. We argue that it is incorrect to use relation $\theta \approx k_w z$ in the expression for ϕ_h as done in [2]. On the one hand, the radiation diffraction size for a single particle is of order $\sqrt{\lambda L_w}$. On the other hand, the electron rotation radius is given by $r_w = (K/\gamma)\lambda_w$. It follows that $r_w^2/\lambda L_w \ll 1$, that holds independently of the value of K, because $N_w \gg 1$. Thus, the electron rotation radius is always much smaller than the radiation diffraction size. Moreover, straightforward geometrical considerations show that it makes sense to talk about a transverse beam size $\sigma_\perp$ only when $\sigma_\perp^2 \gg r_w^2$. This is the case in practical situations of interest. There is still room to compare the beam size $\sigma_\perp$ with the radiation diffraction size. In the case $\sigma_\perp \ll \sqrt{\lambda L_w}$ we deal with a filament electron beam. In the opposite case the filament beam approximation breaks down. We are interested in this last case, where single-particle results cannot be used. We have therefore established a hierarchy in the characteristic scales of interest: $\sigma_\perp^2 \gtrsim \lambda L_w \gg r_w^2$. It follows that the azimuthal coordinate of each electron, θ, is fixed during the motion inside the undulator with the accuracy of the resonance approximation, scaling as $1/N_w$. In contrast to this, the identification $\theta \approx k_w z$ is made in [2]. This is a kinematical mistake. If $\theta \approx k_w z$ each electron would be rotating around the origin of the coordinate system, that is not the case. Thus, the azimuthal resonance condition is a misconception following from this mistake. This misconception is subsequently passed on to simulations in [2], resulting in incorrect outcomes. Harmonic emission exists for a single electron, and it also exists for an electron bunch. However, qualitative properties are different with respect to what has been predicted in [2]. In particular, as we have seen before, on-axis power vanishes.

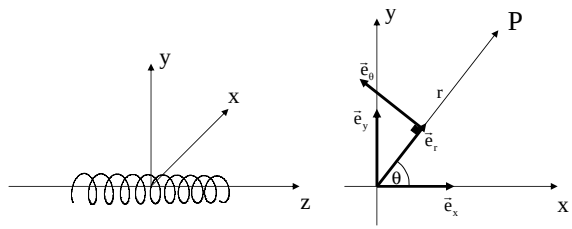

Figure 3: Cylindrical coordinate system and setup.

CONCLUSIONS

In this paper we discussed NHG in helical undulators, with particular emphasis on second harmonic generation. First we considered the NHG mechanism in helical undulators in all generality. Then we specialized our study to the case of second harmonic generation. Finally, to exemplify our results, we treated a simplified model where the beam modulation wavefront is orthogonal to the z axis, has a Gaussian transverse profile and is independent on the position inside the undulator. Our results show that on-axis harmonic generation from helical wigglers vanishes. This applies to any harmonic of interest with the exclusion of the fundamental, and independently of the form of the electron beam modulation (assuming that the electron beam as a whole propagates on-axis). Important consequences follow regarding the two mainstream development paths in FEL physics. First, as concerns short wavelength (x-ray) SASE FEL devices, vanishing on-axis harmonics make the option of a helical undulator less attractive as regards the exploitation of NHG radiation. Second, as concerns high average-power FEL oscillators, vanishing on-axis harmonics suggest that helical undulators carry relevant advantages over planar undulators, as potential for mirror damage is reduced. Previous studies reported non-vanishing on-axis power, due to the nature of a particular azimuthal resonance condition. We showed that this resonance condition is a misconception, arising from a kinematical mistake. This misconception was passed on to simulations, that confirmed the presence of on-axis power out of NHG from helical wigglers. Such result is incorrect.

For details on our work we refer the interested reader to [1].

REFERENCES

[1] G. Geloni, E. Saldin, E. Schneidmiller and M. Yurkov, preprint DESY 07-058, http://arxiv.org/abs/0705.0295, accepted for publication in Nucl. Instrum. and Methods in Phys. Res. A

[2] H.P. Freund, P.G. O'Shea and S.G. Biedron, Physical Review Letters, 94, 074802 (2005)

UNDULATOR RADIATION IN A WAVEGUIDE

G. Geloni, E. Saldin, E. Schneidmiller and M. Yurkov
Deutsches Elektronen-Synchrotron (DESY), Hamburg, Germany

Abstract

We propose an analytical characterization of undulator radiation near resonance, when the presence of the vacuum-pipe affects radiation properties, as for the far-infrared undulator beamline at FLASH, that is designed to deliver pulses in the THz range. Such line can be used for pump-probe experiments where THz pulses are naturally synchronized to the VUV pulse from the FEL, as well as the development of novel electron-beam diagnostics techniques. Since the THz radiation diffraction-size exceeds the vacuum-chamber dimensions, characterization of infrared radiation must be performed accounting for the presence of a waveguide. We developed a theory of undulator radiation in a waveguide based on paraxial and resonance approximation. We solved the field equation with a tensor Green's function technique, and extracted figures of merit describing the influence of the vacuum-pipe on the radiation pulse as a function of the problem parameters. Our theory, that makes consistent use of dimensionless analysis, allows treatment and physical understanding of many asymptotes of the parameter space, together with their region of applicability. **A more detailed report of our study is given in [1]**.

INTRODUCTION AND THEORY

The accelerator complex at FLASH produces ultrashort bunches approaching sub-100 fs duration. FLASH will soon operate together with a FIR electromagnetic undulator providing coherent FIR radiation intrinsically synchronized with the VUV pulses. The wavelength range ($\lambda = 60 \div 200$ μm) will overlap with a large part of the THz-gap. This will allow pump-probe experiments combining FIR and VUV radiation, and non-destructive electron beam diagnostics. Vacuum chamber effects are expected to play an important role at longer wavelengths. Optimization of the radiation transport system calls for a precise characterization of THz pulses along the photon beamline. In the present work we focus on the characterization of undulator radiation from a filament beam (as for the FIR line at FLASH) in presence of a waveguide. One should solve the field equations in paraxial approximation with proper boundary conditions, e.g. $\mathcal{D}[\vec{\vec{E}}_\perp(z,\vec{r}_\perp)] = \vec{f}(z,\vec{r}_\perp)$, where $(\vec{n}\times\vec{\vec{E}}_\perp)_{|_S} = 0$ and $(\vec{\nabla}_\perp\cdot\vec{\vec{E}}_\perp)_{|_S} = 0$. Here S is the internal surface of the pipe, $\mathcal{D} \equiv (\nabla_\perp{}^2 + 2i\omega/c\cdot\partial/\partial z)$, $\nabla_\perp{}^2$ being the Laplacian operator over transverse cartesian coordinates and $\vec{f} = 4\pi e/c\cdot\exp\{i\int_0^z d\bar{z}\omega/[2\gamma_z^2(\bar{z})c]\}[i\omega/c^2\cdot\vec{v}_\perp(z) - \vec{\nabla}_\perp]\delta(\vec{r}_\perp - \vec{r}'_\perp(z))$. Solution must accounting for the tensorial nature of the Green's function. In the UR case, the resonance approximation can be exploited too. We thus consider planar undulator with a large number of undulator periods and a frequency range of interest close to the fundamental harmonic, where the free-space field exhibits horizontal polarization (for undulator field in the vertical direction) and azimuthal symmetry. An explicit expression for the field is calculated as a superposition of TE and TM modes. We introduce normalized units: $\hat{\vec{\vec{E}}}_\perp = [-c^2/(A_{JJ}\omega e\theta_s)]\vec{\vec{E}}_\perp$, $\hat{C} = 2\pi N_w\Delta\omega/\omega_r$, $\hat{z} = z/L_w$, $\hat{r} = r/\sqrt{L_w\lambda\!\!\!^{-}}$, $\Omega = R^2/L_w\lambda\!\!\!^{-}$, $\hat{C}_k^\mu\mu_{1k}^2/(2\Omega)$ and $\hat{C}_k^\nu = \nu_{1k}^2/(2\Omega)$. Here $\Omega = R^2/(\lambda\!\!\!^{-}L_w)$ is the main parameter of our theory, comparing the pipe area with the radiation diffraction area, while μ_{mk} and ν_{mk} are, respectively, solutions of $J'_m(\mu_{mk}) = 0$ and $J_m(\nu_{mk}) = 0$. We obtain for $\hat{E}_{x,y}(\hat{r},\phi,\hat{z})$:

$$\hat{E}_x = i\sum_{k=1}^{\infty}\left\{\mathcal{A}_k^\mu(\hat{z})\left[J_o\left(\frac{\mu_{1k}\hat{r}}{\sqrt{\Omega}}\right) + J_2\left(\frac{\mu_{1k}\hat{r}}{\sqrt{\Omega}}\right)\cos(2\phi)\right] + \mathcal{A}_k^\nu(\hat{z})\left[J_o\left(\frac{\nu_{1k}\hat{r}}{\sqrt{\Omega}}\right) - J_2\left(\frac{\nu_{1k}\hat{r}}{\sqrt{\Omega}}\right)\cos(2\phi)\right]\right\} \quad (1)$$

and

$$\hat{E}_y = i\sum_{k=1}^{\infty}\left\{\mathcal{A}_k^\mu(\hat{z})J_2\left(\frac{\mu_{1k}\hat{r}}{\sqrt{\Omega}}\right) - \mathcal{A}_k^\nu(\hat{z})J_2\left(\frac{\nu_{1k}\hat{r}}{\sqrt{\Omega}}\right)\right\}\sin(2\phi), \quad (2)$$

where we set $\mathcal{A}_k^\mu(\hat{z}) = \hat{C}_k^\mu\exp[-i\hat{C}_k^\mu\hat{z}]/[(\mu_{1k}^2-1)J_1^2(\mu_{1k})]\,\mathrm{sinc}[1/2(\hat{C}_k^\mu + \hat{C})]$ and, moreover, $\mathcal{A}_k^\nu(\hat{z}) = \hat{C}_k^\nu\exp[-i\hat{C}_k^\nu\hat{z}]/[\nu_{1k}^2J_0^2(\nu_{1k})]\mathrm{sinc}[1/2(\hat{C}_k^\nu + \hat{C})]$. The sinc(·) functions in the expressions for $\mathcal{A}_k^{\mu,\nu}$ is consequence of instantaneous switching of the undulator field. However, our theory applies with a finite accuracy related to the use of the resonance approximation. We thus introduce a spatial frequency filter in the field by redefining

$$\mathcal{A}_k^\mu(\hat{z}) = \frac{\hat{C}_k^\mu\exp[-i\hat{C}_k^\mu\hat{z}]}{(\mu_{1k}^2-1)J_1^2(\mu_{1k})}\mathcal{F}\left\{S(\hat{z}'),\left(\hat{C}_k^\mu + \hat{C}\right)\right\} \quad (3)$$

and

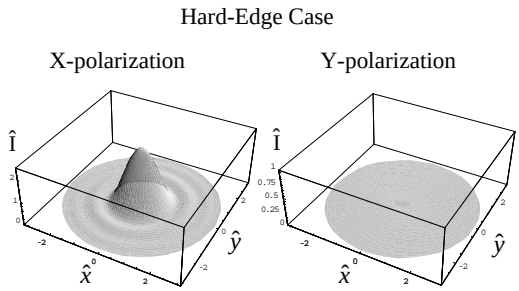

Figure 1: Three-dimensional view of the virtual source in the free-space limit for $\Delta = 0$ (hard-edge case) and $\hat{C} = 0$ (perfect resonance) .

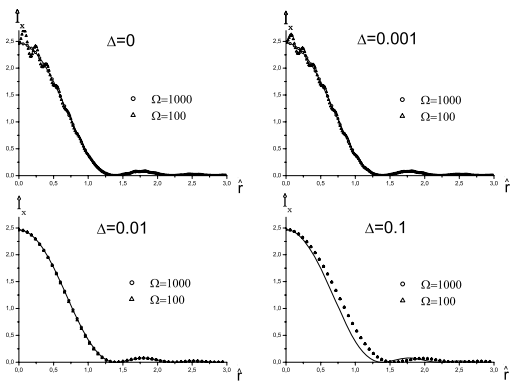

Figure 2: Intensity profiles of the virtual source ($\hat{z} = 0$) at large values of $\Omega = R^2/(\lambda L_w)$ for different values of Δ and $\hat{C} = 0$ (perfect resonance). This 2D plot is obtained cutting the 3D intensity profile at $\hat{y} = 0$ (i.e. at $\phi = 0$).

$$\mathcal{A}_k^{\nu}(\hat{z}) = \frac{\hat{C}_k^{\nu}\exp[-i\hat{C}_k^{\nu}\hat{z}]}{\nu_{1k}^2 J_0^2(\nu_{1k})}\mathcal{F}\left\{S(\hat{z}'),\left(\hat{C}_k^{\nu}+\hat{C}\right)\right\} . \qquad (4)$$

Here $\mathcal{F}\{S(\hat{z}'),(\hat{C}_k^{\mu,\nu}+\hat{C})\}$ is the Fourier transform of the function S with respect to $(\hat{C}_k^{\mu,\nu}+\hat{C})$. The where function $S(z')$ introduces some smoothing of the rectangular undulator profile on a scale of λ_w. We model $S(\hat{z}')$ as a constant function along the undulator length with exponentially decaying edges on a typical distance Δ. The value of Δ is chosen to cut off high spatial frequencies that are outside the region of applicability of the resonance approximation, i.e. $\Delta \sim 1/N_w$. A three-dimensional view of the virtual source in the middle of the undulator in the free-space limit $\Delta = 0$ (hard-edge case) is presented in Fig. 1, while intensity profiled for different values of Δ are given in Fig. 2.

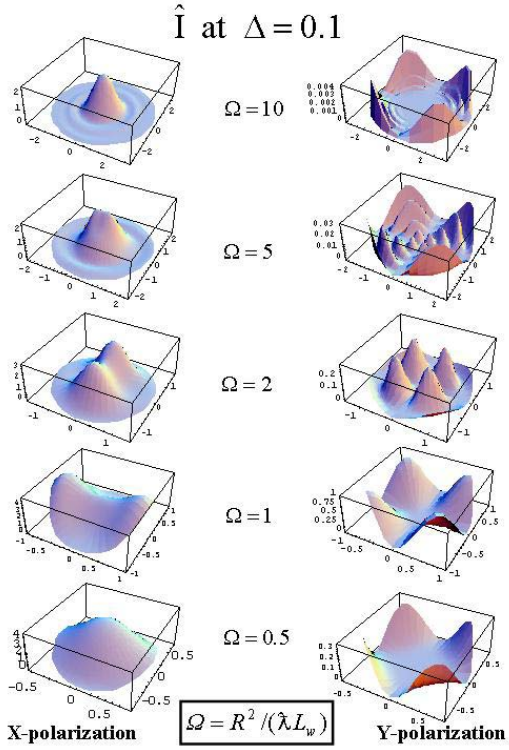

Figure 3: Intensity profiles of the virtual source ($\hat{z} = 0$) at different values of $\Omega = R^2/(\lambda L_w)$ for $\Delta = 0.1$ and $\hat{C} = 0$ (perfect resonance).

We also studied the impact of wall-resistance effects. We concluded that propagation through the pipe is strongly affected by wall-resistance effects even for relatively large values of Ω. This effect strongly depends on the material considered. Estimations allowed us to formulate the recommendation that the internal part of the vacuum pipe for the infrared undulator line at FLASH should be copper-coated.

RESULTS

Some figure of merit should be extracted from the full information carried by the expression for the field about how the metallic pipe influences radiation properties. We separately studied, for horizontal and vertical polarization components, two-dimensional intensity distributions on a transverse plane at arbitrary distance from the undulator, for different choices of the problem parameter. These plots are shown in Fig. 3 and Fig. 4. Another figure of merit of interest is the ratio between the power density for a specific value of Ω integrated over the waveguide cross-section and the angle-integrated power density in free space:

$$\hat{W} = \int d\vec{\hat{r}}_{\perp}\left|\vec{\hat{E}}_{\perp}(\Omega)\right|^2 \Big/ \left(\int d\vec{\hat{r}}_{\perp}\left|\lim_{\Omega\to\infty}\vec{\hat{E}}_{\perp}\right|^2\right) . \qquad (5)$$

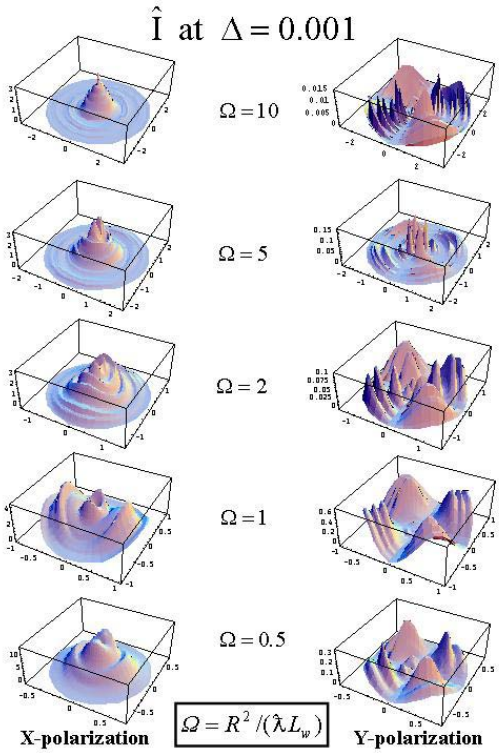

Figure 4: Intensity profiles of the virtual source ($\hat{z} = 0$) at different values of $\Omega = R^2/(\lambda L_w)$ for $\Delta = 0.001$ and $\hat{C} = 0$ (perfect resonance).

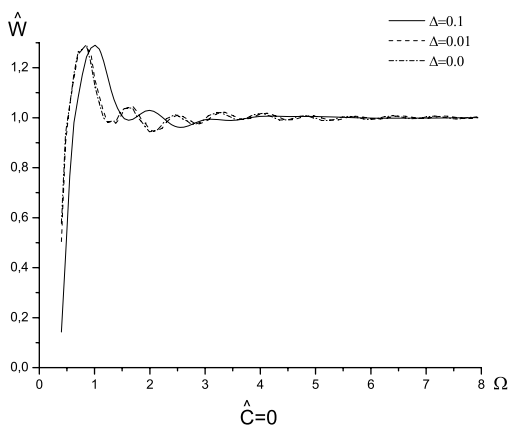

Figure 5: Plot of $\hat{W}$ as a function of $\Omega = R^2/(\lambda L_w)$ for $\hat{C} = 0$ (perfect resonance) at different values of Δ.

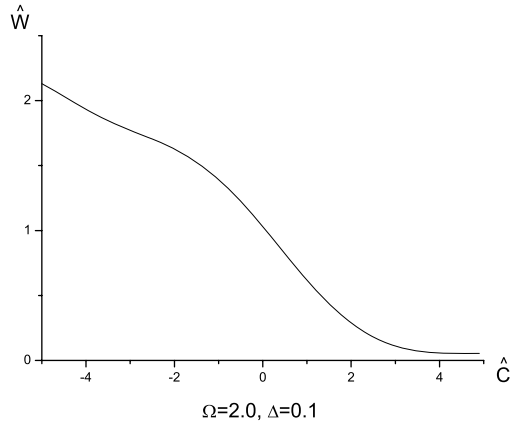

Figure 6: Plot of $\hat{W}$ as a function of $\hat{C} = 2\pi N_w \Delta\omega/\omega_r$ for $\Omega = 2.0$ at $\Delta = 0.1$.

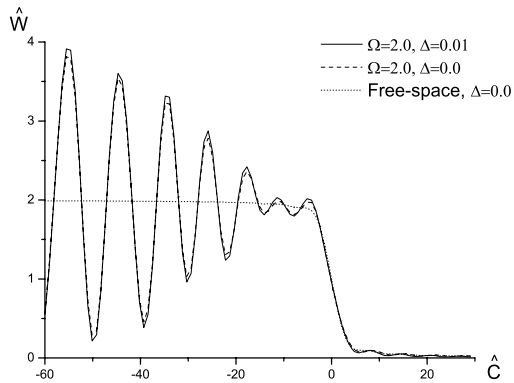

Figure 7: Plot of $\hat{W}$ as a function of $\hat{C} = 2\pi N_w \Delta\omega/\omega_r$ for $\Omega = 2.0$ at different values of $\Delta = 0.01$ and $\Delta = 0$. The far-field limit ($\Omega \longrightarrow \infty$) is also shown for comparison (dotted line).

We studied $\hat{W}$ as a function of Ω at perfect resonance (see Fig. 5). Conversely, once Ω is fixed, one can investigate how the total power changes as a function of the detuning from resonance (see Fig. 6 and 7).

We also proposed a comparison between the magnitude of the horizontally and vertically polarized fields, defined as

$$P_x(\hat{r}) = \mathrm{Abs}\left[\hat{E}_x(\hat{r}, 0, 0)\right]\Big|_{\Omega\longrightarrow\infty} \tag{6}$$

and

$$P_y(\hat{r}, \Omega) = \mathrm{Abs}\left[\hat{E}_y\left(\hat{r}, \frac{\pi}{4}, 0\right)\right]\Big|_{\Omega} . \tag{7}$$

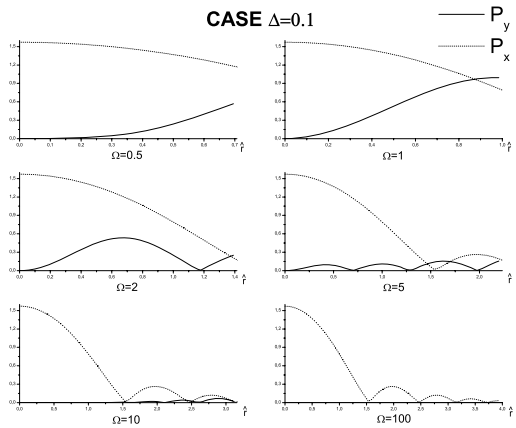

Figure 8: Comparison of P_x (dotted line) and P_y (solid line) for $\Delta = 0.1$ at different values of $\Omega = R^2/(\lambda L_w)$ and $\hat{C} = 0$ (perfect resonance). Plots refer to the virtual source position ($\hat{z} = 0$).

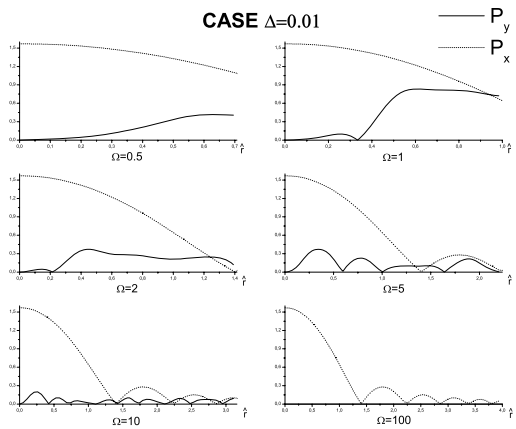

Figure 9: Comparison of P_x (dotted line) and P_y (solid line) for $\Delta = 0.01$ at different values of $\Omega = R^2/(\lambda L_w)$ and $\hat{C} = 0$ (perfect resonance). Plots refer to the virtual source position ($\hat{z} = 0$).

Plots are given in Fig. 8 and Fig. 9.

Finally, evolution of the intensity profiles at $\Omega = 2$ and $\hat{C} = 0$ is given in Fig. 9.

CONCLUSIONS

We presented a theory of undulator radiation within a waveguide and we exemplified it in the case of the infrared undulator beamline at FLASH. Relation between current electromagnetic sources and field is more complicated with respect to the free-space case. Analysis of the problem is performed with the help of

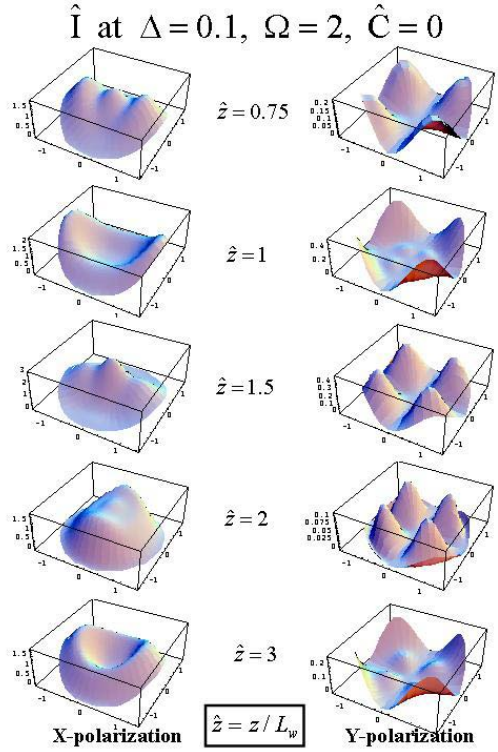

Figure 10: Intensity profiles at different values of $\hat{z} = z/L_w$ for $\Omega = 2$, $\hat{C} = 0$ (perfect resonance) and $\Delta = 0.1$.

a tensor Green's function, complicating equations that now depend on the undulator type and on the waveguide geometry. We treated a circular waveguide in particular, and we implemented the planar undulator case within the applicability region of the resonance approximation. The electric field was found as a superposition of the waveguide modes, and was studied for different values of parameters. The main parameter involved in the problem is the waveguide parameter Ω. When Ω is comparable, or smaller than unity, waveguide effects become important, under the assumption of a perfect conductor.

For details on our work we refer the interested reader to [1].

REFERENCES

[1] G. Geloni, E. Saldin, E. Schneidmiller and M. Yurkov,submitted to Elsevier Science, also DESY 07-31 (2007) http://arxiv.org/abs/physics/0703049.

THREE-DIMENSIONAL ANALYSIS OF THE SURFACE MODE SUPPORTED BY A REFLECTION GRATING *

Vinit Kumar†, RRCAT, Indore, M.P. 452013, India
Kwang-Je Kim, ANL, Argonne, IL 60439, USA

Abstract

In a Smith-Purcell Free-Electron Laser (SP-FEL), the electron beam interacts with the surface mode supported by a metallic reflection grating to produce coherent radiation. All the previous analyses of SP-FEL had considered the localization of the surface mode only in the direction perpendicular to the grating surface and assumed translational invariance along the direction of grooves of the grating. In this paper, we include the localization of the surface mode along the direction of grooves as well and study the three-dimensional structure of the surface mode in order to include diffraction effects in the analysis of SP-FELs. Full three-dimensional Maxwell-Lorentz equations are derived for the self-consistent nonlinear analysis of SP-FELs.

INTRODUCTION

Smith-Purcell Free-Electron Laser (SP-FEL) is seen as an attractive option for a compact coherent terahertz source using low energy electron beam. In an SP-FEL, coherent electromagnetic radiation is generated due to the interaction of an electron beam with the surface electromagnetic mode supported by a reflection grating. Several authors have recently studied this interaction using analytical as well as numerical techniques [1-4]. In all the previous analyses, the three-dimensional effects have been either ignored or included only approximately. This is because these analyses consider the interaction of the electron beam with the two-dimensional surface mode, where the electromagnetic field has no variation along the direction of grooves of the reflection grating. The two-dimensional surface mode is therefore not localized in the direction of grooves, although it is localized in the direction perpendicular to the grating surface. We call such surface modes as nonlocalized surface modes in this paper. The diffraction of surface mode along the direction of grooves, which affects the overlap with the electron beam and hence the build-up of power is therefore not included in these analyses. It is important to include three-dimensional effects in the analysis to accurately study the performance of the system and also to accurately calculate the start current, which is the threshold electron beam current for coherent growth of power. In this paper, we study the three-dimensional surface mode, which is localized in both the transverse directions that are perpendicular to the direction of propagation. We also discuss the coupled Maxwell-Lorentz equation to describe the interaction of the electron beam with the three-dimensional surface mode.

In the next section, we discuss the dispersion relation of an off-axis nonlocalized surface mode supported by a reflection grating. The construction of three-dimensional localized surface mode using a combination of off-axis nonlocalized modes is discussed in the following section. Maxwel-Lorentz equation for the interaction of the electron beam with the three-dimensional surface mode is discussed after that and finally, we present some conclusions in the last section.

DISPERSION RELATION OF A SURFACE MODE PROPAGATING OFF-AXIS

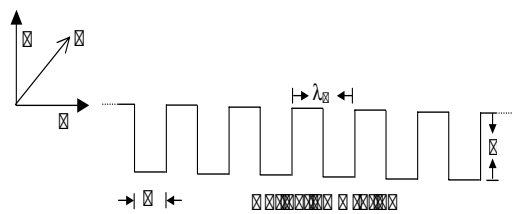

Figure 1: Schematic of a rectangular reflection grating. The top surface of the grating is in the plane y = 0.

Figure 1 shows the schematic of a rectangular metallic reflection grating having period λ_g, groove depth d, and groove width w. We want to study the self-consistent electromagnetic field supported by this structure. All the previous analyses of this problem assumed the system to have translational invariance in the x-direction and hence these are two-dimensional analyses. Here, we assume an exp($ik_x x$) type variation in EM field along the x-direction. In order to find out the dispersion relation of the surface mode, we follow our earlier approach [3, 5], where the surface mode appears in terms of singularities of the reflection matrix $\underline{\mathcal{R}}$. The EM field in the region $y > 0$ is composed of the incident and reflected wave having the following Floquet-Bloch expansion for the H-polarization:

$$H_x^I = \sum_{n=-\infty}^{+\infty} A_n^I \exp\left(ik_n z + ik_x x - ip_n y - i\omega t\right), \quad (1)$$

$$H_x^R = \sum_{n=-\infty}^{+\infty} A_n^R \exp\left(ik_n z + ik_x x + ip_n y - i\omega t\right). \quad (2)$$

* Work supported by the U.S. Department of Energy, Office of Science, Office of Basic Energy Sciences, under Contract No. DE-AC02-06CH11357.

† vinit@cat.ernet.in

Here n is the spectral order, $A_n^R = \sum \mathcal{R}_{nm} A_m^I$, $k_n = k_z - nk_g$, $k_z = k/\beta$, $k = \omega/c$, $k_g = 2\pi/\lambda_g$, $p_n = i\Gamma_n = \sqrt{k^2 - k_x^2 - k_n^2}$, and the sign of the square root is chosen such that $[\mathrm{Re}(p_n) + \mathrm{Im}(p_n)] \geq 0$, which is essentially the outgoing wave condition [6]. The phase velocity of the zeroth-order component along the z-axis is β in the unit of the speed of light c. Note that the plane wave components described by Eqs. (1-2) are in general, propagating off-axis in the xz plane. The total electromagnetic field $\vec{E}$ and $\vec{H}$ in the region $y > 0$ is obtained by combining the contribution from the incident and reflected waves. In addition to H_x, the EM field will have E_z, E_y, H_z and H_y components also. Defining $\vec{E} = \vec{\mathcal{E}}(y,z)\exp(ik_x x - i\omega t)$ and $\vec{H} = \vec{\mathcal{H}}(y,z)\exp(ik_x x - i\omega t)$, these components are given by [7]

$$(k^2 - k_x^2)\mathcal{E}_z = -i\omega\mu_0(\partial\mathcal{H}_x/\partial y), \quad (3)$$

$$(k^2 - k_x^2)\mathcal{E}_y = i\omega\mu_0(\partial\mathcal{H}_x/\partial z), \quad (4)$$

$$(k^2 - k_x^2)\mathcal{H}_z = ik_x(\partial\mathcal{H}_x/\partial z), \quad (5)$$

$$(k^2 - k_x^2)\mathcal{H}_y = ik_x(\partial\mathcal{H}_x/\partial y), \quad (6)$$

where μ_0 is the permeability of vacuum. Note that since we are considering H-polarization as opposed to E-polarizationn due to its strong interaction with co-propagating electron beam, we take E_x = 0.

The electromagnetic field inside the grooves can be expressed as a superposition of cavity modes, and the expression for $\mathcal{H}_x$ in the M^{th} groove $(M\lambda_g + b < z < M\lambda_g + \lambda_g)$, where $b = \lambda_g - w$ can be written as [8]

$$\mathcal{H}_x^{(M)} = \sum_{s=0}^{\infty} A_s^{(M)} \cos[q_s(z - z_M)]cos[Q_s(y + d)], \quad (7)$$

where $q_s = \pi s/w, Q_s = [k^2 - k_x^2 - q_s^2]^{1/2}, z_M = M\lambda_g + b$. The remaining components of EM field inside the groove can be determined in the same way as described above by Eqs. (3-6). In the metallic portion of the grating, the electromagnetic field can be assumed to be vanishing. The following expression for the reflection matrix $\underline{\mathcal{R}}$ is obtained by satisfying the boundary condition at the interface y=0 for E_z and H_x:

$$\underline{\mathcal{R}} = (\underline{I} + \underline{Z})^{-1}(\underline{I} - \underline{Z}), \quad (8)$$

where $\underline{I}$ is the identity matrix and $\underline{Z}$ is the impedance matrix given by

$$Z_{mn} = -\frac{w}{\lambda_g}\frac{1}{\Gamma_m}\sum_{s=0}^{\infty}\frac{Q_s\tan(Q_s d)}{g_s} \times \mathcal{L}(p_n;s)\mathcal{L}^*(p_m;s). \quad (9)$$

Here, $\mathcal{L}^*$ in the complex conjugate of $\mathcal{L}$, $g_0 = 1, g_{s\neq 0} = 1/2$, and $\mathcal{L}$ is given by

$$\mathcal{L}(p_m;s) = e^{ik_m b}\frac{1}{2}\left[e^{-i\theta_-}\frac{\sin\theta_-}{\theta_-} + e^{-i\theta_+}\frac{\sin\theta_+}{\theta_+}\right],$$

where $\theta_{\pm} = (-wk_m \pm \pi s)/2$. The above expression for $\underline{\mathcal{R}}$ has the same form as given in Ref. [8] except that it is now generalized to include non-zero value of k_x. We make an important observation here that the effect of introducing a finite value of k_x is that ω in earlier expression simply gets replaced with $\sqrt{\omega^2 - c^2k_x^2}$. With the help of this replacement rule, we can use the earlier calculation performed for the k_x = 0 case even for a finite k_x case.

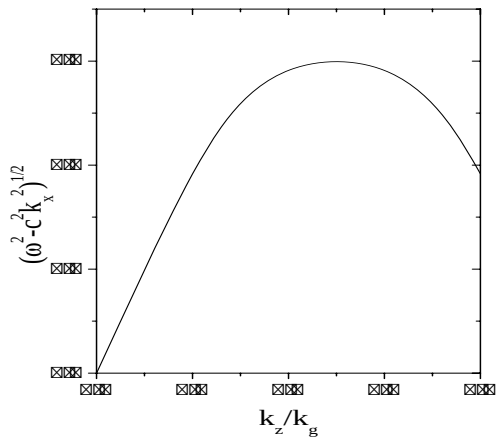

Figure 2: Typical dispersion relation for a rectangular reflection grating for a surface mode propagating off-axis.

Next, we discuss the dispersion relation of the surface mode. The surface mode appears as a singularity in the reflection matrix. For example, for a given value of ω and k_x, we can find a value of k_z for which the reflection matrix becomes singular. This means that reflected components given by Eq. (2) are supported self-consistently by the grating without the need of incident waves. Also, the reflected components corresponding to different values of n in Eq. (2) add in a certain fixed ratio of amplitudes such that the boundary conditions are satisfied on the grating surface [3]. In this way, by studying the singularity of $\underline{\mathcal{R}}$, we can find out the dispersion relation of the surface mode. We have earlier discussed the calculation of dispersion relation for k_x = 0 case in Refs. [3,5]. The same calculation can be used to get the dispersion relation for a finite k_x case, using the replacement rule that we have discussed in this section. Fig. 2 shows a typical dispersion relation plotted for a certain set of grating parameters. For a given value of ω and k_x, there is a certain fixed value of k_z and also the values of A_n/A_0 for all values of n are fixed and can be calculated. As has been discussed earlier [1, 3], the group velocity of the surface mode co-propagating with low energy electron beam is negative, meaning that the energy flows backward if the phase velocity is in the forward direction.

Hence, in this section, we have discussed surface mode which propagates off-axis, but is still nonlocalized in the x direction. In the next section, we use this to construct a set of fully localized surface modes.

THREE-DIMENSIONAL STRUCTURE OF THE LOCALIZED SURFACE MODE

In the last section, we have discussed the surface mode that is composed of plane waves which propagate, in general, off-axis in the xz plane. We can combine such surface modes with suitable weight function in k_x to obtain a mode that is localized in the x direction as follows

$$E_z^T = \sum_n \int dk_x A_n(k_x) \exp(ik_n z + ik_x x - \Gamma_n y). \quad (10)$$

Note that it is here understood that all the field quantities have $\exp(-i\omega t)$ type time dependence. Here, E_z^T stands for the total longitudinal electric field and Γ_n is real, meaning that the field decays and is localized in the y direction. Note that for a given k_x, the relative magnitudes of the amplitude A_n (i.e., the ratio A_n/A_0 for all values of n) as well as the relation between k_z and ω can be calculated as mentioned in the last section. The k_z and Γ_n are therefore functions of k_x in the above integral for a given value of ω. In the above expression, only the zeroth-order component corresponding to $n = 0$ term interacts strongly with the co-propagating electron beam and we will therefore focus on this term only in the remaining of the paper. However, all other components are present there with an amplitude in a fixed ratio with the amplitude of the zeroth-order component such that boundary conditions are satisfied at the grating surface.

Let us introduce the angle ϕ in the xz plane via $k_x = k_z \sin\phi$. Under the paraxial approximation $\phi \ll 1$, we obtain the following expressions for the ϕ-dependence of k_z and Γ_0:

$$k_z(\phi) = k_z(1 + \frac{\phi^2}{2\beta\beta_g}), \quad (11)$$

$$\Gamma_0(\phi) = \Gamma_0 + \frac{k_z^2\phi^2}{2\Gamma_0}(1 + \frac{1}{\beta\beta_g}), \quad (12)$$

where we have simplified the notations by writing $k_z = k_z(0)$ and $\Gamma_0 = \Gamma_0(0)$. Here β_g is the magnitude of the group velocity ($d\omega/dk_z$ for $k_x = 0$) of the surface mode in the unit of c. As mentioned earlier, the group velocity is negative. We can substitute the above expressions for k_z and Γ_0 in the Eq. (10) and only retain the $n = 0$ term and get the following expression for the field in the zeroth-order component:

$$E_z^0 = e^{-\Gamma_0 y} e^{ik_z z} \int \underbrace{A_0(\phi) e^{i\frac{k_z\phi^2 z}{2\beta\beta_g}} e^{-\frac{k_z^2\phi^2}{2\Gamma_0}(1+\frac{1}{\beta\beta_g})y}}_{\times e^{ik_z\phi x} d\phi.} \quad (13)$$

We note that E_z^0 appears as a Fourier transform in ϕ of the underbraced term in the above expression. We can take the orthonormal set of Gauss-Hermite functions for $A_0(\phi)$ and obtain a set of Gauss-Hermite orthonormal surface modes which are localized in the x direction. This is exactly the same way in which one can get the localized Gauss-Hermite modes for a laser beam in free space [9]. Here, we consider only the fundamental Gaussian mode by choosing $A_0(\phi) = \exp(-\phi^2/4\sigma_\phi^2)$ for which we obtain the following expression for the rms beam size Σ_x [10]

$$\Sigma_x^2(y;z) = \Sigma_x^2(y;0) + \Sigma_\phi^2(y) z^2. \quad (14)$$

Note that the above equation is in the form of paraxial diffraction with a waist at z = 0, the rms waist beam size of $\Sigma_x(y;0)$, and an rms diffraction angular divergence of $\Sigma_\phi(y)$. The quantities on the right-hand side of Eq. (14) are determined by the following relations:

$$\Sigma_x^2(y;0) = \sigma_x^2 + \frac{y}{2\Gamma_0}(1 + \frac{1}{\beta\beta_g}), \quad (15)$$

$$\sigma_x\sigma_\phi = \frac{1}{2k_z}, \quad (16)$$

$$\Sigma_x(y;0)\Sigma_\phi(y) = \frac{1}{2k_z\beta|\beta_g|} = \frac{\lambda}{4\pi|\beta_g|}. \quad (17)$$

These reduce to the well-known relations between the rms size and angular divergence in free space when $|\beta_g| = 1$. Eq. (14) can also be written in a form familiar in paraxial optics discussions:

$$\Sigma_x^2(y;z) = \frac{\lambda}{4\pi|\beta_g|}(Z_R + \frac{z^2}{Z_R}), \quad (18)$$

where the Rayleigh range Z_R is given by

$$Z_R = \frac{4\pi|\beta_g|}{\lambda}\Sigma_x^2(y;0). \quad (19)$$

We have thus derived in this section the three-dimensional structure of fully localized surface mode. The fundamental Gaussian mode is discussed in detail and the analysis can be easily extended to derive the structure of higher order Gauss-Hermite surface modes. Note that compared to Gauss-Hermite modes propagating in free space, the wavelength λ is here replaced with λ/β_g.

THREE-DIMENSIONAL MAXWELL-LORENTZ EQUATIONS

We now discuss the interaction of the localized mode that we discussed in the last section with the co-propagating electron beam. For the two-dimensional case, where the system is assumed to have translational invariance in the x direction, we had earlier derived the coupled nonlinear Maxwell-Lorentz equation for the interaction of the surface mode with the sheet electron beam [3]. Using the Maxwell equation with the source term and using the slowly varying envelope approximation and the paraxial approximation, we can write down the equation for the evolution of the electromagnetic field given by Eq. (13). Leaving the details of the derivation to another publication [11], we present here the final result:

$$\frac{\partial E_z}{\partial z} - \frac{1}{2i\beta\beta_g k_z}\frac{\partial^2 E_z}{\partial x^2} - \frac{1}{\beta_g c}\frac{\partial E_z}{\partial t} = \frac{Z_0\chi}{2\beta\gamma}\int dy j_z e^{-\Gamma_0 y}\langle e^{-i\theta}\rangle, \quad (20)$$

where $Z_0 = 377\Omega$ is the characteristic impedance of free space, χ is the residue of the singularity associated with the surface mode as defined in Ref. [3], j_z is the electron volume current density at the given location, θ is the phase of the electron and $\langle \cdots \rangle$ denotes averaging over electrons. Note that E_z is the amplitude of the electric field in the zeroth-order component of the surface mode at the grating surface, i.e., $y = 0$. Once E_z is known, one can calculate $A_0(\phi)$ using Eq. (13) and then as discussed earlier in this paper, we can calculate $A_n(\phi)$ for all n. Substituting these in Eq. (10), we get the total electromagnetic field. Note that by construction, this electromagnetic field satisfies the boundary condition on the grating surface and also evolves due to interaction with co-propagating electron beam as given by Eq. (20). It is interesting to observe that the structure of this equation is similar to that for the case of conventional FELs. The second term on the left side this equation represents diffraction and compared to the conventional FEL case, here λ is replaced with $\beta_g \lambda$. This is same as we observed in the last section, where the same replacement occurs in the formula for the Rayleigh range in Eq. (19).

The equation for the evolution of phase and energy of the electrons, as derived earlier [3] are given by

$$\frac{1}{\beta c}\frac{\partial \gamma_i}{\partial t} + \frac{\partial \gamma_i}{\partial z} = \frac{eE_z}{mc^2} e^{i\psi_i} + c.c, \qquad (21)$$

$$\frac{1}{\beta c}\frac{\partial \theta_i}{\partial t} + \frac{\partial \theta_i}{\partial z} = \frac{k}{\beta^3 \gamma^2}\frac{(\gamma_i - \gamma_p)}{\gamma_p}, \qquad (22)$$

where γ_p is the energy of the electron resonant with the surface mode in the unit of rest mass energy, γ_i is the energy of the i^{th} electron in the unit of rest mass energy and θ_i is the phase of i^{th} electron. Note that here we have ignored space-charge term in Eq. (21) for simplicity. Eqs. (20-22) are the coupled three-dimensional time-dependent Maxwell-Lorentz equations, which describe the interaction between the surface mode and the electron beam. If there are focusing forces, there will be equations for the evolution of transverse dynamical variables of electrons, in addition to Eqs. (21-22).

Finally, we give the expression for the power flowing in the surface mode in the backward direction. In general, power will flow along x direction also in addition to z direction in 3-D case. However, under paraxial approximation, we can assume that power flowing along the x direction is not very significant. The expression for the power P flowing along the (negative) z direction, which is further generalization of the expression obtained for 2-D case in Refs. [3,12] is given by

$$P = 2\frac{\beta\gamma}{Z_0 \chi}\int |E_z|^2 dx. \qquad (23)$$

Note that the above expression is for the total power corresponding to EM field in all the components corresponding to diiferent values of n in Eq. (10).

CONCLUSIONS

In this paper, we have discussed the three-dimensional surface electromagnetic modes supported by a reflection grating that are localized along the direction of grooves as well as in the direction perpendicular to the grating surface. We have then discussed the nonlinear three-dimensional time-dependent coupled Maxwell-Lorentz equations for the interaction of the surface mode with the electron beam. These equations can be numerically solved to study the evolution of power in an SP-FEL taking diffraction effects into account, which has so far not been accurately studied. We can linearize the corresponding Maxwell-Vlasov equation and solve it approximately to get an analytic expression for start current taking three-dimensional effects into account. This will be taken up in the future.

REFERENCES

[1] H. L. Andrews and C. A. Brau, Phys. Rev. ST Accel. Beams 7 (2004) 070701.

[2] J. T. Donohue and J. Gardelle, Phys. Rev. ST Accel. Beams 8 (2005) 060702.

[3] V. Kumar and K.-J. Kim, Phys. Rev. E 73 (2006) 026501.

[4] D. Li et al., Phys. Rev. ST Accel. Beams 9 (2006) 040701.

[5] V. Kumar and K.-J. Kim, Proceedings of PAC05 (2005) 1616.

[6] *Electromagnetic Theory of gratings*, edited by R. Petit (Springer-Verlag, Berlin, 1980).

[7] P. M. Van den berg, Appl. Sci. Res. 24, (1971) 261.

[8] L. Schachter and A. Ron, Phys. Rev. A 40, (1989) 876.

[9] A. Seigman, *Lasers*, University Science Books, Sausalito, 1986.

[10] K.-J. Kim and V. Kumar, to appear in Phys. Rev. ST Accel. Beams.

[11] V. Kumar and K.-J. Kim, under preparation.

[12] V. Kumar and K.-J. Kim, Proceedings of FEL05 (2005) 274.

COMPARISION BETWEEN KINETIC AND FLUID DESCRIPTION OF PLASMA-LOADED FREE-ELECTRON LASER

B. Maraghechi* , S. Babaei, Department of Physics, Amirkabir University of Technology, P.O. Box 15875-4413, Tehran, Iran

Abstract

In the kinetic treatment of the plasma-loaded FEL single particle equation of motion for both beam and plasma electrons in the radiation fields are used. Therefore, interaction terms between the wiggler and the space-charge wave, in the transverse velocity of electrons, which are important elements in the fluid model, are neglected. A dispersion relation of a plasma-loaded FEL with kinetic theory is used that takes into account the velocity spread of both beam and plasma electrons. In the present analysis a dispersion relation is obtained, by the fluid theory, with the interaction terms between the wiggler and the space-charge wave in the transverse velocity of electrons taken into account. Since these interaction terms are inherently missing in the kinetic theory the two dispersion relation are compared to find out about the importance of these terms. It was found that although the absence of these terms has considerable effects on the growth rate, the general kinetic dispersion relation may be used to study the temperature effects of a warm beam/plasma on the instability of a free-electron laser with a plasma background.

INTRODUCTION

The effects of background plasma on the interaction of electrons with the radiation have been of considerable interest in devices for the generation of coherent electromagnetic radiation. There are several investigations on the plasma loaded FEL[1-11]. A kinetic dispersion relation (DR) of a plasma loaded FEL is derived in Ref. 1 that takes into account the velocity spread of both beam and plasma electrons

In all of the above fluid methods[1-9] and in the kinetic treatments,[1,12,13] of the plasma- loaded FEL, single particle equation of motion for beam or plasma electrons in the radiation fields are considered. Therefore, interaction terms between the wiggler and the space-charge wave, in the transverse velocity of electrons, which are important elements in the fluid model, are neglected.

In the present work, the kinetic theory of Ref. 1 and its DR of a plasma-loaded FEL is considered. Since in this kinetic model single particle treatment of electrons in the radiation field is inherent in the theory a fluid model is used to find a DR that takes into account the interaction terms between the wiggler and the space-charge wave in the transverse velocity of electrons. The fluid DR is compared with the kinetic DR to find the importance of these interaction terms. It is found that the absence of these interaction terms in the kinetic treatment has considerable effects on the growth rate. However, characteristic behaviour of the kinetic DR is found to be satisfactory and, consequently, the general kinetic DR may be used to study the temperature effects of a warm beam/plasma on the instability of a plasma–loaded FEL.

KINETIC DESCRIPTION

Consider a relativistic electron beam propagating in the z direction through background plasma and a helical wiggler magnetic field. A general DR for a plasma-loaded FEL, using kinetic theory, is derived in Ref. 1 as

$$c^2k^2D^L(k,\omega)D^T(k-k_0,\omega)D^T(k+k_0,\omega)$$
$$=\frac{1}{2}a_w^2[D^T(k-k_0,\omega)+D^T(k+k_0,\omega)]\times$$
$$\times\{[\chi^{(1)}(k,\omega)]^2-c^2k^2D^L(k,\omega)[\alpha_3\omega_b^2+\chi^{(2)}(k,\omega)]\}. \qquad (1)$$

In order to compare the kinetic DR with that of the fluid model a relatively weak wiggler is assumed. In this case, the resonant space-charge wave $D^L(k,\omega)\approx 0$ couples to the resonant right circular wave $D^T(k-k_0,\omega)\approx 0$, which leaves the left circular wave nonresonant, i.e., $D^T(k+k_0,\omega)\neq 0$. Moreover, terms containing a_w^2 are also neglected in the coupled equations and the cold beam and plasma is assumed to obtain the following DR

$$(\omega^2-c^2k_r^2-\frac{\omega_b^2}{\hat{\gamma}_b}-\omega_p^2)(1-\frac{\omega_b^2}{\hat{\gamma}_b\gamma_z^2[\omega-kV_{\|}]^2}-\frac{\omega_p^2}{\omega^2})$$
$$=\frac{1}{2}a_w^2\frac{\omega_b^4}{\hat{\gamma}_b^4}\frac{(\omega\beta_{\|}-ck)^2}{(\omega-kV_{\|})^4}, \qquad (2)$$

where, $k_r=k-k_0$ is the radiation wave number and all other quantities are defined in Sec. III and in Ref. 1. Kinetic model DR (2) has been solved numerically to find the imaginary part of the frequency. Figure 1 shows the variation of growth rate with radiation wave number for $B_w=1$ kG, $\hat{\gamma}_b=4$, and $\hat{n}_b=1\times10^{13}$ cm^{-3}. Curves 1, 2, 3, 4, and 5 corresponding to the density of background plasma at 0.8, 1.25, 1.75, 2, and 2.3, respectively (in units of 10^{13} cm^{-3}).

FLUID DESCRIPTION

We now consider the fluid theory description of a relativistic and cold electron beam that passes through a background plasma and a static helical wiggler magnetic

* Electronic mail: behrouz@aut.ac.ir

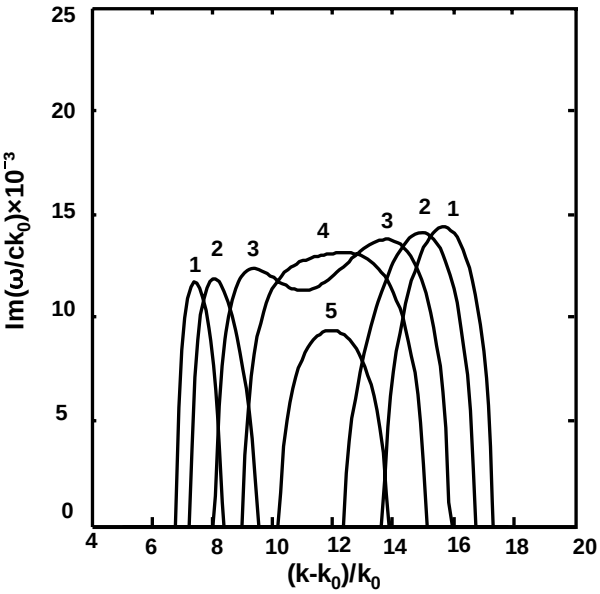

Fig. 1. Kinetic-model growth rate verses radiation wave number

field $\mathbf{B}_w$. The unperturbed state consists of

$$\mathbf{B}_w = B_w(\hat{\mathbf{e}}_x + i\hat{\mathbf{e}}_y)\exp(ik_0 z) + c.c., \quad (3)$$

$$\mathbf{v}_w = v_w(\hat{\mathbf{e}}_x + i\hat{\mathbf{e}}_y)\exp(ik_0 z) + c.c., \quad (4)$$

with equilibrium velocity given by $\mathbf{v}_w + \mathbf{v}_\parallel$, where $v_w = -eB_w/\hat{\gamma}_b mck_0$ is the transverse velocity and $\hat{\gamma}_b = [1-(v_w^2+v_z^2)/c^2]^{-1/2}$ is the total beam electron energy.

The perturbation quantities associated with the right circularly polarized electromagnetic wave (radiation) and the space-charge wave are

$$\delta\mathbf{E},\ \delta\mathbf{B},\ \delta\mathbf{A} \sim (\hat{\mathbf{e}}_x - i\hat{\mathbf{e}}_y)\exp[i(k_r z - \omega t)], \quad (5)$$

$$\delta\mathbf{E}_z,\ \delta\mathbf{v}_{bz},\ \delta\mathbf{v}_{pz},\ \delta n_b,\ \delta n_p \sim \exp[i(kz - \omega t)], \quad (6)$$

where $k = k_r + k_0$. In Eq. (5) subscripts minus, like δA_-, is removed in transverse field quantities for brevity. The relativistic momentum equation in the lab frame, for the electron beam,

$$m\gamma_b\frac{d\mathbf{v}}{dt} + m\mathbf{v}\frac{d\gamma_b}{dt} = -e\mathbf{E} - \frac{e}{c}(\mathbf{v}\times\mathbf{B}), \quad (7)$$

with

$$\frac{d}{dt}\gamma_b = -\frac{e}{mc^2}(\mathbf{v}.\mathbf{E}), \quad (8)$$

can be linearized using the linearized relativistic factor

$$\gamma_b = \hat{\gamma}_b + \frac{\hat{\gamma}_b^3}{c^2}(\mathbf{V}_\parallel.\delta\mathbf{v}_{bz} + \mathbf{v}_w.\delta\mathbf{v}_{b\perp}). \quad (9)$$

The transverse component of the momentum equation for the electron beam and plasma will be found as follows

$$\hat{\gamma}_b m(\frac{\partial}{\partial t} + V_\parallel\frac{\partial}{\partial z})\delta\mathbf{v}_{b\perp} + \hat{\gamma}_b m\delta v_{bz}\frac{\partial}{\partial z}\mathbf{v}_w^*$$

$$+m\hat{\gamma}_b^3\frac{V_\parallel}{c^2}(\mathbf{V}_\parallel.\delta\mathbf{v}_{bz} + \delta\mathbf{v}_{b\perp}.\mathbf{v}_w)\frac{\partial}{\partial z}\mathbf{v}_w^* - \frac{e}{c^2}\mathbf{v}_w^*(\mathbf{v}_w.\delta\mathbf{E}_r)$$

$$= \frac{e}{c}(\frac{\partial}{\partial t}\delta\mathbf{A} - \mathbf{V}_\parallel\times\delta\mathbf{B} - \delta\mathbf{v}_{bz}\times\mathbf{B}_w^*), \quad (10)$$

$$m\frac{\partial}{\partial t}\delta\mathbf{v}_{p\perp} = \frac{e}{c}(\frac{\partial}{\partial t}\delta\mathbf{A} - \delta\mathbf{v}_{pz}\times\mathbf{B}_w^*). \quad (11)$$

Neglecting the terms proportional to a_w^2, Eqs. (10) and (11) will yield

$$\delta v_{b\perp} = \frac{e}{\hat{\gamma}_b mc}\delta A - \frac{\hat{\gamma}_b\beta_{ze}^2 ck_0 a_w^*}{\sqrt{2}(\omega - k_r V_\parallel)}\delta v_{bz}, \quad (12)$$

$$\delta v_{p\perp} = \frac{e}{mc}\delta A + \frac{ck_0 a_w^*}{\sqrt{2}\omega}\delta v_{pz}, \quad (13)$$

where $a_w = eB_w/mc^2k_0$.

The wave equation for the radiation field is

$$(\omega^2 - c^2k_r^2)\ \delta\mathbf{A} = 4\pi c\delta\mathbf{J}_\perp, \quad (14)$$

where $\delta\mathbf{J}_\perp = e\hat{n}_b\delta\mathbf{v}_{b\perp} + e\hat{n}_p\delta\mathbf{v}_{p\perp} + e\delta n_b\mathbf{v}_w$, δn_b is the electron beam density, and $\mathbf{v}_w$, $\delta\mathbf{v}_{b\perp}$ are transverse velocities of the electron beam due to the wiggler and radiation field, respectively. The longitudinal electrostatic field, i.e., space-charge wave, is produced by the perturbed electron density of the beam and background plasma and is given by

$$ik\delta E_z = -4\pi e(\delta n_b + \delta n_p). \quad (15)$$

The longitudinal component of the momentum equation for the electron beam and plasma will be found as follows

$$i\hat{\gamma}_b m(\omega - kV_\parallel)\delta v_{bz} = \frac{e}{\gamma_z^2}\delta E_z + \frac{e}{c}(\mathbf{v}_w\times\delta\mathbf{B}).\hat{\mathbf{e}}_z$$

$$+\frac{e}{c}(\delta\mathbf{v}_{b\perp}\times\mathbf{B}_w).\hat{\mathbf{e}}_z - \frac{e}{c^2}V_\parallel(\mathbf{v}_w.\delta\mathbf{E}), \quad (16)$$

$$im\omega\delta v_{pz} = e\delta E_z + \frac{e}{c}(\delta\mathbf{v}_{p\perp}\times\mathbf{B}_w).\hat{\mathbf{e}}_z. \quad (17)$$

Substituting $\delta v_{b\perp}$ and $\delta v_{p\perp}$ from Eqs. (12) and (13) and $\mathbf{v}_w$ from Eq. (4) into Eqs. (16) and (17) we have

$$\hat{\gamma}_b m(\omega - kV_\parallel)\delta v_{bz}$$

$$= -ie\gamma_z^2\delta E_z + (ea_w\hat{\gamma}_b^{-1}/\sqrt{2})(k - V_\parallel c^{-2}\omega)\delta A, \quad (18)$$

$$m\omega\delta v_{Pz} = -ie\delta E_z + (ek_0 a_w/\sqrt{2})\delta A. \quad (19)$$

Using the continuity equation, the perturbed beam and plasma densities are given by

$$\delta n_b = \frac{k}{(\omega - kV_\parallel)}(\hat{n}_b\delta v_{bz} + V_\parallel\delta n_b), \quad (20)$$

$$\delta n_p = \frac{k}{\omega}\hat{n}_p \delta v_{pz} . \quad (21)$$

With substitution of δv_{bz} and δv_{pz} from Eqs. (18) and (19) into Eqs. (20) and (21) δn_b and δn_p are obtained to be inserted in Eq. (15). This will give

$$(1-\frac{\omega_b^2}{\hat{\gamma}_b\gamma_z^2(\omega-kV_\parallel)^2}-\frac{\omega_p^2}{\omega^2})\delta E_z$$

$$= i\frac{a_w}{\sqrt{2}}[\frac{\omega_b^2}{\hat{\gamma}_b^2(\omega-kV_\parallel)^2}(k-\beta_\parallel c^{-1}\omega)+\frac{\omega_p^2}{\omega^2}k_0]\delta A . \quad (22)$$

Similarly, substitution of $\delta v_{b\perp}$, $\delta v_{p\perp}$ from Eqs. (12) and (13), v_w from Eq. (4), and δn_p from Eq. (21) into Eq. (14) will give

$$(\omega^2-c^2k_r^2-\frac{\omega_b^2}{\hat{\gamma}_b}-\omega_p^2)\delta A = i\frac{c^2k_0a_w}{\sqrt{2}}(\frac{\beta_\parallel^2}{\gamma_z^2(\omega-k_rV_\parallel)}\frac{\omega_b^2}{(\omega-kV_\parallel)}$$

$$-\frac{\omega_b^2}{\gamma_z^2\hat{\gamma}_b^2(\omega-kV_\parallel)^2}\frac{k}{k_0}-\frac{\omega_p^2}{\omega^2})\delta E_z , \quad (23)$$

where terms proportional to a_w^2 are neglected. Equations (22) and (23) will easily yield the DR as follows

$$(\omega^2-c^2k_r^2-\frac{\omega_b^2}{\hat{\gamma}_b}-\omega_p^2)(1-\frac{\omega_b^2}{\hat{\gamma}_b\gamma_z^2(\omega-kV_\parallel)^2}-\frac{\omega_p^2}{\omega^2}) =$$

$$\frac{1}{2}c^2a_w^2(\frac{\omega_b^2k}{\gamma_z^2\hat{\gamma}_b^2(\omega-kV_\parallel)^2}+\frac{\omega_p^2}{\omega^2}k_0-\frac{\beta_\parallel^2}{\gamma_z^2(\omega-k_rV_\parallel)}\frac{\omega_b^2k_0}{(\omega-kV_\parallel)})$$

$$\times[\frac{\omega_b^2}{\hat{\gamma}_b^2}\frac{(k-V_\parallel c^{-2}\omega)}{(\omega-kV_\parallel)^2}+\frac{\omega_p^2}{\omega^2}k_0] . \quad (24)$$

Equation (24) is the fluid-model DR to second order in wiggler amplitude.

In the fluid DR (24) transverse velocity components of radiation, given by Eqs. (12) and (13), contain interaction terms between the wiggler and space-charge wave, which are given by the second terms in the right-hand sides (RHS) of Eqs. (12) and (13). In contrast, these interaction terms are absent in the derivation of the kinetic DR (2). In order to asses the importance of these interaction terms the fluid DR is derived with the second terms in the RHS of Eqs. (12) and (13) removed, which will yield

$$(\omega^2-c^2k_r^2-\frac{\omega_b^2}{\hat{\gamma}_b}-\omega_p^2)(1-\frac{\omega_b^2}{\gamma_z^2\hat{\gamma}_b(\omega-kV_\parallel)^2}-\frac{\omega_p^2}{\omega^2}) =$$

$$\frac{1}{2}\frac{c^2a_w^2\omega_b^2k}{\gamma_z^2\hat{\gamma}_b^2(\omega-kV_\parallel)^2}[\frac{\omega_b^2}{\hat{\gamma}_b^2}\frac{(k-V_\parallel c^{-2}\omega)}{(\omega-kV_\parallel)^2}+\frac{\omega_p^2}{\omega^2}k_0] . \quad (25)$$

Equation (25) is the fluid model DR to second order in wiggler amplitude and with the interaction terms in the transverse velocities of radiation, i.e., Eqs. (12) and (13), neglected. This fluid-model DR is equivalent to the

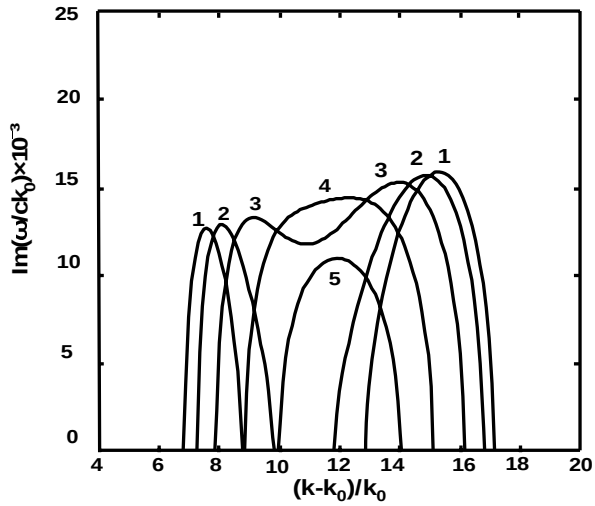

Fig. 2. Fluid-model growth rate verses radiation wave number with the interaction terms in the transverse velocities of radiation neglected.

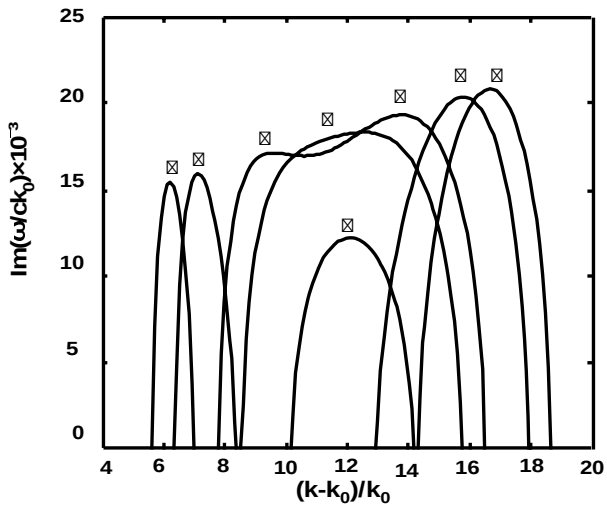

Fig. 3. Fluid-model growth rate verses radiation wave number with the interaction terms in the transverse velocities of radiation retained.

kinetic DR (2) and, therefore, they can be compared. Figure 2 shows the growth rate found from fluid DR (28) with the same parameters as in Fig. 1. Since interaction terms in the transverse velocities of radiation are absent in both Figs. 1 and 2 they compare quite well with each other. The highest value for the kinetic growth rate at around 0.0144, in Fig.1, is about 10% below that of the fluid-model growth rate at around 0.016, in Fig. 2. Moreover, location of the left (right) peak, for curve 1, in Fig. 1 at $(k-k_0)/k_0 \approx 7.2$ (≈ 15.5) differs by only about 4% (1.3%) from the corresponding peak in Fig. 2 at $(k-k_0)/k_0 \approx 7.5$ (≈ 15.3). The critical density at around 2.41×10^{13} cm^{-3} is about 3% higher than in Fig.1. The widths of unstable spectrums in the two figures are also in satisfactory agreement. Therefore, due to the absence of interaction terms in the transverse velocities of radiation

in the kinetic DR (2) as well as in the fluid DR (24) the two DRs compare quite well both quantitatively and characteristically.

Equation (24) is the fluid-model DR to second order in wiggler amplitude and with the interaction terms in the transverse velocities of radiation, i.e., Eqs. (12) and (13), retained. The fluid-model growth rate, found from this DR, is illustrated in Fig. 3. Due to the absence of interaction terms in the transverse velocities of radiation, in the kinetic-model growth rate in Fig.1, its peak value at around 0.0144 is about 31% lower than that of the fluid growth rate in Fig. 3 at around 0.021. This shows that the absence of these interaction terms in the kinetic DR has profound effects on its growth rate. Characteristics of the two figures can also be compared. Location of the left (right) peak, for curve 1, in Fig. 1 at $(k-k_0)/k_0 \approx 7.2$ (≈ 15.5) differs by about 18% (7%) from the corresponding peak in Fig. 3 at $(k-k_0)/k_0 \approx 6.1$ (≈ 16.7). The critical density at around 2.52×10^{13} cm^{-3} is about 7% higher than in Fig. 1. Therefore, characteristic behavior of the kinetic DR compares relatively better than its quantitative behavior with the fluid DR. Consequently, the general kinetic DR (1) may be used to study the temperature effects of a warm beam/plasma on the instability of a plasma-loaded FEL.

CONCLUSION

In the derivation of the kinetic DR, in Eq. 1, the transverse velocities of electrons in the radiation fields are found from the conservation of the transverse component of canonical momenta, which themselves are found from the single particle equations of motion. Therefore, no interaction with the wiggler field is present. On the other hand, in the fluid-model DR (24) the transverse velocity components of radiation, found from the fluid momentum equations and given by Eqs. (12) and (13), contain interaction terms between the wiggler and space-charge wave. To first order in a_w, these are the second terms in the RHS of Eqs. (12) and (13), which are missing in the kinetic treatment.

In order to study the importance of these interaction terms the kinetic-model DR has been compared with the fluid-model DR. For this purpose a weak coupling regime, i.e., small wiggler amplitude, is assumed under which the left circularly polarized electromagnetic wave is nonresonant, i.e., $D^T(k+k_0,\omega)\neq 0$, and terms containing a_w^2 in the coupled equations are neglected. It was found that the resulting kinetic DR (2) compares fairly well with the corresponding fluid DR (25), which does not contain the interaction terms in the transverse velocities of radiation. However, the kinetic DR (2) does not agree quantitatively with the fluid DR (24), which does contain the interaction terms. Nevertheless, characteristic behavior of the two DRs are of better agreement so that the general kinetic DR (1) may be used to study the temperature effect of a warm beam/plasma on the growth rate of a plasma-loaded FEL. This DR is full and contains both the Compton regime DR and the Raman regime DR. Therefore, a complete numerical investigation of the kinetic DR (1) should include a warm beam/plasma in both Compton and Raman regime.

ACKNOWLEDGMENT

One of the authors (B.M) would like to thank the Center of Excellence in Computational Aerospace Engineering for financial support.

REFERENCES

[1] S. Babaei and B. Maraghechi, Phys. Plasmas, **14**, 053114 (2007).
[2] P. Wen-Bing and C. Ya-Shen, Int. J. Electron. **65**, 551 (1988).
[3] V. K. Tripathi and C. S. Liu, IEEE Trans. Plasma Sci. **18**, 466 (1990).
[4] A. Serbeto and M. V. Alves, IEEE Trans. Plasma Sci. **21**, 243 (1993).
[5] V. Petrillo, A. Serbeto, C. Maroli, R. Parrella, and R. Bonifacio, Phy. Rev. E **51**, 6293 (1995).
[6] K. H. Tsui and A. Serbeto, Phy. Rev. E **58**, 5013 (1998).
[7] V. Petrillo and C. Maroli, Phys. Rev. E **62**, 8612 (2000).
[8] R. N. Agarwal, V. K. Tripathi, and P. C. Agarwal, IEEE Trans. Plasma Sci. **24**, 1197 (1996).
[9] B. Qian, Y. Liu, and C. Li, Phys. Plasmas **1**, 4089 (1994).
[10] J. Parashar, H. D. Pandey, A. K. Sharma, and V. K. Tripathi, J. Plasma Phys. **58,** 613 (1997).
[11] K. K. Pant and V. K. Tripathi, IEEE Trans. Plasma Sci. **22**, 217 (1994).
[12] Y. Seo and E. H. Choi, IEEE Trans. Plasma Sci. **25**, 360 (1997).
[13] A. Sharma and V. K. Tripathi, Phys. Fluid B. **5**, 171 (1993).
[14] A. Sharma and V. K. Tripathi, Phys. Plasmas. **3**, 3116 (1996).

CONSERVATION LAWS IN QUASILINEAR THEORY OF RAMAN FREE-ELECTRON LASER

B. Maraghechi, Department of Physics, Amirkabir University of Technology, Tehran, Iran
A. Chakhmachi, Plasma Physics and Nuclear Fusion Research School,
Nuclear Science and Technology Research Institute, AEOI, Tehran, Iran
and Department of Physics, Amirkabir University of Technology, Tehran, Iran

Abstract

A quasilinear theory of the free-electron laser, in Raman regime, is presented to establish that conservation laws on number, energy, and momentum are upheld. A high density electron beam is assumed so that the space-charge potential is no longer negligible. A sufficiently broad band spectrum of waves is assumed so that saturation will be due to the quasilinear spread of the beam electrons. Otherwise, for the single mode excitation, saturation will be due to the electron trapping in the space-charge potential. It is shown that the quasilinear slow variation of the background distribution function is in the form of the diffusion equation in momentum space. An expression for the time evolution of the spectral energy density is derived. Conservation laws to the quasilinear order (second order) are derived and are proved to be satisfied. Results of the present investigation may be used to study the quasilinear saturation of a free-electron laser in the presence of the space-charge wave.

INTRODUCTION

Saturation and nonlinear evolution of free-electron lasers (FEL) are of considerable importance both experimentally and theoretically. The main reason is that saturation determines the efficiency of the device.

For sufficiently broad spectrum of unstable waves, saturation is due to quasilinear energy spread of the beam electrons. This problem has been studied only in the Compton regime, where the electrostatic potential of the space-charge wave is negligible due to low density of the electron beam [1-5]. On the other hand, when there is only a single exited mode, saturation of the amplification is considered to be caused by electrons trapped in the electrostatic field of the space-charge wave in the Raman regime or the pondermotive wave in the Compton regime [6-8].

The purpose of the present investigation is to derive conservation laws in the quasilinear analysis of an FEL in the presence of the space-charge field of electrons. The method of analysis and notations are similar to Ref. 1. The quasilinear slow variation of the background distribution function is in the form of the diffusion equation in momentum space. An expression for the time evolution of the spectral energy density is derived. Conservation laws, to the quasilinear order (second order), for particle, energy and momentum are derived and are proved to be satisfied.

PHYSICAL MODEL

We consider a collisionless, relativistic, electron beam with uniform cross section propagating in the z direction. The electron beam propagates through a constant amplitude helical wiggler magnetic field specified by

$$\mathbf{B}_0 = -B_w cos(k_0 z)\widehat{\mathbf{e}_x} - B_w sin(k_0 z)\widehat{\mathbf{e}_y}, \qquad (1)$$

The transverse electromagnetic and longitudinal electrostatic perturbed fields $\delta\mathbf{E}$ and $\delta\mathbf{B}$ are defined as

$$\delta\mathbf{E} = -\frac{1}{c}\frac{\partial}{\partial t}\delta\mathbf{A} - \nabla\delta\varphi, \qquad \delta\mathbf{B} = \nabla\times\delta\mathbf{A}. \qquad (2)$$

The relativistic, nonlinear Vlasov equation for the electron beam distribution function $f_b(z,\mathbf{p},t)$ is given by

$$[\frac{\partial}{\partial t}+v_z\frac{\partial}{\partial z}-e(\delta\,\mathbf{E}+\frac{\mathbf{v}\times(\mathbf{B}_0+\delta\mathbf{B})}{c}).\frac{\partial}{\partial\mathbf{p}}]f_b(z,\mathbf{p},t)=0. \qquad (3)$$

In the present analysis, we investigate the class of exact solution to Eq. (3) of the form

$$f_b(z,\mathbf{p},t) = n_0\delta(P_x)\delta(P_y)G(z,p_z,t), \qquad (4)$$

where $n_0 = const$, and P_x and P_y are the canonical momenta transverse to the beam propagation direction. Substituting the distribution function (4) into Eq. (3) and integrating the resting equation over p_x and p_y, gives

$$[\frac{\partial}{\partial t}+v_z\frac{\partial}{\partial z}-\frac{\partial}{\partial z}H(z,p_z,t)\frac{\partial}{\partial p_z}]G(z,p_z,t)=0. \qquad (5)$$

In this equation, $H(z,p_z,t)$ is defined by

$$H(z,p_z,t) = \gamma_T mc^2 - e\delta\varphi(z,t)$$

$$= [m^2c^4 + c^2p_z^2 + e^2(A_x^0+\delta A_x)^2 + e^2(A_y^0+\delta A_y)^2]^{(1/2)}$$

$$-e\delta\varphi(z,t), \qquad (6)$$

which is the particle energy for $P_x = 0 = P_y$, and $\gamma_T mc^2$ is the kinetic energy. In the absence of perturbed fields, the energy is given by

$$\gamma mc^2 = (m^2c^4 + c^2p_z^2 + e^2B_w^2/k_0^2)^{1/2}. \qquad (7)$$

It is assumed that the distribution function $G(z,p_z,t)$, $H(z,p_z,t)$, and $\delta\varphi(z,t)$ are spatially periodic with periodicity length $2L$ so it is convenient to introduce the specially averaged distribution function $G_0(p_z,t)$ defined by

$$G_0(p_z,t) = \langle G\rangle = \frac{1}{2L}\int_{-L}^{L} dz G(z,p_z,t). \quad (8)$$

For small $\delta\mathbf{A}$ and $\delta\varphi$,

$$G(z,p_z,t) = G_0(p_z,t) + \delta G(z,p_z,t), \quad (9)$$

$$H(z,p_z,t) = H_0(p_z,t) + \delta H(z,p_z,t) = \gamma mc^2 + \delta H, \quad (10)$$

and therefore

$$\delta H(z,p_z,t) = (e^2/\gamma mc^2)(A_x^0\delta A_x + A_y^0\delta A_y) - e\delta\varphi(z,t). \quad (11)$$

Equation (11) shows that the space-charge wave constitute the electrostatic potential of the perturbed Hamiltonian or energy. By substituting $v_z = p_z/\gamma_T m = p_z c^2/(H+e\delta\varphi)$, Eq. (6) can be expressed as

$$\frac{\partial}{\partial t}G + p_z c^2\frac{\partial}{\partial z}(\frac{G}{H+e\delta\varphi}) - \frac{\partial}{\partial p_z}(G\frac{\partial}{\partial z}H) = 0,$$

which can be averaged over the spatial periodicity length 2L to obtain

$$\frac{\partial}{\partial t}G_0 = \frac{\partial}{\partial t}\langle G\rangle = \frac{\partial}{\partial p_z}\langle \delta G\frac{\partial}{\partial z}\delta H\rangle. \quad (12)$$

In the approximation where only linear wave-particle interactions are retained in the description, δG evolves according to [1]

$$\frac{\partial}{\partial t}\delta G + \frac{p_z}{\gamma m}\frac{\partial}{\partial z}\delta G - (\frac{\partial}{\partial z}\delta H)\frac{\partial}{\partial p_z}G_0 = 0. \quad (13)$$

Equation (13) will be recognized as the linearized Vlasov equation for perturbations about spatially uniform distribution function $G_0(p_z,t)$, which varies slowly with time according to Eq. (12).

TIME EVOLUTION OF DISTRIBUTION FUNCTION AND ENERGY

We introduce the Fourier series representations

$$G(z,p_z,t) = G_0(p_z,t) + \sum_k{}'\delta G_k(p_z,t)\exp(ikz), \quad (14)$$

$$H(z,p_z,t) = H_0(p_z,t) + \sum_k{}'\delta H_k(p_z,t)\exp(ikz), \quad (15)$$

$$\delta\psi(z,t) = \sum_k \delta\psi(k,t)\exp(ikz), \quad (16)$$

where $\delta\psi$ is δA_x, δA_y, or $\delta\varphi$ and $k = n\pi/L$ with n an integer and the summations run from $k=-\infty$ to $k=+\infty$. The prime on the summations denotes that the $k=0$ term is omitted. From Eqs. (11), and (14)-(16) it follows that (for $k\neq 0$)

$$\delta H_k = (\frac{e^2 B_w}{2\gamma mc^2 k_0})[\delta A_x(k+k_0) + i\delta A_y(k+k_0)$$
$$+\delta A_x(k-k_0) - i\delta A_y(k-k_0)] - e\delta\varphi(k). \quad (17)$$

The time dependence of perturbed quantities is assumed to be of the form $\exp(-i\int_0^t \Omega_k(t')dt')$ in circumstances where the time variation of $G_0(p_z,t)$ is sufficiently slow $\Omega_k = \omega_k + i\gamma_k = -\omega_{-k} + i\gamma_{-k}$. By use of $\bar{\gamma}mc^2 = const$ that denotes the characteristic mean energy of the unperturbed beam electrons we can write the perturbed amplitudes in terms of dimensionless amplitudes $\delta\Phi(k)$ and $\delta A^{\pm}_{k\pm k_0}$. In Fourier variables, Eq. (12) becomes

$$\frac{\partial}{\partial t}G_0 = -\frac{\partial}{\partial p_z}\sum_k ik\delta H_{-k}\delta G_k. \quad (18)$$

Solving Eq. (13) and neglecting free-streaming contributions to $\delta G_k(p_z,t)$, we obtain for the perturbed distribution function

$$\delta G_k(p_z,t) = -[(\frac{\bar{\gamma}eB_w}{2\gamma k_0})(\delta A^+_{k+k_0} + \delta A^-_{k-k_0}) - \bar{\gamma}mc^2\delta\Phi(k)]$$
$$\times(\frac{k\partial G_0/\partial p_z}{\Omega_k - kv_z})\exp(-i\int_0^t \Omega_k(t')dt'). \quad (19)$$

Substituting Eqs. (17) and (19) into Eq. (18) yields the quasilinear kinetic equation for $G_0(p_z,t)$:

$$\frac{\partial}{\partial t}G_0(p_z,t) = i\sum_k k^2\frac{\partial}{\partial p_z}(\frac{|\delta H_k|^2\partial G_0/\partial p_z}{\Omega_k - kv_z}). \quad (20)$$

Note that Eq. (20) has the form of a diffusion equation for $G_0(p_z,t)$ in momentum space.

Linear Dispersion Relation and Energy Equation

The complex oscillation frequency $\Omega_k(t)$ is obtained adiabatically in terms of $G_0(p_z,t)$ from the linear DR. For the present configuration the linear DR is derived in Ref. 9 and 10 as follows

$$c^2k^2 D_k^L(\Omega_k)D^T_{k-k_0}(\Omega_k)D^T_{k+k_0}(\Omega_k) =$$
$$(1/2)a_w^2[D^T_{k-k_0}(\Omega_k) + D^T_{k+k_0}(\Omega_k)]$$
$$\times\{[\chi_k^{(1)}]^2 - c^2k^2D_k^L(\Omega_k)[\chi_k^{(2)} + \alpha_3\omega_{pe}^2]\}, \quad (21)$$

where the dielectric functions D_k^L, $D^T_{k-k_0}$, $D^T_{k+k_0}$, and the effective susceptibility $\chi_k^{(n)}$ are defined by

$$D^T_{k\pm k_0}(\Omega_k) = \Omega_k^2 - c^2(k\pm k_0)^2 - \alpha_1\omega_{pe}^2, \quad (22)$$

$$\chi_k^{(n)}(\Omega_k) = \bar{\gamma}^{n+1}mc^2\omega_{pe}^2\int\frac{dp_z}{\gamma^n}\frac{k\partial G_0/\partial p_z}{\Omega_k - kv_z}. \quad (23)$$

$$D_k^L(\Omega_k) = 1 + \frac{\chi_k^{(0)}(\Omega_k)}{c^2k^2}, \quad (24)$$

Here $\omega_{pe}^2 = 4\pi n_0 e^2/\bar{\gamma}m$, $a_w = eB_w/\bar{\gamma}mc^2k_0$ and $\alpha_n = \bar{\gamma}^n \int \frac{dp_z}{\gamma^n} G_0$. We will now obtain the wave kinetic equation. The average energy density in the electromagnetic and electrostatic fields is given by

$$\frac{1}{8\pi}\sum_k [|\delta \mathbf{E}_k|^2 + |\delta \mathbf{B}_k|^2] =$$

$$(\frac{\bar{\gamma}mc^2}{2e})^2 \frac{1}{4\pi c^2}\sum_k \{|\delta A^+_{k+k_0}|^2[|\Omega_k|^2 + c^2(k+k_0)^2]$$

$$+|\delta A^-_{k-k_0}|^2[|\Omega_k|^2 + c^2(k-k_0)^2] + 2c^2k^2|\delta\Phi(k)|^2\}$$

$$\times exp(2\int_0^t \gamma_k(t^{'})dt^{'}) = \sum_k \epsilon_k(t), \qquad (25)$$

where $\varepsilon_k(t)$ is the spectral energy density. From Eq. (25), it follows that $\epsilon_k(t)$ evolves according to

$$\frac{\partial}{\partial t}\epsilon_k(t) = 2\gamma_k(t)\epsilon_k(t), \qquad (26)$$

where the linear growth rate $\gamma_k(t)$ is determined adiabatically in terms of $G_0(p_z, t)$ from Eq. (21). Equations (20), (21), and (26) then form a closed quasilinear description of the system including the effects of linear wave-particle interactions.

CONSERVATION OF PARTICLE, MOMENTUM AND ENERGY

The fully nonlinear Vlasov-Maxwell equations possess three exact conservation relations. These are: average density,

$$\int_{-L}^{L}\frac{dz}{2L}\int d^3p f_b(z, \mathbf{p}, t) = const, \qquad (27)$$

total average plasma kinetic energy density plus electromagnetic and electrostatic field energy density,

$$\int_{-L}^{L}\frac{dz}{2L}\{\int d^3p(\gamma_T - 1)mc^2 f_b(z, \mathbf{p}, t)$$

$$+\frac{1}{8\pi}[(\delta\mathbf{E})^2 + (\mathbf{B}_0 + \delta\mathbf{B})^2]\} = const, \qquad (28)$$

and total average plasma momentum density plus electromagnetic field momentum density,

$$\int_{-L}^{L}\frac{dz}{2L}\{\int d^3p p_z f_b(z, \mathbf{p}, t) + \frac{1}{4\pi c}(\delta\mathbf{E}\times\mathbf{B}_0$$

$$+\delta\mathbf{E}\times\delta\mathbf{B})_z\} = const. \qquad (29)$$

We now demonstrate that the conservation relations (27)-(29) are upheld by the quasilinear kinetic equations derived in Eq. (20). The distribution function f_b is taken to be of the form of Eq. (4). In Eqs. (27)-(29), we expand quantities such as $\gamma_T mc^2$ and retain up to second-order terms in perturbation amplitudes.

Particle conservation: Substituting Eq. (4) into Eq. (27), and making use of Eq. (9), we obtain

$$\frac{\partial}{\partial t}\int_{-\infty}^{\infty} dp_z n_0 G_0(p_z, t) = 0. \qquad (30)$$

Clearly this is true for $\partial G_0/\partial t$ given by Eq. (20) since Eq. (20) is in the form of a diffusion equation in momentum space and the integrand is an exact differential.

Energy conservation: To show energy conservation from quasilinear theory, the quantity $\gamma_T mc^2$ [Eq. (6)] is expanded to second order, by this we have

$$\langle\mathbf{KED}\rangle = \int_{-L}^{L}\frac{dz}{2L}\int_{-\infty}^{\infty} dp_z n_0((\gamma-1)mc^2 G_0$$

$$+\frac{e^2}{\gamma mc^2}[(A_x^0\delta A_x + A_y^0\delta A_y)\delta G - (\delta A_x^2 + \delta A_y^2)G_0]$$

$$-\frac{1}{2}\frac{e^4}{\gamma^3 m^3 c^6}(A_x^0\delta A_x + A_y^0\delta A_y)^2 G_0) \qquad (31)$$

In above equation $\langle\mathbf{KED}\rangle$ is the average plasma kinetic energy density. Then the quasilinear analog of the exact energy conservation relation in Eq. (28) can be expressed as

$$\frac{\partial}{\partial t}\langle\mathbf{KED}\rangle = -\frac{\partial}{\partial t}\langle\frac{1}{8\pi}[(\delta\mathbf{E})^2 + (\mathbf{B}_0 + \delta\mathbf{B})^2]\rangle, \qquad (32)$$

To verify Eq. (32), we proceed by taking the derivative of Eq. (31) with respect to time, and substituting Eq. (20) for $\partial G_0/\partial t$ into the first term on the right-hand side of Eq. (31). The perturbed distribution function δG appearing in second term is obtained from Eq. (19). Then by use of DR (21) we can eliminate the integrals over momentum in favor of dielectric functions $D^T_{k+k_0}$, $D^T_{k-k_0}$, and D^L_k. Relations between the perturbed amplitudes and dielectric functions are also used.

$$\frac{\partial}{\partial t}\langle\mathbf{KED}\rangle = (\frac{\bar{\gamma}mc^2}{2e})^2\frac{1}{2\pi c^2}$$

$$\sum_k\{(i\omega_k + \gamma_k)[D^T_{k+k_0}|\delta A^+_{k+k_0}|^2 + D^T_{k-k_0}|\delta A^-_{k-k_0}|^2]$$

$$+\gamma_k(\omega_{pe}^2\alpha_1)[|\delta A^+_{k+k_0}|^2 + |\delta A^-_{k-k_0}|^2]$$

$$+(i\omega_k - \gamma_k)[2c^2k^2|\delta\Phi(k)|^2]\}exp(2\int_0^t \gamma_k(t^{'})dt^{'}). \qquad (33)$$

Substituting Eq. (22) into Eq. (33), and eliminating terms in the k summations, which are odd functions of k, yields

$$\frac{\partial}{\partial t}\langle\mathbf{KED}\rangle = -(\frac{\bar{\gamma}mc^2}{2e})^2\frac{1}{4\pi c^2}\frac{\partial}{\partial t}\sum_k exp(2\int_0^t \gamma_k(t^{'})dt^{'})$$

$$\times([|\delta A^+_{k+k_0}|^2(|\Omega_k(t)|^2 + c^2(k+k_0)^2)$$

$$+|\delta A^-_{k-k_0}|^2(|\Omega_k(t)|^2 + c^2(k-k_0)^2)] + [2c^2k^2|\delta\Phi(k)|^2]). \qquad (34)$$

The right-hand side of Eq. (32) can be evaluated

$$-\frac{\partial}{\partial t}\langle[\frac{1}{8\pi}(\delta\mathbf{E})^2 + (\delta\mathbf{B} + \mathbf{B}_0)^2]\rangle =$$

$$-(\frac{\bar{\gamma}mc^2}{2e})^2\frac{1}{4\pi c^2}\frac{\partial}{\partial t}\sum_k exp(2\int_0^t \gamma_k(t^{'})dt^{'})$$

$$([|\delta A^+_{k+k_0}|^2(|\Omega_k(t)|^2+c^2(k+k_0)^2)$$

$$+|\delta A^-_{k-k_0}|^2(|\Omega_k(t)|^2+c^2(k-k_0)^2)]+[2c^2k^2|\delta\Phi(k)|^2]). \quad (35)$$

Comparing Eqs. (35) and (34) completes the proof of Eq. (32).

Momentum conservation: We will now show that the average total axial momentum is conserved in the quasilinear theory. To obtain the quasilinear analog of Eq. (29), Eq. (4) is substituted into Eq. (29), the resulting equation is differentiated with respect to time, use is made of Eq. (12), and we integrate by part with respect to p_z:

$$-\frac{n_0e}{mc}\int_{-L}^{L}\frac{dz}{2L}[(\frac{e}{c}(A^0_x+\delta A_x)\frac{\partial}{\partial z}(A^0_x+\delta A_x)$$

$$+\frac{e}{c}(A^0_y+\delta A_y)\frac{\partial}{\partial z}(A^0_y+\delta A_y))\int_{-\infty}^{\infty}\frac{dp_z}{\gamma_T}G]$$

$$+\frac{\partial}{\partial t}\int_{-L}^{L}\frac{dz}{2L}\frac{1}{4\pi c}(\delta\mathbf{E}\times\mathbf{B}_0+\delta\mathbf{E}\times\delta\mathbf{B})_z=0. \quad (36)$$

Where $\int_{-L}^{L}\frac{dz}{2L}\frac{1}{4\pi c}(\delta\mathbf{E}\times\mathbf{B}_0)_z = 0$. We can expand the transverse current density $-e\int d^3p(v_x\hat{\mathbf{e}}_x+v_y\hat{\mathbf{e}}_y)f_b$ in powers of perturbed quantities. Thus, for the form of f_0 given in Eq. (4) and by expanding G and $1/\gamma_T$ to first order perturbed amplitudes the time rate of change of the average plasma momentum density is given by

$$\frac{\partial}{\partial t}\langle\mathbf{PMD}\rangle=\int_{-L}^{L}\frac{dz}{2L}\int_{-\infty}^{\infty}dp_z(-\frac{n_0e^2}{mc^2})$$

$$\times[\frac{1}{\gamma}A^0_x\delta G\frac{\partial}{\partial z}\delta A_x+\frac{1}{\gamma}A^0_y\delta G\frac{\partial}{\partial z}\delta A_y$$

$$-\frac{e^2}{\gamma^3m^2c^4}(A^0_x\delta A_x+A^0_y\delta A_y)G_0(A^0_x\frac{\partial}{\partial z}\delta A_x+A^0_y\frac{\partial}{\partial z}\delta A_y)] \quad (37)$$

correct to second order in the perturbation amplitude. The analogue equation to Eq. (29) in quasilinear theory is

$$\frac{\partial}{\partial t}\langle\mathbf{PMD}\rangle=-\frac{\partial}{\partial t}\langle\frac{1}{4\pi c}(\delta\mathbf{E}\times\delta\mathbf{B})_z\rangle. \quad (38)$$

Rearranging the terms in Eq. (37) and by use of the DR (21) and the relation between perturbed amplitudes and dielectric functions we have

$$\frac{\partial}{\partial t}\langle\mathbf{PMD}\rangle=-(\frac{\bar{\gamma}mc^2}{2e})^2\frac{1}{2\pi c^2}\frac{\partial}{\partial t}\sum_k exp(2\int_0^t\gamma_k(t^{'})dt^{'})$$

$$\times\omega_k[(k+k_0)|\delta A^+_{k+k_0}|^2+(k-k_0)|\delta A^-_{k-k_0}|^2]. \quad (39)$$

We can now evaluate the second term of Eq. (29) by use of Eqs. (3), (14)-(16)

$$-\frac{\partial}{\partial t}\langle\frac{1}{4\pi c}(\delta\mathbf{E}\times\delta\mathbf{B})_z\rangle=\frac{1}{4\pi c}$$

$$-\frac{\partial}{\partial t}\sum_k\frac{ik}{c}(\delta A^*_x(k,t)\frac{\partial}{\partial t}\delta A_x(k,t)+\delta A^*_y(k,t)\frac{\partial}{\partial t}\delta A_y(k,t))$$

$$=-(\frac{\bar{\gamma}mc^2}{2e})^2\frac{1}{2\pi c^2}\frac{\partial}{\partial t}\sum_k exp(2\int_0^t\gamma_k(t^{'})dt^{'})$$

$$\times\omega_k[(k+k_0)|\delta A^+_{k+k_0}|^2+(k-k_0)|\delta A^-_{k-k_0}|^2], \quad (40)$$

Then, Eq. (38) is directly proved by comparing Eqs. (39) and (40).

CONCLUSION

In the Raman regime, due to the high density of the electron beam, the space-charge potential is not negligible compared to the pondermotive potential. In this paper we have derived conservation laws in the quasilinear analysis of an FEL in the presence of the space-charge field of electrons.

The assumption of a broad spectrum of waves ensures that the saturation takes place through the quasilinear diffusion of electrons in the momentum space rather than by the particle trapping.

The presence of space-charge wave, that is resonant in the Raman regime, with the real parts of the frequency and wave number satisfying the linear DR, modifies the problem considerably compared to the Compton regime in which space-charge potential is negligible in comparison to the pondermotive potential.

The quasilinear kinetic theory used to derive three exact conservation relations, corresponding to conservation of (average) particle density, total energy, and total axial momentum. These results may be used to study the quasilinear saturation of a FEL in the raman regime.

ACKNOWLEDGMENT

One of the authors (B.M.) would like to thank the Center of Excellence in Computational Aerospace Engineering for financial support.

REFERENCES

[1] A. M. Dimos, R. C. Davidson, Phys. Fluids. **28**, 677 (1985).

[2] T. Taguchi, K. Mima, and T. E. Mochizuki, Phys. Rev. Lett **46**, 824 (1981).

[3] W. P. Marable and P. A. Sprangle, J. Appl. Phys. **67**, 3576 (1990).

[4] R. C. Davidson and Y.-Z. Yin, Phys. Fluids. **28**, 2524 (1985).

[5] N. A. Vinokurov, Z. Huang, D. A. Shevchenko, and K. -J. Kim, Nucl. Instrum. Methods. Phys. Res. A **475**, 74 (2001).

[6] N. M. Kroll, P. L. Morton, and M. N. Rosenbluth, IEEE J. Quantum Electron. **QE-17**, 1436 (1981).

[7] W. H. Louisell, J. F. Lam, and D. A. Copeland, Phys. Rev A **18**, 655, (1978).

[8] T. Kwan and J. M. Dawson, Phys. Fluids. **22**, 1089 (1979).

[9] R. C. Davidson and H. S. Uhm, Phys. Fluids. **23**, 2076 (1980).

[10] R. C. Davidson, *Physics of Nonneutral Plasmas* (Addision-Wesley, Redwood City, CA. 1990), Chap. 7 .

LIMIT FOR HARMONIC CONVERSION IN A SINGLE CASCADE OF COHERENT HARMONIC GENERATION

E. Allaria, G. De Ninno, Sincrotrone Trieste, Trieste, Italy

Abstract

Harmonic generation is a reliable method for producing coherent high-brightness photon pulses from relativistic electron bunches. The standard process leading to Coherent Harmonic Generation is initiated by a powerful seed laser. As a consequence, reaching short wavelengths generally requires a high order frequency conversion. For that reason some of the projects which are presently under development for coherent VUV and soft-Xray emission are based on a series of two or more consecutive "cascades". In these setups, the radiation produced into one stage is used as a seed in a following cascade. The required number of cascades depends on the maximum harmonic conversion which can be obtained in single stages. In this paper we study the mechanism underlying CHG, i.e. the bunching creation into the modulator, and we investigate the physical limits of the single-stage CHG.. The identification of the limiting parameters may allow the implementation of new methods for enhancing the conversion efficiency. One of these methods, which rely on a simple modification of the standard CHG scheme, has been recently proposed [3] and shown to be able to significantly improve the system performance. Results are confirmed by 3D numerical simulations using the FERMI electron beam parameters as initial conditions.

INTRODUCTION

It is well known that the electron bunching, which is needed for effective High Gain Harmonic Generation (HGHG), rapidly decreases with the harmonic number, unless a strong energy modulation is produced in the modulator. However, the exponential light amplification that follows the first quadratic growth is strongly sensitive to the total energy spread,i.e., the quadratic combination of initial incoherent energy spread and of the coherent modulation.

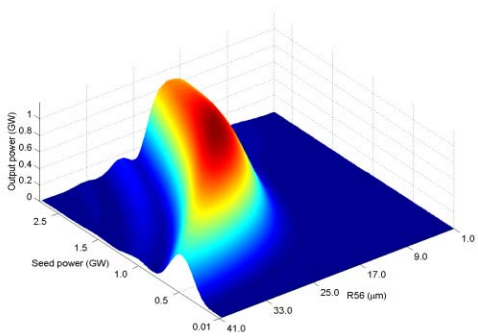

Figure 1: Example of Optimized output power for the HGHG FEL setup as a function of seed power and R56.

As a consequence, the optimization of a HGHG scheme relies on a compromise between the production of a sufficiently high bunching in the modulator (allowing a significant quadratic growth) and the need of keeping the total energy spread below the FEL parameter ρ. An example of the dependence of the produced FEL output power on the seed power and dispersive section strength (R56) is shown in Fig.1.

In this paper we study the possibility of optimizing the CHG setup once the electron-beam and the radiator parameters are given. For the presented work, electron beam parameters have been chosen to be those of the FERMI@Elettra project [1], see Table 1.

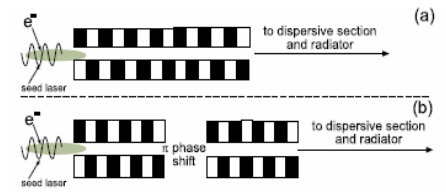

Figure 2: a) Schematic layout for the modulator in a standard HGHG setup. b) Proposed modified layout considering a phase shifter in between two modulator subsections.

The optimization is based on a modification of the standard modulator scheme, involving both the ondulator configuration and the power of the seed laser (Fig.2). The study has been done by perfomring numerical simulations with well established 3D FEL codes ginger and genesis.

Table 1: FERMI electron-beam parameters

Parameter	*Value*	*Units*
Electron Beam Energy	1.2	GeV
Peak current	1	kA
Uncorrelated energy spread	200	keV
Norm. Transverse Emittance	1.5	mm-mrad

CASCADE LIMIT IN A STANDARD CHG SCHEME

According to theoretical predictions [2], the induced energy spread needed for efficient CHG increases with the harmonic number.

Figs.3 and .4 show that, while the optimum value of energy spread increases when reducing the emitted wavelength, the optimum bunching is approximately constant (order of 4% in our case). This result can be explained considering that in HGHG bunching is necessary to induce the quadratic emission occurring in the first part of the process, AND SIMPLY HAS TO BE LARGER THAN SHOT NOISE. However, the main contribution to the final output power comes from the

successive exponential growth, which is rapidly depressed when the (total) energy spread increase.

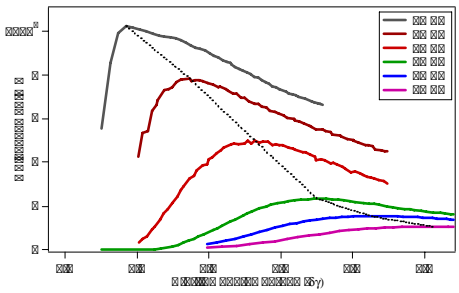

Figure 3: For each wavelength the maximum output power, obtained after optimization, is plotted as a function of the total energy spread ($\delta\gamma$) at the entrance of the radiator, which is correlated to the seed power .

Indeed, in first approximation, the required value for the bunching is independent from the harmonic we are interested in.

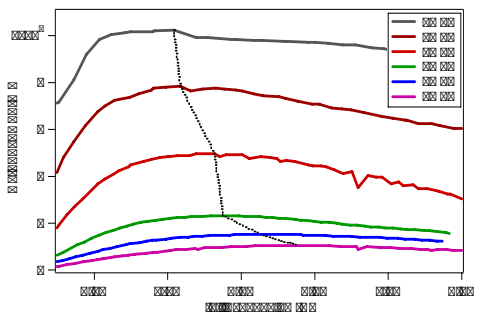

Figure 4: For each wavelength the maximum (optimized) output power is plotted as a function of the bunching produced after the dispersive section.

The fact that shorter wavelengths require larger energy spread implies that the final output power monotonically decreases (see inset of fig. 5) when going to shorter wavelengths.

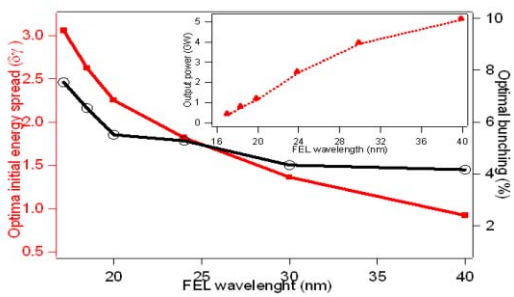

Figure 5: Form the data of figs. 3 and 4 we can see a strong dependence of the $\delta\gamma$ necessary to optimize the output power as a function of the desired wavelength (red curve). On the contrary, the bunching (black curve) shows only a weak dependence. The inset shows the decrease of output power as a function of λ.

A limit in wavelength for HGHG to occur is provided by the harmonic at which it is no more possible to produce the required amount of bunching. In the considered setup (see Table 1) HGHG become inefficient for λ<20nm (N>12) and cannot be obtained for λ<17nm (fig.5).

We focus now on the 20nm case, that is the 12th harmonic of a frequency multiplied Ti:Sa tuned at 240nm. As shown in previous figures, a power of about 1 GW for the considered system can be obtained. Fig.6 shows the evolution of the radiation power (red) and bunching (black) along the radiator starting from a properly optimized initial condition. The considered radiator parameters are those used for the first FEL of the Fermi@Elettra project [1], with the only difference that the radiator period has been reduced to 55mm from the original 65mm in order to extend the tunability to shorter wavelengths.

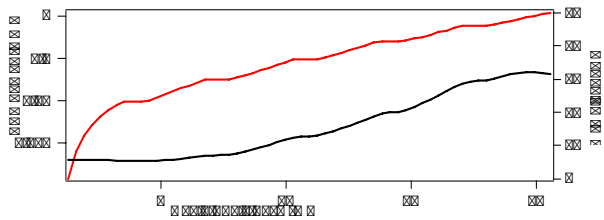

Figure 6: Results showing the quadratic (z<5) ad the exponential growth of the FEL power in the optimized standard setup for 20nm.

The mechanism underlying the FEL process during HGHG can be understood looking at the electron phase space at the entrance of the radiator, as shown in fig.7a. Figure 7b shows the localized density distribution of electrons, which is at the origin of initial bunching. Bunched electrons (blue in Fig.7a) are responsible for the coherent quadratic emission (z<5m in Fig.6). Remaining electrons interact with the produced radiation in the rest of radiator (z>5m) and are eventually responsible for the exponential growth.

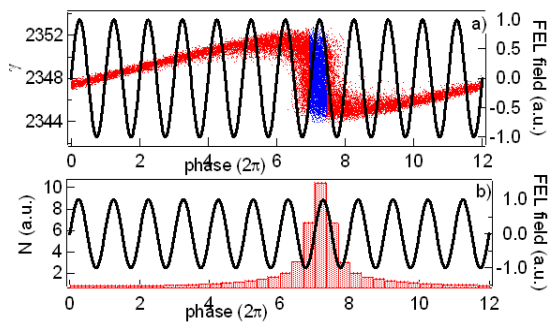

Figure 7: a) Phase-space representation of electrons at the entrance of the radiator in the optimized standard configuration for the 20nm case. b) Histogram of the electron density distribution. In both figures, the field evolution at 20 nm is reported as a reference.

Due to the energy modulation necessary for HGHG, "blue" electrons are characterized by a large energy spread and will only participate to the initial coherent emission. The rest of electrons (red) are characterized by a small "slice" energy spread, but their mean energy present quite large variations along the original phase (0-

24π referring to one period of the 12th harmonic of the seed wavelength, i.e. 20nm). Such a detuning limits the exponential growth.

NEW OPTIMIZED CONFIGUATIONS

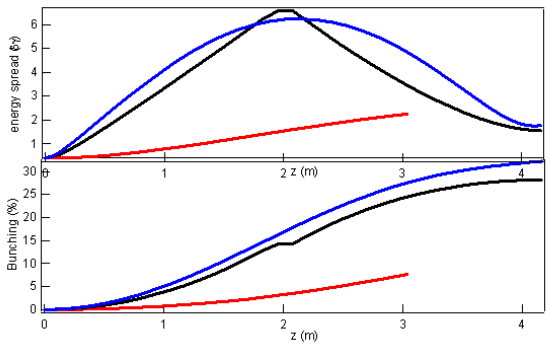

Figure 8: Evolution of the energy spread (a) and bunching (b) inside the modulator for the three considered setups: standard (red curve), double modulator (black curve) and detuned modulator (blue curve).

The modulator of a HGHG system can be optimized if one is able to produce the needed amount of bunching by inducing a smaller amount of coherent energy spread. For this purpose, in [3] we have proposed a simple scheme relying on a two-segment modulator separated by a de-phasing unit (Fig.1). In the first segment, electrons interact with the coherent radiation and coherent energy spread is produced. After the de-phasing unit, electrons and radiation are de-phased by about π, so that the interaction in the second modulator section is used to partially absorb the coherent energy spread.

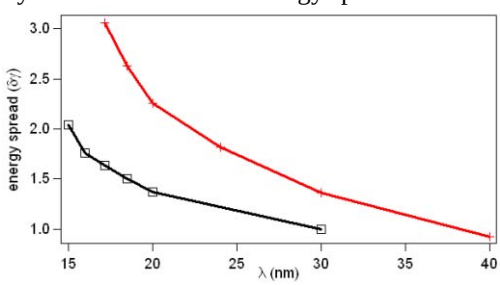

Figure 9: Comparison between the standard setup and the one based on the double modulator in terms of the energy spread necessary for creating a certain amount of bunching (4%) at the desired λ. Red curve refers to the standard configuration while the black one refers to the double modulator scheme.

We propose here a new setup which is able to produce the same effect on the electron beam using a single modulator section. The method exploits the natural de-phasing that occurs to electrons moving in a detuned undulator. As demonstrated by the data reported in Fig.8, by properly choosing the detuning value it is possible to obtain the same effect of the two modulator sections with π de-phasing in-between. The benefits of using one of the proposed methods with respect to the standard one are shown in Fig.8, where the minimum energy spread necessary to induce a bunching of 4% is reported as a function of the wavelength.

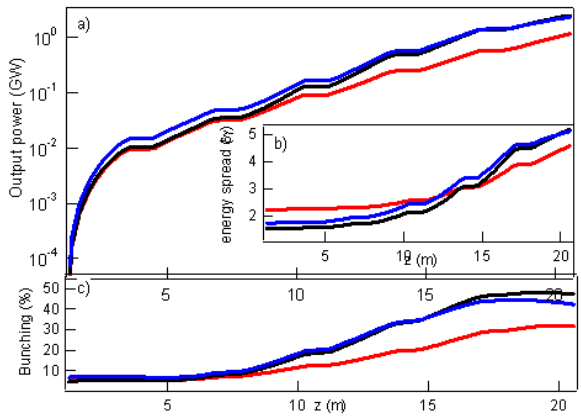

Figure 10: Example of the improved performance at 20nm obtained by using the proposed modified modulators. FEL power evolution along the radiator for the setup using the standard modulator (red curve), the double modulator (blue curve) and the detuned modulator (black curve).

Data show that for the same wavelength the new proposed methods allow to obtain the required bunching with about half of the energy spread with respect to the standard method (Fig.9). This implies that a significantly larger output power can be reached. This is shown in Fig.10 where the evolution along the radiator of the output power and bunching for the 20nm case is shown for the standard and two new proposed methods. A factor two can be gained with the new modulator schemes.

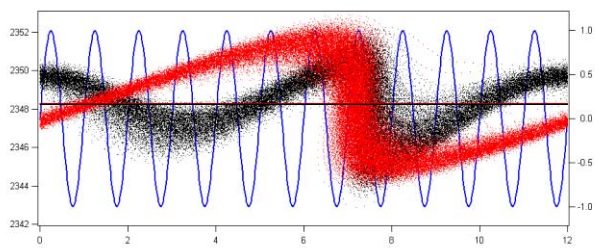

Figure 11: Phase space representation of the bunched electrons at the entrance of the radiator in the case of the standard modulator scheme (red dots) and the one using the 2 modulator sections with a π de-phasing unit (black dots).

Looking at Fig.10, one can appreciate the difference between the standard and new methods. While the bunched electrons (ϕ~7), responsible for coherent emission, are very similar for the two considered configurations, the unbunched electrons look different. Indeed, electrons that have been modulated by using the double modulator setup (black dots) have in general an energy which is closer to the nominal one.

EXTENDING THE LIMIT

According to data shown in fig.9, using the proposed optimized modulator setups is possible to extend the limit for HGHG to shorter wavelengths. Indeed, data show that with the same induced energy spread using the new proposed schemes it is possible to obtain a bunching of 4% at a wavelength which is about half of the one that can be reached with the standard method.

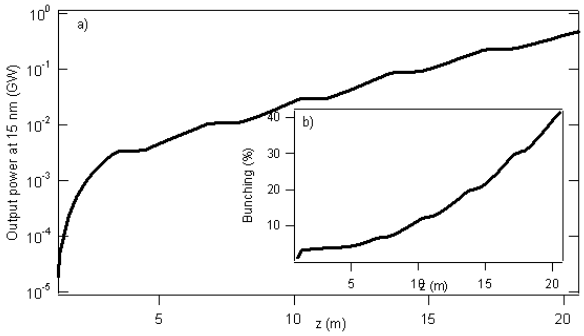

Figure 12: Power growth of the FEL into the radiator at the 16th harmonic (15nm) The use of the new proposed schemes allow to reach more than half GW, In the inset the evolution of the bunching is shown.

This is confirmed by data reported in Fig.12 showing the power evolution along the radiator using an electron bunch which has been passed through the two- modulator scheme for creating the bunching. Data shows that with the proposed modified methods it is possible to go close to saturation at 15 nm. It is important to note that better results in terms of extracted power can be obtained at shorter wavelengths by optimizing the radiator period..

CONCLUSIONS

The limit for the harmonic conversion which can be obtained with the standard HGHG scheme in a realistic machine has been analyzed. Moreover two methods have been presented allowing to extend the limit of HGHG toward shortest wavelengths. These methods only require a modification of the undulator used in the modulator section and a more powerful seed laser.

REFERENCES

[1] FERMI design technical report, in press.
[2] L. H. Yu, Phys. Rev. A **44**, 5178 (1991).
[3] E. Allaria, G. De Ninno, PRL **99,** 014801 (2007).

1D LINEAR INTENSITY SPIKING EVOLUTION IN A SINGLE SHOT OF A SASE FEL

C. Maroli, L. Serafini, INFN-Sezione di Milano,Via Celoria 16, 20133 Milano, Italy
V. Petrillo, Dipartimento di Fisica dell'Università di Milano-INFN Sezione diMilano,
Via Celoria 16, 20133 Milano, Italy

Abstract

It is shown that the simple system of equations used by Bonifacio et al. in 1994, leads to signals characterized by the usual spiky behaviour of the FEL radiation intensity, as well as to "coherent" signals in which the spiking is reduced to a small amplitude random fluctuation on a smooth and nearly constant average value. The two types of signals are obtained with different classes of initial conditions. In particular, coherent signals correspond to initial shot-noise configurations whose closely spaced spikes have widths much smaller than the cooperation length.

INTRODUCTION

The intensity spiking in the radiation of a high-gain free-electron laser starting from noise consists of a sequence of random spikes with wide top-to-bottom variations in the signal received at the end of the undulator [1-4]. The random nature of the spiking is a direct consequence of the random character of the small electromagnetic fields created on the electron beam as it enters the undulator field and the main aspects of the spiking are described accurately by the linear form of the one-dimensional FEL equations.

Starting from the Maxwell-Lorentz 1D equations, the disturbances in the radiation field $\delta A(z,t)$ and bunching factor $\delta b(z,t)$ are given by the following simple linear system in the limit of small radiation fields and when the radiation wave length λ is much smaller than the cooperation length $L_C = \lambda/4\pi\rho$ (ρ is the FEL parameter):

$$\left(\frac{\partial}{\partial t} + c(1-\beta_0)\frac{\partial}{\partial z}\right)\delta A(z,t) = \delta b(z,t),$$
$$\frac{\partial^2}{\partial t^2}\delta b(z,t) = \frac{i}{T_G^3}\delta A(z,t) \qquad (1)$$

These equations are written in the frame moving with the undisturbed beam velocity $c\beta_0$, $T_G = \lambda_w/4\pi c\rho$ is the gain time and λ_w the undulator period. The reason why we reconsider this very simple system of equations is that it may lead to final situations in which there is no spiking and the signal found at the end of 10-20 gain times T_G consists of one single and smooth bump, even when the length L_b of the beam is much longer than the cooperation length L_C.

ONE SINGLE SPIKE

We consider the particular solution of (1)

$$\delta A(\bar{z},\bar{t}) = \int_{-\infty}^{+\infty} dh\, \delta A_0(h) e^{i(h\bar{z}-\omega(h)\bar{t})}$$

where $\omega(h)$ is the root of the dispersion relation $\omega^3 - h\omega^2 - 1 = 0$ with positive imaginary part. The integral in the preceding equation is solved numerically for the case of a Gaussian spike at t=0 and different values of the parameter $\alpha = L_0/L_C$, where L_0 is the FWHM value of the initial Gaussian spike.

Fig.1 shows that the time evolution of the spike depends on the value of its width at t=0 as compared with L_C. In particular, when $L_0 \approx L_C$, the spike increases exponentially while its width increases only slightly. Instead, when $L_0 << L_C$, the width of the spike increases by several orders of magnitude starting from the very small value at t=0.

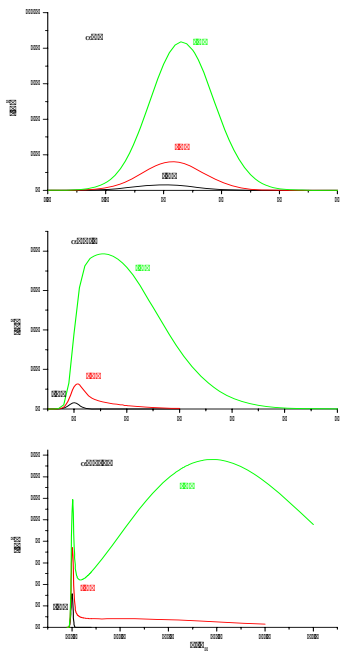

Fig.1(color) – Values of $|\delta A|^2$ *vs* z/L_C. Top figure $\alpha = 1$, curves (a, black),(b, red),(c, green) for $t/T_G = 0, 1, 2$, respectively; middle figure $\alpha = 0.1$, (a),(b),(c) for $t/T_G = 0, 2, 4$; bottom figure $\alpha = 0.01$, (a),(b),(c) for $t/T_G = 0, 4, 6$.

Fig.2 shows what happens for large values of t/T_G and for α = 1, 0.1, and 0.01, while Fig.3 gives the value of the radiation intensity at the peak of the spike vs t/T_G.

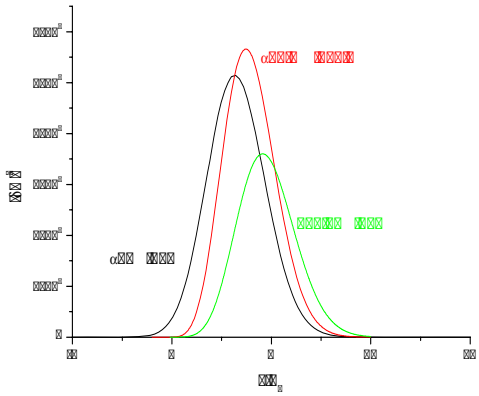

Fig.2 (color) – Values of $|\delta A|^2$ *vs* z/L_C. Curve (a, black) α = 1, t/T_G = 10; curve (b, red) α = 0.1, t/T_G = 12.5; curve (c, green) α = 0.01, t/T_G = 15.

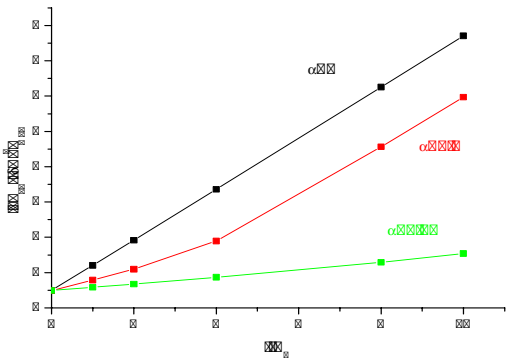

Fig.3 (color) – $|\delta A|^2$ at the maximum of the spike *vs* t/T_G for: (a, black) α = 1; (b, red) α = 0.1; (c, green) α = 0.01

RANDOM SEQUENCE OF SPIKES

Infinitely long electron beam

In this case we assume $\delta A(z,0)$ as the following random sequence of Gaussian spikes

$$\delta A(\bar{z},0) = \sum_{j=1}^{N_{sp}} A_{0j} e^{-\mu_j(\bar{z}-\bar{z}_{0j})^2 + i\theta_j \bar{z}}$$

where N_{sp} is the number of spikes, the peak of each single spike being at $z=z_{0j}$ while the complex numbers A_{0j} and the real numbers μ_j, θ_j and z_{0j} are all random functions of the integer j defined in terms of their average values and r.m.s. deviations.

Fig.4 shows modulus and phase of the complex number δA at t=0 and $t=10T_G$ for an initial random sequence in which all spikes have widths comparable with L_C, the average distance D_{sp} between successive spikes being $5L_C$. At $t=10T_G$, $|\delta A|^2$ has the usual spiky form with wide top-to-bottom variations of the signal intensity. Fig.5 shows modulus and phase of δA at t=0 and 10 T_G, for a sequence of spikes whose widths are all much smaller than L_C. In this case the signal at t = 10 T_G has only a small amplitude fluctuation on top of a smooth and nearly constant average value. The number of "spikes" that characterise the shape of the signal intensity at this time follows approximately the usual rule, i.e., number of spikes ~ bunch length/ $2\pi L_C$ ~ $40/2\pi$ ~ 6-7 but the amplitude of the spikes as compared with the average value of the intensity is much reduced. The two parts (d) in figures 4 and 5 show the profile of the signal intensity at t=10 T_G for the two cases, together with the corresponding incoherent and interference terms.

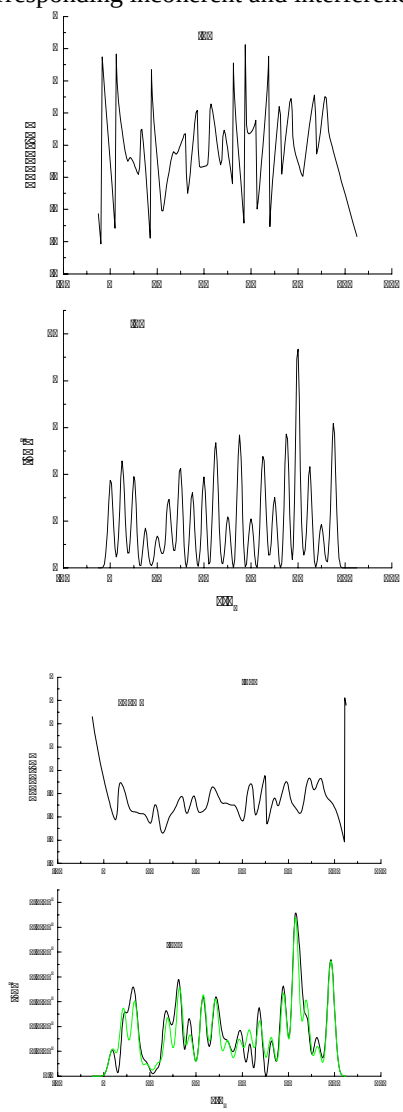

Fig.4 (color) – Phase and modulus squared of δA *vs* z/L_C at t=0 (first column, parts (a) and (b)) and $t=10T_G$ (second column, (c) and (d)). (d) shows the signal intensity (curve 1, black) and the incoherent part (curve 2, green). N_{sp}=20, $D_{sp}=5L_C$, α=1.

While $|\delta A|^2$ in Fig.4 is practically equal to its incoherent part indicating that the interference between different signals is always negligible, in Fig.5 the final signal intensity is the result of a strong process of constructive interference. If it seems appropriate to classify as "incoherent" the signal produced in the case of Fig.4, it seems likewise appropriate to consider as "coherent" the signal produced in the case of Fig.5.

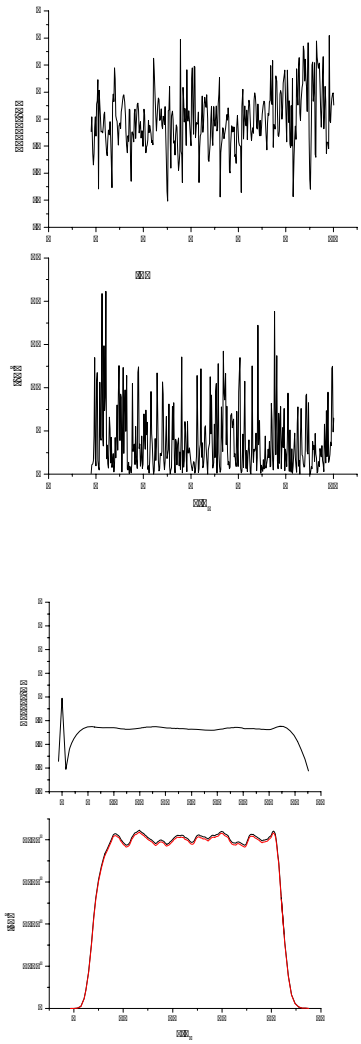

Fig.5 (color) – Same as Fig.6 with N_{sp}=1000, D_{sp}=0.04 L_C, α=0.007. Only part of the signal has been plotted at t=0. Part (d) shows the signal intensity (curve 1, black) and the interference part (curve 2, red).

As a third example, we consider the case in which the signal at t = 0 contains two characteristic lengths, the first of the order of the cooperation length L_C and the second much shorter than L_C. Fig.6 shows what happens in a case in which the initial signal is made up by 225 narrow spikes whose widths are uniformly of the order of 10^{-1} L_C (the average distance between narrow spikes is 0.2 L_C), together with 15 large spikes whose widths are uniformly of the order of L_C (average distance between large spikes 3 L_C). The whole signal at t = 0 covers about 45 cooperation distances. As one can see, spiking develops also in this case after a considerable "cleaning" of the signal, because at t = 10 T_G it is composed by 8 large spikes (number of spikes ~ $45/2\pi$ ~ 7-8) with the usual wide top-to-bottom oscillations. This is due to the long spikes at t = 0 increasing immediately with the largest growth rates.

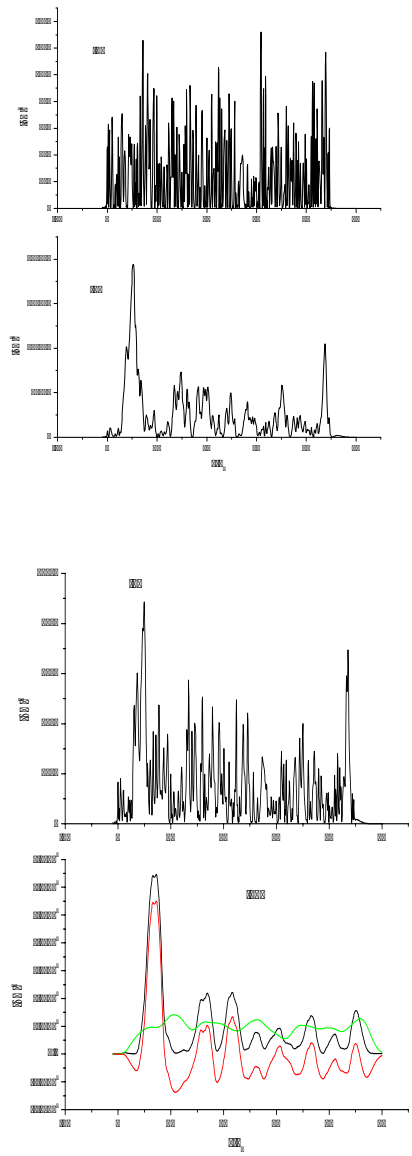

Fig.6 (color) - $|\delta A|^2$ *vs* z/L_C at t/T_G=0,2,4,10 (part (a),(b),(c),(d) respectively). (d) shows also the incoherent (curve 2, green) and interference (curve 3, red) parts of the total signal (curve 1, black) at $t=10T_G$.

Finite-length electron beam

System (1) has been integrated numerically also in the case of a beam of finite length. Fig.7 shows the behaviour of the signal intensity as obtained by solving the system with appropriate initial and boundary conditions. The initial condition for this case consists of 8000 Gaussian spikes with the average distance between successive spikes $D_{sp} = 0.01L_C$. The bunch length is $L_b = 80\ L_C$.

CONCLUSION

The main result of this paper is that according to system (1), the light emitted by an FEL is not always a chaotic light even if the initial signal is noisy [5]. In fact, this system leads to signals dominated by the spiking as well as to signals in which the spiking is reduced to a small amplitude fluctuation superimposed on a smooth pulse. Spiking in the usual sense is associated with initial conditions characterized by a scale-length L_0 of the order of the cooperation length L_C, while absence of spiking requires that the initial shot-noise condition consists of a random sequence of uniformly narrow spikes with widths of the order of $10^{-2}\ L_C$ or smaller, i.e., that $L_0 << L_C$. Since system (1) is based on the slowly-varying envelope approximation (SVEA), the initial conditions are consistent with its nature only if the characteristic length L_0 is longer than the wave-length λ of the emitted radiation. Absence of spiking as deduced on the basis of (1), therefore, requires that L_0 satisfies the inequality $\lambda < L_0 << L_C$. This means small values of the FEL parameter ρ, of the order of 10^{-4} or smaller which are typical of FELs based on static or optical undulators and operating in the regime of very high frequencies or even X-ray FELs.

REFERENCES

[1]R.Bonifacio,L.DeSalvo, P.Pierini, N.Piovella, C.Pellegrini, Phys.Rev.Letters **73**,70(1994)

[2]L.H.Yu, S.Krinsky, Nucl.Instrum.Methods Phys.Res., Sect.A **407**,261(1998)

[3] E.L.Saldin, E.A.Schneidmiller, M.V.Yurkov, Opt.Commun. **148**,383(1998)

[4]K.-Je Kim, in *Towards X-ray Free Electron Lasers*, edited by R.Bonifacio and W.Barletta, AIP Conference Proceedings No.413 (AIP,New York,1997), p.3

[5] Zhirong Huang, K.-Je Kim, Phys. Rev. STAB **10**,034801(2007)

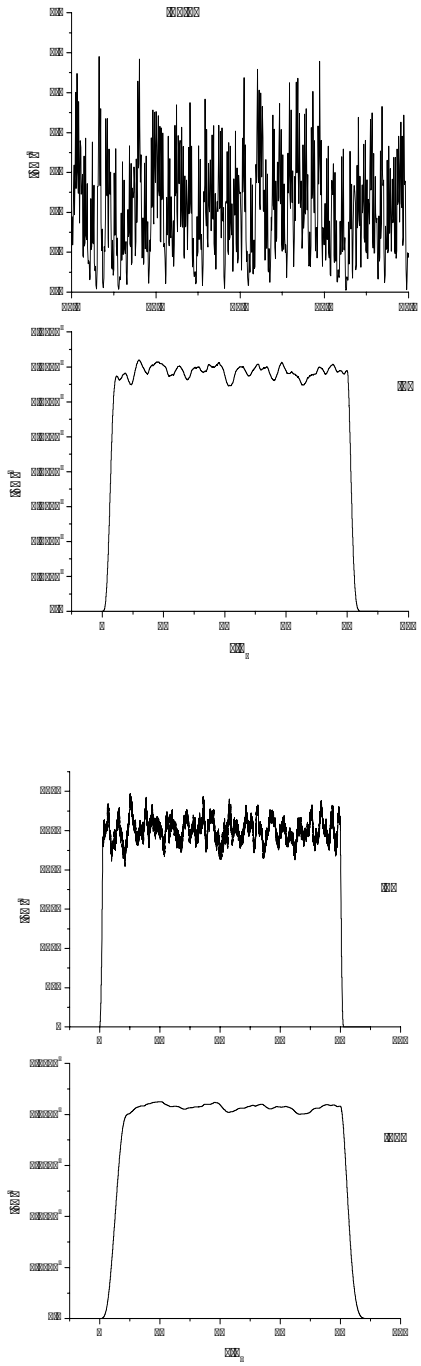

Fig.7 – Signal intensity *vs* z/L_C at times $t/T_G = 0.01$, 1, 5, 10 (parts (a), (b), (c) and (d)) in the case of a finite-length electron beam with $L_b = 80\ L_C$. $N_{sp} = 8000$, $D_{sp} = 0.01L_C$. Only part of the signal is given at t=0.01.

OPTIMIZED DESIGNS FOR CAEP IR FREE-ELECTRON LASER

Xiaojian Shu#, Yuhuan Dou, Institute of Applied Physics and Computational Mathematics, P. O. Box 8009, Beijing 100088, P. R. China

Abstract

The characteristics of CAEP IR free-electron laser are estimated and the optimized designs of the resonator parameters such as the radius of output hole, the size of mirror and the length of the resonator are carried out using our 3D FEL oscillator code. With the appropriate parameters, the saturated power, output power, gain and the construction of optical modes are calculated.

INTRODUCTION

Infrared free-electron lasers (FELs) have broken important ground in optical science for many attractive features such as most notably wavelength tunability, control of spectral and temporal pulse width. In order to bring along the development of correlative technologies such as superconducting technology, linear accelerator technology and optical cavity technology, an infrared FEL device is built at the China Academy of Engineer Physics (CAEP) which driven by superconducting linear accelerator. The radiation wavelength of the device will be in the range from 3 to 8μm.

In this paper, The characteristics of CAEP IR free electron laser devices will be estimated and the optimized design of the resonator parameters such as radius of output hole, the size of mirror, the resonator length will be carried out by using our 3D FEL oscillator code (OSIFEL)[5-7]. The design is achieved by considering two factors as optical cavity character and the transverse optical modes. Based on the appropriate parameters, the saturated power, output power, the resonator gain, the construction of optical modes are calculated.

THE ESTIMATE OF THE OPTICAL CHARACTERISTICS

Table 1: CAEP IR FEL Parameters

Electron beam	
Energy (MeV)	37
Peak current (A)	30
Micro bunch (ps FWHM)	2.5
Energy spread (%)	1
Emittance (π mm mrad)	20
Wiggler	
Period (cm)	3.2
Peak field strength (kG)	3.2
Number of periods	44
Optical	
Wavelength (μm)	4.4
Cavity length (m)	2.769
Mirror curvature (m)	1.499

#shu_xiaojian@iapcm.ac.cn

The electron-beam and wiggler parameters used are listed in Table 1. The energy spread and emittance are specified as FWHM and RMS. Using the parameters of the optical cavity, we can attain that the Rayleigh length is 40cm, the optical waist radius is 0.7mm, and the radius of the optical beam on the cavity mirror is 2.6mm.

THE NUMERICAL SIMULATIONS

To attain optimized the radius of the mirror of the optical cavity and the coupling hole, the numerical simulations are performed using the 3-D OSIFEL code. In the simulations, the distribution functions of transverse position and velocity, energy of the electron are assumed as Gaussian. The corresponding initial values of the sample electrons are given by Monte Carlo method and the initial phases are loaded according to the 'quiet start' scheme to eliminate the numerical noise.

Selection of the Radius of Coupling Hole

The influences of the hole-coupling on the gain, power, output and the mode construction are simulated and studied, as shown in Table 2, where r is the radius of the coupling hole, G_{net} the net gain, P_{in} the saturated intracavity power, P_{out} the output power, η_{loss} the total loss of the resonator, f_{00} the ratio of the fundamental mode, η_{out} the coupling efficiency, which is defined as the ratio of the useful loss to the total loss. It can be seen that the total loss of resonator and coupling efficiency decrease as a reduction in the size of hole, however, the ratio of the fundamental mode increases. If the size of hole is increase, the interaction of the optical radiation with the electrons will become weaker so the net gain of resonator is decreased. According to Table 2, we may select the optimum size of radius r as 0.3 to 0.4mm.

Table 2 Characteristics of resonator as a function of the radius of the coupling hole

r /mm	G_{net} /%	P_{in} /MW	P_{out} /MW	η_{out} /%	η_{loss} /%	f_{00} /%
0.30	23.4	131	3.58	52.7	5.40	98.0
0. 35	20.0	110	3.61	53.0	6.60	97.1
0. 40	15.5	67	3.41	54.6	10.1	94.2
0. 50	10.3	41	2.82	56.0	14.0	90.0

Effects of the Mirror Size

There are mainly two aspects from the influence of the cavity mirror size. One is the influence on the characteristics of the resonator, the other is the influence on the structure of transverse optical modes. That is, when the radius of cavity mirror becomes large, the net gain and the saturated intracavity power will increase; however, the proportion of fundamental mode will decrease because the loss of the high order modes is small. So the optimum

size of the mirror of the resonator must be selected. The characteristics of the resonator as a function of the radius of the mirror of the resonator R are simulated as shown in Table 3, the evolvement curves of fundamental mode as a function of optical pass for different radius of the mirror of the resonator are plotted in Fig. 1. It can be seen from Table 3 as the radius of the mirror of the resonator increases, the quality of resonator becomes better such as the little loss of the resonator, lager output power, and higher coupling efficiency. However, from Fig. 1, it can be seen that when the radius of the mirror of the resonator increases, the distributing of modes becomes more complex and the proportion of fundamental mode will decrease. When the radius of the mirror of the resonator is 1.5cm, the proportion of fundamental mode is about 75%. Considering the quality of resonator and structure of mode, it is suggested that the suitable range of mirror-radius is 0.8-0.9cm. In this range, the proportion of fundamental mode is above 90% in the whole cavity.

Table 3 The characteristics of resonator as a function of the radius of the mirror of the resonator

R/cm	G_{net}/%	P_{in} /MW	P_{out}/MW	η_{out} /%	η_{loss} /%
0.5	20.0	107	3.50	51.4	6.8
0. 8	20.0	110	3.61	53.0	6.6
0.9	20.4	108.6	3.81	55.9	6.68
1.0	20.5	108	4.29	63.4	6.8
1.2	20.0	114	4.38	63.9	6.37
1.5	20.0	117	4.46	66.2	6.1

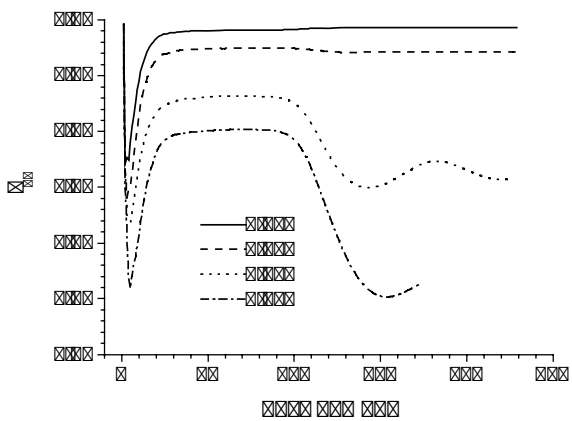

Fig. 1. The evolvement of fundamental mode for different radius of the mirror.

The Detuning Curve

Furthermore, the detuning curves of free-electron laser oscillators are calculated using the 3-D OSIFEL. The result is shown in Fig. 2. It can be seen that the range of the detuning curve is from about –0.2 μm to –7 μm and the detuning length is about 7 μm. Note that the curve is very sharp and the detuning length is shorter because the small signal gain of CAEP IR FEL device is smaller.

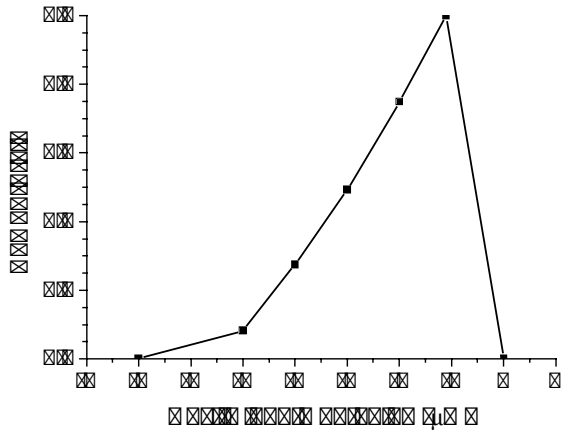

Fig. 2. Detuning curve of CAEP IR FEL from 3D simulations.

Simulation Results

Based on the above numerical simulations, we select the radius of the coupling hole as 0.35mm, the radius of the mirror as 0.8cm. The evolvement curves of the total gain G_t and the net gain G_{net} are shown in Fig. 3. The evolvement curves of intracavity optical power P_{in} and the output power P_{out} are shown in Fig. 4. It can be seen that after 100 pass number, the intracavity optical power is saturated, the total gain is about 28%, the net gain is about 20%, the saturated power is about 110MW, the output peak power is about 3.6MW. The proportion of fundamental mode is about 97%.

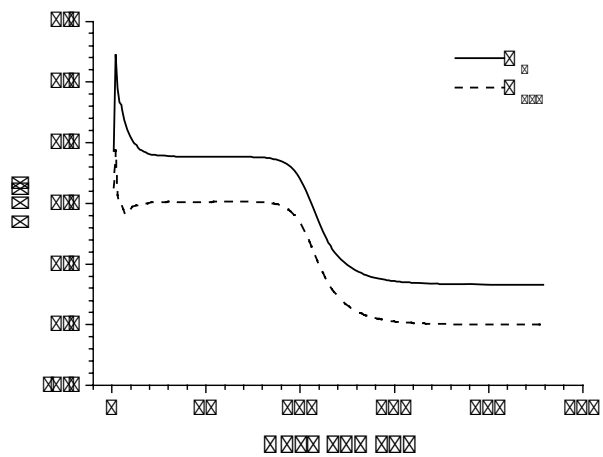

Fig. 3. The evolvement curves of the total gain (G_t) and the net gain (G_{net}).

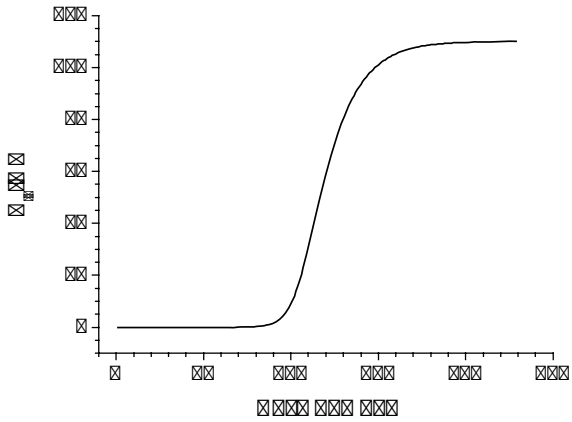

Fig. 4a. The evolvement of the intracavity power.

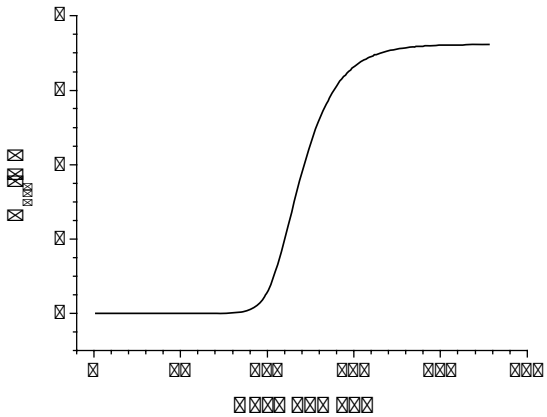

Fig. 4b. The evolvement of the output power.

CONCLUSIONS

In general, the simulation and optimized design of the CAEP IR FEL has been made with the help of our 3-D OSIFEL code. Considering the quality of resonator and structure of mode, the optimum radius of the coupling hole and the radius of the mirror of the resonator have been chosen. It can be attained that the range of the detuning curve is from about –0.2 μm to –7 μm and the detuning length is about 7 μm. With the appropriate parameters, the saturated power, output power, the resonator gain, the construction of optical modes are calculated.

REFERENCES

[1] G.R. Neil, et al., Phys. Rev. Lett., 84 (2000) 662.
[2] C. Behre, et al., Nucl Instr And Meth, A528 (2004) 19.
[3] R. Hajima, et al., "Recent Results of the JAERI Energy-Recovery Linac FEL", 26th International FEL Conference &11th FEL Users Workshop, Trieste, Italy, August 2003.
[4] E.A. Antokin, R.R. Akberdin et al., Nucl Instr And Meth. A528 (2004) 15.
[5] Xiaojian Shu, Yuanzhang Wang, Nucl. Instr. And Meth. A 483 (2002) 205.
[6] Xiaojian Shu,Yuanzhang Wang, Yunqing Jiang, et al.,Optical Engineering, 39 (2000) 1543.
[7] Xiaojian Shu, Yuanzhang Wang, et al., Nucl. Instr. And Meth. A407 (1998) 76.

FEL WITH OROTRON TYPE FEEDBACK*

N.S. Ginzburg#, A.M. Malkin, N.Yu. Peskov, R.M.Rozental, A.S. Sergeev, IAP RAS, Nizhny Novgorod, Russia
K. Kamada, R. Ando, Kanazawa University, Kanazawa, Japan.

Abstract

In this paper we discuss a novel scheme of the free-electron laser in which the electromagnetic wave excited by the electron beam is coupled to the mode of a two-mirror quasioptical resonator by means of corrugation one of the mirrors. The described scheme allows to combine selective properties of quasioptical resonator with relativistic frequency up-conversion of a free electron laser.

INTRODUCTION

In microwave electronics orotron [1] is widely used as a source of radiation in millimeter and submillimeter wavebands. In this device an electron beam is coupled to a mode of quasi-optical resonator by means of the periodical grating one of the resonator mirrors. In our paper we discuss a relativistic modification of such a device which can be useful for providing spatial coherence radiation from large size electron beam

In orotron (Fig.1a) a rectilinear electron beam moving along the periodical grating on the mirror of a quasioptical cavity to be in Cherenkov synchronism to a spatial harmonic of the resonator mode. A novel FEL scheme (Fig. 1b) is suggested in which the slow wave structure of orotron is replaced by shallow Bragg corrugation which provides the coupling of the transverse (with respect to direction of beam propagation) mode of a quasi-optical resonator with longitudinally propagating wave. The latter can be excited by the relativistic electron beam wiggling in undulator field in condition of Dopper frequency up-shift. It should be noted that such a scheme is similar to FEL based on coupling between the quasi cutoff and the propagating mode in cylindrical waveguides which was described in [2,3] (above interaction mechanism will be tested on a 8 mm FEL based on high current accelerator 0.7 MeV/2 kA/200ns at Kanazawa University, Japan). In considered case we replace the waveguide by open quasi-optical resonator and suggest that FEL will be driven by large size sheet electron beam. As in [2] the transverse propagating (cut-off) mode provides the feedback in the system thus leading to self-excitation, while the longitudinal propagating wave is responsible for energy extraction in the steady-state regime of operation. But additionally as will be shown in this paper in considered geometry the cut-off mode provides spatial coherence radiation from sheet electron beam.

*Work supported by RFBR under Grant 06-02-17129-a and the Dynasty foundation.
#ginzburg@appl.sci-nnov.ru

THE ELECTRODYNAMIC MODEL

We consider a resonator consisting of two metallic mirrors . One of the mirrors is corrugated with a period *d*. This corrugation provides coupling between the modes possessing longitudinal (in *z* direction, see Fig.1b) wavenumbers differing by factor $\bar{h} = 2\pi / d$. In the simplest case of the sinusoidal corrugation

$$b(z) = b_0 \cos(\bar{h} z),$$

where $b(z)$ is the deviation of the mirror surface, $2b_0$ is tthe corrugation depth. In the case of more complicated corrugation (for example, meander type corrugation) b_0 is equal to the amplitude of the first space harmonic We assume corrugation to be shallow in the wavelength scale, so that $\bar{h} b_0 << 1$.

We use coupling between the propagating in *z* direction wave and the *q*-th mode of the quasioptical resonator (in the system with the closed waveguide [2] this mode corresponds to the quasi cut-off mode). Above coupling requires that the wavenumber of the longitudinal propagating wave $h = \omega / c$ and the wavenumber of the transverse propagating mode quasioptical resonator ($q\pi / L_y$) should be equal to the translation vector of the Bragg structure:

$$h \approx \frac{q\pi}{L_y} \approx \bar{h},$$

where ω is the operation frequency, *c* is the velocity of light, L_y is the distance between the mirrors (in *y* direction).

Note that due to the symmetry of the considered system not only the forward + *z* direction propagating wave is coupled to the transverse mode, but also a

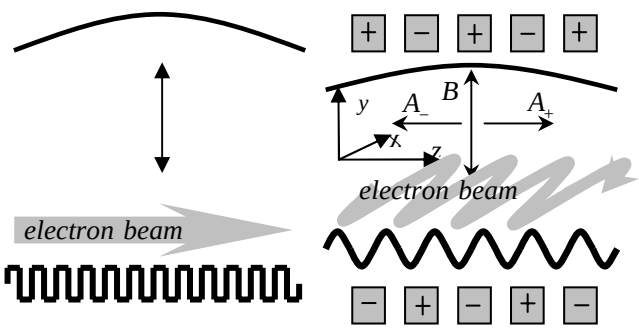

Fig.1. Schematic of the orotron (a) and FEL with orotron-type feedback (b).

backward propagating one. This wave in the FEL does not interact with electrons but provide an additional channel of extraction of electromagnetic energy out of the system.

We present the electromagnetic fields of the coupled modes in the following form, separating its transverse (over *y*-axis) structures and the slowly varying amplitudes over z and x coordinates:

$$\vec{E}_{\pm} = \mathrm{Re}\left(A_{\pm}(t,z,x)\vec{E}_{\mathrm{A}}(y)\mathrm{e}^{\mp ih_A z}\mathrm{e}^{i\omega_c t}\right) \quad (1)$$

$$\vec{E} = \mathrm{Re}\left(B(t)\,f(x,z)\vec{E}_{\mathrm{B}}(y)\mathrm{e}^{i\omega_c t}\right) \quad (2)$$

Here z is the coordinate along the corrugation vector, y is directed between the mirrors an *x* is the transverse coordinate parallel to the mirrors (fig.1b).

The coupling equations describing the scattering of the three modes in assumption of shallow corrugation can be derived from the Maxwell equations using the surface magnetic current technique developed in [4]. These equations include the equations for the propagating modes (1) and the equation of resonator mode excitation (2).

$$\pm\frac{\partial A_{\pm}}{\partial z} + \frac{1}{c}\frac{\partial A_{\pm}}{\partial \tau} + i\delta A_{\pm} = i\alpha B f(x,z) \quad (3)$$

$$\frac{\partial B}{\partial t} + \frac{\omega}{2Q}B = ic\alpha\iint f(x,z)(A_{+}+A_{-})dXdZ\,, \quad (4)$$

Here $\delta = \omega - \dfrac{q\pi c}{L_z}$ is the geometrical detuning from the wave synchronism,

$$\alpha = \frac{hb_0}{4L_y}\frac{1}{\sqrt{hL_z}}$$

is the coupling coefficient proportional to the depth of the corrugation, the factor *Q* describes the quality factor of the mode of regular two-mirror resonator (this factor takes into account both diffraction losses of the mode and Ohmic losses in the resonator walls).

We use the open boundary conditions for the amplitudes of the propagating modes:

$$A_{+}(z=L_z)=0\,,\ A_{-}(z=0)=0\,. \quad (5)$$

where L_z is the length of the mirrors in *z* direction. We also assume that the corrugation is shallow so that the perturbation of the quasioptical resonator modes is small which structure specifies by the function *f(x,z.)* .

It should be noted that the spatial structure of the propagating waves $A_{\pm}$ (z, x) is not fixed and can be found from simulations.

FEL INTERACTION IN THE QUASIOPTICAL RESONATOR WITH CORRUGATED MIRROR

A FEL oscillator can be realised within the described electrodynamic system. We consider a sheet beam of electrons and wiggling in the periodical undulator field and interacting with synchronous A_{+} wave propagating in +z direction Corresponding synchronism condition can be presented as

$$\omega - hv_{\|} \approx \Omega\,,$$

where Ω is the oscillation (bounce) frequency of the particles in the undulator field, $v_{\|}$ is the electrons longitudinal velocity. Electrons wiggling parallel to the *y*-axis generate RF current, which density can be written in thel form

$$j(x,z,t) = I_0(x)J(x,z,t)\,, \quad (6)$$

$$J(x,z,t) = \frac{1}{\pi}\int_0^{2\pi} e^{-i\theta(x,z,t)}d\theta_0\,.$$

Here $I_0(x)$ is the unperturbed beam current density,

$$\theta = \omega t - hz - \int\Omega\mathrm{d}t$$

is the slowly varying electrons phase in the field of synchronous wave, θ_0 is its value in the point of entry in the interaction space. Current (6) excites the synchronous wave so the currant density enters the right hand part of Eq.(3) in a usual way.

Equations of electron motion can be written in the forms

$$\left(\frac{\partial}{\partial Z} + \frac{1}{\beta_{\|}}\frac{\partial}{\partial\tau}\right)^2\theta = \mathrm{Re}\left(\hat{A}_{+}e^{i\theta}\right) \quad (7)$$

Here we use the following dimensionless variables and parameters: $Z = zCh$, $X = 2x/L_x$ $\tau = \omega Ct$, $\beta_{\|}$ is normalized electron velocity, $\hat{A}_{\pm} = e\kappa\mu A_{\pm}/mc\bar{\omega}\gamma_0 C^2$ is the propagating wave norm, $\theta = \bar{\omega}t - hz - \int\Omega\mathrm{d}t$ - is the electron phase in the field of the synchronous wave,

$$C = \left(\frac{eI_0}{mc^3}\frac{c\lambda^2K^2\mu}{4\pi^2\gamma_0 N_{\mathrm{A}}}\right)^{1/3}$$

is the Pierce parameter, μ is an inertial bunching parameter, K is the electron-wave coupling parameter proportional to the amplitude of transverse oscillation of electrons, N_{A} is the norm of the propagating mode.

Electron efficiency of the oscillator is defined by relations

$$\eta = \frac{C}{\mu\left(1-\gamma_0^{-1}\right)}\bar{\eta}\,,\ \bar{\eta} = \frac{1}{2\pi}\int_0^{L_x}\int_0^{2\pi}\left(\frac{\partial\theta}{\partial Z}-\Delta\right)\Bigg|_{Z=L} d\theta_0 dx\,.$$

We suppose the characteristic time of the changing of the resonator mode amplitude B to be substantially greater than the electrons transit time $l/v_{\|}$ and forward and backward waves propagation time l/v_{gr} . In this case it is possible to assume that amplitude of the above mode is constant during intervals $l/v_{\|}$ and l/v_{gr} and neglect time derivatives in the equations of electron motion (7) as well as the propagating wave excitation equations (3).

It is convenient to overwrite the coupled-waves equations in the form:

$$\frac{\partial \hat{A}_+}{\partial Z} + i\delta\hat{A}_+ = i\alpha' B f(x,z) + J \qquad (8)$$

$$\frac{\partial B}{\partial t} + \frac{\omega}{Q_{\mathrm{mod}}} B = i\alpha' \iint f_n(X) A_+ dX dZ$$

$$\left(\frac{\partial \theta^2}{\partial Z^2}\right) = \mathrm{Re}\left(\hat{A}_+ e^{i\theta}\right)$$

These equations form the self-consistent set describing the dynamics of electron-wave interaction in the system under consideration.

The function *f(x,z)* for the lowest mode of two-mirror resonator can be approximated as follows:

$$f(z) = \sin\frac{\pi z}{L_x}\sin\frac{\pi z}{L_z}.$$

Deriving the equations (8) we took into account that the backward wave A_- is not coupled to the electrons, consequently the equation for the backward wave with boundary condition (5) can be integrated. After substitution the result of integration the cutoff mode equation and the second integration one can get the value of losses coefficient which takes into account the scattering of the mode into the backward wave and write the equation (9) entering the modified Q-factor

$$Q_{\mathrm{mod}} \approx \left(\frac{1}{Q} + \frac{2\alpha^2\pi^2 L_z^2 \cos^2(\delta L_z/2)}{\left(\delta^2 L_z^2 - \pi^2\right)^2}\right)^{-1}.$$

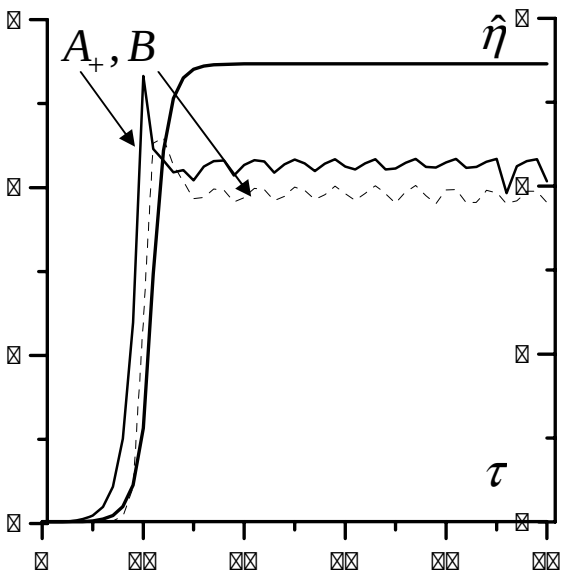

Fig.2. The process of establishment of steady-state oscillations.

The equations (8) were solved numerically. The results of simulations are presented in Fig.2,3 at $L_x = 2$, $L_z = 4.5$, $\Delta = -1$, $\delta = 1.7$, $\alpha' = 2$. In Fig 2 one can see the process of establishment of steady-state oscillation regime. Fig.3 demonstrates the transverse and longitudinal structures of the propagating wave A_+. It is important to note that output phase distribution of propagating wave arg A_+ (x) does not depend on initial conation that actually means spatial synchronization of output radiation associated with this wavethrough the coupling with the cut-off mode *B*. Thus considered FEL scheme provides mode control in oversized microwave system. According to estimations the dimension of the system in the transverse (x and y) directions is sufficient for using above scheme for producing powerful spatially coherent radiation in short millimeter and submillimeter bands from moderately relativistic sheet electron beams.

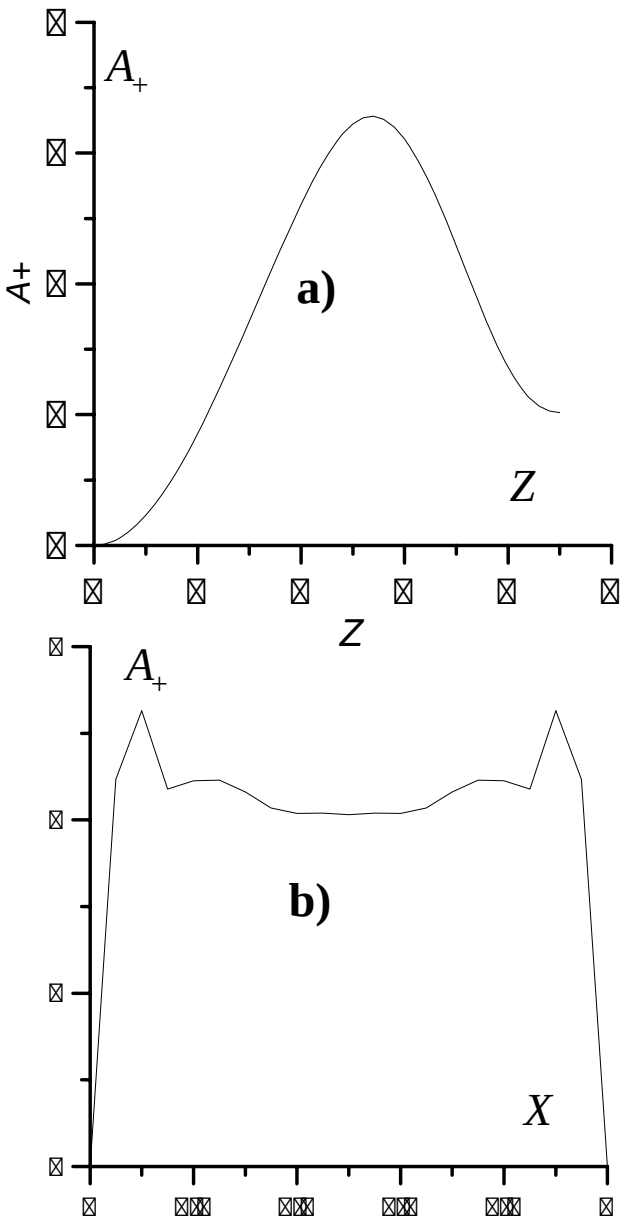

Fig.3. Longitudinal (a) and transverse (b) structure of the propagating wave in the steady state regime.

Note in conclusion that it is interesting to consider situation when the transverse (over y axis) structure of propagating mode A_+ is not fixed and is defined by its interaction with electron beam.

REFERENCES

[1] F.S Rusin,. G.D Bogomolov, in *Proceedings of the IEEE* vol. 57, 1969, p.720
[2] N.S.Ginzburg, A.M.Malkin, N.Yu.Peskov, et. al., *Phys. Rev. ST Accel. Beams* vol. 8, 2005, p. 040705.
[3] N. S. Ginzburg, A. M. Malkin, N. Yu. Peskov, and A. S. Sergeev, *Technical Physics Letters*, Vol. 32, 2006, p. 896
[4] N.F. Kovalev, I.M. Orlova, M.I. Petelin, *Izv. VUZov, Radiofizika* vol.2, 1968, p. 783 (in Russian).

A DESCRIPTION OF GUIDED FEL RADIATION WITH DIELECTRIC WAVEGUIDE EIGENMODES

E. Hemsing*, G. Andonian, J. Rosenzweig, Particle Beam Physics Laboratory, UCLA, USA
A.Gover, Deptartment of Physical Electronics, Tel-Aviv University, Israel

Abstract

We present a description of free-electron laser (FEL) radiation in the high-gain, small-signal regime through an expansion of eigenmodes of a virtual dielectric waveguide. A set of coupled differential equations is derived for the slowly-varying mode expansion coefficients and the electron beam density modulation amplitudes. The equations are decoupled into an algebraic matrix equation for solutions of the self-similar FEL supermodes that propagate with a self-similar profile. For a suitable choice of the form of the virtual dielectric, this virtual dielectric waveguide expansion (VDE) approach has the advantage of describing gain-guided FEL radiation over many Rayleigh lengths in terms of a basis that parallels the standard gaussian modes of free-space paraxial optics.

INTRODUCTION

The optical guiding of light in free-electron lasers (FELs) is a well-known phenomena that results during amplification as the coherent interaction between the electron beam (e-beam) and the electromagnetic (em) field introduces an inward curvature in the phase front of the light, refracting it back towards the lasing core of the e-beam[1, 2]. During the exponential gain process the e-beam can behave like a guiding structure that suppresses diffraction, reducing transverse power losses and enhancing the em field amplification (gain-guiding). The guided em field eventually settles into a propagating, self-similar eigenmode of the FEL system (supermode) with a fixed transverse profile distribution and spot size[3, 4].

Guided modes have been previously explored analytically by direct derivation of the eigenmode equations from the coupled Maxwell-Vlasov equations[3, 5, 6], and through expansions of the FEL signal fields in terms of hollow, conducting-boundary waveguide eigenmodes[4], step-index fiber modes[2], and free-space paraxial waves[7, 8]. Since, in an FEL, the e-beam operates simultaneously as an optical source and as a wave-guiding structure, an em mode description permits investigation of the coupling efficiency and guiding characteristics of individual modes to the e-beam. Of particular interest is the coupling to the well-known Hermite-Gaussian or Laguerre-Gaussian modes that describe free-space waves in the paraxial limit. The propagation and guiding of these modes over many Rayleigh lengths in an FEL interaction can be investigated directly by an expansion of the radiation field in terms of guided eigenmodes that have the form of paraxial modes evaluated at the waist. This connection is useful both in characterizing the free-space propagating radiation fields emitted from the FEL, but also in understanding input radiation coupling, as in the case of seed radiation injection.

FIELD EXPANSION AND MODE EXCITATION IN A WAVEGUIDE

In a structure of axial translational symmetry, the radiation fields can be expanded in terms of transverse radiation modes with amplitudes that vary only as a function of the symmetry axis, z. Neglecting backward propagating waves and approximating the fields as dominantly transverse, the radiation field expansion in terms of waveguide modes is,

$$\underline{\tilde{E}}_\perp(\underline{r}) = \sum_q C_q(z)\underline{\tilde{\mathcal{E}}}_{\perp q}(r_\perp)e^{ik_{zq}z}$$

$$\underline{\tilde{H}}_\perp(\underline{r}) = \sum_q C_q(z)\underline{\tilde{\mathcal{H}}}_{\perp q}(r_\perp)e^{ik_{zq}z}. \quad (1)$$

where $\underline{\tilde{\mathcal{H}}}_{\perp q} = (1/Z_q)\hat{e}_z \times \underline{\tilde{\mathcal{E}}}_{\perp q}$, k_{zq} is the q^{th} mode axial wavenumber, and $Z_q = (k/k_{zq})\sqrt{\mu_0/\epsilon_0}$ for TE modes. The modes are orthogonal and normalized to

$$\mathcal{P}_q = \frac{1}{2}\mathrm{Re}\Big[\int\int[\underline{\tilde{\mathcal{E}}}_{\perp \mathrm{q}}(\mathrm{r}_\perp) \times \underline{\tilde{\mathcal{H}}}^*_{\perp \mathrm{q}}(\mathrm{r}_\perp)] \cdot \hat{\mathrm{e}}_\mathrm{z}\mathrm{d}^2\mathbf{r}_\perp\Big]. \quad (2)$$

The mode $\tilde{\mathcal{E}}_{\perp q}$ is an eigenmode of a dielectric medium with transverse variation in the refractive index $n(r_\perp)$. Assuming $\nabla n^2 \ll k$, the eigenmode equation is

$$\nabla^2_\perp \underline{\tilde{\mathcal{E}}}_{\perp q}(r_\perp) + [n(r_\perp)^2k^2 - k^2_{zq}]\underline{\tilde{\mathcal{E}}}_{\perp q}(r_\perp) = 0 \quad (3)$$

where $k = \omega/c$. With equations (1) and (3) and under the paraxial approximation ($|d^2C_q/dz^2| \ll |k^2C_q|$) for the slowly-growing coefficients, the excitation equation for the mode q in the presence of a source current is given by,

$$\frac{d}{dz}C_q(z) = -\frac{1}{4\mathcal{P}_q}e^{-ik_{zq}z}\int\int \underline{\tilde{J}}_\perp(\mathbf{r}) \cdot \underline{\tilde{\mathcal{E}}}^*_{\perp q}(r_\perp)d^2\mathbf{r}_\perp - i\sum_{q'} C_{q'}(z)e^{-i\Delta k_{zqq'}z}\kappa^d_{q,q'} \quad (4)$$

where

$$\kappa^d_{q,q'} = \frac{\omega\epsilon_0}{4\mathcal{P}_q}\int\int[n(r_\perp)^2 - 1]\underline{\tilde{\mathcal{E}}}_{\perp q'}(r_\perp) \cdot \underline{\tilde{\mathcal{E}}}^*_{\perp q}(r_\perp)d^2\mathbf{r}_\perp \quad (5)$$

and $\Delta k_{zqq'} = k_{zq} - k_{zq'}$ is the difference between the axial wavenumbers of the modes q and q'. The term $\kappa^d_{q,q'}$ characterizes the mode coupling and represents the virtual polarization currents and charges that must be subtracted when using eigenmodes of a dielectric waveguide, since no such structure exists in the physical system.

* ehemsing@physics.ucla.edu

ELECTRON BEAM FLUID MODEL AND COUPLED EXCITATION EQUATIONS

A linear plasma fluid model for a cold e-beam (negligible energy spread) can be used to describe the small-signal excitation in an FEL interaction[4]. A relativistic e-beam in an FEL experiences transverse oscillations driven by an interaction with a periodic structure. This motion drives an axial ponderomotive force that modulates the axial electron velocity such that, to first-order, the axial velocity of a cold beam within a static undulator can be expanded as $v_z(\underline{r},t) = v_{z0} + \mathrm{Re}[\tilde{v}_{z1}(\underline{r})e^{-i\omega t}]$ where $v_{z0} = \beta_z c$ is the d.c. component and $\tilde{v}_{z1}$ is the perturbation oscillating at signal frequency ω. Longitudinal variations in the velocity like the half-frequency modulation found in planar undulator systems are ignored here. The velocity modulation $\tilde{v}_{z1}$ develops a density bunching modulation that is similarly described in a linear model as $\mathsf{n}(\underline{r},t) = \mathsf{n}_0(r_\perp) + \mathrm{Re}[\tilde{\mathsf{n}}_1(\underline{r})e^{-i\omega t}]$ where $\mathsf{n}_0(r_\perp)$ is the transverse density profile of the e-beam. The a.c. component of the longitudinal current density results from both the axial velocity and density perturbations and is $\tilde{J}_{z1}(\underline{r}) = -e[\mathsf{n}_0(r_\perp)\tilde{v}_{z1}(\underline{r}) + v_{z0}\tilde{\mathsf{n}}_1(\underline{r})]$. If the transverse divergence of the current perturbation is assumed small $\nabla_\perp \cdot \tilde{J}_{\perp 1} \ll \partial \tilde{J}_{z1}/\partial z$, the continuity equation can be written as $d\tilde{J}_{z1}/dz = -i\omega e\tilde{\mathsf{n}}_1(\underline{r})$. The transverse component of the current density that excites the signal wave is written in terms of the density perturbation as

$$\underline{\tilde{J}}_\perp(\underline{r}) = -\frac{1}{2}e\tilde{\mathsf{n}}_1(\underline{r})\underline{\tilde{v}}_{\perp w}e^{-ik_w z}. \tag{6}$$

where $\underline{\tilde{v}}_{\perp w}$ is the transverse velocity vector and k_w is the axial wavenumber of the periodic undulator lattice.

From the expressions for the current density and the relativistic force equation for the axial velocity perturbation, the density bunching can be expressed as a second order differential equation[4]. It is useful to define the density bunching parameter

$$\tilde{\mathbf{i}}_q(z) = \frac{e}{8\mathcal{P}_q}e^{-i\frac{\omega}{v_{z0}}z}\int\int \tilde{\mathsf{n}}_1(\underline{r})\underline{\tilde{v}}_{\perp w}\cdot\underline{\tilde{\mathcal{E}}}^*_{\perp q}(r_\perp)d^2\mathbf{r}_\perp. \tag{7}$$

By combining the density modulation equation from Ref [4] with Eqs (4) and (7) we obtain a coupled form for the mode excitation evolution equations:

$$\frac{d}{dz}C_q(z) = \tilde{\mathbf{i}}_q(z)e^{i\theta_q z} - i\sum_{q'}\kappa^d_{q,q'}C_{q'}(z)e^{-i\Delta k_{z;qq'}z}$$

$$\Big[\frac{d^2}{dz^2} + \theta^2_{pr}\Big]\tilde{\mathbf{i}}_q(z) = i\sum_{q'}Q_{q,q'}C_{q'}(z)e^{-i\theta_{q'}z} \tag{8}$$

where $\theta_q = \omega/v_{z0} - (k_{zq} + k_w)$ is the characteristic detuning parameter for a given mode. The coupling between the e-beam with transverse density distribution function $f(r_\perp)$ and the FEL radiation field is given by the parameter $Q_{q,q'} = \theta^2_p\kappa_{q,q'}$ in Eq (8) where $\theta^2_p = e^2\mathsf{n}_0/\gamma\gamma^2_z\epsilon_0 m_e v^2_{z0}$ and the e-beam mode-coupling coefficient $\kappa_{q,q'}$ is

$$\kappa_{q,q'} = \frac{\epsilon_0}{8\mathcal{P}_q}(k_{zq} + k_w)\int\int f(r_\perp)\tilde{\mathcal{E}}_{pm,q'}\underline{\tilde{v}}^w_\perp\cdot\underline{\tilde{\mathcal{E}}}^*_{\perp q}d^2\mathbf{r}_\perp. \tag{9}$$

The radiation field and the undulator field are assumed to be polarization matched. The axial ponderomotive field is $\tilde{\mathcal{E}}_{pm,q}(r_\perp) = \frac{1}{2}[\underline{\tilde{v}}_{\perp q}\times\underline{\tilde{\mathcal{B}}}^*_{\perp w} + \underline{\tilde{v}}^*_{\perp w}\times\underline{\tilde{\mathcal{B}}}_{\perp q}]\cdot\hat{e}_z$ where $\tilde{v}_{\perp q}$ is the transverse electron velocity due to the Lorentz force of the q^{th} mode of the signal field, $\tilde{\mathcal{B}}_{\perp w}$ is the transverse magnetic field of the undulator, $\tilde{v}_{\perp w}$ is the transverse velocity due to the undulator field and $\tilde{\mathcal{B}}_{\perp q} = \mu_0\tilde{\mathcal{H}}_{\perp q}$. The term $JJ = [J_0(\alpha) - J_1(\alpha)]^2$ can be included in the coupling parameter $\kappa_{q,q'}$ for a strong planar undulator ($JJ = 1$ for a helical undulator geometry), where J_0 and J_1 are the first and second order Bessel functions and $\alpha = \omega cK^2/(8\gamma^2 v^2_{z0}k_w)$ where $K = e|\tilde{\mathcal{B}}_{\perp w}|/mck_w$ is the undulator parameter. The relativistic factor is $\gamma = \gamma_z\sqrt{1 + K^2/2}$ with $\gamma^2_z = 1/(1 - \beta^2_z)$. The effect of the longitudinal space-charge in the beam is represented by the finite-width beam parameter $\theta_{pr} = \bar{r}\theta_p$ where $\theta_p = \omega_{p0}/v_{z0}$ is the longitudinal space-charge parameter (plasma wavenumber) of a uniformly distributed electron beam profile used in a 1D model. The plasma reduction factor satisfies $|\bar{r}| \le 1$, and can be calculated numerically for a specific e-beam geometry[7]. In the limit that $\lambda\beta_z \ll r_0$ where r_0 is the e-beam radius, one can make the approximation $\bar{r} \simeq 1$.

The first equation in Eqs (8) describes the excitation of the mode amplitude C_q of a virtual dielectric waveguide eigenmode due to the density perturbation and transverse wiggling motion of the electrons throughout the FEL interaction. The second equation in (8) highlights the evolution of the modal density bunching parameters through the e-beam coupling to the expansion modes.

The initial conditions for Eqs (8) specify the operating characteristic of the FEL. For example, when operating as a single-pass amplifier (seeded FEL) there is no initial density and velocity modulation $\tilde{\mathbf{i}}_q(0), d\tilde{\mathbf{i}}_q(z)/dz|_{z=0} = 0$ and the initial seed field is non-zero $C_q(0) \neq 0$. Alternately, for a self-amplified spontaneous emission FEL (SASE), the amplified shot noise can be related to the pre-bunching conditions $\tilde{\mathbf{i}}_q(0) \neq 0, d\tilde{\mathbf{i}}_q(z)/dz|_{z=0} = 0$ and the input signal field vanishes $C_q(0) = 0$.

SUPERMODE MATRIX SOLUTION

In the high-gain regime of an FEL the radiation field is optically guided towards the beam axis. After a sufficiently long interaction length, prior to the onset of saturation, a balance is reached between the natural diffraction effects of the radiation and the focusing effects of the gain-guiding. The FEL settles into a period of steady exponential growth, characterized by a radiation field profile that propagates self-similarly which can be descried by a specific, fixed combination of expansion modes called the *supermode*. In

order to find the system supermodes, it is enough to find the characteristic solutions to Eq (8). These are the combinations of expansion modes that propagate with a distinct wavenumber k_{SM}, and can be found by looking for a solution of the form

$$\underline{\tilde{E}}_{SM}(\underline{r}) = \Big[\sum_q b_q \ \underline{\tilde{\mathcal{E}}}_q(r_\perp)\Big] e^{ik_{SM}z} \qquad (10)$$

where the mode amplitude coefficients b_q are constants and the z-dependence is contained solely in the exponential term. The excitation equations for this supermode expansion can be found by transforming the mode amplitude coefficents $C_q(z)$ via:

$$C_q(z) = b_q e^{i(k_{SM}-k_q)z}. \qquad (11)$$

Plugging this expression into the coupled excitation evolution equations (8), a single equation is obtained for the supermode coefficients:

$$(\theta_{pr}^2 - \theta_{SM}^2)\Big[(k_{SM}-k_{zq})b_q + \sum_{q'} \kappa^d_{q,q'} b_{q'}\Big] = \sum_{q'} Q_{q,q'} b_{q'}, \qquad (12)$$

where $\theta_{SM} = \theta + k - k_{SM}$ is the supermode detuning parameter, and θ is the detuning parameter for a 1D model ($k_{zq} = k$). Since we anticipate that the supermode propagates with a slightly modified axial wavenumber from that of free-space, we define $k_{SM} = k + \delta k$ and Eq (12) can be written in matrix form

$$\left[\Big[(\delta k - \theta)^2 - \theta_{pr}^2\Big][\underline{\underline{\mathbf{I}}}\delta k + \underline{\underline{\kappa}}^d - \underline{\underline{\Delta k}}] + \underline{\underline{Q}}\right]\underline{b} = \underline{0} \qquad (13)$$

where $\underline{\underline{\Delta k}}$ is diagonal with matrix elements given by $\Delta k_q = k_{zq} - k$.

Solutions to the determinant equation $|[(\delta k - \theta)^2 - \theta_{pr}^2][\underline{\underline{\mathbf{I}}}\delta k + \underline{\underline{\kappa}}^d - \underline{\underline{\Delta k}}] + \underline{\underline{Q}}| = 0$ result in $3N$ solutions for δk, where N is the number of expansion modes. Each δk can then be inserted in Eq (13) to find a non-trivial solution (if one exists) for the mode amplitude vector $\underline{b}$, the components of which are the expansion coefficients of a supermode of the FEL system. From Eq (10) and the definition of k_{SM} it can be seen that the solution for δk with the largest imaginary component drives the highest gain, and dominates over the rest of the supermodes. This value, δk_{SM}, used in solving Eq (13) will yield the coefficients of the dominant supermode.

We note that when $\underline{\underline{\Delta k}}, \underline{\underline{\kappa}}^d = 0$, as in the case of an expansion into a free-space mode basis, the matrix equation in (13) reduces to a generalized matrix form of the canonical FEL cubic equation. Further, in the limit of a large transverse beam profile, $Q_{q,q'} \to Q$ and Eq (13) is the familiar 1D FEL cubic equation for the mode independent beam coupling parameter Q.

LAGUERRE-GAUSSIAN MODE EXPANSION

The choice of the refractive index in Eq (3) determines the form of the basis expansion used in the excitation equations (8). For quadratic refractive index of the form $n^2(r_\perp) = n_0^2[1 - 2\Delta(r/a)^2]$ with $\Delta \ll 1$, the constituent VDE expansion basis consists of a complete, orthogonal set of either Hermite-Gaussian (HG)[9] or Laguerre-Gaussian (LG) functions[10]. Since both HG and LG modes also occur as solutions to the paraxial wave equation, this choice for the refractive index identifies a connection between the VDE method and a description of the FEL system using paraxial, diffracting modes of free-space. The intrinsic advantage of the guided mode expansion formalism is the ability to efficiently model the signal field during high-gain over many Rayleigh lengths with only a few modes.

For geometries that are largely axisymmetric over the interaction length, LG modes provide a convenient working basis to model the FEL radiation. They have the form

$$\tilde{\mathcal{E}}_{\perp;p,l}(r,\phi) \propto e^{-il\phi} e^{-\frac{r^2}{w_0^2}} \Big(\frac{r\sqrt{2}}{w_0}\Big)^{|l|} L_p^{|l|}\Big(\frac{2r^2}{w_0^2}\Big) \qquad (14)$$

where L_p^l is an Associated Laguerre polynomial. The mode index q takes on two values (p, l) corresponding to the radial and azimuthal mode numbers, respectively. The argument of the LG polynomials contain the parameter defined as $w_0^2 \equiv 2a/kn_0\sqrt{2\Delta}$ which sets a characteristic waist size in terms of the refractive index parameters.The field modes in Eq (14) are thus identical to free-space LG fields that satisfy the paraxial wave equation, when the free-space modes are evaluated at the waist. This waist definition specifies a characteristic dielectric profile form for a quadratic dielectric, in which a free-space Laguerre-Gaussian mode with waist size w_0 will propagate as a guided eigenmode.

It is noted that the LG modes of Eqn (14), as well as those of a free-space system, possess an axial field component for both the electric and magnetic fields for modes with $|l| > 0$. The magnitude of the axial electric field component is on the order of λ/w_0 by comparison to the principle transverse component, and can be neglected, validating the approximation made in deriving the amplitude evolution equation (4)[11].

It is instructive to cast the associated Rayleigh range for a free-space paraxial wave in terms of the dielectric parameters $z_R = kw_0^2/2 \equiv a/n_0\sqrt{2\Delta}$, which yields a refractive index $n^2(r) = n_0^2 - (r/z_R)^2$. The axial wavenumber $k_{zq} = k_{z;p,l}$ is given by

$$k_{z;p,l}^2 = k^2 n_0^2 - \frac{4}{w_0^2}(2p + l + 1). \qquad (15)$$

The refractive index on axis can be taken as $n_0^2 \simeq 1$ and the FEL signal field can be expanded into a sum of LG guided modes given by Eq (14), each with wavenumber $k_{z;p,l}$. The expansion waist w_0 is arbitrary, but can be chosen to be on the order of the e-beam size to facilitate efficiency in modeling the beam evolution with a finite number of modes included in the expansion[12].

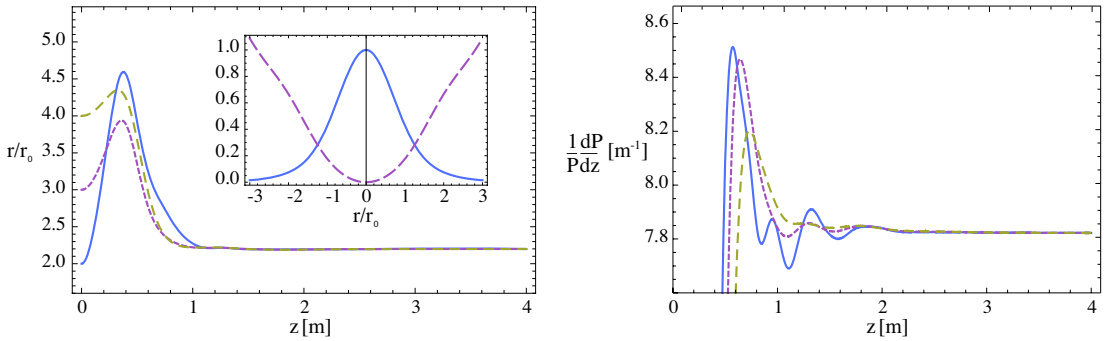

Figure 1: Left: Numerically modeled evolution of the radiation spot size throughout undulator for VISA FEL at $\lambda = 1064$nm for $\theta = 0$ detuning. Three spot sizes ($w_{s0} = 2r_0, 3r_0$, and $4r_0$) for a $P = 0.1\mu W$ gaussian seed are introduced at the undulator entrance with a $r_0 = 115\mu$m gaussian e-beam $f(r) = e^{-r^2/r_0^2}$. During the start-up period early on, the seed beam diffracts briefly until exponential gain develops. The self-focusing effects then guide the beam toward a fixed spot size, characteristic of the FEL supermode. Inset: Normalized field intensity (solid) and phase (dashed) profiles of supermode. Right: Normalized differential radiation power evolution for each input seed. The power slope for each input spot size evolves towards the same value after the supermode is established halfway through the 4 m VISA undulator.

SIMULATIONS

Results generated by the VDE method that uses an LG mode expansion basis to model the Visible to Infrared SASE or Seeded Amplifier (VISA) FEL currently in operation at Brookhaven National Laboratory are shown in Figure 1. The VISA FEL is ideal for investigations using an LG expansion since it has generated both hollow and spiral transverse em intensity patterns that are suggestive of single or multiply interfering LG modes[13]. The results in Figure 1 show the evolution of various injected radiation fields towards the supermode, both in the transverse spot sizes (left) and in the differential power curves (right) as a function of the longitudinal coordinate. Both the inwardly curved phase front (dashed line – inset) and the "pinched gaussian" intensity profile (solid line – inset) of the radiation at the undulator exit (z=4 m) display the signature characteristics of a gain-guided FEL supermode.

CONCLUSIONS

We have presented a description of the FEL electromagnetic signal field during high-gain through an expansion into a complete set of eigenmodes of a virtual dielectric waveguide. The FEL supermode can be found in the small-signal limit by finding the eigenfunction solutions to the coupled mode excitation equations derived from a cold e-beam fluid model. The choice of a quadratic index medium for the virtual dielectric yields a set of guided Hermite-Gaussian or Laguerre-Gaussian modes that relate to paraxial modes of free-space. Future work will involve comparisons of the VDE formulation with 1) experiments at VISA, where plans are underway to measure the phase and mode content of the em radiation[14] and, 2) numerical simulations using GENESIS 1.3 to verify and support the analytic and experimental results. The coupling to higher-order radial and azimuthal modes will also be investigated.

REFERENCES

[1] N. M. Kroll, P. L. Morton, and M. N. Rosenbluth, IEEE Journal of Quantum Electronics 17, 1436 (1981). G. T. Moore, Nuclear Instruments and Methods in Physics Research A 239, 19 (1985).

[2] E. T. Scharlemann, A. M. Sessler, and J. S. Wurtele, Phys. Rev. Lett. 54, 1925 (1985).

[3] M. Xie and D. A. G. Deacon, Nuclear Instruments and Methods in Physics Research A 250, 426 (1986).

[4] Y. Pinhasi and A. Gover, Phys. Rev. E 51, 2472 (1995).

[5] M. Xie, Nuclear Instruments and Methods in Physics Research A 445, 59 (2000). M. Xie, Nuclear Instruments and Methods in Physics Research A 445, 67 (2000).

[6] E. L. Saldin, E. A. Schneidmiller, and M. V. Yurkov, Optics Communications 97, 272 (1993).

[7] Y. Pinhasi and A. Gover, Phys. Rev. E 48, 3925 (1993).

[8] P. Sprangle, A. Ting, and C. M. Tang, Phys. Rev. Lett. 59, 202 (1987).

[9] A. Yariv, Optical Electronics in Modern Communications (Oxford University Press, USA, 1997)

[10] L. Yu, et al, Journal of Physics A 31, 9353 (1998). O. Georg, Applied Optics 21, 141 (1982).

[11] W. L. Power, et al Phys. Rev. A 52, 479 (1995).

[12] E. Hemsing, A. Gover, and J. Rosenzweig, unpublished.

[13] G. Andonian, et al, Proceedings of FEL 2006 Conference, 443-446, Berlin, Germany.

[14] E. Hemsing, et al, Proceedings of PAC 2007 Conference, 1263-1265, Albuquerque, New Mexico, USA.

ENHANCING FEL POWER WITH PHASE SHIFTERS*

Daniel Ratner†, Stanford University, CA, 94305 USA
Alex Chao, Zhirong Huang, SLAC, Stanford, CA 94309 USA

Abstract

Tapering the undulator parameter is a well-known method for maintaining the resonant condition past saturation, and increasing Free Electron Laser (FEL) efficiency. In this paper, we demonstrate that shifting the electron bunch phase relative to the radiation is equivalent to tapering the undulator parameter. Using discrete phase changes derived from optimized undulator tapers for the Linac Coherent Light Source (LCLS) x-ray FEL, we show that appropriate phase shifts between undulator sections can reproduce the power enhancement of undulator tapers. Phase shifters are relatively easy to implement and operate, and could be used to aid or replace undulator tapers in optimizing FEL performance.

INTRODUCTION

Despite the projected six orders of magnitude increase in peak power for Self-Amplified Spontaneous Emission (SASE) x-ray FELs, some applications, including single molecule imaging, may require still higher photon flux [1]. To increase the power in higher harmonics, it is possible to shift the FEL electron phase relative to the radiation, suppressing the power in the fundamental wavelength and prolonging growth of the harmonics [2]. We have studied the related use of phase shifts to correct slippage at saturation and boost the power output of the fundamental wavelength. Similar methods have been mentioned in the past in connection with harmonic radiation [2] and numerical simulations [3]. Here we undertake a detailed analytical and numerical study of enhancing FEL power with phase shifters. We explore the relation between phase shifts and undulator tapers to calculate optimal phase shifts for SASE FELs in the saturation regime. The phase shift method, while equivalent to tapering the undulator parameter, provide an independent knob to maximize the FEL performance.

ONE-DIMENSIONAL ANALYSIS

The resonant condition

$$\lambda_1 = \lambda_u \frac{1 + K^2/2}{2\gamma_0^2} \tag{1}$$

sets the radiation wavelength, λ_1 for an FEL; after each undulator period, λ_u, the electron bunch slips behind the radiation by exactly λ_1. It follows that when the resonant condition holds, the phase, Ψ, between the electron bunch and radiation stays constant (up to 2π). Near saturation, the bunch loses significant energy to the radiation, and the FEL resonant condition begins to fail. As $\gamma_0 \to \gamma < \gamma_0$, the resonant wavelength increases, and the electrons slip more than one radiation wavelength during each undulator period. Introducing a phase shift (by means of a small chicane) can correct for the increase in slippage by shifting the bunch backwards into the previous bucket. (If, over many undulator periods, the bunch has accumulated extra slippage of $\Delta\theta$, then the chicane shifts the electrons an additional $2\pi - \Delta\theta$. There is no easy way to shift electrons forward.) After the shift, the electron bunch is once again in phase with the radiation, preserving the resonant condition farther into saturation.

To show that compensating for the additional slippage can optimize the radiation power in the undulator, we use a simplified 1-D FEL model and neglect the effect of detuning. The slowly varying radiation field $\tilde{a}$ is given by

$$\frac{d\tilde{a}}{d\bar{z}} = -\langle e^{-i\theta_j} \rangle \,. \tag{2}$$

The phases, $\theta \equiv (k + k_u)z - \omega t + \text{const}$, are the longitudinal positions of the electrons relative to the electron bunch given in units of $\lambda_1/2\pi = 1/k_u$. The variable $\bar{z} \equiv 2k_u\rho z$, is the scaled position along the undulator. Here ρ is the dimensionless FEL parameter [4]. Finally, the average in Eq. (2) is taken over all electrons. Taking $\tilde{a} \equiv Ae^{i\Psi}$, with Ψ the phase of the radiation relative to the electron bunch, we can separate out the magnitude and phase components of the radiation field:

$$\frac{d\tilde{a}}{d\bar{z}} = e^{i\Psi}\left[\frac{dA}{d\bar{z}} + iA\frac{d\Psi}{d\bar{z}}\right] . \tag{3}$$

Inserting Eq. (3) into Eq. (2) and separating real and imaginary parts gives

$$\frac{dA}{d\bar{z}} = -\left\langle \cos(\theta_j + \Psi) \right\rangle , \tag{4}$$

$$\frac{d\Psi}{d\bar{z}} = \frac{1}{A}\langle \sin(\theta_j + \Psi) \rangle \,. \tag{5}$$

Our strategy is to maximize A by introducing an arbitrary phase shift, ϕ between the radiation and electrons, and then maximize $\frac{dA}{d\bar{z}}$ with respect to ϕ at all points along the undulator. (A chicane delays all particles relative to the radiation, introducing an arbitrary change in relative phase of the bunch.) Our goal, then, is to choose ϕ to maximize the quantity $-\langle \cos(\theta_j + \Psi + \phi) \rangle$.

Adding the arbitrary phase, ϕ, gives

$$\frac{dA}{d\bar{z}} = \langle \cos(\theta_j + \Psi) \rangle \cos(\phi) - \langle \sin(\theta_j + \Psi) \rangle \sin(\phi) \tag{6}$$

*Work supported by Department of Energy contract DE–AC02–76SF00515.

† dratner@slac.stanford.edu

To find the optimal phase shift, we differentiate with respect to ϕ to find

$$\phi_{max}(\bar{z}) = \arctan\left[-\frac{\langle\sin(\theta_j+\Psi)\rangle}{\langle\cos(\theta_j+\Psi)\rangle}\right]. \quad (7)$$

Carrying out the maximization then requires the calculation of $\phi_{max}(\bar{z})$ at all points past saturation along the undulator. (ϕ is a function of $\bar{z}$, because θ_j and Ψ are also functions of $\bar{z}$.)

Substituting the result from Eq. (7) into Eq. (6) we find, for $\langle\cos(\theta_j+\Psi)\rangle > 0$,

$$\left(\frac{dA}{d\bar{z}}\right)_{max} = \sqrt{\langle\cos(\theta_j+\Psi)\rangle^2 + \langle\sin(\theta_j+\Psi)\rangle^2} \equiv |b|\,, \quad (8)$$

where b is the bunching factor of the electrons.

We originally motivated the phase shift by the need to maintain a constant Ψ, the phase between the electron bunch and the radiation. We would like to check that our best phase, ϕ_{max}, optimized to increase the radiation amplitude, A, will simultaneously keep Ψ fixed. Returning to Eq. (5), now with an arbitrary phase inserted, we have

$$\frac{d\Psi}{d\bar{z}} \propto \langle\sin(\theta_j+\Psi)\rangle\cos\phi + \langle\cos(\theta_j+\Psi)\rangle\sin\phi\,. \quad (9)$$

Plugging in ϕ_{max} from the optimization condition, Eq. (7), gives

$$\frac{d\Psi}{d\bar{z}} \propto \langle\sin(\theta_j+\Psi)\rangle - \langle\cos(\theta_j+\Psi)\rangle\frac{\langle\sin(\theta_j+\Psi)\rangle}{\langle\cos(\theta_j+\Psi)\rangle} = 0\,. \quad (10)$$

We find that implementing the phase shifts, ϕ_{max}, does indeed keep the phase, Ψ, fixed, consistent with our initial goal of maintaining the correct slippage length.

EQUIVALENCY TO UNDULATOR TAPER

To find the optimal phases, Eq. (7), we can numerically evaluate $\langle\sin(\theta_j+\Psi)\rangle$ and $\langle\cos(\theta_j+\Psi)\rangle$ at each desired phase shifter location. This, of course, is not very practical for an actual SASE FEL. However, we motivated this approach by the need to maintain the resonant condition (Eq.1). Tapering the undulator, an established method for optimizing FELs, works through the same principle [5]. From the resonant condition, we see that shifting the phase is equivalent to decreasing the undulator parameter. To express a phase shift in terms of a taper, we start with the ponderomotive phase equation

$$\frac{d\theta}{d\bar{z}} = k_u - k_1\frac{[1+K^2/2]}{2\gamma^2}\,. \quad (11)$$

relating the change in phase, $\phi = \Delta\theta$, to the undulator parameter, K. An undulator taper is a small shift $K_0 \to K(\bar{z})$. Plugging into Eq. (11), dropping the second order term, and using the resonant condition, $k_u/k_1 = (1+K_0^2/2)/(2\gamma_r^2)$ gives

$$\frac{d\theta}{d\bar{z}} = k_u - k_u\frac{\gamma_r^2}{\gamma^2} + k_u\frac{\gamma_r^2}{\gamma^2}\frac{K_0(K(\bar{z})-K_0)}{1+K_0^2/2}\,. \quad (12)$$

Using the notation $\eta = (\gamma-\gamma_r)/\gamma_r$, $|\eta| \ll 1$ yields the usual FEL phase equation with a correction term of order $K_0 - K(\bar{z})$:

$$\frac{d\theta}{d\bar{z}} = 2k_u\left[\eta - \frac{K_0(K_0-K(\bar{z}))}{2+K_0^2}\right]. \quad (13)$$

Thus we find a change, $K_0 \to K(\bar{z})$, results in a change, $\theta \to \theta + \Delta\theta$, with accumulated phase shift

$$\Delta\theta(\bar{z}) = -2k_u\int_{\bar{z}_0}^{\bar{z}}\frac{K_0(K_0-K(\bar{z}'))}{2+K_0^2}d\bar{z}' \quad (14)$$

where $K(\bar{z})$ is some arbitrary function (i.e. an optimized taper) and the integral starts from the last phase shift at position $\bar{z}_0$.

The advantage of deriving phase shifts in this manner is that SASE FEL undulator tapers are well understood, and the optimal function $K(\bar{z})$ can be calculated from the FEL parameters, for instance by the GINGER self-taper algorithm [6]. With a predetermined taper function, we can plug into Eq. (14) and calculate the optimal phase shifts for an arbitrary FEL.

We have shown that shifting the phase continuously is identical to tapering the undulator parameter. However, the phase shift is most interesting if implemented discretely, with the taper from each undulator section replaced by a single shift. In this case, the exact equivalence breaks down. The larger the shift, the more time the FEL spends at a suboptimal phase, and for long undulators the accumulated difference $K(\bar{z}') - K_0$ might require large phase shifts, $\Delta\theta(L_u)$, near the end of the undulator (Eq. 14). To determine the practicality of discrete shifts, we use FEL parameters similar to the LCLS at 1.5 Å [7] for numerical examples (Table 1). Although LCLS does not currently have periodic phase shifters, designs for similar projects such as the European XFELs [8] have incorporated phase shifters between undulator sections. Using Eq. (14), we find the taper-equivalent shifts for LCLS have $\Delta\theta < 1$, suggesting that the method of phase shifts will match the performance of an undulator taper.

Table 1: SASE Simulation Parameters

Radiation wavelength (λ_1)	1.5 Å
Bunch current	3.4 kA
Undulator period (λ_u)	3 cm
Undulator parameter (K)	3.5
Electron energy	13.6 GeV
Relative RMS energy spread	$1x10^{-4}$
Normalized transverse emittance	1.2 μm
Beta function	25 m

NUMERICAL RESULTS

1-D Simulations

To simulate phase shifts, we started with a 1-D FEL code, including energy spread but not emittance effects. We used four different types of optimization:

1. Phase scan,
2. Numerically optimized phase shifts,
3. Linear energy taper, and
4. Phase shifts derived from a linear taper.

First we used a brute force phase scan. To determine the n^{th} phase shift at position z_n, we optimized the power at position z_{n+1} by trying 5 (or more) different phase shifts. Then, picking the best phase for the n^{th} position, we optimized position z_{n+1}.

Second, we used the results from Eq. (7) to calculate optimal phase shifts numerically. We calculate the phase for 2 cases: shifts every 1m and every 3m. The 3m shifts are less effective than the phase scan because the shifts are infrequent, and $\Delta\theta > 1$. The results for the first two methods are given in Fig. 1.

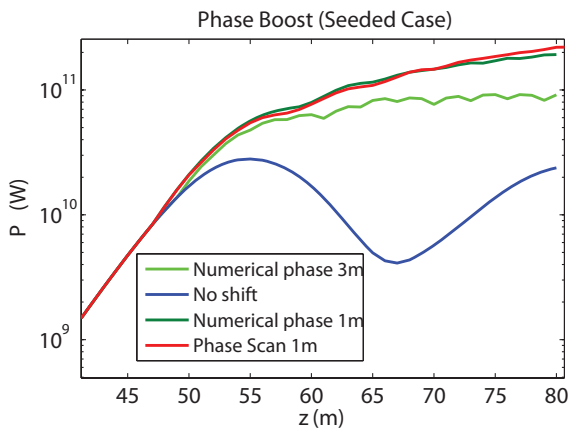

Figure 1: Fundamental radiation power from phase shifts. Phases done 3 ways: Numerical optimization every 1m (dark green), Numerical optimization every 3m (light green), Phase scan every 1m (red). The fourth plot (blue) has no phase shifts.

Third, we used a linear taper to boost the fundamental power. Fourth, we calculated the taper-equivalent phase shifts (Eq. (14)), implemented every 1m. The final two methods are computationally identical if the phase is shifted on each iteration. However, the results still match for less frequent phase shifts, so long as the shifts are small ($\Delta\theta < 1$). Results for both seeded and SASE cases are given in Figs. 2 and 3. Performance is worse for the third harmonic (green), because the shifts are relatively larger than in the case of the fundamental.

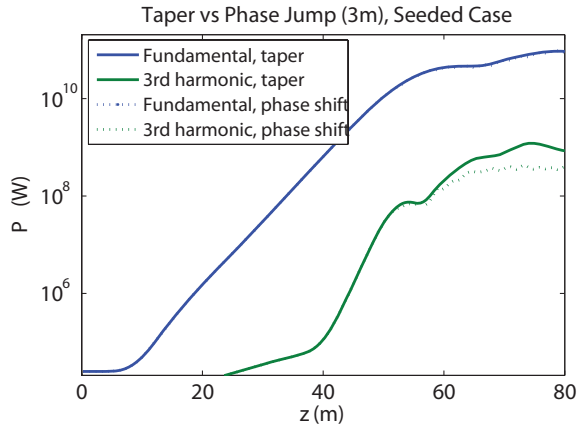

Figure 2: Comparison of taper and equivalent phase shifts every 3m for Seeded FEL, 1-D simulation.

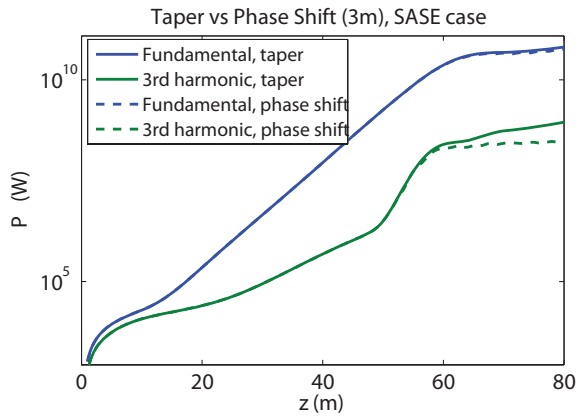

Figure 3: Comparison of taper and equivalent phase shifts every 3m for SASE FEL, 1-D simulation.

Finally, we compare phase shifts derived from the optimal linear taper to numerically optimized phase shifts (Eq. (7)), and the results from the phase scan. The phase shifts are all well matched (Fig. 4), confirming the equivalence of the four optimization methods.

3-D Simulations

We repeated the same study using the FEL code GINGER. To find an optimal undulator taper, $\Delta K(z)$, we used GINGER's self-taper algorithm [6]. With η defined above

$$\frac{d\eta}{dz} = -\frac{1}{\gamma_0}\frac{d\gamma_r}{dz} - \frac{eK[JJ]}{2\gamma_0^2 mc_2} E\sin(\theta + \Psi)$$

When the energy change is small (in the exponential regime), we can ignore the $\frac{d\gamma_r}{dz}$ term. However, at saturation, the energy loss is significant (of order ρ), and the resonant energy γ_r changes. Following [5], we define a synchronous phase Ψ_r from

$$-\frac{1}{\gamma_0}\frac{d\gamma_r}{dz} \equiv \frac{eK[JJ]}{2\gamma_0^2 mc_2} E\sin(\Psi_r).$$

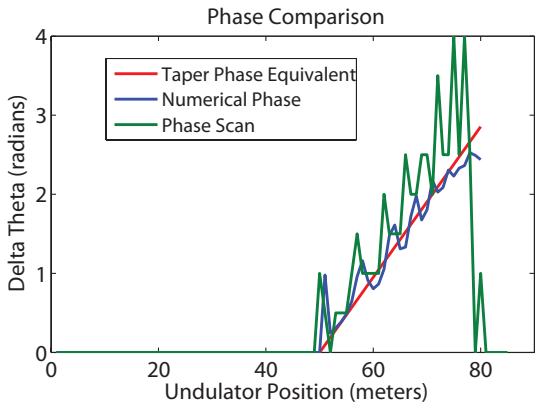

Figure 4: Phases determined by phase scan, numerical optimization and taper equivalent (Seeded case).

with Ψ_r determined by both $\frac{d\gamma_r}{dz}$ and K. Any particle with the synchronous phase will then define the center of the bucket, with particles nearby in phase space performing a synchrotron oscillation around the synchronous phase. (By definition, the energy η is constant.) An optimal phase Ψ_r is determined by optimizing bucket size and $d\gamma_r/dz$, which together set the energy transferred from electrons to radiation. We can then find a function $K(z)$ to maintain the phase Ψ_r as a constant throughout the saturation regime. Alternatively, we can manipulate the phase directly through periodic phase jumps, as described in Eq. (14) above. If the phase jumps are frequent enough so that $\Delta\theta < 1$ (or equivalently, $\Delta\Psi$), the system will effectively maintain the resonant condition without resorting to altering K.

Using GINGER's self-design taper function we created an optimal taper and then found the equivalent phase shifts (Fig. 5). We confirm the 1-D results, showing an equivalence between a taper and phase shift for an LCLS-like SASE FEL (Fig. 6, Table 1). The equivalence starts to fail at the very end of the undulator, when $\Delta\theta > 1$.

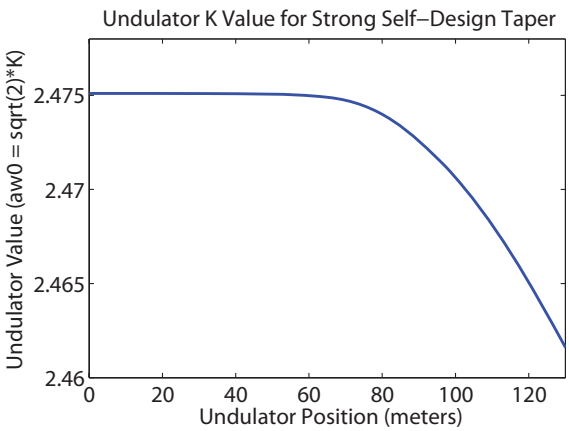

Figure 5: Taper for Seeded and SASE cases. Simulation using GINGER's 3D code.

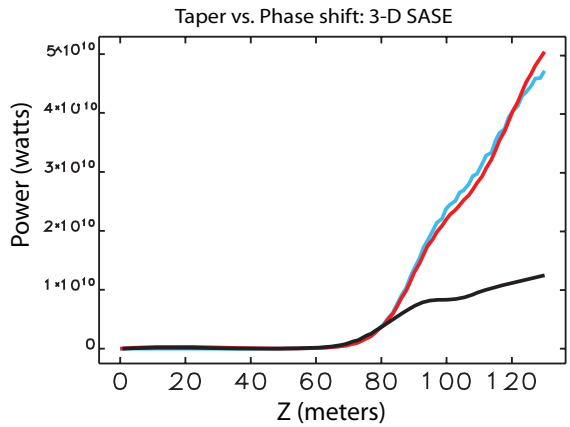

Figure 6: Power for normal (black), tapered (red) and phase-shifted (blue) LCLS-like SASE FEL, 3-D simulation. 12 Phase shifts between undulator sections (3.8 m).

CONCLUSION

We demonstrate the equivalence between phase shifts and undulator tapers. If the required phase shifts are small ($\Delta\theta < 1$), then the shifts can be implemented discretely and still mimic the effect of an undulator taper. In particular, we simulate phase shifts placed between undulator sections for an x-ray FEL and find the results are equivalent to those of an optimized taper. The phase shift method could be useful as a replacement or enhancement of undulator tapers when the use of tapers is constrained by technical issues. Even when the undulator parameter of each undulator section can be individually adjusted, placing phase shifters between the undulator sections provides independent control and fine tuning capability over the FEL power.

ACKNOWLEDGMENTS

We would like to thank W. Fawley, B. McNeil, and H.-D. Nuhn for many helpful discussions.

REFERENCES

[1] H. Chapman, S. P. Hau-Riege and J. Hajdu, *Prepared for 28th International Free Electron Laser Conference (FEL 2006), Berlin, Germany, 27 Aug - 1 Sep 2006*

[2] B. McNeil et al., Phys. Rev. Lett. 96, 084801 (2006).

[3] A.A. Varfolomeev et al., Nucl. Instr. and Meth. A 407, 296 (1998).

[4] R. Bonifacio, C. Pellegrini and L. Narducci, Opt. Commun. **50**, 6 (1985).

[5] N. M. Kroll, P. L. Morton and M. N. Rosenbluth, IEEE J. Quant. Electron. **17**, 1436 (1981).

[6] W.M. Fawley et al., Nuclear Instruments and Methods in Physics Research A 483 (2002) 537541

[7] Linac Coherent Light Source Conceptual Design Report, SLAC-R-593, UC-414 (2002).

[8] TESLA Technical Design Report, TESLA FEL 2002-09, DESY, 2002.

THREE-DIMENSIONAL THEORY OF THE CERENKOV FREE-ELECTRON LASER

H. L. Andrews* and C. A. Brau
Department of Physics and Astronomy, Vanderbilt University, Nashville, Tennessee, 37235, USA

Abstract

We present an analytical theory for the operation of a Cerenkov free-electron laser which includes diffraction of the optical mode in the direction transverse to the electron beam. Because the width of the optical mode depends on gain, the usual cubic dispersion relation is replaced by a 5/2-power dispersion relation, which allows two roots. These roots both have positive real parts, indicating that they are slow waves. For a narrow electron beam, the optical mode is much wider than the beam, thus reducing the gain by an order of magnitude from that predicted by the two-dimensional theory. In the limit of a wide electron beam, the two-dimensional theory is recovered.

INTRODUCTION

Compact narrow-band far-infrared, or terahertz (THz), sources have potential applications in a large number of fields including biology, chemistry, and materials science[1, 2]. The current THz sources in existence either produce short-pulsed broadband radiation, or require very large facilities. The exceptions to these are CO_2 pumped FIR lasers and backward-wave oscillators (BWOs). FIR lasers only have discreet lines, making them impractical for spectroscopy, and BWOs do not reach short enough wavelengths. Free-Electron Lasers (FELs) based on either the Smith-Purcell effect or Cerenkov radiation offer the possibility of a source capable of producing narrow-band THz radiation.

In a Cerenkov FEL the electron beam interacts with the evanescent wave of a single-sided dielectric waveguide. Since the wave has a forward group velocity, the instability is convective and the device works as an amplifier. Oscillation is achieved by feedback from reflections at the ends of the structure. The most powerful CFELs use ampere beams in cylindrical waveguides [3] but smaller devices can be constructed using milliampere beams in planar geometries [4]. The theory of cylindrical devices has been developed in detail, and the agreement with experimental results is good [3]. The theory for planar geometries has been worked out in two dimensions [5]. We extend this theory to three dimensions by including diffraction of the optical beam in the direction transverse to the electron beam, parallel to the surface of the dielectric [6]. We show that the gain is reduced by an order of magnitude and the fundamental nature of the conventional three-wave interaction is altered.

* heather.l.andrews@vanderbilt.edu

THEORY

To model the CFEL in three-dimensions we let the electron beam pass above a dielectric slab, bounded below by a conductor, as shown in Figure 1. The electron beam travels in $\hat{z}$, while $\hat{x}$ extends above the slab and $\hat{y}$ is the transverse direction. We assume a beam of width W, and a dielectric slab of depth H.

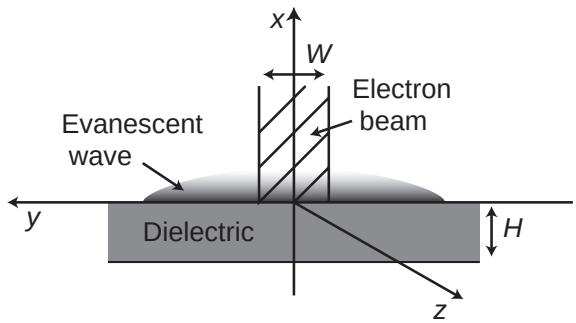

Figure 1: Geometry used for the three-dimensional model. The electron beam has a width W and is allowed to extend to infinity in x. The dielectric had a depth H and is wide compared to both the evanescent scale height and mode width.

To make the problem tractable, we start by making three assumptions. First, we assume the electron beam is uniform and extends infinitely far in $\hat{x}$. This introduces negligible errors to the theory because the electron beam height is actually on the order of the evanescent scale height. The assumption is corrected at the end of the calculation by using a filling factor. Next, we assume the operating frequency of the device is much larger than the plasma frequency or $\omega \gg \omega_e$. This is justified by considering the operating parameters of the most recent CFEL experiments at Dartmouth [4], shown in Table 1. For these parameters $\omega \approx 10^{12}$ Hz and $\omega_e \approx 10^9$ Hz. Finally, we assume that the mode width, Δy, is much greater than the evanescent scale height, Δx. For the Dartmouth parameters $\Delta x = \beta\gamma\lambda/4\pi \approx 80\mu$m, where βc is the electron beam velocity, $\gamma = 1/\sqrt{1-\beta^2}$ and λ is the operating wavelength. Diffraction arguments suggest that the evanescent mode width is on the order of $\Delta y = \sqrt{\beta\lambda Z_g/2\pi}$ ≈mm where Z_g is the gain length.

We find the fields within and above the dielectric by solving Maxwell's equations and requiring the solutions to meet the appropriate boundary conditions. Only TM modes

Table 1: Parameters used in the Dartmouth experiments and all theoretical predictions [4]

Dielectric thickness	350 μm
Index of refraction	3.6
Beam energy	30 keV
Beam thickness	70 μm
Beam current	1 mA

of the form

$$\begin{aligned} E_z &= E_0(x,y)\, e^{i(kz-\omega t)} \\ \mathbf{H}_t &= \mathbf{H}_0(x,y)\, e^{i(kz-\omega t)} \end{aligned} \tag{1}$$

are considered, where k is the wave vector in the $\hat{z}$ direction. We find the fields above the dielectric by starting in the electron rest frame, where we can treat the electron beam as an isotropic dielectric. We then transform the fields into the laboratory frame. By setting the fields above and within the dielectric equal at the boundary, we find the dispersion relation. When there is no beam present, we find the two-dimensional dispersion relation,

$$D(\omega,k,k_y) = \frac{n^2\left(\omega^2-k^2c^2\right)}{n^2\omega^2-k^2c^2}\kappa(k_y)\cot\left[\kappa(k_y)H\right]+\alpha(k_y) \tag{2}$$

where n is the index of refraction of the dielectric slab, k_y is the $\hat{y}$ component of the wave vector, $\kappa(k_y)$ is the $\hat{x}$ component of the wave vector within the dielectric, and $\alpha(k_y)$ is the $\hat{x}$ component of the wave vector above the dielectric. The dispersion relation is plotted in Figure 2.

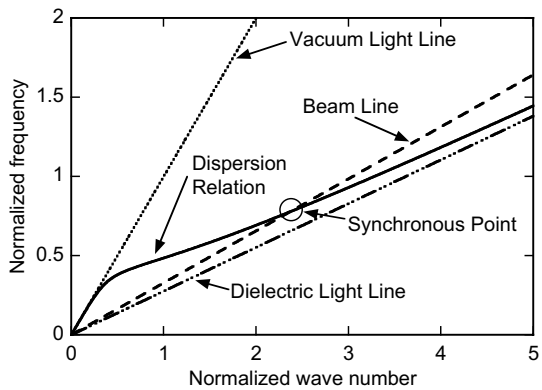

Figure 2: The two-dimensional dispersion curve for the parameters used in experiments at Dartmouth (see Table 1). Only the first order branch is shown.

When the electron beam is present, we anticipate that the highest gain will be found in the vicinity of the synchronous point, shown in Fig. 2, where the electron-beam line intersects the dispersion curve or, $\omega_0 = \beta c k_0$. We also assume that most waves are traveling parallel to the direction of beam travel so $k_y \approx 0$. We can then expand the dispersion relation about this point and find,

$$\begin{aligned} &(\delta\omega-\beta c\delta k)\left[D_\omega(\delta\omega-\beta_g c\delta k)+D_y k_y^2\right]\bar{E}(k_y) = \\ &\quad \frac{W}{2\pi}\frac{\omega_e^2\alpha_0}{\gamma^3}\int_{-\infty}^{\infty} dk_y'\bar{E}'\left(k_y'\right)\mathrm{sinc}\left[\frac{W}{2}\left(k_y-k_y'\right)\right] \end{aligned} \tag{3}$$

where

$$\begin{aligned} D_\omega &= \left.\frac{\partial D(\omega,k,k_y)}{\partial\omega}\right|_{(\omega_0,k_0,0)} \\ D_y &= \left.\frac{\partial D(\omega,k,k_y)}{\partial k_y^2}\right|_{(\omega_0,k_0,0)} \end{aligned} \tag{4}$$

and $\delta\omega$ and δk are the shifts in frequency and wave vector from the synchronous point, β_g is the group velocity, $\alpha_0 = \alpha(\omega_0, k_0, k_y = 0)$ and k_y' is a dummy variable. Computations show that $D_\omega > 0$, $D_y < 0$ and $\beta_g > 0$. In general this equation must be solved numerically, but for either a wide or narrow electron beam, analytical solutions to the dispersion relation can be found.

Wide Electron Beam

When the electron beam is wide, $W \gg \Delta y$, the sinc function behaves like a delta function, so we evaluate the integral at $k_y' = k_y$. We recover the two-dimensional cubic dispersion relation,

$$(\delta\omega-\beta c\delta k)^2(\delta\omega-\beta_g c\delta k) = \frac{\omega_e^2}{\gamma^3}\frac{\alpha_0}{D_\omega}, \tag{5}$$

the roots of which are shown in Figure 3. As in the two-dimensional case, one root corresponds to a fast wave, one to a slow wave which gains energy from the electron beam, and one to the structure wave, which decays. For steady-state amplifier operation we take $\delta\omega = 0$ and find that the gain in three dimensions with a wide beam,

$$\mu_{3D-wide} = -Im(\delta k) = \frac{\sqrt{3}}{2}\left(\frac{\omega_e^2}{\gamma^3\beta^2\beta_g c^3}\frac{\alpha_0}{D_\omega}\right)^{1/3} \tag{6}$$

is identical to the two-dimensional gain.

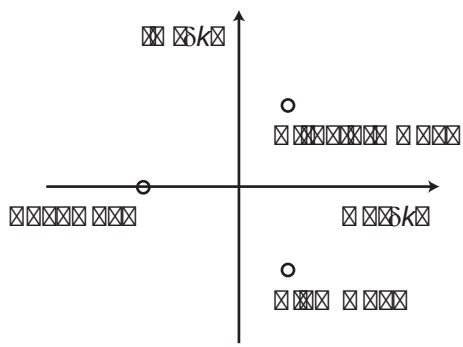

Figure 3: Roots of the dispersion relation for a wide electron beam. These are the same as for the two-dimensional result.

Narrow Electron Beam

When the electron beam is narrow, $W \ll \Delta y$, we approximate sinc $(x) \approx 1$. The integral becomes trivial, and we are able to invert the Fourier transform of the field using contour integration. The dispersion relation in this limit is

$$E_0(0,y) = \frac{W}{2}\frac{\omega_e^2}{\gamma^3}\frac{\alpha_0}{D_y}\frac{E_0(0,0)}{(\delta\omega - \beta c\delta k)^2}\frac{e^{y\Delta k_y}}{\Delta k_y} \quad (7)$$

where

$$\Delta k_y^2 = \frac{D_\omega}{D_y}(\delta\omega - \beta_g c\delta k) \quad (8)$$

and the sign of the root is chosen such that for positive y $Re(\Delta k_y) < 0$ and for negative y $Re(\Delta k_y) > 0$. Solving this dispersion relation on axis for the steady-state amplifier case, $y = 0$ and $\delta\omega = 0$, we find the roots are

$$\delta k_n = K^{2/5} e^{i(4/5)n\pi} \quad (9)$$

where

$$K = \frac{W}{2}\frac{\omega_e^2}{\gamma^3\beta^2\beta_g^{1/2}c^{5/2}}\frac{\alpha_0}{\sqrt{D_\omega |D_y|}}. \quad (10)$$

Figure 4 shows these five roots. Only two, $n = 2$ and

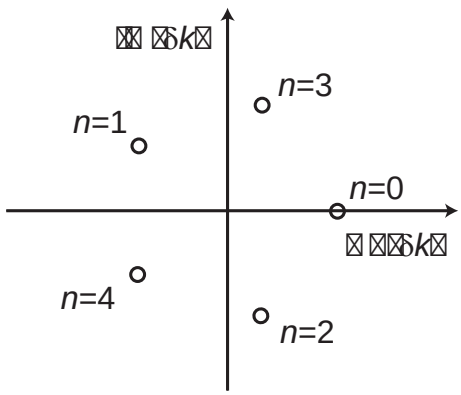

Figure 4: Roots of the dispersion relation for a narrow electron beam. Because of physical constraints, only $n = 2$ and $n = 3$ roots are true solutions. The $n = 2$ root has positive gain, while $n = 3$ has negative gain. Both modes have the same width and are slow waves $(Re(\delta k) > 0)$.

$n = 3$ are physically admissible solutions; for the others, the fields diverge at $y = \pm\infty$. Of these the $n = 2$ root has positive gain and the $n = 3$ root has negative gain where the gain is given by

$$\mu_{3D-narrow} = -Im(\delta k_2) = K^{2/5}\sin\left(\frac{2}{5}\pi\right). \quad (11)$$

From Equation 7, we find the mode width at the $1/e$ point to be

$$\Delta y = -\frac{2}{Re(\Delta k_y)} = \frac{2}{K^{1/5}}\left|\frac{D_y}{\beta_g c D_\omega}\right|^{1/2}\sec\left(\frac{\pi}{5}\right). \quad (12)$$

DISCUSSION AND COMPARISON WITH EXPERIMENT

Using the parameters in Table 1, we can compare the results of the two-dimensional theory with the three-dimensional theory and experimental observations. The vertical and transverse field profiles for the three-dimensional theory using a narrow electron beam are shown in Figures 5 and 6, respectively. The transverse

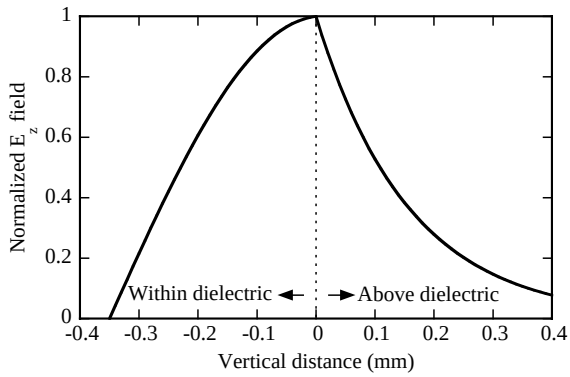

Figure 5: Vertical profile of the electric field. The field height is much smaller than the field width shown in Figure 6.

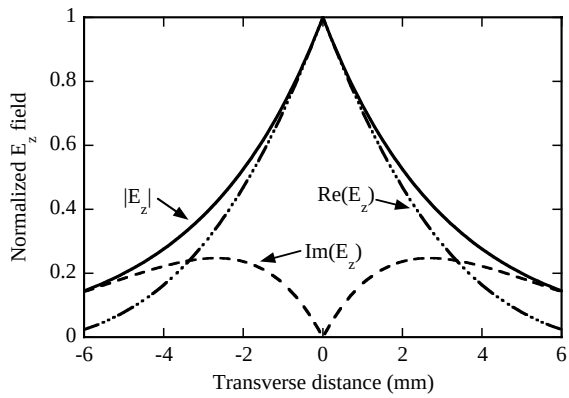

Figure 6: Transverse profile of the electric field. The field is much wider than the electron beam used in experiments. It is also wide compared with the evanescent scale height.

field profile shows that the mode width, $\Delta y \approx 6$ mm, is large compared to both the width of the electron beam and the scale height of the evanescent wave, as initially assumed.

In computing the gain, we recognize that the electron beam only extends above the dielectric a distance comparable to the scale height of the evanescent wave, rather than well beyond the wave. To correct for this we reduce the electron density, or equivalently ω_p^2, by a filling factor [7, 8]

$$F_{fill} = 1 - e^{-W/\Delta x}. \quad (13)$$

We find that the two-dimensional gain is $\mu_{2D} \approx 50/\text{m}$, in good agreement with the theoretical prediction of $60/\text{m}$

by the Dartmouth group [4, 5]. The three-dimensional gain, $\mu_{3D} \approx 10/\mathrm{m}$, is a factor of 5 smaller. This can be understood as diffraction diluting the effective current density by spreading the optical mode over an area much larger than the electron beam. The experimental value for gain reported by the Dartmouth group [4] is $\mu_{exp} \approx 250-450/\mathrm{m}$. This is $5-9$ times larger than the two dimensional theory and $25-45$ times larger than the three-dimensional theory. The origin of this discrepancy is not understood.

Equally interesting are the structure of the dispersion relation in three dimensions and the location of the roots. In place of the cubic dispersion relation characteristic of two-dimensional geometries and axially symmetric structures, we obtain and $5/2$-power dispersion relation. The two roots which satisfy the dispersion relation are labeled $n = 2$ and $n = 3$ in Figure 4. The $n = 2$ root has gain while the $n = 3$ root has loss. Both roots have the same real part, corresponding to the same mode width and indicating that both are slow waves ($Re\,(\delta k) > 0$). This result is surprising because it suggests that transverse diffraction in a three-dimensional structures forbids fast waves. We can understand this result physically by recognizing that when waves are confined to the region near the electron beam the situation is similar to waves guided by a dielectric waveguide. Because its index of refraction exceeds unity, the dielectric waveguide only supports slow waves, so optical modes supported by the CFEL can only be slow waves.

ACKNOWLEDGEMENTS

The authors gratefully acknowledge helpful discussions with J. H. Brownell, C. H. Boulware and J. D. Jarvis. This work was supported by the Medical Free Electron Laser Program and the Department of Defense under grant number F49620-01-1-0429.

REFERENCES

[1] P. H. Siegel, IEEE Trans. Microwave Theory and Techniques 50, 910 (2002).

[2] S. P. Mickan and X.-C. Zhang, Int. J. High Speed Electron. 13, 601 (2003).

[3] I. de la Fuente, P. J. M. van der Slot and K. J. Boller, Proceedings of the 2004 FEL Conference, p. 314 (http://JACoW.org).

[4] I. J. Owens and J. H. Brownell, J. Appl. Phys. 97,104915 (2005).

[5] I. J. Owens and J. H. Brownell, Phys. Rev. E. 67, 036611 (2003).

[6] H. L. Andrews and C. A. Brau, J. Appl. Phys. 101, 104904 (2007).

[7] H. L. Andrews, C. H. Boulware, C. A. Brau, J. T. Donohue, J. Gardelle and J. D. Jarvis, New J. Phys. 8, 298 (2006).

[8] G. F. Mkrtchrian, Phys. Rev. ST-AB 10, 080701 (2007).

THREE-DIMENSIONAL THEORY OF THE SMITH-PURCELL FREE-ELECTRON LASER

J. D. Jarvis and H. L. Andrews,
Department of Physics and Astronomy, Vanderbilt University, Nashville, TN 37235, U.S.A.

Abstract

We present an analytic theory for the exponential-gain (growth) regime of a Smith-Purcell free-electron laser amplifier (oscillator), which includes the effects of transverse diffraction in the optical beam. The optical mode is guided by the electron beam, having a mode width that depends upon the gain length. For the case of a wide electron beam, the dispersion relation converges with that of the 2-D theory. When the electron beam is narrow, the conventional cubic-dispersion relation is replaced by a five-halves dispersion. The dispersive properties of the grating divide device operation into four distinct regions, two amplifier and two oscillator. The number and location of physically allowed roots changes depending on operating region. Additionally, in the narrow-beam case, new challenges arise in satisfying the boundary conditions required for operation as an oscillator

INTRODUCTION

The wide range of potential applications for THz radiation is currently driving interest in the development of intense, compact, tunable THz sources. Such applications include: resonant excitation and spectral analysis of chemical and biological molecules and systems, medical and industrial imaging, and investigations in materials science and nanostructures [1,2]. Electron-beam-based devices are very promising sources of THz radiation. These include synchrotrons, conventional FELs, and slow-wave devices, such as backward-wave oscillators. While synchrotrons and conventional FELs are large and expensive, slow-wave devices can be compact, laboratory-scale instruments.

Slow-wave structures support subluminal electromagnetic modes, which may interact resonantly with an electron beam passing in close proximity. This resonant interaction causes bunching in the electron beam and amplitude growth of an evanescent optical field. For an open-grating structure, superradiant Smith-Purcell radiation may be extracted at harmonics of the evanescent wave [3]. This configuration is known as a Smith-Purcell free-electron laser (SPFEL). The SPFEL may be operated as an amplifier (convective instability), or as an oscillator (absolute instability), depending on the sign of the laser wave's group velocity. The two-dimensional theory of such a device has been examined in detail for the exponential gain/growth regime [4,5,6,7], and is closely supported by PIC simulations [6,8,9]. A two-dimensional numerical treatment of device operation from startup to saturation, with one-dimensional electron dynamics, has also been performed [7].

In this work, we include the effects of transverse diffraction in the optical beam of an SPFEL. The approach used is similar to that used for the 3-D theory of the Cerenkov FEL [10]. As expected, three-dimensional effects increase the gain length and oscillator start current substantially. Furthermore, compared to the 2-D theory, their dependence on the beam current increases due to gain guiding. We find that diffraction of the optical beam in the periodic-grating structure subdivides device operation into two amplifier regions and two oscillator regions. For the amplifier and oscillator regions furthest from the Bragg point, we find the inclusion of a fast wave in the physically allowed solutions. This is very surprising, considering the nature of a guided system. For the oscillator region closest to the Bragg point there are only two physically allowed solutions. It is not known how the required boundary conditions on the electron and optical beams can be satisfied in this region.

DISPERSION

In an SPFEL, resonant energy exchange between the electron beam and bound surface modes gives rise to spatial modulations in the beam density. These density modulations lead to superradiant enhancement of the emitted SP radiation, and subsequent modification of its angular distribution [3]. In the following analysis we calculate the fields subject to the Maxwell equations and boundary conditions and solve for the dispersion relation. We then introduce the electron beam as a perturbation and calculate the resulting wavenumber and frequency shifts for solutions to the dispersion relation.

Table 1: Dartmouth grating and beam parameters

Grating period	173 μm
Groove width	62 μm
Groove depth	100 μm
Grating length	12.7mm
E-beam width/height	60 μm
E-beam current	1 mA
E-beam height above grating (measured from bottom of beam)	0 μm

For an electron beam energy of $150\ \mathrm{kV}$ and the grating parameters of Table 1, the intensity scale height of the evanescent wave is $\Delta x = \beta\gamma\lambda / 4\pi \approx 38\ \mu\mathrm{m}$, where $\beta \sim 0.43$ is the normalized electron velocity,

$\gamma = 1/\sqrt{1-\beta^2}$, and $\lambda \sim 10^{-3}$ m is the free-space wavelength. We anticipate from simple diffraction arguments that the transverse mode width is of order $\Delta y \approx \sqrt{\beta\lambda Z_g / 2\pi}$ (~millimeters), where Z_g (~centimeters) is the gain length. Schematics of the device geometry with all pertinent dimensions are given in Figures 1 and 2.

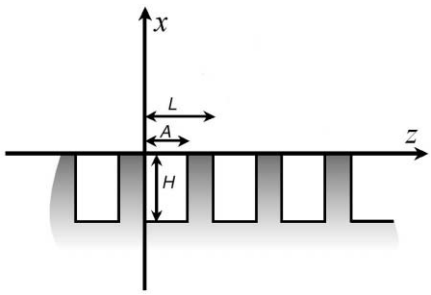

Fig. 1 Geometry of grating structure, viewed from the side

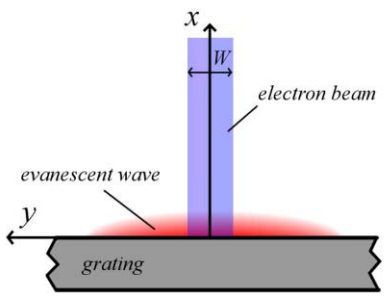

Fig. 2 Geometry of evanescent wave and electron beam, viewed from front

Because the fields vanish exponentially above the scale height, we simplify the theory by allowing the electron beam to extend to infinity in the x direction. A filling factor can be used to correct for errors introduced by this approximation [6,11]

To calculate the dispersion relation for the grating, in the absence of the electron beam, we expand the field above the grating in Floquet series and the field in the grooves as Fourier series. Invoking the Maxwell equations and matching the fields at the grating surface, we arrive at the empty grating dispersion function $D\left(\omega, k, k_y^{\,2}\right)$, where ω is the frequency, k is the longitudinal wavenumber, and k_y is the wavenumber in the y direction. We then expand the dispersion function about the synchronous point ($\omega_0 = \beta c k_0$) in ω, k, and $k_y^{\,2}$, introducing the electron beam as a perturbation. In the limit where the electron beam is infinitely wide the dispersion relation matches the 2-D theory [5]. For the case of a very narrow beam the resulting dispersion relation is

$$\left(\delta\omega - \beta c\delta k\right)^2 \left[\frac{D_\omega}{D_y}\left(\delta\omega - \beta_g c\delta k\right)\right]^{\frac{1}{2}} = \Delta \quad (1)$$

where β_g is the evanescent wave's goup velocity, $\delta\omega$ and δk are the complex frequency and wavenumber shifts respectively, D_ω and D_y are partial derivatives of the no-beam dispersion function with respect to ω and $k_y^{\,2}$, and

$$\Delta = \frac{\beta^3 c^2 W}{ALD_y}\frac{\omega_e^{\,2}}{\gamma^2\omega_0^{\,2}}\tan\left(\frac{\omega_0}{c}H\right)\left[1-\cos\left(k_0 A\right)\right]. \quad (2)$$

Calculations show that D_ω is negative, irrespective of k, but D_y changes such that $D_y > 0$ near the center of the Brillouin zone $\left(k/K = 1/2\right)$ and $D_y < 0$ towards the edges of the zone $\left(k = 0, K\right)$. This subdivides operation of the SPFEL into the four distinct regions pictured in Figure 3 with the dispersion relation. Some roots are eliminated in each region of operation because they do not allow the fields to vanish at $y = \pm\infty$. A diagram detailing this selection is given in Figure 4. We now consider the amplifier and oscillator regimes of the SPFEL.

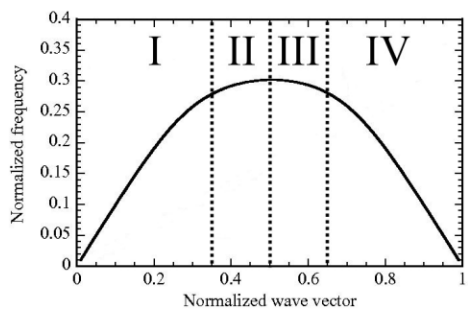

Fig. 3 Dispersion relation with different regions of operation

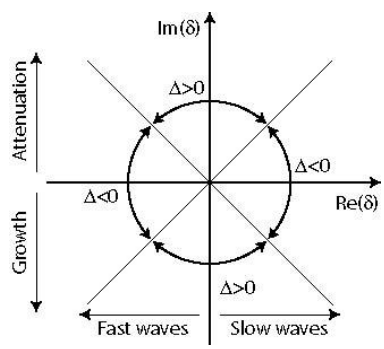

Fig. 4 Diagram for selection of allowed roots

AMPLIFIER

When the device operates as a steady-state amplifier, $\delta\omega = 0$ and β_g is positive. In region II, the roots of the dispersion relation are

$$\delta k_n = \Gamma^{\frac{2}{5}} e^{i\frac{4}{5}n\pi} \tag{5}$$

where

$$\Gamma = \frac{1}{\beta^2 c^2}\left|\frac{D_y \Delta}{D_\omega \beta_g c}\right|^{\frac{1}{2}}. \tag{6}$$

Similarly, in region I the roots are

$$\delta k_n = \Gamma^{\frac{2}{5}} e^{i\left(\frac{4}{5}n\pi + \frac{\pi}{5}\right)}. \tag{7}$$

In region II only two roots are physically allowed, $n = 2,3$. From Figure 5 we see that these are slow waves, i.e. they have a phase velocity lower than that of the no-beam-operating point.

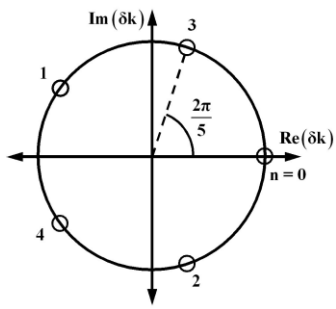

Fig. 5 Roots for region II in the complex plane

In region I, however, there are three physically allowed roots including one fast wave solution. It is surprising that a fast wave is allowed in a gain-guided system. In region II, the $n = 3$ root has loss and the $n = 2$ root has gain. The gain for the $n = 2$ root is given by

$$\mu_{3D} = -\mathrm{Im}\left(\delta k_2\right) = \Gamma^{\frac{2}{5}} \sin\left(\frac{2}{5}\pi\right) \tag{8}$$

and has a corresponding $1/e$ optical mode width of

$$\Delta y = 2\left(\left|\frac{D_\omega}{D_y}\beta_g\right| c\right)^{-\frac{1}{2}} \Gamma^{-\frac{1}{5}} \cos\left(\frac{\pi}{5}\right). \tag{9}$$

The relationship given in (9) is simply understood to be the manifestation of gain guiding in the SPFEL. As an example, we consider the grating and beam described in Table 1. The three-dimensional gain is plotted in Figure 6, along with the two-dimensional gain, which has been scaled down by a factor of three to appear on the same graph.

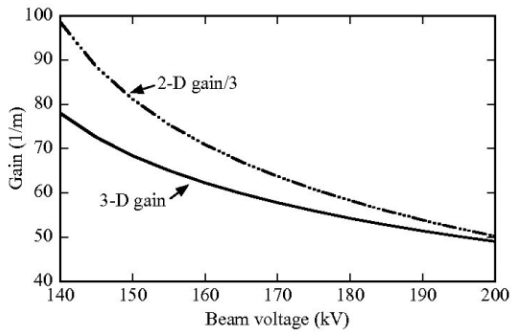

Fig. 6 Computed gain for 2-D and 3-D theories as a function of beam voltage

The transverse profile of the electric field is given in Figure 7, and the $1/e$ mode width is found to be $\Delta y \approx 4.4\mathrm{mm}$. By examining the geometry of this mode, it is clear that the initial assumptions made concerning its dimensions are justified

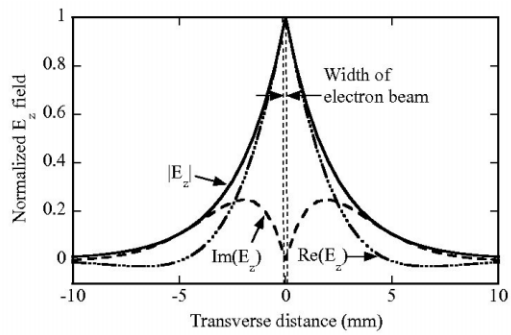

Fig. 7 Transverse profile of the electric-field strength

OSCILLATOR

In regions III and IV the group velocity of the evanescent mode is negative. This allows information about the bunching of the electron beam at the grating exit to be carried back upstream. This serves as an intrinsic form of feedback and, provided that the beam current exceeds the so-called start current, allows the device to oscillate. For a solution to exist in the oscillator case, three boundary conditions must be satisfied in conjunction with the dispersion relation (1). The electron beam must be free of density and velocity modulations at the upstream end of the grating, and the input optical field at the downstream end must vanish [5,6]. These boundary conditions are satisfied by interference of the three waves that compose the mode. Solutions to the inhomogeneous system can have different transverse widths due to the presence of gain guiding. Therefore, if only inhomogeneous solutions are used, the boundary condition on the input field cannot be satisfied for all y. For a general solution to the system, arbitrary amounts of the homogeneous solutions may be added. In the following analysis we require that

the boundary conditions be satisfied only on the beam axis. We find that while region IV has three physically allowed roots, only two waves are admitted in region III. It is not clear how all three boundary conditions may be satisfied without the presence of a third wave. We therefore restrict our analysis of the oscillator regime to region IV.

To form a mode of the oscillator, each wave must have the same frequency shift $\delta\omega$. The boundary conditions are defined by

$$\begin{vmatrix} 1/\delta_1^2 & 1/\delta_2^2 & 1/\delta_3^2 \\ 1/\delta_1 & 1/\delta_2 & 1/\delta_3 \\ e^{i\xi\delta_1} & e^{i\xi\delta_2} & e^{i\xi\delta_3} \end{vmatrix} = 0 \qquad (10)$$

where δ_j and ξ are dimensionless variables given by

$$\delta_j = \left[\frac{\beta^2 c^{\frac{5}{2}} |\beta_g|^{\frac{1}{2}}}{\Delta} \left(\frac{D_\omega}{D_y} \right)^{\frac{1}{2}} \right]^{\frac{2}{5}} \left(\delta k_j - \frac{1}{\beta c} \delta\omega \right), \qquad (11)$$

$$\xi = \left[\frac{\Delta}{\beta^2 c^{\frac{5}{2}} |\beta_g|^{\frac{1}{2}}} \left(\frac{D_y}{D_\omega} \right)^{\frac{1}{2}} \right]^{\frac{2}{5}} Z . \qquad (12)$$

To find the start current we require $\mathrm{Im}\left[\kappa(\xi_0) \right] = 0$, where

$$\kappa = -\left[\frac{\beta^2 |\beta_g|^{\frac{1}{2}}}{\Delta} \left(\frac{D_\omega}{D_y} \right)^{\frac{1}{2}} \right]^{\frac{2}{5}} \left(\frac{1}{|\beta_g|} + \frac{1}{\beta} \right) \delta\omega \qquad (13)$$

and solve the dispersion relation

$$\delta_j^2 \sqrt{\delta_j - \kappa} \pm 1 = 0 \qquad (14)$$

subject to (10). The lowest dimensionless root found is $\xi_0 = 1.194$, $\kappa(\xi_0) = 1.802$. Both the 2-D and 3-D start currents are plotted as a function of operating voltage in Figure 8.

CONCLUSIONS

We have presented a three-dimensional theory of SPFEL oscillator (amplifier) operation for the exponential growth (gain) regime. We find that 3-D effects substantially increase both gain length (amplifier) and start current (oscillator). Unexpected consequences result from inclusion of diffraction in the grating's periodic structure. Device operation is divided into four regions, which are characterized by the number and location of physically allowed roots to the dispersion relation. Fast waves are included in some regions of operation despite the guided nature of the interaction. In the present theory the mode width vanishes mathematically at the boundaries of these regions $\left(D_y \to 0 \right)$. These consequences are not fully understood at present.

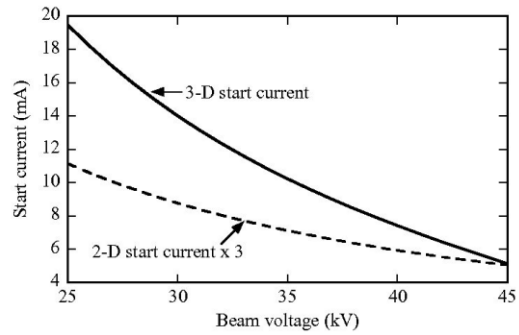

Fig. 8 Oscillator start current as a function of electron beam voltage

ACKNOWLEDGEMENTS

The authors gratefully acknowledge helpful discussions with C. A. Brau and K.-J. Kim. This work was supported by the Medical Free Electron Laser Program of the Department of Defense under grant number F49620-01-1-0429.

REFERENCES

[1] S. P. Mickan and X.-C. Zhang, Int. J. High-Speed Electron. and Sys. **13**, 601 (2003).
[2] P. H. Siegel, IEEE Trans. Microwave Theory and Techniques **50**, 910 (2002).
[3] H. L. Andrews, C. H. Boulware, C. A. Brau, and J. D. Jarvis, Phys. Rev. ST-AB **8**, 110702 (2005).
[4] H. L. Andrews, C. A. Brau, Phys. Rev. ST-AB **7**, 070701 (2004).
[5] H. L. Andrews, C. H. Boulware, C. A. Brau, and J. D. Jarvis, Phys. Rev. ST-AB **8**, 050703 (2005).
[6] H. L. Andrews, C. H. Boulware, C. A. Brau, J. T. Donohue, J. Gardelle, and J. D. Jarvis, New J. Phys. **8** (2006) 289.
[7] V. Kumar and K. J. Kim, Phys. Rev. E **73**, 026501 (2006)
[8] D. Li, Z. Yang, K. Imasaki, and Gun-Sik Park, Phys. Rev. ST-AB **9**, 040701 (2006).
[9] J. T. Donohue and J. Gardelle, Phys. Rev. ST_AB **8**, 060702 (2005).
[10] H. L. Andrews and C. A. Brau, J. Appl. Phys. **101**, 104904 (2007)
[11] G. F. Mkrtchian, Phys. Rev. ST-AB **10**, 080701 (2007)

ON NMR PROBING OF THE KINETICS OF A FREE-ELECTRON LASER-INDUCED CHEMICAL EXCHANGE

S.P. Babailov, IIC SB RAS, Novosibirsk, Russia

Abstract

Determination of the rate constants of chemical exchange reactions (at dark conditions, Figure 1) and the quantum yields of photo-induced chemical exchange (PICE, in particular, molecular photoisomerization reactions) is an efficient application of NMR spectroscopy [1,2].

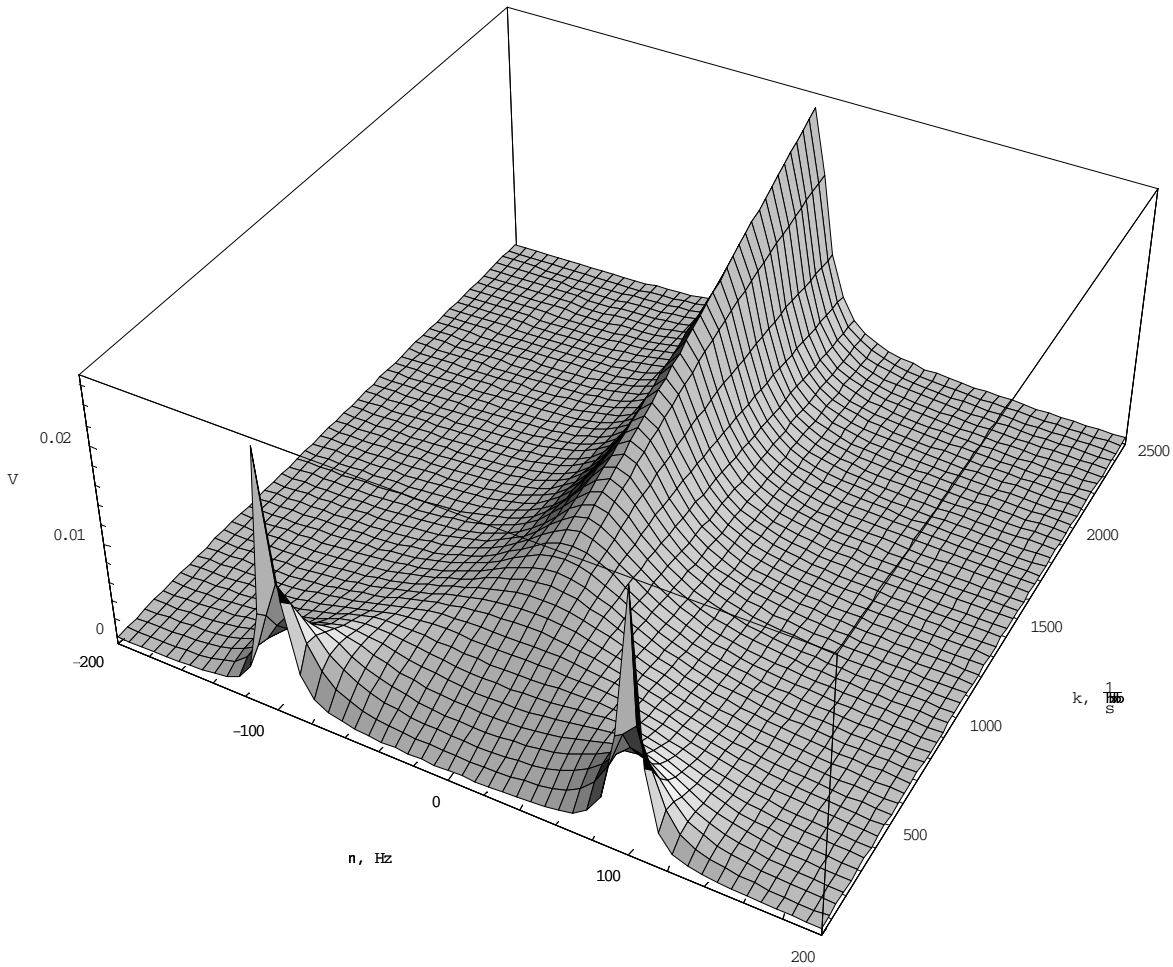

Figure1: Calculated NMR line-shape for a two-site chemical exchange at dark condition (T_1=T_2=10 c, Δν=200 Гц, the rate constant (k) changes from 38 to 2500 c^{-1}).

We are proposed a combined approach for study the kinetics of photo-induced chemical exchange (PICE) reactions (see (1), (2)), which involves a free-electron laser (FEL) and NMR spectroscopy [3].

$$A \underset{h\nu_2}{\overset{h\nu_1}{\rightleftharpoons}} B \qquad (1)$$

$$A + B \underset{h\nu_2}{\overset{h\nu_1}{\rightleftharpoons}} C \qquad (2)$$

Continuous and pulse irradiation of the chemical system in the presence of PICE can be achieved using FEL.

THEORETICAL

Based on the analytical equations derived in the work we consider the time-dependent dynamics of variation of the instant NMR line shape for two-site chemical exchange.

$$v(\nu,t)=\mathrm{Im}\left[e^{-(R_2+i\Delta\omega)t}\vec{G}_0-ik_1\int_0^t e^{-(R_2+i\Delta\omega)(t-\tau)}\left(e^{-R_1\tau}\vec{M}_{z0}-M_0R_1^{-1}(e^{-R_1\tau}-1)I_1\cdot\vec{P}\right)d\tau\right] \quad (3)$$

If one induce an abrupt increase in the rate constant of chemical exchange (for example, by quickly heating the system or PICE), then the NMR line shape will change with time, ultimately reaching another new steady state. Our calculations show that there are beats and oscillations (on the NMR line shape) damped with time (see Figure 2, (3)).

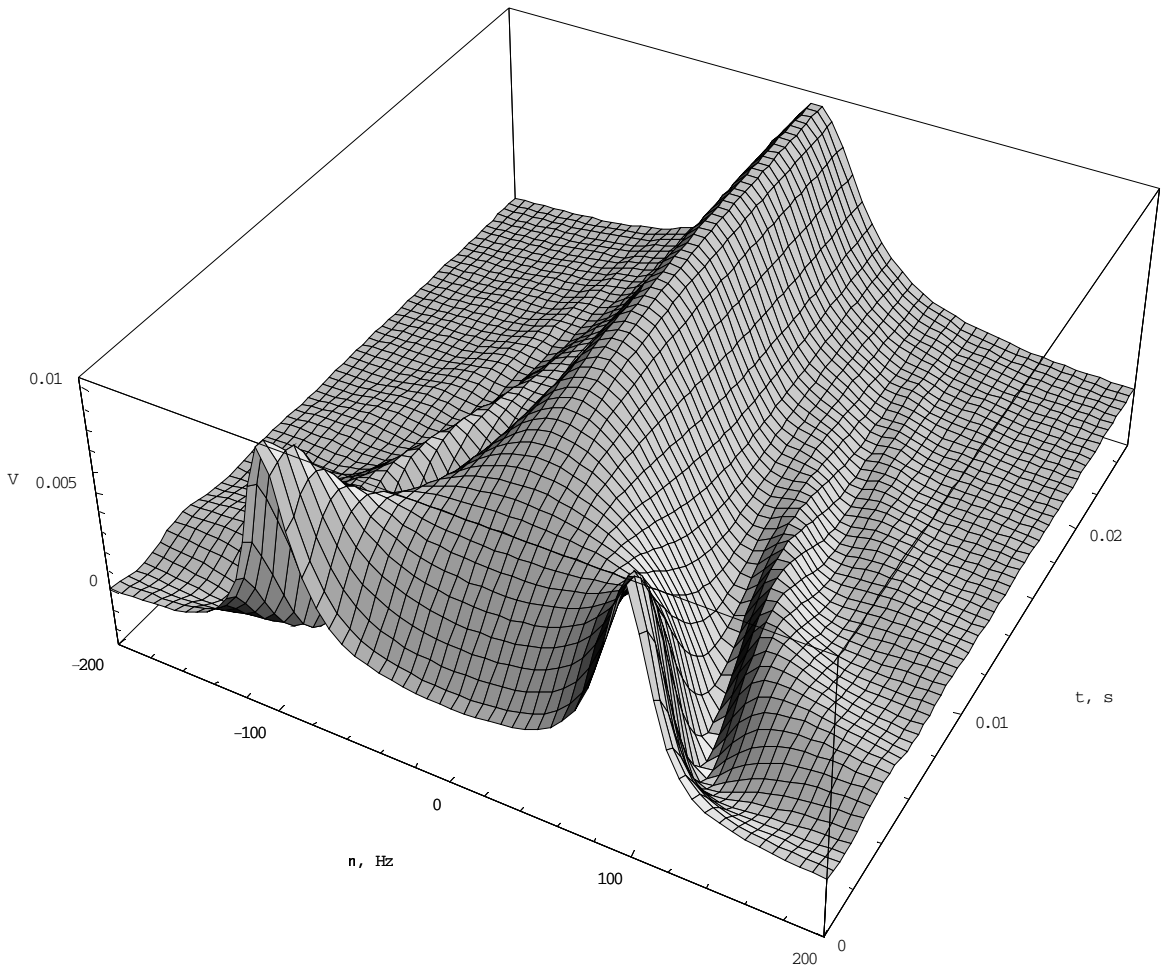

Figure 2: Calculated time-dependent NMR line-shape for a two-site chemical exchange at photo-induced chemical exchange condition (T_1=T_2=10 c, Δν=200 Гц, k changes from 100 to 2500 c^{-1} (at abrupt increase)).

CONCLUSION

The information about the time-dependent instant line shapes provides possibility to predict the real kinetics of PICE. Prospective objects are molecular conformers and spin isomers. So, FEL can be used in the setup for PICE studies in combination with a NMR spectrometer.

REFERENCES

[1] S.P. Babailov, E.M. Glebov, A.I. Kruppa, and V.F. Plyusnin, "NMR in Photo-Induced chemical Exchange Systems. Double-Resonance Inverse Fractional Population Transfer Application for Investigation of 1,2-(2,2'-Dipyridyl) Ethane Photoisomerization Kinetics", Concepts in Magnetic Resonance, 2006, 8, P.571.

[2] S.P. Babailov, "Lanthanide Paramagnetic Probes for NMR spectroscopic studies of Molecular Conformational Dynamics in Solution. Applications to Macrocyclic molecules", Progress in Nuclear Magnetic Resonance Spectroscopy, 2007, (doi:10.1016/j.pnmrs.2007.04.002) http://dx.doi.org/10.1016/j.pnmrs.2007.04.002

[3] S. P. Babailov, "Photo-induced chemical exchange in solutions: NMR spectroscopic detection of the kinetics", Russ. Chem. Bull., Int. Ed., 2006, 10, p.1631.

TERAHERTZ IMAGING AND RADIOSCOPY WITH 160X120 MICROBOLOMETER 90 FPS CAMERA*

A.L. Aseev, D.G. Esaev, M.A. Dem'yanenko, I.V. Marchishin, Rzhanov Institute of Semiconductor Physics SB RAS, 630090 Novosibirsk, Russia
B.A. Knyazev, G.N. Kulipanov, N.A. Vinokurov, Budker Institute of Nuclear Physics SB RAS, 630090 Novosibirsk, Russia.

Abstract

An uncooled micromolometer matrix camera has been developed for IR and THz high-speed imaging. The 120x160 matrix consists of resistive vanadium oxide elements on a silicon nitride bridge. The element size is 46x46 micron at the array period of 51 micron. We describe device fabrication process and matrix operational characteristics. Application of the camera in quasi-optical systems with Novosibirsk terahertz free electron laser as a radiation source is described. Recording rate up to 90 frames per second has been achieved.

INTRODUCTION

TERAHERTZ imaging is critically important for many applications. Appearance of high power terahertz sources, such as free electron lasers, enables using "parallel" recording techniques rather than recording images point-by-point with scanner. The last technique is routinely used in the time domain spectroscopy (TDS) systems, where recording an image takes minutes and hours. Recently commissioned Novosibirsk terahertz free electron laser generates terahertz radiation at the fundamental mode in a range of 120 – 240 μm with the average power 100 – 200 W at the repetition rate 5.6MHz and second and third harmonics with the average power of about several Watts. A number of imaging techniques employing the thermal effect of terahertz radiation were developed during past two years for recording images on the user stations [1 – 2]. These imaging techniques have many advantages, but each of them has at the same time certain drawbacks. One of them has a good spatial resolution, but pure sensitivity. Other being sensitive has no good spatial resolution. In this paper we describe the application of a microbolometer matrix to the recording of images in the terahertz spectral region.

MATRIX DESCRIPTION

The expansion of application sphere of thermal imager and others infrared (IR) devices along with increase of its sensitivity demands of decrease of cost, power consumption and weight, more convenience to use and high reliability. All these requirements are satisfied by uncooled focal plane array (FPA) actively developed last two decades. Microbolometer FPAs, based on thermoresistance effect have got the greatest expansion. Vanadium oxides (VOx) and amorphous silicon are mainly used as thermoresistance material. In the latter case process of microbolometer fabrication is carried out completely within the framework of usual silicon technology.

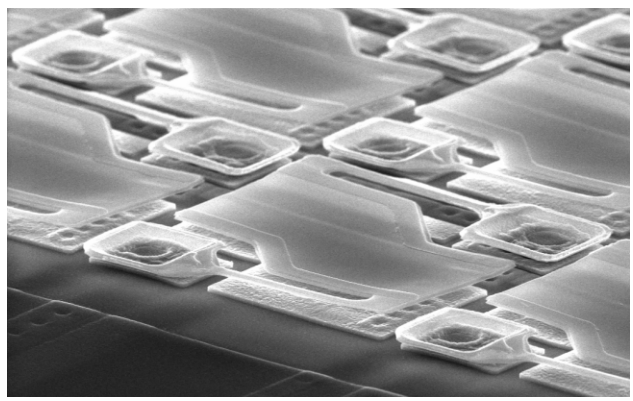

Fig. 1: Scanning electronic microscope photograph of 160x120 microbolometer FPA fabricated on silicon readout circuit.

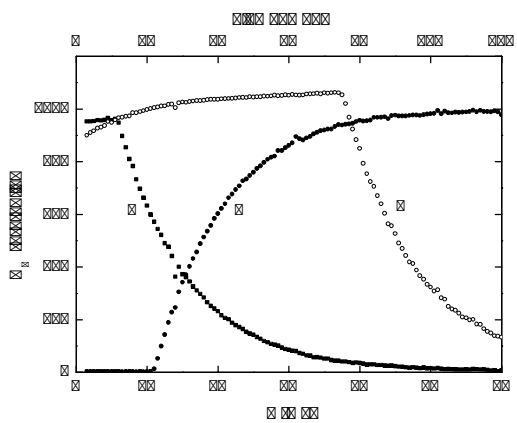

Fig. 2. Time dependence of 160x120 microbolometer FPA output signal normalized on sensitivity at pulse illumination. (1) the decay of FPA output signal after illumination: (2) the increasing of the signal during illumination, (3) is an intermediate situation.

*This work was supported in part by SB RAS under Integration Grant 174/6, by grant RNP.2.1.1.3846 from the Russian Ministry for Education and Science, and grant 07-02-13547 from Russian Foundation for Basic Research

The high performance of uncooled FPA mentioned above is achieved the mainly due to development of technologies of thermosensitive layers preparation and microbridge structure fabrication. Since uncooled FPA are fabricated in integrated-circuit form the basic requirement to the technologies mentioned above is their compatibility with fabrication technology of the silicon readout integrated circuit (ROIC). The traditional methods of thermosensitive vanadium oxides layers preparation - reactive magnetron and ion-beam sputtering - are enough complicated and require the complex expensive equipment. For preparation of thermosensitive amorphous silicon layers the technology of plasma enhanced chemical vapor deposition (PECVD) from monosilane with addition phosphine is used that creates additional difficulties.

Vanadium oxide 160×120 pixel matrix was designed for the operation in the middle infrared spectral region (8 – 14 μm). The fabrication technology and operational characteristics of the matrix in this spectral region are described in paper [3]. In this paper we describe the application of this matrix for the recording of the monochromatic radiation in the spectral range 130 – 150 μm.

TERAHERTZ IMAGING WITH VO_X MATRIX

Though the matrix was not optimal for terahertz radiation, it approves itself as a very perspective tool for terahertz imaging. It appears to be more sensitive than previously developed technique. It has a spatial resolution close to the wavelength limit. We have demonstrated the recording of a moving object image with a rate up to 90 frames per second.

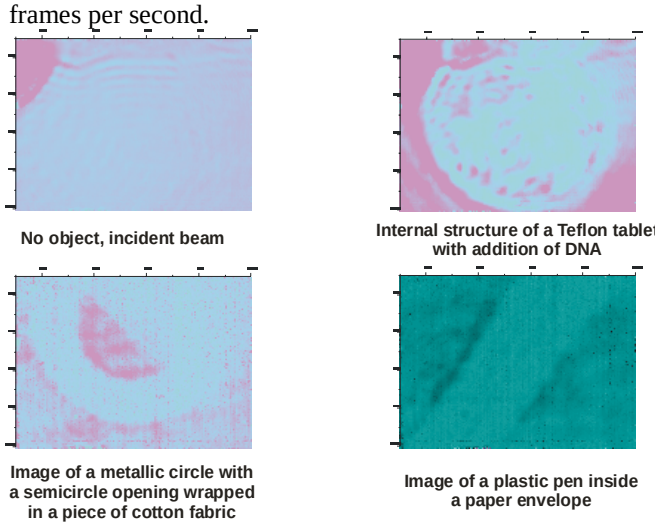

Fig. 3. Imaging terahertz radioscopy, λ = 130 mm. Imager: microbolometer matrix. Matrix size: 160x120 pixels, 16 bit, 8,2x6,2 mm, Recording rate: up to 90 frames per second.

The microbolometer matrix was applied for study of focusing terahertz radiation with a reflective kinoform (Fresnel) lens [4]. It was used for imaging radioscopy of rat bones that is necessary for study of osteoporosis development [5].

The matrix was used as a recorder in a number of quasi-optical systems developed at Novosibirsk free electron laser. In the right upper corner in Fig.3 the internal structure of a tablet pressed from Teflon powder with addition of DNA is shown. The image was recorded by means of the radioscopy of the tablet with FEL as a source (see schematic in Fig. 2, ref. [5]).

Other application of the matrix was the radioscopy of wrapped objects and substances. Two pictures in the lower row in Fig. 3 demonstrates the capability of the matrix for the examination of partially transparent to terahertz radiation substances for the inspection of illegal objects and for the control of the box and container contents in industry and stores by means of the radioscopy. Fig. 4 demonstrates a capability of the matrix for imaging of the objects illuminated by terahertz radiation (reflection/scattering mode).

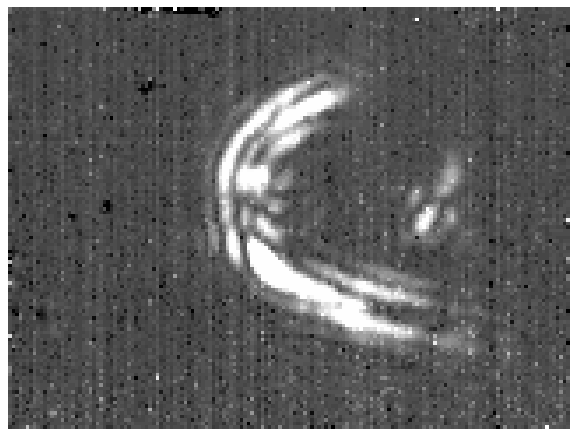

Fig. 4. Image of a wire spring with diameter of 2 mm.

CONCLUSION

A microbolometer matrix approves itself as a powerful tool for terahertz imaging both in transmission and reflection modes. Further development of the technique will be directed on the increasing matrix elements and optimizing matrix design for the terahertz region.

REFERENCES

[1] V.S. Cherkassky, B.A. Knyazev, V.V. Kubarev, et al.” Imaging techniques for a high-power THz free electron laser”, Nuclear Instruments and Methods in Physics Research A, vol. 543, p. 102-109, 2005.

[2] V.S Cherkassky, V.V. Gerasimov, G.M. Ivanov, et al. “Techniques for introscopy of condense matter in terahertz spectral region”, *Nuclear Instruments and Methods in Physics Research A* 575, pp. 63-67, 2007.

[3] M.A. Dem’yanenko, V.N. Ovsyuk, V.V. Shashkin, et al. Uncooled 160x120 microbolometer IR FPA based on sol-gel VOx, International congress on Optics and Optoelectronics, *Proceedings of SPIE*, 5957, 340 (2005).

[4] B.A. Knyazev, G.N. Kulipanov, I.A. Polskikh, et al. ""Diffraction optical elements and optical systems with a high power monochromatic terahertz source", *These Conferenc,* Paper *MOPPH033*

[5] M. Gonchar, V. V. Gerasimov, B. A. Knyazev, "Spectroscopy and spectrally resolved radioscopy of biological substances using terahertz free electron laser radiation", *These Conference,Paper MOPPH031*

SPECTROSCOPY AND SPECTRALLY RESOLVED RADIOSCOPY OF BIOLOGICAL SUBSTANCES USING TERAHERTZ FREE ELECTRON LASER RADIATION*

A. M. Gonchar, Institute of Cytology and Genetics SB RAS, Novosibirsk
V. V. Gerasimov, Novosibirsk State University
N.G. Gavrilov, B. A. Knyazev, Budker Institute of Nuclear Physics, SB RAS, 630090, Russia

Abstract

Osteoporosis is a major cause of morbidity of older people. Direct financial expenditure for the treatment of osteoporosis fracture in the U.S. is estimated at $10-$15 billion per year. Though there are a number of methods for diagnostics of osteoporosis, X-ray radioscopy, NMR, element analysis, densitometry, etc., the development of new methods, which are complementary to the existing ones, is highly desirable. We have carried out first experiments on the examination of spectroscopic characteristics of healthy and osteoporosis-affected bone tissues in the terahertz spectral range. The samples were prepared by pressing of grounded bone tissue obtained from the intact rats Wistar and from the senescence-accelerated rats OXYS. The OXYS rats suffered hereditary osteoporosis developed early in life are, therefore, a useful model for examining osteoporosis. The first experiments using a Fourier-spectrometer showed considerable difference in the bone tissue absorbance for two strains, though statistic tests are still required. Because the bone tissue is a highly-absorbing substance, the attenuated total reflection spectroscopy seems to be the most adequate method for detailed bone study. Imaging radioscopy of bone samples using a matrix of microbolometers as a sensor and the Novosibirsk free electron laser as a source of monochromatic terahertz radiation is described.

INTRODUCTION

Osteoporosis is a systemic skeletal disorder characterized by low bone mass and micro architectural deterioration of bone tissue, leading to enhanced bone fragility and an increased tendency to fracture. Osteoporosis has a long latent period and clinically reveals already in the presence of fractures when the bone mineral density is reduced significantly [1]. Thus, for preventing and treatment this disease the early diagnosis is necessary. Today there are several experimental techniques in diagnostic of the osteoporosis such as dual X-ray densitometry and computer tomography, NMR, etc. In spite of high developing and routine of such technique for bone research, the using of terahertz radiation can give complementary information about the bone tissue characteristics that can be valued for diagnostic of osteoporosis.

Recently, the capabilities of terahertz spectroscopy for bones research have been started to investigate. Until now, a few researches of bones using the terahertz time-domain spectroscopy (TDS) have been done. This technique allows obtaining information on the bone density and the complex refractive index. Bone A technique for the computer tomography of bones based on TDS had been demonstrated in the paper [2]. The information about the optical properties of three-dimensional (3D) structures of the investigated bone in the far-infrared region was obtained. Newly developed high-power terahertz sources, such as the Novosibirsk free-electron laser, open up new possibilities for bone radioscopy and imaging, including study of dynamical processes [3].

The goal of this study was the investigation of capabilities of osteoporoses diagnostics by comparison absorption spectra of normal and osteoporosis bone tissue. As a modal for the investigation two genetic strains of rats were chosen, Wistar (intact rats) and OXYS (senescence-accelerated rats with the early onset of osteoporosis). The strain OXYS was founded at the experimental animal laboratory of Novosibirsk Institute of Cytology and

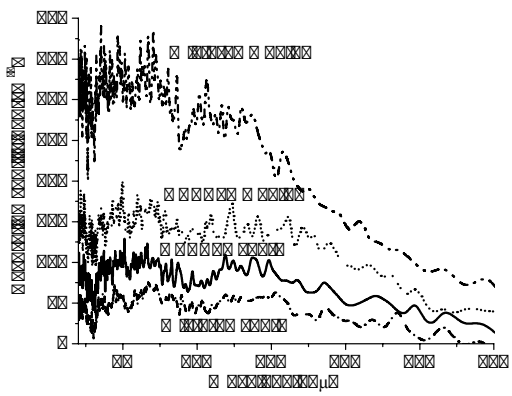

Figure 1: Absorbance vs. wavelength for the bone samples of intact (Wistar) and senescence-accelerated (OXYS) rats of different ages.

Genetics. The animals of this strain have a particularly short life span and accelerated development of age-

*This work is partially supported by Integration Grant 174/6 from SB RAS, by grant RNP.2.1.1.3846 from the Russian Ministry for Education and Science, and grant 07-02-13547 from Russian Foundation for Basic Research

associated pathological phenotypes similar to several geriatric disorders observed in humans.

METHODS AND RESULTS

Fourier-spectrometer measurements

The transmission spectra in the region of 30-300 μm for the bones of two-month and two-year Wistar and OXYS rats were recorded using a Fourier-spectrometer Bruker IFS66v/S (Fig. 1). The samples were prepared by pressing of grounded bone tissue into 200-400 μm thick tablets. Previously, bones from rats were lyophilized and reduced to fragments into the powder in the agathic mortar. The characteristic size of the powder particles was less then wavelength of the THz radiation used in our experiments.

Measurements of the tablet spectra reveal significant absorption of terahertz radiation. So high absorption can be attributed to the absorption of liquid water, which is present in bone tissue in the free and bonded state. The plots in Fig. 1 show clear difference between the extinction coefficients for two-month Wistar and OXYS rats, as well as (may be not so clear) for the two-year animals. Unfortunately the signal magnitude at the Fourier spectrometer detector in these experiments was near the FS noise. To increase the reliability of the measurements we have started study of the extinction coefficient using an attenuated total reflection (ATR) spectroscopy.

Attenuated total reflection technique

ATR is a one of the most adequate techniques for the spectroscopy of highly absorbing substances. The comparison of capabilities of spectrometers for terahertz spectral range is shown in Table 1. Recently, a two-beam ATR spectrometer meant for the operation with tunable FEL was developed [4]. This system was tested using the samples with known optical constants (water, hexane, and benzene) and are showed a good agreement with reference data. Measurements of bone spectra using the ATR spectrometer are in progress.

Table 1: Comparison of capabilities of spectrometers for terahertz spectral range

Capability	Spectrometer type		
	FS	AS	ATR
Measurement of highly absorbing samples	∓	∓	+
Measurement of low absorbing samples	+	+	∓
No impact of reflection	−	−	+
No impact of scattering	−	−	+
Measurement of real and imaging parts of the refraction index	−	−	+
Capability for 2D imaging spectroscopy	−	+	+

Radioscopy with microbolometer matrix

Spectrally resolved terahertz radioscopy of the bones is a prospective technique for the examination of internal bone structure and detection of osteopathy location. We applied a 120×160 pixel microbolometer matrix [5] for the radioscopy of the rat bones. The experimental setup is shown in Fig. 2 and two recorded images are presented in Fig. 3. Intensity distributions along one of the matrix rows are shown in the plot for the initial beam and for the beam passed the bone.

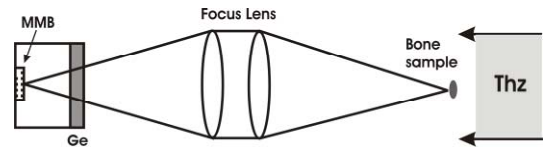

Figure 2: Experimental scheme of radioscopy using MMB with a polyethylene lens.

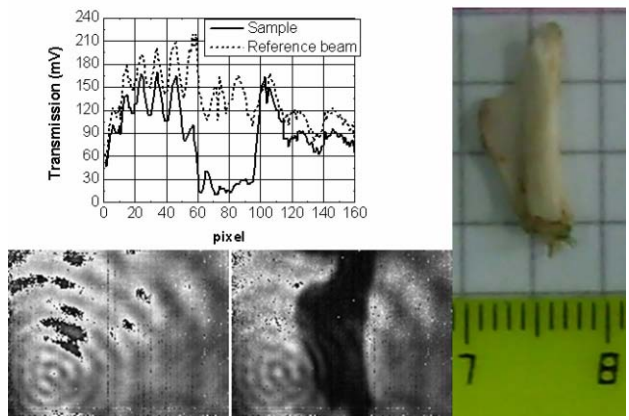

Figure 3: Imaging of rat bones using the MMB: rate 90 frames per second at the bottom (from left to right): reference beam, pass beam through the bone, the bone's photo; at the top: horizontal profile of intensity of the reference beam (dash line) and pass beam (solid line).

CONCLUSION

Thus, the first experiments on rat bone spectroscopy revealed obvious correlation between the absorbance and the strain of two month rats OXYS and Wistar and between of two-year OXYS and Wistar rats. The first radioscopy experiments using MMB showed the capability, in spite of high bone absorption, recording of radioscopic images of bone tissue using terahertz FEL radiation. Further investigations of the bone spectra using ATR technique and radioscopy will give the answer where or not the spectral differences between Wistar and OXYS can be applied for pre-clinical screening analysis of the efficiency of pharmaceutical medicines for osteoporosis treatment.

REFERENCES

[1] D. Faibish, "Mineral Changes in Osteoporosis Review," *Clin Orthop Relat Res.*, vol. 443, pp. 28–38, 2006.

[2] B. Ferguson, X.-C. Zhang, "T-ray computed tomography," *Optics Letters*, vol. 27, no. 15, 2002.

[3] V. S. Cherkassky, V. V. Gerasimov, G. M. Ivanov et al. "Techniques for introscopy of condense matter in terahertz spectral region," *Nuclear Instruments in Physics Research*, no. 575. pp. 63-67, 2007.

[4] V. S. Cherkassky, N. G. Gavrilov, V. V. Gerasimov et al. "Attenuated total reflection spectrometer with terahertz free electron laser as a source," in Proc. of Int. Conf., IRMMW-THz 2006 Shanghai, pp. 459.

[5] A.L. Aseev, D.G. Esaev, M.A. Dem'yanenko, et. al. *These Conference, Paper* MOPPH030.

DEVELOPMENT OF METAL MESH BASED QUASI-OPTICAL SELECTIVE COMPONENTS AND THEIR APPLICATION IN HIGH-POWER EXPERIMENTS AT NOVOSIBIRSK TERAHERTZ FEL*

S.A. Kuznetsov#, BINP SB RAS, Novosibirsk State University,
Novosibirsk, 630090, Russian Federation
V.V. Kubarev, P.V. Kalinin, B.G. Goldenberg, V.S. Eliseev, E.V. Petrova, N.A.Vinokurov
BINP SB RAS, Novosibirsk, 630090, Russian Federation

Abstract

In this paper we discuss main types of metal mesh based passive selective components of THz-quasi-optics required for applications in experiments at Novosibirsk terahertz free electron laser. The first experimental results on development of thin-film metal mesh polarizing beamsplitters and frequency filters by methods of photolithography and electroforming are presented. The technological aspects of the promising LIGA-technique being in progress in the Siberian synchrotron radiation centre and destined for production of thick metal mesh components with thickness compared to radiation wavelength are described.

INTRODUCTION

Successful realization of scientific programs of the Siberian Centre of Photochemical Research [1, 2] operating on basis of Novosibisk terahertz free electron laser (NovoFEL), which fundamental generation harmonics overlaps a spectral range 1.3÷2.5 THz, requires application in user experiments different types of passive quasi-optical selective devices intended for spatial and frequency gating of powerful beams of NovoFEL radiation. The necessary instrumentation includes beam-splitters, attenuators, frequency filters and some elements of focusing optics. Along with desired selective characteristics such devices should be capable of operating over a long period of time under high-power load conditions without noticeable degradation of their properties. It admits to employ in selective components only low absorbing and thermostable materials, such as high conductivity metals and special types of polymers. The best solution is in use of metal mesh structures with specially designed subwavelength topology of mesh cells. For minimizing absorption the metal structures should be wafer-free, however in case of non-self-bearing topology or small metallization thickness structure fastness requires presence of supporting thin-film polymeric substrates.

In this report we discuss selective properties of the main types of metal mesh structures required for NovoFEL experiments and present first results of development of metal mesh components by three different manufacturing techniques: a) contact photolithography; b) electroforming; c) LIGA. Dealing with a minimal topological size of the mesh pattern about a few microns, each of these techniques enables to produce mesh components within its own corresponding range of metallization thickness: a) ≤1 μ; b) ~10 μ; c) ~100 μ.

It should be elucidated that conventional photolithography is considered to be the most adequate, relatively cheap and well-proven technology for manufacturing metal mesh quasi-optical components traditionally used in low- and moderate-power THz-applications. In NovoFEL user experiments employment of such "photolithographic" components is restricted due to high average power of NovoFEL radiation, reaching 400 W nowadays and expected to be raised in the future. Small thickness of metallization and presence of dielectric carrier substrates in such components limit their surface and volumetric thermal conductivity resulting in danger of quick overheating and destruction under high-power load conditions. The best "high-power" alternative to "photolithographic" components (in case of self-bearing topology) are the components based on substrate-free self-supporting thick metal mesh structures manufactured by conventional electroforming and LIGA techniques. In spite of higher technological costs such components are of great interest for NovoFEL applications since they are much more thermostable and mechanically firm and have a much higher radiation destruction threshold. Another inherent and important feature of thick metal structures is much stronger low-frequency attenuation due to a waveguide cut-off effect that can be effectively used for solving problems of harmonics filtration and THz-beams intensity control discussed below.

THZ-COMPONENTS REQUIRED FOR NOVOFEL APPLICATIONS

By fundamental practical purpose influencing on choice of mesh pattern topology the metal mesh based selective components should be divided into three main groups (see Fig.1): 1) beam-splitters (attenuators); 2) frequency harmonics filters; 3) diffractive optical elements.

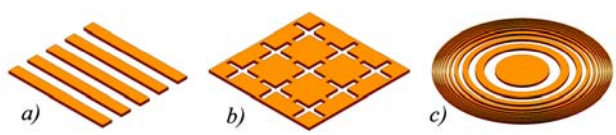

Figure 1: Fundamental types of metal mesh based components required for NovoFEL experiments: *a*) polarizing beam-splitter; *b*) frequency filter; *c*) diffractive optical element (amplitude transparency).

* This work is supported in part by the Russian Foundation for Basic Research (project No. 07-02-01459-a).
# sakuzn@inp.nsk.su

Wideband beam-splitters and attenuators

Urgency of these components is connected with necessity of NovoFEL radiation distribution over simultaneously operating different user stations, as well as THz-beams multiplexing and beam intensity control in various user experiments. Due to almost 100% polarization linearity of FEL's radiation [3] the best solution is in use of polarizing grids or 1-D meshes (Fig. 1a) with a grid pitch g much less than operating wavelength λ. Such grids reflect effectively the E-polarized component of the incident radiation and transmit its H-polarized component that enables to control intensity of transmitted or reflected radiation by choosing an appropriate orientation angle of the grid. For simultaneous operation of different user stations the NovoFEL facility needs beam-splitters with clear aperture diameter up to ~250 mm at minimally realized grid pitch values.

It should be pointed out that for a fixed value of $min(g)$, which is determined by technological limitations, operational efficiency of a polarizing beam-splitter can be greatly enhanced by increasing its metallization thickness t. As t grows the grid slots begin to manifest waveguide properties that results in exponential decrease of the spectral transmittance for the E-polarized incident wave due to a waveguide cut-off effect (Fig. 2a). For H-polarization there is no prohibition on waveguide mode propagation but in contrast to the case $t \to 0$ the transmittance appears to be frequency modulated (Fig. 2b). The last effect is explained by excitation of standing waves inside waveguide slots due to partial reflection of the propagating wave from the input and output slot boundaries. The approximate spectral positions of H-transmission minima and maxima can be obtained from the formulas of Fabry-Perot resonances:

$$\lambda_{min} \approx 2t/(m+1/2),\ \lambda_{max} \approx 2t/m,\ m \in \mathrm{N}.$$

In practice, for eliminating the negative effect of H-transmission modulation it is recommended to mount a polarizing beam-splitter at the angle of incidence $\varphi = \arcsin(q)$, where q is relative width of grid slots. In this case reflection of the H-polarized wave vanishes due to Malyuzhinets effect.

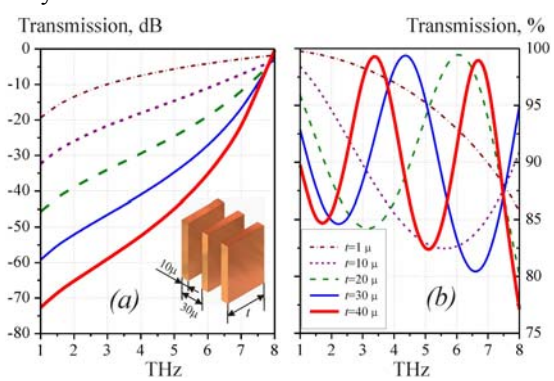

Figure 2: Numerical simulation of influence of metallization thickness t on frequency response of a copper polarizing beam-splitter (normal incidence): *a*) E-polarization (**E** || slots); *b*) H-polarization (**H** || slots).

Harmonics filters

Detailed spectral measurements of NovoFEL radiation show that along with a fundamental generation harmonics (λ = 118−235 μ) the laser spectrum contains the second and the third ones which relative power in optimized regimes reaches relatively high values: 2 % and 0.6 % respectively [4]. A study of these short-wave spectral components and their interaction with investigated samples is a subject of great interest.

For filtering the higher FEL's harmonics at simultaneous strong (≥40 dB) suppression of the 1st one the following 2-D metal mesh structures can be applied:

– Nonresonat "inductive" meshes with circular openings (Fig. 3a, 6). At thickness t compared to radiation wavelength such meshes act as effective high-pass filters, which efficiency of low-frequency attenuation below the point $\nu_{cutt\text{-}off} \approx 1.841 \cdot c/(\pi d)$ is enhanced by the factor $\sim 32 \cdot t/d$ (dB) in comparison with similar thin meshes due to a waveguide cut-off effect.

– Resonant "inductive" meshes of crossed dipole slots (Fig. 3b, 5b) with resonant band-pass transmission at wavelength close to doubled slot length L. For small metallization thickness (t~1 μ) such single meshes provide not higher than ~20 dB out-of-band attenuation. It can be augmented at low frequencies by increasing t.

– Resonant "capacitive" meshes. Such meshes comprised by disjointed resonant conducting elements are effective for rejecting undesirable spectrum frequencies. Meshes with hexagonally packed ring elements (Fig. 4) are recommended for proving a widest rejection band (FWHM~100%) at the maximal theoretical attenuation level ~35-40 dB.

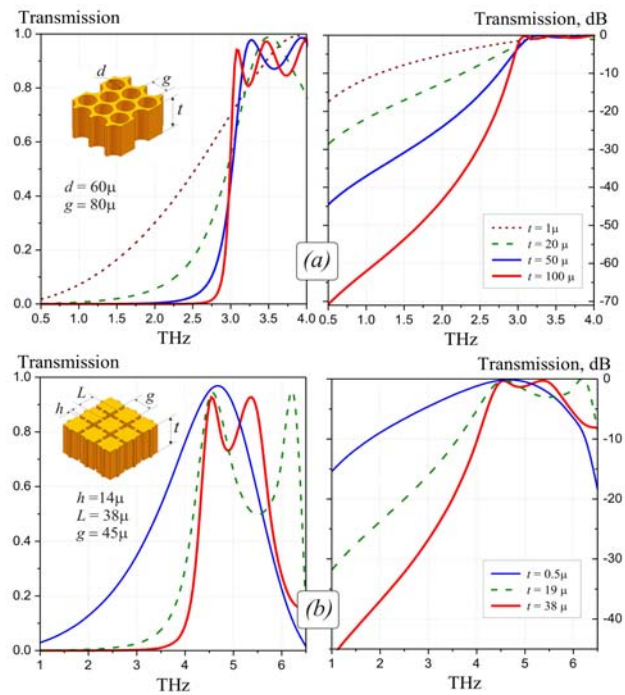

Figure 3: Frequency response of nonresonant high-pass (a) and resonant band-pass (b) copper single-layer mesh filters for different metallization thickness t.

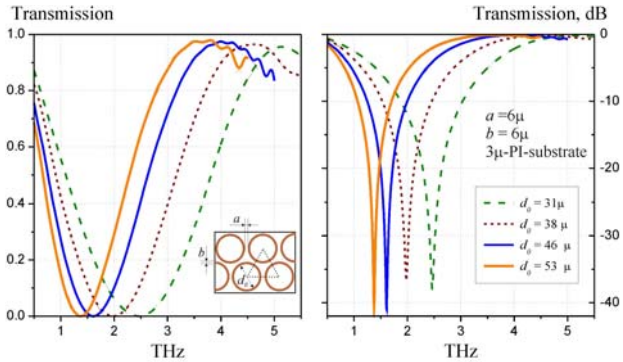

Figure 4: Simulated band-stop properties of thin single resonant meshes with hexagonally packed circular ring elements (t~0.45μ, *Al*) deposited on a 3μ-polyimide film.

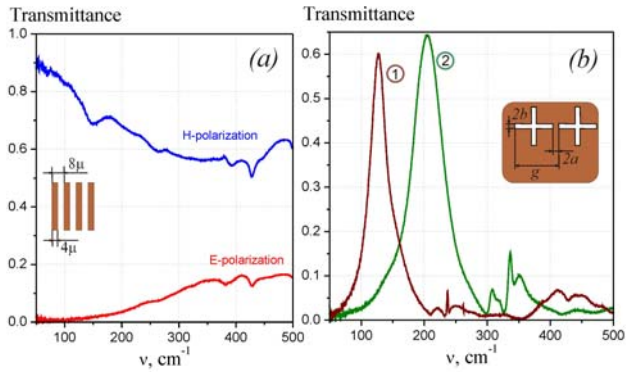

Figure 5: Spectral transmittance of experimental samples of 0.45μ-*Al*-mesh structures deposited on 3.5μ-PI-films: 1) g=41.4μ, 2a=12μ, 2b=6μ; 2) g=28.5μ, 2a=10μ, 2b=5μ.

Diffractive optical elements (DOEs)

DOEs (Fig. 1c), conditionally called as "irregular 2-D mesh structures", are intended for focusing THz-radiation into a spot of a desirable shape. Such a problem arises for instance in scheduled THz-experiments on governing supersonic gas flows by controlling radiation energy deposition inside a specified volume [5]. In contrast to "non-diffractive" mesh structures considered above DOEs operate in a high order diffraction mode that is provided by the greater topological size of a "mesh" pattern ($g > 2\lambda$). Detailed consideration of DOEs is beyond the scope of our paper and can be found for instance in [6].

SAMPLE THZ-COMPONENTS PRODUCED BY PHOTOLITOGRAPHY AND ELECTROFORMING

In the framework of the THz-instrumentation development task we have adapted and successfully tested the technology of contact micro-photolithography for manufacturing thin-film free standing terahertz polarizers (Fig. 1a) and resonant band-pass filters (Fig. 1b) at minimal topological size of the mesh pattern 4–6 μ and clear aperture diameter ∅ 66 mm. The polyimide films 3.5 μ thick were used as bearing substrates for *Al*-mesh structures with metallization thickness 0.45 μ. The typical FIR transmission spectra of manufactured samples obtained at the "Bruker IFS 66v/s" Fourier-transform spectrometer are presented in Fig. 5. Since a radiation source used in the FT-spectrometer is originally nonpolarized an auxiliary polarizer was used for obtaining a reference signal during FIR characterization of 4x8μ-polarizers. The manufactured samples were also tested in 50 W THz-beams of NovoFEL radiation that let us measure directly transmittances of mesh samples in a low-transmission region without using a cryogenic technique. E.g. the transmittance of 4x8μ-polarizers for E-polarization appeared to be ~$3.2 \cdot 10^{-3}$ at λ = 126 μ.

The choice of thin polyimide substrates is conditioned by their satisfactory optical characteristics, high

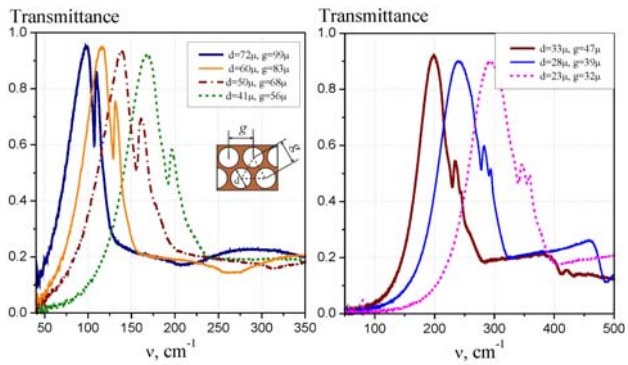

Figure 6: High-pass properties of free standing substrate-free nonresonant 9μ-*Ni*-meshes with hexagonally packed circular openings.

mechanical fastness and thermostability enabling to withstand radiation heating up to 350^0C. By now polyimide-film based mesh structures were successfully tested at radiation power flows ~2 kW/cm^2.

Successive use of photolithographic and electroforming techniques enables to increase mesh metallization thickness resulting in elimination of supporting polymeric substrate in case of self-bearing structures. We successfully tested this technology for production a set of dichroic high-pass filters based on electroformed *Ni*-meshes 8÷10 μ thick (Fig. 6). As such thickness is close to the upper technological limit the only alternative for its further increase is use of the LIGA-technique.

PRODUCTION OF THICK THZ-COMPONENTS BY LIGA-TECHNIQUE

In comparison with conventional photolithography the LIGA-technique being developed at the Siberian Synchrotron Radiation Centre (BINP SB RAS) is based on deep X-ray lithography and destined for producing microstructures in a wide range of their thicknesses: from a few units up to hundreds microns [7, 8]. Such an advantage of the LIGA-technology over optical and UV techniques is realized due to high penetrability of X-ray radiation into X-ray-sensitive resists and negligible effects of parasitic Fresnel diffraction that makes LIGA to

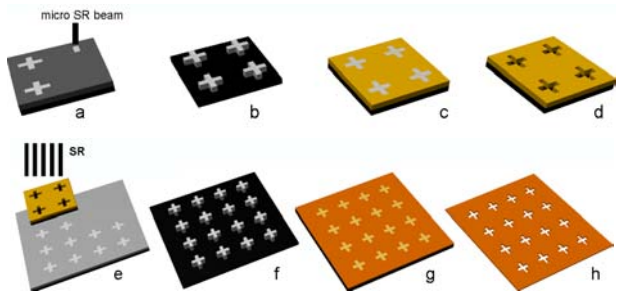

Figure 6: Main stages of the LIGA-technique: a-d) X-mask production; e-h) X-mask application for obtaining a thick metal mesh structure.

be ideal for manufacturing thick metal mesh based THz-components with extremely high aspect ratios unachievable by any other methods.

The principal stages of LIGA include production of an X-ray contrast mask which topological pattern replicates the pattern of a desired mesh structure, deep X-ray lithography via the prepared X-mask and subsequent growing of an output thick mesh structure by electroforming. At present, we master the LIGA-technique for producing self-bearing copper 2-D mesh filters 50÷100 μ thick at the minimal topological size of mesh pattern about 10 μ. The main steps of the used technology are shown in Fig. 6.

We use a direct method of X-mask creation [8] based on direct forming a latent image of the required microstructure or its fragment in the 30 μ-layer of the X-ray sensitive negative resist SU-8 deposited onto roentgenoparent wafer by irradiation under a collimated microbeam of synchrotron radiation (SR) with photon energy 4÷30 keV (Fig 6a). SR provides uniform irradiation of the SU-8 layer over its depth that result in verticality of walls in output microstructures. As roentgenoparent wafers the polished plates of special carbonic glass 500÷600 μ thick are used. After removal of the unirradiated resist by wet etching technique (Fig 6b) a thin 1÷3 μ copper sublayer and a subsequent 10÷20 μ layer of rhenium or gold are deposited onto the wafer by electroforming (Fig 6c). The layer of rhenium (gold) acts as a roentgenopaque material required for the X-mask, whereas a copper sublayer provides better adhesion of Re (Au) to the wafer surface. After final removal of the residual resist (Fig 6d) the finished X-mask with typical operating area 10x10 mm^2 is ready for next applications.

The stage of production of the output metal mesh structure (Fig 6e-h) includes steps similar to the considered above. X-ray exposure of a thick SU-8 resist deposited onto a carbonic glass wafer is realized via the prepared X-mask with subsequent multiplication of the X-mask pattern over desired area (Fig 6e). Irradiated regions of SU-8 material cross-linked after exposure and cleaned from unirradiated resist (Fig 6f) form the mask with deep vertical walls which is used for the following electroforming of a thick metal structure (Fig 6g). The maximal metallization thickness of the output mesh structure corresponds to the thickness of the SU-8 resist which is 50÷100 μ thick in our LIGA-experiments. The main problem appearing at the final step of production is separation of a copper structure from the carbonic glass wafer after removing the residual resist by wet etching (Fig 6h). This problem is solved by galvanic deposition of an auxiliary 1μ-Re-layer onto the carbonic glass wafer before electroplating of copper. It leads to decreasing copper adhesion due to passivation of Re-surface.

CONCLUSION

Rapid progress in terahertz researches connected with appearance of high-power FELs requires detailed development, designing and optimization of selective components of terahertz quasi-optics necessary for high-power applications. For future experiments at NovoFEL user stations the THz-components produced by conventional thin-film based photolithography and electroforming are considered as supplementary to thick LIGA-components which are of primary importance. We place the emphasis on development of the LIGA-technique and expect to obtain first high-quality THz-LIGA-structures in 2007-2008.

REFERENCES

[1] V. P. Bolotin, N. A. Vinokurov, D. A. Kayran et al., “Status of the Novosibirsk terahertz FEL”, Nuclear Instrum. Methods, vol. A543, pp. 81-84, 2005.

[2] N. A. Vinokurov et al., “Status of Novosibirsk ERL and FEL”, in these Proceedings.

[3] V. P. Bolotin, V. S. Cherkassky, E. N. Chesnokov et al., “Novosibirsk terahertz free electron laser: status and survey of experimental results”, Proc. Joint IRMMW-THz-2005 Conf., Williamsburg, USA, 2005, p. 495.

[4] V. V. Kubarev, N. A. Vinokurov, V. V. Kotenkov et al., “Harmonic Generation in the Novosibirsk Terahertz FEL”, in Proc. Joint IRMMW-THz-2006 Conf., Shanghai, China, 2006, p. 162.

[5] V. V. Yakovlev, V. M Fomin. “Possibilities of laser radiation application for solving aerodynamic problems”, in Proc. 1st Russian THz-Workshop “Generation and application of terahertz radiation”, 24-25 Nov., 2005, Ed. B.A. Knyazev, Novosibirsk, Russia, pp. 123.

[6] I. A. Polskikh, A. Fanova, B. A. Knyazev et al, “Diffraction Optical Elements and Optical Systems with High Power Monochromatic Terahertz Source”, in these Proceedings.

[7] W. Ehrfeld and H.Lehr. "Deep X-ray lithography for the production of three dimensional microstructures from metals, polymers and ceramics". Radiat. Phys. Chem., vol. 45, No. 3, pp. 349-365, 1995.

[8] E.V. Petrova, B.G. Goldenberg, V.I. Kondratiev et al., “Production of thick wafer based X-masks for deep X-ray lithography”, J. Surface Investigation. X-Ray, Synchrotron and Neutron Tech., 2007 (in press).

DIFFRACTION OPTICAL ELEMENTS AND OPTICAL SYSTEMS WITH A HIGH POWER MONOCHROMATIC TERAHERTZ SOURCE *

V.S. Cherkassky, A. V. Fanova, L.A. Merzhievsky, S.A. Zhigach, NSU, Novosibirsk, Russia
Young Uk Jeong, Hyuk Jin Cha, B.A., Korean Atomic Energy Research Institute
N.G.Gavrilov, B.A. Knyazev#, G.N. Kulipanov, I.A. Polskikh, N.A. Vinokurov, S.A., BINP, Novosibirsk, Russia.

Abstract

We have developed reflective diffraction optical elements (DOE) for focusing radiation of terahertz free electron lasers (FEL). Metal-dielectric Fresnel zone plates and metallic kinoform "lenses" were fabricated and tested using FEL radiation. A microbolometer camera (see the paper by Esaev et al. at this conference) sensitive to THz radiation had been applied for recording both terahertz beam caustic and terahertz images. Diffraction efficiency of a kinoform lens appears to be about unity. Quality of images obtained with the kinoform lens was studied. The lens was used as a key element for a Toepler optical system, which were used for studying condense matter non-uniformities and deformations. The experiments were performed at Novosibirsk and KAERI FELs.

INTRODUCTION

Imaging in the terahertz spectral region (1 – 10 THz) is a subject of special interest for many applications such as biological researches, medical diagnostics, study of materials, security systems and many other applications. Each optical system consists of a source of radiation, optical elements and an imager. In this paper we describe optical elements and recorders developed for imaging with free electron laser (FEL) as a source. Most of the experiments were carried out at high power Novosibirsk FEL. Some of them have been done at KAERI FEL.

Because the refractive optical elements can be damaged by high power terahertz radiation, we have developed a number of reflective diffraction optical elements (DOE). Large-scale reflection DOE are often used in the microwave spectral region, and the application of DOE in terahertz optical systems is, obviously, very prospective.

Previously [1 – 3] we have developed (or adapted) three recorders for the visualization of intense terahertz radiation: a near-IR thermograph, a thermal-sensitive Fizeau interferometer, and a "thermal image plate". In this paper we first used as a terahertz imager [4] a microbolometer matrix, initially developed for the MIR range 0. The matrix has higher sensitivity and better spatial resolution, than the imagers mentioned above.

*Work supported by Integration grants 174/6 and 22/6 from Siberian Branch of Russian Academy of Science, by grant RNP.2.1.1.3846 from the Russian Ministry for Education and Science, and grant 07-02-13547 from Russian Foundation for Basic Research.…
#knyazev@inp.nsk.su

TERAHERTZ OPTICAL ELEMENTS AND SYSTEMS

Fresnel zone plates

Three Fresnel zone plates (with zone numbers of 91, 46, and 30, respectively, and the first Fresnel zone radii of 5.2, 7.35 and 9.0 mm) had been designed and fabricated for focusing terahertz radiation with simultaneous reflection under the right angle. The elliptically shaped plates with the minor semi-axis of 5 cm and the aspect ratio of 1:1.41 were formed by etching a copper foil clad on a fiber-glass plastic. The central zone of each plate was reflecting.

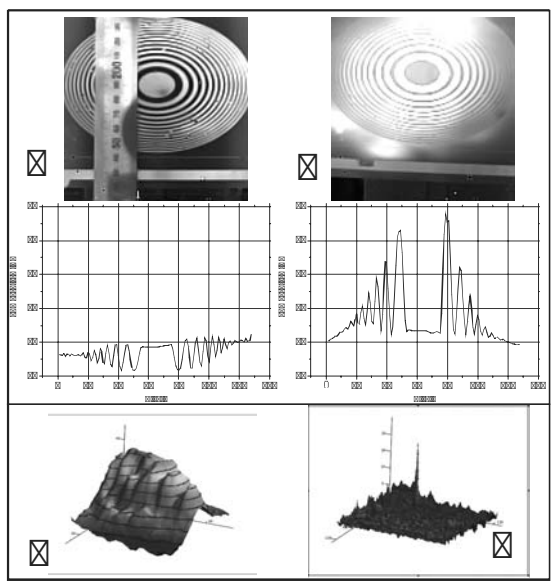

Figure 1: A thermographic image of a zone plate recorded with no radiation (*a*) and with THz irradiation (*b*); plots – effective temperature distribution along the major ellipse axis. Intensity distribution in the initial THz beam (*c*) and in the zone plate focus (*d*) recorded with the thermal image plate.

The images of a zone plate taken at 2.5 – 3.0 μm with the thermograph (Fig.1) show growing the temperature of the dielectric zones up to 55 C, nevertheless, the zone plate focuses THz radiation well. The focal lengths for all zone plates exactly correspond to designed values. Since the principle focal length of a zone-plate is inversely proportional to the radiation wavelength, $f_1 = r_1^2/\lambda_0$, it can be used at arbitrary wavelength, but low diffractio efficiency (~10%) constrains its application.

Reflecting kinoform lens

More effective in comparison with a zone plate is a kinoform or Fresnel lens, in which each zone surface is parabolically profiled. First, we tested a simplified kinoform lens with elliptical zones, similar to the above described zone plates, and with the profile designed for focusing radiation at $\lambda_0 = 130$ μm with $f = 250$ mm. The kinoform lens was manufactured by drilling on a NC machine. Minor radius of the first Fresnel zone was equal to 8.06 mm. Measured diffraction efficiency of the lens appears to be close to unity.

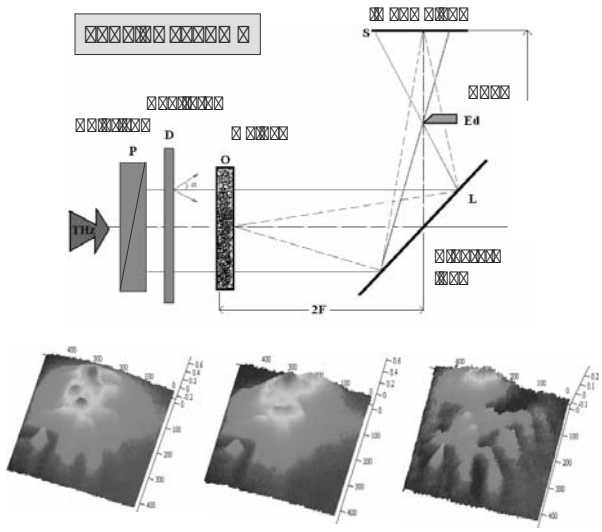

Figure 2: Toepler optical system and images obtained for a polyethylene film as an object: undistorted film (left picture) and stretched ones.

Optical systems with kinoform lenses

The kinoform lens was used as a focusing element in a Toepler quasi-optical system (Fig.2) intended for the study of loaded solid samples and stretched films by means of terahertz radioscopy. Experiments were performed both at NovoFEL and KAERI FEL. Dynamic range and linearity of Toepler system response critically depend on the focal spot quality. Using a 160×120 pixel, 51 μm period microbolometer focal plane array 0, we recorded the distribution of terahertz radiation intensity (Fig. 3) in the caustic surface of the elliptical kinoform lens without scatterer, object and knife-shaped edge.

The kinoform lens has a relatively small focal spot size in the vertical direction (at $L = 250$ mm), which enables using the lens for the study of vertical optical path gradients, but the horizontal spot size is too large and the intensity distribution is uneven, which does not enable measurement of horizontal nonuniformities. The origin of the horizontal focal spot distortion lies, obviously, in the simplified Fresnel zone and surface shapes. The correct shape must be an emulation of the off-axis parabolic mirror that is not easy to fabricate.

To obtain a good focal spot, we fabricated axisymmetric kinoform lens, and by inclining it under a small angle, extracted the reflected terahertz radiation onto a small plane mirror that enabled displacing the focal spot out of the initial beam. 2D surface plot in Fig. 3 demonstrates high quality of the focal spot for the axisymmetric kinoform lens.

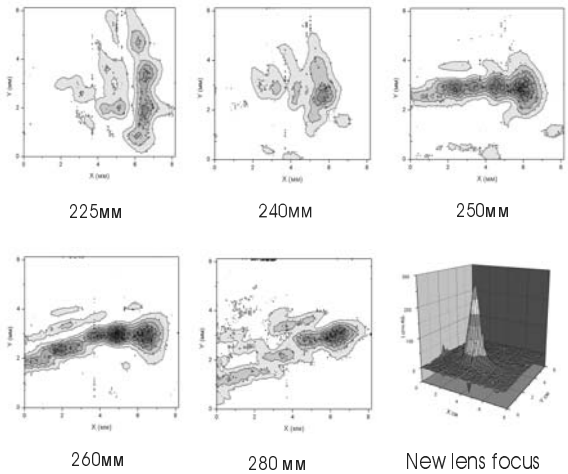

Figure 3: Distribution of terahertz beam intensity in the elliptical kinoform lens caustic surface (2-D plots) and in the focus of axisymmetric kinoform lens (the last plot) recorded with the microbolometer focal plane array.

CONCLUSION

Focusing elements and detectors developed in this study enable designing of quasi-optical systems for imaging and radioscopy with a high power terahertz free electron laser. Examples of optical path gradients recorded when THz beam passed through stretched polyethylene film are shown in the bottom Figure 2.

REFERENCES

[1] V. S. Cherkassky, V. V. Gerasimov, G. M. Ivanov, et al. “Techniques for introscopy for a high-power THz free electron laser”, Nucl. Instrum. Methods in Phys. Res. vol. A 543, pp. 102-109, 2005.

[2] N. A. Vinokurov, B. A. Knyazev, G. N. Kulipanov, et al. “Visualization of radiation from a high-power terahertz free electron laser using a thermosensitive interferometer”, Tech. Phys., vol. 52, no.7, pp. 911–919, 2007.

[3] V. S. Cherkassky, B. A. Knyazev, V. V. Kubarev, et al. “Imaging techniques for introscopy of condense matter in terahertz spectral region”. Nucl. Instrum. Methods in Phys. Res. vol. A 575 pp. 63-67, 2007.

[4] Dem’yanenko M.A.,Ovsyuk V.N., Shashkin V.V., et al. “Uncooled 160x120 microbolometer IR FPA based on sol-gel VOx”, in Proc. SPIE, vol. 5957, 340-347, (2005).

DIAGNOSTICS OF AN ELECTRON BEAM USING COHERENT CHERENKOV RADIATION*

R. Tikhoplav#, P. Musumecci, J. Rosenzweig, S. Tochitsky, UCLA, Los Angeles, CA 90095
G. Gatti INFN/LNF, 00044 Frascati (RM) Italy

Abstract

The use of coherent Cherenkov radiation as a diagnostic tool for longitudinal distribution of an electron beam is studied in this paper. This method will be employed for the 7th harmonic bunching experiment at Neptune linear accelerator facility at UCLA. Coherent Cherenkov radiation is produced in an aerogel with an index of refraction close to unity.

THEORETICAL BACKGROUND

Radiation due to a relativistic electron beam traversing a medium, such as transition radiation (TR), has proved itself to be a powerful tool for beam diagnostics, e.g., determining the transverse distribution and position of an electron beam as in TR screen technique. Such radiation could also be used for reconstruction of the longitudinal profile of the electron beam if the coherent part of such radiation is known [1].

Regardless of the source of radiation (Cherenkov (CR), Synchrotron (SR), or TR), the spectral response of the electron bunch can be represented as following [2],

$$T(\lambda) = S(\lambda)\left(N + N(N-1)\left|F_{3D}(\lambda)\right|^2\right) \quad (1)$$

where $S(\lambda)$ is the spectrum of a single particle, λ is wavelength, N is the number of particles in the bunch, F_{3D} is the 3-D Fourier transform of the bunch particle distribution, called the form factor,

$$F_{3D}(\lambda) = F(\lambda)F_T(\lambda) \quad (2)$$

where F and F_T are longitudinal and transverse form factors respectively. Coherent part of radiation is proportional to the number of emitters squared, thus it gives a much stronger signal than the incoherent part. It is also a function of a form factor which depends on the shape of the bunch. If a longitudinal modulation of a certain period λ_0 (micro-bunching) is introduced to the bunch with longitudinal Gaussian distribution of rms size σ, such modulation would change the form factor resulting in enhancement of a corresponding frequency of radiation and its harmonics.

$$F(\lambda) = \exp\left(-2\pi^2\sigma^2/\lambda^2\right)\left(1+\sum_n h_n(\lambda_0)\right) \quad (3)$$

where $h_n = a_n \exp\left(-2n^2\pi^2\sigma^2/\lambda_0^2\right)\cosh\left(4n\pi^2\sigma^2/\lambda\lambda_0\right)$ is the modulation factor, n and a_n are the harmonics number and its weight respectively. Such radiation would be analyzed and a temporal distribution of the electron beam could be deducted.

Coherent Cherenkov Radiation in the Aerogel

Cherenkov radiation induced by a single particle can be expressed in terms of number of photons per unit frequency,

$$\frac{\partial N_{ph}^{Ch}}{\partial k \partial \theta} = L\alpha\theta_c^2\delta(\theta-\theta_c) \quad (4)$$

here α is the fine structure constant, θ_c is Cherenkov angle, L is the length of the electron path in the medium. In the case of a bunched electron beam, the total number of photons for Coherent Cherenkov Radiation (CTR) can be expressed as the following,

$$N_{ph}^{Ch} \approx \sqrt{\pi}LN^2\frac{\alpha}{\sigma}a_n^2\theta_c^2\left|F_T(\lambda)\right|^2 \quad (5)$$

We are particularly interested in using the aerogel as a medium for CTR. Aerogel, or 'frozen smoke' is a low-density solid-state material made by high temperature and pressure-critical-point drying of a gel composed of colloidal silica structural units filled with solvents [3].

Table 1: Aerogel Parameters

Parameter	**Value**
Material	SiO_2
Density	20 kg/m^3
Refractive Index, n	1.008
Cherenkov Angle, θ_c	7.25^O
Melting Point	1200^{O}C

Its low density provides nearly non-destructive tool for the electron beam diagnostics (see Table 1) and its small refractive index $n=1+\Delta$ gives a small Cherenkov angle $\theta_c \approx \sqrt{2\Delta}$.

The form factor (and consequently, the enhancement of coherent radiation) depends on the transverse shape of the electron beam as well. A Gaussian transverse distribution $f(\rho) \propto \exp(\rho^2/2\sigma_T^2)$ leads to suppression of shorter wavelengths (see Fig. 1), unless the transverse size σ_T is infinitely small. The corresponding form factor is given by the following:

$$F_T(\lambda) = \exp\left(-2\pi^2\theta_c^2\sigma_T^2/\lambda^2\right) \quad (6)$$

This could be overcome if other transverse shapes are employed. For example, transverse hard-edge distribution

*Work supported by US Department of Energy
#rodion@ucla.edu

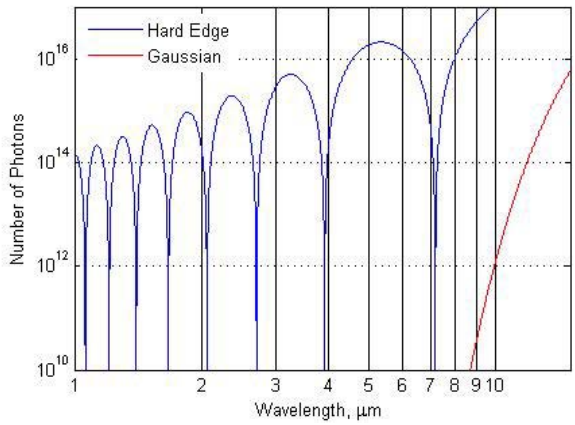

Fig. 3: Number of photons of the Cherenkov radiation induced by 160 pC electron beam for Gaussian and hard edge transverse distributions.

$f(\rho) \propto rect_{\sigma_T}(\rho)$ gives a stronger signal than the Gaussian, see Fig. 1. The corresponding form factor is

$$F_T(\lambda) = \frac{J_1\left(2\pi^2\theta_c^2\sigma_T^2/\lambda^2\right)}{2\pi^2\theta_c^2\sigma_T^2/\lambda} \quad (7)$$

Hard edge distribution is not the only one that gives a good response in the high frequency range. Other techniques such as putting a grid of wires across the beam could be used [4].

Angular Distribution of the Cherenkov Radiation

The delta-function nature of the theoretical representation for the angular distribution of Cherenkov radiation makes unrealistically strict requirements for the transverse emittance of the electron beam. Indeed, spatial coherence of radiation is not achievable unless all the electrons trajectories in the medium are perfectly parallel.

To treat the problem properly, one needs to take into account the fact that the speed of an electron decreases by a small jump every time a photon is emitted. Interestingly, this process is analogues to a spectral line broadening due to finite life of an excited state.

L.I. Schiff [5] treated this problem and got the following distribution for intensity of Cherenkov radiation as a function of an angle between the direction of the motion of an electron and direction of radiation:

$$I(\theta) = I(\theta_c)\frac{\sin^2 y}{y^2} \quad (8)$$

where

$$y = 2\pi\frac{l}{\lambda}(\cos\theta_c - \cos\theta) \quad (9)$$

l is the length of a free path. Distribution (8) has a certain width. Let $\Delta\theta$ to be FWHM of (8), i.e., $I(\theta_c + \Delta\theta/2) = I(\theta_c - \Delta\theta/2) = I(\theta_c)/2$ or $\sin y = y/\sqrt{2}$, and $y \approx 1.4$; therefore from (9) it follows that

$$\Delta\theta \approx 2.8/(2\pi\frac{l}{\lambda}\sin\theta_c) \quad (10)$$

Finding the exact value for the length of the free path l theoretically is challenging due to partial coherence between different elementary waves emitted by different parts of an electron path [6]; but its upper limit is easily set to be the total length of the medium L, which is in our case is 2.5 mm. Hence, the lower limit for $\Delta\theta$ is 14 mrad.

EXPERIMANTAL SET-UP

The Neptune facility at UCLA consists of a 15 MeV Photoinjector linac which can provide a charge of up to 0.5 nC and a CO_2 laser with peak energy of up to 100 J [7]. Using a CO2 regenerative amplifier (10.6 um) with 5-10 MW of power, we expect the electron beam to be fully bunched after traversing a 10 period undulator tuned to the 7th harmonic of the laser [8], see Table 2.

Table2: Neptune Bunching Experiment Parameters

Parameter	**Value**
Undulator Length	33 cm
Undulator Period, λ_u	3.3 cm
Undulator Constant, K_u	1.8
Electron Energy	12.4 MeV
Electron Charge	100 pC
Normalized Emmitance	5 mm-mrad
Laser Energy	1 mJ
Laser Pulse Length	200 ps
Laser Intensity, I	1 GW/cm^2
Laser Beam rms Size	0.65 mm

SUMMARY

A novel method for micro-bunching diagnostics of an electron beam using aerogel has been analyzed and will be tested at Neptune facility at UCLA. By measuring the relative intensities of different harmonicas the whole longitudinal modulation can be reconstructed. The lower limit for the angular width of the Coherent Cherenkov Radiation was found to be 14 mrad which corresponds to the beam parameters available at the Neptune facility.

REFERENCES

[1] R. Tikhoplav, PhD Dissertation (2006).
[2] O. Grimm, *et al.*, DESY April 24, 2006 Internal report (2006).
[3] http://stardust.jpl.nasa.gov/tech/aerogel.html
[4] G. Gatti, *et al.*, Proc. of 2007 Part. Accel. Conf. 998 (2007).
[5] L.I. Schiff, Quantum Mechanics (1949).
[6] J.V. Jelley, *Physics-Uspekhi* **58**, 231 (1956).
[7] http://pbpl.physics.ucla.edu
[8] P. Musumeci, *et al.*, these proceedings.

FIRST EXPERIENCES WITH THE FIR-FEL AT ELBE

U. Lehnert, P. Michel, W. Seidel, G. Staats, J. Teichert, R. Wünsch
Forschungszentrum Dresden-Rossendorf e.V., 01314 Dresden, Germany

Abstract

We show the design and the parameters of operation of the long-wavelength (U100) FEL at ELBE. First lasing has been shown in August, 2006. Since then, the laser has undergone thorough commissioning and is available for user experiments since fall, 2006. Besides in-house users the IR beam is available to external users in the FELBE (FEL@ELBE) program witch is a part of the integrated activity on synchrotron and free electron laser science in the EU. At the beginning of 2007 lasing in the full designed wavelength range from 20 µm to 200 µm was demonstrated. The laser power typically reaches several Watts in cw operation but drops for very long wavelengths depending on the size of the used out-coupling hole. However, there exists a serious problem with small gaps in the wavelength spectrum. We attribute this behaviour to the transmission characteristics of the overmoded partial waveguide used from the undulator entrance to the first mirror.

INTRUDUCTION

At Forschungszentrum Dresden-Rossendorf, Germany, the radiation source ELBE (Electron Linac with high Brilliance and low Emittance) operates on the basis of a superconducting linear accelerator for electron energies up to 40 MeV with an average beam current of 1 mA in quasi continuous wave (cw) mode. The electron linac serves as a driver to generate several kinds of secondary radiation and particle beams. Two free-electron lasers generate radiation in the mid and far infrared for a very large field of applications reaching from semiconductor physics to biology. In addition, MeV Bremsstrahlung for nuclear (astro) physics, monochromatic hard-X-ray channelling radiation for radiobiological experiments, and in near future also neutrons and positrons for studies in nuclear reactor science and materials research are provided. The quality and range of the provided beams will be extended even further when the superconducting photo-electron gun [1] which is tested at present will become operational. The first FEL to become operational at ELBE was the mid-IR FEL [2] using two undulators with 27.3 mm period. With the available beam energies it covers a wavelength range from 3-24 µm. To extend the wavelength range into the far-IR a second FEL with a 100 mm period [3] undulator was installed. It now provides laser light from 20-200 µm. After first lasing in August, 2006 it is in routine user operation since fall, 2006. The relevant user facilities comprise 6 optical laboratories. Some of these are also used by in-house groups, mainly in the areas of semiconductor physics, and radiochemistry, and experiments there will require a certain level of collaboration with the in-house researchers. In particular noteworthy is the fact that a number of additional optical sources from the visible to the THz frequency range are available, e.g. for two-colour pump-probe experiments. These sources (Ti:sapphire laser and amplifier, OPO, OPA, broad-band THz generator) are all based on Ti:sapphire oscillators which are synchronized to the FEL with an accuracy better than a ps. Two laboratories are intended to provide users with utmost flexibility for their own experiments, also in scientific areas not covered by in-house groups (e.g., surface physics, molecular physics).

U100-FEL SETUP

The FIR-FEL at ELBE (see Fig. 1) uses a hybrid undulator with 100 mm period length. It consists of 38 periods equipped with SmCo magnets which were chosen due to their better radiation resistance with respect to NdFeB. With a minimum gap of 24 mm a maximum K_{rms} parameter of 2.7 is reached. The whole wavelength range from 20-200 µm is covered with electron beam energies from 20-35 MeV. To allow small undulator gaps a waveguide optical beam transport through the undulator is necessary. The ELBE FIR-FEL uses a partial waveguide spanning from the undulator entrance to the downstream mirror. The interior height was chosen to 10 mm. In horizontal direction the waveguide is wide enough to allow essentially free propagation. Thus, an overmoded parallel-plate waveguide is formed which shows low losses for the principal mode. The downstream mirror was placed as a cylindrical mirror inside the waveguide. On the upstream side the optical beam propagates freely through the focusing quadrupoles and the dipole to a toroidal mirror. To optimize the coupling between the waveguide mode and the free propagation the horizontal curvature of both mirrors was chosen to correspond to a Rayleigh range of 180 cm. The vertical curvature of the upstream mirror, however, equals its distance of 361 cm from the waveguide entrance. Round-trip optical losses inside the U100 resonator were computed using the GLAD [4] code. The mode conversion between waveguide and free propagation was approximated taking only the fundamental waveguide mode into account. The efficiency computed this way is above 94 % for all wavelengths yielding a reasonably high Q of the optical resonator. To allow for a near-optimum out-coupling over the whole wavelength range the upstream mirror chamber is equipped with three interchangeable mirrors of identical curvature but with 2.0, 4.0 and 7.0 mm out-coupling holes.

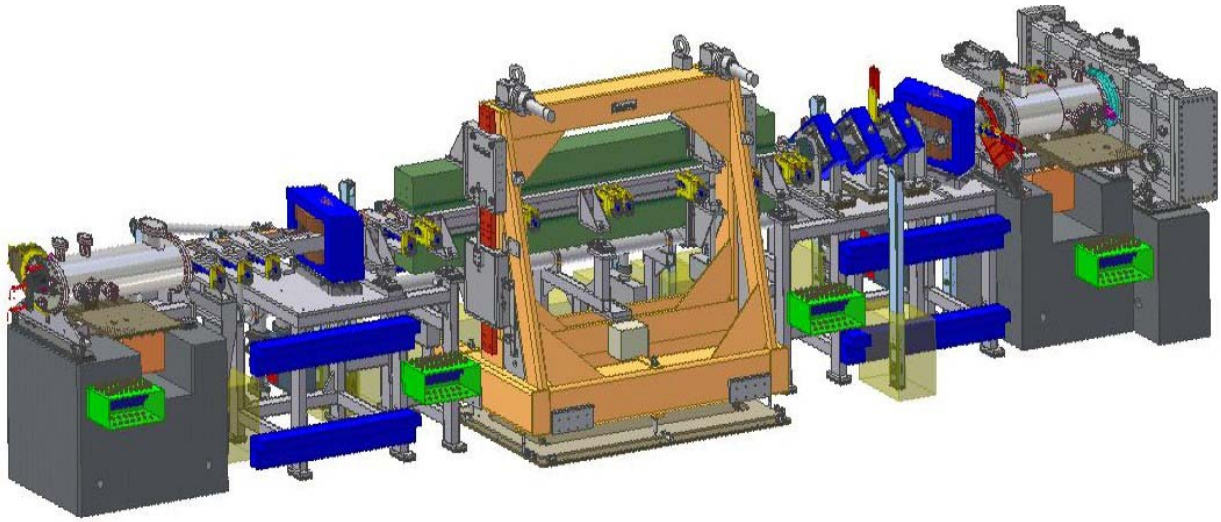

Figure 1: The setup of the FIR-FEL of ELBE. The electron beam enters from the right side through the blue bending magnet and quadrupole triplet. The upstream mirror chamber contains three interchangeable mirrors with different size out-coupling holes.

FEL OPERATION AND DIAGNOSTICS

Since the FEL gain is linearly proportional to the beam peak current it is highly desirable to minimize the electron bunch length in the vicinity of the undulator. Accordingly, calculations of the laser gain yield an optimum at minimum bunch length (see Fig. 2), even though this is bought at the expense of an increased energy spread of the electron beam. When tuning the electron beam the bunch length can be optimized by maximizing the signal of coherent optical transition radiation from a viewscreen. For the mid-IR FEL we have this way reached a minimum 1.5 ps bunch length for an optimized beam. It turns out, however, that for the startup of the FIR laser it is way more critical to minimize the energy spread of the beam even though adjusting the accelerator for energy spread drastically increases the bunch length at the undulator. The optical losses inside the U100 resonator do not exceed 6 % per pass (see Fig. 3), even when only the lowest order hybrid waveguide mode is considered. When out-coupling is included the losses rise by approximately twice the out-coupled fraction due to diffraction losses at the hole. These calculations are in good agreement with a recently measured value of 10 % loss per pass at 30 µm wavelength with the 2 mm out-coupling hole. The calculated average FEL output power reaches levels of 50 W for both maximum electron energy and undulator K parameter. In practise about 12 W were measured and delivered for user operation (see Fig. 4). To measure the energy spectrum at the exit of the FEL has proven an extremely versatile tool to start-up the lasing and to optimize the FEL operation. In the mid-IR FEL one typically can see the spontaneous emission and some spikes of increased intensity which one can use to

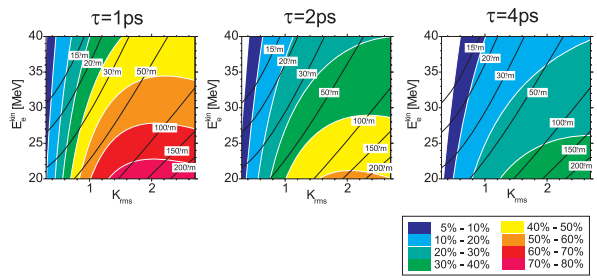

Figure 2: Computed small-signal gain in the low-gain approximation.

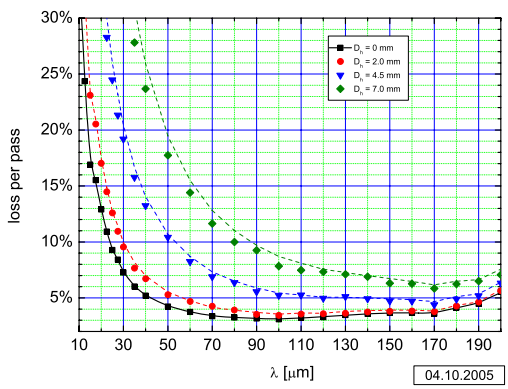

Figure 3: Round-trip losses of the optical beam in the U100 optical resonator. The black line shows the mode conversion losses only. The coloured data additionally include the out-coupling and diffraction losses at different out-coupling hole sizes. At 30 µm the 10 % loss per pass could be confirmed by cavity ring down measurements.

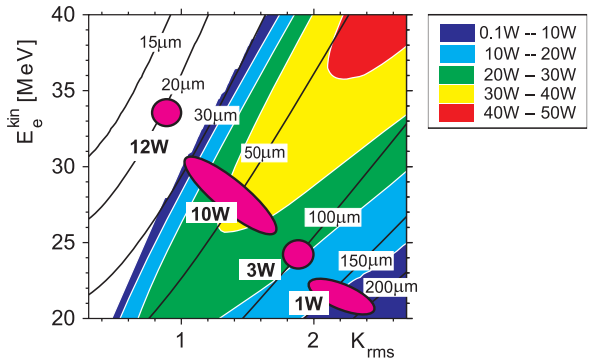

Figure 4: Typical output power of the FEL in CW operation. The best measured values are higher for most wavelengths but do not fully reach the predictions. For small wavelengths the computations show low power output due to high optical losses which was not seen this significantly in the experiment.

optimize the tuning until the laser starts. In the FIR-FEL the detection efficiency of our normally used reference detector is too low to see the spontaneous emission or small spikes of lasing startup. One, however, immediately notices the increase in energy spread on a viewscreen in the dispersive section after the FEL as soon as the FEL starts. It is even possible to use the energy spread as a measure for the amplitude of the optical field inside the resonator. Fig. 5 shows the energy spectrum when tuning the length of the optical resonator.

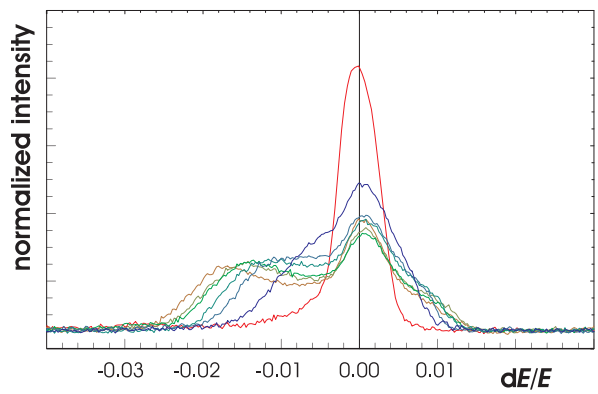

Figure 5: Energy spectra of the electron beam after passage through the FEL. The red trace shows the spectrum for a negative optical cavity detuning where the laser is off. Over green to blue the colours than indicate an increasing detuning with laser action. For minimum detuning (brown trace) the maximum power is out-coupled from the electron beam with some electrons loosing about 2 % of their initial energy. One notes that a certain fraction of the beam does not take part in the laser interaction and remains unchanged in energy.

INACCESSIBLE WAVELENGTH

While the combination of a partial waveguide in the undulator up to the downstream mirror with free optical propagation between the undulator entrance and the upstream mirror showed a reasonably high Q in theory there seam to be problems in practice. We made the observation that at some particular wavelengths it is impossible to start the laser. In addition, the optical spectra show well-defined suppressed wavelengths distributed over the whole range of operation. One example for this is shown in Fig. 6. At a fixed setting of the electron beam, the emission wavelength of the FEL was shifted by changing the undulator gap. For all recorded spectra the emission is suppressed at 30.3 µm wavelength with a marked drop in efficiency and output power when the nominal lasing wavelength just meets the dropout. An absorption line in the optical beam path to the diagnostic station can be excluded because the suppression effect is seen in the energy spread of the electron beam as well.

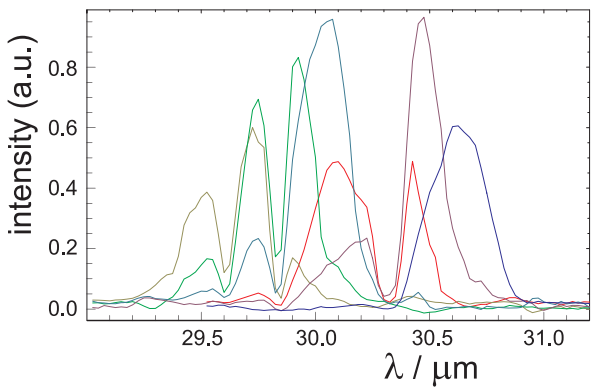

Figure 6: Optical spectra of the laser output shifting the nominal FEL wavelength over a wavelength gap at 30.3 µm.

We presently try to explain this effect with an interference of different optical waveguide modes. The re-circulated optical beam mainly couples into the fundamental transverse waveguide mode essentially spread over the whole waveguide gap. The light created by the laser interaction inside the undulator, however, is emitted in a localized area where the much smaller electron beam overlaps with the optical beam and therefore has a completely different mode structure. We have tried, to compute the phase of the emitted radiation with respect to the fundamental mode assuming a certain combination of modes which yields an angular emission pattern known for undulator radiation. This is propagated through the waveguide to the downstream mirror and back to the exit of the waveguide and yields the phase transfer function pictured in Fig. 7. It is obvious that for phase angles larger than $\pi/2$ the gain vanishes or even becomes negative due to destructive interference with the circulating fundamental mode. Fig. 8 compares the relative gain computed in this strongly simplified model to the wavelengths at which we have observed difficulties

to start lasing or drop-outs in the measured wavelength spectra. Obviously, the match is not perfect and further detailed study of the phenomenon is required.

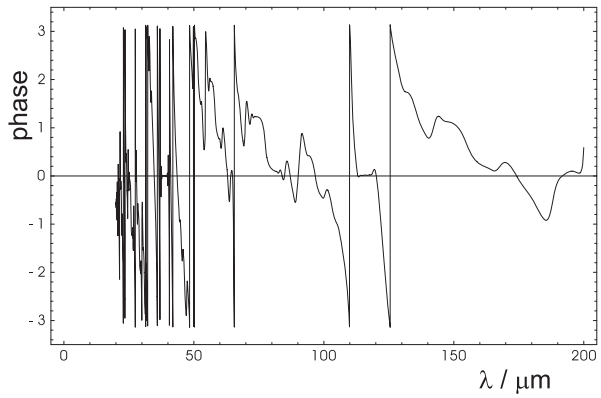

Figure 7: Transfer function of the waveguide for light generated with a gaussian profile at the interaction with the electron beam.

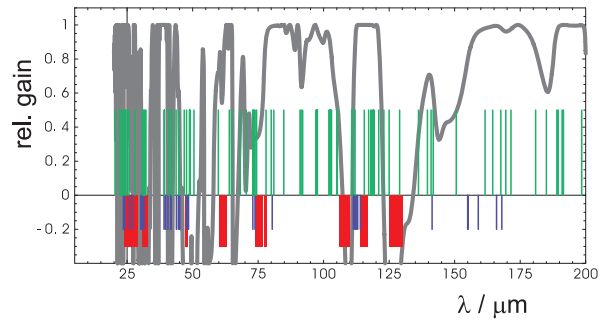

Figure 8: Computed relative FEL gain over the wavelength range. The green lines denote wavelengths at which the FEL was operated so far. The red stripes underline areas in which we had problems to start the lasing and blue lines show wavelengths at which the FEL showed prominent drop-outs in the optical spectrum.

OUTLOOK

Since first lasing in August, 2006, the FIR-FEL at ELBE was commissioned successfully and has since been put into full user operation. The full wavelength range has been demonstrated with the major beam parameters meeting specifications. With this, ELBE is established as a radiation source for the whole IR range from 3 to 200 μm. Both FELs are operated as a user facility, being open to users worldwide, provided their scientific proposals have been favourably evaluated by the panel responsible for distribution of beam time. Under the name ``FELBE'' the facility is member of the EC funded ``Integrating Activity on Synchrotron and Free Electron Laser Science (IA-SFS)'', which comprises most synchrotron and FEL facilities in Europe and provides financial support to users from EC and associated states. Instructions for beam time applications are available on the FELBE website (www.fzd.de/FELBE). A world novelty is the possibility to use the Elbe IR radiation for experiments in high magnetic fields. The beams of both FELs can be delivered into the new High Magnetic Field Lab Dresden (HLD) [5,6] which was built recently in immediate vicinity to the ELBE building. First experiments have been run this year and scientific results are soon to be expected.

REFERENCES

[1] C. A. Arnold, H. Büttig, D. Janssen, T. Kamps, G. Klemz, W.D. Lehmann, U. Lehnert, D. Lipka, F. Marhauser, P. Michel, K. Möller, P. Murcek, Ch. Schneider, R. Schurig, F. Staufenbiel, J. Stephan, J. Teichert, V. Volkov, I. Will and R. Xiang, Development of a superconducting radio frequency photoelectron injector, Nuclear Instruments and Methods in Physics Research A 577 (2007) 440-454

[2] P. Michel, P. Evtushenko, U. Lehnert, T. Dekorsy, F. Gabriel, E. Grosse, M. Helm, M. Krenz, W. Seidel, D. Wohlfarth, A. Wolf, R. Wünsch, First Lasing at the ELBE mid-IR FEL, 26th International Free Electron Laser Conference FEL 2004, Trieste, Italy

[3] E. Grosse, U. Lehnert, P. Michel, R. Schlenk, W. Seidel, A. Wolf, U. Willkommen, U. D. Wohlfarth, R. Wünsch, A Far-Infrared FEL for the Radiation Source ELBE, 27th Free Electron Laser Conference FEL 2005, Palo Alto, USA

[4] GLAD, Applied Optics Research, Woodland, WA 98674, USA

[5] F. Pobell, A.D. Bianchi, T. Herrmannsdörfer, H. Krug, S. Zherlitsyn, S. Zvyagin, J. Wosnitza, The New High Magnetic Field Laboratory at Dresden: a Pulsed-Field Laboratory at an IR Free-Electron-Laser Facility AIP Conference Proceedings 850 (2006) 1649

[6] J. Wosnitza, A.D. Bianchi, J. Freudenberger, J. Haase, T. Herrmannsdörfer, N. Kozlova, L. Schultz, S. Zherlitsyn, S.A. Zvyagin, Dresden Pulsed Magnetic Field Facility, J. Magn. Magn. Mat. 310 (2007) 2728

A STUDY OF DETECTION SCHEMES IN ELECTRO-OPTIC SAMPLING TECHNIQUE*

Y. W. Parc#, I. S. Ko, POSTECH, Pohang 790-784, Korea
J. Y. Huang, C. Kim, PAL, Pohang 790-784, Korea

Abstract

Electro-Optic Sampling (EOS) is the ingenious tool for the measurement of the electron beam. There are two traditional detection schemes: one is the crossed polarizer scheme and another is balanced detection one. A new detection scheme called 'Near Crossed Polarizer' (NCP) scheme in the EOS technique is developed to increase the signal to noise ratio (SNR) in the experiment. The new detection scheme is studied in detail and the 3D scanning result with electron beam in FLASH is compared with the detection scheme.

INTRODUCTION

The detection schemes for EOS measurement are studied in theoretically and experimentally also. Two traditional detection schemes are the crossed polarizer and the balanced detection scheme. Those have each difficulty to be applied in real diagnostic in the EOS measurement of the electron beam. To overcome those difficulties, new detection scheme called 'Near Crossed Polarizer' scheme is developed. In this letter, the detail study of the NCP scheme is shown with 3D scanning result of the EOS measurement.

THEORY

EO crystals such as ZnTe and GaP have a character of birefringence materials when the electric field is applied to the crystal. The refractive index of the crystal can be calculated from the constant energy surface in the electric displacement vector space and the impermeable tensor that is linear to the electric field strength. The refractive index can be found from the refractive index ellipsoid equation by a principal-axis transformation [1, 2]. The two main refractive indices n_1, n_2 of the crystal along the principal axes are given by

$$n_1 = n_0 + \frac{n_0^3 r_{41} E}{2}, \qquad n_2 = n_0 - \frac{n_0^3 r_{41} E}{2} \qquad (1)$$

where n_0 is the initial refractive index, r_{41} is the electro-optic constant, and E is the electric field applied to the crystal. The difference of the propagation speeds of each laser component, which is due to the different refractive indices, changes the polarization of the incident laser pulse. This brings the relative phase shift, Γ, between the horizontal component of the laser pulse and the vertical one, which is given by

$$\Gamma = \frac{\omega_0 d}{c}(n_1 - n_2) = \frac{\pi d}{\lambda_0} n_0^3 r_{41} E \qquad (2)$$

where d is the crystal thickness, ω_0 is the mean angular frequency of the laser pulse, c is the speed of light, λ_0 is the mean wavelength of the laser pulse, and E is the electric field applied to the crystal.

Detection schemes

There are two traditional methods to detect the polarization change; the crossed polarizer scheme and balanced detection one. In the crossed polarizer scheme, the laser intensity is measured by a polarizer and a detector. The analytic expression of the intensity difference ΔI in the case of the crossed polarizer scheme is given by [1, 2]

$$\Delta I = I_0 \sin^2(\Gamma/2) \qquad (3)$$

where Γ is the relative phase shift between the two polarized parts of the laser field and the I_0 is the initial intensity of the laser pulse. There is another method to detect the polarization change called balanced detection scheme. In the balanced detection scheme, the laser intensity is measured by a quarter-wave plate, a polarizer and two detectors. The quarter-wave plate enhances the relative phase shift by a quarter of one wave length. The analytic expression of the intensity difference ΔI in the case of balanced detection scheme is given by [1, 2]

$$\Delta I \equiv I_h - I_v = |\mathrm{E}_h|^2 - |\mathrm{E}_v|^2 = I_0 \sin(\Gamma) \qquad (4)$$

where all parameters are same with above Eqs., h and v represent 'horizontal' and 'vertical' each. When the relative phase change Γ is 7° in the crossed polarizer scheme, the change of the initial laser intensity is merely 0.37% from Eq. (3). This signal change is too low to be detected in real diagnostics setup. However, in the balanced detection scheme, there is 12% change of the initial laser intensity from Eq. (4) for the same Γ. The signal level is high enough to detect, but the balanced method is difficult to apply in real diagnostic setup. To overcome those difficulties, a new method called Near Crossed Polarizer (NCP) scheme is developed. In the new detection scheme, the laser intensity is measured by a quarter wave plate, a half wave plate, a polarizer, and a detector. The intensity with NCP scheme is calculated by the multiplication of the Jones matrices of the each wave plate [3]. The calculated intensity is given by

$$I(\theta,\ \varphi,\ \Gamma)$$
$$= \left[1 + \cos(\Gamma + 2\varphi - 4\theta)\sin^2\varphi - \cos(\Gamma - 2\varphi + 4\theta)\cos^2\varphi\right]/2$$
$$= \left[1 - \cos(\Gamma)\cos(4\theta - 2\varphi)\cos(2\varphi) + \sin(\Gamma)\sin(4\theta - 2\varphi)\right]/2$$
.....(4)

where the θ is angle of the half wave plate, φ is angle of the quarter wave plate and the I_0 is the initial laser intensity incident to the EO crystal. The signal level and background also are changed according to the angles of the half and quarter wave plates. In Fig. 1, the experimental layout with the NCP scheme is shown.

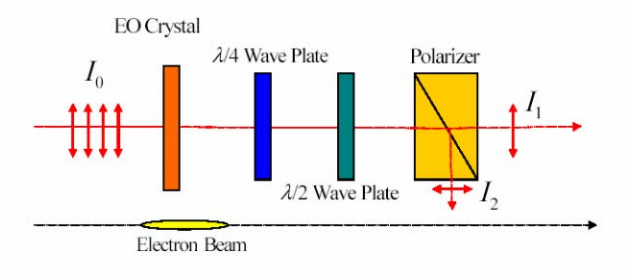

FIG. 1. Layout of the electro-optic sampling.

In Fig. 2, there is a measurement result of the electron beam with the NCP scheme in FLASH [4].

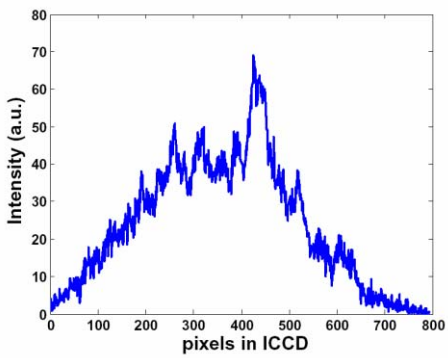

Fig. 2. The typical measurement of the electron beam in FLASH. In this measurement, the quarter wave plate is set as -4 degree and the half wave plate is set as -2 degree. The GaP crystal thickness used in this measurement is 180 μm. The distance between the electron beam and the crystal is 1.5 mm on average. The electron beam energy is 800 MeV and the total electron beam charge is 0.8 nC.

3D view of the signal in NCP scheme

In Fig.3, the theoretical intensity change of EO signal by half and quarter wave plate is shown with 3D plot when Γ is 2 degree. The background intensity change which means Γ is 0 degree is not shown in this paper, however the behaviour of the two graphs is similar.

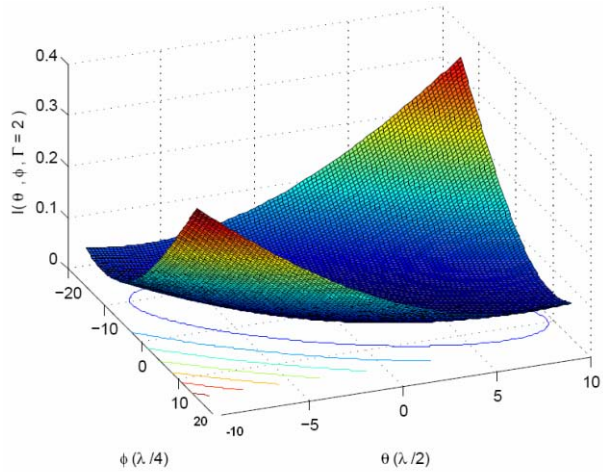

Fig. 3. The intensity with 'crossed polarizer scheme' when Γ is 2 degree. θ is the angle of half wave plate for compensation and φ is the angle of quarter wave plate. Note that y axis is normalized by the initial laser intensity.

In Fig. 4, the measurement result of the theoretical prediction shown in Fig. 3 is plotted.

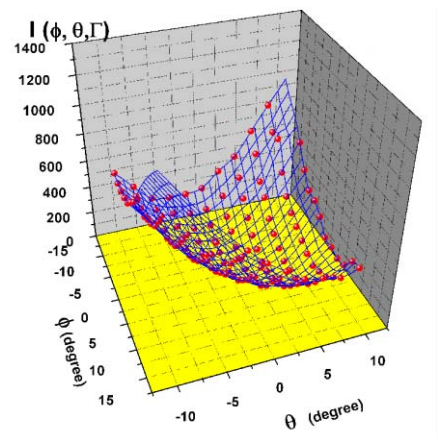

Fig. 4. The intensity with 'crossed polarizer scheme' measured in FLASH. θ is the angle of half wave plate for compensation and φ is the angle of quarter wave plate. Note that y axis is not normalized by the initial laser intensity. The unit is same with the Fig. 2 i.e. the ICCD unit.

SCANNING RESULT IN TEO SETUP IN FLASH

The half and quarter wave plates are scanned to find the best condition to measure the electron beam. In Fig. 5, the theoretical prediction of the SNR function in 3D view is

shown, in which the peak position is where the $\theta = 0$ and $\varphi = 0$ because the theoretical background is 0.

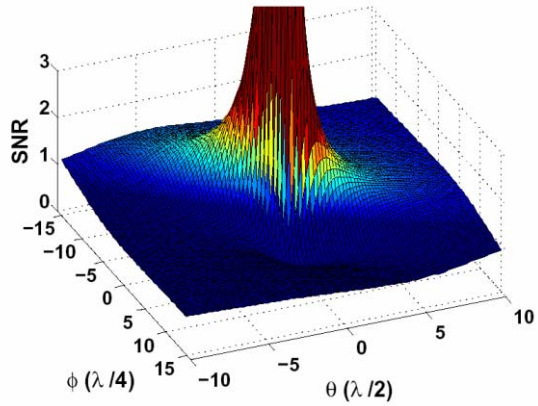

Fig. 5. Theoretical prediction of SNR. θ is the angle of half wave plate for compensation and φ is the angle of quarter wave plate.

There is a region lower than 1 which means the signal is lower than the background. This can be occurred at certain angles of the half and quarter wave plate, because the changed polarization of the laser pulse with the angles is decreased by the modulation of EO crystal.

In Fig. 6, the experimental result of the SNR function in 3D view is shown.

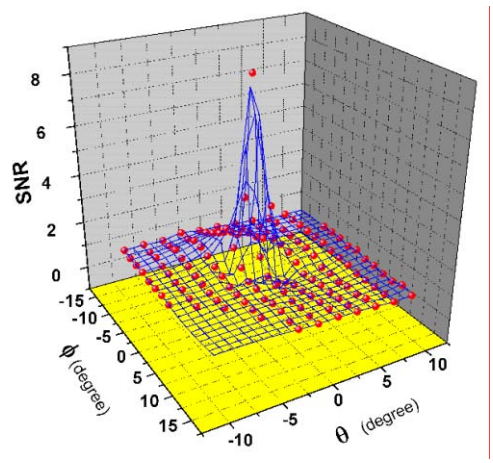

Fig. 6. SNR measured in FLASH. θ is the angle of half wave plate and φ is the angle of quarter wave plate.

In Fig. 6, the peak position is not at $\theta = 0$ and $\varphi = 0$ point due to the leakage of the laser due to the imperfection of the polarizer. The background is not 0 even at $\theta = 0$ and $\varphi = 0$, so the denominator of the SNR function is not 0. That makes the shift of the maximum position of SNR. With $\theta = 0$ and $\varphi = 0$, the NCP scheme is same with the CP scheme, that means the level of signal is quite low to be detected in some situation. In the real diagnostics experiment, the maximum SNR point should be searched in each diagnostics setup to make balance between the SNR and the absolute signal level to be detected with good resolution.

ACKNOWLEDGMENT

This work was supported by Grant No. R01-2006-000-11309-0 from the Basic Research Program of the Korea Science & Engineering Foundation and the Center for High Energy Physics (CHEP) at the Kyungpook National University. One of authors (Y. W. Parc) extends his thanks to DESY for the hospitality during his stay (2006.11 ~ 2007.04).

REFERENCES

[1] M. Bruken et al., TESLA Report 2003-11 (2003).
[2] S. Casalbuoni et al., TESLA Report 2005-01 (2005).
[3] B. Steffen, “Electro-Optic Methods for Longi-tudinal Bunch Diagnostics at FLASH” Thesis, The University of Hamburg (2007).
[4] private communication with A. Azima in DESY.

COMPARATIVE STUDY OF ELECTRO-OPTIC EFFECT BETWEEN SIMULATION AND MEASUREMENT *

Y. W. Parc#, I. S. Ko, POSTECH, Pohang 790-784, Korea
J. Y. Huang, C. Kim, PAL, Pohang 790-784, Korea

Abstract

Electro-Optic Sampling (EOS) is a promising method to measure various properties of the electron beam non-destructively. In this Letter, a rigorous analysis procedure of the electro-optic (EO) measurement is introduced. The measured data of electron beam by electro-optic technique is analyzed in terms of the relative phase shift between the horizontal and the vertical components of the laser. A simulation study is done with the pulse propagation method, which utilizes Fourier transform to investigate the evolution of an electromagnetic pulse inside the EO crystal. The analysis result of the EO measurement expressed in terms of the relative phase shift is compared with the simulation, and they show a good agreement.

INTRODUCTION

Non-destructive measurement of the electron bunch length with femtosecond resolution is one of essential issues to operate XFEL facilities successfully [1]. During last several years, the EOS method has been successfully implemented to measure femtosecond electron bunches and arrival time at FELIX, SPPS, and FLASH facilities [2-8].

THEORY

EO crystals such as ZnTe and GaP have a character of birefringence materials when the electric field is applied to the crystal. The refractive index of the crystal can be calculated from the constant energy surface in the electric displacement vector space and the impermeable tensor that is linear to the electric field strength. The refractive index can be found from the refractive index ellipsoid equation by a principal-axis transformation [9, 10]. The two main refractive indices n_1, n_2 of the crystal along the principal axes are given by

$$n_1 = n_0 + \frac{n_0^3 r_{41} E}{2}, \qquad n_2 = n_0 - \frac{n_0^3 r_{41} E}{2} \tag{1}$$

where n_0 is the initial refractive index, r_{41} is the electro-optic constant, and E is the electric field applied to the crystal. The difference in the propagation speeds, which is due to the different refractive indices, changes the polarization of the incident laser pulse. This brings the relative phase shift, Γ, between the horizontal component of the laser pulse and the vertical one, which is given by

$$\Gamma = \frac{\omega_0 d}{c}(n_1 - n_2) = \frac{\pi d}{\lambda_0} n_0^3 r_{41} E \tag{2}$$

where d is the crystal thickness, ω_0 is the mean angular frequency of the laser pulse, c is the speed of light, λ_0 is the mean wavelength of the laser pulse, and E is the electric field applied to the crystal.

Detection scheme

A new method called Near Crossed Polarizer (NCP) scheme is developed. In the new detection scheme, the laser intensity is measured by a quarter wave plate, a half wave plate, a polarizer, and a detector. The intensity with NCP scheme is calculated by the multiplication of the Jones matrices of the each wave plate [11]. The calculated intensity is given by

$$I(\theta, \varphi, \Gamma)/I_0 = \left[1 - \cos(\Gamma)\cos(4\theta - 2\varphi)\cos(2\varphi) + \sin(\Gamma)\sin(4\theta - 2\varphi)\right]/2 \tag{3}$$

where θ is angle of the half wave plate, φ is angle of the quarter wave plate, and I_0 is the initial laser intensity incident on the EO crystal. The signal level and the background are also changed according to the angles of the half and the quarter wave plates. The signal to noise ratio can be increased by the control of the angle of the plates [12].

EXPERIMENT

At the FLASH facility in DESY, there is an EO diagnostic section called Timing Electro-Optic (TEO) setup to measure the electron beam properties. The TEO setup is used to measure the bunch length and the timing jitter of the electron beam by the spatial decoding method with GaP crystal as shown in Fig. 1 [8].

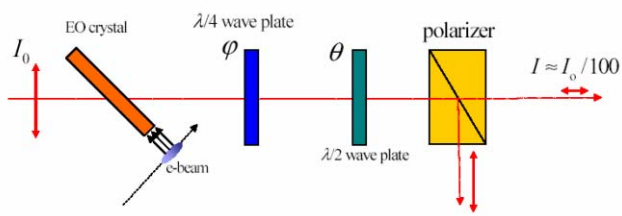

Figure 1. Layout of the electro-optic sampling.

In the spatial decoding method, the laser pulse is propagated through the EO crystal with 45° angle, and the timing information of the electron beam is converted to the spatial information of the image measured by the ICCD camera [5, 8].

In order to study the electro-optic effect induced by the electron beam, it is necessary to know the initial intensity of the laser as shown in Eq. (3). Normally, the initial intensity of the laser for the EO diagnostic is so high to be measured by ICCD camera directly without damaging ICCD itself. Thus, the initial intensity of the laser is extrapolated from the measured data with several angles of the half wave plate using Eq. (3), where ICCD can detect the intensity of the laser passing through the EO crystal and polarizer safely. If the angle of the quarter wave plate is fixed, the laser intensity at the ICCD is controlled by the half wave plate in front of the polarizer as shown in Fig. 1. The extrapolated initial intensity of the laser is 4466 which will be shown elsewhere.

A measurement result is shown in Fig. 2 which shows a signal with 47.6 unit of the ICCD at 12.6 ps position in the measurement window.

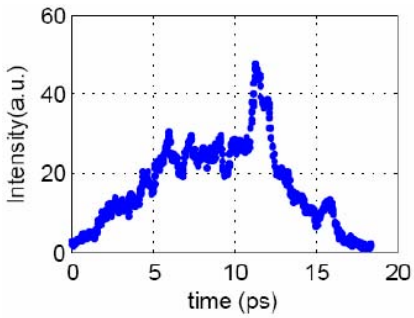

Figure 2. Electron beam measurement by TEO setup at FLASH. The GaP crystal thickness is 180 μm. The distance between the electron beam and the laser at the crystal is 2 mm on average. The half wave plate angle is 0^o. The quarter wave plate angle is -2^o.

There is a small peak at 16 ps position, which is generated by the reflection of THz radiation at the back surface of the EO crystal [10]. The time duration between the main peak and the small one is determined by the thickness of the EO crystal and the speed of THz radiation in the EO crystal. The GaP crystal thickness used in this experiment is 180 μm. It makes the travel distance of THz radiation 360 μm which corresponds to 3.4 ps travel time. The radial distance from the electron beam and the EO crystal can be controlled by a remote control system. The radial distance between the electron beam and the crystal in the measurement is 2 mm on the average which can be known from the radiation detection by glass optic fibers in FLASH [13].

The maximum relative phase shift Γ of the measured pulse can be calculated from Eq. (5) with the peak value of the measured data in Fig. 2. In the measurement, the angle θ of the half wave plate is set to 0^o and the angle φ of the quarter wave plate is set to -2^o. Analysis of the peak in Fig. 2 with the initial laser intensity I_0 = 4466 is shown as

$$I\left(\theta=0^{\circ},\ \varphi=-2^{\circ},\ \Gamma\right)=47.6 = \frac{4466}{2}\left[\begin{array}{l}1-\cos(\Gamma)\cos\left(-2\times(-2^{\circ})\right)\cos\left(2\times(-2^{\circ})\right)\\ +\sin(\Gamma)\sin\left(-2\times(-2^{\circ})\right)\end{array}\right] \quad (4)$$

From the solution of Eq. (4), we can get the relative phase shift Γ = 7.13^o which represents that the laser passing through the EO crystal is elliptically polarized.

SIMULATION

In the simulation, the electric field inside the crystal is calculated from the longitudinal profile of the electron beam. The pulse propagation method, which utilizes Fourier transform of the electric field to investigate the evolution of the electric field inside the EO crystal, is used in this simulation.

An electron beam with Gaussian charge distribution is generated to simulate the measurement. The beam charge Q is set as 0.06 nC and the rms pulse width σt of the electron beam is set as 40 fs which corresponds to the bunch length of the electron beam 12 μm. The thickness of GaP is the same 180 μm as the experimental condition. Simulation results for different distances between the electron beam and the crystal are shown in Fig. 3, and the peak values for different distances are shown in Fig. 4.

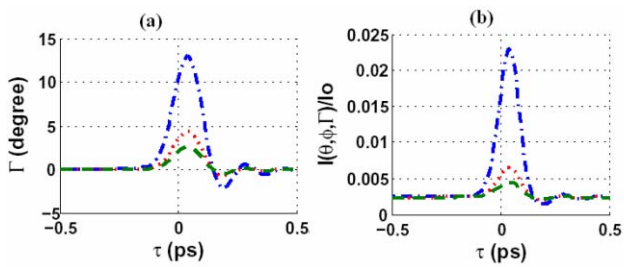

Figure 3. Simulation results: (a) The relative phase shift Γ, and (b) the intensities from NCP scheme are shown. The dash-dot line (top) represents the result of the distance between laser and the EO crystal R = 1 mm, the dotted line (middle) represents the result of the R = 3 mm, and the dashed line (bottom) represents the result of the R = 5 mm. The charge of the electron beam is 0.06 nC and the rms pulse width is 40 fs. The half wave plate angle θ is 0^o and the quarter wave plate angle φ is -2^o.

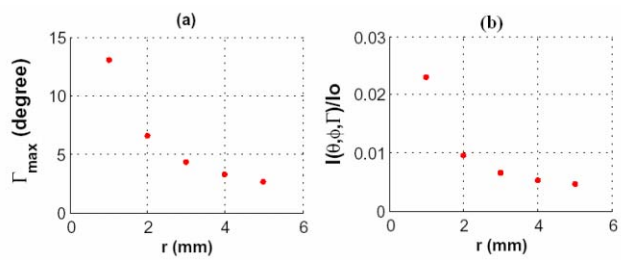

Figure 4. Simulation result for different distance R. (a) Maximum points of Fig. 6 (a) are plotted along R. The data is fitted by Eq. (10) shown as a solid line. (b) Maximum points of Fig. 6 (b) are plotted along R. The curve is the fitting result with Eq. (11).

SUMMARY

This Letter introduces a rigorous procedure to analyse the EO technique to measure the electron beam non-destructively. The initial intensity of incident laser is obtained by the extrapolation of the data measured at lower intensity. Accurate relative phase shift obtained by precisely estimated incident laser intensity and NCP scheme provides EOS as a tangible technique for non-destructive measurement of electron beams. Simulation results with the pulse propagation method are well matched with the analysis result of the measurement.

ACKNOWLEDGMENT

This work was supported by Grant No. R01-2006-000-11309-0 from the Basic Research Program of the Korea Science & Engineering Foundation and the Center for High Energy Physics (CHEP) at the Kyungpook National University. One of authors (Y. W. Parc) extends his thanks to DESY for the hospitality during his stay (2006.11 ~ 2007.04).

REFERENCES

[1] PAL/POSTECH, “4-th Generation Light Source Conceptual Design Report,” November 2004.
[2] X. Yan et al., Phys. Rev. Lett., 85, p. 3404 (2000).
[3] I. Wilke et al., Phys. Rev. Lett., 88, p. 124801 (2002).
[4] G. Berden et al., Phys. Rev. Lett., 93, p. 114802 (2004).
[5] A. L. Cavalieri et al., Phys. Rev. Lett., 94, p. 114801 (2005).
[6] J. Rossbach et al., Eur. Phys. J. D, 37, p. 297 (2006).
[7] B. Berden et al., Proceedings of European Particle Accelerator Conference 2006, Edinburg, Scotland, p. 1055 (2006).
[8] A. Azima et al., Proceedings of European Particle Accelerator Conference 2006, Edinburg, Scotland, p. 1049 (2006).
[9] M. Bruken et al., TESLA Report 2003-11 (2003).
[10] S. Casalbuoni et al., TESLA Report 2005-01 (2005).
[11] E. Hecht, Optics, 4th ed., Addison-Wesley, Inc., 2002, p. 377
[12] private communication with B. Steffen in DESY
[13] private communication with A. Azima in DESY
[14] H. J. Bakker et al., J. Opt. Soc. Am. B, 15, p. 1795 (1998).

LOSSES IN OPTICAL RESONATOR OF NOVOSIBIRSK TERAHERTZ FEL: THEORY AND EXPERIMENT

V.V. Kubarev#, BINP, Novosibirsk, Russia

Abstract

A direct comparison of the simple universal analytical theory used earlier to design an optical resonator for the Novosibirsk terahertz free electron laser (NovoFEL) and numerous subsequent experiments is presented. A good agreement of the theory with the experiments is shown. A possibility of future optimization of the optical resonator is described.

INRODUCTION

Round trip losses are the main parameter of most laser resonators. There are many different numerical methods to calculate losses of resonators with given geometries. However, an optimal geometry is not known when a new resonator is being created. A simple search for different geometries is ineffective. In this case we need some analytical theory. In [1], the author of this paper proposed a simple universal analytical method to calculate small losses in stable open laser resonators. A comparison of the method with well-known papers in which numerical [2, 3] and cumbersome analytical [4] methods were used only for certain types of losses and geometries shows a good agreement.

On the other hand, the free electron laser gives us a unique possibility of direct experimental measurement of such losses, which is practically impossible in conventional lasers due to the inertia of their active media. First measurements of this type on NovoFEL with the start optical resonator were published in [5]; they shown a good agreement of the theory and experiment. In this paper, a nominal optical resonator with larger output coupling was investigated in a wider spectral range.

THEORY

Diffraction losses c_i caused by different small perturbations at the center of a Gaussian mode (openings) and at its periphery (mirror apertures, diaphragms, scrapers) are equal, according to [1], to double "geometrical" losses $c_i = 1 - (1 - c_g)^2 \approx 2c_g$. Geometrical losses c_g are a part of the mode cross-section overlapped (cut) by a perturbation. The total resonator losses can be evaluated as:

$$c_\Sigma = 1 - \prod_i (1 - c_i) \approx \sum_i c_i \qquad (1)$$

This property of additivity for losses at the openings and outer apertures of mirrors is shown in paper [1]. For one-type aperture losses at the periphery of a beam (mirrors, diaphragms, scrapers), the additivity condition is satisfied if the elements with losses are divided by a distance exceeding the length $L_a = d \cdot \delta/\lambda$, where d and δ are typical sizes of the mode and perturbation, and λ is the wavelength. The mode fills the cutoff part of its periphery at this distance. This condition is satisfied for the main components of our resonator losses. The losses in other sections of the resonator can be ignored because of the exponential sensitivity of the Gaussian beam to narrower diaphragms.

The calculation model of our optical resonator after some optimization of diaphragm diameters and their positions is shown in Fig.1. Values of the diameters and axial distances between the resonator center and the diaphragms are presented in Table 1. We assume that the diaphragms are full absorbing because many of them have a special absorbing ceramic coating [5] and the cross-section of vacuum pipes of our resonator is sufficiently large.

Thus, the resonator losses per round trip (for removed scrapers and symmetrical positions of all diaphragms to the resonator center) are:

$$c_\Sigma = 1 - (1 - c_{mo})^2 (1 - c_{md})^4 (1 - c_{mh1})^2 (1 - c_{mh2})^2 \times \times (1 - c_{d1})^8 (1 - c_{d2})^8 (1 - c_{d3})^8, \qquad (2)$$

where c_{mo} and c_{md} are the ohmic and outer aperture losses of mirrors; c_{mh1} and c_{mh2} are the losses on openings in the mirrors; c_{d1}, c_{d2} and c_{d3} are diaphragm losses (pick-up sensor aperture, banding magnet camera aperture, and undulator aperture, respectively). For simplicity, we use one-index numeration of the losses in Fig.1, Table 1, and Fig.6, according to equations (1) and (2).

From the well-known experimental data for optical properties of solid gold, we can obtain the ohmic losses of our mirrors with gold coating: $c_{mo} = 10^{-2}(0.71 - 1.2\lambda$ [mm] $)$.

For losses of the Gaussian TEM_{00} - mode with the radial field distribution $E \sim exp(-r^2/r_0^2)$; $r_0 = \{\lambda L_f/\pi [1 + (z/L_f)^2]\}^{1/2}$, where L_f is the Rayleigh length, one can obtain the following formulas:

$$c_{dk,md} = exp\{-\pi d_k^2 L_f/[2\lambda(L_f^2 + z_{dk,md}^2)]\} \qquad (3)$$

$$c_{mh} = \pi d_{mh}^2/\{2\lambda L_f[1 + (L_0/2L_f)^2]\}, \qquad (4)$$

where $k = 1, 2, 3$; d is the diameter of the losses component, and $L_0 = 26.589$ m is the resonator length.

The dependences of total losses as functions of wavelength for different Rayleigh lengths are shown in Fig.2. The value $L_f = 5$ m and mirror radiuses $R = L_0[1 + (2L_f/L_0)^2]/2 = 15$ m were chosen as optimal in the

wavelength range from 100 to 300 μm. Different losses components for this Rayleigh length are shown in Fig.6.

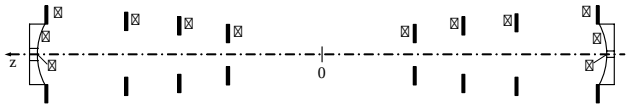

Figure 1: Calculation model of the optical resonator. Numbers at elements are *i* indexes according to equations (1) and (2).

Table 1: Diameters and positions of losses elements

Index *i*	**Diameter *d* [mm]**	**Position *z* [mm]**
2	190	13294.5
3	9	13294.5
4	3.5	13294.5
5	105	7500
6	101	6300
7	78	4500

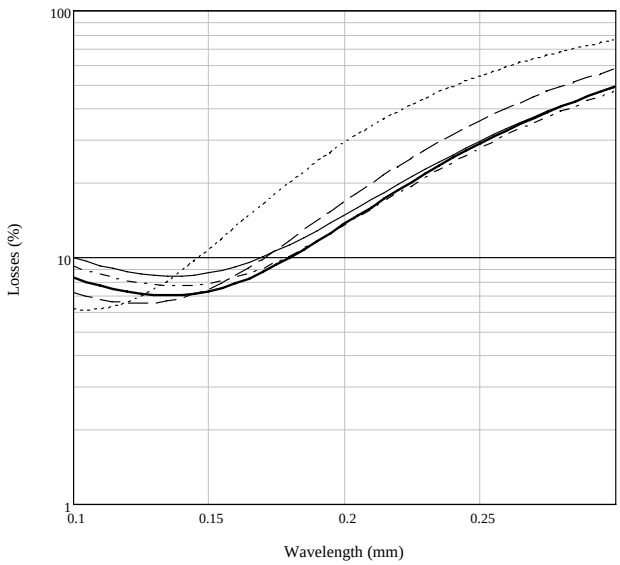

Figure 2: Total losses per round trip of NovoFEL versus wavelength for different Rayleigh lengths: L_f = 3 m (dotted line), L_f = 4 m (dashed line), L_f = 5 m (thick solid line), L_f = 6 m (dash-dotted line), L_f = 7 m (thin solid line).

EXPERIMENT

As before [5], we used in the experiments a detector on the basis of the Schottky diode matrix with a traveling wave antenna in the corner cube reflector [6]. We specially used a not the fastest Schottky detector to have a sufficient number of measured points on one light pulse. Though we checked many times the detector linearity in the measurement of CW submillimeter power, we also investigated the parameter for pulsed measurement. It is easy to see in Fig.3 that our detector is also linear in this case.

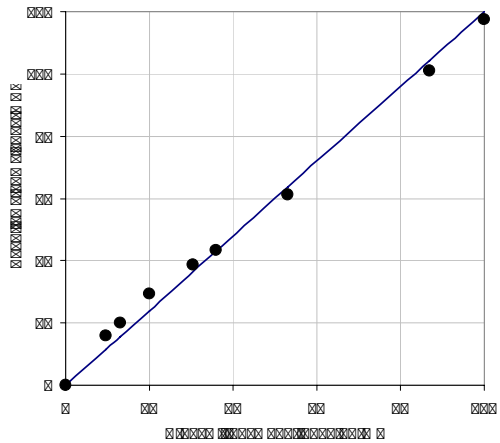

Figure 3: Signal of the Schottky diode detector versus transmission of the attenuator for working conditions of the detector.

We measured the losses of the nominal optical resonator just after its assemblage (in 2004) and recently (in June 2007) for a wider spectral range. The last experiment is shown in Fig. 4. Electron pulses of NovoFEL were switched off at the time marked by arrows. After this time, light pulses decayed exponentially for the wavelength range from 120 to 200 μm. The losses were calculated as $c = 1 - T/\tau$, where T = 177.4 ns is the repetition period of pulses, τ is the decay time of the best exponential asymptotic. When the losses constituted about twenty percent, we did not find an exponential power decay. The losses for different periods averaged over four oscillograms are shown in Fig.5. In this case, we assume that the losses of the first decay period are more close to real losses of the NovoFEL optical resonator in the stationary regime. Thus, it is this value that is used in a comparison with the theory in the next section.

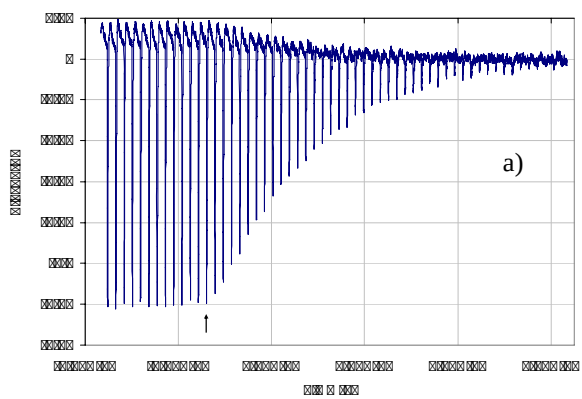

Figure 4: Time evolution of NovoFEL light pulses after switch-off of electron pulses for radiation at a wavelengths 129.8 μm (a). Switch-off time is shown by arrows.

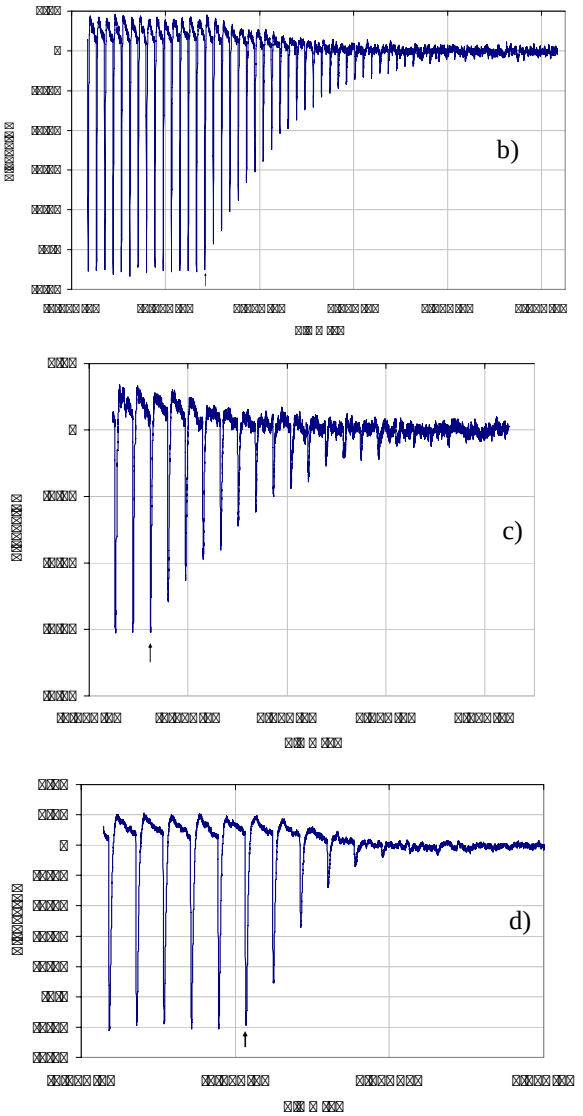

Figure 4: Time evolution of NovoFEL light pulses after switch-off of electron pulses for radiation with different wavelengths: 152.5 μm (b), 197.3 μm (c), and 229.4 μm (d). Switch-off time is shown by arrows.

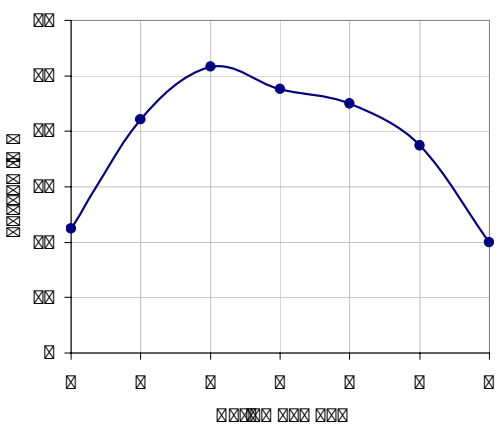

Figure 5: Losses averaged over four oscillograms versus the number of periods after switch-off for λ = 229.4 μm.

COMPARISON OF THE THEORY AND THE EXPERIMENT

A comparison of the theory and the experiment is presented in Fig.6. Different lines in the figure show various components of losses and total round trip losses according to the scheme of Fig.1 and expressions (1)-(4). We can see that the main components of losses for short wavelengths are hole losses whereas in the long wavelengths range these are diaphragm losses. Two sets of experimental points were measured in 2004 and 2007. We can see that there is a good agreement of the theory and the experiment within the accuracy of the calculation and measurement (≈ 10 %).

Nevertheless, we can assume that experimental losses somewhat exceed theoretical values. A first probable explanation of this can be some depreciation of theoretical ohmic losses in the mirrors, especially in the short-wavelengths range. These losses were calculated for an ideal optical solid gold surface. The real surface of our mirrors is a diamond machined copper surface of optical quality with a gold coating.

Most out-of-order experimental point for λ =152.5 μm was measured in regime with modulation sideband instability, which probably has a small influence on the mode intensity distribution. We plan to repeat the experiment with damped sideband instability.

Another possible correction of the long-wavelengths losses is connected with inexact axial position of the absorption diaphragms (Fig.1). Geodetic measurements give such transversal displacements of the diaphragms, which increase the total losses for λ = 200 μm by 1 %.

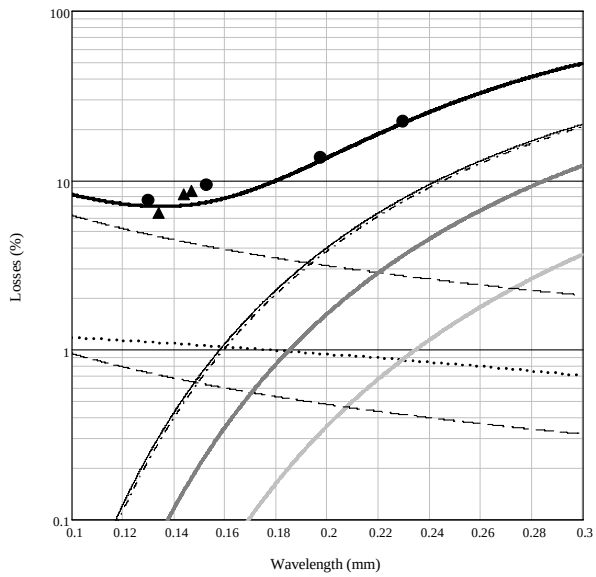

Figure 6: Theoretical (curves) and experimental (points) losses of nominal NovoFEL resonator. Theoretical curves fit the following notation in Fig.1: dotted line (1), dashed lines (3, 4), light gray line (2), gray line (6), dash-dotted line (5), and thin solid line (7); thick solid line is total round trip losses. Experimental points: circles (2007 experiment), triangles (2004experiment).

PROBABLE OPTIMIZATION OF THE OPTICAL RESONATOR

A probable optimization of the optical resonator is in increasing of the useful part of optical resonator losses, which is output power of NovoFEL. Now the power is output through circular openings at the centers of mirrors. According to the presented theory, additional diffraction losses at the openings are equal to useful losses. Thus, if we use some uniform output coupling system not perturbing the mode intensity distribution, the NovoFEL output power can be increased at least two times. A Michelson interferometer with a CVD-diamond film beam-splitter can be such a system. If the beam-splitter thickness is 53 μm and the electric field vector of laser radiation is perpendicular to the incident plane of the beam-splitter, it can overlap optimally the entire operating NovoFEL range. An additional possibility of the system is tuning of optimal output coupling for different regimes and wavelengths. The maximal value of output coupling as a function of wavelength is shown in Fig.7. The output coupling can be tuned from zero to this value. In the figure, the present fixed useful output coupling is given for comparison. Measured optical properties of CVD-diamond in terahertz range are presented in [7]. They allow an installation of the material into optical resonator.

Thus, in the future the NovoFEL output power can be increased more than two times with such sufficiently large CVD-diamond film.

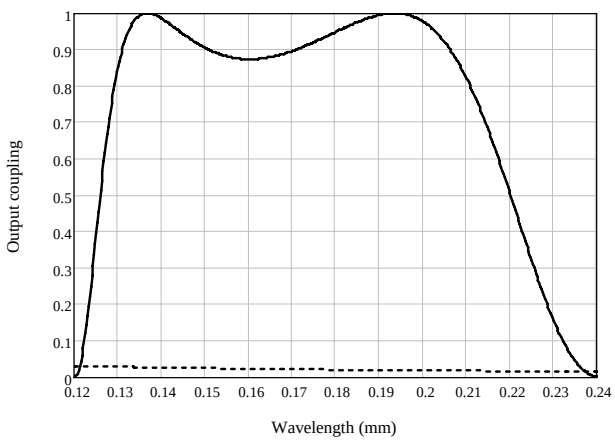

Figure 7: Maximal output coupling of tunable CVD-diamond Michelson output coupling system (solid line) and present fixed output coupling through openings (dashed line).

CONCLUSION

Losses in the NovoFEL optical resonator were measured in its operating range. There is a good agreement between the measurements and a theory which was used for design of the optical resonator. On basis of the theory, upgrade the optical resonator is proposed. The uniform tunable CVD-diamond output coupling system can increase the NovoFEL output power more than two times.

REFERENCES

[1] V.V. Kubarev, "Babinet principle and diffraction losses in laser resonators", Quantum Electronics 30 (2000) 824-826.

[2] T. Li, "Diffraction losses and selection of modes in maser resonators with circular mirrors", Bell Syst. Techn. J. 44 (1965) 917-932.

[3] D.E. McCumber "Eigenmodes of a symmetric cylindrical confocal laser resonator and their perturbation by output-coupling apertures", Bell Syst. Techn. J. 44 (1965) 333-363.

[4] V.V.Lyubimov, I.B. Orlova "Approximate calculation of oscillations in resonators with concave mirrors", Opt. Spectrosk. 29 (1970) 29.

[5] V.V. Kubarev, B.Z. Persov, N.A. Vinokurov, A.V. Davidov, "Optical resonator of powerful free-electron laser", Nucl. Instr. & Meth. A 528 (2004) 199-202.

[6] V.V. Kubarev, G.M. Kazakevich, Y.U. Jeong, B.J. Lee, "Quasi-optical highly sensitive Schottky-barrier detector for a wide-band FIR FEL", Nucl. Inst.& Meth. A 507 (2003) 523-526.

[7] V.V. Kubarev, "Optical Properties of CVD- diamond in Terahertz Range and Its Applications on the NovoFEL", Proc. of conf. IRMMW-THz 2007, Cardiff, Great Britain, September 2-7, 2007.

CONTROL AND DIAGNOSTIC SYSTEM FOR NOVOSIBIRSK FEL RADIATION

V.V.Kubarev, E.V.Makashov, K.S.Palagin, S.S.Serednyakov. Budker Institute of Nuclear Physics, 630090, Novosibirsk, Russia.

Abstract

The architecture and main capabilities of the control and diagnostic system for the Novosibirsk FEL coherent radiation are described. The software managing this system employs a client-server model. The software developed is able to work both in client and server modes. It can also control various equipment – from the FEL optical cavity mirrors to the local equipment of user stations. The mode of control program operation and controlled equipment are determined by external configuration files. Some results of the system operation are also presented.

INTRODUCTION

The first stage of the free electron laser (FEL) based on energy recovery linac is now working at Budker Institute of Nuclear Physics [1]. Generation of coherent radiation in the wavelength range of 120 to 200 microns has been achieved. This radiation is applied in a number of user and diagnostic experiments. To apply the radiation successfully, it is necessary both to know its main parameters and to transmit them to the user stations and FEL control panel. In addition, it is necessary to control some radiation parameters (wavelength) and to set up the system.

To solve these and some other tasks, a control system has been developed. It performs the following:

1. Measurement and diagnostics of the main radiation parameters, i.e. wavelength, power and transversal shape of radiation beam.
2. Control over some FEL components (optical cavity) as well as over the radiation wavelength.
3. Real-time transmission of the main radiation parameters to the computers of user stations.

Operation of this system is considered in more details below.

SYSTEM ARCHITECTURE

This system consists of a certain set of equipment (ADCs and controllers of step motors) and a program to manage this equipment. Besides, the program uses a remote control interface for a set of parameters of the energy recovery linac as well as reading some parameters necessary for users. Figure 1 presents a scheme of the entire system. The program can work in client and server modes. The program mode and configuration of equipment to control (step motor controllers, numbers of ADC channels, etc.) are set in external configuration files. Thus, applying various configuration files, the program can work in various modes and control different equipment.

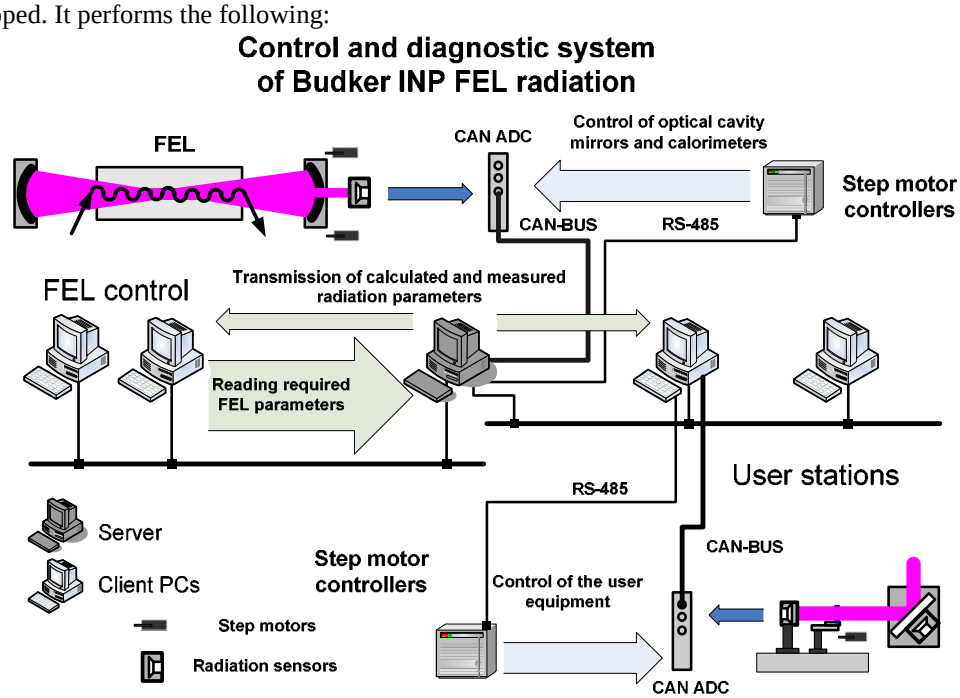

Figure 1: Scheme of the system

The server program runs only on one computer, which is linked with two local networks – a FEL control network and a network of user computers (see Fig.1). The server captures required parameters of FEL operation, transforms them, calculates needed values and yields them to both networks. The server also has means to control the radiation wavelength and the FEL optical cavity. These means are inaccessible for the client part of the program.

The client programs work both the computers controlling the FEL and those at the user stations. The client programs have a number of sub-programs to measure radiation characteristics that are inaccessible in the server part of the program.

CONTROL OVER THE PARAMETERS OF THE OPTICAL SYSTEM AND FEL RADIATION

FEL operation is frequently linked with the necessity of setting up separate components of the optical system. For instance, it is necessary to periodically adjust the position of the mirrors of the optical cavity as to the maximum of extracted radiation with the help of step motors. Sometimes it is also necessary to measure radiation power in a cavity with the help of calorimeters. Since these parameters are linked with the FEL as a whole, the system has been developed in such way that they could be controlled only from one computer, the server program is running on, and they would be inaccessible for other client programs. The configuration files of the server program contain information about the step motors connected to the mirrors of cavity and scrappers as well as information about the ADC channels intended for radiation measurement in several places – immediately at the cavity output (see Fig.1) and at the accelerator hall output. Control over all these parameters makes it possible to set up different operational modes of the FEL optical system and work with them.

As is known, the main merit of FEL is the possibility of rapid re-tuning of radiation wavelength. That is why scanning over the radiation wavelength is another radiation control function of the server. The FEL radiation wavelength dependence is expressed by the following formula:

$$\lambda = \frac{d}{2\gamma^2}\left(1+\frac{k^2}{2}\right),$$

where

λ is the radiation wavelength;

d is the period of undulator;

γ is the electrons' relativistic factor;

k is the undulator parameter, $k = k_0 \cdot I$,

where I is the current in the windings of the undulator and k_0 is the coefficient of proportionality.

The best way to rapidly re-tune radiation wavelength is through varying undulator current. Undulator current is managed from the control program for the magnetic system, so current value variation has to be realized via the option of magnetic system remote control with the Epics Channel Access protocol [2]. A scheme of scanning cycle is presented in Fig.2. The server organizes a cycle of sequential variation of undulator current within set limits and with a given step. The program sends client requests for undulator current adjustment to the server of the control program for the magnetic system, waits for 3 seconds (for the field to reach the steady state) and then reads the indications of radiation sensors. In addition, in order to compensate the possible influence of undulator field variation on the beam path, requests for adjustment of some other elements of the magnetic system are sent (see Fig.2). The total (incident) power of radiation and power of radiation absorbed in a sample or transmitted radiation are measured in the course of retuning cycle. The desired spectrum is obtained after normalization of the obtained dependence of the second value on the undulator current as to the first value (the total power), since the total power can vary a little during the measurement cycle. By now, the maximal range of continuous scanning is 120 to 150 microns, while the total range of radiation wavelength is 120 to 230 microns.

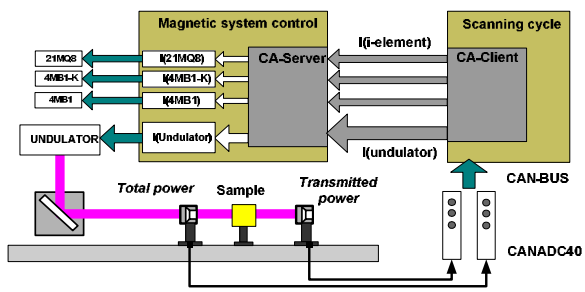

Figure 2: Cycle of scanning over the radiation wavelength.

MEASUREMENT OF MAIN PARAMETERS OF RADIATION

For experiments with FEL radiation it is necessary to know its main parameters, i.e. the radiation wavelength, radiation beam shape and its power. Since these parameters can vary with time, it is necessary to measure them periodically. Most of these measurements are done at a specially-created diagnostic station. In the system being described, these functions are realized as a set of sub-programs, which are only accessible in the client part of program. The following have been done by now:

1. Radiation wavelength measurement with the help of Fabri-Perot interferometer.
2. Radiation power measurement with the help of sapphire calorimeter.
3. Measurement of the transversal distribution of radiation beam power via two-coordinate scanning.

Radiation wavelength has been measured via a cycle of scanning over the angles of rotation of Fabri-Perot etalon [3] relative to the incident radiation beam. In the course of

this cycle, the program displays a graph of radiation intensity vs. this angle. A typical plot is shown in fig.3

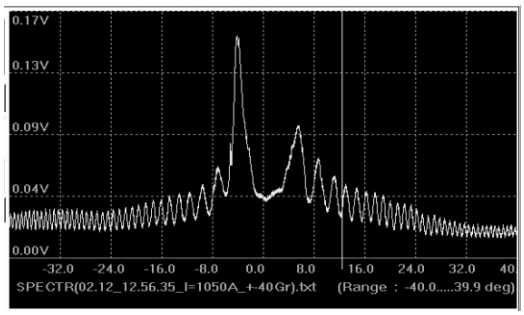

Figure 3: Radiation wavelength measurement with the help of Fabri-Perot interferometer

The radiation wavelength is calculated from the positions of maximums in the graph, by the following formula:

$$\lambda = \frac{2d}{n}\left(\cos\theta_1 - \cos\theta_n\right)$$

where:

λ is the radiation wavelength to measure;

d is the distance between the lattices;

θ_1 and θ_n are the rotation angles corresponding to the 1st and nth maximums.

It can be seen from the formula that the accuracy of radiation wavelength determination is in proportion to the ***n***, the number of the last maximum, or to the maximal rotation angle. That is why the cycle is organized over a maximal possible range of angles.

Transversal beam distribution was measured with the help of a two-row array of piroelectric radiation detectors, installed in the path of the incident FEL radiation. The array is connected with a shifter, which moves in a direction normal to the line of detectors. In the course of measurement the program organizes a cycle over the coordinate of line shift. All detectors in the line are inquired between the steps of this cycle. As a result, radiation power on a rectangular area of scanning gets measured. This area covers the entire radiation beam and amounts to about 15x20 cm. The spatial measurement resolution equals the distance between adjacent detectors and is less than 1 cm in one coordinate and about 4 mm in the other. Fig. 4 presents a graph of the picked-up distribution of radiation power.

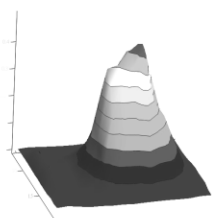

Figure 4: Transversal distirbution of power in the radaition beam.

TRANSMISSION OF MAIN PARAMETERS OF RADIATION TO THE USERS

For experimental work with radiation, a user station needs real-time information on radiation parameters – wavelength and power – as well as on the main parameters of the accelerator – frequency and energy of the beam and current of the undulator. In this system, this information is transmitted from the program working in the server configuration to programs running in the client mode. The Epics Channel Access protocol is used as the communications protocol. A scheme of this interaction is shown in Fig.1. The server program gets main parameters of FEL operation from other control systems of the FEL. Then the program computes a theoretical wavelength of radiation from these parameters. Then the Channel Access Server specifies this wavelength and some other of main FEL parameters under other names, making them accessible for reading by clients. Besides, the computer the server is running on is connected to an ADC on which measurements of radiation are terminated. These values are also specified by the server and are accessible for all client programs.

As it is shown in the fig. 1, the computer the server is running on is connected to two local networks – a control network for the FEL and a network of user computers. As a result, all information yielded by the server program is accessible both on control computers and on the user stations. In any of its configurations (server or client), the program has means for displaying these values in real time. Besides, it is able to write the history of all parameter values for the last working session on a hard disc, which can be useful at long-term experiments since radiation power can vary during FEL operation.

CONCLUSION

This system is now used in FEL operation. Capabilities of the system allow one both to control FEL radiation and carry out experiments on measurement of its characteristics. Different configurations of program work make it possible both to transmit and receive main parameters of system operation as well as to control different devices, e.g. the mirrors of the optical cavity and equipment at the user stations.

REFERENCES

[1] N.G. Gavrilov, B.A. Knyazev, E.I. Kolobanov, et al. Status of Novosibirsk high-power terahertz FEL. NIM 2007, Vol. A575, p 54-57.

[2] Philip Stanley EPICS R3.13, Channel Access Portable Server, http://lansce.lanl.gov/organization/EPICSdata/ca/castout/server-1.html

[3] M. Born, E. Wolf Principles of optics, Nauka, 1973 (in Russian)

OPERATION OF NEAR-INFRARED FEL AT NIHON UNIVERSITY*

K. Hayakawa#, Y. Hayakawa, K. Nakao, K. Nogami, T. Tanaka, LEBRA, Funabashi, Japan
A. Enomoto, S. Fukuda, K. Furukawa, S. Michizono, S. Ohsawa, KEK, Ibaraki, Japan
M. Inagaki, T. Kuwada, T. Sakai, I. Sato, Nihon University, Tokyo, Japan

Abstract

The near-infrared FEL at Laboratory for Electron Beam Research and Application (LEBRA) in Nihon University has been operated for a variety of scientific applications since 2003. The stability of the FEL power was improved appreciably by the advanced stability of the 125MeV electron linac. Currently fundamental FEL wavelength ranges from 1 to 6 microns, which is restricted by the electron energy and the optical devices. The higher harmonics in the visible region is also available [1]. The maximum macropulse output energy of 60mJ/pulse has been obtained at a wavelength of 1725 nm. The short FEL resonator length at LEBRA results in relatively high optical energy density on the surface of the resonator mirrors; present copper-based Ag mirrors in use at LEBRA are not durable enough for long-term operation. Generation of intense harmonics by means of nonlinear crystals has been tested. The preliminary results have demonstrated the conversion efficiencies of 3 to 9% for the second harmonic generation by the fundamental FEL in the wavelength region from 1400 to 1800nm.

INTRODUCTION

The electron linac at LEBRA has a conventional configuration. It consists of the DC electron gun with a dispenser cathode, the prebuncher which is a 7-cell travelling wave structure, the buncher which is a 21-cell travelling wave structure and three 4-m long regular accelerating sections. The specifications of the electron linac are listed in Table 1. Schematic layout of the accelerating structures, the RF system and the beam lines for FEL and parametric X-ray (PXR) generations are shown in Fig. 1.

The FEL beam line and the optical resonator system have been installed to provide the near-infrared FEL for various studies [2]. To increase the FEL gain, magnetic bunch compression has been performed in the 90-degree bending system [3].

Table 1: Main parameters of the LEBRA linac.

Accelerating rf frequency	2856	MHz
Klystron peak output rf Power	30	MW
Number of klystrons	2	
Electron energy	30~125	MeV
Energy spread (FWHM)	0.5~1	%
Macropulse beam current	200	mA
Macropulse duration	20	μsec
Repetition rate	12.5	Hz

Table 2: LEBRA undulator parameters.

Resonator length, *L*	6.718	m
Undulator period	48	mm
Undulator length	2.4	m
Number of periods	50	
Maximum *K* (rms)	1.35	

To generate a monochromatic and spatially coherent X-ray beam, the PXR beam line has been installed next to the FEL beam line.

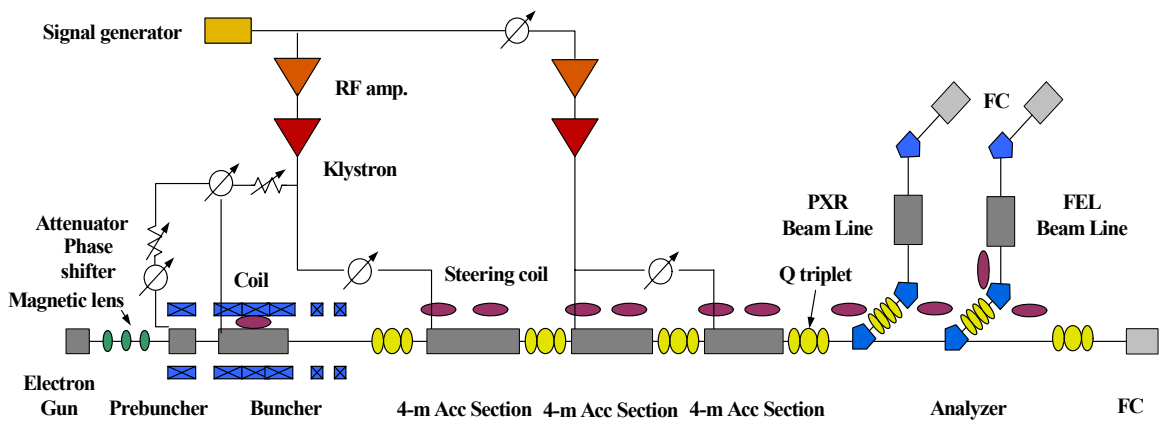

Figure 1: Schematic layout of the accelerating structures, RF system and the FEL and the PXR beam lines

*"Academic Frontier" Project for Private Universities: matching fund subsidy from MEXT, Japan, 2005-2007
#hayakawa@lebra.nihon-u.ac.jp

The undulator consists of a planar Halbach-type permanent magnet, where the electron beam is wiggled in the vertical plane. The specifications of the FEL system are listed in Table 2. The optical beam is extracted through the small coupling hole made in the mirror center. The light beam extracted from the optical resonator is collimated using the beam expander that consists of an ellipsoidal mirror and a parabolic mirror, and then transported to the experimental rooms through the vacuum ducts.

In this paper, the wavelength dependence of the FEL intensity, the time structure of the FEL pulse and the problem of the resonator mirror damage are reported. Also, the results of the experiments for generating the harmonics by means of nonlinear optical crystals (NLO) are discussed.

CHARACTERISTICS OF FEL LIGHT

Correlation between the oscillating wavelength and the optical energy per macropulse

The FEL output power is very sensitive to the change of the orbit and the focusing of the electron beam, and it also depends on the adjustment of the optical resonator and the extent of damage of the resonator mirrors. Hence, the reproducibility of the FEL power level is not very good even at the same electron energy and the same undulator gap width. However, there is a rough correlation between the oscillating wavelength and the optical energy per macropulse. The dependences of the output FEL energy on the wavelength have been obtained for various electron energies in the wavelength region from 1160 to 6130nm as shown in Fig. 2.

In the short wavelength region the saturation level is relatively high, though the gain is small and the loss is large. The FEL macropulse duration becomes short near the oscillation limit at the short wavelength end where the saturation is not achieved stably. In the long wavelength region the macropulse duration is relatively long and the saturation is stable. However, due to the relatively low saturation level and small output coupling, the energy of the FEL extracted from the optical resonator decreases gradually with increased wavelength.

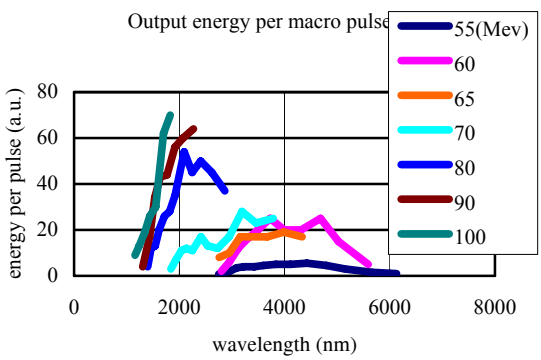

Figure 2: Wavelength dependence of the output energy per macropulse.

In the LEBRA FEL, the output energy per macropulse has the maximum at the wavelengths around 2000 nm. The maximum record of 60mJ/pulse has been achieved at the wavelength of 1725nm.

Pulse structure

To increase the peak electron beam current, the electron bunch has been compressed by using the 90–degree bending magnet system placed just upstream of the FEL system. The analysis of the energy spectra of 100-MeV electron beam obtained by the acceleration in different RF phases suggests that the bunch length of approximately 3ps (FWHM) at the exit of the linac has been compressed to 1ps (FWHM) or less at the entrance of the FEL system. This implies that we can expect a very short FEL pulse.

Since the FEL pulse is a coherent wave packet, the approximate pulse length can be deduced from the measurement of autocorrelation width. A typical shape of the autocorrelation traces measured at a wavelength of 1500 nm by using a Michelson interferometer is shown in Fig. 3. In this figure the horizontal axis expresses the position of the movable mirror measured along the optical axis in the interferometer, in units of micron, and the vertical axis expresses the relative intensity of the light detected by means of an InGaAs photo diode. The FEL pulse width of approximately 60 μm in spatial domain or 200 fs in time domain has been deduced from this trace.

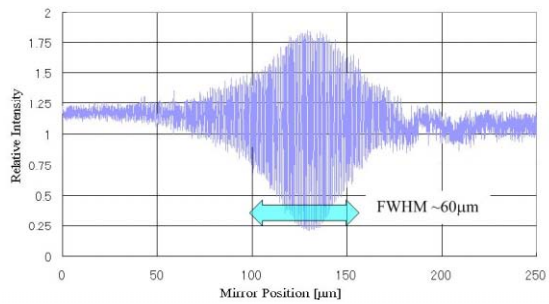

Figure 3: Autocorrelation trace at the wavelength of 1500nm.

By using the same method, the pulse width of the second and the third harmonics have been deduced approximately to be a half and two third the width of the fundamental FEL, respectively. The intensities of these harmonics have been measured by means of a Si photo diode.

Mirror damage

To oscillate FEL over the wide region of wavelengths, protected silver-coated copper mirrors have been used for the optical resonator. In fact, this type of mirror has an extremely high reflectance at the wavelength region longer than 0.4 μm, and has demonstrated the highest durability ever experienced at LEBRA as a FEL resonator mirror. Use of protected silver-coated silicon mirrors was attempted. The mirrors suffered serious damage soon

after the FEL oscillation started. A photograph of the damaged silicon mirror and its expanded image around the coupling hole are shown in Fig. 4. In this figure, it looks that the coated silver was melted and the silicon substrate was excavated. On the contrary, the copper mirrors were usable at least several months, although the FEL power level decreased gradually and the mirrors eventually had to be replaced.

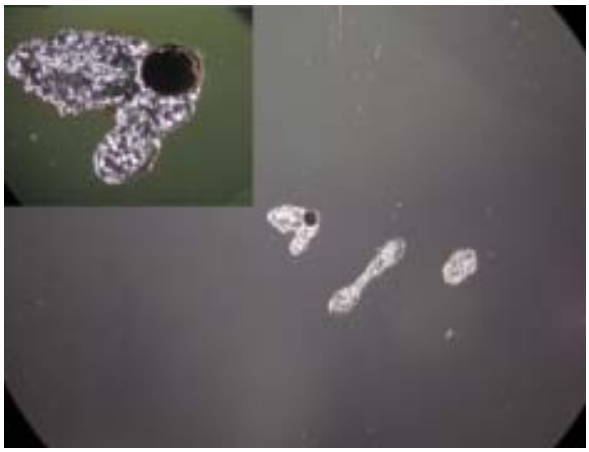

Figure 4: Damages on the surface of the Ag coated silicon. Entire mirror (25mm in diameter) and close up around the coupling hole.

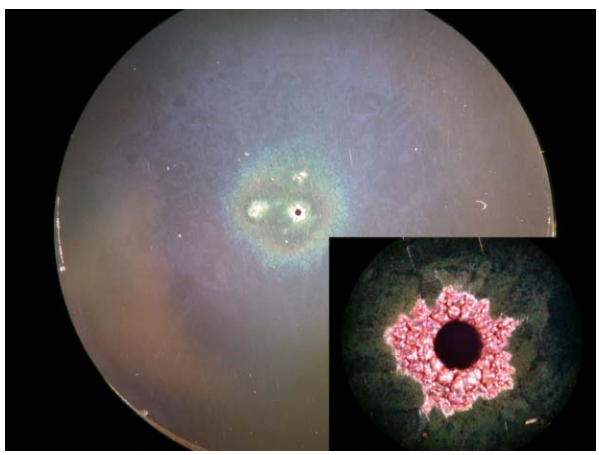

Figure 5: Damages and discoloration on the surface of the Ag-coated copper mirror. Entire mirror (25mm in diameter) and close up around the coupling hole.

A demounted mirror and its expanded image around the coupling hole are shown in Fig. 5. Different from the case of the silicon mirror, the surface over the wide area near the center of the mirror has discolored. The coated silver around the coupling hole has been lost; the copper substrate is visible and it looks melted. Degradation of the resonator mirrors by the damage on the surface is a serious problem in generating a high power FEL. As mentioned previously, the micropulse width of the LEBRA infrared FEL has been estimated to be as short as 200 fs. Therefore, damage to the mirrors could be due to extremely high energy density caused by very short FEL pulses in the optical resonator. Under the present situation, the resonator mirrors have to be replaced every three or four months.

The FEL beam radius on the resonator mirror can be enlarged by shortening the Rayleigh range. Then the energy density may be reduced sufficiently so that mirror damages can be avoided. When the Rayleigh range is shortened, the resonator mirrors have to be adjusted very precisely so as to keep the confocal condition. Since there has been found no other efficient solutions, mirrors with smaller curvature radii will be tested if the lifetime of the mirror can be increased.

HARMONIC GENERATION USING NLO

Preliminary experiments for generating harmonics [4] of the FEL by using NLO devices have been performed. The $KTiOPO_4$ (KTP) crystals have been used for second harmonic generation (SHG) and third harmonic generation (THG). The cutting angle and the antireflective coating of the crystal for SHG were optimized for the fundamental wavelength of 1500 nm and the second harmonic of 750 nm. Similarly the crystal for THG was optimized for corresponding wavelengths. The conversion efficiencies of SHG obtained with the NLO have been 3 to 9% for the fundamental wavelengths from 1400 to 1800nm as listed in table 3. Typical macropulse waveforms of fundamental FEL, nonlinear second harmonic and SHG are shown in Fig. 6. The SHG waveform is similar to the fundamental one. The THG waveform was also observed, however the conversion efficiency was far smaller than 1%.

Table 3: Fundamental and second harmonic wavelengths, energies per macropulse and conversion efficiencies.

1st nm	2nd nm	1st mJ	2nd mJ	efficiency %
1400	700	~3	~0.15	~5
1500	750	~4.5	~0.4	~9
1600	800	~6	~0.45	~7.5
1700	850	~7.5	~0.6	~8
1800	900	~9	~0.3	~3

A KTP crystal works under Type-II phase matching

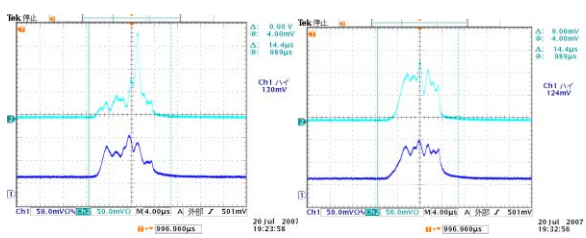

(a) (b)

Figure 6: Macropulse waveforms of fundamental and second harmonic: (a) fundamental (lower trace) and nonlinear harmonic (upper trace), (b) fundamental and SHG.

condition. Hence the second harmonic is generated from two fundamentals with their polarization planes at right angles to each other. Due to the group velocity mismatch between the two components of fundamental light, the conversion phenomenon occurs only within about 1 mm in depth from the surface of the crystal, which restricts the conversion efficiency. If it is necessary to increase the conversion efficiency, other kinds of crystal should be used.

REFERENCES

[1] Y.Hayakawa, et al, "Characteristics of the fundamental and the higher harmonic generation at LEBRA", Nucl. Inst. and Meth. A 507 (2003) 404-408.

[2] K.Hayakawa, et al, "The LEBRA 125 MeV electron linac for FEL and PXR generation", Proc. LINAC2004, Luebec, Aug. 2004, p 90.

[3] K.Yokoyama, et al. "Bunch length measurements at LEBRA", Proc. LINAC2004, Luebec, Aug. 2004, p 411.

[4] P.A.Franken, A.E.Hill, C.W.Peters, and G.Weinreich. "Generation of Optical Harmonics", Phys. Rev. Lett. 7, 118-119 (1961).

ARC-EN-CIEL project electron beam dynamics

C. Bruni *, A. Loulergue, M. E. Couprie, Synchrotron SOLEIL, Saint-Aubin, France

Abstract

ARC-EN-CIEL project is based on the development of fourth generation tunable light source of high brilliance in the VUV to soft X-ray wavelength domain. The project will evolved into three phases : first and second phases are in single pass configuration, while third phase comports recirculation loops. For delivering a high brilliance light source with high peak power short pulses, the high charge electron beam should have subpicoseconde duration with low emittance and energy spread. In order to keep optimal slice characteristics for light production, phase space non linearities due to optics aberrations and collective effects should be minimized. In ERL configuration, the accelerator scheme and focusing should be optimized to take into account collective effects as Beam Break Up instability.

INTRODUCTION

This project is based on the development of a fourth generation subpicosecond light source, with a high brilliance and tunable in the VUV to soft X-ray wavelength domain[1]. ARC-EN-CIEL views two simultaneous modes of operation :

- A high charge, low emittance electron beam for HGHG (High Gain Harmonic Generation) operation : a 1 nC electron bunch charge compressed by two chicanes, with 1 to 10 kHz repetition rate and 1 to 10 μA average current,
- A high average current electron beam for synchrotron radiation operation : a 0.2 to 1 nC electron bunch charge, with 1 to 100 MHz repetition rate and 1 to 100 mA average current.

The HGHG based FEL sets requirements on the beam : high charge, sub-picosecond duration, and low emittance. Optics aberration or collective effects, which are accentuated by high charge, are able to generate non linearities, which damage beam characteristics [2, 3].

Adding recirculation loops allows high average current operation and the energy to be increased by keeping high densities subpicosecond bunch. However, collective effects as Beam Break up instability, form a feedback loop between electron beams and RF cavities. Then, hereafter a threshold current, the oscillation amplitude of the beam transverse position exponentially grows leading to the beam loss [4].

* christelle.bruni@synchrotron-soleil.fr

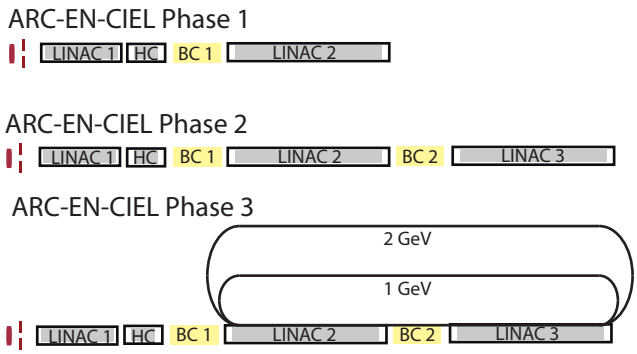

Figure 1: Representation of the ARC-EN-CIEL accelerator for the different phases. LINAC : Linear accelerator composed of cryomodules, HC : third harmonic cavity, BC : bunch compressor. To view all components, the representation is not scaled. Phase 1 is 70 m long, phase 2 : 200 m, phase 3 : 200 m with a radius of the arcs of 15 and 30 meters.

This paper presents the electron beam dynamics for the ARC-EN-CIEL project in single pass and ERL configuration, especially on the conditions for minimizing non linearities and Beam Break Up instability.

SINGLE PASS CONFIGURATION

ARC-EN-CIEL phase 1 and 2 (see fig. 1) aim at providing a 220 MeV and 1 GeV electron beam. The technology employed is a RF gun [5] followed by superconducting TESLA type [6] cryomodules. Chicanes are used to compress the beam duration. In this section, simulations realized for both single pass cases of ARC-EN-CIEL are presented by pointing out the optimisation for the light production.

The RF gun and the cavity modules have been simulated using ASTRA [7]. The laser, which lights the photocathode is 20 ps long (2.1 mm rms) with a cylindrical uniform distribution. To take into account the Coherent Synchrotron Radiation (CSR) in the chicane, the CSRTrack code [8] has been employed to model the compression scheme.

ARC-EN-CIEL phase 1

The RF gun produces a 1.1 π mm $mrad$ total emittance with a total charge of 1 nC. Then a first cryomodule (LINAC1) leads to an energy of 120 MeV. A third harmonic cavity (HC) tuned in order to suppress non linearities (RF and magnetic) is placed before the chicane [9]. Figure

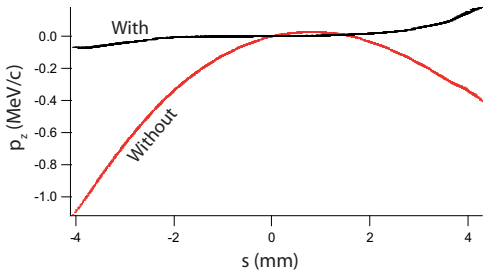

Figure 2: Comparison of the longitudinal phase space of the electron bunch before the chicane without or with a harmonic cavity in the case of ARC-EN-CIEL phase 1. Charge 1 nC, energy 110 MeV.

2 illustrates the effect of the harmonic cavity after the first cryomodule, which highly distorts the beam. However the distortion in the edges of the distribution remains due to the space charge force, which could be linearized by an ellipsoidal shaping of the laser at the cathode [10, 2]. The compression, from 7 to 500 fs rms long is realized thanks to a magnetic chicane (BC1). A compromise between a smaller energy beam chirp and a reduced effect of CSR leads to a ten meters long chicane with a R_{56} coefficient set at $0.2\ m$. The compression increases the total emittance from 1.1 to 2 $\pi\ mm\ mrad$ (see figure 3). Whereas with an adequate optics [11], the slice emittances along the bunch remain almost unchanged (ranging from 1 to 1.5) with a small mismatch from slice to slice. The compressor creates a correlated emittance that reaches $0.2\ \pi\ mm\ mrad$, which denotes a spread of the slices in the transverse phase space. Although weak, it is the main contributor to the total emittance increase by strong mismatching.

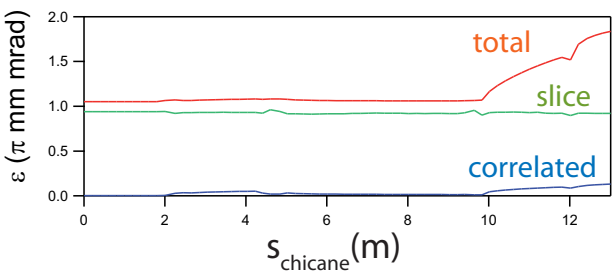

Figure 3: Evolution of the total, central slice and correlated emittance along the chicane at 110 MeV in the case of ARC-EN-CIEL phase 1. Charge 1 nC, energy 110 MeV, compression from 7 ps to 500 fs, R_{56}= 0.2 m, $L_{chicane}$=10m.

Then, the second linac, formed by two cryomodules with a phase adjusted to obtain a minimized energy spread at the end of the accelerator, increases the energy from 110 MeV to 220 MeV. The slice energy spread remains low and of the order of 0.05 %.

Figure 4a illustrates the longitudinal phase space representation of the electron beam at the end of the accelerator. It presents distorsions due to the space charge force and the CSR effect in the chicane. In spite of this non linearities, the slice emittance along the bunch remains almost constant with a low value around 1 $\pi\ mm\ mrad$ (see figure 4b). The peak current at the center of the bunch attains 0.9 kA.

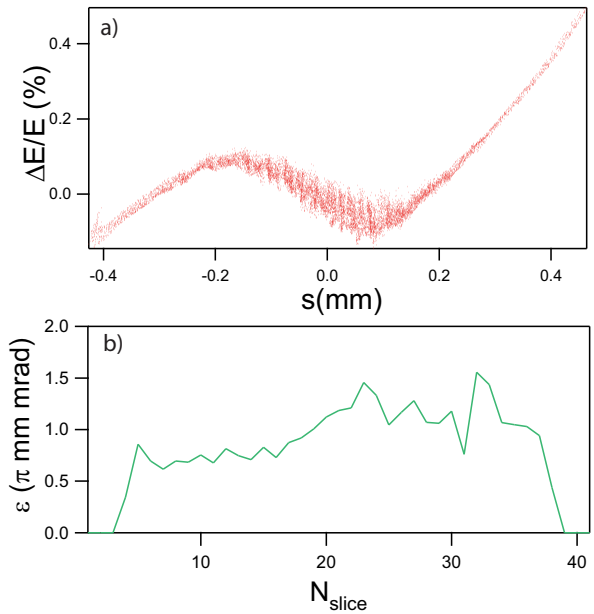

Figure 4: Electron bunch simulations for ARC-EN-CIEL phase 1. a) Longitudinal phase space representation, b) slice emittance along the bunch at the end of the linear accelerator. Charge 1 nC, Energy 220 MeV, bunch duration 500 fs

ARC-EN-CIEL phase 2

For this case, the compression uses a second chicane placed at an energy around 500 MeV. The compression is relaxed in the first chicane from 7 ps to 800 fs compared to ARC-EN-CIEL phase 1. This leads to a conserved slice and total emittance whereas a correlated emittance is created in the chicane. Then, a second linac composed by four cryomodules increases the energy from 110 MeV to 550 MeV and enables adjusting the energy spread chirp for a second chicane ($R_{56} = 0.05\ m$), which compresses the beam from 800 fs to 250 fs with very small degradation of the total and slice emittances. A third linac (five cryomodules) tuned to redress the energy spread brings the energy to 1 GeV. The electron beam slice energy spread and emittance are represented in figure 5. They remain small along the bunch around 0.04% of central slice energy spread, 1.2 $\pi\ mm\ mrad$ of slice emittance, and a peak current of 3 kA.

ERL CONFIGURATION

ARC-EN-CIEL phase 3 consists in adding two recirculation loops. The electrons beam is first accelerated during a first pass in the accelerating cavities, and decelerated with

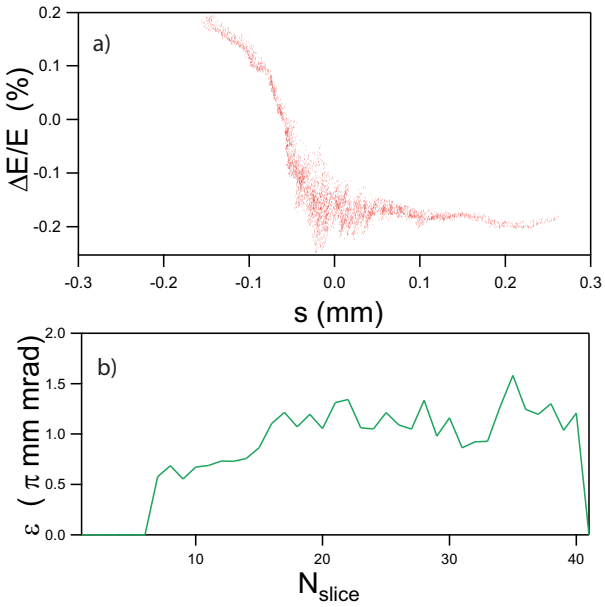

Figure 5: Electron bunch simulations for ARC-EN-CIEL@1 GeV. a) Longitudinal phase space representation, b) slice emittance along the bunch at the end of the linear accelerator. Simulations parameters are : charge=1 nC, Energy=1 GeV, bunch duration =250 fs

an opposite phase during a second pass, while restoring the energy to the high frequency structures. By way of limited numbers of turns, the electron bunch duration can stay in the picosecond order contrarily to storage rings. For Energy Recovery Linac (ERL) mode, higher average current can be obtained. A high current operation requires a separate cw gun based on a DC photoinjector (Jlab type), which provide a 1 to 100 MHz pulsed electrons beam at 0.2 to 1 nC charge. A SRF gun will be employed depending on their development [13].

Arcs optics

Two recirculating loops at 1 and 2 GeV are added to ARC-EN-CIEL phase 2. There lattices are based on the Double Bend Achromat of SOLEIL storage ring without straight sections. Each arc are respectively 50 and 100 m long for 1 end 2 GeV. The optics is design in order to control globally and locally the first and second order isochronism (R_{56} and R_{566}) to prevent over compression or lengthening of the bunches. The chromaticities are also tunable. The optical functions of the 1 GeV arc are sketched on figure 6.

Beam Break up and linac focusing

ARC-EN-CIEL design should takes into account the required conditions, particularly on the transverse focusing, to minimize the Beam Break Up current threshold. Studies of this instability for ARC-EN-CIEL is realized thanks to BI code [12]. From a collective point of view, instabilities become more critical as the case of linear accelerator. Instabilities lead to beam loss at a threshold current, which depends on optics, number of recirculations and cavity quality factor. Transverse beam break up appears to be the limiting factor for ERL [4]. To simulate the transverse transport of the ERL configuration, a code has been developed under Matlab. It allows the parameters of the accelerator and the optical function to be adjusted. Simultaneously the transfer matrix calculated for each element is written in the lattice file BI code input. The matlab code scans the optical functions and optimizes the threshold current for a given accelerator configuration. The quadrupoles are approximated by thin lenses surrounded by two straight sections. The straight length is half the quadrupoles ones L_{qp}. The arc is not yet relevant and is just considered as an ellipse transport with imposed conditions at the entrance and at the exit. The phase advance of the arc is adjusted to maximize the threshold current. The β functions are the same at the entrance and at the exist of the arc, and the α functions are of opposed sign to keep the symmetry.

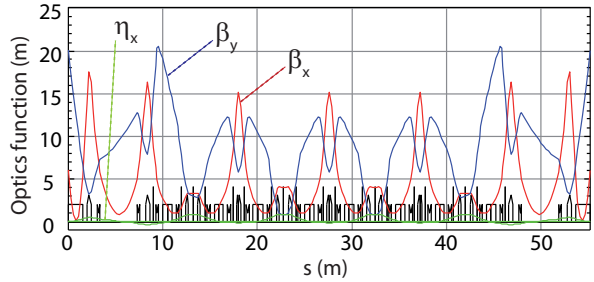

Figure 6: Optics functions versus the position along the arc at 1 GeV. β_x: vertical beta function, β_x: horizontal beta function, η_x: dispersion function.

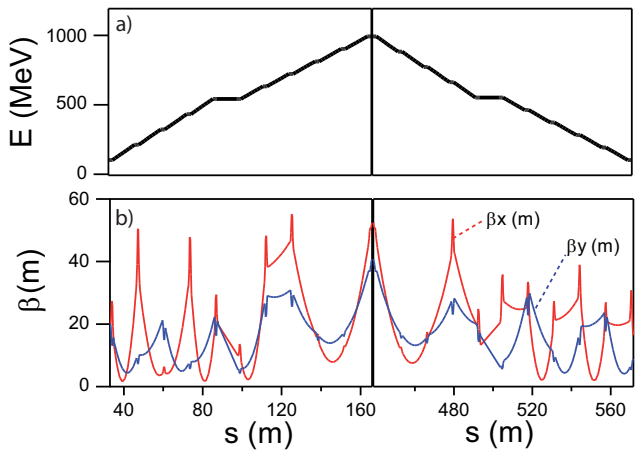

Figure 7: a) Energy and b) beta functions versus the position along the accelerator. Parameters are : drift between the quadrupoles and between the cryomodule and the quadrupole is set at 0.3 m and the length of the quadrupoles at 0.3 m, focusing strength of 2.5 m^{-2} and threshold current of 30 mA for 1 MHz repetition rate.

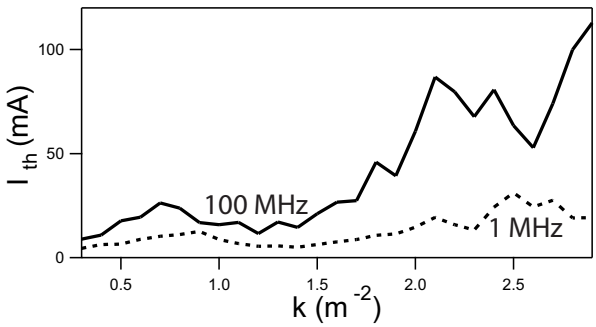

Figure 8: Intensity threshold as a function of the focusing strength of the quadrupoles. Drift between the quadrupoles and between the cryomodule and the quadrupole is set at 0.3 m and the length of the quadrupoles at 0.3 m.

The simulations presented here consider a graded gradient transverse focusing scheme [14] with triplet quadrupoles with a focusing strength arrangement $(-k/2,\ k,\ -k/2)$. In order to keep the symmetry of the optical functions, there are quadrupoles sets between each cryomodules, at the beginning and at the end of the linear accelerator section. Preliminary simulations with a simplified design considering a 1 GeV linear accelerator, have been done with one recirculation. The focusing strength is choose to be constant in the first half of the linear accelerator, when the electrons increase their energy. As a consequence, it results from the simulations an evolution of the current threshold as a function of the focusing strength. Figure 7 illustrates the energy variation along the recirculations loops and the optical function. The focusing scheme enables to adapt the optical function to the case of lower energy of the electrons : in the first half of the accelerator, when the energy increases and in the second half one when the energy decreases. The optical function presented (see Figure 7b) are symmetric compared to the center of the arc. They are comprise between 2 and 55 m.

With a maximum charge in ERL configuration of 1 nC, the average current is 1 mA (resp. 100 mA) for 1 MHz (resp. 100 MHz) repetition rate. As a consequence, the Beam Break Up threshold current should be larger than 1 mA for 1 MHz and 100 mA for 100 MHz. The dashed curve of figure 8 shows that whatever the focusing strength the threshold current of the beam break up instability is higher than 1 mA. So the Beam break up instability does not limit the current of the ERL operation at 1 MHz repetition rate. On the other hand, an operation at 100 mA can be done only for few focusing strength. In fact, the Beam Break up instability is more critical at 100 MHz repetition rate and will need a careful design of the optics.

In a next step, simulations have to be done versus different parameters acting on the transfer matrix from turn to turn and from element to element. For the case of N_r recirculation loops, the Beam Break Up instability becomes critical as the threshold current is smaller of a factor $N_r(2N_r - 1)$. As a consequence, the maximum current for the two recirculations needed for $2\ GeV$ is predicted to be around $20\ mA$.

CONCLUSION

ARC-EN-CIEL single pass accelerator has been designed in order to maximize the electron beam brilliance and to optimize parameters as the energy spread for the production of HGHG light. ERL loops could provide in addition synchrotron radiation from undulators and FEL oscillation in the UV-X wavelength domain. BBU instabilities does not limit a high average current operation. But further investigations have to be realized to obtain a high average current with two recirculation loops.

ACKNOWLEDGMENT

The support given by EUROFEL contract No 011935 is acknowledged.

REFERENCES

[1] M.E Couprie (these proceedings).

[2] C. Limborg-Deprey and P. R. Bolton, Nucl. Instrum. Methods A **557**, 106 (2006).

[3] S. Heifets, G. Stupakov, and S. Krinsky, Phys. Rev. ST Accel. Beams **5**, 064401 (2002).

[4] G. H. Hoffstaetter and I. V. Bazarov, Phys. Rev. ST Accel. Beams **7**, 054401 (2004).

[5] Y.kim, F. Lohl, S. Schreiber, and K. Flottmann, proceedings of LINAC **http://accelconf.web.cern.ch**, 391 (2006).

[6] B. Aune, R. Bandelmann, D. Bloess, B. Bonin, A. Bosotti, M. Champion, C. Crawford, G. Deppe, B. Dwersteg, D. A. Edwards, et al., Phys. Rev. ST Accel. Beams **3**, 092001 (2000).

[7] K. Flottman, ASTRA, a space charge tracking algorithm, http://www.desy.de/ mpyflo.

[8] M. Dohlus and T. Limberg, CSRTrack, http://www.desy.de/xfel-beam/csrtrack/index.html.

[9] D. Dowell, T. D. Hayward, and A. Vetter, proceedings of Particle Accelerator Conference **http://accelconf.web.cern.ch**, 992 (1995).

[10] F. Sacherer, IEEE Trans. Nucl. Sci. NS **18**, 1105 (1971).

[11] M. Dohlus and T. Limberg, proceedings of Particle Accelerator Conference **http://accelconf.web.cern.ch**, 1015 (2005).

[12] I. Bazarov, BI, http://www.lns.cornell.edu/ ib38/bbucode/src/.

[13] A. Todd, Nucl. Instrum. Methods A **557**, 36 (2006).

[14] D. Douglas, Report JLAB-TN-00-027 (2000).

STATUS OF THE UNDULATOR SYSTEM OF THE SEEDED HGHG-FEL TEST BENCH AT MAX-LAB*

J. Bahrdt, W. Frentrup, A. Gaupp, K. Goldammer, K. Holldack, M. Scheer,
BESSY, Berlin, Germany
M. Brandin, F. Lindau, D. Pugachov, S. Thorin, S. Werin, Lund University, Lund, Sweden,
J. Kuhnhenn, Fraunhofer INT, Euskirchen, Germany

Abstract

Within the EUROFEL Design Study a seeded HGHG-FEL will be set up at the 450 MeV linac at MAX-lab. The undulators and the dispersive section have been installed. Two different glass fiber based radiation dose monitors have been integrated. We report on the performance of these components. The impact of electron losses on undulator magnets and the Cherenkov fibers have been simulated. The THz radiation as produced by the bunched electron beam in the dump magnet can be used as a measure of the longitudinal and transverse overlap of the electron beam and the laser beam which has been concluded from simulations.

INTRODUCTION

Within the European FEL Design Study a single stage seeded HGHG FEL [1] test bench is currently set up at MAX-lab [2]. The electrons will be accelerated in the injection linac of the MAX-I-III rings. The FEL experiment is located inside the MAX-II storage ring and the electron beam will be available between the injections into the MAX-lab rings. A new low emittance photocathode gun [3] will be installed at the end of 2007. The commissioning of the complete setup will start in September 2007 using an existing gun which provides a bunch charge of 0.08nC.

BESSY has built and installed the two permanent magnet undulators (modulator and radiator) and the electromagnetic chicane. Permanent magnets are sensitive to radiation damage and the deposited doses have to be monitored. For this purpose two glass fiber systems have been implemented: i) A Cherenkov system delivers fast signals which will be used for a laser interlock system in case of an electron beam missteering. ii) Absolute dose measurements are done with a powermeter system which is based on another type of glass fiber. A detailed study and comparison of both measurements systems in combination with numerical simulations will be very helpful for the design of future FEL sources.

The alignment of the electron beam with respect to the laser beam is crucial for a reliable operation of the seeded FEL and a robust diagnostic is required. Simulations show that the spectral distribution of the THz radiation as produced by the electron bunch in the dump magnet changes significantly if the seed laser interacts with the electron beam. Thus, the THz will be helpful in the commissioning phase and also later during normal operation as an input for feedback systems.

*This work has been partially supported by the EU Commission in the Sixth Framework Program, Contract No. 011935 – EUROFEL.

THE UNDULATORS

The parameters of the undulators and the chicane have been described in [4]. The electron beam height at the FEL location of 520mm requires a horizontal operation of the two undulators. The undulators have been measured and shimmed in the vertical position at the BESSY field measurement bench. After shimming the devices have been rotated by 90° and mounted onto three columns each. Fig. 1 shows the radiator in operating position at MAX-lab. In the final position the field integrals will be checked with a pulsed wire system and air coils at the undulator ends will be used to compensate residual field errors.

Figure 1: Radiator of the APPLE II type in operating position without vacuum chamber. Four power meter sensors (see below) at each undulator end (orange cable) are installed.

THE CHICANE

The chicane consists of four electromagnets (Fig. 2). Each magnet is made of two low carbon steel pieces (C < 0.01%) which are bolted together. The poles have been wire cut. The number of windings per coil is 432. The measured field integrals per Ampere for the four magnets are: 10.9, 10.9, 10.6, 10.7 Tmm / A.

The magnetic hysteresis of the four magnets as measured with a moving wire is ±0.25 Tmm (Fig. 3).

Hall probe measurements show a reproducibility of the field setting below 5e-4 after two cycles (Fig. 3).

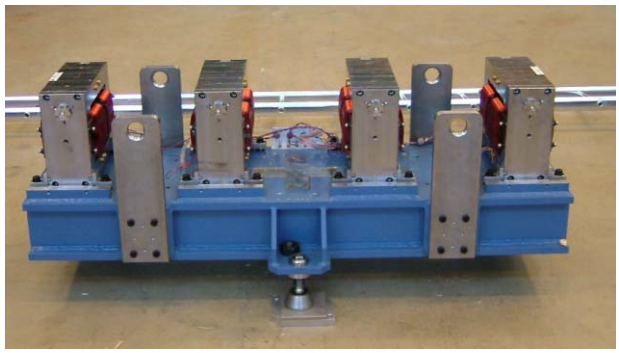

Figure 2: Electromagnetic Chicane.

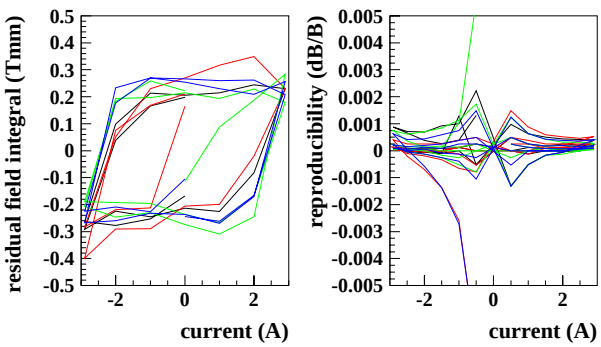

Figure 3: Left: Hysteresis of field integrals of the four magnets. The measurement noise is due to the presence of up to 30Tmm field integrals. Right: Reproducibility of field settings within a sequence of several current cycles of the magnets.

RADIATION PROTECTION OF THE MAGNETS

Significant demagnetization of undulator permanent magnets in storage rings have been reported in the literature [5-7]. The risk of demagnetization is even higher in single pass devices like linac based FELs. Extensive studies have been performed to get a quantitative understanding of demagnetization effects [8, 9]. Collimation systems have to be designed such that the radiation dose deposited into the magnets remains below an acceptable limit [10].

In the MAX-lab FEL a stainless steel capillary (length: 100mm, diameter 3mm, wall thickness: 12.5mm) is located in front of the modulator preventing the electron beam from hitting the circular beam pipe in case of a failure of the two vertical deflecting dipole magnets at the laser beam port (vertical beam displacement due to the dipole magnets: 20mm).

The electron losses will be monitored with two different systems, a Cherenkov system for fast beam loss detection and a powermeter system for absolute dose measurements. GEANT simulations have been performed to estimate the radiation doses in the magnets and to evaluate the corresponding number of produced Cherenkov photons. The experiences gained with these systems will be valuable for the BESSY Soft X-Ray FEL [11].

Cherenkov System

A Cherenkov fiber system [12] is fast and the signal can be used to switch off the electron beam in case of intolerable beam losses. During the commissioning phase the relative intensities of the individual fibers can be used to align the electron beam properly.

The system installed at the MAX-lab FEL consists of four radiation insensitive glass fibers (core: 300µm, cladding: 300 µm) mounted directly onto the circular undulator vacuum chamber which has a diameter of 10mm (Fig. 4). Thus, the fibers will provide detailed spatial information even for large undulator gaps. The sensitivity of the fibers is small as compared to large luminescence detectors. The small size, however, permits an installation close to the electron beam over many meters.

The GEANT [13] simulations are based on a 1nC bunch hitting the vacuum chamber wall of the modulator under zenith angles of 0.1 and 1mrad and azimuthal angles of 0, 45 and 90°, respectively. Four Cherenkov fibers and one Thermo Luminescence Detector (TLD) are included in the model (Fig. 4). The evaluated radiation doses induced in the TLD and the magnets and the produced Cherenkov photons are summarized in (Tab. 1). The given number of photons is the number detected by the photomultiplier (applying a numerical aperture of 0.22 inside the fiber and including the spectral characteristics of the multiplier).

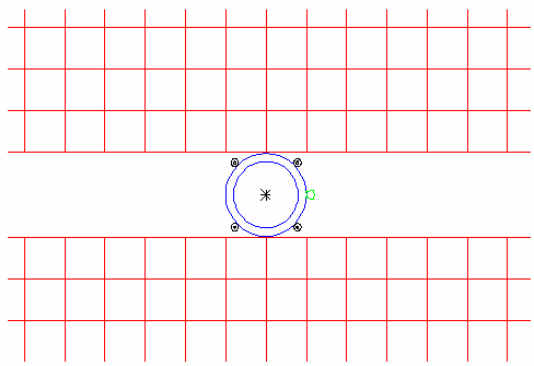

Figure 4: Cross section of the modulator including the permanent magnets (red), vacuum chamber (blue), Cherenkov monitors (black) and TLD monitor (green).

Table 1: Results from GEANT simulations.

angles mrad / °	TLD mGy / nC	max. dose in magnet mGy / nC	Cherenkov photons/nC	
			forward direction	backward direction
0.1 / 0	1207	57	6.7e7	1.1e7
0.1 / 45	131	205	9.7e7	1.5e7
0.1 / 90	77	287	7.2e7	1.2e7
1.0 / 0	2730	188	1.2e8	2.1e7
1.0 / 45	412	487	1.6e8	2.7e7
1.0 / 90	279	588	1.3e8	2.3e7

Maximum doses of 0.59 Gy/nC are detected for the 1mrad case (Fig. 5). It has been shown [14] that a maximum reduced dose (electron energy > 20MeV) of 70kGy can be tolerated in case of the BESSY Soft X-Ray FEL which represents a rather conservative number for the short MAX-lab FEL. Thus, the number of generated Cherenkov photons is sufficiently high to detect even small electron beam losses long before the magnets are damaged. The exact detection limit of the Cherenkov fibers will be subject to future combined numerical and experimental studies at the FEL.

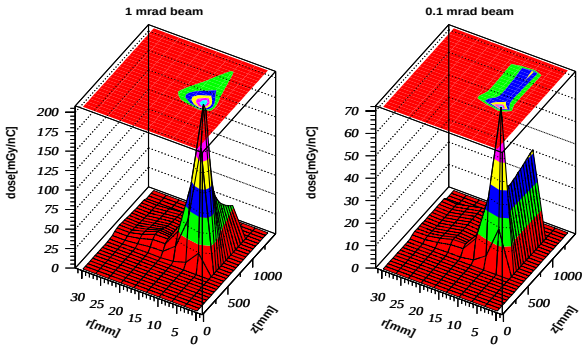

Figure 5: Radiation doses inside the magnets induced by a 1nC electron bunch hitting the vacuum chamber. The data are averaged over the 0°, 45° and 90° scenarios.

Powermeter System

Absolute radiation dose measurements can be done with calibrated glass fibers [15]. The fibers can be installed along the region of interest (e.g. the complete undulator system) providing spatial information of the beam losses (Optical Time Domain Reflectometer, OTDR). Another approach is a system of several local sensors which are multiplexed. The spatial resolution of the latter system is slightly lower (depending on the number of channels) but the complete dynamic range is available for each channel whereas in the OTDR system the dynamic range is available only for the whole system. A system with 16 local sensors has been installed at the MAX-lab FEL.

Glass fibers for telecommunication applications are not optimized for radiation dosimetry. Usually, the optical parameters which are relevant for dose measurements can vary by orders of magnitude. This requires a careful selection of the fibers. Four germanium and phosphorous doped polyimid coated 50/125/145 µm graded index fibers from different suppliers have been tested by the Fraunhofer INT, Euskirchen, Germany. A fiber fabricated by J-Fiber, Jena, Germany, has been selected for the MAX-lab FEL. The calibration of this fiber as determined with a Co-60 source is plotted in figure 6.

The figure of merit for the fiber selection is a combination of various parameters: i) high dynamic range; ii) radiation sensitivity; iii) annealing after irradiation; iv) linear response on total radiation dose; v) low sensitivity on dose per time.

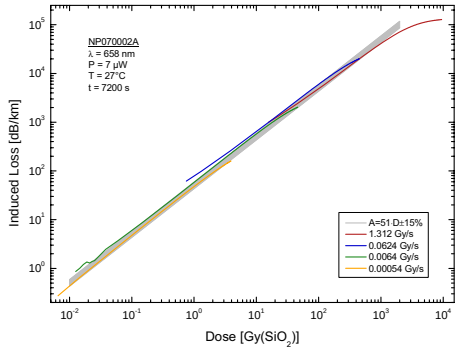

Figure 6: Calibration of the selected fiber.

The chosen fiber has the following performance (Fig. 6): i) in combination with the currently installed light source and the power meter the dynamic range is 30-40 dB ii) the attenuation is described by: (dB / km) = dose (Gy) * 51. For comparison: the sensitivity of conventional germanium doped 50/125/250 µm graded index fibers as used to connect the sensor modules to the light source and the analyzer is two orders of magnitude lower. iii) 24h after irradiation less than 10%. iv) The deviation from a linear curve within the range from 0.01-1000Gy is smaller than ±15%. v) A linear response has been demonstrated for dose rates between 0.0005 Gy/s up to 1.3 Gy/s.

The MAX-lab system consists of sixteen channels. One channel serves as a reference. The read out time for all 16 channels is less than 60s. The light source consists of an LED (658 nm) powered by a stable constant current power supply. 10% of the output power is measured directly (excluding the optical coupler, the optical switches and all fibers) with a power meter. In a temperature stabilized environment the source drifts are only 0.01dB / day. The influence of typical source drifts in a rough environment of 0.02-0.05dB / day can easily be compensated.

The reference fiber has no sensor module attached but is shortcut at the FEL location. It can be used to compensate for drifts of the support fibers.

The sensor fibers are wound to rectangular flat coils (50x50mm**2) and the radiation exposed length of one fiber is approximately 2m. The coils are mounted onto the magnet girders close to the upstream and downstream ends of the undulators. At smallest gap the distance to the electron beam is 7mm for the modulator and 28mm for the radiator. Radiation sensitive fibers are used only for the coils. The distance of 40m between the FEL and the electrical cabinet is bridged with radiation insensitive fibers.

The system has been installed in March 2007 and the drifts have been monitored since that time. The optical transparency of the 15 fibers has been corrected for fluctuations of the light source. The signals show a long term drift of ±0.03dB per day and a periodic structure superimposed to it (Fig.7, left). The drifts are dominated by temperature fluctuations which is concluded from a correlation diagram (Fig. 7, right). The various fibers show individual temperature dependencies. The data can

be corrected using a specific temperature coefficient for each fiber. Two temperature sensors are installed at each undulator end. After correction the residual drifts are well below ±0.01dB for a period of several days. This guarantees a long term system sensitivity of better than 0.2Gy. The remaining differences between the fibers are due to the individual characteristics of the cascaded optical coupler behind the light source.

In case the fibers have reached the upper limit of the linear regime of 1000Gy they can be thermally annealed at a temperature of up to 350°C in order to recover the full transmission.

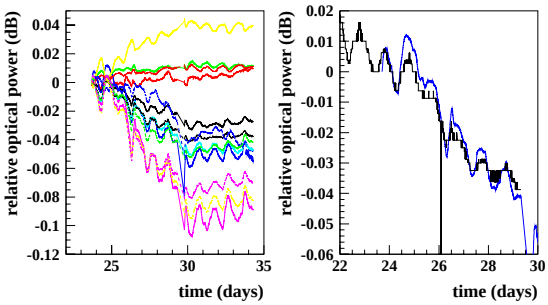

Figure 7: Left: Long term stability of the system consisting of 15 fibers. Right: The day by day fluctuations (blue) are closely correlated to the temperature variations (black).

THZ DIAGNOSTICS

The diagnostics of the FEL resonance in the modulator will be performed using a strong difference in coherent THZ emission [16,17] from the seeded and unseeded bunch after propagating through an additional bending magnet (dump magnet) behind the radiator. Since the electrons are gathering path length differences controlled by R56 along the magnet, the bunch shape in time domain is different for the seeded and unseeded case. This is caused by the change in energy spread due to the FEL resonance (Fig. 8 left).

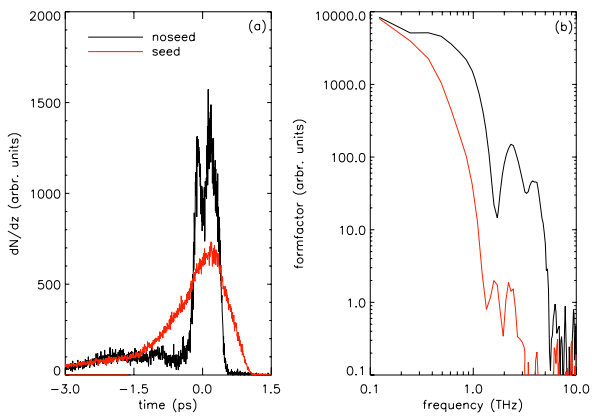

Figure 8: Left: Projection of the seeded and unseeded electron density in the bunch according to start-to-end simulations [2] after passing an R56 of 0.05 m. Right: Expected envelopes of THz spectra (formfactor) emitted by theses bunches for the seeded and unseeded case.

The THz power spectral density emitted there is ~ N(N+1)f, where f is the square of the Fourier transformation of the longitudinal electron density and N=0.6x10^9 (0.1 nC) is the number of electrons.

The calculated form factor f for the two cases (Fig. 8, right) demonstrates that the coherent far infrared emission in the range between 1 and 10 THz can be employed to detect the overlap between seed laser and bunch in the modulator. By setting an appropriate high pass filter the signal from a THz detector will almost completely drop to zero for a successful energy modulation of the electrons.

REFERENCES

[1] L. H. Yu, J. Wu, Nucl. Instr. and Meth. in Nucl. Res. A 483 (2002) 493.
[2] S. Werin, al., these proceedings.
[3] S. Werin et al., Proceedings of the EPAC 2006, Edinburgh, Scotland, 2006, pp 130-132.
[4] J. Bahrdt et al., Proceedings of the EPAC 2006, Edinburgh, Scotland, 2006, pp 59-61.
[5] P. Colomp, T. Oddolaye, P. Elleaume, “Partial Demagnetization of ID6 and Dose Measurements on Certain Ids”, Machine Technical Note 1-1996/ID, 1996.
[6] M. Petra et al., Nucl. Instr. and Meth. in Phys. Res. A, 507 (2003) pp. 422-425.
[7] P. Colomp, T. Oddolaye, P. Elleaume, “Demagnetization of Permanent Magnets to 180 MeV Electron Beam”, Technical Report ESRF/MARCH-ID/93-09, European Synchrotron Radiation Facility, ESRF March 1993.
[8] T. Bizen, T. Tanaka, Y. Asano, D.E. Kim, J.S. Bak, H.S. Lee, H. Kitamaru, Nucl. Instr. and Meth. in Phys. Res. A 467-468 (2001) 185-189.
[9] M. Marechal, T. Shintake, SRI2003, Conference Proceedings, AIP 705, (2004) pp 282-285.
[10] H. Schlarb, “Collimation System for the VUV Free-Electron-Laser at the TESLA Test Facility”, Thesis Work, Universität Hamburg, DESY-THESIS-2001-055, Nov. 2001.
[11] “The BESSY Soft X-Ray FEL”, Technical design Report, D. Kraemer et al., Berlin, 2004.
[12] M. Körfer, W. Göttmann, F. Wulf, J. Kuhnhenn, Proceedings of DIPAC 2005, Lyon, France, 2005, p301.
[13] GEANT 3.21, Detector Description and Simulation Tool, Computing and Networks Division, CERN, Geneva, Switzerland.
[14] J. Bahrdt et al., Proceedings of the FEL Conference 2006, Berlin, Germany, 2006, pp521-528.
[15] H. Henschel, M. Körfer, J. Kuhnhenn, U. Weinand, F. Wulf , Nucl. Instr. and Meth. in Phys. Res. A 526 (2004) pp. 537-550.
[16] Holldack et al. PRL 96, 054801 (2006).
[17] A. A. Zholents and K. Holldack, Proceedings FEL Conference 2006, Berlin, Germany, 2006, pp725-727.

NONLINEAR HARMONIC GENERATION IN THE BESSY SOFT X-RAY FEL*

K. Goldammer, BESSY, Berlin, Germany.

Abstract

Free Electron Lasers (FELs) do not only radiate at the fundamental frequency, they may also radiate coherently at higher harmonics. This process is referred to as nonlinear harmonic generation or NHG. NHG is of high interest, because it extends the output wavelength of FELs to several harmonics of the FEL resonant frequency. In cascaded High Gain Harmonic Generation (HGHG) FELs, harmonic radiation may be used to improve frequency-conversion and reduce the number of HGHG-stages. BESSY proposes to build a cascaded HGHG FEL with three FEL lines [1]. They cover a wavelength range of 51 nm (Low-Energy FEL) to 1.2 nm (High-Energy FEL) and consist of up to four HGHG-stages. In this paper, we present studies of the BESSY High-Energy FEL harmonic content performed with the upgraded version of the simulation code Genesis 1.3 [2].

INTRODUCTION

The BESSY High-Energy (HE-) FEL uses a cascade of four HGHG stages to convert a seed laser of 297.5 nm down to 1.24 nm. Each stage consists of a modulator, dispersive chicane and radiator. Analytic studies [3] predict that the signal-to-noise ratio (SNR) in HGHG FELs decreases by the square of the harmonic nbumber used during conversion. As the total conversion factor in the BESSY HE-FEL is 225, degradation of the radiation due to noise is a critical issue. In order to conserve the excellent temporal coherence of the seeded FEL radiation, a new design is proposed that uses harmonic radiation to reduce the number of HGHG-stages. Its prospects are investigated in this paper.

Harmonic radiation is intrinsically produced during the FEL process in planar undulators and leads to coherent emission at higher harmonics of the FEL resonance [4]. It becomes significant in the high gain regime of an FEL and typically provides for power levels in the range of 1% or 0.1% of the fundamental depending on the harmonic number.

The new design uses harmonic radiation from the first stage radiator. Its fifth harmonic has a wavelength of 11 nm and could hence be applied directly as a seed for the third stage modulator. Figure 3 illustrates the idea.

HARMONIC CONTENT OF FIRST STAGE

The BESSY High Energy FEL first radiator is a planar undulator with the period length of λ_u=92 mm and a total length of 3.69 m. The radiator has to be prolonged significantly to yield sufficient fifth harmonic power for seeding the third stage. The harmonic power in the first radiator then evolves as depicted in Fig. 2.

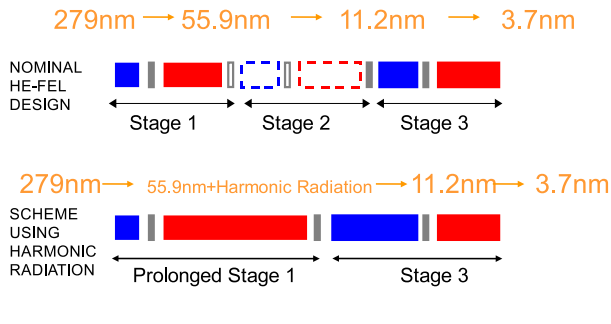

Figure 1: Schematic picture of new proposal for BESSY High Energy FEL: harmonic radiation from first stage radiator could be used to the seed third stage. The second stage could be omitted. Stages 1 to 3 depicted.

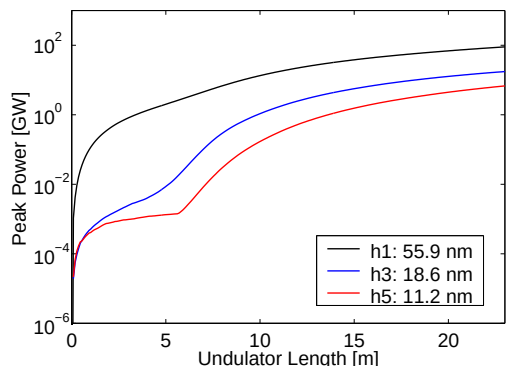

Figure 2: Simulation of BESSY High-Energy FEL radiation power along first radiator. From top to bottom: fundamental, third and fifth harmonic radiation. Simulation performed with new version of Genesis 1.3 [2].

It can be observed that the harmonics start later than the fundamental and enter their exponential gain regime after approximately 5 to 7 m. After that they rapidly reach a significant output power because they have a shorter gain length (higher gain) than the fundamental. This corresponds well to analytic predictions [5].

* Work supported by the Bundesministerium für Bildung und Forschung, the State of Berlin and the Zukunftsfonds Berlin

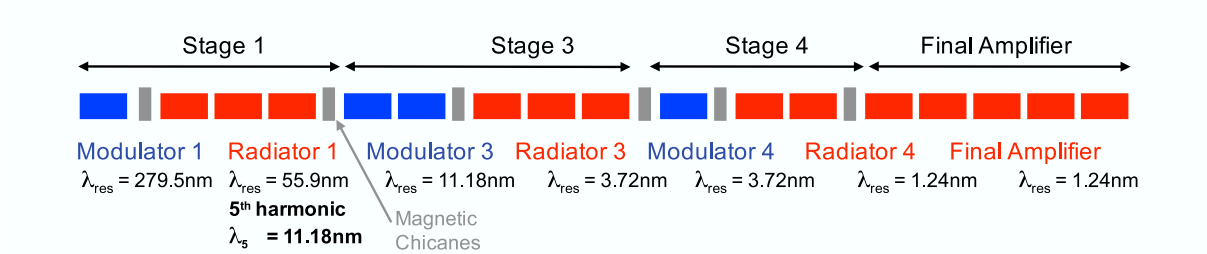

	Mod1	Rad1	Mod3	Rad3	Mod4	Rad4	FA
λ_u [mm]	122	61.2	70	50	50	28.5	28.5
No. of undulator periods	1x18	3x51	2x50	3x56	1x69	2x110	5x110

Figure 3: Schematic view of new design BESSY High Energy FEL with table of undulator properties.

NEW DESIGN

The choice of λ_u and K plays an important role in FEL performance. In order to find the optimal undulator settings for the first radiator with respect to a short gain length and high output power, a range of FEL configurations were studied. The combination of K=6 and λ_u=61.2 mm is a good compromise that reduces the fundamental gain length by about one fourth [6]. With the assumption of a 10 mm undulator gap, this corresponds to a peak flux of 1.6 T in the undulator magnets which is technically feasible [7].

A schematic view of the new design is given in Fig. 3. The radiator length is fixed at 9.4 m (153 periods) where the fifth harmonic power is in the range of 230 MW. Simulation studies of the fresh bunch parts show that this keeps the increase of energy spread at a tolarable level.

The temporal and spectral power distribution of the fifth harmonic at the end of the radiator then evolve as depicted in Fig. 4. However, the fifth harmonic power at the end

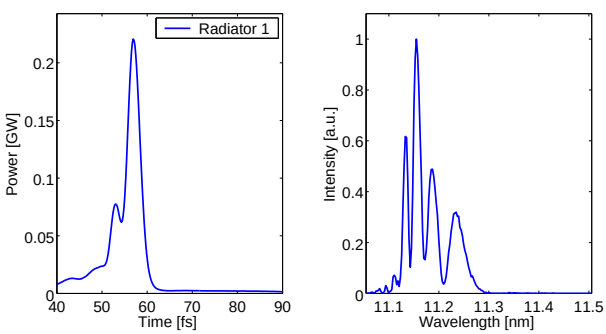

Figure 4: Temporal and spectral power distribution of fifth harmonic radiation of first radiator at 9.4 m. Undulator period 61.2 mm, K=5.98.

of the prolonged radiator is about a factor eight lower than the original seed power for the third stage. This requires a careful readjustment of the undulator lengths in all subsequent stages. The total length of the first stage is now 15.5 m including the dispersive section in between modulator and radiator and the fresh bunch chicane after the first radiator. In order to maintain sufficient energy modulation in the third stage modulator, it has to be extended from 30 to 100 periods, equal to about 5 m of undulator. However, the extension of the first and the third stage does not exceed the original length reserved for the second stage.

RESULTS

Maintaining the nominal undulator configurations for the third and fourth stage, the power at the end of the third and fourth radiator evolves as depicted in Fig. 5. The power

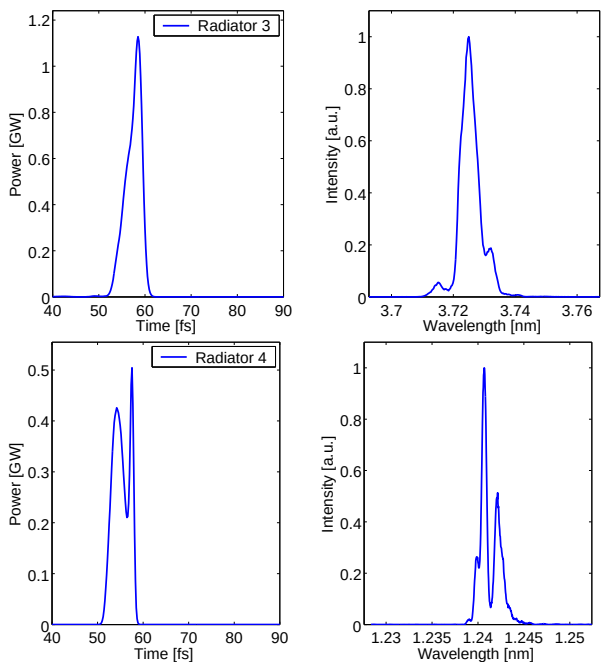

Figure 5: Simulation of temporal and spectral power distribution at end of third radiator, top, and fourth radiator, bottom, in scheme 1.

levels compare well to the output power in the original design. When using the radiation from the fourth radiator to seed the final amplifier, it reaches an output power of 2.5 GW. This slightly exceeds the nominal output power of 1.8 GW. The temporal and spectral power distribution at the end of the final amplifier are depicted in Fig. 6. The

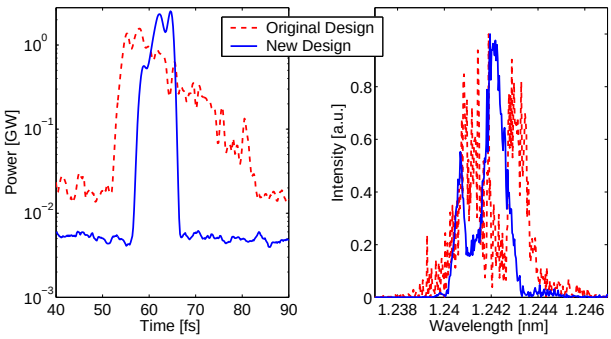

Figure 6: Simulation of temporal and spectral power distribution at end of final amplifier.

output power of the final amplifier in the new design compares well to the output power of the original HE-FEL design. The pulses have become shorter, which is due to the fact that the harmonic pulses at the end of the first radiator are significantly shorter than the fundamental pulses. Radiation from unseeded bunch parts, the background in Fig. 6, left, is also greatly reduced. This can be attributed to the reduced number of HGHG stages. Figure 6, right, shows the improvement of the final amplifier spectrum. The new design results in fewer temporal spikes and the output radiation is concentrated in a smaller bandwidth (30% net reduction), thus showing improved temporal coherence.
However, there are still two peaks visible in the spectrum. The shorter wavelength spike is a sideband which is amplified because it lies within the FEL bandwidth[1]. It already appears in the output of the fourth radiator, see Fig. 5, bottom, which has been used to seed the final amplifier. It probably results from the bunching distribution of the electrons in the radiator. Ref. [1] explains that the electrons can get *overbunched*, meaning that they move too far in the potential bucket, and generate a modulation of the emitted radiation frequency. This could be avoided by readjusting R_{56} in the dispersive chicanes at the expense of output power.

HARMONIC CONTENT OF THIRD STAGE

Harmonic radiation might be used again for an additional change in the design. The third harmonic radiation of the third radiator has a wavelength of 1.24 nm and can be used to directly seed the final amplifier.
However, this idea is more of a theoretical than a practical option. The gain length in the third radiator is significantly longer than in the first radiator (L_{G1D}=1.8 m as opposed to 1 m). This means that the radiator has to be prolonged significantly to yield sufficient fundamental gain for the harmonic power to become noticeable. As a consequence, the total undulator length in this case would exceed the nominal HE-FEL length, which is certainly a drawback. The long undulators also provoke a significant SASE background from the unseeded buch parts. Figure 7 depicts the temporal and spectral profile of the third harmonic at 23 m along the third radiator. The peak power is about a factor of

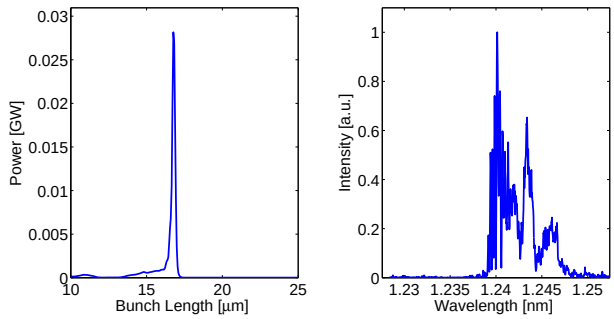

Figure 7: Temporal and spectral power distribution of third harmonic radiation of third radiator at 23 m.

six lower than the output of the fourth radiator in the nominal design. As a result of the degradation of electron beam quality in the long undulator, the spectrum shows several spikes and sidebands.
When using the harmonic radiation from the third radiator to seed the final amplifier, the HE-FEL line yields the temporal and spectral power depicted in Figure 8. The final amplifier spectrum is dominated by a spiky SASE spectrum and does not convey the advantages of High Gain Harmonic Generation any more.

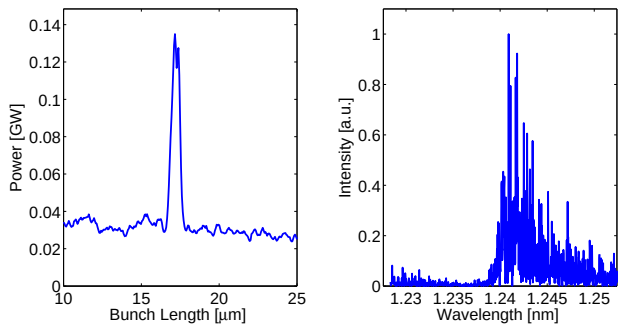

Figure 8: Temporal and spectral power distribution at end of final amplifier when using third harmonic radiation from stage three.

CONCLUSION

The use of harmonic radiation from the first stage for seeding the third stage is a promising option for the BESSY High Energy FEL. The simulation studies performed with

[1]The relative FEL bandwidth of the order of the FEL parameter ρ which is about 1e-3 in the final amplifier.

the new version of Genesis [2] show that it is a feasible option and yields an output power and spectral bandwidth comparing well to the original design. Moreover, the new scheme that uses harmonic radiation has a number of benefits:

1. The complexity of multi-stage cascading is reduced as the number of HGHG stages decreases from four to three. This can be expected to greatly improve the practicability of the proposed machine both during commissioning as well as during operation.

2. The constraints on the electron beam are relaxed. The BESSY Soft X-Ray FEL implements the serial use of the fresh-bunch technique in each HGHG stage [8]. As a consequence, a long electron bunch with a high current region in the range of several hundreds of femtoseconds is required[2]. In order to reach a peak current of 1.75 kA current along the entire bunch, an initial bunch charge of 2.5 nC needs to be generated in the injector. Saving one HGHG-stage reduces the required bunch length by a few hundred femtoseconds. The bunch charge could be lowered to 1.5 to 2 nC such that the effects of space charge could be reduced. As a consequence, the beam emittance decreases and the FEL efficiency is enhanced.

3. The total undulator length decreases. This is beneficial due to two reasons: a) the FEL pulses are less prolonged by slippage in the undulators. This results in shorter output pulses. b) The fresh parts of the electron beam are less degraded in energy-spread before they come to use in their corresponding stages. This improves the quality of the electron beam and the FEL performance.

However, it has to be noted the experimental experience with harmonic emission in the soft X-ray regime is still small. FEL theory also shows that harmonic radiation is critically dependant on strong FEL gain on the fundamental. If a only a few of the relevant electron beam parameters (e.g. peak current or energy-spread) do not meet the expectations, the first radiator might saturate significantly later and not yield high intensity harmonic emission as predicted. Experiments with harmonic emission from HGHG FELs should hence be conducted to further investigate this issue.

REFERENCES

[1] D. Krämer, E. Jaeschke, W. Eberhardt (Editors), The Bessy Soft X-Ray Free Electron Laser, ISBN 3-9809534-0-8, 2004

[2] S. Reiche, K. Goldammer, P. Musumeci, “Recent Upgrade to the Free-electron Laser Code Genesis 1.3,” *To be Published In the Proceedings of Particle Accelerator Conference (PAC 2007)*.

[2]The length was chosen to allow for seeding five consecutive bunch parts, accounts for slippage of FEL radiation in the radiators and includes a safety margin for timing difficulties.

[3] E. Saldin, E. Schneidmiller, M. Yurkov, “Study of a noise degradation of amplification process in a multistage HGHG FEL,” Opt. Comm. 202 (2002) pp. 169-187.

[4] Z. Huang and K.-J. Kim, ”Nonlinear harmonic generation of coherent amplification and self-amplified spontaneous emission”, Nuclear Instruments and Methods in Physics Research A 475 (2001), pp. 112-117.

[5] Z. Huang and K.-J. Kim, ”Three-dimensional analysis of harmonic generation in high-gain free-electron lasers”, Phys. Rev. E 62, 7295 (2000)

[6] K. Goldammer, ”Studies of Harmonic Generation in Free Electron Lasers”, PhD Thesis, Humboldt-Universität Berlin, 2007

[7] Johannes Bahrdt, private communication, 2007.

[8] Li-Hua Yu and I. Ben-Zvi, ”High-gain harmonic generation of soft X-rays with the fresh bunch technique”, Nuclear Instruments and Methods in Physics Research A 393 (1997), pp. 96-99.

OUTPUT PERFORMANCE OF THE STARS HGHG DEMONSTRATOR AT BESSY*

B. Kuske †, K. Goldammer, A. Meseck, BESSY, Berlin, Germany

Abstract

BESSY is planning to construct a free-electron laser facility, STARS - **S**uper conducting **T**est-**A**ccelerator for **R**adiation by **S**eeding, to demonstrate cascaded high-gain harmonic generation (HGHG) FELs. A 325MeV superconducting linear accelerator will drive two HGHG-stages, where the second stage is seeded by the radiation from the first stage. Such a cascading of the HGHG scheme allows for a reduction of the STARS output wavelength down to the few 10nm range. This paper describes the layout and the expected performance of the facility, the achievable wavelength range, the harmonic content of the radiation, the potential of super-radiant pulses and first tolerance studies for bunch parameter mismatch.

INTRODUCTION

In 2004, BESSY presented the Technical Design Report for a 2.25GeV linac driven Free-Electron Laser (FEL) user facility, covering the VUV to soft X-ray spectral range [1]. The facility utilizes the high-gain harmonic generation principle (HGHG), first demonstrated at Brookhaven National Labratory, USA, in 2000 [2]. In order to reach the short wavelength range, several cascaded HGHG stages are foreseen. In 2006, the German Science Council recommended the construction of a demonstrator to investigate the possibility of cascading HGHG stages. A Conceptual Design Report for this demonstrator, 'STARS'- **S**uper conducting **T**est-**A**ccelerator for **R**adiation by **S**eeding, has been published in 2006 [3]. STARS will consist of a normal conducting RF gun, a superconducting 325MeV linac, a collimation and diagnosis section and a 27.5m undulator section [4]. It will produce pulses in the spectral range from 18eV to 31eV. For further details see [5]. This paper details the layout of the undulator section and presents the performance of STARS at different wavelengths and operational modes. A few preliminary calculations concerning the stability of the machine are shown.

MECHANICAL LAYOUT OF THE UNDULATOR SECTION

The undulator section will consist of two HGHG stages separated by a fresh bunch chicane, that delays the electron bunch so that the radiation of the first stage seeds a preceeding, fresh part of the beam. Each stage starts with a short undulator to modulate the energy of the electron bunch (modulator). It is followed by the dispersive section consisting of four identical dipoles. The adjacent undulator, called radiator, consists of two respectively three separated segments tunable to the harmonics of the modulators' resonant frequency. Table 1 lists the important parameters for all four undulators.

Table 1: Characterization of the STARS undulators (Modulators: M1, M2, Radiators R1, R2.)

	M1	**R1**	**M2**	**R2**
Type	planar	planar	planar	Apple III
Period [m]	0.05	0.05	0.05	0.022
No. Periods	10	2*40	30	3*150
Aper. [mm]	10	20	20	7
Max. B_y[T]	1.1	1.1	1.1	0.839
Max. B_x[T]	-	-	-	0.621
Length [m]	0.5	2* 2.0	1.5	3*3.3
Res. λ [nm]	800	160/200	160/200	40/50/66

The fresh bunch chicane is mechanically identical to the dispersive sections. In order to control the electron beam size along the length of almost 30m, a total of 9 quadrupoles are distributed, one before and after each chicane and one in between undulator segments. The matching into the section will be handled in the preceding collimator. The total length of the chicanes is 2.5m; the distance between undulator segments is 1.0m. The chicanes will also host all necessary diagnostics, as well as all vacuum components, which shall not be incorporated into the undulators. Phase shifters and further diagnostics are placed between undulators segments. The correctors necessary to control the trajectory of the bunch are incorporated into the quadrupoles.

OPERATIONAL MODES

A tunable 800nm Ti-Saphir laser will be used to seed the first modulator. There will be a small chicane right in front of the modulator as a port for the beam. The 4th or 5th harmonic of the beam modulation can be amplified in the following radiator by tuning the dispersive section and driving the undulator gap. After the radiator the electron bunch is delayed by 100 fs in the fresh bunch chicane. Thus, in the second modulator, the preceding, unused part of the bunch is seeded by radiation 160nm and 200nm. The second radiator can be tuned to the 4th or 3rd harmonic of the resonant frequency of the second modulator, so that the final output

* Funded by the Bundesministerium für Bildung und Forschung (BMBF), the State of Berlin and the Zukunftsfond Berlin

† Bettina.Kuske@bessy.de

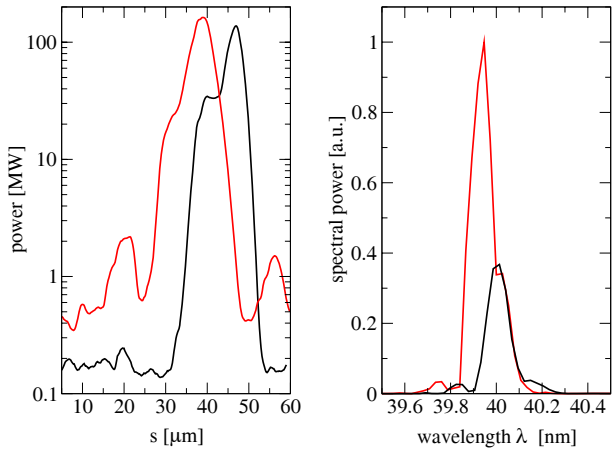

Figure 1: The temporal and the spectral power, at 40nm and helical polarization, when optimizing the output of the first radiator segment (black) and the second segment (red).

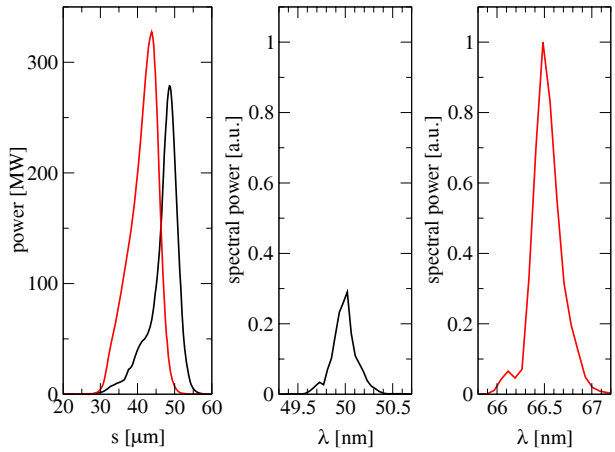

Figure 2: Temporal and spectral power at 50nm (black) and 66nm (red) for planar radiation, optimized for the first radiator segment.

ranges from 40nm to 66nm. Despite changing the combination of the harmonics, the tunability of the seed laser frequency allows for delivering any intermediate frequency. The second radiator consists of three undulator segments. Depending on the final bunch parameters and the chosen wavelength, the saturation length varies, and the gaps of one or two segments might be opened for certain operating conditions. The second radiator will be an APPLE III type undulator [7], so that the polarization is variable. Due to the segmented layout of the radiators and the tunability of the dispersive sections, a wide range of operational modes are feasible. By increasing the fields in the chicanes, the FEL process can be pushed to saturate at the end of the first segment of Radiator 2, with a very good signal to noise ratio of 10^3. The saturation point moves towards the end of the second segment of Radiator 2, when the chicane strength is relaxed. Higher temporal as well as a much higher spectral power can be reached, at the expense of a smaller signal to noise ratio, see Fig 1.

Furthermore, the tolerance of STARS to bunch parameter deviations, like the finally achievable emittance or the energy spread is largely increased. Best results for a bunch emittance of 1.0 πmm mrad e.g. are reached by using only one segment of Radiator 1. In this sense, the following performance characteristics are only examples of what is achievable.

PERFORMANCE

All calculations presented have been performed using GENESIS1.3 [6]. As the performance strongly depends on the bunch parameters, only start-to-end bunches, i.e. results from particle tracking studies in the gun, linac and collimator were used as input for the performance calculations. The dispersive chicanes were modeled using the transfer matrix feature of GENESIS and the bunch part used in the second stage has also been tracked through the first HGHG stage, to include any possible spontaneous radiation effects. The bunches are seeded at 800nm by a 275MW, 30fs Gaussian shaped seed pulse. The average sliced emittance extracted from the start-to-end simulation is 1.0 πmm mrad, a value much smaller than measured so far in state-of-the art normal conducting guns for 1nC bunch charge. On this account, the sliced emittance of the bunches has been raised to 1.5 πmm mrad. The averaged bunch parameters are listed in Table 2.

Table 2: The main average bunch parameters vary slightly for the two bunch parts used in the two stages

	part 1	**part 2**
Gamma	639.6	638.5
Emittance$_{x,y}$ [π mm mrad]	1.44	1.50
Rel. energy spread	3.3 10^{-5}	3.1 10^{-5}
Beam size$_{x,y}$ [μm]	126, 118	130, 134
current [A]	508	512
total bunch charge [nC]	1.0	

The calculations do not include any magnetic errors or trajectory offsets, except for those inherent to the bunch, or any bunch-to-bunch fluctuations.

Fig. 2 shows the temporal and spectral power for 50nm and for 66nm and planar polarization taken behind the first radiator segment. In order to switch from 50nm to 66nm only the second radiator has to be re-tuned to the third harmonics of 200nm. Due to the increased undulator K-value the power increases. For the longer wavelengths it becomes increasingly difficult to suppress the background radiation and avoid the onset of super-radiance to maintain a pure spectrum when optimizing the output of the second radiator segment.

Table 3 displays the three main operational modes and

their performance parameters optimized for clean spectra and maximal power. Any intermediate wavelength can be achieved by varying the seed laser wavelength and adjusting the undulator gaps.

Table 3: Main STARS performance parameters for planar (P) and helical (H) polarization.

Wavelength	**40nm**		**50nm**		**66nm**
Polarization	P	H	P	H	P
No. segments	2	2	1	1	1
Power [MW]	120	163	275	336	328
Pulse energy [μJ]	2.8	3.8	6.1	7.4	9.2
Pulse width [fs]	18	19	16	16	24
% of pulse energy in 0.1 % bandwidth	53	53	41	41	23
background energy / pulse energy [%]	6.6	5.9	6.6	7.1	2.3

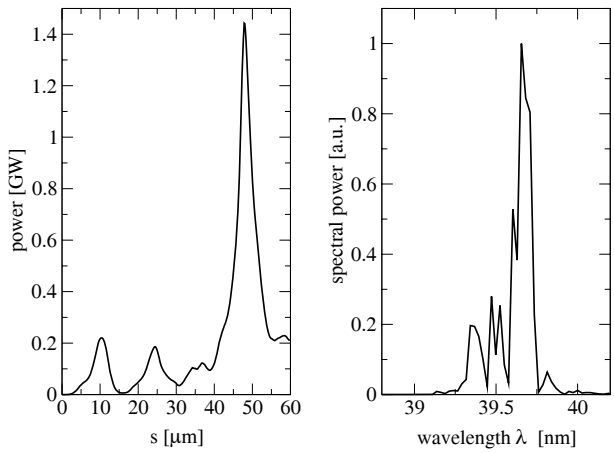

Figure 3: Temporal and spectral power of the super-radiant pulse at the end of the third radiator segment. Still 40% of the power are located within 0.1% bandwidth. The FWHM pulse length is 14fs.

The FEL power can be increased beyond saturation by slightly detuning the undulator. This leads to the onset of the super-radiant regime, [8]. The coherence length, i.e. the slippage within one gain length, becomes comparable to or larger than the pulse length. When the radiation power is high enough, bunching occurs instantly in a small fraction right ahead of the pulse, the power is further increased and the electrons immediately debunch again. As a result, much higher peak powers at very short pulse lengths can be achieved, at the expense of a deteriorated spectral purity. Fig. 3 displays the results achievable at 40nm planar polarization and an emittance of 1.0 πmm mrad taken behind the third undulator segment, when the undulator K-value is reduced by 1.7%. The peak power is 1.4GW, the pulse energy is 43μJ. Despite the deteriorated spectrum, still 40% of the energy is located within 0.1% of the spectral bandwidth. The FWHM pulse length is 14fs.

SENSITIVITY TO BUNCH PARAMETERS

In preliminary tolerance studies, the sensitivity of the STARS performance to large changes of single bunch parameters has been studied for the most sensitive case at 40nm and planar polarization. These calculations model basic parameter deviations, e.g. when the calculated energy spread or the emittance differ from the predictions. In this case, the undulator section can be adjusted to achieve the best performance under the given conditions. To achieve the following results, the structural flexibility of STARS as explained above has been exploited. In order to preserve the typical variation of the parameters over the bunch, the parameters have been scaled for each slice. Please note that the expected shot to shot parameter variations are much smaller than the given offsets. Shot to shot fluctuations can not be counteracted and have to be studied separately. The most critical parameters for the performance are the emittance, the energy spread and the current. Their values and the maximum output power are listed in Table 4.

Table 4: Maximal achievable power, in case major bunch parameters should not match the predictions. The reference values are indicated by italic letters. By using the second radiator segment, even the 68MW reached for an emittance of 2.0 πmm mrad could be improved.

Parameter	**Value**	**Segment**	**Peak power [MW]**
Emittance [πmm mrad]	1.0	1	145
	1.5	*1*	*120*
	2.0	1	68
Rel. energy spread	*3e-5*	*1*	*120*
	1e-4	2	127
current [A]	450	2	100
	500	*1*	*120*
	550	2	156

HARMONIC CONTENT

Recently, an upgrade of GENESIS has been developed that allows for the computation of harmonics in the FEL output for planar undulators [9]. This program has been used to investigate the STARS output at 13.3nm. Fig. 4 shows the results for two radiator segments. To increase the harmonic content of the radiation, a longer duration of the FEL process, i.e. using two radiator segments is profitable. 20% higher peak power and a much cleaner spectrum can be found after the second segment.

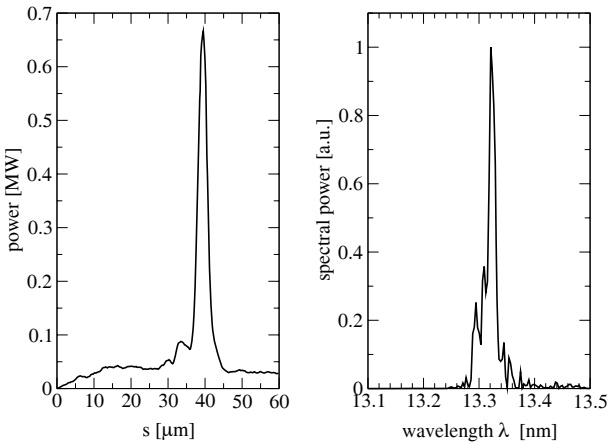

Figure 4: Temporal and spectral power of the 3rd harmonic in the second radiator segment when tuned to 40nm planar radiation.

CONCLUSION

BESSY proposes the construction of a demonstrator, STARS, to investigate the possibility of cascading HGHG stages in order to provide reproducible fs pulses in a wavelength range much shorter than provided by available lasers. The general layout of the undulator section of the machine has been presented, and simulation results of the expected performance of different operational modes have been shown. The proposed layout proved to be flexible enough to cope with a wide range of bunch parameters, due to the modular construction of the radiators and the flexibility provided by the dispersive sections. Calculation with an emittance of 1.5 πmm mrad and an energy spread of $1.0{\cdot}10^{-4}$ predict almost the same peak power as calculations for an emittance of 1.0 πmm mrad and an energy spread of $3.3{\cdot}10^{-5}$, when the undulator section is properly optimized and the second radiator segment is used.

It is known that the synchronization between the bunch and the seeding radiation is one of the critical aspects of HGHG FELs. The effects of timing jitters is expected to be large, but has yet to be studied. The influence of magnetic errors, trajectory offsets and undulator errors will be studied in the near future, but their influence is expected to be far less critical.

REFERENCES

[1] "The BESSY Soft X-ray Free Electron Laser, Technical Design Report", March 2004, eds.: D. Krämer, E. Jaeschke, W. Eberhardt, ISBN 3-9809534-0-8, BESSY, BERLIN (2004).

[2] A. Doyuran et al., "Characterization of a High-Gain Harmonic-Generation Free-Electron Laser at Saturation", Phys. Rev. Lett. 86, 5902 (2001). URL: http://link.aps.org/abstract/PRL/v86/p5902.

[3] The STARS Design Group, "STARS - Proposal for the Construction of a Cascaded HGHG FEL", BESSY Internal Report, Berlin, October 2006.

[4] M. Abo-Bakr et al., "STARS — A Two-Stage High-Gain Harmonic Generation Demonstrator", Proc.of thr Particle Accelerator Conference (PAC 2007), Albuquerque, New Mexico.

[5] J. Knobloch et al., "STARS — An FEL to demonstrate Cascaded High Gain Harmonic Generation", FEL'07, this proc.

[6] S. Reiche, "GENESIS 1.3: A Full 3D Time Dependent FEL Simulation Code", Nuclear Instruments and Methods A429 (1999) p. 243.

[7] J. Bahrdt, W. Frentrup, A. Gaupp, B. Kuske, M. Meseck, M. Scheer, "Undulators for the BESSY Soft X-ray Free Electron Laser", Proc. of the 26th International Free Electron Laser Conference (FEL 2004) Trieste, Italy.

[8] L. Giannessi, S. Spampinati and P. Musumeci, "Non Linear Pulse Evolution in Seeded and Cascaded FELs", Proc. of the 27th International Free Electron Laser Conference (FEL 2005), Stanford, California, USA.

[9] S. Reiche, K. Goldammer, P. Musumeci, "Recent Upgrade to the Free-electron Laser Code Genesis 1.3,", Proc.of thr Particle Accelerator Conference (PAC 2007), Albuquerque, New Mexico.

SMALL-APERTURE VACUUM-CHAMBER DESIGN FOR STARS*

J. Bahrdt, V. Dürr, A. Meseck†, M. Scheer, G. Wüstefeld
BESSY GmbH, Berlin, Germany

Abstract

To demonstrate and investigate the cascaded high-gain harmonic generation (HGHG) scheme proposed for the BESSY Soft X-ray FEL, BESSY plans to build a test-facility called STARS consisting of two HGHG stages. The radiator in the second stage is planned as an APPLE III device which provides the highest field for a circular beam pipe. It's minimum Gap of 7 mm translates into a 5 mm inner diameter of the vacuum chamber, which leads to a higher pressure and an increase of the wakefields. An analysis of the impact of the wakefields and the expected vacuum profile is thus required. Results of this analysis and vacuum calculations and measurements are presented.

INTRODUCTION

To provide radiation with high power, short pulse length and full coherence in the VUV and soft X-ray regime, BESSY plans to build a seeded FEL facility based on the high-gain harmonic generation scheme [1, 2]. The technical design report of the BESSY Soft X-ray FEL facility [3] was evaluated in 2006 by the German Science Council and recommended for funding subject to the condition that its key technology, the cascaded HGHG scheme, be demonstrated beforehand. To address this issue, BESSY is proposing the proof-of-principle facility STARS [5] for a two-stage HGHG cascade which will serve as a user facility even after the commissioning of the BESSY FEL. The STARS is seeded by a tunable laser covering the spectral range of 700 nm to 900 nm. The target wavelength ranges from 70 nm to 40 nm with peak powers up to a few hundred MWs and pulse lengths less than 20 fs (rms). The polarization of the fully coherent radiation is variable. For efficient lasing a 325 MeV driver linac is required. It consists of a normal-conducting gun, superconducting TESLA-type modules modified for CW operation and a bunch compressor, for more details see please [4, 5, 6].

The STARS comprises a cascade of two HGHG stages each consisting of an undulator (acting as modulator) / dispersive chicane / undulator (acting as radiator) section. The two modulators and the first radiator of the STARS are planned as planar devices. The second (final) radiator needs to be helical to provide full polarization control of the output radiation. This radiator consists of three undulator modules and will be realized as an APPLE III [7] device.

The period lengths and the minimum gaps, i.e. free aperture between the magnet rows, of the undulators are chosen such that the desired wavelength range can be covered for an electron beam energy of 325 MeV. The planar devices have a period length of 50 mm and a minimum gap of 20 mm and 10 mm respectively. The period length of the final radiator amounts to 22 mm and the minimum gap is 7 mm. This small gap translates into 2.5 mm for the vacuum chamber inner radius.

Generally, the small conductance caused by such a small aperture leads to a higher pressure, which has to be counteracted by a suitable vacuum pumping scheme as far as possible. An other impact of the small aperture is the enhancement of the wakefields. In spite of the moderate peak current of 500 A predicted for STARS, an increase of the undulator wakefields can be expected.

The degradation of the electron beam quality due to the higher pressure and the change in the electron energy by the wakefields decline the FEL output radiaton. We present a analysis of their impact on the FEL performance.

CIRCULAR BEAM PIPE AND APPLE III TYPE RADIATOR

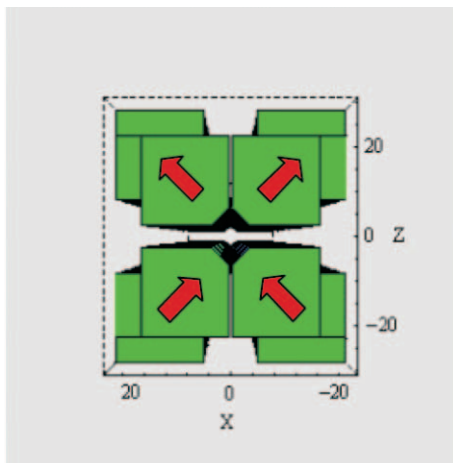

Figure 1: A sketch of the magnetic structure of an APPLE III device.

The second radiator will be realized as an APPLE III device providing full polarization control of the radiation. This APPLE type requires a round beam pipe to allow for more magnetic material located close to the electron beam, see Figure 1. For the second radiator of STARS, the free aperture between the magnets is 7 mm and the smallest vertical distance amounts to 4.4 mm which provides enough space for Hall probe measurements as well as for a fixture to support the vacuum chamber. An APPLE III type structure has been chosen for a number of reasons:

*Work supported by the Bundesministerium für Bildung und Forschung and the Land Berlin
† meseck@bessy.de

- For the same minimum aperture (7mm in this case) the APPLE III device provides a factor of 1.35 higher fields when compared to the APPLE II design. Note that the minimum aperture of 7 mm is limited by the acceptable aperture of the electron collimation system and the alignment concept.
- The natural focusing of an APPLE III design is smaller than that of an APPLE II. The natural focusing depends on the transverse field profiles which changes with gap and row phase of the variably polarizing Radiator. The focusing strength has an impact on the electron beam size and has to be compensated by a superposed external quadrupole lattice.
- The APPLE III design provides space for the installation of glass fiber radiation monitors (to detect beam loss) close to the electron beam without sacrificing gap (the diameter of Cherenkov glass fibers is 0.7mm) [8, 9].

However, the needed circular beam pipe with the small inner radius of 2.5 mm reduces the vacuum conductance, even more than an elliptical beam pipe with a short axis of 2.5 mm. Therefore a suitable pumping scheme has been designed.

VACUUM SYSTEM

A carefully designed pumping system for the second radiator requires 3 m long modules with 1 m long sections between them. The intersections will comprise the pump,focussing quadrupoles, phase shifter and diagnostic. Figure 2 shows the calculated vacuum profile for this scheme. The peak value is in the 10^{-6} mbar range. Measurements with a commercially available copper tubing (with a inner radius of 2 mm) have yielded a value of 5×10^{-7} mbar. After several weeks of measurement the pressure fell to 2×10^{-8} mbar. Therefor pressures less than 1×10^{-7} mbar can be expected for the final radiator.

Gas pressures in this range are not expected to produce significant radiation damage in the undulators or impact the photon flux. The question, whether the elastic scattering on nuclei, which provides the major contribution to the scattering process for 300 MeV electrons, can cause a noticeable angle error, has been investigated by analytical models [10, 11, 12] and Monte-Carlo simulations. The results of the calculation and simulations with GEANT3 and GEANT4 [13, 14] are summarized in Figure 3. Depicted is the number of scattered electrons per solid angle versus the scattering angle (for 300 MeV electrons). The electrons are scattered on N_2 in a target length of 4 m with a pressure of 10^{-5} mbar. Most electrons are scattered in a very small angle, less than 0.01% have a scattering angle larger than 10 μrad. Therefore, for a vacuum pressure less than 10^{-5} mbar the scattering on rest gas can be neglected.

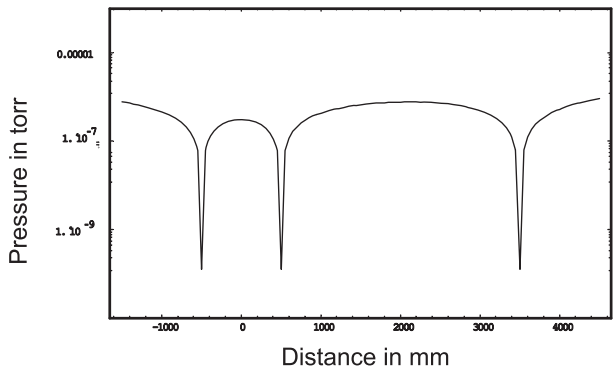

Figure 2: The calculated vacuum profile of the second radiator with a module length of 3 m.

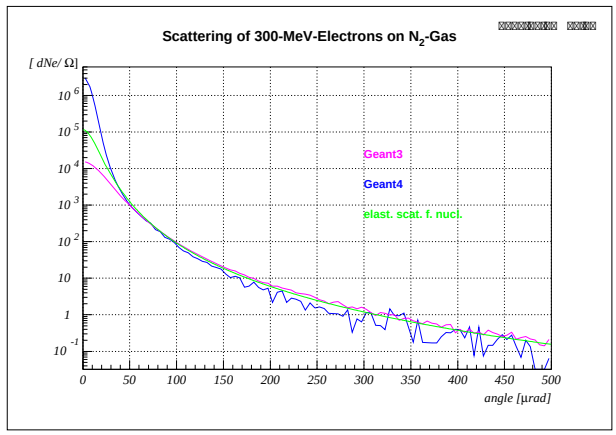

Figure 3: The number of scattered electrons per solid angle versus the scattering angle for 300 MeV electrons scattered on N_2 in a target length of 4 m with a pressure of 10^{-5} mbar.

WAKEFIELDS

Due to the small aperture of the second radiator, measurable wakefields are expected in spite of the low peak current of 500 A. The change of the electron energy by these wakefields could perturb the FEL interaction by pushing the electrons off-resonance. An analysis of the wakefields was performed to estimate their impact on the FEL performance.

Figure 4 shows the temporal profile of the wakefields, where the black line is the resistive wake, the blue line is the geometrical wake, the red line is the sum of them and the green line is the current profile. Two examples are shown for different inner radii (r) of a copper pipe. The aperture for the diagnostic box (gap) is 20 mm. The temporal profile of the wakefields for different aperture of diagnostic box are depicted in Figure 5, also an example with aluminum pipe is shown.

The dominant sources were found to be the resistive wall wakes and the effect of geometry at the diagnostic ports, each contributing about 50% to the total wakefield. Max-

imum calculated values were of order 5 kV/m for a pipe inner radius of 2.5 mm.

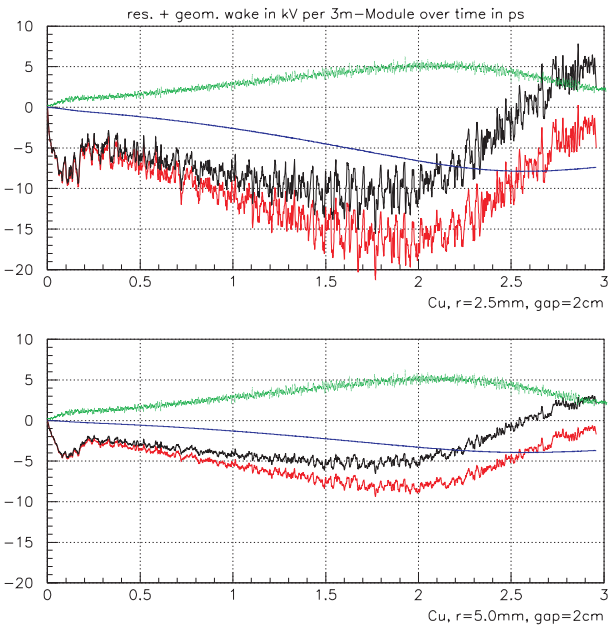

Figure 4: Temporal profile of the wakefields, where the black line is the resistive wake, the blue line is the geometrical wake, the red line is the sum of them and the green line is the current profile in [a.u.].Two examples are shown for different inner radii (r).

Compared with published LCLS wakefield calculations [15, 16] the peak current in STARS is more than 20 times smaller and in turn much weaker wakefields are expected. There is no advantage of the use of aluminum pipe for the second radiator of STARS, see Figure 5. Note that for STARS the AC component of the resistive wall wakefields can be neglected, as the STARS bunch ($500\mu m$ rms [6]) is much longer than the LCLS bunch ($20\mu m$ rms [15]).

The energy loss due to the wakefields (5 keV/m) was included in the calculation of the FEL radiation using GENESIS [17]. Figure 6 compares the FEL performance with and without the energy loss. The temporal and spectral profiles of the FEL output are shown for the shortest target wavelength of STARS. For a beam pipe with a inner radius of 2.5 mm and the expected beam properties of STARS, the impact of the wakefields is negligible.

CONCLUSION

A small-aperture vacuum-chamber with an inner radius of 2.5 mm is planned for the second radiator of STARS. Generally, such a small aperture leads to a higher pressure and an increase of the wakefields. Thus it causes a degradation of the FEL output.

The expected pressure and its impact on the electron beam has been calculated for the second radiator. Additionally, the pressure was measured in a test setup. The

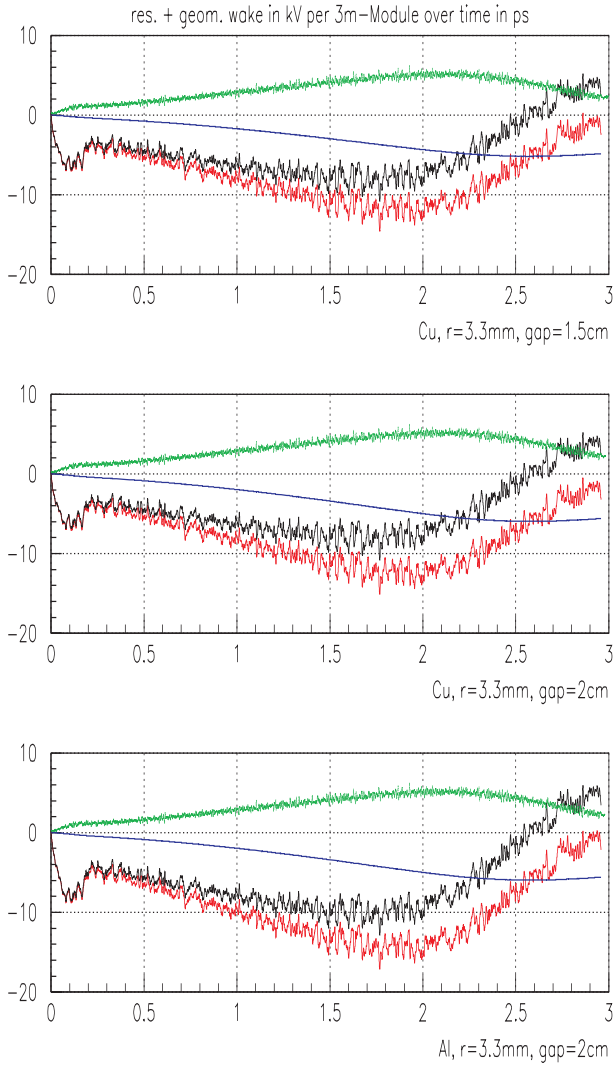

Figure 5: Temporal profile of the wakefields, where the black line is the resistive wake, the blue line is the geometrical wake, the red line is the sum of them and the green line is the current profilein [a.u.]. Three examples are shown for different aperture of diagnostic box (gap) and materials.

increase of the pressure seems to be very moderate. Thus the electron beam will not be disturbed.

Due to the wakefields, an energy loss of 5 keV/m is expected for the second radiator. Including this in the FEL simulations, almost no impact could be observed. We conclude that the small-aperture beam-pipe of the second radiator causes almost no degradation of the FEL performance.

REFERENCES

[1] L. Yu,“Theory of high gain harmonic generation: an analytical estimate ,” NIM A 483 (2002) 493.

[2] L. Yu, “High-gain harmonic generation of soft X-ray with the “fresh bunch” technique,” NIM A 393 (1997) 96.

[3] “The BESSY Soft X-ray Free Electron Laser, Technical De-

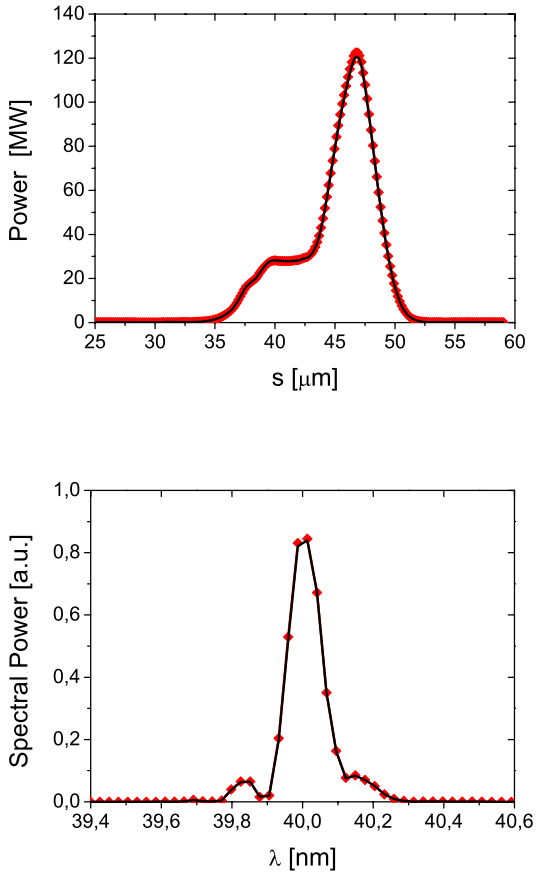

Figure 6: Temporal (top) and spectral (bottom) profiles of the FEL output are shown for the shortest wavelength (i.e. 40 nm) aimed at STARS with (black line) and without (red diamond) the energy loss due to the wakefield.

sign Report", March 2004, eds.: D. Krämer, E. Jaeschke, W. Eberhardt, ISBN 3-9809534-08, BESSY, Berlin (2004).

[4] B. Kuske, K. Goldammer, A. Meseck, "Output Performance of the STARS HGHG Demonstrator at BESSY", this conference.

[5] "STARS - Proposal for the Construction of a Cascaded HGHG FEL", eds.: J. Knobloch, E. Jaeschke, W. Eberhardt, BESSY, Berlin (2006).

[6] T. Kamps et al., "STARS - A Two-Stage High-Gain Harmonic Generation FEL Demonstrator", proceedings PAC07.

[7] J. Bahrdt, W. Frentrup, A. Gaupp, B. Kuske, A. Meseck, M. Scheer, "UNDULATORS FOR THE BESSY SOFT-X-RAY FEL", proceedings FEL 2004, Trieste, Italy.

[8] J. Bahrdt,"APPLE UNDULATORS FOR HGHG-FELS",proceedings FEL 2006, Berlin, Germany.

[9] J. Bahrdt," Status of the Undulator System of the Seeded HGHG-FEL Test bench at MAX-Lab", this Conference

[10] J.D. Jackson, "Classical Electrodynamics", 2.Edition (1975).

FEL projects

[11] W. A. McKinley, "The Coulomb Scattering of Relativistic Electrons by Nuclei", Phys.REV.74 (1948) 1759.

[12] J. Le Duff, "Current and Current Density Limitations in Existing Electron Storage Rings," NIM A 239 (1985) 83.

[13] S. Agostinellia et al.,"GEANT4 - A Simulation Toolkit", NIM A506 (2003), 250-303R. Brun et al.

[14] "GEANT Detector Description and Simulation Tool", v. 3.21, CERN Program Library CERN (1993).

[15] K. L. F. Bane, G. Stupakov, "Resistive Wall Wakefield in the LCLS Undulator", proceedings PAC05.

[16] S. Reiche et al., "Optimization of the LCLS X-ray FEL output performance in the presence of strong undulator wakefields", proceedings PAC05.

[17] S. Reiche, "GENESIS 1.3", NIM A 429(1999) 243.

MEASUREMENT OF THE PROJECTED NORMALIZED TRANSVERSE EMITTANCE AT PITZ*

L.Staykov†, J. Bähr, C. Boulware, H. J. Grabosch, L. Hakobyan, M. Hänel, S. Khodyachykh, S. Korepanov, M. Krasilnikov, S. Lederer, A. Oppelt‡, B. Petrosyan, S. Rimjaem, A. Shapovalov§, F. Stephan, DESY, Zeuthen, Germany
J. Rönsch, Hamburg University, Hamburg, Germany
D. Richter, BESSY, Berlin, Germany
K. Flöttmann, DESY, Hamburg, Germany
G. Asova, K.Boyanov, I.Tsakov, INRNE-BAS, Sofia, Bulgaria

Abstract

The main objective of the Photo Injector Test facility at DESY in Zeuthen (PITZ) is the production of electron beams with minimum transverse emittance at 1 nC bunch charge. PITZ consists of a photo cathode RF gun, solenoids for compensation of the space charge induced emittance growth and a booster cavity. In order to study the emittance evolution along the beam line three Emittance Measurement SYstems (EMSY's) were installed downstream of the booster cavity [1]. In a first operation period in October 2006 the emittance was measured for gun gradients of about 40 MV/m. A new gun cavity is presently installed at PITZ and conditioning up to a gradient of 60 MV/m is ongoing. In this work we present recent results from measurements of the normalized projected transverse emittance of the electron beam. The emittance is measured using the so called single slit scan technique. Measurements are presented for different gun and booster gradients, solenoid strengths and initial beam size at the photocathode.

INTRODUCTION

Major goal of PITZ is the development and optimization of electron sources that fulfill the requirements for SASE FEL's such as FLASH and XFEL. The optimization process is conducted by extended numerical simulations using ASTRA [2], and closely followed by research and development of appropriate instruments for electron and laser beam characterization (see [3, 4]).

A simplified scheme of PITZ is shown on Figure 1. It consists (right-to-left) of a 1.5 cell L-band RF gun equipped with a Cs_2Te cathode, pair of solenoids for space charge compensation, low energy beam diagnostics, a booster cavity, high energy diagnostics including three EMSY's (installed at 4.3, 6.6 and 9.9 m downstream the cathode) and a beam dump. A photocathode laser system provides carefully shaped laser pulses with variable transverse diameter and flat hat longitudinal distribution (see [4, 5]).

In this paper we present results from the emittance measurements made in October 2006 and summer 2007 using two different gun cavities:

- prototype 3.1 conditioned in summer 2006 and optimized in October 2006 up to the maximum requirements for FLASH with a peak power of 3.5 MW resulting in gun gradient of about 40 MV/m [6];
- prototype 3.2 which was conditioned and optimized this summer with a peak power of up to 6.9 MW resulting in a gun gradient of $\sim$60 MV/m [7].

For gun prototype 3.1 the emittance was measured using the three existing EMSY's as a function of the main solenoid focusing current for various booster phases. For prototype 3.2 the emittance was measured only at the first EMSY (distance from the cathode 4.3 m) for various beam sizes at the cathode and different energy gain from the booster. In addition the optimized settings for gun 3.1 were applied to gun 3.2 and the emittance was measured, the results are compared and discussed.

EMITTANCE MEASUREMENT SETUP

The transverse emittance at PITZ is measured using the so called *single slit scan* technique. A schematic representation of the technique is shown on Fig. 2. For this technique the uncorrelated local divergence is estimated by cutting the electron beam into thin slices and measuring their size on a screen after propagation in a drift space. The so called sheared normalized RMS emittance is then calculated using the following definition [8]:

$$\varepsilon_n = \beta\gamma \cdot \sqrt{\langle x^2 \rangle \cdot \langle x'^2 \rangle}. \quad (1)$$

Here $\langle x^2 \rangle$ and $\langle x'^2 \rangle$ are the second central moments of the distribution of the electrons in the so called trace phase space where $x' = p_x/p_z$ represents the angle of a single electron trajectory with respect to the whole beam trajectory[1]. The RMS beam size is measured on an additional OTR or YAG screen at the position of the slits. The uncorrelated divergence is obtained by analyzing the profiles of

* This work has partly been supported by the European Community, Contract Number RII3-CT-2004-506008, and by the 'Impuls- und Vernetzungsfonds' of the Helmholtz Association, contract number VH-FZ-005.

† Presenting author, e-mail: lazaraza@ifh.de
‡ now at PSI, Vilingen
§ on leave from MEPHI, Moscow

[1] valid for small momentum spread within the bunch, otherwise more precise definition should be used (i.e. [9]).

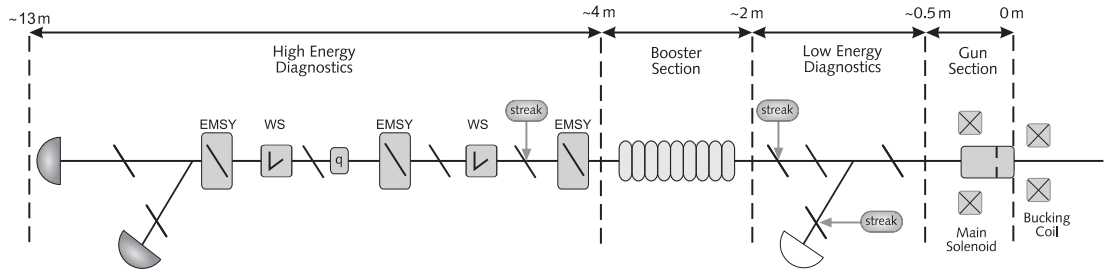

Figure 1: Layout of PITZ.

the beamlets produced from the slits which drift some distance L_d downstream. There the spatial distribution of the beamlets corresponds to the local uncorrelated divergence, $\langle x'^2 \rangle_{local}$ which can be derived from the size of the beamlet using:

$$\sqrt{\langle x'^2 \rangle_{local}} = \frac{\sqrt{\langle x_b^2 \rangle}}{L_d}. \quad (2)$$

Here $\sqrt{\langle x_b^2 \rangle}$ is the RMS size of the beamlet on the screen after distance L_d. The total uncorrelated divergence of the beam is estimated by a weighted average of several measurements of the local divergence taken from different locations across the beam:

$$\langle x'^2 \rangle = \sum_{i=1}^{N} w_i \cdot \langle x'^2 \rangle_i. \quad (3)$$

The Lorentz factors $\beta\gamma$ is measured using a dispersive section downstream of EMSY.

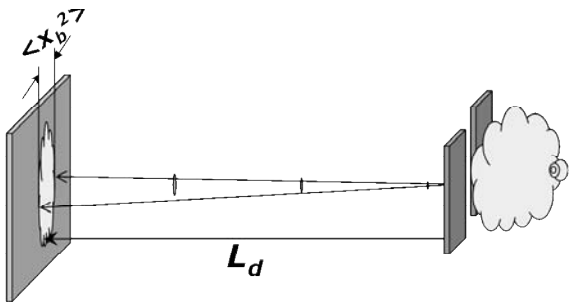

Figure 2: Schematic representation of the single slit scan technique.

The measurement system was optimized to measure emittance as low as 1 mm.mrad for 1 nC charge per bunch with precision better than 10 % (see [10]). The slits are mounted on two orthogonal actuators which host also the YAG and OTR screens for transverse beam distribution measurements. Single slit masks with slit opening of 10 and 50 μm and thickness of 1 mm. Rotating and goniometric stages are providing precise angular adjustment of the actuators for improved angular acceptance of the system.

EMITTANCE MEASUREMENTS

On Fig. 3 the evolution of the beam emittance as simulated with ASTRA[2] is shown for the two different accelerating gradients, 40 and 60 MV/m, used for the measurements. The simulation parameters are set close to PITZ machine parameters, shown in Table 1. The curves look different since for 40 MV/m the goal of the optimization was to have the slowest rise of the emittance along the beam axis in order to resemble the conditions for emittance conservation. At 60 MV/m the goal was to have the minimum emittance at 4.3 m downstream the cathode (location of EMSY1).

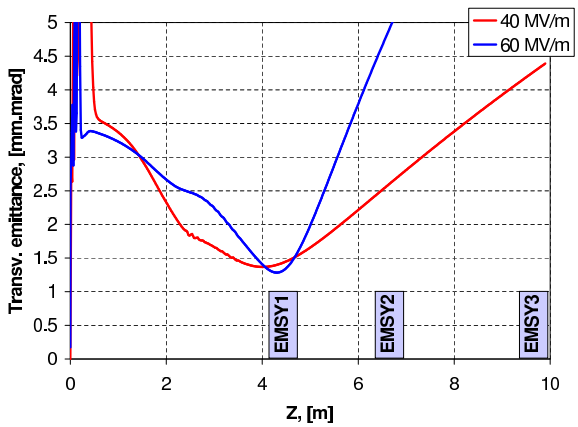

Figure 3: Emittance evolution along the beamline for two different gun gradients.

40 MV/m accelerating gradient at the cathode

The characterization of gun 3.1 was done with maximum input power of 3.5 MW. Therefore, all the emittance measurements were made with a maximum accelerating gradient of about 40 MV/m which resulted in a maximum mean beam momentum right after the gun of up to about 5 MeV/c. In addition, at solenoid currents below 280 A, the full beam size at z=1.0 m was approaching 12 mm which is the size of the vacuum chamber at the low energy dispersive arm located at this position (see Fig. 1). This was a further limitation to our available optimization range.

[2] all the RF phases are relative to the phase of maximum mean momentum gain in ASTRA

Table 1: Machine parameters for emittance measurements.

par.	gun 3.1	gun 3.2	Units
E_{acc}	43	∼60	MV/m
ϕ_{gun}	-2	0	deg
I_{main}	274-290	365-376	A
P_{mean}	12.85	11 to 14.8	MeV/c
$\phi_{booster}$	0 to -20	0	deg
XY_{ini}	0.51	0.33 to 0.55	mm
r_t/f_t	6-8	6-8	ps
$FWHM$	∼18	∼20	ps

On Fig. 4 the dependence of the projected normalized transverse emittance on the current in the main solenoid at three different locations along the beamline is shown. All other injector parameters are fixed as shown in the Table 1, $\phi_{booster}$ = ϕ_{ref}-10 deg. A minimum is visible for EMSY1 around $I_{main} = 282$ A. For the other two stations the minimum of the emittance could not be characterized because of the above mentioned limitations in the optimization range. Another notable fact is the large disagreement between the results at EMSY3, $I_{main} = 284$ A, and the simulations shown on Fig. 3. This can be explained by a large error of the beam size measurements due to the fact that the beam at EMSY3 is of a size comparable with the screen. Also the narrow dipole chamber in the low energy section could cause a dilution of the phase space.

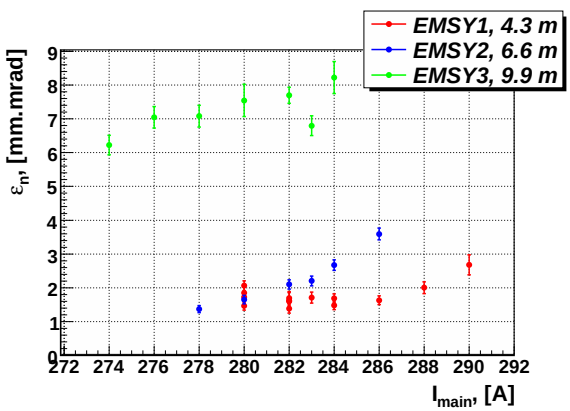

Figure 4: Emittance as a function of the current in the main solenoid. Gun at 40 MV/m and booster phase with respect to the maximum acceleration phase is -10 deg.

On Fig. 5 a comparison between gun 3.1 and 3.2 is shown, the machine settings were set such to reproduce the conditions during the measurements with gun 3.1, namely the mean momentum from the gun (4.95 MeV/c), final momentum after the booster (12.85 MeV/c) and the laser spot size on the cathode (initial beam size ∼ 0.51 mm). Altough there is agreement within the error bars between the minimum values, $\varepsilon_{n,3.1} = 1.37 \pm 0.14$, $\varepsilon_{n,3.2} = 1.54 \pm 0.15$, there is obvious large discrepancy between the minimum

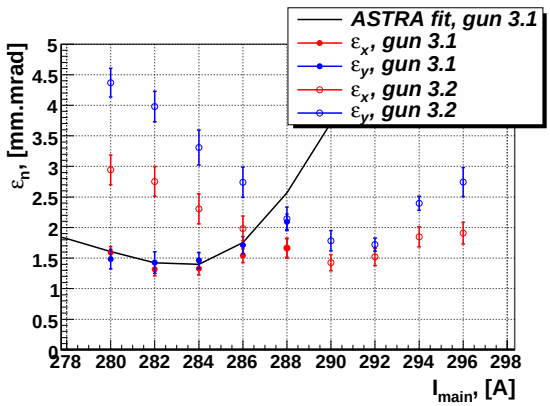

Figure 5: Comparison of the measurement with gun 3.1 and gun 3.2 as well as with ASTRA simulations for the gun 3.1 case. The machine was set to have the same mean momentum at about 40 MV/m, booster phase with respect to the maximum acceleration phase is -5 deg, initial beamsize is 0.5 mm.

position with respect to I_{main} of about 8 A. This large discrepancy is still to be understood.

60 MV/m accelerating gradient at the cathode

For the gun 3.2 the RF power in the cavity was increased up to the limit of our RF system (∼ 7 MW in the gun). This corresponds to an accelerating gradient of about 60 MV/m or mean beam momentum after the gun up to 6.5 MeV/c However the problem with the aperture at the low energy dispersive arm remained therefore we decided to use only the first EMSY (z=4.3 m) and to optimize for lowest emittance at this location. One of the optimization parameters was initial beam size (laser spot size at the cathode) The main solenoid current (I_{main}) was scanned around the beam waist at EMSY1. The energy gain from the booster cavity was varied such that the final beam momentum was tuned to 9.5, 11.0, 13.0 and 14.5 MeV/c.

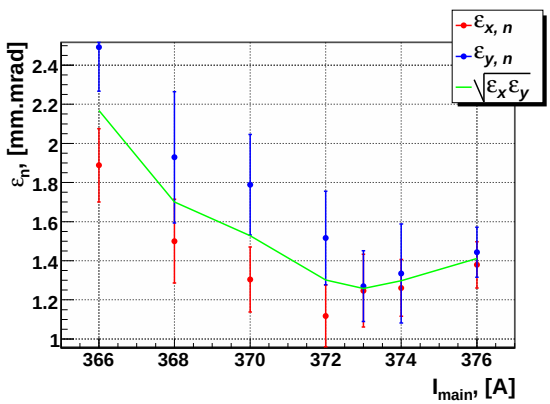

Figure 6: Emittance as a function of the main solenoid focusing strength. Gun 3.2, mean momentum after the booster 14.45 MeV/c.

On Fig. 6 one sees the dependence of the projected emittance on the focusing strength of the main solenoid. The geometrical average minimum of the measured emittance is 1.26 $\pm$ 0.18 mm mrad. Analog scans have been performed at different momentum gain from the booster. For fixed laser parameters, gun gradient and phase, as well as booster phase the minimum emittance obtained from a scan of I_{main} is shown in Fig. 7 as a function of the momentum gain in the booster.

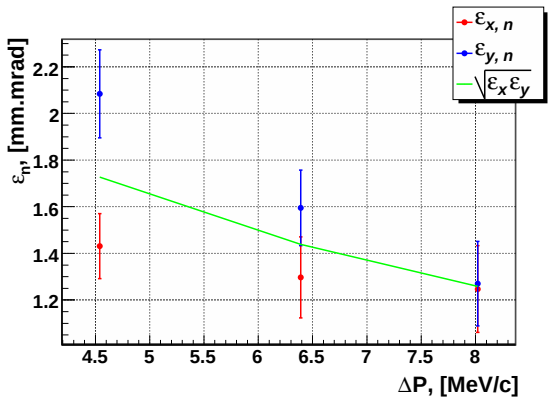

Figure 7: Minimum of the emittance as a function of the momentum gain in the booster.

The beam emittance has been re-measured in details for the best machine parameters: $P = 14.45$ MeV/c, $I_{main} = 373$ A, $XY_{ini} = 0.33$ mm. A very good reproducibility of about 2-3% has been demonstrated. Furthermore we did a very detailed scan with the slit technique, using as small as 25 μm separation between the individual slit positions. The phase space distribution is shown on Fig. 8. To the authors knowledge this image has unprecedent resolution in the trace space for such beam parameters. The ultimate resolution of our current system is estimated to be 36 μm x 15.4 μrad.

CONCLUSIONS

Gun 3.1 was conditioned up to 40 MV/m and characterized resulting in normalized beam emittance of 1.37 $\pm$ 0.14 mm mrad.

Corresponding machine parameters were applied to gun 3.2 at 40 MV/m yielding 1.54 $\pm$ 0.15 mm mrad.

Gun 3.2 was conditioned up to 60 MV/m and delivered minimum transverse normalized emittance of 1.26 $\pm$ 0.18 mm.mrad.

REFERENCES

[1] L.Staykov et al., "Commissioning of a New Emittance Measurement System at PITZ", FEL'06.

[2] K.Flötmann, ASTRA, http://www.desy.de/˜mpyflo

[3] S.Khodyachykh et al., "New beam diagnostic developments at PITZ", Proceedings of the PAC'07

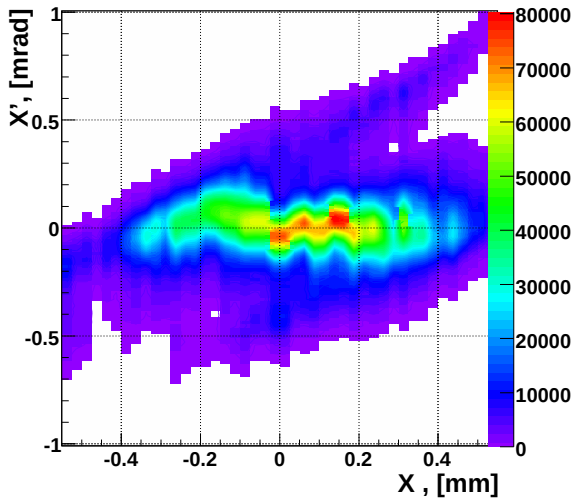

Figure 8: Phase space distribution at $P = 14.45$ MeV/c, $I_{main} = 373$ A, on crest phases of gun and booster.

[4] M.Hänel et al., "Photocathode Laser Pulse Diagnostics at PITZ", Proceedings of the FEL'07

[5] J.Bähr et al., "Upgrades of the Laser Beam-line at PITZ", Proceedings of the FEL'05

[6] A.Oppelt et al., "Tuning, Conditioning and Dark Current Measurements of a New Gun Cavity at PITZ", Proceedings of the FEL'06

[7] S.Rimjaem et al., "Status and Perspectives of the PITZ facility upgrade", Proceedings of the FEL'07

[8] V.Miltchev, "Investigations on the transverse phase space at a photo injector for minimized emittance", PhD thesis, Humboldt University Berlin

[9] K. Flöttmann, Some basic features of the beam. emittance, Phys. Rev. ST Accel. Beams 6

[10] L.Staykov et al., "Design Optimization of an Emittance Measurement System at PITZ", Proceedings of the DIPAC'05.

STATUS OF THE SPARX FEL PROJECT*

C.Vaccarezza, D.Alesini, M.Bellaveglia, S.Bertolucci, M.E Biagini, R.Boni, M.Boscolo, M.Castellano, A.Clozza, L.Cultrera, G.Di Pirro, A.Drago, A.Esposito, M.Ferrario, D.Filippetto, V.Fusco, A.Gallo, A.Ghigo, S.Guiducci, M.Migliorati, L.Palumbo, L.Pellegrino, M.Preger, C.Sanelli, M.Serio, F.Sgamma, B.Spataro, A.Stella, F.Tazzioli, M.Vescovi, C.Vicario, INFN Frascati, Italy
F. Ciocci, G.Dattoli, A.Doria, F.Flora, G.Gallerano, L.Giannessi, E.Giovenale, G.Messina, P.L. Ottaviani, G.Parisi, L.Picardi, M.Quattromini, A.Renieri, C. Ronsivalle ,ENEA C.R. Frascati, Italy
S.Cialdi, C.Maroli, V.Petrillo, M. Rome, L.Serafini, INFN-Milano, Italy
L.Catani, E.Chiadroni, A. Cianchi, C.Schaerf, INFN-Roma II, Roma, Italy
P.Musumeci, M.Petrarca, INFN Roma, Italy
F.Alessandria, A.Bacci, F.Broggi, C.De Martinis, D.Giove, M.Mauri, INFN/LASA, Segrate, Italy
L.Ficcadenti, M.Mattioli, A.Mostacci, University La Sapienza, Roma, Italy
P.Emma, SLAC, Menlo Park, CA, U.S.A.
S.Reiche, J. Rosenzweig, UCLA, Los Angeles, CA, U.S.A

Abstract

The SPARX project consists in an X-ray-FEL facility jointly supported by MIUR (Research Department of Italian Government), Regione Lazio, CNR, ENEA, INFN and Rome University Tor Vergata. It is the natural extension of the ongoing activities of the SPARC collaboration. The aim is the generation of electron beams characterized by ultra-high peak brightness at the energy of 1 and 2 GeV, for the first and the second phase respectively. The beam is expected to drive a single pass FEL experiment in the range of 13.5-6 nm and 6-1.5 nm, at 1 GeV and 2 GeV respectively, both in SASE and SEEDED FEL configurations. A hybrid scheme of RF and magnetic compression will be adopted, based on the expertise achieved at the SPARC high brightness photoinjector presently under commissioning at Frascati INFN-LNF Laboratories [1,2]. The use of superconducting and exotic undulator sections will be also exploited. In this paper we report the progress of the collaboration together with start to end simulation results based on a combined scheme of RF compression techniques.

THE SPARX LAYOUT

A spectral range from 13 nm to 1 nm has been considered for the radiation. SASE-FEL's in this wavelength range require high brightness beam at the undulator entrance. In Table 1 the electron beam parameter list is reported for such a source, while in Fig. 1 the schematic layout of the accelerator is shown. A 150 MeV SPARC-like photoinjector [1] is meant to provide a 300-500 A beam, adopting the velocity bunching compression scheme. A first linac section L1 rises the beam energy up to 300 MeV, where a first magnetic chicane is foreseen mainly for comparing the overall efficiency between the two compression methods at low energy. After a second linac section L2, i.e. at the energy around 0.6 GeV, the main magnetic compressor BC2 is located rising the beam peak current up to I_{pk}≈1 kA, according to a 'hybrid' compression scheme consisting in one RF compression stage at low energy, plus one magnetic chicane at 0.6 GeV. A third accelerating section L3 brings the beam energy up to E≈1GeV and a first extraction dogleg DL1 drives the beam through a diagnostic section and to the first undulator where both SASE and seeding experiments in the radiation wavelength range of λ_r≈ 13 ÷5 nm are foreseen. This is what is meant for the first phase of the SPARX project. For the Phase II another linac section will bring the beam energy up to 1.5 GeV where a third magnetic chicane BC3 is foreseen to compress the beam and reach peak currents of the order of I_{pk}≈2÷2.5 kA. The last linac L4 brings the final energy up to E=2GeV. A second extraction dogleg DL2 provides the beam diagnostics and delivery to the second undulator for the wavelength range λ_r≈ 5÷1.5 nm

Table 1: Electron beam parameters

Beam Energy	1÷2	GeV
Peak current	1-2.5	kA
Emittance (average)	2	mm-mrad
Emittance (slice)	1	mm-mrad
Energy spread (correlated)	0.1	%
Repetition Rate	50	Hz

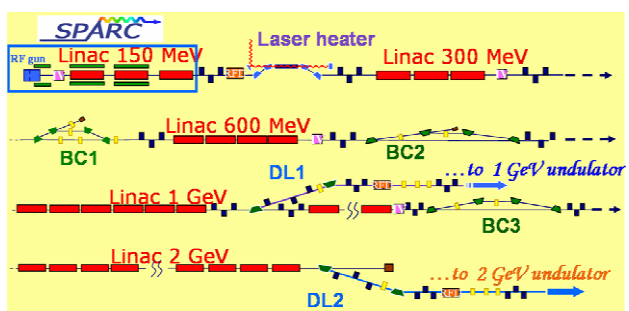

Fig. 1: SPARX Linac schematic layout

*Work partially supported by MIUR for the realization of "Grande Infrastruttura Laser ultrabrillante per raggi X multiscopo"

The RF Photoinjector

The injector design is based on the SPARC high brightness photoinjector presently under commissioning at Frascati Laboratories [1,2]. It considers a 1.1 nC bunch 10 ps long (flat top) with 1.1 mm radius, generated inside a 1.6-cell S-band RF gun of the same type of the BNL-SLAC-UCLA one [3] operating at 120 MV/m peak field equipped with an emittance compensating solenoid. Three standard SLAC type 3-m TW structures each one embedded in a solenoid boost the beam up to 150 MeV. According to the simulation results the beam compression at low energy (<150 MeV), still in the space charge dominated regime, turns out to be feasible provided that a proper emittance compensation technique is adopted [4], Moreover the propagation of a short bunch in the following accelerating sections reduces the potential emittance degradation caused by transverse wake fields, while a proper phasing of the linac can control the longitudinal wake fields. A systematic study based on PARMELA code simulations has been done in order to optimize the parameters that influence the compression [5], the results of computations show that peak currents up to kA level are achievable at the injector exit with a good control of the transverse and longitudinal emittance by means of a short SW section operating at 11424 MHz [6] placed before the first accelerating section. On the other side the results obtained without the IV harmonic correction prior the RF compressor, show that is anyway possible to reach good compression factors but paying for a heavy deformation of the longitudinal bunch distribution, a strong sensitivity to RF compressor phase, and a highly non linear longitudinal phase space. In Table 2 a summary is reported of the RF compression studies results. A medium RF compression factor has been chosen and presented here as the first referring case for the SPARX beam dynamics studies, it gives an average peak current I_{pk}≈400 A at the exit of the photoinjector, as highlighted in Table 2 and shown in Fig. 2.

The Linac

In the present configuration the SPARX accelerator (PHASE I and II) is composed of four separate S-band linac sections L1, L2, L3, L4, with E= 25 MV/m accelerating field, located downstream a SPARC-like photoinjector (see Fig. 1). At the entrance of each of the three magnetic chicanes an X-band section is provided to linearize the beam longitudinal phase space prior the magnetic compression. For the 1 GeV channel of Phase I, both L1 and L2 sections are meant to work off crest, to provide the required energy chirp to compress the beam in BC2, while the on crest L3 section rises the beam energy up to E=1 GeV and contributes to the energy spread reduction. For the magnetic compression in BC3, the proper off-crest acceleration is applied also to the L3 section, while L4 contributes to the energy spread cancellation and brings the beam energy up to E=2GeV.

Table 2: RF compressor parameter

RF phase range	B1,B2,B3 (gauss)	Current (A)	Emittance (μm)
-60°/-75°	1200,0,0	117-151	0.7
-75°/-83°	1200,1400,0	151-249	0.8
-83°/-87°	1200,1400,0	249-458	1.3
-87°/-91°	1200÷1800	458-1180	2.8

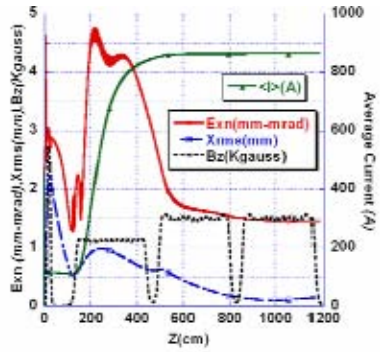

Fig. 2: Average current, transverse emittance and envelope, axial magnetic field vs. z for a final 450 A electron beam., tracked with PARMELA [7].

The invariant envelope matching condition will be applied to the lattice as proposed by Ferrario *et al* [8].

The Bunch Compression

To increase the beam current up to the kA order magnitude a magnetic compression stage is foreseen in the BC2 chicane for the beam with final energy E=1GeV, I_{pk}≈1 kA (Phase I), and in the BC3 chicane for the beam with final energy E=2 GeV, I_{pk}≈2.5 kA (Phase II). With the previously described setting for the RF photoinjector, a further compression factor of 2 in the BC2 chicane produces an average peak current I_{pk}≈1 kA, able to reach SASE saturation in the wavelength range of λ_r≈ 10÷6 nm at the energy of 1GeV. The parameters of the BC2 compressor for this case are shortly listed in Table 3. The photoinjector incoming beam has been generated with PARMELA, considering a thermal emittance value of ε_x≈0.6 μm, the downstream tracking in the chicane has been performed with ELEGANT [9]. The tracking in the BC2 chicane has also been checked with PARMELA and CSRtrack [10] codes in order to clarify the role played by the space charge effect in the transverse emittance dilution [11]. The three codes outputs show substantially that for a peak current around I_{pk}≈1 kA the space charge effect doesn't heavily contribute to dilution of the transverse emittance.

Table 3: BC2 compressor parameters .

Beam Energy	E	GeV	0.5
Initial rms bunch length	σ_{zi}	mm	210
Final rms bunch length	σ_{zf}	mm	90
Incoming energy spread	$\sigma_{\delta i}$	%	.45
Momentum compaction	R_{56}	mm	-27
2nd order mom. compaction	T_{566}	mm	+42

A hybrid compression scheme with velocity bunching and BC2 only is nevertheless foreseen and RF compression tests will be performed at the SPARC facility in the second half of 2007. After the BC2 compressor the energy of the beam is raised up to 1 GeV and the first dogleg DL1 delivers the beam to the 1 GeV undulator system, where both SASE and seeded radiation schemes are foreseen for a radiation length in the range of $\lambda_r \approx 13 \div 5$ nm. After the 1 GeV DL1 dogleg insertion another linac section brings the beam energy up to 1.5

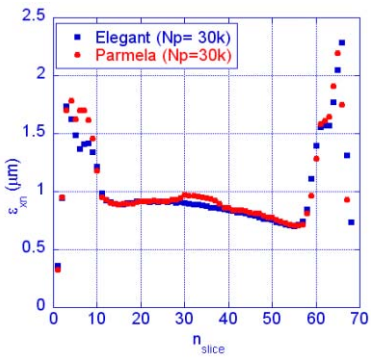

Figure 3: Slice analysis of the horizontal beam emittance after BC2 compressor as obtained with Elegant and Parmela code simulation.

GeV where the third magnetic compressor BC3 is located, in order to reach a peak current of the order of $I_{pk} \approx 2.5$ kA. After the last linac, at around 2 GeV, a second dogleg DL2 brings the beam to the second undulator system for radiation length in the range of $\lambda_r \approx 1.5 \div 5$ nm. A special attention is devoted to the space charge effect relevance in both the BC2 and BC3 compressors: in Fig. 3 the simulation results for the transverse beam emittance are reported as obtained with the Elegant and Parmela codes. A projected emittance dilution of the 30% is obtained so far; the compressor optimization is still in progress in order to further reduce the transverse dilution due to the space charge effect.

The undulator and FEL

Both SASE and seeded radiation modes are foreseen at each of the two energy steps of the SPARX channel. As an example in Table 4 the very preliminary parameter list is reported for the two undulators of a possible seeding experiment at 2.3 GeV. In Fig. 4 the radiation spectrum is shown for the fifth harmonic of the λ=13 nm seed. An intensive study is ongoing to explore the most suitable configurations according to the user community needs.

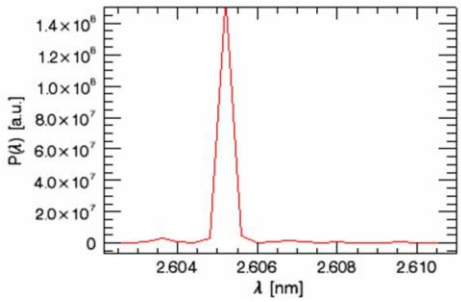

Figure 4: Radiation Spectrum of the fifth harmonic for a possible seeded scheme at 2.3 GeV.

Table 4: Preliminary Parameter list of Seeding Experiment example at 2.3 GeV. (Fig. 7)

	Undulator 1	Undulator 2
Periods	21	42
Sections	9	10
Period(cm)	5.4	2.7
K	4.299	2.51

CONCLUSIONS

The SPARX project aim is the generation of electron beams characterized by ultra-high peak brightness at the energy of 1 and 2 GeV, (Phase I and II), for SASE and SEEDED FEL experiments in the range of $\lambda_r \approx 13.5 \div 1.5$ nm. It is jointly supported by the Italian Government and Regione Lazio with a five years schedule for the first phase. The critical components such as the RF-compression scheme, magnetic chicane, etc. will be tested during the phase II of the SPARC project. A first general layout for SPARX has been proposed and first start to end simulations for the 1 GeV channel of Phase I, have been presented using a "hybrid" scheme of bunch compression with RF and magnetic compression techniques involved together.

REFERENCES

[1] http://www.lnf.infn.it/conference/sparx05/Giornate di Studio SPARX e Applicazioni
[2] A. Cianchi, *et al.*, Proc. of DIPAC07, Venice, Italy
[3] M. Ferrario, *et al.*, "Experimental results with the SPARC emittance-meter", Proc. of PAC07, Albuquerque, New Mexico, USA.
[4] C.Vicario, *et al.*, "Laser and RF Synchronization Measurements at SPARC", Proc. of PAC07, Albuquerque, New Mexico, USA.
[5] C. Ronsivalle *et al.* "Comparison Between SPARC E-Meter Meas. and Simulations", Proc. of PAC07, Albuquerque, New Mexico, USA.
[6] http://www.lnf.infn.it/acceleratori/sparc/SPARC Technical Design Report

[7] B. Spataro, *et al*, "A Bi-periodic X-band RF cavity for SPARC", Proc. of EPAC06, Edinburgh, Scotland
[8] L. Ficcadenti, *et al*, "RF measurements results of the final brazed SPARC RF deflector", Proc. of PAC07, Albuquerque, New Mexico, USA.
[9] L. Giannessi, *et al*, "Future Seeding Experiment at SPARC", Proc. of FEL 2006, Berlin, Germany.
[10] M.D. Dohlus, T. Limberg, "CSRtrack: Faster Calculation of 3-D CSR Effects, FEL04, Trieste.
[11]C.Vaccarezza, *et al*, "Status of SPARX FEL project", Proc. of EPAC06, Edinburgh, Scotland.

THE DRIVE LASER SYSTEM FOR CFEL

Li Weihua,Chen Yanan
Institute of Applied Electronics,CAEP,China

Abstract

A reliable and compact drive system is one of the key components for the stable operation of FEL.We have developed a solid-state drive laser system to meet the requirements of the CFEL(CAEP FEL) research.The system consisted of a passive mode-locked oscillator with a timing stabilizer,a regenerative amplifier and a frequency conversion part.After the 4-th harmonics,the duration of 15 picoseconds Gaussian pulses with wavelength 266nm at a repetition rate 54.17MHz were obtained.These micropulses were contained within a macropulses envelope as long as 1 to 6μs,which was emitted from the drive laser at a repetition rate at 3Hz,6Hz or 12Hz,one single micropulse energy as large as 4μJ was achieved.The design specifications, configuration and diode-pumped amplifier of the drive laser system are also described.

INTRODUCTION

A reliable and compact drive laser system is one of the key components for the stable operation of FEL.It will strongly affect the performance of the FEL,such as the specifications as following:the micropulse duration of electron beam,the micropulse current of electron beam,the jitter of micropulse-peak-current,and so on[1].We have developed a all-state-solid drive laser system to meet the requirements of the CFEL research,as shown in table 1.The laser stablility,e.g.,energy stability,timing stability and the pointing stability,was also requested stringently during the course of the research[2].

DRIVE LASER SYSTEM

The drive laser system,which was shown in Fig.1,was consisted of a passive mode-locked oscillator with a timing stabilizer,a regenerative amplifier and a frequency conversion part.

Oscillator

The seeding laser GE-100-XHP,is a passive mode-locked laser with a semiconductor absorber mirror (SESAM),developed by Time-Bandwidth Products Ltd, Switzerland[3].Its repetition rate is 54.167 MHz,equal to 1/24 of 1300MHz L-band radio frequency, which was used for the photocathode RF gun.The timing stabilizer measured the phase and the frequency offset between the laser pulses and the reference RF signal,and adjusted the cavity length to synchronize the two signals[4].

Regenerative Amplifier

It was composed of one-double-pass and two-single-pass stages.A Pockels Cell captured a “maropulse” from the continuous pulses output to increase the pulse energy.Every “macropulse” contains 50 to 300 micro-pulses,as long as 1us to 6us.

Harmonics Generator

This component coverted the fundamental output to the 4-th harmonics,which would illuminate the photocathode Cs_2Te.The net conversion efficiency was close to 20% from the fundamental to the 4-th harmonics.The UV energy was obtained up to 1.2mJ per “macropulse”,4uJ per micropulse.

LASER PERFORMANCE

Amplitude Uniformity

The amplitude uniformity from micropulse to micropulse in the same macropulse was quested stringently for the CFEL research.We have measured it at the port of regenerative amplifier,2-th harmonics and 4-th harmonics,as shown in Fig.2,Fig.3,Fig.4.The variation of amplitude uniformity from micropulse to micropulse was 3% rms or less.

Energy Stability

UV energy stability was measured for 300 shots by a power meter.The statistical results showed that the Energy fluctuation was 2.8%rms or less.The curve of energy deviation from the mean value was shown in Fig.5,which were 84 data from the 300 shots.

Timing Jitter

The timing jitter of the laser oscillator was estimated from the output of the phase detector in the feedback loop.A phase detector measured the phase difference between the fast photodiode signals of laser pulses and the reference RF signal,and generated an “error signal”.This phase difference was related to the timing jitter between the laser phase and the reference RF phase.The timing jitter of the oscillator was estimated as 0.4ps rms.

Pointing Stability

The pointing stability of 266nm output pulses was measured by a CCD camera.Beam profiles were measured on a screen plate at 30 meters away form the laser output port.Pointing stability of the beam centroid was estimated to be 0.1mrad rms in Y direction,and 0.01mrad rms in X direction,as showed in Fig.6 and Fig.7.The scale between the pixel to actual dimension was 13.7 pixels to 1mm.Fig.8 was the beam profile.

Other specifications and the laser performance were listed on Table 2.

CONCLUSION

The all-solid-state drive laser system has been developed on the basis of the laser diode pumping,the passive mode-locked oscillator with SESAM and the feedback timing stabilizer.The drive laser was reliable,compact and satisfying to meet the requirements of the CFEL research.

REFERENCES

[1] Li Zhenghong,Hu Kesong,Yang Maorong etc.The RF Photoinjector Research,High Power Laser and Particle Beams,2000,12(3):366

[2] F.Sakai,M.Yorozu,Y.Okada etc.All-Solid-State Picosecond Laser System for Photocathode RF Gun.

[3] High Power Mode-locked Diode-Pumped Picosecond Laser,User Mannual,Time-Bandwidth Ltd,Switzerland.

[4] Timing Stabilizer Feedback System Accessory,User Mannual,Time-Bandwidth Ltd,Switzerland.

[5] A.R.Fry,M.J.Fitch etc.Laser System for The TTF Photoinjector at FERMILAB.IEEE,1998

[6] J.Early,J.Barton etc.The Los Alamos FEL Photoinjector drive laser,Nuclear Instruments and Methods in Physics Research ,A318(1992)381-388

Tab.1 The Parameters of CFEL

1	Electron Energy/MeV	35-40
2	Beam Pulse Current/A	>30
3	Beam Pulse Duration/ps	3-5
4	Pulse Repetition Rate/MHz	54.17
5	Maropulse Duration/μs	1-6
6	Maropulse Rep. Rate/Hz	3-6-12
7	Pulse Timing Jitter/ps	<2
8	Micropulse Amplitude Jitter/rms	<3%
9	Energy Spread	<1%

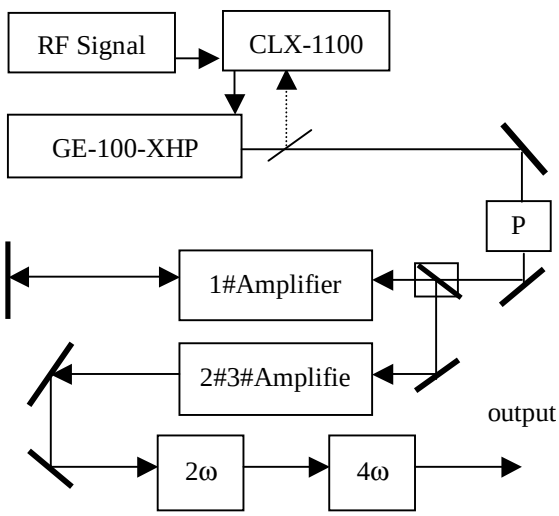

Fig.1 Layout of the Drive Laser System for CFEL

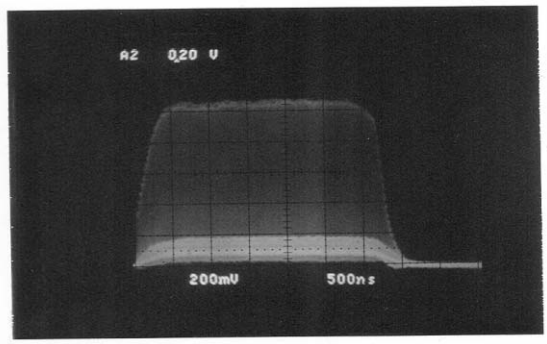

Fig.2 The amplitude uniformity at the port of amplifier

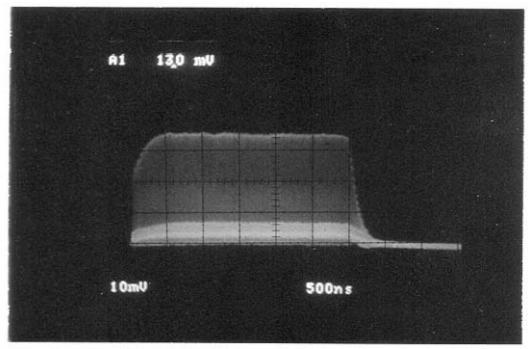

Fig.3 The amplitude uniformity at the port of 2-th harmonics

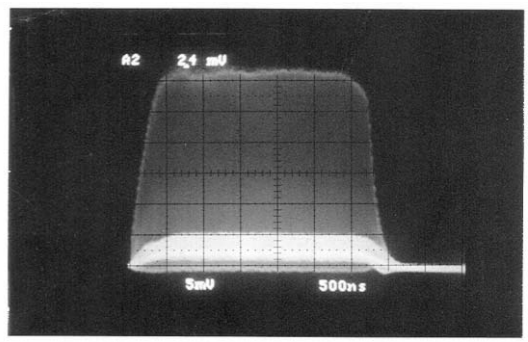

Fig.4 The amplitude uniformity at the port of 4-th harmonics

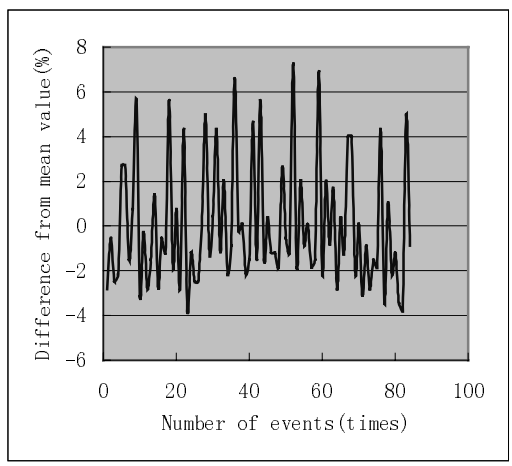

Fig.5 The UV energy fluctuation from mean value

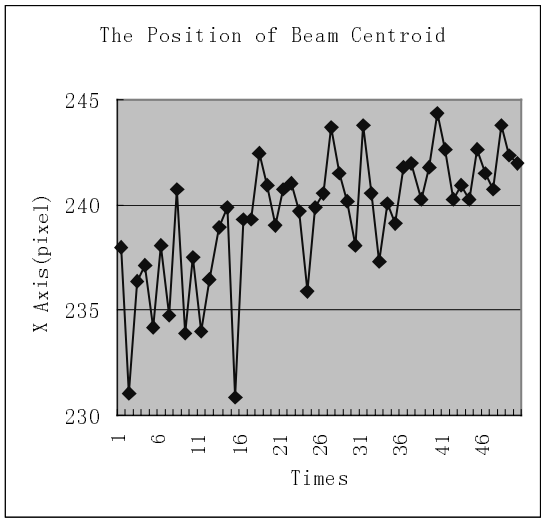

Fig.6 The pointing stability at X direction

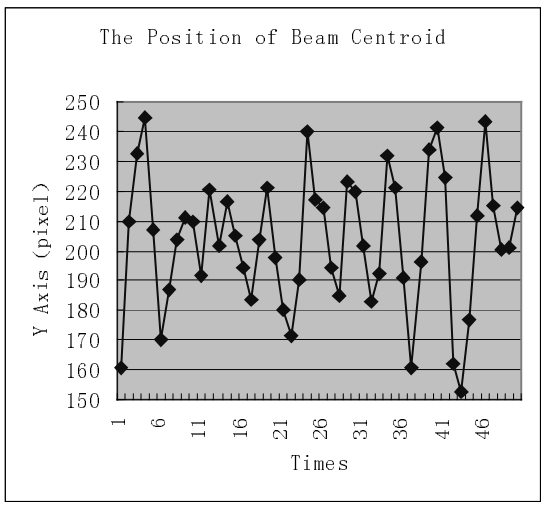

Fig.7 The pointing stability at Y direction

Tab.2 The performance of the drive laser system

1	Wavelength/nm	266
2	Pulse width/ps	10-15
3	Frequency/MHz	54.17
4	Pulse Energy/μJ	3-5
5	Maropulse duration/μs	1-6
6	Maropulse repetition. rate/Hz	3-6-12
7	Micropulse timing jitter/ps	<2
8	Amplitude jitter/rms	3%
9	Pointing stability/mrad	0.11

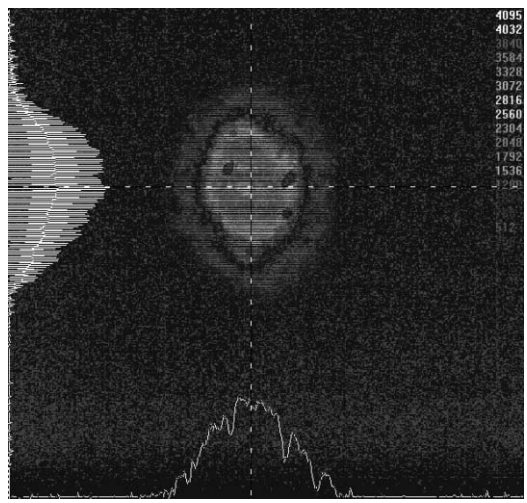

Fig.8 The profile of UV pulse spot

DESIGN OF THE PAL TEST FEL MACHINE

Mungyung Kim*, Jinhyuk Choi, Jung Yun Huang, Heung-Sik Kang, In Soo Ko, Tae-Yeon Lee, Jong-Seok Oh, Sung Ju Park, PAL, Pohang, South Korea

Chang-Mook Yim, POSTECH, Pohang, South Korea

Abstract

In order to the PAL-XFEL, the 1st stage will be to build a test machine, whose design parameters are presented here. It will be a 200 MeV machine that has the target wavelength of visible range. The design details and simulation results are shown in this paper.

INTRODUCTION

The Pohang Accelerator Laboratory (PAL) is going to build a new X-ray free electron laser (XFEL) machine based on the self-amplified spontaneous emission (SASE) scheme [1]. For the first step of the project, a test machine is considered to build. But it means extra time and budget is required. Fortunately, we have found sufficient area in the linac building. Usually PAL linac is operated as an injector for the 2.5 GeV storage ring. So another linac, test linac, beside of the preinjector area in the linac building, is operated for low energy experiments with 60 ~ 100 MeV. Furthermore RF cathode gun system is installed to test as an injector of the PAL FEL in the assembly room of the building. The injector consists of two accelerator columns with about 80 MeV. If we combine with two machines, the test linac and the injector, we need only one acceleration column and one chicane to have a 200 MeV linac for the test machine of PAL FEL project. It means we can save time and budget to construct a building of the test machine. So the test machine is designed to install in the area. Fig 1 shows the structure of the PAL preinjector area and schematic layout of the test machine. In this paper, the simulation results and detail designs of the machine will be reported.

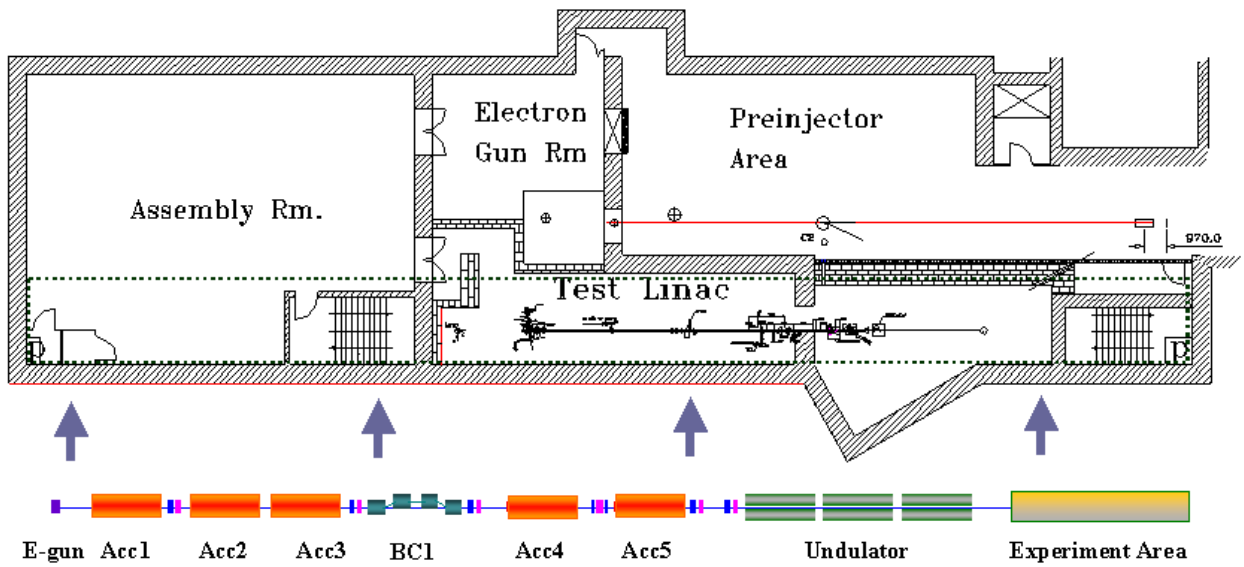

Figure 1: Drawing with preinjector area in the linac building and schematic layout of the test machine. The test machine is designed to install in the dashed block.

BEAM DYNAMICS DESIGN

The test machine consists of a 78 MeV injection part, linear accelerator with a chicane, beam transport line, SASE radiation area with three undulators and experiment area as shown in Fig. 1.

The injection part consists of a photo-cathode RF gun and two accelerating columns. The beam charge from the RF gun is 0.5 nC with 10 ps pulse length 60 Hz repetition rate in maximum, and the final energy of the injector is 78 MeV. After the injector, the beam pulse length is 777 μm, peak current is 60 A, energy spead is 0.3 % and rms normalized eimttances are 0.9 μmrad both direction with horizontal and vertical. PARMELA is used to simulate the injection part.

The linear accelerator is composed of two parts, bunch compressing and accelerating. The bunch compressing part consists of one accelerating column, L1, and one chicane bunch compressor BC1. At the exit of the injection part the electrons enter the L1 where they are

*mungyung@postech.ac.kr

accelerated to ~ 120 MeV. Acceleration occurs off-set crest to provide correlated energy spread along the bunch that will compress it in the compressor BC1 shown in Fig.1. The momentum spread for bunch compressing depends on RF phase (off-set crest) and power. The accelerating column is limited to accelerate up to ~ 50 MeV. And there is only one accelerating column in the L1. Because it limits the RF power, we have small variation about RF phase. The other component for bunch compressing is momentum compaction factor (R56) of BC1.

BC1 is located at that point of 110 MeV, and compresses the beam pulse length from 773 μm to around 228 μm to have peak current above 300 A. Because of the RF power limitation, momentum compaction factor (R56) of BC1 is also limited. RF phase affects on energy spread of the beam, and R56 affects significantly on emittance of the electron beam. We choose lower emittance, we get higher energy spread, and vice versa. For example, figure 2 shows the slice beam pulse shapes with the same peak current 390 A in the case R56 is varying. When R56 is -31.8 mm, the RF power of L1 is 16.7 MV/m and RF phase of L1 is –49.8°. When R56 is -63.1 mm, the RF power of L1 is 15.0 MV/m and the RF phase of L1 is –28.8°.

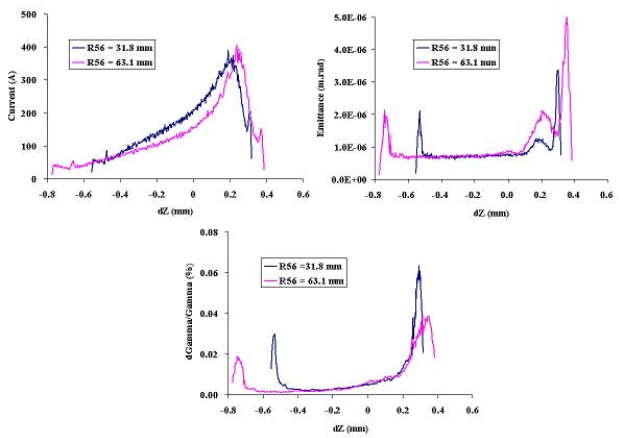

Figure 2: Slice beam pulse shapes at the entrance of the undulator. In the simulation particle number is 200,000 and slice number is 300. It shows current profiles (left), x-axis emittance profiles (Right) and energy spread (down).

From the tedious calculations with elegant code, we choose R56 is -31.8 mm. In the case, beam energy is 110 MeV, projected RMS energy spread is about 1.25 % at BC1. The bending angle of the BC1 is 7.2°, drift length between two dipole magnets is 1.2 m, and the length of each of four dipole magnets is 0.3 m.

2nd accelerating part (L2) consists of two accelerating columns with 15.4 MV/m RF power. Because L2 is also used in low energy experiment like as test machine in the same time, the structure is almost fixed. For the low energy experiments, another thermionic electron gun will be connected to the branch of the L2 at entrance.

The beam transport line from L2 to undulator is very short because of the space problem. So we have no dog-leg structure [2]. It consists of two quadrupole doublets to adjust beta function of the beam at the entrance undulator. At this point the beta-x is 6.22 m, alpha-x is –1.48, beta-y is 6.67 m and alpha-y is 1.44.

At the entrance of undulator, in this test machine, above 300-A peak current, below 1.5 μmrad emittance and below 0.2% energy spread are required for visible wavelength FEL. In this design, the simulation results using ELEGANT code satisfies the demands. At the entrance of undulator, the peak current is about 390 A, normalized slice emittance is 1.2 μmrad and energy spread is about 0.012 %.

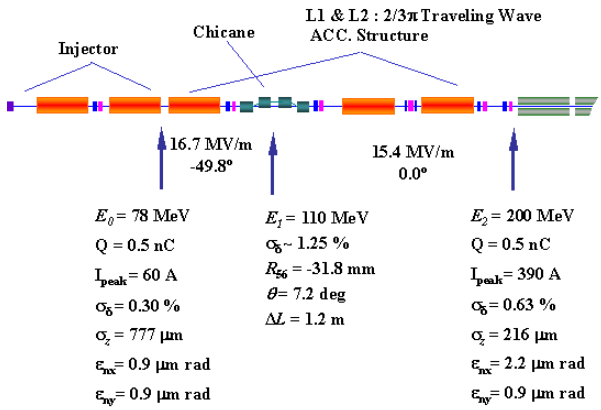

Figure 3: Layout of test machine for PAL XFEL

The figure 3 shows layout of the test machine and various beam dynamic simulation results. The figure 4 shows beta functions and eta functions along beamline, and figure 5 shows beam profiles in dE/E-dz plane. Table 1 summarize parameters of the test machine.

Table 1: Parameters of the Test Machine

Parameter	Value	Unit
Nominal electron energy	200	MeV
Peak current	390	A
Final bunch length	228	μm
RMS slice energy spread	0.012	%
Normalized slice emittance	1.2	μmrad
Radiation wavelength	visible	
Full undulator Length	10	m
Saturation undulator length	6 ~ 7	m

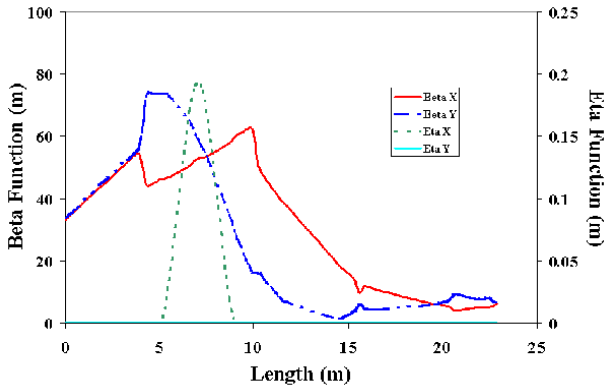

Figure 4: Beta and Eta functions along beamline of the test machine.

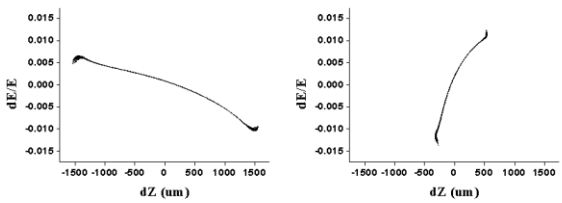

Figure 5: 200,000 particle profiles in dE/E-dZ plane at injector (left) and at entrance of the undulator (Right).

SUMMARY

The test machine with visible FEL using SASE for completion of 3.7 GeV PAL X-FEL is designed to satisfy demands of time and budget to construct. The simulation results are acceptable. We need more study about beam diagnosis system in the machine.

REFERENCES

[1] T. Y. Lee, Y. S. Bae, J. Choi, J. Y. Hunag, H. S. Kang, M. G. Kim, D. H. Kuk, J. S. Oh, Y. W. Parc, J. H. Park, S. J. Park and I. S. Ko, "Design and Physical Issues of the PAL-XFEL" Journal of the Korean Physical Society, Vol. 48, No. 4, April 2006, pp. 791 ~ 795.

[2] Linac Coherent Light Source (LCLS) Conceptual Design Report, SLAC-R_593, April 2002, UC-414.

FEATURES OF THE PAL-XFEL DESIGN*

T.-Y. Lee†, J. Choi, and H. S. Kang
Pohang Accelerator Laboratory, San 31, Hyoja-dong, Pohang, Kyungbuk 790-784, KOREA

Abstract

PAL-XFEL, the new XFEL project of Pohang Accelerator Laboratory, aim to emit hard X-ray of $1 - 1.5$ Å, although its beam energy is only 3.7 GeV. To achieve the goal, coherent third harmonic radiation will be utilized. This paper discusses schemes of hard X-ray generation with 3.7 GeV electron beam and concludes that use of the third harmonic is the only possible way.

INTRODUCTION

The storage ring based third generation light source has spread all over the world in the last twenty years and is now a useful and common facility for scientific research. However, even more advanced X-ray source, the XFEL facility, is not likely to be so. Apparently, the X-ray FEL (XFEL) is achievable only by a high energy electron beam. To make $1 - 1.5$ Å hard X-ray FEL, the electron energy has been chosen 14.35 GeV for the Linac Coherent Light Source (LCLS) in SLAC [1] that is under construction and 17.5 GeV for the European XFEL in DESY [2] that is approved. Not only the linear accelerator but also the undulator in XFEL is long; the LCLS undulator is 112 m long and the European XFEL undulator is even longer, 260 m. We may have to conclude that hard X-ray FEL is too expensive to be available in most countries. Is it possible to reduce the machine size? The SPring-8 Compact SASE Source (SCSS) project in Japan tries to reduce the whole facility size by using an in-vacuum undulator and the new technology of C-band linear accelerator [3]. It is going to need only 8 GeV electron beam to generate hard X-ray. However, building and maintaining an 8 GeV electron machine still costs a lot even with the new technology. A natural question is how compact an XFEL facility can be.

PAL-XFEL, the new XFEL project of Pohang Accelerator Laboratory (PAL) [4], tries to achieve the goal by utilizing the third harmonic SASE radiation. It will uses 3.7 GeV electron beam. Below it will be shown that $1 - 1.5$ Å hard X-ray FEL can not be achieved by 3.7 GeV electron energy, if we insist to use only the fundamental SASE radiation. Therefore, PAL-XFEL may be the lowest energy hard X-ray FEL machine. The only defect is that the transverse coherence of the PAL-XFEL third harmonic radiation would be far from perfect. Basic parameters of the PAL-XFEL are listed in Table 1 for unfamiliar readers.

* Work supported by Korean Ministry of Science and Technology
† tylee@postech.ac.kr

Table 1: Parameters of PAL-XFEL

Beam Parameters	**Value**	**Unit**
Electron energy	3.7	GeV
Peak current	3	kA
Normalized slice emittance	1	mm mrad
RMS slice energy spread	0.01 %	
Full bunch length	270	fs
Undulator Parameters		
Undulator period	1.5	cm
Segment length	4.5	m
Full undulator length	80	m
Peak undulator field	1.19	T
Undulator parameter, K	1.49	
Undulator gap	4	mm
Average β-function	10	m
FEL Parameters		
Radiation wavelength	3	Å
FEL parameter, ρ	5.7×10^{-4}	
Peak brightness	5×10^{31}	1)
Peak coherent power	1	GW
Pulse repetition rate (Max.)	60	Hz
1D gain length	1.2	m
Saturation length, L_{sat}	45	m

1) photon/(sec mm^2 mrad^2 0.1%BW)

BEAM ENERGY DEPENDENCE OF XFEL FACILITY SIZE

To find the possibility of using low electron beam energy for an hard X-ray FEL, we need to know its beam energy dependence. To find out the beam energy dependence of an hard X-ray FEL, recall that the resonant wavelength of an undulator is given by

$$\lambda_r = \frac{\lambda_u}{2\gamma^2}\left(1 + \frac{K^2}{2}\right), \quad (1)$$

where λ_r is the resonant wavelength, λ_u the undulator period, γ the Lorentz factor, and K the undulator parameter. K is defined by

$$K = 0.934 B_0[\text{Tesla}]\lambda_u[\text{cm}], \quad (2)$$

where B_0, the undulator peak magnetic field, depends not only on the undulator gap and period but also on the magnet material. If we consider a hybrid undulator with vanadium permendur, it is given by

$$B_0 = 3.694 \exp\left[-5.068\frac{g}{\lambda_u} + 1.520\left(\frac{g}{\lambda_u}\right)^2\right] \quad (3)$$

with g denoting the gap. In LCLS, for $\lambda_r = 1.5$ Å, the beam energy is 14.35 GeV, $\lambda_u = 3$ cm, and $g = 0.65$ cm. If we want to use lower beam energy, we have to use shorter λ_u and smaller K that depends on λ_u and B_0. Since B_0 depends on g/λ_u, we have two parameters (λ_u and g/λ_u) to be controlled to compensate for the decreasing beam energy. Hence, we fix g/λ_u (and thus B_0) and use only λ_u. Solving Eq. (1) for λ_u while keeping the LCLS value of the ratio $g/\lambda_u = 0.217$, we can determine λ_u that gives 1.5 Å hard X-ray at a lower electron energy. First, arranging Eq. (1) for λ_u, we obtain a cubic equation

$$\lambda_u^3 + \frac{2}{a^2}\lambda_u = \frac{4\lambda_r\gamma^2}{a^2}, \tag{4}$$

where $a = 0.934B_0$. Solving this cubic equation, we obtain λ_u as a function of γ or E, the electron energy. The graph of λ_u versus E is shown in Fig. 1. As E decreases from the LCLS energy, λ_u decreases almost linearly. Since g/λ_u is fixed, $g = 0.217\lambda_u$ also decreases making in-vacuum undulator an inevitable choice at lower electron energies. Figure 1 may imply that hard X-ray FEL is achievable by using very low energy electrons if the undulator period is properly short. However, the undulator gap g should also be very small, which causes serious problems. Hence, both λ_u and g can not be arbitrarily small and electron energy can not be very low.

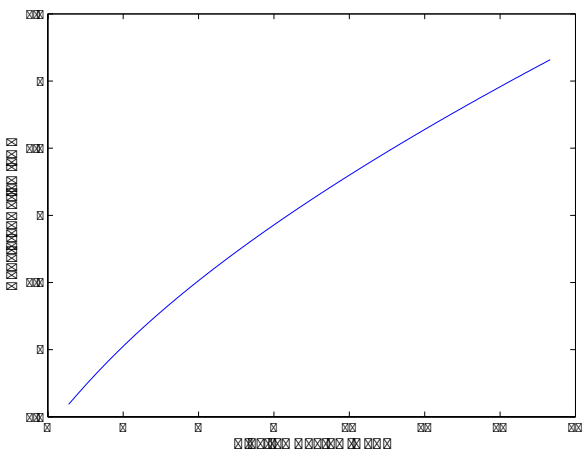

Figure 1: Graph of λ_u that gives 1.5 Å radiation as a function of E. The ratio g/λ_u is fixed to 0.217, the LCLS value.

To build a compact XFEL, we also have to reduce the undulator length. To estimate the SASE saturation length, L_{sat}, and find its energy dependence, a key parameter is the FEL parameter ρ defined by

$$\rho = \frac{1}{2\gamma}\left[\frac{I}{I_A}\frac{\lambda_u^2 K^2 [JJ]^2}{8\pi^2\sigma_x^2}\right]^{1/3}, \tag{5}$$

where $I_A = 17045$ A is the Alfen current, I is the beam peak current, σ_x is the cross sectional beam size, and $[JJ]$ is defined by

$$[JJ] = J_0\left(\frac{K^2}{4+2K^2}\right) - J_1\left(\frac{K^2}{4+2K^2}\right). \tag{6}$$

Note that ρ roughly defines the upper bound of the electron energy spread σ_E/E in a slice. The SASE process begins only when $\sigma_E/E < \rho$ and it stops (saturates) when σ_E/E grows and reaches ρ. Hence, ρ should not be too small for successful power growth.

The fundamental length scale to determine the saturation length is the one-dimensional gain length defined by

$$L_{1D} = \frac{\lambda_u}{4\sqrt{3}\pi\rho}. \tag{7}$$

In general, a large ρ is preferred not only for high gain, but also for a short gain length. In Eq. (5), note that $\sigma_x^2 = \beta\epsilon_n/\gamma$ where ϵ_n is the normalized emittance and β is the betatron function. The currently achievable value for ϵ_n is around 1.2 μ-rad and β is free to choose. The optimal β that gives the shortest saturation length is given by [5]

$$\beta_{opt} = 11.2\left(\frac{I_A}{I}\right)^{1/2}\frac{\epsilon_n^{3/2}\lambda_u^{1/2}}{\lambda_r K[JJ]}. \tag{8}$$

Using β_{opt} in Eq. (5), we obtain

$$\rho = \frac{1}{2}K[JJ]\left(\frac{I}{I_A}\frac{\lambda_u}{\epsilon_n}\right)^{1/2}\left(\frac{\lambda_r}{89.6\pi^2\epsilon_n\gamma^2}\right)^{1/3}. \tag{9}$$

Using the LCLS value $I = 3.4$ kA, the dependence of ρ on E as λ_u moves on the line of Fig. 1 is shown in Fig. 2. Note that ρ also decreases as E decreases. The requirement $\sigma_E/E < \rho$ gives a severe restriction for a compact XFEL source. The LCLS value of σ_E/E is approximately 0.01%, which means $\sigma_E \approx 1.4$ MeV. As the electron energy E is lowered, the relative energy spread σ_E/E increases while ρ decreases. At around $E = 4.5$ GeV, σ_E/E is comparable to ρ. Hence $E = 4.5$ GeV seems the lowest possible energy for 1.5 Å XFEL.

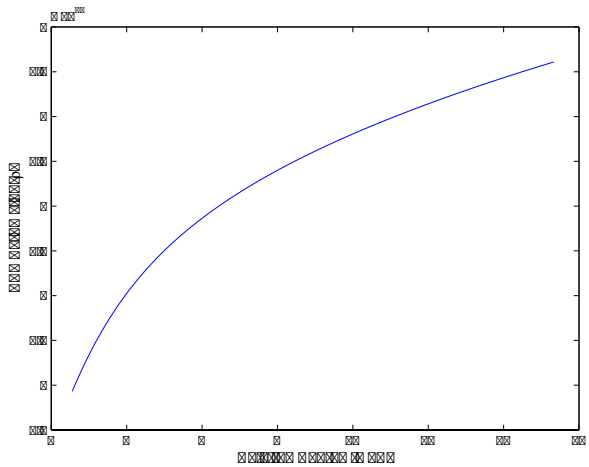

Figure 2: Graph of ρ as a function of E.

The three dimensional parameter L_{3D} is usually described as

$$L_{3D} = L_{1D}(1+\eta), \tag{10}$$

where η measures the deviation from the one dimensional theory due to diffraction, emittance, and energy spread.

L_{sat} and P_{sat}, the saturated peak radiation power, are approximately given by

$$P_{sat} = 1.6\rho\left(\frac{L_{1D}}{L_{3D}}\right)^2 \frac{I\gamma mc^2}{e},$$
$$L_{sat} = L_{3D}\ln\left(\frac{P_{sat}\lambda_r}{2\rho^2 Ec}\right). \quad (11)$$

Certainly, L_{sat} is an important factor to determine the whole machine size. Using Eqs. (5) and (10) in Eq. (11), the E-dependence of L_{sat} is revealed and shown in Fig. 3. L_{sat} also decreases as E decreases from the LCLS energy and reaches the minimum at around $E = 5 - 6$ GeV. In Fig. 3, the part below $E = 4.5$ GeV is meaningless, because the energy spread exceeds ρ and there is no SASE process. The abnormal abrupt increase of the saturation length indicates the meaninglessness. P_{sat} is depicted in Fig. 4 on the logarithmic scale. Note that P_{sat} decreases slowly as E decreases from the LCLS energy to $E \sim 4.5$ GeV and drops rapidly outside of it. P_{sat} is still above 1 GW. Therefore, a compact XFEL does not sacrifice the radiation power. Overall, the shortest XFEL for 1.5 Å can be built at around $E = 4.5$ GeV.

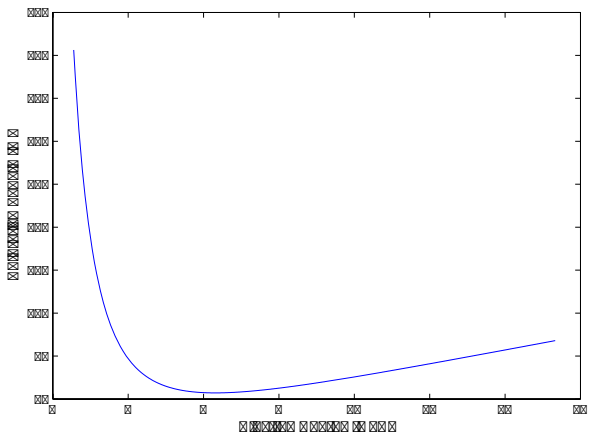

Figure 3: Graph of L_{sat} as a function of E.

TRANSVERSE COHERENCE

The condition for the transverse coherence is roughly given by

$$\frac{\epsilon_n}{\gamma} \sim \frac{\lambda_r}{4\pi}. \quad (12)$$

This rough condition claims that the beam energy has to be high enough to secure the transverse coherence for a very small λ_r (hard X-ray). Since Eq. (12) is an order of magnitude relation, accurate estimate of transverse coherence needs a computer. Especially, the degree of transverse coherence at the saturation was obtained as a function of $\hat{\epsilon} = 2\pi\epsilon_n/(\lambda_r\gamma)$ [5]. Converting this result to our purpose, we obtain Fig. 5, which shows clearly that the degree of transverse coherence for 1.5 Å hard X-ray decreases as the electron energy decreases. According to Fig. 5, the degree

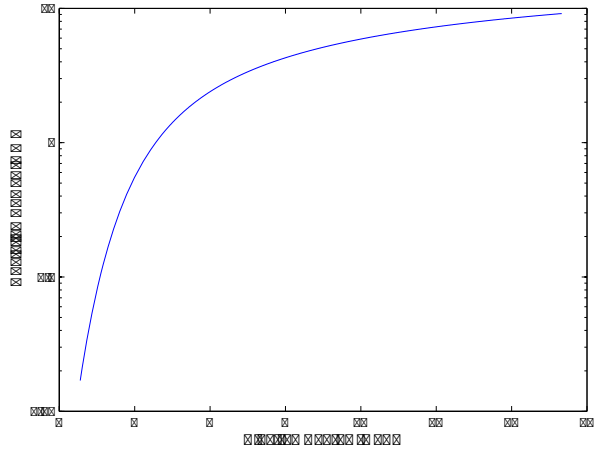

Figure 4: Graph of P_{sat} as a function of E.

of transverse coherence of LCLS is approximately 0.83. At a lower energy and shorter undulator period, the transverse coherence would be worse. Therefore, we conclude that hard X-ray FEL is achievable at a lower electron energy but its transverse coherence may not be perfect.

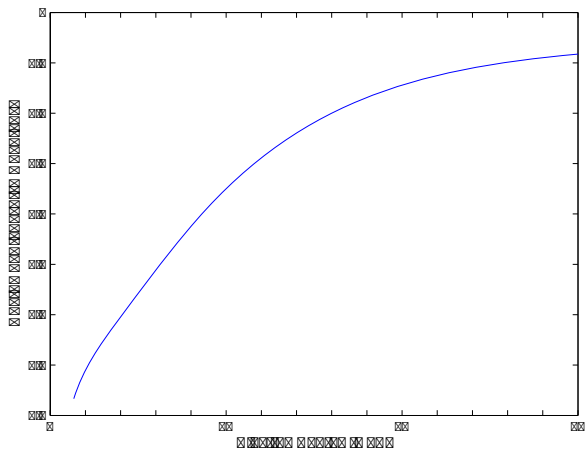

Figure 5: Degree of transverse coherence for 1.5 Å XFEL as a function of E.

CHOICE OF PAL-XFEL

Although hard X-ray FEL is possible by using $E = 4.5$ GeV, note from Fig. 1 that the undulator period and thus the undulator gap is very small at the energy. The gap is around only 2.5 mm. This may not be an unreasonably small number. However, it causes not only beam handling difficulty but also severe wakefield effect that reduces the radiative power. If we try to choose a safer gap (maybe larger than 3 mm), the beam energy should be at least 6 GeV, which is not compact at all. Therefore, it may be concluded that hard X-ray FEL is not achievable by a compact XFEL machine of beam energy lower than 4 GeV. That is why PAL-XFEL chose to use the third harmonic radiation [8, 9, 10]. Then

even smaller hard X-ray FEL facility is possible. If we generate 3 Å fundamental radiation at a even lower energy of 3.7 GeV, its 1 Å third harmonic radiation is usable. Since the needed undulator is shorter than using the fundamental radiation, the whole facility size is really compact.

The only problem is the output power. The output power of the third harmonic is much lower than that of the fundamental mode. The ratio of the third harmonic power to the fundamental power is given by [11])

$$\frac{P_3}{P_1} = 0.094 \times \left(\frac{K_3}{K_1}\right)^2. \quad (13)$$

K_1 and K_3, coupling factor of the fundamental and third harmonic respectively, are special cases of K_h defined by

$$K_h = K(-1)^{(h-1)/2}[J_{(h-1)/2}(Q) - J_{(h+1)/2}(Q)], \quad (14)$$

where $Q = hK^2/(4+2K^2)$. It is straightforward to compute $(K_3/K_1)^2$ as a function of K. As shown in Fig. 6, it increases from zero and becomes almost flat after $K > 2.5$ saturating to $(K_3/K_1)^2 = 0.22$, which gives the asymptotic value $P_3/P_1 \approx 0.02$. Hence, P_3 can not exceed 2% of P_1. With $K = 1.49$, the PAL-XFEL value, P_3 is approximately 1% of P_1. Parameters of the two harmonics are listed in Table 2. The peak power and peak brightness of the third harmonic radiation is still very high. Finally the degree of transverse coherence of the third harmonic radiation, obtained at this low energy, is also low.

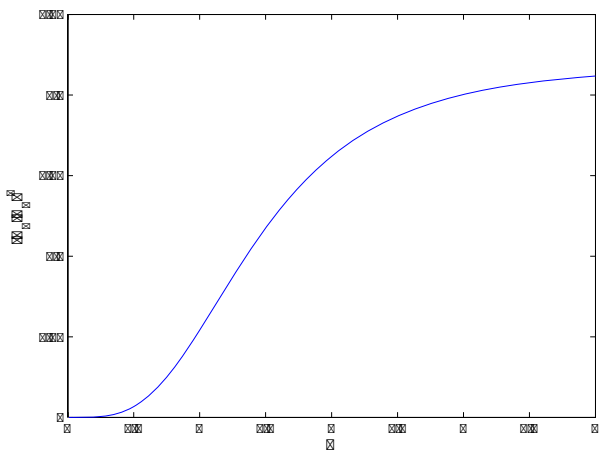

Figure 6: Graph of $(K_3/K_1)^2$ as a function of K.

Table 2: Parameters of the two harmonics

Parameters	**Fundamental**	**Third harmonic**
Wavelength (Å)	3	1
Peak power (GW)	1	0.01
Peak brightness [2)]	1×10^{32}	3×10^{29}
Photons/pulse	5×10^{11}	1.5×10^{9}

[2)] photon/(sec mm^2 mrad^2 0.1%BW)

SUMMARY

We have seen, in this paper, that it is possible to generate 1.5 Å hard X-ray FEL with lower electron energy (down to 4.5 GeV) and shorter undulator at the expense of reduced degree of transverse coherence. However, the facility size can be reduced even further by utilizing the third harmonic radiation whose power is less than 2% of the fundamental one and transverse coherence is also poor. PAL-XFEL is one such example. We can not build a compact hard X-ray FEL that has all three special properties. However, XFEL with incomplete transverse coherence is still very useful, because the majority of experiments do not need the transverse coherence.

REFERENCES

[1] J. Arthur *et al.*, Linac Coherent Light Source Conceptual Design Report, Stanford, SLAC (2002).

[2] A. Aghababyan *et al.*, The European XFEL Technical Design Report, Hamburg, DESY (2006).

[3] SCSS XFEL R&D Group, SCSS XFEL Conceptual Design Report, RIKEN/SPring-8 (2005).

[4] T.-Y. Lee, Y. S. Bae, J. Choi, J. Y. Huang, H. S. Kang, C. B. Kim, D. E. Kim, M. G. Kim, Y. J. Kim, I. S. Ko, J. S. Oh, Y. W. Parc, and J. H. Park, Proceedings of FEL 2006, Bessy, Berlin, Germany, (2006) 210.

[5] E. L. Saldin, E. Schneidmiller, and M. Yurkov, Proceedings of FEL 2006, Bessy, Berlin, Germany, (2006) 206.

[6] K. L. F. Bane and G. Stupakov, SLAC-PUB-10707, LCLS-TN-04-11, (2004).

[7] P. Emma, Z. Huang, C. Limborg-Deprey, J. Wu, W. Fawley, M. Zolotorev, and S. Reiche, Proceedings of 2005 Particle Accelerator Conference, Knoxville, USA, (2005) 344.

[8] W. Colson, IEEE J. Quantum Electron. **17**, (1981) 1417.

[9] R. Bonifacio, C. Pellegrini, and L. Narducci, Opt. Commun. **50**, (1984) 373.

[10] Z. Huang, and K.-J. Kim, Phys. Rev. E **62**, (2000) 7295.

[11] E. L. Saldin, E. Schneidmiller, and Yurkov, Proceedings of FEL 2005, SLAC, Stanford, USA, (2005) 51.

POTENTIALITIES OF ELMI DEVICE FOR SUBMILLIMETER GENERATION BY STIMULATED INTERCAVITY SCATTERING IN PLANAR FEM *

A. V. Arzhannikov*, V. T. Astrelin, A. S. Kuznetsov, S. A. Kuznetsov, P. V. Kalinin, S. L. Sinitsky, V. D. Stepanov, BINP, Novosibirsk, Russia
N. S. Ginzburg, N. Yu. Peskov, A. S. Sergeev, V. Yu. Zaslavsky, I. V. Zotova, IAP, N-Novgorod, Russia

Abstract

Paper describes main features of a project on two-stage generation of submillimeter radiation at the ELMI device. This novel variant of a two-stage scheme is based on stimulated intercavity scattering. In accordance with the scheme, at the first stage a sheet electron beam drives a 2D Bragg free electron maser (FEM) of planar geometry to generate 4-mm pump wave. At the second stage this wave undergoes stimulated scattering at the supplementary electron beam to produce submillimeter radiation. In the paper we describe results of theoretical and experimental investigations of various aspects of the two-stage scheme and some testing experiments on units for realization of this scheme at the ELMI device.

INTRODUCTION

In recent experiments at the ELMI-device the single frequency operation of 4-mm planar FEM with 2D distributed feedback has been demonstrated [1]. These results created a basis for development of a two-stage generator for the sub-mm band. A key feature of the scheme proposed earlier in [2], is the use of two sheet beams with a few kAmps currents that transported in two parallel slit channels with a guiding longitudinal magnetic field, which are connected by a special waveguide. At the first stage one of the sheet beams passing in a slit channel with static undulator magnetic field drives 2D Bragg FEM of planar geometry to generate 4-mm pump wave as well as in the recent ELMI experiments. This intensive 4-mm radiation accumulated in the FEM resonator is transported through the special waveguide to the second slit channel where it is used as an EM-undulator for the secondary stage of sub-mm FEL.

The special waveguide connection will be realized in similar way as it was suggested earlier in the project of multibeam FEM with 2D distributed feedback where it was used for synchronization of radiation generated in different channels [3], [4]. Production of the two sheet beams by one accelerator diode with two cathodes is also similar to the process of operation of the multibeam diode described in Ref. [4].

SCHEMATIC OF PROPOSED EXPERIMENTS

At the first stage we plan to use a FEM with hybrid Bragg resonator which was developed in the recent experiments [1]. Hybrid two-mirror resonator consisting of upstream 2D and downstream 1D Bragg reflectors provides spatial coherence of radiation in a FEL driven by a large-size sheet e-beam [5], [6]. In the ELMI-experiments generated radiation has wavelength $\lambda_0 = 4$ mm with pulse duration up to 0.5 μs. The existence of regimes with high level of the mm-radiation spectral density near the frequency close to one of hybrid Bragg resonator eigen modes during all the pulse has been registered.

One of the typical shots shown in the Fig. 1 demonstrates the FEM operation on the mode with frequency 75.3 GHz. The single mode generation lasts 330 ns.

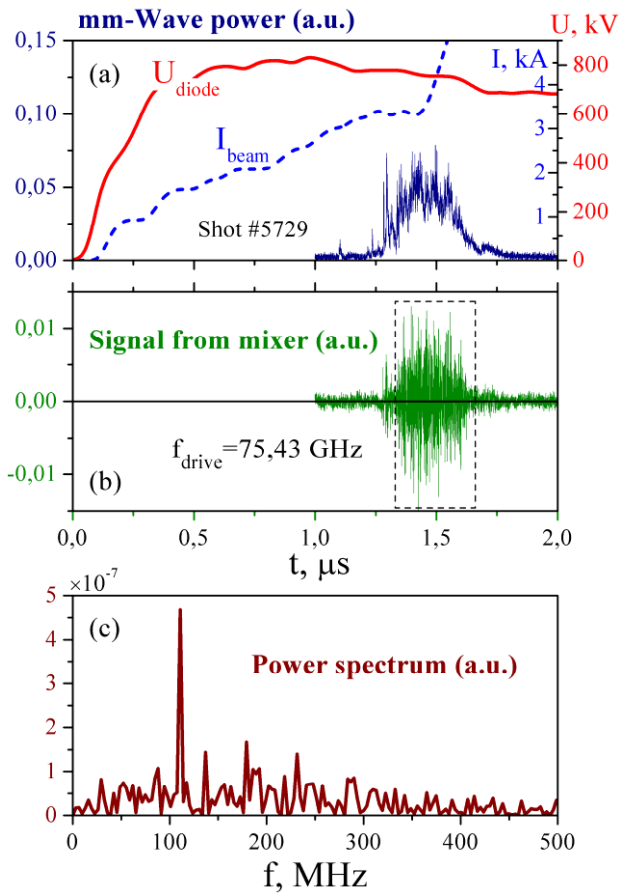

Fig. 1 Single frequency operation of 4-mm FEM: a) diode voltage (U_{diode}), beam current (I_{beam}) and mm-wave power; b) intercarrier frequency signal from heterodyne mixer (heterodyne frequency f_{drive}=75.43 GHz); c) mm-wave power spectrum.

*arzhannikov@inp.nsk.su

In a two-stage scheme such mm-radiation as an incident wave should be scattered by the electrons with energy ~1 MeV at the second stage of generation. Using the formula for the double Doppler effect the wavelength of scattered radiation λ will be the following:

$$\lambda = \lambda_0 \frac{(1-\beta\cos\theta_s)}{(1-\beta\cos\theta_i)}, \qquad (1)$$

where $\beta = v/c$ is the electron velocity, θ_i and θ_s — angles of incident and scattered waves with respect to direction of the electron velocity (Fig. 2).

For two cases of back-scattering and 90°-scattering formula (1) gives $\lambda \approx \lambda_0/4\gamma^2$ and $\lambda \approx \lambda_0/2\gamma^2$ respectively, where $\gamma = 1/\sqrt{1-\beta^2}$ is an electron relativistic factor. The expected wavelengths of the scattered radiation at output of the two-stage scheme are presented in Fig. 2. As it is seen the radiation in the band of 0.1–0.3 mm can be obtained in case of back-scattering of 4-mm radiation whereas 90°-scattering provides radiation wavelength in the band of ~0.2–0.5 mm for γ in the range 2–3.4.

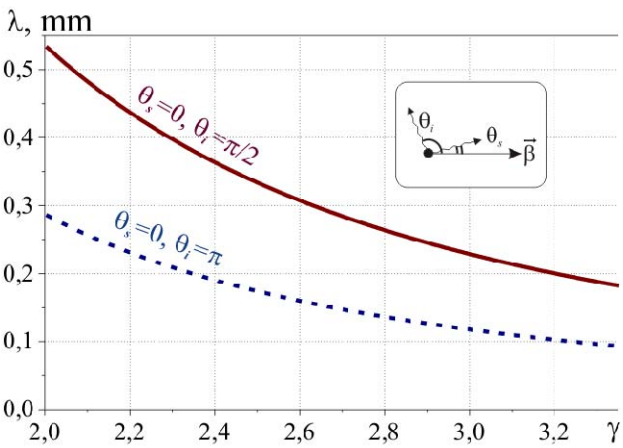

Fig. 2 Conversed wavelength due to scattering of 4-mm radiation on beam electrons as the function of the beam γ-factor

Schematic drawings of experimental realization of sub-mm generator based on two different scattering schemes are presented in Fig. 3 and Fig. 5. For both variants we suppose to use sheet beams with 3–4 mm thickness and 10–20 cm width and a current density more than 1 kA/cm. The e-beams pass the slit channels at presence of longitudinal guiding magnetic field with the strength ~1 T. In the channel #1 of both variants the electrons oscillate in undulator magnetic field and generate 4 mm pump wave. Theoretical studies of planar FEM at ELMI accelerator demonstrates that the electric field strength of 4-mm radiation inside the FEM resonator can amount to 10^5–10^6 V/cm. In Fig. 4 results of simulation of interactivity fields are presented for configuration shown in Fig. 3 (z coordinate is measured along e-beam velocity and 2D Bragg reflector). The 2D Bragg resonator is optimized such a way to increase amplitude of transverse propagating energy fluxes B. These fluxes by connecting waveguides are transported in the channel #2 for pumping electron transverse oscillations.

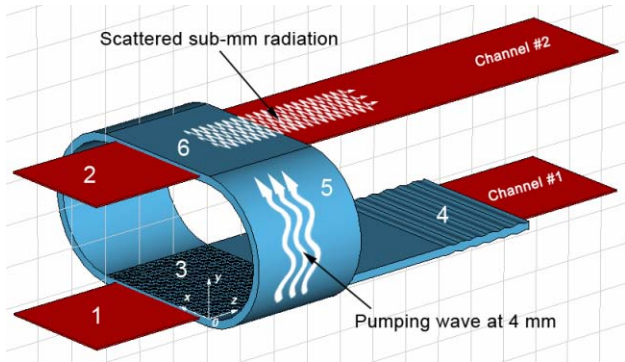

Fig. 3 Scheme of two-stage generation for the band of 0.2–0.5 mm: 1 — sheet REB for driving the planar FEM-oscillator; 2 — sheet REB for mm-wave scattering; 3 — 2D Bragg reflector; 4 — 1D Bragg reflector; 5 — special waveguide; 6 — area of 4-mm radiation scattering on e-beam.

For the first experiments we plan to observe scattered signal amplification in the SASE (self-amplified spontaneous emission) [7] regime in the absence of the resonator (mirrors) for sub-mm radiation. The spatial growth rate for scattered short-wave radiation is given by the expression [8], [9]:

$$\Gamma[\mathrm{cm}^{-1}] = 6.8 \cdot \left(\frac{j_b[\mathrm{kA/cm}]}{\lambda_0[\mathrm{mm}] \cdot b[\mathrm{mm}]} \right)^{1/3} \cdot \frac{a_o^{2/3}}{\gamma}, \qquad (2)$$

where j_b is the linear current density in the second beam, $a_0 = 2.3 \cdot 10^{-8} \lambda_0[\mathrm{mm}] E_i[\mathrm{V/cm}]$ is the pump wave strength parameter, E_i is the pump wave amplitude and b is the gap between the channel plates. For the pump radiation with

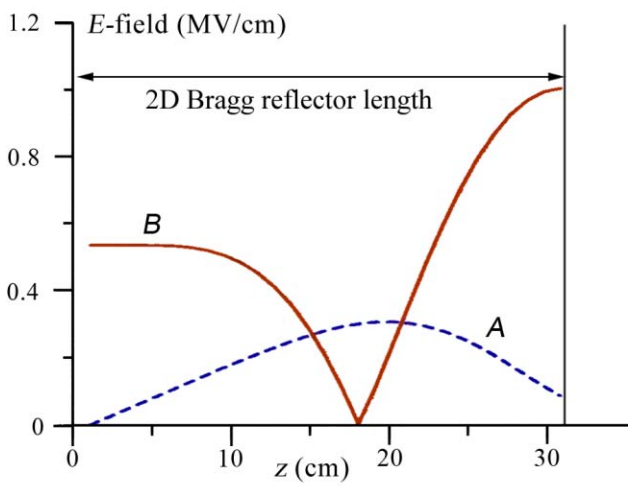

Fig. 4 Results of simulation of 4-mm generation in the 2D Bragg FEM: profile of transverse *(B)* and longitudinal *(A)* propagating partial waves inside 2D Bragg structure.

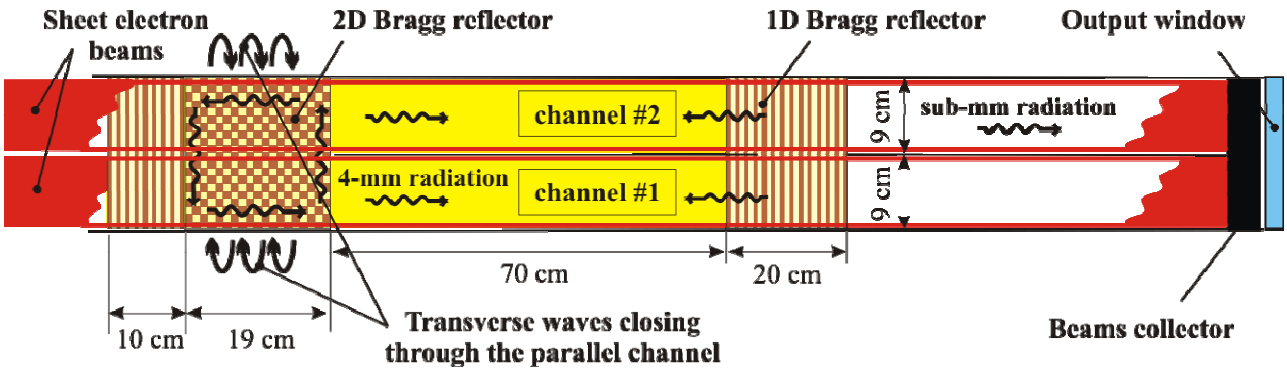

Fig. 5 Scheme of two-stage generation for the band of 0.1–0.3 mm

λ_0=4 mm and E_i =1 MV/cm this parameter is estimated on the level $a_0 \sim 0.05$–0.1. Thus, for the relativistic factor $\gamma = 3$, j_b = 1 kA/cm and b = 10 mm the spatial growth rate of sub-mm radiation is estimated as $\Gamma \sim 0.1$ cm^{-1}.

Expression for the gain (2) is valid for a "cold" beam with rather small velocity spread

$$\frac{\delta v}{c} << \lambda \cdot \Gamma \approx 0.04 . \qquad (3)$$

The required value of the velocity spread can be obtained by an accurate choice of geometry of magnetic field configuration in accelerator diode and an appropriate strength of guiding magnetic field. Analysis of this problem has shown that for experimental conditions of the ELMI-accelerator in order to satisfy (3) we should increase the guiding magnetic field up to 2.5–3 T. In addition to these changes some reconstructions in the accelerator diode and vacuum slit channels should provide appropriate parameters for the first step of two-stage experiments on production of sub-mm radiation in SASE regime. After that it will be possible to use either quasi-optical or some modifications of Bragg resonators to obtain generation regime with corresponding narrowing the radiation spectrum.

One of the problems related with observation of SASE regime in the overmoded waveguide is suppression of interaction with low frequency modes. Such a problem can be solved by using waveguide with variable gap between plates. According to the results of KARAT simulation of 200 GHz SASE (see [2]) the waveguide tapering provides possibility for suppression of low frequency amplification. This result is explained that variation of the waveguide parameters affects more strongly near cut-off modes with the large Brillouin angles.

TWO BEAMS PRODUCTION

As a first step for implementing the two-stage generation scheme we have provided passing of two similar sheet e-beams through the parallel slit channels with the guide magnetic field 1.75 T. The scheme of this experiment was just like one shown in Fig. 5 only that the Bragg resonator has been replaced with the regular planar waveguide. The result of this experiment is shown in Fig. where beams currents measured on the collectors are presented together with accelerator diode voltage. As one can see the traces of beams currents are practically the same. Minor difference can be minimized by varying the cathodes positions in the accelerator diode if required.

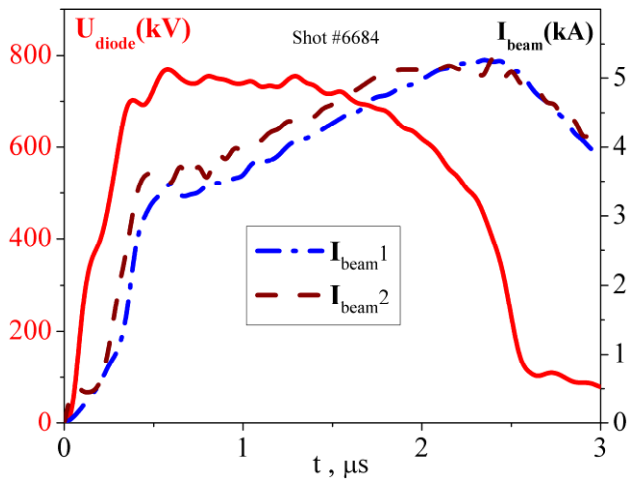

Fig. 6 Production of two sheet e-beams in a common diode with two cathodes and transportation of these beams through the parallel slit channels: U_{diode} — accelerating voltage; $I_{beam}1,2$ — currents of the beams.

CONCLUSION

Basing on the results of the experiments on generation of 4-mm radiation in a planar FEM together with the results of theoretical investigations and computer simulations, we proposed the submillimeter radiation generator based on stimulated scattering of pumping mm-wave on a high-current sheet REB with electron energy ~1 MeV. Power level up to 1 MW of 100 μm wavelength radiation with 0.1–1 μs pulse duration can be reached by constructing this generator on basis of already operating planar FEM with appropriate technical upgrading at low financial costs. Thus technical implementation of such solution seems to be highly prospective.

ACKNOWLEDGMENT

The work was partially supported by CRDF (grant NO-008-X1) and RFBR (grants 04-02-17118 and 05-02-17036) and is supported now by RFBR (grant 06-08-01506) and Scientific Program "Problems of Radiophysics" of RAS.

REFERENCES

[1] A. V. Arzhannikov, N. S. Ginzburg, V. G. Ivanenko et al. "Investigation of Mode Structure for mm-wave Radiation Pulses Generated by Planar FEM at 2-D Distributed Feedback", Abstracts of 16th Int. Conf. on High-Power Particle BEAMS, BEAMS'2006, Oxford, UK, 2006, No. 19, p. 54.

[2] A. V. Arzhannikov, N. S. Ginzburg, P. V. Kalinin et al. "Intercavity Scattering Scheme for Two-stage Generation of Submillimeter Radiation on the Base of Planar 2D Bragg FEM", in Proc. VI Int. Workshop "Strong Microwaves in Plasmas", N. Novgorod, Russia, 2006, vol. 1, p. 228.

[3] N. S. Ginzburg, N. Yu. Peskov, A. S. Sergeev et al, Nucl Instrum Meth Phys Res A, 475 (2001) 173.

[4] A. V. Arzhannikov, V. T. Astrelin, V. B. Bobylev et al, Nucl. Instrum. Meth. Phys. Res. A, 507 (2003) 129.

[5] N. S. Ginzburg, N. Yu. Peskov, A. S. Sergeev et al. Thech. Phys. J, 26 #16 (2000) 8 (in Russian).

[6] N. S. Ginzburg, V. Yu. Zaslavsky, N. Yu. Peskov et al. Thech. Phys. J, 76 n. 12 (2006) 80 (in Russian).

[7] R. Bontfacio, C. Pellegrini, L. M. Narducci, Optic. Comm, 50 iss. 6 (1984) 373.

[8] V. L. Bratman, N. S. Ginzburg, M. I. Petelin, J. Exp. Theor. Phys, 76 (1979) 930.

[9] P. Sprangle, C. M. Tang, W. M. Manheimer, Phys. Rev. A, 21 (1980) 302.

A PROJECT OF SC ERL AT KAERI

A.V.Bondarenko, S.V.Miginsky, Budker Institute of Nuclear Physics, Novosibirsk, Russia
B.C.Lee, S.H.Park, Y.U.Jeong, Y.H.Han, Korea Atomic Energy Research Institute, Daejeon, Korea

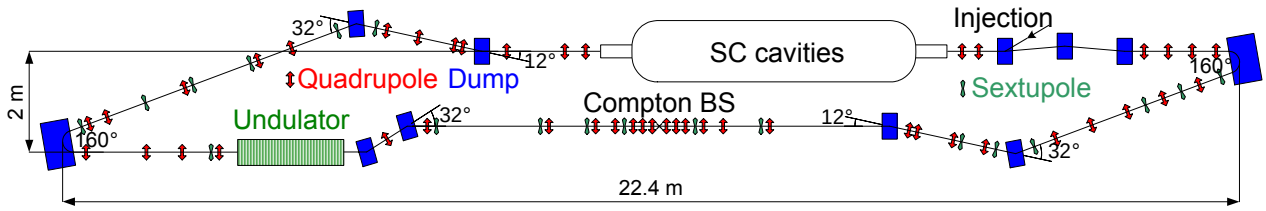

Figure 1. The layout of the ERL.

Abstract

A project of an ERL at Korea Atomic Energy Research Institute is described. The ERL will be connected to the existing machine without any modification. It consists of two 180° bents and two straight sections: one is for an FEL, another for a Compton X-ray source. One can choose the regime controlling the lenses. The total ERL is isochronous to avoid any problem with longitudinal beam instability. It will be possible to control both Sx and Sy transformation matrix elements independently to suppress longitudinal beam instability and allow the increase of beam current. Sextupoles will be installed in bents to suppress chromatic aberration. This design provides operation in FEL regime with high electron efficiency in the range of electron energies 12–22 MeV.

INTRODUCTION

At present time, a superconductive linear accelerator successfully operates at KAERI. It consists of an injector with injection energy 2 MeV, injection beamline, cryogenic accelerating module, which contains two cavities. Electron beam parameters are following:

- bunch duration: 100 ps;
- number of electrons per bunch: 10^{10};
- electron energy (full): 10 MeV;
- repetition rate: 5.6 MHz;
- emittance: 2π mm·mrad;
- energy spread (relative): $6 \cdot 10^{-3}$.

A future ERL based on this linac will be build at KAERI. An FEL and a Compton source will be driven by it. A project of the ERL should meet the following requirements:

- Accelerator should have two regimes, one for the FEL and the other for the Compton source. The regimes will be switched with magnets.
- The machine should operate in a wide energy range in order to provide broad band FEL retuning. The ERL will operate at the energy from 12 MeV up to 22 MeV.
- The possibility to control both S_x and S_y transport matrix elements independently and total isochronism of the ERL is necessary to suppress longitudinal and regenerative transverse beam instability. This possibility permits to increase the beam current and the FEL power.
- Low beam emittance degradation in the beamline is necessary for successful FEL operation and beam

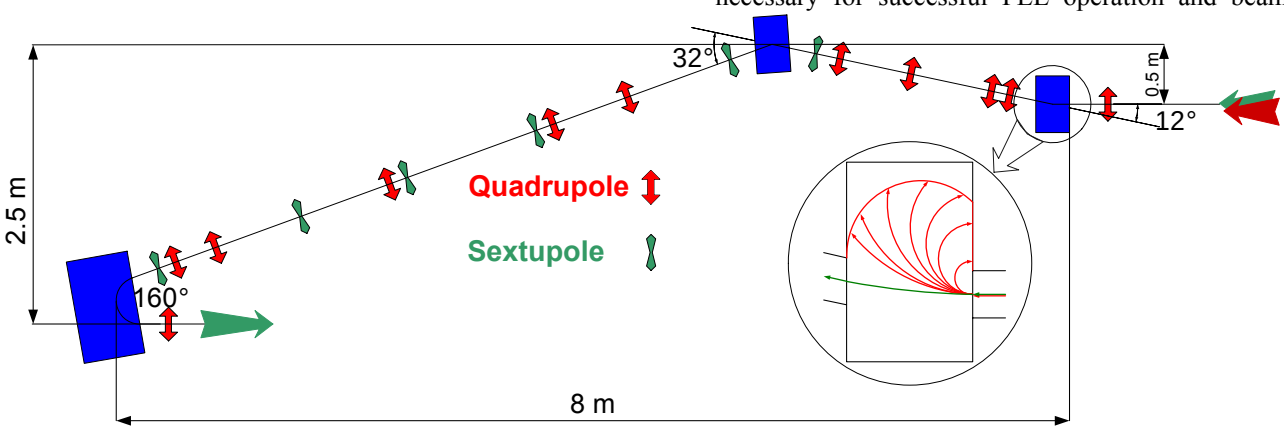

Figure 2. The layout of the first bent.

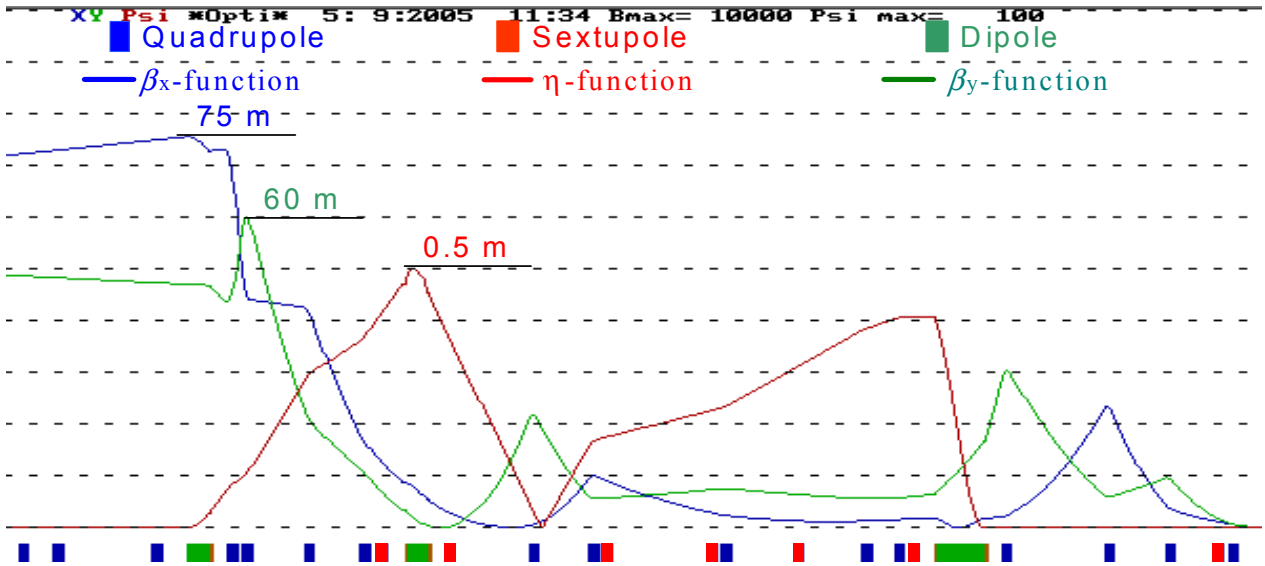

Figure 3. The lattice functions in the first bent.

energy recovery. Therefore we should use sextupoles to suppress chromatism which is the main reason of emittance dilution.

- Large energy aperture of the dump and the beamline after the undulator is necessary to obtain high FEL efficiency, as the energy spread after the FEL is proportional to its electron efficiency.

The machine will consist of two isochronous near achromatic bents (their small chromatism compensates $v < c$), and two straight beamlines separated by a dogleg. The FEL and the Compton source will be installed on these straight parts. The layout of accelerator optics is shown in figure 1.

FIRST BENT

Consider the first bent. It is necessary to control the longitudinal dispersion from 7 up to 17 cm to compensate that of the whole machine due to $v < c$. Emittance degradation in the bent should be low to keep FEL radiation quality. The dump is installed inside the first dipole of the bent. This design allows to avoid an extraction chicane. It also has a big energy aperture (> 1 MeV in the whole energy range) to collect the whole

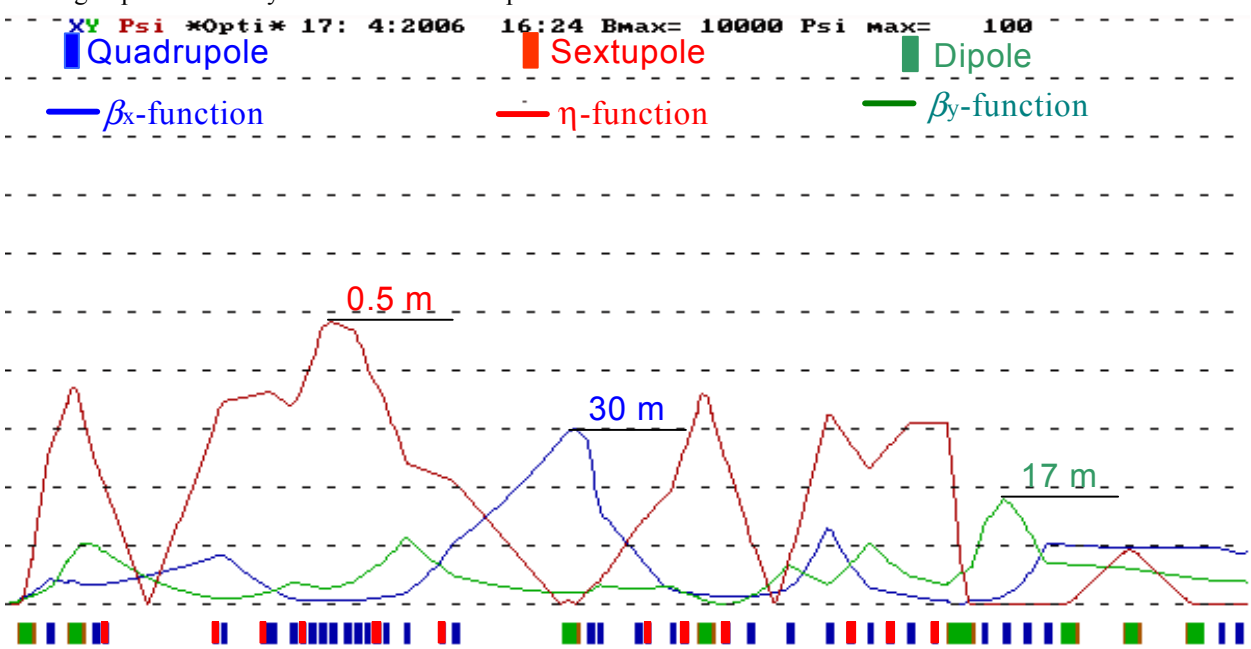

Figure 4. The lattice function in the beamline after the undulator in the FEL regime.

waste beam without loss. The accelerated beam moves through the common track together with the decelerated beam. Due to that, the capability to control the common track optics is very limited. Also the beam state at the entrance of the accelerating module is known only approximately. So the bent should operate successfully in the following range of the entrance lattice functions:

$$\begin{cases} \beta_z \quad \text{from} \quad 25\,\text{m} \quad \text{to} \quad 80\,\text{m} \\ \beta_x \quad \text{from} \quad 35\,\text{m} \quad \text{to} \quad 140\,\text{m} \\ \left|\alpha_{x,z}\right| \le 3 \end{cases}$$

The layout of the first bent is shown in figure 2.

It consists of three bending dipoles for 12°, 32° and 160°, the first dipole bends beam to the right while the two others to the left. It allows setting large negative η-function in the second dipole to compensate the longitudinal dispersion which gains in the mirror. The lattice functions in the bent in the FEL mode are shown in figure 3. Controlling η-function in the second dipole modifies the longitudinal dispersion in the whole bent within the necessary range. Sextupoles are installed in the bent in places with big η-function and small β-function to suppress chromatic aberration. The strengths of sextupoles are selected to zero $\partial\eta/\partial p$ and $\partial\eta'/\partial p$, and to decrease $\partial\alpha_{xy}/\partial p$ and $\partial\beta_{xy}/\partial p$ to the level where emittanse dilution due to chromatic aberration is equal to one due to nonlinear focusing in the sextupoles. This optimization leads to comparably small emittance dilution through the whole bent $\sqrt{\Delta\varepsilon^2}/\varepsilon \le 0.75$.

BEAMLINE AFTER UNDULATOR

The beamline after the undulator consists of a dogleg (two 32° dipoles), a strait beamline for the Compton source, the second bent similar to the first one, and an injection chicane. The main feature of the beamline after the undulator is big energy spread of the beam in the FEL regime. It leads to high emittance degradation as a result of chromatic aberration. Also large beam size due to nonzero η and high energy spread leads to significant edge aberration in quadrupoles. Chromatic aberration can be suppressed by sextupoles while edge aberration prevents to conduct a beam with relative energy spread greater than 0.06. Suppression of chromatic aberration is made similar to the first bent. The only difference is the beamline needs more sextupoles as their strengths are limited by emittance degradation. This method of suppression of chromatism provides a possibility to conduct a beam with relative energy dispersion 0.05 through the beamline with emittanse degradation $\sqrt{\Delta\varepsilon^2}/\varepsilon \approx 1$. The lattice functions in the beamline after the undulator in the FEL mode are shown in figure 4.

The beamline was simulated with OPTI code based on the linear transverse single-particle dynamics model. This model neglects space charge effect, so can't be used for the extraction beamline. In that case it is necessary to take space charge effect into account due to small beam energy in this part of the accelerator. It was made by code I&Eps [1]. In this simulation, focusing of the cavity was considered as concentrated at the edges of the cavity.

CONCLUSION

This design provides operation with high electron efficiency in the range of electron energies from 12 up to 22 MeV. It also allows suppressing longitudinal and regenerative transverse beam instability to increase beam current. The output power of a future FEL will be a few kW in the wavelength range from 35 to 70 μm.

The most desirable upgrade is one more pair of SC cavities. In this case the maximum beam energy of the ERL exceeds 40 MeV. It provide possibility to make an FEL in the near-IR region. Of course, a new beamline is to be designed in this case.

REFERENCES

[1] S.V.Miginsky An optimizer for high-current beamlines, NIM **A 558** (2006) 127-130.

THE NIJMEGEN FEL, A FEL OSCILLATOR WITH HIGH SLIPPAGE

P.J.M. van der Slot*, E. van Geijn, K.J. Boller
Mesa+, Department of Applied Technology, University of Twente, Enschede, NL
J. Jalink, W.J. van der Zande, IMM, Radboud University Nijmegen, Nijmegen, NL

Abstract

The Nijmegen Free-Electron Laser (FEL) aims at producing narrow bandwidth radiation for high resolution spectroscopy in the THz regime. To this end, the radio frequency accelerator based FEL will produce a train of phase locked optical pulses. We use the Medusa1D code to simulate the performance of this system at various wavelengths and undulator lengths and estimate the power available in a single line of the phase locked spectrum.

INTRODUCTION

The High Field Magnetic Laboratory at the Radboud University Nijmegen, and other such laboratories worldwide, have made it possible to study molecules in materials in fields with strengths approaching 40 Tesla. All elementary excitation energies increase proportionally. As a consequence strong (> 100 W) and coherent radiation sources are needed from 100 μm to 1.5 mm, the so-called THz gap. Narrow bandwidth radiation is best suited for coherent, saturation, and pulse-echo studies. Pulsed intense radiation is best suited for non-linear and time-resolved studies. The parameters of the Nijmegen Free-Electron Laser (NijFEL) have been chosen to provide such a radiation source. An RF accelerator based electron source will provide short electron bunches creating a train of intense micropulses of picosecond duration. A narrow bandwidth, ($\Delta\lambda/\lambda \simeq 10^{-5}$), equals the generation of bandwidth limited pulses (BWL) of hundreds of nanosecond duration. This is achieved by ensuring that the micropulses in the macropulse are fully coherent, either using spontaneous coherence or forcing coherence using an intra-cavity interferometer. It is expected that spontaneous coherence is helped by using electron pulses with lengths comparable to the wavelength to be generated. This implies the design of a FEL oscillator with high slippage.

The zero design parameters to achieve this performance with NijFEL are shown in table 1, and fig. 1 shows the resonant wavelength of NijFEL as a function of the undulator parameter K for different values of the electron beam energy E_b. The ratio of the electron bunch length l_e to the slippage distance Δz_s ($= N_u\lambda$ at resonance) varies approximately from 0.015 to 0.3 depending on the actual number of undulator periods and wavelength used. The performance of the NijFEL system is therefore highly dominated by short pulse effects [1]. Because of the long wavelengths (see fig. 1), NijFEL will use a half open resonator

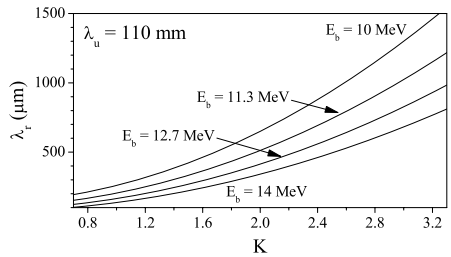

Figure 1: FEL resonant wavelength λ_r as a function of the undulator K parameter for different values of the electron beam energy E_b.

that provides waveguiding between the poles of the undulator.

To determine the performance for various undulator lengths and wavelengths, we use the Medusa1d code. This code retains, in the 1d approximation, all the features of the 3D Medusa code [2, 3]. It includes a simple oscillator model where the the radiation output at the undulator's

Table 1: Zero design values for NijFEL. $L_u = N_u\lambda_u$ is the undulator length

Accelerator			
RF frequencye	f_{RF}	3	GHz
Bunch charge	Q_b	300	pC
micro pulse duration	t_p	3	ps rms
Beam energy	E_b	10-14	MeV
Emittance (norm.)	ϵ_n	50	mm mrad
Energy spread (rms)	$\Delta\gamma/\gamma$	0.25	%
Duration macropulse	T_m	10-12	μs
Rep. rate macropulses	f_{rep}	≤ 5	Hz
Undulator			
Period	λ_u	110	mm
K (rms)	K	0.7-3.3	
Number of periods	N_u	30-40	
Oscillator & radiation			
Wavelength	λ	0.1-1.5	mm
Final rel. bandwidth	$\Delta\lambda/\lambda$	10^{-5}	
Power (after filtering)	P_u	>100	W
Total roundtrip loss	α_L	5-20	%
Waveguide heigth	h	10	mm
Length	L_r	L_u+2	m

* p.j.m.vanderslot@tnw.utwente.nl

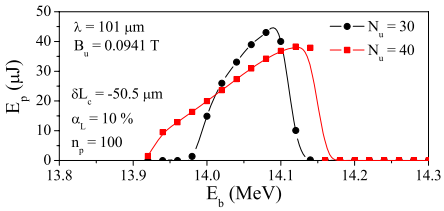

Figure 2: E_p versus E_b after $n_p = 100$ passes for $N_u = 30$ (circles) and 40 (squares).

exit is multiplied by $1 - \alpha_L$, α_L being the total single pass cavity loss, and, after appropriate shifting in the time to compensate for slippage Δz_s and cavity detuning δL_c, is used as input for the next pass. Furthermore, Medusa1d incorporates some 3D effects through Xie's fitting formula [4] which results in an increase of the energy spread of the electrons and a filling factor that includes both diffraction and guiding effects.

1D SIMULATION RESULTS

Medusa1d is not able to model the hybrid resonator that is planned for NijFEL. A geometric filling factor can be used to model overlap between electrons and optical field. However, this does not include possible guiding effects due to the FEL interaction [5, 6]. We therefore compared the filling factor for the hybrid waveguide and the one derived from Ming Xie's fitting formula for an open resonator. The latter is found to be larger than the filling factor for the hybrid waveguide. Apparently, guiding effects in NijFEL are sufficiently strong to influence the filling factor. We therefore consider an open resonator in the remaining part of the paper and use Xie's fitting formula to calculate the filling factor.

Furthermore, an up- and down taper of 2 periods is used at the entrance respectively exit of the undulator to allow proper injection and extraction of the electron beam. Values for parameters are taken from Table 1 unless otherwise specified.

Performance at $\lambda = 100$ μm

In order to produce a narrow bandwidth, the train of coherent optical pulses within the macropulse must be as long as possible. We want to minimize transient effects at the beginning of the macropulse. We therefore evaluate the performance of NijFEL at λ = 100 μm for both maximum gain and maximum efficiency settings of the electron beam energy. For an electron beam energy of 14 MeV and a peak undulator field of B_u = 0.0941 T we find a maximum single pass, small signal gain for $\lambda = 101$ μm. Figure 2 shows the intracavity optical pulse energy E_p after $n_p = 100$ passes as a function of E_b. The cavity detuning is $\delta L_c = -0.5\lambda$ with respect to a synchronous cavity that is defined by the roundtrip time of an optical pulse in an empty cavity being

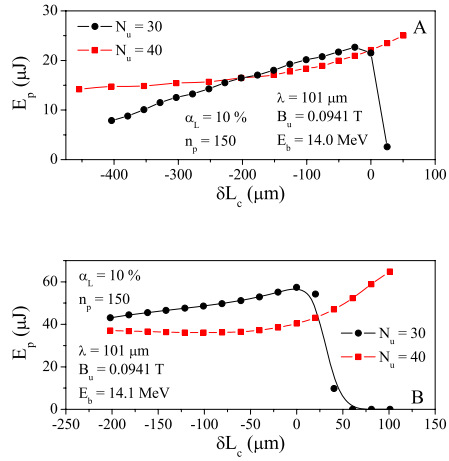

Figure 3: E_p after $n_p = 150$ passes versus δL_c for $N_u = 30$ (circles) and 40 (squares) at maximum single pass, small signal gain (A) and maximum efficiency (B).

a multiple of the time separating two consecutive electron bunches [1]. Fig. 2 shows that maximum efficiency is found at slightly higher value for E_b compared to the one required for maximum gain. We therefore have determined the detuning curve for both $E_b = 14$ MeV and 14.1 MeV. The results are shown in fig. 3. Fig. 3A shows that for maximum gain, E_p is about the same for the short and long undulator for $-2\lambda < \delta L_c < 0$ and the longer undulator has a higher pulse energy for smaller cavity lengths. Also the longer undulator shows considerable output energy for $\delta L_c > 0$, where the shorter undulator fails to lase. At maximum efficiency, we find the short undulator having higher optical energies over most of the detuning range investigated, except for cavity lengths larger than the synchronous length where the gain for $N_u = 40$ results in a sharp increase of E_p. We observe that E_p for maximum efficiency setting is about a factor of 2.5 larger than for maximum gain setting.

The number of roundtrips n_b required to reach maximum E_p is shown in fig. 4. This figure shows that indeed for the case of maximum gain significantly fewer roundtrips are required for the optical field to build up to saturation inside the resonator. At this wavelength, a minimum of about 50 roundtrips is required at maximum gain for negative cavity detuning and $N_u = 40$. It increases sharply for positive detuning. The shorter undulator requires at least 50 more roundtrips ($\sim 1.5\mu$s) to saturate. Also for maximum efficiency we find that the reduced gain results in a larger value of n_b.

The repetition rate of the optical micropulses will be f_{rep} = 3 GHz. As a consequence, if all the optical pulses are fully coherent, the resulting frequency spectrum of the train of optical pulses will consist of very narrow lines (linewidth of the order of 10 MHz) separated by the 3 GHz. Filtering of one of the narrow lines does not require a high

[1] $\delta L_c < 0$ means a shorter cavity length

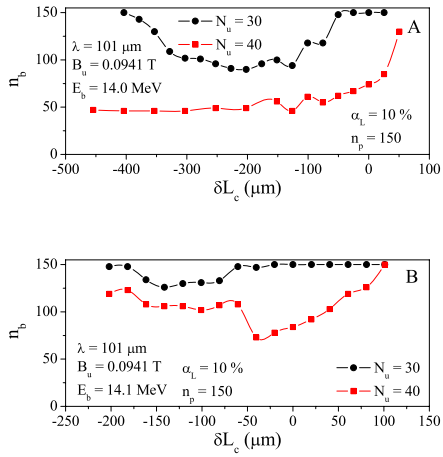

Figure 4: n_b versus δL_c for $N_u = 30$ (circles) and 40 (squares) at maximum single pass, small signal gain (A) and maximum efficiency (B).

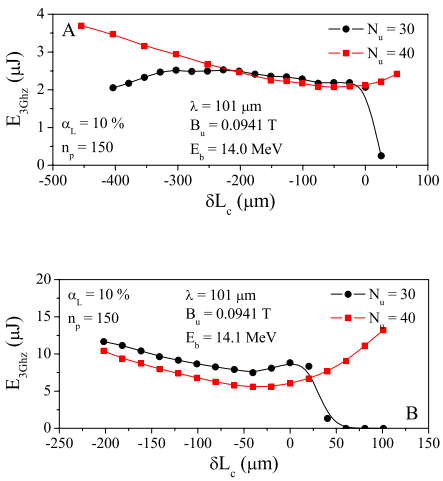

Figure 5: E_{3GHz} versus δL_c for $N_u = 30$ (circles) and 40 (squares) at maximum gain (A) and maximum efficiency (B).

quality etalon as a consequence of the large 3 GHz line spacing. To estimate the energy available after filtering, we have also determined the intracavity optical energy E_{3GHz} of a single optical micropulse in a bandwidth of 3 GHz around the central wavelength. This is an important figure of merit for narrow bandwidth operation of the NijFEL system, as this energy may be concentrated in a line with a width of 10 MHz. This figure of merit is shown in fig. 5 for both the case of maximum gain and maximum efficiency, and again for the two undulator lengths. As expected, we find for $N_u = 40$ that E_{3GHz} increases away from zero detuning [7]. For positive detuning this is due to both a higher pulse energy and an increasingly longer optical pulse. For negative detuning the micropulse energy decreases, however this is more than compensated by the increase in pulse length and hence a narrower spectrum, at least when the detuning is not too large. As a result, the figure of merit increase more rapidly for increasing positive detuning then for decreasing negative detuning. For $N_u = 30$, the behaviour is very similar, albeit that the gain becomes too low for positive detuning values and hence both E_p and E_{3GHz} drop quickly to zero (at least when we limit ourselves to at most 150 roundtrips). Fig. 5A also shows that, for large negative detuning, the figure of merit drops as the increase in pulse duration can not compensate the drop in energy any more.

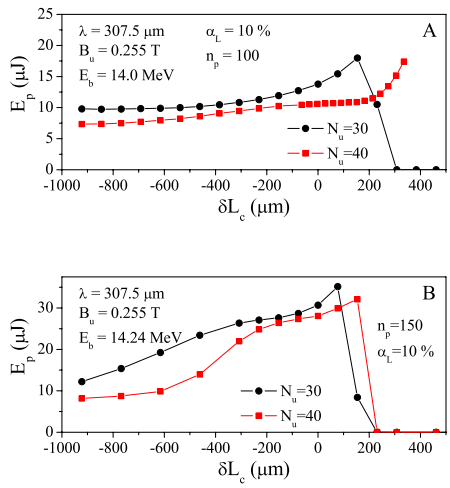

Figure 6: E_p versus δL_c for N_u = 30 (circles) and 40 (squares) at maximum gain and 100 passes (A) and maximum efficiency and 150 passes (B).

Performance at $\lambda = 300$ μm

Similar simulations as in the previous section have been done at a wavelength near λ = 300 μm as well, using the same beam energy of 14 MeV. Using $B_u = 0.255$ T, we find that the maximum single pass, small signal gain is found for $\lambda = 307.5$ μm. Using this wavelength, and varying the beam energy again around the value of 14 MeV, we find, that the maximum efficiency is now near $E_b = 14.24$ MeV. Because we expect a higher gain than for $\lambda = 101$ μm, we have taken a maximum of 100 and 150 passes for the high gain respectively maximum efficiency setting. The same results as for $\lambda = 101$ μm but now for $\lambda = 307.5$ μm are shown in figs. 6 to 8. Much of the features found for $\lambda = 101$ μm are also present for the 307.5 μm wavelength. However, for the case of high gain, the figure of merit is higher for the 30 period undulator than for the 40 period one, except for the longest resonator lengths investigated. Also, the higher gain at this wavelength results in an extension of the detuning curve to positive detuning values for the 30 period undulator. For the maximum efficiency setting, and moderate cavity de-

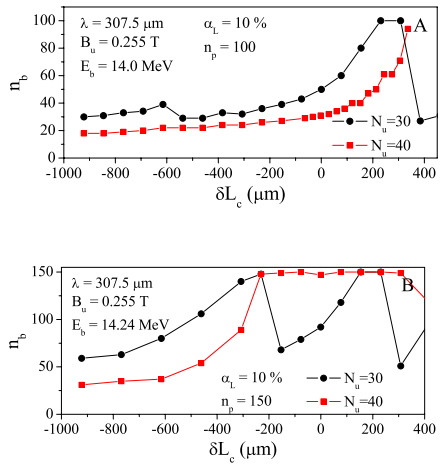

Figure 7: n_b versus δL_c for N_u = 30 (circles) and 40 (squares) at maximum gain (A) and maximum efficiency (B).

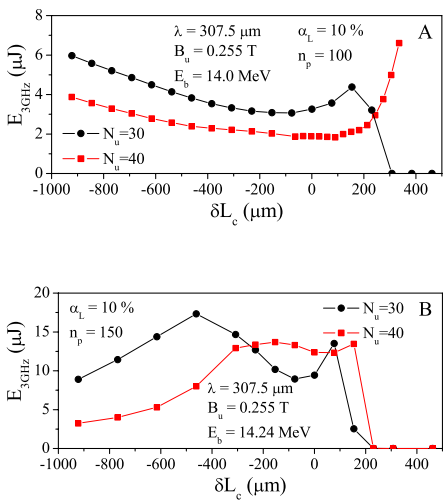

Figure 8: E_{3GHz} versus δL_c for N_u = 30 (circles) and 40 (squares) at maximum gain and 100 passes (A) and maximum efficiency and 150 passes (B).

tuning, the 40 period undulator has a slightly higher figure of merit, while for large negative detuning, the 30 period undulator has the higher figure of merit. This may be due to the fact that we used the same E_b for both undulator lengths while the actual value for optimum energy extraction may differ slightly (see fig. 2). Note, that for $N_u = 40$ and $\delta L_c > -300$ μm, E_p is limited by the maximum number of roundtrips used in the simulation. Comparing the two wavelength, we find that for $N_u = 40$ the minimum figure of merit is about the same for both wavelengths at maximum gain setting, while for maximum efficiency and at slightly negative detuning values the figure of merit is a factor of two higher at 307.5 μm. For the shorter undulator it is the other way around: at maximum gain, the figure of merit is about a factor of 2 larger for the wavelength $\lambda = 307.5$ μm, and for maximum efficiency it is about the same for the two wavelengths.

DISCUSSION AND CONCLUSION

In the simulation, the NijFEL system can either be set to produce maximum gain or maximum efficiency. For the first setting, the buildup time is smallest and we would expect the smallest bandwidth after filtering provided that the whole train of micropulses is fully coherent. The optical micro pulse energy is however significantly lower than can be obtain for the maximum efficiency settings. As a consequence, the figure of merit is also significantly higher for the maximum efficiency setting. Note that since Medusa1d is set up to use one frequency, it only calculates the optical energy in a finite bandwidth around this frequency. Thus, the resulting bandwidth may be smaller than the gain bandwidth of the laser. Hence, Medusa1d will under estimate the optical energy that can be produced by NijFEL.

The range of values for the figure of merit available through tuning the length of the cavity is the same for both undulator lengths at the longer wavelength, while for $\lambda = 101$ μm the range is larger for $N_u = 40$.

For the parameters investigated, the minimum figure of merit is 2 μJ. Assuming that half of α_L is due to outcoupling of the radiation, and using the 3 GHz repetition rate of the micropulses, we expect at least 300 W to be available in the strongest spectral line of a fully coherent macropulse. By optimising the detuning, the figure of merit can be at least a factor of 3 to 5 larger, hence, it seems that the design goals for narrow bandwidth operation of NijFEL can be realised with either undulator length. The performance has to be evaluated at other wavelengths as well before the optimum undulator length can be determined.

ACKNOWLEDGEMENT

We would like to thank Lex van der Meer of the FOM Institute for Plasma Physics Rijnhuizen for the useful discussions.

REFERENCES

[1] W.B. Colson, in “Free-Electron Laser Handbook”, eds. W.B. Colson, C. Pellegrini and A. Renieri (Elsevier, Amsterdam, 1990), Chap. 5.

[2] H.P. Freund, S.G. Biedron, and S.V. Milton. IEEE J. Quantum Electron. **36**, 275 (2000).

[3] H.P. Freund. Phys. Rev. STAB, **8**, 110701 (2005).

[4] M. Xie. Nucl. Instrum. Methods Phys. Res., A**445**, 59 (2000).

[5] E.T. Scharlemann, A.M. Sessler, J.S. Wurtele. Phys. Rev. Lett. **54**, 1925 (1985).

[6] G.T. Moore. Nucl. Instrum. Methods Phys. Res., A**250**, 381 (1986).

[7] A.M. Macleod, et.al., Phys. Rev. E **62**, 4215 (2000).

3D MODELLING OF THE ERLP IR-FEL

D.J. Dunning, N.R. Thompson and J.A. Clarke, ASTeC, STFC Daresbury Laboratory, UK.
B.W.J. M[c]Neil, SUPA, Department of Physics, University of Strathclyde, Glasgow, UK.

Abstract

The Energy Recovery Linac Prototype (ERLP) facility is currently being commissioned at Daresbury Laboratory. It serves as a testbed for technologies to be used in the proposed 4th Generation Light Source (4GLS) facility. As part of the ERLP facility, an infra-red oscillator FEL is due to be commissioned early in 2008. In this paper we present full three dimensional, time-dependent modelling of the ERLP IR-FEL using Genesis 1.3 in combination with a paraxial optical propagation code (OPC). We also discuss how this work will be used to inform commissioning of the FEL.

INTRODUCTION

The full details of the design for the ERLP IR-FEL are presented in [1] and summarised in Table 1 and a plan of the FEL is shown in Figure 1. Commissioning of the FEL is scheduled to begin early in 2008, and in preparation for this, full three dimensional modelling of the FEL has been carried out using Genesis 1.3 [2] in combination with a paraxial optical propagation code (OPC [3]). Both steady state and time-dependent simulations have been performed for three different modes of operation of the FEL. The results detailed in this paper will serve as a guide to the expected performance of the FEL during the commissioning period and will allow a comparison with experimental results so as to better inform FEL modelling for the 4GLS project.

Table 1: ERLP IR-FEL design parameters.

Parameter	Value
Wiggler period	0.027 m
Gap (fixed)	12 mm
Number of periods	40
Wiggler length	1.08 m
Deflection parameter, K	1.0
Nominal electron beam energy	35 MeV
Bunch charge	80 pC
Bunch length (rms)	<0.6 ps
Normalised emittance	10 mm-mrad
Energy spread (rms)	0.1 %
Optical cavity length	9.22438 m
Radiation wavelength (at 35 MeV beam energy)	4.394 μm

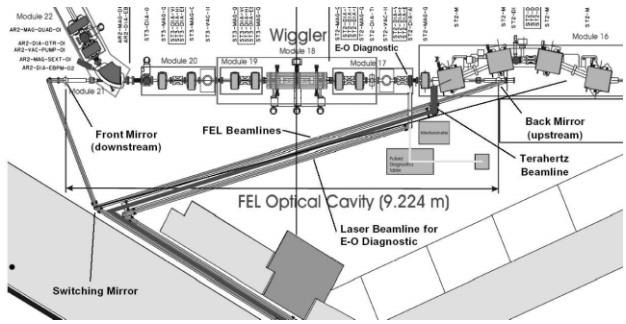

Figure 1: Plan of the FEL.

Operating Modes

The three proposed operating modes of the FEL are as follows: **normal mode**, **commissioning mode**, and **transmissive outcoupling mode**. A summary of the parameters for the different operating modes is given in Table 2. In transmissive outcoupling mode the electron bunch length is doubled, apart from this, the differences between different modes are in the mirror radii of curvature (ROC) and outcoupling method.

NORMAL MODE

The normal operating mode is designed to have maximum gain [4] and optimum output power. Details of this optimisation are included in the next section. The cavity is of a symmetric near-concentric design, of length $D = 9.22438$ m, with mirror ROC $R = 4.75$ m. The mirror angular alignment tolerance is $\ll 76$ μrad. Outcoupling is via a 1.5 mm radius hole in the downstream mirror, giving a 12 % outcoupling fraction (chosen to maximise the output power).

The optical mode radius at the centre of the wiggler is $w_0 = 1.04$ mm. At this location the matched electron beam radii are $\sigma_x = 0.24$ mm and $\sigma_y = 0.30$ mm. The electron beam jitter (in transverse position) is expected to be no more than 10 % of the beam radius. This means that the jitter in electron beam position is no greater than 3 % of the optical mode size and ensures the coupling between electrons and radiation is near-optimal. The optical mode radius on the mirror surface, assuming the fundamental transverse mode TEM_{00} is $w_{mirror} = 6.15$ mm compared to a mirror aperture radius of $a = 19$ mm. The ratio $a/w_m \approx 3{:}1$: this is large enough to ensure that diffraction losses from the fundamental mode are minimal. All higher order transverse modes are wider, and will therefore suffer more diffraction loss - this is advantageous because it encourages lasing at the fundamental mode. In effect the limited mirror aperture acts as a crude method of transverse mode control.

Table 2: A summary of parameters for the different operating modes (the abbreviations "US" and "DS" refer to upstream and downstream respectively). The parameters: stability, angular alignment tolerance, mode size, cavity loss and single pass gain are calculated using standard design formulae.

Mode	**Normal**		**Commissioning**		**Transmissive**	
	US mirror	*DS mirror*	*US mirror*	*DS mirror*	*US mirror*	*DS mirror*
Mirror Material	Cu/Au	Cu/Au	Cu/Au	Cu/Au	Dielectric	Cu/Au
Reflectivity	>98%	>98%	>98%	>98%	3% trans.	>98%
ROC (m)	4.75	4.75	4.75	4.75	5.0	5.0
Mirror aperture radius (mm)	19	19	19	19	19	19
Hole radius (mm)	No hole	1.5	0.75	0.75	No hole	No hole
Outcoupling type (location)	Hole (DS)		Holes (DS + US)		Transmissive (US)	
Stability g^2	0.88		0.88		0.71	
Angular alignment tolerance θ_m (μrad)	$\ll 76$		$\ll 76$		$\ll 157$	
Mode at waist w_0 (mm)	1.04		1.04		1.36	
Mode at mirror w_{mirror} (mm)	6.15		6.15		4.61	
Total cavity loss (%)	16		10		5	
Single pass gain (%)	72		72		25	
Electron bunch length σ_t (ps)	0.6		0.6		1.2	

Cavity optimisation

The cavity geometry has been varied around the proposed working point by changing the ROC of the mirrors simultaneously such that the waist position of the lowest order cold-cavity mode is kept constant. Figure 2 shows the effect of varying the radius of the outcoupling hole and the ROC of the cavity mirrors on the output power after 100 passes (by which time the FEL output is stable for almost all parameter sets used). This work has been carried out using Genesis 1.3 and OPC in steady-state mode. The results show that the proposed working point for normal mode operation (hole radius = 1.5 mm, mirror ROC = 4.75 m) is near optimum in terms of output power (~7.5 MW). The reduced output power around ROC = 4.8 m can be explained by considering the shape of the power profile at the downstream mirror (see Figure 4); the intensity cross-section peaks off-axis, hence the on-axis power outcoupled through the hole is lower.

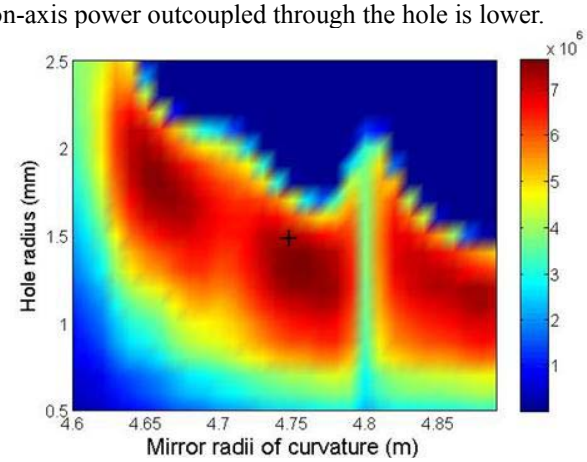

Figure 2: Output power (W) as a function of hole radius and mirror radii of curvature (i.e. keeping waist position constant). For normal operation, the hole radius is 1.5 mm and mirror ROC is 4.75 m.

For the proposed working point, the normalised intensity cross sections at saturation are shown in Figure 3 at different points within the optical cavity.

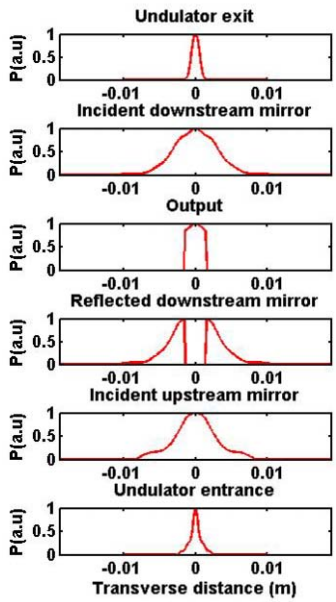

Figure 3: The normalised intensity cross sections at saturation, for different points within the optical cavity. Mirror radii of curvature = 4.75 m. The extent of the figure in the x-direction is equal to the mirror size (radius = 19 mm).

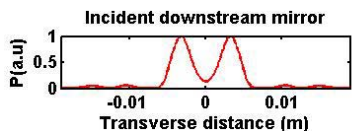

Figure 4: The normalised intensity cross section at the downstream mirror, at saturation, for mirror radii of curvature = 4.8 m.

Time-dependent simulations

Using Genesis 1.3 in time-dependent mode allows us to model the effects of cavity detuning, we are however, limited to detune the cavity only to half-integer multiples of the wavelength. Figure 5 show the cavity detuning curve for simulations of the FEL operating in normal mode. Higher peak output power (~16 MW at a cavity detuning of 2.2 μm) is seen compared to the steady state result (~7.5 MW).

Shown as a comparison is the corresponding cavity detuning curve for simulations performed using the one-dimensional code FELO [5]. There is a fairly good agreement between the two codes, particularly at smaller detuning values. Shown in Figure 6 is a comparison of the results from Genesis/OPC and FELO for a cavity detuning value of 4.4 μm (where the output power agreement between the two codes is closest); the longitudinal profile of the output radiation at saturation is plotted. There is a good agreement between the two codes for the longitudinal profiles of the FEL output at saturation.

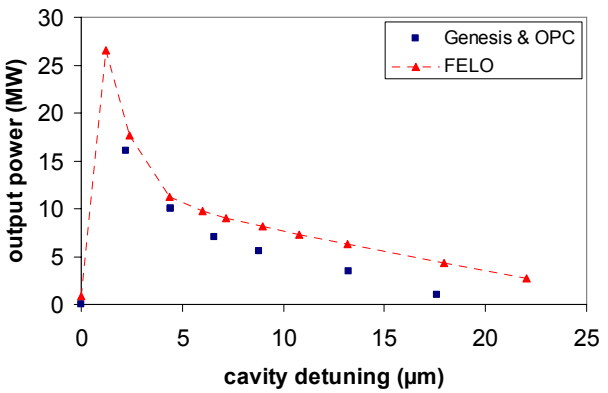

Figure 5: Output power at saturation against cavity detuning value for simulations of the FEL operating in normal mode, using Genesis 1.3/OPC and FELO.

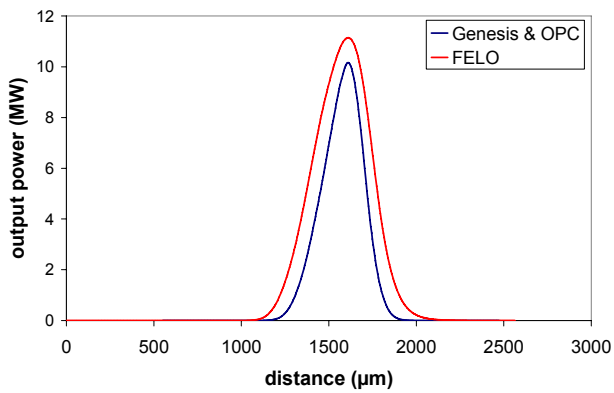

Figure 6: Longitudinal profile of the FEL output at saturation for a cavity detuning of 4.4 μm. Comparison between Genesis/OPC and FELO.

Shown in Figures 7 and 8 is the variation of longitudinal profile of the output radiation with cavity roundtrip number for two different cavity detuning values. Figure 7 shows the results with a cavity detuning of 2.2 μm; the width of the pulse is seen to be narrower than for the detuning value of 13.2 μm shown in Figure 8.

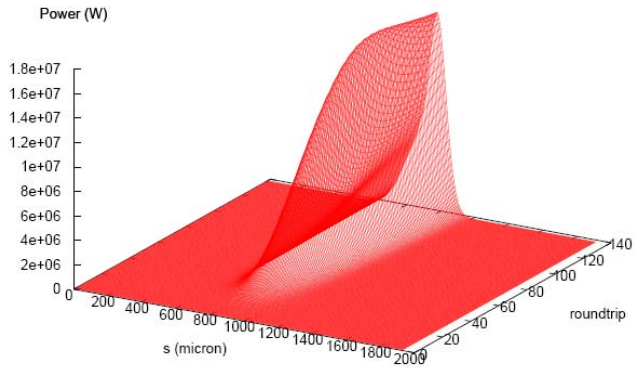

Figure 7: Variation of longitudinal profile of the output radiation with cavity roundtrip number for cavity detuning = 2.2 μm.

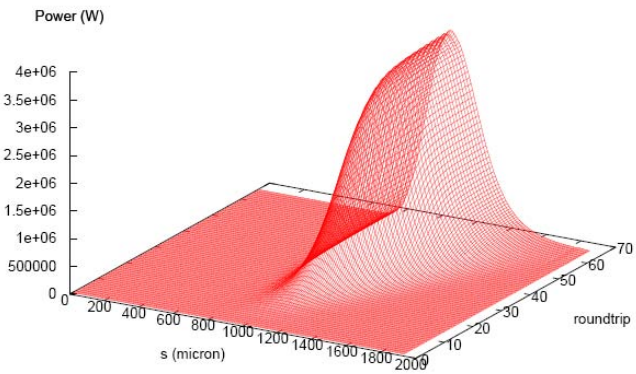

Figure 8: Variation of longitudinal profile of the output radiation with cavity roundtrip number for cavity detuning = 13.2 μm.

COMMISSIONING MODE

The commissioning mode of operation is designed for achieving first lasing; the cavity geometry is the same as for normal mode but outcoupling is via both mirrors. During commissioning we plan to monitor the FEL output directly at the upstream mirror while simultaneously monitoring the output from the downstream mirror in the diagnostics room. We therefore decouple the two problems of correctly steering the cavity to achieve lasing and correctly steering the output radiation down the beampipe to the diagnostics room.

Since outcoupling in this mode of operation is from both mirrors, smaller holes (0.75 mm radius) will be used, compared to the single hole used in normal mode operation. It is anticipated that this will reduce transverse mode distortion. Figure 9 shows the normalised intensity cross sections at saturation, at different points within the optical cavity. From the undulator entrance cross section it is evident that there is some higher order mode content in the radiation field.

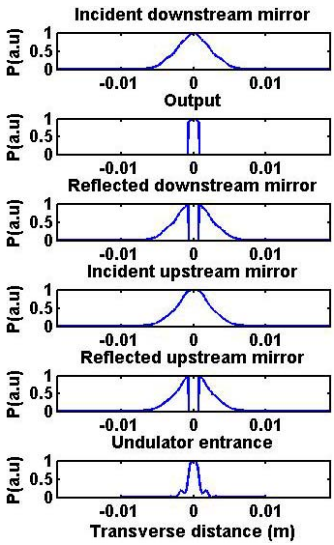

Figure 9: The normalised intensity cross sections at saturation for the FEL operating in commissioning mode, for different points within the optical cavity.

Time dependent simulations using Genesis 1.3 and OPC have been performed for the FEL operating in commissioning mode. Figure 10 shows the variation of output power with cavity detuning value. Figure 11 shows the variation of longitudinal profile of the output radiation from the downstream hole with cavity roundtrip number, for a cavity detuning of 2.2 μm.

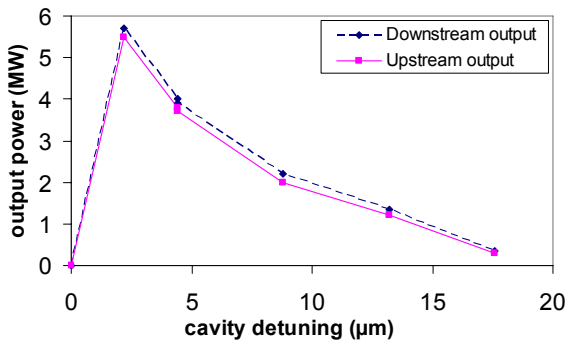

Figure 10: Output power at saturation against cavity detuning value for the simulations of the FEL operating in commissioning mode, using Genesis 1.3/OPC and FELO.

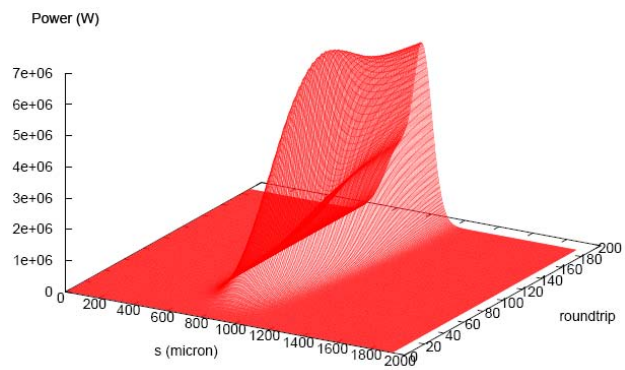

Figure 11: Variation of longitudinal profile of the output radiation from the downstream mirror with cavity roundtrip number for cavity detuning = 2.2 μm.

TRANSMISSIVE OUTCOUPLING MODE

The transmissive outcoupling mode of operation is designed to give us experience of using the transmissive outcoupling method and to increase the tolerances to electron beam transverse and longitudinal jitter and mirror angular alignment. The mirror cavity is designed to be further from concentric; increasing the mirror ROC to 5.0 m increases the optical waist to w_0 = 1.36 mm, reduces the cavity stability parameter g^2 to 0.71 and relaxes the angular alignment tolerance to $\ll$ 157 μrad. The electron bunch length is doubled to σ_t = 1.2 ps which halves the peak current but the calculated single pass gain is still 25 %, sufficient to lase easily with the outcoupling fraction reduced to 3 %.

The potential problem of mode distortion caused by hole outcoupling is removed by outcoupling using a partially transmitting (3 %) dielectric mirror. Because the cavity is further from concentric (compared to normal mode), the mode sizes shown in Figure 12 are wider at the waist and narrower at the mirrors compared to Figure 3. Time dependent simulations using Genesis 1.3 and OPC have been performed for the FEL operating in this mode and output powers of up to 12 MW are seen.

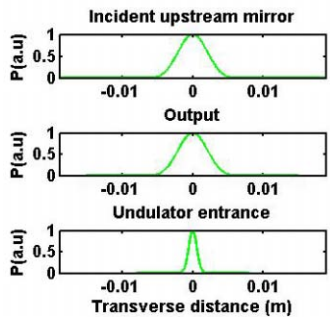

Figure 12: The normalised intensity cross sections at saturation for the FEL in transmissive outcoupling mode, at different points within the optical cavity.

CONCLUSION

Full three dimensional modelling of the ERLP IR-FEL has been carried out for the three different modes of operation of the FEL. For normal mode operation, the proposed cavity geometry and outcoupling hole radius have been shown to be near optimum in terms of output power. Time dependent simulations indicate a peak output power of ~16 MW at a cavity detuning of 2.2 μm.

REFERENCES

[1] N. Thompson, ERL Prototype FEL, internal report, *erlp-ofel-rpt-0001*, 2003.
[2] S. Reiche, Nucl. Inst. Meth. Phys. Res. A, 429, 243, (1999).
[3] J. G. Karssenberg et al, FEL-Oscillator Simulations with Genesis 1.3, FEL Conf 2006, 407.
[4] N. Thompson, ERL Prototype FEL: Electron Beam Matching, internal report, *erlp-ofel-rpt-0006*, 2004.
[5] B.W.J. McNeil et al, FELO, a one dimensional time dependent FEL oscillator code, FEL Conf. 2006, 59.

THE IR-BEAM TRANSPORT SYSTEM FROM THE ELBE-FELs TO THE USER LABS

W. Seidel, E. Grosse, M. Justus, K.-W. Leege, D. Proehl, R. Schlenk, A. Winter,
D. Wohlfarth, R. Wuensch
Forschungszentrum Dresden-Rossendorf, Dresden, Germany

Abstract

In the Forschungszentrum Dresden-Rossendorf, two free-electron lasers (FELs) have been put into operation. They produce laser light in the medium and the far infrared wavelength range (4-150 μm). The IR ligh is transported to several laboratories in the same building and to the adjacent building of the High Magnetic Field Laboratory as well, where the experimental setups are up to 70 m away from the FELs. Constructional peculiarities, the large wavelength range, the high average power in cw regime, and the beam property requirements of the users pose a challenge to the beam line design. The transport system includes vacuum pipes, diagnostic elements, plane and toroidal gold-covered copper mirrors, and exit windows. The designed transport system produces a beam waist at selected spots in each laboratory representing a magnified image of the outcoupling hole. Spot size and position are independent of the wavelength.

INTRODUCTION

The Radiation Source ELBE [1] at the Forschungszentrum Dresden-Rossendorf is centered around a superconducting Electron Linear accelerator of high Brilliance and low Emittance (ELBE), constructed to produce cw electron beams up to 1 mA beam current at 12-34 MeV. The electron beam is used to generate various kinds of secondary radiation, mainly to drive two free-electron lasers in the infrared region (4-150 μm). Starting in the summer 2005, beam time is offered to external users in the frame of the EC funded "Integrating Activity on Synchrotron and Free Electron Laser Science" (FELBE project [2]).

The IR radiation is produced in one of the two hybrid magnet undulators U27 and U100. Changing the undulator gap or the electron energy the wavelength of the produced IR beam can be varied from 4 to 22 μm (U27) and from 20 to 150 μm (U100). Additionally, a 633 nm beam from a HeNe laser used for mirror alignment has to be transported by the beam line.

The outcoupled laser power to be transported by the beam line depends strongly on the parameters of the electron beam and of the FEL undulator and resonator. Till now a maximum average cw power of 25 W has been obtained. Theoretical estimates predict a maximum cw power of about 35 W.

The IR light is transported to several laboratories in the same building and to the adjacent building (through a tunnel which is 27 m long) of the Dresden High Magnetic Field Laboratory (HLD, [3]) as well, where the experimental setups are up to 70 m away from the FELs.

The beam arriving at the user laboratories should be sufficiently narrow (a few millimeters). Its Rayleigh range should be long enough (10 cm at minimum). The profile should be circular with a Gaussian shape. It should not vary to much with the wavelength, with the size of the outcoupling hole and the used FEL. Linear polarization in horizontal or vertical direction should be conserved.

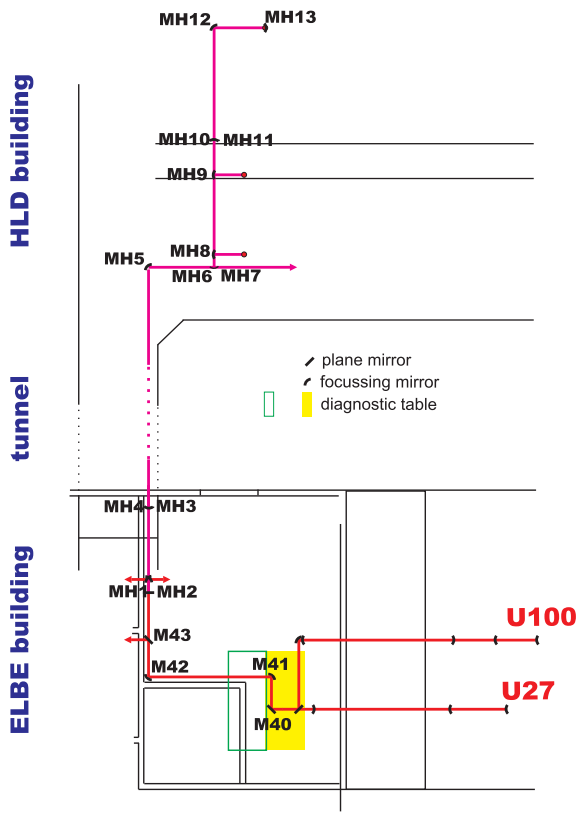

Figure 2: Top view of the beam line from the U100 and U27 FEL in the ELBE building to the user station in the HLD building via diagnostic table and tunnel.

DESCRIPTION OF THE BEAM LINE

The designed beam line is able to transport IR light in the wavelength range between 4 and 200 μm without noticeable diffraction and absorption losses. The HeNe adjustment beam is visible in the whole transport system. To avoid the absorption of IR light in the ambient air the beam is guided in pipes which are either evacuated or purged with

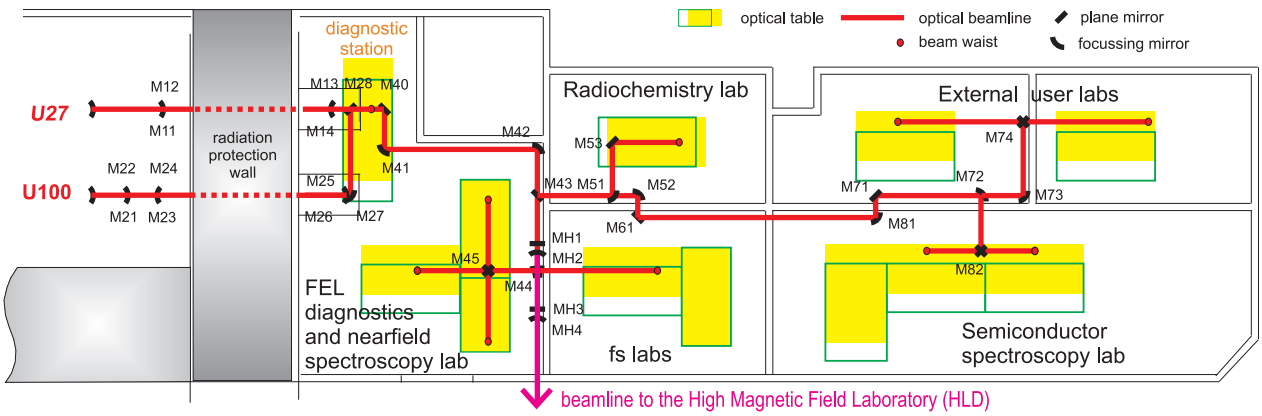

Figure 1: Top view of the beam line (red line) from the outcoupling holes of U27 and U100 through the diagnostic station to the optical tables in the various user laboratories.

dry nitrogen gas. The mirrors are mounted along the walls of the laboratories on supports 105 cm above floor, in general. Because of the large wavelength range we use reflective optics with metal mirrors [4] (gold-coated copper and stainless steel). Their reflectivity is 98.8% [4], the surface roughness is below 0.2 μm. In many cases the mirrors are used simultaneously to deflect and to refocus the beam. The distance between refocusing mirrors must be considerably smaller for the far infrared than for visible light.
Altogether 16 flat and 27 focusing mirrors are used in the transport system (all are fixed in gimbal mounts). They deflect the beam by 90 degrees. We use bifocal toroidal mirrors to have the same focal length in the meridional and in the saggital plane. In this way we reduce the number of mirrors to a minimum. To keep spherical aberration small the radii of curvature must be larger than the beam radius is. In general, the distance between two focusing mirrors is short enough to keep the beam narrow enough for a 10 cm beam pipe. In the tunnel to the HLD, a long straight distance has to be covered without any corner. Here we chose a 20 cm pipe to avoid refocusing within a straight section of the beam line. Farther, in the magnetic laboratories the beam pipe can be reduced to 16 cm. The effective diameter of the mirrors (viewed in beam direction) is 10, 20 and 16 cm accordingly. The path of the IR beam from the FELs to the experimental tables in the user laboratories is displayed in Fig. 1.
The beamline starts in the FEL cave at the outcoupling holes in one of the resonator mirrors of the U27- or U100-FEL (left side of Fig. 1). There is a diamond window roughly 4 cm behind the outcoupling holes. It separates the ultra-high vacuum in the resonator from the beam line. The window is mounted under the Brewster angle of 67 degrees to let pass horizontally polarized light without reflecting it. The window aperture has a diameter of 8 mm (U27) and 12 mm (U100), respectively. To sustain the static and dynamic pressure difference the diamond slab is 350 μm (U27) and 570 μm thick. Further windows are placed on the diagnostic table (Diamond) and at the ends of each particular beam line (ZnSe, KRS-5, TPX, Quartz, Diamond, respectively the beam properties). From the outcoupling hole the beam is transported to a diagnostic table in the neighboring room where the beam parameters can be measured. Some of them (average power, repetition rate) can also be modified [5].

The FEL cave is separated from the user laboratories by a radiation protection wall which is 2.6 m thick (see Fig. 1). This wall has to be by-passed by the laser beam. A straight connection between these rooms would allow γ-quanta and free neutrons produced by the high-energy electron beam in the FEL cave to enter the diagnostic laboratory.
Behind the diagnostic table the beam is transported into 6 laboratories in the ELBE building and additionally into the High Magnetic Field Laboratory in a separate building. The latter is connected with the ELBE building by a tunnel which is 27 m long. The branch guiding the beam to the HLD is shown in Fig. 2.
To evaluate the beam propagation theoretically we used the method of the equivalent Gaussian beam [6]. The beam passing the outcoupling hole is described as a circular Gaussian beam with a waist at the hole. The slight curvature of the wave front at the outcoupling hole can be neglected. The waist size w_0 in the hole is determined by the diameter D_h of the hole according to $w_0 = 0.7 * D_h/2$. The same relation is used to assign a nominal diameter $D_b = 2 * w/0.7$ to the Gaussian beam at any place in the beam line. The description as a Gaussian beam is considered an approximation which allows analytically to evaluate the propagation of the outcoupled beam. We have tested this approximation in several cases by means of the wave optical code GLAD [7]. The diameter of apertures in the beam line should be larger than the beam diameter D_b, to avoid power losses and diffraction ripples in the beam profile. Fig. 3 shows the beam diameter D_b along the beam line from the outcoupling hole to the diagnostic table for both FELs. On its path, the beam is sufficiently slight to

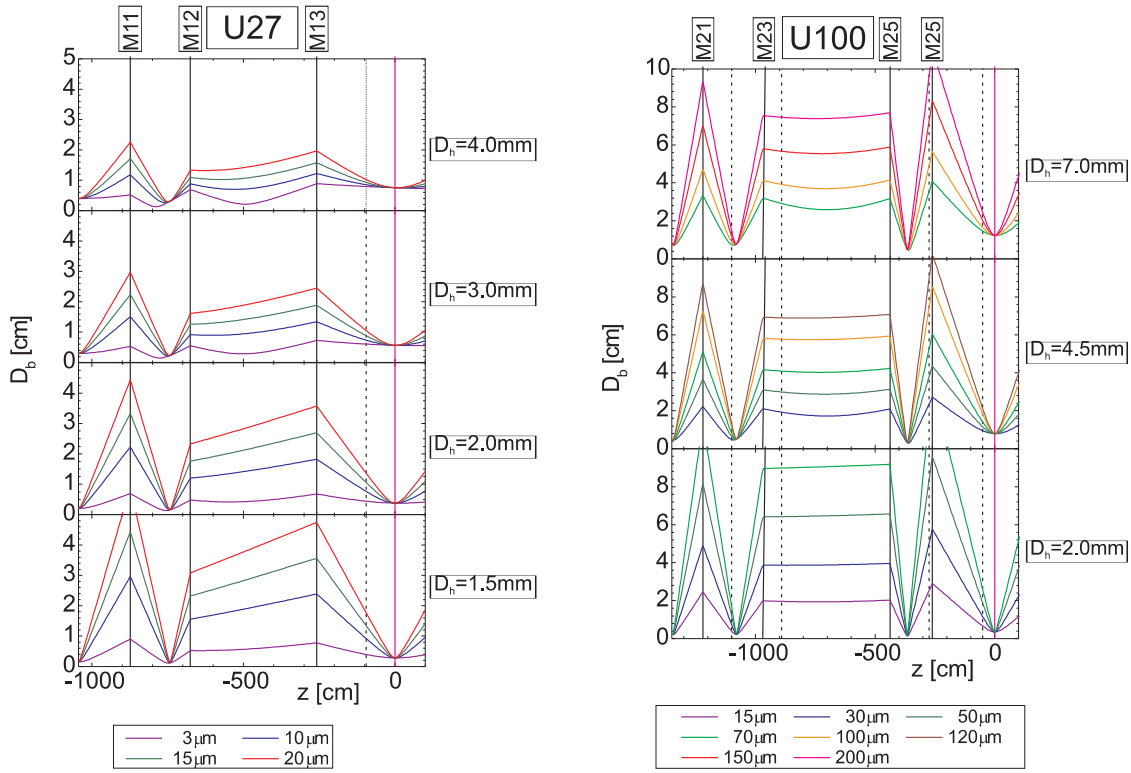

Figure 3: Diameter D_b of the IR beam calculated along the beam line from the outcoupling hole to the waist on the diagnostic table (z=0) for various wavelengths and outcoupling holes with diameter D_h. Focusing (Mik) and flat mirrors are indicated by vertical solid and broken lines, respectively. The position of the diagnostic waist is indicated by the magenta line. Left panel: U27-FEL, right panel: U100-FEL.

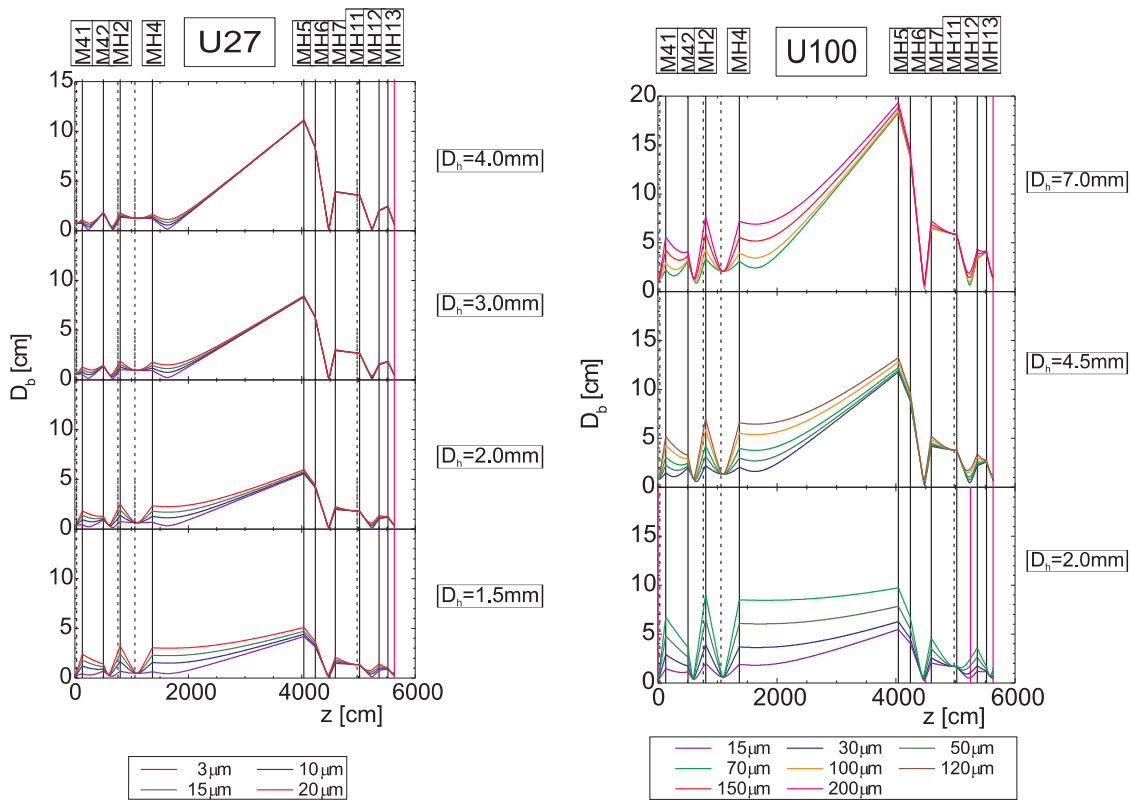

Figure 4: The same as in Fig. 3 for the beam line from the waist on the diagnostic table (z=0) to the HLD.

fit into a 10 cm beam pipe. On the other hand, it is broad enough not to damage the mirror surfaces by a big power density. The waist on the diagnostic table ($z = 0$ in Fig. 3) is common to the beams from each outcoupling hole in either FEL and to all wavelengths as well. Only the waist size is proportional to the diameter of the outcoupling hole. The narrow beam in the vicinity of the waist is used for beam measurements and modifications.

The beam line to the HLD is a particular branch of the general line delivering the laser light from the IR FELs to several user laboratories. It branches off from the general line behind mirror M43 by inserting the flat mirror MH1 (see Fig. 1) into the beam line. It bents the beam down to a specific line guiding the beam via mirrors MH2 - MH4 into a tunnel on basement level which connects the ELBE building with the HLD. Arriving the tunnel the beam is refocused (MH4) to a nearly parallel beam. However, diffraction increases the IR-beam size much stronger than in the range of visible light. Towards the end of the tunnel the beam is too thick for a 10 cm pipe and the pipe diameter has to be increased to 20 cm. The beam size calculated along the beam line is shown in Fig. 4.

In order to test the validity of the approximation by a Gaussian beam, the beam profile behind the outcoupling hole and on several positions in the beam line has been measured. These profiles are in conformity with the corresponding Gaussian profile. The power transmission of the beam line depends strongly from the used windows, the wavelength and the length of the beam line and was measured to be 15-90 %.

REFERENCES

[1] P. Michel et al., Proceedings of the 2004 FEL Conference, p. 8-13, Trieste, Italy

[2] www.fz-rossendorf.de/felbe

[3] J. Wosnitza et al., J. Phys.: Conf. Ser. 51, 619 (2006)

[4] LT Ultra-Precision, www.lt-ultra.com

[5] W. Seidel et al., Proceedings of the 2006 FEL Conference, p. 341-344, Berlin, Germany

[6] H. Kogelnik, Appl. Opt. **4** (1965) 1562-1569

[7] GLAD, Applied Optics Research, Woodland, WA 98674, USA

THERMAL AND NON-THERMAL LASER CUTTING UTILIZING ADVANCED INDUSTRIAL LASERS AND ERL-FELS *

Eisuke J. Minehara,
JAEA, 2-4 Shirakata-shirane, Tokai, Naka, Ibaraki 319-1195, JAPAN.

Abstract

The JAEA and JLAB energy-recovery IR free-electron lasers (ERL-FEL) have successfully demonstrated their capabilities of a sub ps pulse, high efficiency, GW high peak power, kW average power, and wide tunability. Utilizing the high power FEL and ERL technologies, we could realize a more powerful and more efficient FEL than 20kW and 25%, respectively, for nuclear industry, pharmacy, medical, defense, shipbuilding, semiconductor industry, chemical industries, environmental sciences, space-debris cleaning, power beaming and so on very near future. We have performed their thermal and non-thermal cutting experiments using advanced industrial lasers like fiber, and water-jet guided ones and the ERL-FELs, and have characterized them according to their resultant effects.

INTRODUCTION

Two nuclear power plants of the 166MW Tokai power station and 165MW Fugen power stations have been prepared and partially started to decommission in Japan recently. The Tokai power station is the first nuclear power plant for commerce in Japan and decommissioning of the Tokai power station is the first project of the nuclear power plant for commerce in Japan. The Fugen is the advanced thermal reactor prototype using heavy water moderator, light water cooling, and dense piping structure in the core. Feasibility studies of laser cutting are discussed here to compare a few kinds of commercially-available advanced industrial lasers and ERL-FELs with each other.

The currently-available CW lasers like CO_2, YAG, and fiber lasers are widely used to cut, to drill and to peel-off the material sheet, rod, and pipes of stainless steel, zirconium alloy, and others in the power plants, factories and laboratories. Cutting mechanisms of all the lasers listed above to machine the materials are blown off or burn out the melted one by feeding the assisting gases of highly-pressurized inert gases and oxidation gases like N2, O_2 and others. Therefore, we can easily expect that there are some intrinsic difficulties to cut, to drill and to peel-off the materials wherever and whenever we cannot feed either one of the laser power and pressurized gases to the machining point. We can cut the stainless steel sheet at the speed of 10 meter per minute or even the higher one whenever we can feed enough amounts of the laser power and gas at the cutting point. Double-layered, and multi-layered sheets, and rod and pipe bundles are intrinsically difficult to cut completely using the mechanism discussed here and all the lasers being commercially-available in the world. Therefore, we have to give up cutting the layered sheets and bundles at once simply using the mechanism and all the lasers. We can only cut the layered sheets layer by layer, and bundles step by step after removal of the cut layer, cut rod, and cut pipe as long as we will use all the commercially-available lasers. The layer by layer and step by step cutting with all the lasers is not so quick enough to decommission the power station facilities. There is no commercially-available sub-ps or a few ps ultra-fast, GW peak power, kW average power free-electron lasers [1] to cut the multi-layered and bundled structures at once. As they have been under development over last 10 years, they will be commercially available next 10 years.

ADVANCED INDUSTRIAL LASERS

The figures 1 and 2 show the fiber laser device and cut sample as one of the typical industrial laser examples.

Figure 1: 1 to 50kW CW Ytterbium fiber lasers are manufactured by IPG Photonics. A typical example of the commercially-available advanced industrial CW lasers.

*Work supported by in part by Grants-in-Aid for Scientific Research (A19206103).
minehara.eisuke@jaea.go.jp

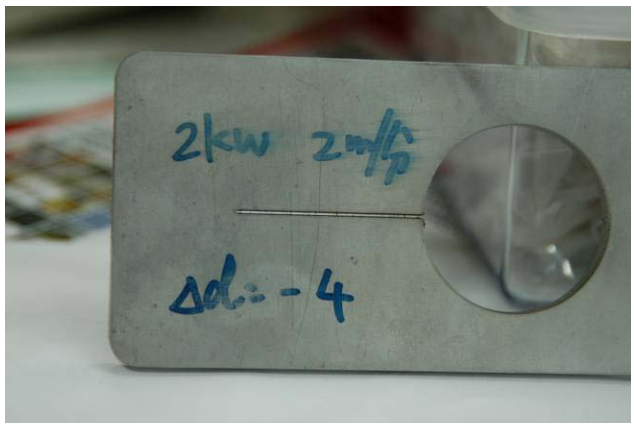

Figure 2: A Stainless-steel plate of 4mm thick and 40mm wide and 80mm long was successfully and quickly cut using 20 bar compressed and focused N_2 gas flow and IPG made 2 kW CW Ytterbium fiber laser. The 2kW fiber laser system usually has a capability of thick metal plate cutting from a few mm up to ten and several mm.

The fiber lasers have been often used to produce the CW power output ranging from several hundred W to 100 kW. In decommissioning the Fugen power station, we can expect about 4000 tons of radioisotope-contaminated waste and 370000 tons of dismantled materials. Especially, we can easily apply the currently and commercially available lasers like fiber lasers to cut and to dismantle the dense piping structure and the thick tank in the Fugen power station.

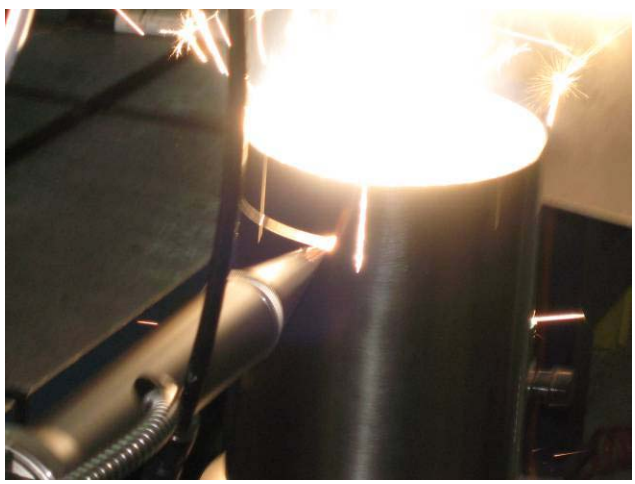

Figure 3a: A Fugen Zirconium alloy pressurized tube of about 4.3mm thick and 117.8mm inner diameter was successfully and quickly cut with 6m per a minute using 20 bar compressed and focused N_2 gas flow and IPG 5kW fiber laser.

The pressurized tube and Carandoria tube of Zirconium alloy were originally tried to cut at the same instant in the Fugen station. As it is very difficult for currently and commercially available industrial lasers to cut at the same instance, here we tried to cut them one by one by the fiber lasers shown in Figs.3a and 3b. Because the speed of the laser cutting is very fast and reliable in 5-6 m per minute or even faster, we can directly cut them into the small pieces from the inside to outside using a small and specially -designed laser nozzle one by one.

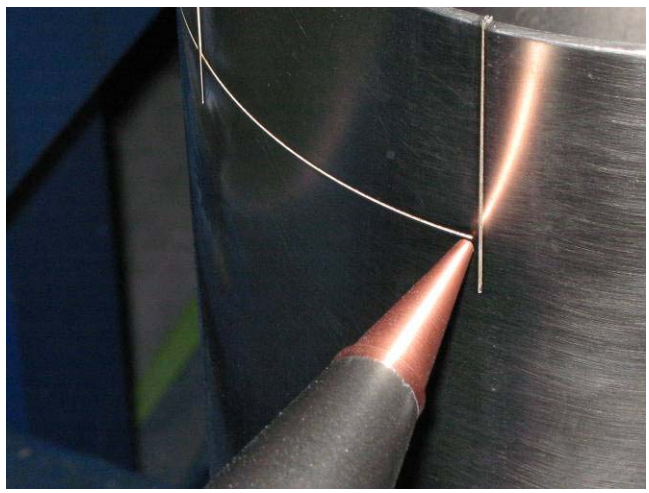

Figure 3b: The Zirconium alloy tube was cut with very high speed of 6m per a minute, and cut-width was as narrow as 0.25mm more or less. Surface condition of the cutting edges is very beautiful and very smooth and slightly narrower than the Stainless steel cases.

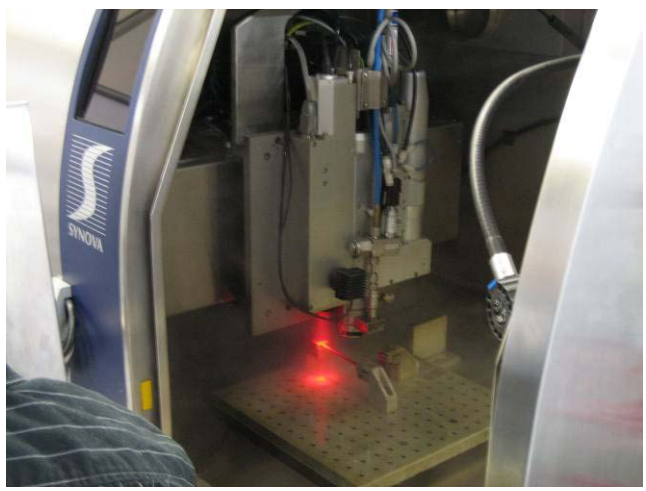

Figure 4: Water jet-guided laser named LMJ(Laser Micro-Jet) driven by 100-200W pulsed YAG laser manufactured by Synova S.A., Switzerland is another typical example of the new, commercially-available, and advanced industrial lasers.

A so-called water jet-guided laser named Laser Micro-Jet(LMJ) shown in Fig.4 is the newest laser - manufacturing tool and applicable to decommissioning of nuclear power plants. The LMJ was recently-invented by the researchers in the early nineties at the Federal Institute of Technology in Lausanne, Switzerland. We already have tried to cut, to drill and to peel-off non-radioactive metal samples. We hope to increase the available laser power in LMJ system from 100W to one kW, and we can easily estimate that the needed duty factor is not so large to be several % more or less.

ERL-FELS

Figure 5 shows the JAEA free-electron laser that we can convert them from quasi-CW machine to full CW or higher duty ones to cut the multi-layered and bundled materials at once. After the conversion, we can sharply cut the very thick tank wall with a very small gap width, drill and peel-off without producing a large amount of radioisotope (RI)-contaminated dusts during the decommissioning operation.

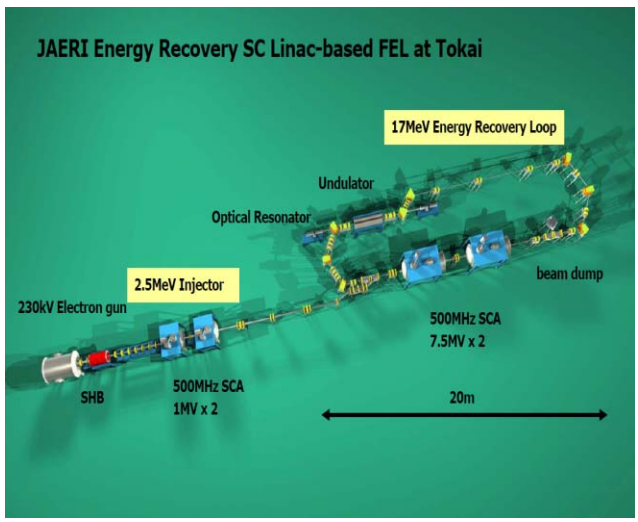

Figure 5: The JAEA energy recovery super-conducting linac-based free-electron laser(ERL-FEL) at Tokai.

Very good cutting performances of ERL-FELs are expected for Stainless-steel and Zirconium alloys because of millions times larger peak power, the same kW high average one, and very good laser divergence.

Three industrial FEL models having the reflextron[2] or similar geometry are illustrated in Fig. 6. Three of them are infrared FELs, and the fourth ultraviolet or visible FEL. As shown in Fig.6, the far-infrared FEL (FIR FEL) ranging from 200 to 50micron wavelengths uses the 500MHz UHF band cavity of 5-10MeV electron energy with the reflextron energy recovery geometry.

A mid-infrared FEL (MIR FEL) ranging from 50 to 8 micron wavelengths will use the 500MHz UHF band cavity of 12-24MeV electron energy with the reflextron geometry. Possible and typical applications are expected to be large-scaled photochemical processing, medical, pharmacy, rare-material separation, radio isotope separation in nuclear decommissioning and so on. A near infrared FEL (NIR FEL) ranging from 12 to 2 micron uses the same 500MHz cavity of 24-48MeV electron beam energy with the reflextron.

As shown in Fig.7, 1.3micron high peak power and high average power JLAB FEL light could instantly cut the 316L stainless-steel bar sample like boiling water reactor components and stainless-steel thick bar without high pressurized blow-off gas. All conventional laser cutters must need a focused and very high pressurized gas flow to blow off narrow part of the laser-heated and melted metal material.

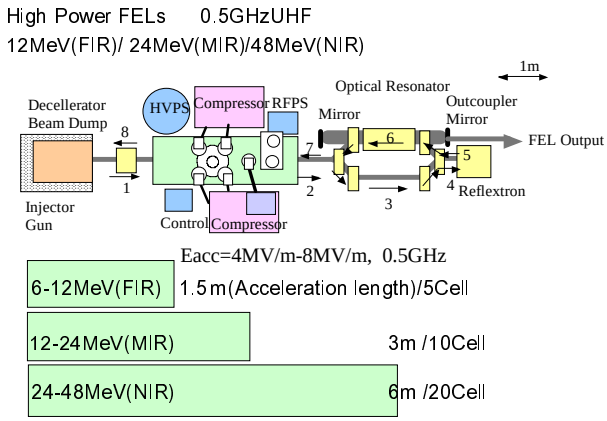

Figure 6: Three industrial FEL models for lasing in the FIR, MIR, and NIR wavelength regions with the reflextron geometry. All of them use the 500MHz UHF band cavities of 5, 10 and 20 cells, respectively.

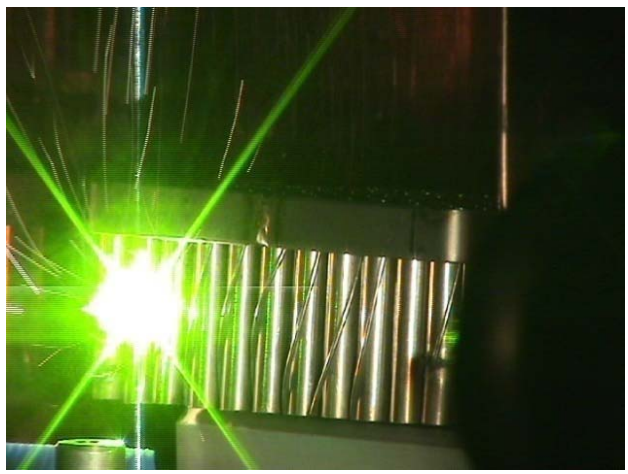

Figure 7: High peak power and high average power JLAB FEL light could instantly cut the 316L stainless-steel bar sample like boiling water reactor components and stainless-steel thick bar without high pressurized blow-off gas.

A 10 or 20kW industrial FEL which can lase at around a fiber-transmittable wavelength of 1.3 micron and at around water transmittable wavelength centered around 0.5 micron will be very useful to transmit their power to a pin-pointed position in a distant area from the FEL. The FEL will be widely used in the many factories like a shipyard, automobile factory, civil engineering, nuclear power plant and so on.

A few FEL application examples will cover the application of non-thermal peeling, cutting, and drilling to decommission the nuclear power plants, and to prevent stress-corrosion cracking in the nuclear decommissioning industry. As a very thin cutting width has been thought to realize a so-called RI contamination free decommissioning, we plan to use a water-jet guiding of FEL light for non-thermal peeling, cutting, and drilling in decommissioning the nuclear power plants. And we also

have demonstrated to prevent cold worked stress-corrosion cracking of the vital components like pressure vessel shroud and recirculation pump piping in the nuclear power plant. The cold worked stress-corrosion cracking sample like BWR shroud is shown in Fig. 8.

A preliminary characterization of the 316L stainless-steel samples shows that the KW CW fiber laser cutting resulted molten zone, high residual tensile stressed area, and high Vickers number hardened layer in the surface, on the other hands, the water jet-guided and JLAB ERL-FEL lasers no molten one, almost no residual tensile stressed one, and the low Vickers number one as the same with the material deep inside.

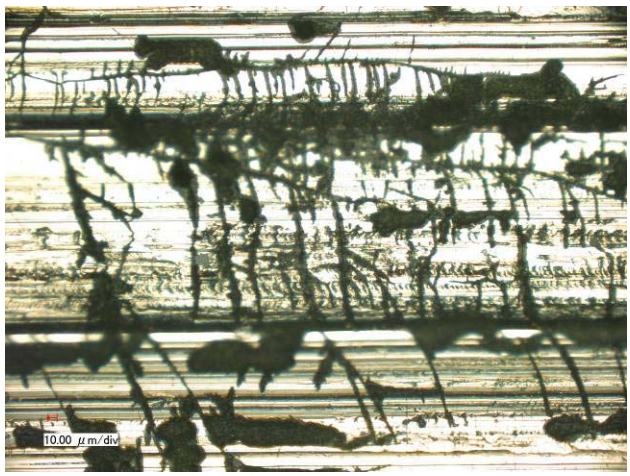

Figure 8: A large number of typical cold worked stress-corrosion cracking(CWSCC) are found in the 316L stainless-steel sample which have often been used in the boiling light water reactor (BWR) shroud and other reactor internal components after the JIS(Japan Industry Standard) defined $MgCl_2$ SCC test of 20 hours.

CONCLUSIONS

The FELs driven by the superconducting RF linac have intrinsically very high average power capability because the linac driver is highly efficient and powerful. Relatively low efficiency converted from the electron beam to FEL power can be overcome, and increased to recover the remained beam power after the lasing by the ERL. The ERL technology can be usable to make the FEL efficient drastically, and to realize the industrial FELs for many major industry fields including the nuclear power ones soon. The reflextron like geometry can be applied to make the industrial FELs compact, powerful, and efficient because an absolute value of the velocity difference is very small between the acceleration and deceleration along the accelerator cavity at the same position, and we can recover very efficiently the beam power at a few MeV or less electron energy.

We can also add that the preliminary characterization of the 316L stainless-steel samples using ERL-FELs and water jet-guided laser show very clear and promising results for their non-thermal machining capabilities.

ACKNOWLEDGMENTS

The author gratefully express his thanks to Drs. G. Neil, M. Shin, S. Benson, G. Williams, J. Kevin, J. Gubeli and many other colleagues in JLAB FEL facility and all members of JAEA ERL-FEL one for their valuable and kind suggestions and helps on the FEL machining trials, and Profs. H. Horike and T. Fukuda of Osaka University for his continuous encouragement. This work has been supported in part by Grants-in-Aid for Scientific Research (A19206103).

REFERENCES

[1] Minehara, E.J., et al., ‘‘Development and operation of the JAERI superconducting energy recovery linacs’’ , Nucl. Instr. and Meth. in Physics Research Section A, Vol. 557, Issue 1, 1 Feb. 2006, pp 16-22.

[2] E. A. Heighway, “Magnetic Beam Defection System”. Canadian Patent 993124, issued 1976.

PRELIMINARY DESIGN OF THE PROPOSED IR-FEL IN INDIA

Srinivas Krishnagopal*, Vinit Kumar
RRCAT, Indore, M.P. 452013, India

Abstract

We discuss preliminary design studies of an infrared (IR) free-electron laser (FEL) proposed to be built at the Raja Ramanna Centre for Advanced Technology (RRCAT). The design calculations and optimisations have been performed using the three-dimensional time-dependent oscillator code GINGER [1].

INTRODUCTION

A terahertz free electron laser, the CUTE-FEL, designed to lase around a wavelength of 80 μm using a 10 MeV linac is in an advanced stage of construction at RRCAT [2]. In the next step in our FEL activities, we have proposed to build an IR-FEL. In this context, we have performed design studies of an IR FEL to lase between 12-50 μm, which will use a 15-25 MeV linac. In this paper, we focus mainly on 30 μm simulations and briefly discuss the results at 12.5 μm and 50 μm also. The high power, short pulse and widely tunable coherent radiation from this IR-FEL can be used for performing a wide range of interesting research applications that include experiments on direct as well as indirect band-gap semiconductors, IR microscopy of biological samples, multi-photon dissociation experiments, isotope separation, reaction dynamics studies, etc.

In the next section, we discuss the basic design considerations and then in the following section, we discuss design simulation results. We finally conclude in the last section.

DESIGN CONSIDERATIONS

After preliminary consultaions with users, we found that a wavelength range of 12-50 μm is interesting for a wide range of many interesting experiments. Using a 15-25 MeV electron beam from an electron linac, and an undulator having period (λ_u) of 40 mm and undulator parameter K in the range 1-2, it should be possible to cover this wavelength range, as can be seen from the following formula:

$$\lambda_R = \frac{\lambda_u}{2\gamma^2}(1 + \frac{K^2}{2}), \tag{1}$$

where λ_R is the radiation wavelength, γ is the electron energy in units of its rest mass energy and $K = eB_u\lambda_u/2\pi mc$, B_u is the peak undulator field, m is the rest mass of electron and c is the speed of light. Note that we have chosen maximum value of $K = 2$ such that we get a wavelength tunability up to a factor of two by varying K in the range 1-2. We will use a Halbach configuration of pure permanent magnets for the undulator, where the dependence of peak magnetic field on the gap g between the jaws of the undulator is given by[3]

$$B_u = 1.43B_r \exp(-\pi g/\lambda_u). \tag{2}$$

Here B_r is the remanent field of the permanent magnet used in the undulator. Using B_r = 1.2 T for NdFeB magnets, we obtain the gap to be 15 mm for $K = 2$. We therefore will need to use an undulator vacuum pipe having inner diameter (ID) of 11 mm.

The number of undulator periods N_u is chosen to be 60 on the basis of gain considerations. The 2.4 m long undulator will be immersed in a 4.1 m long optical cavity. The undulator will be asymmetrically placed in the optical cavity such that we have 1.05 m of space available for beam transport and diagnostic on the upsteam side and 0.65 m of space available on the downstream side. Assuming a Rayleigh range of 0.8 m, which is one third of the undulator length, the rms optical beam size at the waist is 1.4 mm. We therefore chose the rms electron beam horizontal size σ_x at the waist to be around 1 mm for good overlap with the optical beam. The rms electron beam size σ_y in the vertical direction is taken to be the matched beam size in the undulator given by [3]

$$\sigma_y = \sqrt{\frac{\epsilon_n\lambda_u}{\sqrt{2}\pi K}}, \tag{3}$$

where ϵ_n is the normalized rms electron beam emittance. We choose ϵ_n = 30 mm-mrad for our design calculation.

For the electron beam, we will use a micropulse charge in the range 0.2-0.5 nC. The electron beam rms pulse width is taken to be 4 ps and the relative rms energy spread is taken to be 0.5%. These parameters are easily acheivable. In the next section, we present the results of design simulations.

DESIGN CALCULATIONS

For performing the design simulations, we have used the FEL code GINGER [1], a multidimensional [full 3D for macroparticles and 2D ($r - z$) for radiation], time-dependent code to simulate the FEL interaction in single-pass amplifier as well as oscillator configurations. GINGER utilizes the KMR [4] wiggle-period-averaged electron-radiation interaction equations and the slowly-varying envelope approximation (SVEA) in both time and space for radiation propagation. For propagation outside the undulator for oscillator problems, the code uses a Huygens integral method. Shot noise is modeled by giving a controlled amount of randomness to the initial longitudinal

* skrishna@cat.ernet.in

phases of macroparticles; the algorithm [5] generates the statistically-correct shot noise at the fundamental as well as at harmonics.

The design parameters of the IR-FEL are given in Table 1. For the 30 μm simulations reported here, we have used γ = 45.25. We first performed the time-independent simulation using the code TDAOSC [6] which is an oscillator version of the code TDA [7]. For the parameters mentioned in Table 1, we obtained the single pass, small-signal gain of 135%, saturated cavity power of 9.8 MW and hole out-coupled power of 2.0 MW. The resonator parameters were optimized using TDAOSC and we obtained optimum performance for the Rayleigh range of 0.8 m and the location of the waist in the middle of the optical cavity. The optical mode profile at both the mirrors and the entrance of the undulator is shown in Fig. 1. We find the modes are nearly Gaussian.

Table 1: Design parameters used in the simulation

Electron beam energy (E)	22.6 MeV
Peak beam current (I)	20 A
RMS energy spread (σ_γ/γ)	0.5%
RMS normalised emittance	30 mm-mrad
RMS pulse width (σ_z)	1.2 mm
Micropulse rep. rate	36.62 MHz.
RMS e-beam size (σ_x, σ_y)	0.37 mm, 1.00 mm
Electron macropulse width	8 μs
Undulator period (λ_u)	40 mm
Peak und. parameter (K)	2.0
Undulator length ($N_u\lambda_u$)	2.4 m
Undulator gap	15 mm
Beam pipe diameter	11 mm (ID)
Radiation wavelength (λ_R)	30 μm
Optical cavity length	4.1 m
Location of down mirror	65 cm from und. exit
Location of up mirror	105 cm from und. entr.
Mirror radii of curvature	2.36 m (d), 2.36 m (u)
Mirror reflectivity (power)	99%
Hole radius in down. mirror	2 mm

Next, we performed time-dependent simulations using GINGER. We simulated the time-structure of the electron bunch as Gaussian with rms width of 4 ps. A time window of six times the rms width has been used for simulating the electron bunch, which is discretized into 60 electron slices, the separation between slices being 4 radiation wavelengths. A total number of 96 such radiation slices were used in the simulation. We studied the effect of cavity length detuning on the performance of the FEL. Fig. 2 shows the dependence of out-coupled power on cavity length detuning ΔL_c. Here, ΔL_c is defined as the reduction in the cavity length compared to the synchronized length. We find that the optimum performance is obtained at ΔL_c = 27 μm. We used this value for further simulations done at this wavelength.

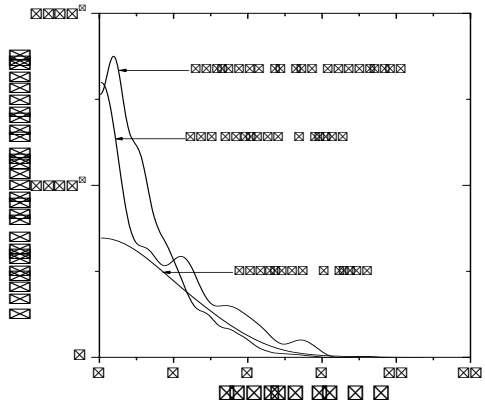

Figure 1: Mode profile of the radiation beam at different locations as indicated in the figure.

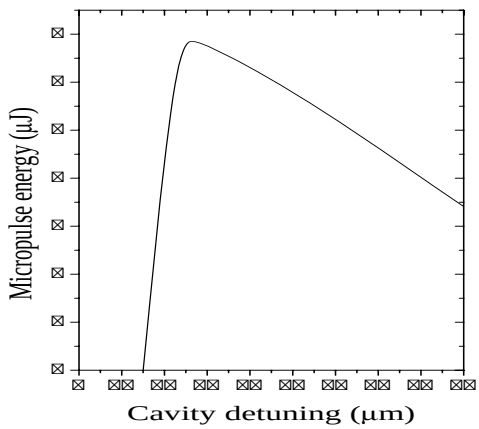

Figure 2: Energy in the out-coupled micropulse as a function of cavity detuning.

Next, we studied the growth of power starting from shot noise, which is shown in Fig. 3. The saturated intracavity average power is 5 MW, where averaging is done over effective electron pulse width, which is approximately 2.5 times the rms width for a Gaussian bunch. As seen in Fig. 3, it takes around 150 round trips for the power to saturate. This means that the start-up time is around 4 μs since cavity length is 4.1 m.

The time structure of the out-coupled power is shown in Fig. 4. We find that the peak out-coupled power is 1.35 MW and the total energy in the micropulse is 6.9 μJ.

We thus find that assuming a modest set of design parameters mentioned in Table 1, it should be possible to lase and generate around 1 MW of peak out-coupled power at 30 μm. We have also performed preliminary simulations at 12.5 μm and 50 μm and found that the lasing is possi-

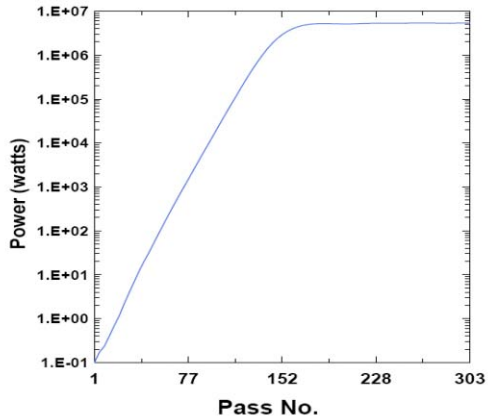

Figure 3: Growth of average intracavity power from noise. Parameters used in the simulation are given in Table 1.

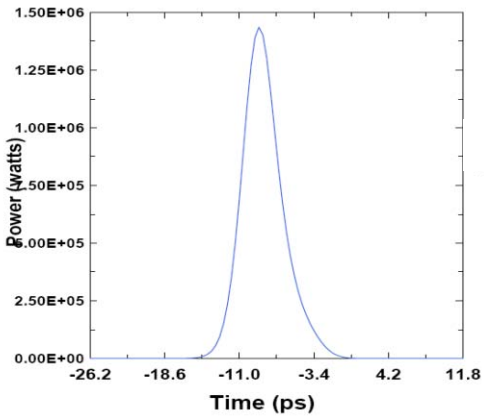

Figure 4: Time structure of the out-coupled power. A hole of radius 2 mm in the downstream mirror is used for this calculation.

ble even at these wavelengths with these parameters. Fig. 5 shows the growth of power from shot noise for these two cases. Note that we have assumed an electron energy of 25.32 MeV ($\gamma = 50.55$) and $K = 1.0$ for the 12.5 μm simulation. For the 50 μm simulation, the electron beam energy is assumed to be 17.4 MeV ($\gamma = 35.07$) and $K = 2.0$. We have used a peak electron beam current of 50 A for the 12.5 μm simulation. Since the gain is less at shorter wavelengths, we have used a larger current for this case. Also, we have taken the radius of the out-coupling hole in the downstream mirror to be 1 mm since the radiation beam size is smaller for this case. The peak out-coupled power for the 12.5 μm case is around 3.2 MW and for the 50 μm case, it is 1.1 MW.

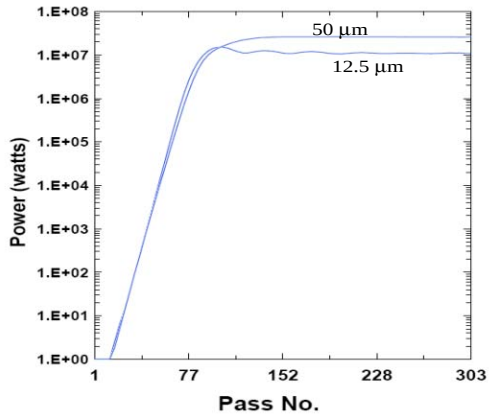

Figure 5: Growth of average intracvity power from shot noise for the 12.5 μm and 50 μm cases. Parameters used in the simulation are discussed in the text.

DISCUSSIONS AND CONCLUSIONS

We have not included the effect of wave-guiding in our calculation. Since we are planning to use a rather smaller beam pipe ID, the effect of wave-guiding may become important. We plan to focus on this issue in the future.

To summarize, we have presented the results of preliminary design calculations for an IR FEL proposed to be built at RRCAT. We find that with modest design parameters, it should be possible to lase in the range 12.5 - 50 μm and obtain peak out-coupled power more than 1 MW. Detailed design simulations and optimization are still underway.

ACKNOWLEDGEMENT

It is a pleasure to thank Bill Fawley for many useful and stimulating discussions on FEL simulation using GINGER and for his generous help by including the hole-outcoupling in this code.

REFERENCES

[1] W. Fawley, *A user Manual for GINGER and Its Post-Processor XPLOTGIN*, LBNL-49625-Rev. I ed., Lawrence Berkley National Laboratory (2004).

[2] S. Krishnagopal et al., Proceedings of FEL Conference (2006) 496.

[3] C. A. Brau, *Free-Electron Lasers*, Academic Press Inc., San Deigo, 1990.

[4] N.M. Kroll, P.L. Morton, and M.R. Rosenbluth, IEEE J. Quantum Elec. QE-17, (1981) 1436.

[5] W.M. Fawley, PRST-AB 5 (2002) 070701.

[6] S. Krishnagopal et al., Nucl. Instr. and Meth. A 318 (1992) 661.

[7] T. M. Tran, J. S. Wurtele, Computer Phys. Commun. 54 (1989) 263.

SHORT WAVELENGTH REGENERATIVE AMPLIFIER FREE-ELECTRON LASERS

N. R. Thompson and D. J. Dunning, ASTeC, Daresbury Laboratory, Warrington WA4 4AD, UK*
B. W. J. M^{c}Neil, SUPA, University of Strathclyde, Glasgow G4 0NG, UK

Abstract

In this paper we discuss extending the operating wavelength range of tunable Regenerative Amplifier FELs to shorter wavelengths than current design proposals, notably into the XUV regions of the spectrum and beyond where the reflectivity of broadband optics is very low. Simulation studies are presented which demonstrate the development of good temporal coherence in generic systems with a broadband radiation feedback of less than one part in ten thousand.

INTRODUCTION

A regenerative amplifier free-electron laser (RAFEL) is a high-gain resonator FEL which achieves saturation in a few round-trips of the radiation in a high-loss, and hence low feedback, optical cavity. Because the radiation feedback fraction is low it is feasible that the use of low reflectivity optics in the resonator makes the RAFEL a candidate for short wavelength operation [1]. Several RAFEL proposals have been made in the VUV [2, 3] and X-ray [4] and some experimental results obtained [5, 6].

There are several expected advantages of the RAFEL over other types of FEL. The RAFEL should be less sensitive to radiation-induced mirror degradation than a low gain oscillator FEL, and the small number of passes required to reach saturation should relax the longitudinal alignment tolerances. The optical feedback also allows the undulator length to be reduced compared to a Self Amplified Spontaneous Emission (SASE) FEL, and it is expected that because of the feedback a RAFEL source can deliver higher quality and more stable pulses than a SASE FEL.

The properties of the transverse modes within the cavity differ from those of a low-gain oscillator FEL. Because of the high loss of the resonator the radiation is not stored over many passes, and because of the high-gain of the FEL the radiation does not propagate freely within the cavity but experiences gain guiding. The cavity's primary function is to return a small field to the start of the undulator to seed the interaction with the subsequent electron bunch. For these reasons it is equally valid to refer to a RAFEL as a High-Gain Self-Seeding Amplifier FEL.

In this paper we present 1D modeling results for a system with a very low feedback factor that returns only $\sim 10^{-5}$ of the undulator output. Such low feedback may occur when mirror reflectivities are very poor, for example into the XUV and x-ray regions of the spectrum. The results are encouraging and suggest that, in principle, a low feedback RAFEL may prove a viable source at these photon energies.

* n.r.thompson@dl.ac.uk

A GENERIC HIGH-GAIN RAFEL

We now consider a generic high gain system shown schematically in Fig. 1 and investigate the properties of such a system when the feedback fraction is reduced to very low levels. First we optimise the feedback fraction using two criteria—the output power and the pulse temporal coherence should both be maximised. We work in the units of the universal scaling [7] where $\bar{z} = z/l_g$ and $l_g = \lambda_w/4\pi\rho$ is the nominal gain length, with λ_w the undulator period and ρ the FEL parameter.

It can be shown from [8] that the electron beam equivalent shot-noise power is:

$$|A_0|^2 \approx \frac{6\sqrt{\pi}\rho}{N_\lambda\sqrt{\ln\left(N_\lambda/\rho\right)}}, \tag{1}$$

where N_λ is the number of electrons per radiation wavelength. In the exponential gain regime the radiation intensity after a single pass through an undulator of scaled interaction length $\bar{z}$ is then given by

$$|A_1|^2(\bar{z}) \approx \frac{|A_0|^2}{9}\exp(\sqrt{3}\bar{z}) \tag{2}$$

and after returning a fraction F of the output power to the start of the undulator, via some as yet undefined optical system, the seed power at the start of the second pass is $F \times |A_1|^2$. The necessary condition for the development of longitudinal coherence is that this seed power is greater than the shot noise power, i.e.

$$F \times |A_1|^2 > |A_0|^2.$$

A feedback factor criterion to dominate the shot noise can then be defined as:

$$F_N > 9\exp(-\sqrt{3}\bar{z}). \tag{3}$$

The feedback factor necessary to optimise the output power in the steady state regime only has been determined from 1D simulations, with the results shown in Fig. 2. A fit to the numerical data, valid over the range $3 \leq \bar{z} \leq 12$, gives

$$F_P \approx 25\exp(-\sqrt{3}\bar{z}). \tag{4}$$

It is seen from comparison of (3) and (4) that $F_P \simeq 3F_N$ implying that optimising feedback to maximise the output power will necessarily prove sufficient to dominate the

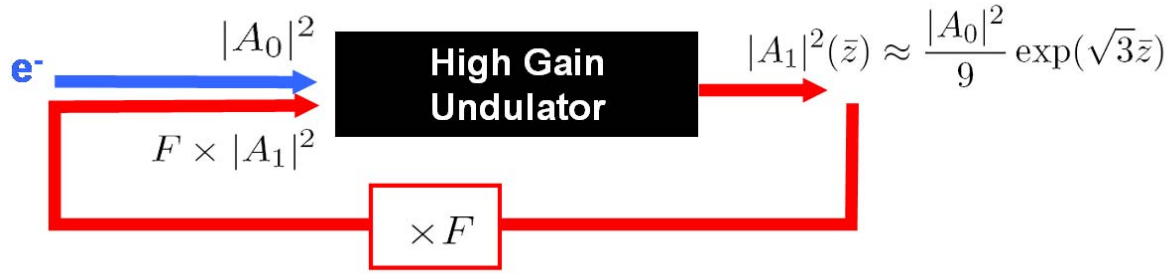

Figure 1: Schematic representation of a generic high gain RAFEL system.

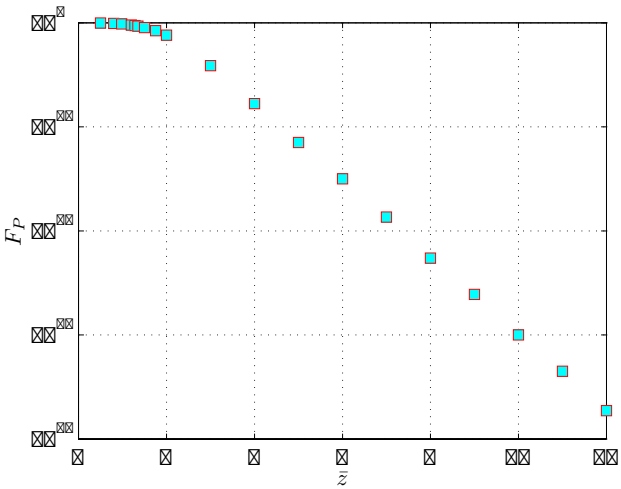

Figure 2: Results of one-dimensional steady-state simulations to determine the feedback factor F_P that maximises the output power. A fit to the numerical data over the range $3 \leq \bar{z} \leq 12$, gives $F_P \approx 25\exp(-\sqrt{3}\bar{z})$

electron beam shot noise and enable the development of coherent pulses. This postulate is tested with 1D time-dependent numerical simulations in the next section.

TIME DEPENDENT SIMULATIONS

Simulation Method and Parameters

We choose a low feedback factor of $F_P = 10^{-5}$ and use (4) to derive the appropriate scaled interaction length of $\bar{z} = 8.67$. An FEL parameter of $\rho = 2.9 \times 10^{-3}$ is used, typical of XUV FELs, with a peak number of electrons per wavelength of $N_\lambda \approx 3.8 \times 10^5$. The macroscopic profile of the electron bunch is gaussian, and the input electron beam is monoenergetic. The system is modelled using a 1D time dependent code FELO [9] which solves the 1D FEL propagation equations

$$\begin{aligned} \frac{d\theta_j}{d\bar{z}} &= p_j, \\ \frac{dp_j}{d\bar{z}} &= -(A(\bar{z},\bar{z}_1)\exp[i\theta_j] + c.c.) \\ \left(\frac{\partial}{\partial\bar{z}} + \frac{\partial}{\partial\bar{z}_1}\right) A(\bar{z},\bar{z}_1) &= \chi(\bar{z}_1)\langle\exp[-i\theta]\rangle \equiv b(\bar{z},\bar{z}_1) \end{aligned}$$

where p is the particle energy $p = (\gamma - \gamma_r)/\rho\gamma$ with γ_r the resonant electron energy in units of the electron rest mass, θ the particle phase within the ponderomotive well, $\bar{z}_1$ is the length along the electron bunch from the bunch tail in units of the cooperation length $l_c = \lambda_r/4\pi\rho$ and $\chi(\bar{z}_1)$ the function describing the macroscopic electron current profile.

The feedback factor was varied from $F = 10^{-3}$ to $F = 2 \times 10^{-6}$, and the cavity detuning value δ_c, in units of $\bar{z}_1$, varied from $\delta_c = 0$, defining cavity synchronism, to a detuned cavity length of $\delta_c = 9.0$. For each combination of these parameters the system was allowed to evolve over 200 cavity round trips.

In order to compare the numerical results of the low feedback RAFEL system with a SASE system, 200 separate simulations were done for an equivalent SASE system with $\bar{z} = 14$ where saturation of the pulse energy is seen to occur.

Simulation Results

An analysis has been carried out to determine key parameters of the output pulses pass-by-pass. The parameters of interest are the peak intensity $|A|^2_{\rm peak}$, the rms pulse length $\sigma_{\bar{z}_1}$, the rms relative linewidth σ_λ/λ and the time bandwidth product $\Delta\nu\Delta t$ which is used to quantify the development of the temporal coherence. The definition used is

$$\Delta\nu\Delta t = \frac{1}{\lambda}\left(\frac{\Delta\lambda}{\lambda}\right)\Delta z \qquad (5)$$

with Δz the pulse width. The numerical value obtained depends on the definition of width chosen. The choice used here here is $\Delta x = 2\sqrt{2\ln 2} \times \sigma_x$ under which definition

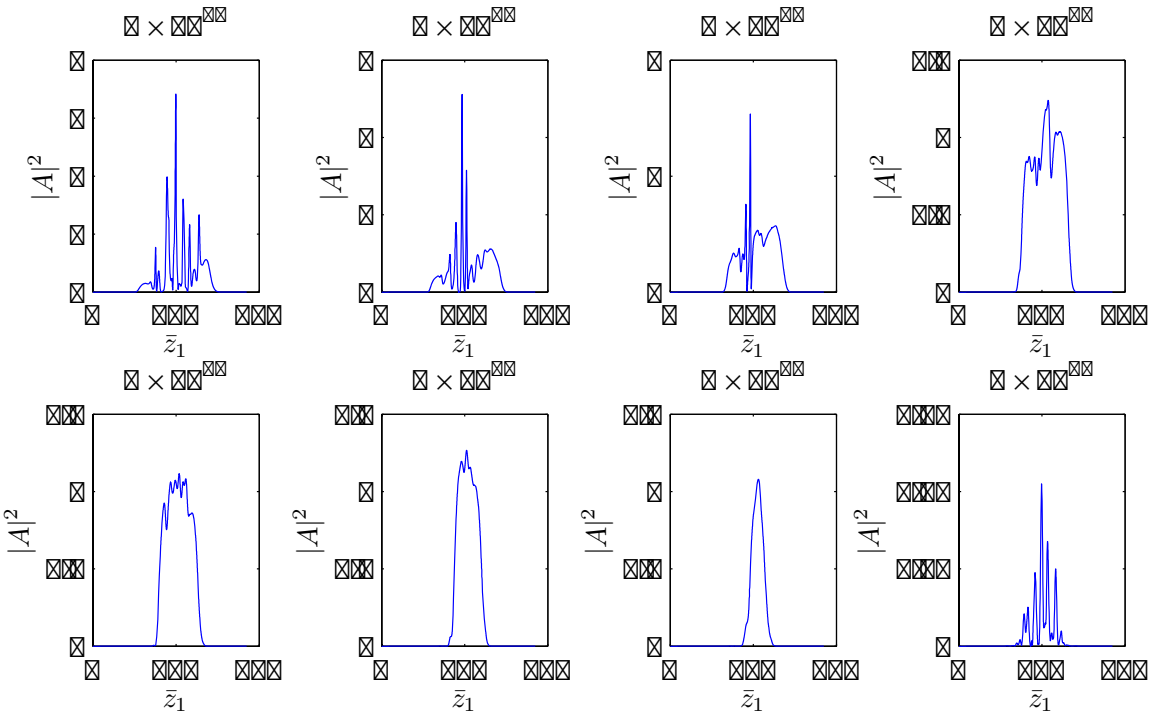

Figure 3: Typical output pulses of the low feedback RAFEL system. The feedback fraction is shown above each plot, and varies from $F = 1 \times 10^{-3}$ (top left) to $F = 2 \times 10^{-6}$ (bottom right). The cavity detuning value is $\delta_c = 6.0$ for all pulses.

a transform limited gaussian intensity pulse would give the result obtained using FWHM values of $\Delta\nu\Delta t \simeq 0.44$ (the relationship between σ and FWHM for a gaussian given by $\mathrm{FWHM}(x) = 2\sqrt{2\ln 2} \times \sigma_x$).

SASE results The results of the SASE simulations are as follows: the root mean square (rms) linewidth over 200 simulations was $\langle \sigma_\lambda/\lambda \rangle = 2.77 \times 10^{-3}$ with an rms pulse length $\langle \sigma_{\bar{z}_1} \rangle = 14.01$ giving a time-bandwidth product of $\langle \Delta\nu\Delta t \rangle = 5.9$. The peak intensity $\langle |A|^2_{\mathrm{peak}} \rangle = 2.2$.

Low feedback RAFEL Results To identify some features of the RAFEL output, pulse profiles for a feedback fraction decreasing from $F = 10^{-3}$ to 2×10^{-6} are shown first in Fig. 3 for a cavity detuning value of $\delta_c = 6.0$. It is seen that for $F = 10^{-3}$ the pulse profile is spiky with a peak intensity $|A|^2_{peak} = 7$. The bandwidth for these parameters, averaged over 200 post-saturation passes, is $\langle \sigma_\lambda/\lambda \rangle = 4 \times 10^{-3}$, greater than the mean SASE value of $\langle \sigma_\lambda/\lambda \rangle = 2.77 \times 10^{-3}$, and the time bandwidth product is $\langle \Delta\nu\Delta t \rangle = 12$ compared to the SASE value of $\langle \Delta\nu\Delta t \rangle = 5.9$. This data indicates that the RAFEL pulse is over-saturated. The feedback fraction is too high so that the seed power is too great and the RAFEL saturates before the end of the undulator.

Fig. 3 shows that as the feedback fraction is decreased the pulse profile becomes cleaner, with the front and back of the pulse cleaning up first, leaving a spiky region in the centre of the pulse. This behaviour is attributed to the gaussian electron current profile—the front and back of the pulse experience less gain and do not oversaturate whereas the centre of the pulse oversaturates. The time bandwidth product falls below the SASE value at a feedback fraction of $F = 5 \times 10^{-5}$. For lower feedback, the time bandwidth product continues to fall until it reaches a minimum value of $\langle \Delta\nu\Delta t \rangle = 1.0$ at a feedback of $F = 5 \times 10^{-6}$. Examination of the pass-by-pass data shows individual pulses with $\Delta\nu\Delta t = 0.68$, close to that of a transform limited gaussian pulse. Finally, as the feedback fraction is reduced further to $F = 2 \times 10^{-6}$ it is seen that there is insufficient feedback for growth to saturation, and the pulse shown represents a pre-saturation SASE pulse for an interaction length $\bar{z} = 8.67$. This conclusion is supported by the fact that the pulse parameters (except peak intensity) have reverted back to close to their values for the SASE simulations.

The complete data for all simulations, in each case averaged over 200 post-saturation pulses, are summarised in the contour plots of Fig. 4 and Fig. 5. In each of these plots the vertical axis gives the feedback F and the horizontal axis the cavity detuning δ_c. The bold contour represents the averaged value of the 200 SASE simulations so that, for example, in the top left plot showing time-bandwidth product, the area below the bold contour represents all those feedback and detuning combinations in which the low feedback RAFEL pulses have a lower time-bandwidth product, and hence improved temporal coherence, than the SASE case.

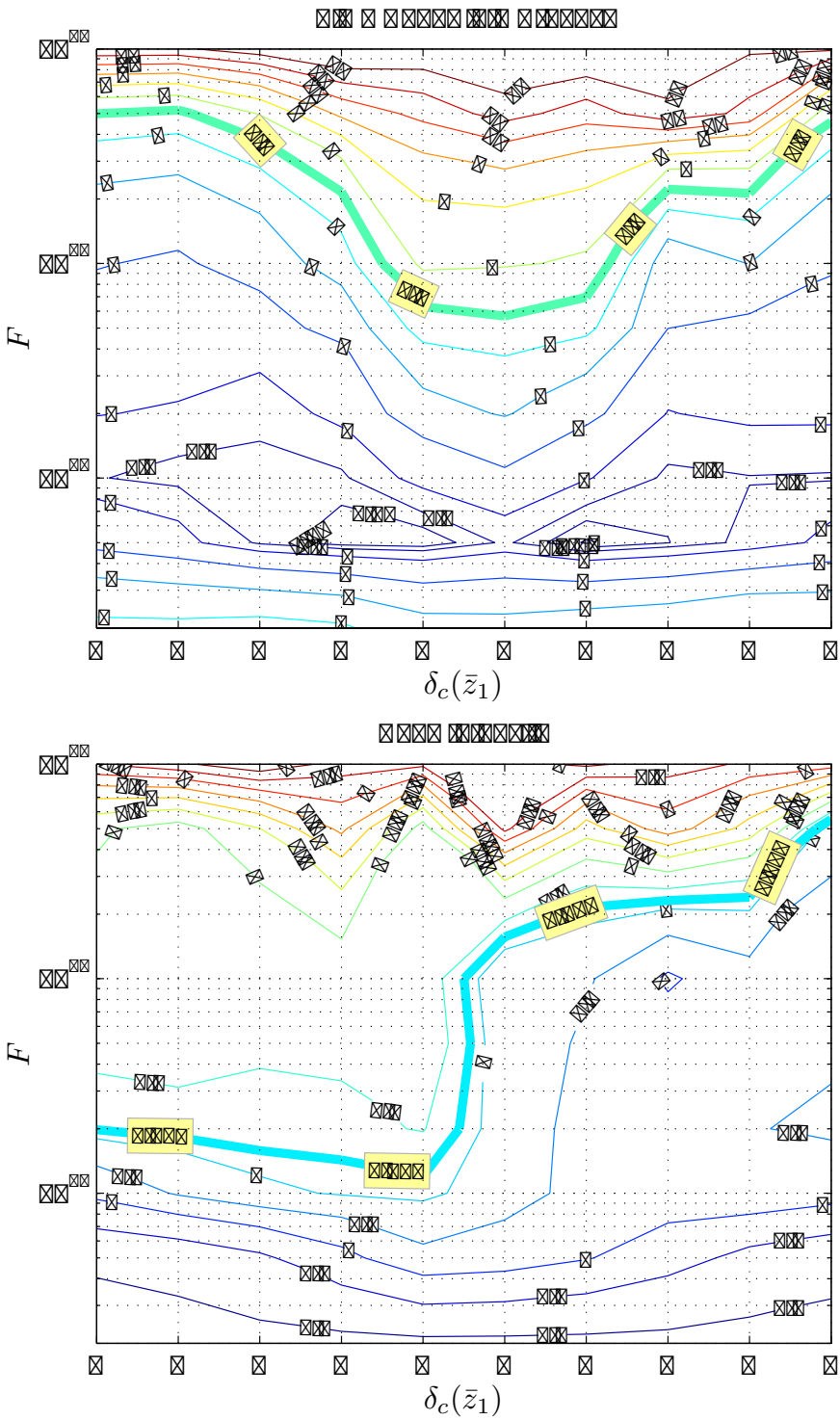

Figure 4: The complete data for all simulations, in each case averaged over 200 post-saturation pulses, for time-bandwidth product $\langle \Delta\nu\Delta t \rangle$ (top), and peak intensity $\langle |A|^2_{\mathrm{peak}} \rangle$ (bottom). In each plot the vertical axis gives the feedback F and the horizontal axis the cavity detuning δ_c. The bold contour represents the averaged value seen for the 200 SASE simulations.

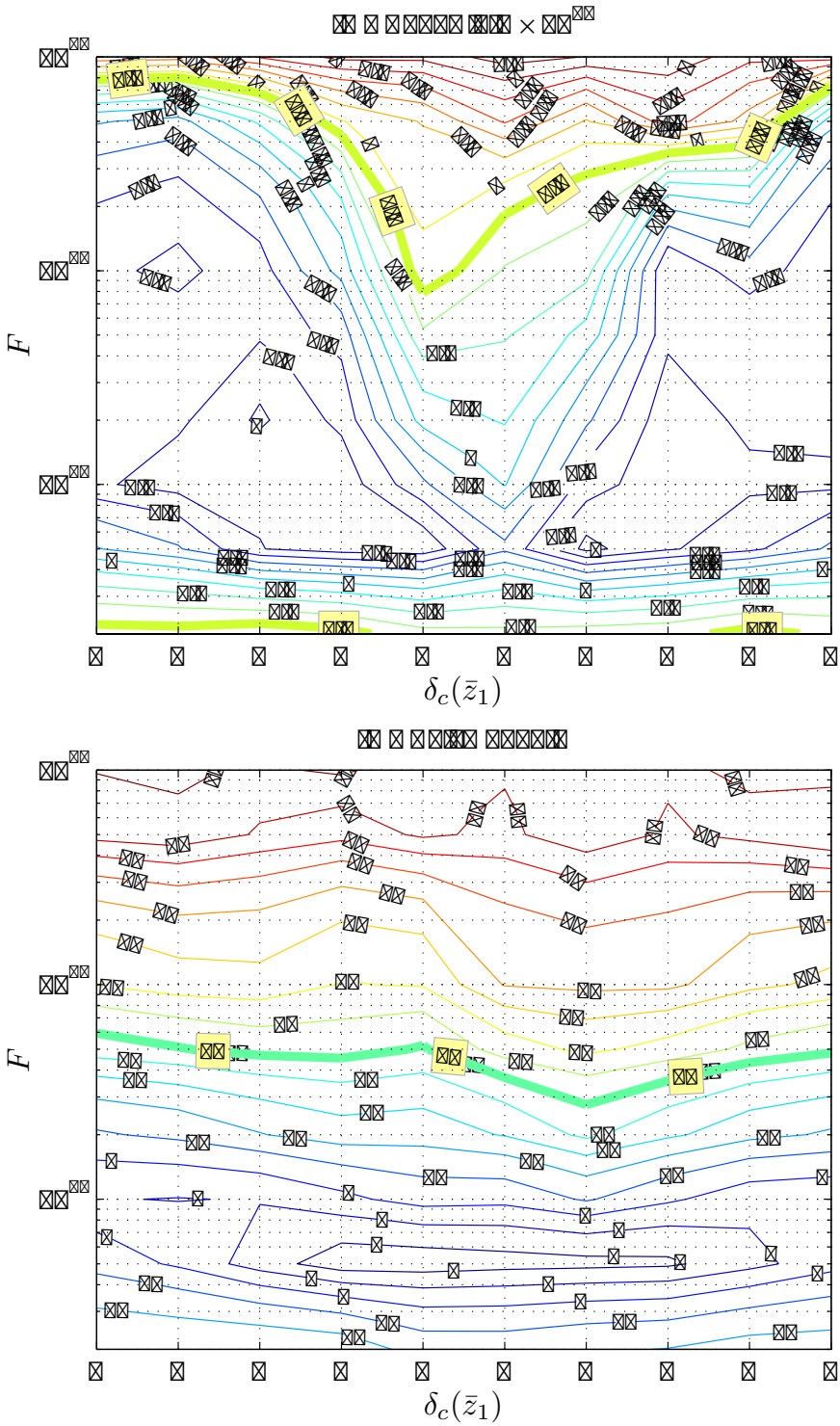

Figure 5: The complete data for all simulations, in each case averaged over 200 post-saturation pulses, for rms bandwidth $\langle \sigma_\lambda / \lambda \rangle$ (top) and rms pulse length $\langle \sigma_{\bar{z}_1} \rangle$ (bottom). In each plot the vertical axis gives the feedback F and the horizontal axis the cavity detuning δ_c. The bold contour represents the averaged value seen for the 200 SASE simulations.

Discussion of Results

It is clear from these simulations that the feedback factor derived in (4), with a value $F_P = 10^{-5}$ and for interaction length $\bar{z} = 8.67$, is sufficient to significantly improve the temporal coherence of the output compared to SASE, over the full range of cavity detuning values. The feedback corresponding to the best temporal coherence is $F = 5 \times 10^{-6}$ which is a factor of two larger than the criterion derived in (3) required to dominate shot noise which gives $F_N > 2.7 \times 10^{-6}$.

From examination of the contour plots in Fig. 4 and Fig. 5, and considering the previous discussions, three broad regimes can be identified:

- For $F \gtrsim 10^{-4}$: the output has the characteristics of over-saturation;
- For $10^{-4} \gtrsim F \gtrsim 5 \times 10^{-6}$: the applied feedback improves the pulse coherence over SASE;
- For $F \lesssim 5 \times 10^{-6}$: the feedback is insufficient to give growth to saturation or improve the coherence, giving unsaturated SASE output.

CONCLUSION

An overview of the properties of Regenerative Amplifier FELs has been presented and a one-dimensional feasibility study of a generic high-gain RAFEL system which functions using cavity feedback factors as low as 5×10^{-6}. It has been shown that such a system may generate radiation pulses of greatly improved quality than that possible using SASE. The greatest temporal coherence is seen when the power feedback is approximately double the shot noise power. Here the time bandwidth product, averaged over 200 pulses, is $\langle \Delta\nu\Delta t \rangle \approx 1.0$, approximately double that of a transform limited gaussian pulse. This is more than five times better than the equivalent SASE result, with individual pulses having a time bandwidth product as low as $\Delta\nu\Delta t \approx 0.68$.

It is also seen that if the feedback factor is too high the pulses oversaturate and their properties are similar to, or worse than, the equivalent SASE case.

Methods of attaining the low feedback factors were not discussed, however the fact that they may be so small indicates that there is significant scope in extending the low feedback RAFEL concept into the XUV and possibly further. The possibility of combining harmonic generation methods [10, 11, 12, 13] and RAFEL also exists and these exciting possibilities will be the subject of future research.

REFERENCES

[1] McNeil BWJ 1990 *IEEE J. Quantum Electron.* **26** 1124

[2] CCLRC 2006 *4GLS Conceptual Design Report* Council for the Central Laboratory of the Research Councils (UK) online at http://www.4gls.ac.uk/documents.htm#CDR

[3] McNeil BWJ, Thompson NR, Dunning DJ, Karssenberg JG, van der Slot PJM and Boller K-J 2007 *New J. Phys.* **9** 239

[4] Huang Z, Ruth RD 2006 *Phys. Rev. Lett.* **96** 144801

[5] Nguyen DC, Sheffield RL, Fortgang CM, Goldstein JC, Kinross-Wright JM and Ebrahim NA 1999 *Nucl. Instrum. Methods Phys. Res.* A **429** pp 125-30

[6] Faatz B, Feldhaus J, Krzywinski J, Saldin EL, Schneidmiller EA and Yurkov MV 1999 *Nucl. Instrum. and Meth. Phys. Res. A* **429** pp 424-8

[7] Bonifacio R, Pellegrini C and Narducci L 1984 *Opt. Commun.* **50** pp 373-8

[8] Kim KJ 1986 *Phys. Rev. Lett.* **57** pp 1871-4

[9] McNeil BWJ, Robb GRM, Dunning D and Thompson NR 2006 *Proc. 28th Int. Free Electron Laser Conf. (Berlin, Germany)* pp 59-62 Joint Accelerator Conferences Website, http://www.jacow.org

[10] Bonifacio R, De Salvo Souza L, Pierini P and Scharlemann ET 1990 *Nucl. Instrum. Methods Phys. Res.* A **296** 787

[11] Yu L-H 200 *Science* **289** 932

[12] McNeil BWJ, Robb GRM, Poole MW and Thompson NR 2006 *Phys. Rev. Lett.* **96** 084801

[13] McNeil BWJ, Robb GRM and Poole MW 2004 *Phys. Rev.* E **70** 035501(R)

NUMERICAL SOLUTION OF THE FEL CORRELATION FUNCTION EQUATION

O.A. Shevchenko[#], N.A. Vinokurov,
Budker Institute of Nuclear Physics, 11 Acad. Lavrentyev Prosp., 630090, Novosibirsk, Russia

Abstract

The equation for two-particle correlation function in FEL was derived recently to provide a new way of noise calculations in SASE FELs [1]. In this paper this equation is solved numerically for the simplest case of narrow electron beam. Time independent solution with saturation is obtained. It is compared with the results of quasilinear theory and results of previous SASE linewidth estimates.

INTRODUCTION

High gain FELs operated in SASE mode are considered now as one of the most perspective high-brightness radiation source in the x-ray region. Therefore it is very important to know the radiation properties of such FELs. Parameters of radiation in a single shot are determined by the shot noise in the beam current which has stochastic nature. Because of that these parameters fluctuate from shot to shot and they can not be determined without exact solution of the particle motion and Maxwell equations. On the other hand the parameters averaged over many shots can be found by the methods of statistical mechanics.

The statistical approach has been treated by many authors but usually it was limited to the linear case when one can introduce the Green function and the averaging becomes straightforward [2,3]. Some authors considered the averaged results of simulations obtained by macroparticle based codes [4]. But in this case it is not evident that artificially constructed initial distribution of macroparticles leads to correct results at saturation stage.

The regular nonlinear approach to the start-up from noise has been proposed in [1]. It is based on the BBGKY set of equations which is truncated to two equations for single-particle distribution function and two-particle correlation function. In this paper we obtain the numerical solution of these equations for the simplest model of narrow beam comprised of charged disks with Gaussian transversal charge distribution.

BASIC EQUATIONS

In the case of the charged disks model the equations (4-5) of [1] for the single-particle distribution function and two-particle correlation function have the following form:

$$\left(\frac{\partial}{\partial\theta}+\nu_1\frac{\partial}{\partial z_1}\right)F(1,\theta)=-N\int d\{2\}\Phi(1,2)\frac{\partial}{\partial\Delta_1}G(1,2;\theta) \qquad (1)$$

$$\left(\frac{\partial}{\partial\theta}+\nu_1\frac{\partial}{\partial z_1}+\nu_2\frac{\partial}{\partial z_2}\right)G(1,2,\theta)=-N\frac{\partial F(1)}{\partial\Delta_1}\int\Phi(1,3)G(2,3,\theta)d\{3\}-$$
$$-N\frac{\partial F(2)}{\partial\Delta_2}\int\Phi(2,3)G(1,3,\theta)d\{3\}-\left(\Phi(1,2)\frac{\partial}{\partial\Delta_1}+\Phi(2,1)\frac{\partial}{\partial\Delta_2}\right)F(1)F(2) \qquad (2)$$

where $(i)=(z_i,\Delta_i)$, $d\{i\}=dz_i d\Delta_i$, $\nu_i=(1+2\Delta_i)$, Δ_i - relative electron energy deviation, z_i - electron longitudinal coordinate in undulator, N - number of electrons in the beam, $\theta=2\gamma_\parallel^2(t-z),(c=1)$ - "time" variable and $\gamma_\parallel$ - relativistic factor of electron longitudinal motion. The longitudinal interaction force $\Phi(1,2)$ can be determined from eq. (6) of [1]. In the considered model it should be averaged over transversal distribution:

$$\langle\Phi(1,2)\rangle_\perp=-\frac{r_e}{2\sigma^2k_w\gamma}\frac{K^2}{1+K^2}\left(\frac{e^{ik_w(z_1-z_2)}}{1+i\alpha k_w(z_1-z_2)}+c.c.\right) \qquad (3)$$

here σ is r.m.s transversal beam size, r_e - classical electron radius, $\alpha=1/2k_0k_w\sigma^2$ - small dimensionless parameter which characterizes the beam "thickness", k_0 - radiation wave number and k_w - undulator wave number. We assume that undulator has constant deflection parameter K and helical symmetry.

From this point we shell consider stationary case, therefore the time derivative in Eq. (1-2) can be omitted and N should be replaced by the number of electrons per unit of length. In this case the single-particle distribution function has to be renormalized the following way:

$$\int\nu_1F(z_1,\Delta_1)d\Delta_1=1$$

To eliminate the fast oscillating terms it is convenient to introduce the slow varying complex amplitude $\tilde{G}$ of the correlation function:

$$G(z_1,\Delta_1;z_2,\Delta_2)=2\,\mathrm{Re}\left(\tilde{G}(z_1,\Delta_1;z_2,\Delta_2)e^{i(z_1-z_2)}\right) \qquad (4)$$

Here we have replaced k_wz_i by dimensionless variable z_i. Substituting (4) into (1-2) and neglecting fast oscillating terms we obtain the final system of equations:

[#]O.A.Shevchenko@inp.nsk.su

$$\nu_1 \frac{\partial}{\partial z_1} F(1) = -2\,\mathrm{Re}\left(\frac{\partial}{\partial \Delta_1} I(z_1, \Delta_1; z_1) \right) \tag{5}$$

$$\frac{1}{2}\left[(\nu_1+\nu_2)\left(\frac{\partial}{\partial z_1}+\frac{\partial}{\partial z_2}\right)+(\nu_1-\nu_2)\left(2i+\frac{\partial}{\partial z_1}-\frac{\partial}{\partial z_2}\right)\right]\tilde{G}(1;2) =$$
$$= -\frac{\partial F(1)}{\partial \Delta_1} I^*(z_1; z_2, \Delta_2) - \frac{\partial F(2)}{\partial \Delta_2} I(z_2; z_1, \Delta_1) -$$
$$-\frac{2\pi}{N_{\lambda_0}}\left(\tilde{\Phi}^*(z_1 - z_2)\frac{\partial}{\partial \Delta_1} + \tilde{\Phi}(z_2 - z_1)\frac{\partial}{\partial \Delta_2}\right) F(1)F(2) \tag{6}$$

where function $I(z_1; z_2, \Delta_2)$ is determined as

$$I(z_1; z_2, \Delta_2) = \int_0^{z_1}\int_{-\infty}^{\infty} \tilde{\Phi}(z_1 - z_3)\tilde{G}(2;3)\,d\{3\}, \tag{7}$$

$\tilde{\Phi}(z) = -2\rho^3 \dfrac{1}{1 - i\alpha z}$ is renormalized complex amplitude of the longitudinal force (3), $\rho = \left(\dfrac{1}{(2\gamma)^3}\dfrac{I}{I_A}\dfrac{K^2}{k_w^2\sigma^2}\right)^{\frac{1}{3}}$ - Pierce parameter (I - beam peak current, $I_A = mc^3/e$ - Alfven current), N_{λ_0} - the number of electrons in the beam on one wavelength.

The solution of eq. (5-6) can be obtained by numerical methods which are described in the next section. It seems natural that initial electron distributions in different shots are not correlated. Then the boundary conditions for eq. (5-6) are $\tilde{G}|_{z_1=0} = \tilde{G}|_{z_2=0} = 0$, $F|_{z_1=0} = F_0(\Delta_1)$, where $F_0(\Delta_1)$ is the electron energy distribution at the entrance to undulator. It is sufficient to find the solution only for $z_1 \ge z_2$ as the symmetry of the correlation function imposes additional condition

$$\tilde{G}(1,2) = \tilde{G}^*(2,1) \tag{8}$$

It should be noted that one-time two-particle correlation function allows to find only the radiation peak power averaged over different shots. The averaged spectral distribution is determined by two-time two-particle correlation function which obeys the following equation:

$$\left(\frac{\partial}{\partial \theta_1} + \nu_1 \frac{\partial}{\partial z_1}\right) G_2(1, \theta_1; 2, \theta_2) = -N \frac{\partial F(1)}{\partial \Delta_1} \int \Phi(1,3) G_2(3, \theta_1; 2, \theta_2)\, d\{3\} \tag{9}$$

In the stationary case $G_2(1, \theta_1; 2, \theta_2) = G_2(1,2; \theta_1 - \theta_2)$ and this equation has to be solved with the initial condition $G_2(1,2; \theta_1 - \theta_2)|_{\theta_1=\theta_2} = G(1,2)$.

The beam current correlation function at given longitudinal coordinate in undulator z can be found from the following expression:

$$\langle \delta I(z, t_1)\delta I(z, t_2)\rangle = A\int \nu_1\nu_2 G_2(z, \Delta_1, \theta_1; z, \Delta_1, \theta_2)\, d\Delta_1 d\Delta_2$$

where A is some constant and $\theta_i = 2\gamma_\parallel^2(t_i - z)$. It can be shown that if we neglect the dependence of longitudinal "velocities" ν_i on energy coordinates Δ_i then

$$\langle \delta I(z, t_1)\delta I(z, t_2)\rangle \equiv J(z, \theta_1 - \theta_2) =$$
$$= A\int G\left(z - \frac{1}{2}(\theta_1 - \theta_2), \Delta_1; z + \frac{1}{2}(\theta_1 - \theta_2), \Delta_2\right) d\Delta_1 d\Delta_2$$

The current spectral density is determined by the expression:

$$J_\nu(z) = \int J(z, \tau) e^{i(1+\nu)\tau} d\tau$$

NUMERICAL SOLUTION

The system of equations (5-6) has been solved numerically using finite difference method. The difference scheme was obtained by replacing of partial derivatives by centered differences. The integral in Eq. (7) was approximated using method of central rectangles. The numerical algorithm is illustrated in Fig. 1. Indexes (n,m) correspond to energy coordinates, index (j) is related to the coordinate z_2.

The letters "M", "O" and "P" denote three layers in z_1 direction. To find the solution at the layer "P" one has to know the values of correlation function at two preceding layers. Therefore it is required to keep in the computer memory only these three layers. The solution above the line $z_1 = z_2$ is obtained from the symmetry condition (8).

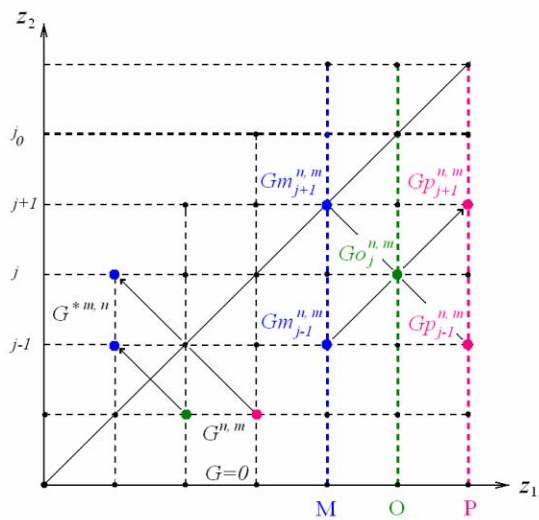

Figure 1. The finite difference scheme.

SIMULATION RESULTS

In this section we present an example of simulation results obtained for the following set of parameters: Pierce parameter $\rho = 0.01$, beam energy spread $\sigma_e = 0.2\rho$, $\alpha = 50\rho$.

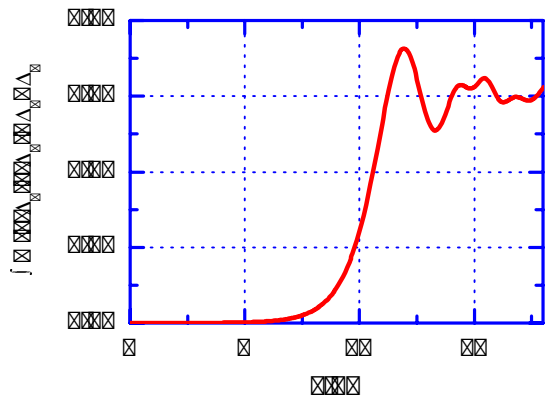

Figure 2. Dependence of the microbunching square on the longitudinal coordinate in undulator. L_g - the gain length at the linear stage.

At Fig. 2 one can see the dependence of the beam microbunching on the longitudinal coordinate in undulator. The amplitude gain length at linear stage $L_g \approx 40\lambda_w$, where λ_w is undulator period. Therefore the Fresnel number $1/2\alpha k_w L_g$ [1] is small and the narrow beam approximation is valid. The exponential growth starts at $z \approx 4L_g$ and comes to saturation at $z \approx 10L_g$.

Fig. 3 shows variation of the r.m.s. spectral bandwidth along undulator. The final value of the bandwidth is in very good agreement with the asymptotic formula (21) obtained in [1].

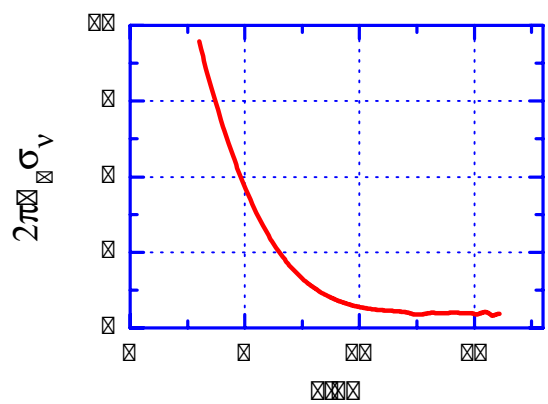

Figure 3. Dependence of the r.m.s. spectral bandwidth on the longitudinal coordinate in undulator. N_g - number of undulator periods per one gain length.

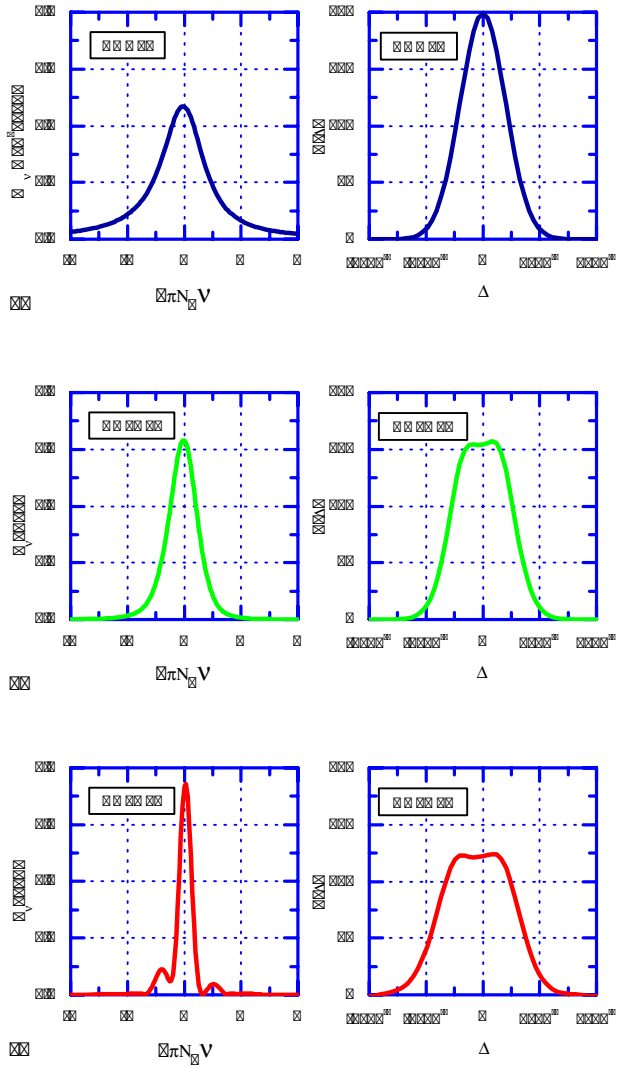

Figure 4. The spectral and energy distributions at different longitudinal positions: a) – start of the exponential growth, b) – start of saturation process, c) – saturation stage.

The saturation process is illustrated in Fig. 4. At the beginning of the exponential growth the spectrum is wide and the energy distribution function is unperturbed (a). Before saturation the bandwidth reduces rapidly and the energy spread starts growing (b). At the saturation stage the energy distribution becomes wide and amplification stops (c). The saturation mechanism is very similar to the quasilinear one [5].

Fig. 5 shows distribution of the correlation function amplitude integrated over energy in the (z_1, z_2) plane.

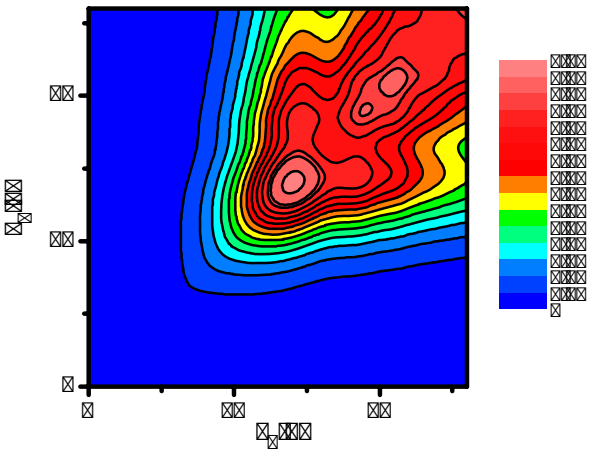

Figure 5. Two coordinate distribution of the correlation function amplitude integrated over energy.

CONCLUSION

In this paper we developed the description for saturation in SASE FEL based on rigorous statistical approach. By our knowledge it is the only existing method to consider nonlinear stage of noise amplification in FEL now. For the simplest case of narrow electron beam we first obtained non-trivial solution for the correlation function nonlinear behaviour.

From the other hand, the SASE FEL is an explicit illustration of fundamental ideas of statistical physics. Indeed, the averaging over the abstract assembly of macroscopically equivalent systems is simply the averaging over different electron bunches, which pass through undulator. It is also the clear example of ergodicity, as the averaging over bunches is a kind of time-averaging.

REFERENCES

[1] O.A. Shevchenko, N.A. Vinokurov, NIM A507 (2003) 84-88.
[2] K. J. Kim. NIM A250 (1986) 396
[3] S. Krinsky and L.-H. Yu, Phys. Rev. A35 (1987) 3406.
[4] E.L. Saldin, E.A. Schneidmiller, M.V. Yurkov, NIM A407 (1998) 285-290.
[5] N.A. Vinokurov, Z. Huang, O.A. Shevchenko, K.-J. Kim, NIM A475 (2001) 74.

NUMERICAL PROPAGATION SIMULATIONS AND COHERENCE ANALYSIS OF SASE WAVEFRONTS*

O. Chubar#, M.-E. Couprie, F. Polack, SOLEIL, 91191 Gif-sur-Yvette, France
M. Labat, G. Lambert, O. Tcherbakoff, CEA, DSM/SPAM, 91191 Gif-sur-Yvette, France

Abstract

Examples of wavefront propagation simulation and coherence analysis of Self-Amplified Spontaneous Emission (SASE), seeded and started-up from noise, are presented. The calculations are performed using SRW – the wave-optics computer code optimized for Synchrotron Radiation (SR), and the 3D FEL simulation code GENESIS. To ensure easy inter-operation and data exchange between the two codes, GENESIS has been integrated into the "emission" part of the SRW, which is dedicated for calculation of initial wavefronts in the form ready for subsequent propagation simulations. After each run of GENESIS in time-dependent mode, the resulting electric field is transformed from time to frequency domain, and the wavefront obtained this way is numerically propagated, using Fourier-optics methods implemented in SRW, from the exit of FEL undulator to a destination plane of a beamline containing several optical elements separated by drift spaces. Interferometer-type optical schemes, which allow for "probing" spatial and temporal coherence of SASE wavefronts, are used in the examples. Intensity distributions of the propagated radiation are extracted and analysed in time and frequency domains. The presented examples show that the SRW code can be used for optimization of optical beamlines for 4th generation synchrotron radiation sources, which require accurate treatment of wave-optical phenomena in frequency and time domains.

INTRODUCTION

Synchrotron Radiation emitted by relativistic electrons in magnetic fields of storage ring sources of the 3rd generation is a proven tool for research in many areas of science, from physics and chemistry to biology and medicine. An outstanding feature of the SR is a very broad emission spectrum extending from far infrared to hard X-ray range. Besides, undulator-based 3rd generation SR sources offer relatively high average spectral flux, brightness and degree of spatial coherence of the output radiation, and a possibility to use this radiation simultaneously for various experiments at a large number of beamlines.

The new emerging sources of the 4th generation – free-electron lasers and energy-recovery linacs – extend the domain of SR applications to time-resolved research, by providing femtosecond and, prospectively, even attosecond time scale pulses of radiation with extremely high peak brightness [1, 2].

To fully exploit all great SR features in the 3rd and 4th generation sources, high-accuracy simulation tools for the processes of emission and wavefront propagation through various optical elements of a beamline should be used. In the frame of classical electrodynamics, such simulation tools, dedicated both for the emission and propagation parts, would operate with 3D electric field of radiation [3]. Whereas this requirement seems absolutely natural for the emission part, it is much less evident for the propagation, where simple geometrical optics based approximation exists and is extensively (and successfully) used for incoherent sources and systems dominated by optical aberrations. Nevertheless, with decrease of electron beam emittance in storage rings [4] and continuous progress in the quality of optical elements [5-7], the radiation gradually approaches diffraction limit for shorter and shorter wavelengths, making physical-optics approaches to simulation of wavefront propagation increasingly important.

Two physical-optics based approaches to wavefront propagation simulation are currently popular: Fourier optics [8] and asymptotic expansions (mainly, the stationary phase method) [9, 10]. This paper deals with the Fourier optics approach, as it is implemented in the SRW computer code [11, 12].

The following are proven "strong points" of the Fourier optics method:

- very high CPU efficiency;
- possibility to take into account multiple diffractive/ refractive/ reflective optical elements in "uniform" way without any increase of the overall complexity;
- stability in case of "noisy" wavefronts (these methods are extensively used for simulation of scattering);
- availability of large amount of data on electric field after only one propagation pass.

Among "weak points" of this method one can mention:

- large amount of memory required for "standard" near-field propagator through free space, and
- poor accuracy of the "thin" element approximation for simulating grazing incidence optics and/or optics with very wide angular apertures.

We note that for the 3rd generation sources, it is often enough to simulate wavefront propagation through a beamline only in frequency domain – at one central or eventually at several different frequencies / photon energies. On the other hand, the 4th generation sources require a combined frequency- and time-domain analysis because of the necessity to preserve (or at least to keep track of) temporal characteristics of propagating wavefronts. To profit of CPU efficiency of the Fast Fourier Transforms (FFT), which are used by the free-space propagator and at changing the electric field representation between the frequency and time domains, it is preferable to keep in memory at each step of

*Work supported by EuroFEL
#oleg.chubar@synchrotron-soleil.fr

propagation an entire "instant" wavefront, meshed not only vs two transverse coordinates, but also vs frequency (or time). This makes the memory constraint even more important. In the following sections, we show that despite of this constraint, the Fourier optics method can be very efficiently used for simulating propagation of time-dependent SASE wavefronts produced by FELs.

BRIEF METHOD DESCRIPTION

Time- and Frequency-Domain Representations

Time- and frequency-domain complex electric fields $\vec{E}(\vec{r},t)$ and $\tilde{\vec{E}}(\vec{r},\omega)$ are well known to be related by the Fourier transform:

$$\tilde{\vec{E}}(\vec{r},\omega) = \int_{-\infty}^{\infty} \vec{E}(\vec{r},t)\exp(i\omega t)dt$$
$$\vec{E}(\vec{r},t) = \frac{1}{2\pi}\int_{-\infty}^{\infty} \tilde{\vec{E}}(\vec{r},\omega)\exp(-i\omega t)d\omega \quad (1)$$

where t is time, ω is cyclic frequency (linked to photon energy via the reduced Planck constant $\varepsilon = \hbar\omega$), $\vec{r}$ is observation point.

Initial SASE wavefronts are often calculated in time domain [13]; however, propagation of the electric field in free space or in media is described in the frequency domain [14]. Besides, it is often necessary to follow the evolution of both temporal and spectral characteristics of a wavefront at different propagation steps. It is therefore important to use an efficient algorithm for Eq. (1). Such algorithm can be based on a prime-factor FFT [15], which would be applied "in place" to a "flat" (or "C-aligned") complex electric field data structure – for many space points $\vec{r}$ in parallel.

Fourier-Optics Propagators

The propagation of transverse components of the frequency-domain electric field in free space is well known to be described by the Huygens-Fresnel principle, which, for small emission and observation angles is [14]:

$$\tilde{\vec{E}}_{\perp}(\vec{r}_2,\omega) \approx \frac{-i\omega}{2\pi c}\iint_{\Sigma_1} \tilde{\vec{E}}_{\perp}(\vec{r}_1,\omega)\frac{\exp[i\omega|\vec{r}_2-\vec{r}_1|/c]}{|\vec{r}_2-\vec{r}_1|}d\Sigma_1 \quad (2)$$

where the integration is performed over surface Σ_1; $\vec{r}_1$ is point on that surface (varying at the integration), $\vec{r}_2$ is an observation point, c is speed of light. If Σ_1 is a plane, e.g. perpendicular to Z axis, and $\vec{r}_2$ belongs to another plane, located at distance Δz from Σ_1, then $d\Sigma_1 = dx_1 dy_1$, $|\vec{r}_2-\vec{r}_1| = [\Delta z^2 + (x_2-x_1)^2 + (y_2-y_1)]^{1/2}$, and Eq. (2) is a convolution-type integral, which can be quickly calculated using 2D FFT.

In practice, direct application of the convolution theorem to Eq. (2) for the case of propagation between parallel planes may result in the necessity of very dense sampling of the electric field vs transverse coordinates x_1 and y_1 (and/or x_2, y_2), because the phase of the field at some distance from source depends quadratically on these coordinates and all oscillations of the field within given wavefront limits must be resolved (otherwise accuracy may be lost). There are several possibilities to walk around this problem. One consists in distinguishing more economic (in terms of sampling) "special cases" of propagation, such as propagation to or from waist, when Eq. (2) can be reduced to one Fourier transform and multiplication of the field by phase factors which depend on the transverse coordinates.

More generally, if approximate values of wavefront radii and centres with respect to transverse coordinates are known, one can "subtract" the quadratic phase terms from the initial wavefront; then, within the quadratic phase approximation, Eq. (2) can still be reduced to a convolution, with the necessity to re-scale (and eventually shift) the resulting wavefront, and add a new (modified) quadratic phase term to it. This simple manipulation can dramatically reduce the amount of memory required for the propagation, while preserving high efficiency and accuracy of the Fourier optics method.

Electric field transformation at propagation from a transverse plane before an optical element (e.g. lens, mirror, aperture, zone plate, grating,...) to a plane immediately after it can be formally represented as:

$$\tilde{\vec{E}}_{\perp out}(x_2,y_2,\omega) \approx \mathbf{G}(x_2,y_2,\omega)\exp[i\omega L(x_2,y_2)/c]\times \\ \times \tilde{\vec{E}}_{\perp in}(x_1(x_2,y_2),y_1(x_2,y_2),\omega) \quad (3)$$

where, in general case, $\mathbf{G}(x_2,y_2,\omega)$ is a 2x2 matrix function of the output transverse coordinates and frequency, which can take into account eventual anisotropy of the optical element with respect to transverse components of the input electric field; the optical path function $L(x_2, y_2)$ and the input/output coordinate transformation $x_1(x_2,y_2), y_1(x_2,y_2)$ can be deduced from geometrical optics, or by applying the stationary phase method. We note that for a "thin" optical element, Eq. (3) is reduced to simple multiplication of the input field by a complex transmission function.

Wavefront Resizing and Resampling

Transverse dimensions and/or oscillation rates of electric field may strongly vary during the propagation. In order to keep the electric field sufficiently well dimensioned and resolved at each step of the propagation (as required by the propagators being used to simulate optical elements and free spaces) and, at the same time, stay within reasonable memory consumption, efficient mechanisms of wavefront resizing (changing limits) and resampling (changing steps of the grid) should be used. The resampling can be performed either by using interpolation, or by applying FFT and resizing the electric field on the Fourier side. E.g., if there is a necessity to decrease step of transverse position(s), one can perform forward FFT and increase limit(s) by padding zeros on the Fourier side, and then perform backwards FFT. At manipulations with time-dependent wavefronts, the use of

the resizing and resampling procedures is particularly important, and it should be used not only to transverse coordinates (/angles), but also for time (/frequency).

APPLICATIONS FOR TIME-DEPENDENT SASE WAVEFRONTS

To illustrate application of the Fourier-optics based method, as it is implemented in the SRW code, for simulating propagation of time-dependent SASE wavefronts, we use two simple interference-type optical schemes, one of them being sensitive to spatial, and the other one to temporal coherence of an input wavefront. Of course, the range of potential applications of the method is not limited by these types of optical schemes.

Two different wavefronts are numerically propagated through the optical schemes: (almost fully) saturated radiation wavefront obtained at seeded FEL operation and a wavefront of unsaturated SASE.

All calculations described in this section were performed on a regular laptop PC with 1 GB of memory under 32-bit Windows. In all considered cases, the simulation of wavefront propagation took small amount of CPU time (in the range of minutes) compared to the calculation of initial time-dependent wavefronts.

Wavefronts at FEL Exit

The two initial wavefronts were calculated using GENESIS (integrated into SRW) for the parameters corresponding to the phase 2 of the ArcEnCiel project [16]:

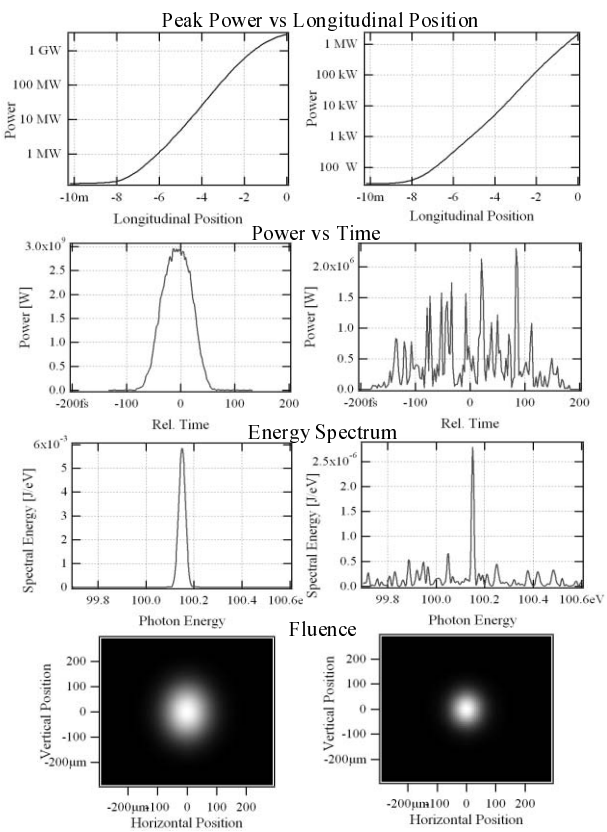

Figure 1: Radiation characteristics at FEL exit for two cases: seeded (left) and started up from noise (right).

electron beam at 1 GeV energy, 1.5 kA peak current, 60 μm RMS bunch length, 1.2 π mm-mrad normalized emittance; planar undulator with 30 mm period and deflecting parameter ~2.06, composed out of five 2 m long sections. In one case, a seeding radiation pulse of 50 kW peak power and 22 fs RMS duration, at 100.15 eV average photon energy was used (the seed was assumed to be produced by the process of generation of high harmonics in gas [17]). In the other case, no external seed was applied. The results of time-dependent calculations (peak power, pulse profile, energy spectrum, fluence/intensity distribution at FEL exit) obtained for the two cases are presented in Fig. 1.

Young's Double-Slit Interferometer

The Young's double-slit interferometer scheme, shown in Fig. 2, allows one to test transverse coherence of input radiation [14].

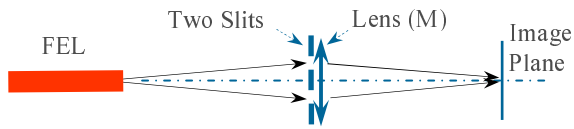

Figure 2: Double-slit interferometer scheme.

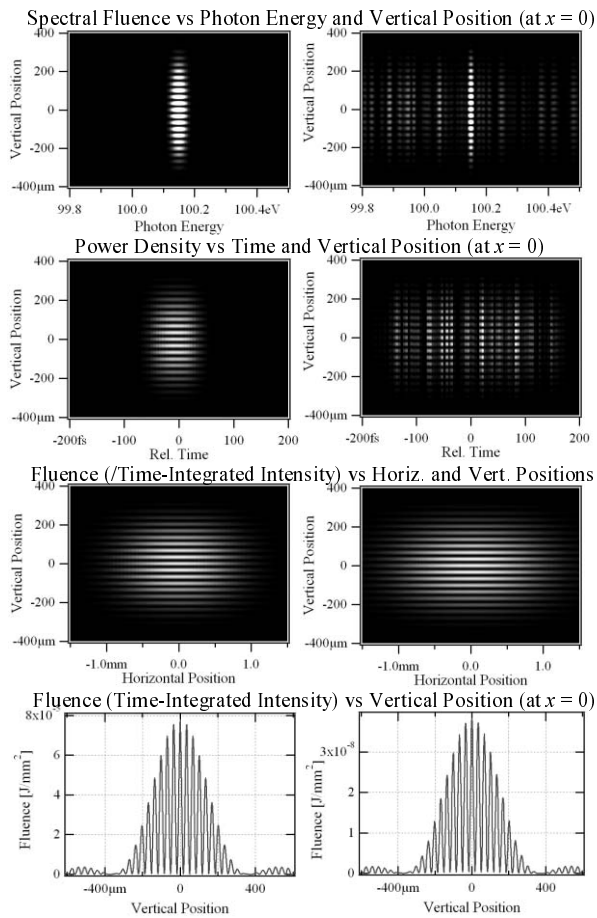

Figure 3: Wavefront characteristics in the image plane of double-slit interferometer scheme for two FEL regimes: seeded (left) and started up from noise (right).

The following parameters of this scheme were used for SASE wavefront propagation calculations: 20 m distance from the FEL exit to the slits, 1 mm vertical distance between the slits, 0.1 mm slit widths, 2.6 m/18 m vertical/horizontal focal distance of an astigmatic lens (mirror), and 3 m distance from the lens to the image plane. The calculation results obtained for the image plane in the two wavefront cases (as described above) are presented in Fig. 3. One can see that in both cases, the visibility of interference fringes, characterizing the degree of spatial coherence, is ~1.

Double-Slit Interferometer with Grating

A simple scheme for probing temporal coherence can be obtained by inserting a grating into the double-slit interferometer, just before (or immediately after) the slits and the mirror, as shown in Fig. 4.

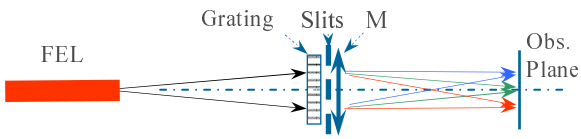

Figure 4: Double-slit interferometer with grating.

Simulation results on wavefront propagation to the observation plane for the two cases of input SASE are illustrated in Fig. 5. At this calculation, the vertical and horizontal focal distances of the mirror were 3.7 m and 100 m; the observation plane was at ~3.8 m from the mirror. The grating was assumed to be flat, with groove density of 150 l/mm; the incidence angle ~2.5° (in vertical plane).

We see from Fig. 5 that for both wavefront cases, the interference patterns are strongly modified by the grating. Vertical positions of interference peaks depend now on photon energy (see upper image plots), and this reduces the visibility of fringes in the resulting frequency- (or time-) integrated patterns. As one can see from the graphs, the poor visibility of fringes in the seeded case has also simple time-domain interpretation: because of the delay introduced by the grating, the radiation pulses from the two slits almost don't overlap in time.

We note that in the case of SASE started from noise, the interference pattern depends on pulse micro-structure (having stochastic origin) and can therefore appear further "smoothed-out" after averaging over ensemble of pulses. The corresponding analysis can be easily performed using the described methods.

ACKNOWLEDGEMENTS

We would like to thank Dr. M. Bowler (4GLS) and Dr. P. Dumas (SOLEIL) for precious help in benchmarking and reviewing wavefront propagation functions of SRW.

REFERENCES

[1] C. Pellegrini, S. Reiche, in Optics Encyclopedia, Wiley-VCH Verlag, Berlin 2003, p. 1111-1134.
[2] A. Zholents, W. Fawley, Phys. Rev. Lett. 92, 224801 (2004).

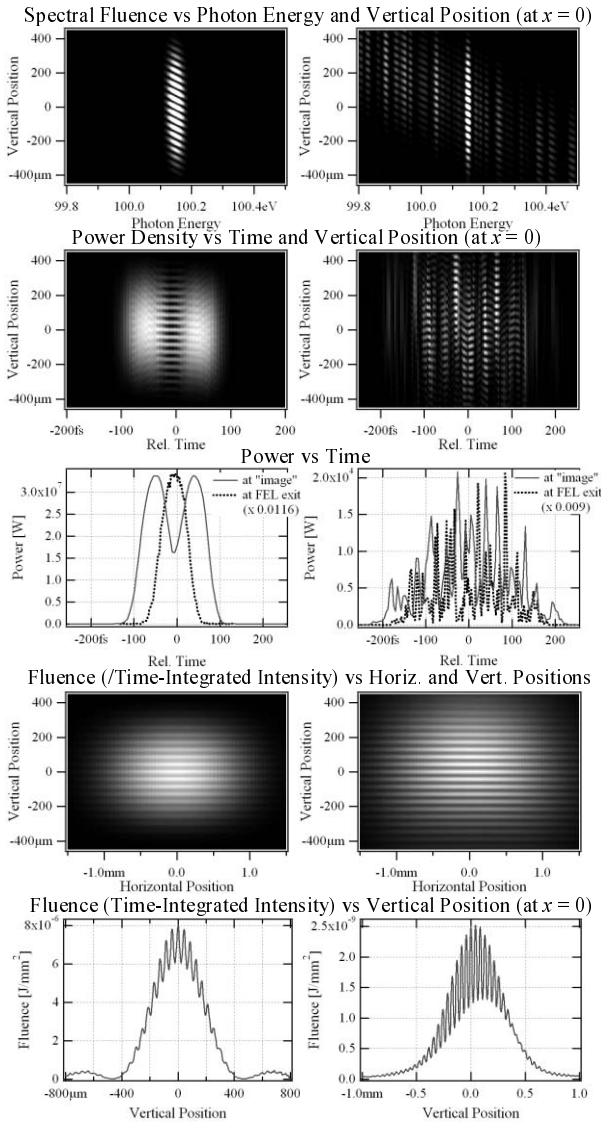

Figure 5: Wavefront characteristics in observation plane of double-slit interferometer with grating, for two FEL regimes: seeded (left) and started up from noise (right).

[3] K.-J. Kim, Nucl. Instr. and Meth. A246 (1986) p.71-76.
[4] K.-J. Kim, Synchr. Rad. News, Vol. 19 (6), Dec. 2006, p. 2-6.
[5] A. Snigirev et. al., Nature 384 (1996) p.49.
[6] M. Hart, L. Berman, Acta Cryst. A54 (1998) p. 850-858.
[7] E. Di Fabrizio et. al., Nature 401 (1999) p. 895-898.
[8] J.W. Goodman, Introduction to Fourier Optics, 2nd ed., McGraw-Hill, 1996.
[9] J. Bahrdt, Applied Optics 36 (19) 1997, p. 4367.
[10] J. Bahrdt, Phys. Rev. ST - Acc. and Beams 10, 060701 (2007).
[11] O. Chubar, P. Elleaume, Proc. EPAC-98, p.1177-1179.
[12] O. Chubar et. al., Proc. SPIE Vol. 4769 (2002) p. 145-151.
[13] S. Reiche, http://corona.physics.ucla.edu/~reiche/.
[14] M.Born, E.Wolf, Principles of Optics, 4th ed., Pergamon Press, 1970.
[15] S.C. Chan and K.L. Ho, IEEE Trans. Circuits and Systems 38 (8), 1991, p. 951-953.
[16] M.-E. Couprie et. al., these proceedings.
[17] Z. Chang et al, Phys. Rev. Lett. 79 (16) 1997, p. 2967.

IMPACT OF LONGITUDINAL SPACE-CHARGE WAKE FROM FEL UNDULATORS ON CURRENT-ENHANCED SASE SCHEMES

G. Geloni, E. Saldin, E. Schneidmiller and M. Yurkov
Deutsches Elektronen-Synchrotron (DESY), Hamburg, Germany

Abstract

We present a description of longitudinal wake fields in XFELs that is of relevance in relation with Enhanced Self-Amplified Spontaneous Emission (ESASE) schemes. We consider wakes in XFELs, in the limit when the electron beam has gone inside the undulator for a distance longer than the overtaking length (the length that electrons travel as a light signal from the tail of the bunch overtakes the head of the bunch). We find that the magnitude of the resulting energy chirp constitutes a reason of concern for the practical realization of ESASE schemes. **A more detailed report of our study is given in [1]**.

INTRODUCTION

This article presents a description of longitudinal wake fields in XFELs. Our study is of importance in connection with ESASE schemes, demanding for a detailed study of longitudinal wake fields arising after the dispersive section. For XFEL setups, the undulator parameter K obeys $K^2 \gg 1$. As a result, the average longitudinal Lorentz factor $\bar{\gamma}_z = \gamma/\sqrt{1+K^2/2}$ is such that $\bar{\gamma}_z^2 \ll \gamma^2$, γ being the Lorentz factor of the beam. Based on $\bar{\gamma}_z^2 \ll \gamma^2$, we demonstrate that the presence of the undulator strongly influences the space-charge wake. In contrast to this, in literature, wake calculations for the LCLS case are given in free-space, as if the presence of the undulator were negligible. In this paper we pose particular attention to the LCLS case, for which ESASE schemes have been first proposed. We thus restrict our attention to a specific region of parameters. First, the longitudinal size of the beam is much larger than the FEL wavelength, i.e. $\sigma_z \simeq \lambda \gg \lambda_r$. Second, we assume a long saturation length compared with the overtaking length, i.e. $L_s \gg 2\bar{\gamma}_z^2\lambda$. Third, effects of metallic surroundings can be neglected, i.e. $a \gg \bar{\gamma}_z\lambda$. We present a general theory based on these three assumptions. These are satisfied for the LCLS case, together with an extra-assumption on the transverse electron-beam size $\sigma_\perp$: $\sigma_\perp^2 \gg \lambda\lambda_w$, λ being the reduced wavelength. Due to this last condition, major simplifications arise in the general theory. Radiation from the undulator is drastically suppressed and calculations of impedance and wake function can be performed considering a non-radiating beam, and thus accounting for space-charge interactions only. Space-charge impedance and wake function is found to reproduce the free-space case. Only, γ must be consistently substituted with $\bar{\gamma}_z$. We apply our theory to the ESASE setup referring to the LCLS facility. We calculate the energy chirp associated with wakes inside the undulator and between dispersive section and undulator. Subsequently, the magnitude of their effect is estimated by calculating the linear energy chirp parameter. We find that the gain of the FEL process is sensibly reduced, and that longitudinal wake fields constitute a reason of concern regarding the practical realization of ESASE schemes.

FIELD CALCULATION

Calculation of longitudinal wake field and impedance from an FEL undulator first demand characterization of the electric field generated at a given position by the bunch. We perform an analysis in terms of harmonics, i.e. $\vec{E} = \vec{E}(\vec{r},\omega)\exp[-i\omega t] + C.C.$, the symbol "C.C." indicating complex conjugation[1]. The complex amplitude $\vec{E}(\vec{r},\omega)$ can be considered as the electric field in the space-frequency domain, "the field". Transverse and longitudinal fields can be found by solving paraxial Maxwell's equation in the space-frequency domain: $\mathcal{D}[\vec{\bar{E}}(z,\vec{r}_\perp,\omega)] = \vec{g}(z,\vec{r}_\perp,\omega)$. Here $\vec{\bar{E}}_\perp = \vec{E}_\perp \exp[-i\omega z/c]$ is the electric field envelope that does not vary much along z on the scale of the reduced wavelength $\lambda = \lambda/(2\pi)$. The differential operator $\mathcal{D}$ is defined by $\mathcal{D} \equiv (\nabla_\perp{}^2 + (2i\omega/c)\cdot\partial/\partial z), \nabla_\perp{}^2$ being the Laplacian operator over transverse cartesian coordinates. The source-term $\vec{g}(z,\vec{r}_\perp)$ is specified by the trajectory of the source electrons, and can be written in terms of the Fourier transform of the transverse current density, $\vec{\bar{j}}(z,\vec{r}_\perp,\omega)$, and of the charge density, $\bar{\rho}(z,\vec{r}_\perp,\omega)$, as $\vec{g} = -4\pi\exp[-i\omega z/c](i\omega/c^2\vec{\bar{j}} - \vec{\nabla}\bar{\rho})$. Thus, we recognize current and gradient terms in the field. Here $\vec{\bar{j}}$ and $\bar{\rho}$ are regarded as given data. They will be treated as macroscopic quantities, and can be written as $\bar{\rho}(\vec{r}_\perp,z,\omega) = \rho_o(\vec{r}_\perp - \vec{r}'_{o\perp}(z))\bar{f}(\omega)\exp[i\omega s_o(z)/v_o]$ and $\vec{\bar{j}} = \vec{v}_o\bar{\rho}$. Here $f(\omega)$ is the Fourier transform of the longitudinal bunch-profile, while ρ_o is related with the transverse bunch-profile. $\vec{r}'_{o\perp}(z)$, $s_o(z)$ and v_o pertain a reference electron with Lorentz factor γ that is injected on axis with no deflection and is guided by the undulator field only. In particular, $r'_{ox}(z) = r_w\cos(k_w z)$ and

[1]For simplicity we will consider $\omega > 0$. Expressions for the field at negative values of ω can be obtained based on the property $\vec{E}(-\omega) = \vec{E}^*(\omega)$ starting from explicit expressions for $\vec{E}$ at $\omega > 0$.

$r'_{oy}(z) = 0$, where the transverse amplitude of oscillations is $r_w = K/(\gamma k_w)$. The correspondent velocity is described by $\vec{v}_{o\perp}(z) = v_{ox}\vec{e}_x + v_{oy}\vec{e}_y$. Finally, $s_o(z)$ is the curvilinear abscissa measured along the trajectory of the reference particle. Solution of Maxwell's equation is performed with the help of a perturbation theory in the small parameter $\lambda_r/\lambda \ll 1$. Calculations yield [1]:

$$\begin{aligned}\vec{\tilde{E}}_\perp(z,\vec{r}_\perp) = &-\frac{i\omega\bar{f}(\omega)}{c}\int d\vec{r'}_\perp \rho_o\left(\vec{r'}_\perp\right)\exp\left[\frac{i\omega z}{2c\bar{\gamma}_z^2}\right]\\ \times\Bigg\{ &+\exp[+ik_w z]\frac{K\vec{e}_x}{i\gamma}K_0\left(\sqrt{2}\frac{|\,\vec{r}_\perp-\vec{r'}_\perp\,|}{\sqrt{\bar{\lambda}\bar{\lambda}_w}}\right)\\ &-\exp[-ik_w z]\frac{K\vec{e}_x}{i\gamma}K_0\left(-\sqrt{2}i\frac{|\,\vec{r}_\perp-\vec{r'}_\perp\,|}{\sqrt{\bar{\lambda}\bar{\lambda}_w}}\right)\\ &+\exp[+ik_w z]\frac{icr_w}{\omega}\Bigg[-\frac{\sqrt{2}K_1\left(\sqrt{2}\frac{|\vec{r}_\perp-\vec{r'}_\perp|}{\sqrt{\bar{\lambda}\bar{\lambda}_w}}\right)\vec{e}_x}{\sqrt{\bar{\lambda}\bar{\lambda}_w}\,|\,\vec{r}_\perp-\vec{r'}_\perp\,|}\\ &\quad+\frac{2(x-x')(\vec{r}_\perp-\vec{r'}_\perp)}{\bar{\lambda}\bar{\lambda}_w\,|\,\vec{r}_\perp-\vec{r'}_\perp\,|^2}K_2\left(\sqrt{2}\frac{|\,\vec{r}_\perp-\vec{r'}_\perp\,|}{\sqrt{\bar{\lambda}\bar{\lambda}_w}}\right)\Bigg]\\ &-\exp[-ik_w z]\frac{icr_w}{\omega}\Bigg[-\frac{\sqrt{2}iK_1\left(-\sqrt{2}i\frac{|\vec{r}_\perp-\vec{r'}_\perp|}{\sqrt{\bar{\lambda}\bar{\lambda}_w}}\right)\vec{e}_x}{\sqrt{\bar{\lambda}\bar{\lambda}_w}\,|\,\vec{r}_\perp-\vec{r'}_\perp\,|}\\ &\quad+\frac{2(x-x')(\vec{r}_\perp-\vec{r'}_\perp)}{\bar{\lambda}\bar{\lambda}_w\,|\,\vec{r}_\perp-\vec{r'}_\perp\,|^2}K_2\left(-\sqrt{2}i\frac{|\,\vec{r}_\perp-\vec{r'}_\perp\,|}{\sqrt{\bar{\lambda}\bar{\lambda}_w}}\right)\Bigg]\\ &-\left[\frac{ic}{\omega}\frac{\vec{r}_\perp-\vec{r'}_\perp}{|\,\vec{r}_\perp-\vec{r'}_\perp\,|}\right]\frac{2}{\bar{\gamma}_z\bar{\lambda}}K_1\left(\frac{|\,\vec{r}_\perp-\vec{r'}_\perp\,|}{\bar{\gamma}_z\bar{\lambda}}\right)\Bigg\} \qquad (1)\end{aligned}$$

and

$$\begin{aligned}\widetilde{E}_z(z,\vec{r}_\perp) = &-\frac{i\omega\bar{f}(\omega)}{c}\int d\vec{r'}_\perp \rho_o\left(\vec{r'}_\perp\right)\exp\left[\frac{i\omega z}{2c\bar{\gamma}_z^2}\right]\\ \times\Bigg\{ &+\frac{\sqrt{2}}{\sqrt{\bar{\lambda}\bar{\lambda}_w}}\exp[+ik_w z]\left[\frac{cK}{\omega\gamma}\frac{x-x'}{|\,\vec{r}_\perp-\vec{r'}_\perp\,|}\right]\\ &\qquad\times K_1\left(\sqrt{2}\,\frac{|\,\vec{r}_\perp-\vec{r'}_\perp\,|}{\sqrt{\bar{\lambda}\bar{\lambda}_w}}\right)\\ &+\frac{\sqrt{2}i}{\sqrt{\bar{\lambda}\bar{\lambda}_w}}\exp[-ik_w z]\left[\frac{cK}{\omega\gamma}\frac{x-x'}{|\,\vec{r}_\perp-\vec{r'}_\perp\,|}\right]\\ &\qquad\times K_1\left(\sqrt{2}i\frac{|\,\vec{r}_\perp-\vec{r'}_\perp\,|}{\sqrt{\bar{\lambda}\bar{\lambda}_w}}\right)\\ &+\frac{2}{\bar{\gamma}_z^2}K_0\left(\frac{|\,\vec{r}_\perp-\vec{r'}_\perp\,|}{\bar{\gamma}_z\bar{\lambda}}\right)\Bigg\}. \qquad (2)\end{aligned}$$

Terms not including $\exp[\pm k_w z]$ are entangled with the electron beam. We identify them as space-charge terms. The formation length of the space-charge field is $2\bar{\lambda}\bar{\gamma}_z^2$, while the correspondent diffraction size is $\bar{\gamma}_z\bar{\lambda}$. Terms including $\exp[\pm ik_w z]$ are indicative of radiation fields. Phase velocity of terms including $\exp[+ik_w z]$ is slower than that of the beam harmonic. Phase velocity of terms including $\exp[-ik_w z]$ is faster than that of the beam harmonic. The formation length of radiation field terms is $\bar{\lambda}_w$, while the correspondent diffraction size is $\sqrt{\bar{\lambda}\bar{\lambda}_w}$. The first and the second integral in the transverse field are (radiative) current density terms. The third and the fourth term are (radiative) gradient terms, while the last term is a (space charge) gradient term. As regards the longitudinal field instead, the third integral is a (space-charge) term originating from a mixture of gradient and current sources. It is possible to cross-check our expressions for the field with the help of Gauss law $\vec{\nabla}\cdot\vec{E} = 4\pi\bar{\rho}$. In particular, it can be seen that $\vec{E} = \vec{E}_{\rm rad} + \vec{E}_{\rm sc}$ separately verifies: $\vec{\nabla}\cdot\vec{E}_{\rm sc} = 4\pi\bar{\rho}$ and $\vec{\nabla}\cdot\vec{E}_{\rm rad} = 0$. This confirms that radiation field is not entangled with sources, while space-charge field is.

IMPEDANCE

The impedance is defined accounting for the transverse size of the beam as $Z(\omega,z) = 1/|\bar{f}(\omega)|^2 \cdot \int_0^z dz' \int_A d\vec{r}_\perp \vec{\bar{j}}^{*} \cdot \vec{E}$. The integration volume is a cylinder of base A including the undulator up to position $z' = z$. Integration in z' is performed from 0 to z, because we are interested in impedance generated inside the undulator, that begins at $z = 0$. The wake function can be obtained by Fourier transformation of the impedance. Using Eq. (1) and Eq. (2) we obtain the total impedance $Z = Z_{\rm r} + Z_{\rm sc}$. The real part Z_R is given by

$$\begin{aligned}Z_R = &-\frac{K^2\pi\omega z}{4\gamma^2}\int d\vec{r'}_\perp \int d\vec{r''}_\perp \rho_o^*(\vec{r'}_\perp)\rho_o\left(\vec{r''}_\perp\right)\\ &\times J_0\left(\frac{\sqrt{2}\,|\vec{r'}_\perp-\vec{r''}_\perp|}{\sqrt{\bar{\lambda}\bar{\lambda}_w}}\right). \qquad (3)\end{aligned}$$

The imaginary part Z_I amounts to

$$\begin{aligned}Z_I = &-\frac{K^2\omega z}{2\gamma^2}\int d\vec{r'}_\perp \int d\vec{r''}_\perp \rho_o^*(\vec{r'}_\perp)\rho_o\left(\vec{r''}_\perp\right)\\ &\times\Bigg\{\frac{\pi}{2}Y_0\left(\frac{\sqrt{2}\,|\vec{r'}_\perp-\vec{r''}_\perp|}{\sqrt{\bar{\lambda}\bar{\lambda}_w}}\right)-K_0\left(\frac{\sqrt{2}\,|\vec{r'}_\perp-\vec{r''}_\perp|}{\sqrt{\bar{\lambda}\bar{\lambda}_w}}\right)\\ &+\frac{4+2K^2}{K^2}K_0\left(\frac{|\vec{r'}_\perp-\vec{r''}_\perp|}{\bar{\gamma}_z\bar{\lambda}}\right)\Bigg\}. \qquad (4)\end{aligned}$$

Z_R can be entirely traced back to the fast-wave part of the transverse radiative field. Z_I is composed of different contributions instead. The term in Y_0 follows from the fast-wave transverse radiative field. The second term (in K_0) follows from the slow-wave transverse radiative field. The last term (also in K_0) can be traced back to the longitudinal space-charge field.

Asymptotic case for $\sigma_\perp^2 \ll \bar{\lambda}\bar{\lambda}_w$

It is interesting to derive asymptotic limits of Eq. (3) and Eq. (4) in the case for $\sigma_\perp^2 \ll \bar{\lambda}\bar{\lambda}_w$. Bessel

functions in Eq. (3) and Eq. (4) can be expanded for small argument values. In particular, using $J_0(x) \simeq 1$ for $x \ll 1$, the real part of the impedance becomes $Z_R = -K^2\pi z/(4c\bar{\lambda}\gamma^2)$, independently of the choice of ρ_o. Subsequently, we use $K_0(x) \simeq -\gamma_E - \ln(x/2)$ and $Y_0 \simeq 2/\pi[\gamma_E + \ln(x/2)]$, $\gamma_E \simeq 0.577216$ being the Euler Gamma constant in the imaginary part of the impedance, Eq. (4). We obtain $Z_I = -K^2 z/(c\bar{\lambda}\gamma^2)\ln(\sqrt{\bar{\lambda}/\bar{\lambda}_r}) + 2z/(c\bar{\lambda}\gamma^2)\ln(\sqrt{1+K^2/2}) + Z_{I\,\mathrm{free}}$, where $Z_{I\,\mathrm{free}} = 2z\gamma_E/(c\bar{\lambda}\gamma^2) + 2\omega z/\gamma^2 \int d\vec{r}'_\perp \int d\vec{r}''_\perp \rho_o^*(\vec{r}'_\perp)\rho_o(\vec{r}''_\perp)\ln[|\vec{r}'_\perp - \vec{r}''_\perp|/(2\bar{\lambda}\gamma)]$. $Z_{I\,\mathrm{free}}$ is the only model-dependent part of the impedance. Assuming a Gaussian transverse profile $\rho_o(r_\perp) = 1/(2\pi\sigma_\perp^2 c)\exp[-r_\perp^2/(2\sigma_\perp^2)]$, we obtain $Z_{I\,\mathrm{free}} = 2z\gamma_E/(c\bar{\lambda}\gamma^2) + 2z/(c\bar{\lambda}\gamma^2)\ln[\sigma_\perp/(\gamma\bar{\lambda})]$. Thus, $Z_{I\,\mathrm{free}}$, is logarithmically divergent on $\sigma_\perp$. This is the free-space impedance. The renormalized impedance, i.e. the difference $Z - i\,Z_{I\,\mathrm{free}}$ is independent of $\sigma_\perp$ and constitutes a result valid for any value of K. These results are in agreement with limiting cases discussed in literature.

Asymptotic case for $\sigma_\perp^2 \gg \bar{\lambda}\bar{\lambda}_w$

Transverse scales pertaining radiation field and space-charge field are present in Eq. (3) and Eq. (4). The first two terms in Y_0 and K_0 in Eq. (4), as well as the entire real part of the impedance, are linked to the presence of transverse current density and to radiation field. The last term in Eq. (4) is due to the presence of longitudinal space-charge field, a combination of current and gradient terms. The corresponding Bessel functions yield different characteristic transverse scales. Bessel functions related with the radiation field yield $\sqrt{\bar{\lambda}\bar{\lambda}_w} \sim \sqrt{\bar{\lambda}\bar{\lambda}_r\bar{\gamma}_z^2}$. Those related with the longitudinal space-charge field yield $\bar{\lambda}\bar{\gamma}_z \sim \sqrt{\bar{\lambda}\bar{\lambda}\bar{\gamma}_z^2}$. Since $\bar{\lambda} \gg \bar{\lambda}_r$, it follows that $\sqrt{\bar{\lambda}\bar{\lambda}_w/2} \ll \bar{\lambda}\bar{\gamma}_z$. By inspection of Eq. (3) and Eq. (4) one can see that the value of $\left|\vec{r}'_\perp - \vec{r}''_\perp\right|$ is limited by $\sigma_\perp$, because of the presence of the exponential functions under the integration sign. Therefore, assuming constant total charge of the beam, when the electron beam transverse size $\sigma_\perp$ increases beyond $\sqrt{\bar{\lambda}\bar{\lambda}_w}$ the radiation contribution is suppressed with respect to the space-charge one. Summing up, when $\sigma_\perp^2 \gg \bar{\lambda}\bar{\lambda}_w$, we may neglect the real part of the impedance Z_R and approximate the total impedance with

$$Z = -i\frac{2\omega z}{\bar{\gamma}_z^2}\int d\vec{r}' \int d\vec{r}''\rho_o^*(\vec{r}')\rho_o\left(\vec{r}''_\perp\right)K_0\left(\frac{\left|\vec{r}' - \vec{r}''\right|}{\bar{\lambda}\bar{\gamma}_z}\right). \quad (5)$$

This means that, in the limit $\sigma_\perp^2 \gg \bar{\lambda}\bar{\lambda}_w$, the only field to be accounted for when calculating impedance (and wake), is the effective longitudinal space-charge field.

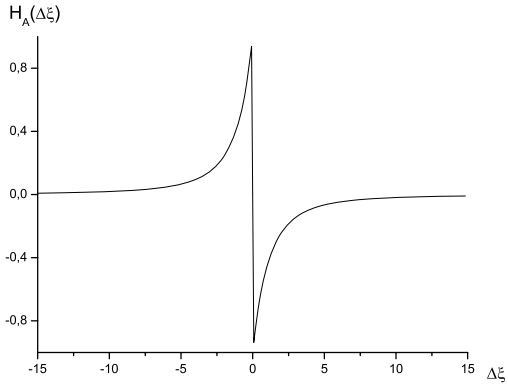

Figure 1: Plot of the universal function H_A.

STEADY STATE WAKE FOR $\sigma_\perp^2 \gg \bar{\lambda}\bar{\lambda}_W$

Our derivations drastically simplify for $\sigma_\perp^2 \gg \bar{\lambda}\bar{\lambda}_w$. We consider transverse and longitudinal gaussian profiles. When $\sigma_\perp^2 \gg \bar{\lambda}\bar{\lambda}_w$, an expression for the wake can be found by Fourier-transforming the impedance given in Eq. (5). Eq. (5) is mathematically identical to the free-space expression where γ is substituted by $\bar{\gamma}_z$. We find that the antisymmetric part of the wake G_A is given by $G_A(\Delta\xi) = \bar{\gamma}_z\eta\hat{z}/\sigma_\perp \cdot H_A(\Delta\xi)$, where $H_A(\Delta\xi) = -\Delta\xi/(2\sqrt{\pi})\ \{2\sqrt{\pi}/|\Delta\xi| - \pi\exp[(\Delta\xi)^2/4]\mathrm{erfc}[|\Delta\xi|/2]\}$. Here we defined $\Delta\xi = \bar{\gamma}_z(\Delta s)/\sigma_\perp$, $\eta = \bar{\gamma}_z\sigma_z/\sigma_\perp$ and $\hat{z} = z/(2\bar{\gamma}_z^2\sigma_z)$. A plot of the universal function H_A as a function of $\Delta\xi$ is given in Fig. 1.

The energy change of a single particle at position s within the bunch due to the reactive part of the wake (averaged over transverse coordinates) is given by $\Delta\mathcal{E}_A(s) = (-e)\int_{-\infty}^{\infty} G_A(\Delta s)f(s-\Delta s)d(\Delta s)$. An explicit expression for $\Delta\mathcal{E}_A/\mathcal{E}_o$, with $\mathcal{E}_o = \gamma m_e c^2$, as a function of $\xi = \bar{\gamma}_z s/\sigma_\perp$ is:

$$\frac{\Delta\mathcal{E}_A}{\mathcal{E}_o}\left(\frac{s}{\sigma_z};\eta\right) = \frac{I_{\max}\hat{z}}{\gamma I_A}F\left(\frac{s}{\sigma_z};\eta\right) \quad (6)$$

and

$$F\left(\frac{s}{\sigma_z};\eta\right) = \int_{-\infty}^{\infty} d(\Delta\xi)\eta H_A\left(\eta\frac{s}{\sigma_z} - \Delta\xi\right)\exp\left[-\frac{(\Delta\xi)^2}{2\eta^2}\right]. \quad (7)$$

A plot of F is given as a function of s/σ_z in Fig. 2 for different values of η.

APPLICATION TO ESASE SCHEMES

We now calculate the impact of longitudinal wake fields on ESASE schemes. We propose an analysis on a set of parameters referring to LCLS. Similar calculations may be performed on other parameter

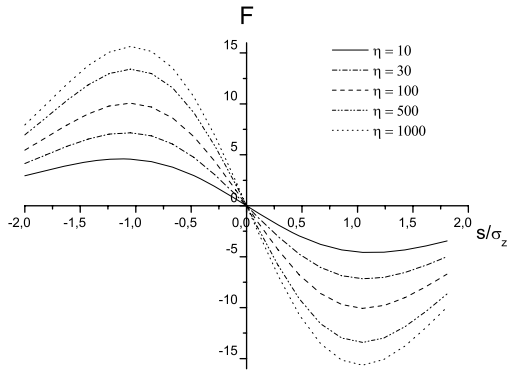

Figure 2: Plot of F for different values of η.

sets like those for the European XFEL. We consider a beam with normalized emittance after the dispersive section $\epsilon_n \simeq 1.2$ mm mrad. We take the average betatron function in the focusing lattice $\beta_f = 18$ m, and $\gamma = 2.8 \cdot 10^4$. This gives a transverse beam size $\sigma_\perp = (\epsilon_n \beta_f/\gamma)^{1/2} \simeq 30\ \mu$m. The longitudinal size of the bunch is $\sigma_z = 50$ nm. The maximal current is about the Alfven current $I_A \simeq 17$ kA; in fact, $I_{\rm peak} \simeq 18$kA. Finally, the undulator has a period $\lambda_w = 0.03$ m, $K = 3.7$, and the vacuum chamber dimension is $a = 2.5$ mm. We consider a wavelength $\lambda\!\!\!^{-} \simeq \sigma_z = 50$ nm. We can neglect the vacuum chamber influence, because $\bar{\gamma}_z \lambda\!\!\!^{-} = 500\ \mu$m, as $\bar{\gamma}_z \simeq 10^4$, and $\bar{\gamma}_z \lambda\!\!\!^{-} \ll a = 2.5$ mm. The overtaking length is $2\lambda\!\!\!^{-}\bar{\gamma}_z^2 \simeq 10$ m. The saturation length is about $L_s = 50$ m. Thus $\hat{z} = 5$, and we can use our asymptotic expression. Moreover $\eta = \bar{\gamma}_z \sigma_z/\sigma_\perp \simeq 16.7$. From fig. 2 (or from direct calculations) one can see that the maximal value assumed by $F(s/\sigma_z, \eta)$ for $\eta = 16.7$ is about $F_{\rm max} \simeq 6$. It follows that the energy-chirp peak-to-peak is given by $\Delta\mathcal{E}_{A,\rm peak} = 2m_e c^2 (I_{\rm max}/I_A) \cdot \hat{z} F_{\rm max} \simeq 30$ MeV. In contrast to this, estimations in literature indicate "a swing in energy of 2.4 MeV". The reason for this large discrepancy is due to the fact that, in literature, the Lorentz factor γ is incorrectly used in place of $\bar{\gamma}_z$. Energy chirp is also accumulated in the free-space between the dispersive section and the undulator, worsening the situation even more. In the LCLS case the dispersive section is a dogleg located about 200 m from the undulator. The overtaking length is now $2\lambda\!\!\!^{-}\gamma^2 \simeq 80$ m, so that $\hat{z} = 2.5$. Using the same procedure as for the wake inside the undulator (but considering γ instead of $\bar{\gamma}_z$), we obtain an extra energy chirp of about $\Delta\mathcal{E}_{A,\rm peak} \simeq 20$ MeV. The sum of contributions from the straight section after the dogleg and from the undulator amounts to about 50 MeV. In order to estimate the magnitude of the effect we can use the linear energy chirp parameter $\hat{\alpha} = -(\gamma\omega\rho_{1D}^2)^{-1} \cdot d\gamma/dt$, where ρ_{1D} is the one-dimensional ρ-parameter in FEL theory. For ESASE schemes at LCLS $I_{\rm peak} = 18$ kA, and we have $\rho_{1D} \simeq 10^{-3}$. Using an estimated peak-to-peak chirp of 50 MeV we obtain $\hat{\alpha} \simeq 1$. Thus, the saturation length is significantly modified. This is a reason of concern, because ESASE schemes are based on the assumption that the nominal saturation length of about 80 m is shortened to about 50 m, that is only 37.5% less.

CONCLUSIONS

We presented a theory of wake fields in an XFEL system. Specific constraints on parameters (fulfilled in XFEL setups) were considered. We derived expressions for the steady state impedance, that is composed of a radiative and a space-charge part. Radiation field and space-charge field are characterized by different formation lengths: the undulator period $\lambda\!\!\!^{-}_w$ and the overtaking length $2\lambda\!\!\!^{-}\bar{\gamma}_z^2$ respectively. As a result, the steady state radiative part of the impedance can be applied for any undulator system (with $N_w \gg 1$). The steady state space-charge part of the impedance can be used only assuming that the saturation length is long with respect to the overtaking length, which limits its practical region of applicability. After having dealt with a generic expression for the steady-state impedance, we specialized our theory to the case $\sigma_\perp^2 \gg \lambda\!\!\!^{-}\lambda\!\!\!^{-}_w$. Major simplifications arise: space-charge contributions to impedance and wake dominate with respect to radiative contributions. We showed that the (antisymmetric) wake can be given in terms of an asymptotic expression for the wake generated by a beam in uniform motion along the longitudinal axis provided that γ is consistently substituted with $\bar{\gamma}_z$. Final expressions are presented in the case of a planar undulator. However, there are no specific effects related with such choice, and our work may be straightforwardly extended to the case of a helical undulator. In the limit $\sigma_\perp^2 \gg \lambda\!\!\!^{-}\lambda\!\!\!^{-}_w$ radiation is suppressed, so that the beam can be considered as non-radiating, and only space-charge impedance is present. Such impedance amounts to the free-space impedance, where γ is consistently substituted with $\bar{\gamma}_z$. Eq. (5) gives the correct impedance at position z inside the undulator, as an asymptotic limit for $\sigma_\perp^2 \gg \lambda\!\!\!^{-}\lambda\!\!\!^{-}_w$ of our general theory. We used our theory to estimate the effect on ESASE schemes, and we found reason for concern. Our results are in contrast with literature, where the Lorentz factor γ is incorrectly used in place of $\bar{\gamma}_z$ in the calculation of the impedance.

For details on our work we refer the interested reader to [1].

REFERENCES

[1] G. Geloni, E. Saldin, E. Schneidmiller and M. Yurkov, DESY 07-087 (2007) at http://arxiv.org/abs/0706.2280, submitted to Elsevier Science

SPACE CHARGE EFFECT IN AN ACCELERATED BEAM *

G. Stupakov and Z. Huang
Stanford Linear Accelerator Center, Stanford University, Stanford, CA 94309

Abstract

It is usually assumed that the space charge effects in relativistic beams scale with the energy of the beam as γ^{-2}, where γ is the relativistic factor. We show that for a beam accelerated in the longitudinal direction there is an additional space charge effect in free space that scales as E/γ, where E is the accelerating field. This field has the same origin as the "electromagnetic mass of the electron" discussed in textbooks on electrodynamics. We then consider the effect of this field on a beam generated in an RF gun and calculate the energy spread produced by this field in the beam.

INTRODUCTION

Modern light sources such as free electron lasers and energy recovery linacs require high-peak current, small-emittance beams. One of the important characteristics of such a beam is its energy spread. It determines the limits of a possible bunch compression, the stability against microbunching, and properties of the beam as a radiator of photons. There are several mechanisms that contribute to the energy spread in radio frequency electron guns with the dominant one, for nanocoulomb bunches, being the space charge effect.

Traditionally in accelerator physics the space charge effect is computed as a self field of a beam moving with constant velocity along a straight line. The longitudinal field in such a beam causes the energy exchange between the particles; it typically scales with the beam energy as γ^{-2} [1, p. 128], where γ is the relativistic factor, and usually becomes small for highly relativistic beams. In a broader sense, the space charge effect might be understood as a self field of the beam, even when it moves with acceleration. With this understanding, acceleration adds to the beam self field. One such contribution, that attracted a lot of attention lately, is due to the coherent radiation of the beam and is called the coherent synchrotron radiation wake (or CSR wake) [2]. The CSR wake is the radiation reaction force that keeps balance between the electromagnetic energy that is carried away by the radiation and the kinetic energy of the beam particles. It occurs when the beam is being accelerated in the direction perpendicular to the beam velocity in bending magnets or undulators.

Another type of radiation reaction force has been considered in recent papers [3, 4]—it is a self field that arises inside the beam during a violent longitudinal acceleration. Such a field can play a role in plasma acceleration experiments, where the pace of acceleration is much larger than in a conventional RF cavities.

In this paper we point out to a new component of the space charge field that arises during longitudinal acceleration of the beam. We assume that the acceleration is not strong enough to cause a noticeable radiation. What it does, however, it changes the velocity of the beam. Because the beam electromagnetic field depends on how fast it moves, the electromagnetic energy of the beam field changes during acceleration. Similar to the case of a converging beam, one should expect an additional component of the self field that keeps balance between the beam and the field energy. We call this field the *acceleration field*. Being proportional to the acceleration, on average, it is equivalent to a renormalization of the mass; it is discussed in textbooks on electrodynamics in connection with a so called electromagnetic "mass" of a point charge [5, 6]. In this paper we are interested in the spatial distribution of the field and, more specifically, the energy spread in the beam induced by the acceleration field.

The model that we consider in this paper assumes that the beam does not change its shape during the acceleration. We neglect a component of self field that is associated with the converging (or diverging) beams (see [7] and references therein).

ENERGY OF ELECTROMAGNETIC FIELD OF A MOVING GAUSSIAN BUNCH

Consider a Gaussian bunch of charged particles moving with velocity v in the z direction with the particle distribution function given by

$$n(x,y,\zeta) = \frac{N}{(2\pi)^{3/2}\sigma_z\sigma_\perp^2}\exp\left(-\frac{r^2}{2\sigma_\perp^2}-\frac{\zeta^2}{2\sigma_z^2}\right), \quad (1)$$

where N is the number of particles in the bunch, $r = \sqrt{x^2+y^2}$, $\zeta = z - vt$, $\sigma_x = \sigma_y = \sigma_\perp$ is the rms bunch size in the transverse direction, and σ_z is the rms bunch length in the longitudinal direction. The electromagnetic field of such a bunch can be calculated using the Lorentz transformation from the beam frame, see, e.g., [8]. The integrated electromagnetic energy over the whole space

$$W = \int \frac{E^2+H^2}{8\pi}dV\,, \quad (2)$$

grows with γ, as shown in Fig. 1. Note that this energy tends to infinity when $\gamma \to \infty$. As a detailed analysis shows, at $\gamma \gg 1$ the asymptotic expression for W is

$$W = \frac{Q^2}{\sqrt{\pi}\sigma_z}\log\gamma\,, \qquad \gamma \gg 1\,. \quad (3)$$

* Work supported by Department of Energy contract DE–AC02–76SF00515.

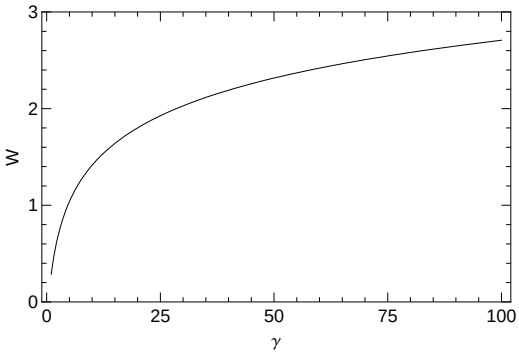

Figure 1: Integrated electromagnetic energy density in units Q^2/σ for a spherical Gaussian bunch ($\sigma_\perp = \sigma_z = \sigma$) as a function of γ.

Imagine now that the beam is being accelerated from rest to velocity v corresponding to some value of γ. The increased electromagnetic energy is taken from the kinetic energy of the beam via a longitudinal electric field E_z induced by the acceleration. Such a field is known from the theory of the radiation reaction force [6, p. 386], where it is responsible for the electromagnetic field contribution to the mass of a charged particle. This force is linear in acceleration, and changes sign when the acceleration is reversed. It is not related to the radiation; in addition to transferring energy from the beam to the electromagnetic field during acceleration (and transferring it in the opposite direction during deceleration) it introduced an energy spread in the beam. In the next section we derive an expression for E_z using the retarded potentials.

SPACE CHARGE AND ACCELERATION FIELDS

Consider a beam moving along the z axis with velocity $v(t)$ that varies with time and is the same for all particles of the beam. If $n(x, y, z)$ is the particle density at initial time, then at time t the charge density ρ and the current density j_z are: $\rho = en(x, y, z - z_0(t))$, $j_z = ev(t)n(x, y, z - z_0(t))$, with $v = dz_0/dt$, and e the elementary charge. The scalar and vector potentials of the beam are given by the following equations [5]

$$\phi(\boldsymbol{r}, t) = \int \frac{\rho(\boldsymbol{r'}, t - \tau)}{|\boldsymbol{r} - \boldsymbol{r'}|} d^3r' \,,$$
$$\boldsymbol{A}(\boldsymbol{r}, t) = \frac{1}{c} \int \frac{\boldsymbol{j}(\boldsymbol{r'}, t - \tau)}{|\boldsymbol{r} - \boldsymbol{r'}|} d^3r' \,, \qquad (4)$$

where the retarded time $t - \tau$ is defined by $c\tau = |\boldsymbol{r} - \boldsymbol{r'}|$. We will assume that the acceleration $a(t) = dv/dt$ is small and expand the potentials in Taylor series keeping only linear terms in acceleration. We have approximately

$$z_0(t - \tau) \approx z_0(t) - v(t)\tau + \frac{1}{2}a(t)\tau^2$$
$$v(t - \tau) \approx v(t) - a(t)\tau \,. \qquad (5)$$

This gives for the scalar potential

$$\phi(\boldsymbol{r}, t) = e \int \frac{d^3r'}{|\boldsymbol{r} - \boldsymbol{r'}|} \times n\left(x', y', z' - z_0(t) + v(t)\tau - \frac{1}{2}a(t)\tau^2\right) . \qquad (6)$$

We now expand the function n to obtain $\phi \approx \phi_{\rm sc} + \tilde{\phi}$, where $\phi_{\rm sc}$ is the space charge potential that does not depend on acceleration, and $\tilde{\phi}$ is a part of the potential proportional to the acceleration:

$$\phi_{\rm sc}(\boldsymbol{r}, t) = e \int \frac{n\left(x', y', z' - z_0(t) + v(t)\tau\right)}{|\boldsymbol{r} - \boldsymbol{r'}|} d^3r' \,,$$
$$\tilde{\phi}(\boldsymbol{r}, t) = -\frac{e}{2}a(t) \int \frac{\tau^2}{|\boldsymbol{r} - \boldsymbol{r'}|} d^3r' \times \partial_z n\left(x', y', z' - z_0(t) + v(t)\tau\right) \,, \qquad (7)$$

with $\partial_z n = \partial n(x, y, z)/\partial z$. Similarly, we expand the vector potential $\boldsymbol{A}$ which has the z component only,

$$A_z(\boldsymbol{r}, t) = \frac{e}{c} \int \frac{(v(t) - a(t)\tau)}{|\boldsymbol{r} - \boldsymbol{r'}|} d^3r' \times n\left(x', y', z' - z_0(t) + v(t)\tau - \frac{1}{2}a(t)\tau^2\right) , \qquad (8)$$

to obtain $\boldsymbol{A} \approx \boldsymbol{A}_{\rm sc} + \tilde{\boldsymbol{A}}$, with

$$A_{z,\rm sc}(\boldsymbol{r}, t) = \frac{e}{c} \int \frac{v(t) n\left(x', y', z' - z_0(t) + v(t)\tau\right)}{|\boldsymbol{r} - \boldsymbol{r'}|} d^3r'$$
$$\tilde{A}_{z,}(\boldsymbol{r}, t) = -\frac{e}{2c^3}a(t)v(t) \int |\boldsymbol{r} - \boldsymbol{r'}| d^3r' \times \partial_z n\left(x', y', z' - z_0(t) + v(t)\tau\right)$$
$$- \frac{ea(t)}{c^2} \int n\left(x', y', z' - z_0(t) + v(t)\tau\right) d^3r' \,. \qquad (9)$$

One can formulate conditions of applicability of the approximations used above by requiring that the terms discarded in the Taylor expansions are small compared to those left. There are two such conditions

$$a \ll \frac{c^2}{l} \,, \qquad \left|\frac{\dot{a}}{a}\right| \ll \frac{c}{l} \,, \qquad (10)$$

where l is the characteristic size of the bunch. These conditions mean that the acceleration is not large and does not change fast.

The electric field of the beam is a sum of the space charge field and a component that vanishes in the limit when $a = 0$, $\boldsymbol{E} \approx \boldsymbol{E}_{\rm sc} + \tilde{\boldsymbol{E}}$, where $\boldsymbol{E}_{\rm sc} = -\nabla\phi_{\rm sc} - c^{-1}\partial\boldsymbol{A}_{\rm sc}/\partial t$ and $\tilde{\boldsymbol{E}} = -\nabla\tilde{\phi} - c^{-1}\partial\tilde{\boldsymbol{A}}/\partial t$. The electric field $\boldsymbol{E}_{\rm sc}$ (and related to it the magnetic field $\boldsymbol{B} = \boldsymbol{v} \times \boldsymbol{E}_{\rm sc}/c$) is traditionally associated in accelerator physics with the the space charge effect. The total energy of this field is plotted in Fig. 1.

In this paper, we are interested in the electric field $\tilde{\boldsymbol{E}}$, and more specifically in the longitudinal component $\tilde{E}_z$

$$\tilde{E}_z = -\frac{\partial\tilde{\phi}}{\partial z} - \frac{1}{c}\frac{\partial\tilde{A}_z}{\partial t} \,, \qquad (11)$$

that changes the kinetic energy of the beam particles. Using Eqs. (7) and (8) for calculation of $\tilde{E}_z$ we find that in addition to terms proportional to a it also contains terms that involve $\dot{a}$ and a^2. We discard the latter as being small because of the conditions (10). This approximation gives the following expression for $\tilde{E}_z$,

$$\begin{aligned}\tilde{E}_z = &-\frac{e}{c^2}a\int\frac{n\left(x',y',z'+v\tau\right)}{|\boldsymbol{r}-\boldsymbol{r}'|}d^3r' \\ &-\frac{e}{2c^2}a\beta\int\left(\beta|\boldsymbol{r}-\boldsymbol{r}'|-(z-z')\right)d^3r' \\ &\times\partial_{zz}n\left(x',y',z'+v\tau\right) \\ &+\frac{e}{2c^2}a\int\left(\frac{z-z'}{|\boldsymbol{r}-\boldsymbol{r}'|}-4\beta\right)\partial_z n\left(x',y',z'+v\tau\right)d^3r'\,.\end{aligned} \tag{12}$$

In this equation we set $t = z_0 = 0$ (which means that the density distribution of the beam at the observation time is now $n(x, y, z)$), and suppressed the argument t in a and v. In what follows, for brevity, we call $\tilde{E}_z$ the *acceleration field*.

ACCELERATION FIELD FOR A GAUSSIAN BUNCH

For a Gaussian bunch with the charge distribution function given by Eq. (1) the calculation of the acceleration field can be reduced to a one dimensional integral. The expression for this field is derived in Ref. [9] and is given by the following equations

$$\tilde{E}_z(x,y,z) = -\frac{eNa}{\sqrt{2\pi}c^2\sigma_z}G\left(\frac{r}{\sigma_\perp},\frac{z}{\sigma_z}\right)\,, \tag{13}$$

with

$$\begin{aligned}G\left(R,Z\right) = &\int_0^\infty dvF(v,Z) \\ &\times\exp\left[-\frac{R^2A^2}{2\left(A^2+v\gamma^2\right)}-\frac{Z^2}{2(v+1)}\right]\,,\end{aligned} \tag{14}$$

where

$$\begin{aligned}&F(v,Z) = \frac{\gamma^2}{2(v+1)^{9/2}\left(A^2+\gamma^2v\right)}\times \\ &\left[v\left(5Z^2+\left(2(v-2)(v+1)Z^2+v(v+3)^2-vZ^4\right)\gamma^2\right)\right. \\ &\left.+\,v\left(4\gamma^2+v\left(Z^4-(v-4)Z^2-v\right)+3\right)+2\right]\,.\end{aligned} \tag{15}$$

Using the relation between the acceleration and the rate of change of the gamma factor, $a = (c/\gamma^3\beta)d\gamma/dt$, we can write the energy change of a particle in the beam due to the acceleration field as

$$\Delta\mathcal{E}(r,z) = \int ve\tilde{E}_z dt = -\frac{I_0}{I_A}mc^2\int_{\gamma_i}^{\gamma_f}\frac{d\gamma}{\gamma^3}G\,, \tag{16}$$

where $I_0 = Nec/\sqrt{2\pi}\sigma_z$ is the peak current in the bunch, $I_A = mc^3/e$ is the Alfvén current, γ_i and γ_f are the initial and final values of the gamma factor, and the function G is given by Eq. (14).

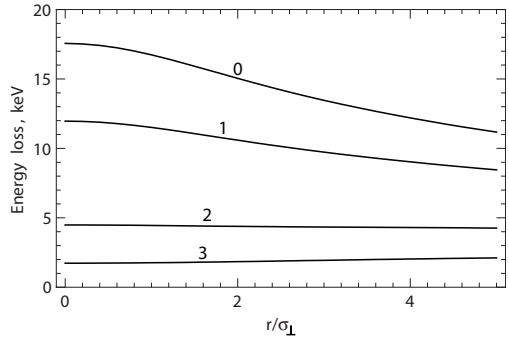

Figure 2: Energy loss induced by the acceleration field for four different slices in the bunch ($z/\sigma_z = 0$, 1, 2, and 3; this number is indicated near the curves) as a function of electron radial position.

In the ultrarelativistic limit $\gamma \gg 1$, one can find from Eqs. (14) and (15) that $G \approx 2\gamma^2 e^{-z^2/2\sigma_z^2}$. The longitudinal acceleration field in this limit does not depend on radius. Taking into account that in the external field $E_{\rm ext}$ the acceleration of a relativistic particle is $a = eE_{\rm ext}/m\gamma^3$ we arrive at the following expression for $\tilde{E}_z$

$$\tilde{E}_z = -\sqrt{\frac{2}{\pi}}\frac{r_eN}{\sigma_z\gamma}E_{\rm ext}e^{-z^2/2\sigma_z^2}\,,\qquad \gamma\gg 1\,, \tag{17}$$

with $r_e = e^2/mc^2$. We see that the acceleration field is directed against the external field $E_{\rm ext}$ and scales as $E_{\rm ext}/\gamma$. This contrasts to the usual scaling $\propto \gamma^{-2}$ of the longitudinal space charge forces. Note that due to the scaling $G \propto \gamma^2$ the integral (16) diverges logarithmically when $\gamma_f \to \infty$. This is related to the fact that the electromagnetic energy of the bunch logarithmically tends to infinity when $\gamma \to \infty$, as indicated by Eq. (3). In reality, the beam is being accelerated inside a vacuum volume that has a characteristic transverse size b. The electromagnetic energy of a relativistic beam propagating in a pipe of radius b does not change with γ when $\gamma \gtrsim b/\sigma_z$. To take into account this shielding effect of the metallic pipe, for rough estimates, we will assume that $\gamma_f = b/\sigma_z$. Note that typically $b/\sigma_z \gg 1$, and because our result has only a logarithmic dependence on γ, it is rather insensitive to the exact value of γ_f.

For a numerical example we consider now parameters of the LCLS rf-gun beam. Because our model assumes Gaussian distribution and the LCLS beam has a flat longitudinal profile, we choose the model parameters in such a way that σ_x and σ_z are equal to the corresponding rms values for the LCLS beam. We have $\sigma_z = 0.86$ mm, $\sigma_x = 0.6$ mm, and $Q = 0.72$ nC (corresponding to the peak current of $I_0 = 100$ A). We also choose $\gamma_i = 1$ and $\gamma_f = 20$, corresponding to the beam pipe radius of about 1.2 cm. Using Eq. (16) we calculated the energy loss of each particle in the beam. Note that for the nominal LCLS rf gun accelerating field of 120 MV/m the applicability conditions (10) are reasonably well satisfied. The plot of the radial dependence of the function $\Delta\mathcal{E}(r, z)$ for several values of z is shown in Fig. 2. The energy loss for the same beam aver-

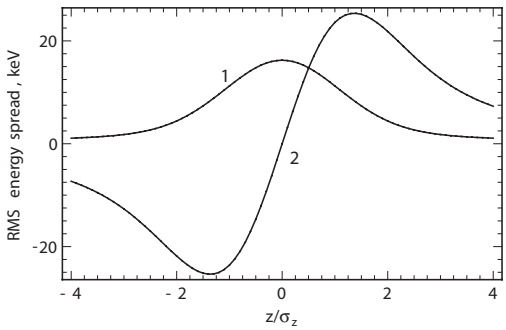

Figure 3: Energy loss induced by the acceleration field (averaged over transverse dimensions) as a function of electron longitudinal position, curve *1*. For comparison, we also show the energy loss introduced by the space charge effect, curve *2*.

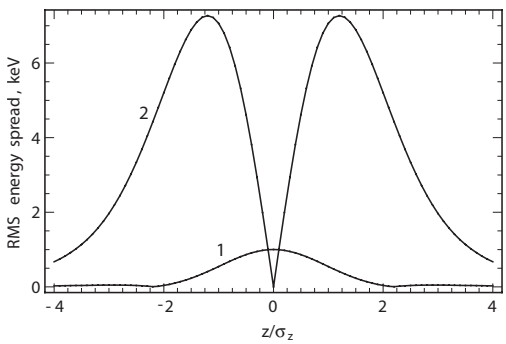

Figure 4: RMS energy spread induced by the acceleration field as a function of electron longitudinal position, curve *1*. For comparison, we also show the energy spread introduced by the space charge effect, curve *2*.

aged over the transverse coordinate is shown in Fig. 3 as a function of the position z. Finally, Fig. 4 shows the rms energy spread in slices as a function of z. In Figs. 2 and 3 we also show the energy loss and the rms energy spread introduced by the space charge forces (due to the longitudinal component of the field $\boldsymbol{E}_{\rm sc}$). The space charge effects were calculated using the theory of Ref. [10].

DISCUSSION

As was mentioned in the introduction, the acceleration field keeps balance between the electromagnetic energy of the beam and the kinetic energy of the particles. Mathematically, this property is formulated as the equality between the rate of change of the electromagnetic energy W and the work of the field $\tilde{E}_z$ on the moving particles

$$\frac{dW}{dt} = -e \int \tilde{E}_z v n d^3 r \,. \qquad (18)$$

Although we do not prove this statement here (see [9]), we demonstrate its validity with the numerical example from the previous Section. We calculated the electromagnetic energy difference for the beam at the final state with $\gamma_f = 20$ and the initial state with $\gamma_i = 1$, which gave us $\Delta W = 22.5$ μJ. When we integrated the right side of Eq. (18) over time from the initial to the final state, we found that the work of the acceleration numerically is equal to ΔW, in perfect agreement with the energy balance equation.

Computation of beam self-fields is a critical aspect in numerical simulations of high-brightness electron beam generation. Many simulation codes (ASTRA, IMPACT, PARMELA) employ the quasi-static approximation and compute only the space charge fields. There exist a few codes that calculate the beam fields from the exact solutions of Maxwell's equations (i.e., the retarded potentials). A review of different computational approaches can be found in Ref. [11]. In this paper, starting with the retarded potentials and separating explicitly the self-fields into space charge and acceleration ones, we give an analytical expression for the longitudinal component of the acceleration field. Using a Gaussian bunch model and typical (LCLS) RF gun parameters, we calculate the energy spread introduced by the acceleration field and show that it gives rise to a small correction of the energy spread introduced by the space charge field. These results may be useful in guiding the simulation studies of high-brightness beams.

References

[1] A. W. Chao and M. Tigner. *Handbook of Accelerator Physics and Engineering*. 3nd edition, 2006.

[2] L. V. Iogansen and M. S. Rabinovich. *Sov. Phys. JETP*, **37**, 83, 1960; Ya. S. Derbenev et al. DESY Report TESLA-FEL 95-05, 1995; J. B. Murphy, S. Krinsky, and R. L. Gluckstern. *Part. Accel.*, **57**, 9, 1997.

[3] G. Geloni et al. *Nuclear Instruments and Methods in Physics Research A*, **578**, 34, 2007.

[4] R. A. Bosch. *Phys. Rev. ST Accel. Beams*, **10**, 050701, 2007.

[5] J. D. Jackson. *Classical Electrodynamics*. Wiley, New York, third edition, 1999.

[6] W. Panofsky and M. Phillips. *Classical Electricity and Magnetism*. Addison-Wesley, 2nd edition, 1962.

[7] K. L. F. Bane and A. W. Chao. *Phys. Rev. ST Accel. Beams*, **5**, 104401, 2002.

[8] G. Stupakov. *Lecture notes on Classical Mechanics and Electromagnetism in Accelerator Physics*. The US PAS, Lansing, MI, 4-15 June 2007.

[9] G. Stupakov and Z. Huang. Space charge effect in an accelerated beam. to be published, 2007.

[10] Z. Huang et al. In *Proceedings of the 2005 Particle Accelerator Conference*, page TPAT062, Knoxville, Tennessee USA, May 2005.

[11] L. Serafini. In *Proceedings of the 2nd ICFA Workshop on the Physics of High Brightness Beams*, page 27, 1999.

ELECTRON OUTCOUPLING SCHEME FOR THE NOVOSIBIRSK FEL

A.N. Matveenko*, O.A. Shevchenko, V.G. Tcheskidov, N.A. Vinokurov
Budker Institute of Nuclear Physics, Novosibirsk, Russia

Abstract

One of the main problems of contemporary high power FELs is the mirror heating. One of the possible solutions of this problem is the use of electron outcoupling [1, 2]. In this case the mirrors of optical resonator are not transparent and the coherent radiation from an additional undulator in the FEL magnetic system is used. To provide the output of this radiation the electron beam in the auxiliary undulator is deflected from the optical resonator axis. To save bunching it is preferable to use the achromatic deflecting bend. The project of electron outcoupling for the Novosibirsk FEL is described. Simulation results are presented.

INTRODUCTION

The output power of high power oscillator FELs [3] are limited by mirrors heating, leading to surface distortion. Typical gain in oscillator FEL is tens per cent. Correspondingly, optical cavity "quality factor" must be of the order of 10 to make losses lower then amplification. Consequently, intracavity power is at least an order of magnitude higher, than extracted power, and optical cavity mirrors are most loaded compared to mirrors in the user beamlines. Electron outcoupling is one of the possible ways to decrease the power density on the mirrors at the same FEL output power.

The basic idea of electron outcoupling is to output the coherent radiation of the bunched electron beam in the second undulator section (see Fig. 1.), while the bunching is generated in the first section, which is put into optical cavity. In this case the lasing power in the first section can be limited some way (e.g. installing long undulator, or using beam scraper to control cavity losses), but the beam bunching can be preserved. An isochronous bend between the sections brings the beam into the second undulator.

The angle between undulators must be larger then undulator radiation divergence angle $\sim \frac{1}{\gamma}\sqrt{\frac{1+K^2/2}{2N}}$, where N is the number of periods in the undulator, γ is the relativistic factor, K is the planar undulator deflection parameter.

Lengths of the undulator sections are chosen from a condition $\frac{1}{N} \sim 4\pi\frac{\Delta E}{E}$, where ΔE is the r.m.s. energy spread of the electron beam.

Numerical simulations for different electron outcoupling schemes were performed earlier in [4-7]. Here we present design and simulation results for Novosibirsk high power FEL.

*A.N.Matveenko@inp.nsk.su

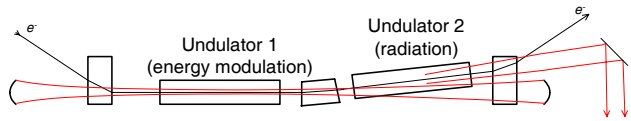

Fig. 1. Electron outcoupling scheme with two undulators and bending section between them. Electron beam path and laser output are shown.

ELECTRON OUTCOUPLING SCHEME OF NOFOSIBIRSK FEL

Electron outcoupling is planned to be used on the 4-th track of the second stage of Novosibirsk FEL. General layout of the second stage is shown in Fig. 2. Main electron beam and laser radiation parameters are summarized in Table 1.

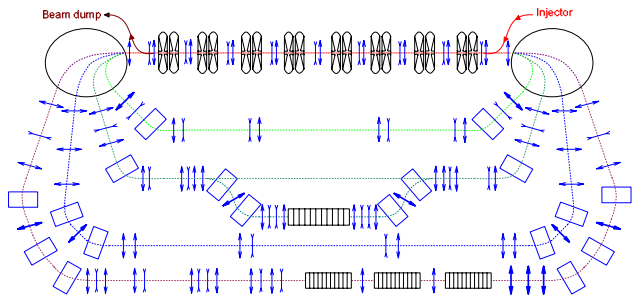

Fig. 2. Layout of the second stage of Novosibirsk FEL.

Table 1. Electron beam and laser radiation parameters.

Energy, MeV	40
Peak current, A	100
Electron beam emittance (normilized), μm	20
Maximum K	2
Undulator period, cm	6
Number of periods in each undulator	28
Deflection angle in second undulator, mrad	3
Relative energy spread	$3\cdot10^{-3}$
Radiation wavelength, μm	15
Optical cavity length, m	40
Mirror radius of curvature, m	25
Mirror reflectivity, %	90
Optical cavity β_x, β_y on mirrors, m	50
Optical cavity β_0 (Raleigh length), m	10

The scheme of the electron outcoupling of Novosibirsk FEL is shown in Fig. 3. It uses three undulators instead of two. The idea lying behind this modification is that in the basic scheme shown in Fig. 1 beam bunching reaches saturation at the end of the first undulator, therefore the efficiency of radiation in the second undulator is reduced. So, if one puts the third undulator (effectively, we divide the first undulator into two) one gets best beam bunching

inside the second undulator and better outcoupling efficiency.

Planar permanent magnet undulators are used.

In order to reduce the length of the bends between undulators, we use combined function elements. The achromatic bend between first and second undulators consists of two correctors on the nearest ends of the undulators and a quadrupole shifted off axis to provide both bending and focusing. As the bend is achromatic (R_{16}= R_{26}=0), it has also R_{51}= R_{52}=0. The last conditions are necessary to tilt electron slices in the bend, saving the bunching, obtained in the first undulator. Bend with shift between second and third undulators is done similarly, though it is not achromatic.

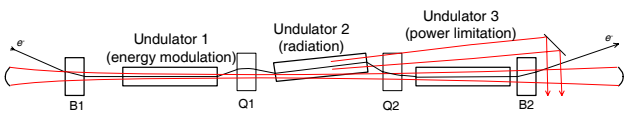

Fig. 3. Electron outcoupling scheme of Novosibirsk FEL. Electron beam path is shown in black. Laser output is shown with red arrows.

Optical functions of the beam in undulators are shown in Fig. 4. All undulators focus in "y" direction with matched β_{y0}=0.529 m at K=2. 4 quads before and 4 after the undulators (see Fig. 2) are necessary to provide appropriate matching to external beamline.

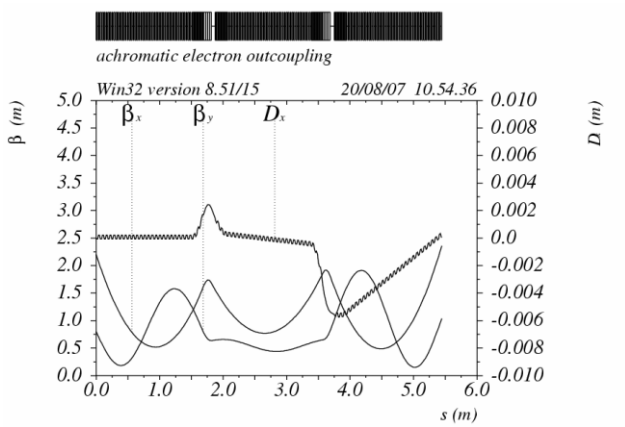

Fig. 4. Optical functions of the beam in undulators.

Optical mode inside the second undulator is partially overlapped with the electron beam, therefore the beam radiates into the mode too. So, simulation of lasing is needed to optimize the outcoupling.

SIMULATION RESULTS

Simulation of electron outcoupling is done with GENESIS [8] and OPC [9] codes. GENESIS is used to simulate the operation of FEL and electron outcoupling itself. OPC is used to propagate radiation field in optical cavity. Beam and optical cavity parameters from Table 1 are used in simulation.

Fig. 5 shows the bunching factor in undulators. The bunching is maximal in the second undulator. GENESIS calculates bunching in axes of the first undulator. The bunching in the second undulator in the axes of second undulator is a little bit higher. (Since the bend between undulators is achromatic, there is no bunching reduction.)

Total (eigenmode and coherent undulator) radiation power growth is shown in Fig. 6.

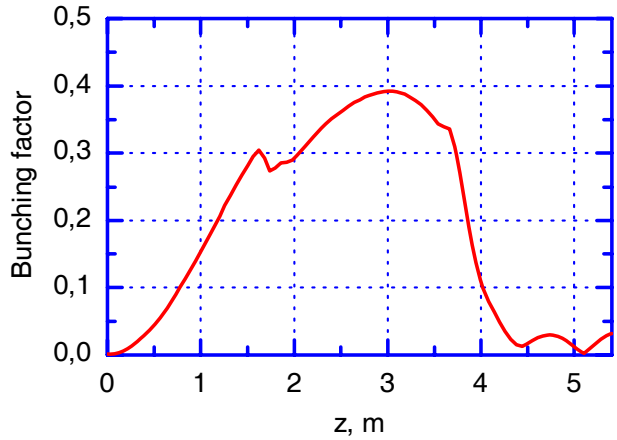

Fig. 5. Bunching factor in undulators.

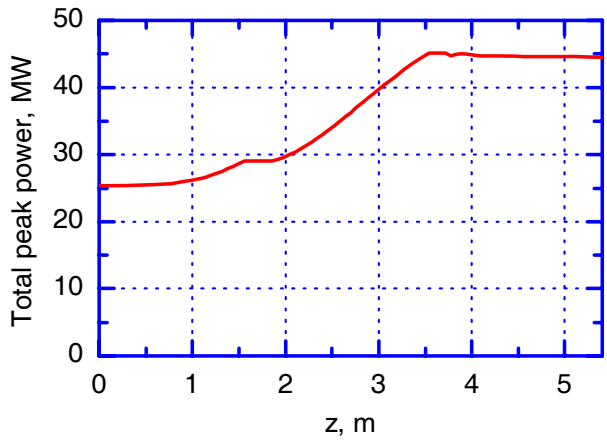

Fig. 6. Total radiation power vs. length.

Figures 7 and 8 demonstrate the power distribution on the optical cavity mirror and on the outcoupling mirror surface (Intensity scales are different for visualisation purposes). Outcoupling mirror is located near the mirror of the optical cavity. Its edge is at the distance of approximately 2.5 cm from the optical axis. The profiles at y=0 are shown in Fig. 9.

Red cross in Fig. 8 shows the expected center of the radiation spot from the second undulator. Circular interference patterns we interpret as interference of radiation from the first and the third undulators. A portion of radiation from the first and the third undulators is also outcoupled. Basic mode in the optical cavity is distorted (it's center moves off axes) which is seen in Fig. 9.

Total power and intensity on the optical cavity mirrors and outcoupler are listed in Table 2. Given values are for bunch repetition rate 3.75 MHz (which is the optical cavity fundamental frequency) and average current about 6 mA. It is seen that the ratio of the outcoupled power to the intracavity power is more than 25%.

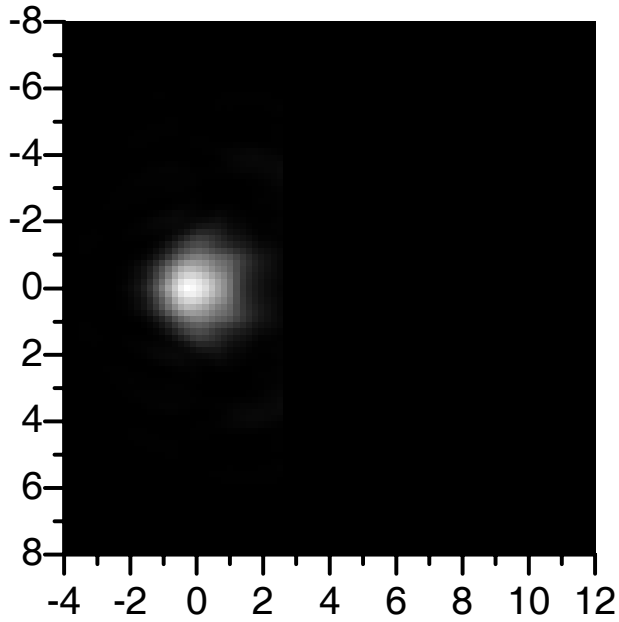

Fig. 7. Power distribution on the forward optical cavity mirror surface. Transverse coordinates are in cm.

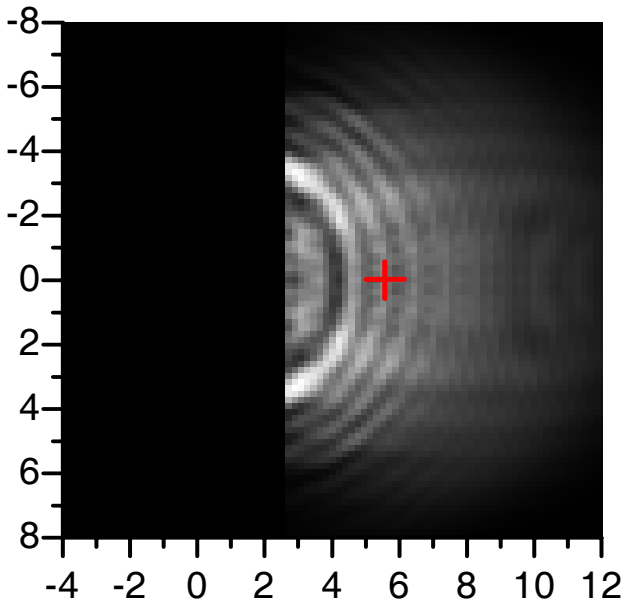

Fig. 8. Power distribution on the outcoupling mirror (scraper) surface. Transverse coordinates are in cm.

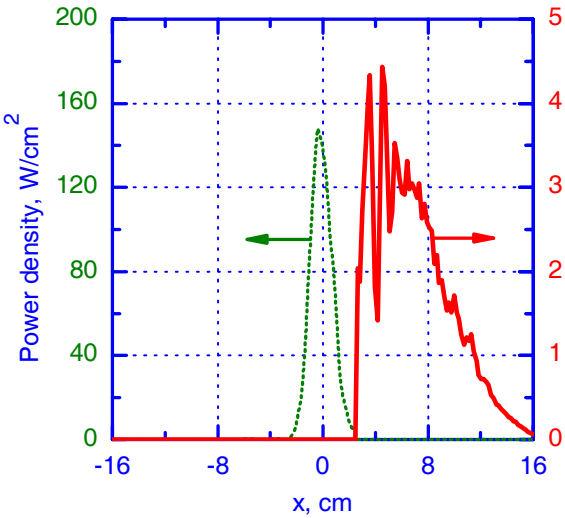

Fig. 9. Intensity profiles: green - on the optical cavity mirror surface, red – on the outcoupling mirror surface. Scales are shown with arrows.

Table 2. Radiation parameters on the forward mirror of the optical cavity and outcoupling mirror.

Total average power on the cavity mirror, W	990
Total outcoupled power, W	260
Max. intensity on the cavity mirror, W/cm^2	170
Max. intensity on the outcoupling mirror, W/cm^2	5

CONCLUSION

In this paper we considered the electron outcoupling scheme with trajectory deflection in the second undulator (radiator). The scheme with deflection in the third undulator was also simulated, but the FEL output power was less for our beam parameters. The results of calculations look reasonable and understandable and show that the chosen parameters of FEL magnetic system are close to optimal.

REFERENCES

[1] N.G. Gavrilov et al., NIM A304 (1991) 63-65.
[2] G.N. Kulipanov, A.S. Sokolov, N.A. Vinokurov, NIM A375, (1996) 576-579.
[3] G. Neil et al., NIM A557, (2006) 9.
[4] D.D. Quick, et. al., NIM A341, ABS92, 1994.
[5] J. Blau, et. al., NIM A341, ABS94, 1994.
[6] S.J. Hahn, et. al., NIM A358, p. 167, 1995.
[7] S.J. Hahn and W.M. Fawley, Proc. of SPIE 2376, pp. 116-124, 1995.
[8] S. Reiche, NIM A429, (1999) 243.
[9] J.G. Karssenberg, et al., Proc. of FEL 2006, pp. 407-410.

MODELLING MIRROR ABERRATIONS IN FEL OSCILLATORS USING OPC

P.J.M. van der Slot*, J.G. Karssenberg, K.J. Boller
Mesa+ Institute for Nanotechnology, University of Twente, Enschede, NL

Abstract

Several high power free-electron lasers (FELs) are currently under design, operational or being upgraded. One central issue is the beam outcoupling and mirror deformation due to absorbed power. Here we present an extension to the OPC code that allows it to model mirror distorions. We use this code to model the high average power vacuum ultra violet FEL oscillator of the 4th generation light source. Both Genesis 1.3 and Medusa are used to calculate the gain provided by the undulator. Our findings indicate that the high gain oscillator is quite resilient to thermal mirror deformation and operation well into the kW range of average power can be expected.

INTRODUCTION

Several high average power Free-Electron Lasers (FELs) are currently operational [1, 2] or planned [3]. One of the issues in these devices is the thermal distortion of the mirrors that can alter the optical mode and degrade performance. Including this and other mirror distortions in simulation of these devices is important to understand and further improve these devices. Several attempts have already been made to model thermal mirror distortions [4, 5, 6, 7], however, a full integration of the FEL gain medium, optical propagation in the non-amplifying section and mirror distortions for both steady state and time dependent simulations is not readily available. Here we present an extension to the OPC package [8] that allows it to model mirror distortions. OPC implements paraxial optical propagation in the non-amplifying sections of a resonator, while either Genesis 1.3 [9] or Medusa [10] is used to simulate the gain provided by the undulator.

It is well know that various mirror distortions can be described using the circle polynomials of Zernike [11]. Within OPC these polynomials are used to calculated a phase difference $d\theta$ according to

$$d\theta = A_{nm} R_n^{|m|}(\rho) \times \begin{cases} cos(m\phi) & m \geq 0 \\ sin(m\phi) & m < 0 \end{cases} \qquad (1)$$

where $R_n^{|m|}$ is the circle polynomial of order (n,m), ρ is the scaled radial distance $\sqrt{x^2+y^2}/\rho_c$, ρ_c being a characteristic distance, ϕ is the angle $\tan^{-1}(y/x)$, and A_{nm} is the amplitude of the aberration. These aberrations define a phase mask that is applied to the optical field at the position of the corresponding optical component. The scaling constants A_{nm} and ρ_c can either be kept constant or made dependent on certain properties of the optical field, e.g., the total power or the root-mean-square (rms) width of the optical beam.

Different type of aberrations can be modeled using Zernike polynomials. For example, $n = 4$ and $m = 0$ corresponds to spherical aberration, $n = 3$ and $m = 1$ to coma and $n = 2$ and $m = 2$ to astigmatism [11]. A combination of Zernike polynomials can also be used to model a cylindrical lens. Here we focus on the the use of Zernike polynomials to model thermal mirror distortions [6, 4].

As an example of a high average power FEL we consider here the vacuum ultra violet FEL (VUV-FEL) oscillator that is part of the 4th generation light source (4GLS) project of Daresbury laboratory [3]. This high gain oscillator uses a low Q cavity to generate coherent output with photon energies in the range 3 to 10 eV. The VUV-FEL will operate in the 600 MeV high average current branch of the energy-recovery linac, and is driven by ~ 80 pC electron bunches at multiples of $4\frac{1}{3}$ MHz up to a maximum of 1.3 GHz. A system of distributed bunch compression along the beam line is expected to compress the bunch to lengths as short as 100 fs, generating a peak current of ~ 300 A before injection into the VUV-FEL. The main system parameters used in the simulations are given in table 1. Since the average output power will be of the order of 300 W or multiples thereof, and the mirror only reflects 60 % of the radiation falling on the surface, significant mirror heating is expected.

We will first briefly discuss the mirror thermal expansion and the resulting phase distortion. We then continue with a simulation of the VUV-FEL with and without the mirror expansion included.

MIRROR EXPANSION UNDER A THERMAL LOAD

The mirrors considered for the VUV-FEL oscillator consist of a protected aluminium coating on a silicon substrate. The reflectivity R of the mirror is expected to be 60 % [3]. Radiation is extracted at the downstream (DS) mirror through a hole with a radius of $r_h = 1.8$ mm. We approximate the mirror loading in the form of a train of optical pulses by an average power and determine the steady state displacement $\delta z(r)$ of the reflecting mirror surface under the assumption that the average absorbed power P_{abs} will have a Gaussian profile with rms width σ_m.

We use the finite element program MultiPhysics with the Structural Mechanics Module [12] to calculate the temper-

* p.j.m.vanderslot@tnw.utwente.nl

Table 1: Baseline VUV-FEL parameters as used in the simulations.

Undulator	
Undulator period λ_u	58 mm
Undulator parameter K (rms)	1.9799
Periods per module	52
Number of modules	3
Electron Beam	
Electron beam energy	549.3 MeV
Relative energy spread (rms)	0.1 %
Bunch charge	80 pC
Peak current	300 A
Normalised emittance	2 mm-mrad
Optical Cavity	
Wavelength λ	123.89 nm
Cavity length L_{cav}	34.618067 m
Upstream ROC r_1	14.5 m
Downstream ROC r_2	21.7573 m
Mirror reflectivity R	60 %
Rayleigh length z_r	3.67 m
Fundamental mode waist w_0	0.38 mm
Waist position (from US mirror)	13.5 m
Outcoupling hole radius r_h	1.8 mm
Cavity stability $g_1 \times g_2$	0.82

ature distribution and the resulting surface displacement, δz. The DS mirror considered here has an outer diameter of 20 mm and a thickness of 10 mm. The thermal conductivity and thermal expansion are taken to be 1.2 W/cmK and 2.8×10^{-6} K^{-1} respectively. Although taken constant here, these can be allowed to vary with temperature. A heat flux with a Gaussian profile having a rms width σ_m and total flux of αP_o is used to load the reflecting surface of the mirror, where α is the absorption coefficient and P_o is the average optical power incident on the mirror. Note that only the fraction with $r > r_h$ will be absorbed by the mirror. The mirror is cooled at the outer edge, where we assume a heat transfer coefficient $h_T = 1000$ W/m^{2}K to a thermal sink that is kept at 293 K. The heat transfer coefficient of the backside of the mirror is set to $h_T/1000$. Mechanically, the mirror is considered to be mounted stress free with the reflecting surface pushed against a stable reference plane. Hence, the outer edge of the reflecting surface can only move radially. The rest of the mirror is allowed to expand freely. Taking the spot size of the heat flux on the mirror equal to the rms size of the optical beam found for the VUV-FEL in stationary state without mirror distortions, and using $P_o = 300$ W, $\alpha = 0.4$, we find that P_{abs} and σ_m are 35.3 W and 2.3 mm respectively for $r_h = 1.8$ mm. For these numbers, the temperature profile, $T(r)$, and mirror displacement, $\delta z(r/2\sigma_m)$ are shown in figure 1. For comparison, the profiles for the case $r_h = 2$ mm are also included. In this figure 1B δz is shown as a function of the

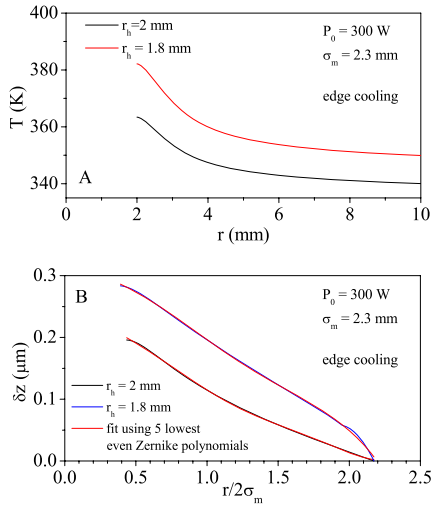

Figure 1: Temperature profile (A) and surface displacement (B) of the mirror for $P_{abs} = 35.3$ W ($r_h = 1.8$ mm) and $P_{abs} = 25.5$ W ($r_h = 2.0$ mm). Here $P_o = 300$ W and $\sigma_m = 2.3$ mm.

Table 2: Fit parameters for Zernike polynomials for the parameters of figure 1. The resulting δz is in [m].

	$r_h = 1.8$ mm	$r_h = 2.0$ mm
A_{00}	2.446e-7	1.639e-7
A_{20}	-5.544e-8	-5.641e-8
A_{40}	5.480e-9	8.037e-9
A_{60}	-2.9344e-10	-6.050e-10
A_{80}	3.773e-12	1.648e-11

scaled variable $r/2\sigma_m$, along with a fit to δz using Zernike polynomials:

$$\delta z(r/2\sigma_m) = \sum_{n=0}^{n=8} A_{n0} R_n^0(r/2\sigma_m) \qquad (2)$$

where n only takes on even values. Figure 1 shows that the difference between the calculated displacement and the fit is far below $\lambda/10$. The fitting coefficients are given in table 2 for both $r_h = 1.8$ mm and 2 mm. To convert the surface displacement to a phase change we use

$$d\theta(r/2\sigma_m) = -\frac{4\pi\delta z(r/2\sigma_m)}{\lambda} \qquad (3)$$

Since the phase shift is proportional to twice the surface displacement and the minus sign has to be chosen to be in agreement with the phase advancement used in OPC.

VUV-FEL OSCILLATOR WITH MIRROR DISTORTION

OPC is set up to use the fitting coefficients of table 2 to calculate the mirror displacement and then convert it to a phase mask using eq. 3. This phase mask is then applied to the DS mirror. As long as the spot size of the optical beam on the mirror does not significantly change, we do not need to recalculate the temperature and displacement profile. The amplitude of the phase shift can then be found by multiplying $\delta z(r)$ with the ratio $P_{abs}(t)/P_{abs,0}$ where $P_{abs}(t)$ is the instantaneous average power absorbed by the mirror and $P_{abs,0}$ is the absorbed power used to calculate the thermal expansion $\delta z(r)$.

One problem with modeling the mirror's thermal deformation is the difference between the time scale for the oscillator to reach saturation and the mirror to reach a stable thermal profile. The latter is determined by the thermal relaxation time, which is estimated to be of the order of 1 s for the DS mirror. On the other hand, the roundtrip time for the cavity is about 230 ns and the laser reaches steady state after about 20 roundtrips (~ 4.6 μs). Ideally, one would want to apply the absorbed energy of a single optical pulse to the mirror, and use a time dependent analysis to determine $T(r)$ and $\delta z(r)$ at the arrival time of the next optical pulse. The build up of the radiation and the thermal distortion would then be determined iteratively until a steady state was obtained. Although such a simulation can be set up with OPC using an appropriate finite element solver,this requires considerable computational resources and we have choosen to demonstrate the effect of thermal mirror distortions in a different way.

In view of the short time the VUV oscillator requires to produce a stationary output, we first let the oscillator reach this state and then apply the full thermal distortion instantaneously at the DS mirror and observe how the laser reacts. Although this ignors the temporal development of the distortions it gives a first impression of how the distortions affect the laser. Figure 2 shows the total power in and cross section of the optical field at various places along the resonator and in the far field (power only) after $n = 25$ and 50 roundtrips. The mirror distortion is applied after 30 roundtrips. Here Genesis 1.3 is used in steady state mode to propagate the optical field through the undulator and $f_{rep} = 4\frac{1}{3}$ MHz. It is clear that at these power levels the laser quickly adapts to the distortions in the phase front of the optical field without seriously affecting the power in the field. We do observe that the surface expansion focusses the field more towards the upstream (US) mirror and hence the spot size on this mirror is decreased and the intensity increased (about a factor of 2 on axis). The profile has changed as well and the intensity is now maximum on axis. Figure 3 shows the cross section of the field at the undulator's entrance as a function of the roundtrip. This figure shows that only a few roundtrips are required for the laser to adapt to the full mirror distortion.

The thermal load on the mirror increases when f_{rep} is

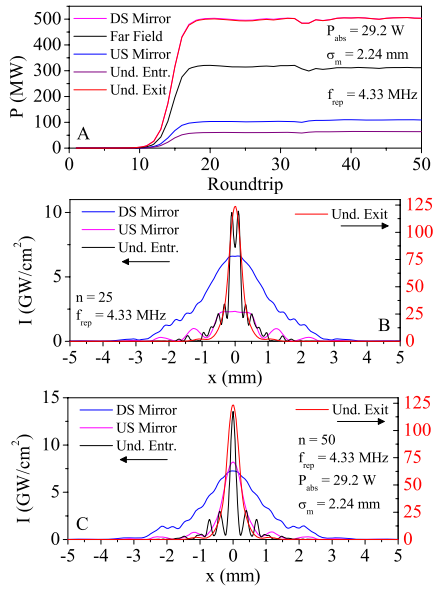

Figure 2: Total power as a function of roundtrip (A) and cross section of the field at various places in the cavity for $n = 25$ (B) and $n = 50$ (C). $f_{rep} = 4\frac{1}{3}$ MHz.

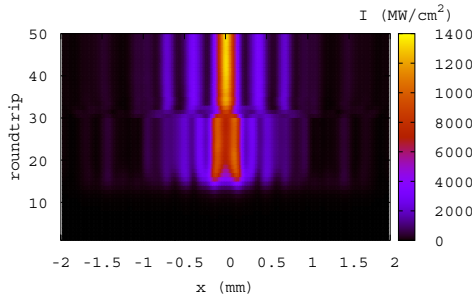

Figure 3: Cross section of the optical field at the undulator's entrance as a function of the roundtrip n. The thermal distortion is applied at $n = 31$ and $f_{rep} = 4\frac{1}{3}$ MHz.

increased. Figures 4 and 5 show the same data but now for $f_{rep} = 21\frac{2}{3}$ MHz. Again, the profiles at $n = 25$ are equal to the ones shown in figure 2B. Figure 4 shows that when the distortions are applied, the total output power at the undulator's exit drops by almost a factor of 50. Still, after about 10 roundtrips the laser finds a new equilibrium, albeit at an output level that is 70 % of the power without mirror distortions. Although a realistic model of the temporal behaviour of the mirror's thermal distortion is not used, these results indicate that an average optical output power of the order of several kW is feasible. This can still be further improved if the mirror can be cooled more efficiently.

OPC can also use Medusa [10] to calculate the gain and we have also simulated the VUV-FEL oscillator using this code. As Genesis 1.3 can not start from noise in steady

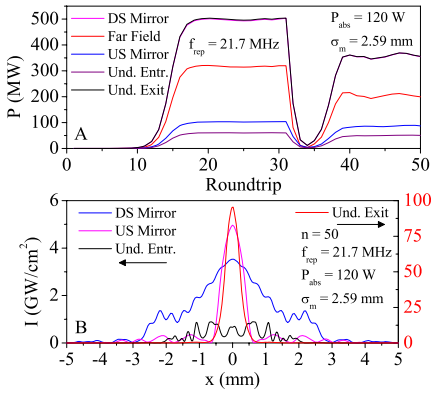

Figure 4: Total power as a function of roundtrip (A) and cross section of the field at various places in the cavity for $n = 50$ (B). $f_{rep} = 21\frac{2}{3}$ MHz.

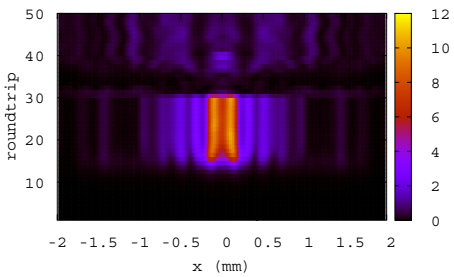

Figure 5: Cross section of the optical field at the undulator's entrance as a function of the roundtrip n. The thermal distortion is applied at $n = 31$ and $f_{rep} = 21\frac{2}{3}$ MHz.

state mode, both codes used a seed power of 2 W based on Ming Xie's formula for shot noise [13]. Preliminary results indicate that Medusa shows less optical guiding in the undulator during start-up. It predicts a larger spot size for the optical beam at the undulator's exit and consequently, the spot size at the DS mirror is found to be smaller. The feedback is then too small for the laser to start. Medusa can also start from noise in steady state mode. In this case, the field in the oscillator builds up and saturates at about 366 MW intracavity after about 40 passes without distortions. This is about double the number of roundtrips required by Genesis 1.3. Initial results with the mirror's thermal distortion turned on and using $f_{rep} = 4\frac{1}{3}$ MHz showed a similar behaviour. The differences found between Genesis 1.3 and Medusa are still under investigation.

DISCUSSION AND CONCLUSIONS

We have extended the OPC package to include mirror distortions using Zernike polynomials. These distortions are applied as a phase mask at the appropriate optical component in the resonator. Alternatively, the user may provide an external file that defines an arbitrary phase mask. OPC can easily be adjusted to interface with an apropriate time dependent finite element program that calculates the time dependent surface expansion resulting from a train of optical pulses incident on a mirror. Alternatively the instantaneous absorbed power based on the optical pulse energy and f_{rep} can be weighted with a thermal relaxation time that allows the mirror deformation to build up more slowly than the instantaneous average power. As an example we applied a simple implementaton of the thermal distortion by applying instantaneously the full distortion to the DS mirror of the 4GLS VUV-FEL oscillator after the oscillator has saturated. We used both Genesis 1.3 and Medusa for the gain calculation and there are some some differences in their predictions related to the startup of the laser that are currently under investigation. Nevertheless the case considered here shows that the laser is expected to be quite resilient to the mirror's thermal distortion.

ACKNOWLEDGEMENT

We would like to thank David Dunning, Brian McNeil and Neil Thompson of the 4GLS design team for the useful discussions, and Henry Freund and Buff Miner of SAIC for the Medusa simulations and discussions.

REFERENCES

[1] G. Neil, et. al., Nucl. Instrum. Methods Phys. Res. A**557** 9 (2006).

[2] E.J. Minehara, Nucl. Instrum. Methods Phys. Res. A**557** 16 (2006).

[3] B.W.J. McNeil, et. al., New J. Phys. **9** (2007) 239.

[4] S.V. Benson, et.al., Nucl. Instrum. Methods Phys. Res. A**407**, 401 (1998).

[5] A.R.B. de Castro, and T. Möller, Rev. Sci. Instrum, **76**, 063104 (2005).

[6] J.C. Goldstein, B.D. McVey, and B.E. Newman, Nucl. Instrum. Methods Phys. Res. A**296**, 288 (1990).

[7] H.P. Freund, M. Shinn, and S.V. Benson, *Proceedings 28th Free-Electron Laser Conference*, FEL'06, Berlin, Germany, Aug. 2006, p. 444, http://www.JaCoW.org

[8] J.G. Karssenberg, et.al., J. Appl. Phys. **100**, 093106 (2006).

[9] S. Reige, Nucl. Instrum. Methods Phys. Res. A**429**, 243 (1999)

[10] H.P. Freund, S.G. Biedron, and S.V. Milton. IEEE J. Quantum Electron. **36**, 275 (2000).

[11] M. Born and E. Wolf. *Principles of Optics*, 6th edition. Pergamon Press, 1980.

[12] Comsol Multiphysics V3.3a and Stuctural Mechanics module are from Comsol AB, Stockholm, Sweden. http://www.comsol.com

[13] M. Xie. Nucl. Instrum. Methods Phys. Res., A**445**, 59 (2000).

FLASH UPGRADED - PREPARING FOR THE EUROPEAN XFEL

H. Schlarb* for the FLASH and the XFEL Project Team,
DESY, D-20607 Hamburg, Germany

Abstract

Since 2005, the Free electron LASer in Hamburg, FLASH, has delivered a high brilliance photon beam to users with a wavelength range between 13 nm and 40 nm. To meet the user demands for 4 nm wavelengths, sub-50 fs timing stability, and better pointing stability, the accelerator will be continuously upgraded within the next few years. The upgrade to an energy of 1.3 GeV, the development of a transverse and longitudinal intra-train feedback system, and a 3^{rd} harmonic cavity at 3.9 GHz are key prototype tests for the European XFEL. FLASH also serves as a test bench for an entirely new approach to accelerator facility synchronization involving optical pulses distributed in length stabilized fibres. Increased stabilization of the electron beam peak current and its arrival time should provide the possibility to reliably seed the electron bunch with higher laser harmonics. In this paper, an overview of the planned upgrades for FLASH will be presented with respect to their usefulness for the European XFEL.

INTRODUCTION

Since 2005, the high-gain **F**ree electron **LAS**er in **H**amburg, FLASH, successfully delivers to user experiments in the VUV-wavelength range between 13 nm and 40 nm ultra-short photon pulses (10-25 fs FWHM) with peak power at the Gigawatt level [1]. The peak brilliance of the FLASH photon beam exceeds that of state-of-the-art synchrotron radiation sources by seven orders of magnitude. Observations of the high degree of transverse and longitudinal coherence, intensity stability of the self-amplified spontaneous emission process, amplification gain measurements along the undulator and the content of high harmonics down to 2.6 nm are in full agreement with theoretical prediction.

The 13 nm wavelength achieved with this FEL is limited only by the 700 MeV maximum electron beam energy and is an important milestone for FLASH and the European XFEL as they set goals of reaching wavelengths of 6 nm and 0.1 nm, respectively. Besides photon production for users, FLASH serves as a small scale ($\sim$ one tenth) prototype for the larger XFEL facility. The layouts of the facilities are shown in Fig.1 [3, 4].

The electron beam is produced in a laser-driven photoinjector using a normal conducting RF gun. The beam is accelerated in a linear accelerator comprised of eight 9-cell superconducting cavities housed in cryogenic modules. The kilo-Ampere's peak currents are achieved though two magnetic bunch compressors before the beam enters the main linac section. Passing beam cleaning and protecting collimators, the electron bunches of typically 100 fs duration produce the SASE-FEL photons in long undulators. Key parameters of the machines are listed in Tab. 1[3, 4].

Most of the accelerator parameters impacting the electron beam dynamics, beam instrumentation, mechanical or RF tolerances are quite similar for the two facilities. The main differences are related to the electron beam energy, the accelerator and undulator length, the electron and the photon beam transport, and the photon diagnostics for Angstrom wavelengths. The large number of devices in the XFEL - about 100 acceleration modules - requires reliable mass-production by industry. FLASH can provide for the prototyping of single XFEL units and, within certain limitations, can also provide long-term reliability tests.

Table 1: Key parameter of FLASH and the European XFEL

Parameter	**FLASH**	**XFEL**
norm. emittance	2 μm	1.4 μm
peak current	2.5 kA	5.0 kA
bunch rep. rate	1(9) MHz	5 MHz
pulse rep. rate	10 Hz	10 Hz
bunch charge	1 nC	1 nC
beam energy	1.0 GeV	17.5 GeV
photon wavelength	6.3 nm	0.1 nm
acc. freq.	1.3/3.9 GHz	1.3/3.9 GHz
flat top duration	800 μs	650 μs
facility length	260 m	3.4 km
undulator length	30 m	250 m
orbit tolerance und.	5 μm	3 μm

Bunch compression for the XFEL takes place at beam energies that are $\sim$4 times higher than in FLASH. The higher energies and the smaller R_{56} of the XFEL chicanes reduce the sensitivity to micro-bunch instabilities and relax the tolerances on the RF amplitude stability. Dedicated diagnostics for temporal and spatial bunch profiling up to the second bunch compressor - the most critical part of the accelerator - are essentially the same. Therefore, almost all critical accelerator sub-systems can be tested and prototyped at FLASH, allowing for reduced costs, a rapid XFEL commissioning, and minimized risk. In this paper, the various FLASH upgrades relevant for the XFEL are described.

ENERGY UPGRADE TOWARD 1.3 GEV

During the spring shutdown of 2007, a new accelerator module ACC6 - almost the XFEL design module - has been installed. The average gradient of ACC6 is 28.5 MV/m

* holger.schlarb@desy.de

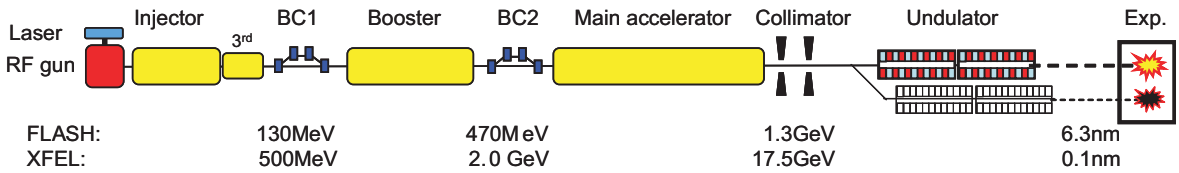

Figure 1: Generic layout of the Free Electron Laser FLASH and the European XFEL.

measured at the cryo-module test stand at DESY. In addition, the coupler of ACC5 has been repaired and module ACC3 has been exchanged, allowing FLASH to reach the design beam energy of 1 GeV or 6 nm photon wavelength.

At the exit of the FLASH linac, space for a seventh acceleration module is foreseen. To meet the user demands for shorter photon wavelength, the installation of ACC7 is planned for 2009. This boosts the beam energy toward 1.3 GeV and allows the users to reach the water window with wavelengths below 4.3 nm in the first FEL harmonics.

This new accelerator module (No. #8) will be assembled at DESY by industry. The four acceleration modules (ACC4-ACC7) correspond to a baseline RF section of the XFEL. It will, therefore, allow for testing of the complete high- and low-power RF control system, as foreseen for the Angstrom machine; this includes the waveguide distribution and 32-cavity field regulation.

3.9 GHZ LINEARIZING CAVITIES

Ultra-short FEL pulses of some ten femtosecond duration are produced at FLASH by inhomogeneous electron bunch compression, causing a sharp leading high-peak current spike with a picosecond-long trailing tail. The longitudinal profile is mainly a consequence of the non-linear energy chirp from the time-dependent RF fields and the linear shearing of the longitudinal phase space that occurs in the magnetic bunch compressor chicanes.

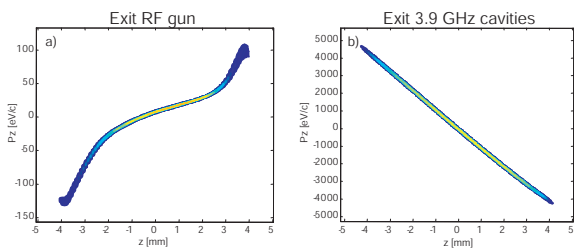

Figure 2: Simulation of longitudinal phase space at the entrance of ACC1 and at the exit of the 3^{rd} linearizer cavities.

Of significant importance for he bench marking of beam dynamics and operational aspects of the XFEL with homogeneous bunch compression is the installation of the third harmonic superconducting linearizer cavity operated at 3.9 GHz (see Fig. 2(b)).

At FLASH, the first bunch compression takes place at 130 MeV beam energy. Four 3^{rd} harmonic cavities operated at a gradient of 15 MV/m (20 MV voltage total) are sufficient to remove non-linearities caused by accelerating RF, time-momentum correlations exiting the RF gun (Fig. 2(a)), higher order chicane momentum compaction (T_{566}) and distortions due to collective effects. The XFEL requires a total voltage of 108 MV at 3.9 GHz due to the higher energy of 500 MeV at the first compressor. The voltage can be achieved by 24 cavities at a gradient of 13.5 MV/m.

Cavity treatments, assembly and vertical performance tests have been successfully carried out at Fermilab [5, 6]. The delivery of a complete cryostat housing the four cavities for FLASH (Fig. 3) by Fermilab is foreseen for Spring 2008 [7]. An integral test of the cryostat is planned at the DESY cryo-module test bench before installation in 2009.

The preservation of the projected beam emittance requires an alignment of the cavities to each other better than 0.5 mm. In addition, a good orbit control through the cavity string is needed.

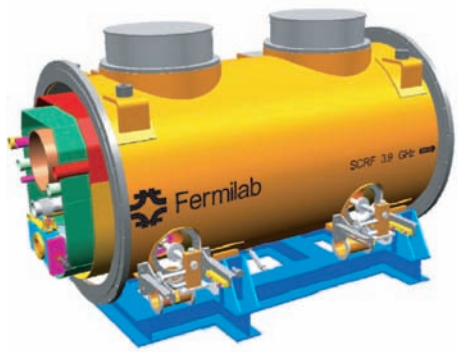

Figure 3: Cryostat housing the four 3^{rd} harmonic cavity for FLASH.

DIAGNOSTICS DEVELOPMENTS

Intra-bunch train feedback

The long duration of the XFEL electron macro-pulses enables active stabilization of the transverse beam offsets by means of a fast intra-bunch-train feedback (IBFB) system. The Paul Scherrer Institute agreed to develop the IBFB which will be tested in its prototype version at the FLASH linac [8, 9].

The proposed IBFB topology, shown in Fig. 4, consists of two upstream beam position monitors (BPM) followed by two kicker magnets for each transverse plane and two downstream BPMs. From position measurements

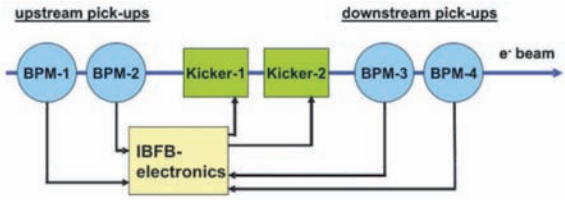

Figure 4: Topology of the intra-bunch train feedback system

of the upstream BPMs transverse kicks are applied with a latency preferably below the bunch spacing of 200 ns and 1000 ns for the XFEL and FLASH. Optimization of the feedback parameters is derived from the downstream BPMs. The proposed IBFB system will damp perturbations up to frequencies of some 100 kHz. The FPGA-based digital IBFB electronics include a DSP that enables adaptive feed-forward correction of repetitive intra-train variations. Resonant stripline pickups were developed to meet the desired orbit resolution of 1-2 μm and latency requirements. A test of the IBFB at FLASH is planned for 2008.

Single-shot THz spectrometry

Coherent radiation produced at diffraction and transition screens or bending magnets provides an excellent opportunity for diagnosing and controlling the bunch compression process. The radiation is emitted mid and far infrared wavelength range, corresponding to the electron bunch length. To measure this radiation, a single-shot THz spectrometer based on three staged diffraction gratings has been developed (see Fig. 5(a))[11, 12]. The diffracted radiation is recorded by an array of pyro-electric sensors (shown in Fig. 5(b)), that can be read out simultaneously. To suppress water absorption in air, the spectrometer and detector unit is housed in a vacuum vessel.

Correlations between the FEL intensity and different wavelengths ranging from 12 μm to 80 μm clearly show that the spectral information reveals significantly more information than a simple integral power determination. For example, the FEL intensity is correlated with the THz intensity at 30 μm, but anti-correlated to wavelengths around 12 μm, indicating a large destructive compression of the beam. The measurements were carried out using a single kicked bunch onto an transition screen. An online device suited for macro-pulse operation that detects the coherent synchrotron radiation emitted at the last bending magnet of the chicane is in preparation.

Fiber laser based electro-optic bunch profiling

The longitudinal bunch profile has been successfully measured by detecting the Coulomb field of the bunch with electro-optics (EO) techniques. The Coulomb field is encoded into the polarization of a broadband laser pulse (Ti:Sa laser) and decoded by transforming the polarization variation into a laser intensity modulation. Cross-

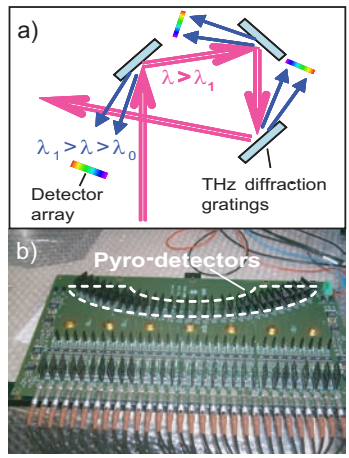

Figure 5: (a) Scheme of single-shot spectrometer covering 12-80 μm radiation. (b) Pyro-detector array with 30 channels.

comparison with a transverse deflecting RF structure turning the longitudinal charge distribution into a transverse streak on an observation screen[10] reveals a time resolution of 60 fs rms, limited by electro-optic crystal [13, 14].

Unlike the transverse deflector, EO-techniques are non-invasive and allow for single-shot detection of all bunches in an macro-pulse. This requires the development of a fast readout system for detection of the laser intensity modulation in a line-array, and, in a second step for intra-train feedbacks, a high speed FPGA based profile processing.

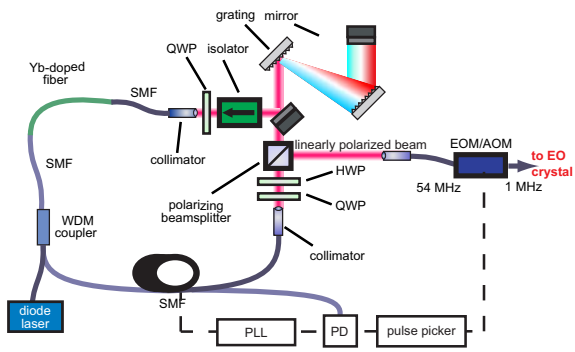

Figure 6: Scheme of Yb-fiber laser for EO bunch profiling.

Suited for tunnel installation and for every day operation, an ultra-broadband Ytterbium-fiber laser, sketched in Fig. 6, is considered. The fiber laser has been developed in corporation with Bilkent Uni. [15]. The repetition frequency of the cavity is 54 MHz and will be reduced with a pulse-picker to match the bunch frequency. Fiber amplification allows for boosting of the pulse energy to 1-10 μJ with pulse durations below 50 fs (FWHM).

Optical replica synthesizer

Femtosecond time-resolutions can be achieved with an optical replica synthesizer (ORS), proposed in Ref. [16]. It

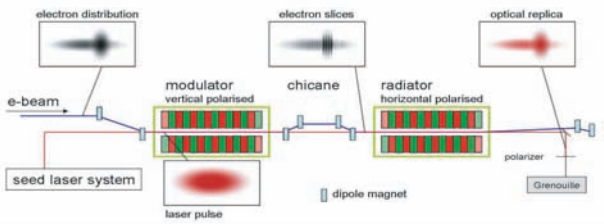

Figure 7: Scheme of optical replica synthesizer.

operates like an optical klystron FEL seeded by an infrared laser (Fig. 7) [17]. In the modulator undulator, the interaction of the laser with electrons causes an energy modulation. A small chicane turns the energy modulation into a density modulation at the wavelength of the laser light. The micro-bunched beam radiates coherently in a radiator undulator. The emitted light pulse with the same longitudinal profile as the electron beam is analyzed by a commercially available second-harmonic generation FROG (frequency resolved optical gating) device.

In a collaboration effort between Uni. Stockholm, Uni. Uppsala, Uni. Hamburg, BESSY and DESY, the ORS experiment was assembled at FLASH. The commissioning of the novel diagnostic device is scheduled for Autumn 2007. Beside the diagnostics aspect, the ORS experiment will provide valuable experience with the design and the operation of a laser heater, as foreseen in the XFEL design.

FEMTOSECOND SYNCHRONIZATION

A drift-free synchronization distribution system with femtosecond accuracy is of key importance for the stability of X-ray FELs and is an indispensable prerequisite for laser seeded FELs. The most critical devices of an FEL are the photo-injector laser, the RF gun, the acceleration section upstream of the bunch compressors, and pump-probe and seed lasers for user experiments. Their locations are separated by 260 m for FLASH and by 3.4 km for the XFEL. Femtosecond accuracy at these large distances cannot be achieved with conventional coaxial RF cable distributions. Laser based synchronization, however, can provide the desired stabilities [18]. At FLASH, a prototype system for the XFEL of a laser based synchronization is under construction [19]. The large complexity of such a system, comprised of multiple feedback loops, needs a careful design of the sub-components and optical devices to meet the reliability, stability and maintainability requirements.

The new synchronization system consists of an passively mode-locked Erbium-doped fiber laser producing ultra-short pulses at central wavelength of 1550 nm and a repetition rate of 216 MHz. The fiber laser is narrow-bandwidth locked to the low-noise RF master oscillator of FLASH. The laser pulses are distributed throughout the facility in dispersion compensated optical length stabilized fiber links. Length stabilization is accomplished by Piezo-transducers. The error signal is generated by the precise temporal overlap of pulses exiting the laser with pulses back-reflected at the end of the fiber link in a balanced second harmonic optical cross-correlator. A 400 m long fiber link test bench installed in an accelerator hall has been setup to develop the link stabilization unit. First out-of-loop measurements show a short time (≈10 min.) link accuracy of 4.4 fs rms and drifts of 20 fs peak-to-peak during 12 hours are observed. At the same time, the optical fiber length has changed due to environmental temperate change by more than 40 ps [20].

At the link exit, three different front-end systems can be classified: a) the synchronization of optical lasers using sum-frequency optical cross-correlation; b) the direct use of the optical synchronization pulses for sub-50 fs bunch arrival measurements [21], bunch position monitoring in large apertures [22], and RF signal sampling. The optical pulses are also most suited as seeds for laser amplifier, e.g. the ORS-experiment; c) the conversion to RF for the acceleration field control, for example, by means of a Sagnac-loop interferometer [23].

Figure 8 shows the layout of the FLASH optical links and their front-ends. The system will be suited to stabilize the electron beam arrival by fast intra-train feedbacks for the RF control and to synchronize all relevant devices.

LASER SEEDING (S-FLASH)

Implementation of a femtosecond stable synchronization system and further improvements of the RF controls should produce a reduction of the electron timing jitter below 100 fs (FWHM). The 3.9 GHz linearizer cavities allows for longer electron bunches (400 fs FWHM) with uniform peak currents that are comparable to what we use today. This will enable the stable temporal overlap for external seeding of FLASH (s-FLASH) at VUV wavelengths.

A technical feasibility study to demonstrate electron beam seeding with the high harmonics generated by an optical laser impinging on a gas target has been approved by the German funding agency. The goal of s-FLASH is to initially reach saturation at 30 nm seed wavelength (29^{th} harmonics) with 100 kW seed power. The desired FEL intensity fluctuation would be smaller than 5 % at the Gigawatt level, the radiation would have full longitudinal coherence with a SASE background below 1 % and the pump-probe timing would be stable below 10 fs.

To avoid impacts on the normal FLASH user operation, the layout of the experiment (Fig. 9) allows for parasitic operation. The ten meter long, variable-gap undulator will be installed after the collimation dogleg, providing the required wavelength tunability at fixed electron beam energies. The seed is transported from a neighboring laser building and coupled into the electron beam line at the last dogleg bending dipole. The Gigawatt seeded FEL pulses with a duration of about 20 fs FWHM are coupled out a few meters behind the undulator. The out-coupling mirror is located in the center of a small chicane to vertically offset the electron beam by ~ 10 mm. The FEL beam is then

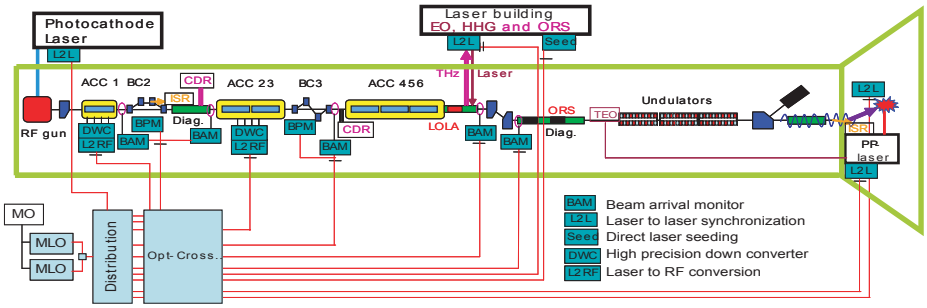

Figure 8: Prototype of a laser based synchronization system for the XFEL at FLASH

transported to an experimental building outside of the accelerator tunnel. A portion of the optical laser is split after the multi-pass amplifier and transported to the pump-probe experiment. Installation of s-FLASH is planned for 2009.

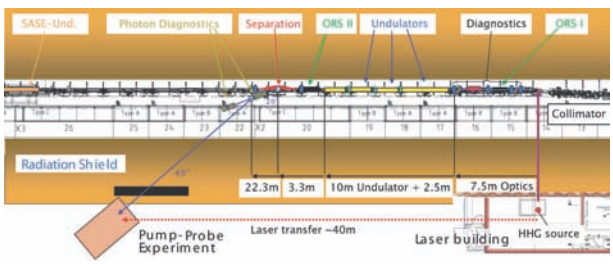

Figure 9: Layout of the laser-seed FLASH (s-FLASH).

SUMMARY

Future upgrades of FLASH will provide important opportunities for prototyping XFEL components such as a complete RF section, the 3^{rd} harmonic cavity, novel diagnostics for beam stabilization, a synchronization system with femtosecond accuracy, and an external seeding system.

REFERENCES

[1] V. Ayvazyan et al.,"First operation of a free-electron laser generating GW power radiation at 32 nm wavelength", Eur. Phys. J. D 37, p. 297-303 (2006)

[2] W. Ackermann, et al., "Operation of a free-electron laser from the extreme ultraviolet to the water window", Nature Photonics 1, 336 - 342 (2007)

[3] J. Rossbach, "A VUV Free Electron Laser at the TESLA Test Facility at DESY", NIM A375, (1996) 269.

[4] "XFEL Technical Design Report", DESY 2006-097, http://xfel.desy.de.

[5] T. Khaboulline, et al., "3.9 GHz Superconducting Accelerating 9-cell Cavity Vertical Test Results", PAC'07, June 2007, Albuquerque, USA, p. 2295

[6] E. Harms, et al., "Status of the 3.9-GHz Superconducting RF Cavity Technology at Fermilab",PAC'07, June 2007, Albuquerque, USA, p. 2256

[7] Private communication E. Vogel, DESY

[8] V. Schlott, et al., "Intra Bunch Train Feedback for teh European X-FEL", EPAC'06, Edinburgh, Scotland, p. 3017

[9] B. Keil, et al., "Design of an Intra-Bunch-Train Feedback system for the European X-ray FEL", DIPAC'07, May 2007, Venice, Italy

[10] M. Huning, et al., FEL'05, Aug. 2005, Stanford, CA, p. 538.

[11] H. Delsim-Hashemi et al., "Single-Shot Longitudinal Diagnostics with THz radiation at the Free-Electron Laser FLASH", FEL'06, Aug. 2006, Berlin, Germany, p. 594

[12] B. Schmidt, "Overview on diagnostics for X- ad XUV-FEL", , FEL'06, Aug. 2006, Berlin, Germany, p. 761

[13] G. Berden, et al., "Benchmarking ultrafast electron bunch length monitors", accepted for publication, Phys. Rev. Lett.

[14] B. Steffen, et al., "Single-Shot Longitudinal Bunch Profile Measurements at FLASH Using Electro-Optic Detection", this conference, WEBAU04.

[15] A. Winter, O. Ilday and B. Steffen, "Femtosecond Yb-doped fiber laser system at 1 μm of wavelength with 100-nm bandwidth", DIPAC'07, May 2007, Venice, Italy

[16] E. Saldin, E. Schneidmiller, M. Yurkov, "A simple method for the determination of the structure of ultrashort relativistic electron bunches", NIM A539 (2005) 499.

[17] G. Angelova, et al., "Installation of the Optical Replica Synthesizer in FLASH", this conference.

[18] J. W. Kim, et. al., "Large scale timing distribution and RF synchronization for FEL facilities", FEL'04, Trieste, Italy.

[19] A.Winter, et.al., "High-precision laser master oscillators for optical timing distribution systems in future light sources", EPAC'06, July 2006, Edinburgh, Scotland, p. 2747.

[20] F.Loehl, et al., "Sub-10 Femtosecond Stabilization of a Fiber Link Using a Balanced Optical Cross Correlator", PAC'07, June 2007, Albuquerque, USA, p. 3804

[21] F. Loehl, et. al., "A Sub-50 fs Bunch Arrival Time Monitor System for FLASH" DIPAC'07, Venice, Italy, 2007.

[22] K. Hacker, et al., "Large Horizontal Aperture BPM for use in Dispersive Sections of Magnetic Chicanes", EPAC'06, July 2006, Edinburgh, Scotland, p. 1043.

[23] J. W. Kim, et. al., "Long-Term Stable Microwave Signal Extraction from Mode-Locked Lasers", Optics Express, July 2007, Vol. 15, Issue 14, p. 8951

STATUS OF SCSS & X-RAY FEL PROJECT IN JAPAN

Tsumoru Shintake# and XFEL/SPring-8 Team
RIKEN/JASRI/SPring-8, Hyogo 679-5148 Japan

Abstract

The XFEL/SPring-8 project has been funded in FY2006, which is aiming at generating 1 Å coherent intense X-ray laser using 8 GeV normal-conducting accelerator. The construction period is scheduled 2006-2010, and FEL operation will start in 2011. XFEL/SPring-8 is based on unique concept of SCSS: SPring-8 Compact SASE Source. It requires low emittance and high peak current electron beam, i.e., normalized emittance of 1 π.mm.mrad and 3 kA peak current. We decided to employ the thermionic electron gun, which generates 1 A beam from single crystal cathode, followed by the multi-staged bunching system to achieve 3000 times compression. The design is based on the "Adiabatic Bunch Compression" scheme, i.e., compressing bunch length as inversely proportional to the beam energy, thus the bunch length on electron rest frame is kept constant, and as a result the low slice emittance is preserved. To prove this concept, the SCSS prototype accelerator of 250 MeV beam energy was build. On June 2006, the first lasing has been observed at 49 nm. From the FEL gain measurement, the beam brightness was determined as high as 300 $A/(\pi.mm.mrad)^2$, which is enough value for the beam quality for the 8 GeV XFEL/SPring-8 project.

INTRODUCTION

We started SCSS project in 2001[1] for developing technology required for X-ray FEL. SCSS stands for SPring-8 Compact SASE Source, in which by means of in-vacuum type short period undulator, the required electron beam energy becomes lower, additionally the C-band accelerator drives the beam at high gradient as high as 35 MV/m, as a result, the total system length becomes "compact", and it fits to available site length at SPring-8.

In the course of SCSS R&D, we developed a low emittance electron gun using single crystal CeB6 cathode shown in Fig. 2 and 500 kV gun driven by pulse modulator power supply: We also developed various hardware components required for SCSS: injector rf system, C-band klystron modulator with oil-filled compact design, high resolution beam position monitor, and digital rf signal processing system[2]. In order to check the developed hardware components and verify system performance, especially the low emittance electron injector, we constructed SCSS prototype accelerator in 2004-2005. The tunnel length is 60 m long, the maximum electron beam energy is 250 MeV, the shortest lasing wavelength is around 50 nm. In July 2006, we observed first lasing. The user beam run will start in October 2007.

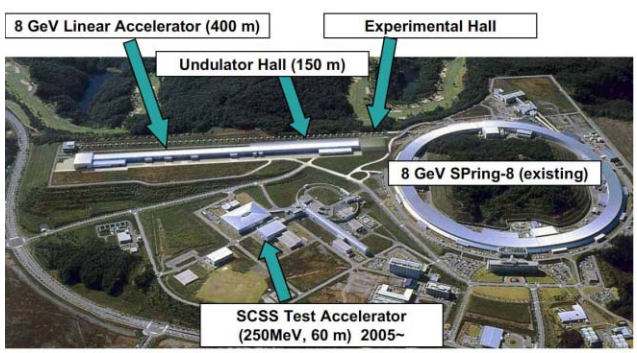

Fig. 1 The XFEL will be build at SPring-8 site.

On FY2006, the Japanese MEXT: Ministry of Education, Culture, Sports, Science and Technology has decided construction of XFEL at SPring-8 site. The project is aiming at generating 1 Å coherent intense X-ray laser, which is based on SASE using 8 GeV normal-conducting accelerator. A big benefit to have XFEL at SPring-8 site is to share human resources and facilities for sample preparation with existing 8 GeV synchrotron light source.

We have decided to use normal conducting linear accelerator technology at C-band frequency (5712 MHz), which was originally developed at KEK for the e+e- linear collider project. It is "warm" technology, not super conducting "cold" technology; therefore it can be constructed with much lower cost. The C-band accelerator is capable of running at high accelerating gradient, as high as 35 MV/m. The 50 MW C-band klystron was developed and it is now available from industries as a standard component. C-band accelerator technology is available right now.

CHOICE OF ELECTRON SOURCE

SCSS is unique and beneficial, however, it requires extremely low normalized emittance: ~ 1 π.mm.mrad and high peak current: 3 kA. We decided to employ the thermionic electron gun, which generates 1 A beam from single crystal cathode, followed by the multi-staged bunching system to achieve 3000 times compression (3000 = 20 x 5 x 10 x 3). The design is based on "Adiabatic Bunch Compression" scheme as shown in Fig. 3, i.e., compressing bunch length as inversely proportional to the beam energy, thus the bunch length on electron rest frame is kept constant, and as a result the low slice emittance is preserved. We carefully manipulate bunch length and avoid "over bunching", thus we do not mix particle between head and tail within bunch. The bunch length on the electron rest frame is kept almost constant, in practice it is about 30 cm long, while the diameter of the beam is a few mm only, therefore the electric field of space charge is fairly uniform and linear, and has only the radial component, as a result emittance break due to the space charge effect becomes negligibly small.

#shintake@spring8.or.jp

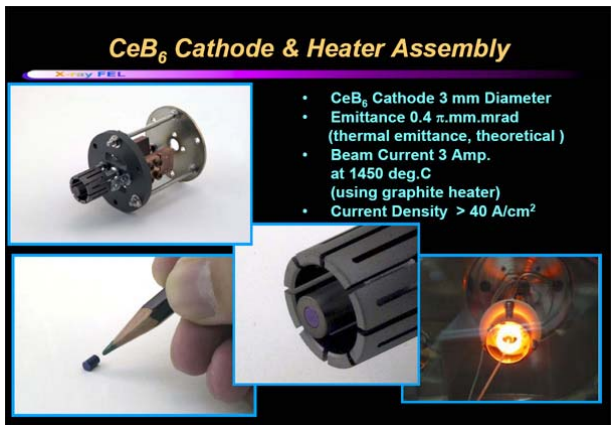

Fig. 2 CeB_6 single crystal thermionic cathode for low emittance electron source.

We use rod shape CeB_6 of 3 mm in diameter as shown in Fig. 2. We extract 1 A beam by 10 MV/m acceleration field in the gun (500 kV/5cm), which is in the temperature limited condition. The theoretical normalized emittance due to thermal motion at the cathode is 0.4 π.mm.mrad. The emittance was carefully measured at the gun using double slits. The measured emittance of core beam was 0.6 π.mm.mrad [3].

MACHINE CONFIGURATION AND BEAM OPTICS

Figure 4 shows the machine configuration and its parameter is listed in Table-1. The thermionic electron gun generates only 1 A, and then we compress the bunch length 3000 times in the injector and chicane magnets. We designed the compression factor as 20, 5, 10, 3 in the injector, the first, second and third bunch compression systems, respectively. The highest compression is made in the injector, it is basically velocity bunching using energy chirping on rf field. In the optics design, we introduced new concept "Adiabatic Bunch Compression Scheme"[4], where we maintain the longitudinal bunch length as constant on the electron rest frame (moving frame) during acceleration. In practice, we squeeze the bunch length as inversely proportional to the beam energy, that is, 1 nsec, 500 keV, $\gamma = 2$ at the gun, followed by 0.6 nsec, 1 MeV, $\gamma = 3$ after booster, and 10 psec, 30 MeV, $\gamma = 60$ after bunch compressor 1. In this scheme, we maintain constant bunch length on the electron rest frame, and never over compress, thus we can maintain "laminar flow" of electron beam from the gun down to the undulator.

Table-1. Machine parameter of SCSS prototype accelerator and XFEL/SPring-8

		Prototype	X-ray FEL	
Beam Energy	E	0.25	8.0	GeV
X-ray Wavelength	λ	60	0.1	nm
Beam Emittance	ε_n	2	1.0	π.mm.mrad
Bunch Length	Δz	100	100	μm
	FWHH	0.3	0.3	psec
Transverse Beam Size	$\sigma_{x,y}$	100	25	μm
Peak Current	I_p	1	3	kA
Charge per bunch	q	0.3	1	nC
Undulator Parameter	λ_u	15	18	mm
	K	1.3	1.3	
Length	L	10	80	m
FEL Saturation Length	L_{sat}	20	60	m

In the SCSS prototype accelerator[5], the projected emittance was measured as 3~4 π.mm.mrad, while it was dominated by the resolution limit of profile monitor and also including the tail component associated from beam deflector right after the gun. To determine the emittance in the beam core, we performed FEL gain measurement by varying K-parameter of the undulator, and peak current, from which we obtained beam brightness 300 $A/(\pi.mm.mrad)^2$. To determine peak current, we performed bunch length measurement by chirping the beam energy in C-band accelerator, and observed the transverse beam size variation in the downstream chicane. The full width was 1 psec. Therefore we obtained the beam current as 300 A, and the emittance derived as 1 π.mm.mrad. This is enough beam quality for 8 GeV XFEL machine.

From the SCSS prototype accelerator to 8 GeV XFEL/SPring-8, we need further bunch compression by factor of 10. This is straightforward by simply adding another two magnetic chicane bunch compressors as shown in Fig. 4.

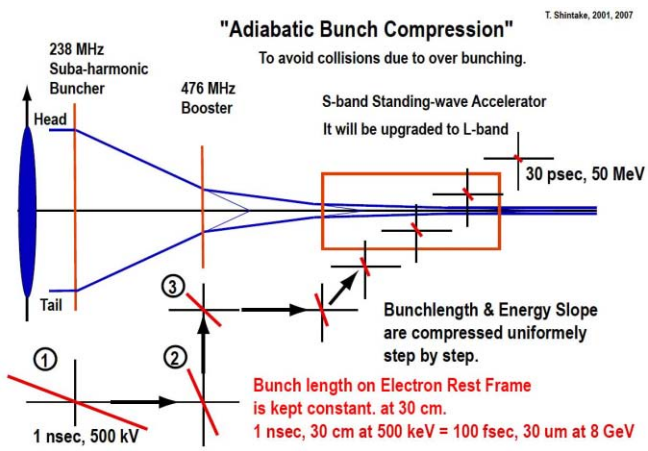

Fig. 3 Adiabatic bunch compression scheme.

One special care is taken in the design of 8 GeV machine to make linear the beam shape in the (z, E) phase space. Overlapping the higher order harmonic field on the dominant rf-field, we may flatten the effective acceleration field. This technique will be applied in the 476 MHz booster cavity with L-band correction cavity and L-band accelerator with C-band correction cavity.

The frequency of the rf acceleration is designed as lower in the injector and gradually raised higher in the following accelerator. This is a part of the "Adiabatic Bunch Compression" scheme, where the wavelength of the rf field is also varied to maintain constant bunch to wavelength ratio. Ideal way is to use static field everywhere until beam energy reaches to 8 GeV, since the static field does not cause emittance dilution associated from time varying transverse kick from radial electric field or azimuthally magnetic field in the rf cavity.

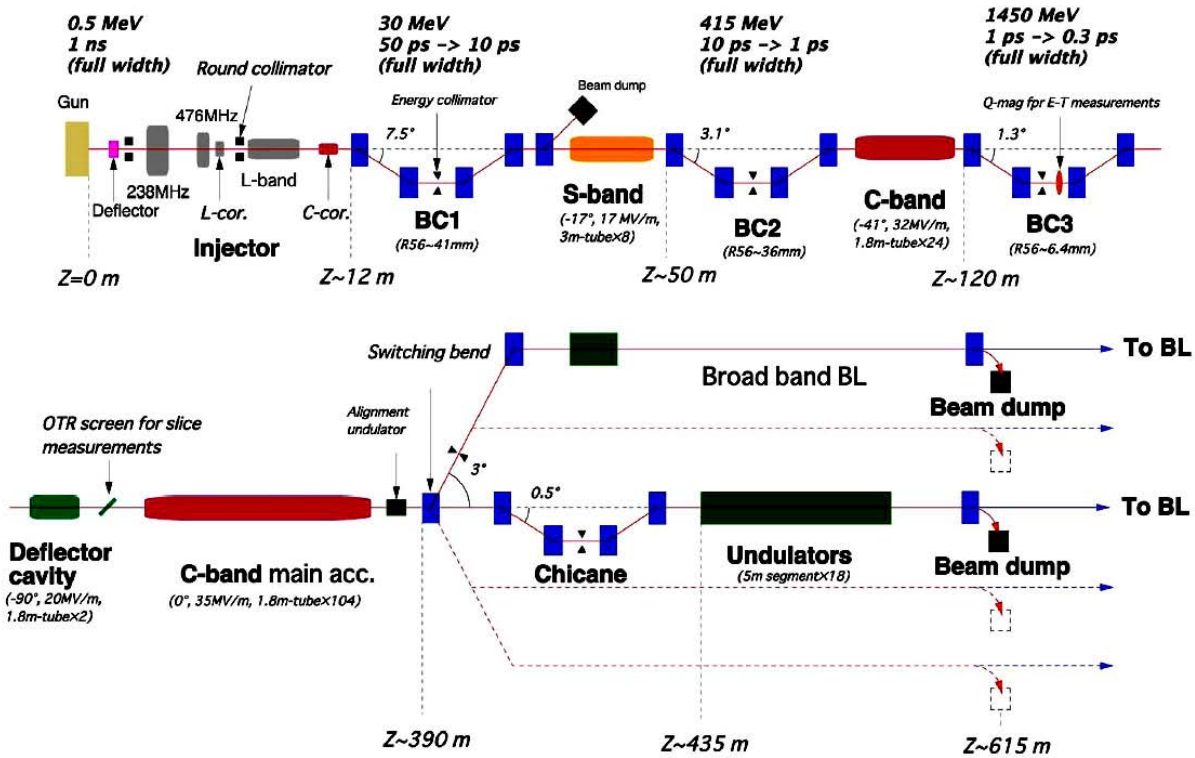

Fig. 4 Machine configuration.

In practice the attainable electric field gradient is lower at lower frequency, especially at DC field. HV break down is caused by avalanche mechanism driven by ion bombardment on metallic electrode followed by gas emission and successive ionisation, which results in more ion bombardment. When the rf frequency becomes higher, the field polarity changes faster than the ion reaches to the electrode, thus the cycle gain of ion population becomes lower, and HV breakdown stops. From this technical point, the higher frequency is desirable for high field acceleration. On the other hand, to minimize the emittance dilution due to the time varying transverse kick, lower frequency is desirable. To make an optimum design for those two constraints under the "Adiabatic Bunch Compression" scheme, we chose the rf frequency lower in the injector and higher in main linac. We start 238 MHz in the sub-harmonic buncher, and 476 MHz in the booster, then 1428 MHz (L-band) in bunch accelerator, 2856 MHz (S-band) in the upstream 30 MeV → 415 MeV in the main accelerator, at the last 5712 MHz (C-band) in the main linac up to 8 GeV. They are schematically drawn in Fig. 5.

A question will be arise, why don't we go even higher frequency. In principle, the answer is "Yes", but "No" in practice. The high frequency accelerator requests smaller size of accelerating cavity structure, whose fabrication becomes harder and harder as frequency becomes higher. The C-band is determined by the technical consideration amount the higher gradient and the practical engineering capability.

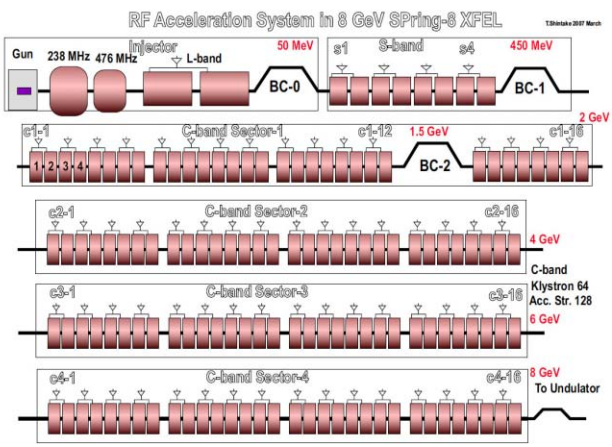

Fig.5 Accelerating structures.

UNDULATOR

Figure 6 shows the undulator for 8 GeV XFEL/SPring-8. The magnet array is hybrid type consist from permanent magnet and iron yoke. It is in-vacuum design with variable gap (2 mm ~ 40 mm). Nominal operation point is gap = 4 mm and K = 1.9. One advantage to use in vacuum undulator is that we have fairly wide beam aperture by opening the gap to 40 mm, where we can transport guide laser beam for alignment of cavity BPMs. Temperature control of the permanent magnet is one of the most important issue in precise undulator design, in this point the in vacuum undulator design provides ideal heat isolation from the environmental temperature change.

Figure 7 shows one example simulation results on the SASE-FEL amplification with nominal beam parameter.

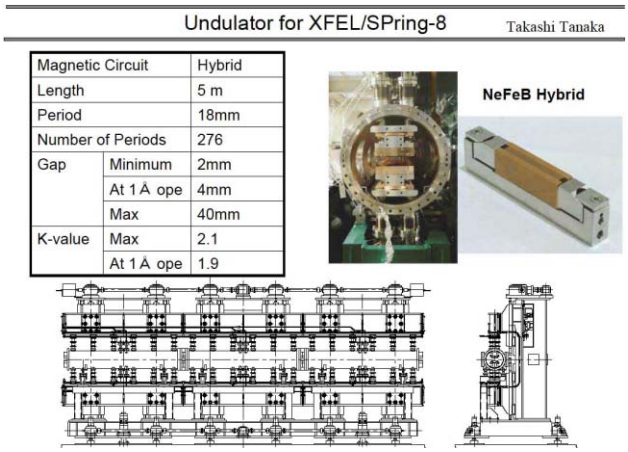

Fig. 6 Undulator for 8 GeV XFEL/SPring-8. The magnet array is hybrid type consist from permanent magnet and iron yoke.

It predicted that the FEL will be saturated within 120 m long undulator line. The estimated saturation power is 2 GW.

STABILITY ISSUE

As discussed in previous sections, our system uses very high bunch compression factor, thus the beam parameter, such as peak current, is very sensitive to the machine parameter change in the upstream section. By simple analysis, to make the peak current stability better than a few %, it was shown that the voltage and phase stability on the rf acceleration field in the injector has to be 10^{-4} level and 0.1 degree, respectively. In order to achieve this requirement, we have been carrying out R&D on stable high-voltage power supply for klystron modulator. By means of parallel operation of high-power fast inverter-type power converter and a small power precise power supply, we successfully demonstrated 10^{-4} level of pulse-to-pulse stability in 50 kV, 35 kW power supply. Using this type of power supply in the electron gun, and S-band buncher, the measured beam energy jitter in the SCSS prototype accelerator becomes 6 x 10^{-4}. The R&D will be continued during the construction period to achieve 1 x 10^{-4}. The beam arriving time jitter was measured at the entrance to the undulator. It was 46 fsec, which is reasonable value if we consider R56 (40 mm) parameter of chicane multiplying with the energy jitter. This is very promising result for pump-probe experiment. And also, this is a surprising result that we have such stable beam timing even through the bunch was made after high compression from a long pulse of thermionic gun.

To obtain 0.1 degree phase stability, we are currently developing optical fiber link. For slow drift, phase detection system in optical fiber by reflecting optical signal from one end, and apply feedback on fiber mechanical stretcher. Recently, we stretched 2 km fiber around the SPring-8 ring, where the phase drift was maintained within 10 fsec range.

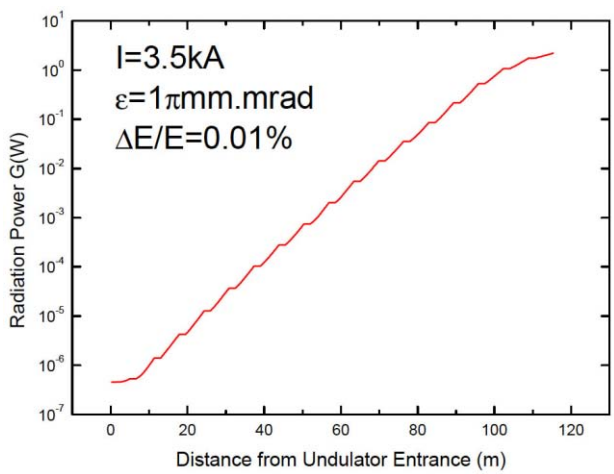

Fig. 7 Simulated FEL power growth along undulator line.

CONCLUSION & SCHEDULE

Our design concept on low emittance electron gun and injector, based on thermionic cathode and adiabatic bunch compression, has been proven at SCSS prototype accelerator. XFEL/Spring-8 aiming at generating 1 Å X-ray was designed and its construction has been started in FY2006. The construction will be completed in FY2010 and the first X-ray beam test is scheduled in the end of FY2010.

REFERENCES

[1] T. Shintake *et al*., "SPring-8 Compact SASE Source", SPIE2001, San Diego, USA, June 2001
[2] http://www-xfel.spring8.or.jp
[3] K. Togawa *et al*., "Emittance Measurement on the CeB6 Electron Gun for the SPring-8 Compact SASE Source", FEL2004, Trieste Italy, August 2004
[4] T. Shintake, "Status of SCSS Project", FEL2006 conference, Berlin, August, 2006.
[5] H. Tanaka *et al*., "Low Emittance Injector at SCSS", FEL2006 conference, Berlin, August, 2006.

STARS—AN FEL TO DEMONSTRATE CASCADED HIGH-GAIN HARMONIC GENERATION*

M. Abo-Bakr, W. Anders, J. Bahrdt, K. Bürkmann, P. Budz, O. Dressler, H. Dürr, V. Dürr, W. Eberhardt, S. Eisebitt, J. Feikes, R. Follath, A. Gaupp, R. Görgen, K. Goldammer, S. Hessler, K. Holldack, E. Jaeschke, T. Kamps, J. Knobloch†, O. Kugeler, B. Kuske, P. Kuske, D. Krämer‡, F. Marhauser§, A. Meseck, R. Mitzner¶, R. Müller, A. Neumann, M. Neeb, K. Ott, D. Pflückhahn, T. Quast, M. Scheer, T. Schroeter, F. Senf, G. Wüstefeld
BESSY, Albert-Einstein-Strasse 15, 12489 Berlin, Germany

Abstract

BESSY is proposing a new facility to demonstrate the cascading of two high-gain harmonic-generation stages for the generation of FEL radiation. This facility, called STARS, is planned for lasing in the wavelength range 40 nm to 70 nm. A 325-MeV CW driver linac provides a peak current of 500 A at a bunch charge of 1 nC. The linac consists of a normal-conducting gun, three superconducting TESLA-type modules modified for CW operation, a third-harmonic unit to linearize the RF potential and a single-stage bunch compressor. This paper discusses the facility layout and the main operating parameters.

MOTIVATION

Femtosecond pulses from linac-based free-electron lasers are unique tools for future time-resolved experiments. In March 2004, BESSY published the TDR for a free-electron laser user facility that covers the VUV to soft X-ray range (BESSY FEL) [1]. This second-generation FEL facility is seeded and uses the high-gain harmonic generation (HGHG) [2] scheme to produce coherent radiation down to the 1-nm range. This scheme offers the possibility to generate photon pulses of variable femtosecond duration, gigawatt peak power, full shot-to-shot pulse reproducibility, wide-range tunability and full transverse and longitudinal coherence. To reach the highest energies, HGHG cascades with up to four stages must be employed.

Following the evaluation of the TDR in 2005/06 by the German Science Council, it was recommended that the BESSY FEL be realized on condition that its enabling technology, the HGHG *cascade*, be demonstrated beforehand.

To address this important issue, BESSY is therefore proposing to build a two-stage HGHG cascade with a superconducting driver linac called STARS (Superconducting Test Accelerator for Radiation by Seeding) [3, 4]. Although its primary purpose is to validate the cascading of HGHG stages, many components and technical issues are nearly identical to those of the BESSY FEL. Hence, STARS serves as an ideal test bed for operating CW superconducting technology, diagnostics, synchronization, and for studying beam generation, manipulation and transport.

To demonstrate the capabilities and potential of seeded, ultra-short-pulse FEL radiation, prototype user experiments will also be installed at STARS. The location of STARS is planned such that it will remain operational even after construction of the BESSY FEL. By expanding the experiments, STARS will therefore migrate towards a full user facility to enhance the BESSY FEL and to enable the exploration of new techniques before they are adopted for the BESSY FEL.

OVERVIEW

STARS will be located on the same site as BESSY-II in Berlin-Adlershof, making use of some of the existing infrastructure while leaving room for the BESSY FEL facility to be built later. The philosophy behind the layout of STARS, as depicted in Figure 1, is to adopt a conservative configuration that provides for "safe" operation in view of the main goal of demonstrating the cascading of HGHG at 70 nm. Hence, components for the driver linac and system parameters were adopted which have already been demonstrated experimentally elsewhere. Nevertheless, "optional upgrades" of the linac are included, some from the outset, that will enhance the FEL's performance to make STARS attractive for future user experiments.

A normal-conducting photoinjector generates high-brightness electron bunches. Three superconducting TESLA-type cryomodules, modified for CW operation, then boost the energy up to 325–380 MeV.[1] The cryomodules contain twenty 9-cell TESLA-type cavities with the possibility to add four further ones at a later date. Bunch compression is achieved in a magnetic chicane following the second module. A collimator and diagnostic beam line preceed the HGHG cascade, permitting linac commissioning before the beam is injected into the FEL section consisting of two HGHG stages and a fresh bunch chicane.

For bunch compression, off-crest acceleration is required. Non-linearities in the longitudinal bunch profile introduced by the RF potential result in a strongly peaked current distribution after compression. STARS thus in-

* Supported by the Bundesminsiterium für Bildung und Forschung, the State of Berlin and the Zukunftsfonds Berlin.

† knobloch@bessy.de
‡ now at GSI, Darmstadt
§ now at Jefferson Lab, Newport News
¶ Universität Münster

[1] The final energy depends on whether the third-harmonic cavities, discussed later, are in operation or not.

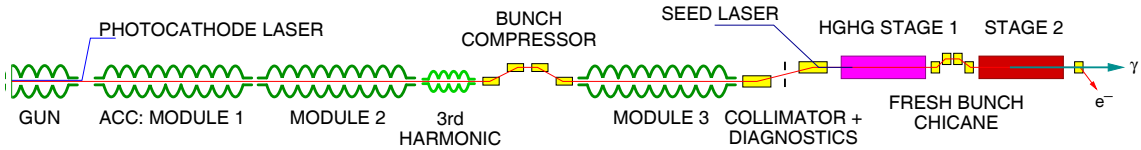

Figure 1: Layout of the main components of STARS.

cludes a third-harmonic cavity system directly after the second module to remove the non-linearities. However, the demonstration of cascaded HGHG is also possible without the linearizing cavities installed, albeit at longer wavelengths and lower power.

ELECTRON-BEAM GENERATION

The electron beam current is generated in an RF photoinjector. Here a modified PITZ normal-conducting system has been adopted [5], primarily because the required beam paramters (slice emittance = 1.5 π mm mrad at 1 nC) have already been demonstrated [6, 7]. A UV photocathode laser illuminates a Cs_2Te cathode with flat-top laser pulses of 20 ps width to release electron bunches of 1 nC charge.

The repetition rate of the STARS injector is a conservative 100 Hz with a pulse length of 25 μs. This is sufficient to demonstrate cascaded HGHG, while operating the gun cavity at a moderate thermal load of 7.5 kW. Stable gun operation, critical to guaranteeing a jitter-free beam, is thus much simpler than for high thermal pulsed loads. An RF pickup is included in the gun-body design to further enhance the control of the RF field. First experiments at low power have demonstrated that the required phase and amplitude stability of 0.3° and 0.1% can readily be achieved and even improved upon [8].

In future, an upgrade to the full 1-kHz operation, as for the BESSY FEL, is planned and the thermal loading will increase to 75 kW. To handle this, the cooling of the PITZ3 gun cavity design was improved and a prototype of the new design was tested successfully to 47 kW power dissipation, limited only by available RF power at the gun [5].

BEAM ACCELERATION

Superconducting RF technology developed by the TESLA collaboration and as described in the BESSY FEL TDR [1] has been chosen for the driver linac of STARS. Although TESLA was originally designed for pulsed operation, both STARS and the BESSY FEL will operate CW for a number of compelling reasons. These include the flexibility to choose bunch patterns more freely and the enhanced RF stability because the RF is alway on. The latter is especially critical to provide jitter-free electron bunches to the HGHG cascade to ensure maximal output and synchronization capabilities for user experiments.

To study the CW operation of TESLA technology, BESSY has already started an intensive R&D program. The Horizontal Bi-Cavity Test facility (HoBiCaT) [9] has been set up for this purpose.

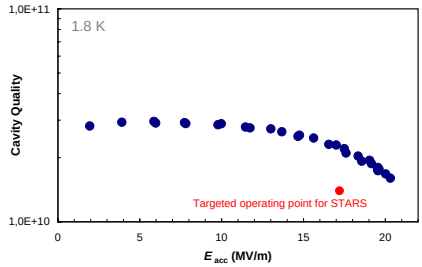

Figure 2: Cavity quality of a CW operated TESLA cavity with all ancillary components (coupler, tuner, HOM pickups, etc.) as measured in the HoBiCaT facility.

Tests of RF couplers [10] and tuners [11] as well as studies such as the optimum bath temperature required for reliable and economic CW operation, have been performed.

Simulations of the HGHG scheme have shown that a beam energy of 325 MeV is sufficient for lasing at wavelengths down to 40 nm. This energy can be reached with three TESLA-type modules containing a total of 20 cavities operating at a moderate 17.2 MV/m. Note that this value takes into account a total decelerating voltage of about 30 MeV in the third-harmonic section. Measurements in HoBiCaT have already demonstrated that CW operation at this field is possible while exceeding the STARS design quality factor of 1.4×10^{10} by 65% (see Figure 2).

At 1 nC bunch charge and a repetition rate of 100 Hz, beam loading in STARS is less than 2 W per cavity. Hence, RF power will be needed primarily to compensate the microphonic detuning in the cavities. Microphonic detuning is also a significant contributor to RF instability and thus should be kept to a minimum.

Measurements in HoBiCaT have shown that the RMS microphonics are of the order of 3 Hz or less with peak excursions around 15 Hz. A significant portion of these microphonics are at frequencies below 1 Hz and are caused by pressure fluctuations in the helium gas-return system, of order 0.03 mbar RMS [12].

It is expected that the larger volume of the STARS helium system will reduce the level of microphonic detuning. Still, it has already been demonstrated that the detuning can also be compensated with a fast, piezo-based cavity tuner to levels below 1 Hz RMS. Even high frequency components at mechanical resonances have been compensated with this system (see Figure 3).

To provide for an ample safety factor, the RF system will be dimensioned to handle microphonic detuning values of 5 Hz RMS and 25 Hz peak. The optimal bandwidth is 50 Hz, or an external coupling of 2.6×10^7. At 17.2 MV/m accelerating field this translates into an RF power requirement of $P_{\mathrm{ave}} = 3.1$ kW and $P_{\mathrm{peak}} = 5.9$ kW, which the

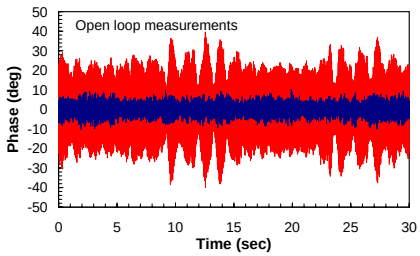

Figure 3: *Open-loop* measurements of the cavity phase stability. The dominant noise source is microphonic detuning resulting in a phase stability of 14.9° RMS (red curve). When detuning compensation is activated with a fast piezo tuner, the stability improves to 2.8° (blue curve).

existing TTF couplers can readily handle, as demonstrated in HOBICAT [10]. The STARS system will consist of 20 individual IOT-based RF transmitters supplying one cavity each via coaxial transmission lines. RF control will be performed by a digital FPGA-based system.

BEAM TRANSPORT

A single bunch compressor at 180 MeV is required to increase the peak current. A combination of off-crest acceleration and subsequent passage through a dispersive magnetic chicane is employed to compress the beam from 45 A to 500 A.

Due to non-linearities in the accelerating RF potential, a very high and short current peak with a long tail results after the compression. As the peak will generate strong SASE background radiation, it limits the compression factor and hence the power of the HGHG output radiation. Although STARS is designed to be able to demonstrate HGHG in this mode, the quality and power is improved upon by installing third-harmonic cavities. They remove most of the non-linearities of the RF potential and the bunch compressor. A superconducting third-harmonic module (with four 9-cell cavities) is currently being developed by Fermilab for the FLASH accelerator [13]. This unit is compatible with the main acceleration modules and is planned for installation in March 2008. Preliminary analyses of the input coupler system suggest that CW operation of the unit is also possible.

Start-to-end tracking of the electron beam, including all components in Figure 1, have been completed. The photoinjector and the first four cavities were simulated with ASTRA to take into account space-charge effects. ELEGANT was used for the remainder of the linac, while tracking in the undulators was performed with GENESIS.

The bunch profile at the entrance of the undulators is depicted in Figure 4. A *slice* emittance of approximately 1 π mm mrad and an energy spread of 12 keV is predicted. Very important for the HGHG process is the fact that a constant profile is maintained in the approximately 1-ps wide peak-current region (500 A) used in the HGHG cascade.

Measurements at PITZ have demonstrated that a *projected* emittance of approximately 1.5 π mm mrad is readily achievable [6, 7]. Also, tests at FLASH have shown that there the energy spread is below the measurement resolution limit of 20 keV [14]. Both results are compatible with the predicted beam parameters for STARS. Nevertheless, for subsequent GENESIS simulations, the *slice* beam emittance was intentionally increased to 1.5 π mm mrad to provide for an additional safety margin in case unexpected beam dilution occurs in the STARS linac. An improved emittance will allow STARS to operate at higher power.

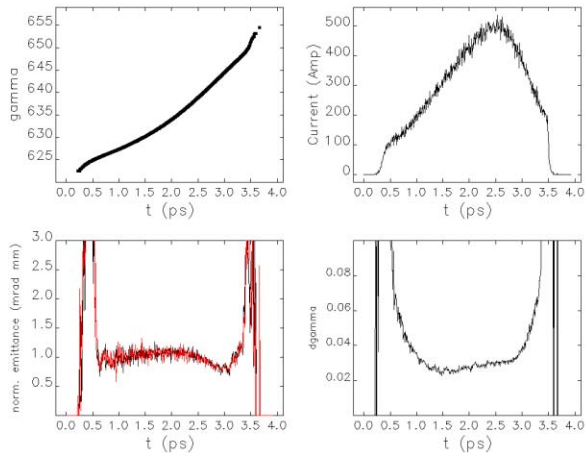

Figure 4: Simulated beam properties at the entrace of the undulator. Top left: Beam energy, top right: current profile, bottom left: slice emittance, bottom right: slice energy spread.

An important consideration for the HGHG cascade is the bunch-to-bunch stability of the beam. Due to the off-crest acceleration, the bunches have an energy chirp of about 5 MeV/ps. Any time jitter of the bunches thus shifts the central energy of the slices used for HGHG which must remain in the energy acceptance of the cascade (of order 2×10^{-3}). Hence the jitter of the seed laser to the bunch may not exceed about 150 fs. Studies of the jitter are still ongoing, but first results based on the cavity performance in HOBICAT have demonstrated that the required stability can be achieved with the CW SRF system.

THE HGHG CASCADE

STARS will cascade two HGHG stages to reach a photon energy of up to 31 eV. Even higher energies can be accessed by tapping into the harmonic content of the radiation.

Figure 5 depicts the layout of the STARS HGHG cascade. STARS will be continuously tunable from 40 nm to 70 nm, the lowest wavelengths placing the most stringent requirements on the electron beam quality. The flexibility is achieved by using different harmonics (three to five) in the cascades in conjunction with gap adjustments of the undulators and variation of the seed wavelength.

Modulators 1 and 2 and Radiator 1 are planar devices, while APPLE-III undulators for Radiator 2 provide full variability of the polarization between 40 nm and 50 nm [15]. APPLE-III devices yield a 35% higher field on axis than APPLE-II undulators, so that at minimum gap

Figure 5: Schematic of the STARS HGHG cascade (note that the quadrupoles between undulators are not shown.)

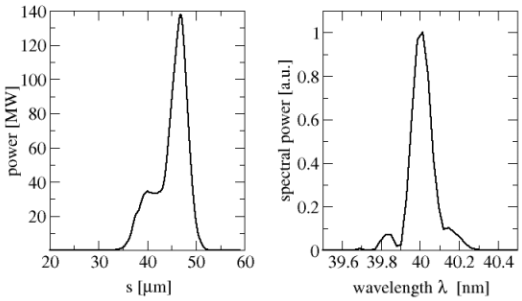

Figure 6: Temporal profile (left) and spectrum (right) of helical radiation at 40 nm.

(7 mm) 70 nm radiation is within reach. Here, the required electron-beam quality is relaxed and STARS can even be commissioned without the third-harmonic cavity system.

Performance predictions for the HGHG process were made using complete start-to-end simulations with the same approach as for the BESSY FEL [16, 17, 18]. Importantly, the HGHG simulations with GENESIS 1.3 are based on the actual electron bunch profiles obtained from the linac start-to-end calculations, only that the slice emittance has intentionally been increased by 50%. Also, both radiating slices have been tracked through the first HGHG stage to ensure that any (detrimental) spontaneous radiation is taken in consideration.

Results for the most challenging case, radiation produced at 40 nm, are depicted in Figure 6 [18]. For helical polarization, an output power of order 140 MW is expected. The length of the seed-laser pulse (approximately 20 fs) is maintained and about 53% of the power is within the 0.1% spectral bandwidth. Even more power is produced at longer wavelengths—nearly 350 MW at 66 nm.

Significant flexibility has been designed into STARS for the final radiator. Here three independent modules are used to permit a wide range of operating modes. One benefit is that STARS is very tolerant to variations of the electron-beam parameters, with saturation attained either after the first or second module. Figure 7 underscores this point for simulations at 40 nm (planar polarization). Two simulations were performed; one with the beam emittance and energy spread as predicted by the start-to-end simulations ($1\ \pi$ mm mrad and 3×10^{-5}, respectively) and one with the emittance and energy spread increased to $1.5\ \pi$ mm mrad and 10^{-4}, respectively. In the latter case, the strength of the dispersive section had to be increased and the second module of Radiator 2 was closed. Nevertheless, nearly the same output performance is achieved.

At the expense of spectral purity and by employing all three radiator modules, the power can be increased further by driving the cascade in the superradiance regime. This mode is able to achieve peak powers above 1 GW at 40 nm (see [18] for more details). Wavelengths below 40 nm are

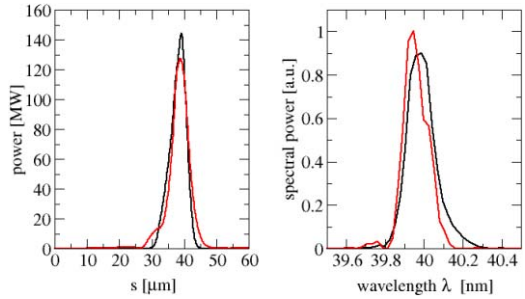

Figure 7: Simulated performance at 40 nm (planar polarization). The black curves were obtained with an emittance of $1\ \pi$ mm mrad and an energy spread of 3×10^{-5}. The calculations were repeated with degraded values of $1.5\ \pi$ mm mrad and 10^{-4}, respectively (red curve) and the 2nd module of Radiator 2 was closed.

also within reach of STARS by tapping into nonlinear harmonic contents of the radiation field. For example, using the third-harmonic (13 nm) approximately 700 kW is expected [18, 19].

REFERENCES

[1] D. Krämer, E. Jaeschke, W. Eberhardt, (editors), "The BESSY Soft X-Ray Free Electron Laser", Technical Design Report, ISBN 3-9809534-0-8, BESSY, Berlin, 2004.

[2] A. Doyuran et al., *Phys. Rev. Lett.* 86, 5902 (2001).

[3] J. Knobloch, E. Jaeschke, W. Eberhardt, (editors), "STARS—Proposal for the Construction of a Cascaded HGHG FEL", BESSY Report, Berlin, 2006.

[4] M. Abo-Bakr et al., *Proc. PAC 2007*, Albuquerque, NM (2007).

[5] F. Marhauser, *Proc. EPAC 2006*, Edinburgh (2006)

[6] A. Oppelt *et al.*, *Proc. LINAC 2004*, Lübeck (2004).

[7] F. Stephan, *these proceedings*.

[8] K. Ludwig, "Analog phase and amplitude controller", BESSY Report 2007.

[9] J. Knobloch et al., *Proc. EPAC 2004*, Lucerne (2004)

[10] J. Knobloch et al., *Proc. PAC 2005*, Portland, OR (2005)

[11] A. Neumann et al., *Proc. EPAC 2006*, Edinburgh (2006)

[12] A. Neumann, "Characterization and Control of Superconducting CW Cavities in the BESSY FEL", PhD thesis (to be published), Humboldt University, Berlin, 2007.

[13] T. Arkan et al., *Proc. PAC 2005*, Knoxville, TN (2005).

[14] M. Röhrs, C. Gerth, M. Hüning, and H. Schlarb, *Proc. EPAC 2006*, Edinburgh (2006).

[15] J. Bahrdt, *Proc. FEL 2006*, Berlin (2006).

[16] B. Kuske et al., *Proc. FEL 2004*, Trieste (2004).

[17] M. Abo-Bakr et al., *Proc. FEL 2005*, Stanford (2005).

[18] B. Kuske, K. Goldammer, A. Meseck, *these proceedings*.

[19] K. Goldammer, "Studies on Harmonic Generation in Free Electron Lasers", PhD thesis (to be published), Humboldt University, Berlin, 2007.

TOWARDS A LOW EMITTANCE X-RAY FEL AT PSI

A. Oppelt*, A. Adelmann, A. Anghel, R.J. Bakker, M. Dehler, R. Ganter, C. Gough, S. Ivkovic, F. Jenni, C. Kraus, S.C. Leemann, F. Le Pimpec, K. Li, P. Ming, B. Oswald, M. Paraliev, M. Pedrozzi, J.-Y. Raguin, L. Rivkin, T. Schietinger, V. Schlott, L. Schulz, A. Streun, F. Stulle, D. Vermeulen, F. Wei, A.F. Wrulich, Paul Scherrer Institute, 5232 Villigen PSI, Switzerland

Abstract

The Paul Scherrer Institute (PSI) in Switzerland is aiming to build a compact and cost-effective X-ray FEL facility for the wavelength range 0.1 – 10 nm. Based on the generation of very low emittance beams, it consists of a low-emittance electron source followed by high-gradient acceleration, and advanced accelerator technology for preserving the initial low emittance during further acceleration and bunch compression. In order to demonstrate the feasibility of the concept and the emittance preservation, a 250 MeV test facility will be built. This machine has been designed to be used as injector for the X-ray FEL at a later date. The accelerator design of the 250 MeV linac will be presented together with the status of the low emittance source and high gradient acceleration.

INTRODUCTION

In order to realize compact free electron lasers for the Angstrom wave length range, electron sources with high brilliance and ultra low emittance are required, allowing for low beam energies and short undulator length, and thus dramatically reducing the size and costs of such a project.
The proposed X-ray FEL at PSI is based on the development of new concepts that enable a substantial reduction in size and costs of the facility with respect to other existing designs.
The successful operation of such a FEL depends on the combination of high peak current, low energy spread, and high brightness of the electron beam. For the PSI-XFEL performance, in order to reach the Angstrom spectral range, a peak current of 1.5 kA, a relative energy spread around 10^{-4}, and a normalized transverse (slice) emittance as low as technically possible (i.e. $\varepsilon_n < 0.1$ mm mrad), are crucial. These stringent requirements shall be met by using new techniques, which include a low emittance source, a high gradient acceleration section, and a sophisticated bunch compression scheme.

LOW EMITTANCE SOURCE

Electrons emitted via field emission from micron sized metallic tips have an intrinsic low emittance due to the small source size. Using a double gated emitter geometry, parallel beamlets are produced from these tips. Combining the tips into a two-dimensional field emitter array (FEA), the required beam current can be reached with minor losses in emittance. Research at PSI focuses on developing suitable field emitter arrays emitting a total current of 5.5 A with an emittance of about 0.05 mm mrad. A scanning electron microscope (SEM) image of such an array, produced in-house at PSI, is shown in figure 1. Currents up to $\sim 10\mu$A per tip have been extracted from such a FEA in DC mode. The performances were studied at a 100 kV test stand [1].

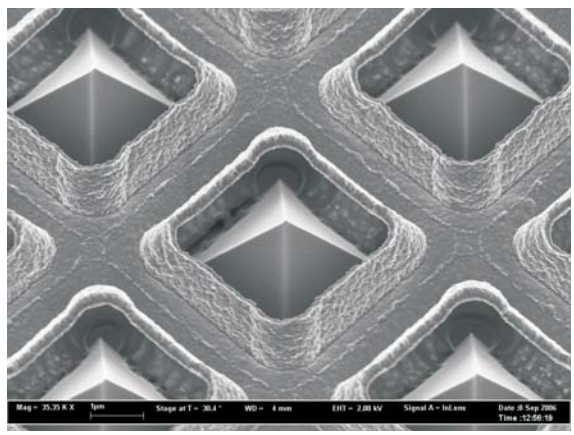

Figure 1: SEM picture of a FEA produced at PSI: the pyramidal shaped Mo tips and the gate layer are clearly visible.

Needle cathodes (single tip field emitters) are also investigated at PSI. Currents up to 470 mA were extracted from a ZrC needle via field emission (pulsed voltage, 2 ns FWHM, 30 Hz) [2]. Laser assisted field emission from needle cathodes allows increasing the extracted current further and offers the possibility of pre-bunching the electron beam. Figure 2 shows the measured current waveforms when applying different voltages (2 ns FWHM, 30 Hz) to a needle cathode in combination with laser illumination (266 nm, 6 μJ, 16 ps RMS). In this way, a peak current of 2.9 A was extracted [3]).
Since the fabrication and operation of the FEA [4] is very challenging, the option of using a conventional photo cathode is also investigated. With the proper choice of parameters (material, bunch charge, peak current), emittances of about 0.1 mm mrad should be reachable. Therefore, a Cu photo cathode will be chosen as start-up version for the injector. For both options, photo emission and field emission, the parameters were chosen equally such that the design of the following accelerator sections is not affected.

* presenting author: anne.oppelt@psi.ch

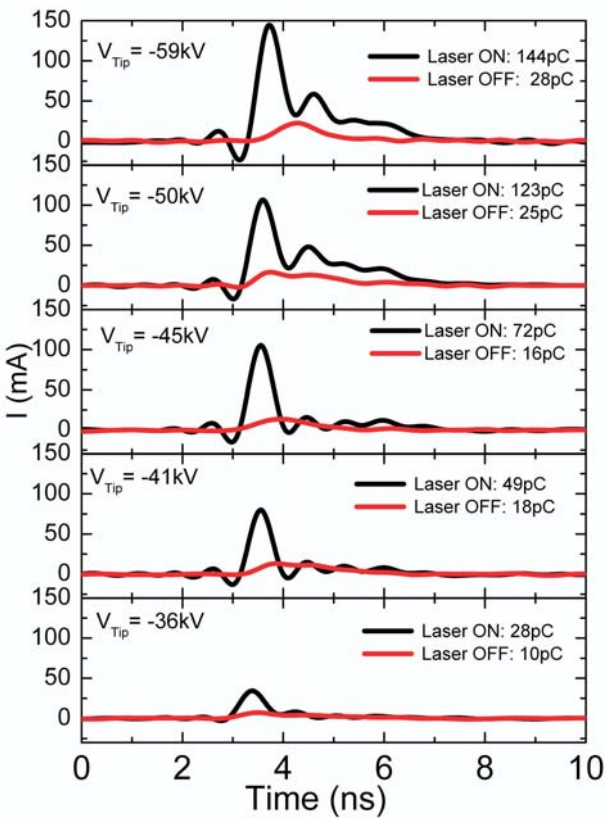

Figure 2: Effect of the laser illumination on the extracted current as function of different voltages applied to a ZrC needle cathode (see text). Note: The photo current pulses are broadened due to the low bandwidth of the oscilloscope (1 GHz).

HIGH GRADIENT ACCELERATION

In order to preserve the low initial emittance produced by the FEA, the field emitter will be operated in a pulsed diode at an accelerating gradient of 250 MV/m (1 MV pulser, 4 mm gap between cathode and anode). The development of such a high voltage pulser is ongoing at PSI. A 500 kV pulser was installed at the PSI site in summer 2007 and commissioning has started. After successfully having passed the high voltage tests, high gradient tests are scheduled and we expect beam operation by the end of the year. Figure 3 shows a photograph of this pulser in the test bunker. Some basic diagnostics for electron beam characterization at 500 keV (mainly emittance and momentum measurements) is being mounted. After demonstrating operation at 125 MV/m, this pulser will be upgraded to the final 1 MV pulser in order to realize the target acceleration gradient of 250 MV/m and produce a 1 MeV electron beam.

Figure 3: The high voltage high gradient test facility at PSI: the 500 kV pulser is installed and being commissioned.

EMITTANCE PRESERVATION AND BUNCH COMPRESSION

Even after the high gradient acceleration process, the electron beam is still fragile at 1 MeV. A concept for preserving the small emittance is therefore necessary, since space charge forces will blow up the beam emittance. Emittance conservation in the first 250 MeV of acceleration, where space charge forces dominate, is therefore a challenging task.

The low beam current (5.5 A) and bunch charge (200 pC) are beneficial to reduce the initial emittance and its dilution due to space charge forces in the low energetic region. But in order to obtain a peak current sufficient for lasing, a large bunch compression ratio of $\sim$270 is needed, which can be realized by controlling the longitudinal phase space. Therefore, after the high gradient section, the electron beam is accelerated off-crest in a two-frequency RF cavity [5]. The fundamental frequency (1.5 GHz) introduces thus an energy chirp which leads to ballistic bunching, while the third harmonic frequency (4.5 GHz) flattens the accelerating field and thus allows controlling the longitudinal bunch shape. In the following L-band TW structure, the RF compression is finished and the bunch length frozen, see figure 4. At this stage, the electron bunches are short enough to be further accelerated in an S-band TW structure,

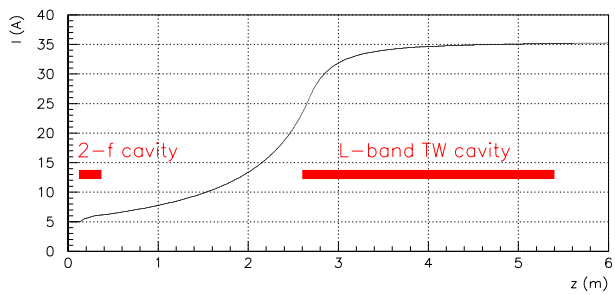

Figure 4: Effect of the two-frequency cavity: current increase due to ballistic bunching (HOMDYN calculation).

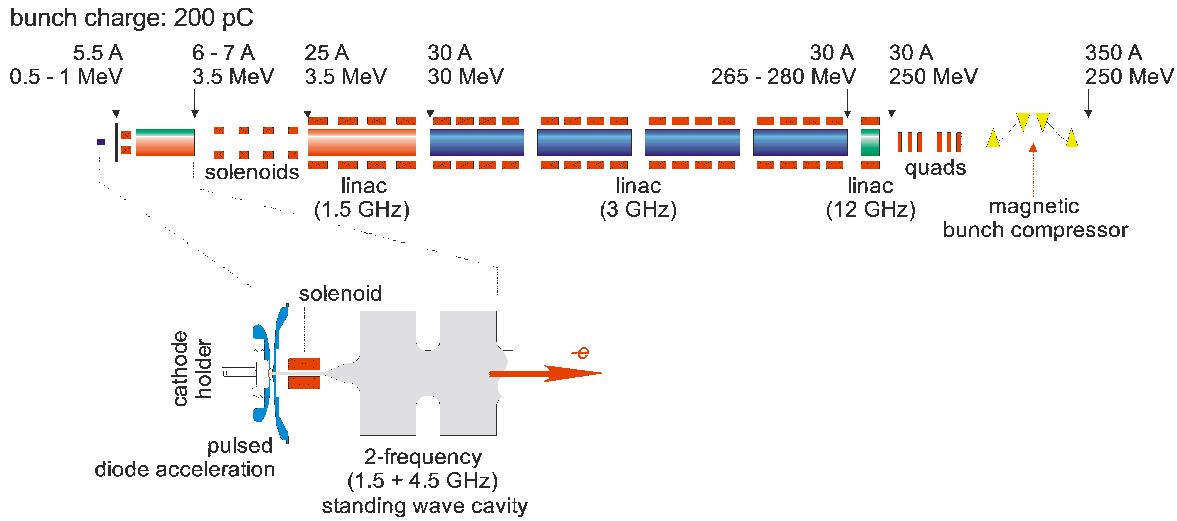

Figure 5: Layout of the 250 MeV injector facility (top) with a detailed sketch of the first accelerating elements (bottom). Target beam currents and energies along the machine are indicated.

running at 3 GHz. Afterwards, a 12 GHz harmonic cavity linearizes the phase space before further bunch compression takes place in the magnetic chicane. Here, an energy of 250 MeV and a peak current of 350 A are reached. At this stage of acceleration, space charge essentially no more influences the electron beam.

After the injector, the beam will be further accelerated to ∼6 GeV, always using normal conducting RF technology (mainly S-band). Another magnetic bunch compressor assures the peak current of 1.5 kA needed for the PSI-XFEL. At the entrance of the 30 m long undulator, a target slice emittance not larger than ε_n = 0.2 mm mrad must be realized.

250 MEV INJECTOR FACILITY

In order to experimentally verify the low emittance accelerator concept described above, a 250 MeV injector facility will be built and operated at PSI in the years 2008–2011. The detailed setup of the 250 MeV injector is described in [6]. Figure 5 represents a schematics of the machine and its space charge dominated beam optics.

If successful, the 250 MeV machine should then serve as injector for the cost-effective 6 GeV PSI-XFEL. The proposed installation of the 250 MeV injector building and the XFEL infrastructure on the PSI site (close to the SLS) is illustrated in figure 6.

Beam dynamics simulations of the complete 250 MeV injector facility have been done using different tools [7]: envelope tracking codes (`HOMDYN` [8], `BET` [9]) and particle codes (e.g. `IMPACT-T` [10]). The simulation results show the feasibility of the accelerator concept: bunch compression and emittance preservation can be realized. As an example, figure 7 represents the emittance growth in the accelerator calculated with `HOMDYN`. The energy distribution along the bunch as well as the current profile at the end of

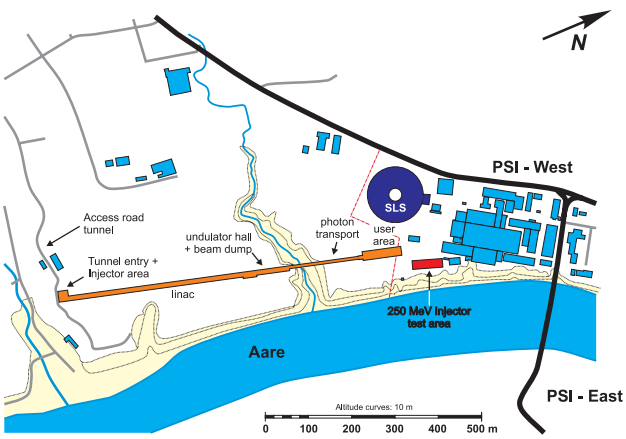

Figure 6: Site plan of the PSI-West area with the planned infrastructure for 250 MeV injector (red) and PSI-XFEL (orange).

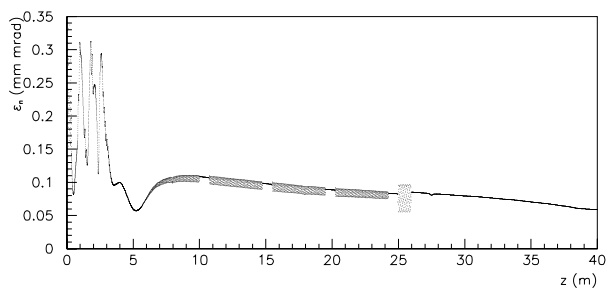

Figure 7: `HOMDYN` calculations of projected emittance growth along the 250 MeV injector.

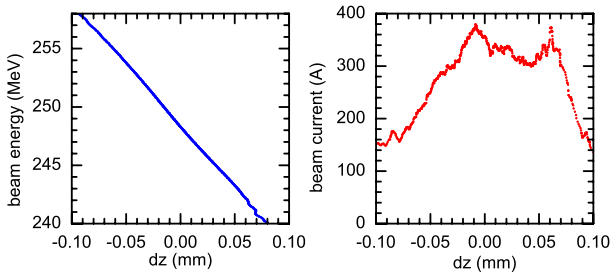

Figure 8: Slice energy distribution (left) and current profile (right) after the bunch compressor at z=40 m.

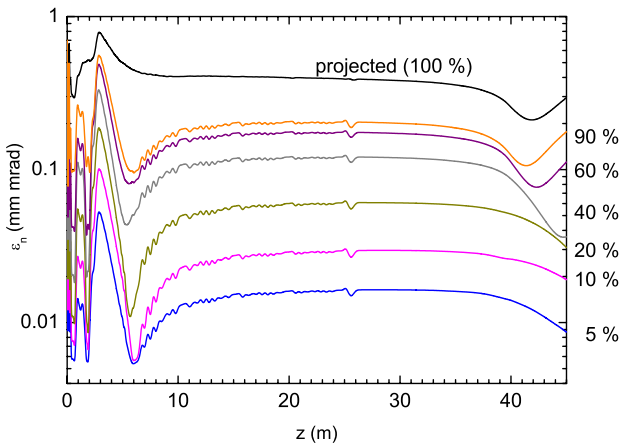

Figure 9: Slice emittance growth as calculated with BET.

the 250 MeV injector are presented in figure 8. Figure 9 shows slice emittances for various slice sizes as simulated with BET (an envelope code based on HOMDYN). These kind of 1D simulations are currently verified by a full 3D simulation of the 250 MeV injector [6].

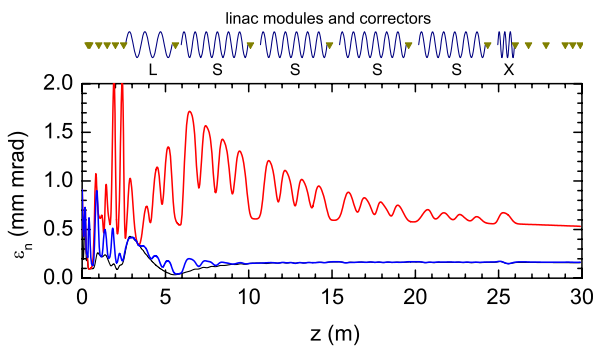

Figure 10: Misalignment studies for the 250 MeV injector: random offsets of beamline elements with $\sigma = \pm 70\mu$m result in an emittance growth due to dispersion (red), but orbit correction (blue) can bring back the emittance to the ideal value (black). On top of the plot, the accelerating structures as well as the position of the corrector coils are depicted.

In addition to beam dynamics simulations for optimizing accelerator components and beam optics, basic tolerance and alignment studies were done using the BET code [3]. For the first beamline elements (pulsed diode, solenoid, two-frequency cavity), the tolerance requirements are fairly stringent: according to the simulation results, relative field variations below 5×10^{-3} have to be realized. For the elements further downstream, the requirements are more relaxed.

Misalignment studies show that the beamline element positioning is not critical: beam orbit correction using steerers brings the emittance back to the ideal value (case of perfect alignment), see figure 10.

SUMMARY AND OUTLOOK

The PSI-XFEL concept is based on new technologies such as field emission, high gradient acceleration, and a two-frequency cavity, which are currently under development. In order to prove the sophisticated bunch compression scheme and the transport of low emittance beyond the space charge dominated regime, a 250 MeV injector facility will be built. Its successful operation will allow the construction of an Angstrom range cost-effective XFEL at PSI in the time period 2011 – 2016.

REFERENCES

[1] S.C. Leemann et al., Beam characterization for the field-emitter-array cathode-based low-emittance gun, Phys. Rev. ST Accel. Beams 10 (2007) 071302.

[2] R. Ganter et al., Nanosecond field emitted and photo-foield emitted current pulses from ZrC tips, NIM A 565 (2006) 423-429.

[3] Conceptual Design Report of the 250 MeV injector for the PSI-XFEL, under preparation.

[4] E. Kirk et al., Development of All-metal Field Emitter Arrays for high Current Applications, Proceedings International Vacuum Electronics Conference 2007, Kitakyushu, Japan.

[5] K. Li et al., A two-frequency rf cavity for the PSI-XFEL: design and beam dynamics simulations, Proceedings International Workshop on Frontiers in FEL Physics and Related Topics 2007, Elba island, Italy.

[6] Th. Schietinger et al., Beam Dynamics of the 250 MeV Injector Test Facility, Proceedings PAC 2007, Albuquerque, USA.

[7] R. Bakker, Ultra high brightness accelerator design, Proceedings FEL 2006, Berlin, Germany.

[8] M. Ferrario, HOMDYN user guide, available at *https://projects.astec.ac.uk/Plone/astec/Software/HOMDYN/*HOMDYN%20User%20Manual.pdf.

[9] R. Bakker, PSI in-house development.

[10] S. Lidia et al., Phys. Rev. ST Accel. Beams 9 (2006) 044204.

HIGH ORDER MODE ANALYSES FOR THE ROSSENDORF SRF GUN

V. Volkov, BINP, Novosibirsk, Russia
D. Janssen, FZD, Dresden, Germany.

Abstract

High Order Modes (HOM) excited by the beam in a superconducting RF gun (SRF gun) could destroy the quality of the electron beam. This problem is studied on the base of frequency domain description by considering of the equivalent RLC circuit contour for each HOM, periodical excited by a pulsed current source [1].

Expression for the voltage, the field amplitude and the phase of the excited HOM has been obtained. The equations for the coupling impedances of monopole TM-HOM and TE-HOM in the RF gun cavity has been derived. In this calculation the change of the particle velocity due to acceleration is taken into account.

Resonance frequencies, coupling impedances, unloaded and external quality factors, excitation voltages and field distributions for each HOM including trapped HOM are calculated for Rossendorf SRF gun up to the frequency of 7.5 GHz, using the complex field solver CLANS. The dependence of the calculated parameters from a cavity deformation has been studied.

The influence of the seven most dangerous HOM on the beam quality has been estimated by particle tracking using the ASTRA code.

DERIVATION OF THE THEORY

In the following considerations the electron beam is represented by a pulsed current with the repetition round frequency Ω. The time dependence of each pulse is given by the Delta-function [2].

Excitation Voltage

The voltage $\Delta U=\omega\cdot(R/Q)\cdot q$ of each HOM is excited when a bunch pass through the cavity. It can be presented as a vector in the complex space, which rotates with the round resonance frequency ω of the HOM:

$$U_0(t)=\Delta U\cdot e^{j\omega t-\omega t/2Q_L}, \qquad (1)$$

whereas R/Q is coupling impedance of the HOM; $\omega/2Q_L$ is attenuation factor; Q_L is loaded quality factor of the HOM and q is bunch charge.

The voltage U_N is the result of N bunch-HOM interaction, where the voltage is changed each time by the amount ΔU and N phase rotation ϕ between the interaction moments. This phase angle is determined by the HOM and the bunch repetition frequency and given by $\phi=2\pi\cdot Fraction(\omega/\Omega)$. Finally for U_N one obtains:

$$U_N(t)=\Delta U e^{i\cdot(\omega t+\varphi)}\sum_{n=0}^{N}\left(e^{i\cdot 2\pi\omega/\Omega-2\pi\omega/\Omega\cdot 2Q_L}\right)^n. \qquad (2)$$

where φ is phase angle at that time, when the bunch starts at cathode of the SRF gun. In the stationary limit $N\to\infty$ the amplitude of excitation voltage U(t) becomes constant. From (2) follows:

$$U(t)=U_N(t)\big|_{N\to\infty}=\frac{\Delta U}{1-e^{i\cdot 2\pi(\omega/\Omega)}\cdot e^{-2\pi(\omega/\Omega)/2Q_L}}\cdot e^{i\cdot(\omega t+\varphi)}, \qquad (3)$$

The time evolution of U in the complex plane is graphical represented in Fig.1.

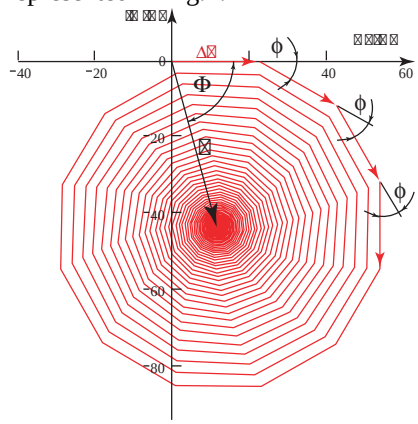

Figure 1: Evolution of excitation voltage of all bunches for low Q values of the HOM.

In the real cavity this excited voltage is equal to the change of the particle energy due to the interaction with the HOM field

$$U\equiv\int dW/e, \qquad (4)$$

whereas W is the change of the kinetic particle energy which can be measured in an experiment.

TM-HOM Excitation by Accelerated Beam

The energy exchange between the HOM and the particles moving through the cavity is defined as:

$$dW=\frac{1}{m\gamma}\cdot\left(dP_\theta\cdot P_\theta+dP_r\cdot P_r+dP_z\cdot P_z\right)=\frac{1}{m\gamma}\cdot\left(d\vec{P}\cdot\vec{P}\right) \qquad (5)$$

Here P_z, P_θ, P_r are particle momentum components which commonly depend from the accelerating and focusing fields in the cavity; The components of the $d\vec{P}$ are the momentum transfer due to the HOM-particle interaction. They are given by:

$$d\vec{P}=e\cdot\vec{E}\cdot dt+\frac{e}{m\gamma}\cdot\left[\vec{P}\times\vec{B}\right]\cdot dt, \qquad (6)$$

whereas e and m are the electron charge and the electron mass respectively, γ is relativistic factor, E and B is the electric and magnetic RF field of the HOM.

For the monopole TM HOM field at cavity axis the equations B=0; $\bar{E}=E_z(z)\cdot\sin(\omega t+\varphi)$ are hold. From (4) and (5) follow:

$$U=\int_0^T E_z(z)\cdot\sin(\omega t+\varphi)\cdot\beta(t)c\cdot dt \qquad (7)$$

The integration interval T is the time of HOM-particle interaction. $E_z(z)$ is the electric field distribution of the HOM on the cavity axis; β(t) and z=z(t) are the particle velocity and its coordinate determined by the acceleration

and can be obtained from (6) if $\bar{E}$ and $\vec{B}$ are the accelerated and focusing fields. The phase φ must be equal to phase of excited HOM when a multiple harmonics n·Ω of the repetition is equal to the HOM frequency ω. In that case U has the maximal possible value. By this consideration and using (7) we obtain for U and φ

$$U=\sqrt{\left[\int_0^T E_z(z)\cdot\sin(\omega t)\cdot\beta c\cdot dt\right]^2+\left[\int_0^T E_z(z)\cdot\cos(\omega t)\cdot\beta c\cdot dt\right]^2} \quad (8)$$

$$\varphi=\arctan\left[\int_0^T E_z(z)\cdot\sin(\omega t)\cdot\beta(t)dt\Big/\int_0^T E_z(z)\cdot\cos(\omega t)\cdot\beta(t)dt\right] \quad (9)$$

dJ = dq·U – exchanging of HOM field saved energy with the particle energy according to energy balance;

dU = ω(R/Q)·dq – HOM voltage excited by the particles in the equivalent circuit;

From previous follow dJ=U·dU/ω(R/Q), integration gets:

$$R/Q=\frac{U^2}{2\omega J} \quad (10)$$

The R/Q values of the Rossendorf SRF gun calculated for different accelerating gradients are presented in table 1. Its values are decreased for a low accelerating gradient.

Excitation of the TE Mode by Accelerated Beam

The TE mode has only one field component $\bar{E}\equiv E_\theta$, which is responsible for the energy transfer between beam and HOM field. Therefore from (4) and (5) follows:

$$dW=\frac{e}{m\gamma}\cdot(\vec{P}\cdot\vec{E})\cdot dt+\frac{e}{(m\gamma)^2}\cdot(\vec{P}\cdot[\vec{P}\times\vec{B}])\cdot dt=\frac{e}{m\gamma}\cdot P_\theta\cdot E_\theta\cdot dt \quad (11)$$

$P_\theta/m\gamma$ is the azimuthally velocity component. It is only different from zero in the present of an external magnetic field. Only in this case the TE HOM can be excited. Therefore we propose the feed of a second TE mode with the axis field $B_{zo}(z,t)=B_{zo}(z)\cdot\sin(\omega_o t+\varphi_o)$. This mode has been used in [3] for focusing and emittance compensation of the electron beam. In the paraxial limit assuming r=const the pulse is given by:

$$P_\theta(t)\cong -e\cdot\frac{r}{2}\cdot B_{zo}(z)\cdot\sin(\omega_o t+\varphi_o)\cdot \quad (12)$$

We assume here $B_{zo}(z) >> B_z(z)\cdot\sin(\omega t+\varphi)$ – the field of excited TE mode. In the same approximation we obtain:

$$E_\theta=-\frac{r}{2}\cdot\frac{\partial B_z(z)\cdot\sin(\omega t+\varphi)}{\partial t}=-\frac{r}{2}B_z(z)\cdot\omega\cdot\cos(\omega t+\varphi) \quad (13)$$

From (11), (12) and (13) follows:

$$U=\frac{e}{m}\cdot\frac{r^2}{4}\cdot\omega\cdot\int_0^T\frac{1}{\gamma}B_{zo}(z)\cdot B_z(z)\cdot\sin(\omega_o t+\varphi_o)\cdot\cos(\omega t+\varphi)\cdot dt \quad (14)$$

After averaging the radius r by $\langle r^2\rangle = \rho^2/2$ we are able to calculate the coupling impedances for the TE modes using the same arguments as in the proceeding sections:

$$R/Q_{TE}=B_{\max}^2\cdot B_{o\_\max}^2\cdot\rho^4\cdot\omega\cdot f(\omega,\omega_o,\varphi_o)/2J \quad (15)$$

The expression $f(\omega,\omega_o,\varphi_o)$ is proportional to $\exp(-(\omega+\omega_o))/\gamma^2$. B_{max} and B_{o_max} are the maximum axis magnetic fields for the excited HOM and for the external focusing TE HOM respectively. Usually the values of $(R/Q)_{TE}$ are in the order of several nanoohms.

The excitation of TE HOM is possible only in the present of external magnetic field. The phase of excitation TE HOM field φ depends from phases φ_o of the external TE mode as $\sim\varphi_o$. If the resonance frequency of the external TE mode is not equal to a multiple of the repetition frequency ($\omega_o\neq k\Omega$) then these phase φ changes with the bunch number n as $\varphi(n)\sim 2\pi\cdot(\omega_o/\Omega)\cdot n$. Assuming this n dependence in the vector sum of the excited voltages (see fig.1) we find, that the voltage excitation of TE HOM can be neglected. These modes could be of interest in the presence of a static magnetic field only.

HOM OF THE ROSSENDORF SRF GUN

In the next step we have calculated the field distribution of the HOM for the 3 ½ cell gun cavity using the CLANS field solver. The external loading caused by the circuits disposed immediately after the choke (Q_{CC}); by the Cu stem surface loses (Q_{Cu}) and by the beam pipe (Q_{BP}), which is responsible for the trapped mode dumping, is taken into account. The resonance frequency, the coupling impedance, the unloaded and the three external quality factors and the field distribution for the TM monopole HOM up to 7.5 GHz has been calculated. The corresponding values are given in Tab.1. Fig. 2 shows the field pattern of a trapped TM HOM with the mentioned three loads.

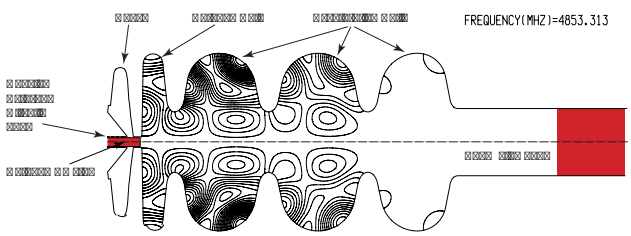

Figure 2: The 3 ½ cell cavity of the SRF gun with the field pattern of a trapped TM HOM.

These loads are simulated by low conducting materials with ε=1, μ=1, $tg\delta_\varepsilon$=1.5, $tg\delta_\mu$=1.5. All incident RF power is dissipated without of any reflecting.

The unloaded quality factor Q_o is equal G/R(f), where G is geometry factor of the HOM; $R(f)=R_{1300}\cdot(f/1300MHz)^2$ is the niobium surface resistance with R_{1300}=23.2 nOhm at a temperature of 2K.

The cathode Cu stem surface resistance is defined as $R_{Cu}(f)=2\pi\cdot(10^{-7}\cdot f/\sigma_{77K})^{1/2}$, where $\sigma_{77K}=5.4\cdot10^8$ 1/Ohm·m is specific conductivity of copper at 77K.

Now we are able by means of (3) to calculate the excitation voltage U in dependence on the repetition frequency Ω. The result is given in Fig. 3. The upper part contains the pass band modes. The repetition frequency Ω = 26 MHz is far from the resonance condition and the excitation voltages for the HOM are lower than 25V. Also in the lower part of the picture no harmonics of 26 MHz is close to a HOM frequency.

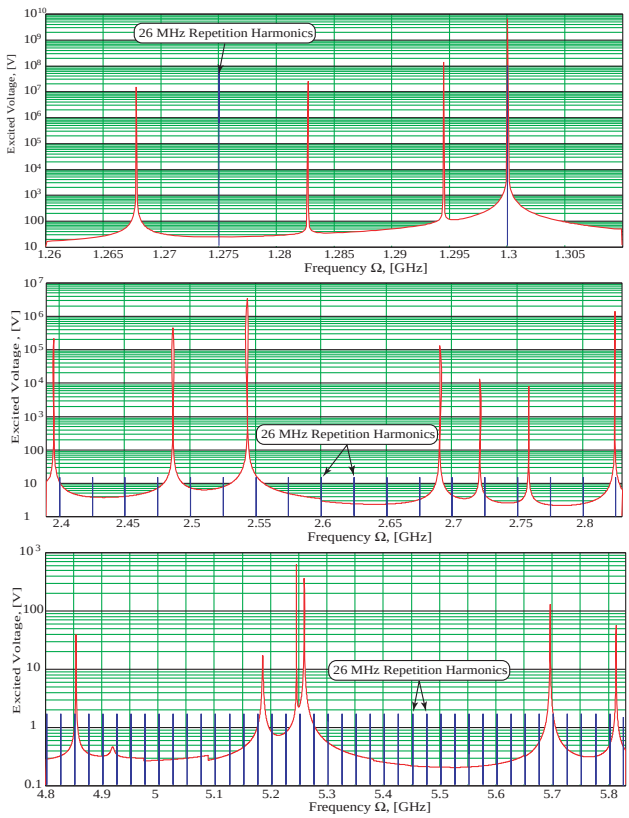

Figure 3: The voltages of the TM HOM.

Table1: Field parameters of the HOM. Trapped HOM marked by blue color. $1/Q_L = 1/Q_o + 1/Q_{CC} + 1/Q_{Cu} + 1/Q_{BP}$.

ω/2π MHz	Q_L	Q_o	R/Q, Ohm		
			β=1	E=25	E=12.5
1268	2.61e8	6.16e9	29.5	21.8	14.55
1283	3.65e9	9.98e9	4.35	2.98	1.694
1294	6.78e9	9.01e9	13.3	9.15	5.196
1300	9.35e9	1.0e10	168.6	170.2	171.2
2395	2.16e8	4.93e9	8.07	8.05	7.948
2487	1.13e7	4.27e9	16.8	12.6	9.957
2544	4.44e7	4.39e9	21.0	20.0	18.94
2690	7.36e6	4.67e9	5.86	5.82	4.536
2721	1.95e6	5.09e9	3.11	2.49	1.706
2758	1.63e6	5.43e9	1.55	1.28	1.243
2824	6.52e7	3.26e9	18.5	11.0	5.395
4043	4273	2.78e9	1.48	1.16	1.086
4853	4.48e4	2.36e9	3.49	1.27	0.22
5184	6631	2.35e9	0.87	0.89	0.641
5244	8.06e5	1.9e9	7.66	2.59	0.195
5257	9.07e6	2.22e9	1.66	1.14	1.383
5694	7.34e4	1.11e9	9.17	3.22	0.713
5811	3.63e7	1.57e9	4.13	1.57	0.291
5944	2.92e4	1.58e9	0.39	0.38	0.358
5992	745.4	2.57e9	1.21	0.89	0.657
6077	6.77e4	1.67e9	0.29	0.18	8.7e-2
6128	5060	1.83e9	0.44	0.37	0.253
6668	1.62e4	1.69e9	2.47	0.25	6.7e-3
7131	3.47e4	1.00e9	0.46	0.22	3.4e-2
7213	1.38e5	1.23e9	0.73	0.34	0.105
7467	4464	1.69e9	29.5	21.8	14.55

DEPENDENCE OF THE HOM SPECTRUM FROM THE CAVITY SHAPE DETUNING

In this section we examine the stability of the obtained result by a simple model. SRF gun is equipped by the mechanism allowing detuning of main resonance frequency of 1300 MHz. The detuning is being due to changing of total length of 3.5 cell cavity. We change the cavity shape by changing the inclination of the straight parts of the cavity cells marked by red colour in Fig.4.

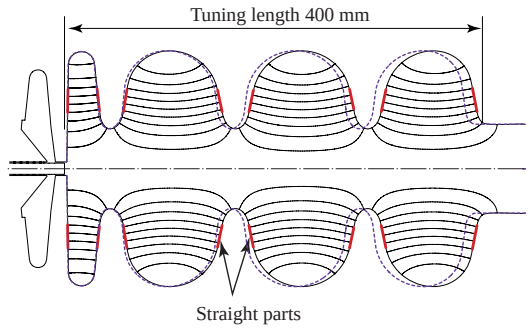

Figure 4: Change of the cavity shape.

Together with the cavity shape changes the HOM frequencies ω and loaded quality factors in dependence of the length variation δ. For a given repetition rate the voltages of (3) are also function of δ. In Fig.5 we plot the sum of all HOM voltages for different repetition rates and constant current

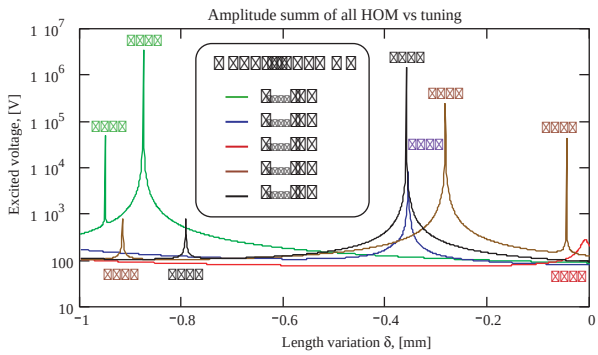

Figure 5: Amplitude sum of all TM HOM excited by 2 mA beams with different repetition frequencies. f_{1300} is accelerating mode frequency changing versus δ.

Again we obtain typical resonance behavior. But in this case the HOM voltages can achieve several MV if a HOM frequency ω approaches to a harmonics of the repetition frequency. This result shows that a certain HOM can destroy the beam quality at a special cavity shape or cavity length and a special repetition rate. We can avoid these approaches by switching between different repetitions frequencies.

In the table 2 the change of HOM parameters in 3.5 cell SRF gun cavity versus of –1 mm detuning is presented. The loaded quality factors changes significantly. It shows the high sensitivity of the trapped HOM with respect to the cavity deformation.

Table 2: The change of HOM parameters in the 3.5 cell SRF gun cavity at δ=–1 mm.

ω/2π, MHz	Δ ω/2π, MHz	ΔQ/Q, %	ΔR/Q, Ohm
1268	-0.72	-4.01	0.05
1283	-0.72	-5.388	0.046
1294	-0.68	-3.958	0.87
1300	-0.66	-0.465	-0.7
2395	0.86	1.431	0.054
2487	1.05	-0.0088	-0.01
2544	1.29	-1.075	-0.22
2690	0.63	-0.6233	-0.017
2721	0.73	-1.786	0.016
2758	0.91	-2.017	0.007
2824	0.76	-0.848	-0.07
4043	1.34	-32.98	-0.039
4853	2.21	-5.549	-0.011
4918	2.15	-2.612	-0.0158
5184	6.79	25.23	0.093
5244	5.23	5.901	-0.202
5257	4.17	-94.95	0.052
5694	2.56	1.148	-0.162
5811	9.36	15.88	0.274
5944	1.56	9.594	-0.0224
5992	3.89	-17.51	0.016
6077	1.31	-30.89	-0.0133
6128	1.96	2.292	0.00468
6668	7.02	405	-0.0075
7131	0.69	-0.9913	-0.001
7213	1.71	38.85	-0.0113
7467	2.9	-3.586	0.0028

THE INFLUENCE OF THE HOM ON THE BEAM PROPERTIES

The influence of HOM on bunch properties has been estimated by particle tracking using the ASTRA code. For this purpose the field of the seven most dangerous HOM was added separately in ASTRA input file.

Bunch charges of 77 and 308 pC, an accelerating field of 12.5 MV/m and a laser spot size of 4 mm with σ=3.5 ps Gaussian temporal distribution has been used in the calculations.

In the first step the optimal values of the launch phase and the field strength of a focusing solenoid disposed after the RF gun are determined by the emittance minimization without HOM fields. In the next step the influence of the HOM with an axis field E_{max}=1 MV/m is calculated. The results are presented in table 3. The values $\Delta\varepsilon$ and $\Delta\sigma_w$ are the changes of the emittance and the energy spread with respect to the undisturbed values.

It is interesting, that for certain HOM and for certain E_{max} values the transverse emittance decreases. The energy spread is always diminishing. In figure 6 the emittance and energy spread dependencies from excited voltage are shown for 2824 MHz HOM.

Table 3: Influence of TM HOM for E_{max}=1 MV/m on the beam properties.

ω/2π	77 pC			308 pC		
	Δε, %	$\Delta\sigma_w$ %	U, KeV	Δε, %	ΔW, %	U, KeV
2395	1.65	-0.37	32.7	1.11	-4.12	32.7
2543	2.27	-0.85	48.5	2.29	-5.46	48.3
2824	-11.7	-14.5	132*	0.93	-14.4	19.
4853	-0.8	-4.14	5.3	0.02	-4.8	5.11
5693	-1.11	-5.88	6.63	2.31	-7.11	6.13
5811	1.33	-6.82	6.01	0.39	-5.05	5.75
5992	1.33	0.29	6.88	3.58	0.33	6.69
Without HOM	ε, μm	σ_w, KeV	-	ε, μm	σ_w, KeV	-
	0.46	17.9	-	1.47	24.5	-

* The excitation corresponds to minimum of emittance at E_{max}=7.72 MV/m

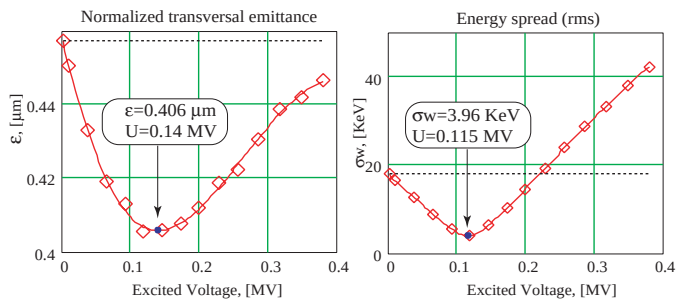

Figure 6: Emittance and energy spread versus excited voltage of the 2824 MHz HOM.

CONCLUSION

At a repetition (cw) frequency of 26 MHz the monopole TM-HOM of the 3 ½ cell SRF gun cavity have no influence on the beam quality. But a relatively small deformation of the cavity can change the situation drastically. In order to avoid this situation it would be useful to have a possibility to change the repetition frequency in a dedicated area.

It is very interesting that for a specific parameter field the excitation of special monopole TM-HOM improve the beam quality.

REFERENCES

[1] Fernando Sannibale, Collective effects. Single and Multibunch Instabilities. Fundamental Accelerator Theory, Simulations and Measurement Lab – Arizona State University, January 16-27, 2006.

[2] This method is successfully used in the practice of BINP by V.M. Petrov et al., Novosibirsk, Russia.

[3] Superconducting RF gun cavities for large bunch charges. V. Volkov, K. Floettmann, D. Janssen. PAC07, 2007.

FEL POTENTIAL OF THE HIGH CURRENT ERLS AT BNL *

D. Kayran#, I. Ben-Zvi, V. N. Litvinenko, E. Pozdeyev,
Brookhaven National Laboratory, Upton, NY, USA,
A.N. Matveenko, O.A. Shevchenko, N.A. Vinokurov,
Budker Institute of Nuclear Physics, Novosibirsk, Russia.

Abstract

An ampere class 20 MeV superconducting Energy Recovery Linac (ERL) is under construction at Brookhaven National Laboratory (BNL) [1] for testing concepts for high-energy electron cooling and electron-ion colliders. This ERL prototype will be used as a test bed to study issues relevant for very high current ERLs. High average current and high performance of electron beam with some additional components make this ERL an excellent driver for high power far infrared Free Electron Laser (FEL). A possibility for future up-grade to a two-pass ERL is considered. We present the status and our plans for construction and commissioning of the ERL. We discus a FEL potential based on electron beam provided by BNL ERL.

INTRODUCTION

The R&D ERL facility at BNL aims to demonstrate CW operation of ERL with average beam current in the range of 0.1-1 ampere, combined with very high efficiency of energy recovery. The ERL is being installed in one of the spacious bays in Bldg. 912 of the RHIC/AGS complex.

The ERL R&D program is pursued by the Collider Accelerator Department (C-AD) at BNL as an important stepping-stone for 10-fold increase of the luminosity of the Relativistic Heavy Ion Collider (RHIC) using relativistic electron cooling of gold ion beams with energy of 100 GeV per nucleon. Furthermore, the ERL R&D program extends toward a possibility of using 10-20 GeV ERL for future electron-hadron/heavy ion collider, eRHIC [2].

These projects are the driving force behind the development of ampere-class ERL technology, which will find many applications including light sources and FELs.

The intensive R&D program geared towards the construction of the prototype ERL is under way: from development of high efficiency photo-cathodes [3] to the development of new merging system compatible with emittance compensation [4].

LAYOUT OF THE R&D ERL

Two operating modes are envisaged, namely the high current mode and the high charge mode. The high current (0.5 A) mode will operate electron bunches with lower normalized emittance, 0.7 nC charge per bunch at 703 MHz rep-rate. In this case, the full energy of electrons at gun exit is limited by the available RF power 2.5 MeV. In high charge mode electron beam will consist of bunches with charge up to 5nC per bunch at 10MHz repetition rate, 50 mA average current. The electrons energy at the exit of the gun can be pushed upto 3.0-3.5 MeV by the maximum field attainable in the super-conducting gun itself.

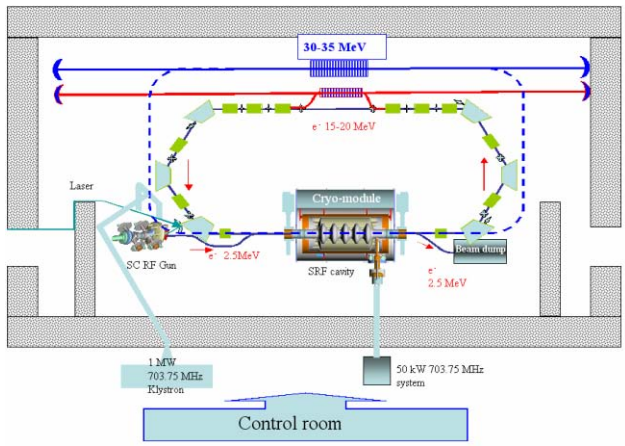

Figure1: Layout of the R&D energy recovery linac in the shielded vault with possible FEL setup. Dashed line shows considered second pass upgrade.

The ERL design (shown in Fig. 1) has one turn: electrons are generated in the superconducting half-cell gun and injected into the main superconductive linac. Linac accelerates electrons 15-20 MeV, which pass through a one turn re-circulating loop with achromatic flexible optics [5].

The photocathode is located in a high electric field for immediate acceleration of the electrons to as high energy as possible, reducing emittance degradation due to strong space charge force. Furthermore, linear part of space charge effects is compensated by applying a suitable external solenoid magnetic field.

In nominal recovery operation regime the path-length of the loop provides for 180 degrees change of the RF phase, causing electron deceleration (hence energy recovery) down to injection energy. The decelerated beam separates from the higher energy beam and goes to the beam-dump.

ERL Injector

The electron injector is a central part of any ERL that has to deliver high brightness electron beam. The BNL R&D ERL injector (see Fig. 2) consist of ½ cell superconducting RF gun with photocathode inside, solenoid, four dipoles and two solenoids turned on in opposite direction (in order to match the electron beam with linac entrance more accurately). The 4th dipole mergers the high and low energy beams.

* Work performed under the auspices of the US Department of Energy
# dkayran@bnl.gov

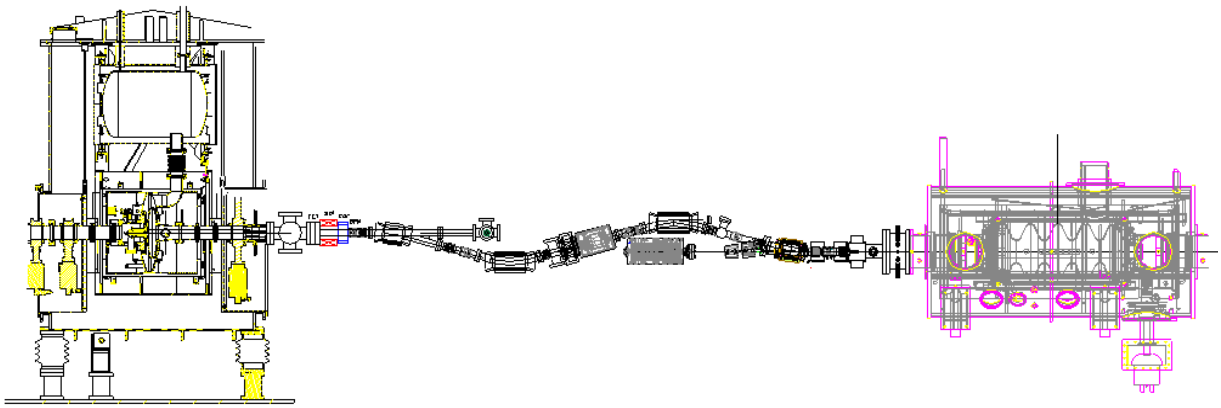

Figure 2: Detailed drawing of SRF Injector for the BNL R&D ERL.

For R&D ERL the superconducting 703.75 MHz RF (SRF) gun was selected (Fig.3). The gun design with a short 8.5 cm cell was chosen in order to provide reasonably high electric field at the cathode at this low accelerating voltage. To provide effective damping of high order mode (HOM) this gun has rather large iris radius of 5 cm. More details on the SRF gun and its photocathode system can be found elsewhere [6].

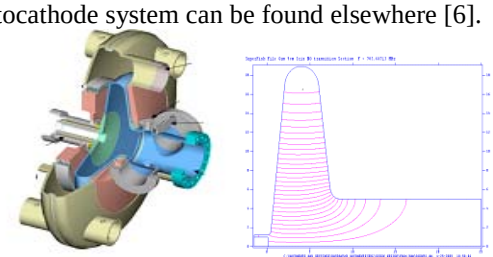

Figure 3: The SRF gun, in helium vessel (cartesy Advance Energy System) and SUPERFISH electric field profile simulation.

Merger

One of the novel systems we plan to use for the R&D ERL is a merging system providing achromatic condition for space charge dominated beam and compatible with the emittance compensation scheme [4].

Table 1: Electron beam parameters of the R&D ERL injector.

Charge per bunch, nC	0.7	1.4	5
Injection energy, MeV	2.5	2.5	3
Max. beam energy, MeV	20	20	20
Average beam current, A	0.5	0.5	0.05
Bunch rep-rate, MHz	700	350	9.38
Normalized emittance ex/ey, μm	1.4/1.4	2.2/2.3	4.8/5.3
Rms energy spread, %	0.35	0.5	0.97
Rms bunch length ps	18.5	21	31

Focusing of the bending magnets in the merging section has significant effect on the low energy electrons. Different focusing in vertical and horizontal planes (astigmatism) makes impossible simultaneous emittance compensation. Hence, the use of combined function magnets [7] with equal focusing strength in x- and y-direction is necessary.

Fig. 4 shows result of PARMELA [8] simulations of the ERL injector for different charge per bunch. Due to the bends in vertical direction the effect of vertical emittance growth is clear. But at the exit of Z-merger both: vertical and horizontal emittances become almost equal. In case of 5 nC per bunch this equality is broken, the next order nonlinearity start playing a role.

The main expected electron beam parameters of this system obtained by PARMELA simulations are listed in Table 1.

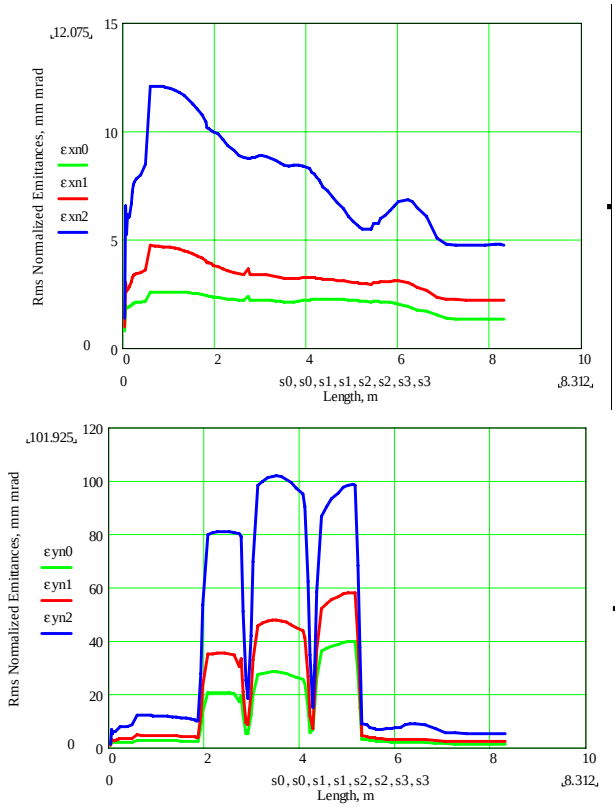

Figure 4: Evolution of normalized beam emittances (top figure – horizontal, bottom figure- vertical) in the ERL injector. Bunch charge: 0.7 nC-GREEN, 1.4 nC- RED, 5nC –BLUE.

5-cell SRF linac

The heart of the ERL facility is 5-cell SRF linac, which is designed for operating with ampere-class CW beam current [9]. The cavity was designed as a "single-mode" cavity, in which all Higher Order Modes (HOMs) propagate to HOM ferrite absorbers through the large beam pipe. This design provides for very low Q's for HOMs and hence very high ERL stability. Measurements of the damped Q and R/Q of the HOMs and simulations show that in nominal operation regime the cavity is stable to over 20 amperes in a one pass ERL and over 2 amperes for two passes ERL.

Figure 5: The ERL cavity following BCP at JLab.

We plan to intentionally tune the lattice of the ERL to a special mode to test the TDBBU predictions for our SRF linac with current limited only to few hundreds of milliamps.

The cavity was built by AES and is undergoing chemistry at Jefferson Laboratory. Figure 5 shows the cavity at JLab after the first BCP. The 5-cell SRF linac built by AES and is planned to be installed and tested in Bldg. 912 this year.

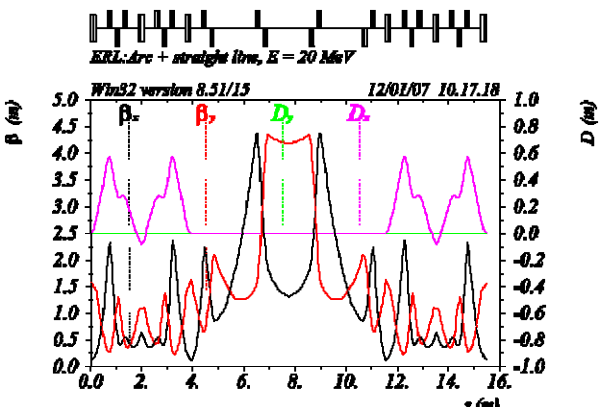

Figure 6: Lattice β and D functions of the R&D ERL for the case of zero longitudinal dispersion $D_s = m_{56}$. The m_{12} and m_{34} elements are controlled independently using quadrupoles in the dispersion-free straight section.

Loop lattice

The lattice of the ERL loop controls the parameters of a symplectic transport matrix, which affect the stability and operation conditions of the ERL. The lattice of the loop is intentionally chosen to be very flexible for the R&D ERL to be a test-bed of new ampere-range of beam currents in ERL technology [10]. The adjustable part of the lattice has two arcs and a straight section. Each arc is an achromat with adjustable longitudinal dispersion. Quadrupoles in the dispersion-free straight section provides for matching of the β-function and for choosing the desirable phase advances independently in horizontal and vertical planes. The lattice functions for isohronus operation regime are shown in Fig.6. The PARMELA tracking result for 0.7 nC per bunch from the cathode to the dump are shown in Fig.7 and Fig. 8.

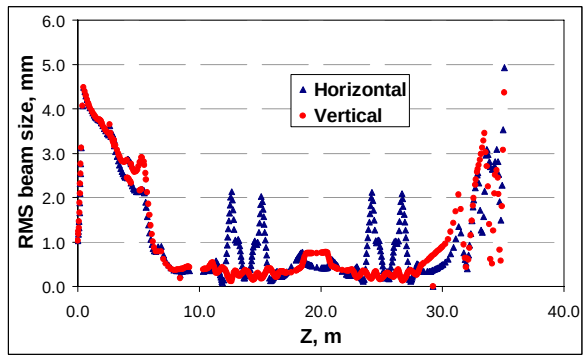

Figure 7: RMS beam size evolution from the cathode to the beam dump as a PARMELA tracking (Q=0.7 nC per bunch).

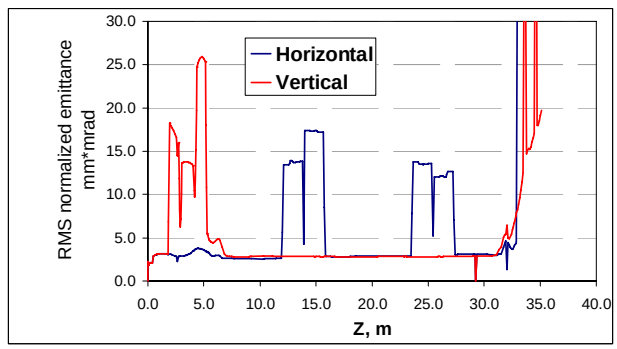

Figure 8: RMS normalized emittances evolution from the cathode to the beam dump as a PARMELA tracking (Q=0.7 nC per bunch).

The PARMELA simulation demonstrates what after the acceleration to 20 MeV the emitances are preserved (Fig. 8). There are effective horizontal emittance jumps due to nonzero dispersion inside the banding arcs. However in dispersion free straight section vertical and horizontal emittances are equal again.

Beam dump

After a cycle of acceleration and deceleration back to the injection energy 2.5 MeV electron beam goes to beam dump. The beam dump has bullet like shape inside with full water cooled jacket around. This beam dump is an exact copy of that is used for 1MW klystron water cooled collector and this beam dump can accept electron upto 2 MW avrage power CW. In order to avoid very hot spots on a surface of the beam dump the electron beam is over focused by short focal length solenoid. The result of simulation shows on Fig 9 what maximum power density is less 200 W/cm^2.

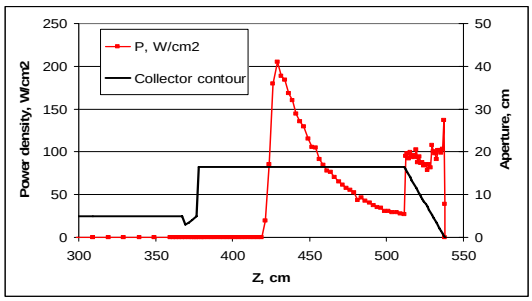

Figure 9: Power density distribution of 1 MW electron beam in the beam dump.

FEL POTENTIAL OF THE R&D ERL

The availability of high current electron beam with low emittance (see Tab. 1) opens new perspective of using BNL R&D ERL as an electron beam provider for free electron laser. The simplest upgrade is to install in the dispersion free straight section bypass with one undulator and mirrors from both side. For shorter wavelength we consider the potential extension of this facility into two turn configuration and installation of IR FEL. The shielded vault is designed for ERL with maximum energy of 54 MeV to accommodate these future up-grades. The loop of the ERL is designed to accommodate large energy spread of electron beam in the case of operating a 100 kW CW FEL [10].

An other option to use the high power electron beam in optics-free (ring [11]) FEL. The simple schematic of such type of FEL layout is shown in Fig. 10. There are two undulators in straight section and isochronous 360 degrees bend. Radiation from the second undulator (amplifier) produces energy modulation of the new coming beam inside the first undulator (modulator). The isochronous bend delivers the modulated electron beam in the amplifier. One of the big issues is to preserve microbunching structure of the electron beam during the 360 degrees turn.

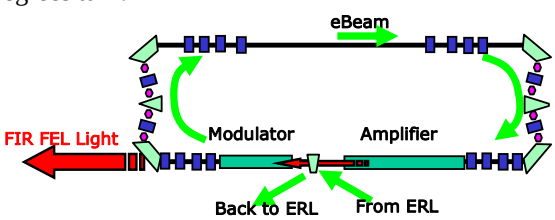

Figure 10: Schematic layout of optics free FEL

For 5 cm undulators period and 0.7 nC electron beam (Tab. 1) at rep. frequency 9.38 MHz the GENESIS [12] simulation gives: wavelength 29 microns, peak power 2 MW and average power 400 W. For full current mode operation rep. rate 703.75 MHz we obtain 30 kW far infrared in CW mode.

CONCLUSSIONS

We are designing, constructing, and commissioning a small (about 20 meters in circumference) R&D ERL to test the key issues of amp-class CW electron accelerator with high brightness beams, required for future nuclear physics experiments at RHIC-II and eRHIC. Extensive R&D program on many novel components to be used in the ERL is under way. The prototype ERL will demonstrate the main parameters of the electron beam required for electron cooling.

This facility, planned to be commissioned in 2009, will serve as the test-bet for new range of beam parameters whose application will extend well beyond the goals set forward by Collider Accelerator Department at BNL.

The high avrage current and nice performance of the electron beam makes BNL R&D ERL opens the potential of using this machine as an electron source for kilowatts class FELs.

REFERENCES

[1] I. Ben-Zvi at al., “Extremely High Current, High-Brightness Energy Recovery Linac”, PAC2005.

[2] T. Hallman, T. Kirk, T. Roser and R.G. Milner, “RHIC II/eRHIC White Paper,” Submitted to the NSAC Sub-Committee on Future Facilities, February 15, 2003, http://www.bnl.gov/henp/docs/NSAC_RHICII-eRHIC_2-15-03.pdf

[3] Multi-Alkali Photocathode Development at BNL, A. Burrill et al., PAC2005.

[4] V.N. Litvinenko, R. Hajima, D. Kayran, NIM A 557, (2006) pp 165-175.

[5] D. Kayran et al, Optics for High Brightness and High Current ERL Project at BNL, PAC 2005, pp. 1775-1777.

[6] A. M. M. Todd et al., “State-of-the-Art Electron Guns and Injector Designs for Energy Recovery Linacs”,.PAC2005, p. 2292.
Rama Calaga, Ph.D. Thesis Stony Brook University, 2006.

[7] Wuzheng Meng et al., Unique features in magnet designs for R&D Energy Recovery Linac at BNL, PAC07 proceedings MOPAS097

[8] L. M. Young, J. H. Billen, "Parmela documentation", LA-UR-96-1835.

[9] R. Calaga et al., “High Current Superconducting Cavities at RHIC”, TUPKF078, Proceedings of EPAC-2004, Geneva, Switzerland, July 5-9, 2004

[10] V. N. Litvinenko et al., FEL 2004, p. 570.

[11] N.A. Vinokurov, O.A. Shevchenko, NIM A528 (2004) 491-496.

[12] S. Reiche, NIM A429, (1999) 243.

ELECTRON BEAM DYNAMICS UNDER COHERENT HARMONIC GENERATION OPERATION AT UVSOR-II

M. Labat, CEA Saclay - 91 191 Gif-sur-Yvette, France
C. Bruni, G. Lambert, M.E. Couprie, Synchrotron SOLEIL - 91 192 Gif-sur-Yvette, France
A. Mochihashi, M. Shimada, M. Katoh, UVSOR Facility - Okazaki, Japan
M. Hosaka, Y. Takashima, Nagoya University - Nagoya , Japan
T. Hara, RIKEN SPring-8 - Hyogo, Japan

Abstract

In the Coherent Harmonic Generation Free Electron Laser configuration, an external laser source is seeded inside a first undulator. The interaction between the electron beam and this seed induces energy modulation of the bunch, further converted into a density modulation, producing coherent radiation in a second undulator. The energy modulation enhances the energy spread of the electron bunch, converted by the machine optics into a modification of its longitudinal distribution. In the case of a storage ring FEL, the electrons are re-circulating: the same bunch keeps interacting with the seeded laser, and relaxation of the distribution is only allowed in between two laser injections. Such specific dynamics has been studied on the CHG FEL of UVSOR-II storage ring (Japan). The electron beam stored at 600 MeV is seeded using a 2.5 mJ, 1 kHz, 1.2 ps Ti:Sa laser at 800 nm wavelength, allowing radiation at 266 nm (third harmonic). A Streak Camera is used to record the evolution of the longitudinal profiles as a function of the repetition rate and average power of the seeding laser, leading to bunch lengthening and distortion dynamical analysis. It appeared that because the heating induced by the interaction remains local, the refreshment process of the electronic distribution is modified. The experimental results are compared to simulations.

INTRODUCTION

The combination of an intense fs laser with synchrotron electron beams now allows delivery of sub–ps light pulses in an extendend spectral domain: from TeraHertz [1] to X–rays [2]. The Coherent Harmonic Generation Free Electron Laser (CHG FEL) results from this assembly. In the CHG FEL [4, 5, 6], the electron beam is modulated in energy by the laser pulse, within the magnetic field of an undulator -so–called "modulator"-. Passing through a dispersive section converts this energy modulation into a density modulation, allowing in a second undulator -so–called radiator-, coherent emission at the seeding laser wavelength and its harmonics. Inversely to HGHG FEL configuration[7], the injected seed does not interact with a fresh bunch but a re–circulating synchrotron beam, which may drive degradation in time of the electronic distribution, and eventually of the output radiation properties. The effect of a ps laser pulse on an electronic distribution has already been studied in oscillator FELs physics (lasing results from the pass by pass amplification of the electrons spontaneous emission which is stored in an optical cavity). The light pulse increases the energy spread of the electron beam, the so–called bunch heating [8, 9], inducing bunch lengthening and shape distorsion [10, 11, 12, 13], until saturation is reached. Depending on the longitudinal overlap between the electrons circulating in the ring and the laser pulse in the optical cavity, the FEL can be operated in continuous or pulsed mode. In this last mode, the electron beam refreshes in between two pulses deliveries [14]. Q-switch operation of oscillator FELs gave similar results on heating dynamics and showed local effects on the electronic distribution [15, 16].

In this paper, we investigate the dynamical response of an electron bunch from a storage ring to the excitation of an external laser with shorter pulse duration (by one order of magnitude) and higher peak power, as it is the case for both Slicing and CHG schemes. A model is given for simulation of the electron-photon interaction inside the storage ring. It is then used, together with experimental results obtained on UVSOR-II CHG FEL, to understand the evolution towards saturation of the electronic distribution under the laser heating. Finally, local aspect of this interaction and its consequence on the dynamics are presented.

BEAM HEATING SIMULATION

The electron bunch distribution is simulated using a pass to pass model following the stored particles in the longitudinal phase space [18]. The initial code [13, 17] has been modified to include single pass interaction with an external laser. The evolution of the j^{th} particle at n^{th} pass is driven by:

$$\tau_{n+1,j} = \tau_{n,j} - \alpha T_0 \epsilon_{n,j} \quad (1)$$

$$\epsilon_{n+1,j} = \epsilon_{n,j} - U_0 + V_{RF,n,j} - D_{n,j} + R_{n,j} + SE + W_{mod,n,j} \quad (2)$$

with $\tau_{n,j}$ its relative longitudinal position and $\epsilon_{n,j}$ its relative normalized energy with respect to the synchronous particule. Energy variation is converted by the machine optics into a longitudinal displacement, which depends on the momentum compaction factor α and the revolution period T_0.

Along each revolution, the particule losses energy by synchrotron radiation (U_0), random emission (R) and spontaneous emission in the optical klystron (SE) [19]. D is the damping term. The interaction with the external laser

induces a maximum energy exchange of [20]:

$$\Delta\gamma_{max} = \frac{2\pi K N \lambda_0}{\gamma \lambda_{Las}} \left(J_0(\xi) - J_0(\xi)\right) a_{Las} \qquad (3)$$

where K is the deflexion parameter, N the number of undulator periods, λ_0 the undulator period, a_{Las} is the peak dimensionless potential vector of the laser electric field, $\lambda_{Las} = 2\pi c/\omega_{Las}$ its wavelength, γ the Lorentz factor, c the light speed, J the Bessel function and $\xi = \frac{K^2}{4(1+K^2/2)}$. Since the electric field experienced by the j^{th} electron depends on its relative position $\tau_{n,j}$ and phase Φ_j, the laser induced energy change is:

$$W_{mod,n,j} = \frac{\Delta\gamma_{max}}{\gamma}\, exp(-\frac{\tau_{n,j}^2}{2\sigma_{Las}^2})\, sin(\omega_{Las}\tau_{n,j} + \Phi_j) \qquad (4)$$

with σ_{Las} the laser pulse duration. This term is set to zero if nT_0 is not a multiple of the laser period. Finally, the RF system provides an energy $V_{RF,n,j}$ to compensate the total losses and ensure equilibrium.

Thanks to this model, simulation of the electron bunch distribution evolution are performed, and compared to experimental results.

BEAM HEATING

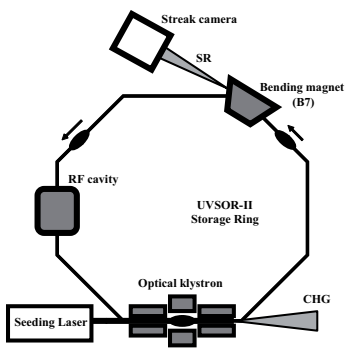

Figure 1: General scheme of the experimental setup for CHG experiment on UVSOR-II storage ring. A Ti:Sa laser is focussed inside the first part of the optical klystron. Coherent radiation (CHG) is collected at the output of the optical klystron and Synchrotron Radiation (SR) at the ouptut of B7 bending magnet for electron bunch profile measurements with a streak camera (Hamamatsu, C5680). Indeed, the distribution of the synchrotron radiation pulse is a replica of the electronic distribution.

The CHG experiments were performed on UVSOR-II [21] storage ring. A general scheme is given in Fig. 1, and the main parameters of the electron beam and laser are summarized in table 1. The intense Ti:Sa laser is focussed inside the modulator onto the electron beam. Using a mechanical light chopper, the laser is alternatively switched ON and OFF. The results are given in Fig. 2. This alternative injection drives clear oscillations of the bunch length

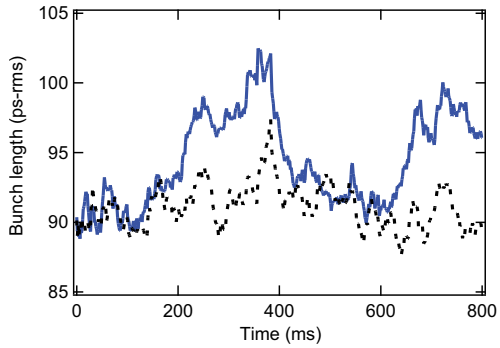

Figure 2: Bunch length measured with the streak camera. Continuous line: a mechanical light chopper at 2 Hz enables periodic laser injection (the laser is seeded during 250 ms at f_{rep} = 1 kHz, and then cut off during the following 250 ms). Dotted line: laser OFF. I = 4.8 mA. The natural bunch length at low current of this measurement is higher than expected because the RF cavity electric field was not optimised. Data are smoothed.

Table 1: Parameters for CHG operation at UVSOR-II.

	Symbol	**Value**
Electron beam		
Energy (MeV)	E	600
RF frequency (MHz)	f_{RF}	90.1
RF voltage (kV)	V_{RF}	94
Number of stored bunches	n_b	1
Period of revolution (ns)	T_0	178
Momentum compaction factor	α	0.028
Synchrotron frequency (kHz)	f_S	19.4
Damping time (ms)	τ_S	20
Natural energy spread (10^{-4})	σ_γ	3.4
Optical Klystron		
Number of periods	N	9
Spatial period (cm)	λ_0	11
Dispersive section length (cm)	L_d	33
Deflection parameter	K	6.06
Laser		
Average power (W)	P	1.5
Pulse duration (ps-fwhm)	σ_{Las}	1.2
Repetition rate (Hz)	f_{rep}	50 - 1000
Wavelength (nm)	λ_{Las}	800

at the laser injection frequency. Indeed, since bunch length can be assumed proportionnal to energy spread (operating at low current in potential well distorsion regime [22]), the bunch lengthening can be correlated to a heating of the distribution. When seeding is enabled (laser ON), the bunch length increases via laser heating (by 12 %); when seeding is disabled, the bunch length decreases back to the laser OFF value through the synchrotron damping process.

The longitudinal profile of the electron beam is then recorded with continuous seeding at 1 kHz, a standard CHG operation. At 1 mA, an increase by 12 % is measured (from 83 to 93 ps-rms), in agreement with the results of Fig. 2. The model reproduces the bunch length laser OFF at zero current, i.e. 80 ps-rms. In CHG operation (using P=1 W, f_{rep}=1 kHz and σ_{Las}=1.2 ps-fwhm), it leads to a bunch lengthening up to 107 ps-rms, a value slighlty higher than the experimental one probably because of non perfect synchronisation and alignment in the experiment.

Using 100 Hz repetition rate, still with 0.15 W seeding power, bunch lengthening could no longer be detected experimentally. Indeed, the simulated bunch length at 100 Hz repetition rate (and 0.1 W seeding power) only rises by 3.5 ps-rms, the limit of the experimental detection.

The simulations are found in good qualitative agreement with the experimental results, allowing further dynamical studies.

BEAM HEATING DYNAMICS

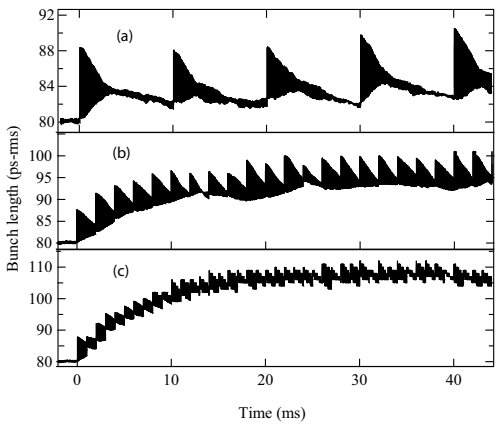

Figure 3: Bunch length evolution from laser OFF to stable CHG operation. (a) f_{rep}=100 Hz, $T_{90\%} \approx$ 20 ms, (b) f_{rep}=500 Hz, $T_{90\%}$ =18 ms, (c) f_{rep}=1 kHz, $T_{90\%}$ =14 ms. Simulation with 15000 particules and the parameters of table 1. $T_{90\%}$ is the time to reach 90% of the bunch length at saturation.

Simulation of Fig. 3 investigates the evolution of the electron beam from laser OFF initial state, to CHG operation state. When seeding is switched on, the average bunch length gradually increases, performing oscillations at the laser repetition rate, until a saturation is reached: the average bunch length becomes constant.

Whatever the simulated repetition rate, the rising time to saturation remains below 25 ms. An upper limit of the rising time of 100 ms is found using the mechanical chopper (see Fig. 2). A precise measurement would require a fast shutter (to be able to neglect rising of the seeding average power) synchronised with the streak camera acquisition. The simulated rising time decreases with f_{rep} (see Fig. 3): it is 20 ms at 100 Hz, 18 ms at 500 Hz and 14 ms at 1 kHz.

Once saturation is reached, the electronic distribution reveals a double oscillating time structure. After each laser injection, the bunch length suddenly increases, and then slowly decreases back to its value before previous injection: the bunch length oscillates at the laser repetition rate. In addition, all along CHG operation, synchrotron motion drives fast oscillations of the distribution at the synchrotron frequency.

Three levels of dynamics are found in the evolution of the electronic distribution. When the laser is injected, the electronic distribution responds to the laser periodic excitation by transiting to a pseudo equilibrium state. Once at saturation, the distribution oscillates at the laser repetition rate, refreshing in between two injections, and at the synchrotron frequency. The refreshment compensates the periodic bunch heating and allows to maintain equilibrium. In addition, the final heated state depends on the initial electron beam quality, but can also be tuned using, for instance, the seeding laser repetition rate. The bunch heating, i.e. energy spread can be controlled. This is of high interest since the coherent output power strongly depends on the energy spread at interaction [23, 24].

LOCAL BEAM HEATING

We now investigate on the local aspect of the electron-photon interaction, since the seeding laser pulse is shorter by nearly two orders of magnitude than the electron bunch. The profiles in CHG operation are simulated, and a typical example is given in fig. 4. Initially, laser is OFF and the distribution starts from Gaussian shape (a). The first injection of the laser causes a local distorsion in the center of the distribution (b): a hole appears one turn after injection and remains only for a few turns (few tens of μs). The edges of the distribution are not yet affected. Once saturation is reached (less than 25 ms later), each laser injection still induces a hole remaining just for a few turns (d), but the diffusion of the heated electrons causes a flattening of the whole distribution, and a density displacement towards the edges (c). The laser induces a local density defect in the profile, which vanishes in between two laser injections.

The electron beam phase space can be recontructed [25] in two dimensions given by the electronic density $N(\tau)$ and its derivative. In the phase space, a defect in the profile, as for instance a hole, will correspond to a large amplitude oscillation A_{hole}.

A_{hole} reduces with the repetition rate. The hole can no longer be detected at repetition rate higher than 5 kHz (and P=5W, σ_{Las}=1.2 ps-fwhm). The heated particules are diffused [13] over the whole bunch, causing strong bunch lengthening. A_{hole} increases with the pulse duration (at given repetition rate and peak power). The digged hole gets wider, still vanishing after a few turns, which eases the diffusion towards edges and causes bunch lengthening.

The laser induces a local distorsion in the distribution at

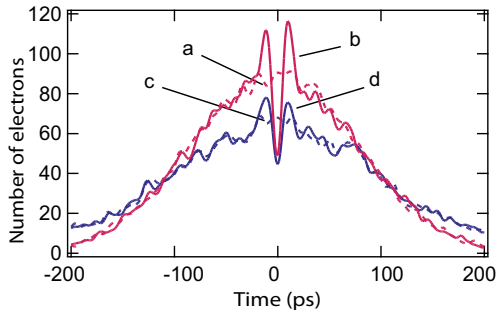

Figure 4: Simulated longitudinal profiles: (a) Laser OFF profile, (b) Profile two turns after first laser injection, (c) Profile in saturated regime 2 turns before a laser injection, (d) Profile in saturated regime two turns after a laser injection. Simulation parameters: f_{rep}=1 kHz, 4 W average power, 4.8 ps-fwhm pulse duration for the laser (optimised to produce a net hole in the distribution), 15000 particules, and other parameters of table 1

each injection which, thanks to a fast diffusion, disappears before next injection: even at saturation, the laser does not experience local density defect. On the other hand, this diffusion increases the bunch length and consequently reduces the electronic density all along the distribution. These local dynamics studies reveal that the tunability of the external laser parameters (f_{rep}, P and σ_{Las}) offers attractive perspectives of adjusting beam heating and consequently CHG ouptut power with possible optimisation between peak and average output power.

CONCLUSION

Electron dynamical response to an external short duration and intense laser has been investigated. Thanks to simulations found in agreement with experimental results obtained on UVSOR-II CHG FEL, we observed that the seeding of the laser causes -via bunch heating- a transition towards a saturated regime with double frequency oscillating structure (at the laser repetition rate and at the synchrotron frequencies). The bunch heating, and consequently the equilibrium state at saturation, can be adjusted using the laser parameters. This opens perpsectives to optimisation of the output radiation, especially in terms of peak or average power. While those results were obtained in CHG FEL configuration, they can be easily extended to any scheme involving interaction between intense electric field and stored electron beam.

ACKNOWLEDGMENTS

The authors would like to thank X. Epiard, J. Yamazaki, S. Bielawski, C. Szwaj. A part of this work was supported by Grant-Aid for Scientific Research of the JSPS and by International Collaboration Program of IMS.

REFERENCES

[1] K. Holldack, S. Khan, R. Mitzner and Quast T., Phys. Rev. Lett. 96 (2006), 054801.

[2] R.W.Schoenlein, S. Chattopadhyay, H.H.W. Chong, T.E. Glover, P.A. Heimann, C.V.Shank, A.A. Zholents and M.S. Zolotorev, Science 287 (2000), 2237.

[3] A. A. Zholents and M. S. Zolotorev, Phys. Rev. Lett. 76 (1996), 912.

[4] R. R. Freeman and B. M. Kincaid, AIP Conference Proceedings 119 (1984), p.277-292.

[5] R.Coisson and F. De Martini, Phys. of Quant. Electron. 9 (1982) 939.

[6] R.Prazeres, J.M. Ortega, C. Bazin, M. Bergher, M. Billardon, M.E. Couprie, M. Velghe and Y. Petroff, Nucl. Instrum. Methods Phys. Res. A 272 (1988), p.68-72.

[7] L.H. Yu et al., Phys. Rev. A 44 (1991) 5178.

[8] J.M.J. Madey, Nuovo Cimento Soc. Ital. Fis. 50 B (1979) 64.

[9] G. Dattoli and A. Renieri, Nuovo Cimento Soc. Ital. Fis. 59 B (1980) 1.

[10] Robinson K.E., Dissertation of the Stanford University, (1984).

[11] M.E. Couprie and P. Elleaume, Nucl. Inst. Meth. A 237 (1987) 77-82.

[12] G.L. Orlandi, C. Bruni, D. Garzella, M.E. Couprie, C. Thomas, R. Bartolini, C. Rippon and G. Dattoli, Phys. Rev. ST. 7 (2004) 060701.

[13] G. De Ninno, M.E. Couprie, D. Nutarelli, D. Garzella, E. Renault and M. Billardon, Phys. Rev. E 64 (2001) 026502.

[14] M. Billardon, D. Garzella and M. E. Couprie, Phys. Rev. Lett. 69 (1992) 2368.

[15] Litvinenko V.N. and Burnham B. and Madey J.M.J. and Wu Y., Nucl. Inst. Meth. Phys. Res. A 358 (1995) 334-337.

[16] I.V. Pinayev, V.N. Litvinenko, K. Chalut, E.C. Longhi and S. Roychowdhurry, Nucl. Inst. Meth. Phys. Res. A 528 (2004) 283-286.

[17] R. Roux and M. Billardon, Nuovo Cimento Soc. Ital. Fis. A 112 (1999) 513.

[18] M. Sands, SLAC Report No. 121 (1970).

[19] J.M.Ortega, Cours de DEA, Rayonnement des onduleurs, Universit d'Orsay, Paris XI (2004).

[20] L.H. Yu and J. Wu, Nucl. Inst. Meth. Phys. Rev. A 483 (2002) 493-498.

[21] M. Katoh et al., Proceedings of the AIP'04 Conference 708 (2004), p.49-52.

[22] G. Dattoli, L. Mezi, M. Migliorati, A. Renieri, M.E. Couprie, D. Garzella, D.Nutarelli, C. Thomas, G. DeNinno and R. Walker, Nucl. Inst. and Meth. A 471 (2001) 403.

[23] R. Prazeres, PhD. Thesis, University of Paris XI, Orsay (1988) Chap.2-3, p.27-71.

[24] J. Wu and L. H. Yu, SLAC-PUB (2004) 10494.

[25] J.D.Farmer, Chaotic attractors of an infinite-dimensional dynamical system, Physica 4D (1982), p.366.

ANALYTICAL STUDIES OF TRANSVERSE COHERENCE PROPERTIES OF X-RAY FELS

E.L. Saldin, E.A. Schneidmiller, and M.V. Yurkov
Deutsches Elektronen-Synchrotron, DESY, Hamburg, Germany

Abstract

The explicit solution of the initial value problem for a SASE FEL operating with a large ratio of electron beam emittance to the wavelength, $\hat{\epsilon} = 2\pi\epsilon/\lambda \gg 1$, is presented. The degree of transverse coherence is explicitly calculated, too. It is shown to be dependent on the ratio of the number of FEL gain lengths to the parameter $\hat{\epsilon}$. In particular, in the multi-mode limit the radiation from a SASE FEL has by the squared number of gain lengths higher degree of transverse coherence than a synchrotron radiation generated by a beam with the same emittance.

INTRODUCTION

Free electron lasing at wavelengths shorter than ultraviolet can be achieved with a single-pass, high-gain FEL amplifier. Due to a lack of powerful, coherent seeding sources short-wavelength FEL amplifiers work in so called Self-Amplified Spontaneous Emission (SASE) mode when amplification process starts from shot noise in the electron beam [1, 2, 3]. The first VUV FEL user facility FLASH ("F"ree-Electron-"LAS"er in "H"amburg) [4, 5] operates in SASE mode and produces GW-level, laser-like radiation pulses with 10 to 50 fs duration in the wavelength range 13-45 nm. Present level of accelerator and FEL techniques holds potential for SASE FELs to generate wavelengths as short as 0.1 nm [6, 7, 8].

The condition $\hat{\epsilon} < 1/2$ is often formulated as necessary one for an optimal design of a SASE FEL. It is meant that under this condition the radiation from SASE FEL has a full transverse coherence. However, as it is shown in [9], the maximal degree of transverse coherence (and brilliance as well) is achieved at $\hat{\epsilon} \simeq 1$. For smaller emittances the degree of transverse coherence decreases due to the effect discovered in [10]. Moreover, the above mentioned condition is strongly violated in the project parameters of hard X-ray FELs [6, 7, 8]: there the parameter $\hat{\epsilon}$ is in the range 2-5. Even without discussing exotic proposals [11, 12], one can notice a general trend towards lower energies of the electron beam, i.e. cost-saving solutions. Since achievable normalized emittance $\gamma\epsilon$ is limited by beam physics and technology issues, this would lead to a further increase of $\hat{\epsilon}$. Thus, theoretical understanding of properties of a SASE FEL, operating in this regime, becomes practically important. In this paper we present the main results of the theoretical analysis performed in Ref. [13] dealing with the limit $\hat{\epsilon} \gg 1$.

EIGENVALUE EQUATION

Let us have at the undulator entrance a continuous electron beam with the current I_0, with the Gaussian distribution in energy

$$F(\mathcal{E}-\mathcal{E}_0) = \left(2\pi\langle(\Delta\mathcal{E})^2\rangle\right)^{-1/2} \exp\left(-\frac{(\mathcal{E}-\mathcal{E}_0)^2}{2\langle(\Delta\mathcal{E})^2\rangle}\right), \quad (1)$$

and in a transverse phase plane

$$f(x,x') = (2\pi\sigma^2 k_\beta)^{-1} \exp\left[-\frac{x^2+(x')^2/k_\beta^2}{2\sigma^2}\right], \quad (2)$$

the same in y phase plane. Here $k_\beta = 1/\beta$ is the wavenumber of betatron oscillations and $\sigma = \sqrt{\epsilon\beta}$.

Using cylindrical coordinates, in the high-gain limit we seek the solution for a slowly varying complex amplitude of the electric field of the electromagnetic wave in the form [14]:

$$\tilde{E}(z,r,\varphi) \propto \Phi_{nm}(r)\exp(\Lambda z)e^{\pm \mathrm{i}\, n\varphi}, \quad (3)$$

where n is an integer, $n \geq 0$. For each $n > 0$ there are two orthogonal azimuthal modes and many radial modes that differ by eigenvalue Λ and eigenfunction $\Phi_{nm}(r)$. The integro-differential equation for radiation field eigenmodes [15, 16, 17] can be written in the following normalized form:

$$\left[\frac{\mathrm{d}^2}{\mathrm{d}\,\hat{r}^2} + \frac{1}{\hat{r}}\frac{\mathrm{d}}{\mathrm{d}\,\hat{r}} - \frac{n^2}{\hat{r}^2} + 2\,\mathrm{i}\,B\hat{\Lambda}\right]\Phi_{nm}(\hat{r}) =$$
$$-4\int_0^\infty \mathrm{d}\,\hat{r}'\hat{r}'\Phi_{nm}(\hat{r}')$$
$$\times\int_0^\infty \mathrm{d}\,\xi\frac{\xi}{\sin^2(\hat{k}_\beta\xi)}\exp\left[-\frac{\hat{\Lambda}_\mathrm{T}^2\xi^2}{2} - (\hat{\Lambda}+\mathrm{i}\,\hat{C})\xi\right]$$
$$\times\exp\left[-\frac{(1-\mathrm{i}\,B\hat{k}_\beta^2\xi/2)(\hat{r}^2+\hat{r}'^2)}{\sin^2(\hat{k}_\beta\xi)}\right]$$
$$\times I_n\left[\frac{2(1-\mathrm{i}\,B\hat{k}_\beta^2\xi/2)\hat{r}\hat{r}'\cos(\hat{k}_\beta\xi)}{\sin^2(\hat{k}_\beta\xi)}\right], \quad (4)$$

where I_n is the modified Bessel function of the first kind. The following notations are used here: $\hat{\Lambda} = \Lambda/\Gamma$, $\hat{r} = r/(\sigma\sqrt{2})$, $B = 2\sigma^2\Gamma\omega/c$ is the diffraction parameter, $\hat{k}_\beta = k_\beta/\Gamma$ is the betatron motion parameter,

$\hat{\Lambda}_{\rm T}^2 = \langle(\Delta\mathcal{E})^2\rangle/(\bar{\rho}^2\mathcal{E}^2)$ is the energy spread parameter, $\hat{C} = \left[k_{\rm w} - \omega/(2c\gamma_z^2)\right]/\Gamma$ is the detuning parameter, $\Gamma = \left[A_{\rm JJ}^2 I_0 \omega^2 \theta_{\rm s}^2 \left(I_{\rm A} c^2 \gamma_z^2 \gamma\right)^{-1}\right]^{1/2}$ is the gain factor, $\bar{\rho} = c\gamma_z^2\Gamma/\omega$ is the efficiency parameter, ω is the frequency of the electromagnetic wave, $\theta_{\rm s} = K_{\rm rms}/\gamma$, $K_{\rm rms}$ is the rms undulator parameter, γ is relativistic factor, $\gamma_z^{-2} = \gamma^{-2} + \theta_{\rm s}^2$, $k_{\rm w}$ is the undulator wavenumber, $I_{\rm A} = 17$ kA is the Alfven current, $A_{\rm JJ} = 1$ for helical undulator and $A_{\rm JJ} = J_0(K_{\rm rms}^2/2(1+K_{\rm rms}^2)) - J_1(K_{\rm rms}^2/2(1+K_{\rm rms}^2))$ for planar undulator. Here J_0 and J_1 are the Bessel functions of the first kind. Note that the efficiency parameter $\bar{\rho}$ is related to the corresponding parameter ρ [18] of the one-dimensional model as follows: $\bar{\rho} = \rho B^{1/3}$. The equation (4) can be reduced to the integral equation by means of the Hankel transformation [17] and then solved numerically.

Effects of emittance play the dominant role in X-ray FELs. In this paper we will mainly concentrate on the case when beta-function is optimized for the highest FEL gain as it happens in practice. Since diffraction parameter depends on beta-function, it is more convenient to go over to the normalized parameters other then those introduced above. Indeed, diffraction parameter can be rewritten as $B = 2\hat{\epsilon}/\hat{k}_\beta$, where $\hat{\epsilon} = 2\pi\epsilon/\lambda$. Then we can go from parameters $(B, \hat{k}_\beta)$ to $(\hat{\epsilon}, \hat{k}_\beta)$. In the following we will consider the case when $\hat{\epsilon} \gg 1$, the energy spread effect can be neglected, and the beta-function is optimized for the maximum growth rate. We apply the variational method [17, 19] to the Eq. (4) with the trial functions [13]

$$\Phi_{nm}(\hat{r}) = \hat{r}^n \exp(-a\hat{r}^2) L_m^n(2a\hat{r}^2)\,, \qquad (5)$$

where L_m^n are assotiated Laguerre polynomials. Solving the obtained equations [13], we find the zeroth-order eigenvalue

$$\hat{\Lambda}_0 \simeq \frac{0.3695 + 0.2735\,{\rm i}}{\hat{\epsilon}} \qquad (6)$$

for the optimal betatron wavenumber $\hat{k}_\beta \simeq 0.503/\hat{\epsilon}^2$ and at the optimal detuning $\hat{C}_0 \simeq 0.391/\hat{\epsilon}$. The diffraction parameter for this operating point is $B \simeq 3.98\,\hat{\epsilon}^3$. Then we find [13] the next order correction (in $\hat{\epsilon}^{-1}$) to the eigenvalue

$$\hat{\Lambda}_{nm} \simeq \hat{\Lambda}_0 - \frac{(1+n+2m)(0.3080 + 0.0988\,{\rm i})}{\hat{\epsilon}^2}\,, \qquad (7)$$

and the mode parameter

$$a \simeq (0.4355 - 0.5123\,{\rm i})\hat{\epsilon}\,. \qquad (8)$$

Eqs. (5), (7) and (8) are the solutions for field distributions and growth rates of eigenmodes of a high-gain FEL with optimized beta-function in the limit $\hat{\epsilon} \gg 1$. We compared these asymptotical solutions with the exact solution [17] at the optimal detuning for different modes and found a good agreement for $\hat{\epsilon} \gg 1$.

Concluding this section, we should analyze some scaling relations. The FEL gain length in the case under consideration scales as $L_{\rm g} = (\mathrm{Re}\,\hat{\Lambda}_0\Gamma)^{-1} \propto \hat{\epsilon}/\Gamma$, while the beta-function as $\beta = k_\beta^{-1} \propto \hat{\epsilon}^2/\Gamma$. In other words, the betatron phase advance per gain length, $k_\beta L_{\rm g}$, is of the order of $\hat{\epsilon}^{-1}$. The size of a radiation mode scales as $\hat{\epsilon}^{-1/2}$, and a typical change of transverse coordinates of particles during the passage of one gain length as $\hat{\epsilon}^{-1}$ in units of the electron beam size. The rms size of the intensity distribution of a fundamental mode (with $n = m = 0$) can be expressed in dimensional units as $\sigma_{rad} \simeq 1.07\sqrt{\beta\lambda/(2\pi)} \simeq 0.92\sqrt{\epsilon L_{\rm g}}$ for the optimal beta-function.

INITIAL VALUE PROBLEM

The solution of initial value problem for a SASE FEL with a parallel electron beam, accounting for diffraction effects, was obtained in [15, 20]. Initial value problem, that also includes emittance effect, was solved in [21, 22, 23] in a general form and then approximated in single-mode limit. Here we present an explicit solution [13] for a large emittance, $\hat{\epsilon} \gg 1$, and the optimal (for the growth rate) focusing, $\hat{k}_\beta \simeq 0.503/\hat{\epsilon}^2$. The normalized output power (normalized FEL efficiency) in high-gain linear regime can be expressed as [13]:

$$\hat{\eta} = \frac{\eta}{\bar{\rho}} \simeq \frac{0.0755\exp(2N_g)}{N_c\hat{\epsilon}^2\sqrt{N_g}\,[f\,(N_g/\hat{\epsilon}) - 1]} \qquad (9)$$

where η is the ratio of the radiation power to the electron beam power, $N_g = \mathrm{Re}\,\hat{\Lambda}_0\hat{z} = 0.3695\hat{z}/\hat{\epsilon}$ is the number of field gain lengths within a given undulator length, $\hat{z} = \Gamma z$, $N_c = I/(e\omega\bar{\rho})$, and the function f is given by

$$f\left(\frac{N_g}{\hat{\epsilon}}\right) = 0.419\cosh\left(1.667\frac{N_g}{\hat{\epsilon}}\right) + 0.581\cos\left(0.535\frac{N_g}{\hat{\epsilon}}\right)\,. \qquad (10)$$

Note that parameter $\bar{\rho}$ for the given operating point is related to the corresponding one-dimensional parameter [18] as $\bar{\rho} = B^{1/3}\rho \simeq 1.58\hat{\epsilon}\rho$.

The expression (9) is valid when $\hat{\epsilon} \gg 1$ and $N_g \gg 1$, but the ratio $N_g/\hat{\epsilon}$ may take any value[1]. In particular, for a sufficiently long undulator, $N_g \gg \hat{\epsilon} \gg 1$, the fundamental TEM_{00} gives the dominating contribution to the total power. In this case Eq. (9) reads

$$\hat{\eta} \simeq \frac{0.360}{N_c\hat{\epsilon}^2\sqrt{N_g}}\exp\left[2N_g(1 - 0.834/\hat{\epsilon})\right] \simeq \frac{0.36}{N_c\hat{\epsilon}^2\sqrt{N_g^{00}}}\exp(2N_g^{00})\,, \qquad (11)$$

[1] In practice the maximal value of N_g is limited by saturation effects that are not considered in the linear theory presented here. For any reasonable set of parameters $N_g < 10$ in linear regime of SASE FEL operation.

where $N_g^{00} \simeq N_g$ is the number of field gain lengths for the TEM_{00} mode. This solution is identical to that given in [23], taken in the limit $\hat{\epsilon} \gg 1$ with the optimal beta-function, and integrated over FEL frequency band. Now let us consider the multi-mode limit, $\hat{\epsilon} \gg N_g \gg 1$. In this case the radiation power (9) is expressed as

$$\hat{\eta} \simeq \frac{0.151}{N_c N_g^{5/2}} \exp(2N_g) \,. \qquad (12)$$

Relative partial contributions to the total power of modes with an azimuthal index n can be calculated as follows [13]:

$$p_0 = \sqrt{\frac{f-1}{f+1}} \qquad for \quad n=0 \qquad (13)$$

$$p_n = \frac{2\sqrt{f-1}}{\sqrt{f+1}(f+\sqrt{f^2-1})^n} \qquad for \quad n>0 \qquad (14)$$

For $n > 0$ we consider the sum of the contributions of the two independently excited azimuthal modes with the angular dependence $\exp(\pm \mathrm{i} n\varphi)$. The contribution of the azimuthal-symmetric mode goes pretty linearly for $N_g < \hat{\epsilon}$:

$$p_0 \simeq 0.5 \frac{N_g}{\hat{\epsilon}}$$

and asymptotically approaches unity when $N_g \gg \hat{\epsilon}$. Other modes have maxima of which locations can be found from the equation

$$f\left(\frac{N_g}{\hat{\epsilon}}\right) = \frac{\sqrt{n^2+1}}{n} \,.$$

Maximal partial contribution of $n-$th azimuthal mode in linear regime of SASE FEL operation is given by

$$\max(p_n) = \frac{2n^n(\sqrt{n^2+1}-n)}{(\sqrt{n^2+1}+1)^n} \qquad for \quad n>0 \qquad (15)$$

For instance, a possible contribution is limited by 34.3% for $n = 1$, by 18.0% for $n = 2$, etc. For large n a maximum is located at $N_g/\hat{\epsilon} \simeq n^{-1}$ and takes the value $\max(p_n) \simeq (ne)^{-1}$, e being the base of natural logarithm.

Especially simple relation for the partial contributions of azimuthal modes can be deduced for the point where $p_0 = p_1$. There we have:

$$p_0 = \frac{1}{3} \,, \qquad p_n = \frac{1}{2^{n-1}3} \,. \qquad (16)$$

Note that the results (15) and (16) are universal since they do not depend on a specific choice of the function f.

DEGREE OF TRANSVERSE COHERENCE

The definition of a degree of transverse coherence was introduced in [9]:

$$\zeta = \frac{\int\int |\gamma_1(\vec{r}_\perp, \vec{r}\prime_\perp)|^2 \langle I(\vec{r}_\perp)\rangle \langle I(\vec{r}\prime_\perp)\rangle \,\mathrm{d}\,\vec{r}_\perp \,\mathrm{d}\,\vec{r}\prime_\perp}{[\int \langle I(\vec{r}_\perp)\rangle \,\mathrm{d}\,\vec{r}_\perp]^2} \,. \qquad (17)$$

where $I(\vec{r}_\perp) = |\tilde{E}(\vec{r}_\perp)|^2$ is the radiation intensity,

$$\gamma_1(\vec{r}_\perp, \vec{r}\prime_\perp) = \frac{\langle \tilde{E}(\vec{r}_\perp)\tilde{E}^*(\vec{r}\prime_\perp)\rangle}{\left[\langle|\tilde{E}(\vec{r}_\perp)|^2\rangle\langle|\tilde{E}(\vec{r}\prime_\perp)|^2\rangle\right]^{1/2}} \qquad (18)$$

is the transverse correlation function, $\tilde{E}$ is the slowly varying amplitude of the electromagnetic wave, and $< \ldots >$ means ensemble average. The definition (17) is valid for any stationary (or quasi-stationary [14, 24]) random process, in particular for the radiation from a SASE FEL with a long electron bunch [14] operating in linear and nonlinear regimes.

The radiation of a SASE FEL, operating in the linear regime, holds properties of a completely chaotic polarized light [14, 24]. In this case, as it was shown in [9], the definition (17) is equivalent to that given by the variance of the instantaneous power [10, 14]:

$$\zeta = \sigma_P^2 = \frac{< (P - < P >)^2 >}{< P >^2} \,, \qquad (19)$$

where $P = \int I(\vec{r}_\perp) d\vec{r}_\perp$. The degree of transverse coherence ζ can be thought of as an inverse number of transverse modes [9, 10, 14]:

$$\zeta = \frac{1}{M_\mathrm{T}} \,. \qquad (20)$$

However, the definitions (17) and (19) cannot be directly used for the purpose of this paper, namely for analytical calculations of the degree of transverse coherence of a SASE FEL. Nevertheless, analyzing the results of numerical simulations in Ref. [9], we found out that the degree of transverse coherence according to the definition (17) is well approximated by the squared partial contribution of azimuthal-symmetric mode:

$$\zeta \simeq p_0^2 \,. \qquad (21)$$

Accuracy of this approximation is connected with the residual effect [10] on transverse coherence originated from the finite frequency bandwidth of a SASE FEL. Indeed, for a sufficiently long undulator the only fundamental TEM_{00} mode survives (other modes are exponentially suppressed), i.e. perfect transverse coherence would be achieved for a monochromatic wave. However, the amplitude and phase distributions of this mode change within the FEL bandwidth. As a result, the degree of transverse coherence approaches unity as [10]: $1 - \zeta \simeq \delta_r/N_g$ but not exponentially as in (21). A numerical factor δ_r is of the order of

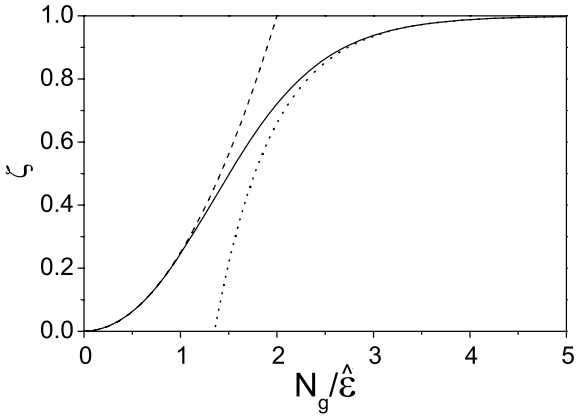

Figure 1: Degree of transverse coherence versus parameter $N_g/\hat{\epsilon}$. The asymptotes (24) and (25) are shown as dot and dash lines, respectively.

one for $\hat{\epsilon} \simeq 1$ [9] and strongly increases in the limit of small electron beam size. However, for considered here case $\hat{\epsilon} \gg 1$ we have found analytically [13] that $\delta_r \simeq 0.026$ for the optimal beta-function:

$$\zeta \simeq 1 - \frac{0.026}{N_g} \,, \tag{22}$$

i.e. this effect is negligible for large N_g. We have seen from numerical simulations [9] that the relative difference between (17) and (21) is indeed very small for large $\hat{\epsilon}$ and N_g in both linear and nonlinear regimes. Thus, despite the definition (21) was introduced heuristically, it is sufficiently accurate and adequate for our purposes. We rewrite it, using (13), in a more explicit form

$$\zeta \simeq \frac{f-1}{f+1} \,. \tag{23}$$

The plot of the degree of transverse coherence versus $N_g/\hat{\epsilon}$ for the function f from (10) is presented in Fig 1. For $N_g \gg \hat{\epsilon} \gg 1$ the degree of transverse coherence is close to one:

$$\zeta \simeq 1 - \frac{2}{f} \simeq 1 - 9.54 \exp\left(-1.667 \frac{N_g}{\hat{\epsilon}}\right) \,, \tag{24}$$

but one should keep in mind the residual effect (22). In the limit $\hat{\epsilon} \gg N_g \gg 1$ we get

$$\zeta = \frac{1}{M_{\rm T}} \simeq 0.25 \left(\frac{N_g}{\hat{\epsilon}}\right)^2 \,, \tag{25}$$

or, in dimensional units

$$\zeta = \frac{1}{M_{\rm T}} \simeq \left(\frac{\lambda N_g}{4\pi\epsilon}\right)^2 \,. \tag{26}$$

Amazingly, a numerical factor in front of the last expression is equal to one (with the accuracy of the order of 10^{-3}, accepted in this paper) for the case of the optimal beta-function. Note that in the case of synchrotron radiation for an axisymmetric beam one would have in the limit $\hat{\epsilon} \gg 1$ for optimal focusing: $\zeta = 1/M_{\rm T} \simeq (\lambda/4\pi\epsilon)^2$. Thus, the radiation from a SASE FEL has N_g^2 higher degree of transverse coherence in this limit.

The asymptotes (24) and (25) are plotted in Fig. One can see that Eq. (25) is pretty accurate for $N_g/\hat{\epsilon} < 1$, and Eq. (24) - for $N_g/\hat{\epsilon} > 3$.

Finally, we present an estimate of the degree of transverse coherence at saturation for the case $\hat{\epsilon} \gg N_g \gg 1$. Number of gain lengths at the end of linear regime (where the formation of transverse coherence stops) can be estimated [13] as $N_g \simeq \frac{1}{2}\ln(N_c/\hat{\epsilon})$. Thus, using (25) we get:

$$\zeta^{sat} \simeq \left(\frac{\ln(N_c/\hat{\epsilon})}{4\hat{\epsilon}}\right)^2 \,. \tag{27}$$

REFERENCES

[1] A.M. Kondratenko and E.L. Saldin, Part. Accelerators **10**(1980)207.

[2] Ya.S. Derbenev, A.M. Kondratenko and E.L. Saldin, Nucl. Instrum. and Methods **193**(1982)415.

[3] J.B. Murphy and C. Pellegrini, Nucl. Instrum. and Methods A **237**(1985)159.

[4] V. Ayvazyan et al., Eur. Phys. J. D **37**(2006)297.

[5] W. Ackermann et al., Nature Photonics **1**(2007)336

[6] M. Altarelli et al. (Eds.), XFEL: The European X-Ray Free-Electron Laser. Technical Design Report, Preprint DESY 2006-097, DESY, Hamburg, 2006 (see also http://xfel.desy.de).

[7] J. Arthur et al., Linac Coherent Light Source (LCLS). Conceptual Design Report, SLAC- R593, Stanford, 2002 (see also http://www-ssrl.slac.stanford.edu/lcls/cdr.

[8] SCSS X-FEL: Conceptual design report, RIKEN, Japan, May 2005. (see also http://www-xfel.spring8.or.jp).

[9] E.L. Saldin, E.A. Schneidmiller and M.V. Yurkov, "Coherence Properties of the Radiation from X-ray Free Electron Laser", DESY report DESY-06-137, August 2006; submitted to Opt. Commun.

[10] E.L. Saldin, E.A. Schneidmiller and M.V. Yurkov, Opt. Commun. **186**(2000)185

[11] F. Gruener et al., Appl. Phys. **B86**(2007)431

[12] A. Bacci et al., Phys. Rev. ST Accel. Beams **9**(2006)060704

[13] E.L. Saldin, E.A. Schneidmiller and M.V. Yurkov, "Analytical Description of Coherent Properties of X-ray Free Electron Lasers", to be published

[14] E.L. Saldin, E.A. Schneidmiller and M.V. Yurkov, "The Physics of Free Electron Lasers", Springer, Berlin, 1999

[15] K.J. Kim, Phys. Rev. Lett. **57**(1986)1871

[16] L.H. Yu and S. Krinsky, Physics Lett. **A129**(1988)463

[17] M. Xie, Nucl. Instrum. and Methods **A445**(2000)59

[18] R. Bonifacio, C. Pellegrini and L.M. Narducci, Opt. Comm. **50**(1984)373

[19] M. Xie and D. Deacon, Nucl. Instrum. and Methods **A250**(1986)426

[20] S. Krinsky and L.H. Yu, Phys. Rev. **A35**(1987)3406

[21] Z. Huang and K.J. Kim, Phys. Rev. **E62**(2000)7295

[22] M. Xie, Nucl. Instrum. and Methods **A475**(2001)51

[23] Z. Huang and K.J. Kim, Nucl. Instrum. and Methods **A475**(2001)59

[24] E.L. Saldin, E.A. Schneidmiller and M.V. Yurkov, Opt. Commun. **148**(1998)383

COMPACT X-RAY FREE ELECTRON LASE BASED ON AN OPTICAL UNDULATOR

C. Maroli, V. Petrillo, Dipartimento di Fisica dell'Università di Milano-INFN Sezione di Milano Via Caloria,16, 20133 Milano, Italy
L. Serafini, A. Bacci, A Rossi, P. Tomassini, *INFN*-Sezione di Milano, Via Celoria,16, 20133 Milano, Italy

Abstract

The interaction between a very high-brilliance electron beams and a relativistically intense counter-propagating laser pulses produces X rays via FEL collective amplification. The phenomenon is, however, very selective, so that the characteristics of both electron and laser beam must satisfy tight requirements in terms of beam current, emittance, energy spread and laser amplitude stability within the pulse. The three dimensional equations governing the radiation phenomenon have been studied in both linear and non linear regime and solved numerically for the particular interesting values of wavelengths of 1 Ang, 1nm and 12 nm. The performance of the collective Thomson source has been compared with that of an equivalent static undulator.

INTRODUCTION

The collective effects that develop in the classical Thomson back-scattering give rise to intense X-ray pulses easily tunable and highly monochromatic at a level a few orders of magnitude larger than the incoherent radiation. Due to recent technological developments in the production of high brilliance electron beams and high power CPA laser pulses, it is now even conceivable to make steps toward their practical realisation.

The phenomenon of the impact between the electron beam and the laser pulse has characteristics similar to the free electron laser and has been studied in previous papers[1-2]. The lasing is rather difficult to start up and the power saturation level is lower than that achieved in conventional static wigglers. It is however large enough to be interesting for application as fast probing for chemical process, monochromatic X imaging, phase contrast imaging, deep probing for inertial fusion research, considering moreover the fact that this kind of set-up is compact and considerably less expensive than static FEL.

In this paper we present several details about this X-ray production phenomenon, analysing various beam lines producing different electron bunches as well as various situations relevant to the synchronization between the electron beam and the laser pulse. Finally, we have compared the results of the radiation levels obtained with our 'ad hoc' radiation code EURA (for Electromagnetic Undulator Radiation Analysis) with those provided by the code GENESIS 1.3 currently used in FEL simulations [3], which is however not presently able to model electro-magnetic undulators. The answers given by both codes are qualitatively similar and also the quantitative estimates of saturation power and gain length are very close, when magnetostatic undulators are considered.

NUMERICAL SOLUTION OF 3D EQUATIONS

We have first studied the use of a CO_2 laser of wavelength λ_L=10 micron. High power lasers of this frequency are characterized by 70-100 GW of power and up to 300 psec of time pulse length.

By fixing the mean energy of the electron beam around the value <E>=30 MeV, i.e. $<\gamma>=60$, using the resonance condition for the back-scattering Thomson, $\lambda_R=\lambda_L(1+a_{L0}^2)/4\gamma^2$ and assuming the laser parameter $a_{L0}\leq 0{,}5$, X rays of wavelengths λ_R of the order of 7-9 Angstrom can be obtained. For this case, collective effects and FEL instability develop when the beam transverse normalized emittance does not exceed the value ε_x=0.5, and if the energy spread $\Delta\gamma/\gamma$ is contained in few 10^{-4}. Values of this kind are out of the current state-of-the-art of high–brightness beams but represent an interesting challenge for a possible future operation scenario.

Our numerical simulations for the case of the electromagnetic undulator have been performed with the 3D code EURA, which is a three-dimensional, time dependent code that integrates equations (2-5) using a forth order Runge-Kutta method for the particles and an explicit finite difference scheme for the radiation equation. The bunching factor is calculated along the beam by selecting, around each point, a moving portion of the bunch including several buckets.

The data obtained with EURA for a static undulator have been compared with similar data produced with the code GENESIS 1.3 widely used in the FEL analysis. The comparison is presented in Fig 3 where data from EURA (black curve (b)) and from GENESIS 1.3 time dependent (red curve (a)) are reported.

The data chosen for the comparison are: undulator parameter a_w=0.3, undulator period λ_w=10μm, radiation wavelength λ_R=1.515 nm, ε_x=0.3 mm mrad, r.m.s. transverse dimension σ_x=12.5 μm (corresponding to a

maximum radius of 25 μm), a constant external magnetic field. EURA simulates the entire bunch, which has been taken 1 mm long, while GENESIS 1.3 simulates a fraction of N=1000 slices of width λ_R, separated by $z_{sep}=N_{sep}\lambda_R$ with $N_{sep}=20$, corresponding to approximately 75 cooperation lengths.

We note that in both simulations with EURA and GENESIS 1.3 it is very important to set the correct detuning with respect to the nominal resonance frequency, because otherwise the growth of the instability is strongly damped. The computed gain lengths are of L_g =3,6 mm for EURA and L_g =4.08 mm for GENESIS 1.3, while the analytical expressions by Ming Xie [3] give

$$L_g=L_{1D}(1+\eta) \qquad (1)$$

with L_{1D}, the one-dimensional gain length, estimated numerically as about 1.97 mm,

$$\eta=(0.45\eta_d^{0.57}+0.55\eta_\varepsilon^{1.6}+3\eta_\gamma^{2}+\text{[illegible]}) \qquad (2)$$

and:

$$\eta_d=L_{1D}\lambda_R/(4\pi\sigma_x^{2}) \qquad (3)$$

$$\eta_\varepsilon= L_{1D}2\pi\varepsilon_{,x}^{2}/(\gamma^{2}\sigma_x^{2}\lambda_R) \qquad (4)$$

$$\eta_\gamma= 4\pi L_{1D}(\delta\gamma/\gamma)/\lambda_w \quad . \qquad (5)$$

It can be seen that for the case analysed η_d is about 1,5 10^{-3} , η_γ =0.24, negligible respect to η_ε which in this case can be evaluated through (24) as η_ε =1.31 yielding on the whole to L_g =3,96 mm.

As shown in fig 3, EURA gives a gain length slightly shorter than GENESIS 1.3, with a faster saturation, but at a smaller power level. Other characteristics are an initial growth in the first gain length less steep and stronger post-saturation power oscillations due probably to a deeper entrapment of the particles. A zero-order comparison on the time independent behaviour is impossible, because EURA is, for its nature, only time dependent. The scenario is similar to that pointed out in the GENESIS 1.3 versus GINGER comparison [4,5]. Other data relevant to the analysis made with GENESIS 1.3 are reported in Fig 2 where the signal on the bunch at z=3 cm is presented.

In fig 3 the radiation obtained with a conventional static undulator (already presented in fig 3) has been plotted together with the case of an electromagnetic wiggler of equal intensity and wavelength, in the case of $a_w=a_{L0}=0.3$, $\lambda_w=\lambda_L=10$ μm, $\varepsilon_x=0.3$ mm mrad, $\sigma_x=12.5$ μm (corresponding to a maximum radius of 25 μm).The differences introduced by the resonance condition lead, however, to a radiation wavelength smaller than a factor of two respect to the static undulator, so that, for the electromagnetic undulator, $\lambda_R=0.7578$ nm. The simulations show that the electromagnetic undulator produces a power saturation value of 1.93 MW in less than 2.5 cm, with an average gain length of about 1.8 mm, while the static undulator reaches 1.33 MW of power in about 3 cm, with a gain length near to 3.5 mm.

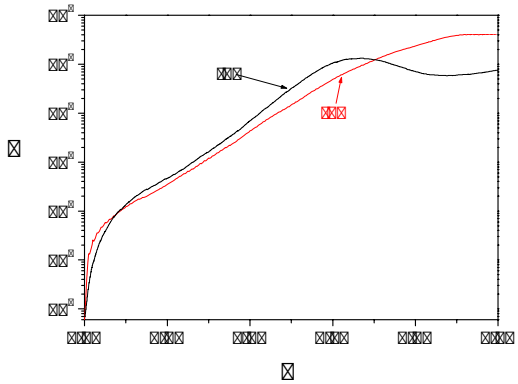

Fig 1: Radiated power P in Watt versus z coordinate in meter for (a) simulations made with GENESIS 1.3 and (b) with EURA for $a_w=0.3$, $\lambda_w=10$ μm, $\lambda_R=1.515$ nm, $\varepsilon_x=0.3$ mm mrad, $\sigma_x=12.5$ μm (corresponding to a maximum radius of 25 μm), a constant external static magnetic field.

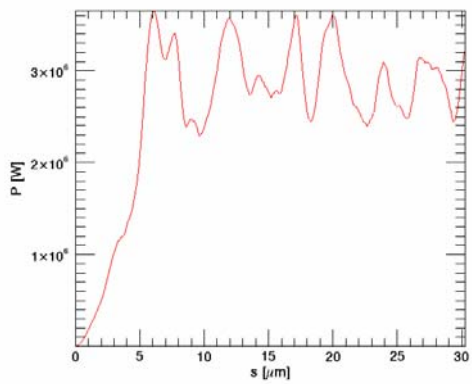

Fig 2: Radiated power P (in Watt) versus the coordinate along the bunch s (in microns) at z=3 cm and for the same case as fig 5. Simulation made with GENESIS 1.3

In fig 4 a case analogous to fig 3 is presented, but the emittance value, that in this case has been increased to 0.6. In this case the power level achieved by electromagnetic and static undulators are respectively 0.36 MW and 0.26 MW, with gain lengths of respectively 2.9 and 5.08 mm. In Fig 5 a summary of data is presented showing the gain lengths ((a) and (b)) deduced by a fitting of the numeral data (on the left scale) and the saturation radiation intensity ((c) and (d)) (on the right scale) for both electromagnetic (in blue) and static (in black) undulators. A case particularly important for its applications is the production of radiation characterized by wavelength λ_R of about 1 Angstrom. . This value can be reached with a Ti:Sa laser with $\lambda_L=0.8$ μm, $a_{L0}=0.8$, $\langle\gamma\rangle=55$, $L_b=300$ μm, $r_b=7$ μm, a total charge of 3 nC, for a current of 3 KA.

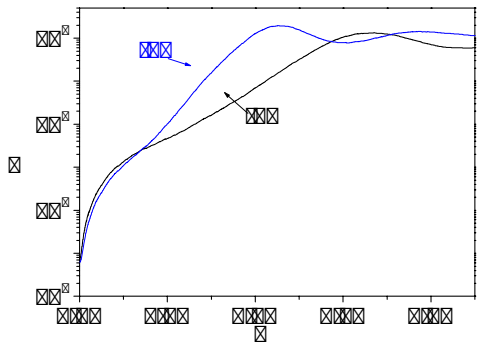

Fig 3: Radiated power P (in Watt) vs z (in meter) for (a) static undulator and (b) electromagnetic undulat a_w=0.3, λ_w=10 μm, ε_x=0.3 mm mrad, σ_x=12.5 μm or. (corresponding to a maximum radius of 25 μm).For the static undulator λ_R =1.515 nm, while for the e.m. undulator λ_R =0.7578.

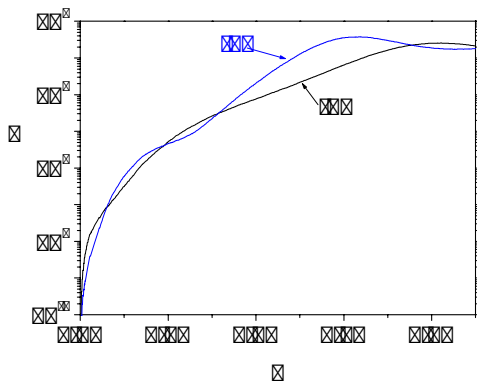

Fig 4: Same as Fig 3 but with ε_x=0.6 mm mrad.

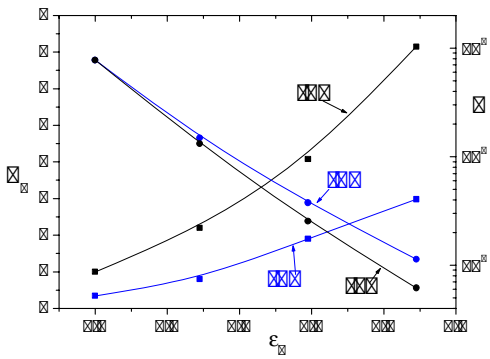

Fig 5: Gain length L_g in mm (left scale) versus ε_x in mmmrad. Radiation power P (in Watt) versus ε_x in mmmrad on the right scale for a_w=0.3, λ_w=10 μm, σ_x=12.5 μm (corresponding to a maximum radius of 25 μm). (a) and (c) refer to a static undulator case, while (b) and (d) to an electromagnetic one.

Cases with emittance ε_x=0.26 mm mrad (curve (a)) ε_x =0.54 mm mrad (curve (b)) and ε_x =0.8 mm mrad (curve (c)) are presented in Fig 6, where the power obtained in Watt is plotted versus z (in meter).

The factor $\rho = \frac{1}{\gamma}\left(\frac{\omega_b^2 \bar{a}_{L0}^2}{16\omega_L^2}\right)^{\frac{1}{3}}$ (ω_b being the plasma frequency of the beam and ω_L the laser frequency) is 4.17 10^{-4} and the radiation wavelength is λ_R =1.13 A. In this case we are at the limit of validity of the classical model, because the quantum factor q is 0.9, and quantum effects, arising when q>1, can play an important role [7,8]. However, the previous condition on q relies on one-dimensional models. Three-dimensional considerations [9] seem to point out a relaxation of the above condition due to the enlargement of the bandwidth associated to non-ideal and geometrical effects so that the requirement q>1 should be rather replaced by $q\rho > \max(\rho, \Delta\gamma/\gamma, \varepsilon_{n,x}^2/\sigma_x^2)$, where qρ is the relative energy separation between the quantum lines, ρ is the one-dimensional natural bandwidth and $\Delta\gamma/\gamma$ and $\varepsilon_{n,x}^2/\sigma_x^2$ are respectively the inhomogeneous line broadening due to energy spread and emittance effects [10]. In our case we have $q\rho=4\ 10^{-4}$, but for the case (a) $\varepsilon_{n,x}^2/\sigma_x^2$ does never go under $7\ 10^{-4}$. The cases with larger emittance are, in this sense, even less critical respect to the presence of quantum effects. The cases presented require an amount of laser power outside the present status of the art, but achievable in the near future [11]. In fact, for instance, in the case (b) with emittance ε_x =0.54 mm mrad, at saturation the beam has a maximum radius of about 15 μm; assuming for the laser in the waist a spot size of 20 μm, we obtain the needed laser power of more than 17 TW for at least 1.5 mm, corresponding to a total laser energy of about 85 J.

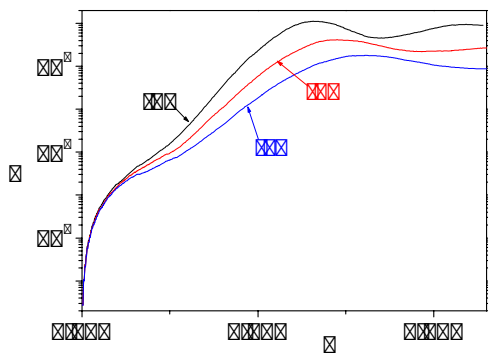

Fig 6: Radiated power P (in Watt) vs z (in meter) for an electromagnetic undulator. a_{L0}=0.8, λ_L=0.8 μm, σ_x=3.5 μm, (corresponding to a maximum radius of 7 μm), $\Delta\gamma/\gamma=10^{-4}$, λ_R=1.13 Angstrom. (a) ε_x=0.26 mm mrad .(b) ε_x=0.54 mm mrad (c) ε_x=0.8 mm mrad.

Also the properties of the electron beam are extreme, due to the required condition of large current, low emittance, minimum energy spread, high focusing and relatively small γ.

A case equally interesting, but less difficult to realise is a radiation wavelength of about 1 nm. In addition to the case presented in the previous paragraph relying on the

use of the CO_2 laser (characterized by a radiation wavelength λ_R of about 7.57 A), we present here the possibility of producing X-rays in the range of the nanometer with the Ti:Sa laser.

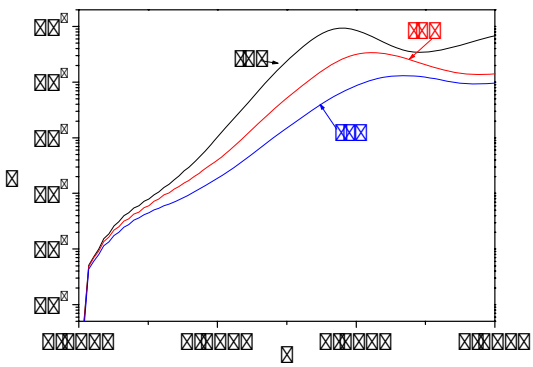

Fig 7 Radiated power P (in Watt) vs z (in meter) for an electromagnetic undulator. a_{L0}=0.8, λ_L=0.8 μm, σ_x=5 μm, (corresponding to a maximum radius of 10 μm), I=600 A, $\Delta\gamma/\gamma=10^{-4}$, λ_R=1.06 nm. (a) ε_x=0.26 mm mrad .(b) ε_x=0.54 mm mrad (c) ε_x=0.8 mm mrad..

In this case, in fact, the factor γ has been assumed γ=18.11 and a_{L0}=0.8, the resonant wavelength being about 1 nm. The total charge is Q=2 10^{-9} C, L_b=1 mm, so that the current I is I=600 A. Cases with different emittance are presented in Fig 11. The radiation power reaches 1 MW for the case with ε_x=0.26. The requirement of laser power can be evaluated by assuming a channel of 17 μm of maximum radius with a length of 1.1 mm for a power of 12 TW and a total energy of 48 J.

Finally, we present the possibility of producing 12 nm radiation by means of the CO_2 laser. For this case, the properties of the electron beam have been relaxed. In fact, we have assumed a γ of 16.5, a current of 150 A, an emittance of $\varepsilon_{,x}$=1.06 mm mrad , a maximum radius of 30 μm (σ_x=15. μm), an energy spread of 1.3 10^{-4}, conditions inside the present status of the art of the production of high brightness electron beams. The saturation value of the radiation power is very low, namely ten Kilowatt, but larger by a factor 20 than the incoherent radiation produced in the same bandwidth. The power saturation value can be considerably incremented up to 10 MW by shifting the focus of the beam. In Fig 8 the radiation power and the rms radius are presented for a_{L0}=0.5 and for the focus of the beam shifted at z=0.68 cm in correspondence of the middle of the exponentiation phase.

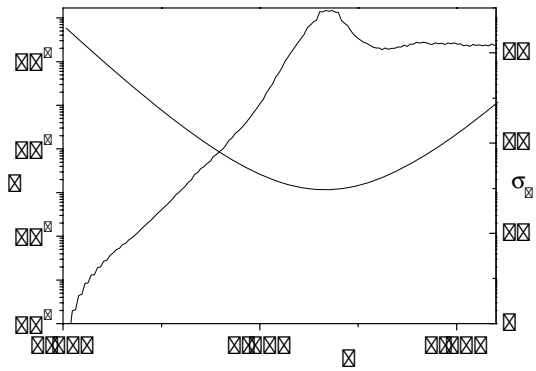

Fig 8: Left axis: radiated power P in Watt vs zin meter. Right axis: rms radius (in micron) vs z.

The laser power required is in this last case 100 GW with total energy 2.3 J, but considerable value of power radiation (namely P= 100 KW at 1 cm) can be reached also by limiting the laser parameter to a_{L0}=0.2, corresponding to 16 GW of laser power and 0.6 J of total energy.

REFERENCES

[1] A.Bacci, C. Maroli, V. Petrillo , L. Serafini: 'Eur. Phys. Jour. Appl. Phys', (2006), 2006080

[2] A.Bacci, M Ferrario, C. Maroli, V. Petrillo, L.Serafini: 'PRST AB',Vol.: 9 , (2006) 060704

[3]S. Reiche: Genesis 1.3 http:// pbpl.physics.ucla.edu/~reiche/

[4] Ming Xie, "Design Optimization for an X-Ray Free Electron Laser Driven by SLAC Linac," Proc. 1995 PAC, Dallas, May 1-5, 183.

[5] William M. Fawley, "A user manual for GINGER and its post-processor XPLOTGIN" (February 19, 2002). Lawrence Berkeley National Laborat*ory*. Paper LBNL-49625. http://repositories.cdlib.org/lbnl/LBNL-49625

[6]W.M. Fawley: 'X-Ray FEL Simulation:Beam Modeling' ICFA 2003 Workshop on Start to end Numerical Simulations of X-RAY FEL's Fawley-ICFA03-Zeuthe..>http://citeseer.ist.psu.edu/xie95design.

[7] J.B. Murphy and C. Pellegrini: 'J Opt.Soc. Am. B', Vol.: 2, (1985), pg.:259 .

[8] R. Bonifacio et al.: 'Nucl. Instrum. And Meth. A', Vol.: 543 ,(2005), pg.:645.

[9] Smetanin, I.V., Nakajima, K, Proceedings of the Second Symposium on Advanced Photon Research (JAERI-Con 2001-011) : 236-40, 2001

[10] Winthrop J. Brown and Frederic V. Hartemann: 'Phys.Rev. ST A B', Vol.:7 (2004), 060703.

[11] M. D. Perry et al., "Petawatt Laser Pulses," Optics Letters, Vol. 24 (1999), p. 160, E. Hugonnot, J. Luce, and H. Coïc, "Optical parametric chirped-pulse amplifier and spatiotemporal shaping for a petawatt laser", Appl. Opt. 45, 377-382 (2006)

PRODUCTION OF FEMTOSECOND PULSES IN A FREQUENCY DOUBLER AND PERSPECTIVES OF FLASH USER FACILITY FOR PUMP-PROBE EXPERIMENTS WITH FEMTOSECOND RESOLUTION

E.L. Saldin, E.A. Schneidmiller, and M.V. Yurkov
Deutsches Elektronen-Synchrotron (DESY), Hamburg, Germany

Abstract

Free Electron Laser in Hamburg (FLASH) operates successfully since the year of 2000. Permanent upgrades of the facility did allow to reduce operating wavelength from 100 nm in 2000 down to 13 nm in 2006. An upgrade of the year of 2007 is in the progress, and after its completition FLASH will reach design value of the wavelength of 6.4 nm. An attractive feature of FLASH is production of intense, ultra-short radiation pulses of sub-10-fs duration. In this paper we describe perspective upgrades of FLASH aiming at extension of the operating wavelength range while conserving the feature of ultra-short pulse production. We show that an upgrade of FLASH with a frequency doubler will allow to reduce the wavelength down to 3 nm, thus covering the "water window" – the wavelength range that is crucially important for the investigation of biological samples. We show also that recent installations at FLASH of far infrared undulator (FIR) and optical replica synthesizer (ORS) open up the possibility for implementation of schemes allowing to perform pump-probe experiments with 10 femtosecond temporal resolution.

INTRODUCTION

During last years we observe rapid progress of Self-Amplified Spontaneous Emission Free Electron Lasers (SASE FELs) [1–3]. Jump in the wavelength was by about three orders of magnitude, from 12 μm in 1997 down to 13 nm in 2006 [4–9]. Presently FLASH (Free Electron Laser in Hamburg) has produced unprecedented powers for EUV radiation at a fundamental wavelength of 13.7 nm, and harmonics with wavelengths as low as 2.75 nm [9]. After an energy upgrade to 1 GeV of the FLASH driving linac minimum wavelength in the fundamental harmonic of FLASH will be 6.4 nm.

FLASH demonstrated unique femtosecond mode of operation [6–9] which was not considered at an early design stage of the project [10]. Thorough analysis has shown that due to nonlinear compression and small local energy spread the short high-current leading peak (spike) in the bunch density distribution was produced by beam formation system. Despite strong collective effects (of which the most critical was the longitudinal space charge after compression) this spike was bright enough to drive FEL process up to the saturation for the wavelengths down to 13 nm. Analysis of the latest experimental results [9] indicate that the peak current in the spike is 2 to 2.5 kA, the FWHM length of the high current spike is approximately 30 fs and the normalized emittance is 1 to 1.5 mm-mrad. Note that the latter value is significantly less than the project one of 2 mm-mrad [10], and encouragingly approaches to the values predicted by start-to-end simulations. For FLASH this result is of crucial importance allowing to reach shorter wavelengths with fixed electron energy of 1 GeV. The first scenario for reaching "water window" at FLASH equipped with efficient frequency doubler has been analyzed a few years ago [11, 12]. That analysis has been based purely on refined start-to-end simulations. Now, with an experimentally proven update of the beam parameters we present further development of a concept of frequency doubling for generation of powerful femtosecond pulses. Application of frequency doubler at FLASH will allow to cover the water window (wavelength range between the K-absorption edges of oxygen ($\lambda = 2.34\mathrm{nm}$) and carbon ($\lambda = 4.38\mathrm{nm}$)) that is crucially important for the investigation of biological samples.

Two-color pump-probe experiments are very attractive for time-resolved studies. In this paper we show that present configuration of FLASH holds great potential for pump-probe experiments with 10 femtosecond temporal resolution. This potential stems from recent installation at FLASH of far infrared undulator (FIR) and optical replica synthesizer (ORS) [13–16]. In the case of FIR undulator optical pulses from FIR and XUV pulses from FEL are naturally synchronized since they are produced by the same electron bunch. In the case of pump-probe experiments with an external optical laser an ORS setup is used as a selection trigger for perfectly synchronized pump-probe pulses.

CONCEPT OF FREQUENCY DOUBLER

An idea of using two undulators, with the second undulator resonant to one of the harmonics of the first one, was considered in [17–19] (it is also referred to as the "afterburner" method). The first undulator is long enough to reach saturation and produce strong spatial bunching in harmonics. The bunched beam generates coherent radiation in the second undulator which follows immediately the first one. The main problem with this approach is the large induced energy spread which significantly degrades the performance of the radiator section at the harmonic fre-

quency [11, 12]. Another method to generate higher harmonics is high-gain harmonic generation scheme from the external seed (see [20] and references therein). However, it is technically complicated and is not flexible enough for production of tunable radiation.

The concept of effective frequency doubler scheme for SASE FEL has been proposed in [11, 12]. This scheme essentially exploits the feature of a small local energy spread in the driving electron beam of SASE FEL. It consists of undulator tuned to the first harmonic, dispersion section, and undulator tuned to the second harmonic. The latter one can be also tapered in order to increase output power above saturation level. The first stage is a conventional SASE FEL. The gain of the first stage is controlled in such a way that the maximum energy modulation of the electron beam at the XFEL exit is about equal to the local energy spread, but still far away from saturation. When electron bunch passes through dispersion section this energy modulation leads to effective compression of the particles. Then bunched electron beam enters the 2nd harmonic undulator, and from the very beginning produces strong radiation because of a large value of spatial bunching, low value of the emittance and relatively small induced energy spread. Saturated power has the same level as for conventional SASE FEL, but is reached in significantly shorter undulator.

PRODUCTION OF ELECTRON BUNCHES

We illustrate operation of the frequency doubler for the energy of the driving beam of 1 GeV (see Fig. 1). The electron beam is produced in a radio frequency gun and brought up to an energy of 1000 MeV by six accelerating modules ACC1 to ACC6. At energies of 130 and 380 MeV the electron bunches are compressed in the bunch compressors BC1 and BC2. The electron beam formation system is based on the use of nonlinear longitudinal compression. When the bunch is accelerated off-crest in the accelerating module, the longitudinal phase space acquires a radio frequency induced curvature. Downstream of each bunch compressor, this distortion results in a non-Gaussian distribution within the bunch and in a local charge concentration. It is the leading edge of the bunch, with its high peak current, which is capable of driving the high intensity lasing process (see Fig. 2). Collective effects play a significant role in the bunch compression process for short pulses. One can see on Fig. 2 that an increase in the peak current and a narrowing of the width of the spike leads to an increase in the induced energy chirp due to space charge effects.

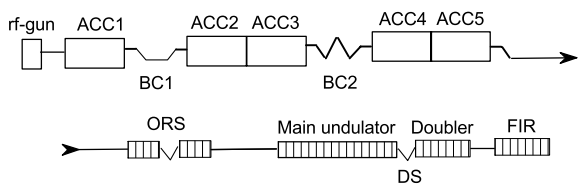

Figure 1: Schematic layout of the FLASH facility equipped with frequency doubler. Undulator of frequency doubler is placed just after the main undulator. Abbreviations ACC, BC, and DS stand for accelerating module, bunch compressor, and dispersion section, respectively. The scheme also shows far infrared undulator (FIR) and optical replica synthesizer (ORS) setups installed at FLASH in 2007.

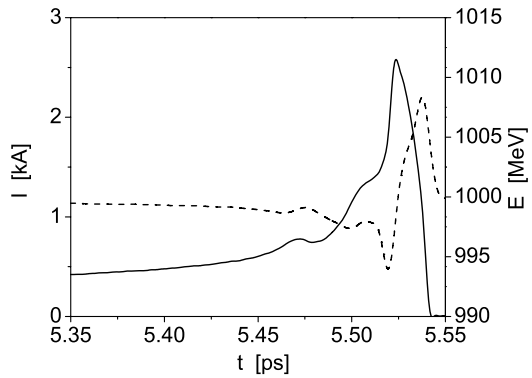

Figure 2: Structure of the electron bunches at FLASH: current I (solid line) and mean energy E (dashed line) along the electron bunch at the undulator entrance (simulations of [9] scaled to 1 GeV). The bunch head is located at the right hand side of the figure.

PROPERTIES OF THE RADIATION

We illustrate operation of the frequency doubler at FLASH for the case of FEL process driven by short-spike electron bunch with energy of 1 GeV (see Fig. 2). The main undulator of FLASH is a fixed 12 mm gap permanent magnet device with a period length of 2.73 cm and a peak magnetic field of 0.48 T. The frequency doubler is 9 m long undulator (1.95 cm period and 0.39 T peak magnetic field). Simulations have been performed with time-dependent code FAST [21] upgraded for simulation of higher harmonics. Prior presenting results for the frequency doubler it is worthwhile to overview operation of SASE FEL with a uniform undulator. Simulations of the femtosecond mode of operation of FLASH at 6 nm show that present undulator length of 27 meters is sufficient to reach deep saturation in the main undulator. Expected level of the average energy in the radiation pulse is up to 70 μJ for an ideal tuning of the machine and emittance in the bunch head of 1.4 mm-mrad. Expected radiation pulse duration is in sub-10 fs range.

Electron bunch quality is high enough to drive SASE FEL optimized for production of 3 nm radiation (see Fig. 3). Saturation is achieved at the undulator length of about 30 meters with the level of the energy in the radiation pulse about 15 μJ. We present this number for the further comparison with the frequency doubler.

When operating as a frequency doubler, the level of output radiation energy in the main undulator should be tuned

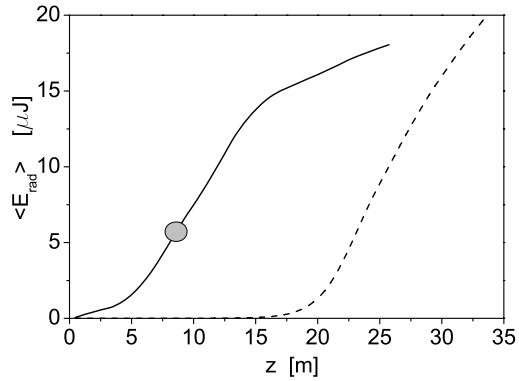

Figure 3: Energy in the radiation pulse in the frequency doubler (solid line). Electron energy is 1 GeV, undulator period is 1.95 cm, and peak magnetic field is 0.39 T. Radiation wavelength is 3.2 nm. Dashed line shows operation of SASE FEL with the same undulator.

to the value about one microjoule. At this stage of amplification process induced energy modulations become to be about local energy spread in the lasing spike. Then electron bunch passes dispersion section with the net compaction factor about one micrometer, and energy modulations transforms to the density modulation with high content of the second harmonic. Finally, electron bunch is directed to the undulator resonant at the second harmonic (frequency doubler undulator) and readily starts to produce powerful radiation from the very beginning. Since the electron beam still has high quality, a self-consistent process of radiation amplification takes place. Peak radiation intensity is nearly the same as in conventional SASE FEL, but saturation occurs at a shorter undulator length. We see from Fig. 3 that the level of the average radiation energy is 5 μJ at the undulator length of 9 meters. Temporal and spectral properties of the radiation pulse at this point are illustrated with Fig. 4. FWHM pulse length is well below 10 fs, and average power exceeds gigawatt level. Contribution of the 3rd harmonic into the full radiation power is about 0.08%, and peak power is in a megawatt range.

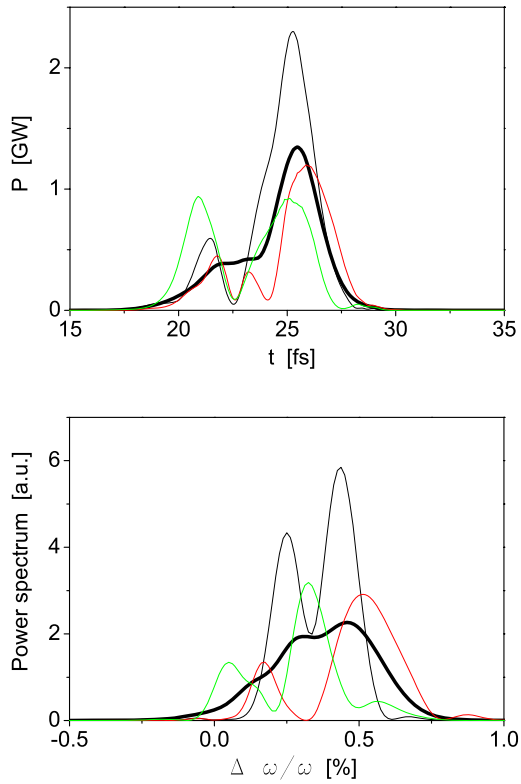

Figure 4: Temporal (top) and spectral (bottom) properties of the radiation pulse at the length of the frequency doubler of 9 meters. Bold lines show averaged values, and thin lines are single shots.

PERSPECTIVES FOR PUMP-PROBE EXPERIMENTS ON A 10-FS TIME SCALE

Recently FLASH facility has been extended with the far infrared undulator (FIR) and optical replica synthesizer (ORS) [13–16]. These devices hold great potential for organization of pump-probe experiments on a 10-fs pulse scale at FLASH operating in a femtosecond mode.

Current plans for FIR undulator foreseen pump-probe experiments with VUV and FIR pulses (wavelength range from a few to 200 μm) [14]. While initially FIR and VUV pulses are synchronized on a 10 fs timescale (they both are produced by the same electron bunch), additional jitter may be introduced by mechanical vibrations of optical components because different beamlines are used for transport of VUV and FIR pulses. Here we propose jitter-free scheme (see Fig. 5). Combination of modulator of ORS and FIR undulator as a radiator will allow to produce powerful pulses of coherent radiation with the wavelength of driving laser around one micron. Then both pulses are transported to the experimental area using the VUV opti-

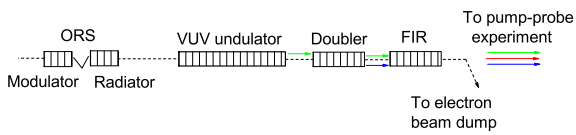

Figure 5: Scheme for pump-probe experiments with VUV FEL pulses and pulses produced by infrared undulator. Operation of the scheme is based on production by the same electron bunch of naturally synchronized VUV FEL pulses and pulses produced by the infrared undulator. Relative synchronization of the pulses is preserved by means of using the same optical system for transportation of the pulses to the experiment.

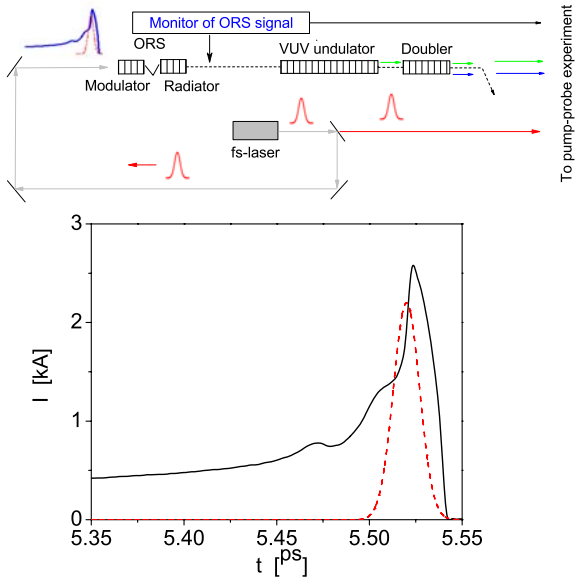

Figure 6: Scheme for pump-probe experiments with VUV FEL pulses and optical pulses from external femtosecond laser (top). ORS setup driven by the same external laser produces selection trigger for well synchronized pulses. Bottom plot illustrates overlapping of electron pulse (solid line) and optical pulse (dashed line) in the modulator of ORS setup.

cal system which conserves mutual synchronization. Calculations of the photon beam transport show that both radiation pulses, VUV and infrared one, can be effectively transported through existing optical system. Separation of infrared and VUV pulses and organization of required time delay is performed just near the experimental sample.

ORS setup can be also used for organization of pump-probe experiments involving femtosecond pulses from VUV FEL and powerful optical pulses from femtosecond optical laser. Key problem of such experiments is precise synchronization of laser and electron pulses having timing jitters of different physical nature. Instead of solving synchronization problem we propose to use pulse selection scheme based on ORS setup. Operation of this scheme is illustrated in Fig. 6. An optical beam from fs-laser is split into two beams, one is directed to the sample, and another one is used as a seed for ORS. Output signal from the ORS exhibits strong dependence on the time jitter between the lasing spike and short laser pulse, and achieves maximum value at perfect overlapping. Selection signal is generated in this case which marks events with perfectly synchronized pump-probe pulses.

Installation of frequency doubler at FLASH is natural, cost-effective way for complete covering of the "water window", the wavelength range which is of crucial importance for studying biological samples. But it is not just simple extension of the operating wavelength range of the facility: production of ultra-short pulses with gigawatt level of output power extends an opportunity for studies of time-dependent processes on a sub-10-fs time scale described above. In addition, the frequency doubler setup produces two radiation pulses of different frequencies which are naturally synchronized on a few femtosecond scale. The frequency doubler scheme is rather flexible allowing to negotiate with the intensity of the radiation pulses. In particular, it is rather simple to produce VUV pulses (with fundamental and doubled frequencies) with similar intensity in the range of a few microjoules which reveals an opportunity for performing pump-probe experiments with powerful VUV pulses of different colors.

ACKNOWLEDGEMENT

We thank R. Brinkmann, J. Rossbach, and J.R. Schneider for interest in this work.

REFERENCES

[1] A.M. Kondratenko and E.L. Saldin, Part. Accelerators **10** (1980)207.

[2] Ya.S. Derbenev, A.M. Kondratenko, and E.L. Saldin, Nucl. Instrum. and Methods **193**(1982)415.

[3] J.B. Murphy and C. Pellegrini, Nucl. Instrum. and Methods A **237**(1985)159.

[4] M. Hogan et al., Phys. Rev. Lett. **81**(1998)4867.

[5] S.V. Milton et al., Science **292**(2001)2037.

[6] V. Ayvazyan et al., Phys. Rev. Lett. **88**(2002)104802.

[7] V. Ayvazyan et al., Eur. Phys. J. D **20**(2002)149.

[8] V. Ayvazyan et al., Eur. Phys. J. D **37**(2006)297.

[9] W. Ackermann et al., Nature Photonics, 1 (2007)336.

[10] T. Åberg, et al., A VUV FEL at the TESLA Test Facility at DESY, Conceptual Design Report, DESY Print TESLA-FEL 95-03 , May 1995.

[11] J. Feldhaus et al., DESY Print DESY 03-092, July 2003.

[12] J. Feldhaus et al., NIM A528(2004)471.

[13] B. Faatz et al., Nucl. Instrum. and Methods **A475**(2001)363.

[14] M. Gensch et al., "New THz undulator beamline at the VUV FEL FLASH", submitted to Infrared Physics & Technology.

[15] E.L. Saldin, E.A. Schneidmiller and M.V. Yurkov, Nucl. Instrum. and Methods **A539**(2005)499.

[16] P. van der Meulen et al., Proc. of FEL 2006 Conference, Berlin, 2006, p. 296.

[17] R. Bonifacio, L. De Salvo, and P. Pierini, Nucl. Instrum. Methods Phys. Res. A 293, 627(1990)

[18] Ciocci, et al., IEEE J. Quantum Electron. 31 (1995)1242

[19] W. M. Fawley et al., Proceedings of the IEEE 1995 Partice Accelerator Conference, 1996, p219

[20] I. Ben-Zvi et al., Nucl. Instrum. Meth. **A304**(1991)151.

[21] E.L. Saldin, E.A. Schneidmiller, and M.V. Yurkov, Nucl. Instrum. and Methods **A 429**(1999)233.

GENERATION OF X-RAY FEL LIGHT USING LASER WAKEFIELD ACCELERATED ELECTRON BEAMS

O.A. Shevchenko[#] , N.A. Vinokurov, Budker Institute of Nuclear Physics, 11 Acad. Lavrentyev Prosp., 630090, Novosibirsk, Russia
Kim Ta Phuoc, Antoine Rousse, Laboratoire d'Optique Appliquée, ENSTA, CNRS UMR 7639, Ecole Polytechnique, Chemin de la Hunière, 91761, Palaiseau, France

Abstract

We consider a new class of high gain FELs based on femtosecond electron bunches with extra high current density produced by Laser Wake Field Acceleration (LWFA). The FELs of this kind can be used for generation of high power femtosecond x-ray pulses. We present the results of simulations of FEL operation with some reasonable beam parameters which will be obtained in future. We focus our attention on the advantages which can be gained from the unique possibility of the use of femtosecond hundred-kiloamperes bunches, generated by LWFA. We also consider the impact of the relatively poor electron beam properties on FEL characteristics.

INTRODUCTION

The possibility of the laser wake field acceleration (LWFA) of electron beams in plasma was explored in detail many years ago [1]. Until the present time practical application of this acceleration technique was impossible because of absence of lasers with required parameters. The rapid development of high power laser technique recently gave rise to intensive experimental investigation of LWFA [2]. At present one can obtain the laser peak power up to 1 PW with the pulse duration several tens of femtoseconds. This enables one to expect the creation of laser-plasma accelerators which can provide the peak currents several hundreds of kiloamperes with relatively small slice emittance and energy spread. Such accelerators could have very compact design as the gradient in the laser wake field can reach 300 GeV/m. They certainly would find many applications. One of them could be a source of electron bunches for the compact (tabletop) X-ray FEL [3].

The FEL operation may strongly depend on the details of the 6-D electron distribution function which can not be measured directly. Therefore it seems reasonable to make the LWFA experiments simultaneously with observation of the electron beam radiation from undulator. This way one can optimize the plasma accelerator parameters for the requirements of the X-ray SASE FEL.

In this paper we consider a possible scheme of the combined LWFA and SASE FEL experiment. We discuss some essential physical and technical problems of this experiment. They include space charge and wakefield effects, beam transport and undulator construction. Assuming some reasonable beam parameters which can be achieved in LWFA we obtain the FEL radiation parameters.

[#]O.A.Shevchenko@inp.nsk.su

DESCRIPTION OF THE ACCELERATOR AND FEL LAYOUT

Based on the X-ray FEL requirements one can imagine the scheme of the experimental setup which is shown in Fig. 1.

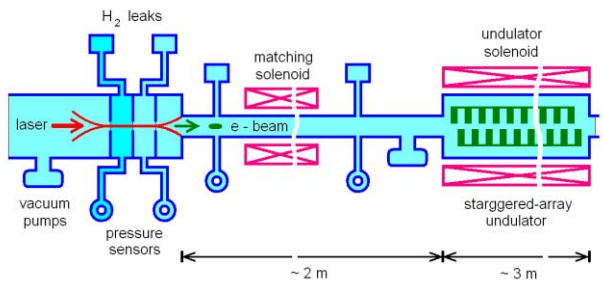

Figure 1. Possible scheme of the combined LWFA and X-ray FEL experiment.

In most of the existing LWFA experiments plasma volume is created in a gas jet or capillary and the transverse laser beam size does not exceed 10 microns [2]. For the laser pulse energy available now it seems worthwhile to increase the transverse laser beam size one order of magnitude and use the gas volume with optimized pressure profile. In addition one can use the gas focusing in the beam transport line after accelerator and inside undulator which matches very well with the electron acceleration in the same gas.

At the scheme presented in Fig. 1 the accelerator region is separated from the vacuum channel by narrow orifice through which the laser radiation is injected into the gas volume. To minimize multiple scattering the gas is hydrogen. The gas pressure is chosen to be $\sim 5\times10^{-3}$ atm so that acceleration up to 1 GeV occurs at the distance 10 cm. Additional diaphragms are placed along the accelerator axis. It allows to optimize the pressure profile.

For the compactness of the experimental setup it is desirable to obtain the FEL gain length no more then several tens of centimetres. The electron beam β-function in undulator should be of the same order of magnitude. It can be achieved by applying of gas focusing which works effectively at high beam peak currents. The focusing occurs because the beam electrical field is partly screened due to gas dielectric permeability and beam focuses itself by magnetic field (at high beam currents collective electric field may ionize atoms, and therefore effective permeability will increase). Usually the gas permeability

influence is very small but for such big peak currents which can be obtained in LWFA it is sufficient to focus the beam. In our case the required gas pressure is relatively small (~ 100 Pa) and beam scattering can be neglected. To match the beam β-function from the accelerator exit to the undulator entrance one can also use superconducting solenoid.

To obtain X-ray radiation with 1 GeV electron beam one has to use undulator with the period several millimetres. The staggered array undulator seems to be the optimal choice for such small period [4]. The vanadium permendur poles of the undulator can be placed directly to the gas-filled volume. It should be noted that longitudinal impedance of vacuum chamber does not depend on its roughness in the case of short beam and relatively low conductivity of vacuum chamber material. The critical value of the conductivity is determined by the expression $\sigma_{cr} \sim \frac{1}{2\pi}\left(\frac{a}{l_b}\right)^2 \frac{c}{l_b}$ where l_b is the bunch length, a - radius of vacuum chamber, c - speed of light. Taking $l_b \sim 1\,\mu m$ and $a \sim 0.5\,mm$ we obtain $\sigma_{cr} \sim 10^{19}$ which is much higher then copper conductivity. Therefore the undulator poles do not require shielding by smooth metallic plates and thus the gap can be increased which slightly reduces the "resistive" wakefield.

Undulator parameters which have been used in simulations are listed in Table 1.

Table 1: Undulator parameters

Undulator period, mm	3.6
Undulator gap, mm	1.0
Undulator K - parameter	0.3
Longitudinal field, Tesla	1

ASSUMED ELECTRON BEAM PARAMETERS AND SOME KNOWN PROBLEMS

Electron beams obtained by LWFA should have very large correlated energy spread. Electron energy can change from zero to maximum value at the distance equal to the quarter of plasma oscillation wavelength. For the assumed gas pressure $\lambda_p \sim 100\,\mu m$. So the energy difference at distance $1\,\mu m$ can reach 5 %. On the other hand the local energy spread should not be very large. Therefore in our simulations we assume zero local energy spread and energy chirp 5 % at distance $1\,\mu m$.

Utilization of laser beam with larger transverse size allows one to hope that the beam slice emittance can become noticeably smaller then in present experiments. There also may be some correlations between longitudinal and transverse electron motion which can improve FEL operation.

Taking into account all these considerations we assume the beam parameters which are summarized in Table 2.

We also assume homogeneous focusing and constant transverse size of the beam in undulator. As it was mentioned above the focusing in our scheme is realized by beam magnetic field due to the partial screening of beam electrical field in gas. Therefore the transverse space charge defocusing is automatically taken into account.

Table 2: Electron beam parameters

Electron energy, GeV	1
Beam charge, nC	0.8
Pulse duration (r.m.s.), fs	1.5
Peak current, kA	200
Normalized slice emittance, mm×mrad	0.5
Beam transverse size in undulator, μm	8.75
Local energy spread	0
Energy chirp, %/ μm	5

One has to consider carefully the space charge longitudinal wakefield. In our case it is smaller then resistive wakefield and we do not include it in simulations (it depends on current derivative and can be reduced by increase of the bunch length). There is also fast oscillating component of the longitudinal field which is created by microbunching. Its influence is also not very significant because the plasma oscillation length is larger then the gain length.

Another space charge effect which we do not take into account is that the particles with large amplitudes of betatron oscillations gain additional energy in transverse electrical field. This effect creates correlations between electron energy and betatron amplitude which can be favourable for the FEL operation. Unfortunately in our case it is not strong enough for that.

The strongest collective effect which we include in our simulations is resistive wakefield. As the beam length is small we assume that the wakefield is simply proportional to the charge in front and proportionality constant is determined by the undulator gap [5]. The gas pressure is to be low enough to decrease the Cherenkov wakes.

SIMULATION RESULTS

To simulate FEL operation we used the code GENESIS [6]. The results are presented below.

In Fig. 2 one can see the increase of FEL radiation pulse energy (expressed in terms of photon number) in undulator. The gain length at the exponential growth stage (from 1 to 1.75 m) is about 28 cm. Difference between straight and dotted curve illustrates the efficiency degradation due to the resistive wakefield. Influence of the fast component of longitudinal electrical field created by microbunching is illustrated by dashed curve.

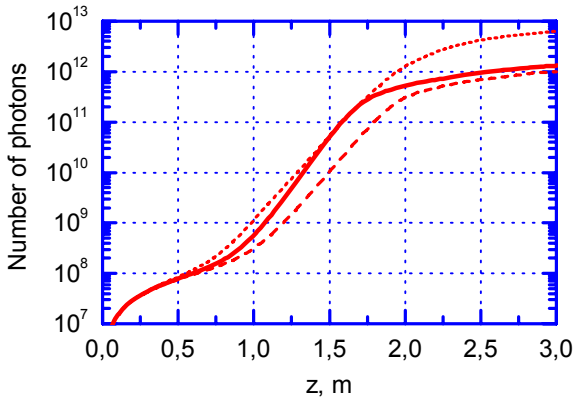

Figure2. Number of photons in the FEL radiation pulse as a function of longitudinal coordinate in undulator. Dotted curve corresponds to the resistive wake free case; dashed curve includes the influence of space charge.

Radiation power and spectral distributions at different positions in undulator are shown in Fig. 3.

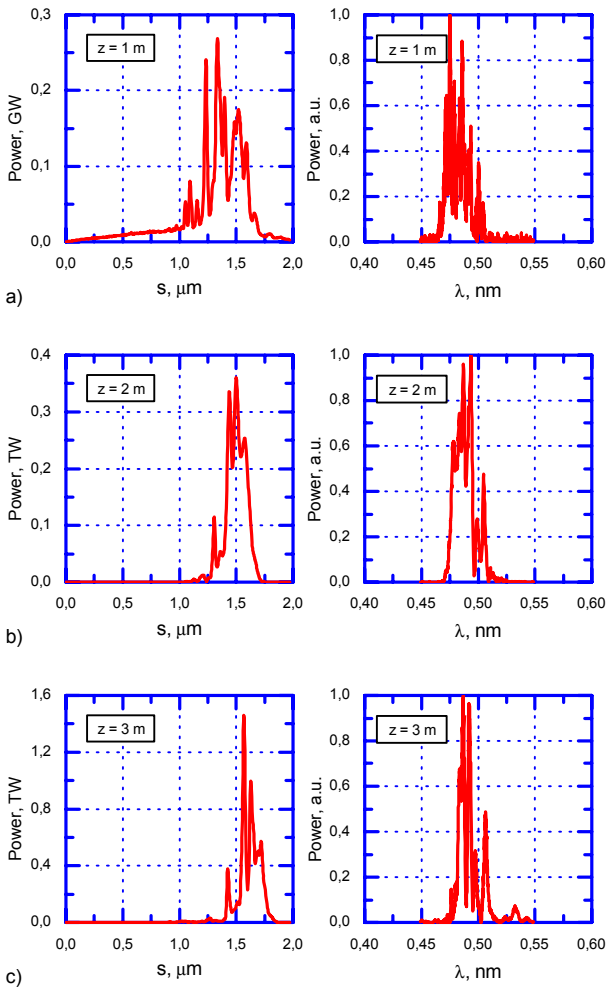

Figure 3. Radiation power and spectral distributions at different distances from the undulator entrance.

The peak power at saturation (3 m from the beginning of undulator) is about 1.5 TW. The spectral bandwidth is rather large which is typical for SASE FELs.

Beam bunching distribution at different stages is presented in Fig 4. The bunching reaches its maximal value at linear stage and starts dropping down at saturation.

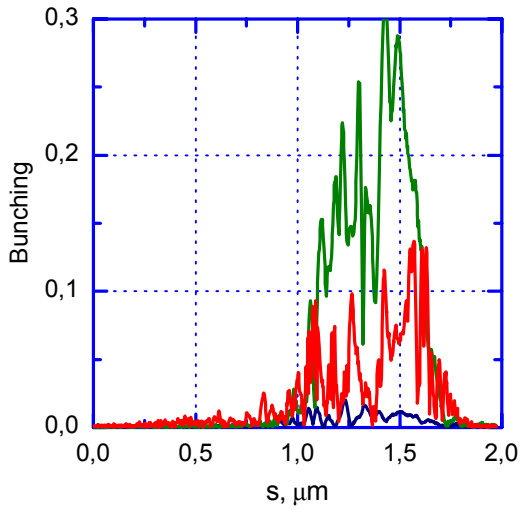

Figure 4. Beam bunching distribution at the distance 1 m (blue), 2 m (green) and 3 m (red) from the undulator entrance.

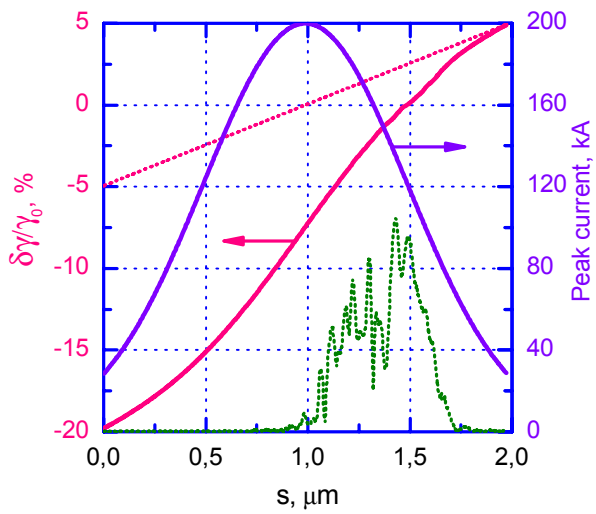

Figure 5. Relative energy deviation created by resistive wake in undulator and initial energy chirp (pink) and beam current profile (violet). Dotted pink curve corresponds to initial energy chirp and green curve shows beam bunching distribution in the middle of undulator.

The resistive wakefield is illustrated in Fig. 5. It is seen that microbunching grows only in front of the beam where the energy deviation is not very large.

The basic FEL parameters are summarized in Table 3.

Table 3: FEL parameters

Gain length, cm	28
Saturation length, m	~3
Radiation wavelength, Å	5
Number of photons	10^{12}
Peak power, TW	1.5
Spectral bandwidth (r.m.s.), %	2
Pulse duration (r.m.s), fs	0.37

CONCLUSION

In this paper we proposed the scheme of test installation for compact x-ray FEL based on laser-plasma accelerator. The main idea is that it is easier to optimize acceleration parameters (laser beam size, plasma pressure longitudinal dependence, etc.) looking at measured x-ray parameters, than to measure details of electron distribution in extremely short bunch with hopefully low slice emittance and energy spread. The lack of reliable data on beam parameters in LWFA makes impossible to predict gain length and power of FEL. Therefore our calculations demonstrate only some set of beam parameters for accelerator optimization. From the other hand, the available peak power of femtosecond lasers and their energy per pulse are increasing from year to year. This gives us the possibility of further LWFA beam parameters improvement (for example, by the increase of the laser beam transverse size for having more homogeneous accelerating field and less focusing aberrations).

REFERENCES

[1] T. Tajima and J. M. Dawson, Phys. Rev. Lett. **43**, 267 (1979).

[2] J. Faure *et al.*, Nature **431**, 541 (2004); C. G. R. Geddes *et al.*, Nature **431**, 538 (2004); S.P.D. Mangles *et al.*, Nature **431**, 535 (2004).

[3] F. Grüner *et al*., Appl. Phys. B 86, 431-435 (2007).

[4] A. Ho, R. H. Pantell, J. Feinstein, and Y. C. Haung, *IEEE* J. Quantum Electronics **27**, 2650 (1991).

[5] A. W. Chao, *Physics of collective beam instabilities in high energy accelerators* (John Wiley & Sons, New York, 1993); K. Bane, G. Stupakov, SLAC-PUB-10707

[6] S. Reiche, Nucl. Instrum. Methods Phys. Res. A **429**, 243 (1999).

DIFFRACTION EFFECTS IN THE COHERENT TRANSITION RADIATION BUNCH LENGTH DIAGNOSTICS *

G. Kazakevich, V. Lebedev, S. Nagaitsev,
FNAL, P.O. Box 500, Batavia, Illinois 60510, USA

Abstract

Diffraction effects in the Coherent Transition Radiation (CTR) bunch length diagnostics are considered for the A0 Photoinjector and the NML injection module. The effects can cause a noticeable distortion of the measured CTR spectra depending on the experimental setup and the bunch parameters and resulting in errors of the bunch length measurenents. Presented calculations show possible systematic errors in the bunch length in measurements based on the CTR spectra at A0 Photo injector and the NML injection module.

INTRODUCTION

Application of the CTR diagnostics for the sub-picoseconds bunch length measurements was proposed more than 10 years ago and a number of articles have been devoted to the experiments in this field. The diagnostics employing the Transition Radiation (TR), [1], are based on the measurements of the CTR spectra to restore the bunch length through the Fourier transform. In this article we consider low-frequency TR range where the coherent part of the spectrum dominates and the wavelengths are about the bunch length. For such low-frequency harmonics one should not neglect the diffraction effects in the coherent radiation diagnostics, [2, 3, 4]. They can strongly distort the measured CTR spectra depending on the beam energy and the experimental setup. We discuss computations of the CTR diffraction effects in application to the measurements at A0 Photoinjector, [5], and the NML injection module [6].

ELECTRIC FIELD OF THE TR AND CTR

Most experimental techniques using CTR spectra for the bunch length measurements employ backward TR generated at 45^0 incidences of electrons on the mirror-quality metallic screen. This radiation has a spectral density practically similar to the one for the backward TR at the normal incidence. For simplicity we consider only this case. To estimate the diffraction effects we assume a finite radius *a* of the TR screen. Finite size of vacuum chamber we do not consider for sake of simplicity though it also affects the bunch longitudinal profile. We also assume that the screen is located at the origin of the cylindrical frame η: $(\rho, \phi, z = 0)$, and the *z* axis is directed along the momentum of the electron beam. The observation point is displaced at a distance *D>>a* along *z*. A derivation of required formulae generally follows to Ref. [4], where the consideration is based on the virtual-photon method applicable for ultra relativistic electrons.

The Fourier harmonic of the radial electric field for the incident single electron is expressed as, [7, 4]:

$$\tilde{E}_r(\omega,\rho) = \frac{-e\omega}{(2\pi)^{3/2}\varepsilon_0\beta^2c^2\gamma} K_1\left(\frac{\omega\rho}{\beta c\gamma}\right), \quad (1)$$

where: ε_0 is the permittivity of vacuum, $K_1(u)$ is the second kind modified Bessel function. We assume that the virtual photon constituting the electron self-field is converted into the real TR photon. Considering continuity of the normal components of the electric induction and tangential components of the electric field of the virtual and real (reflected) photons, [8], one can conclude that the amplitudes of the radial components of virtual and real photons are same, i.e. the electric field of an ultra relativistic electron is almost completely reflected from metal screen. The small element of the TR screen with coordinates $(\rho,\phi,0)$ gives following contribution to the field (this field is also radial) in the point of observation *(x,0,D)* :

$$d\tilde{E}_x(x,0,D,\omega) = \frac{-i\omega}{2\pi c}\tilde{E}_r(\omega,\rho)\cos\phi\frac{e^{\frac{i\omega R'}{c}}}{R'}\rho d\rho d\phi \cdot \quad (2)$$

Here: R' is a distance between the points $(\rho,\phi,0)$ and (*x*,0,*D*),

$$R' = \sqrt{D^2 + (x-\rho\cos\phi)^2 + (\rho\sin\phi)^2} \approx R - \frac{x\rho\cos\phi}{R} + \frac{\rho^2}{2R}, \quad (3)$$

and: $R = \sqrt{D^2 + x^2}$. Substitution (1) and (3) into (2) with $x/R = \sin\theta$ and integration over the TR screen area yields for the electric field in the point (*x*,0,*D*):

$$\tilde{E}_x(x,0,D,\omega) \approx \frac{ie\omega^2}{(2\pi)^{5/2}\varepsilon_0\beta^2c^3\gamma}\cdot\frac{e^{\frac{i\omega R}{c}}}{R}\times \int_0^a\left[\int_0^{2\pi}K_1\left(\frac{\omega\rho}{\beta c\gamma}\right)\cos\phi\cdot e^{\frac{-i\omega\rho\sin\theta\cos\phi}{c}}d\phi\right]\cdot e^{\frac{i\omega\rho^2}{2cR}}\rho d\rho \cdot \quad (4)$$

In this expression the integration over angle ϕ gives the first kind Bessel function $J_1(z)$:

$$\int_0^{2\pi} e^{\frac{-i\omega\rho\sin\theta\cdot\cos\phi}{c}}\cos\phi\cdot d\phi = -i2\pi\cdot J_1\left(\frac{\omega\rho\sin\theta}{c}\right),$$

That yields:

*Work supported by Fermi Research Alliance LLC. Under DE-AC02-07CH11359 with the U.S. DOE
#kazakevi@fnal.gov

$$\tilde{E}_x(x,0,D,\omega) \approx \frac{e\omega^2}{(2\pi)^{3/2}\varepsilon_0\beta^2 c^3\gamma}\cdot\frac{e^{\frac{i\omega R}{c}}}{R}\times$$
$$\int_0^a J_1\left(\frac{\omega\rho\sin\theta}{c}\right)K_1\left(\frac{\omega\rho}{\beta c\gamma}\right)\cdot e^{\frac{i\omega\rho^2}{2cR}}\rho d\rho\,. \qquad (5)$$

The flow of the TR energy in the observation plane is: $S_z = (1/2\mu_0)\tilde{E}_x\tilde{B}_y^*$, where the magnetic field Fourier component is: $\tilde{B}(\omega) = \tilde{E}(\omega)/c$, and μ_0 is the permeability of vacuum. Total energy per unit area radiated through element $ds=dx\cdot dy$ is [8]:

$$\frac{d^2U}{d\omega d\Omega} = I(\omega,\theta) = 2\varepsilon_0 cR^2\left|\tilde{E}_x(\omega,\theta)\right|^2, \qquad (6)$$

where: $ds = R^2 d\Omega$.

Eqs. (5) and (6) include both: the Fraunhofer diffraction in far-field zone and the Fresnel diffraction in the near-field zone. The inequalities: $a < \gamma\lambda$ and $D < \gamma^2\lambda$ (λ is the wavelength of the TR harmonic), [9], give a region where the Ginzburg-Frank formula [1] has to be corrected for the diffraction. The Fraunhofer diffraction approximation considering finite size of the TR screen neglects the third term in Eq. (3); while the Fresnel diffraction approximation neglects the second term in Eq. (3). For the far-field measurements one can omit the Fresnel diffraction effect.

In ultra relativistic case and $a\to\infty$ results obtained from Eq. (5) for far-field zone coincide with those obtained with Ginzburg-Frank formula, therefore, for TR in the optical wavelength range at the electron energy of tens-hundreds MeV the diffraction effects are negligible and there is no need to use the above expressions to calculate the angular distribution of the radiation, however at the TR wavelength in the sub millimeter-millimeter range the diffraction effects become noticeable.

Using Eq. (5), derived for point like charge, one can obtain an expression for finite size bunch with charge *Ne* using the following method. First, we consider Fourier spectrum of the current of point-like bunch moving with velocity of $\vec{v}$ along *z* axis. The corresponding Fourier harmonics are:

$$j_{k\omega} = \int_{-\infty}^{\infty} Nev\delta(r-vt)e^{i(\omega t-kr)}\frac{dtdr}{(2\pi)^4} = \frac{Nev\cdot\delta\left(\omega-(\vec{k}\vec{v})\right)}{(2\pi)^4}.$$

Then we consider Fourier spectrum for a bunch with Gaussian distribution along *z* axis and infinitely small transverse sizes:

$$j_{k\omega} = \frac{Nev}{(2\pi)^4\sqrt{2\pi}\sigma}\int_{-\infty}^{\infty} e^{-\frac{(z-vt)^2}{2\sigma^2}}\cdot e^{i(\omega t-\vec{k}\vec{r})}dtdr^3.$$

Introducing new variable: $z`=z-vt$ and taking into account that: $\left(\frac{(z`)^2}{2\sigma^2}+ik(z`)\right) = \frac{\left(z`-i\sigma^2k\right)^2+\sigma^4k^2}{2\sigma^2}$,

$$\int_{-\infty}^{\infty} e^{-2i\cdot\pi\cdot kx}dk = \delta(x),\quad \int_{-\infty}^{\infty} e^{-x^2}dx = \sqrt{\pi} = \int_{-\infty}^{\infty} e^{-(x+ai)^2}dx,$$

one can write:

$$j_{k\omega} = \frac{Nev}{(2\pi)^4}\delta(\omega-kv_0)\exp\left(\frac{-\sigma^2k_z^2}{2}\right).$$

Here: k_z is projection of $\vec{k}$ on *z* axis. For small angles $k_z^2 \approx k^2(1-\theta^2)$, this results in:

$$j_{k\omega} = \frac{Nev}{(2\pi)^4}\delta(\omega-k_zv_0)\exp\left(\frac{-\sigma^2k^2(1-\theta^2)}{2}\right).$$

Comparing this expression with the Fourier harmonics of the point-like bunch current one obtains the term describing TR for finite size bunch. The term in a frequency domain is expressed as:

$$S(\omega) = N\exp\left(-\omega^2(1-\theta^2)/2\sigma_\omega^2\right). \qquad (8)$$

Thus in the case of longitudinal Gaussian distribution Eqs. (5) and (7) have to be supplemented by term $S(\omega)$. For $\theta<<1$ it results in,

$$S(\omega) \approx N\exp\left(-\omega^2/2\sigma_\omega^2\right).$$

Corresponding form-factor for spectral density of coherent radiation of the *N* electrons is:

$$F(\omega) = \left(S(\omega)\right)^2. \qquad (9)$$

That yields the total CTR spectral power within the angle θ_0 to be equal to:

$$I_{cd}(\omega) = 2\pi\int_0^{\theta_0} F(\omega)\cdot I(\omega,\theta)\sin\theta\cdot d\theta\,. \qquad (10)$$

Using this spectral power one can determine the bunch length through the inverse Fourier transformation.

DIFFRACTION EFFECTS IN THE SINGLE ELECTRON TR

Angular distributions of the backward TR generated by passage of single electron through the TR screen were computed using Eqs. (5), (6). The results for the wavelengths, λ, of 1, 0.3, 0.1 mm and the electron energies of 15 and 40 MeV are plotted in Figs. 1, 2.

The TR screen radius, *a*=12.5 mm of existing real setup and the distances *R* =250 mm and *R* >>250 mm (far field zone) were used in the computations.

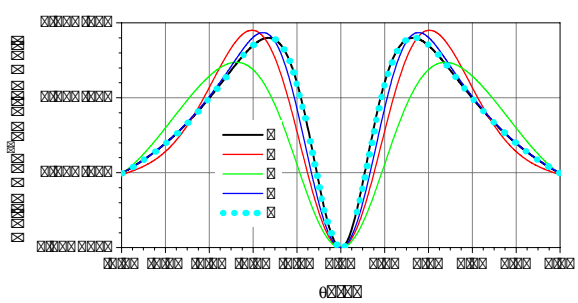

Fig. 1. Angular distribution of the backward TR for different wavelengths and 15 MeV electrons. C- λ=1 mm, far-field zone; D- λ=1 mm, R=250 mm; E- λ=0.3 mm,

R=250 mm; F- λ=0.1 mm, R=250 mm. Curve B was computed using Ginzburg-Frank formula.

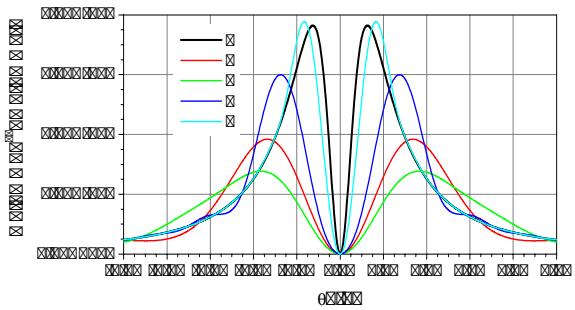

Fig. 2. Angular distribution of the backward TR for different wavelengths and 40 MeV electrons. C- λ=1 mm, far-field zone; D- λ=1 mm, R=250 mm; E- λ=0.3 mm, R=250 mm; F- λ=0.1 mm, R=250 mm. Curve B was computed using Ginzburg-Frank formula.

For comparison the angular distributions of the backward TR calculated using the Ginzburg-Frank formula (where the spectral density does not depend on the frequency in a wide range) are also shown in these figures.

The plots show that the diffraction effects caused by finite TR screen size noticeably change the angular distribution of the TR especially for low frequencies. Computation of the angular distribution using Eq. (5) and (6) for the TR screen radius $a > \gamma\lambda$ and detection of the TR in the far-field zone results in excellent agreement with calculation using the Ginzburg-Frank formula; but for $a < \gamma\lambda$ and/or detection of the TR at $D < \gamma^2\lambda$ a noticeable difference appears. An increase of the energy of electrons magnifies the difference for long-wavelength TR due to diffraction effects, in spite of the narrower angular distribution of the TR at higher energy. The diffraction phenomenon becomes apparent in a broadening of the TR angular distribution for longer waves.

Since the CTR exists in long-wave part of spectrum, the broadening in the angular distribution causes a distortion of the measured CTR spectra in a real experimental setup. This additionally complicates determination of the bunch length in methods employing the CTR techniques.

DIFFRACTION EFFECTS IN THE CTR SPECTRA

The spectra for the Gaussian distributions with rms bunch duration of σ_t = 1.5 ps, 0.5 ps. and 0.15 ps are presented by Gaussians with rms frequency width σ_f = 0.107 THz, 0.322 THz and 1.07 THz, respectively.

The CTR spectra corresponding to real setups were calculated using Eqs. (5), (6) and (10) for θ_0 = 0.05 rad. and 0.1 rad. Dependences of the spectra on the σ_t of the bunch, beam energy and setup condition are shown in Figs. 3-5.

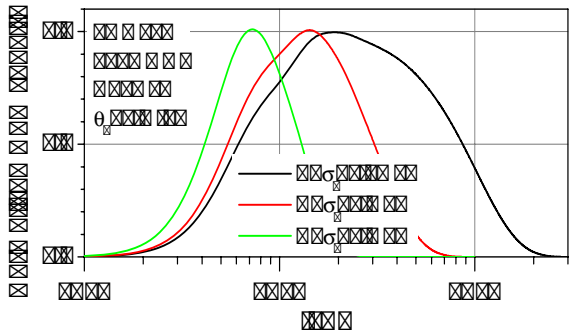

Fig. 3. Calculated normalized CTR spectra for 15 MeV for different σ_t at a=25 mm, θ_0=0.1 rad.

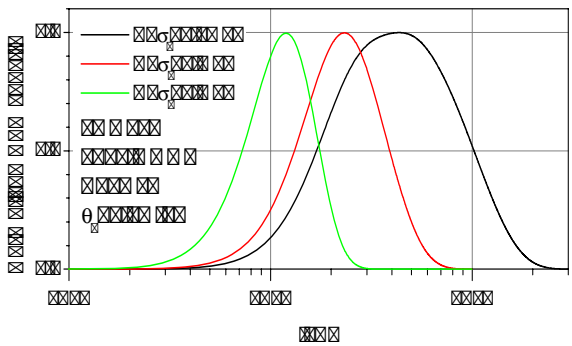

Fig. 4. Calculated normalized CTR spectra for 15 MeV for different σ_t at a=12.5 mm, θ_0=0.05 rad.

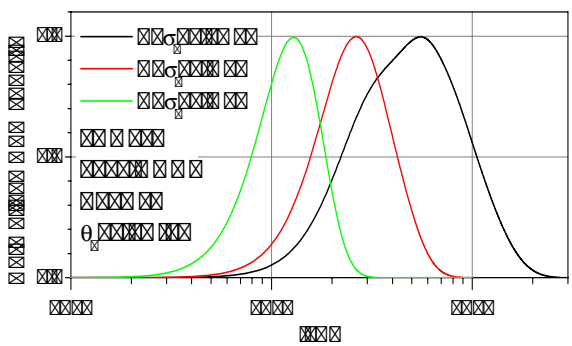

Fig. 5. Calculated normalized CTR spectra for 40 MeV for different σ_t at a=12.5 mm, θ_0=0.05 rad.

The plotted curves show significant variation of the CTR spectra with parameters of the experiment because of diffraction effects. The effects noticeably shift low frequency boundary of the CTR spectra to higher frequencies at limited size of the TR screen and limited detector acceptance. In fact these phenomena lead to the "shortening" of the electron bunch length if it is computed using the inverse Fourier transform. Corresponding results are shown in Fig. 6 for different σ_t values at 15 MeV, a=12.5 mm and θ_0=0.05 rad.

We introduce the dimensionless relative σ_r as the ratio of the computed (using inverse Fourier transform of the

CTR spectra) σ_t value to the real σ_t value of the bunch with Gaussian longitudinal distribution. It is plotted in Fig. 7 for different beam energies and setup parameters.

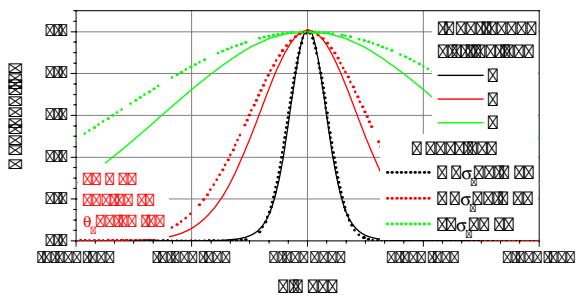

Fig. 6. "Shortening" in the bunch duration caused by diffraction. Curves *B, C, E* correspond to σ_t=0.5, 1.5, 5 ps, respectively.

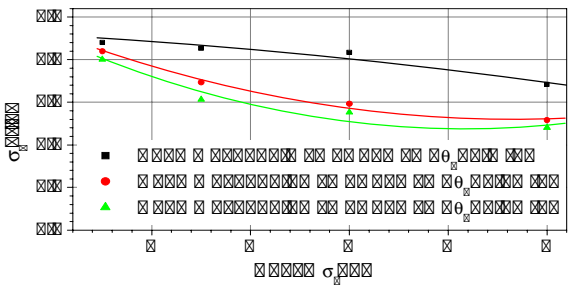

Fig. 7. Bunch "shortening" caused by diffraction effects for different bunch durations, setup geometries and beam energy.

Presented plots evaluate systematic errors in the bunch length caused by diffraction, if distortion of CTR spectra is unaccounted. The effects become noticeable at low frequencies (longer bunch length) and they are caused by both: the finite size of the TR screen (the Fraunhofer diffraction) and the finite distance to the detecting device at finite acceptance of the detecting device (the Fresnel diffraction) as well.

Note that the same systematic errors are inherent to all methods based on the measurements of the coherent radiation, including methods utilizing non-linear optical crystals.

The ordinary experimental setup employing the TR screen of 25 mm in diameter at detection of the CTR in the range of ± 0.05 rad. gives relative systematic error in the bunch length of ≈ 10% at the bunch length of 0.5 mm and at the electron beam energy of 15 MeV. At longer bunch the diffraction more distorts the CTR spectra and systematic error in the bunch length should be bigger if the CTR diagnostics are used. For the bunch length of ≈ 3 mm the relative systematic error is increased up to ~24% for Gaussian longitudinal bunch profile. Higher energy of the electrons causes bigger distortion of the CTR spectra and, correspondingly, bigger systematic error in the bunch length determination. Figure 8 presents systematic errors of the bunch length calculations caused by diffraction for Gaussian longitudinal bunch profiles.

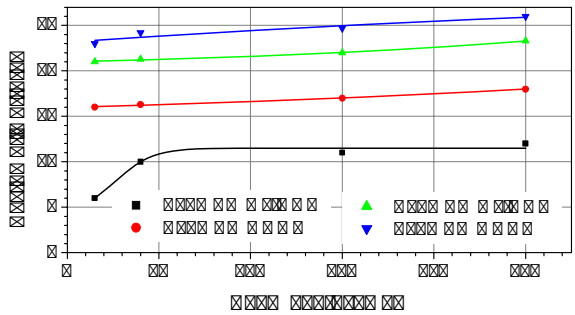

Fig. 8. Systematic errors caused by diffraction effects in finding of the bunch length based on the CTR techniques for different beam energies.

The presented plots were calculated at *a =1.25 cm, R = 25 cm, θ_0 =0.05* rad. As follows from Fig. 8 those setup parameters provide systematic errors ≤ 5% for the bunch length ≤ 0.3 mm at the beam energy up to 15 MeV and ~ 12% at the beam energy of 250 MeV. Increase of the bunch length causes a stronger distortion of the result. Increase of the beam energy also amplifies a distortion of the result.

SUMMARY

If uncounted, the diffraction distortions of the CTR spectra result in systematic errors of the bunch length measurements depending on the setup and the bunch parameters. The diffraction corrections should be considered in the planned experiments at the A0 Photoinjector and the NML injection module.

REFERENCES

[1] V.L Ginzburg and I.M. Frank, J. Exp. and Theoret. Phys., Vol. 16, pp. 15-21, 1946

[2] M. Castellano and V.A. Verzilov, PRST-AB V1, 062801, (1998)

[3] M. Castellano et al., NIM A 435, (1999), 297-307

[4] S. Casalbuoni et al., TESLA Report 2005-15

[5] J.P. Carneiro et al., "First Results of the Fermilab High-Brightness RF Photoinjector", Proc. of the 1999 PAC Conference, NY, 1999, pp. 2027-2029

[6] M. Church et al., "Plans for a 750 MeV Electron Beam Test Facility at Fermilab" PAC 2007 report, PAC Conference, Albuquerque, New Mexico, 2007

[7] J.D. Jackson, Classical Electrodynamics, J. Wiley & Sons, 1998

[8] L.D. Landau and E.M. Lifshitz, Electrodynamics of Continuous Media, Pergamon, New York, 1960

[9] V.A. Lebedev, NIM A 372, (1996), 344-348

SIMULATIONS FOR THE LCLS INJECTOR

C.Limborg-Deprey*, D.H. Dowell, P.Emma, R.Iverson, J.Frisch, H.Loos, J.Turner, J.Schmerge, J.Welch, J.Wu, Y.Ding, Z.Huang, J.Castro, G.Hays, P.Hering, S.Gilevich, A Miahnahri, W.White
SLAC[#], MS 18, SLAC 2575 Sand Hill Road, Menlo Park, CA , U.S.A.

Abstract

The Linac Coherent Light Source (LCLS) Injector has now been commissioned for five months. Measurements made at the end of the Injector beamline show that the beam quality meets the specifications. The transverse projected emittances at 135MeV are in the range of 1.2 mm-mrad for 1nC/100A and the horizontal slice emittances are below 1 mm-mrad. In this paper, we discuss the validity of both emittance and bunch length measurements by comparing them with results from simulations made with a multi-particle tracking code.

INTRODUCTION

The LCLS Injector commissioning started on April 5th 2007 after several years of design, manufacturing and installation. After a few months of commissioning, the beam quality at 135 MeV reached design performances with projected emittances varying from 1 to 1.5 mm-mrad at 1nC and peak current of 100A [1] .

A bunch charge of 1nC charge was obtained after "passive" and "active" laser cleaning were done. "Passive" cleaning is done at nominal laser fluence while operating. In particular, when the laser radius was decreased from 1.0 to 0.7 mm, to minimize the transverse emittances, a factor two increase in quantum efficiency was obtained after one week of operation at that new setting. "Active" cleaning was then performed switching off the RF and forcing the laser fluence to 2.5 times higher levels than nominal while scanning the cathode position. It then allowed us to reach 1nC at 300 μJ on the cathode and 30 degrees laser injection phase.

In this paper, we discuss the validity of transverse emittance numbers deduced from the measurements by comparing them to numbers obtained from simulated data after processing those latter following the same method as that applied to measured data. In the 135 MeV section of the LCLS Injector, the emittance can be obtained by either determining beam sizes at three screens (separated by 60 degree phase advance) or at a single screen while scanning an upstream quadrupole (quad scan). The beam sizes are measured using OTR screens or wire scanners. All combined, this gives at least four types of measurements. The rms beam sizes can be extracted following various algorithms which truncate the tails of the distributions at different levels. Similar truncation levels were applied to the simulated data. The first part of this paper shows that the emittance value rapidly decreases when long tails are truncated. Emittances as low as 1.2 mm-mrad in both planes for 1nC seem realistic for 90-95% of the particles constituting the core of the bunch.

* Corresponding author: limborg@slac.stanford.edu
# SLAC is operated by Stanford University for the Department of Energy under contract number DE-AC03-76SF00515

In the second part of this paper, we report on the effort made to benchmark the simulation code IMPACT [2] to the experimental data. Multi-particle tracking codes [3,4] had been used intensively at the design stage of the LCLS injector to specify tolerances of the beamline components and of the drive laser [5]. In this paper, we present results calculated with the 3D algorithm of the IMPACT code. 3D simulations are essential to represent our asymmetric beam. IMPACT can run on parallel processors, making 3D calculations time efficient.

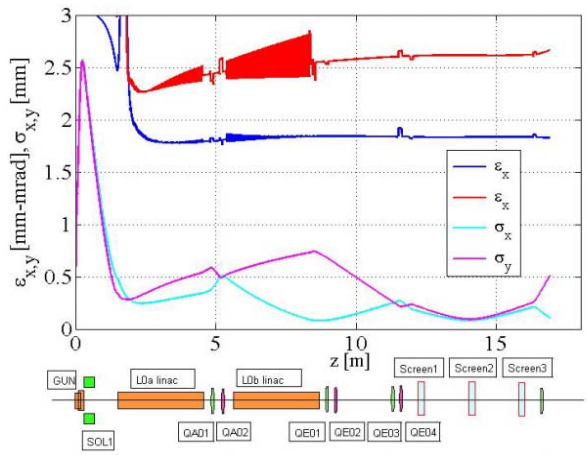

Figure 1: Beam size and 100% projected emittance for optimized beamline – the beam is matched to the 3-screens – the three OTR screen locations are shown

EMITTANCE

Transverse Tails

The initial distribution used in the simulations presented in this chapter uses the virtual cathode drive laser image as a transverse profile. The laser spot on the cathode, and thus the virtual cathode, is the image of an aperture limiting our transversally Gaussian laser profile. Even if the emission profile has hard edges, see figure2-a, the photo-electron beam develops large transverse tails. To evaluate the effect of those tails on the emittance calculations, simulations with 2 levels of meshing were used: 32 x 32 x 32 or 128 x 128 x 64. The first set was run with 200k particles and the second one with 4 million particles. No noticeable difference was seen in the generation of transverse tails and emittance results were within a few percent. In both cases some islands of higher density were preserved down the beamline as shown in the three screen profiles of figure 3. The 4 million particle distribution case shows finer structure in the profile than the 200k distribution. But, the 12μm

resolution of the screens sets the limit to the fine structure visible on the experimental data. The long transverse tails seen in the simulations are similar to those observed in the experiment (see figure 3d). The longitudinal profile used in the simulations (see figure 2-b) is directly the laser one measured with the cross-correlator.

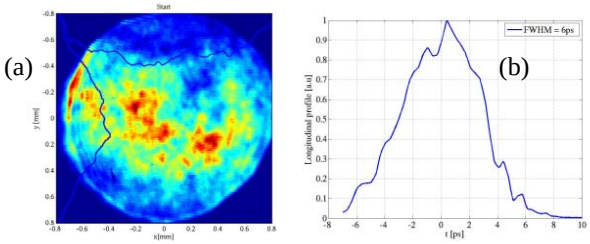

Figure 2: Laser profiles July 13th 2007 (a) virtual cathode (b) Longitudinal profile

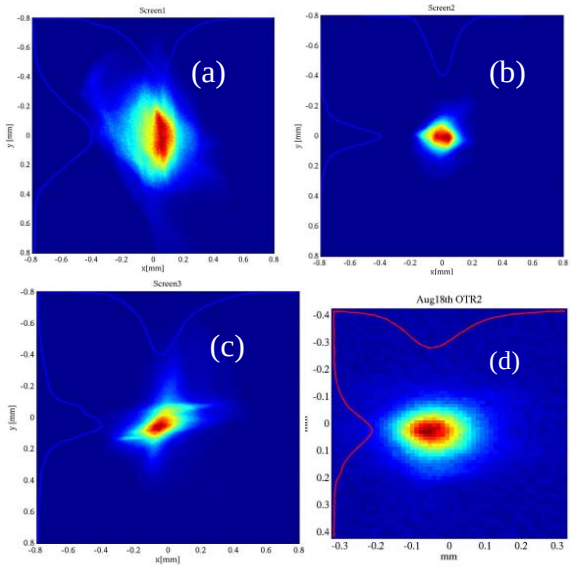

Figure 3: Transverse profiles ; Simulations data (a) OTR1; (b) OTR2 ; (c) OTR3 ; Experimental data (d) OTR2 (scale different to show graininess)

Rms Beam Size Calculation

The rms beam size of the profiles can be computed following various methods, but the "rms area cut" is most commonly used. The rms beam size is typically computed by integrating each measured 1D transverse profile and cutting out 2.5% of the area (charge) on each side. Accordingly, the truncated profile then contains 95% of the charge at the beam core. Other methods are applied less commonly, including Gaussian fits, and full 100% rms calculations, but the 95% core emittance value is less sensitive to baseline profile noise as well as weak beam tails, which will likely not contribute to the FEL gain in any case. Applying the same robust method uniformly in both measurement and simulation allows a fair, reproducible comparison. Accordingly, the intensity profile, after these cuts, should then contain 95% of the charge.

Three Screen Emittance Measurement

The beamline quadrupoles are tuned such that the beam sees a 60 degree betatron phase advance between each successive screen of the three screen emittance station. The transverse phase space is then probed optimally in size and angle. Both experimental and simulations data correspond to a well matched beam as the one presented in figure 1. Slightly different magnet settings were used in the simulations compared to the experimental one in order to compensate for small inaccuracies in the beamline model and beam characteristics. In figure 4, the emittance numbers are computed from the three profiles after appropriate truncation. Figure 4 shows that the horizontal and vertical emittances get respectively close to 1.2 and 1.5 mm-mrad in the horizontal plane for 5% cut area, while the numbers are 1.8 and 2.6 mm-mrad for the distribution containing all the particles.

Quadrupole Scan Emittance Measurement

A simulation of the quadrupole scan using QE04 (see figure 1) was performed. For each of the quadrupole setting, the appropriate truncation levels were applied to the profiles. The numbers obtained are nearly identical to those obtained for the 3-screen emittance calculations and are plotted in figure 4. Once again, the simulations were done starting from a matched configuration. Running 4 million particles instead of 200k did not change the results by more than a few percent.

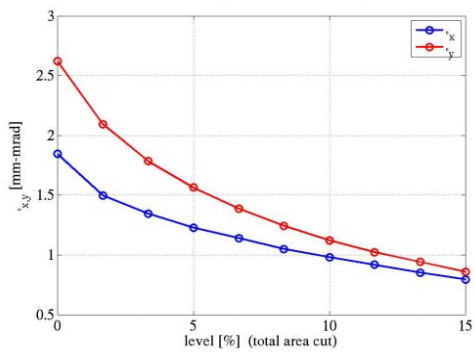

Figure 4: Emittance calculated from simulations for different levels of area cut on the transverse profile; the curves are identical for both quadrupole scan simulated data (using 7 profiles) and the three screen simulated data

SIMULATIONS VS EXPERIMENT

Initial Distribution

The initial particle distribution needs to be as close as possible to the emitted photo-electron distribution.
In the transverse plane, the intensity of the emission profile can differ dramatically from that of the virtual cathode image due to variation in quantum efficiency across the cathode. To measure the emission profile, a point-to-point imaging of the cathode is performed at extremely low charges. Such images show that our

cathode presents some high density emission spots. It is not clear that those emission spots were generated by high intensity spots in the drive laser beam or by some RF arcing in the gun at the early stage of commissioning. Since we operate in the space charge limit regime, it is not certain that the intensity emission profile is the same at high charge and at low charge [6]. However, in the simulations presented below, we used the intensity profile measured at low charge on the first imaging screen and transported back to the cathode.

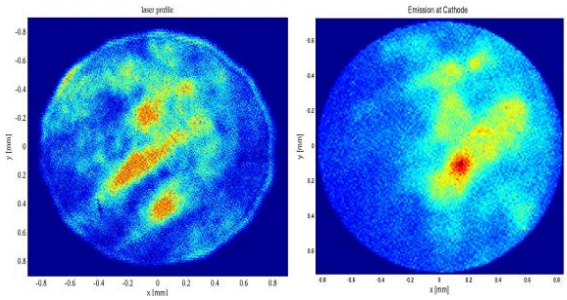

Figure 5: (a) virtual cathode; (b) emission scaled and rotated from point-to-point image at first screen

In the longitudinal plane, we used directly the laser longitudinal profile measured with the cross-correlator (mixing the UV and the IR of the Ti:Sa laser), see figure 6. This profile should in theory be corrected for Schottky effect, see figure 7, but the intensity variation is small over the 6 ps, i.e. the 6 degrees of the bunch extent.

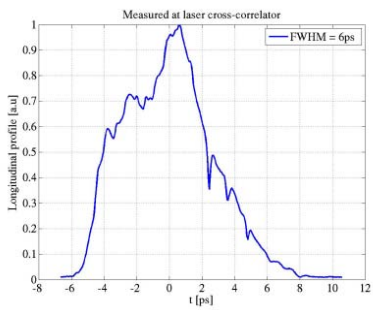

Figure 6: Longitudinal profile measured at the cross-correlator

The distributions of the transverse momenta are Gaussian with rms values giving a thermal emittance of 0.6 mm-mrad per mm of cathode radius. Thermal emittance measurements were done early in the run confirming this level.

A six-dimensional distribution is then generated numerically using a quiet start algorithm based on Halton sequences [7].

Beamline Model

The beamline components have been described in [5] and are briefly summarized at the bottom of figure 1. Other magnetic fields present in the gun region have been ignored as of now, but will be included in a second round of simulations. The beam is assumed to be on axis and not perturbed by wakefields. The beam is usually steered into the linac section to prevent wakefield-based emittance growth.

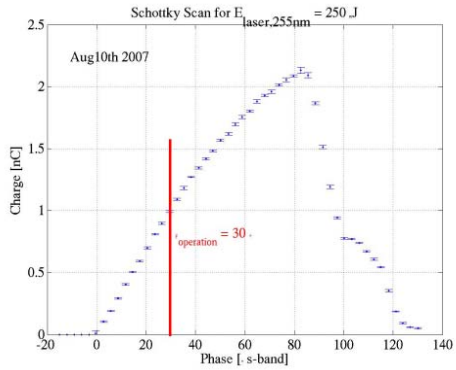

Figure 7: Schottky scan; charge vs laser injection phase

Operating Parameters

The nominal parameters are

- Laser pulse (6ps FWHM, 1.66 mm diameter)
- Charge from 200pC to 1nC
- 30 degrees injection phase
- Gun gradient 110MV/m (more recently 115 MV/m)
- Linac sections 20 MV/m , 24 MV/m

Machine Tuning

The standard procedure for tuning the LCLS Injector follows these steps:

(1) verify laser injection phase to 30 degrees by performing a Schottky scan (charge vs laser injection phase)
(2) realign the laser on the solenoid axis (the solenoid was aligned to the gun very accurately before installation)
(3) matching to emittance station
(4) perform emittance minimization by scanning solenoid, steering into the linac section

Solenoid Scan Emittance Measurement

Solenoid scans are done on a regular basis for operating the LCLS Injector. The optimum solenoid value changes mostly when gun RF parameters and slightly with charge.

Figure 8 and Figure 9 show the same measurement of emittance as a function of solenoid value but for two types of analysis. Figure 8 shows the result using the 100% rms, i.e for no truncation of the tails of the profiles. The shape of the curve of measured horizontal emittance is very similar to that obtained with the simulations and computed with 0% truncation level. But the mimimum value differs by 25%. A better agreement on the minimum emittance value is obtained if a 2.5% level cut is applied on the simulated data, in particular for the vertical plane. Figure 9 shows the results from the measurements when the standard 5% rms cut area is used on the profile. Simulations results based on the 5% level give slightly higher emittance numbers. However, if a truncation at 7.5 % level is applied on the simulated data, the agreement with the measurements becomes quite good.

The solenoid currents used in the simulations were scaled by a factor 0.986 to make the solenoid values

giving the minimum emittance coincide in both cases. Such an error of 1.4% is within the tolerance of the gun energy measurement done at the gun exit.

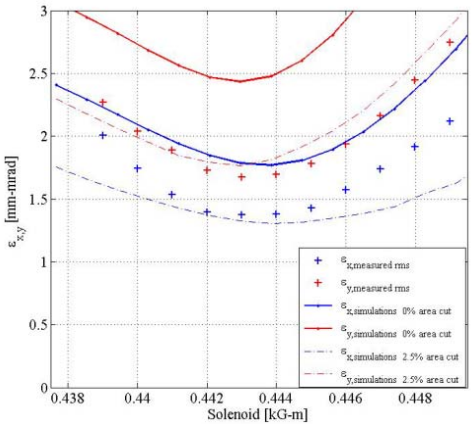

Figure 8: Emittance vs solenoid- Comparison between experimental and simulated data for rms values calculated with no cut on the tails- simulations results at 2.5 % cut level have also been superimposed

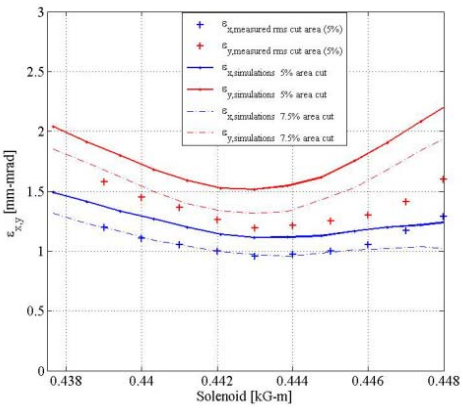

Figure 9: Emittance vs solenoid- Comparison between from experimental data and simulations based on the 5% rms cut area - simulations results at 7.5 % cut have also been superimposed

Bunch Length vs Charge

Bunch lengths are measured using a transverse deflecting cavity. A careful calibration is regularly performed to accommodate the effects of the variation in klystron power. The experimental data presented in figure 10 were taken within less than an hour. Simulations were based on the optimization of the beamline for 200 pC as was the case the day of that measurement. The agreement between the measurement and the simulations is quite satisfactory. The measured longitudinal laser profile used in the simulation was that measured with the cross-correlator and had a 5ps FWHM, i.e. it was slightly smaller than the nominal 6ps long laser pulse used for most of our 2007 run.

At 1nC, when the laser pulse is 6ps long, the rms bunch length of the electron beam at 135 MeV is 1.05mm. It is larger than the design value of 0.84 mm. The space charge induced bunch lengthening is stronger when starting with both a shorter laser pulse and a smaller radius than those calculated at the design stage. The design laser pulse for 1nC was 10ps FWHM and 1mm radius.

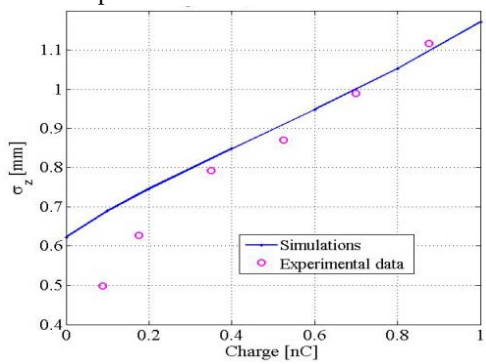

Figure 10: rms bunch length measured compared to results from simulations

CONCLUSION

This first series of simulations seem to validate the acceptable emittance numbers measured at 1nC during the first LCLS Injector run. A fairly good agreement is obtained between measurement and simulations. More experimental data are required to characterize the physics of the emission in the space charge limited regime in which we are running. The related physics might explain the 25% higher emittance numbers obtained in the simulations. A second series of simulations remains to be done including the complete set of known magnetic fields. Further comparisons will include longitudinal phase space characterization and data for low charges.

ACKNOWLEDGEMENTS

The authors would like to thank Ji Qiang (IMPACT) for his very valuable help in setting up the LCLS deck in IMPACT. The authors are indebted to L.Young (PARMELA) and K.Floetmann (ASTRA) for their great support over the years and for the development of multiparticle tracking codes for photo-injectors. The authors are also very grateful to the engineers, technicians and operators involved in the Injector construction and commissioning.

REFERENCES

[1] D.Dowell, "LCLS Injector Commissioning Results" these proceedings
[2] J.Qiang , IMPACT-T User Document Version 1.5, LBNL, rep 62326,2007
[3] L.Young, J.Billen, PARMELA, LANL codes, laacg1.lanl.gov/laacg/services/parmela.html
[4] K.Floettmann, ASTRA, K.Floetmann, http://www.desy.de/~mpyflo/Astra_dokumentation/
[5] C.Limborg-Deprey, "Modifications of the LCLS Injector Beamline", EPAC 04, Lucerne, Switzerland
[6] J.Rosenzweig, "Initial Measurements of the UCLA RF PhotoInjector ", NIM A 341 (1994) 379-385
[7] Halton sequences, http://orion.math.iastate.edu/reu/2001/voronoi/halton_sequence.html

PRELIMINARY STUDY OF QUIET START METHOD IN HGHG FEL SIMULATION*

Y.Hao#, L.H.Yu, BNL, Upton, NY 11973, U.S.A.
Y.Hao, Indiana University, Bloomington, IN 47405, U.S.A.

Abstract

Quiet start scheme is broadly utilized in Self Amplified Spontaneous Radiation (SASE) FEL simulations, which is proven to be correct and efficient. Nevertheless, due to the energy modulation and the dispersion section, the High Gain Harmonic Generation (HGHG) FEL simulation will not be improved by the traditional quiet start method. A new approach is presented to largely decrease the number of macro-particles per slice that can be implemented in both time-independent and time-dependent simulation, accordingly expedites the high order harmonic cascade simulation or other small modulation HGHG cases.

INTRODUCTION

Great interest has been focused in single pass free electron laser (FEL) for many years for the capability of generating coherent radiation with high intensity and short pulse duration in short wavelength from deep ultraviolet (~100 nm) to hard x-ray (~0.1nm). The scheme, self amplified spontaneous radiation (SASE), has been carefully study in both theory and experiment. The simulation of SASE FEL process is achieved by using the quiet start method[1,2], which reduces the macro particle number and simulation time dramatically. However, SASE FEL is seeded by the shot noise of electron bunch; hence produce limited temporal coherence and large shot-to-shot intensity fluctuation.

An alternate approach for SASE FEL is the high gain harmonic generation (HGHG) FEL. As the first HGHG FEL experiment is accomplished successfully and overcome the limit of SASE FEL [3], increasing projects were proposed to produce fully coherent VUV and soft X-ray radiations sources using cascade HGHG scheme.

The Quiet Start scheme, which reduces the number of macro particles largely in SASE simulation, uses only small number of distinguished phase ψ (usually 4). Each phase is filled with identical macro particle distribution of other 5 dimensions (γ, x, y, p_x, p_y), which is generated by pseudo random number generator or Hammersley quasi-random sequence. However, the quiet start scheme does not lead to correct bunching factor in terms of HGHG process.

A quiet start method scheme for HGHG is introduced in [4]. In the article, we consider a more dedicate method to realize 'Quiet Start' initial particle loading in small modulation case when the modulator and dispersion sessions exist, in order to achieve correct bunching factor at the entrance of radiator. When energy modulation is small because of a weak seed laser, the beam energy spread is large or dispersion effect is large so that the beam is over bunched, the signal (bunching factor) generated by modulator and dispersion section will be small. Such small bunching factor will be overwhelmed by the noise of initial loading method such as Hammersley sequence, if the number of macro particles is not large enough. The quiet start loading method is to find a way to generate less noise with same number of macro particles compared with normal loading methods. To introduce our method on the small modulation HGHG FEL simulation, first we will derive the bunching factor errors produce by this quiet start scheme in 1-D case theoretically. Then 3-D scheme is carried out with utilizing Hammersley sequence on transverse dimensions to reduce noise. One example of small modulation HGHG scheme is demonstrated to show the effectiveness of the method in the last section.

ONE DIMENSION ANALYSIS

In the HGHG FEL scheme, the bunching factor after energy modulation and dispersion section can be calculated theoretically using a simplified one dimension model. Assuming that the phase space distribution is described by distribution written in variable $\gamma = E/mc^2 - \gamma_c$, $\theta = (k_0 + k_w)z - \omega_0 t$, where E is the energy of electron, mc^2 is electron mass, γ_c corresponds to the resonance energy, k_0 and ω_0 is the resonance wave number and resonance angular frequency, k_w is the undulator wave number.

The initial distribution function can be written as Eq. (1), with energy spread σ_γ,

$$f(\gamma_0, \theta_0) = \frac{1}{\sqrt{2\pi}\sigma_\gamma} \exp\left(-\frac{\gamma_0^2}{2\sigma_\gamma^2}\right) \tag{1}$$

After the modulator, the electron bunch energy is modulated to (γ', θ')

$$\begin{aligned} \gamma' &= \gamma_0 + \Delta\gamma \sin(\theta_0) \\ \theta' &= \theta_0 \end{aligned} \tag{2}$$

The energy modulation strength $\Delta\gamma$ can be calculated from the modulator strength and seed laser power.

The dispersion section gives rotation on the longitudinal phase space and change the energy modulation to density modulation. The new coordinate (γ'', θ'') is given by

$$\begin{aligned} \gamma'' &= \gamma' = \gamma_0 + \Delta\gamma \sin(\theta_0) \\ \theta'' &= \frac{d\theta}{d\gamma}(\gamma_0 + \Delta\gamma \sin(\theta_0)) + \theta_0 \end{aligned} \tag{3}$$

*Work supported by U.S.DOE under contract No DE-FG02-92ER40747 and NSF under contract No PHY-0552389
#yhao@bnl.gov

Before the bunch enters the radiator, the distribution function is shown in Eq.(4). Here we change the notation (γ'', θ'') to $(\gamma + \gamma_0, \theta)$ for simplicity.

$$f(\gamma,\theta) = \frac{1}{\sqrt{2\pi}\sigma_\gamma}\exp\left(-\frac{\left(\gamma-\Delta\gamma\sin\left(\theta-\frac{d\theta}{d\gamma}\gamma\right)\right)^2}{2\sigma_\gamma^2}\right) \quad (4)$$

The bunching factor after modulator and dispersion section can be calculated as

$$b_m = J_m\left(m\frac{d\theta}{d\gamma}\Delta\gamma\right)\exp\left(-(m\frac{d\theta}{d\gamma}\sigma_\gamma)^2/2\right) \quad (5)$$

In HGHG simulation, the traditional quiet start method does not produce the desired bunching factor as derived in equation (5) using finite number macro-particles. To obtain the correct bunching factor after energy modulation and dispersion section, we must carefully consider two dimensional initial longitudinal phase space variables (γ_0, θ_0) to choose the macro-particles used in the simulation. Assuming the initially configuration is evenly distributed in phase variable θ, and has Gaussian distribution with energy spread σ_γ in γ. We choose the phase to be some equal-space discrete value $\theta_{0j} = 2\pi \times j/N_j$, where N_j is the total number of discrete value θ_{0j}. In each θ_{0j}, same configuration of energy γ_{0k}, totally N_k energy values, is assigned. Using this configuration, we need $N_j \times N_k$ macro-particles for 1-D analysis.

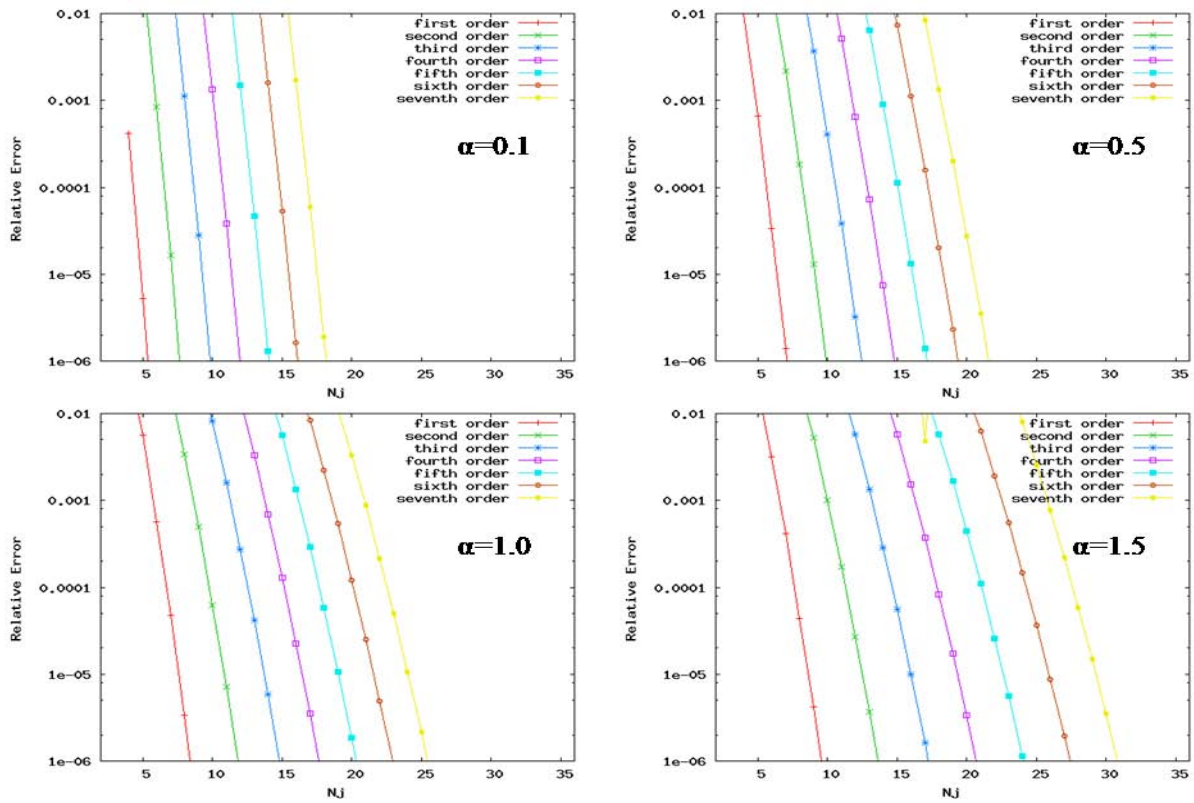

Figure 1. Bunching factor error as function of N_j

Now we can find the bunching factor of these $N_j \times N_k$ particles before entering the radiator, using the Eq (3). Here we use θ_l as the final phase of l^{th} particle after energy modulation and dispersion section, where l varies from 1 to $N_j \times N_k$. Parameter $\alpha = d\theta/d\gamma \times \Delta\gamma$ is introduced for simplicity.

$$b_m = \langle e^{im\theta_l}\rangle = \sum_{l=1}^{N_j\times N_k} e^{im\theta_l} = \frac{1}{N_j N_k}\sum_{j=1}^{N_j}\sum_{k=1}^{N_k} e^{im\left(\frac{d\theta}{d\gamma}(\gamma_{0k}+\Delta\gamma\sin(\theta_{0j}))+\theta_{0j}\right)} \quad (6)$$

$$= \frac{1}{N_j N_k}\sum_{j=1}^{N_j} e^{im\theta_{oj}+im\alpha\sin(\theta_{0j})}\sum_{k=1}^{N_k} e^{im\frac{d\theta}{d\gamma}\gamma_{0k}}$$

Now the two sums are decoupled and can be evaluated separately. The first sum only depends on N_j; while the second relies on each γ_{ok}.

The first sum in Eq. (6) can be calculated easily using Jacobi-Anger expansion $e^{izsin(\theta)} = \sum_{p=-\infty}^{+\infty} J_p(z)e^{ip\theta}$, where $J_p(z)$ is Bessel function of the first kind.

$$\frac{1}{N_j}\sum_{j=1}^{N_j} e^{im\theta_{oj}+imasin(\theta_{0j})} = \frac{1}{N_k}\sum_{j=1}^{N_j}\sum_{p=-\infty}^{+\infty} J_p(m\alpha)\, e^{\frac{i(p+m)2\pi j}{N_j}} \quad (7)$$

After simple steps, the bunching factor gives

$$b_m = \sum_{t=-\infty}^{+\infty} J_{tN_j-m}(m\alpha) \times \sum_{k=1}^{N_k} e^{im\frac{d\theta}{d\gamma}\gamma_{0k}} \quad (8)$$

Equation (8) shows the criteria of choosing N_j. Quantitatively, we can define the bunching factor error E(m,α) by comparing Eq. (8) and (5).

$$E_1(m,\alpha) = \frac{\left|\sum_{t=-\infty}^{\infty} J_{tN_j-m}(m\alpha)\right| - J_m(m\alpha)}{J_m(m\alpha)} \quad (9)$$

Figure 1 is the bunching error of the first sum with respect to N_j, at different harmonic number m and parameter α. It shows that, as N_j increases, the error decrease dramatically. For large harmonic number m, more discrete phase values are needed to maintain the same error value. Also, larger N_j is chosen as parameter α increases. If the dispersion strength is optimized to yield maximum bunching factor, the parameter α makes $J_m(m\alpha)$ reach the maximum at around $\alpha\sim1$. For example, if harmonic number is 3, other parameters are optimize to achieve maximum bunching factor, N_j is selected to be no less than 16 to keep the error less than 1%. This also explains why quiet start for SASE FEL process (usually $N_j = 4$) does not yield correct result.

The accuracy of second sum in Eq. (8) depends on the distribution of N_k energy values deviated from ideal Gaussian distribution. Just follow the method which we treat the first sum, we use sequence $a_k = (k - 1/2)/N, (k = 1\cdots N_k)$ to represent uniform distribution in [0,1]. A transformation as (15) forms uniform Gaussian distribution.

$$b_k = \sqrt{2}Erf^{-1}(-1+2a_k) \quad (10)$$

One option is to simply choose N_k energy values as $\gamma_k = \sigma_\gamma b_k$. When N_k is approaching to infinity, the second sum will approaching right value expressed in second factor of equation (5). When N_k is not large enough, the error of second error is cannot be neglected. But in reality, we need to decrease N_k as small as possible to save computation time; meanwhile, the N_k energy values must produce the second sum with acceptable error.

In order to achieve the requirement listed above, we choose the N_k energy value as shown in (15).

$$\gamma_k = \sigma_\gamma b_k + c_k \quad (11)$$

c_k is the small deviation from the number calculated in (10). The requirement can be listed in (15). All sums in (15) are added from 1 to N_k.

$$\sum c_k = 0$$
$$\frac{1}{N_k}\sum \gamma_k^2 = \sigma_k \quad (12)$$
$$\frac{1}{N_k}\sum e^{im\frac{d\theta}{d\gamma}\gamma_k} = \exp\left(-(m\frac{d\theta}{d\gamma}\sigma_\gamma)^2/2\right)$$

With the restriction above, we can minimize the rms value of c_k. By minimize the rms value, we expect all c_k values become zero when N_k approches infinity.

Here we follow the procedure of Lagrangian multiplier to seek the minimum of $\sum c_k^2$ with conditions in (15). First we define a new function in (15) after introducing new parameter λ_1, λ_2 and λ_3, where s_2 is the right-hand side constant of last equation in (12).

$$\begin{aligned} f(c_1,\cdots,c_{N_k},\lambda_1,\lambda_2,\lambda_3) &= \sum_{k=1}^{N_k} c_k^2 - \lambda_1\sum_{k=1}^{N_k} c_k \\ &- \lambda_2\left(\sum_{k=1}^{N_k}\gamma_k^2 - \sigma_k\right) \\ &- \lambda_3\left(\sum_{k=1}^{N_k} e^{im\frac{d\theta}{d\gamma}\gamma_k} - s_2\right) \end{aligned} \quad (13)$$

Then we can write down N_k equations from the newly defined function as in (15). Combined with 3 equations in (12), we can solve these $N_k + 3$ equations with $N_k + 3$ variables $c_1,\cdots,c_{N_k},\lambda_1,\lambda_2,\lambda_3$. By accomplishing all the procedures we can get a deviated Gaussian distribution with correct bunching factor in the simplified 1-D analytical model.

$$\frac{\partial f(c_1,\cdots,c_{N_k},\lambda_1,\lambda_2,\lambda_3)}{c_k} = 0, (k = 1\cdots N_k) \quad (14)$$

LIMITATION OF THE MODEL

There are limitations of this simplified model. The first one comes from the fact that we ignore the dispersion in the modulator. When the modulator is long, the dispersion effect can't be ignored, and equation (2) should be replaced by a set of coupled equations. Approximately, the dispersion of the modulator can be represented as (15), where N_u is the number of modulator period. We can include it in to the chicane dispersion and perform the Lagrangian multiplier procedure.

$$\left.\frac{d\theta}{d\gamma}\right|_{modulator} \cong \frac{2\pi N_u}{\gamma_0} \quad (15)$$

The second limitation is the Lagrangian multiplier process only generates sequence that leads to correct bunching factor at one specific position (the entrance of radiator). Along the undulator the dispersions at each

point are different; there will be errors when other points are calculated.

3-D SIMULATION

In one dimension model, we already had the $N_j \times N_k$ multi-particles. To extend it to 3D case, we need to generate N_t different transverse distribution (x, y, p_x, p_y) sets for each one in $N_j \times N_k$ multi-particles. Totally the number of particle in 3-D simulation is $N_j \times N_k \times N_t$. For the transverse distributions we can use Hammersley pseudo random sequence to reduce fluctuation in transverse phase space distribution.

Here, as an example, we simulate the 2nd order HGHG scheme in soft X-ray regime. Main parameter used in simulation is shown in Table 1. In this example, the energy spread is larger than the energy modulation amplitude; the beam is slight over bunched after dispersion section. This leads the bunch factor at radiator entrance to be small (around 0.012).

Table 1: Simulation parameter

Beam energy (in electron mass)	8806
Energy spread	6e-4
Seed laser power (W)	1.0e8
Dispersion strength $d\theta/d\gamma$	0.171
Modulator period (m)	0.06
Modulator length (m)	4
Radiator period (m)	0.05

As the harmonic number is 2, N_j is selected to be 16 for enough accuracy at given dispersion strength according to Figure 1. For each phase value (θ, γ), we fill N_t sets of transverse Gaussian distribution using Hammersley pseudo random sequence. Now the left variance is N_k, the number of gamma values. And the total number of macro particles is $N_t \times N_k \times 16$. N_k needs to relatively large because small number of N_k will lead to large error at the dispersion other than the optimized point. N_t also need a large number because the energy modulation varies at different transverse location. Table 2 shows the choice of each dimension

Table 2: Number of particle in each dimension

N_k	32, 64
N_j	16
N_t	100, 200, 300, 400, 500

We use our method to generate initial distribution of above HGHG FEL process and import the initial distribution to Genesis 1.3. As comparison, we also use the loading method of Genesis, which uses Hammersley sequence for all 6 dimensions.

Figure 2 shows gain length in Radiator as function of different number of total macro particles. We can see that the result converges as macro particle number increases (both N_t and N_k increases). When N_k is small, the gain length calculation shows a small offset because the gain length depends on the energy distribution.

We can also compare this quiet start scheme with the 6-D coordinate generated by Hammersley sequence. Using quiet start scheme we can achieve accurate bunching factor before entering radiator by utilizing small amount of macro-particles (Figure 3) The systematic error caused by limitation stated in last section is small compare with the signal (<1%).

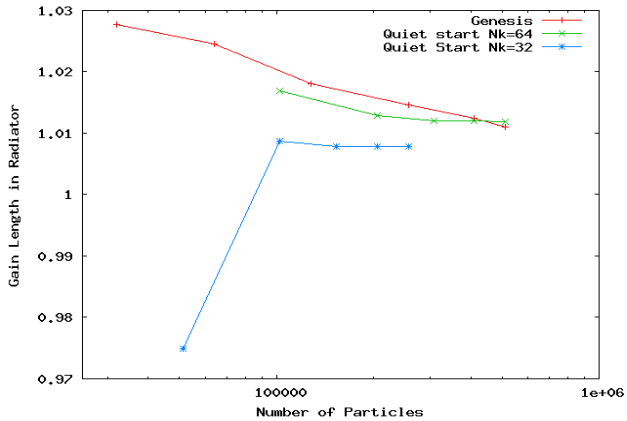

Figure 2. Comparison of Gain Length in Radiator

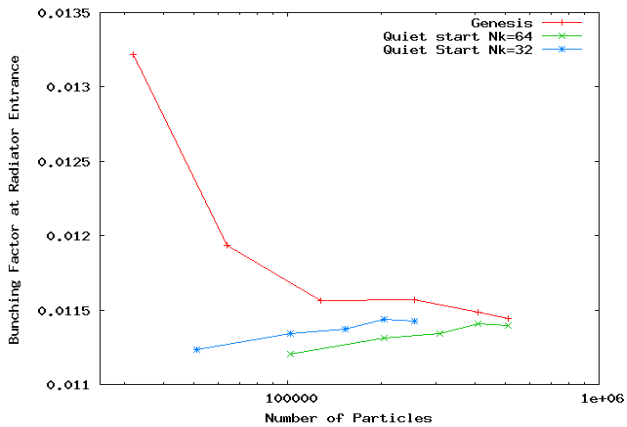

Figure 3. Comparison of bunching factor before radiator

CONCLUSION

The quiet start scheme for HGHG FEL simulation is promising and easy scheme to save more macro particle. We generate the initial distribution of macro particles and import to an existing FEL simulation code. The total number of particle can be largely reduced by achieving precise bunching factor in radiator in small modulation case. But because we use some approximations in the analysis, there is systematic error in the result, which needs more study to correct.

REFERENCES

[1] L.H. Yu and S. Krinsky, Phys. Rev. A 35, 8 (1987)
[2] L.H. Yu and, S. Krinsky, R.L. Gluckstern, Phys. Rev. Lett. 64,3011 (1990)
[3] L.H. Yu et al, Science 289, 932 (2000)
[4] Y. Hao and L.H. Yu, Proceeding of 2007 Particle Accelerator Conference, Albuquerque

FREE ELECTRON LASERS AND HIGH-ENERGY ELECTRON COOLING*

Vladimir N. Litvinenko, BNL, Upton, Long Island, NY, USA#
Yaroslav S. Derbenev, TJNAF, Newport News, VA, USA)

Abstract

Cooling intense high-energy hadron beams remains a major challenge in modern accelerator physics. Synchrotron radiation of such beams is too feeble to provide significant cooling: even in the Large Hadron Collider (LHC) with 7 TeV protons, the longitudinal damping time is about thirteen hours. Two cooling methods (or combination of them) – stochastic cooling (CS) based on broad-back RF feedback(s) and electron cooling (EC) driven by energy recovery linac (ERL) – are under development for cooling high energy hadron colliders.

In this paper we focus on Coherent Electron Cooling (CEC), an unique technique which promising significantly better efficiency that the above-mentioned techniques, in a wide energy range. In the early 1980s, CEC was suggested as a possibility for using various microwave instabilities in an electron beam to enhance its interaction with hadrons (i.e., cooling them). The capabilities of present-day accelerator technology, ERLs, and high-gain Free-Electron Lasers (FELs), finally caught up with the idea and provided the all necessary ingredients for realizing such a process at energies typical for hadron colliders.

In this paper, we discuss the principles, and the main limitations of the CEC process based on a high-gain FEL driven by an ERL. We also present, and summarize in Table 1, some numerical examples of CEC for ions and protons in RHIC and the LHC.

INTRODUCTION

In contrast with electron- and positron-beams, hadron beams in storage rings (colliders) do not have strong loss mechanism (such as synchrotron radiation for electrons) and, therefore, do not have a natural damping mechanism to reduce their energy spreads and emittances.

There are several reasons why cooling high-energy hadron beams, mostly at the top energy range of a collider, is strongly desirable.

First, any increases in the longitudinal- and transverse-emittances of a hadron beam accumulated during multi-stage acceleration from a source to the store energy (collision) remain in the beam. Any instability causing the growth of emittance (for example, that of the electron cloud that is the limiting factor for most modern hadron colliders) may entail the need to discard accelerated beams and start the process again. In any case, present-day high-energy hadron colliders do not have control of beam emittances at the collision energy, and are forced to use beams as they are; this is not always the optimum approach.

The main figure of merit of any collider is its average luminosity, i.e., its average productivity for an appropriate branch of physics. Cooling hadron beams at top energy may further this productivity.

For a round beam, typical for hadron colliders, the luminosity is given by a simple expression:

$$\mathcal{L} = f_c \frac{N_1 N_2}{4\pi\beta^*\varepsilon} \cdot h\left(\frac{\sigma_s}{\beta^*}\right) \qquad (1)$$

where N_1, N_2 are the number of particles per bunch, f_c is their collision frequency, β^* is the transverse β-function at the collision point, ε is the transverse emittance of the beam, σ_s is the bunch length, and $h \le 1$ is a coefficient accounting for the so-called hourglass effect [1]:

$$h(x) = \frac{\sqrt{\pi}}{x} e^{1/x^2} erfc(1/x).$$

The hourglass effect is caused by variations in the beam's size $\sigma_r^2 = \beta^*\varepsilon\left(1 + s^2/\beta^{*2}\right)$ along the length of the collision region, which is defined by the bunch-length, σ_s. Accordingly, for h >0.75, β^* should be limited to values $\beta^* \ge \sigma_s$. Hence, longitudinal cooling of hadron beam may allow reduction of β^* and increase the colliders' luminosity. Plans are to use a non-zero crossing angle at the Large Hadron Collider (LHC) at CERN. In this case, reducing the bunch's length would directly contribute to increasing the luminosity and eliminating the necessity of having a complicated crab-crossing system.

The effect of transverse emittance cooling on the collider's luminosity is less straightforward, but is also important. For beams with limited intensities, the luminosity (1) grows as the transverse emittance decreases. Furthermore, reduction of the beam emittance (in combination with bunch shortening) provide favorite conditions for lowering β^* using final focusing quadrupoles with smaller aperture.

In many colliders luminosity is limited by beam-beam effects. In this case reduction of the transverse emittance would require also proportional reduction of the bunch intensities, N_1 (and sometimes N_2) in eq.(1), which may cause reduction of luminosity per bunch. Possible luminosity improvements in these cases are collider specific.

In eRHIC – BNL's plan for electron-hadron collider (EIC)- polarized electrons accelerated in an ERL will collide with hadrons stored in the RHIC's storage ring [2]. In this case, a reduction of the transverse emittance of the hadron beam engenders a proportional reduction of the electron beam's intensity while maintaining its ultimate luminosity constant [3]. Reduction of the electron beam's current has multiple advantages: reducing the strain on the polarized electron source, proportionally lowering synchrotron radiation (the main source of the

* Work performed under the auspices of the U.S. Department of Energy.
# Corresponding author vl@bnl.gov

Table 1. Comparison of estimations for various cooling mechanisms in RHIC and LHC colliders.
The sign ∞ is used to indicate helplessly long damping times.

Machine	Species	Energy GeV/n	Synchrotron radiation, hrs	Electron cooling, hrs	**CEC, hrs**
RHIC	Au	100	20,961 ∞	~ 1	**0.03**
RHIC	protons	250	40,246 ∞	> 30	**0.8**
LHC	protons	450	48,489 ∞	> 1,600	**0.95**
LHC	protons	7,000	13 (energy)/26 (transverse)	∞∞	**< 2**

To estimate electron cooling in LHC we used an energy scaling $\gamma^{7/2}$ typical for RHIC's electron cooler design [8,9], i.e., cooling protons in LHC at 7 TeV is ~10^{10} harder that cooling antiprotons in the Fermilab recycler [7]. Hence, our usage of ∞∞ in an appropriate column.

detector's background); and, offering the possibility of increasing the electron beam's energy.

ELIC - Jlab's version of EIC – plans also to take full advantage of transverse cooling of hadron beam. This plan calls for increase of the collision frequency to 1.5 Ghz to compensate for reduced number of particles per bunch and to reduce β^* to 0.5 cm [4].

Hence, high-energy cooling may play important role in increasing the performance of high-energy hadron and lepton-hadron colliders, including RHIC and eRHIC at Brookhaven National Laboratory, BNL, ELIC at Jefferson Laboratory, the Tevatron at Fermilab, and potentially the LHC at CERN.

Electron cooling proved to be very efficient method of cooling intense hadron- and ion-beams at low and medium energies [6]. The electron cooler of 9 GeV antiprotons in the Fermilab recycler represents state-of-the-art technology [7], which already led to significant increase in Tevatron's luminosity. Development of the ERL-based electron cooler at BNL promises effective cooling of gold ions with energies of 100 GeV per nucleon [8]. An advanced electron cooling scheme based on ERL and circulator-ring is under consideration for ELIC [5], promises to advance electron cooling techniques even further. Nevertheless, the effectiveness of electron cooling is weaker for protons than it is for ions (it scales with Z^2/A, where Z is the change number of an ion and A its atomic number, viz., $Z^2/A=1$ for protons and $Z^2/A=31.7$ for $_{197}Au^{79}$). Efficiency of conventional electron cooling scheme also falls sharply with the beam's energy (for RHIC it falls as $\gamma^{7/2}$ [9]). Hence, traditional electron-cooling of protons with energies from about 100 GeV in RHIC to a few TeV in LHC with conventional techniques is hardly possible within the realm of present accelerator technology.

It was noted by earlier works [10], that potential of an electron beam based cooling techniques may not be exhausted by the classical electron cooling scheme. The idea of coherent electron cooling (CEC) encompasses various possibilities of using collective instabilities in the electron beam to enhance the effectiveness of the interaction between hadrons and electrons [11]. In this paper, we focus on a specific case of using a high gain FEL (driven by an ERL) for CEC. CEC combines the advantages of electrostatic interaction with the broad band of FEL-amplifiers: examples in this paper span from tens of THz to hundreds of PHz. Such systems are naturally fit into a straight section of modern high-energy hadron colliders. The proposed CEC method has following differences compared with the concept of *optical stochastic cooling* [12]:

a) it may not entail significant modifications to the lattice of the hadron machine ;
b) it uses electrostatic interaction instead of rather inefficient radiation and interaction with TEM waves by protons in a wiggler;
c) it is not limited to few potential choices of laser frequencies and their bandwidths in THz range.

Similar to other coherent cooling techniques, the CEC's cooling rate is limited by the cross-talk of neighboring hadrons (and the short noise in the electron beam). Thus, the cooling rate is limited by an effective number of particles in a coherent sample, which is inversely proportional to the amplifier's bandwidth. In the CEC scheme, the FEL frequency can be chosen appropriately to match the energy of the electron beam. Consequently, for LHC energies the FEL wavelength naturally extends into the soft-X-ray range (nm), where frequencies are measured in ExaHertzs (10^{18} Hz). Even a tiny fraction of this frequency extends far beyond the bandwidth of any other amplifier.

PRINCIPLES OF HIGH ENERGY COLLECTIVE ELECTRON COOLING

Figure 1 shows two (of many) possible layouts of a longitudinal coherent electron cooler. As in a regular electron-cooling scheme, electrons and hadrons should have the same relativistic factor in the CEC:

$$\gamma_o = E_e / m_e c^2 = E_h / m_h c^2. \qquad (2)$$

The simplest (and most economical) version of the CEC allows electrons and hadrons to co-propagate along the same straight section. It has a small, weak chicane at the end of the FEL section for adjusting the timing between the electron-beam's modulation and that of the hadron. This scheme imposes limitations on the value of the wiggler parameter, $\boldsymbol{a_w}$ (see discussion in the following sections). A more elaborate scheme (which also is more flexible and complicated) separates the hadron- and electron- beam so each can be individually manipulated.

For simplification, let us initially consider longitudinal (energy) cooling of the hadron beam. As shown in

Section 3, this cooling can be redistributed to include transverse cooling. Otherwise, the principles of the FEL-based coherent cooling remain the same. It has three parts: The Modulator, the FEL Amplifier/ Dispersion, and the Kicker.

Many processes discussed in this paper are easier to describe in a co-moving (CMS) frame propagating with beam velocity along the straight sections:

$$\beta_o = \frac{v_o}{c} = \sqrt{1-\gamma_o^{-2}} \qquad (3)$$

For high-quality ultra-relativistic ($\gamma_o >> 1$) hadron- and electron-beams of interest for this paper, the motion of the particles in the CMS frame usually is non-relativistic (***v*** << ***c***, where ***c*** is the speed of the light). In addition, the velocity distribution function is highly anisotropic with the root-mean-square (RMS) velocity spread in the longitudinal direction:

$$\sigma_{V//,CSM} \cong c \cdot \sigma_\delta \qquad (4)$$

(where $\delta = E/E_o - 1$ is the relative energy deviation of a particle) that is much smaller compared with that in the transverse direction

$$\sigma_{V\perp,CSM} \cong c \cdot \gamma_o \sigma_\theta , \qquad (5)$$

where σ_θ is the angular spread of electron beam in the laboratory -frame.

Let us next consider the principle of CEC using this simple model, which is discussed in more detail in the following sections.

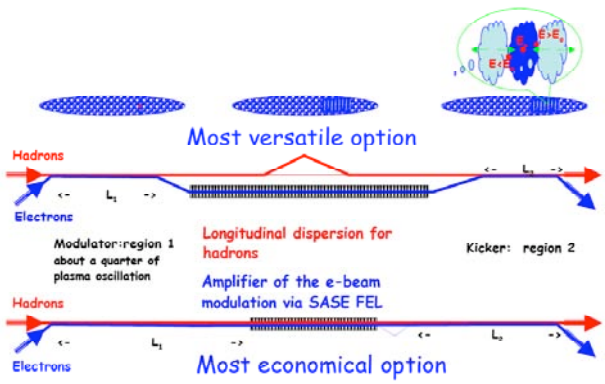

Fig. 1. Schematic layout of the Coherent Electron Cooler with three sections: a) A modulator, where the electron beam is polarized (density modulated) by presence of hadrons; b) an FEL, where density modulation in the electron beam is amplified / longitudinal dispersion for hadrons; c) a kicker, where the longitudinal electrostatic field in the electron beam accelerates or decelerates hadrons. The cooling mechanism is based upon longitudinal dispersion in the hadron beam, i.e., dependence of the time-of-flight on their energy.

In the modulator, individual hadrons attract* electrons and create local density (and velocity) modulation centers at the position of individual hadrons. The process is a linear one, and density modulation on the ensemble of the hadrons is the direct superposition of density modulations induced by individual hadrons. Because of the flat velocity-distribution, the shape of the charge-density modulation resembles that of a flat pancake, with longitudinal extent significantly smaller that the transverse size. When translated into the lab-frame, the longitudinal extent of the pancake shrinks by a factor of γ_o into the nanometer range (see next sub-section). If the length of modulator is chosen to allow a quarter of the plasma oscillation to occur within the electron beam, then, at the end of this section, the electron beam density has a pancake-like distortion with a total excess charge of ***–Ze*** centered at the location of the hadron.

In a FEL-amplifier this modulation of charge density in the electron beam is amplified via the well-known mechanism of exponential FEL growth [13]. Maximum gain in the optical power of such a FEL amplifier is limited by saturation [14,15] to about few millions. Thus, a linear FEL power gain of $\leq 10^6$ and a corresponding amplitude gain, $G_{FEL} \leq 10^3$, are conceivable. In this case, at the exit of the FEL, the individual charge pancake will become a wave-packet (stack) of such pancakes separated by the FEL's resonant wavelength

$$\lambda_o = \frac{\lambda_w}{2\gamma_o^2}(1 + a_w^2), \qquad (6)$$

(where λ_w and a_w, respectively, are the wiggler period and wiggler parameter), and, most importantly, with a G_{FEL} -times larger charge in the pancake. The duration of such a wave-packet (i.e., the thickness of the individual pancake stack) is equal to the coherence length of SASE FEL radiation [14,15], and can be as short as a few or a few tens of FEL wavelengths (see the corresponding section below). This pancake stack of charge-density modulation will generate a periodic longitudinal electrostatic field with period of the FEL wavelength: $k_o = 2\pi/\lambda_o$,

$$E(z) = E_o \cdot \sin(k_o z + \varphi) \ . \qquad (7)$$

Hadrons' time of flight *through the dispersion section* depends on the hadrons' energy:

$$(t - t_o)v_o = -D \cdot \delta , \qquad (8)$$

where t_o is time of flight of a hadron with ideal energy and longitudinal dispersion; in general cases, it is a combination of velocity dependence (in drifts) and pass-length (in chicanes) on the hadrons' energy:

$$D = D_{free} + D_{chicane};$$
$$D_{free} = \frac{L}{\gamma^2}; \quad D_{chicane} = l_{chicane} \cdot \langle \vartheta^2 \rangle , \qquad (9)$$

where ϑ is the angle of trajectory in the chicane.

The pass-time of hadron with ideal energy should be equal to that of the space-charge wave-packet. This crude synchronization can be achieved by properly choosing their trajectories (or a_w and small chicane for straight-

* Repel, in the case of antiprotons or negatively charged ions

pass option – see details below). We note that charge-density modulation induced by a hadron propagates with the average longitudinal speed of the electron beam everywhere except at the FEL. There, the wave-packet of charge-modulation propagates with the group velocity of the FEL's optical wave-packet, which falls in between the speed of light and the longitudinal velocity of electrons [16]:

$$v_g \cong c\left(1-\frac{1+a_w^2}{3\gamma_o^2}\right). \qquad (10)$$

Fine tuning the chicane provides for synchronization between the space-charge wave-packet induced by a hadron in such away that the hadron with central energy, E_o, arrives at *the kicker section* just on the top of the pancake of increased electron density (induced by the hadron)[†], wherein the longitudinal electric field is zero. Hadrons with higher energy will arrive at the kicker ahead of their respective pancake in the electron beam, and will be pulled back (decelerated) by the coherent field of the electron beam; we note that positively charged hadrons are attracted to high-density pancakes of electrons. Similarly, a hadron with lower energy falls behind and, as a result will be dragged forward (accelerated) by the clump of electron density. While propagating in a kicker section of length, L_2, the hadrons will experience an energy kick of

$$\Delta \mathbf{E} = -eZ \cdot E_o \cdot L_2 \cdot \sin\{kD\delta\} \quad , \qquad (11)$$

where Ze is the hadron's charge ($Z=1$ for protons and $Z=79$ for Au ions). Thus, hadrons with energy deviation within the $|\delta| < \pi/kD$ range will experience a coherent cooling, strength of which is proportional to FEL gain. We dedicated the next section to calculations/estimations of the CEC strength. In Section 4, we discuss the effect of surrounding particles on the cooling mechanism.

Table 2: Main parameters of BNL's ERL

Parameter	**Units**	**Value**
Energy	MeV	54.34
RF Frequency	MHz	703.75
Charge per bunch	nC	5
Normalized transverse emittance	mm mrad	3.2
Relative energy spread		$3.6\ 10^{-4}$
Bunch length	cm	0.76

[†] Again, for negatively charged particle like antiprotons or negatively charged ions, it will be low-density valley. The synchronization conditions are independent of the sign of the hadrons' charge.

DETAILS OF THE CEC MECHANISM

A complete and detailed theoretical description of CEC is deeply embedded in early publications on CEC [10, 11, 17] and extends well beyond the scope and size of this paper. Here we focus on discussing a specific scheme of CEC using the ERL-driven high-gain FEL.

For estimating the values we will adopt the parameters of the ERL's electron beam designed at BNL for electron cooling of RHIC [18,19], but scaled to the appropriate energy of interest. Table 2 lists the main beam parameters of this ERL.

Modulator.

The modulator in the CEC scheme represents the easiest, but all-important section, from where information about the position and charge of each individual hadron (with charge Ze) is imprinted into the co-moving electron beam. It is desirable to choose the length of the modulator section equal ~ 1/4 of the electron-beam's plasma oscillation, which occurs with frequency of

$$\omega_{pe} = \sqrt{\frac{4\pi n_e e^2}{\gamma_o m_e}} \qquad (12)$$

where n_e is the electron beam's density in the laboratory-frame. After a quarter of a plasma oscillation [20], each hadron will be surrounded by a cloud of electrons with total excess charge of –Ze [‡] It is important to note that screening of the hadron is a dynamic process, i.e., electron cloud screening of a hadron moving with a velocity v_h with respect to the electron plasma also will move with the same velocity, while individual electrons will have very small drag velocity. The process is similar to waves in the water, where the water molecules do not move in average. It also is important to note that the hadron's velocity will affect the size of its surrounding electron cloud. Thus, the velocity spreads of both the electrons and hadrons will determine the size of the Debye ellipsoid. The longitudinal extent of the Debye ellipsoid (electron cloud) in the CSM frame will be a simple product of the plasma's period and the RMS velocity spread:

$$r_{D\,//,CSM} \sim T_{1/4} \cdot \sigma_{V\,//,CSM}\,. \qquad (13)$$

In the lab-frame, this dimension is Lorenz-contracted to

$$r_{D\,//,lab} \sim \frac{\pi c}{2\omega_p} \cdot \frac{\sigma_\delta}{\gamma_o}. \qquad (14)$$

With ω_p~5 10^9 Hz being typical for the electron- beam's parameters, we plan to use for CEC (by keeping n_e/γ ~ const), $r_{D\,//,lab}$ ~ 750 nm for 100 GeV/u Au ions and $r_{D\,//,lab}$ ~ 170 nm for 250 GeV proton in RHIC. For 7 TeV protons in LHS, $r_{D\,//,lab}$ ~0.17 nm lies in the soft X-ray range.

[‡] for very cold electron plasma waiting 1/2 of the period will make this value to be –2Ze, which is not very important improvement and which also diminishes in warm plasma.

Similarly, the transverse Debye radius will be given by

$$r_{D\perp} \sim \frac{\pi c}{2\omega_p} \cdot \gamma\sigma_\theta , \qquad (15)$$

which is frame-independent and covers the range from 0.1 mm to 3 mm for the range of parameters we consider in this paper.

Overall, there are no problems with assuming density modulation in electron beam to be point-like longitudinally and flat transversely, i.e., perfectly suited for amplification in a high-gain short-wavelength FEL.

The only problem with the modulator length required for 1/4 of the plasma oscillation that it is proportional to γ because of the Lorenz time-contraction in the CMS frame (see Table 3). As a practical outcome from such dependence, the length of the modulator for LHC energies becomes impractical. Fortunately, it is possible to employ velocity modulation of the electron along with a buncher similar to that in an optical klystron [21] to effectively modulate the electron beam's density even for LHC energies.

Table 3: Plasma oscillations in CEC's modulator

Machine, Energy, Hadrons, GeV/u	**Electron peak current, A**	**Length of 1/4 plasma oscillation in lab frame, m**
RHIC, 40 GeV, Au	50	4.8
RHIC, 100 GeV, Au, p	50	8.5
RHIC, 250 GeV, p	100	30
LHC, 7 TeV, p	100	1325

A detailed expansion of the theory of this process will not fit into this short paper; hence, we consider the following simple case where hydrodynamics equations can be used, but which contain the most important underlying physics. Let us consider a hadron in rest[§] in cold, uniform electron plasma and its density perturbation caused by the hadron $\tilde{n}(\vec{r},t)$ obeying the equation:

$$\frac{\partial^2 \tilde{n}}{\partial t^2} + \omega_e^2 \tilde{n} = Z\omega_e^2 \delta(\vec{r}). \qquad (16)$$

For amplification in the FEL, we are interested in longitudinal density modulation

$$\rho(z) = \iint \tilde{n}(\vec{r})dxdy , \qquad (17)$$

and, to be exact, in its spatial harmonic on FEL with k-vector $k_{cms} = k_o / 2\gamma\beta_z$:

$$\frac{\partial^2 \rho_k}{\partial t^2} + \omega_e^2 \rho_k = \frac{Z\omega_e^2}{2\pi}. \qquad (18)$$

Equation (18) has a straightforward solution

$$\rho_k = \frac{Z}{2\pi}\left(1 - \cos\omega_e t\right), \qquad (19)$$

which indicates that initially the growth of density modulation $\sim(\omega_e t)^2$ is very inefficient for $\omega_e t << 1$, i.e., for a short modulator, as in the LHC case. Fortunately, velocity modulation grows linearly and for the case of $t = L_1/\gamma_o v_o << 1/\omega_e$, one can easily calculate the average longitudinal CMS velocity field induced by presence of a hadron in electron beam with a radius *a* and the resulting energy modulation in the lab-frame:

$$\left\langle \frac{\delta E}{E} \right\rangle \cong -2Z\frac{r_e}{a^2} \cdot \frac{L_1}{\gamma} \cdot \left(\frac{z}{|z|} - \frac{z}{\sqrt{a^2/\gamma^2 + z^2}} \right). \qquad (20)$$

Propagating such electron distribution through a simple buncher with longitudinal dispersion $D = \lambda_o / 2\pi\sigma_{\delta_e}$ [21] will create maximum density modulation with wave-vector k_o.

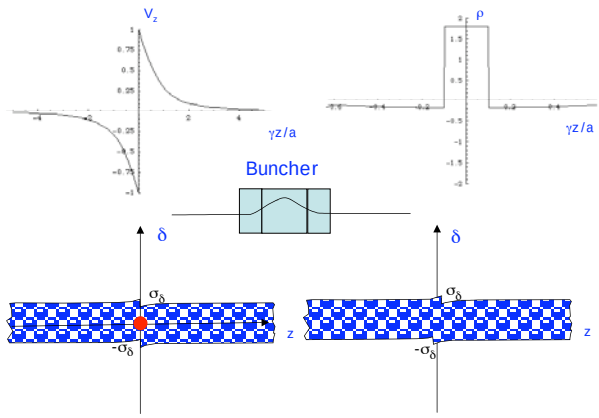

Fig. 2. Longitudinal velocity map (left upper graph) and resulting density modulation (right upper corner graph) after propagation through a simple 3-pole buncher (depicted in the middle). The simulations were done with Mathematica [22].

The two pictures in the bottom of Fig. 2 illustrate the process in the case of a simple phase-space distribution: an initial continuous electron beam (very long, compared with a a/γ_o), with energy spread $\pm\ \sigma_\delta$ that experiences energy modulation in the presence of a hadron (left picture). In a buncher, electrons with higher energies slip forward and those with lower energies slip backwards to create density modulation at the location of the velocity rift. In short, proper use of buncher for electron beam[**] facilitates the generation of density modulation proportional to first order of the phase of plasma oscillations, $\Delta Q \sim -eZ \cdot (\omega_e t)$. In the case CEC for 7 TeV LHC protons, the use of a short modulator section (by LHC standards) of 100 m and a buncher provides for very short cooling times of less than one hour.

[§] Obviously we are using CMS fame of electron beam. Generalization for a case of moving hadron is straightforward: $\frac{\partial^2 \tilde{n}}{\partial t^2} + \omega_e^2 \tilde{n} = Z\omega_e^2 \delta(\vec{r} - \vec{v}t)$ and does not change physics of the process in any significant manner

[**] in kinematics terminology buncher is nothing else but a devise reducing effective longitudinal mass and increasing electrons mobility in z-direction

FEL amplifier for electrons and the dispersion for hadrons

FEL amplifier: It is well known that initial modulation (and noise) in the electron beam density will be amplified. The resulting TEM field, energy modulation, and density modulation, all evolve together in FEL. If the FEL gain is limited to below G~10^3 (to stay away from saturation), the resulting amplitudes represent the simple linear superposition of amplified signals from each hadron plus noise from the electrons [14]. In particular, density modulation in electron beam at the exit of FEL (and the entrance of the kicker section) can be expressed as

$$\rho = -k_o e \begin{pmatrix} Z \sum_{hadrons} K_{FEL}\left(t - t_h - T_f\right) \\ + \sum_{electrons} K_{FEL}\left(t - t_e - T_f\right) \end{pmatrix}. \quad (21)$$

where K_{FEL} is the Green function of FEL in response to a δ-function charge perturbation, and T_f is the time-of-flight of electron "wave-packet" from the end of modulator section to the beginning of the kicker section. The main features of the Green function are that it has carrying frequency at FEL wavelength $\omega_o = k_o c$, has a duration of so-called correlation length (i.e., the number of oscillation is ~ number of wiggler periods per FEL gain length). The inverse duration of this "wave-packet" defines the FEL amplifier's bandwidth.

In addition, this "wave-packet" propagates with the group velocity of FEL signal (10), i.e., the peak of its amplitude moves forward with respect to electron beam. As the result, for $a_w^2 < 1/2$, the group velocity in FEL is larger that that of the hadron.

This situation affords an excellent opportunity to use simple co-propagation of electrons and hadrons through the FEL with a small chicane to delay the electrons, which are lighter and easier to manipulate. This delay for few FEL wavelengths puts the hadron on the top of the charge density "wave-packet" that it induces itself in the modulator.

In the case of $a_w^2 > 1/2$, such simple scenario is not applicable, and the electrons and hadrons should be separated. The hadrons should be delayed for the equivalent of a few FEL wavelengths so to overlap with the maximum of the "wave-packet"– the peak of K_{FEL}.

In both cases, hadrons with designed energy should finish in a zero electric field. This will require sub-FEL-wavelength adjustments, which do not interfere with large-scale timing. The process is similar to maximizing gain in an optical klystron by tiny variation of longitudinal dispersion in its buncher [21].

We take a simple approach for estimating FEL parameters. We assume that wiggler period of 5 cm with reasonable a_w works for all cases, and that selected FEL wavelength is significantly longer that $r_{D//,lab}$. We use analytical formulae derived by Ming Xie [23] to estimate the lengths of the FEL gain,

$$L_{G3D} = L_{G1D}(1+\Lambda); \quad L_{G1D} = \frac{\lambda_w}{4\pi\rho\sqrt{3}}; \quad (22)$$

and the necessary FEL length for a desirable gain. Table 4 gives some resulting parameters.

The optimum longitudinal dispersion for hadrons can be chosen from two considerations: a) Maximum cooling decrement for the typical RMS energy spread δ: $\sin kD\delta = 1$; b) the requirements for cooling all particles within the energy spread {-δ_{max},+δ_{max}}: $\sin kD\delta_{\max} = 0$. Reasonable compromises can be chosen, viz., $D = 1/k\sigma_\delta$, which we will use for our further estimations.

Table 4: Main parameter of FELs for CEC

Machine, Energy, Hadrons, GeV/u	**λ_0**	**FEL Length, m**	**FEL Gain, *amplitude***
RHIC, 40 GeV/n, Au	18 μm	6.5	100
RHIC, 100 GeV, Au, p	3 μm	9	200
RHIC, 250 GeV, p	500 nm	15	100
LHC, 7 TeV, p	10 nm	25	500

Kicker section

In the kicker section, we have sinusoidal modulation of the electron beam's density, which, in the CMS frame is

$$\tilde{\rho} = \frac{k}{2\gamma_o}\frac{G_{FEL}\cdot Z\cdot e}{B}\cdot\sin\left(kz/2\gamma_o\right) \quad (23)$$

where G_{FEL} is the FEL amplification (for amplitude!) and $B = 2\pi\beta_\perp\varepsilon_n/\gamma_o$ is the beam's transverse area, ε_n is the normalized transverse emittance of electron beam, and $\beta_\perp$ is the transverse beta-function. In the CMS frame the field is electrostatic and it is sufficient to solve a trivial $div\vec{E} = 4\pi\tilde{\rho}$ to find it. Since the electron beam in the ERL has close to a uniform distribution and the transverse size of the beam is significantly larger the modulation wavelength, the field near the beam's axis is predominantly longitudinal. Because Lorentz transformation does not change the amplitude of a longitudinal field component, we have in the lab-frame:

$$E_z \cong \frac{2G_{FEL}\cdot Ze}{\beta_\perp\varepsilon_n}\gamma_o\cdot\sin\left(k_o\left(z - \mathrm{v_o}t\right)/\beta_\mathrm{o}\right). \quad (24)$$

This field will exist for about a quarter of the plasma's oscillation and, therefore, for a short kicker length, L_2, one can finally write the change of the hadron's energy per turn in CEC ($r_p = e^2/m_p c^2$ is the classical radius of proton, and A is atomic number of hadron):

$$\Delta\delta = -G_{FEL}\cdot\frac{r_p\cdot L_2}{\beta_\perp\varepsilon_n}\frac{Z^2}{A}\cdot\sin\left(kD\delta\right) \quad . \quad (25)$$

For the natural choice of dispersion $D = 1/k\sigma_\delta$, the cooling decrement for small energy deviations per turn will be

$$J_{CEC} = 2G \cdot \frac{r_p}{\sigma_\delta \varepsilon_n} \cdot \frac{L_2}{\beta_\perp} \cdot \frac{Z^2}{A}. \quad (26)$$

It worth noting that this expression is energy independent, i.e., it promises to be effective in high-energy colliders like the LHC.

Cooling heavy ions using CEC is easier than cooling protons because of $Z^2/A > 1$ (factor 31.7 for $_{197}Au^{78}$ ions in RHIC). It is also important to point out that because of synchrotron oscillations, the value of the CEC decrement (26) should be divided by 2, i.e., the standard ratio for an oscillator.

Table 5: Main parameter of kickers for CEC

Machine, Energy, Hadrons, GeV/u	**L_2, m**	**Hardon bunch length, nsec**	$\frac{\sigma_{s,e}}{\sigma_{s,h}}$
RHIC, 40 GeV, Au	3	2.5	100
RHIC, 100 GeV, Au, p	5	1	200
RHIC, 250 GeV, p	10	1	100
LHC, 7 TeV, p	50	0.25	500

In practice, hadron bunches are usually much longer than electron bunches. In this case, the decrement (26) should be multiplied by the ratio of the bunch lengths:

$$\langle J_{CEC} \rangle = J_{CEC} \cdot \frac{\sigma_{s,e}}{\sigma_{s,h}} \quad (27)$$

These values, listed in Table 5, were used for calculating the cooling times in Table 1.

TRANSVERSE COOLING

Similarly to re-distribution of the damping increments of synchrotron radiation, it is possible to re-distribute decrements of CEC within the boundaries of the "sum of decrement" theorem:

$$J_s + J_x + J_y = J_{CEC}. \quad (28)$$

One easy way of providing cooling of the horizontal emittance is to use a chromatic chicane, as shown in Fig.3 below. In a chromatic chicane, symplectic conditions couple the arrival time of these wave fronts with the transverse coordinates and angles, which provides an energy gain in the kicker's dependence of

$$\Delta \mathbf{E} = -eZ^2 \cdot E_o \cdot L_2 \cdot \sin\left\{k\left(D\delta + R_{16}x' - R_{26}x + R_{36}y' + R_{46}y\right)\right\}; \quad (29)$$

where R_{nm} are elements of transport matrix through chicane (indexes 1,2,3,4,5,6 belong to canonical variables x,x',y'y', -ct and δ).

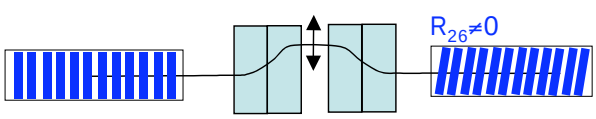

Fig. 3 Chromatic chicane tilts the wave-fronts of charge-density modulation in an electron beam and couples the energy kick with the horizontal position.

The energy change causes a local change in the closed orbit, and hence, a change in the horizontal betatron displacement that is proportional to horizontal dispersion η: (*sin* in eq. (29) is linearized for simplicity)

$$\Delta x = -\eta \cdot eZ^2 \cdot E_o \cdot L_2 \cdot kR_{26}x + ... \quad (29)$$

The typical decrement in horizontal cooling for such system will be

$$J_x \sim \frac{\eta \sigma_\varepsilon}{\sigma_x} J_{CEC}.$$

Cooling of both transverse directions will require at least local transverse coupling (see eqs. (29) and (30)) and non-zero projection of the dispersion vector on both eigen vectors of the betatron modes. A detailed description of such scheme goes beyond the scope of this paper.

COLLECTIVE EFFECTS AND LIMITATIONS ON THE CEC DECREMENT

As we discussed earlier, the electric field in the electron beam is a linear superposition of "wave-packets" excited by all hadrons and electrons, which carry information about their origin, i.e., the position of each hadron and electron in the beam (note that hadrons with a non-unit charge have an additional Z in front of the identical field-function, E_o).

$$E_z = Z \cdot \sum_{i,hadrons} E_o(v_o t - z + z_i) \cdot \sin k(v_o t - z + z_i) - \sum_{j,electrons} E_o(v_o t - z + z_j) \cdot \sin k(v_o t - z + z_j)$$

Hence, the energy kick for each hadron will contain kick from all hadron and electrons within the extent of the ''wave-packet". The action of the self-induced field, which we already considered separately in the previous section, is coherent and is repeated turn after turn. At the same time, the relative phases of hadrons at an optical (μn and nm) scale are completely random, and any correlations are completely eliminated after each turn (similar to the storage ring in FELs [24]). Let us define $\tilde{N} = \tilde{N}_h + \tilde{N}_e / Z^2$, where $\tilde{N}_h$ and $\tilde{N}_e$ is the number of electrons in the FEL coherence length[††] $L_c = N_c \lambda_o$, which "communicate with each other". Writing the equation of evolution of RMS energy and averaging <sin^2> of the random phase, we get the standard equation for RMS spread (analogous to stochastic cooling calculations):

$$\frac{d\sigma_E^2}{dn} = -2\Delta \frac{kD}{\mathbf{E}_o} \sigma_E^2 + \frac{1}{2}\Delta^2 \tilde{N}; \quad \Delta = eZ^2 \cdot L_2 \cdot E_o,$$

[††] again, for simplicity of we used N_c=10 and 20 for numerical example in this paper. There is a rigorous way of defining the correlating length for a specific FEL by using correlation length of its Green function K:

$$L_c = \frac{1}{|K_{\max}|^2} \int_{-\infty}^{\infty} |K(z)|^2 dz$$

with two important consequences. First is that maximum cooling rate can not be larger that 1/Ñ per turn. This limitation is taken into account by properly selecting the FEL gain for cooling rates shown in Table 1.

Table 6: Other parameters for the CEC

Machine, Energy, Hadrons, GeV/u	**Nc**	**Lc, μm**	N_h per bunch	Ñ
RHIC, 40 GeV, Au	20	360	$1\ 10^9$	$6\ 10^5$
RHIC, 100 GeV, Au	20	60	$2\ 10^9$	$5\ 10^5$
RHIC, 250 GeV, p	10	5	$2\ 10^{11}$	$7\ 10^6$
LHC, 7 TeV, p	10	0.2	$1.15\ 10^{11}$	$0.4\ 10^6$

Second consequence is that the stationary (self-consistent) energy spread is proportional to the number of particles in the coherence length (i.e., it is desirable to operate the FEL at as short wavelength as possible!), and also to the cooling rate:

$$\frac{\sigma_E^2}{\mathbf{E}^2{}_o} = \frac{1}{4kD} \cdot \frac{\Delta}{\mathbf{E}_o} \cdot \tilde{N} \qquad (30)$$

Finally, we mention that throughout the entire suite of numerical examples used in this paper we ensured that emittances of both the electron- and hadron- beams did not exceed the FEL wavelength divided by 4π, This action ensures the preservation of phase correlations at the scale of the FEL wavelength.

CONCLUSIONS

In this paper, we showed that coherent electron cooling (CEC) can be very promising method of cooling beams in high-energy hadron colliders. The CEC takes full advantage of high-gain FELs based on high brightness ERLs. Cooling of 100 GeV/n ions and 250 GeV protons in RHIC seems to be straightforward with this method.

Cooling protons in LCH at 7 TeV also seems to be possible, but may require a slightly more elaborate scheme (such as a buncher and separating the beams).

Proof-of-principle experiment to cool Au ions in RHIC at ~ 40 GeV/n is feasible using the existing R&D ERL, which is under construction in BNL's Collider-Accelerator Department (C-AD). Commissioning this ERL is planned for early 2009. Moving this accelerator into RHIC tunnel may take from two to three years.

In this paper we assumed standard statistical shot-noise in the electron beam and did not relied on any possible noise suppression, which is being actively discussed by the electron- cooling community.

ACKNOWLEDGEMENTS

We want to thank Ilan Ben Zvi and Thomas Roser (BNL) for encouraging discussions and well-pointed questions and suggestions, which lead to some of the technical solutions presented in this paper. We are grateful to Anatoly Kondratenko for his wiliness to share his knowledge of processes in high-gain FELs. The first author also would like to thank C-AD's electron cooling and R&D ERL groups for being a test-bed for our initial discussion of ideas used for the FEL-based CEC, and for generating several valuable suggestions.

REFERENCES

[1] M. A. Furman, Proc. 1991 Particle Accelerator Conf., San Francisco, May 6-9, 1991, p. 422.
[2] V. Ptitsyn et al, http://www.bnl.gov/cad/eRhic/Documents/AD_Position_Paper_2007.pdf
[3] V.N. Litvinenko et al., Proc. PAC 2005 http://cern.ch/AccelConf/p05/PAPERS/TPPP043.PDF
[4] Y. Derbenev et al., in Proc. of PAC 07
[5] Y. Derbenev et al., in Proc. of COOL 07
[6] I.Meshkov, Phys. Part. Nucl., 25, 6 (1994) 631
[7] S.Nagaitsev et al., Phys. Rev. Lett. **96**, 044801 (2006)
[8] Ilan Ben-Zvi, et. al., NIM **A532**, 177, (2004)
[9] A.V.Fedotov et al, New J. of Physics **8** (2006) 283.
[10] Ya. S. Derbenev, Proc. of 7th All-Union Conference on Charged Particle Accelerators, 14-16 October 1980, Dubna, USSR, p. 269 (in Russian); Ya. Derbenev, AIP Conf. Proc. No. 253, p.103 (1992)
[11] Ya. Derbenev, in Proc. of Cool 07
[12] A. Mikhalichenko, M. Zolotorev, Phys. Rev. Lett., **71**, p.4146 (1993).
[13] A.M.Kondratenko, E.L.Saldin, Part. Acc. **10** (1980) 207
[14] E.L.Saldin, E.A.Schneidmiller, M.V.Yurkov, The Physics of Free Electron Lasers, Springer, 1999
[15] C.Pelegrinni, NIM **A475**, 177, (2001) p.1
[16] see Ref. [14], page 365
[17] Ya.S. Derbenev, Dissertation, Novosibirsk, 1978
[18]http://www.bnl.gov/cad/ecooling/docs/PDF/Electron_Cooling.pdf
[19] D. Kayran et al., Proc. of PAC 2007 http://accelconf.web.cern.ch/AccelConf/p07/PAPERS/THPAS096.PDF
[20] see for example, C.L. Longmire, Elementary plasma physics, Interscience publishers, 1963
[21] N.A.Vinokurov, A.N.Skrinsky, Preprint of Institute of Nuclear Physics, INP 77-67, 1977, Novosibirsk
[22] Mathematica, © Wolfram Research, Inc
[23] M. Xie, NIM **A445**, 59 (2000).
[24] V.N.Litvinenko et al, NIM **A475**, 177, (2001) p.65

COMMISSIONING RESULTS OF THE LCLS INJECTOR*

D. H. Dowell#, R. Akre, Y. Ding, P. Emma, J. Frisch, S. Gilevich, G. Hays, Ph. Hering, Z. Huang, R. Iverson, C. Limborg-Deprey, H. Loos, A. Miahnahri, J. Schmerge, J. Turner, J. Welch, W. White, J. Wu, *SLAC*, *Stanford*, CA 94309, USA,
L. Froelich, T. Limberg, E. Prat, *DESY*, *Hamburg*, Germany

Abstract

The Linac Coherent Light Source (*LCLS*) is a SASE x-ray Free-Electron Laser (FEL) project presently under construction at SLAC [1]. The injector section, from drive-laser and RF photocathode gun through first bunch compressor chicane, was installed in fall 2006. Initial system commissioning with an electron beam has recently been completed. The second phase of construction, including second bunch compressor and full linac, is planned for 2008. In this paper, we report experimental results and experience gained during the first phase of machine commissioning. This includes the cathode, drive laser, RF photocathode gun, linac booster section, S-band and X-band RF systems, first bunch compressor, and the various beam diagnostics.

INTRODUCTION

The months of April through August 2007 have been spent commissioning the *LCLS* injector. This is the first phase of machine commissioning, with the second phase starting in Dec. 2007 after a 3-month downtime, and the final phase in Nov. 2008, culminating in FEL light in 2009. First electrons from the new photocathode RF gun were observed on April 5 and beam was quickly established to the full (injector) energy of 250 MeV in the main SLAC linac on April 14, 2007 [2]. Over the next five months all the injector systems were commissioned and the beam accelerated to 15 GeV at the end of the SLAC linac. The bunch charge (1 nC) and the measured projected emittance of 1.2 microns meets the design requirements of LCLS.

DESCRIPTION OF THE INJECTOR

Figure 1 shows the major components of the LCLS injector at the 2 kilometer point of the 3 kilometer SLAC linac. The off-axis housing was built during the original construction of the linac in 1962 [3], anticipating future injection beamlines such as LCLS.

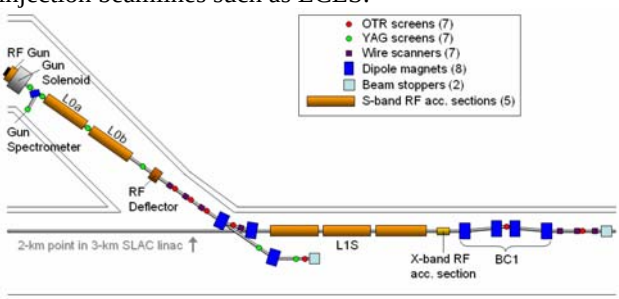

Figure 1: The injector for LCLS located in the off-axis housing at Sector 20, at the 2/3-point along the linac.

The LCLS injector begins with a photocathode RF gun followed by two modified SLAC linac sections producing a beam at 135 MeV, 100 amps peak current and transverse normalized emittance of 1.2 microns for 1 nC bunches. The cathode drive laser is located in a reconstructed alcove above the RF gun. The 135-MeV beam is deflected onto the main linac axis by a two-dipole 35 degree doubly achromatic bend or, with the first 17.5 degree dipole magnet turned off, the beam drifts to a 35 degree straight ahead spectrometer for energy and energy spread measurements. Once on the axis of the main linac, the electrons are accelerated to 250 MeV in three linac structures before entering the first chicane bunch compressor, BC1. Between the three linacs and BC1 is a short x-band structure whose 4th harmonic straightens the beam's longitudinal phase space for linear compression.

THE DRIVE LASER

The RF gun's copper cathode is illuminated by a UV laser operating at 255 nm delivering up to 450 microjoules per pulse at 120 Hz. In addition to the wavelength and energy, the laser must meet stringent stability and reliability requirements as well as strict transverse and longitudinal shaping specifications. The stability specifications were achieved with a pulsed Ti:sapphire system pumped by two quasi-cw, diode pumped Nd:YAG lasers (Figure 2); however the shaping requirements have not been met.

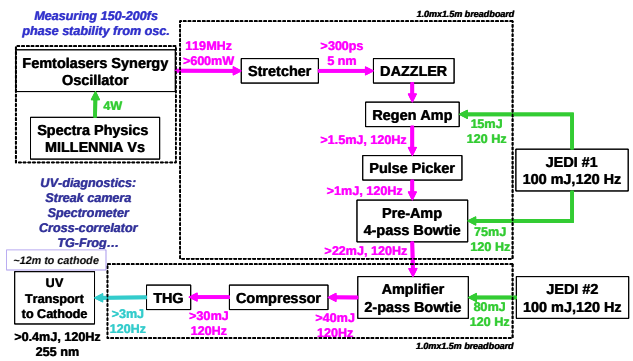

Figure 2: A block diagram of the RF gun drive laser designed and built by Thales Lasers.

The laser pulse shape is measured by combining a short pulse from the oscillator with the UV pulse in a non-linear crystal allowing back-conversion of the mixed signal to the second harmonic. A cross correlation measurement of the UV pulse sent to the cathode is shown in Figure 3.

* Work supported by US DOE contract DE-AC02-76SF00515.
# dowell@SLAC.Stanford.edu

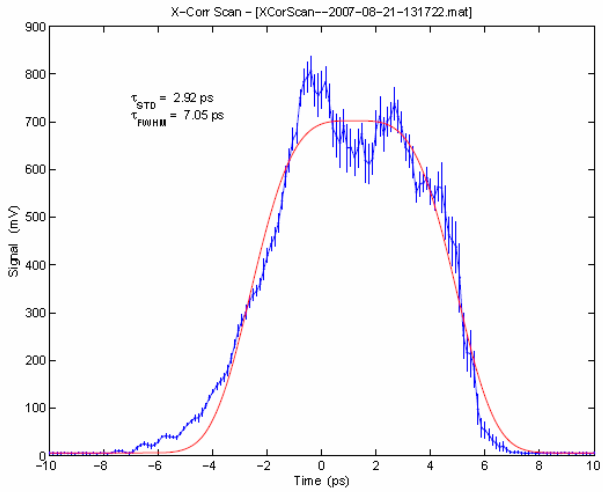

Figure 3: The laser pulse shape as measured in a cross correlator and fit with an n-order super Gaussian.

The short-term charge stability which results both from the laser's energy and the laser-RF phase jitter is shown for a measurement period of 53 seconds in Figure 4. The charge was determined with a beam position monitor (BPM) located immediately after the gun and demonstrates 1.1% (rms) charge stability, which easily meets the 2% specification for stable operation of the LCLS FEL. The long-term variation is controlled using a feedback loop which varies the laser energy using an adjustable wave-plate inside the IR to UV tripler.

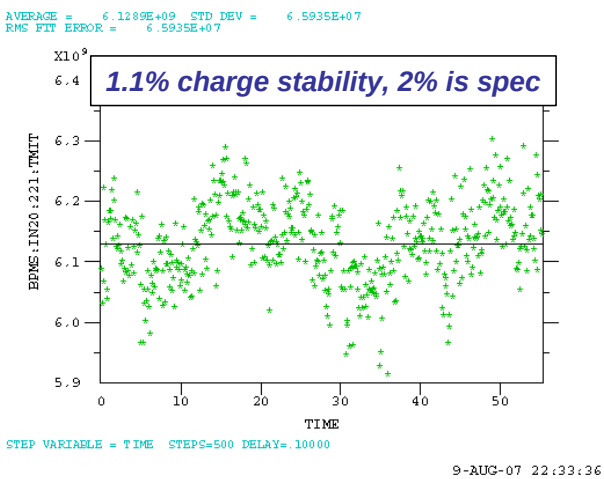

Figure 4: The laser's short-term energy stability of 1.1% (rms) is better than the design specification of 2%.

The laser transverse profile is monitored on the virtual cathode camera (VCC) which views the light from a beam splitter located just before the UV beam enters the beamline vacuum. Figure 5 shows a typical VCC image which is used in a feedback loop with a steering mirror to maintain the laser beam at a fixed point on the cathode. The details of this optical system have been described in ref [4].

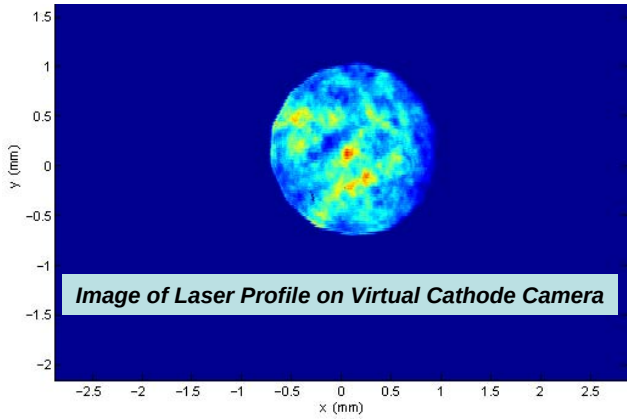

Figure 5: A typical image of the laser transverse profile on the virtual cathode camera.

THE PHOTOCATHODE RF GUN

The LCLS photocathode RF gun has been described elsewhere [5,6] and only its general features are summarized here. The gun fields are fully rotationally symmetric by incorporating dual feed (to eliminate the dipole fields) and a racetrack geometry (to cancel the quadrupole fields induced by the dual feed) for the full cell into which the RF is coupled.

Since this gun is the sole electron source for the LCLS user facility, it needs to operate reliably at the relatively high repetition rate of 120 Hz as well as producing exceptional quality beam. This was done by making several changes to the BNL/SLAC/UCLA gun.

The LCLS gun was made more reliable by replacing the commonly used azimuth angle RF coupling with much larger z-coupled ports running the full length of the full cell. This approach combined with careful design of the coupler-hole lip radii greatly reduced the pulsed heating which otherwise would have limited the gun lifetime. In addition, any field emission from the tuning slugs was eliminated with deformation tuners. These tuners where found to be unnecessary during the tuning process. In addition, the shape of the iris between the two cells was modified to reduce its surface fields below that of the cathode. The resulting cathode surface field is approximately 10% higher than the iris fields. With these modifications the gun was easily conditioned to 120 MV/m and 60 Hz repetition rate. Conditioning at 120 Hz was limited to 107 MV/m due to excessive heating of the gun probes, a limitation which will be corrected by the installation of re-designed probes in 2008. Therefore to reduce any risk of damaging the gun, it was decided to limit the repetition rate to 30 Hz during the 2007 commissioning run. As a result, the gun operated continuously at 30 Hz for more than 3 x 10^8 pulses during the April 5, 2007 to August 24, 2007 commissioning period.

Another important innovation of the gun which improved its beam quality was to greatly increase the frequency separation of the 0- and pi-modes. Previous s-band guns had been built with 3.2 MHz separation resulting in excitation of the undesired 0-mode by the low

frequency components of RF envelope waveform, allowing it to beat against the pi-mode. The presence of the 0-mode increases the correlated energy spread and unbalances the fields between the two cells both during transient and in steady state [5,6]. Increasing the mode separation to 15 MHz greatly reduces excitation of the 0-mode, giving a pure pi-mode in the gun.

THE CATHODE

The cathode quantum efficiency was quite low for the first two months of commissioning. To complicate the issue, the QE had the appearance of being even lower due to incorrect Faraday cup measurements. Once the beam was transported to the main linac, its charge was more accurately measured using known SLAC-standard charge and beam position monitors. However this correction was only a factor of 1.45, while the QE was initially almost 20-times lower than the design requirement.

In order to understand the poor cathode performance, the cathode was imaged optically with white light and a camera in reflection geometry, and the emission distribution imaged with the gun solenoid adjusted to create a point-to-point image of the cathode photo-emission on the second YAG screen [7]. Illumination for the white light image was done by directing light through the UV optics and vacuum window, and reflecting light off the in-vacuum mirror onto the cathode. A digital camera viewed the cathode with the opposing in-vacuum mirror (installed for wakefield compensation) and vacuum window. The photo-emission imaging was done at approximately 10pC bunch charge in order to minimize space charge forces blurring of the image. A comparison of these two methods of imaging is shown in Figure 6. The resolution with both techniques is excellent and the correspondence between the white light features and the areas of high photo-emission is striking.

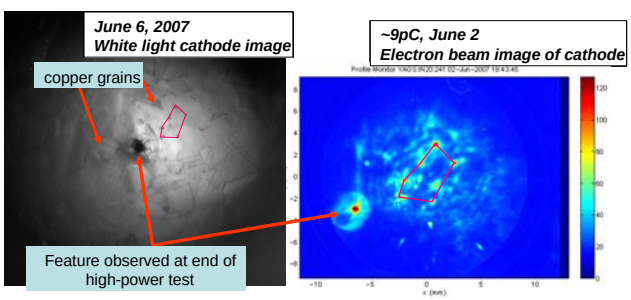

Figure 6: Images of the cathode taken using a white light source and a camera (left), and an electron emission image on a YAG screen approximately 100 cm from the cathode. The gun solenoid is adjusted to image the cathode electrons on the 100 micron thick YAG screen.

The initial QE at the start of commissioning was approximately 2 to 3 x 10^{-6} which is 20-times lower than the design specification of 6 x 10^{-5}. This very low QE limited the maximum beam charge to 200pC during the first half of commissioning. However, reducing the laser size on the cathode during the emittance studies increased the laser fluence to the degree that vacuum activity in the form of low-level RF arcs were observed which cleaned the cathode. The result has been a fortuitous, steady rise in QE during the last three months of commissioning as can be seen in Figure 7.

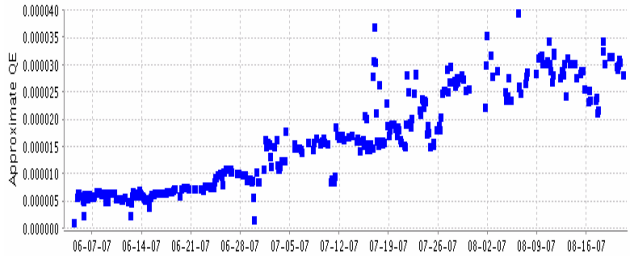

Figure 7: The quantum efficiency during the last two and one-half months of commissioning.

A mild laser cleaning of the cathode was also performed. The fluence was deliberately kept low and only one pass of the scan was done to limit any possible damage to the cathode surface. The QE before and after cleaning is shown in Figure 8, which was done in the presence of low rf power of 1 MV rather than the nominal 6MV, equivalent beam energy. The laser-RF phase was also nominal at 30 degS from the zero crossing. The laser fluence was approximately 360 microjoules per sq. mm in a 0.67 mm diameter laser spot slowly moved over a 2 mm x 2 mm area. The dwell time was 10 seconds at each position with a 100 micron step size. The initial and final QE's were 1.6x10^{-5} and 2.8x10^{-5}, respectively.

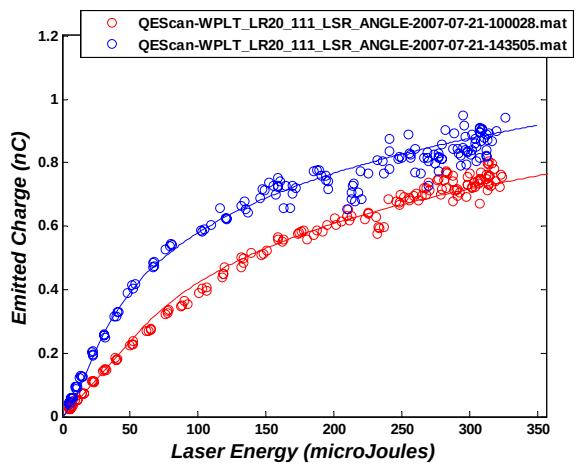

Figure 8: The measured charge vs. laser energy before (red) and after (blue) laser cleaning.

The QE history shown in Figure 7 is an approximation based upon the charge emitted at the RF phase producing the maximum cathode field (approximately 90 degS from the zero field phase), normalized to the laser energy. A more precise measurement is given in Figure 9 where the charge is given as a function of the laser energy at the laser-RF phase of 30 degS from the RF zero crossing. The linear portion at low laser energies gives the quantum efficiency and the onset of the space charge limit is

indicated by the roll-over of the curve from this linear dependence. The space charge limit is quantified by an effective transverse rms radius assuming a Gaussian distribution [8,9]. The inserted image in Figure 9 shows the actual transverse emission distribution as imaged on the YAG screen as described above. This image corresponds to the laser iris completely opened while the charge vs. laser energy data was taken with the iris set to a 1.3 mm diameter cathode illumination.

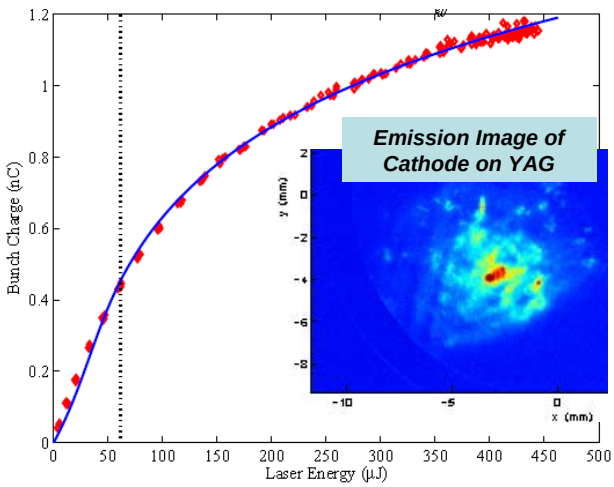

Figure 9: The measured bunch charge vs. laser energy fit with an analysis for the QE and the space charge limit. The QE in this case was 3.7×10^{-5} and the effective transverse radius 0.34 mm (rms). The inset shows the emission distribution with the laser iris fully open when this data was taken. The scale corresponds to the beam size on the YAG screen.

MEASUREMENT AND ANALYSIS OF THE TRANSVERSE EMITTANCE

The LCLS injector transverse emittance at 135 MV is measured using optical transition radiation (OTR) with a 1-micron thick aluminum foil. The images are acquired with a digital camera, background subtracted and analyzed using a variety of methods to eliminate spurious results due to long tails of the distribution. The on-line software allows x- and y-plane projections of the images to be analyzed for rms beam size based on several methods, including: 1) rms of the entire profile, 2) Gaussian fit, 3) asymmetric Gaussian fit, 4) 5% amplitude cut, and 5) 5% area (charge) cut.

The results reported here use the 5% area cut technique. In this method the background subtracted image is integrated in the two transverse dimensions over the region of interest (ROI) and the threshold level corresponding to 5% of the area-integrated image is found. The rms beam sizes for the projections above this threshold are used to compute the emittance.

The emittance results using the 5% area cut analysis are given in Figure 10. The plots on the left show the rms beam size as a function of the quadrupole field with fitted curve overlaid. The beam emittance, Twiss and matching parameters, as well as the goodness of fit are listed on the plot. The ellipses on the right represent the reference phase space of the x- and y-planes at the OTR screen location for the nominal quadrupole field. The straight lines represent the beam size at each quadrupole setting, transformed to the reference phase space.

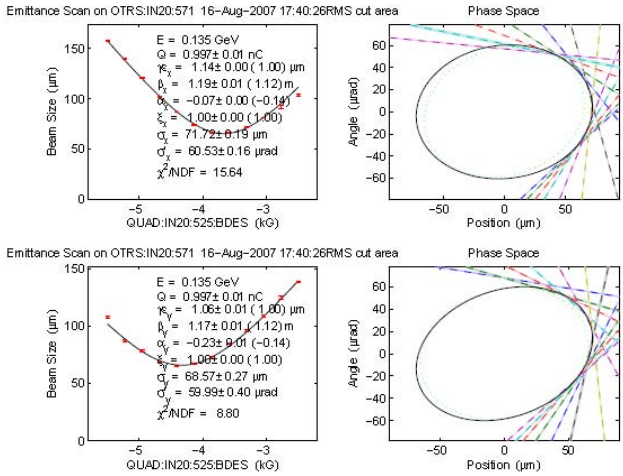

Figure 10: Projected normalized emittance measured for a 1 nC bunch at 135 MeV ($\gamma\varepsilon_x$ = 1.14 μm, $\gamma\varepsilon_y$ = 1.06 μm).

The electron bunch slice emittance is measured on the same OTR screen with the transverse RF deflector switched on, applying the same 5% area cut analysis method to the data. A typical image with the deflector switched on is shown in the center image of Figure 13. In Figure 11, the bunch has been binned into 12 slices and the horizontal emittance calculated for each slice.

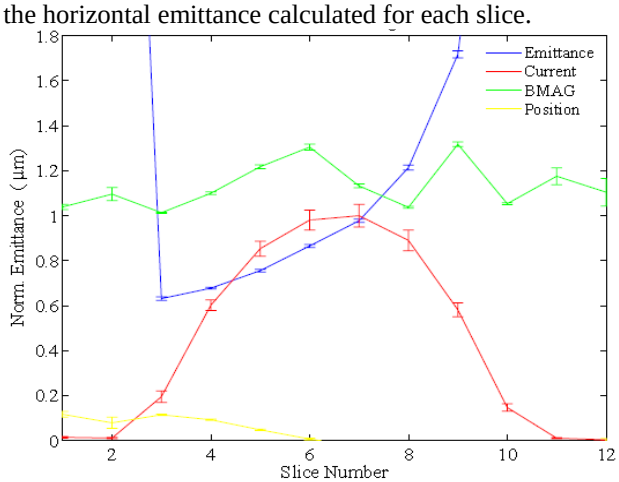

Figure 11: The slice horizontal emittance for a 1-nC, 100-ampere bunch at 135 MeV, with emittance values <1 μm in the beam core.

Simulations of the beam emittance measurement were performed using the IMPACT particle tracking code [10]. In these calculations the electron emission images shown in Figures 6 and 9 and the laser pulse shape given by the cross correlator were used for the starting particle distributions at the cathode surface. Therefore both the transverse and longitudinal asymmetries associated with the initial conditions were included in the simulation. This realistic electron beam distribution was accelerated to 135 MeV and propagated to the OTR screen to

simulate the quadrupole scan technique. The computed transverse profiles were analyzed with the same area cut method as done in the experiment to obtain the emittance as a function of the area cut percentage.

The result of this analysis is summarized in Figure 12 where the transverse emittances are plotted as functions of the percentage of area cut. The higher y-plane emittance results from the asymmetry of the initial electron distribution and is typical of the emittance asymmetry observed in the measurements.

Comparing the measured emittances of Figure 10 with the curves in Figure 12, indicate that a percentage cut of 8 to 9% would result in good agreement with simulation. Whereas the measurement technique described above used 5% for the cut area, it is possible that a few per cent of the measured distribution is lost in the camera noise or there is a subtle difference between the measured and simulated tails at the level of a few percent. In any case, this discrepancy is relatively small, and at worse would imply the measured emittances are for 90 to 93% of the beam charge rather than 95%.

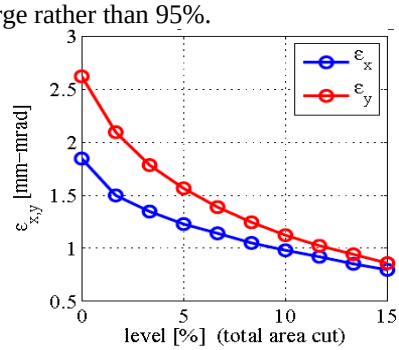

Figure 12: Simulations of the emittance as a function of the percentage area of the tails cut from the data.

BUNCH LENGTH COMPRESSION

The LCLS injector includes a 4-dipole magnetic chicane (BC1) at 250 MeV as the first bunch compression stage. (The second compressor, BC2, will be located 350 m downstream at 4.3 GeV and installed in fall 2007.) Nominally, the bunch is compressed by a factor of 4-5 in BC1, but in the extreme, with X-band 4th harmonic RF switched 'ON' to linearize the energy chirp (see Fig. 15), the bunch can be compressed down to a few microns [11]. The chicane includes an OTR screen, adjustable collimator, and a BPM at its center.

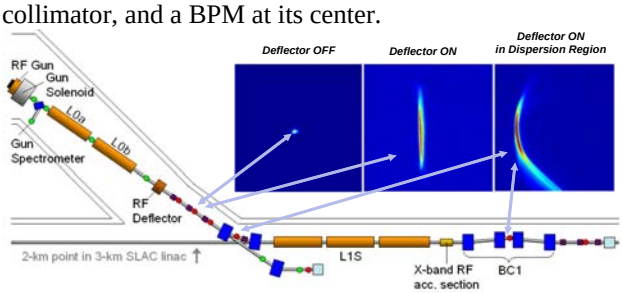

Figure 13: OTR foil images with 1st RF-deflector cavity 'OFF' (left), then cavity 'ON' to measure slice emittance (center), and again 'ON' with an OTR foil at high dispersion to measure longitudinal phase space (right).

The absolute bunch length after BC1 has been measured using a 2.4-m long vertical RF deflecting cavity (LOLA) 900 m downstream of BC1, which acts as a streak camera [11]. The bunch length measurements are shown in Fig. 14 at 1 nC, where the energy spread induced by the off-crest phase of the L1S and X-band RF sections (see Fig. 2) is varied, producing the rms relative energy spread on the horizontal axis of this plot. The compression factor was also measured simultaneously by using two beam phase monitor cavities, one up and one downstream of BC1, to measure the ratio of phase variations at each location as the phase of the drive laser is scanned. This compression factor is multiplied by the measured initial bunch length and plotted for easy comparison with the measured bunch length data. This measurement is presently resolution limited by a phosphor screen, which will be replaced during the fall 2007 installation period with a new OTR foil at 4.3 GeV. The poor agreement of the data in the range $\sigma_E/E > 4\%$ may be due to coherent synchrotron radiation in the compressor.

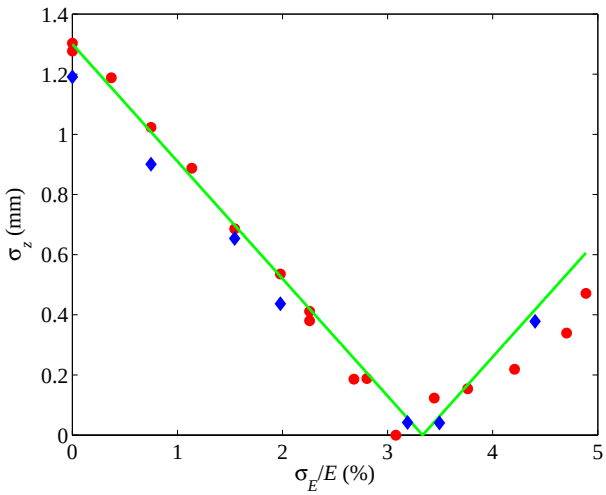

Figure 14: Bunch length after BC1 measured using the RF deflector (red-circles), and initial bunch length times compression factor (blue-diamonds) measured using two beam phase monitor cavities up and downstream of BC1. The calculated bunch length is also shown (green line).

The 2.4-m LOLA cavity will be relocated closer to the BC2 in fall '07, but is presently near the linac end at 14 GeV. A shorter transverse cavity is also located upstream of BC1 (Figs. 1 and 13) and used to measure the initial bunch length and longitudinal distribution (Fig. 16, left). The 14-GeV bunch was also compressed to 170 micron rms bunch length (Fig. 16, right), and smaller, but with a resolution limit of about 100 μm rms, which will be upgraded in 2007 with a new OTR foil at 4.3 GeV.

The BC1 dipole fields are unfortunately of poor quality, including a significant sextupole field and linear field gradient, which generates large horizontal dispersion and emittance growth beyond BC1. The linear dispersion has been corrected using two small quadrupoles placed in BC1 for this purpose, but the sextupole field limits the minimum horizontal emittance growth to about 40% ($\gamma\varepsilon_x$

from 1.2 μm before BC1 up to 1.7 μm after BC1). The dipole magnets will be re-worked in the fall of 2007.

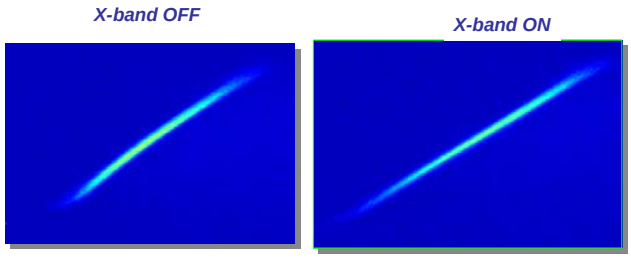

Figure 15: OTR screen in BC1 chicane with its horizontal dispersion. The first RF deflector is 'ON' here, with the X-band cavity 'OFF" at left, and 'ON' at right, demonstrating linearization of the energy chirp.

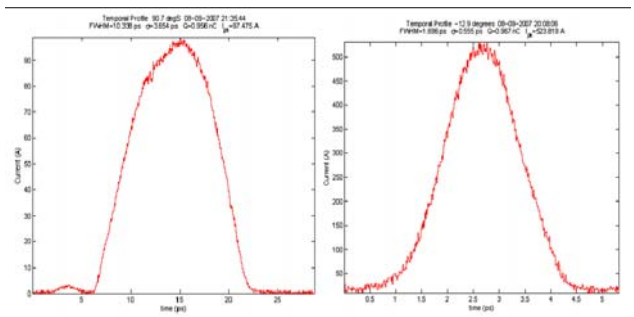

Figure 16: Bunch length distribution measured using both RF deflectors. The first measurement is at 135 MeV (left, $\sigma_z \approx 1.1$ mm, $I_{pk} \approx 97$ A) and the second is at 14 GeV (right, $\sigma_z \approx 0.17$ mm, $I_{pk} \approx 520$ A), representing the bunch length before and after BC1 compression at 1 nC.

BC1 BUNCH LENGTH MONITORS

The bunch length is monitored after BC1 using two techniques. One, referred to as BL12, incorporates a ceramic gap incorporated into the beam pipe downstream of the compressor. The microwave radiation generated by the short bunch's wakefields is transmitted through the ceramic and is detected by two fast, microwave detectors which are sensitive to 100 and 300 GHz. Once calibrated against the bunch length measurements using the LOLA transverse deflecting cavity, these signals are used to feedback the L1S RF phase and regulate the bunch length.

Another bunch length monitor located immediately after the last BC1 dipole measures the coherent synchrotron radiation, edge radiation and diffraction radiation generated by the short bunch as it passes through the dipole and a holed mirror. A collection lens images the diffraction radiation onto a pyroelectric detector. The general layout is given schematically in Figure 17.

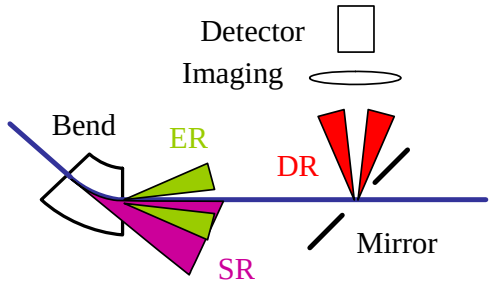

Figure 17: The radiation sources viewed by bunch length monitor, BL11. The pyroelectric detector measures the combined sources of synchrotron radiation (SR), edge radiation (ER) and diffraction radiation (DR) reflected into the detector by a mirror with a hole through which the electron beam passes.

Further details of the BL11 bunch length monitor are shown in Figure 18. The system splits the radiation into two detectors each of which has two high-pass filters at 0.5 mm and 1.0mm which can be inserted for selecting the wavelengths of interest. The responses of these detectors for the cases of no filter, and with the 0.5 mm and 1.0 mm filters inserted as functions of the L1S phase are plotted in Figure 19. Increasing L1S accelerator phase increases the bunch energy chirp resulting in stronger compression in BC1.

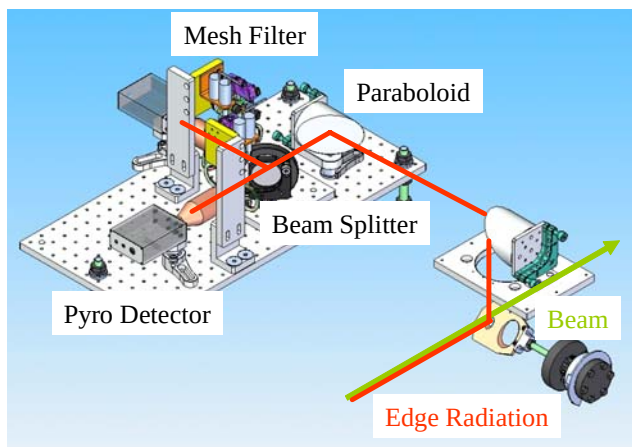

Figure 18: A computer generated drawing of the BL11 bunch length monitor system.

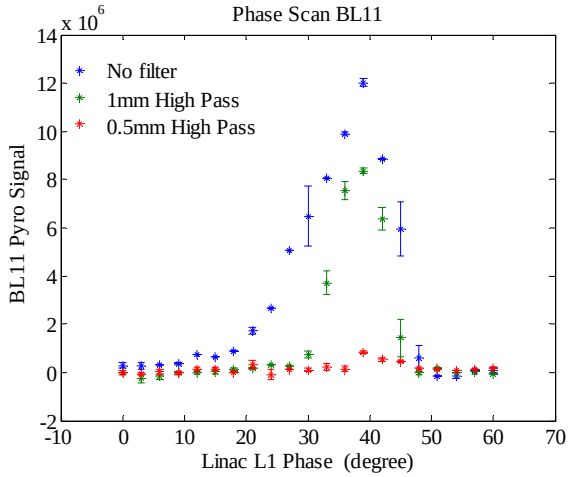

Figure 19: The response of the pyroelectric detector as a function of the phase of the linac section before the bunch compressor. The signal is given for no wavelength filter, a 1mm high pass filter and a 0.5mm high pass filter.

UNEXPECTED PHYSICS

During the beam emittance studies after BC1, we began observing a strong enhancement of the optical signal from the OTR foils when the bunch was highly compressed. The effect is illustrated in Figure 20 where the BL12 microwave detector signals and the OTR optical signal obtained by integrating OTR image are given vs. the L1S RF phase in a semi-log plot. Recall that increasing the L1S phase, decreases the electron bunch length where the L1S phase for nominal LCLS operation is 25 degS. The data show expected behavior for the two microwave signals. The lower frequency 100 GHz signal is first to respond, followed by the 300 GHz detector near 35 degS. The 300 GHz signal saturates above 40 degS.

What is unexpected is the large increase in the OTR optical signal, rising at least an order of magnitude above the unbunched signal. This behavior of the optical signal strength suggests there is micro-bunching of the electron beam at optical wavelengths.

In addition to this large increase in the optical signal, the beam image greatly varies from pulse to pulse. This can be seen in the large error bars at high-compression phases shown in Figure 20, which reflect the large shot-to-shot variation. Similar variations are seen in the profile projections given in Figure 21 for a sequence of beam pulses. The images themselves are similarly striking, displaying chaotic patterns of random spots which can be organized into a ring-like shape with the proper settings of the upstream quadrupoles. This fascinating effect can be seen in Figure 22. And again, these phenomena indicate the generation of coherent optical radiation due to micro-bunch instability.

Another indication of this interesting phenomenon is shown in Figure 23. In this study, the OTR optical signal for the foil is shown, but in this case, BC1 is articulated to zero degrees so as to have zero R_{56}. The quadrupole singlet between the two 17.5 degree dipoles of DL1 (see Fig. 1) is varied and the optical intensity is found to vary with a Gaussian shape, centered exactly at the setting which makes the DL1 dipole-quadrupole-dipole bend doubly achromatic.

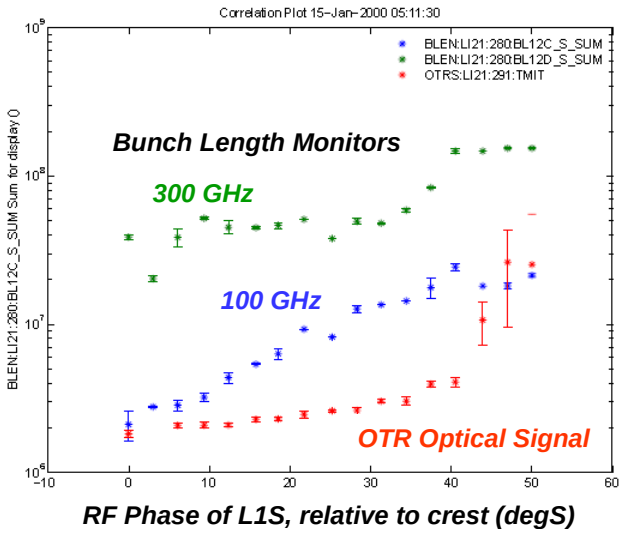

Figure 20: The signals of the BL12 microwave detectors at 100 (blue) and 300 (green) GHz, and the image-integrated OTR optical signal (red) as seen by a digital camera are plotted as functions of the L1S phase relative the crest.

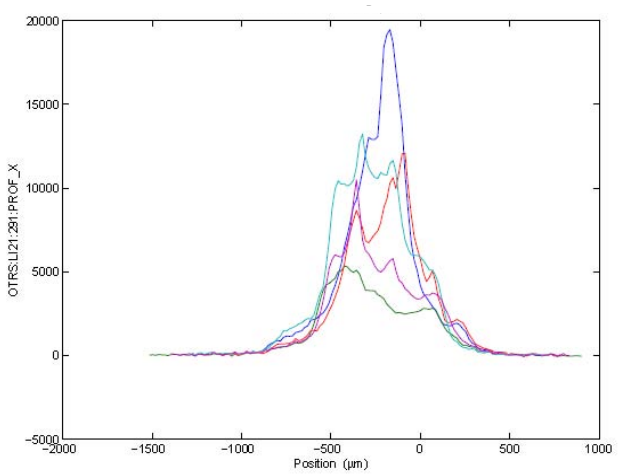

Figure 21: Profile projections for five consecutive beam pulses when the RF phase is set at 50 degS.

The data in Figure 22 can be explained by assuming the bunch has an energy modulation on the scale of optical wavelengths before entering DL1. This modulation is converted to current modulation by the 4 mm R_{56} of DL1 which then coherently radiates transition radiation at the OTR foil. Varying the quadrupole from its design field not only makes the bend dispersive but also results in non-zero values for the R_{51} and R_{52} matrix elements which can mix the bunches by tilting them in the transverse direction, smearing the current modulation and reducing the COTR signal. The coherent optical radiation (COTR) is the strongest when the quadrupole is set for DL1 achromatic with R_{51} and R_{52} equal to zero. A possible source of the initial energy modulation is shot-noise, as the drive laser doesn't have enough bandwidth to produce

such optical scale modulations. Experimental and theoretical investigations are in progress.

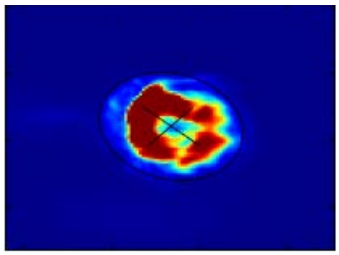

Figure 22: An image of the COTR radiation obtained by careful adjustment of the quadrupoles after the bunch compressor.

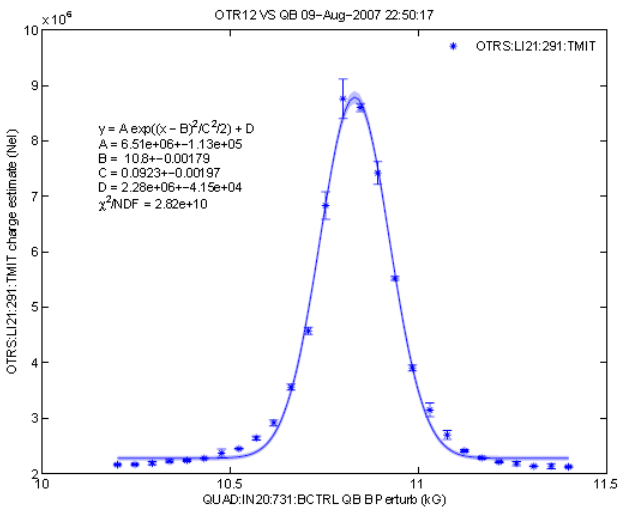

Figure 23: The integrated optical transition radiation signal as a function of the quadrupole single between the 17.5 degree bends. The optical signal is a maximum at the quadrupole setting which makes the DL1 bend doubly achromatic.

SUMMARY AND DISCUSSION

The design and beam properties measured during the five month commissioning run are listed in Table I. These results unambiguously show the injector meets all the beam requirements for the LCLS.

The five month commissioning period not only successfully validated the injector design and its operation, but also observed strong coherent effects in the beam diagnostics and transport on the optical scale. These effects are yet another indication of excellent beam brightness, and show we are now entering a new era of beam physics where coherence dominates not only with the FEL interaction, but also during the production, acceleration, transport and manipulation of these dense electron bunches. The LCLS injector commissioning additionally makes it clear that coherence and interference effects will play a major role in future beam diagnostics. Hence LCLS ushers in a new era not only of 4th generation light sources, but also of bright electron beams which coherently radiate all too easily.

Table I: The design and measured beam properties.

Parameter	sym	dsgn	meas.	unit
Final e^- energy	γmc^2	14	14	GeV
Bunch charge	Q	1	1	nC
Init. bunch length (fwhm)	Δt_0	10	10	ps
Fin. bunch length (fwhm)	Δt_f	2.3	1.5-10	ps
Initial peak current	I_{pk0}	100	100	A
Projected norm emittance	$\gamma\varepsilon_{x,y}$	1.2	1.1 - 1.2	μm
Slice norm. emittance	$\gamma\varepsilon^s_{x,y}$	1.0	0.7 - 1.0	μm
Single bunch rep. rate	f	120	10-30	Hz
RF gun field at cathode	E_g	120	115	MV/m
Laser energy on cathode	u_l	250	300	μJ
Laser wavelength	λ_l	255	255	nm
Laser diameter on cath.	$2R$	1.5	1.3	mm
Cathode material	-	Cu	Cu	
Cathode quantum eff.	QE	6	3.5	10^{-5}
Commissioning duration	-	8	5	mo

REFERENCES

[1] J. Arthur *et al.*, SLAC-R-593, April 2002.
[2] R. Akre, *et al.*, PAC'07, Albuquerque, NM, 2007.
[3] "The Stanford Two-Mile Accelerator," R. B Neal, Ed., W. A. Benjamin 1968, pp.1123-1124.
[4] D. H. Dowell, J. Castro, P. Emma, J. Frisch, S.Gilevich, G. Hays, P. Hering, C. Limborg-Deprey, H. Loos, A. Miahnahri and W. White, "LCLS Injector Drive Laser," PAC'07, Albuquerque, NM, 2007.
[5] C. Limborg-Deprey, D. Dowell, J. Schmerge, Z. Li and L. Xiao, "RF Design of the LCLS Gun" LCLS-TN-05-3, Feb. 2005.
[6] L. Xiao, R.F. Boyce, D.H. Dowell, Z. Li, C. Limborg-Deprey, and J.F. Schmerge, "Dual Feed RF Gun Design for the LCLS", SLAC-PUB-11213 and PAC'05, Knoxville, TN, 2005.
[7] D.H. Dowell, E. Jongewaard, C. Limborg-Deprey, J. Schmerge and A. Vlieks, "Measurement and Analysis of Field Emission Electrons in the LCLS Gun," PAC'07, Albuquerque, NM, 2007.
[8] J. Rosenzweig *et al.*, "Initial Measurements of the UCLA RF PhotoInjector", NIM A 341 (1994) 379-385.
[9] J. L. Adamski *et al.*, "Results of commissioning the injector and construction progress of the Boeing one kilowatt free-electron laser", SPIE Vol. 2988, p158-169.
[10] C. Limborg-Deprey, D. H. Dowell, P. Emma, R. Iverson, J. Frisch, H. Loos, J. Turner, J. Schmerge, J. Welch, J .Wu, Y. Ding, Z. Huang, J. Castro, G. Hays, P. Hering, S. Gilevich, A. Miahnahri and W. White, "Simulations for the LCLS Injector," These Proceedings.
[11] P. Emma *et al.*, PAC'07, Albuquerque, NM, 2007.
[12] R. Akre *et al.*, PAC'01, Chicago, IL, June 2001.

DIRECT MEASUREMENT OF PHASE SPACE EVOLUTION IN THE SPARC HIGH BRIGHTNESS PHOTOINJECTOR*

E. Chiadroni[a†], D. Alesini[a], A. Bacci[c], M. Bellaveglia[a], R. Boni[a], M. Boscolo[a], M. Castellano[a], L. Catani[b], S. Cialdi[c], A. Cianchi[b], A. Clozza[a], L. Cultrera[a], G. Di Pirro[a], A. Drago[a], A. Esposito[a], M. Ferrario[a], L. Ficcadenti[e], D. Filippetto[a], V. Fusco[a], A. Gallo[a], G. Gatti[a], A. Ghigo[a], L. Giannessi[d], M. Incurvati[a], C. Ligi[a], M. Migliorati[e], A. Mostacci[e], P. Musumeci[f], E. Pace[a], L. Palumbo[e], L. Pellegrino[a], M. Petrarca[g], M. Quattromini[d], R. Ricci[a], C. Ronsivalle[d], J. Rosenzweig[f], A.R. Rossi[c], C. Sanelli[a], L. Serafini[c], M. Serio[a], F. Sgamma[a], B. Spataro[a], F. Tazzioli[a], S. Tomassini[a], C. Vaccarezza[a], S. Vescovi[a], C. Vicario[a]

[a]INFN-LNF, via E. Fermi, 40 - 00044 Frascati, Rome, Italy

[b]INFN-Roma "Tor Vergata", via della Ricerca Scientifica, 1 - 00133 Rome, Italy

[c]INFN-Milano, Via Celoria 16, 20133 Milan, Italy

[d]ENEA C.R., via E. Fermi, 00044 Frascati, Rome, Italy

[e]Università di Roma "La Sapienza", Dip. Energetica, via A. Scarpa, 14 - 00161, Rome, Italy

[f]UCLA - Dept. of Physics and Astronomy, 405 Hilgard Avenue, Los Angeles, California 90095, USA

[g]INFN-Roma I, p.le A. Moro 5, 00185 Roma, Italy

Abstract

The characterization of the transverse phase space for high charge density relativistic electron beams is a fundamental requirement in many particle accelerator facilities, in particular those devoted to fourth-generation synchrotron radiation sources, such as SASE FEL.
The main purpose of the SPARC initial phase was the commissioning of the RF photoinjector. At this regard, the evolution of the phase space has been fully characterized by means of the emittance meter diagnostics tool, placed in the drift after the gun exit.
The large amount of collected data has allowed for the first time a detailed reconstruction of the transverse phase space evolution downstream the RF, giving evidences of the emittance compensation process as predicted by theory and simulations.
In particular the peculiar behavior of a flat top longitudinal electron distribution compared to a gaussian distribution has been studied giving important insights for the correct matching with the following linac whose working point is based on the double emittance minimum effect.

INTRODUCTION

The SPARC project is an R&D activity oriented to the development of a high brightness photoinjector to drive SASE FEL experiments [1]. In the first phase, the SPARC layout (Fig.1) consisted of a 1.6 cell RF gun operated at S-band (2.856 GHz, of the BNL/SLAC/UCLA type) and high peak field on the cathode ($\simeq$ 120 MV/m) with incorporated Copper photo-cathode, generating a 5.6 MeV energy beam. The first few meters of beam propagation, where space charge effects and plasma oscillations dominate the electron dynamics, have been studied by means of the movable emittance meter [2]. This device, based on the 1D

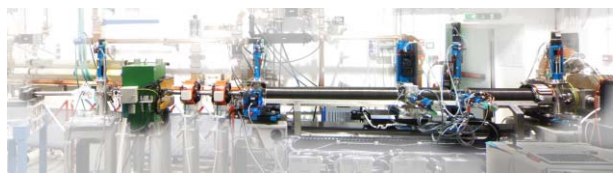

Figure 1: The SPARC photoinjector in the initial phase: from the right to the left, the RF gun with the solenoid, the emittance meter, quadrupoles and dipole magnets, the energy spectrometer and the beam dump.

pepper-pot technique, has allowed not only to measure the beam size and emittance, but also to reconstruct the transverse phase space at different positions along the direction of motion. Due to the high sensitivity of this method, a very precise emittance value can be calculated directly from the phase space analysis. For this reason, suitable data processing algorithms have been developed.
In the next phase of SPARC, which will start in Autumn, the beam emerging from the gun will be focused and matched into 3 accelerating sections of the SLAC type (S-band, TW), to boost the beam energy up to 155-200 MeV and to drive a SASE FEL at 530 nm.

SYSTEM DESCRIPTION AND OPTIMIZATION

To reach its goal SPARC requires a temporally flat, pico-second laser source. This source [3] is based on a Ti:sapphire oscillator that generates 100 fs pulses with a

* Work partially supported by the EU Commission in the sixth framework program, Contract No. 011935 EUROFEL-DS1 and from the MIUR Progetti Strategici DD1834.

† enrica.chiadroni@lnf.infn.it

repetition rate of 79.33 MHz locked with the 36^{th} subharmonic of the SPARC S-band master clock. The measured time jitter is within 1 ps. An acousto-optic dispersive filter, called DAZZLER, is placed between the oscillator and the amplifier to modify the spectral amplitude and phase function to obtain the target temporal profile [4]. The amplifier delivers pulses at 800 nm with energy of 50 mJ and a repetition rate of 10 Hz. The pulses go to the third harmonic generator and UV pulses at 266 nm are produced. At the end of the laser chain there is a grating stretcher to stretch the pulses temporally up to 8-12 ps [5]. After that the optical transfer line transports the laser beam at normal incidence to the cathode with an energy between 50 and 100 μJ.

Since the uniformity of the transverse distribution strongly influences the beam brightness, a dedicated laser cleaning has been performed with 10 μJ and 100 μm spot size diameter, resulting in the increase of the mean quantum efficiency (QE) from 2.3 10^{-5} to 10^{-4} (Fig.2). An improvement of the emission uniformity has been found over a 4 mm square area, which allowed to get the nominal beam parameters (1 nC electron beam charge, with 50 μJ laser pulse energy at 120 MV/m peak field on the cathode).

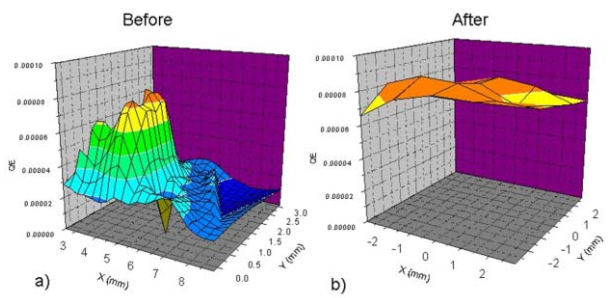

Figure 2: Copper cathode quantum efficiency before (left) and after (right) the laser cleaning.

The Emittance Meter

At the gun exit the beam is quasi-relativistic and conventional methods to measure the transverse emittance are not adequate due to the fact that internal collective forces play a fundamental role in the beam transport. For such space charge dominated beams, the most appropriate technique to measure RMS (root mean square) transverse emittance is the one based on the pepper pot method. This technique, which consists in splitting the beam into several beamlets by means of a multislit mask intercepting the beam or, alternatively, a single slit moving across the beam spot, is implemented in a device, called emittance meter, able to scan the 2 meters long region downstream the gun along the beam line. The emittance can be measured in both x and y planes at different positions along the direction of beam propagation in the range 1098 - 2100 mm following the emittance oscillations. In particular, due to the high measurement resolution, the entire distribution in space and angles can be precisely reconstructed from the sampling in both directions, allowing the full characterization of the beam transverse dynamics.

The complete knowledge of the beam parameters at different distances from the cathode is important also for defining the injector settings which optimize the emittance compensation process and for code validation.

Beyond a transverse diagnostics, the emittance meter allows also to get information on the beam longitudinal parameters. By selecting the central part of the beam with a slit, the evolution of the energy spread can be measured at different z positions. The very good agreement between measurements and PARMELA model, which does not take into account the wake-fields effect, points out that the influence of the long emittance meter bellows is negligible (Fig.3).

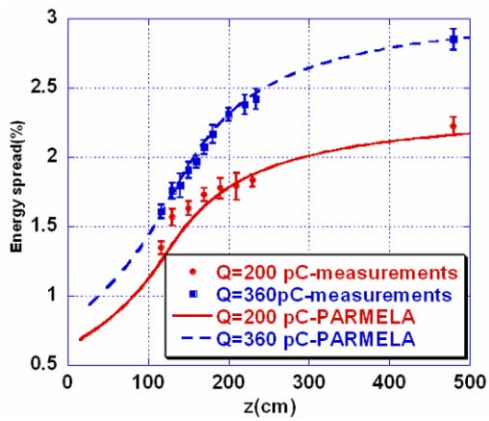

Figure 3: Evolution of the energy spread versus z for two different bunch charges compared with a PARMELA simulation.

DATA ANALYSIS

For the first time direct emittance evolution measurements and experimental studies of dynamical behavior have been done.

Since the beam appears different during its propagation along z, the estimation of the right beam halos and the preservation of the same cut level at different locations are critical issues to deal with. Indeed, conventional image processing tools might introduce artifacts which could cover small fluctuations in the beam emittance dynamics.

Furthermore, the large amount of data collected has demanded the development of an automatic procedure for data processing. At this purpose, three independent algorithms, based on different approaches, have been developed for the emittance calculations: i) a single image analysis and data extrapolation [6], ii) a trace space plot filtering [7] and iii) a genetic-based algorithm [8].

Single Image Analysis and Data Extrapolation

The main program data flow is shown in Fig.4. It consists of four routines.

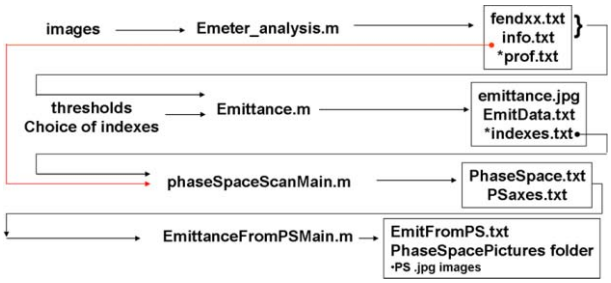

Figure 4: The analysis software data flow. The central column corresponds to the routine names, the left one shows the input parameters while the right one the output parameters.

The first one is the core of the algorithm oriented to distinguish the signal from noise; it takes raw beamlets images as input and after processing their profiles it calculates from them the moments of the beamlet charge distribution, i.e. beamlet area, centroid and rms width along the direction perpendicular to slit edges.
The second routine takes as input the files saved by the first one, cleans data from bad values and calculates the emittance in two different ways: i) by averaging slit parameters and/or ii) by averaging different emittances calculated from each single parameter. The third routine reconstructs and saves the trace space for each single emittance measurement and the fourth one interpolates the trace space in order to have more sampling along the abscissa and then calculates the emittance from the trace space with the desired cut in charge.
This analysis procedure automatically operates a cut on the charge effectively considered in the emittance computation, whose level cannot be trivially retrieved. For this reason and to validate and support the data analysis method, two more algorithms have been developed, both starting from the transverse phase spaces.

Phase Space Filtering

The goals of this code are the calculation of the emittance value directly from the phase space data and the quantification of the cut level introduced on the beam by the previous algorithm.
The idea is to quantify the contribution of every pixel to the total emittance, retrieving the value of the x, x' and using it in the Courant-Snyder invariant to calculate the emittance. The emittance can then be used as sorting parameter, so that pixels with the highest contribution on the emittance value, probably outside the beam core, are withdrawn.
Starting from these pixels the total charge and the second derivative of the emittance with respect to the charge is calculated. A phenomenological evidence has shown a deep, sharp peak in the second derivative in all the reconstructed trace spaces.
Montecarlo simulations have demonstrated that this peak appears in the transition between signal and noise, if the signal-to-noise ratio and the speed of the signal increment over the noisy background are high enough. Assuming this point to be 100% of the beam charge, it is possible to define an emittance value depending on the charge cut level.

Genetic Algorithm

The basic concept relies on the fact that a real beam can be thought as composed by N sub-beams of different densities drawing concentric ellipses in the trace space, with different slopes and covering areas of different intensities.
Starting from the interpolated phase space, the code generates an intensity distribution function from which the total intensity and the cut parameter are retrieved. Each ellipse is described by the three Twiss parameters and the trace space centroid by two coordinates. A family of N solutions, called chromosomes, is generated, each of which corresponding to 2+3N parameters. Therefore the best set of ellipses is found by maximizing the Intensity/Area function, the area corresponding to the beam geometric emittance.
The code is optimized for N=8, but it can accept any number of ellipses. Fig.5 shows a very good agreement between the genetic solution, given by the union of the eight analytical ellipses, and the projected distribution of the real bunch.

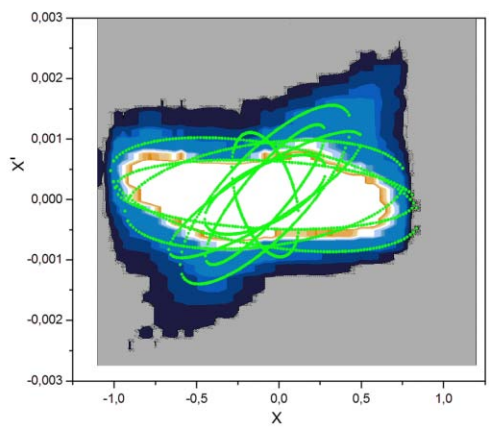

Figure 5: Real beam sampled with 8 ellipses representing the best chromosome.

Comparison

Many different emittance curves have been analyzed and here is shown one of the most significant to compare all the codes. Indeed, the small amplitude of the double minimum oscillation is an excellent candidate to check that every method is able to resolve it. Experimental data are compared in Fig.6 to a numerical fit with the PARMELA tracking code, showing a very good agreement [9].

The cutting level is 95% for the phase space algorithm and 97% for the genetic-based algorithm.

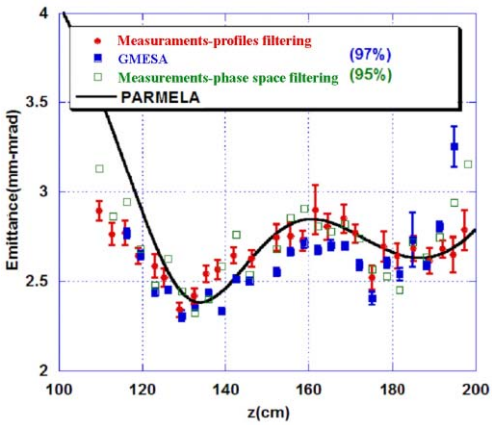

Figure 6: Comparison between different algorithms and PARMELA simulation.

RESULTS HIGHLIGHTS

Comparison between Gaussian and Flat-Top Pulse

An accurate study, supported by PARMELA simulations (Fig.7), has been done to show how the beam dynamics strongly depends on the laser pulse rise time. It is evident

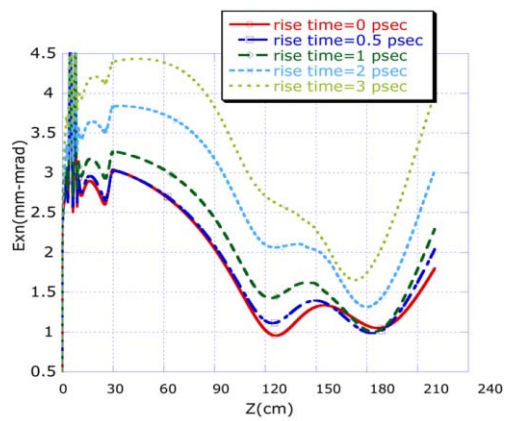

Figure 7: PARMELA simulation of the emittance evolution for pulses with different rise time.

that under the same conditions, the shortest rise time gives not only the smallest emittance minimum, but it makes also the double minimum oscillation more pronounced, whereas at longer rise time it turns into a knee.

Experimentally we compared two different pulse shapes with the same FWHM equals to 8.7 ps, but with different rise time: 5 ps for the Gaussian-like pulse and about 2.5 ps for the flat-top-like pulse (Fig.8a). The resulting emittance evolution in the vertical plane, for a beam of 0.31 mm rms spot size, 0.74 nC charge and 5.4 MeV energy, is shown in

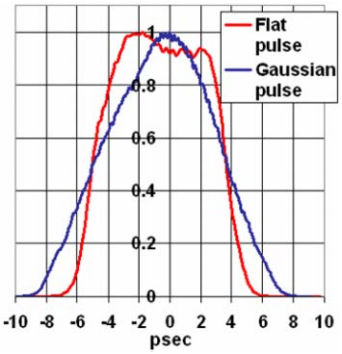

(a)

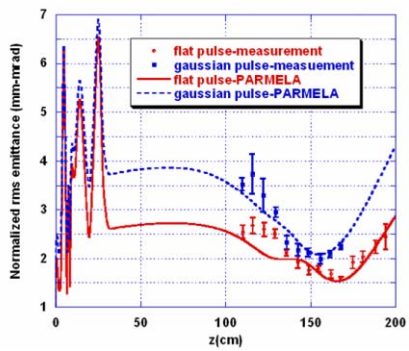

(b)

Figure 8: a) Gaussian-like and flat-top-like pulse shapes with the same FWHM = 8.7 ps. b) Measured emittance evolution of Gaussian and flat top beams compared with PARMELA simulations.

Fig.8b. The comparison points out that the minimum emittance value is reduced from 2 to 1.5 mm-mrad by using a flat-top shape instead of a gaussian pulse, accordingly with PARMELA simulations.

High Brightness Beam

A large number of runs were devoted to maximize the brightness by minimizing the transverse emittance. The best result, obtained with the flat-top longitudinal profile shown in Fig.9, is presented in Fig.10 [10]. The minimum

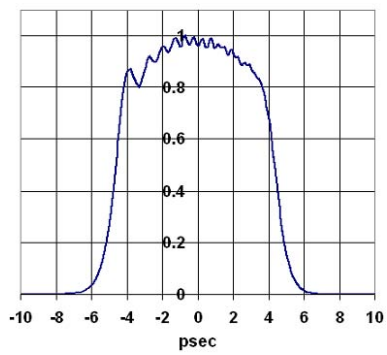

Figure 9: Laser pulse longitudinal profile: FWHM = 9 ps, rise time = 2.7 ps.

emittance, for a beam with peak current of 92 A, is 1.6 mm-mrad, giving a peak brightness of 7 10^{13} A/mm^2. The injection phase was set to -8 deg with respect to the maximum energy gain phase and the rms spot size was 360 μm. The simulation made with PARMELA (solid line in the plot of Fig.10) reveals a very good agreement with the experimental data.

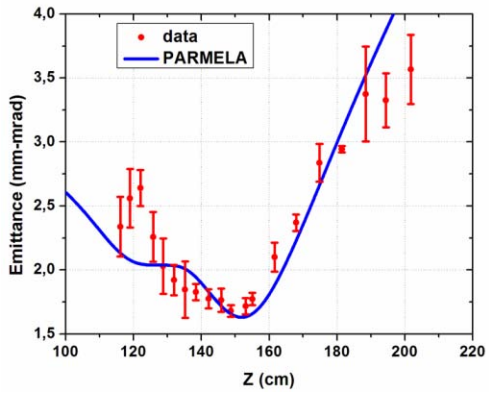

Figure 10: Emittance as function of the longitudinal coordinate for high brightness beam.

Double Minimum Signature

The peculiar space charge regime which, in the flat top pulse mode, gives rise to the emittance oscillation, observed up to now in numerical simulations only and on which photoinjectors worldwide have based the most common compensation design, has been revealed [11] by strongly reducing the rise time down to 1.5 ps (the longitudinal profile is shown in Fig.11) and moving the injection phase of 12 degrees behind the phase of maximum energy gain in order to increase the beam energy spread accordingly with the chromatic nature of the effect. The bunch

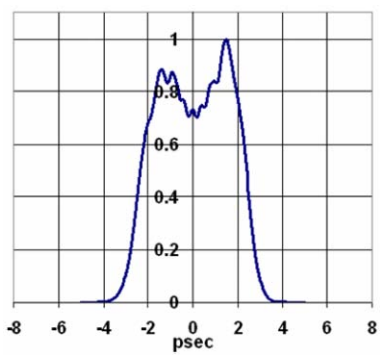

Figure 11: Laser pulse longitudinal profile: FWHM = 5 ps, rise time = 1.5 ps.

charge was 0.5 nC in a 5 ps FWHM laser pulse length, corresponding to 100 A peak current. The beam energy was 5.5 MeV.
The evolution of the emittance along z, in very good agreement with PARMELA simulations, is shown in Fig.12. The amplitude of the oscillation is about 0.3 μm which is above the resolution of our measurement system.

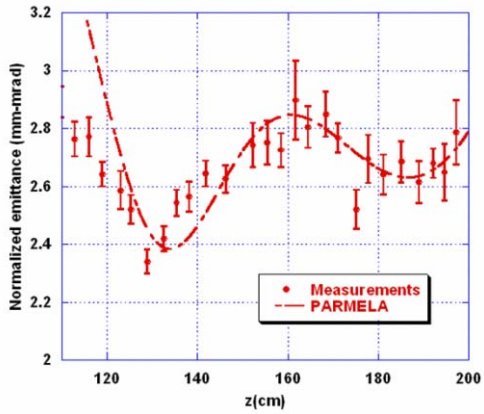

Figure 12: Double minimum emittance oscillation with corresponding PARMELA simulation.

Phase Space Analysis

Emittance oscillations have been explained as produced by a beating between head and tail particles oscillating with different plasma frequencies caused by correlated chromatic effects in the solenoid [12].
In the space charge dominated regime, simulations show a cross shape in the transverse phase space of a flat top distribution at its relative emittance maximum, corresponding to the beam waist (Fig.13b), due to the fact that each slice, which shapes the beam up, has the same weight in current. Thus, under laminar condition, the space charge dominated waist is reached at different positions by the head and the tail of the bunch (Fig.13b, left picture), so that when the bunch tail (green slice) is already diverging the bunch head (red slice) is still converging, resulting in the observed cross shaped transverse phase space.
In the Gaussian pulse case (Fig.13a), this effect is less pronounced since the amount of current at the bunch tails is smaller, thus causing the bunch tails to go through a crossover and only the central slices through a waist [13], [14].
A comparison of the transverse phase space at the beam waist as retrieved from beam measurements for both Gaussian and flat top distribution is reported in Fig.14. According to theory, experimental data show that a flat top beam goes through a space charge dominated waist passing from convergent to divergent, resulting in the typical cross shape in the reconstructed transverse phase space (Fig.14b), while it is absent in case of Gaussian beam (Fig.14a).

CONCLUSIONS

The initial phase of the SPARC project is concluded showing, for the first time experimentally and due to a movable diagnostics, the oscillation of the emittance in the region, downstream the RF gun, where the emittance com-

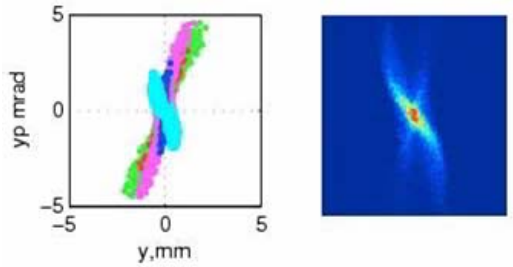

(a) Gaussian beam

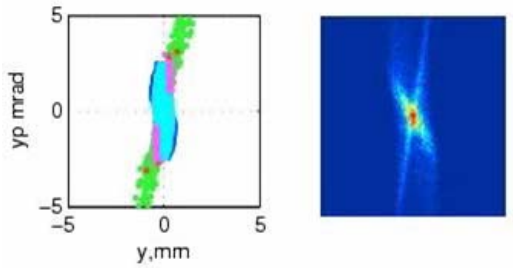

(b) Flat top beam

Figure 13: PARMELA simulation of the transverse phase space for a beam approaching its waist. Left pictures show the ensemble of slices shaping the beam up: green is the bunch tail, light blue the center of the bunch and red the head.

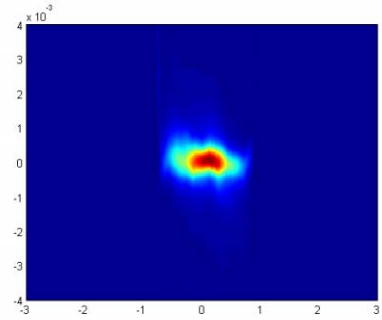

(a) Gaussian beam

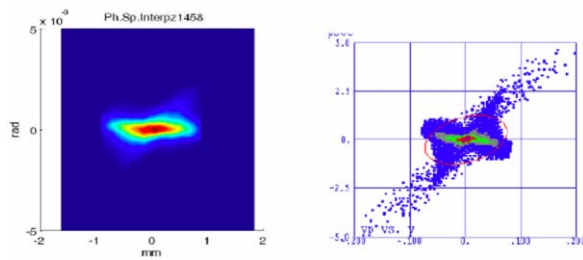

(b) Flat top beam

Figure 14: Reconstructed (left) transverse phase space at the beam waist compared with PARMELA simulation (right).

pensation process is predicted by theory. The high sensitivity of this diagnostics has allowed also to fully reconstruct the beam transverse phase space from which, due to the very high sampling rate, the emittance dynamics has been reproduced in excellent agreement with the simulation.
The large amount of data collected has required the development of automatic tools for data processing which gives a validation of measurement results, being all quantitatively consistent with simulations and with each other.

ACKNOWLEDGMENTS

The authors wish to thank V. Lollo for his contribution to the system mechanical design, engineering and bench testing, F. Anelli and S. Fioravanti for their work on motor controllers. Thanks also to A. Battisti, L. Cacciotti, L.A. Rossi, R. Sorchetti and S. Strabioli.

REFERENCES

[1] SPARC Project Team, Technical Design Report for the SPARC Advanced Photoinjector, http://www.lnf.infn.it/acceleratori/sparc (2004)

[2] L. Catani et al., Review of Scientific Instruments **77**, (2006) 93301.

[3] C. Vicario et al., "Drive Laser System for SPARC Photoinjector", Proceedings of the PAC'07, Albuquerque, NM, USA, June 2007.

[4] S. Cialdi et al., Optics Letters **31**, (2006) 2885.

[5] S. Cialdi et al., Applied Optics **46**, 22, (2007) 4959.

[6] D. Filippetto, "A robust algorithm for beam emittance and trace space evolution reconstruction", SPARC/EBD-07/002, LNF-INFN, June 2007.

[7] A. Cianchi et al., "Accurate emittance calculation from phase space analysis", SPARC/EBD-07/003, LNF-INFN, July 2007.

[8] A. Bacci et al., "A Genetic Code able to compute the emittance value of a real beam by a Multiple Ellipse Slice Analysis of the transversal phase-space image", SPARC/EBD-07/004, LNF-INFN, July 2007.

[9] C. Ronsivalle et al., "Comparison between SPARC e-meter measurements and simulations", Proceedings of the PAC'07, Albuquerque, NM, USA, June 2007.

[10] A. Cianchi et al., "High brightness electron beam emittance evolution measurements in SPARC RF photoinjector", submitted to Phys. Rev., ST-AB.

[11] M. Ferrario et al., "Direct measurement of double emittance minimum in the SPARC high brightness photoinjector", submitted to Physical Review Letters.

[12] M. Ferrario et al., "Recent Advances and Novel Ideas for High Brightness Electron Beam Production Based on Photo-Injectors", The Physics and Application of High Brightness Electron Beam (World Scientific Publishing Co. Pte. Ltd., 2002).

[13] B.E. Carlsten, Nucl. Instrum. & Methods A **285**, (1989) 313.

[14] L. Serafini, J.B. Rosenzweig, Phys. Rev. E **55** (1997) 7565.

SUPERCONDUCTING PHOTOINJECTOR

Ilan Ben-Zvi, Andrew Burrill, Rama Calaga, Xiangyun Chang, Ranjan Grover, Ramesh Gupta, Harald Hahn, Lee Hammons, Dmitry Kayran, Jorg Kewisch, Robert Lambiase, Vladimir N. Litvinenko, Gary McIntyre, Damayanti Naik, David Pate, David Phillips, Eduard Pozdeyev, Triveni Rao, John Smedley, Roberto Than, Robert J. Todd, Dan Weiss, Qiong Wu, Alex Zaltsman, BNL, Upton, Long Island, New York
Michael Cole, Michael Falletta, Douglas Holmes, John Rathke, Tom Schultheiss, Robert Wong, AES, Medford, New York
Alan Murray Melville Todd, AES, Princeton, New Jersey

Abstract

One of the frontiers in FEL science is that of high power. In order to reach power in the megawatt range, one requires a current of the order of one ampere with a reasonably good emittance. The superconducting laser-photocathode RF gun with a high quantum efficiency photocathode is the most natural candidate to provide this performance. The development of a 1/2 cell superconducting photoinjector designed to operate at up to a current of 0.5 amperes and beam energy of 2 MeV and its photocathode system are the subjects covered in this paper. The main issues are the photocathode and its insertion mechanism, the power coupling and High Order Mode damping. This technology is being developed at BNL for DOE nuclear physics applications such as electron cooling at high energy and electron ion colliders..

INTRODUCTION

In the past few years we are witnessing the growth of a new class of particle accelerators: high-power, high-brightness electron beams. This emerging technology is enabled by the combination of high-brightness electron sources and high-current SRF Energy Recovery Linacs (ERL). While the current state-of-the-art is at about 10 mA current [1] (the Jefferson Laboratory FEL upgrade), there is interest in much higher currents, in the range of 0.1 ampere to over 1 ampere CW, with emittances that are of the order of under 1 to a few 10's microns normalized rms, depending n the application, in particular on the bunch charge.

What are the applications driving this interest? First, as the Jefferson Laboratory example suggests, high power Free-Electron Laser (FEL) is one candidate. The high-brightness is required for the lasing conditions at UV or shorter wavelength, and significantly higher currents are desirable for high power FEL applications [2]. The energy required for such applications is not very high, in the range of 100 MeV to less than 1 GeV for UV high-power FELs.

The next application is also for the production of electromagnetic radiation, but for mostly spontaneous emission. This is the ERL based light sources [3,4]. For this application the current may be in the range of 100 mA, less for the extremely high brightness X-ray radiation or higher for flux dominant applications. The required energy is between 3 and 10 GeV.

Another application is in an altogether different field, electron ion colliders [5]. In this type of machine a current of hundreds milliampere electrons or polarized electrons is needed at energy of up to 10 or 20 GeV.

A somewhat specialized application is electron cooling of hadron storage rings, in particular heavy ion beams [6]. This application requires electron beams at currents of up to 0.1 amperes but relatively low energies of under 100 MeV. Finally, there are a host of other applications that have been demonstrated but are still under development: X-ray sources via Thomson scattering of laser on the electron beam and terahertz radiation a examples.

The electron gun and injector design is arguably the most critical part of the ERL. It is here that the ultimate performance of the ERL is determined: What will be its current, its bunch structure, and its transverse and longitudinal emittances. These parameters can only be degraded in subsequent parts of the ERL, never improved. The gun and injector are also the most dynamic elements, with rapid progress being made. It has some of the most intractable problems, in particular the issue of providing a good photocathode and dealing with severe space-charge interaction and limited space. The flip side of this is that any improvement made in this relatively small element affects the performance of the complete ERL and can easily lead to dramatic improvements.

In this paper we will look at the technology and challenges confronting the development of high-current, high-brightness electron sources and describe the approach taken by the few laboratories which are actively developing this technology: Brookhaven National Laboratory and Advanced Energy Systems, KF Rossendorf, the University of Peking and DESY.

THE CURRENT STATUS OF SRF GUNS

The first pioneering experimental work on a superconducting RF gun took place about 15 years ago in Wuppertal by Michalke [7]. The activity in the area of SRF guns around the world is growing steadily. Successful milestone operation of a SRF gun with a superconducting half-cell cavity were carried out in 2002

*Work done under the auspices of the US Department of Energy
#benzvi@bnl.gov

at the Forschungszentrum Rossendorf [8], and a new SRF photoinjector for CW operation at the ELBE linac is under development [9]. The conclusion from the successful operation of the half-cell SRF injector cavity at Rossendorf is addressing the crucial question if the photocathode inside the superconducting cavity reduces the quality factor due to particle pollution. During about 200 hours operation time, such an effect was not seen using $CsTe_2$ cathodes. It also demonstrates convincingly that a reliable mechanism for inserting a normal-conducting cathode stem into a superconducting cavity does not affect the good performance of the SRF cavity. Following this initial success the Rossendorf group embarked on the design and production of a 3 ½ cell gun which has also various other improvements for getting the smallest emittance out of the device, including careful shape optimization, bunch focusing by a high-order RF mode, symmetrized input coupler and improved tuner system [9]. Other SRF guns have been built and operated. An all niobium RF gun developed by BNL, AES and JLab demonstrated large charge (10 nC) in a short (~10 ns) bunch train [10,11]. The University of Peking started very early on a novel hybrid pulsed DC - a half cell niobium gun [12]. The team at Beijing is now proceeding with a 3 ½ cell gun [13, 14]. Superconducting photocathodes in a superconducting RF gun are pursued by a DESY-JLab-BNL collaboration [15], where good SRF performance has been combined in proof-of-principle ½ cell gun and photoemission has been measured. This led to a new 1 ½ cells gun with sophisticated RF design [16]. Following early successes, a new generation of guns is emerging, where multi-cell guns with improved geometries, focusing and coupling aim at a small emittance at higher average currents, 1 to 10 mA, as called by UV or x-ray FELs.

THE BNL – AES SRF GUN

The main feature of the BNL-AES gun, seen in Figure 1., is the design for a very high current, up to 0.5 ampere, for a variety of applications as described above, in particular for electron cooling and electron-ion colliders. Table 1 shows the parameters of the BNL-AES SRF gun. It has been optimized [17] to obtain a small emittance at a large charge by shaping the gun cavity, selection of its frequency and field.

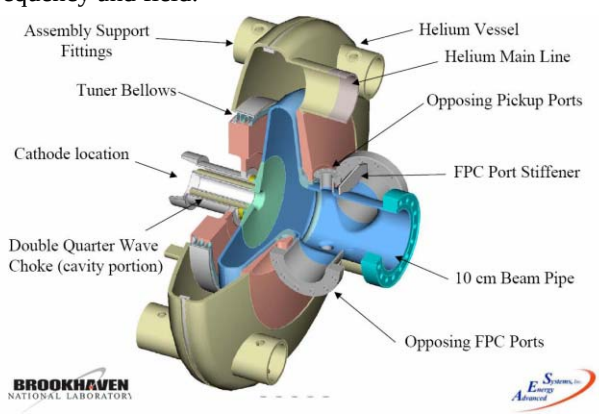

Fig. 1. The BNL-AES SRF electron gun.

The gun design is dictated by the objective of a high current but at a limited (1 MW) CW klystron power. Thus a single cell design is used, which allows for a high accelerating field at a limited total voltage of 2 MV.

The choice of frequency was dictated by the need to maintain the frequency a harmonic of the RHIC frequency with 360 bunch pattern of 28.15 MHz, lower the frequency to a value where beam breakup threshold current in the ERL will be large and, finally, a frequency where CW MW klystrons are available. That led to the choice of 703.75 MHz.

This SRF gun is equipped with a demountable photocathode capable of being inserted and retracted while maintaining the vacuum integrity and cleanliness of the photoinjector. A schematic of the photoinjector and associated helium vessel is shown in figure 1.

The cavity iris had to be made small for beam dynamics reasons (reduction of effective length of the cavity). That precluded damping all HOMs through the beam pipe.

HOM damping is an important issue. It was found that the beam pipe diameter could be kept at 10 cm, the same dimension as the iris of the cavity and still adequately propagate most of the HOMs. Other benefits of having reduced beam pipe size is simplification of strong coupling of the 1 MW RF power to the beam, as well as reduction of the size of the gate valve needed at the end of the beam pipe, a tremendous weight and cost savings.

Table 1: BNL-AES SRF Gun Specifications

Parameter	**Units**	**Value**
Frequency	MHz	703.75
Iris radius	cm	5
Equator Diameter	cm	37.9
Cavity length	cm	25
Beam kinetic energy	MeV	2
Peak electric field	MV/m	35.7
Peak magnetic field	A/m	58740
Stored energy	Joule	8.37
QR_s (geometry factor)	Ω	3.52
R/Q	Ω	96
Q_e (external Q)		37000
Power input	MW	1
Maximum current	mA	500
Emittance at 1.4 nC	μm rms normalized	1.4
Cathode recess	mm	1
Cathode spot size	mm diameter	5
Emission phase	Degrees	25
Longitudinal loss factor	V/pC	0.7
Transverse loss factor	V/pC/m	32

Additionally, a focusing solenoid, constructed from a high temperature superconductor, will be inserted just inside the gate valve in order to help decrease the beam emittance. This will be much easier with the reduced beam pipe size as it will significantly reduce the amount of material needed to make the solenoid, significantly reducing the power needed to drive the solenoid and subsequently the heat generated during its operation.

The gun propagates all but 3 of the HOMs down the beam pipe to be strongly absorbed by a ferrite HOM absorber at room temperature. The three trapped modes can be easily missed by harmonics of the beam repetition frequency and detailed calculations have shown that the effect of long range wake fields can be neglected if the beam amplitude and phase noise are under a reasonable limit. It is expected that the strong coupling of the fundamental power couplers will damp some or all of these modes. Work is in progress on this question.

The gun design accommodates a load-lock cathode insertion mechanism, which is introduced through a double quarter-wave choke joint which accepts a UHV cathode transporter. The photocathode will be extended approximately 1 meter into the photoinjector and positioned at the exact location for operation.

The cathode transporter, in turn, couples to a UHV cathode preparation chamber. The locking mechanism has been designed with UHV requirements and introduction of minimal particulate matter into the cavity. The quarter wave choke joint is much easier to fabricate than the alternative proven design, presently used by Rossendorf, which incorporates a more complex arrangement including an additional, detuned cavity. The quarter wave choke joint concept has undergone preliminary testing and will be subsequently tested using a fully SRF 1.3 GHz photoinjector presently in place at BNL.

PHOTOCATHODE ISSUES

The photocathode is the single most difficult issue for a high-current electron gun.

What are the requirements for a high-current photocathode suitable for this gun?

1. Avoid contamination of the SRF gun.
2. Provide high quantum efficiency.
3. Long life.
4. Prompt emission.
5. Ideally, allow exposure to air to simplify installation.
6. Provide a low thermal emittance.

The initial choice of a cathode for this gun is the multi-alkali photocathode. As described above, there is a provision for inserting an independently cooled, electrically isolated photocathode into the photoinjector. The cathode insertion device is a complicated arrangement that must satisfy a number of different criteria. It must be electrically and thermally isolated from the cavity in order to avoid additional heat loads to the cryogenic system due to the fact that the cathode is maintained at an elevated temperature relative to the cavity and because of the high average current being extracted from the photocathode. It must also be designed such that when inserted there is a means of avoiding multipacting or other RF losses through the insertion mechanism. This is being addressed using the quarter wave choke joint mentioned above.

The photocathode we have pursued is CsK_2Sb [18], and was selected based on its high quantum efficiency and convenient operational wavelengths. (QE of 2-14% at 532 nm and 10-30% at 355 nm) The fabrication of the photocathode is a process that is highly dependent on the exact deposition system configuration, thus making it difficult to directly import a recipe from another source. The general technique, obtained through our collaboration with David Dowell at SLAC, formerly at Boeing, is to deposit ~200 Å of antimony followed by the deposition of ~150 Å of potassium and then deposition of cesium while monitoring the QE. The cesium deposition is terminated when the QE reaches a maximum.

The technological challenges presented by using a CsK_2Sb photocathode in a SRF photoinjector revolve around the vacuum conditions to which the photocathode is exposed. All the multi-alkali photocathodes require extremely good vacuum conditions, 10^{-10} Torr or better, in order to maintain their designed QE for a reasonable length of time. At BNL we demonstrated over 2 months storage of CsK_2Sb photocathodes in $2x10^{-10}$ Torr vacuum. Vacuum degradation during operation in the gun should not be a problem in an SRF photoinjector as it is maintained at 2K.

The temperature of the photocathode in the gun is reduced to bellow room temperature. The operation of the CsK_2Sb photocathode has been tested down to 170 K and has seen only a 10% decrease in QE.

Another possible approach to photocathodes has been proposed and is under investigation [19. The idea is to “amplify” the emission from a photocathode. A thin (of the order of 30 micrometers) diamond window is positioned between the photocathode and the gun. The diamond has a thin metal coating facing the photocathode, and a monolayer hydrogen facing the gun. A DC voltage is applied between the metal layer on the diamond and the photocathode. The primary electrons are generated in the photocathode by a laser, accelerated in the gap between the photocathode and the diamond and strike the diamond with 5 to 10 KeV. The primary electrons produce a large shower of secondary electrons and holes (using about 13 eV of primary energy per electron-hole pair). The electrons and holes are separated quickly by the field in the diamond (produced by the RF gun). The holes are absorbed into the metal layer. The electrons drift through the diamond, thermalizing to a small fraction of an electron volt in the process, and exit the diamond to the gun. A critical element here is endowing the diamond side facing the gun with a negative electron affinity, by bonding hydrogen to the diamond’s dangling bonds.

The emission is prompt and has very low thermal energy. The diamond properties are such that the heat generated by the various processes (mainly the primary energy deposition, RF heating of the metal layer and the

heat generated by the transport of the electrons through the diamond) is conducted efficiently to the walls with an insignificant temperature gradient. In addition, the mechanical strength of the diamond promises that the capsule may hold atmospheric pressure for transporting the evacuated photocathode. The hydrogenated diamond surface is very robust, and can be carried through air for installation without losing its negative electron affinity.

The main difficulty with the diamond amplification process is trapping of electrons in the surface boundary layer, either a hydrogenised diamond facing an anode (emission measurement) or a metal coating on the diamond, serving as an anode (transmission measurement).

In the work done so far we demonstrated that the expected gain of about 77 secondary electrons per 1 keV of a single primary electron's energy can be achieved in transmission measurements by removing trapped electrons either by the transmission of holes (while the field in the diamond is reversed) or by a small amount of light (such as a laser pointer). This can be seen in Figure 2, where gain (defined as the ratio between the collected anode current and primary current) is shown as a function of the field in the diamond for various primary electron energies. The loss in the metal layer is measured to be 3.5 keV. At every primary energy we see the gain curve for "single pulse", which avoids the accumulation of trapped charge, and a curve for continuous operation using a few milliwatts of green laser for de-trapping.

Work is in progress on hydrogenised diamond, in which the trapping is deeper.

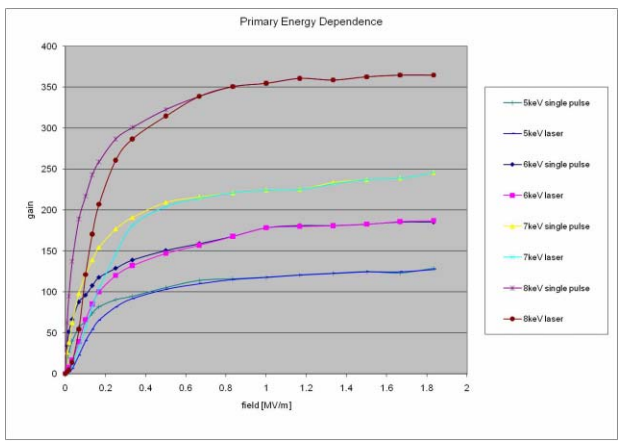

Fig. 2. Gain in transmission with trapping eliminated.

REFERENCES

[1] S. Benson, D. Douglas, P. Evtuschenko, K. Jordan, G. Neil, and T. Powers, "Operational Aspects of High Power Energy Recovery Linacs", Proceedings LINAC 2006, Knoxville, Tennessee, August 20-25, 2006.

[2] V. Litvinenko, I. Ben-Zvi "Potential Use of eRHIC's ERL for FELs and Light Sources", Proceedings, 2004 International FEL Conference, Trieste, Italy, August 29-September 3, 2004.

[3] C. Sinclair, "ERL Based Synchrotron Radiation Light Sources", Proceedings ERL'05 workshop, Newport News, VA, March 20-23, 2005.

[4] I. Ben-Zvi and S. Krinsky, "Future Light Sources Based upon Photo-injected Energy Recovery Linac", Synchrotron Radiation News 14, 20 (2001),

[5] I. Ben-Zvi, et. al., "ERLs in High Energy and Nuclear Physics", Proceedings ERL'05 workshop, Newport News, VA, March 20-23, 2005.

[6] Ilan Ben-Zvi, et. al., "R&D towards cooling of the RHIC Collider", 2003. Nuclear Instruments and Methods in Physics Research A532, 177, (2004)

[7] A. Michalke, "Feasibility of a photoemission source with superconducting RF cavity", AIP Conference Proceedings 279, 761, (1993).

[8] D.Janssen et al., "First operation of a superconducting RF-gun", NIM A, 507 (2003) pp 314-317.

[9] A. Arnold et al, "Development of a superconducting radio frequency photoelectron injector", NIM A **577** (2007) 440–454

[10] H. Bluem, M.D. Cole, A.M.M. Todd, I. Ben-Zvi, T. Srinivasan-Rao, J. Schill, "Photocathode Electron Source Development at Advanced Energy Systems", Proceedings EPAC 2000, June 2000.

[11] T. Rao, I. Ben-Zvi, A. Burrill, H. Hahn, D. Kayran, Y. Zhao, P. Kneisel, M. Cole, "Photoemission Studies on BNL/AES/JLab All Niobium, Superconducting RF Injector", Proceedings PAC 2005, Knoxville, Tennessee, May 16-20, 2005.

[12] C. E. Chen, R. L. Geng, J. H. Song, L. F. Wang, J. Yu, B. C. Zhang, K. Zhao, "A Hybrid Laser-driven E-beam Injector Using Photo-cathode Electron Gun and superconducting Cavity", Proceedings EPAC 1996, Sitges, Spain, June 10-14, 1996.

[13] Kui Zhao, Private communication, August 2007.

[14] S. Huang et al, "Beam Loading Tests on DC-SC Photoinjector at Peking University", Proceedings 2004 FEL Conference, Trieste, Italy, August 29 – September 3, 2004.

[15] J. Sekutowicz et al, Nb-Pb Superconducting RF-Gun, Proceedings EPAC'06, Edinburgh, Scotland, June 26-30, 2006.

[16] Jacek Sekutowicz, Private communication, August 2007

[17] R. Calaga, I. Ben-Zvi, M. Blaskiewicz, X. Chang, D. Kayran and V. Litvinenko, "High current superconducting gun at 703.75 MHz", Physica C: Superconductivity, **441**, 159, (2006)

[18] A. Burrill, I. Ben-Zvi, T. Rao, D. Pate, Z. Segalov, D. Dowell, "Multi-Alkali Photocathode Development at Brookhaven National Lab for Application in Superconducting Photoinjectors", Proceedings PAC 2005, Knoxville, Tennessee, May 16-20, 2005.

[19] T. Rao, I. Abdel, I. Ben-Zvi, X. Chang, J. Grimes, R. Grover, J. Smedley, R. Todd, J. Warren, Q. Wu, J. Bohon, D. Fischer, D. Dimitrov, "Status of Diamond Secondary Emission Enhanced Photocathode", Proceedings 2007 ERL Workshop, Daresbury, England, May 21-25, 2007.

A COMPACT ELECTRON SPECTROMETER FOR AN LWFA*

A.H. Lumpkin**, R. Crowell, Y. Li, and K. Nemeth
Argonne Accelerator Institute, Argonne National Laboratory, Argonne, IL 60439, U.S.A

Abstract

The use of a laser wakefield accelerator (LWFA) beam as a driver for a compact free-electron laser (FEL) has been proposed recently. A project is underway at Argonne National Laboratory (ANL) to operate an LWFA in the bubble regime and to use the quasi-monoenergetic electron beam as a driver for a 3-m-long undulator for generation of sub-ps UV radiation. The Terawatt Ultrafast High Field Facility (TUHFF) in the Chemistry Division provides the 20-TW peak power laser. A compact electron spectrometer whose initial fields of 0.45 T provide energy coverage of 30-200 MeV has been selected to characterize the electron beams. The system is based on the Ecole Polytechnique design used for their LWFA and incorporates the 5-cm-long permanent magnet dipole, the LANEX scintillator screen located at the dispersive plane, a Roper Scientific 16-bit MCP-intensified CCD camera, and a Bergoz ICT for complementary charge measurements. Test results on the magnets, the 16-bit camera, and the ICT will be described, and initial electron beam data will be presented as available. Other challenges will also be addressed.

INTRODUCTION

One of the challenges of the laser wakefield accelerator (LWFA) project is generation of robust, quasi-monoenergetic electron beams. At the AAC06 Workshop a number of laboratories reported observation of such beams ranging in energies from 10s of MeV to 1 GeV with charges ranging from 10 s to 100 s of pC [1]. The Chemistry Division is currently using and developing an LWFA within their Terawatt Ultrafast High Field Facility (TUHFF) [2]. Although pulsed radiolysis chemistry experiments are the primary objective, an initiative to demonstrate an LWFA operating in the bubble regime [3] with quasi-monoenergetic beams is being driven by Strategic LDRD funds. A long-range goal of this project is to use the beam to drive an undulator for generation of ultrafast spontaneous radiation. Other laboratories have targeted the possible driving of a free-electron laser (FEL) [4]. As part of the present ANL project, characterization of the electron beams generated is a critical aspect. Towards this end an electron beam spectrometer is needed to measure the electron beam spectrum to look for the energy peak and energy spread. This is in addition to a basic charge measurement and a beam divergence measurement. The compact spectrometer design is based on that reported by Glinec et al. [5].

*Work supported by the U.S. Department of Energy, Office of Science, Office of Basic Energy Sciences, under Contract No. DE-AC02-06CH11357.
**lumpkin@aps.anl.gov

EXPERIMENTAL BACKGROUND

The 20-TW laser at TUHFF consists of a three-stage chirped-pulse amplified Ti:Sapphire laser system running at 10 Hz. The 15-fs (FWHM) seed pulse train from the oscillator is stretched to 440 ps in a double-pass single grating stretcher, and then a Pockels cell pulse picker is used to lower the repetition rate to 10 Hz. The beam passes through a three-stage amplifier and then is directed into a two-grating pulse compressor resulting in a 600-mJ, 30-fs (FWHM) pulse of 20 TW. A schematic is shown in Fig. 1. A more detailed description of the laser system can be found elsewhere [6]. The compressed laser beam is then directed into the interaction chamber and focused to about 30 μm size onto the 1.2-mm-diameter supersonic He gas jet. Electron pulses of relativistic energies are generated and pass through a rotating Cu disk that blocks the laser beam, but transmits the electrons to a sample or the electron spectrometer or other diagnostics.

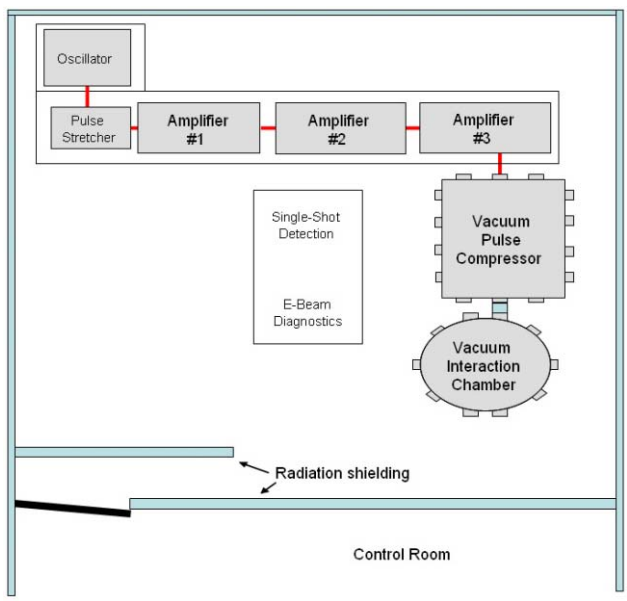

Figure 1: Schematic of the TUHFF with the Ti:Sapphire oscillator, pulse stretcher, three amplifiers, pulse compressor, and the interaction chamber.

Compact Electron Spectrometer

The major components of a compact electron spectrometer based on the Ecole Polytechnique University LOA design [3,5] are the permanent magnet dipole; the scintillator screen at the dispersive plane; the 16-bit CCD camera with optics, which views the screen; and an integrating current transformer (ICT) for complementary charge measurements.

Permanent Magnet Dipole: The two NdFeB magnets are 5 cm long by 2.5 cm wide by 1.2 cm thick. Magnet characterization was performed by the APS Magnetic

Devices Group in their ID magnet measurement facility. Both magnets were characterized and their reference files generated. This was requested in case there is subsequent radiation damage to the magnets from energetic electrons in the LWFA. A collimator may be appropriate before the magnets. The one magnet field strength vs. z plot was determined. A gap was selected to replicate the 0.45 T values of the LOA magnets [4]. That gap is 12 mm for two magnets, although there is an end effect that may reduce the effective dispersion. This provides coverage for 20-, 50-, 100-, and 200-MeV electrons with varying dispersion resulting in energy resolutions of 6, 14, 27, and 53%, respectively [5]. In addition, effective energy resolution can be limited by the natural divergence and beam size at the scintillator screen.

With the completion of the magnet holder assembly, the two magnets were positioned with a 12-mm gap, and the combined fields in this configuration were measured in the APS magnet measurement facility. The plot of field strength versus z is shown in Fig. 2. The total field is about 0.46 T as expected with some end effects again that will reduce the effective dispersion 5-10%.

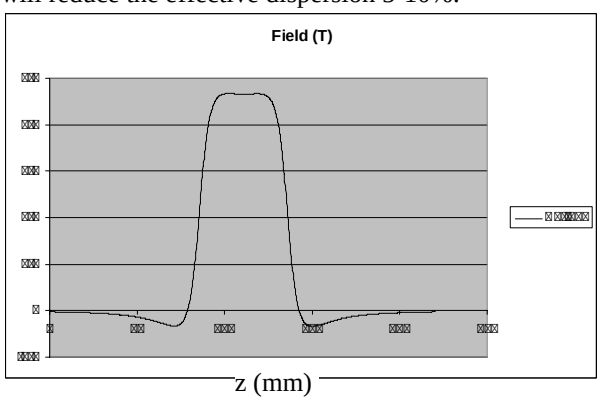

Figure 2: Map of the field strength along the z axis for two 5-cm long magnets with a 12-mm gap. The horizontal axis is in mm (courtesy of Isaac Vasserman, APS).

LANEX Scintillator: Extensive tests have been done previously with the Kodak x-ray screen called LANEX [4]. This is essentially a Gd_2O_2S:Tb inorganic scintillator with efficient conversion of both x-ray and electron incident energies. It has been reported to give similar energy absorption per electron for electron energies from 10 MeV to 500 MeV so it is a good candidate for the converter screen in the spectrometer [4]. These emit in the blue-green with a strong component at 548 nm, which is a good wavelength match to CCD quantum efficiency curves.

16-bit ICCD Camera: A Roper Scientific 16-bit camera was selected for use as the readout of the energy information displayed on the screen. The camera is Peltier-cooled and has a 1024 × 1024 array with 13-µm-square pixels. It has a PCI card that includes the digitizers to provide 16-bit deep images. The microchannel plate (MCP) intensifier tube is of a high quality with 6-µm-diameter channels for the 18-mm-diameter tube. There is a Roper software package loadable on the PC to display and minimally process images. Other programs are used for profile analysis.

The ICCD was taken to the APS S35 optics lab for calibration and resolution tests. We also simulated a working configuration of the PCs being 100 ft away in another lab from the camera control unit and camera head. This is basically how it would run in the LWFA lab.

The camera was mounted on a rail with carriers so the 105-mm F-mount Nikon zoom lens could be used at different working distances. The calibration lab has a platform holding a filter wheel that includes a back-illuminated 15-µm diameter pinhole as a resolution test object and a grid pattern for spatial calibrations. The platform can be moved in three dimensions for centering the source or scanning the field of view and for precise z-motion relative to the camera lens distance to optimize focus. A photograph of the setup is shown in Fig. 3.

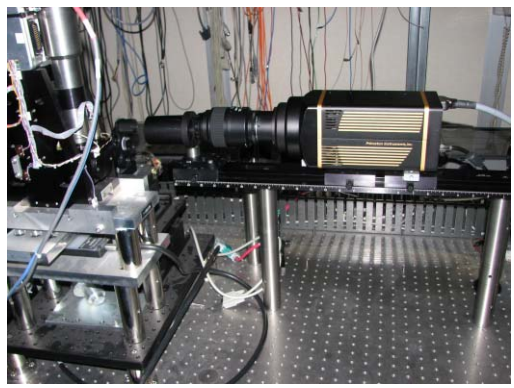

Figure 3: Photograph of the ICCD camera on the S35 optical calibration table. Calibration factors and resolution tests were done for various lens distances.

The tests were initially done at working distances of 14 cm, 17.3 cm, and 29 cm. The grid pattern was used to obtain the calibration factor in each case. A bright square, 10 mm on each side, was used as the main reference. Fine features in the pattern were used for initial focus adjustments. We then selected the pinhole source and scanned the z direction over several mm. An example of the preliminary depth-of-focus results for a working distance of 17.3 cm is shown in Fig. 4, where the FWHM resolution is 2.5 ch or 50 µm. These data show that for this lens setting, resolution can be degraded if the z position is off by 3 mm from the center of the focus curve. A separate Air Force line-pair pattern was used as well at this working distance.

Additional working distances were used at 40, 50, 60, and 70 cm, but the resolution test was not done because we had consistently obtained the 2.5-ch FWHM result, just with different calibration factors. The calibration factors and expected field-of view (FOV) are shown in Table 1. With our LWFA geometry we will view the scintillator back at the 40-70 cm working distance with the camera located outside the chamber looking through the port. A pumpout port was moved, and we installed a window in the port more directly downstream of the

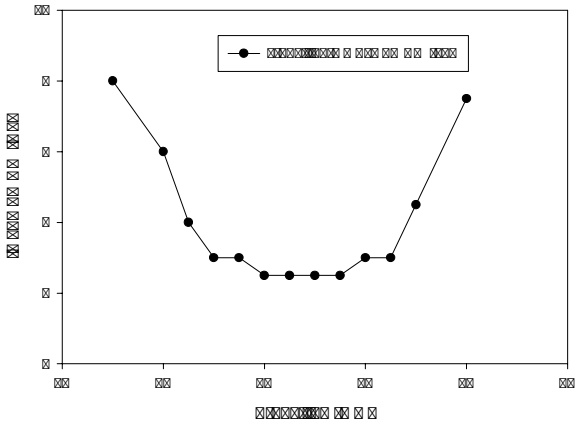

Figure 4: Depth-of-focus scan for a working distance of 17.3 cm for the 105-mm lens. The 2.5 ch (FWHM) resolution would be 50 μm for this calibration factor.

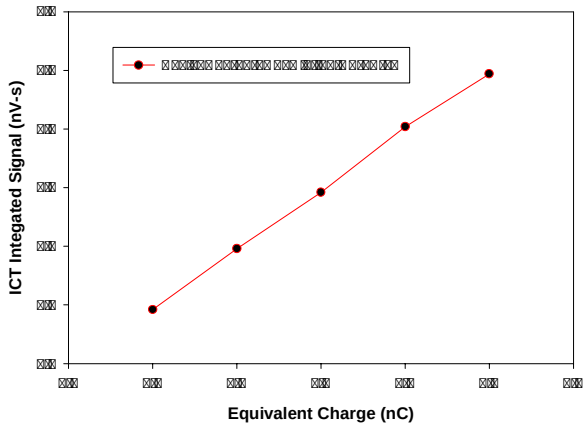

Figure 5: Test results for the Bergoz ICT showing the equivalent charge input and the signal response output (integrated) of the ICT in nV·s.

interaction zone for viewing images on the back of the scintillator.

Table 1: Summary of the Calibration Factors and FOVs for 105-mm Zoom Lens Working Distances

Working Distance (cm)	Calibration Factor (μm/pixel)	FOV (cm)
14.0	13.7	1.4
17.3	19.6	2.0
29.0	36.9	3.8
40.0	50.0	5.1
50.0	62.5	6.3
60.0	74.0	7.6
70.0	89.3	9.1

ICT: A Bergoz ICT is expected to be used in vacuum with a return loop added to provide complementary charge measurements (although the LOA experiments indicated background issues and gave a large error bar on absolute measurements [5]). Initially the existing Faraday cup will be used for experiments.

The ICT was tested using an HP 8114A pulse generator. With the pulse width set at 10 ns, one could set the level to 1 V to have 10 nV·s injected on a wire passing through the center of the ICT. This corresponded to 0.2 nC into a 50-ohm test load. The voltage level was adjusted to vary the injected charge, and the results are shown in Fig. 5. The integrated ICT signal output was determined using the Agilent Infinium 54854A oscilloscope operating in the "integrate mode." The scope trace had ~16 mV peak with 30 ns (FWHM) for the 0.2-nC input. This means that a low-noise environment is needed for seeing 10 s of pC pulses in the LWFA.

Proposed Layout

The LWFA main chamber is ~1.3 m in diameter; however the location of the gas jet nozzle is on one side of a 30-cm-diameter pumpout port centered in the chamber floor and is ~35 cm from the chamber wall. This latter distance is a constraint for installing hardware downstream of the nozzle. First the rotating copper disk is put in, which blocks the intense laser beam and transmits generated electrons. A 6.2-cm lead collimator with a 10-mm-diameter hole at beam centerline may be needed. The magnets are 5 cm long with a 12-mm gap, and the LANEX screen is positioned 17 cm downstream from the entrance edge of the magnets. The LANEX is fronted by a thin Aluminum foil to block laser light leakage if there is any. The screen is about 10 cm wide by 2.5 cm high. The ICCD camera with lens has been positioned at the port to view the back of the LANEX at a working distance TBD, but on the order of 40-70 cm to give the FOV in energy. Two mirrors in the optical path outside the chamber redirect the scintillator light to the lead-shielded camera location. The camera is mounted on a Newport rail supported by a small optical breadboard. The small Faraday cup will initially be positioned for charge measurements. Installation is nearly completed except for final alignment and electrical signal connections.

An initial experiment will be done with no magnets to look for low divergence beams at the LANEX with the FC and camera behind the LANEX. If there is a low-divergence electron beam, there should be quasi-monoenergetic beam as well based on our interpretation of the literature [3]. Also, we can check for the calculated beam size asymmetry with the larger size in the direction of the incident laser polarization as reported by Nemeth et al. [7]. Since the polarization is horizontal in the ANL LWFA, we may need to rotate the spectrometer plane. With enough charge and signal, the complementary OTR experiments from the disk downstream side and a thin foil could be pursued. If there is any microbunching of the beam at blue-shifted wavelengths of the fundamental laser wavelength, the signature should be confirmable with a visible light spectrometer.

EXPERIMENTAL AND ANALYTICAL RESULTS

As mentioned in the previous section, the ANL results are only in an early phase although prompt electrons were generated and used for photolysis experiments in the past

[2]. Simulations were done at ANL using the code VORPAL to evaluate the expected performance of the present LWFA [7,8]. Beam energies of the order of 100 MeV are expected with a plasma density of ~5 × 10^{18} e/cm^3 and the properly focused laser spot (10^{18} W/cm^2) at the gas jet. As shown in Fig. 6, the e-beam should actually exhibit some longitudinal structure which is analogous to SASE-induced microbunching in an FEL. In this case it is the structure impressed by the co-propagating laser fields as the trapped electrons are accelerated though the plasma. Coherent OTR would be generated when such beams transit a dielectric boundary. Such an effect has been reported in the last year by Glinec et al. [9]. In another development, the use of colliding laser beams to produce a more controlled injection of electrons into the LWFA process has resulted in tunable beam energies and more reproducible performance as reported by J. Faure et al. [10]. The longer range goal to use an LWFA beam to drive undulator radiation is schematically shown in Fig. 7. As techniques improve one can expect continued progress in beam quality in regards to energy, energy spread, charge, and emittance. It is difficult to predict the evolution time at this point, but generation of 10-GeV beam by the time of ACC08 is the community target [1] with 1 GeV already demonstrated [11].

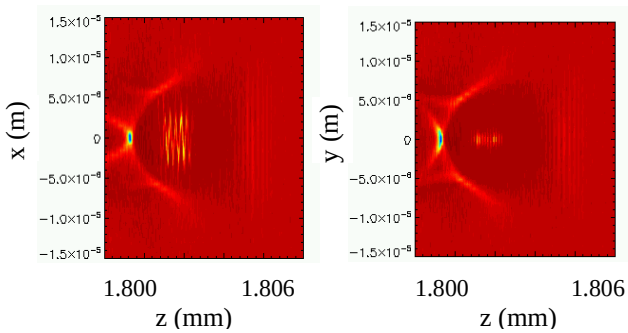

Figure 6: Simulation of the LWFA bubble regime for x-z polarization plane (left) and y-z plane (right) displays of microbunching.

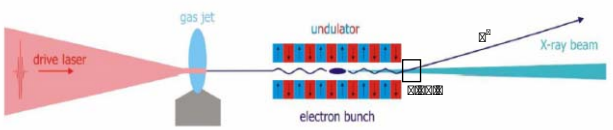

Figure 7: A schematic of the LWFA beam generating spontaneous emission radiation in an undulator.

SUMMARY

In summary, the ANL LWFA project is on the verge of generating electrons again, and a compact electron spectrometer has been installed to look for quasi-monoenergetic beam behavior. The challenge of generating enough charge (100s of pC) with low emittance and energy spread will have to be met before serious work with an undulator would be feasible. The initial ultrafast pulse lengths of the laser can be transferred to the trapped electrons in the bubble regime so generation of short-pulse radiation from an undulator is feasible.

ACKNOWLEDGMENTS

The authors acknowledge the support of R.Gerig and K.-J Kim of the Argonne Accelerator Institute and the assistance of I. Vasserman, B. Yang, J. Power, A. Brill, and T. Pietryla on component testing and of S. Chemerisov for LWFA interaction chamber setup.

REFERENCES

[1] Proceedings of the AAC06, M. Conde and C. Eyberger (Eds.), July 15-22, 2006, Lake Geneva, WI, AIP Conf. Proc. 877 (2006) and references therein.
[2] D.A. Oulianov et al., "Ultrafast Pulse Radiolysis Using a Terawatt Laser Wakefield Accelerator," submitted to J. Appl. Phys. (2006).
[3] V. Malka et al., "Monoenergetic Electron Beam Optimization in the Bubble Regime," Phys. of Plasmas **12**, 056702 (2005).
[4] C.B. Schroeder et al., "Design of an XUV FEL Driven by the Laser Plasma Accelerator at the LBNL LOASIS Facility," Proc. of FEL06, Berlin, Germany, pp. 455-458 (2006); http://www.jacow.org.
[5] Y. Glinec et al., "Broadrange Single Shot Electron Spectrometer," Ecole Polytechnique report dated July 6, 2006.
[6] R.A. Crowell et al., Radiat. Phys. Chem. **70**, 501 (2004).
[7] Karoly Nemeth et al., "Laser driven coherent betatron oscillation in a laser-wakefield cavity," submitted to PRL 2007.
[8] Yuelin Li, private communication, February 14, 2007.
[9] Y. Glinec et al., "Observation of Fine Structures in Laser-Driven Electron Beams Using Coherent Transition Radiation," Phys. Rev. Lett. **98**(19), 194801 (May 2007).
[10] J. Faure et al., Nature **444**, 737 (2006).
[11] W. Leemans et al., "GeV electron beams from a centimeter-scale accelerator," Nature Physics **2**, 696-699 (01 October 2006); Anthony Gonsalves et al., "Experimental Demonstration of 1 GeV Energy Gain in a Laser Wakefield Accelerator," Proc. of PAC07, Albuquerque, NM, June 25-29, pp. 1911-1915 (2007).

ADAPTIVE 3-D UV-LASER PULSE SHAPING SYSTEM TO MINIMIZE EMITTANCE FOR PHOTOCATHODE RF GUN AND NEW LASER INCIDENCE SYSTEM

H. Tomizawa, H. Dewa, T. Taniuchi, A. Mizuno, T. Asaka, K. Yanagida, S. Suzuki, T. Kobayashi, H. Hanaki, Accelerator Division, Japan Synchrotron Radiation Research Institute (JASRI/SPring-8), Kouto, Sayo-cho, Sayo-gun, Hyogo 679-5198, Japan
F. Matsui, Creative & Advanced Research Department, Industrial Technology Center of Fukui Prefecture, 61 Kawaiwashitsuka-cho, Fukui City 910-0102, Japan.

Abstract

We developed an adaptive 3-D shaping (both temporal (1D) and spatial (2D)) short pulse (80 fs~40 ps) UV-laser system as an ideal light source for yearlong stable generation of a low-emittance electron beam with a high charge (1~2 nC/pulse). In its current form, the laser's pulse-energy stability has been improved to 0.2~0.3% (rms; 10 pps, 0.4 TW in femtosecond operation) at the fundamental wavelength and 0.7~1.4% at the third-harmonic generation. Such improvement reflects an ability to stabilize the laser system in a humidity-controlled clean room. The pulse-energy stability of a mode-locked femtosecond oscillator has been continuously held to 0.3% (p-p) for 4.5 months (1% for 10 months), 24 hours a day. In addition, the ideal spatial and temporal profiles of a shot-by-shot single UV-laser pulse are essential to suppress emittance growth in an RF gun. We apply a deformable mirror that automatically shapes the spatial UV-laser profile with a feedback routine, based on a genetic algorithm, and a pulse stacker for temporal shaping at the same time. The 3D shape of the laser pulse is spatially top-hat (flattop) and temporally a square stacked chirped pulse. Using a 3D-shaped laser pulse with a diameter of 0.8 mm on the cathode and pulse duration of 10 ps (FWHM), we obtain a minimum normalized emittance of 1.4 π mm mrad with a beam energy of 26 MeV. We found that the last mirror in the vacuum to make normal incidence is an obstacle for the electron beam. Therefore, we developed the optical elements for a new hollow laser incidence with an axicon final focusing. We fixed temporal parameters with the present mechanical pulse stacker and prepared a new UV-pulse stacking system (fixed parameters) consisting of three birefringence α-BBO crystal rods.

INTRODUCTION

We have been developing a stable and highly effective UV-laser pulse as the light source of a photo-cathode RF gun [1] that in turn provides a high-brightness electron beam source to achieve future X-ray light sources (FEL (free electron laser), Compton back scattering, etc.) since 1996 at SPring-8 (Synchrotron Radiation Research Group). The electron source for several X-ray FEL projects [2-4] requires a very-low-emittance (high-brightness) electron beam as low as 1 π mm mrad. One of the most reliable candidates for this high-brightness electron source is a photocathode RF gun. This type of gun generates an electron beam pulse from a photocathode illuminated by a laser pulse. Our development of this gun is oriented toward a yearlong stable system for user experiments. It is necessary for the copper cathode of this RF gun to have a UV-laser pulse with a pulse width of ~10 ps and a photon energy of ~4 eV. Since we started to develop the laser test facility, two issues related to the laser light source have arisen. One is the energy stability of the UV-laser light source. Therefore, we have stabilized the third-harmonic generation (THG) of a CPA (chirped pulse amplification) Ti:Sapphire terawatt laser system (Figure 1) as the laser light source for the SPring-8 RF gun.

The other problem concerns the spatial and temporal laser profiles. To minimize the beam emittance of a photocathode RF gun, the laser pulse shape should be optimized three-dimensionally. Over the past six years at SPring-8's test facility for the photocathode laser light source, several 3-D shaping systems have been developed from combinations of spatial (transverse: x-, y-axes) and temporal (longitudinal: z-axis) pulse shaping methods (Figure 1). The spatial profile has to be modified with a microlens array [5] or a deformable mirror (DM) [6]. In addition, the temporal profile has to be modified with a spatial light modulator (SLM) [6-7] or the pulse stacker described in this paper. One of the candidates for a reliable 3-D laser pulse shape has been the cylindrical shape (spatially top-hat and temporally square pulse). With a square-shaped 9-ps laser pulse, the lowest beam emittance of 1.2 π mm mrad at 1.0 nC/pulse has already been achieved by J. Yang et al [7]. Previously, we have demonstrated a UV-laser spatial profile shaped as a quasi top-hat (flattop) with a deformable mirror used to automatically optimize it with a feedback routine based on a genetic algorithm. Using this top-hat laser pulse (diameter of 1.0 mm on the cathode) with a pulse duration of 5 ps (note: temporally, not square), we could obtain low-emittance beam generation of 1.7 π mm mrad [6] at a net electron charge of 0.1 nC/pulse. However, the beam emittance at high charge was much larger. This indicates that a 5-ps laser pulse is too short for the laser spot diameter of 1 mm. (The charge density is too high.)

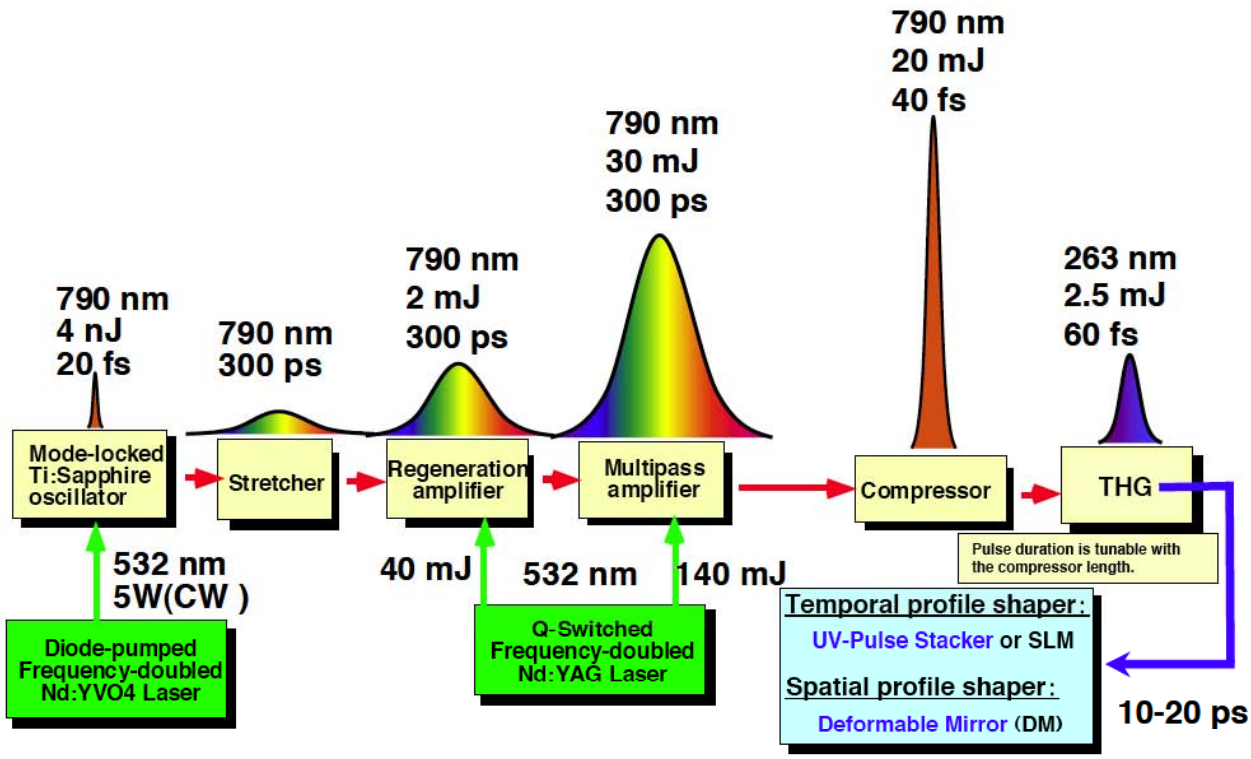

Figure 1: Laser pulse growth and three-dimensional (spatially (2D) and temporally (1D)) shaping process: the pulse duration of THG (263 nm) depends on the group delay dispersion (GDD) introduced by AO-modulator (DAZZLER: FASTLITE) after the stretcher (790 nm). To obtain a 20-ps pulse by stacking eight micro chirped pulses (three stages of pulse stackers), micro chirped pulse duration should be optimized to 2.5 ps at the cathode by changing GDD with DAZZLER (also possible with shifting compressor length).

Therefore, we prepared longer square laser pulses of 10 and 20 ps generated by stacking equivalently split 2.5-ps Gaussian chirped pulses to obtain lower emittance in a higher-charge region. Three stages of pulse stacking can generate a 20-ps pulse from eight 2.5-ps micro chirped pulses. The purpose of introducing longer laser pulses is to make the laser spot size on the cathode smaller while still decreasing the charge density. The small beam size helps to decrease the initial (thermal) emittance, and the small charge density suppresses the space charge effect. A 3-D particle tracking simulation predicted that smaller beam emittance could be obtained with a laser pulse length of about 20 ps at 1.0 nC/pulse [8]. This simulation result implies an important prediction, i.e. that electron pulse length can be maintained around 10 ps with both 10- and even 20-ps laser pulse lengths, due to electron bunch compression during its acceleration in the RF cavity.

DEVELOPMENT OF YEARLONG STABLE LASER LIGHT SOURCE

We chose the THG of a CPA Ti:Sapphire terawatt laser system (repetition rate of 10 Hz) as the laser light source for the SPring-8 RF gun. At THG (central wavelength: 263 nm), the femtosecond UV-laser pulse energy is up to 2.5 mJ/pulse. In its current form, the laser's pulse energy stability has been improved to 0.2~0.3% (rms; 10 pps, 0.4 TW in femtosecond operation) at the fundamental and 0.7~1.4% at the THG. At the first stage of development, this stability had been held for 1.5 months continuously, 24 hours a day. The improvements we had passively implemented were to stabilize the laser system as well as the environmental conditions. We introduced a humidity-control system that maintained humidity at 55% (fluctuating by less than 2% (p-p)) in a clean room to reduce electrostatic charge on the optics. This system keeps dust particles away from the optics and thus avoids burn-out damage. The temperature was kept constant at 21±0.3˚C (p-p), monitored on the laser table. The improvement in THG stability results from the ability to stabilize the laser pumping sources (Q-switched YAG) of the amplifiers with a temperature-controlled base plate in this humidity-controlled clean room. This base plate for YAG stabilization maintained temperature at 25˚C (fluctuating by less than 0.1˚C % (p-p)). In addition, we are testing a feedback system to control the long-term drift of the YAG laser due to the lifetime of the flash lamp, which is now limited to continuous operation of around five months (in our record, 119,380,846 shots at max.) while maintaining the high stability of the laser's pulse energy as mentioned above.

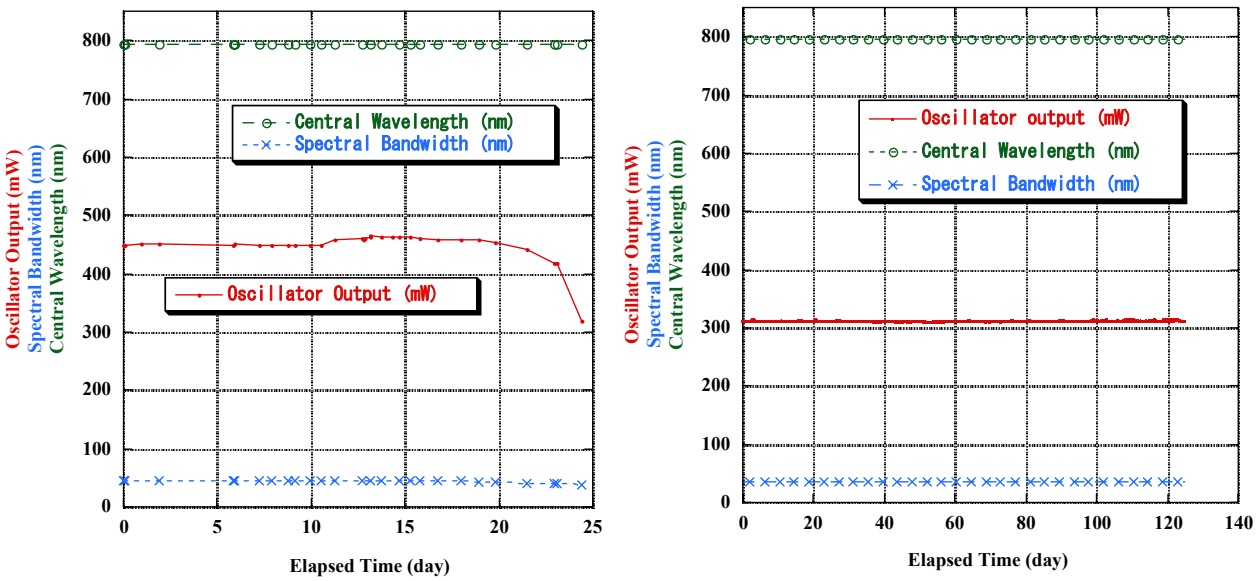

Figure 2: Improvement in laser oscillator's long-term stability (left: just passive, right: full-active, Femto-align & Femto-lock): With full-active feed-backing, the mode-locking and spectral distribution has been kept constant.

Aside from long-term drift of the pumping source YAG, the long-term stability of the total laser system (in THG) depends only on the stability of mode-locking at the oscillator laser. A new oscillator laser (Femtosource Synergy; Femtolasers Produktions GmbH) was installed in our system in April 2005. This oscillator was passively stabilized with a temperature-controlled base plate (21±0.1˚C (p-p)). In the first long-term continuous operation test run, its mode-locking was kept stable without any active stabilization for one month (left figure of Figure 2). However, laser parameters did not remain constant. This indicates that pointing of the pumping laser or laser self-focusing in the crystal (due to change in cavity length) causes drift in the long term (1~2 weeks). When the geometrical configuration of the laser cavity changes with these drifts, its mode-locking becomes unstable. Therefore, for the second test run, we introduced two active feedback systems (Femto-align and Femto-lock; Femtolasers Produktions GmbH) to lock the geometrical configuration of the laser cavity.

Femto-align is designed to compensate for long-term instabilities caused by environmental sources of interference such as thermal deformations or pump-pointing drift. It avoids mode-locking failures and reduces unexpected fluctuations. It monitors the output power and optimizes operations whenever deviations occur. The active controlling mirror can compensate for long-term instabilities of the total laser system. On the other hand, Femto-lock is a sub-ps-jitter synchronization for the oscillators. It allows locking the round-trip frequency of the oscillator pulses to a given reference RF-source (ROHDE & SCHWARZ GmbH & Co. KG: SMHU). The system comprises a fast piezo translator (PZT) in combination with a wide-range translation stage. This arrangement allows the unit to compensate for fast fluctuations (~kHz) as well as for slow long-term drifts (e.g. mechanical deformations due to temperature drifts). This combination of feedback guarantees drift-free yearlong operation.

In the second long-term continuous operation test run, the oscillator was actively stabilized by utilizing both Femto-align and Femto-lock, and it was operated at the locked repetition rate of 89.25 MHz. This long-term stability test had to be stopped for maintenance of the infrastructure. The pulse energy stability of the mode-locked femtosecond oscillator with a temperature-controlled base plate (21±0.1˚C (p-p)) was held at 0.3% (p-p) for 4.5 months continuously, 24 hours a day (right figure of Figure 2). Except for momentary line drop due to natural disasters (thunderbolts, etc.) or infrastructure maintenance, this oscillator has continuous yearlong operation while maintaining constant laser parameters (pulse energy, pulse duration, spectral distribution, etc.) The laser parameters have been kept constant without any sign of instability. This indicates that the drifting deformations of the laser's geometrical configuration could have been locked within the stable region of mode-locking.

3D SHAPING EXPERIMENT WITH UV-LASER PULSE

The 3D UV-laser pulse shaping system combined with a deformable mirror (transverse: 2D) and a chirped pulse stacker (longitudinal: 1D) is shown in Figure 3. Utilizing the long-term stable UV-laser source described above, this system can generate a 3D cylindrical laser pulse. Note that the original micro chirped pulse is optimized in its shape and pulse duration with DAZZLER (AO-modulator) at the fundamental. We explain both shaping techniques in the following.

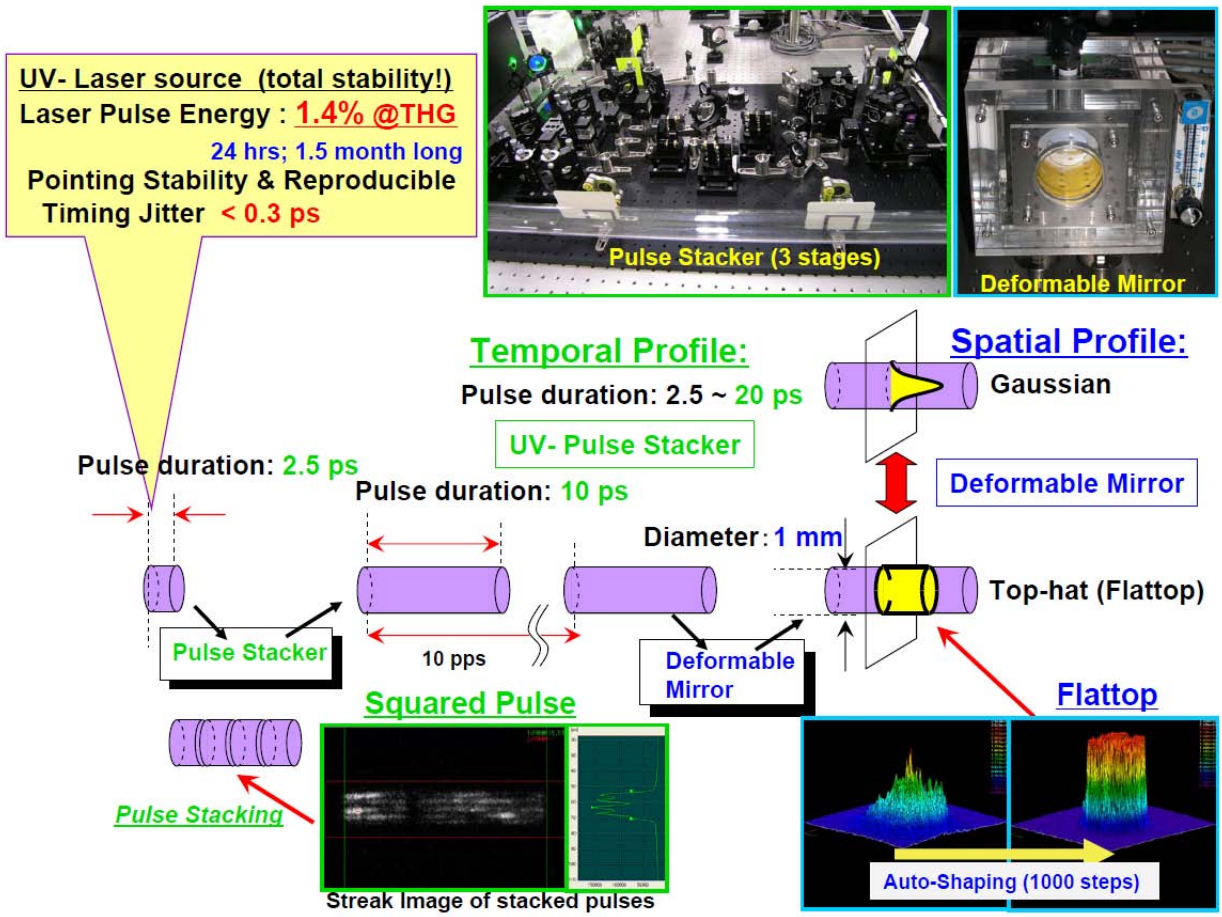

Figure 3: Three-dimensional (spatially (2D) and temporally (1D)) UV-laser pulse shaping system: the 3D shaping system consists of a deformable mirror (DM) and a chirped pulse stacker. These two shaping techniques can be optimized independently because there is no interference between them. The schematic drawing of pulse stacking shows 10-ps pulse generation by stacking four 2.5-ps micro chirped pulses (two stages of pulse stackers).

Top-hat spatial profile optimization with computer-aided deformable mirror

We used a computer-aided deformable mirror (top-right photo in Figure 3) as a spatial shaper. This deformable mirror consists of an aluminium-coated, multilayer silicon nitride membrane and 59 small mirror actuators behind the reflective membrane with a center-to-center distance of 1.75 mm between the actuators. The outermost layer of the reflective membrane is protected with an MgF_2 coating to maintain reflectivity at about ~80% in the ultraviolet region. Adjusting voltages between the control electrodes on the boundary actuators results in fine adjustment of each mirror actuator; the adjustable region of the control voltages is between 0 and 255 V in steps of 1 V, making it possible to shape arbitrary spatial profiles in a total of $256^{59}(\sim 10^{141})$ forming possibilities. However, such high adjustability makes manual as well as simple algorithm adjustment impossible.

Closed loop system for spatial shaping

A closed loop system is essential for a deformable mirror to optimize the laser's spatial profile automatically. We use a PC to control the electrode voltage of the deformable mirror and to measure the spatial profile with a laser profile monitor (Spiricon, Inc.: LBA300-PC). Laser light is reflected with deformation by the deformable mirror and monitored with the profile monitor, whose analyzing program can provide many parameters to evaluate the characteristics of beam profiles. The program is remotely controlled by Active-X [9] control (Object Linking and Embedding), so we could control the deformable mirror while monitoring the laser beam parameters.

Algorithm for automatic control

This spatial shaping method with adaptive optics requires a sophisticated algorithm. We developed software based on a genetic algorithm (GA) to automatically optimize the deformation of the deformable mirror (DM). The set of voltages of whole DM-electrodes are treated as chromosomes in their application. At first, we prepared 50 chromosomes as the initial population and used the MGG (Minimal Generation Gap) method to select the surviving chromosomes. The 59 DM-electrode voltages are applied independently in the range of 0 to 255 V, and these were coded to 59 elements in a chromosome.

In this type of deformable mirror (electrostatic actuator), the displacement in the central region of the membrane is proportional to the square of the electrode voltage. In the initial population, applied electrode voltages (chromosome element values) were randomly selected from the set of discreet voltages (0, 42, 70, 93, 113, 131, 147, 162, 176, 189, 201, 213, 225, 236, 250 V) to linearly change the displacement. In this procedure, chromosomes are treated as follows.

(1) Make a Family consisting of four chromosomes: Two chromosomes are selected randomly from the initial population to make the family, and these chromosomes are placed as "Parents." Then, the other two chromosomes as "Children" are generated through the crossover of the chromosomes of the "Parents." In our program, we prepared three different methods of crossover: random crossover (in our case "58-point crossover"), one-point crossover, and two-point crossover. Thus, four chromosomes are prepared and treated as "Family," which is called "Generation" in GA. The mutation rate was set 1% of the total number of generations.

(2) Drive the deformable mirror and obtain results of the laser parameters from measurements of the laser's spatial profile. In the MGG method, the four chosen chromosomes in the family are compared, and the two best chromosomes survive as superior. Drive the deformable mirror by setting the chromosomes of four members of the "Family" (in the order "Father," "Mother," two "Children") and obtain each result of beam parameters calculated from the analysis program of the laser profile monitor. The beam parameters of the laser's spatial profile are obtained for evaluation in the following step.

(3) Evaluate the resulting parameters using a fitness function. These results are scored by a fitness function defined by top-hat beam shaping. The fitness function is a linear combination of the nine parameters shown in Table 1 with each coefficient as weight. If a chromosome is more highly scored in the evaluation of the fitness function for top-hat, it will be promoted to a higher position in the ranking of "Family." Thus, in this ranking, the chromosomes are ordered by comparing values of the fitness function.

(4) The two best chromosomes are selected as superior and then returned to the population. This procedure makes one generation step forward, and the population is renewed to initiate the next generation.

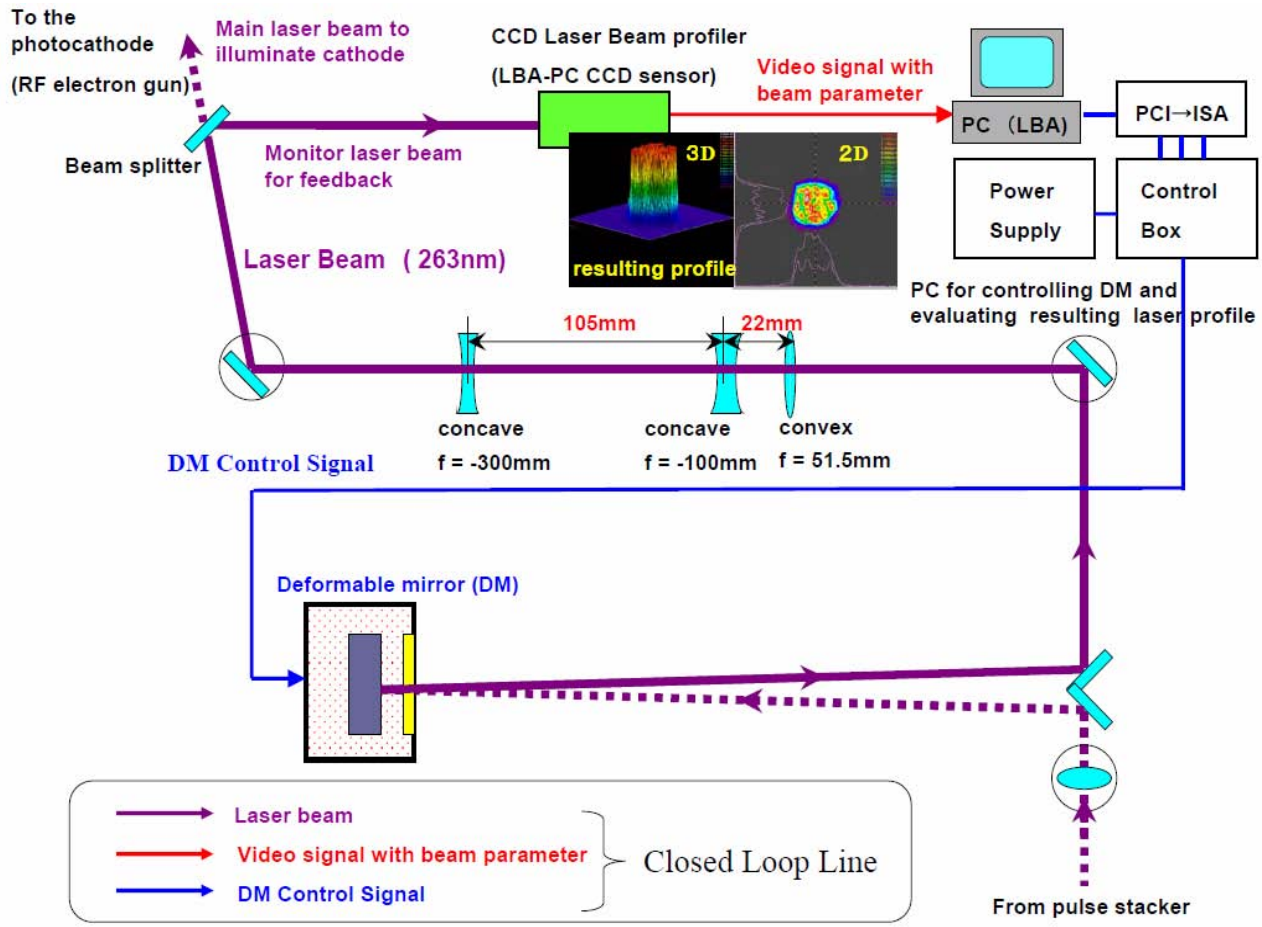

Figure 4: Closed control system for experiment: With evaluation of top-hat (flattop) profiles on laser profiler (LBA300-PC), the deformable mirror (DM) is automatically controlled to optimize the spatial profile toward the top-hat as a target profile.

Fitness function for genetic algorithm to optimize spatial profile through evaluation of beam parameters

We chose nine useful parameters [6] to evaluate the top-hat profiles. These parameters for top-hat shaping and their functions are shown in Table 1. A fitness function is made of the linear combination of these parameters. The fitness function is used as an index for the sophisticated program-based genetic algorithm. The more the laser profile is closed to the target profile (top-hat), the higher the value of the fitness function is. This is calculated for the spatial profile corresponding to each chromosome to evaluate the spatial profile, spot-size diameter, and centre position of the profile. Maximizing the value of the fitness function with the GA-program, the computer-aided deformable mirror optimizes the profile toward a target spatial profile such as the top-hat. The most representative parameter is the Top Hat Factor (THF) [10], where THF is defined as an integral function of the energy fraction as shown in Figure 5. After 2500 generation steps, an inhomogeneous spatial profile was improved to the quasi-top-hat profile shown in Figure 6.

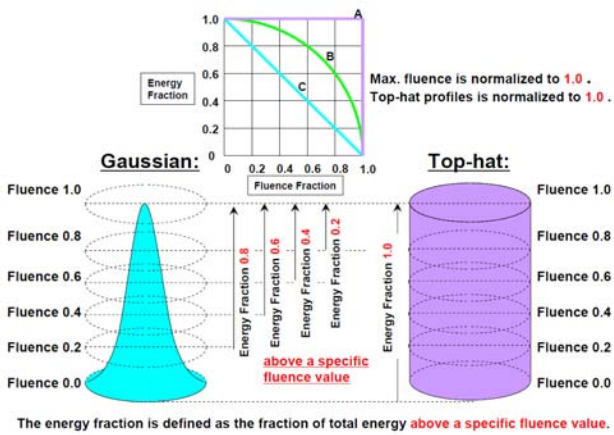

Figure 5: Top Hat Factor (THF) [10] for evaluation of Top-hat profiles: In the top figure, curve A is a Top-hat beam with THF of 1.0, curve C a Gaussian (conoidal) beam, and curve B is beam profile between Top-hat and Gaussian.

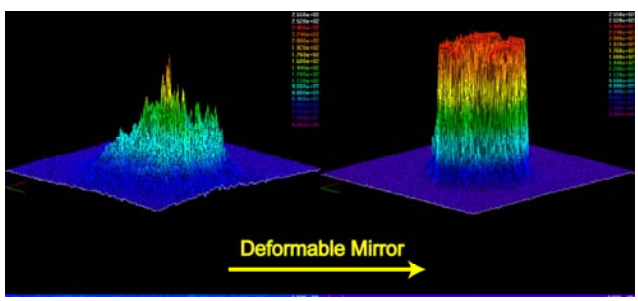

Figure 6: Result of spatial profile optimized to Top-hat with a deformable mirror (Laser profile monitor: LBA300-PC). The figures are normalised with the peak intensity to avoid saturation of laser profiler pixels.

Table 1: Parameters and their uses in fitness function to evaluate spatial profile optimization

Parameters of fitness function for top-hat (flattop) shaping with deformable mirror	
Beam Centre	Minimise the difference from the initial centre position (x, y)
THF	Maximise the Top Hat Factor (0~ 1) (Top-hat: THF=1.0; Gaussian: THF =0.5)
Effective Area	Maximise the integrated energy within the set circle area
Effective Diameter	Minimise the difference from the diameter of set circle
Flatness	Minimise the standard deviation divided by the average in a top-hat area
Peak-to-peak	Minimise the difference between the max. and min. in a top-hat area
Beam Diameter	Minimise the difference from the set diameter
Hot Spot	Minimise the max. in a top-hat area
Dark Spot	Maximise the min. in a top-hat area

SQUARE TEMPORAL PROFILE GENERATION (UV-PULSE STACKER)

Principle and configuration of chirped pulse stacker that is not affected by interference

A pulse stacker is composed of sets of half-wave plates and polarizing beam splitter cubes. One stage of the pulse stacker consists of a pair of a splitter and a half-wave plate. The full s-polarization is rotated to a 45-degree polarization with a half-wave plate. It is then divided into an s-polarized pulse and a p-polarized one with the first polarizing beam splitter at each stage. The p-polarized pulse is delayed with an optical delay line and then combined with the s-polarized pulse after using the next polarized beam splitter at each stage. Finally, as shown in Figure 7, the chirped laser pulse of 2.5 ps is stacked with optical delay at each stage to generate a longer square pulse. By stacking eight micro chirped pulses in three stages, we can obtain a 20-ps square combined pulse. The polarizing beam splitter cubes are the optical contact type (Showa Optronics Co., Ltd.), considering the high power density of the UV-laser pulse. The diagram of the optical system and timing chart of the pulse stacker with a three-stage configuration are shown in Figure 8. At every stage of this pulse stacker, the s-polarization pulse at the first splitter is always the origin of the optical timing delay (see timing chart of Figure 8). This makes it possible to keep the same origin of any

timing delay, even if a 5-, 10- or 20-ps squarely combined pulse is generated by masking a p-polarization pulse at each corresponding stage.

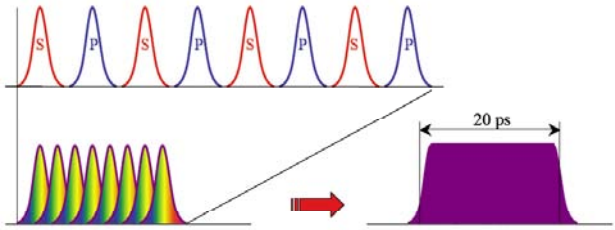

Figure 7: Principle of chirped-pulse stacking (8 pulses: three stages): Avoiding interference, the s- and p-polarized micro chirped pulses are alternatively stacked with the optical delay as long as the micro pulse duration.

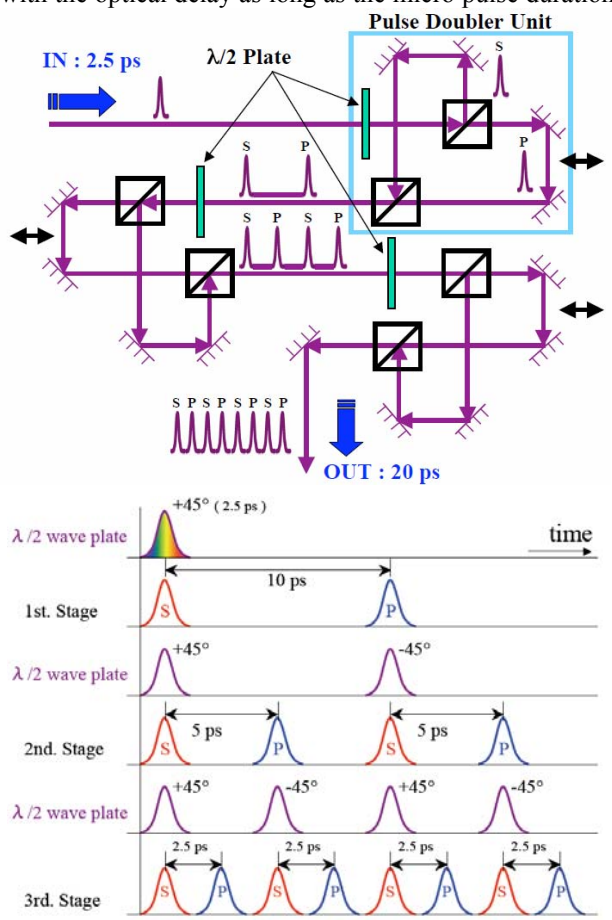

Figure 8: Optical system (upper) and timing chart (lower) of UV-laser pulse stacker: The drawings are shown in the case of three stages (pairs of polarizing UV-laser beam splitter cubes) of pulse stacker. The initial UV-laser pulse duration is set to 2.5 ps for generating a ~20-ps combined macro pulse. The pulse stacker kit is commercially available (http://www.luminex.co.jp/) under license from SPring8 /JASRI.

Finding the origins of optical delay lines

To generate a long pulse without any timing gap or overlap, the origins of the optical delay lines must be determined with a precision of less than 0.5 ps. The origin is defined here as the micrometer-level position in the delay line such that the s- and p-polarized pulses reach the cathode at the same time. The procedure determines the origin by utilizing the electron beam pulse generated at the photocathode as follows [8]. The energy of the electron pulse is measured for two laser pulses divided by each stage of the pulse stacker. The energy of the electron beam is measured as beam positions on a florescence profile monitor after a bending magnet downstream of the RF-gun cavity. To eliminate the positioning jitter and short time drift, the beam positions are measured 5000 times. The micrometer position of the p-polarized pulse is tuned as these two electron beam pulses come to the same position on the profile monitor after several iterations. The timing precision of the origin was about 0.5 ps, estimated from the position jitter distribution. After this procedure, with DAZZLER, micro chirped pulse duration is optimized to make the beam profile at the dispersion section homogeneous.

NEW FIXED 3D-SHAPING SYSTEM WITH HOLLOW LASER INCIDENCE

Through optimization with computer-aided DM and adjustable mechanical pulse stacker, we could improve the laser's 3D profiles and obtain their optimal parameters to minimize emittance. Using a 3D-shaped laser pulse with a diameter of 0.8 mm on the cathode and pulse duration of 10 ps (FWHM), we obtain a minimum horizontal normalized emittance of 1.4 π mm mrad with a beam energy of 26 MeV, holding its net charge to a 0.4 nC/pulse. At a higher net charge of 1.0 nC/pulse, the minimum beam emittance is 2.0 π mm mrad with equivalent diameter and a longer pulse duration of 20-ps (FWHM). However, vertical normalized emittance is around 1.5 times greater than horizontal. Considering the asymmetry of electrical field in the first coupler of the first accelerator tube, we rotated it 90 degrees to check the cause of the difference between x- and y- emittances. Consequently, the vertical emittance was greater than the other, as the emittance difference before the experiment with rotation of accelerator tube.

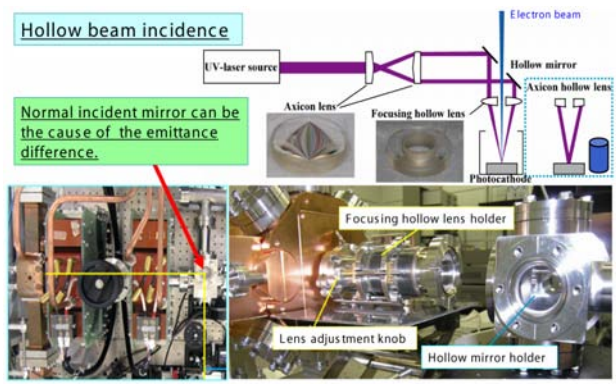

Figure 9: The present normal incident system (left) and new type of incidence with hollow optics (right): the final focusing axicon lens makes the spatial profile of the top-hat at its ray crossing (focus) point (top-right).

Then, we strongly doubt that the normal incident mirror can be the cause of the emittance difference. In particular, the higher charge the electron bunch is, the more significant the difference. Therefore, we developed a new hollow laser incidence system as shown in Figure 9. The hollow inside-out Gaussian laser beam is generated by an axicon lens pair, and then reflected at the hollow mirror for normal incidence through the hollow lens focusing to the photocathode.

In this new incidence system, the strategy for generating top-hat spatial shaping has to change. Up to now, we have obtained enough parameters to optimize the 3D laser pulse shape. There seems to be no difficulty in generating top-hat or homogeneous profiles with fixed (not-adaptive) optics. As shown in the upper right of Figure 9, using the axicon final focusing lens, there is a quasi-flattop region in the depth of a focus (ray crossing).

On the other hand, we fixed temporal parameters with the present mechanical pulse stacker and prepared a new UV-pulse stacking system (fixed parameters) consisting of three birefringence α-BBO crystal rods (Figure 10). When the incident ray injects with an angle to the optical axis, the extraordinary ray delays to an ordinary ray in a birefringence crystal. We utilize this delay in the same manner of the mentioned pulse stacker to generate a 20-ps square stacked chirped pulse. In this method, we rotate the crystal rods on the laser propagation axis independently to control polarisations and compensate angle of rotation, instead of using waveplates.

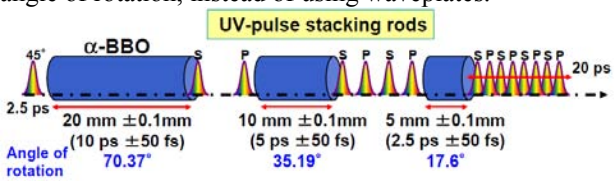

Figure 10: UV-laser pulse stacking rods: The angle of rotation of each rod is shown.

SUMMARY & FUTURE DEVELOPMENTS

For the shot-by-shot optimization of each laser-pulse profile, the laser system should be passively stabilized through environmental controls. At present, if the oscillator is stable without mode-locking failure, the overall laser system can remain stable for yearlong operation with the energy stability described in this paper. During this potentially continuous yearlong operation, every laser parameter was kept constant without any signs of instability.

We demonstrate a 3D shaping (both temporal (1D) and spatial (2D)) short pulse (5~20 ps) laser beam as an ideal light source for yearlong stable generation of a low-emittance electron beam with a high charge. At present, we apply a deformable mirror that automatically shapes the spatial UV-laser profile with a feedback routine, based on a genetic algorithm, and a pulse stacker for temporal shaping at the same time. The 3D shape of the laser pulse is spatially top-hat (flattop) and temporally a square stacked pulse. Using this 3D-shaped laser pulse (diameter: 0.8 mm; 10-ps pulse), we obtain a minimum horizontal normalized emittance of 1.4 π mm mrad.

This high-brightness electron source has maintained almost enough low emittance for X-ray FEL requirements during yearlong continuous operation. However, the vertical emittance is around 1.5 times greater than the other. To solve this, we developed a new incidence method with a hollow laser generator. We have already developed whole hollow optics. For this requirement of renewing 3D-laser pulse shaping, we have developed the hollow axicon final focus lens for spatial top-hat and UV-laser pulse stacking birefringence crystal rods for square macro pulse up to 20 ps.

Precisely optimizing the 3D-shape of the laser pulse, we are striving to generate a further high brightness beam with an emittance as low as possible. Recently, another candidate for a reliable 3D-pulse shape was proposed for even lower emittance [11], which is an ellipsoidal with equivalent fluence along the temporal axis. In this case, a microlens array or deformable mirror cannot help to generate such a three-dimensionally ellipsoidal distribution. A method using a fibre bundle is one solution to avoid the difficulty of adjusting different optical paths [12]. The fibre bundle is a practical system to shape both spatial and temporal profiles at the same time during laser-pulse transportation. The principle of this shaping method involves, in practice, thousands of pulse stackings in defusing the 3-D volume. However, it is difficult to make a smaller laser spot size of ~ 1 mm on the cathode for a realistic working distance of ~1 m in conventional cathode illumination. Therefore, we proposed this shaping technique for only a backward cathode illumination system to shorten the working distance. For this purpose, we are developing a transparent cathode with several materials [13].

REFERENCES

[1] T. Taniuchi et al., Proc. of FEL'96, 1996, p. 137.
[2] "TESLA Technical Design Report, PART V, The X-Ray Free Electron Laser", ed. G. Materlik and Th. Tschentscher, March 2001.
[3] "Linac Coherent Light Source (LCLS) Conceptual Design Report", SLAC-R-593, April 2002.
[4] J. Rivers, "SCSS X-FEL Conceptual Design Report", RIKEN, May 2005.
[5] H. Tomizawa et al., Proc. of EPAC02, 2002, p. 1819.
[6] H. Tomizawa et al., Proc. FEL05, 2005, p. 138.
[7] J. Yang et al., J. Appl. Phys. **Vol. 92**, 2003, p. 1608.
[8] H. Dewa et al., FEL06, 2006, p. 649.
[9] Operator's Manual, Model LBA PC Series, Version 2.50, Spiricon, Inc.: Chapter 9, "ActiveX".
[10] Operator's Manual, Model LBA PC Series, Version 2.50, Spiricon, Inc.: Chapter 6.19, "Top Hat Factor".
[11] C. Limborg-Deprey et al., NIMA 557, 2006, p. 106.
[12] H. Tomizawa et al., NIMA 557, 2006, p. 117.
[13] Japan Patent Application No. 2005-267593.

PERFORMANCE TESTS OF THE PHOTON MONOCHROMATOR FOR SELF-SEEDING AT FLASH *

R. Treusch, U. Hahn, J. Viefhaus, DESY, Hamburg, Germany
H.K. Bechtold, J. Hartvig, H. Juul, V. Toft, Aarhus University, Aarhus, Denmark
S.V. Hoffmann ISA, Aarhus, Denmark
C. Knöchel, LBNL, Berkeley, California, U.S.A.
R. Reininger, Scientific Answers & Solutions, Madison, Wisconsin, U.S.A.
R. Follath, G. Reichardt, F. Senf, F. Siewert, BESSY GmbH, Berlin, Germany

Abstract

A single pass FEL amplifier can produce extremely intense and fully coherent radiation at short wavelengths if it is seeded by a coherent light beam resonant with the magnetic structure and collinear with the electron beam. Since at the present time a single pass SASE[1] FEL is the only source of sufficiently intense, tunable radiation in the soft X-ray region, it has been proposed to use such a source in combination with a narrow-band monochromator for seeding an FEL amplifier [1]. By means of such a "Self-Seeding", the soft X-ray free electron laser FLASH [2] at DESY will be modified so that it can provide coherent radiation in space *and* time in a wavelength range from about 60–6 nm (≈ 20–200 eV).

Here, we will focus on the performance of the photon monochromator beamline for the seeding which was set up and tested at the synchrotron radiation storage ring ASTRID in Aarhus. The optical and mechanical design will be described along with results on the resolving power of the monochromator which have been obtained scanning across rare gas resonance lines at various energies.

INTRODUCTION

Since August 2005 FLASH is providing SASE radiation for users, presently tunable from about 47–13 nm and soon from 60 down to 6 nm. The pulses possess a pulse length of a few 10 fs, almost full transverse coherence, limited longitudinal (temporal) coherence and pulse energies from about 10–100 μJ. By means of the Self-Seeding (or *Seeding Option*) FLASH will be modified in a way that it can provide fully longitudinally coherent, narrow-bandwidth radiation. The output radiation will then exhibit all the characteristic properties of conventional optical lasers but at much shorter wavelengths and with a continuous tunability between 6 and 60 nm. The enhanced beam properties will extend the range of possible applications, particularly for high resolution spectroscopy and for all experiments which need full longitudinal coherence.

The Self-Seeding consists of an additional undulator section, a bypass for electrons and a photon monochromator beamline. R&D in undulator design, FEL theory and electron beam dynamics, as well as on photon beam propagation and optical components were important parts of the project. The photon monochromator beamline aspect will be detailed here. More details, also on all the other components can be found in [3].

The general layout of the Self-Seeding is sketched in figure 1. The first undulator operates in the SASE mode

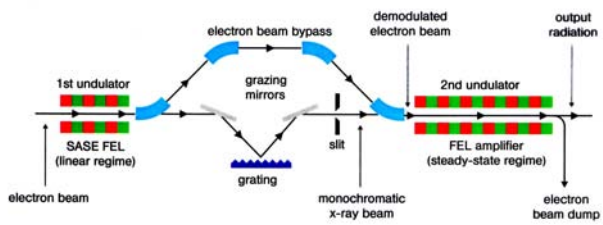

Figure 1: Schematic setup (side view) of the Self-Seeding for FLASH. Behind the first undulator, FEL radiation and electrons are separated. While the electrons travel through the bypass represented by the four blue dipole magnets in the upper part of the figure, the photons propagate across the photon monochromator beamline below in order to provide a narrow-bandwidth seed that is overlayed with the electrons again at the entrance of the second undulator.

in the "linear" (= exponential gain) regime, about 2–3 orders of magnitude below saturation. It produces intense, but structured light pulses as shown in the left part of figure 2. Subsequently electrons and photons are separated. Before they are overlayed again in the second undulator, the electrons travel through a magnetic chicane that is used to remove the longitudinal density modulation ("micro-bunching") of the electron beam which was induced by the FEL process in the first undulator. For the photons, a high resolution grating monochromator together with some matching optics is used as a narrow-band filter to provide the coherent radiation seed which is amplified to saturation in the second undulator section. The resulting spectral distribution is given in the right part of figure 2.

The requirements for the final seeding radiation pulse are obvious: its photon wavelength has to be within the gain bandwidth of the FEL amplifier, the photon bandwidth has to be narrow enough to provide a coherence length as long as the electron bunch length, and the intensity of the

* Work funded through HGF-Strategiefonds (01SF9935/1)
[1] Self-Amplified Spontaneous Emission

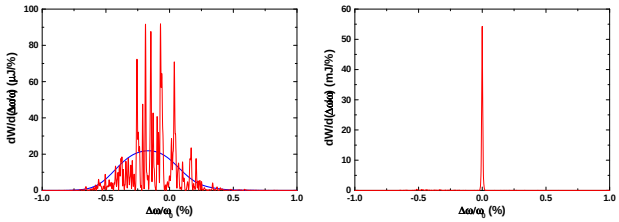

Figure 2: Simulated typical frequency spectrum of a single FEL pulse (from [1]). Left: behind the 1st undulator (SASE, 2 orders of magnitude below saturation). Right: at the exit of the 2nd undulator (seeded FEL in saturation).

seeding radiation has to be much larger than that of the shot noise[2] coming from density fluctuations in the electron beam. Successful seeding then yields a spectral brilliance of FLASH that is up to a factor of 100 higher, i.e. the output power of the seeded FEL is concentrated in a single line which is about a hundred times narrower than the spectrum of the conventional SASE FEL while the pulse energy at saturation remains approximately unchanged. In addition, the pulse now attains full longitudinal coherence.

PHOTON MONOCHROMATOR BEAMLINE

The optical design of the photon beamline was performed applying computer programs that were partly developed for the Self-Seeding at FLASH [4, 5]. The programs combine standard ray tracing with a wavefront propagation of the simulated FEL beam from the end of the first undulator section across the optical elements of the beamline. The output wavefront was used as input for FEL simulations calculating the amplification process in the second undulator. This finally yielded numbers for the efficiency of the seeding process, i.e. the quality of the coupling of the seed pulse with the electron bunch.

In the final, optimized layout, the beamline consists of the monochromator, containing a premirror and a varied line spacing (VLS) spherical grating, and a pair of focusing mirrors at each side of the monochromator. To minimize the number of elements in the beamline, all the reflections and the diffraction are in the same plane. Beside the desired monochromator resolving power of $E/\Delta E \approx 10000 - 20000$, the optical system was designed such that it produces a 1:1 image of the (complex conjugated) wavefront at the entrance of the second undulator section. This way, the optimum coupling, i.e. best longitudinal and transverse overlap between the seed pulse and the electron bunch is achieved [1, 6]. The beamline optics were optimized for the short wavelength end at 6.4 nm and will work satisfactorily up to about 60 nm [7]. The calculated efficiency of the beamline in the wavelength range from 5.8 to 77 nm is better than 10% with carbon coated optics [8]. This ensures that the seed pulse delivered by the monochromator clearly dominates the shot noise in the second undulator and is amplified to saturation. Figure 3 depicts the layout of the beamline, while table 1 summarizes the parameters of the optical elements.

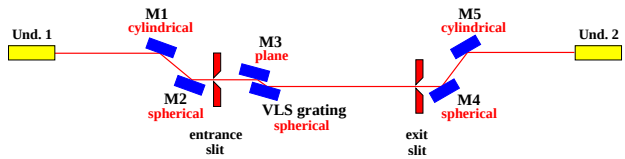

Figure 3: Layout of the photon monochromator beamline of the Seeding Option (side view). M1 to M5 denotes the mirrors. For better visibility, the mirror angles and vertical displacements are greatly exaggerated. The distance between undulator 1 and undulator 2 is 22 m, whereas the maximum vertical distance to the straight line (for the grating and M4) is about 135 mm only (cf. table 1).

Table 1: Parameters of the photon monochromator beamline for the Self-Seeding [7]. Horizontal position means left to right in fig. 3. Incidence angles are given with respect to the surface normal. Positions/angles for M3 and Grating are listed for both ends of the design scan range.

Component	Position (Hor./Vert.) [mm,mm]	Radius [mm]	Angle [Degree]
M1: cylindrical	4500 / 0	345.50 (sagittal)	87.50
M2: spherical	5844.86 / -117.66	41.360×10^3	87.50
Entrance Slit	6844.86 / -117.66		
M3: plane	8879.75 / -117.66 8946.89 / -117.66		86.56 83.52
Grating: VLS, spherical	9020.75 / -134.66	6.0457×10^6	88.28 86.77
Exit Slit	15552.1 / -134.66		
M4: spherical	16502.1 / -134.66	25.70×10^3	86.16
M5: cylindrical	17500 / 0	530.75 (sagittal)	86.16
Start Und. 2:	22000 / 0		

Layout of the mirror chambers

Due to the tight space, the mirror chamber design had to be very compact. It was decided to have all movements of the mirrors outside the vacuum chamber, in order to avoid a production of particles in the vacuum arising from friction of moving parts inside the chamber. From the stringent requirements of positioning accuracy in the μm and sub-mrad range it followed that one needs a very good resolution of the individual movements, in particular the adjustment of beam incidence angle (pitch), and a good reproducibility of the position settings. All, at most six, degrees of freedom had to be "orthogonal", i.e. decoupled. This demanded high precision bearings, translation slides etc., a precise mounting and a robust construction. In the final design, all movements were realized with a twofold suspension, as symmetric to the center of the mirror as possible. Figure 4 shows an exploded view of the mirror chamber for mirror M1. The four mirror chambers for M1, M2, M4 and M5 are, apart from minor differences regarding the mirror holder, almost identical and based on a tested prototype.

[2] = spontaneous undulator emission along the first few gain lengths

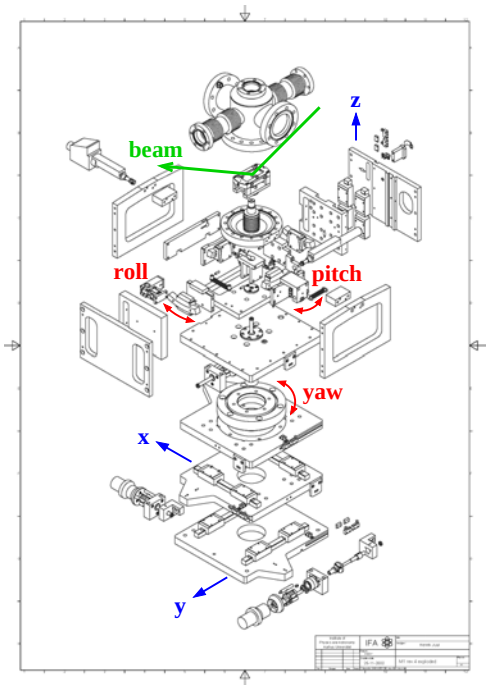

Figure 4: Exploded view of the setup for mirror manipulation used for M1, M2, M4 and M5, including the vacuum chamber. In the lower half one sees stacked tables for x-, y- and yaw-movements which move the complete vacuum chamber, including the mirror. The upper half shows nested roll, pitch and z-movements that manipulate the mirror inside the vacuum chamber through a feedthrough connected with bellows.

Layout of the monochromator

The monochromator is the most crucial component of the beamline with respect to alignment accuracy and desired resolution of the movements [3]. In particular, the required precision and resolution of the pitch of the premirror M3 and the grating made it necessary to put these two rotations inside the vacuum chamber and to attach *state of the art* angle encoders with sub-μrad resolution[3] right at the corresponding axes, similar to some commercially available designs. The basic principle for the movements of the monochromator was adopted from a patented layout [9] that has been applied for high resolution plane grating monochromators. Among its several advantages, this design has a wavelength independent magnification along the dispersion direction. The optical principles of the current monochromator are however, different. The focusing and higher order aberration corrections are achieved with only two elements, the plane mirror (M3) and the variable line spacing spherical grating (a more detailed discussion of the basic principles of the monochromator can be found in refs. [10, 11]). The mechanics for changing the monochromator wavelength setting consist of two nested but separately suspended "cradles" for the grating and M3 which are rotated via external movers that push/pull the respective lever arm of each cradle (Figure 5). High precision radial bearings[4] are employed for the suspension to guarantee the precision and rigidity of the rotational axes.

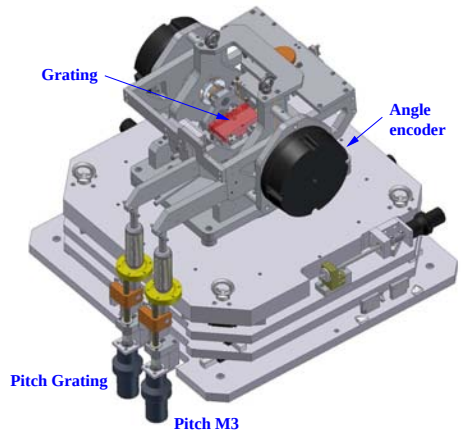

Figure 5: Drawing of the monochromator mechanics showing both, the in vacuum pitch movements via bellow-coupled linear feedthroughs as well as the external stacked tables for x-,y- and yaw-movements. The vacuum chamber mounted on the uppermost table has been omitted.

In order to span the wavelength range from 6-60 nm with proper imaging properties and resolving power including some overlap, one needs three gratings with 800 lines/mm ($\approx$ 4.5–16 nm), 356 lines/mm (10–36.5 nm) and 160 lines/mm (from about 22 to even 83 nm). In contrast to the usual approach with three gratings on independent substrates, we decided to go with three holographically produced gratings side by side on a common spherical Si substrate. That way, the manufacturer (Zeiss) could already – and much better than with individually aligned gratings – ascertain that all gratings are nicely parallel to one another and have all the same incidence (pitch) angle as well as the same roll angle. The perfect optical quality of the gratings regarding parameters such as slope errors, radius of curvature and groove density variation – without and also within the grating holder – was verified at BESSY with the latest generation of nanometrology devices [12].

MONOCHROMATOR PERFORMANCE

In order to test the monochromator performance, in particular its resolving power, the beamline was set up at ASTRID from M1 down to the exit slit (without M4 and M5). A photoionization chamber (gas cell) was put just behind the exit slit to measure the energy dependent ionization of rare gases by monitoring the ion current. Scanning across resonances with linewidths of 1 meV and below – as in the case of doubly excited Helium around 64 eV – directly reveals the resolving power of the monochromator [13]. Other rare gas resonances, e.g. from

[3] Heidenhain RON905 UHV

[4] custom-made by Mahr, Göttingen, Germany

Argon (around 244–250 eV) and Krypton (91–95 eV) with widths of few ten to more than one hundred meV only allow to estimate a lower limit of the resolving power at these energies while still being very useful for accurate energy calibration.

Figure 6 shows a scan across the He resonances after proper alignment and optimization of the beamline at ASTRID. The width of the narrow resonances (e.g. n=7+,8+) of only (3.5 ±0.5) meV yields a resolving power of $E/\Delta E \simeq 19.000$ and is in very good agreement with the respective simulations [14]. Some more results are summarized in figure 7 in comparison to the simulations. Even without a final optimization of all the beamline settings – which would have required a more detailed survey of all degrees of freedom – we reached 90 % of the expected values and surpassed the requirements for the seeding at these energies by about a factor of two already. In addition, the

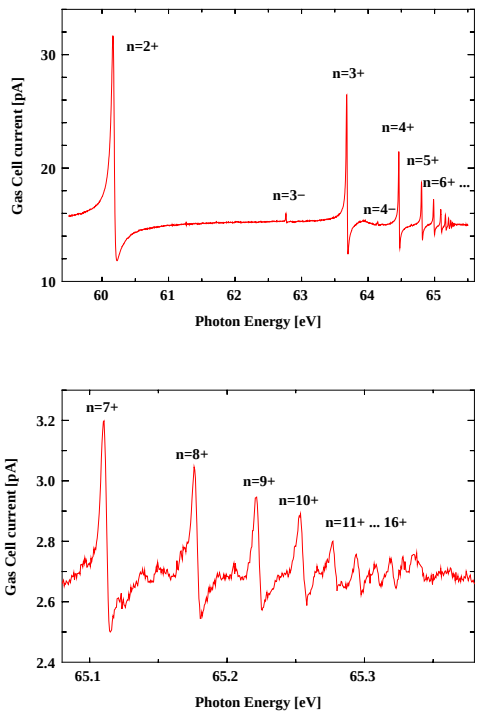

Figure 6: Photoionization yield scan across the He $^1P^0$ resonances (raw data without further normalization). The lower figure is a zoom into the tail of the Rydberg-series (n=7+ to continuum) of the upper figure.

aforementioned common grating substrate very much simplified alignment and operation, as expected. When, e.g., changing after proper energy calibration from one grating to another, the relative energy setting on the new grating was typically 0.2–0.5 ‰ (some 10 meV) off.

Based on our results we conclude that the monochromator beamline is mechanically very stable, precise, reproducible and fully within its specifications with resolving powers between 10000 and 20000, i.e. bandwidths of a few meV only. It meets all requirements for the Self-Seeding.

We would like to acknowledge the technical support from the HASYLAB(DESY) experiment controls and vacuum groups and all the colleagues in the ISA workshops that manufactured most of the beamline mechanics and the vacuum chambers.

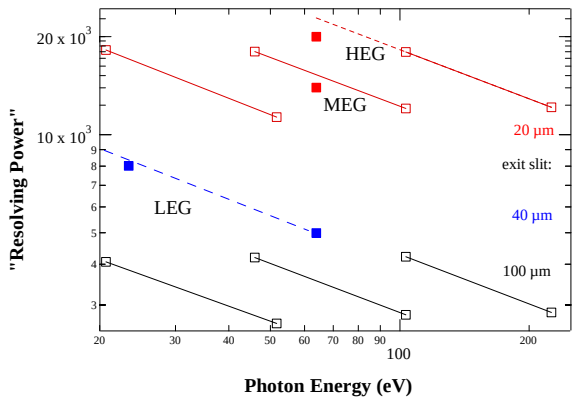

Figure 7: Summary of the measured resolving power. Filled squares: data from resonance measurements, empty squares: simulation results [14] incl. lines to guide the eye. HEG / MEG / LEG=high / medium / low energy grating (800 / 356 / 160 lines/mm), respectively.

REFERENCES

[1] J. Feldhaus et al., Opt. Commun. **140**, 341-352 (1997)

[2] W. Ackermann et al., Nature Photonics **1**, 336-342 (2007)

[3] R. Treusch, *The Seeding Option for the VUV Free Electron Laser at DESY, Final Report*, DESY, Hamburg (2003), available on request (rolf.treusch@desy.de)

[4] R. Reininger et al., AIP Conf. Proc. **521**, 458-462 (1999)

[5] R. Reininger et al., Nucl. Instr. and Meth. A **467-468**, 38-41 (2001)

[6] E.L. Saldin et al., Nucl. Instr. and Meth. A **445**, 178-182 (2000)

[7] R. Reininger, *Optics parameters of the beamline for the seeded FEL*, Internal Project Report (2001), Ref. B7 on the CD-ROM of Ref.[3]

[8] R. Reininger, *VLS grating efficiencies and gratings specifications for the seeded FEL beamline*, Internal Project Report (2002), Ref. B9 on CD-ROM of Ref.[3]

[9] German patent No. 3045931, U.S. patent 4,490,041, see als: H. Petersen et al., Rev. Sci. Instrum. **66**(1), 1-14 (1995)

[10] R. Reininger, *A study of possible PGM beamlines for the seeded SASE free electron laser*, Internal Project Report (1999), Ref. B2 on CD-ROM of Ref.[3]

[11] R. Reininger, *A varied line-spacing spherical grating monochromator for the seeded SASE FEL*, Internal Project Report (1999), Ref. B3 on CD-ROM of Ref.[3]

[12] F. Siewert et al., AIP Conf. Proc. **879**,Part 1, 667-670 (2006)

[13] M. Domke et al., Physical Review A **53**, 1424-1438 (1996) and refs. therein

[14] R. Reininger, *Expected performance of the seeding beamline at ASTRID*, Internal Project Report (2003), available on request (R.T.)

SINGLE-SHOT LONGITUDINAL BUNCH PROFILE MEASUREMENTS AT FLASH USING ELECTRO-OPTIC DETECTION: EXPERIMENT, SIMULATION, AND VALIDATION.

B. Steffen*, E.-A. Knabbe, H. Schlarb, B. Schmidt, P. Schmüser, DESY, Hamburg, Germany
W.A. Gillespie, P.J. Phillips, Dundee University, Dundee, UK
S.P. Jamison, ASTEC, Daresbury Laboratory, STFC, UK
G. Berden, A.F.G. van der Meer, FELIX / FOM Insitute 'Rijnhuizen', Nieuwegein, NL
A.M. MacLeod, Abertay University, Dundee, UK

Abstract

At the superconducting linac of FLASH at DESY, we have installed an electro-optic (EO) experiment for single-shot, non-destructive measurements of the longitudinal electric charge distribution of individual electron bunches. The time profile of the electric bunch field is electro-optically encoded onto a chirped titanium-sapphire laser pulse. In the decoding step, the profile is retrieved either from a cross-correlation of the encoded pulse with a 30 fs laser pulse, obtained from the same laser (electro-optic temporal decoding, EOTD), or from the spectral intensity of the transmitted probe pulse (electro-optic spectral decoding, EOSD). At FLASH, the longitudinally compressed electron bunches have been measured during FEL operation with a resolution of better than 50 fs. The electro-optic process in gallium phosphide was numerically simulated using as input data the bunch shapes determined with a transverse-deflecting RF structure. In this contribution, we present electro-optically measured bunch profiles and compare them with the simulation.

SINGLE-SHOT ELECTRO-OPTIC DETECTION

Precise measurements of the temporal profile of extremely short electron bunches are essential for a detailed understanding of the bunch compression and lasing mechanisms in a SASE FEL. Single-shot electro-optic (EO) detection techniques are ideally suited for this purpose since they are non-destructive and permit correlation studies between the time profile of electron bunches and the properties of FEL pulses produced by the same bunches.

The transverse electric field of a relativistic electron bunch passing close to an electro-optic crystal corresponds to a THz pulse traveling through the crystal. This THz pulse induces a transient birefringence in the EO crystal which can be sampled by a linearly polarized optical laser pulse. In this experiment we use gallium-phosphide (GaP) instead of the more common zinc telluride (ZnTe) as it offers a factor of two better time resolution. The electro-optic temporal decoding (EOTD) technique was applied [1, 2] yielding the best time resolution of the single-shot EO detection methods.

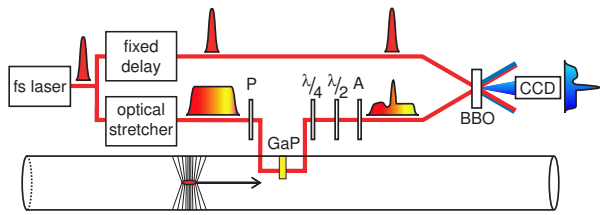

Figure 1: (color) Schematic drawing of the electro-optic temporal-decoding (EOTD) experiment at the FLASH linac. For details see text.

The schematic setup is shown in Fig. 1. The titanium-sapphire (Ti:Sa) laser amplifier (pulse length 30 fs FWHM, central wavelength 795 nm, pulse energy 0.8 mJ, repetition rate 1 kHz) is synchronized to the 1.3 GHz accelerator RF. The laser beam is split into two beams: the probe beam and the gate beam. The probe beam is stretched to 20 ps with a grating-pair optical stretcher and guided through a polarizer P to set the polarization parallel to the [-1,1,0] axis of the EO crystal. It is then injected into the linac vacuum chamber and passes through the GaP crystal placed at a distance of 4-5 mm from the electron beam. The birefringence induced by the Coulomb field of the passing electron bunch is translated into a time-dependent elliptical polarization of the stretched probe beam. This in turn is converted into an intensity modulation with a half wave plate and an analyzer A that is orthogonal to the polarizer P. Any residual birefringence is removed by a quarter wave plate. The EO-induced intensity modulation of the probe pulse is measured through cross-correlation of probe and gate pulse in a frequency-doubling BBO crystal. By overlapping the two pulses non-collinearly, a spatially dependent time delay is introduced between the pulses. The BBO light ($\lambda \approx 400$ nm) is imaged by an intensified CCD camera, and the temporal profile of the electron bunch is derived from the light intensity as a function of position. The intrinsic time resolution of the optical cross-correlator is $\sigma = 25$ fs (rms).

The electric field of the bunch is also arranged to be parallel to the crystallographic [-1,1,0] axis (aligned in horizontal direction), so that the main axis of the refractive

* email: bernd.steffen@desy.de

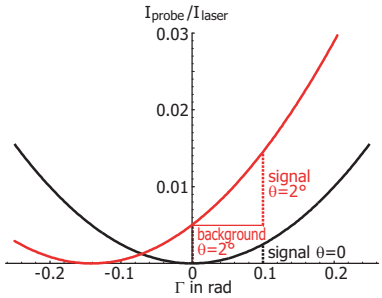

Figure 2: Normalized intensity of the probe beam as a function of the phase retardation Γ for $\theta = 0$, and $\theta = 2°$.

index ellipsoid encloses an angle of 45° with the horizontal axis and hence 45° to the laser polarization. When passing through the birefringent GaP crystal its two polarization components along the main optical axes of the crystal acquire a relative phase retardation:

$$\Gamma = \frac{2\pi\, d}{\lambda_0}\, n_0^3\, r_{41} E_{\mathrm{THz}} \tag{1}$$

Here λ_0 is the optical wavelength, d the thickness of the crystal, $n_0 = n(\lambda_0)$ the optical refractive index of GaP in the absence of an electric field, r_{41} the electro-optic coefficient, and E_{THz} the amplitude of the THz field. Formula (1) is based on the simplifying assumption that THz and laser pulse have the same propagation velocity in the GaP crystal.

Note that in electro-optic sampling (EOS) experiments the delay between THz and probe laser pulse is varied in fine steps and the THz time profile is obtained by averaging over many THz pulses. This scanning method is inadequate at FLASH because the time jitter between the electron bunches and the Ti:Sa laser pulses is too large (> 100 fs). Therefore, single-shot methods are required, the best one being the EOTD technique described above.

The half wave plate shown in Fig. 1 can be used to obtain an EO signal that is either linear or quadratic in the THz field. The intensity of the laser probe pulse impinging on the BBO crystal depends on the phase retardation Γ and the orientation angle θ of the half wave plate in the form [3]

$$I_{\mathrm{probe}}(\theta, \Gamma) = \frac{I_{\mathrm{laser}}}{2}\,[1 - \cos(\Gamma + 4\theta)] \tag{2}$$

Here I_{laser} is the intensity of the incident laser beam. EO detection is frequently made at *crossed polarization*, corresponding to $\theta = 0$. For small values of Γ the EO signal is then proportional to Γ^2, see the black curve in Fig. 2. Hence the EO signal is quadratic in the THz field. Rotating the half wave plate by a few degrees leads to a larger EO signal that is almost linear in E_{THz}, however, there is a non-vanishing background in the absence of an electron bunch (red curve in Fig. 2).

SIMULATION OF THE ELECTRO-OPTIC PROCESS

For ideal electro-optic sampling conditions the THz pulse and the laser pulse should propagate through the EO crystal at the same speed. In reality the THz phase velocity $v_{\mathrm{ph}}(f)$ is frequency dependent and differs from the group velocity v_{g} of the optical laser. A numerical simulation code for the EO process was written [4] to account for the velocity mismatch and to take also into consideration the frequency dependencies of the electro-optic coefficient $r_{41}(f)$ and of the THz amplitude transmission coefficient at the vacuum-crystal interface

$$A_{\mathrm{tr}}(f) = \frac{2}{1 + n(f) + i\kappa(f)} \tag{3}$$

Here $n(f) + i\kappa(f)$ is the complex index of refraction. In the code the EO crystal is subdivided into thin slices of thickness $\delta d = d/N$ (typically $N = 10$ slices for a crystal thickness of $d = 100\ \mu$m), and both the THz pulse and the laser pulse are propagated as wave packets through the crystal. Pulse spreading and attenuation are explicitly taken into account. In each slice the contribution $\delta\Gamma$ to the phase retardation is computed applying Eqn. (1) with the proper delay between the two wave packets in the respective slice. The overall phase retardation Γ is obtained by summation over all slices.

An alternative method is based on the so-called electro-optic response function:

$$G(f, d) = \frac{r_{41}(f)\, A_{\mathrm{tr}}(f)}{d} \int_0^d \exp\left[i\, 2\pi f\, z \left(\frac{1}{v_{\mathrm{ph}}(f)} - \frac{1}{v_{\mathrm{g}}}\right)\right] \mathrm{d}z \tag{4}$$

The phase retardation parameter can be computed from G by inverse Fourier transformation. Figure 3 shows the absolute magnitude of the EO response function of gallium phosphide calculated from published material data [5, 6, 7]. The strong oscillations are caused by the excitation of the lowest transverse-optical lattice resonance of GaP at 11 THz. The vanishing response at about 8 THz is due to the zero-crossing of r_{41} at this frequency. From these curves it is obvious that strong shape distortions will arise if the THz pulse has significant Fourier components in the resonance region of GaP. Moreover, the GaP crystal thickness must be less than 100 μm if one aims for excellent time resolution.

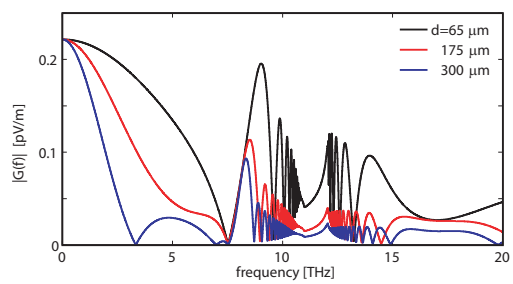

Figure 3: The EO response function of GaP for a crystal thickness of $d = 65$ µm, 175 µm, and 300 µm, respectively.

EXPERIMENTAL RESULTS

For benchmarking the EO process and determining its performance limitations we have carried out simultaneous measurements with the EOTD system and a transverse-deflecting rf structure (TDS), featuring excellent time resolution. The TDS was developed at SLAC [8] and was installed and commissioned at FLASH in cooperation with SLAC [9]. In the TDS, the temporal profile of the electron bunch is transferred to a spatial profile on a view screen by a rapidly varying electromagnetic field, analogous to the sawtooth voltage in conventional oscilloscope tubes. The TDS at FLASH is a 3.6 m long traveling wave structure operating at 2.856 GHz. The bunches pass the structure near zero crossing of the RF field and receive no net deflection but are streaked in the transverse direction. A single bunch out of a train can be streaked. With a fast kicker, this bunch is deflected toward view screen that is imaged by a CCD camera. The other electron bunches are not affected. The time resolution of the TDS for the measurements presented here is about 20 fs (rms).

An EOTD measurement on a longitudinally compressed electron bunch, such as needed for SASE FEL operation, is presented in Fig. 4. The TDS measurement on the adjacent bunch is also shown. The superior time resolution of the TDS is evident. EOTD signals as short as 55 fs (rms) could be measured using a 65 μm thick GaP crystal. The TDS signal shape was used as an input for the numerical simulation of the EO process. The predicted EO signal shape is as is shown in Fig. 4. Its main peak is in excellent agreement with the measured signal. Even the absolute normalization, not shown in the figure, agrees to within 20% to

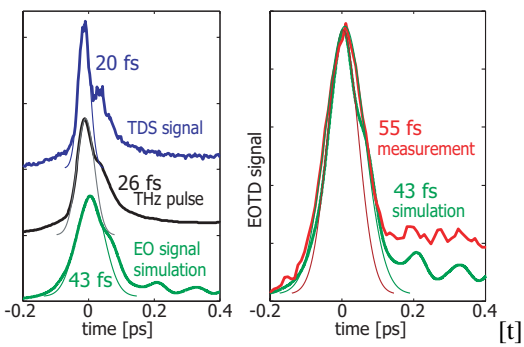

Figure 4: Steps in the comparison between TDS and EOTD signal shapes using a 65 μm thick GaP crystal at an angle $\theta = 2°$ of the half wave plate. Left: From top to bottom: TDS signal, equivalent THz pulse at EO crystal, simulated EO signal. Right: Comparison between simulation and EOTD measurement. The simulated and the measured signals are normalized to the same peak height. The widths correspond to the rms values of the fitted Gaussian pulse shapes.

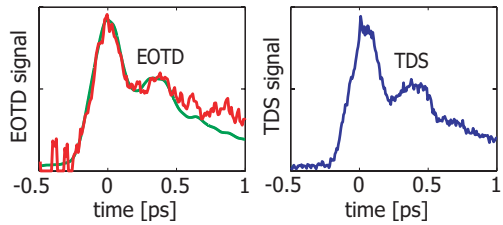

Figure 5: TDS and EOTD signals of bunches showing a double peak structure due to a detuned compression system. The simulated EO signal is shown as a green curve in the left panel.

30%, which is well within the expected fluctuations and the uncertainties of the EO material properties. The measured signal shows a higher tail than the predicted one, which can be attributed to wakefields trailing the electron bunch.

The observed broadening from $\sigma \approx 20$ fs in the TDS data to $\sigma \approx 55$ fs in the EO data is mainly due to the limitations caused by the lattice resonance in GaP. For sufficiently long electron bunches ($\sigma \geq 90$ fs) the time profile as measured by the TDS is faithfully reproduced by the EOTD signal, see Fig. 5.

In another measurement, we employed the simpler EOSD method [10] which does not require a laser amplifier but has the drawback of an inferior time resolution. A GaP crystal of 175 μm thickness was used. From Fig. 3, we infer that frequencies above 5 THz are strongly suppressed in such a thick crystal. As a result both the simulated and the measured EO signals are significantly longer than the real bunch, but both are in perfect agreement. The TDS measurement is shown in the left part of figure 6. The frequency dependent response function of the GaP crystal leads to a significantly stretched equivalent THz pulse inside the EO crystal. In spite of the stretching the THz pulse is still too short to be accurately reproduced by spectrally resolved detection with a Ti:Sa laser pulse chirped to 1.5 ps (rms). Frequency mixing of the effective THz pulse and the laser probe pulse leads to an additional broadening of the predicted EO signal (green curves in fig 6). In the right

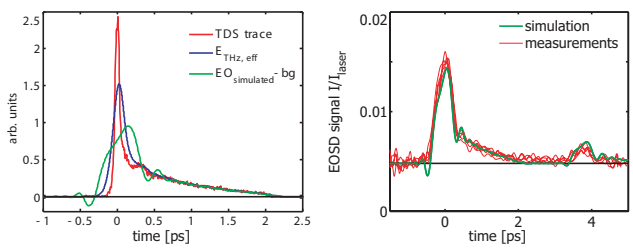

Figure 6: Left: TDS measurement, simulated effective THz pulse and simulated EO signal. Right: EOSD measurements of five consecutive compressed bunches in comparison with the simulated EO signal. Data were taken at $\theta = 2°$ using a 175 μm thick GaP crystal. The laser pulses were stretched by chirping to $\sigma = 1.5$ ps.

part of figure 6 the predicted EO signal is compared to five EOSD electron bunch measurements. Excellent agreement is observed both in shape and amplitude. This indicates that the published GaP material properties and the resulting response function are correct. The comparison between the simulated effective THz pulse and the EOSD signal shows that in this case the signal width is not limited by the response function of the EO crystal but by frequency mixing between chirped laser pulse and THz pulse.

CONCLUSION

The temporal electro-optic decoding method has been benchmarked with a transverse-deflecting RF structure. Simulations based on published EO material data, and using the measured TDS electron bunch profiles as input data, are consistent in shape and amplitude with the EO measurements. Electron bunch profiles with a width of 55 fs (rms) are close to the resolution limit set by the GaP material properties. New electro-optic materials [11] with a broader frequency response than GaP will be needed to improve the temporal resolution.

REFERENCES

[1] G. Berden et al., *Electro-optic technique with improved time resolution for real-time, nondestructive, single-shot measurements of femtosecond electron bunch profiles*, Phys. Rev. Lett., 93:114802, 2004.

[2] S. P. Jamison et al., *Temporally resolved electro-optic effect*, Opt. Lett., 31:1753, 2006.

[3] B. Steffen. *Electro-optic methods for longitudinal bunch diagnostics at FLASH*, PhD thesis, University of Hamburg, 2007. DESY-THESIS-2007-020.

[4] S. Casalbuoni et al., *Numerical Studies on the Electro-Optic Sampling of Relativistic Electron Bunches*, TESLA Report 2005-01 (2005).

[5] D. A. Kleinman and W.G. Spitzer, *Infrared lattice absorption of GaP*, Phys. Rev., 118:110, 1960.

[6] Q. Wu and X.-C. Zhang, *Seven terahertz broadband GaP electro-optic sensor*, Appl. Phys. Lett., 70:14, 1997.

[7] W.L. Faust and C.H. Henry, *Mixing of visible and near-resonance infrared light in GaP*, Phys. Rev. Lett., 17:1265, 1966.

[8] O. H. Altenmueller, R. R. Larson, and G. A. Loew, *Investigations of traveling-wave seperators for the stanford two-mile linear accelerator*, Rev. Sci. Instrum., 35:438, 1964.

[9] M. Hüning et al., *Observation of femtosecond bunch length using a transverse deflecting structure*, Proceedings of the FEL 2005, Palo Alto, CA, USA, 2005.

[10] I. Wilke et al., *Single-shot electron-beam bunch length measurements*, Phys. Rev. Lett., 88:124801, 2002.

[11] X. Zheng et al., *Broadband and gap-free response of a terahertz system based on a poled polymer emitter-sensor pair*, Appl. Phys. Lett., 87: 081115, 2005.

MAGNETIC MEASUREMENTS, TUNING AND FIDUCIALIZATION OF LCLS UNDULATORS AT SLAC*

Y. Levashov, V. Kaplunenko, A. Weidemann, Z. Wolf
SLAC, Menlo Park, CA 94025, USA

Abstract

A new Magnetic Measurement Facility (MMF) has been built at Stanford Linear Accelerator Center (SLAC) to measure, tune and fiducialize LCLS undulators. The climate controlled MMF utilizes two magnetic measurement benches and a large Coordinate Measurement Machine (CMM) to provide a throughput of one undulator per week. Magnetic measurement, tuning and fiducialization processes are presented and first tuning results are discussed.

INTRODUCTION

The Linac Coherent Light Source (LCLS) based on a Self-Amplified Spontaneous Emission Free-Electron Laser (SASE-FEL), is being built at Stanford Linear Accelerator Center (SLAC) by a collaboration of four US-DOE laboratories. A new injector and a part of the existing SLAC linac will be used as an electron source at energy of 13.64 GeV. The 120 m long LCLS undulator line consists of 33 segments. Each segment is a fixed-gap planar undulator assembled of permanent NdFeB magnets and canted poles. The undulator period is 3cm, gap at the beam line is 6.8mm, effective K value varies from 3.500 to 3.485 to account for beam energy loss, and the radiation wavelength will be 1.5A. A prototype of the segment and the first two undulators have been measured and tuned at the Advanced Photon Source (APS) in Argonne National Laboratory (ANL) [1],[2].

Requirements for LCLS undulator tuning and fiducialization are specified in a Physics Requirement Document [3]. The requirements must be met for all beam positions within ±2 mm horizontally and ±200μm vertically of the nominal beam axis. Trajectory excursions for one segment should be less than 2μm, r.m.s. phase errors and particle-wave slippage <10°, first field integrals $<40\times10^{-6}$Tm, second field integrals $<50\times10^{-6}$Tm², and K should be set to 1.5×10^{-4}. The position of the undulator magnetic axis, and the beam trajectory at the nominal K value should be known relative to external mechanical references to 50μm horizontally and 40μm vertically.

Because of their low electrical noise and small planar Hall effects, Sentron XZM12-3-0.6-2T Hall probes are used to sample magnetic fields along an undulator for beam trajectories and K calculations. Field integrals are measured by 3.6m long coils. Additional measurements are made with one period long λ -coils.

The semi-automated process of LCLS undulator tuning allows for a throughput of one undulator per week, which is required to meet the tight project schedule.

MAGNETIC MEASUREMENT LABORATORY

The main concern taken into consideration during construction of the MMF was the temperature. The remnant field of permanent magnet material typically changes by about 0.1% per degree Celsius, which requires the temperature to be constant at ±0.1C° level to meet the tolerance on the K. A high quality air conditioning system keeps the air temperature in the MMF within tolerance, as shown in figure1.

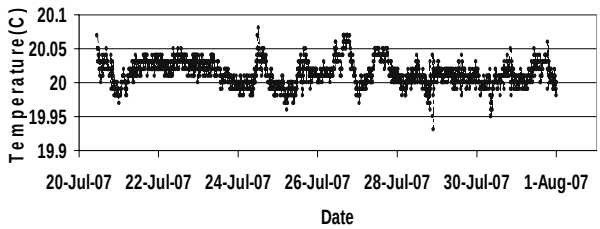

Figure 1. Ambient temperature in MMF

Each undulator stays inside the temperature controlled room for one week prior to the start of measurements to reach thermal equilibrium with the room temperature. During magnetic measurements and tuning, the undulator temperature is monitored by 5 sensors distributed along the length of the device. The difference between the background magnetic field in the laboratory and the magnetic field in the undulator hall at different LCLS tunnel locations was measured to be 0.1G. Many other metal objects, which could affect the ambient magnetic field components, should be taken into account during the tuning process. For that reason all undulators are covered by a μ-metal shield, shown in figure 2, which reduces the ambient magnetic field by a factor of 6. Also they are set in the same orientation in which the segments will be installed in the tunnel, and measured on the same steel support structure.

Initial mechanical acceptance checks and fiducialization measurements of an undulator are made on the 4 meter long CMM. Undulators are tuned on two separate magnetic measurement benches, which allow work to proceed in parallel. The measurement devices are mounted on precision x, y, z - stages with Heidenhain scales and encoders. The instruments are triggered by a National Instruments FPGA in a PXI-1031 chassis. Probe positioning accuracy w.r.t. reference indexes on the scales

* Work supported by US Department of Energy contract DE-AC02-76SF00515.

is better than 5 micrometers. The benches are equipped with cam mover and capacitive sensor systems, which allow alignment of an undulator to the bench in 5 degrees of freedom, with the remaining longitudinal position being only measured. The process of alignment to the bench is completed in approximately 15 minutes to a few micrometers/microradians.

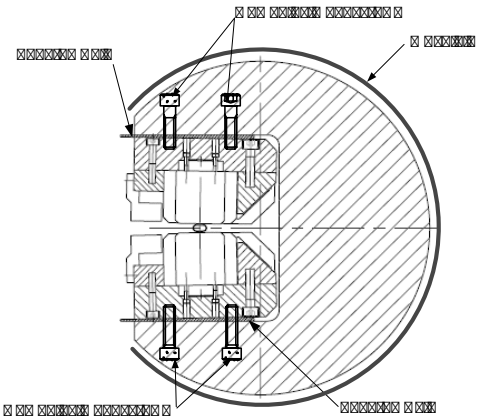

Figure 2. Each undulator is wrapped in a mu-shield, which reduces the ambient magnetic field effect by a factor of 6.

Hall probes are calibrated periodically relative to a Metrolab PT2025 NMR teslameter on a calibration stand. The calibration stand has a special chiller set to 20°C to keep the Hall probe at the same temperature it will have when in use. This increases the accuracy and repeatability of the calibration to 0.3G. The difference between two calibrations is shown in figure 3.

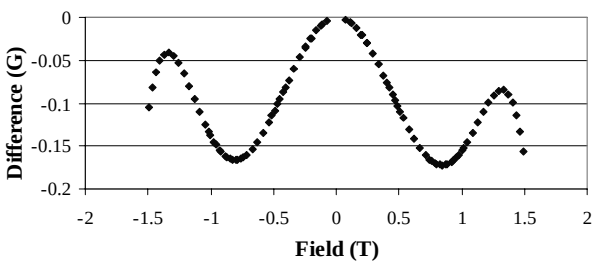

Figure 3. A polynomial fit is made for each Hall probe calibration. The polynomial coefficients are applied to measured data to calculate the corrected field. The difference between two Hall probe calibrations is shown.

Additionally, measurements of a 3.7kG reference magnet are made periodically, right before taking a final set of measurements, to check if the probe calibration has changed.

UNDULATOR TUNING

Undulator tuning is performed in accordance with a plan, in which all steps of tuning and fiducialization are enumerated. On the 4.5m long "rough tuning" bench, trajectories, phases, and K are set to the tolerances. Then a magnetic shield is installed and the undulator is moved to the 7.5m long "fine tuning" bench where a more extensive set of equipment allows field integral measurements, final trajectories, phases, K adjustments and checks to be performed. The undulator support has a steel girder and steel pedestals as will be used in the tunnel to simulate the tunnel conditions. After completion of the tuning process, a final dataset of measurements is made. The fiducialization process also begins on the fine tuning bench and is completed on the CMM.

Tuning trajectories, phases and K

The tuning procedure starts with alignment of a Hall probe to the undulator. Horizontal and vertical scans are made at poles periodically down the undulator. The symmetry point horizontally and the minimum field vertically define the magnetic center at each pole. A fit to the magnetic centers is made to find the axis location. Any magnetic pitch and yaw angles are corrected using the cam mover system. Upon finishing the alignment, scans of the magnetic field, sampling the field every 0.2mm, are made. The Hall probe is moving along the undulator at high speed (80mm/s) which reduces the effect of the probe zero drift. Only a single measurement is required for reproducibility of $2 \cdot 10^{-5}$ which is enough to set K and tune trajectories to better than 1μm. Each Hall probe measurement starts and ends inside zero field chambers located at both ends of the bench. The probe zero offsets and zero drifts are calculated and corrections are made to the measurements. The Hall probe is not used to measure field integrals, since a small DC offset from the probe, when integrated over the segment length, can exceed the required tolerances.

Beam trajectories, phase errors and K are calculated using a special computer program, which also specifies locations and strengths of the shims to be applied to make trajectories straight and to bring phases and K within the tolerances.

Since the magnetic shield blocks access to the gap adjustment screws, as shown in figure 2, an undulator is tuned on the "rough tuning" bench without it and corrections anticipating the shield are made to the measurements. Beam trajectories and phases are tuned by applying special shims, developed at ANL [1]. The K value is set by changing the gap size. All gap adjustment screws should be torqued to the same value to obtain gap adjustment accuracy better than 2μm. After beam trajectories and phases are corrected and K is set, the shield is installed and the undulator is moved onto the "fine tuning" bench.

Measuring and tuning field integrals

Accurate measurements of the small field integrals are made by a 3.6m long integrating coil with 150 turns, wound on a G10 strongback and aligned straight to ±0.1mm. It allows measurement of field integrals in both directions in a small gap by the same coil. The measurements are challenging because the coil is only allowed to move by a half a millimeter due to a small gap, and to minimize averaging over a significant volume of

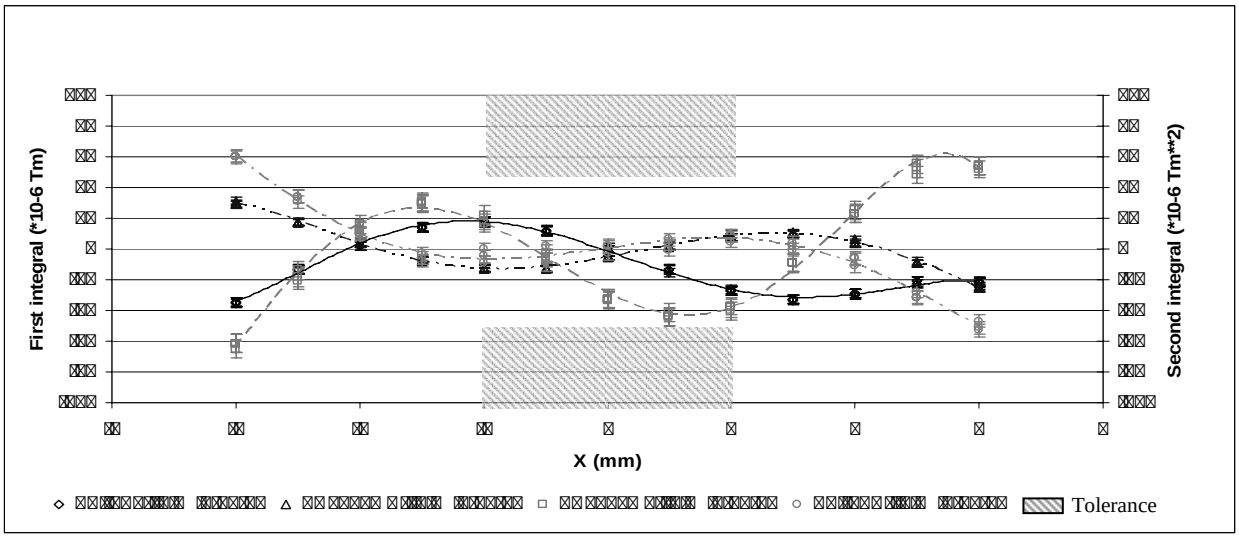

Figure 4. An example of X-dependence of horizontal and vertical field integrals measured by the moving coil. The polynomial fit is of fifth order.

field. Offsets are dealt with by measuring as the coil moves both forward and back. The first integral is measured by fixing return path wires of the coil on the girder and translating both ends of the coil parallel to itself inside the gap by stages. The voltage induced in the coil is sent to a Metrolab PDI-5025 integrator.

The second field integral is measured by holding the exit end of the coil fixed and moving the entrance end, as proposed by P.Vobly [4]. The second field integral has a weighing factor equal to the distance to the end point of the integration.

Heavy filtering is applied to the coil output signal to reduce the electrical noise. The X -dependence of the first and second field integrals in both horizontal and vertical directions is measured and corrected to the tolerances, as shown in figure 4, by applying different types of shims, developed at ANL.

Special tests were done to check the sensitivity and accuracy of the field integral measurement system. The long coil measurements of the small background field integrals were compared to field integrals calculated from fluxgate measurements and to the known field integrals of small magnets placed at various positions. The magnet's strengths were measured by independent means. The tests showed a good 10% agreement between the coil and the fluxgate and 6% level of accuracy in measuring the first and second field integrals by the coil.

Final dataset

When all the measurements are made and the undulator is tuned within the tolerances, the shims are glued in place. Then, the trajectories and the K value are checked and a final dataset of results is made. A map of field integrals is measured in a range of ±6mm with 1mm steps horizontally and ±0.2mm with 0.1mm steps vertically. In addition, Hall probe scans are made in the horizontal direction ±6mm from the magnetic axis location with a step size of 1mm. Small corrections of order of 0.1G are applied to the Hall probe measurements to match the field integrals measured by the long coil.

During the LCLS operation, it is planned to roll an undulator out of the beam line by 80mm. Field integrals are measured by the coil and the magnetic fields are sampled by the Hall probe at the undulator retracted position to have data for future beam trajectory corrections. Since it is outside the magnetic shield, the background field components are measured and taken into account.

To check repeatability of the measurements, a reference undulator is sent through the laboratory for measurements after every 4^{-th} undulator. Results of the reference magnet measurements are shown in table 1.

Table 1
Reference undulator measurement results

		May 2007	**June 2007**	**July 2007**
$\mathbf{I^1_x}$ (10^{-6} T·m)		+30	+20	+44
$\mathbf{I^2_x}$ (10^{-6} T·m^2)		-20	+4	-20
$\mathbf{I^1_y}$ (10^{-6} T·m)		+16	+19	+8
$\mathbf{I^2_y}$ (10^{-6} T·m^2)		+15	+21	+20
Phase Errors (°)	**r.m.s.**	3.7	3.7	3.7
	Entr.	-1.0	-1.5	-1.3
	Exit	-4.4	-4.4	-4.3
	Cell	-5.3	-5.9	-6.0
$\mathbf{K_{corrected}}$		3.498635	3.498567	3.498483
$\mathbf{(\Delta K/K_{nom})}$		$2\cdot10^{-5}$	$-2\cdot10^{-5}$	$-4\cdot10^{-5}$

$I^1_{x,y}$ – first field integrals; $I^2_{x,y}$ – second field integrals; $K_{corrected}$ – effective K, corrected for different magnetic axis x-positions; $\Delta K/K_{nom}$ – relative K error w.r.t. nominal.

FIDUCIALIZATION

Fiducialization is the process of finding how the ideal beam axis, determined magnetically, relates to tangible

objects on an undulator, in our case tooling balls. Special pointed magnets (PM) are used as an intermediate reference [5]. These magnets have a well defined field pattern. The location of the PM centers w.r.t. the PM tooling balls have been found in advance from a calibration. Upon completion of undulator tuning, two magnets are bolted to each end of the undulator and Hall probe scans are made to locate their centers, as shown in figure 5. Horizontal and vertical offsets of the undulator magnetic axis w.r.t. the PM tooling balls are calculated. Then the undulator with the PMs attached to it is moved to the CMM. On the CMM distances between all tooling balls are measured and the fiducialization data calculated.

A number of additional measurements are made to check fiducialization data for possible errors. Two extra PMs are fixed permanently on pedestals next to the bench and measured as references. Horizontal and vertical distances between all tooling balls are measured by optical tools and compared with the CMM data. Additionally, a direct optical measurement of the Hall probe enclosure is made. The accuracy of the optical measurements is about 50μm, but it is a good check of fiducialization data for large errors.

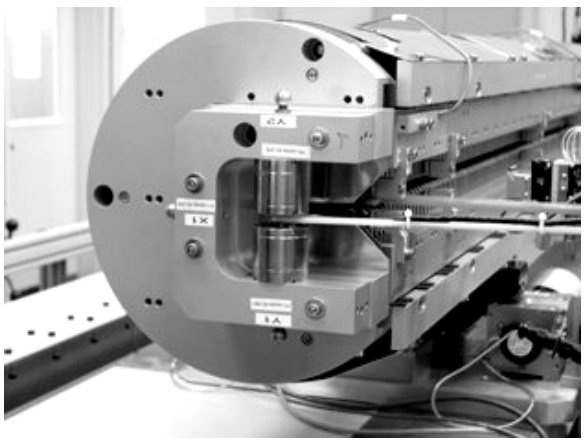

Figure 5. Pointed magnets are attached to the undulator segment for fiducialization.

CONCLUSION

By August 2007, 11 undulator segments have been successfully measured and tuned to specifications in the new climate controlled laboratory at SLAC. All measurement systems are thoroughly calibrated and tested. LCLS undulator measurement and tuning techniques and procedures proved to be adequate to meet the strict tuning requirements. All tuning steps are well documented in a number of technical notes and available online.[†] Raw data and analysis results are saved in a directory structure and available from the SLAC web site[‡].

ASKNOWLEDGMENT

Many thanks to Isaac Vasserman (ANL) for priceless help and tutoring and to Heinz-Deiter Nuhn (SLAC) for valuable discussions.

REFERENCES

[1] I. Vasserman *et al.*, "Magnetic measurements and tuning of the LCLS prototype undulator", Nucl. Instr. and Meth. A 507 (2003) 191.

[2] E. Trakhtenberg *et al.*, "Undulator for the LCLS project--from the prototype to the full-scale manufacturing", Nucl. Instr. and Meth. A 543 (2005) 42.

[3] H.D. Nuhn et al., "General Undulator System Requirements", LCLS Physics Requirements Document, 1.4-001.

[4]. E.I.Antokhin, A.M.Batrakov, P.D.Vobly, N.I.Zubkov, Yu.M.Kolokolnikov, E.G.Miginsky, A.V.Utkin, V.M.Tsukanov, "System for measuring 1 and 2 integrals of the undulator magnetic fields", Preprint BINP, 2002-046, Novosibirsk, 2002.

[5] I.Vasserman "Quadrupole magnetic center definition using the hall probe measurement technique." APS-Pub. LS-285, Argonne, 2004.

[†] LCLS Technical Notes are available at www-ssrl.slac.stanford.edu/lcls/technotes.

[‡] At www-group.slac.stanford.edu/met/MagMeas /MAGDATA/LCLS/Undulator/.

MAGNETIC MEASUREMENTS OF THE FLASH INFRARED UNDULATOR

N.Morozov*, A.Chesnov, E.Matyushevsky, D.Petrov, E.Syresin, JINR, Dubna, Russia,
O. Grimm, J. Rossbach, University of Hamburg, Germany,
Y.Holler, DESY, Hamburg, Germany

Abstract

The FLASH free-electron laser at DESY, Hamburg, has recently been equipped with an infrared electromagnetic undulator, providing radiation in the range 1-200 μm. It will be used both for electron beam diagnostics purposes and as a powerful source synchronized to the VUV and soft X-ray pulses of the FEL. The undulator was constructed at the Joint Institute of Nuclear Research (JINR). This paper summarizes the extensive magnetic measurements that where performed both at JINR and DESY prior to installation of the undulator.

INTRODUCTION

An important feature of the beam formation system of FLASH is the possibility to produce ultra-short (below 50 μm) electron bunches. Such short bunches produce powerful coherent radiation with multi-megawatt power level. Generation of two-colors by a single electron bunch reveals unique possibility to perform pump-probe experiments with VUV and IR radiation pulses [1,4]. Coherent radiation produced by the electron beam in the IR undulator strongly depends on the bunch profile, thus allowing the use of the device for longitudinal profile diagnostics

UNDULATOR MAGNET DESIGN

The undulator (Figure 1) magnetic system [2,3] consists of two ferromagnetic girders with 22 poles each. The exciting coils are set on poles. The coils of the top and bottom girders are connected sequentially and powered by a single electrical supply. Each main coil consists of four layers, and each layer consists of 16 turns. The windings are made of a square-shape copper pipe (8.5x8.5 mm^2) with a cooling channel of 5.3 mm diameter. The maximum current in the winding is 435 A (current density 8.7 A/mm^2). Each regular coil has an additional correction winding to provide fine regulation of the magnetic field. The number of turns in the correction winding is 270, and wire diameter is 1 mm. The corrector winding allows to regulate the number of Amper·turns within 2% of maximum value of the main winding. The correction coils permit to compensate a perturbation of the magnetic field related to an imperfection of magnetic system at its construction. The coils of two end poles differ from the coils of regular periods, and consist of 8 and 36 turns for the first and the second pole, respectively. End-pole coils have also a correcting winding for fine adjustment of the magnetic field.

Figure 1: View of the infrared undulator on the DESY magnetic field measurement bench

SCOPES OF THE MAGNETIC FIELD SHAPING

Undulator magnetic field measurements and correction were provided at the first stage in JINR (Dubna) and finally in DESY (Hamburg). At both sites a Hall probe magnetometer was used for the field measurement. The probe head was moved and controlled in three dimensions by stepping motors and a high accuracy linear encoder (~ some μm). The magnetic field monitoring was realized by reference Hall or NMR probe. During the magnetic field measurement campaign the following goals were realized:

- the first and second total integrals are I_1<200 G·cm and I_2<200 kG·cm^2;
- the first integral in each regular undulator period is I_1<200 G·cm;
- magnetic field reproducibility and long time stability for the first and second total integrals are I_1=±50 G·cm and I_2=±5 kG·cm^2;
- flat beam orbit;
- using one power supply for regular correction coils and as few as possible power supplies for the edge correcting coils.

The above undulator requirements have to be fulfilled in the range of the main coil excitation currents Io = 0 (remanent field) – 435 A (Bo=11000 G).

To achieve those goals, a large amount of simulation work was done at the initial stage of the project design by different codes (POISSON, ANSYS, TOSCA, RADIA) [2]. Those simulations have resulted in a flexible magnetic system with the possibilities to achieve the design goals.

*Corresponding author, email: morozov@nusun.jinr.ru

UNDULATOR MAGNETIC FIELD AND ITS CORRECTION

The measured magnetization curve (central field, pole 4) has shown full correlation of this data with the simulation results by the TOSCA code (Figure 2).

To achieve a minimal first field integral in the regular undulator periods we have realized an iterative correction of the field integral by tuning the values of the correction coils shunt resistors. All regular undulator pole correctors (3-20) were excited by one power supply. The best correction was done first for the main coil current Io=200 A (Figure 3). For other main coil currents the correction was done by tuning the corrector current value. The initial value of the first field integral in the regular periods has achieved 1500 G·cm. The results of the regular periods first integral tuning are shown in Figure 4.

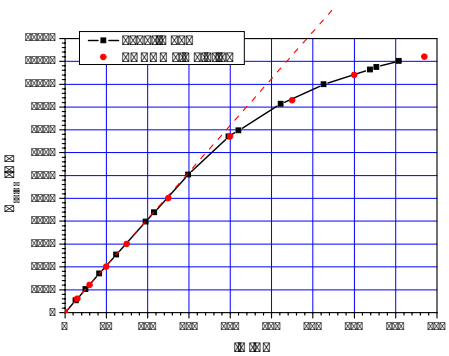

Figure 2: Undulator magnetization curve

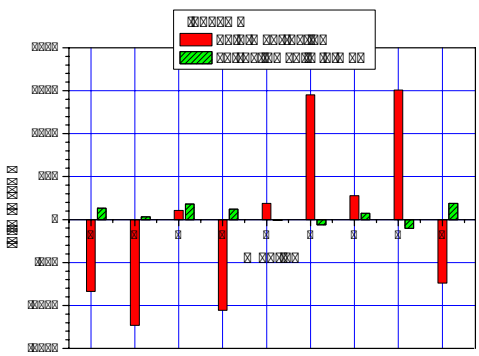

Figure 3: Distribution of the first field integral in the regular undulator periods (Io=200 A) before and after correction

The task of the total first and second field integral correction and minimization was successfully solved by careful tuning of the correctors currents for the pole 1, 2, 21, 22. The maximal correction current is 8 A for these poles. The final first and second field integral is presented in Figure 5 and 6. The corrector coils settings depending from the main coil current are presented in Figure 7. Second integral distributions along the undulator axis are shown in Figure 8 for the maximal main coil excitation currents.

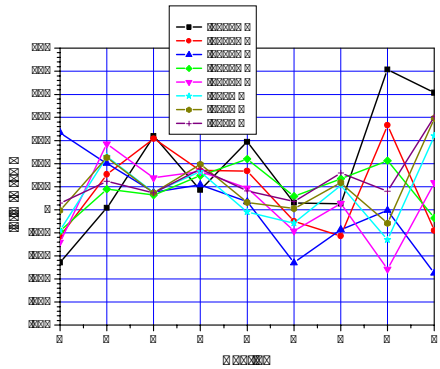

Figure 4: Distribution of the first field integral in the regular undulator periods for some excitation currents

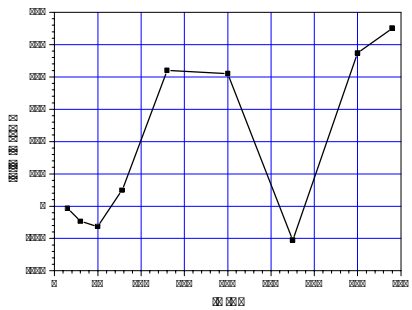

Figure 5: Final first field integral as function of the main coil excitation current

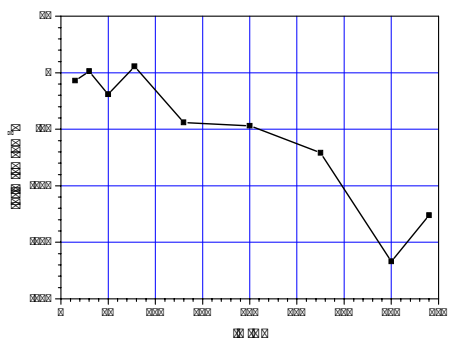

Figure 6: Final second field integral as function of the main coil excitation current

To investigate temperature effects of the undulator, a Fluke Ti45 thermography camera was used. Figure 9 shows an example of such thermographic images. The emissivity for calculating temperatures was taken as 0.95. From a series of such measurement, the coils are in equilibrium after about 30 minutes. The thermal coupling

of the coils to the massive iron yoke and the support structure is weak, however, and a 6 hour time constant is found for the magnetic field.

The results of the reproducibility for the first and second field integral at some test runs are presented in Figure 10 and 11. The study of the undulator magnetic field variation during a 27 hour run at the maximum excitation current Io=435 A has shown that the undulator magnetic field integrals have reached equilibrium some minutes after the working regime setting. The results of the long term measurements are shown in Figure 12.

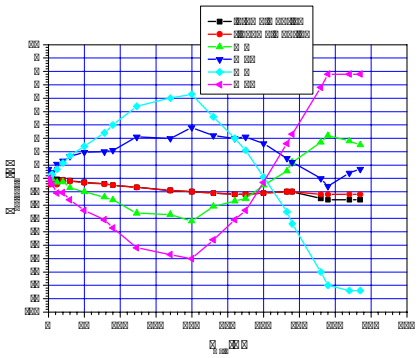

Figure 7: Correctors coils settings

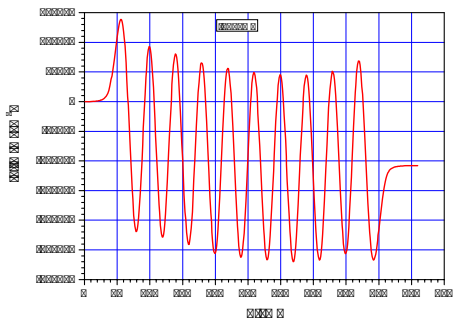

Figure 8: Magnetic field second integral for Io=435 A

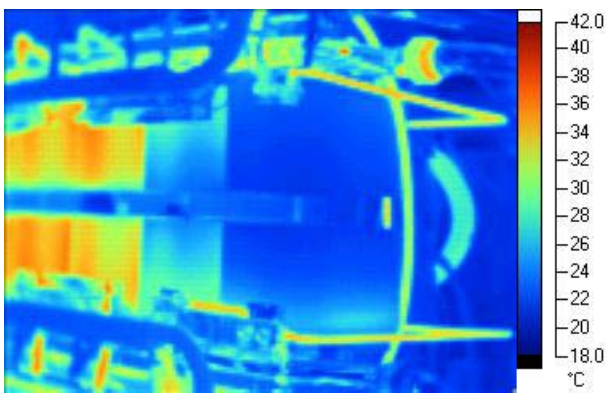

Figure 9: Thermographic image of the infrared undulator 60 minutes after switching on at 435 A current

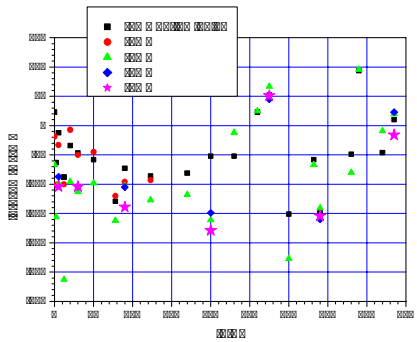

Figure 10: Reproducibility of the first field integral

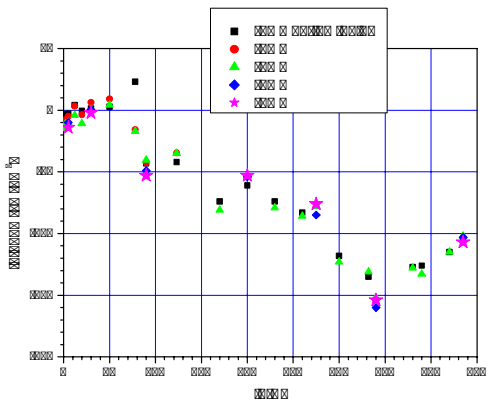

Figure 11: Reproducibility of the second field integral

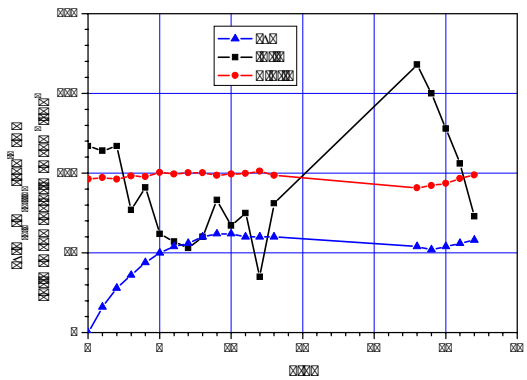

Figure 12: Data from the long test run of the undulator

CONCLUSION

The undulator magnetic field measurement and shaping campaign has approved the technical solution for the magnetic system design. The undulator has shown good stability and reproducibility of the basic magnetic field characteristics.

We would like to thank M. Yurkov, V. Akkuratov, O. Brovko, V. Borisov and A. Shabunov who participated in the undulator design, manufacturing and magnetic field measurements.

REFERENCES

B. Faatz et al., NIM A 475 (2001) 363.

[1] E. A. Matyushevsky et al., JINR E9-2005-168, 2005.

[2] V.Borisov et al, Proceedings of EPAC 2006, Edinburg, Scotland, THPLS133, p.3595-3597.

[3] O.Grimm et al, Proceedings of the 27th International Free-electron laser conference FEL 2005, Stanford, USA, p.183-186.

[4]

NUMERICAL CALCULATIONS OF THE RADIATION EMITTED FROM THE FLASH INFRARED UNDULATOR

O. Grimm*, J. Rossbach, University of Hamburg
V. Kocharyan, DESY, Hamburg, Germany

Abstract

The VUV and soft X-ray free-electron laser FLASH at DESY, Hamburg, has been complemented with an infrared undulator working in the wavelength range of 1 to 200 µm, providing pulses naturally synchronized with the FEL radiation. The results from the magnetic measurements prior to installation are used here as input for calculations of the expected radiation spectrum. Especially the behavior at small excitation currents is important for beam diagnostics using coherent radiation.

INTRODUCTION

Complementing the FLASH facility at DESY, Hamburg, with an undulator working in the mid- and far-infrared regime was first proposed in [1]. There is a strong interest in using such an undulator delivering up to 10 MW peak power in the THz-regime as a radiation source, allowing pump-probe experiments with high temporal resolution. Another equally important application lies within longitudinal bunch shape diagnostics [2, 3]. More details on the undulator have been reported in [4, 5].

The device has been build and installed in the FLASH accelerator, with first beam passing through expected in September 2007. In [6] results of the magnetic measurements that were performed prior to installation are reported. These are used for detailed numerical calculations of the radiation characteristics, some of which are reported in this paper. Such calculations are necessary input to optics codes to quantitatively analyze the transmission characteristics of the infrared beam line.

NUMERICAL CODES

Several numerical codes have been used to perform calculations of the radiation characteristics. Comparisons between the results from different codes are mandatory to get confidence about their validity.

Many calculations are performed with a custom-made code written in Matlab called SynchroSim. The code implements a full time-domain calculation based on using the general Liénard-Wiechert fields from an accelerated charge [7] and a subsequent Fourier transformation to get the spectrum. There are no approximations involved, however the calculation speed is low. Alternatively, a direct calculation in frequency-domain can be done using the paraxial approximation of synchrotron radiation emission [8], giving much higher speed.

The Synchrotron Radiation Workshop (SRW) code has also been used extensively [9]. Some cross-checks were performed with the SPECTRA code [10].

Perfect agreement was found for on-axis spectra calculated with SRW, SPECTRA and SynchroSim. The transverse intensity distribution at 61 µm wavelength and 1 GeV energy is compared between SRW and SynchroSim in Fig. 1. Also here very good agreement is found.

The horizontally asymmetric distribution and interference fringes result mainly from the undulator end poles. Some contribution results also from the inclusion of the dipole magnet that is installed downstream of the undulator. It has a field of about 0.45 T at 500 MeV and is used to dump the electron beam. It should be noted that further along the infrared beam line the relative contribution of the dipole will reduce, as the optics is optimized for the radiation contribution from the undulator.

Further comparisons confirmed the good agreement between different codes, thus calculations in the following were performed with the most convenient program.

SPECTRUM CALCULATIONS

The spectrum calculated for 200 A excitation current of the undulator at 511 MeV electron energy is shown in Fig. 2. On-axis a typical resonance spectrum is obtained containing only odd harmonics. When integrating over a transverse area of $60 \times 60\,\mathrm{mm}^2$ (corresponding to the beam line acceptance at that position), the spectrum acquires a clear baseline. This is an indication of the fact that only a small fraction of the total energy emitted by an electron ends up within the harmonics, see the estimation in the last section.

This effect becomes more pronounced at smaller excitation currents, as Fig. 3 shows for 30 A. This is due to the reduced opening angle of the harmonics at smaller K value, and thus larger contribution of non-resonant radiation when the acceptance aperture is fixed.

TRANSVERSE INTENSITY CALCULATIONS

The transverse distributions of the total radiation intensity (summed over both polarizations) with the undulator current set to the maximum value of 435 A is shown in Fig. 4 for the first and third harmonic (192 µm and 64 µm at 511 MeV, respectively). The 60 mm diameter aperture of

* Corresponding author. E-Mail: oliver.grimm@desy.de

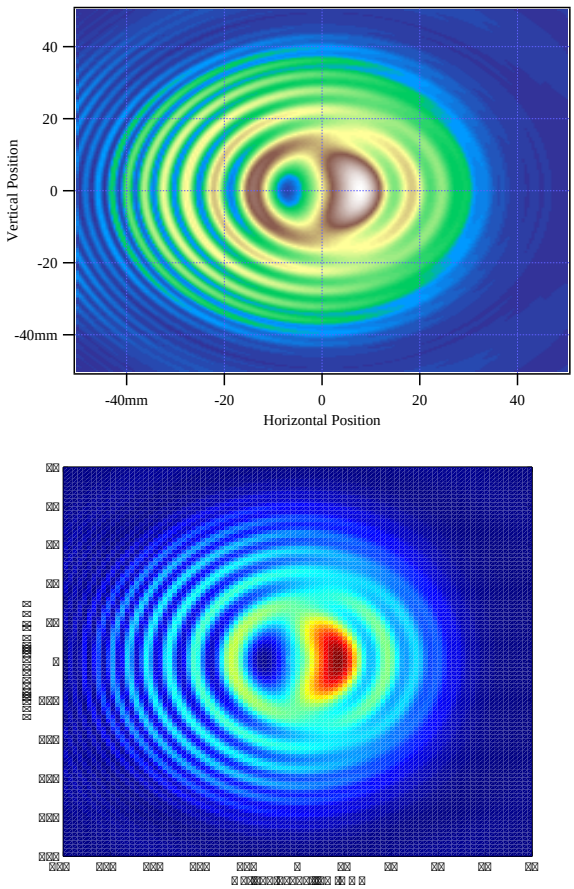

Figure 1: Transverse intensity distribution 9 m behind the undulator centre at 61 µm wavelength and 1 GeV energy. Top: SRW, bottom: SynchroSim.

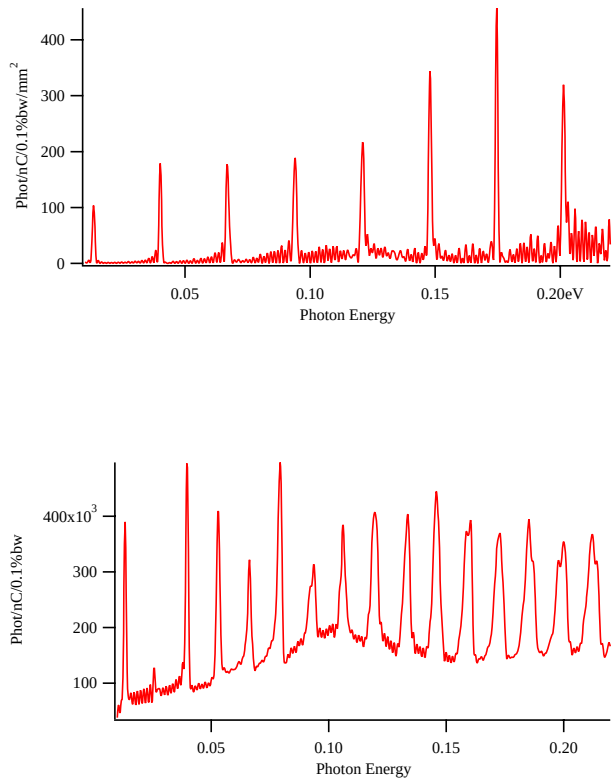

Figure 2: Spectrum at 200 A excitation current and an energy of 511 MeV. On-axis spectrum (top) and integration over a transverse area of $60\times60\,\mathrm{mm}^2$. The first harmonic is at 92 µm.

the beam transport line at that position clips the first harmonic. This reduction of the harmonic amplitude has to be taken this into account for beam diagnostics, as the coherent amplification due to the form factor of the longitudinal charge distribution is imprinted on the relative height of the harmonics.

These plots were calculated at a single wavelength exactly on resonance. Any measurement will integrated over a certain range. Fig. 5 shows the intensity distribution of the first harmonic at 30 A excitation current both for a wavelength on resonance and when integrated over the 10% harmonic bandwidth.

Fig. 6 finally shows the transverse intensity distribution for both polarizations at 30 A when integrated over the full bandwidth of Fig. 3.

TOTAL EMITTED ENERGY

At high K parameter, the spectrum is wiggler-like, consisting of a large number of harmonics. This can be easily understood qualitatively by approximating the undulator for that case as a series of 18 bending magnets of opposite polarity (as the undulator has 9 full periods), separated by half a fundamental wavelength. The spectrum emitted by one bend (approximated as that from circular motion synchrotron radiation) will then be modified into a line spectrum, as Fig. 7 shows.

This approach allows to deduce a scaling of the pulse energy within a given harmonic n. From [11], the bandwidth for an undulator with N periods and fundamental frequency ν_0 is

$$\Delta\nu/\nu \approx 1/(Nn), \qquad \nu = n\nu_0,$$

and the solid angle subtended by the central cone for the relativistic gamma factor γ

$$\Omega \approx \pi\frac{1+K^2/2}{2\gamma^2 Nn} \overset{K\gg1}{\approx} \frac{\pi K^2}{4\gamma^2 Nn}.$$

The envelope $\mathcal{E}$ of the harmonics amplitude in Fig. 7 follows from the low-frequency expression of the synchrotron radiation intensity on axis [7]. It scales for a given magnetic field as $\nu^{2/3}$. The scaling of the energy E within one harmonic can thus be estimated as

$$E \sim \mathcal{E}\cdot\Delta\nu\cdot\Omega \sim n^{-1/3}.$$

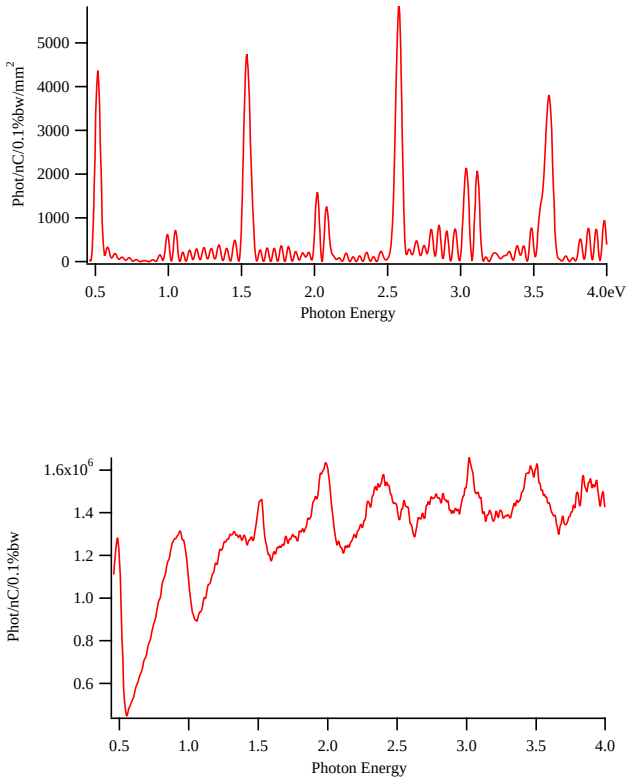

Figure 3: As Fig. 2, but for 30 A excitation current. The first harmonic is at 2.8 µm.

This scaling holds for n much smaller than the harmonic corresponding to the critical frequency: $n \ll 3K^3/8$.

The total energy W_h in all harmonics can be roughly estimated as summing them up to this critical harmonic. Using the expression for the first harmonic energy from [11], this results in

$$W_\mathrm{h} \approx \frac{4\pi e^2\gamma^2}{\epsilon_0 \lambda_u K^2}(J_0(1/2) - J_1(1/2))^2 \cdot \sum_{n=1}^{3K^3/8} n^{-1/3},$$

where λ_u is the undulator period. The total energy W_r radiated by a single electron when passing through an undulator with sinusoidal field can be obtained by integration of the instantaneous power, giving

$$W_\mathrm{r} \approx \frac{\pi e^2 \gamma^2 K^2 N}{3\epsilon_0 \lambda_u}.$$

The ratio becomes, by approximately evaluating the Bessel function expression,

$$\frac{W_\mathrm{r}}{W_\mathrm{h}} \approx \frac{K^4 N}{6\sum_{n=1}^{3K^3/8} n^{-1/3}}.$$

For $K = 42$, corresponding to a first harmonic at 192 µm for 511 MeV, and $N = 9$ this results in $W_\mathrm{r}/W_\mathrm{h} \approx 3400$.

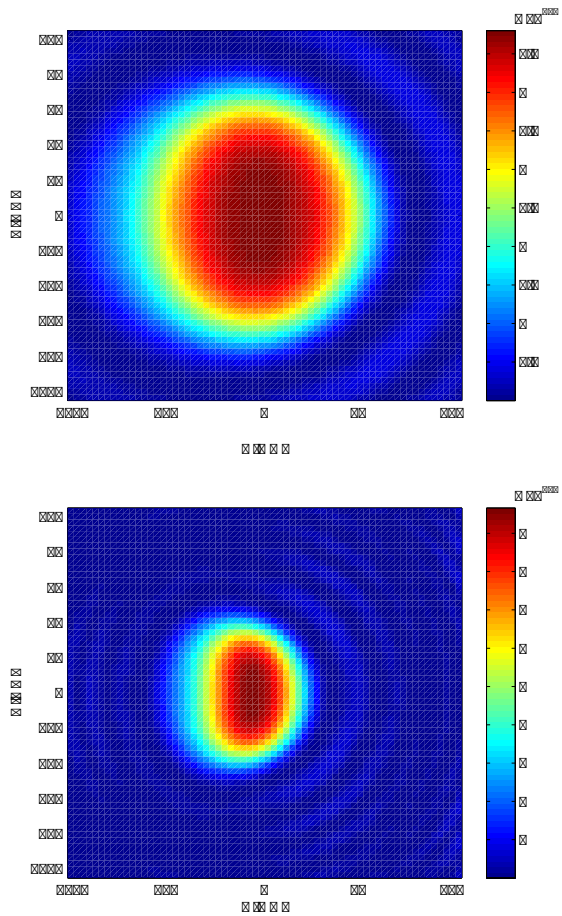

Figure 4: Transverse intensity distribution 10 m behind the undulator centre, at 192 µm (1st harmonic, top) and 64 µm (3rd harmonic, bottom) wavelength. The colour intensity scale is in J/(m²Hz).

Only a very small fraction of the energy lost by an electron actually ends up in one of the harmonics.

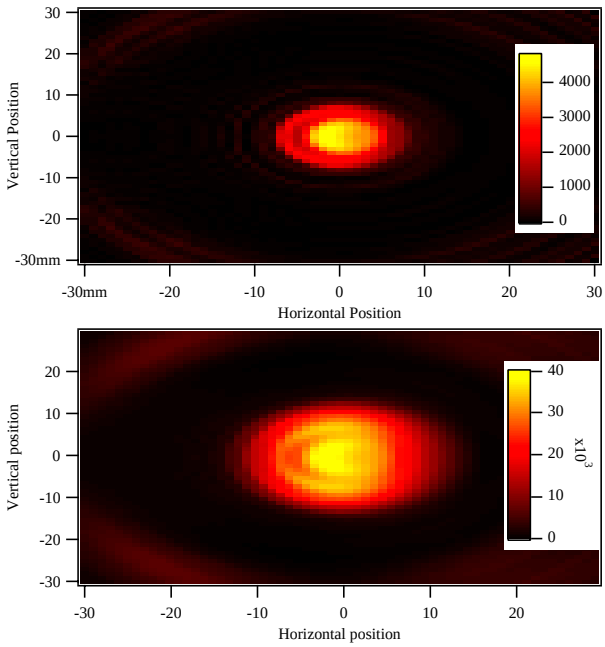

Figure 5: Transverse intensity distribution 10 m behind the undulator centre, on resonance of the first harmonic (2.8 µm, top) and integrated over its 10% bandwidth (bottom). Units of the colour scale are photons/(nC mm^2 0.1% BW) (top) and photons/(nC mm^2) (bottom).

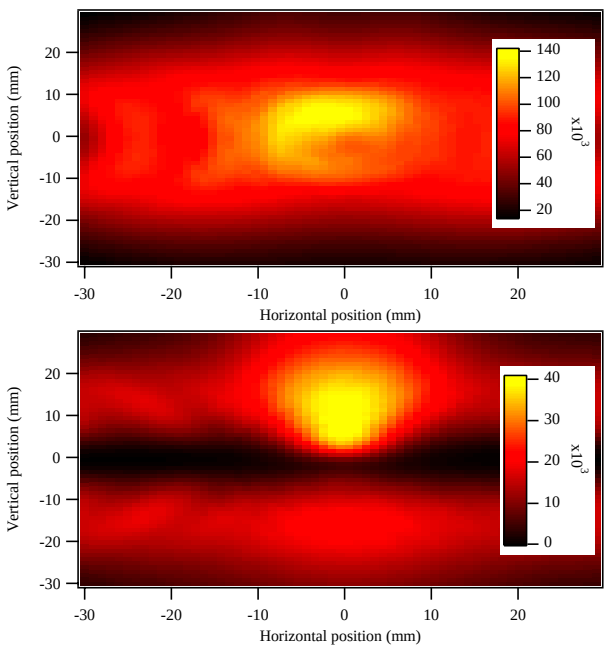

Figure 6: Transverse intensity distribution at 30 A excitation current, 10 m behind the undulator centre, integrated from 300 nm to 3 µm (the range of Fig. 3). Horizontal polarization (top), vertical polarization (bottom). Units of the colour scale are photons/(nC mm^2).

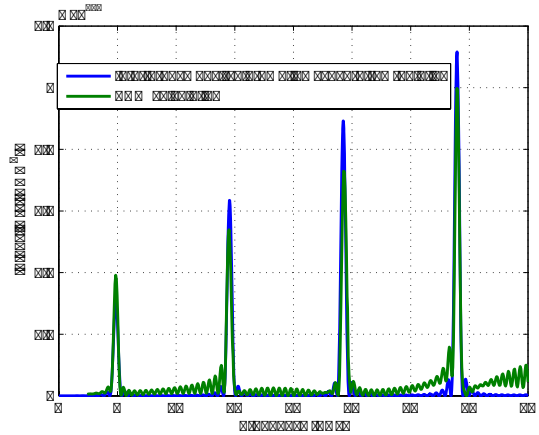

Figure 7: Comparison of the on-axis spectrum 9 m behind the undulator centre as calculated with SRW for the actual undulator field to the effect of interference of circular-motion synchrotron radiation from the individual undulator poles.

CONCLUSIONS

Exemplary calculations of the single-electron radiation generated by the FLASH infrared undulator are presented in this paper. Good agreement is found between different numerical codes. Such calculations allow incorporating a realistic source into Fourier optics codes to evaluate beam line performance and to interpret quantitatively spectral and intensity measurement results. The results presented suggest that angular filtering is needed to obtain well-defined resonance spectra.

REFERENCES

[1] B. Faatz et al., Nucl. Instr. Meth. **A475**, 363 (2001)

[2] G. Geloni et al., DESY 03-031 (March 2003)

[3] O. Grimm, P. Schmüser, TESLA FEL 2006-03 (2006)

[4] O. Grimm et al., Proc. of FEL 2005, Stanford, 21-26 August 2005, p. 183

[5] V. Borisov et al., Proc. of EPAC 2006, Edinburgh, 26-30 June 2006, p.3596

[6] N. Morozov et al., these proceedings

[7] J. D. Jackson, *Classical Electrodynamics*, John Wiley & Sons, New York (1975)

[8] G. Geloni et al., DESY 05-032 (February 2005)

[9] O. Chubar, P. Elleaume, Proc. of the EPAC 1998, Stockholm, 22-26 June 1998, p.1177
`http://www.esrf.eu/Accelerators/Groups/InsertionDevices/Software/SRW`

[10] `http://radiant.harima.riken.go.jp/spectra`

[11] H. Wiedemann, *Particle Accelerator Physics II*, Springer, Berlin (1995)

MAGNET SORTING FOR THE XFEL HYBRID UNDULATOR—COMPARING STUDY

Yuhui Li, Bart Faatz and Joachim Pflueger
Deutsches Elektronen Synchrotron (DESY), Hamburg, Germany

Abstract

Current permanent magnet material quality is insufficient to obtain field qualities in undulators, which satisfy FEL requirements. Therefore position and orientation of magnets have to be carefully chosen in order to obtain mutual cancellation of field errors. In this paper we compare two different sorting schemes, simulated annealing and a straight forward paring method. They are applied to a 5m prototype structure built for the European XFEL facility. The algorithms of these two methods are described in detail and the sorting results and the expected field qualities are carefully compared.

Key words: undulator, sorting, annealing, pairing

INTRODUCTION

The European XFEL will be a user facility in the wavelength range from 0.1 to 1.6 nm [1]. It will use the so-called Self Amplified Spontaneous Emission (SASE) scheme to reach saturation in a single pass [2, 3]. The XFEL will use a technology similar to FLASH [4]. The electron beam is generated in an RF photo cathode gun, accelerated and compressed twice before it reaches its final nominal energy of 17.5 GeV. After acceleration and collimation, the beam will be distributed among several SASE undulators and wigglers for spontaneous emission. The radiation is distributed among 10 user stations. The wavelength can be changed by changing the electron beam energy or by changing the undulator gap.

Studies for FLASH have shown that the transverse overlap between radiation and electron beam has to be better than 20% of the beam size in order not to have a too large reduction in gain and therefore a too large increase in needed undulator length [5]. A similar criterion holds for keeping the resonance condition, i.e. keeping the phase shake within reasonable values. A typical rms deviation here is a few degrees. The undulator magnet quality needed to provide this overlap and phase shake without additional effort does not exist. Therefore, additional methods have to be used in order to guarantee a sufficiently good undulator quality.

Given the quality of the individual magnets, several methods can be used to obtain the appropriate undulator quality. One such method is magnet sorting, i.e. measuring the magnetic properties of the individual magnets and putting them into the structure such that errors in the magnet blocks cancel each other [6]. Another method which can be applied to correct the main field component of the structures that are discussed in this paper is pole-height adjustment [7]. This procedure, which has to take place in any case, is outside of the scope of this report and can only be applied to the main field. Therefore, our main aim is to correct the transverse field components that cannot be corrected by this method.

The structure for which the magnets are sorted is shown in Fig. 1. It consists of magnets separated by iron poles that focus the flux lines resulting in the main magnetic field. Of each magnet, several parameters have been measured: the magnetization in all three directions (M_x, M_y, M_z) and the main magnetic field at a given distance $(B_z^{(n)}, B_z^{(s)})$, thus giving the north-south inhomogeneous field. For a perfect magnet, $M_x = M_y = 0$ and $B_z^{(n)} = B_z^{(s)}$. In order to uniquely identify the orientation of the magnet, each of them is marked as in Fig. 1. Therefore, the direction of the field components is known independent of the orientation of the magnet.

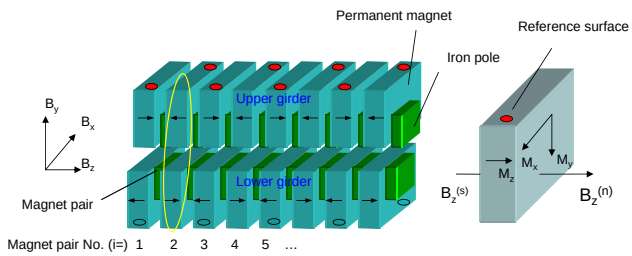

Figure 1: Coordinate system for the undulator and the magnet blocks. The red dot is used to determine the orientation of the magnet under any transformation that may be applied inside the magnetic structure. The arrangement shown here is referred to as the normal state.

With the magnet transverse flux M_x, M_y, the transverse undulator field can be evaluated by:

$$B_{x,i} \propto (F_{l,i} M_{x,l,i} + F_{u,i} M_{x,u,i})(-1)^i$$
$$B_{y,i} \propto F_{l,i} M_{y,l,i} - F_{u,i} M_{x,u,i} \quad (1)$$

The subscript l refers to magnets on the lower girder, u to magnets on the upper girder, i means pole position, F stands for a possible flip of magnet at a certain position, with $F = 1$ the magnet in its normal state and $F = -1$ in its flipped state. $B_{x,i}$ and $B_{y,i}$ are undulator transverse fields on each magnet pair, one in the upper girder, another in the lower girder (see Fig. 1).

In this paper, we will sort the magnets using two different methods, namely simulated annealing and pairing of magnets based on the magnetic measurements.

ALGORITHMS DESCRIPTION OF SIMULATED ANNEALING AND PAIRING

The method of simulated annealing [8, 9, 10] is a technique that has been used for optimization problems. Its main purpose is to avoid getting trapped in a local optimum. Because of the the analogy with the slow cooling down of liquids this process is called (simulated) annealing. In the case of sorting magnets, the magnet position and orientations are changed and the magnetic field for this magnet distribution is calculated. It is quite possible that any single change makes the field quality worse, whereas a combination of changes improves the quality. Simulated annealing offers the possibility to move through a state which is worse to a state which has a better undulator quality needing several magnet permutations in a row. The simulated annealing algorithm can be divided into several steps:

1. Find all possible magnet permutations
2. Find a generator of random changes in this configuration
3. Define a cost function E (analog of energy) whose minimization is the goal of the procedure.
4. Change the system configuration randomly; depending on the values of the cost function before and after changing (E_1, E_2), calculate the value p :

   $$p = exp[-(E_2 - E_1)/T = exp[-\Delta E/T]$$

   If $E_2 < E_1$, the change is accepted; if $E_2 > E_1$, randomly generate a number m in the range of $[0, 1]$. If $m < p$, then this change will still be accepted, if $m > p$, this change will be refused.
5. Control the parameter T (analog of temperature) decreasing during the process. This annealing schedule tells how the T value is lowered, e.g., when and by what amount T is decreased.

A simulated annealing program controls the main annealing progress: first the undulator's configuration is randomly rearranged for 20000 times to determine the range of values of ΔE that will be encountered from move to move, by this the average value $\langle \Delta E \rangle$ can be obtained. Depending on $\langle \Delta E \rangle$ a starting value for the parameter T is chosen which is considerably larger than the largest ΔE which is normally encountered. Then after I_1 times accepted changes or I_2 times refused changes (I_2 is normally larger than I_1), the parameter T decreases by a certain amount. If three times in a row T decreases because of refused changes, the program will be terminated by a last 'quenched' sorting, in which only the change of $\Delta E < 0$ is accepted.

If the undulator is ideal, the field $B_{x,i}$ and $B_{y,i}$ should be zero, so the cost function includes these two elements. Two neighbouring magnet pairs construct one undulator period, so $B_{x,2i-1} + B_{x,2i},\ B_{y,2i-1} + B_{y,2i},\ i = 1, 2, 3...$ represents the transverse field in $i-$th period and these two elements are also included in the cost function. The first and second magnetic field integral of the transverse fields $B_{x,i}$ and $B_{y,i}$ determine the electron beam angle and distance from axis, so the first integral of the transverse field is included too. Consequently six elements are included in the cost function, three in each plane:

- Rms value of transverse field of each magnet pair
- Rms value of transverse field of each undulator period
- Rms value of first integral transverse field on each magnet pair along undulator

So the value of the cost function E is

$$E = w_1 A + w_2 B + w_3 C + w_4 D + w_5 E + w_6 F\,, \quad (2)$$

with $w_1, w_2, w_3, \ldots$ the weights for these six elements, which need to be given each time the annealing program is executed.

Algorithm of pairing magnets

Sorting work can also be done by pairing of magnets. It is divided into two steps: first list all magnets in increasing order of their flux, secondly pairing the magnet with smallest flux to the one with largest flux one by one. The algorithm is:

1. Calculate the absolute transverse field value $|M_x|$ and $|M_y|$ for each magnet, then store them as ascending order in two arrays;
2. Choose another magnet to match the magnet whose absolute value is largest. First step we choose the magnet whose $|M_x|$ and $|M_y|$ is closest to the one that has to be matched. This includes the possibility that by flipping the magnet the sign of M_x and M_y changes at the same time. If matching both cannot be satisfied, then flipping the magnet to make the sign of M_x different has priority.
3. After pairing the magnets, we pair the pairs. Because the x-direction of the field had higher priority during the previous step, the y-direction is considered first during this step. After this treatment, as shown in Fig. 3, the spikes appear by couples and the sign is different, so the integral field can be decreased.
4. After pairing the pairs, we pair double pairs. This time it considers x-direction field more (the result of this step is shown in Fig. 3). Then we pair four pairs by y-direction field, and then eight pairs by x-direction field, and so on.

From the algorithm described above, one can see that the pairing method, unlike to the annealing method, does not

randomly rearrange of the undulator magnet configuration and is therefore less computer intensive. The result of the pairing method and the annealing method will be compared in next section.

SORTING RESULTS OF SIMULATED ANNEALING AND PAIRING

Magnet sorting by simulated annealing

It is known that suitable weight of the elements included in the cost function must be set before running the program. One reasonable method to determine the weight is that first randomly setting the undulator configuration for many times and then observing how much the deviation of each element's contribution to the cost function is. Then each of element weight is set depending on this deviation [11]. The random setting time is 20000. We set as weight of each element the inverse of the deviation of its contribution to the cost function. Table 1 illustrates the different weights. As can be seen, the weight of the field integral is much smaller than the others and in fact can be nearly neglected in the cost function. If the field integral is not neglected, the value of cost function is mainly determined by it.

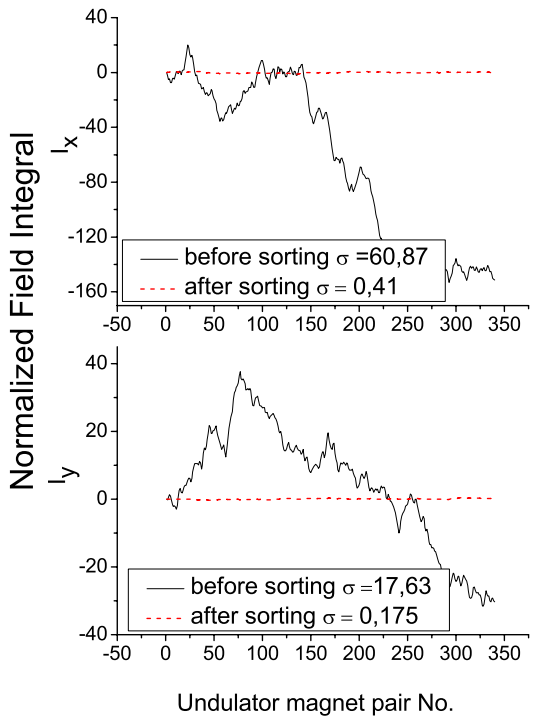

Figure 2: Sorting result by annealing with different element weight listed in Table 1. Both of the field integrals are decreased by two orders of magnitude.

Fig. 2 illustrates the result. One can see that the field integrals decrease by an order of magnitude.

Table 1: Weight for the rms value of each element for cost function

Elements for the cost function	**weight**
B_x on each magnet pair	35971
B_y on each magnet pair	89365
First integral of B_x on each magnet pair	1.513
First integral of B_y on each magnet pair	4.0816
$B_x(i) + B_x(i+1)$ on each undulator period	13210
$B_y(i) + B_y(i+1)$ on each undulator period	33333

Sorting for the 5 m long undulator by pairing

As described earlier, the pairing method is divided into many steps: pairing magnets, pairing magnet pairs, paring double magnet pairs and so on. The result of the different steps on the field at different length scales is shown in Fig. 3.

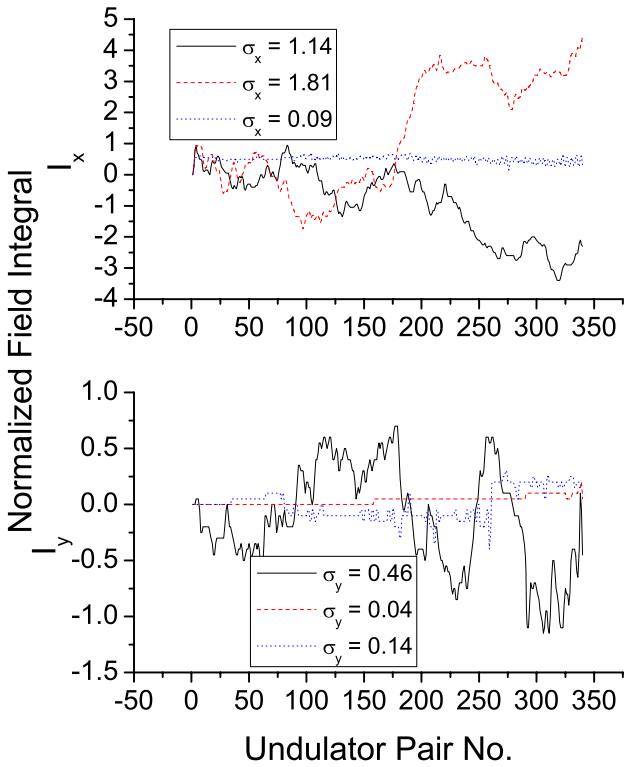

Figure 3: Improvement of the field integral after each step of optimization, pairing of magnets (black curve), pairing of pairs (red curve) and pairing of double pairs (blue curve). The field integral before pairing is the same as in Fig. 2 and therefore not shown.

It illustrates how the field integral depends on the subsequent sorting steps. Because in the first step the magnets are paired, attempting to improve both B_x and B_y, both of the corresponding field integrals improve by about an order of magnitude (black curves in Fig. 3 compared to the original integrals in Fig. 2). Pairing of magnet pairs results in a correlation for B_y such that on the scale of an undulator

period, the errors in B_y compensate each other, resulting in a reduced field integral in this plane after the second step (red curve). Because in this step B_x is not considered, this field integral is changed but not improved. The last step in Fig. 3 shows how sorting magnets on a scale of two undulator periods results in further correlations, now also on B_x which was taken into account in this (final) sorting step (blue curve showing an improvement in teh x-direction).

Comparison of Annealing and Pairing

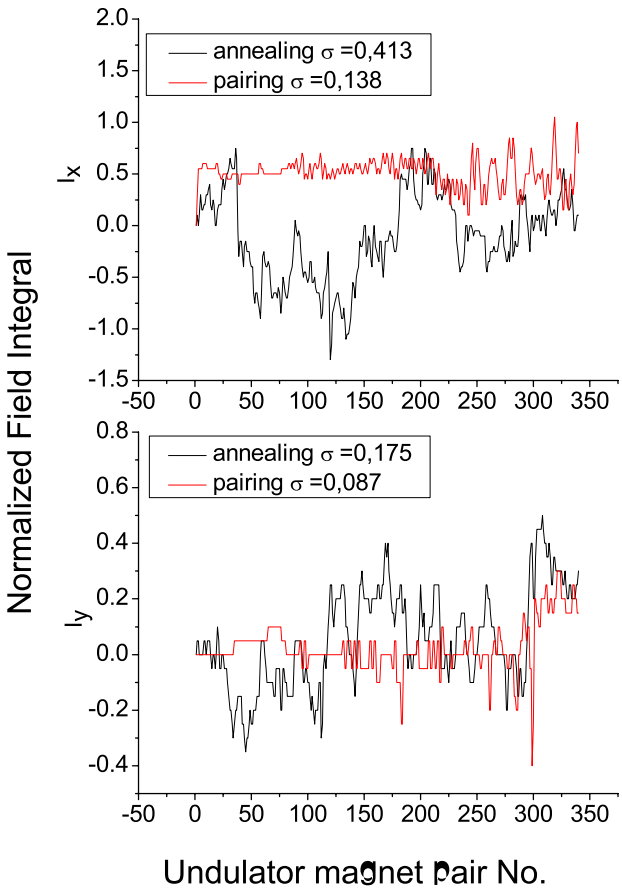

Figure 4: Comparing the transverse field integrals after sorting by annealing and pairing. One can see that for both of transverse field integrals the pairing method gives a factor of 2 smaller errors because the errors are compensated immediately and errors cannot build up to large deviations

The comparison of pairing and annealing is illustrated in Fig. 4. One can see that field integrals are clearly smaller in case of the pairing method. The reason for this is that errors are corrected locally. The results so far show that magnet pairing is much less computer intensive and gives slightly better results. As a consequence, one might say that there is no reason to use simulated annealing. However, in case some magnets have to be exchanged after part of the undulator magnets have already been assembled, the annealing method has the clear advantage that one can resort the remaining part of the undulator with magnets still available, whereas this is more difficult with the pairing method. This is illustrated in Ref. [12].

SUMMARY

In order to reach saturation in an FEL the overlap between electron and photon beam has to be guaranteed. To this aim individual magnets are measured and put into the undulator structure in a special order. The two methods discussed in this paper are simulated annealing and pairing of magnets. Only the transverse field components have been corrected.

As has been shown, both methods can greatly improve the transverse undulator field. The pairing method is more straightforward and gives a better field than the annealing method. The field integral is about a factor of 2 better for pairing, which would result in a better overlap. However, both methods meet and even exceed the required field accuracy.

REFERENCES

[1] Massimo Altarelli et.al., The European X-Ray Free-Electron Laser Technical Design Report, ISBN 3-935702-17-5

[2] A. M. Kondratenko and E. L. Saldin, Part. Accel. 10, 207 (1980)

[3] R. Bonifacio, C. Pellegrini, and L. M. Narducci, Opt. Commum. 50, 373 (1984)

[4] S. Schreiber, Proceedings of the 27th International Free Electron Laser Conference pp, 12-18, 2005, Stanford, California, USA

[5] B. Faatz, J. Pflueger, Y. M. Nikitina, Nucl.Instr. and Meth. A 393 (1997) 380

[6] B. Faatz and J. Pflueger, Magnet Sorting for the TTF-FEL Undulator using Simulated Annealing, TESLA FEL Report 1999-01

[7] J. Pflueger, H. Lu and T. Teichmann, Field fine tuning by pole height adjusting for the undulator of the TTF-FEL, Presented at the 20th International FEL conference, August 17-21, 1998, Williamsburg, USA

[8] Kirkpatrick, S., Gelatt, C.D and Vecchi, M.P. 1983, Science, Vol. 220, pp.671-680

[9] Kirkpatrick, S. 1984, Journal of Statistical Physics, Vol. 34, pp. 975-986

[10] Numerical Recipes, William H. Press, Saul A. Teukolsky, William T. Vetterling and Brian P. Flannery, Cambridge University Press, pp. 436

[11] Duncan Scott, An Introduction to Monte-Carlo Methods for Magnet Block Sorting An APPLE-II Type Helical Undulator, ASTEC-ID-024, 2004

[12] Y. Li, B. Faatz and J. Pflueger, Magnet Sorting for the XFEL Hybrid Undulator — Comparing Study, TESLA-FEL report 2007-06, DESY, Hamburg, Germany

STUDY OF UNDULATOR TOLERANCES FOR THE EUROPEAN XFEL

Yuhui Li, Bart Faatz and Joachim Pflueger
Deutsches Elektronen Synchrotron (DESY), Hamburg, Germany

Abstract

For an X-ray FEL facility, error tolerance simulations for undulator systems are necessary. Previous work mainly took into account random errors for each pole and then simulate their impact. However, some errors, for instance the girder deformation, are not random but periodic. In this paper both random and periodic errors as well as a combination are studied. The results are limited to non-steering errors, i.e. a reduction in overlap between electrons and photon beam has been avoided throughout this study.
Key words: tolerance, undulator, XFEL

INTRODUCTION

In the European XFEL project, photons will be generated in the X-ray range of 3.1 keV to 12.4 keV [1]. High power radiation will be generated using Self-Amplified Spontaneous Emission (SASE). Saturation will be rezched within a typical length of 100 to 150 m [2, 3]. Undulator errors unavoidably exist in this long undulator system. A first estimate for an upper limit on these errors is related to the SASE-FEL bandwidth ρ:

$$\frac{\Delta\lambda_s}{\lambda_s} \approx \frac{2\Delta K}{K} < \rho \qquad (1)$$

With the value of ρ of the order of 10^{-4} for the European XFEL project, undulator gap variation should smaller than 1 μm and the temperature variation should be smaller than 0.08^oC [4]. If Eq. (1) could be satisfied, the power degradation and saturation length increase would be minimal. Because this is far from trivial and a mayor cost driving factor, a more detailed study is neccessary.

The European XFEL facility will supply 0.1 nm to 0.4 nm radiation. Wavelength tuning can be achieved by changing the undulator gap or the electron beam energy. Even though the tolerance level for different modes is different, their behaviour is similar. Therefore in this paper we only list the result of SASE1 with 0.1 nm mode which has the tighest tolerance requirement. A more complete study can be found in [5].

Two kinds of undulator field errors can be distinguished. One kind is random error on each undulator pole. This kind of error can be caused for example by the inhomogeneous field of magnet blocks [6]. Another kind of error changes along undulator as periodic or semi-periodic function. This kind of error exists for instance because of the girder deformation or gap tilt [7]. The previous tolerance simulation work concentrated mainly on the first kind of error. Thus this report only studies the latter one.

Some papers investigating the impact of undulator field errors show that beam wander and phase shake are the key reasons for the increase of gain length [8, 9]. Beam wander reduces the transverse overlap between electron beam and radiation. Phase shake indicates an electron ponderomotive phase variation and therefore a reduction in bunching. In this paper only the impact of phase shake is taken into account.

The FEL simulation code Genesis 1.3 is used for our simulations [10].

DESCRIPTION OF BASIC ERROR TYPES

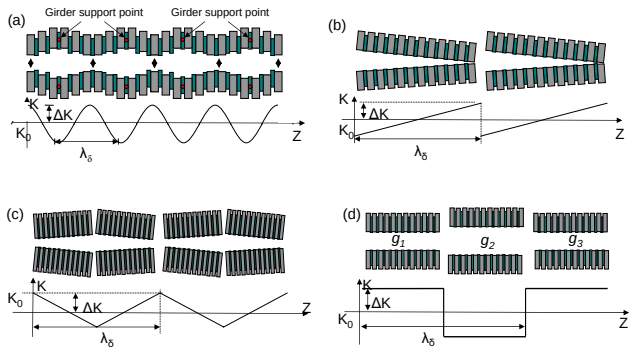

Figure 1: The induced undulator error by girder deformation and gap tilt (a) sinus, (b) sawtooth, (c) triangle and (d) constant

The periodic errors are divided into four basic types: sinus, triangle, sawtooth and (stepwise) constant. The sinus error is used to approximate undulator girder deformation due to the magnetic forces which can be compensated for one gap setting only. Fig. 1 (a) shows this effect. For the European XFEL, a four point support structure is used in order to minimize this effect. A periodic error can also be generated by the inhomogeneous movement of the undulator driving motors. Fig. 1 (b), (c) and (d) illustrate so generated three kinds of periodic errors (sawtooth, triangle and constant). The movement accuracy is assumed to be 1 μm.

Finite motor movement accuracy results some in residual random errors of which the importance has to be quantified. For this purpose, the same error model as shown in Fig. 1 is used, but in this case the resulting amplitude variation ΔK is random. In contrast to this, the undulator girder deformation is always homogeneous and thus a periodic error can always be expected. Therefore, in this paper the simulation of random sinus errors is not investigated. Fig 2 illustrates this random error.

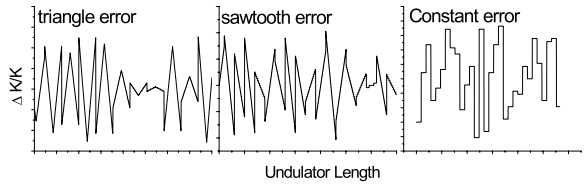

Figure 2: The random error for the three error types. The error amplitude randomly changes from error period to error period.

PHASE SHAKE CALCULATIONS WITH PERIODIC ERRORS

As already mentioned, phase shake is an important reason for radiation power degradation. For the periodic error considered in this paper, the phase shake can be analytically calculated. The undulator parameter K can be written as

$$K(z) = K_0 + \Delta K \cdot f(z) \tag{2}$$

where K_0 is the nominal undulator parameter, $\Delta K \cdot f(z)$ denotes the undulator error. ΔK expresses the error strength and $f(z)$ ($\langle f(z)\rangle = 0$, $\langle f^2(z)\rangle = 1$) the error shape.

It can be shown that the RMS phase shake for a periodic error ($f(z) = f(z + \lambda_\delta)$ with λ_δ the error period) can be approximated by:

$$\sigma_{\Delta\varphi} = \frac{k_u K_0^2}{1 + K_0^2} \cdot \alpha \frac{\Delta K}{K_0} \lambda_\delta \,, \tag{3}$$

where α is a coefficient depending on the error shape. The coefficient values are $1/\sqrt{2}\pi$, $1/\sqrt{30}$, $1/\sqrt{45}$ and $1/\sqrt{12}$ respectively for the sinus, triangle, sawtooth and constant error.

It is important that the RMS phase shake is proportional to the product of $\Delta K/K_0$ times the error period λ_δ. To illustrate this more clearly, Fig. 3 shows simulation results with a periodic sinus field error. One can see that the ΔK of black the sinus error is five times larger than the red error, whereas the error period λ_δ of the black error is ten time shorter than the red error. From Eq. (3) the red error therefore has a larger RMS phase shake. Consequently, the power growth along the undulator with the black error is expected to be closer to the ideal than the red one. This is indeed confirmed by the blue dotted line in the bottom plot of Fig. 3, which is the power growth for the ideal undulator.

ERROR SIMULATION FOR SASE1

In this section we introduce the method of our error tolerance calculation and the results for SASE1, 0.1 nm mode.

Simulation method

As mentioned for each operation mode four error types (sinus, sawtooth, triangle, constant) are simulated. For each error type, the simulation is divided into two steps:

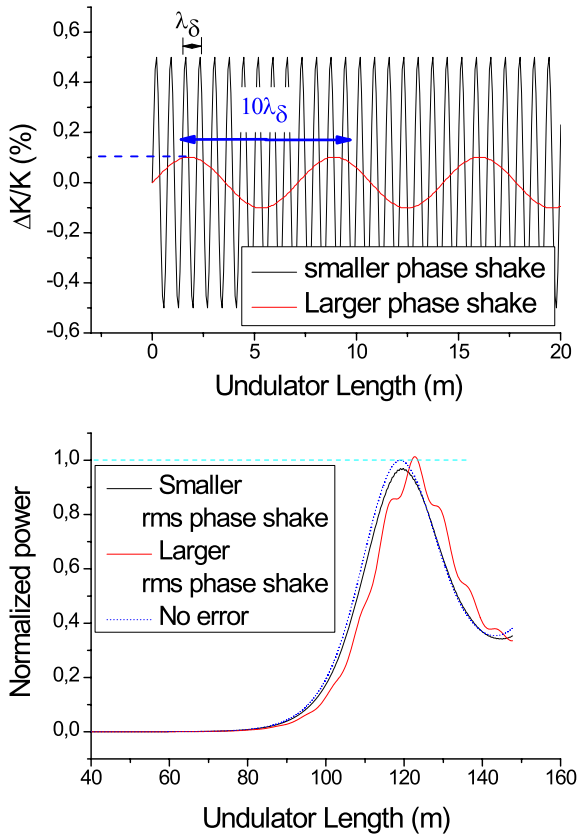

Figure 3: Two sinus error's with different amplitude and period and its impact on the power growth. The ΔK of the black line is larger but because of its shorter λ_δ its rms phase shake is smaller. Thus its power degradation is smaller thanthat of the red curve.

first simulating the periodic error and then the random error. The error models for different types are shown in Fig. 1.

First we calculate the periodic error impact. From Eq. (3) we know that the the RMS phase shake can be changed either by adjusting the error strength $\Delta K/K_0$ or the error period λ_δ. Because the power degradation is determined by the RMS phase shake, any product of $\Delta K/K_0$ and λ_δ with the same phase shake corresponds to a certain power degradation. Therefore first we have taken 9 different error strengths: $\Delta K/K_0 = 0.1\%, 0.15\%, \ldots, 0.5\%$. For each $\Delta K/K_0$, 30 different error periods $\lambda_\delta/\lambda_u = 10, 20, \ldots, 300$ are chosen. Thus the power growth with totally 270 combinations of $\Delta K/K_0$ and λ_δ is calculated.

So far the simulation for periodic error is done. Then the random error is simulated. We choose three points (combination of $\Delta K/K_0$ and λ_δ) where $10\%, 20\%, 30\%$ power degradation can be expected. Thus totally 9 points are chosen. For each point, we fix the λ_δ and set a suitable κ that if $\Delta K_i/K_0$ (i denotes the random error strength in ith period) randomly varies in the range of $[-\kappa, \kappa]$, the RMS phase shake is close to the value of the periodic error. For each combination 100 random simulations are performed

and totally 900 random errors are calculated.

Simulation result for periodic error

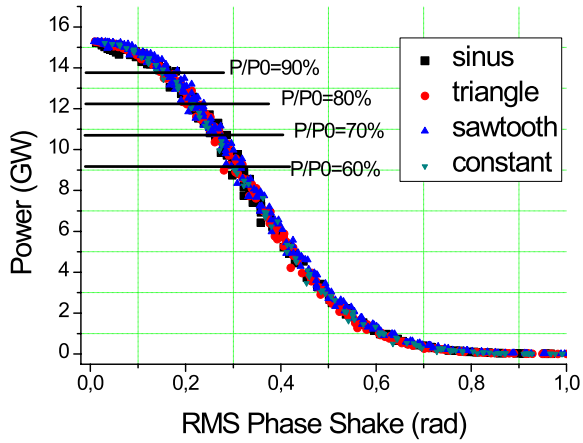

Figure 4: The power degradation versus RMS phase shake at a fixed point inside the undulator before saturation is reached. There is a perfect correlation between power and phase shake, independent of what error shape has been used.

It is interesting to illustrate the power degradation with different RMS phase shake values and different error types. Fig. 4 shows the result. The correlation between the power degradation and the RMS phase shake is good and same RMS phase shake generated by different error types results in the same radiation power. Based on this result we can imagine that for any kind of error type which is not included in our simulation, the power degradation can also be evaluated by the RMS phase shake.

Table 1: Summary of results of tolerance simulations for SASE1, 0.1 nm mode. The numbers quoted here correspond to a power reduction of 10%.

Type	RMS phase shake	λ_δ	$\Delta K/K_0$	Δg (mm)
sinus	0.146	1.2m	0.366%	0.030
triangle	0.156	10m	0.058%	0.005
sawtooth	0.165	5m	0.148%	0.013
constant	0.183	10m	0.043%	0.004

Table 1 shows the tolerance result for SASE1, 0.1 nm mode with a 10% power reduction. From this table one can see that a sinus girder deformation as large as 30 μm can be tolerated which is considerably larger than the estimate based on the Pierce parameter ρ. On the other hand a λ_δ of 10 to 12 m still requires gap control in the μm level. This, hoever, is technically no problem.

the from all of the error types, the girder deformation or the gap movement accuracy can relax to a value larger than 1 μm, which is evaluated by the Perice parameter ρ. On the other hand, the longer periodic length λ_δ brings tighter error strength $\Delta K/K_0$.

Simulation result for random error

Fig. 5 shows the correlation between the power degradation and the RMS phase shake for the random sawtooth error. Comparing to the correlation of periodic error, for the random error the power degradation still correlates to the RMS phase shake. The mean power value for a certain RMS phase shake is similar for random and periodic distributions, but the spread for random errors is larger.

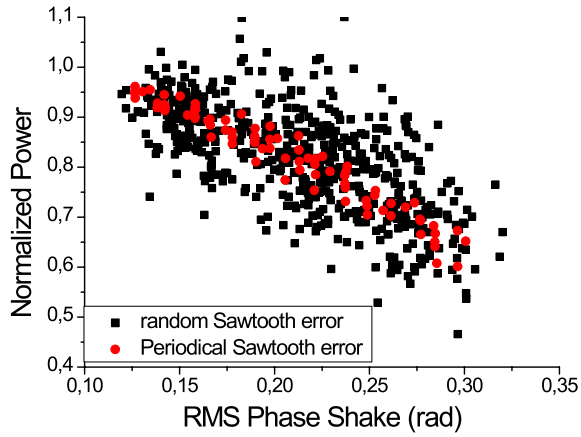

Figure 5: Power versus phase shake in case of a sawtooth error. The back squares show the results of random sawtooth amplitude and length scale. The red circles show the periodic sawtooth errors that are already shown in Fig. 4.

COMBINED ERRORS AND TEMPERATURE COMPENSATION

Combination of different errors

In the sections before, the impact of four different error types have been illustrated separately. Because in practice these errors are combined it is also necessary to study the impact of this kind of combined error.

In principal the sinusoidal girder deformation can be assumed to be always periodic. While the triangle, sawtooth and constant error are all generated because of the inaccuracy of motor movement, they are random. 20 μm of girder deformation, 2 μm motor movement accuracy and 10 μm of girder deformation, 1 μm motor movement accuracy are simulated.

The power degradation and the RMS phase shake are shown in the Fig. 6. One can see that the larger error values bring larger RMS phase shake and therefore the power degradation is larger. The largest power degradation value is about 40%. In addition, the large variation in power is mainly due to the random error, as was already shown in Fig. 5. This means that even though the girder deformation is an order of magnitude larger than the random gap error, the power degradation is not dominated by it, which confirms the result shown in Table 1.

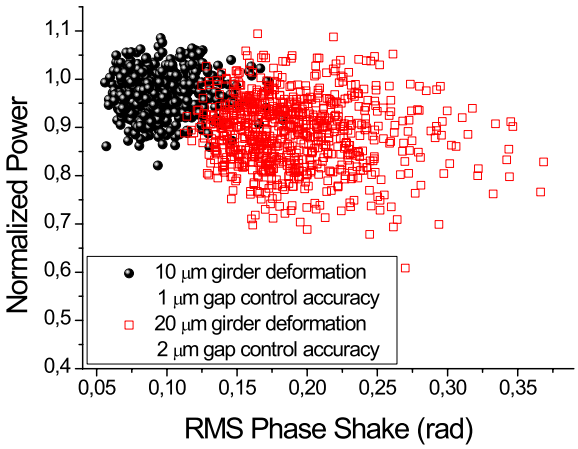

Figure 6: The power reduction due to the combined periodic sinus and random sawtooth/constant error.

Linear temperature gradient and compensation by adjusting the undulator gap

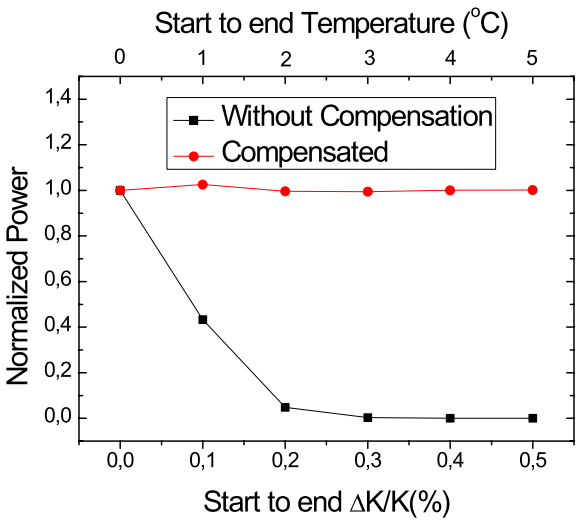

Figure 7: Power reduction due to a temperature gradient over the entire undulatorlength of up to $5\,^o$C and the compensation by an appropriate adjustment of the undulator gap. The gap has been adjusted by 1 μm as soon as the measured temperature exceeds $0.1\,^o$C.

Over the length of the undulator system the temperature may differ. These effects were investigated. From Eq. (1) 0.08^oC are estimated for total temperature variation. This requires a sophisticated air conditioning system with demanding properties. As a simple rule, due to the reversible temperature coefficient of the permanent magnet material 0.1^oC temperature variation corresponds to $\Delta K/K_0 = 10^{-3}$. The effect of the linear temperature variation over the whole undulator system is plotted against the radiation power in Fig. 7, black points. It is seen that a 1^oC variation reduces the power by more than 50%. For 2^oC and above there is no radiated power anymore. An effective way of compensating this effect is to locally correct the undulator gap according to the local temperature. This requires a precise local temperature measurement and a precision temperature sensor on each undulator segment. The local gap is adjusted if a threshold set by the accuracy of the sensor is exceeded. We assume 0.1^oC, which is demanding on an absolute scale. The red points in Fig. 7 show the results. The power loss can be recovered completely.

In terms of Eq. (3) the product $\Delta K/K_0 \cdot \lambda_\delta$ is 0.14 for 1^oC, $\Delta K/K_0 = 10^{-3}$, 140 m error length versus 1.8×10^{-4} for $\Delta K/K_0 = 3.57 \times 10^{-5}$ and 5 m the length of an undulator segment, which is an alternative way of explaining the above result. As shown in Fig. 7 temperature variations as much as 5^oC can be compensated completely.

SUMMARY

Error tolerances for the undulator system of the European XFEL are analyzed in this paper. It has been shown that for non steering errors, the RMS phase shake is a good number to predict the power reduction in an undulator system. For periodic errors the phase shake can be calculated analytically by the product $\Delta K/K_0 \cdot \lambda_\delta$ times a constant depending only on the error shape. Thus for small error period length comparatively large errors can be tolerated, whereas for large error periods the error level are very small. Local temperature measurement and local gap correction was shown to effectively compensate power losses caused by global temperature variation. This method can be effectively used to reduce requirements on temperature stabilization.

REFERENCES

[1] Massimo Altarelli et.al., The European X-Ray Free-Electron Laser Technical Design Report, ISBN 3-935702-17-5

[2] A.M. Kondratenko and E.L. Saldin, Part. Accel. 10, 207 (1980)

[3] R. Bonifacio, C. Pellegrini, and L.M. Narducci, Opt. Commum. 50, 373 (1984)

[4] J. Pflueger, *Undulator Systems and Photon Diagnostics for the European XFEL Project*, Proceedings of the 27th International Free Electron Laser Conference (2005) 378-382

[5] Y. Li, B. Faatz and J. Pflueger, Sutdy of Undulator Tolerances for the European XFEL, TESLA-FEL report 2007-07, DESY, Hamburg.

[6] Y. Li, B. Faatz and J. Pflueger, Magnet Sorting for the XFEL Hybrid Undulator — Comparing Study, presented at this conference

[7] J. Pflueger, M. Tischer, Nucl. Instr. and Meth. **A483** (1999) 388-393

[8] B. Faatz, J. Pflueger, Y.M. Nikitina, Nucl. Instr. and Meth. **A393** (1997) 380-384

[9] B.L. Bobbs et.al, Nucl. Instr. and Meth. **A296** (1990) 574-578

[10] S. Reiche, Nucl. Instr. and Meth. **A429** (1999) 243-248

MCP-BASED PHOTON DETECTOR WITH EXTENDED WAVELENGTH RANGE FOR FLASH

L. Bittner, J. Feldhaus, U. Hahn, M. Hesse, U. Jastrow, V. Kocharyan, P. Radcliffe, E.L. Saldin, E.A. Schneidmiller, K. Tiedtke, B. Timmann, R. Treusch, N. von Bargen, M.V. Yurkov
Deutsches Elektronen-Synchrotron (DESY), Hamburg, Germany
O.I. Brovko, D. Kharlamov, V.I. Lokhmatov, E.A. Matyushevskiy, A.V. Shabunov, E.M. Syresin
Joint Institute for Nuclear Research (JINR), Dubna, Moscow Region, Russia

Abstract

Experimental experience gained at the extreme ultraviolet SASE FEL FLASH (DESY, Hamburg) has shown that successful operation of the facility strongly depends on the quality of the radiation detectors. Here key issues are: wide wavelength range (6 to 100 nm for FLASH), wide dynamic range (from the level of spontaneous emission to the saturation level), and high relative accuracy of measurements which is crucial for detection of a signature of amplification and characterization of statistical properties of the radiation. In this report we describe MCP-based radiation detector for FLASH which meets these requirements. Key element of the detector is wide dynamic range micro-channel plate (MCP) which detects scattered radiation from a target. With four different targets and MCPs in combination with optical attenuators present detector covers operating wavelength range from 6 to 100 nm, and dynamic range of the radiation intensities, from the level of spontaneous emission up to the saturation level of SASE FEL.

INTRODUCTION

The free electron laser FLASH is in operation at DESY since the year 2000 [1–5]. Several upgrades of the facility have been performed, and after an upgrade of 2007 FLASH will cover a wavelength range from 6 to 100 nm. Instrumentation for photon beam characterization has been developed as well [6–11]. An important piece of the photon diagnostics are detectors for measurements of the pulse energy. Originally FLASH has been equipped with PtSi-photodiodes and thermopiles based on YBCO High-Tc-superconductors (HTSCs) [6, 7]. These detectors helped to fix the first signature of light amplification at FLASH [1], but it has been realized soon that they have rather limited possibilities. The first one refers to limited dynamic range, and the other one relates to the physics of interaction of powerful, ultrashort VUV radiation pulses with the detector. In fact, nonlinearities and saturation effects started to occur in PtSi-photodiodes much earlier with respect to calibrations performed with conventional lasers. To solve the problem of limited dynamic range and saturation effects we launched development of MCP-based radiation detector [8], and pretty soon succeeded to tune FLASH to saturation in 2001 [2,3]. An important feature of MCP-detector is high relative accuracy of intensity measurements. This is crucial for detecting the first signature of light amplification and further fine tuning of the machine parameters for increasing the gain. MCP detector is used for measurement of statistical properties of the radiation allowing to determine the pulse length and mode contents of the radiation [12]. In 2004 the energy of FLASH accelerator has been increased to 700 MeV, and a new MCP detector optimized for wavelength down to 10 nm has been installed, and became the primary tool for searching amplification, tuning the gain, and for statistical measurements [4, 5, 9].

In this paper we describe 3rd generation MCP detector at FLASH optimized for the measurement of SASE radiation with the wavelength down to 6 nm.

CURRENT EXPERIENCE WITH MCP-BASED DETECTOR AT FLASH

Photon detectors at FLASH are installed in a beamline downstream the undulator. The most critical step of tuning lasing process is to find the signature of light amplification. The problem relates to a strong background of incoherent radiation produced by the whole bunch (charge 0.5-1 nC)

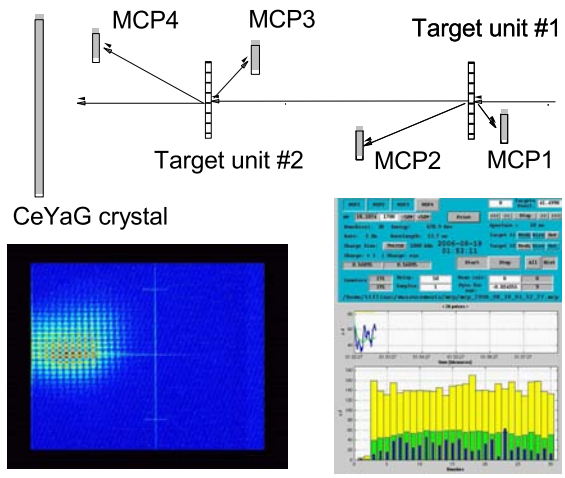

Figure 1: Top: layout of MCP-detector operated at FLASH in 2004-2007 [9]. Detector consists of two identical units for detection of radiation at fixed angles. The targets are semi-transparent gold mesh and gold wire. On-line tuning with this detector allows to have simultaneously quantitative data and visual observation of the photon beam on CeYaG crystal.

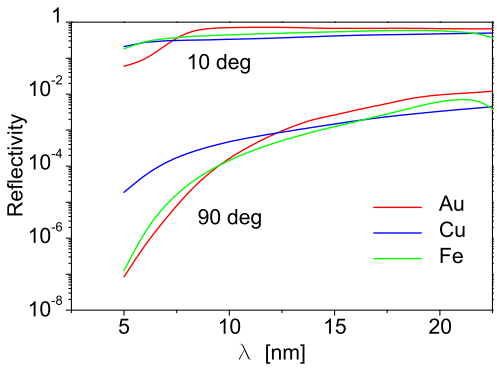

Figure 2: Reflectivies of Au, Cu and Fe versus wavelength for angles of 10 and 90 degrees. Surface roughness is 1 nm [13].

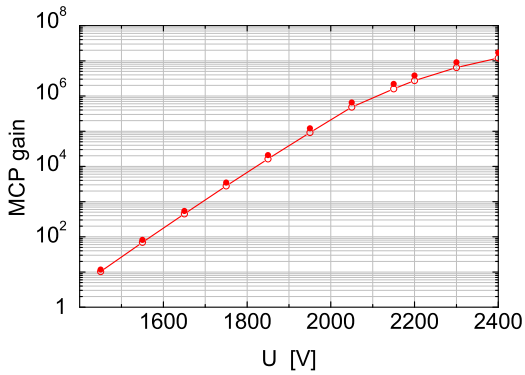

Figure 3: MCP gain versus applied voltage.

passing through the whole undulator length (27 m). In the present experimental conditions, at the energy of electrons of 700 MeV and bunch charge of 0.7 nC the pulse energy of the spontaneous emission is about 40 nJ within the 10 mm aperture of the detector located 18.5 m downstream of the undulator. Thus, it becomes crucial to have high-precision photon detectors permitting the detection of small increases in the radiation intensity. For this purpose a radiation detector equipped with a microchannel plate (MCP) is used [9]. Schematic layout of the detector is shown in Fig. 1. It consists of two identical units, each of them contains removable targets (gold wire of 250 μm diameter and gold mesh with wire of 60 μm diameter, open area 65%) and two MCPs detecting photons at large and small reflection angles. Figure 2 shows reflectivity of the gold for large and small reflection angles. Geometrical positions of MCPs have been chosen such that acceptances of photons (given by convolution of the reflectivity with geometrical factors: reflecting area and angular acceptance) differ by a factor about 300, but overlap at some intermediate light intensity. MCPs detecting backward scattered radiation are

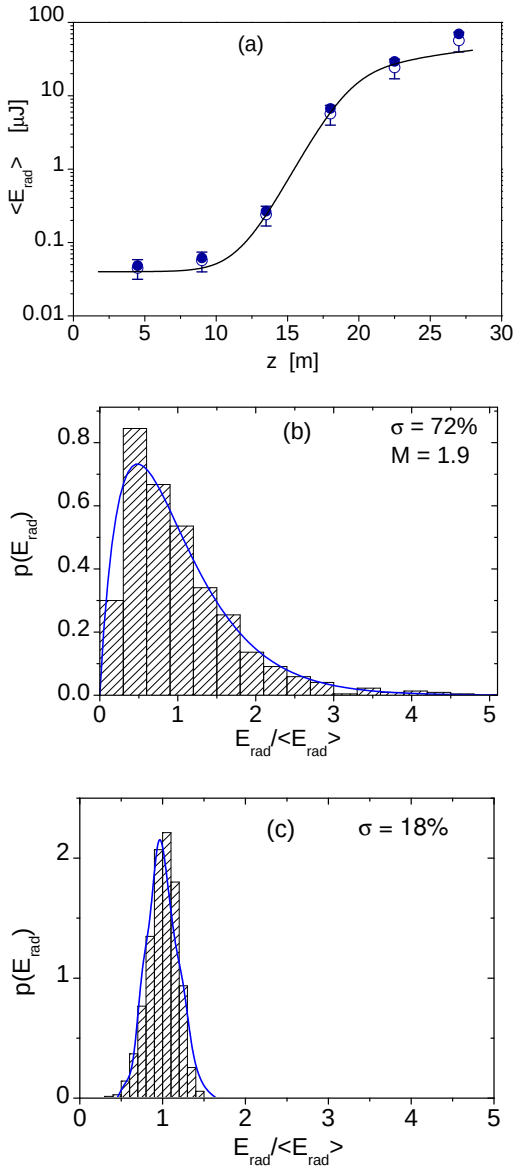

Figure 4: Measured average energy in the radiation pulse versus undulator length (up) showing exponential growth and saturation [5]. Center and lowest panels, probability distributions for the energy in the radiation pulses. Center plot: end of the regime of exponential growth where the average pulse energy is equal to 1 μJ. Lowest plot: saturation regime where the average pulse energy is equal to 40 μJ. Radiation wavelength is 13.7 nm. Solid line on the center plot represents a gamma distribution with the parameter $M = 1.9$. The solid line on the right plot represents simulations with the code FAST [14].

placed very close to the target and accept more photons despite less reflection coefficient. Inspecting the amplification curve of MCP (see Fig. 3) one can wonder why we complicated setup with two different MCPs: one MCP has

very large dynamic range of six orders of magnitude. The choice of such a geometry has been mainly dictated by the following reasons. In the real experimental conditions there is always gamma background originated from the accelerator beamline. In the case of FLASH this background becomes to be significant when high voltage applied to MCP exceeds 1900 V. When light intensity is high, applied voltage needs to be reduced, and below 1400 V space charge effects in MCP channels start to play significant role. Thus, practical operating range of the MCP gain is about three orders of magnitude only, less than the dynamic range of SASE intensity.

The electronics of the MCP-detector itself has low noise, about 1 mV at a level of signal of 100 mV (1% relative measurement accuracy). Another source of disturbances of measurements were fluctuations of the bunch charge. To exclude the influence of bunch charge fluctuations we perform on-line normalization of the radiation energy to the bunch charge. This technique gave us the possibility to detect reliably SASE gain at a 2% level above spontaneous emission. Once amplification is detected, output energy can be easily increased to the level of about ten μJ, the onset of the saturation regime. This occurs due to the exponential dependence of the output signal on a change in any important parameter of the electron beam. Tuning of the radiation energy in the saturation regime above 10 μJ is a delicate procedure, and requires perfect alignment of the orbit in the undulator (on a scale of ten micrometers), and the rf phases of the gun and the first three accelerating modules with relative accuracy of about 0.1 degree.

Absolute calibration of MCP has been performed with spontaneous emission at one operating boundary (nanojoule range of pulse energies), and with gas monitor detector [11] at another operating boundary (from a few to 70 microjoules pulse energies). During experimental run of 2004-2007 years MCP detector demonstrated excellent performance and served as the main tool for SASE search, tuning, intensity characterization and statistical measurements in the wavelength range from 45 to 13 nm (see Fig. 4 from [5]).

We should note that the target of MCP detector (mesh or wire) always produces diffraction pattern resulting in an inhomogeneous intensity distribution at the sample position. Thus, MCP-detector can not be used for online monitoring of the intensity while operating with specific user experiments requiring undisturbed radiation pulse. Gas detector is used in this case [11].

MCP-DETECTOR WITH EXTENDED WAVELENGTH RANGE (MCP07)

For the planned upgrade of the FLASH for operation at 6 nm we also designed and manufactured a new MCP detector. The reason for a new installation is obvious from analysis of reflectivity curve versus the wavelength (see Fig:2). While gold target is perfect for use in the wavelength range above 10 nm, its reflectivity falls dramatically for shorter wavelengths, and different targets and geometry of the detector should be used. General layout of the new detector (MCP07) is shown in Fig. 5. We conserved small/large angle reflection geometry of MCPs which demonstrated to be reliable solution for detection of the radiation above 10 nm.

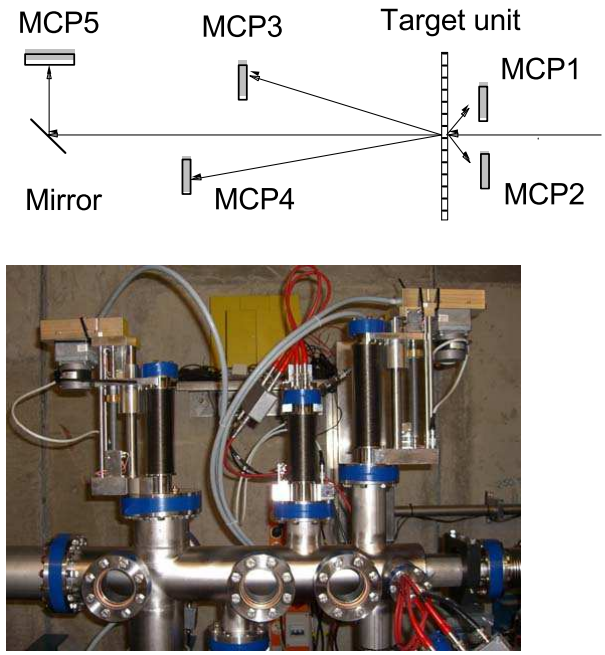

Figure 5: Layout of MCP detector with extended wavelength range installed at FLASH in 2007 (MCP07). Detection of backward reflected radiation is performed with stationary mounted MCP1 a nd MCP2. MCP3 and MCP4 are movable. When positioned off-axis they measure small angle reflected radiation. Measurements of direct photon beam is also possible when positioning MCPs on axis. MCP5 detects radiation reflected by Fe mirror. Target unit contains four grids of different materials (Au, Cu, Fe), and light attenuator.

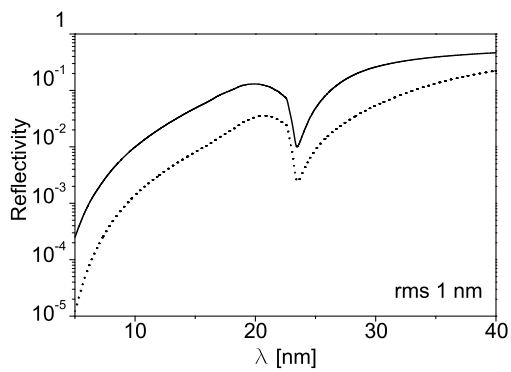

Figure 6: Reflectivies of Fe versus wavelength for angles of 30 and 45 degrees. Surface roughness is 1 nm [13].

Keeping gold mesh, we added three more targets: two iron meshes (88% and 79% open area), and one copper mesh (60% open area). This will help to operate the detector in some range below 10 nm. For tuning SASE at very short wavelengths we assume to use movable MCPs directly facing photon beam. Reduction of the light intensity (if required) will be provided with mechanical attenuator of light (perforated Ni foil located in the target unit, 2% open area). To have full control on light intensity in the wide range we installed side MCP which detects radiation reflected by iron mirror. Mirror serves for two purposes. The first one is to deflect the photon beam off-axis which allows to place MCP in better background conditions. The second function of the mirror is calibrated attenuation of the light (see Fig. 6). With two fixed angles of the mirror (30 and 45 degrees) and with mechanical attenuator we can change the light intensity on MCP in the range of several orders of magnitude. This will allow us to overlap all the range of radiation intensities, from the level of spontaneous emission to the saturation level.

REFERENCES

[1] J. Andruszkow et al., Phys. Rev. Lett. **85**(2000)3825.

[2] V. Ayvazyan et al., Phys. Rev. Lett. **88**(2002)104802.

[3] V. Ayvazyan et al., Eur. Phys. J. D **20**(2002)149.

[4] V. Ayvazyan et al., Eur. Phys. J. D **37**(2006)297.

[5] W. Ackermann et al., Nature Photonics, 1 (2007)336.

[6] R. Treusch, HASYLAB Annual Report, DESY, Hamburg, 2005, p.159-164 (see also http://www-hasylab.desy.de/science/annual_reports/2005_report/index.html).

[7] K. Tiedtke et al., AIP Conf. Proc. **705** (2004)588.

[8] B. Faatz et al., Nucl. Instr. and Meth. A 483(2002)412.

[9] A. Bytchkov et al., Nucl. Instrum. and Methods A **528**(2004)254.

[10] M. Richter et al., Verfahren und Monitordetektor zur Bestimmung der Intensitat von gepulster VUV- oder EUV-Strahlung sowie Verwendung eines derartigen Monitordetektors (Deutsches Patent- und Markenamt, No. 102 44 303.3, Munchen)(2002).

[11] M. Richter et al., Appl. Phys. Lett. **83** (2003)2970.

[12] V. Ayvazyan et al., Nucl. Instrum. and Methods **A507**(2003)368.

[13] Data taken from LBL database

`http://henke.lbl.gov/optical_constants`

[14] E.L. Saldin, E.A. Schneidmiller, and M.V. Yurkov, Nucl. Instrum. and Methods **A 429**(1999)233.

MEASUREMENTS OF PROJECTED EMITTANCE AT FLASH

K. Honkavaara*, Hamburg University, 22761 Hamburg, Germany
F. Löhl, E. Prat, DESY, 22603 Hamburg, Germany

Abstract

FLASH is a SASE FEL user facility at DESY operating with photon wavelengths in the range from vacuum ultraviolet to soft x-rays. Although the slice emittance is a more appropriate parameter to characterize the SASE process, the projected emittance provides a useful measure of the electron beam quality. At FLASH, the projected emittance is measured at three locations along the linac: in the injector (130 MeV), after the collimator, and in the undulator section. The emittance is determined by using a multi-monitor method with OTR monitors and wire scanners. In this paper we describe the measurement set-up and procedure, and report recent results.

INTRODUCTION

FLASH is a SASE FEL user facility at DESY (Hamburg, Germany). It produces short (in order of 10 fs) laser like pulses in the wavelength range from the vacuum ultraviolet to the soft X-ray [1].

Figure 1 shows a schematic layout of the FLASH linac as operated in 2006 and the first half of 2007. Electron bunch trains with up to 800 bunches are generated by a laser-driven RF gun. The macro-pulse repetition rate is 5 Hz, and the bunch frequency 1 MHz. During the measurements reported here, the linac is operated with one or two bunches per bunch train. The bunch charge is 1 nC.

Five accelerating modules, with eight 9-cell superconducting TESLA cavities each, provide electron beam energies up to ∼730 MeV. The electron bunch is compressed by two magnetic chicane bunch compressors. At the location of the first bunch compressor, the beam energy is ∼130 MeV, and at the second one ∼370 MeV. During the measurements reported here, the total beam energy after acceleration is ∼500 MeV. The SASE radiation is produced by six undulator modules with length of 4.5 m each.

The SASE process requires a high quality electron beam in terms of transverse emittance, peak current and energy spread. In the characterization of this process, the slice parameters are the appropriate parameters to consider. However, also the projected emittance, which is relatively easy to measure compared to the slice emittance, provides an important measure of the electron beam quality. In addition to be able to produce a small emittance beam at the injector, it is important to conserve this small emittance up to the undulator, where the SASE radiation is produced.

* katja.honkavaara@desy.de

In this we paper describe the emittance measurements performed at three location along the FLASH linac: at the injector, after the collimation section and at the undulator. These measurements are also discussed in [2].

EXPERIMENTAL SET-UP

We measure the transverse projected emittance using a multi-monitor method. This method is based on measurements of the transverse beam distribution (shape and size) at several locations with fixed beam optics.

There are two diagnostic sections dedicated to emittance measurements along the FLASH linac (see Fig. 1). The first one is located downstream of the first bunch compressor. This section has four OTR (optical transition radiation) monitors combined with wire scanners mounted into a FODO lattice of six quadrupoles with a periodic beta function. Below, we refer this section as the 'BC section'. A second FODO lattice with four OTR monitors is located upstream of the undulator, referred here as the 'SEED section'. A fifth OTR monitor placed upstream of the FODO lattice is used as an additional monitor in the measurements. Along the undulator, the emittance is measured using wire scanners located in front of each undulator module. A seventh wire scanner station is downstream of the undulator.

OTR monitors

OTR monitors are based on detection of backward optical transition radiation. The OTR light is emitted when the electron beam passes through an aluminium coated silicon screen inserted at an angle of 45° with respect to the beam trajectory. The ligth is deflected downwards into an optical set-up consisting of three achromat doublet lenses, three neutral density filters, and a digital CCD camera. Each lens provides a fixed magnification, and can be remotely moved in and out of the optical axis. For accurate measurements we use the lens with the highest magnification (1:1). With this lens the measured resolution is 11 μm rms.

The digital CCD cameras with a firewire interface are connected to a PC in the accelerator tunnel. The PC is connected via local Ethernet to an "image server" in the control room. The read-out system, using a LabView based control software, provides beam images for the on-line visualization and for different applications.

More details of the OTR monitor system are in [3, 4].

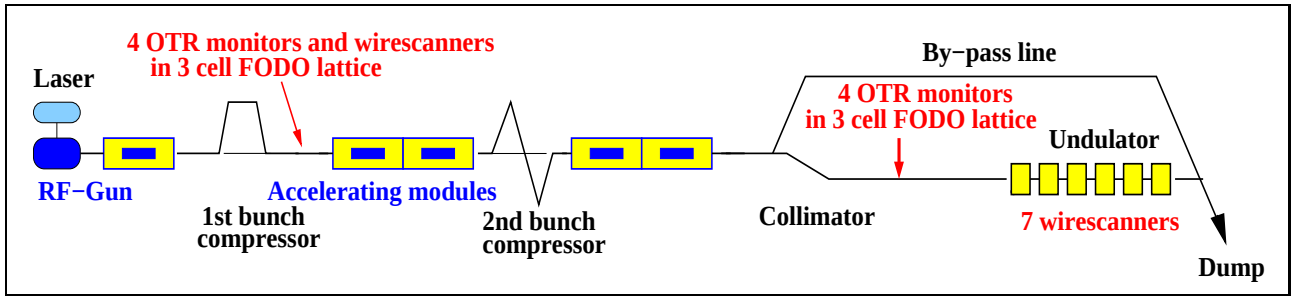

Figure 1: Layout of the FLASH linac (not to scale). Beam direction is from left to right, and the total length is about 250 m. Locations of OTR monitors and wire scanners, used for the emittance measurements, are indicated.

Combined OTR and wire scanner monitors

The OTR monitors in the BC section are combined with wire scanners. Each scanner has a fork with three tungsten wires with a diameter of 18 μm. The wires are oriented such that one of them scans horizontally and another one vertically; the third wire provides information of the coupling between the two planes. The wire scanner is mounted into a common vacuum chamber with an OTR screen, located 5 mm downstream of it. The read-out system, consisting of scintillator panels and photomultipliers, detects secondary particles emitted when the wire passes the electron beam.

In the emittance measurements reported here, we used the OTR monitors only. However, a cross check between profiles measured by the OTR monitors and the wire scanners have been performed showing a good agreement [5].

Undulator wire scanners

Seven wire scanner stations are mounted along the undulator. Each of these stations has two individual wire scanners: one scanning in horizontal direction, and the other one in the vertical. Each scanner has three wires: a 10 μm thick carbon wire, and two tungsten wires with diameters of 10 μm and 50 μm . The read-out is based on detection of secondary emission particles measured with scintillator panels and photomultipliers. More technical details of the undulator wire scanners are in [6].

MEASUREMENTS AND ANALYSIS

During an emittance measurement with OTR monitors, we record 20 beam and background images for each OTR screen. The averaged background is subtracted from each beam image. After that, a sophisticated image analysis procedure is applied to each image [7].

Not only the emittance of the entire beam, but also the emittance of the high density core is of interest. We determine this core by cutting away 10% (an arbitrary choice) of particles in the tails of the two dimensional transverse beam distribution. After that, the horizontal and vertical rms beam sizes of the entire beam and of the 90% core are calculated. These rms sizes are used to calculate the emittance.

In the case of wire scanners, the beam profile is recorded over several macro-pulses (one point per macro-pulse), and only one profile is used when determining the beam size. The rms size of the entire beam is used in the emittance calculations.

The transverse emittance is determined from the measured beam sizes and the transport matrices between the monitors using a least square fitting. A second method is a tomographic reconstruction of the phase space using the maximum entropy algorithm. The results obtained by both methods agree well [7]. Since the fitting technique is faster, we use it in our measurements.

EXPERIMENTAL RESULTS

The projected emittance in the BC section has been routinely measured since early 2005. The emittance measurement procedure is well understood, and we have performed systematic studies on the dependence of the emittance on different machine parameters. A detailed description of these measurements, results and error analysis is in [8].

In the two other sections accurate emittance measurements have been possible only since the beginning of 2007.

Table 1 shows the measured projected emittance at three locations along the FLASH linac. All of the three measurements have been performed within a few hours with the same machine conditions. The second column (Day 2)

	Day 1		Day 2	
Location	ϵ_x	ϵ_y	ϵ_x	ϵ_y
BC	3.7 (2.0)	3.2 (2.0)	3.7 (2.4)	3.8 (2.5)
SEED	3.7 (2.2)	4.7 (3.2)	2.7 (2.0)	3.0 (2.2)
Undulator	4.4	4.1	4.3	4.4

Table 1: Projected emittances measured at three locations along the FLASH linac in two different days. The presented values are normalized rms emittances in units of mm mrad. The value in the bracket is the rms emittance of the 90% beam core. Estimated error of the measured emittances is 0.5 mm mrad.

shows the same measurements repeated 4 weeks later. The presented values are normalized rms emittances of the entire beam. In the BC and SEED sections, where the measurements have been performed using OTR monitors, the rms emittance of the 90% beam core is presented as well. In all the cases, the electron beam charge is 1 nC and the electron beam is accelerated on-crest through the accelerating modules.

The error analysis, taking into account errors in the measured beam size, in the beam energy, and in the transverse matrices, leads to an error estimation of 0.5 mm mrad for the measured emittance values.

No substantial change in the projected emittance can be observed along the linac (Table 1). Similar results have been obtained also on other days, when the linac has been well-tuned.

During these measurements, our goal was not to optimize the emittance but to study the emittance transport. In well optimized conditions, a projected emittance below 2 mm mrad in the BC section has been measured [8].

TECHNICAL ISSUES

The last OTR screen in the SEED section is located only a few meters upstream of the undulator. Losses created when the beam passes through the screen are so high that they may cause degradation of the permanent undulator magnets. Recently, this problem has been solved by mounting a deflecting magnet and a lead shield after the last screen.

At high electron beam energies, the emitted OTR light is concentrated in a very narrow cone. As a consequence, the alignment of the OTR monitors becomes critical. During the measurements in the SEED section, we have observed low beam spot intensities on some of the screens. Especially when the beam is not well-optimized, the intensity depends on the position of the spot on the screen. This indicates a misalignment of the system. During the shutdown in spring 2007, the OTR monitors have been replaced by combined OTR and wire scanners monitors (similar to the ones in the BC section). In addition, the OTR monitors have been realigned.

Matching of the beam to the FODO lattice is important for accurate emittance measurements [8]. In the BC and SEED sections matching works well. In the undulator section, however, it is difficult due to the fact that the so-called transfer matrix condition number is large, an order of magnitude larger than in the BC section. As a consequence, a small error in the measured beam size may lead to a large error in the calculated emittance and Twiss parameters. An additional complication is caused by the small undulator aperture. The beam tube inside the undulator has a diameter of about 10 mm only. In order to avoid losses due to too large beam sizes or missteering of the the beam, matching must be done carefully. Matching has been improved by using more quadrupoles with less changes in the currents, and by cycling the magnets after each matching iteration. We have also observed that the matching to the undulator works better, when we use the sigma of a Gaussian fit instead of the rms beam size as input for the Twiss parameter calculation.

Saturation of the photomultiplier signal has been another problem when measuring the emittance in the undulator. The photon shower generated by the electron beam is squarely proportional both to the wire diameter and to the atomic number of the wire material. As a consequence, when using a 50 μm tungsten wire the amount of light input to the photomultiplieris much larger than with a 10 μm carbon wire. The used photomultiplier has a nonlinear behavior when the light input is too large. This causes an increase of the measured beam size, which leads to an increase of the measured emittance. In order to avoid this artificial increase, the measurements presented here are performed by using the carbon wire only. During the shutdown, filters with an attenuation factor of 32 have been mounted in front of each photomultiplier. This should allow us to use the tungsten wires as well.

SUMMARY AND OUTLOOK

The projected emittance along the FLASH linac has been measured at three locations. No substantial change of the emittance has been observed.

During the shutdown in spring and summer 2007, a sixth accelerating module has been installed in the FLASH linac. This, together with the upgrades of the other accelerating modules, will provide beam energies up to 1 GeV in the near future. We have improved our measurement system in the SEED and undulator sections. In the SEED section, the OTR monitors have been replaced by the combined OTR and wire scanner monitors. In the undulator, attenuators are installed in front of the wire scanner photomultipliers.

Studies on the emittance transport will continue in autumn 2007.

ACKNOWLEDGMENT

We thank the colleagues and the technical staff of DESY (Hamburg and Zeuthen), and of INFN (LNF and Roma Tor Vergata) contributing in the realization and maintenance of the OTR and wire scanner systems. Special thanks are due to M. Sachwitz, A. Wipprecht, P. Castro and L. Fröhlich for studies on the undulator wire scanners, especially concerning the saturation problems. We like to thank V. Balandin and N. Golubeva for their work on the beam optic tools and fruitful discussions on matching problematic in the undulator section. Thanks are also due to W. Decking, T. Limberg and S. Schreiber for many interesting discussions and useful suggestions.

REFERENCES

[1] W. Ackermann *et al.*, "Operation of a free-electron laser from the extreme ultraviolet to the water window", Nature Photonics **1** (2007) 336-342

[2] E. Prat *et al.*, "Beam profile measurements and analysis at FLASH", PAC 2007, Albuquerque, New Mexico, June 25-29, 2007

[3] K. Honkavaara *et al.*, "Design of OTR beam profile monitors for the TESLA Test Facility, phase 2 (TTF2)", PAC 2003, Portland, Oregon, May 12-16, 2003

[4] L. Catani *et al.*, "A large distributed digital camera system for accelerator beam diagnostics", Review of Scientific Instruments **76**, 073303 (2005)

[5] K. Honkavaara *et al.*, "Transverse electron beam diagnostics at the VUV-FEL at DESY", FEL 2005, Stanford, California, August 21-26, 2005

[6] M. Sachwitz *et al.*, "Wire scanners in the undulator section of the VUV-FEL at DESY", DIPAC 2005, Lyon, France, 6-8 June, 2005

[7] F. Löhl, "Measurements of the transverse emittance at the VUV-FEL", DESY-THESIS 2005-014 and TESLA-FEL 2005-03, Diploma Thesis, Hamburg University, 2005

[8] F. Löhl *et al.*, "Measurements of the transverse emittance at the FLASH injector at DESY", Phys. Rev. ST Accel. Beams **9**, 092802 (2006)

RECENT MEASUREMENTS OF THE LONGITUDINAL PHASE SPACE AT THE PHOTO INJECTOR TEST FACILITY AT DESY IN ZEUTHEN (PITZ)*

J. Rönsch†, J. Rossbach, Hamburg University, 22761 Hamburg, Germany
G. Asova‡, J.Bähr, C. Boulware, H. J. Grabosch, M. Hänel, Y. Ivanisenko§, S. Khodyachykh, S. Korepanov, M. Krasilnikov, S. Lederer, B. Petrosyan, A. Shapovalov¶, T.Scholz, L. Staykov, R. Spesyvtsev‖, F. Stephan, DESY, 15738 Zeuthen, Germany
D. Richter, BESSY, 12487 Berlin, Germany
K. Rosbach, Humboldt University Berlin, 12489 Berlin, Germany
L. Hakobyan, YerPhI, Yerevan, Armenia
A. Onuchin, Budker Institut of Nuclear Physics, Novosibirsk 630090, Russia

Abstract

The Photo Injector Test facility at DESY in Zeuthen (PITZ) was built to test and optimize electron guns for short wavelength Free-Electron Lasers (FELs) like FLASH and XFEL at DESY in Hamburg. For a detailed analysis of the behaviour of the electron bunch, the longitudinal phase space and its projections can be measured behind the gun cavity. The electric field at the photo cathode was increased from 40 MV/m to 60 MV/m to optimize the transverse emittance. The momentum distributions for different gradients and gun phases will be presented. In order to study emittance conservation, a booster cavity and additional diagnostics were installed. The evolution of the longitudinal phase space in the booster cavity will be investigated. Measurements of the momentum distribution and longitudinal distribution behind the booster cavity will be discussed.

INTRODUCTION

The main goal of PITZ is to test and to optimize L-Band RF photo injectors for Free-Electron Lasers. The requirements on such a photo injector are small transverse emittances, charge of about 1 nC, short bunches (FWHM of about 20 ps) and the possibility of long bunch trains of 800 pulses emitted with a frequency of 1 MHz. The heart of PITZ is a copper gun cavity with a solenoid magnet that is used to focus the beam. Detailed analyses of the gun cavity at a gradient of 40-45 MV/m were presented in [1, 2, 3]. In order to decrease the effects of space charge forces and thus decrease the transverse emittance, the gradient at the cathode was increased to 60 MV/m. Experience of the conditioning and the first run period at high gradient are presented in [4, 5]. In this paper the influence of the higher gradient on the momentum distribution will be discussed.

MOMENTUM

In order to understand the behaviour of the gun for higher gradients at the cathode, measurements and simulations for different gradients were done. Figure 1 shows measurements and simulations of the maximum mean momentum reached for different powers in the gun. The trend

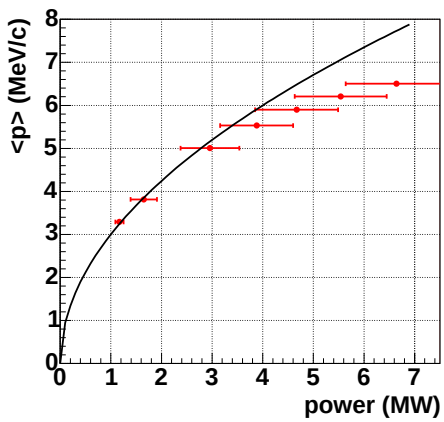

Figure 1: Measured mean momentum as a function of the power in the gun (red dots). the black curve describes the expectation, it is fitted with the square root of the power.

of the measured mean momentum fits to the expectations up to a power in the gun of about 3.5 MW. For higher powers the mean momentum stays below the expectation. The power in the gun cannot be measured directly in the gun and the error of the power measurement is quite large (± 0.5 MW). One possible explanation would be that the measurement of power the is not correct, it is for example possible, that it measures higher order modes or the cavity is misshapen and field balance could change. Another possibility is, that we are loosing power between the point of

* This work has partly been supported by the European Community, contract numbers RII3-CT-2004-506008 and 011935, and by the 'Impuls- und Vernetzungsfonds' of the Helmholtz Association, contract number VH-FZ-005.

† jroensch@ifh.de
‡ On leave from INRNE, Sofia, Bulgaria
§ On leave from IERT, Kharkov, Ukraine
¶ On leave from MEPHI, Moscow, Russia
‖ On leave from NSCIM, Kharkov, Ukraine

power measurement and the gun, for example in the coupler due to misalignment.

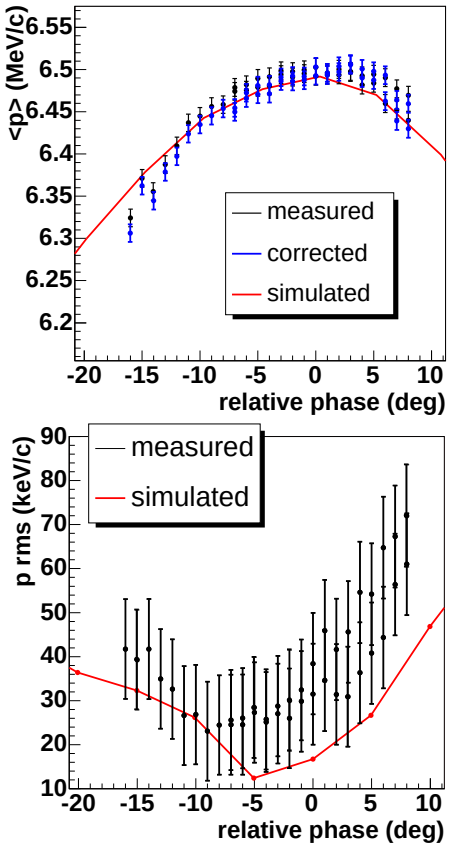

Figure 2: Mean momentum (top) and momentum spread (bottom) as a function of the gun phase.

The maximum mean momentum reached in the gun was about 6.5 MeV/c. Figure 2 shows a measurement and the corresponding simulation of the mean momentum (top) and momentum spread (bottom) as a function of the gun phase. The phase with maximum mean momentum gain was defined as zero for both measurement and simulation. Simulation and measurement of mean momentum fit not completely. The measured momentum spread is larger than the simulation, one reason for the large error bars that the subtraction of the background (dark current), whose momentum is very close to the one of the beam, is not perfect. Another point is that the phase of the minimum is different for measurement and simulation. Due to the large error bars this effect is not so clear in this graph and has to be investigated in more detail.

For the gun phase with maximum momentum gain of 6.4 MeV/c, the momentum was measured after the booster cavity for different booster phases and settings. Figure 3 shows the measured mean momentum and momentum spread of the electron beam as a function of the booster phase for different power (0.6 and 1.9 MW) in the booster. The phase with the smallest momentum spread is in both cases: phase with maximum energy gain - 5 deg. There is a

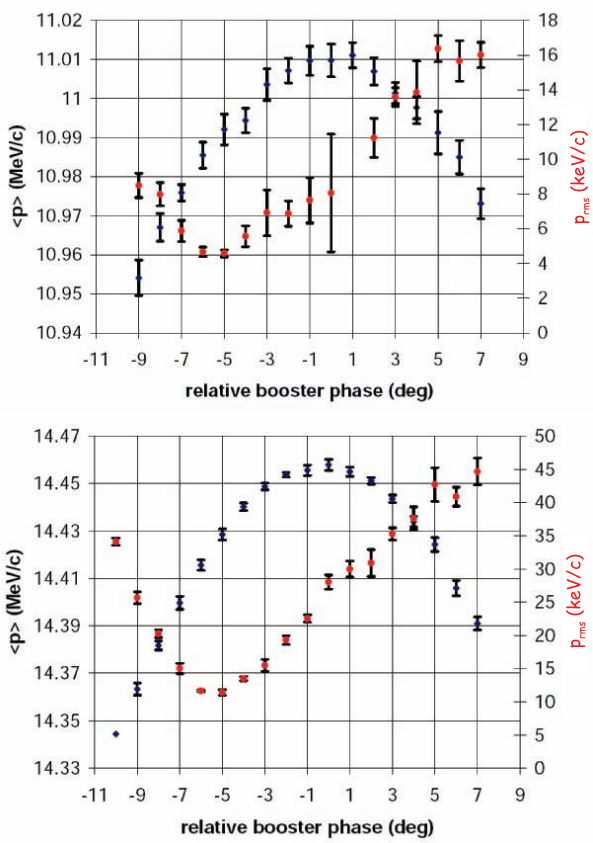

Figure 3: Mean momentum and momentum spread as a function of the booster phase for about 0.6 (top) and 1.9 MW (bottom) in the booster.

strong difference in the value of the momentum spread for the two cases. This might be due to some incorrect setting of the camera or wrong focusing. It was also seen that the YAG-screen, which were used for the measurements were burned, this could falsify the results. More detailed studies have to be performed.

LONGITUDINAL DISTRIBUTION

A screen station (HIGH1.Scr2) for the measurement of the longitudinal distribution of the electron bunch was installed about 1.4 m downstream the exit of the booster cavity (about 5 m downstream the cathode). For the measurement of the bunch length aerogel (n = 1.008), an optical transmission line and a streak camera is used. It was designed such that bunch length measurements can be done with booster cavity turned on and off, i.e. a momentum range from 5 to 40 MeV/c is covered [6]. First measurements were done in the summer of this year with and without booster cavity. Figure 4 shows the measured and simulated rms bunch length done without booster at an energy of about 6 MeV/c for a charge of about 0.6 nC within the measurement range. The phase with the highest momentum gain was determined using dipole magnet and is set to zero in the graph. Unfortunately, it was not possi-

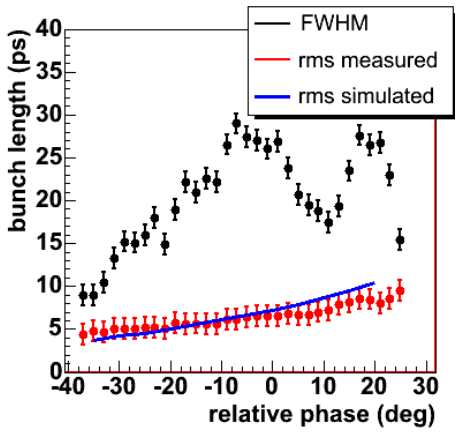

Figure 4: Measurements and simulations of the electron bunch length as a function of the gun phase

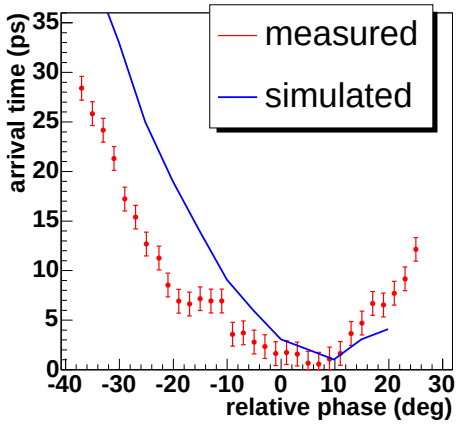

Figure 6: Relative arrival time of the bunch at the streak camera.

ble to make comparable measurements at screen station for bunch length measurement before the booster (about 1.7 m downstream the cathode) due to radiation damage of some components. The rms value is increasing with the phase. The full width half maximum (FWHM) behaves differently. The FWHM is large around the phase with the highest momentum gain (-7 deg to 2 deg), while the rms value is medium range. A large FWHM can be found for higher phases as well, but the rms value of the bunch length is also large. Figure shows the longitudinal distribution for three cases for a better understanding of curve. For the phase

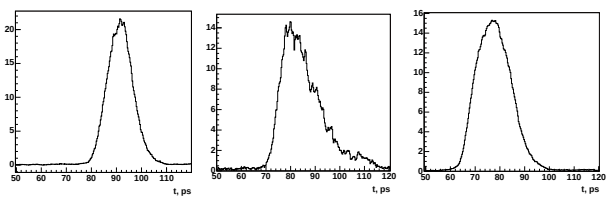

Figure 5: Longitudinal distribution of the electron bunch for phase with maximum mean momentum gain -30 deg +0 deg and 20 deg

with maximum momentum gain (0 deg) the FWHM and the rms values is larger than for -30 deg. This leads to a higher peak current for -30 deg. For 20 deg the FWHM is large, but the rms values as well, due some long tail of the distribution. So cases with large FWHM and and small rms-values is favourable, since the charge is distributed more homogeneous and the influence of space charge forces can be reduced.

The arrival time of the bunches as a function of the gun phase in plotted in figure 6. Here one can see a difference in the arrival time between simulation and measurement. This difference in phase between measurement and simulation is comparable to the one we see in the curve of the momentum spread (Fig. 2). This could be a hint for a systematical error in the set up, but this could be also cause by a shift in the phase during the measurement.

Figure 7 shows the measured and simulated rms bunch length at an energy of about 16 MeV/c, for the gun phase with the highest energy, as a function of the booster phase. The booster phase with the maximum momentum gain was defined as 0 deg. The measurement cover a large phase range (120 deg). The rms bunch length stays almost con-

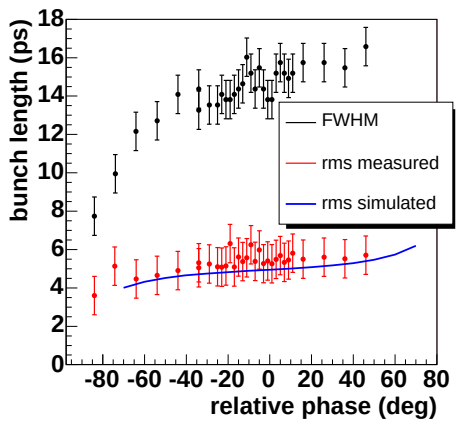

Figure 7: Measurements and simulations of the electron bunch length as a function of the booster phase

stant over a large range around the phase with the maximum momentum gain. For an off-crest the bunch length changes stronger. Figure 8 shows the arrival time of the bunch for the same measurement. Measurement and simulation fit well within the range of -60 to 10 deg. Starting for 10 deg the measurement shows an unexpected behaviour, but the values in the plot of the bunch length seems to be reasonable. It seems to be a measurement artefact, maybe there was a jump in the delay of the streak camera.

SUMMARY

The measurement of mean momentum, momentum spread upstream and downstream the booster was presented. Observed problems and inconsistencies were de-

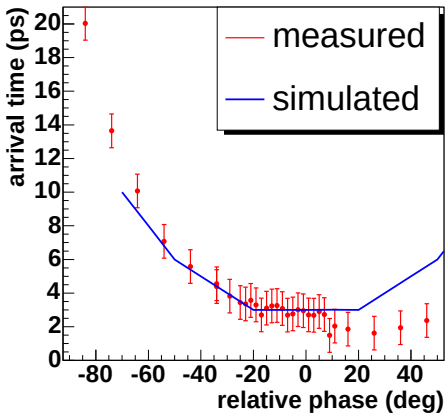

Figure 8: Relative arrival time of the photon pulse produce by the electron bunch at the streak camera as a function of the booster phase. This is assumed to be equal with arrival time of the electron bunch at the screen station

scried and have to be analysed further to understand in detail the problems of this gun and to avoid them in future. A new screen station for the measurement of bunch lengths was put into operation successfully, first measurements were presented and discussed.

REFERENCES

[1] V. Miltchev et al., "Transverse emittance measurements at the photo injector test facility at DESY Zeuthen", FEL'04, Elettra , Triestre, Italy, 2004.

[2] D. Lipka, "Investigations about the longitudinal phase space at a photo injector for minimized emittance", PhD Thesis 2004 Humboldt University Berlin

[3] M. Krasilnikov et al., "Characterization of the electron source at the photo injector test facility at DESY Zeuthen", NIM A 528(2004)360-365.

[4] S. Lederer et al., "Conditioning of a new Gun Cavity Towards 60 MV/m at PITZ", PAC'07, Albuquerque, NM, USA, 2007.

[5] S. Rimjeam et al., "Status and Perspectives of the PITZ Facility Upgrade", FEL'07, Budker Institut of Nuclear Physics, Novosibisk, Russia, 2007.

[6] J. Rönsch et al., "Investigations of the Longitudinal Beam Properties at the Photoinjector Test Facility in Zeuthen", FEL'06, BESSY, Berlin, Germany, 2006.

PHOTOCATHODE LASER PULSE DIAGNOSTICS AT PITZ*

M. Hänel#, J. Bähr, Y. Ivanisenko+, S. Korepanov, M. Krasilnikov, F. Stephan,
DESY Zeuthen, Germany

Abstract

The main objective of the Photo Injector Test facility at DESY in Zeuthen (PITZ) is the development of electron sources that meet the requirements for existing and future FELs such as FLASH or the European XFEL. The goal is the minimization of the transverse emittance of the produced electron bunches. In this respect one of the key issues is the cathode laser system, which should provide longitudinal and transversal flat-top pulses with an excellent long-term stability. In this work we present the full system of laser diagnostics that is currently used at PITZ to monitor the laser pulse parameters.

INTRODUCTION

Laser systems of photo injectors play a crucial role for generating electron bunches with optimum transverse emittance. In our case the laser must produce pulse trains with a repetition rate of 10Hz consisting of up to 800 micro pulses with 1MHz repetition rate. The laser pulses wavelength is 262nm and they have a temporal flat-top shape (FWHM 20ps, rise-/fall-times 6-8ps) as well as a transverse flat-top profile. To extract the required charge of 1nC from the photocathode (Cs_2Te) the laser must provide pulses with an energy of at least 1µJ (for 0.5% quantum efficiency). For further details on the laser system which was developed by the Max Born institute Berlin see [1].

In this paper we present the diagnostics system that is used to monitor the key laser parameters accompanied by recent results.

TEMPORAL LASER PROFILE

The currently used laser system is able to produce flat-top pulses (FWHM 20ps, rise-/fall-times 6-8ps) in the UV utilizing a pulse shaper which consists mainly of a grating stretcher and two birefringent crystals. The effects of the pulse shaper, the subsequent amplification stages, and the conversion of the infrared light into the UV combine to generate flat-top pulses. For tuning the temporal laser shape one can adjust the rotation angles of the birefringent crystals as well as their temperatures. For a detailed description on this pulse shaping technique see [2].

To measure the temporal profile of the laser pulses, a streak camera is used which has a temporal resolution of about 2ps in the UV (Hamamatsu C5680). In addition the measurements of the streak camera can be evaluated using a Matlab script which provides key parameters of the pulse from a fit procedure, i.e. the FWHM, rise- and fall-times as well as the depth of the modulations on the flat-top. Long-term observations show that this method of pulse-shaping is very robust due to its simplicity.

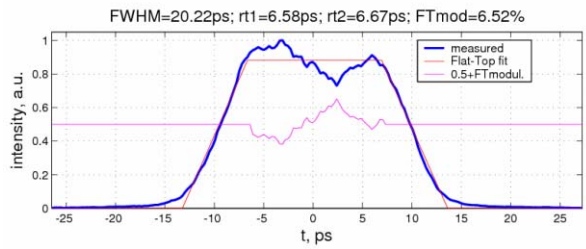

Figure 1: Typical temporal laser pulse shape used during 2007 run period evaluated by the mentioned Matlab script

SPATIAL LASER PROFILE

The spatial flat-top shape of the laser pulses is generated by cutting out a round spot from the center of the widened Gaussian intensity distribution which is produced by the laser. To provide various spot sizes a plate with several apertures of different diameters is mounted on a motorized stage which is remotely controllable. This almost flat-top distribution is then relay imaged onto the photocathode.

For monitoring the transverse profile three different virtual cathodes are used each having the same optical path length as the pulses to the real cathodes have. Two of these virtual cathodes are cameras with a rest-sensitivity in the UV so that the pulses can be shone directly onto the CCD chip. These cameras can be used in different intensity regimes due to different attenuations. The third virtual cathode consist of a Ce:YAG plate which converts the ultraviolet light to visible light. This virtual cathode was introduced recently to develop a method of measurement which does not rely on the rest-sensitivity of the CCD cameras in the UV. Experience shows that this sensitivity rapidly becomes inhomogeneous across the CCD chip. The method using Ce:YAG plates is described in a separate section.

In figure 2a one can see a typical image of the transverse laser profile shown in false colors. Figure 2b displays the same profile in a more intuitive 3D-representation. These images were taken using the direct measurement by shining the laser on the CCD chip. This method has a great disadvantage. Using standard settings for the shutter speed (1/60s) results in smear out effect for the profile. Instead of the one shown in figure 2 one meas-

*This work has partly been funded by the European Community, contract no. RII3-CT-2004-506008 and 011935 and by the 'Impuls- und Vernetzungsfonds' of the Helmholtz Association, contract no. VH-FZ-005.

#marc.haenel@desy.de
+on leave from IERT Kharkiv, Ukraine

ures a profile with less structure and a big halo around the center spot which makes it hard to determine the correct beam size. The reasons for this behavior are not clear and will be investigated.

Because the smear out effect appears to be a slow process the shown profile was measured using a shutter speed of 2µs and the timing was set such that only the first pulse of the train is captured. The shown image is the average over 100 frames.

For this measurement an aperture of 1.2mm diameter was used. The RMS values for x and y differ due to the non symmetric distribution and are slightly higher than the real one because of the position jitter (see corresponding paragraph). The RMS of the flat-top intensity distribution is 7.5%.

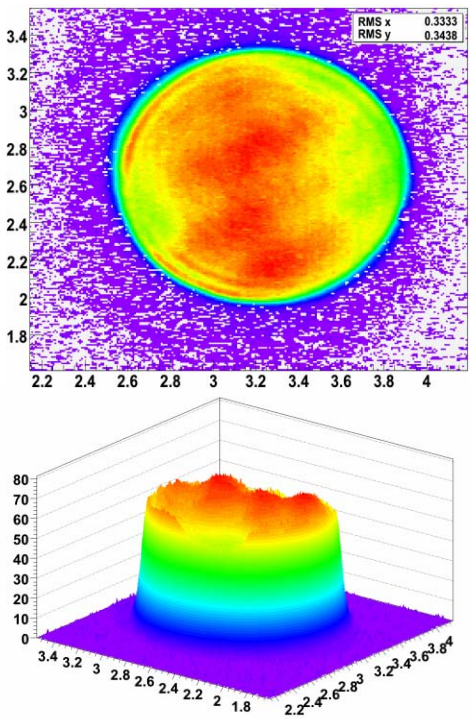

Figure 2a (upper): Transverse laser profile as seen by one of the virtual cathodes.
Figure 2b (lower): The same profile in 3D-view
values on the x and y axes are in mm, z axis is arbitrary intensity.

Measurements with Ce:YAG - plate

The optical scheme for measuring the transverse profile of the laser pulses using the fluorescence properties of Ce:YAG is depicted in figure 3. The laser is directed onto the plate and a part of the ultraviolet light is converted to a broadband signal in the yellow-green wavelength region. The profile in the Ce:YAG plate is imaged onto a CCD-chip by use of a commercial objective. The remaining ultraviolet light is absorbed by the lenses of the objective (BK7).

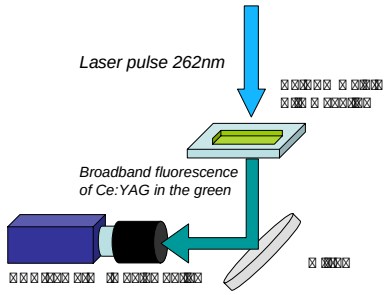

Figure 3: optical setup for the measurement of the transverse laser shape using Ce:YAG

The measurements were performed with three Ce:YAG plates all having the same geometric shape. The surfaces were uncoated. In figure 4 transverse profiles for different plates and positions on the plates are displayed. On every picture pronounced interference structures are visible. These structures vary with position and are different for every Ce:YAG plate. From these pictures one can conclude that it is not possible to get reliable information about the transverse pulse shape by use of this method.

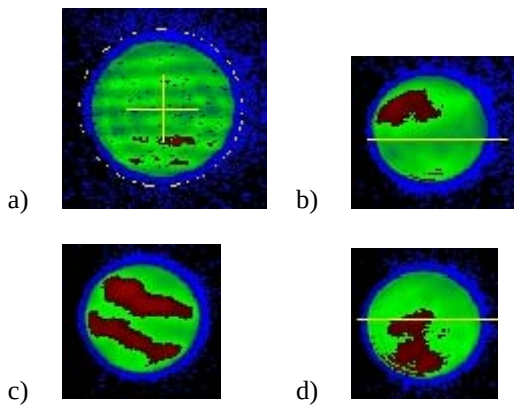

Figure 4: images of the transverse profile for two Ce:YAG - plates and different positions on the plate
a) 1.8mm aperture, 1st plate, pronounced horizontal interference stripes are visible due to non parallel surfaces
b) - d) 1.2mm aperture, 2nd plate, same conditions of the laser but different positions on the plate

The next step is to provide the Ce:YAG plates with an antireflective coating on each surface for further investigation.

LASER PULSE ENERGY JITTER

Besides possibilities to measure the laser pulses energies at the laser output it is more important to know how much energy is actually impinging on the photo cathode. This energy is less than 20% of what the laser produces due to the losses in the beam line which are mainly introduced by the beam shaping apertures. Therefore a photomultiplier tube is used which measures a strongly attenuated part of the beam that is coupled out before the laser enters the vacuum of the gun. Photomultiplier tubes have several advantages. They can provide a linear re-

sponse over a large range of laser pulse energies, they are able to measure at 1MHz repetition rate and by changing the drive voltage the actual amplification can be chosen from several orders of magnitude.

To be able to calibrate the signal of the photomultiplier another measurement device is used. This is based on a commercially available UV sensitive photo diode together with an energy-meter which are externally calibrated and can be read out remotely via RS232 connection (Ophir NOVA II, PD10-pJ-SH-V2). This photo diode is only capable of measuring a repetition rate of 10kHz at maximum. Therefore it cannot be used directly to measure the laser pulse energies within the train. Averaging the signals of both devices for one pulse per train gives the calibration factor.

In Figure 5 the laser pulse energy distribution within a pulse train consisting of 40 pulses is displayed. Every data point represents the averaged energy for the corresponding pulse. The mean value is 54.34 in this case arbitrary units.

As a general criterion for the energy stability one can

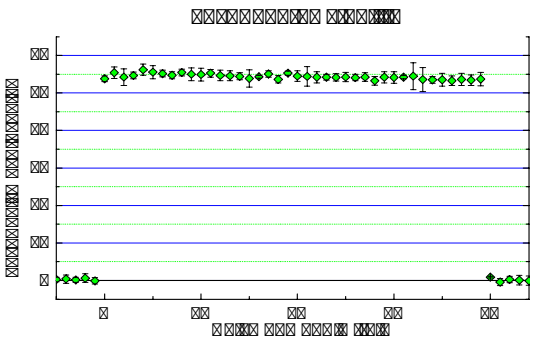

Figure 5: Laser pulse energy for every single pulse in a train of 40 pulses evaluated over 50 trains. The dots show the mean value and the error bars represent the RMS value of the energy for each single pulse.

calculate the overall RMS for all pulses in all measured trains. This turns out to be 1.46 and corresponds to 2.7% pulse energy jitter but contains also a possible slope within the trains. Therefore the average RMS jitter for a single pulse is smaller and was calculated to be 2%. The RMS of the mean values is 1.3%.

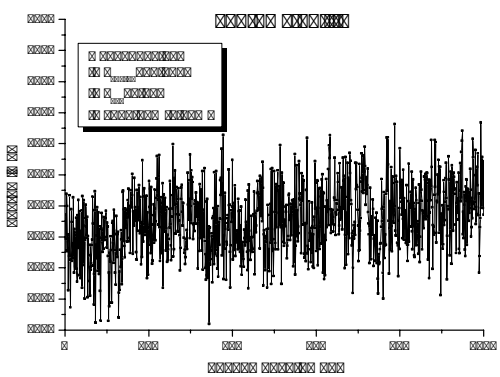

Figure 6: Charge stability measurement

The laser pulse energy is directly linked to a key parameter of the machine, i.e. the extracted charge. The measurement of the charge jitter using an ICT reveals a value of 1.62% (see Figure 6). For this measurement the charge of the first pulse in each train was determined.

At this charge level the slope of the charge vs. laser energy curve is 0.444pC/nJ and therefore a charge stability jitter of 1.62% translates to a laser energy jitter of 2.8% which is in good agreement with the measured one of 2% taking into account that besides the laser energy jitter also other sources exist for the charge jitter.

LASER POSITION JITTER

Another key parameter of the laser system is the position of the spot on the real cathode. While position changes in the order of 0.5mm can be easily measured using the virtual cathodes small scale movements must be monitored by a more sophisticated method. For this reason a procedure was developed which uses a fast quadrant diode. Knowing the transverse laser profile and the signals of the quadrant diode one can extract the actual position of each single laser pulse within the pulse train [3].
Figure 7 shows the measured x- and y-positions within a train of 40 pulses. The position of every pulse is averaged over 200 pulse trains and one can see that there is no significant systematic movement of the pulse position within one train. The error bars are the RMS values for the position of every single pulse. The overall jitter for all pulses in all trains is x_{rms} = 35µm and y_{rms} = 39µm.
There are different possible explanations for this rather

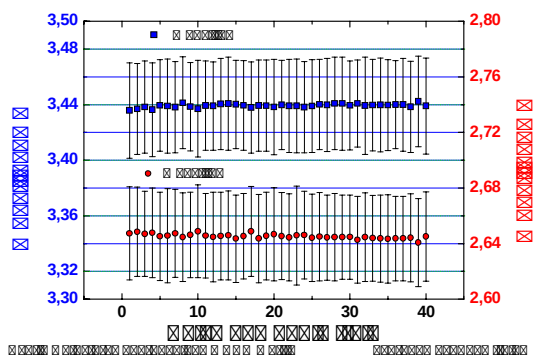

Figure 7: Analysis of the position jitter

high value. The main reason is vibrations of the optical elements in the tunnel. One can estimate that for an optical path length of about 7m in the tunnel the first mirror only needs to turn by 5nrad to introduce 35µm movement on the cathode.

SUMMARY

In this paper the key parameters of the used photo cathode laser system for the 2007 run period were presented.
The temporal profile of the laser pulses are in agreement with the design parameters (20ps FWHM, 6-8ps rise-/fall-times) and show a good long-term stability. The transverse profile has steep edges and exhibits a structure with an RMS of 7.5% on the top. A new system consisting of a Ce:YAG – plate as converter from the UV to visible light was tested and it was found out that this system currently does not meet the demands for this kind of measurement. The laser pulse energy fluctuations were characterized and the value of 2% is in good agreement with the charge stability. Finally the position jitter of the laser pulses on the cathode was determined and shows that the mean position within a pulse train is almost constant but the RMS-values of x_{rms} = 35μm and y_{rms} = 39μm are rather high.

REFERENCES

[1] I. Will, G. Koss, I. Templin, “The upgraded photocathode laser of the TESLA Test Facility”, Nuclear Instruments and Methods in Physics Research A **541** (2005), 467–477

[2] M. Krasilnikov, J. Baehr, M. Hänel, F. Stephan, I.Will, “Experimental Optimization of the Cathode Laser Temporal Profile”, Proceedings of DIPAC 2007, Venice, Mestre, Italy 2007

[3] Ye. Ivanisenko et al., “Photo injector cathode laser beam intensity and pointing position diagnostics and influence on the electron beam emittance measurements”, Proceedings of DIPAC 2007, Venice, Mestre, Italy 2007

INVESTIGATIONS ON THE THERMAL EMITTANCE OF Cs_2Te PHOTOCATHODES AT PITZ*

S. Lederer†, G. Asova‡, J.W. Baehr, K. Boyanov‡, C. Boulware, H-J. Grabosch, M. Haenel, Y. Ivanisenko§, S. Khodyachykh, S. Korepanov, M. Krasilnikov, B. Petrosyan, S.Rimjaem, T.Scholz, R. Spesyvtsev¶, L. Staykov, F. Stephan (DESY, Zeuthen, Germany)
L. Hakobyan (YerPhI, Yerevan, Armenia),
D. Richter (BESSY GmbH, Berlin, Germany)
J. Roensch (University of Hamburg, Hamburg, Germany)

Abstract

The main objective of the Photo Injector Test facility at DESY in Zeuthen (PITZ) is the production of electron beams with minimal transverse emittance. The lower limit of this property of electron beams produced with a photocathode in an RF-gun is determined by the thermal emittance. To understand this crucial parameter for high performance FEL's, measurements under RF operation conditions for cesium telluride (Cs_2Te) photocathodes are done. Results for various accelerating gradients and the dependence on the laser spot size in the cathode plane are presented and discussed in this work.

INTRODUCTION

The thermal emittance determines the lower limit of the normalized emittance of electron beams in injectors. Cesium telluride (Cs_2Te) photocathodes are used at PITZ as sources for electron beams because of their high quantum efficiency (QE) and their ability to release high charge electron bunches in a high gradient RF-gun. In the past several theoretical and experimental studies on the thermal emittance of semiconductor photocathodes like Cs_2Te were performed [1, 2, 3, 4].

In Figure 1 a simplified overview of PITZ is given. The 1.5 cell L-band RF-gun is surrounded by a main and bucking solenoid for compensation of emittance growth due to space charge forces. Under normal operation conditions electrons are emitted from the Cs_2Te cathode by illumination with flat-top laser pulses with temporal FWHM $\approx$ 20 ps and $\lambda = 262$ nm wavelength. A 10 MW klystron provides gradients of about 60 MV/m at the cathode. This gradient is a necessary step toward achieving the required emittance for the European XFEL [5]. More details on the PITZ set-up can be found elsewhere [6].

* This work has partly been supported by the European Community, contracts RII3-CT-2004-506008 and 011935, and by the 'Impuls- und Vernetzungsfonds' of the Helmholtz Association, contract VH-FZ-005.

† sven.lederer@desy.de
‡ on leave from INRNE, Sofia, Bulgaria
§ on leave from IERT, Kharkiv, Ukraine
¶ on leave from NSCIM, Kharkiv, Ukraine

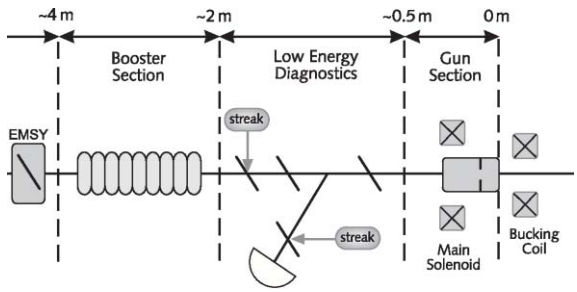

Figure 1: Simplified overview first part of PITZ

At PITZ it is not possible to measure the thermal emittance directly at the cathode. In order to estimate a thermal emittance, a normalized beam emittance has been measured for very low bunch charge and short laser pulses at the first emittance measurement system (EMSY1) 4.3 m downstream (Fig. 1) by the slit scanning technique [7].

In this contribution results from the emittance measurements performed at PITZ are presented for different rms laser spot sizes on the cathode and different accelerating gradients between 30 and 60 MV/m.

THEORETICAL ESTIMATIONS ON THE THERMAL EMITTANCE

The photoemission from semiconductors can be described by a three step model [8]. In the first step an electron from the valence band (VB) is excited to the conduction band (CB) by photon absorption. Due to the energy gap between the conduction and the valence band of $E_g = 3.3$ eV for Cs_2Te, the photon energy must be larger than 3.3 eV [8]. At PITZ a laser with a wavelength of $\lambda = 262$ nm ($E_{ph} \approx 4.72$ eV) is used for the electron excitation into the first density of states maximum in the CB, located 4.05 eV above the VB maximum [8]. The second step involves the electron transport to the surface. In the last step the electron is emitted into vacuum. For the emission process the electron has to overcome the potential barrier at the surface, which for semiconductors can be described by the electron affinity E_A (difference between

the vacuum level and the minimum of the CB). For Cs_2Te E_A is in the order of 0.2 eV [8]. So the threshold photon energy for electron emission is $E_{thr} = E_g + E_A = 3.5$ eV. For PITZ and the above given photon energy this leads to an average kinetic energy of $E_{kin} = 0.55$ eV after emission. It is important to mention, that these results only hold for pure photoemission (i.e. no electric fields at the cathode) and for fresh Cs_2Te cathodes. If the cathodes are used in a photo-injector under operational conditions the electron affinity could be reduced by the high electric field at the cathode. On the other hand changes in the chemical composition of the cathode during operation can result in changed emission conditions (i.e. changed work function) [9].

Based on the argumentation given in [1], the kinetic energy of the emitted electrons can be determined by measuring the thermal emittance. Assuming an isotropic emission into the half sphere in front of the cathode surface the thermal emittance can be written in terms of the rms laser spot size σ_l at the cathode and E_{kin}.

$$\epsilon_{th} = \sigma_l \sqrt{\frac{2E_{kin}}{3m_0c^2}} \tag{1}$$

OPERATIONAL PARAMETERS

The thermal emittance ϵ_{th} adds quadratically to other emittance terms forming the measured transverse emittance ϵ_{meas}.

$$\epsilon_{meas} \approx \sqrt{\epsilon_{th}^2 + \epsilon_{SC}^2 + \epsilon_{RF}^2} \tag{2}$$

This relation has to be taken into account to adjust the operation conditions of the injector to perform thermal emittance measurements. The emittance growth caused by space charge forces reduces with smaller bunch charge. As compromise between small space charge and good signal to noise ratio during measurements, bunch charges of maximum 6 pC were used. The influence of the RF-field at the cathode during the emission on the emittance can be reduced by short gaussian laser pulses instead of flat-top temporal profiles, used for normal operation. The shortest pulses currently producible by the laser system at PITZ have a sigma of 3-4 ps. During measurements the gun RF-phase was adjusted to the phase of maximum mean momentum gain Φ_m. If not commented the data in this paper were obtained with the above mentioned operational conditions and the booster operating at maximal momentum gain. Usually slits of 10 μm width were used at the EMSY1.

EXPERIMENTAL RESULTS

The aim of the emittance measurements presented in this contribution, is to give an estimate on the kinetic energies of the emitted electrons for different RF-gradients at the cathode.

From the measured emittances as function of σ_l one can estimate the kinetic energy right after the emission from the slope $(d\epsilon_{th}/\sigma_l)$ of a linear fit and considering equation 3, which results from the differentiation of equation 1.

$$E_{kin} = \frac{3}{2} m_0 c^2 \left(\frac{d\epsilon_{th}}{d\sigma_l} \right)^2 \tag{3}$$

The variation of the rms laser spot size at the cathodes was achieved by apertures of different diameters put into the laser beam line [10].

In Figure 2 measured emittances of Cs_2Te cathode #83.3 for an accelerating gradient of $E_0 = 30$ MV/m are presented. The field on the cathode during the emission process was determined by $E = E_0 \sin(\Phi_m - \Phi_0)$. The phase Φ_0 was estimated from the rising edge of the charge scan vs. RF-phase. For the current case this results in $E = 17.2$ MV/m. In addition to the experimental data, the linear fits are shown. The resulting kinetic energies for this and the other measured gradients are summarized in Figure 7.

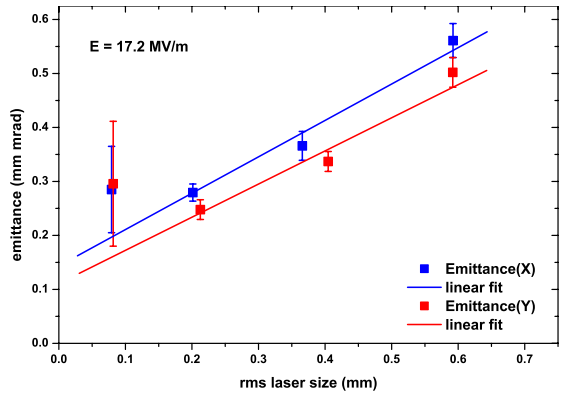

Figure 2: Results from emittance measurements as function of laser spot size for $E_0 = 30$ MV/m for cathode #83.3; symbols: data, lines: linear fit.

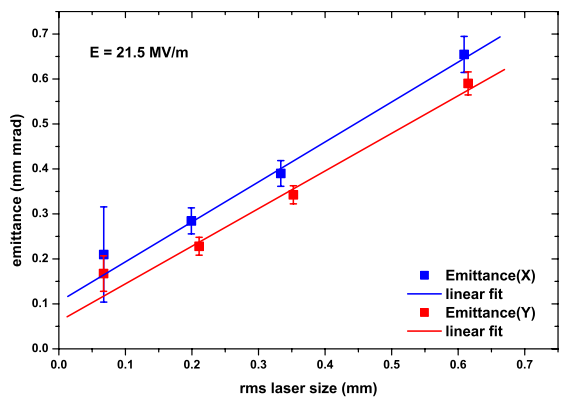

Figure 3: Results from emittance measurements as function of laser spot size for $E_0 = 35$ MV/m for cathode #83.3; symbols: data, lines: linear fit.

Figure 3 shows measured emittances together with the linear fits for an accelerating gradient of $E_0 = 35$ MV/m.

Although for both gradients the measured data can be described by a linear dependence from the rms laser size, deviations to the fits are not small, i.e for the smallest σ_l. A possible reason for the latter one can be the increased charge density of the electron bunch and therefore increased space charge forces. Also neither the data nor the fit end in zero emittance for $\sigma_l = 0$ mm, which could be caused by the accelerating RF-field, also at short laser pulses, and/or by a systematic error during the measurements.

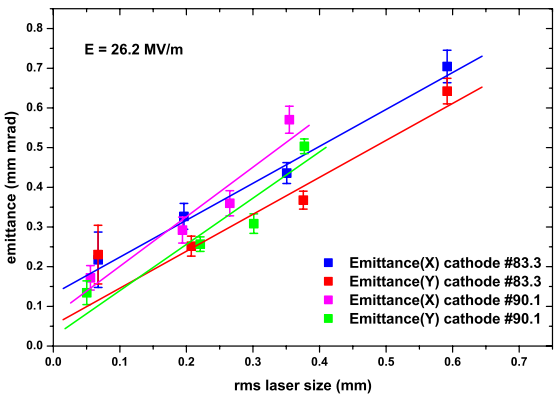

Figure 4: Results from emittance measurements as function of laser spot size for $E_0 = 40$ MV/m; blue and red symbols: data for cathode #83.3, green and magenta symbols: data for cathode #90.1

Figure 4 presents the emittances measured at $E_0 = 40$ MV/m for cathode #83.3 and #90.1. Identical measurements for $E_0 = 60$ MV/m are presented in Figure 6. The datasets were measured with the same operational conditions in the gun section, but the emittances of cathode #90.1 were obtained without booster and with a slit width at EMSY1 of 50 μm. Before the thermal emittance measurements on cathode #90.1, this cathode was used intensely with $\sigma_l = 0.36$ mm, and bunch charges of 1 nC were extracted during the whole period. A QE-map taken in the beginning of the thermal emittance measurements at $E_0 = 60$ MV/m (Fig. 5 right) clearly shows an area in the center region of the cathode with strongly reduced QE. The active area at the right plot in Figure 5 corresponds to the center of the photograph on the left side.

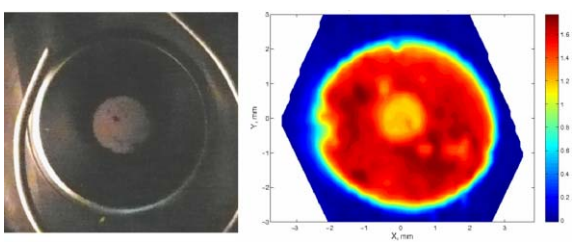

Figure 5: Photograph (left) and QE-map (right) of cathode #90.1

To avoid a mixing of regions with different QE during the emittance measurements, for cathode #90.1 data were only taken for $\sigma_l < 0.36$ mm. The fits in Figure 4 clearly show a different slope obtained from both cathodes, resulting in higher kinetic electron energies for cathode #90.1 (see Fig. 7). In contrary to that, in Figure 6 the slopes for both cathodes are comparable.

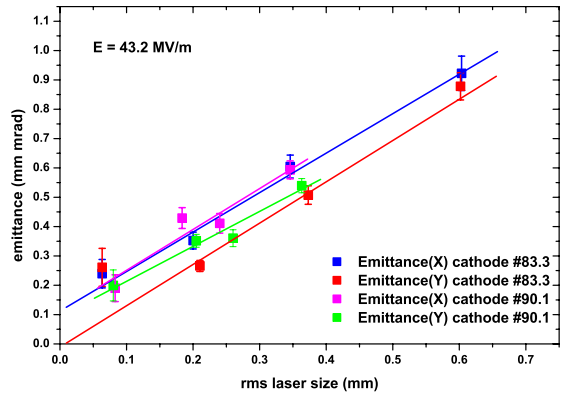

Figure 6: Results from emittance measurements as function of laser spot size for $E_0 = 60$ MV/m; blue and red symbols: data for cathode #83.3, green and magenta symbols: data for cathode #90.1

The kinetic energies obtained from the slopes of the linear fits to the data described above are summarized in Figure 7. Since there is no physical reason for different energies in X and Y direction after the emission, in the figure the geometrical averages of the kinetic energies in both transverse planes are presented. The plot clearly shows the influence of the electric field at the cathode on the kinetic energies, which already was observed for lower gradients [4]. For an accelerating gradient of 60 MV/m ($E = 43.2$ MV/m during emission) we find for both cathodes kinetic electron energies slightly above 1.2 eV. Despite the big uncertainties, this preliminary value is a factor of two higher than for the absence of the electric field (0.55 eV).

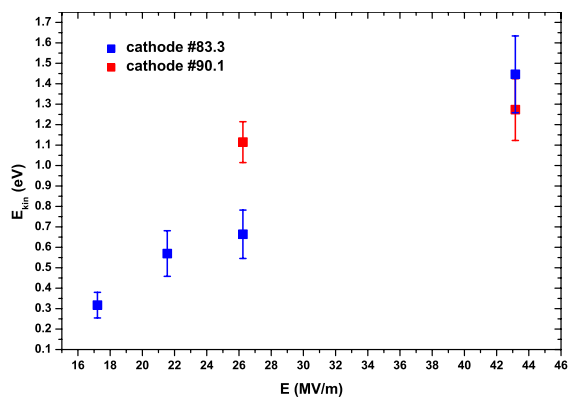

Figure 7: Kinectic electron energies as function of the field at the cathode; blue: cathode #83.3, red: cathode #90.1

SUMMARY

In this contribution measured transverse emittances for different rms laser spot sizes at the photocathode and different gradients are presented. For this measurements the charge was kept to values about 6 pC, and short laser pulses were used. From the thermal emittances the kinetic energies were estimated for two Cs_2Te cathodes. An increase of the kinetic electron energies after the emission with increasing electric field at the cathode was observed. For the highest acceleration gradient available we found kinetic energies of slightly above 1.2 eV. For better understanding of the measured data (i.e. why $\epsilon_{th}\,(\sigma_l = 0) \neq 0$), a more detailed analysis and a comparison with simulations is necessary.

REFERENCES

[1] K. Floettmann, "Note on the Thermal Emittance of Electrons Emitted by Cesium Telluride Photo Cathodes", TESLA-FEL report 1997-01, DESY, 1997.

[2] J.E. Clendenin et al., "Reduction of thermal emittance of rf guns", SLACPUB- 8284, SLAC, 1999.

[3] P. Michelato et al., "Thermal emittance estimation using a time-of-flight spectrometer", Proceedings of the European Particle Accelerator Conference 2000,, Vienna, Austria.

[4] V. Miltchev, et al., "Measurements of thermal emittance for cesium telluride photocathodes at PITZ", Proceedings of the Free Electron Laser Conference 2005, Stanford, USA.

[5] M. Altarelli, et al. (eds.), "The Technical Design Report of the European XFEL", Chapter 4: XFEL accelerator. DESY 2006-097, July 2006, p. 80.

[6] S. Rimjaem, et al., "Status and perspectives of the PITZ Facility Upgrade", to be published in Proceedings of the Free Electron Laser Conference 2007, Novosibirsk, Russia.

[7] L. Staykov et al."Commissioning of a New Emittance Measurement System at PITZ", Proceedings of the Free Electron Laser Conference 2006, Berlin, Germany.

[8] R.A. Powell, W.E. Spicer, G.B. Fisher, and P. Gregory, Phys. Rev. B, **8** 3987 (1973).

[9] S. Lederer, et al., "XPS studies of Cs_2Te photocathodes", to be published in Proceedings of the Free Electron Laser Conference 2007, Novosibirsk, Russia.

[10] J. Baehr et al., "Upgrades of the Laser Beam-line at PITZ", Proceedings of the Free Electron Laser Conference 2005, Stanford, USA.

STATUS AND PERSPECTIVES OF THE PITZ FACILITY UPGRADE*

S. Rimjaem†, G. Asova‡, J.Bähr, C. Boulware, K. Boyanov‡, H.J. Grabosch, M. Hänel, Y. Ivanisenko§, S. Khodyachykh, S. Korepanov, M. Krasilnikov, S. Lederer, A. Oppelt¶, B. Petrosyan, S. Riemann, A. Shapovalov‖, T.Scholz, L. Staykov, R. Spesyvtsev**, F. Stephan, DESY, 15738 Zeuthen, Germany
K. Flöttmann, DESY, 22603 Hamburg, Germany
L. Hakobyan, YerPhI, Yerevan, Armenia
D. Richter, BESSY, 12487 Berlin, Germany
J. Rönsch, University of Hamburg, 22761 Hamburg, Germany
K. Rosbach, Humboldt University, 12489 Berlin, Germany

Abstract

The Photo Injector Test facility at DESY in Zeuthen (PITZ) has been established to develop and optimize electron sources that cover requirements of Free Electron Lasers (FELs) facilities such as FLASH and the European X-ray Free Electron Lasers (XFEL). A major upgrade of the facility is ongoing in steps, in parallel to the commissioning of the extended setup and first experiments. The new setup towards the final design mainly includes a photo cathode RF gun, a post acceleration booster cavity and several diagnostic systems. In order to fulfill the characterization of the high brightness electron source, the diagnostic systems will consist of three emittance measurement systems, two high-energy dispersive arms, an RF deflecting cavity and a phase space tomography module as well as bunch length diagnostics. In this paper, results of the commissioning of the new RF gun, which has been installed and conditioned at PITZ in spring and summer of 2007, the current PITZ status and details of the future facility upgrade will be presented.

INTRODUCTION

Source and injector development has been realized as one of the most important challenges in electron accelerator technology since several accelerators, e.g. FELs, XFEL or Linear Collider, demand excellent beam conditions right from the source. The main requirement for an electron injector is its capability to produce a high brightness beams. PITZ has been designed and built to serve this purpose in order to produce intense electron beams with very small transverse emittance and reasonably small longitudinal emittance. The main objective at PITZ is to generate a reliable electron beam, with transverse emittance of about 1 mm mrad with a bunch charge of 1 nC and an energy spread smaller than 1%. The possibility to achieve small beam emittance has been demonstrated during the successful commission of the facility in the first phase (PITZ1) [1] and intermediate upgraded phase (PITZ1.5) [2].

Further upgrade of the facility towards the final design PITZ2 has been continued to extend the ability to achieve a smaller beam emittance. The so called PITZ1.6 has been finalized and was taken into operation in 2006. PITZ1.6 has completed its tasks with characterization of two new gun cavities (prototype 3.1 and 3.2). Recent commissioning and experimental results from PITZ1.6 with gun 3.2 will be discussed in this paper. Furthermore, the facility upgrade towards the next phases will be described.

PITZ1.6 SETUP WITH RF GUN PROTOTYPE 3.2

The current PITZ setup (PITZ1.6) consists of a 1.5 cell normal conducting RF gun with a Cs_2Te photocathode and a Nd:YLF laser system, a normal conducting booster cavity for post acceleration and diagnostic systems upstream and downstream of the booster cavity. The RF gun and booster cavity are operated with separated L-band (1.3 GHz) RF power systems. The diagnostic sections include devices for characterize the electron beam, e.g. beam size, bunch charge, its position, transverse emittance, longitudinal phase space distribution, electron bunch length, beam momentum and momentum spread. The main upgrade from PITZ1.5 to PITZ1.6 comprises installation of three new emittance measurement systems [3] and a new screen station after the booster for bunch length measurements at electron energies between 4 and 40 MeV [4]. Gun prototype 3.1 was installed and operated up to the maximum requirements of FLASH with maximum peak power of 3.5 MW, resulting in $\sim$40 MV/m gun gradient at the cathode, with RF pulse length of 900 μs at 10 Hz repetition rate [5]. Gun prototype 3.2 was installed in the PITZ1.6 beam line and was taken into operation in April 2006. A main goal for its operation is to study and optimize its properties in the presence of a high accelerating gradient of up to 60 MV/m.

* This work has partly been funded by the European Community, contract no. RII3-CT-2004-506008 and 011935 and by the 'Impuls- und Vernetzungsfonds' of the Helmholtz Association, contract no. VH-FZ-005.

† sakhorn.rimjaem@desy.de
‡ On leave from INRNE, Sofia, Bulgaria
§ On leave from IERT, Kharkov, Ukraine
¶ Presently at PSI, Villigen, Switzerland
‖ On leave from MEPHI, Moscow, Russia
** On leave from NSCIM, Kharkov, Ukraine

Tuning of Gun 3.2

In October 2006, frequency measurements of the gun cavity have been performed and the results showed a detuning from 1.3 GHz of 746 kHz at an expected operation temperature of 55^{o}C. The field profile of the gun 3.2 cavity was measured by using the bead-pull technique and the field at the cathode was about 18% higher than in the full cell. Since a preferable value of the field balance from simulation in order to compromise between high momentum gain and a maximum gradient at the cathode for space charge compensation is about 5-10%, the gun was mechanically tuned by using a convenient tuning device to slightly deform the cavity walls at the cathode plat and at the coupler-facing wall of the iris [5].

The gun was tuned to reach a desired resonant frequency of 1.3 GHz at an operating temperature of 56^{o}C with the field balance between the half and the full cell of 1.03 or the field at the cathode is 3% higher than that in the middle of the full cell. The field distribution before and after the tuning are shown in Fig. 1. Prior to installation at PITZ, water-to-air leak of a cooling channel was found. After the leak was repaired, the frequencies and the quality factor of the gun were re-measured resulted in a higher frequency corresponding to an operating temperature of 64^{o}C. Field profile was not re-measured. RF measurement results of gun 3.2 before and after the tuning process as well as when it was installed at PITZ are summarized in Table 1. The quantities f_π, $Q_{0\pi}$ and $f_{\pi-0}$ stand for the resonant frequency, the unloaded quality factor of π-mode and the mode separation between π- and 0-mode, respectively.

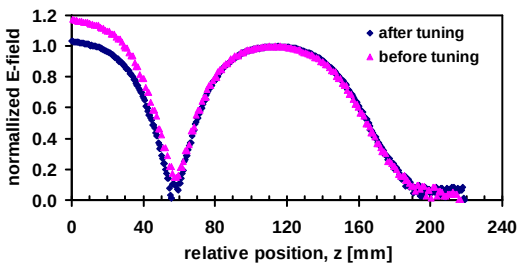

Figure 1: Electric field profile in Gun 3.2 cavity before and after tuning process.

parameter	before	after	at PITZ
f_π [GHz]	1.3013	1.3003	1.3007
$f_{\pi-0}$ [MHz]	5.0	5.1	5.0
$Q_{0\pi}$	-	21316	23853

Table 1: RF measurement results of Gun 3.2 before tuning, after tuning and after installation at PITZ.

Conditioning and Dark current Measurements

After the brazing, the tuning and the cleaning process finished, the gun has been installed and commissioned at PITZ from April to August 2007. It has been conditioned up to a maximum gun gradient of about 60 MV/m at maximum power of 6.9 MW and the stable operation can be achieved with the RF pulse length up to 200 μs. Further, the RF pulse length was increased to 700 μs but only for the short time period because of high level of dark current. Then, the gun cavity conditioning has been continued at RF pulse length of 400 μs for about two weeks before the nominal experiments started. History of the gun gradient and RF pulse length during the conditioning (April-June 2007) is shown in Fig.2. In nominal experiments, the gun has been operated mostly for RF pulses of 140 μs (with 100 μs flat-top) at 10 Hz repetition rate. The nominal peak power in the gun cavity was 6.7 MW corresponding to the average power of 9.4 kW for 140 μs RF pulses.

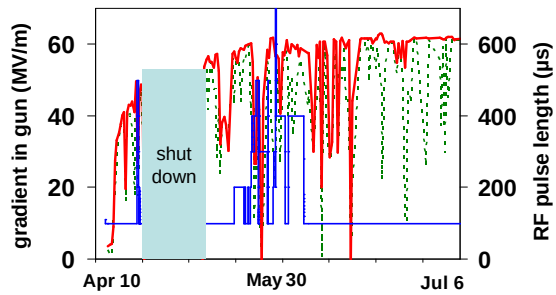

Figure 2: Gun gradient and RF pulse length history of gun 3.2 at PITZ. Maximum gradient (red line) is the highest gradient reached in the cavity, average gradient (green dot) is the average accelerating gradient over operating time period of one hour and the RF pulse length is represented by the blue line.

Cesium telluride (Cs_2Te) photo cathodes are used at PITZ for standard operation, whereas molybdenum (Mo) cathodes have been applied for the conditioning. Dark current measurements have been performed at various gun powers with different cathodes for both Mo and Cs_2Te types. The results are shown in Fig.3, where the maximum dark current is the highest current value measured as a function of the main solenoid currents. One of the measurements is shown in Fig.4 for Cs_2Te cathode no. 109.1. From Fig.3, one can see that the dark current level was improved from conditioning and operation for both Mo and Cs_2Te cathodes except the Mo cathode no. 32.2, which was used at the beginning of the conditioning and a serious damage on its surface has been observed. Another remarkable observation for the Mo electro-polished cathode (no. 55.3) demonstrated lower level of the dark current. These dark current measurements show the progress of conditioning, but the overall dark current level was still high.

Possible reasons may be because of the fabrication error of the area around the cathode plug during the assembling, the bad vacuum condition due the several dismounts (3 times) of the coupler which had vacuum leak after the bake out or the bad condition of the cathode after experiencing high accelerating field. Presumably, the high level of the

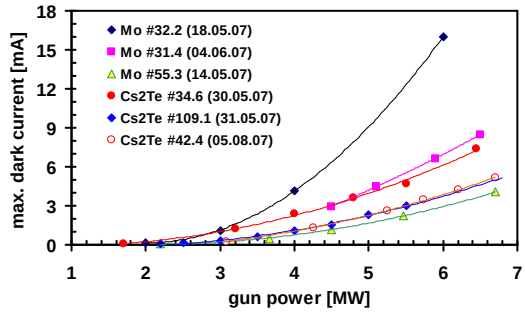

Figure 3: Maximum dark current as a function of gun power for different cathodes of gun 3.2.

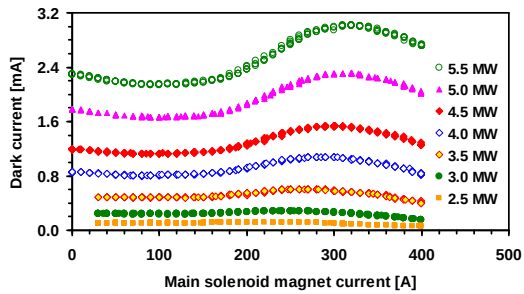

Figure 4: Dark current measurements as a function of the main solenoid magnet current for cathode no.109.1 performing on May 31, 2007.

dark current is responsible for the measured outgassing rate of some parts in double diagnostics cross (DDC, at ∼0.78 m from the photo cathode). Several Teflon parts were found melted during DDC reparation, what explains bad vacuum conditions also in the gun cavity. Moreover, this high dark current has caused a severe radiation level in the accelerator tunnel which damaged several electronic components in the radiation effecting area. More details of the conditioning of gun 3.2 at PITZ and effects of high dark current level to delay the commissioning and experiment at PITZ are described in the reference [6].

Recent Experimental Results

Momentum and longitudinal phase space have been measured at two locations: low energy (LEDA) and high energy dispersive arms (HEDA). Experimental results show that the highest momentum value achieved from gun 3.2 was ∼6.5 MeV/c with an energy spread of about 40 keV/c at gun power of 6.7 MW [9]. This momentum value is lower than the expectation from simulation for the gun gradient of 60 MV/m, which should be about 6.92 MeV/m for the field balance of 1.03. For the post acceleration measurement, the highest momentum measured at HEDA was ∼16 MeV/c with 30 keV/c momentum spread. In fact, the booster can be operated with higher acceleration, but due to a limitation of the dipole current it was not possible to measure the momentum higher than 16 MeV/c.

Projected emittance measurements for gun 3.2 have been performed using the slit mask technique at the emittance measurement station (EMSY1) located ∼0.7 m downstream of the booster exit. The results show that the minimum transverse emittance measured during the commissioning period of gun 3.2 was 1.54 ± 0.15 mm mrad for the gun gradient of 40 MV/m and 1.26 ± 0.18 mm mrad for ∼60 MV/m [10]. Moreover, thermal emittance from the cathode has been investigated and the results reveal that photoelectrons with kinetic energies of 1.4 ± 0.2 eV were emitted from the cathode at the gun gradient ∼60 MV/m [11]. This value is a factor of two larger than the theoretical model.

FUTURE STAGES AT PITZ

Upgrade to PITZ1.7

In mid of August 2007, an upgrade to the intermediate phase PITZ1.7 was started. Main upgrades from PITZ1.6 to PITZ1.7 comprise a modification of the low energy diagnostics section and installation of a new high energy dispersive arm (HEDA1).

- Upgrade of low energy diagnostics section

The dipole at the present low energy dispersive arm (LEDA) at PITZ is a copy of the former injector section at FLASH which was not optimized for PITZ. The solenoid currents necessary for good focusing of the beam downstream of the booster cavity lead to the too large beam size at the dipole chamber. Modification of the pole shoes and vacuum chamber will be performed to increase the vacuum chamber aperture from 12mm to 27mm. In addition, the double diagnostic cross (DDC) in front of the dipole will be upgraded in order to improve the situation of vacuum and wake fields. The new DDC will include a slit which will be used to improve the resolution of the momentum measurements at LEDA.

- The first high energy dispersive arm (HEDA1)

HEDA1 is designed to be a multipurpose system. It will be used as spectrometer to measure momentum, a device to characterize the longitudinal phase space and a system to measure transverse slice emittance. This system includes a 180^o dipole magnet which simplify the reconstruction of the momentum measurement, a slit at the exit of the dipole, a quadrupole magnet and two screen stations. One station will be used for momentum measurements for electron energies up to 40 MeV and the other one, equipped with an optical read-out for streak camera, to investigate longitudinal phase space by using off crest acceleration in the booster and the slit exit of the dipole. HEDA1 can be used to measure the transverse slice emittance at difference longitudinal positions along the bunch.

Upgrade to PITZ2

In order to fulfill the characterization of high brightness electron beam, new diagnostic systems will be in-

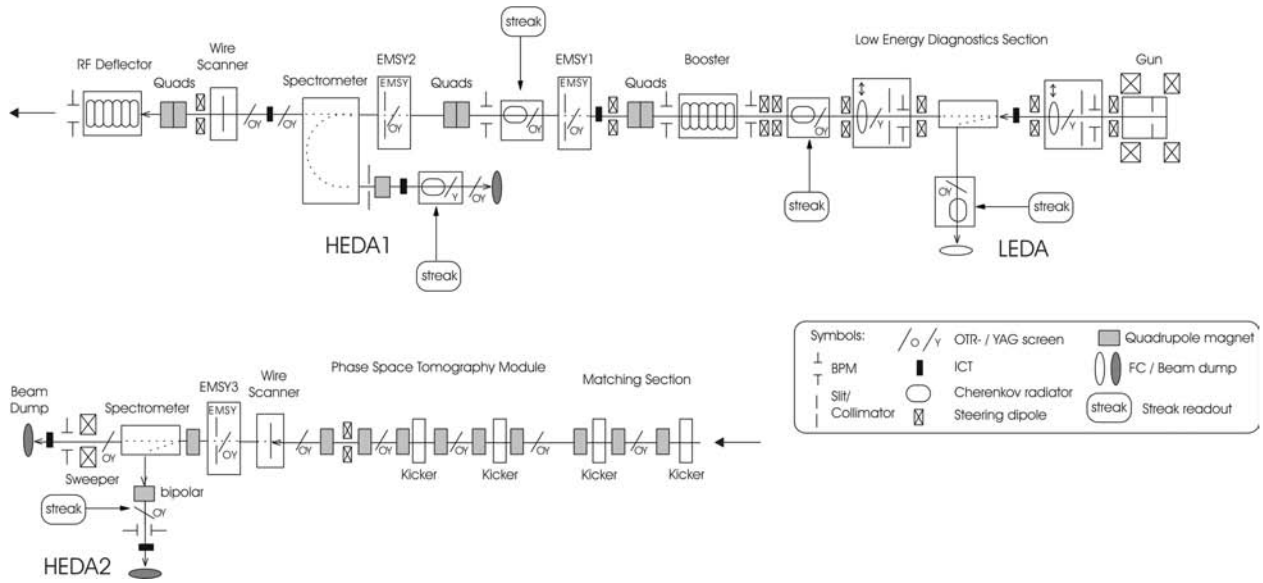

Figure 5: Schematic layout of the future PITZ2 beam line.

stalled at PITZ towards the final design (PITZ2). The PITZ2 setup includes a photocathode RF gun, a post acceleration booster cavity and several diagnostic systems including three emittance measurement systems, two high-energy dispersive arms, an RF deflecting cavity and a phase space tomography module as well as bunch length diagnostics (see Fig.5). The primary goal of PITZ2 is to study the conservation of small emittance beams along the beam line after the booster acceleration. The key parameters for this emittance conservation is the replacement of an existing TESLA booster cavity with a new Cut Disk Structure (CDS) booster, which can provide higher energy gain up to $\sim$24 MeV with the limited RF power and does not degrade the beam quality. An improvement of the laser system is required in order to provide rise/fall time of 2 ps laser pulses with FWHM of 20 ps. Furthermore, additional new diagnostics will be installed in the high energy section downstream of the booster to extend the ability of facility to study more details about the beam properties. An RF deflecting cavity and a phase space tomography module will be included for analysis of the phase space distribution. At the end of the beam line, a third spectrometer will be installed in combination with diagnostics to measure momentum and momentum spread, slice emittance and longitudinal phase space using a Cherenkov radiator and streak camera or the RF-deflector. More details about the beam diagnostics upgrade for PITZ2 can be found in reference [8].

CONCLUSION

The gun 3.2 has been conditioned and taken into operation at PITZ for roughly 4 months in spring and summer of 2007. It has fulfilled the goal to operate at a gun gradient of $\sim$60 MV/m with 140 μs RF pulses length and 10 Hz repetition rate. Several results from the conditioning and experiments of this RF gun with the present PITZ1.6 beam line have been presented in this paper. Further upgrade of the facility to the next phase PITZ1.7 has started in mid of August 2007. After the upgrade is finished next operation period will start in winter 2007/2008.

REFERENCES

[1] F. Stephan et al., "Recent Results and Perspective of the Low Emittance Photo Injector at PITZ", FEL 2004, Trieste, Italy.

[2] A. Oppelt et al., "Status and First Results from the Upgraded PITZ Facility", FEL 2005, Stanford, CA, USA.

[3] L. Staykov, "Commissioning of a New Emittance Measurement System at PITZ", FEL 2006, Berlin, Germany.

[4] J. Rönsch et al., "Investigations of the Longitudinal Beam Properties at the Photoinjector Test Facility in Zeuthen", FEL 2006, Berlin, Germany, 2006.

[5] A. Oppelt et al., "Tuning, Conditioning, and Dark Current Measurements of a New Gun Cavity at PITZ", FEL 2006, Berlin, Germany.

[6] S. Lederer at al., "Conditioning of a new gun cavity towards 60 MV/m at PITZ", PAC 2007, Albuquerque, NM, USA.

[7] K. Flöttmann, A Space Charge Tracking Algorithm (ASTRA), http://www.desy.de/mpyflo.

[8] S. Khodyachykh at al., "New Beam Diagnostic Developments at the Photo-injector Test Facility PITZ", PAC 2007, Albuquerque, NM, USA.

[9] J. Rönsch at al. "Recet Measurements of the Longitudinal Phase Space at PITZ", FEL 2007, Novosibirsk, Russia.

[10] L. Staykov at al. "Measurements of the projected normalized transverse emittance at PITZ", FEL 2007, Novosibirsk, Russia.

[11] S. Lederer at al. "Investigation on the Thermal Emittance of Cs_2Te Photocathode at PITZ", FEL 2007, Novosibirsk, Russia.

PERFORMANCE OF THE FERMI FEL PHOTOINJECTOR LASER*

M. B.Danailov, A.Demidovich, R.Ivanov, I.Nikolov, P.Sigalotti
ELETTRA, 34012 Trieste, Italy

Abstract

The photoinjector laser system for the FERMI FEL has been installed at the ELETTRA laser laboratory. It is based on a completely CW diode pumping technology and features an all-CW-diode-pumped Ti:Sapphire amplifier system, a two stage pulse shaping system, a time-plate type third harmonic generation scheme and aspheric shaper based beam shaping. The paper will present experimental results describing the overall performance of the system. The data demonstrates that all the initially set parameters were met and some largely exceeded. We present what is to our knowledge the first direct measurement of the timing jitter added by a Ti:Sapphire amplifier system and show that for our case it is below 10 fs.

INTRODUCTION

The photoinjector laser (PIL) is known to be one of the very important sub-systems for all single-pass UV and X-ray FELs. The charge and quality of the electron bunch created at the photoinjector (PI) affect dramatically the operation of the FEL and can be a strong limitation in obtaining the expected FEL performance. This is especially true for the challenging projects that are now in construction phase (like LCLS, SLAC, European XFEL). A lot of attention has thus been devoted previously for studying the optimum parameters of the PIL. It is now well accepted that the UV beam should have a nearly flat top spatial profile, while the optimum longitudinal (temporal) shape may vary [1-3]. In addition, laser parameters like energy and beam pointing that may seem easier to control, have also to be very carefully optimised. The overall system design appears to be more difficult in the case of copper photocathode, because of the required very high UV energy (~0.5 mJ for extracting 1 nC). The implementation of beam and pulse shaping techniques at these energy levels in UV is quite challenging. In this paper we describe the schemes and technologic solutions developed at Elettra for the FERMI PIL. As it will be seen the system fully meets and in some aspects exceeds the requirements.

MAIN SYSTEM DESIGN

As it has already been discussed in earlier papers [4], the only laser technology that can meet all the PIL parameters requested for copper photocathode, and is enough mature and reliable, is the one based on Ti:Sapphire as an active material and regenerative amplifier/multipass chirped-pulse amplifier design. The amplifier system described here is a custom system constructed by Coherent Inc. This is in fact the first amplifier system of this type, reaching an energy level above 18 mJ in the infrared, with the use of entirely CW diode pumping technology, which is the base for the extremely high UV energy stability reported below. The amplifier design is shown on Figure 1.

As it is seen, the seed coming from a Ti:Sapphire oscillator (Mira), is stretched and amplified to a mJ level in a regenerative cavity, after which it is further amplified in two two-pass amplifier stages. Each of these is pumped by up to 45 mJ from two Evolution HE Nd:YLF Q-switched pump lasers. As mentioned above, they are pumped by diodes in CW. Table 1 summarizes some of the main laser parameters.

Parameter	Specs	Measured
IR output energy	> 18 mJ	> 18 mJ (~15 mJ in operation)
Pulse duration (Gauss.fit)	<100 fs	~90 fs
Center WL	780+/-5 nm	~783 nm
M^2 value	$M^2_{x,y}$<1.5	M^2_x~1.27, M^2_y<1.17
UV energy before shaping	>2 mJ	>2.3 mJ
Short term energy stability UV (500 shots), RMS	<3%	<0.6%
Long term energy stability UV (8 hours), RMS	<3%	<0.8%
Beam pointing stability	<10 μrad	<5 μrad
Timing jitter (10 Hz-10MHz), RMS	<350 fs	<180 fs

Table 1: Main laser parameters , left- specified, right-measured

We note that the system is capable of delivering >18 mJ energy per pulse in IR, however the reported 2.3 mJ of UV energy is obtained at ~15 mJ in the IR. This regime is preferred for everyday operation because of lower diode current (~19A) and also lower load on the optical components. Conversion efficiency to third harmonic (261 nm) is about 15% and has been fixed after careful balancing of spot-size and pulse duration. Both interferometer like and 'time-plate' designs of the THG unit have been tested with similar results. However, in the latter we have observed a deterioration of the calcite plate which pre-compensates the group velocity mismatch, so at present the interferometric version is in operation.

* This work has been partially supported by the EU Commission in the Sixth Framework Program, Contract No. 011935 EUROFEL

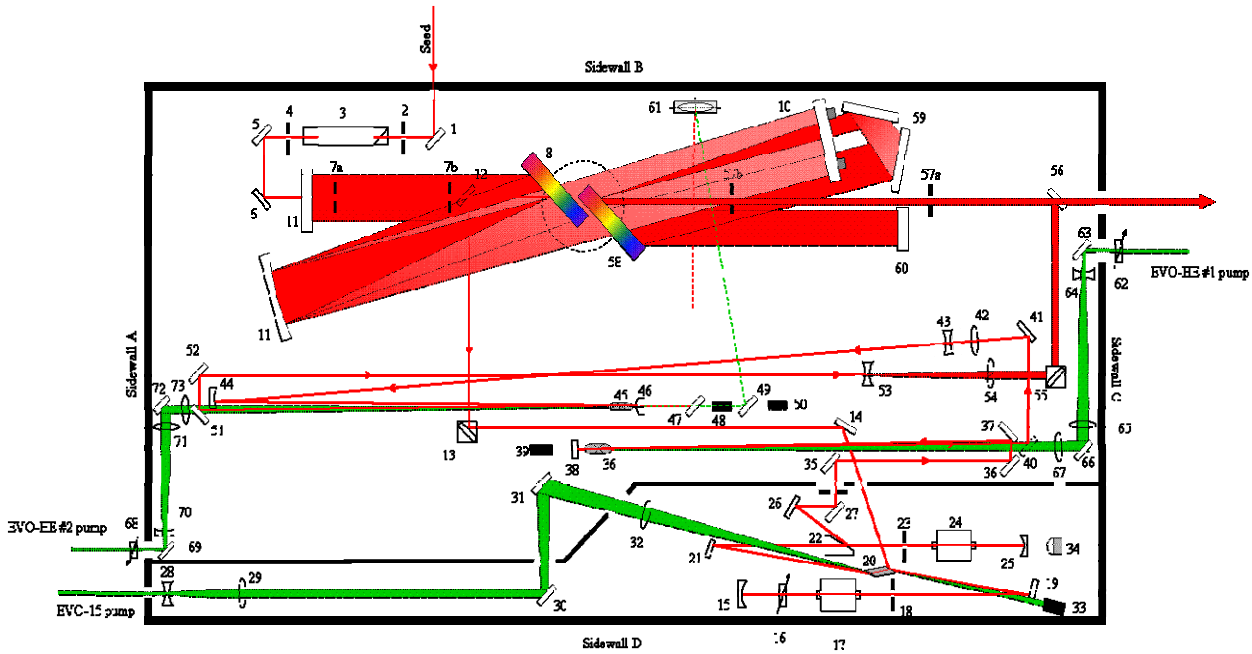

Figure 1: Amplifier design.

TIME SHAPING

The concept chosen for our time-shaping system has been already described previously [4]. In brief, it implements a two-step hybrid shaping system in which a preliminary shaping is performed in IR by an acoustooptic dispersive filter (DAZZLER , Fastlite), and the final shape and duration of the pulse are done in the UV in a Fourie system. In principle the DAZZLER allows both amplitude and phase modulation [5]. We note that the amplitude shaping done by the DAZZLER is partially lost in the amplification process due to the strong 'red' shift of the amplified spectrum with respect to the seeding one. For this reason the DAZZLER alone is not sufficient for producing the required pulse shapes. .

The main temporal shaping is thus performed in UV by the 4-f system shown on Fig.2. The UV pulse coming from the harmonic generation system enters a Fourier-shaping scheme consisting of the grating G1, folding mirror M1, lens L, deformable mirror (DM) and retro-reflecting mirror M2. The modulation is mostly performed by the DM (OKO Technologies). The particular mirror used is a custom made dielectric plate (HR at 260 nm) glued on a 20 piezo transducers (2lines of 10), each of them can be moved by up to 10 micron. As it is seen from the figure we use a configuration where the mirror is used at a large angle, thus increasing the number of useful actuators and the induced phase difference. In alternative configuration, a longer focal distance lens and DM at normal incidence can be used. The DM is used for providing mostly the high order dispersion terms, while half of the large second order dispersion term giving the final (several ps range) pulse lengthening is given by the

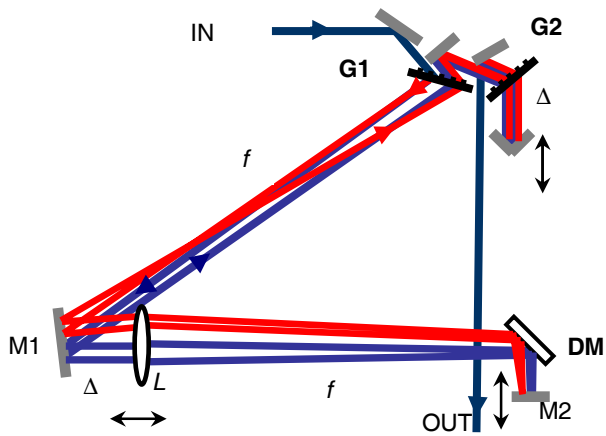

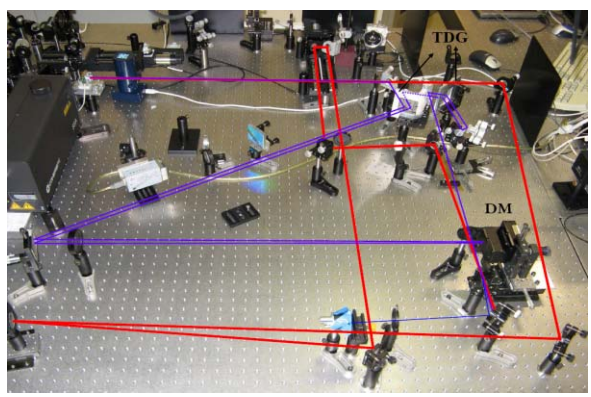

Figure 2: UV pulse shaping optical scheme (up) and photo of the setup (down).

off-focus distance Δ of the grating with respect to the front Fourier plane. The second half of the required group velocity dispersion (GVD) is provided by the double passage through the grating G2, which is also used to cancel the residual spatial chirp introduced by the shaper. The pulse length can be changed by changing Δ in both the shaper and stretcher and respectively adjusting the shape of the DM.

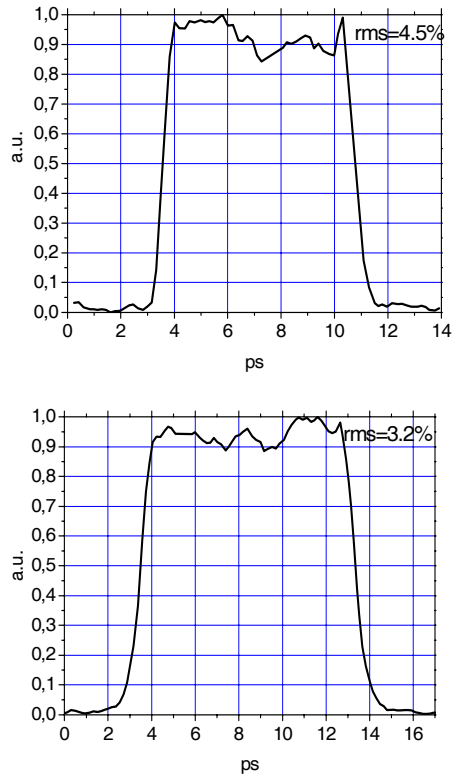

Figure 3: Flat-top pulses with duration of 6 and 10 ps produced using phase modulation by the DM.

Typical examples of the commonly requested flat-top type temporal profile are shown on Figs5. The flat-top duration could be made even longer, up to 15 ps, with the expense of increased modulation (~7% RMS) and fall time (~ 2ps).

As mentioned above, in the case of FERMI a nearly quadratically increasing ramp, as shown on Fig.4 a, is required [3], so the system has at present been optimized for generating such a profile. Fig. 4b presents typical pulse profile measured by cross-correlating the UV pulse with an IR pulse using down-conversion in a 250 micron thick BBO crystal. It was possible to change the duration of the ramp by adjusting the UV stretcher length. For small duration changes the pulse shape was not strongly affected, so no other adjustments were needed. For larger (i.e. more than 2 ps) duration changes, an additional adjustment of the piezo-mirror was necessary.

The transverse shaping of the UV beam is performed by a commercial asperic beam shaper (Moltech). After a proper adjustment of the input Gaussian beam dimension the shaper produces a flat-top distribution which then is relay-imaged on the cathode by the beam transport system. Typical_results at the output of the shaper and after a Relay imaging is shown on Fig.5, left and right, respectively.

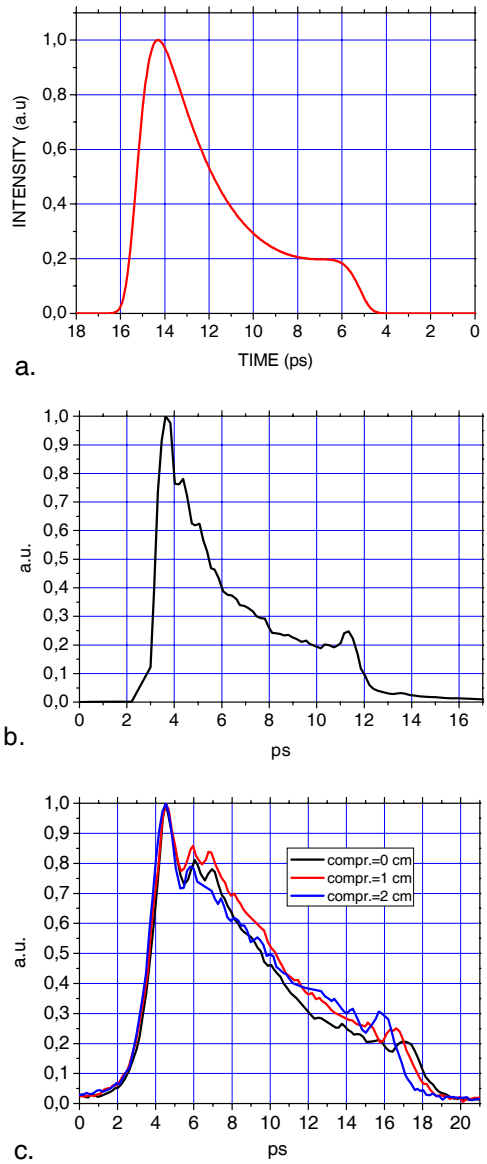

Figure 4: Increasing ramp pulse shapes, a-plot of the required pulse shape; b- cross-correlation trace of the obtained UV pulse; c- pulses of variable duration obtained by adjusting the compressor

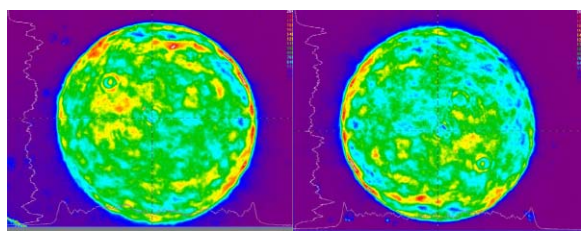

Figure 5: Images of flat-top UV beam after beam shaper (left), and after Relay imaging (right)

TIMING JITTER

The initially requested timing jitter for the FERMI PIL was initially set conservatively at 350 fs RMS , taking into account simulations that were performed at Elettra, as well as the best specs of commercial Ti:Sapphire oscillators. It was expected that the actual system performance will exceed the specs and this was confirmed by the measurements. First, the phase noise of the oscillator locked to an external low noise RF generator was measured. Integrating this curve in the range 10Hz-10MHz an RMS timing jitter of about 180 fs was obtained (blue curve on Fig.6). The red curve on the same graph shows the result of the same type of measurement done using a commercial fibre laser (Menlo Systems). It is seen that, if needed, jitter could be reduced by a factor of two if the latter (after frequency doubling) is used for seeding our amplifier system. At present, however, the jitter performance of the Ti:sapphire oscillator is considered satisfactory for the photoinjector laser.

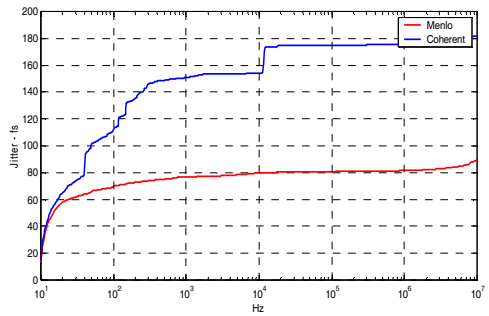

Figure 6. Timing jitter of the Ti:sapphire oscillator (blue) and an Er-doped fibre laser (red)

A question which arises naturally and to our knowledge has not been so far addressed in literature is how much jitter is added by the amplifier system. To clarify this point we pe4rformed a measurement of this jitter by monitoring the cross-correlation signal generated in a thin nonlinear crystal (BBO) by samples of the pulses before and after the amplifier. After measuring the cross-correlation (about 150 fs long nearly Gaussian), the delay was fixed at half-maximum level, so as to have maximum range where the measured fluctuation of the cross-correlation signal was linearly proportional to the timing jitter. A calibration was performed by measuring the signal change by controlled delays. The signal was measured at the rep rate of the amplifier (50 Hz). A typical 10 min record is shown on Figure 7. The jitter value extracted from this measurement was 9.8 fs. At longer time scale, the cross-correlation signal was exhibiting slow drifts, which indicates the need of implementing a beam-path stabilization of the beam-transport when the system will be installed at the photoinjector.

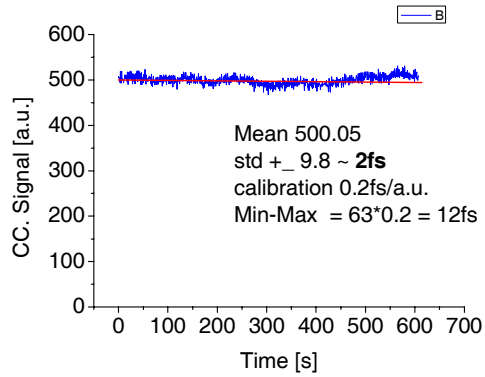

Figure 7. Typical cross-correlation signal by the jitter-measurement

CONCLUSIONS

This paper presents details on the exact setup and performance of the laser system developed for the FERMI photoinjector. The obtained results show that the implemented solutions for amplification, harmonic generation and shaping schemes were correct and allow to guarantee all the required parameters. In particular, we demonstrate for the first time the generation of the prescribed for FERMI increasing ramp UV pulse shape. We also present a first measurement of the timing jitter added by a high energy Ti:sapphire amplifier.

REFERENCES

[1] C. Limborg-Deprey, Proc.27th FEL Conf.(2005), 418.
[2] O.J. Luiten, M.J. Van der Wiel, 27th FEL Conf.(2005) ,paper WEOB003.
[3] G.Penco et al, Proc.FEL 2006, Berlin, Germany, p.625.
[4] M.B.Danailov et al, Proc.FEL 2006, Berlin, Germany, p.617.
[5] P. Tournois, Opt. Comm. 140 (1997), p.245.

A LASER HEATER FOR FERMI@ELETTRA

S.Spampinati, S. Di Mitri, B Diviacco, Sincrotrone Trieste, Italy.

Abstract

To cure the microbunching instability in the FERMI@elettra FEL a laser heater is proposed. The one-dimensional model of the instability predicts a large energy modulation cumulating as the electron beam travels along the linac. According to analytical studies and simulations the longitudinal Landau damping provided by the laser heater is expected to help in suppressing the formation of such a modulation. The efficiency of the beam heating is studied as function of the transverse laser-electron beam mismatch in the laser heater undulator in case of a realistic transverse beam profile.

INTRODUCTION

The FERMI@elettra [1] project will upgrade the Elettra linac with the installation of a photoinjector, a laser heater, an X-band cavity and two magnetic bunch compressors. The linac will then be able to provide the high current, low emittance and low energy spread (high brightness) electron beam needed by the single-pass Free Electron Laser (FEL). In this paper we describe the laser heater.

LASER HEATER

The laser heater is planned to be installed in the linac at a point where the electron beam energy is roughly 100 MeV. This device will provide a controlled increase of the uncorrelated energy spread. According to analytical and numerical studies, the beam heating is expected to help in suppressing the microbunching instability through longitudinal Landau damping [2].

The laser heater layout is shown in Figure 1.

The laser heater consists of an undulator located within a small magnetic chicane that allows an external laser to seed the electron beam. There is space for further diagnostic devices beyond the exit of the laser heater undulator.

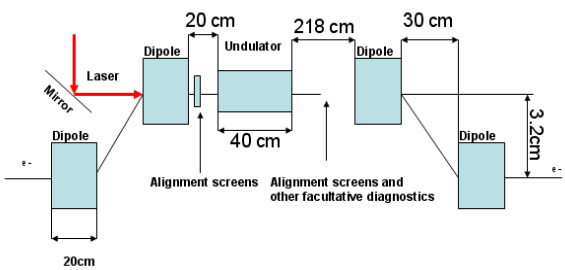

Figure 1: Schematic of the laser heater layout.

The particles interact with the laser in the short undulator and they gain an energy modulation with a periodicity on the scale of the optical wavelength. The corresponding density modulation is negligible; however, the induced energy/position correlation is smeared by the transverse motion in the chicane. As a result, the laser/electron interaction leads to an effective heating of the beam. The main laser heater parameters are listed in the Table 1.

The laser used for the heater will be split from the main beam of the Ti:Sa laser used for the photoinjector laser system. The maximum peak laser power available in the undulator is 10 MW. The IR laser will be stretched to reach a pulse duration of 20 ps. The pulse energy needed is <1mJ, therefore only a small part of the infrared light energy available (for laser heater and photocathode, >18mJ) will be needed for the laser heater. The induced energy spread must be in the rage 10 – 20 keV RMS [3].

Table 1: Mean laser heater parameters

Parameter	**value**
Undulator period	4 cm
Number of periods	12
Bending angle	3.5 degrees
Bending length	20 cm
Drift between bending	30 cm
Drift before undulator	20 cm
Drift after undulator	218 cm
Total length	418 cm

Neglecting changes in the laser and beam transverse dimensions during the interaction, the provided energy modulation for a “hard edge” undulator filed [4] is given by equation.(1):

$$\Delta\gamma_L(r)=\sqrt{\frac{P_L}{P_0}}\frac{K\,L_U}{\gamma_0\,\sigma_r}\left[J_0\left(\frac{K^2}{4+2K^2}\right)-J_1\left(\frac{K^2}{4+2K^2}\right)\right]\cdot e^{-\frac{r^2}{4\sigma_r^2}}\frac{\sin(\frac{\nu_0}{2})}{\frac{\nu_0}{2}}$$

with:

$$\nu_0 = 2\pi N\frac{(\lambda-\lambda_r)}{\lambda} \quad (2)$$

P_L is the laser peak power, $P_0 = 8.7GW$, r is the average radius of the electron beam transverse size, σ_r is the RMS laser spot size in the undulator and $\gamma_0 mc^2$ is the average total energy of the electron beam. J_0 and J_1 are the Bessel functions, K is the undulator parameter, L_u is the undulator length, λ_u is the undulator period, N is the number of periods of the

undulator, I is the laser intensity, γ is the Lorentz factor, λ_r is the resonance wavelength of the laser/electron interaction and λ is the laser wavelength.

The ratio R between the energy modulation $\Delta\gamma_L$ and the energy spread σ_γ depends on the transverse parameter B defined as:

$$B = \frac{\sigma_r}{\sigma_x} \quad (3)$$

where σ_x is the rms horizontal size of the electron beam.

R is 2 for B=1 and it is <2 for B>1. As the Landau damping is less effective for B<1, it is possible to estimate the needed laser power by using R=2 that is:

$$\sigma_\gamma = \frac{\Delta\gamma_L(0)}{2} \quad (4)$$

UNDULATOR

The laser heater undulator is a simple planar permanent magnetic structure. It is designed to be resonant at the 780 nm nominal wavelength of the Ti:Sa photocathode laser for an average beam energy ranging from 85 MeV to 105 MeV. The resonant condition is:

$$\lambda_0 = \frac{\lambda_u}{2\gamma^2}\left(1+\frac{K^2}{2}\right) \quad (5)$$

The undulator period determines the minimum energy at which the undulator is resonant and the minimum gap needed. The undulator is not resonant at a beam energy of 85 MeV for a periods longer than 4.3 cm given the minimum gap required is too tight for a period shorter than 4.0 cm. These considerations are made explicit in Figure 2. A period 4 cm long has been therefore chosen.

The number of periods has to be limited in order to have a large energy acceptance. Figure 3 shows the variation of energy spread as a function of the laser detuning for various number of undulator periods.

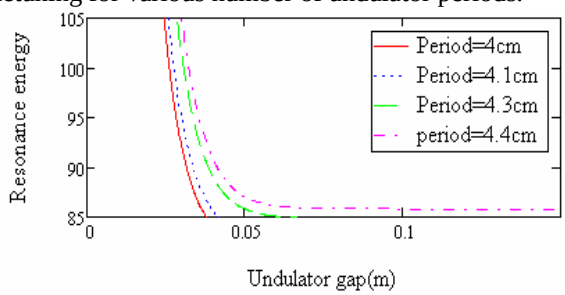

Figure 2: Resonance energy in MeV vs. undulator gap. The undulator tunability has been evaluated for different undulator period lengths.

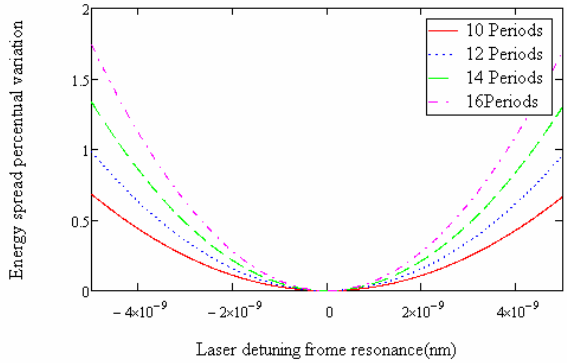

Figure 3: Energy spread percentage variation vs. laser wavelength detuning from the resonance condition.

The present undulator design includes 12 periods (8-10 effective periods) for a total length of 48 cm. The terminations are designed to have no residual dispersion and to provide no orbit displacement. The gap range is 24 – 38 mm for a maximum peak field in the range 0.312 T – 0.102 T.

According to the undulator parameters discussed so far, eq. (4) predicts a peak power of 0.5 MW to induce an energy spread of 20 keV rms.

CHICANE DYNAMICS

The effects of the laser heater chicane on the beam have been analysed. The particle longitudinal coordinate along the bunch (*i.e.*, referred to the beam centre of mass) when the beam reaches the centre of the chicane can be evaluated through the 2nd order transport matrices at the same location and the initial energy and transverse coordinates:

$$z(f) = z(i) + R_{51}x + R_{52}x' + R_{56}\frac{\delta_\gamma}{\gamma_0} + T_{566}\left(\frac{\delta_\gamma}{\gamma_0}\right)^2 \quad (6)$$

For a symmetric achromatic chicane, $R_{51} = 0\text{m}$. The energy/position correlation induced by the interaction is smeared if the following relation is satisfied [5]:

$$|R_{52}|\sigma_{x'} > \frac{\lambda_L}{2\pi} \quad (7)$$

For FERMI, $R_{52} = 0.031\text{m}$, $\beta \approx 2.5\text{m}$ and $\sigma_x' = \sqrt{\varepsilon_x}/\beta_x \approx 55\mu m$. Thus, the correlation is efficiently smeared for a finite emittance beam as shown in Figure 4.

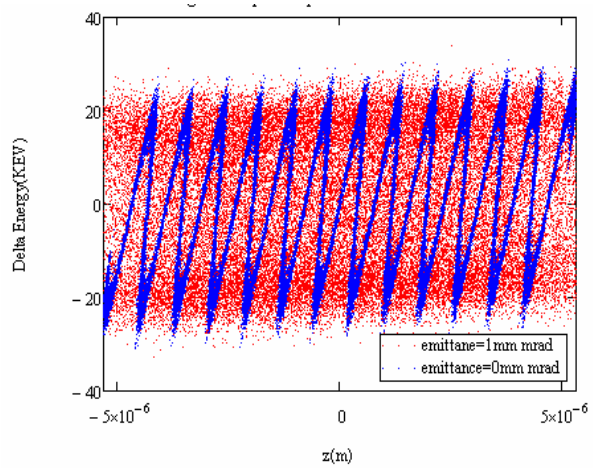

Figure 4: Longitudinal phase space (energy spread in KeV vs. bunch length in m) out of the laser heater chicane. A finite transverse normalized emittance of 1 mm mrad is sufficient to smear the energy/position correlation induced by the laser/electron interaction. For comparison, we show that the smearing effect does not happen for a null emittance, *i.e.* the correlation persists.

Exiting the photoinjector, the bunch head as at a higher energy respect to the bunch tail, therefore eq.(6) describes a beam lengthening. Given the design parameters reported in Table 1 and the known beam energy chirp provided by running off-crest in the upstream linac (the photoinjector accelerates approximately on crest), the laser heater chicane produces an increase of the beam length of about 2%. This effect is not critical for the subsequent compression.

Moreover, as the energy spread increases in the dispersive region, the heating can lead to an emittance dilution by additionally induced betatron motion. The relative emittance growth can be estimated by [5]:

$$\frac{\Delta\varepsilon_x}{\varepsilon_x} = \frac{1}{2}\left(\frac{\sigma_\gamma \eta}{\gamma_0 \sigma_x}\right)^2 \qquad (8)$$

For FERMI this effect is negligible since $\frac{\Delta\varepsilon_x}{\varepsilon_x} = 1.5 \cdot 10^{-5}$

PARTICLE TRACKING

Using the tracking code elegant [x], particle tracking has been performed on a 6 dimensional Gaussian electron beam with elegant code. The energy distribution of the electron beam generated by the photo-cathode has been reproduced in elegant and is shown in Figures 5.

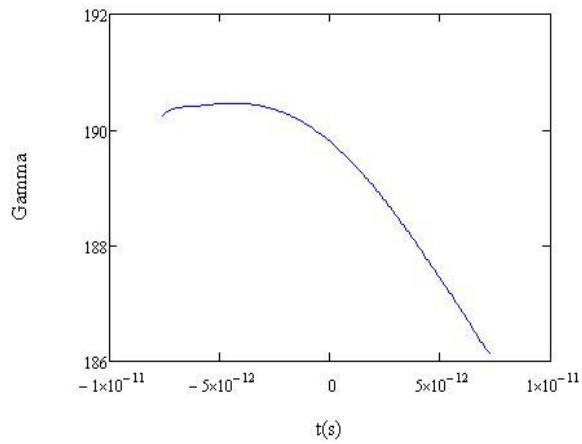

Figure 5: Energy profile of the beam out of the photo-injector.

According to the energy distribution shown in Figure 5, the dispersive motion in the laser heater chicane generates a different transverse displacement of the beam longitudinal slices with respect to the undulator axis (see, Figure 6).

The different overlap of each slice with the seeding laser, together with the variation of the slice transverse dimension also shown in Figure 6, leads to a non-uniform beam heating.

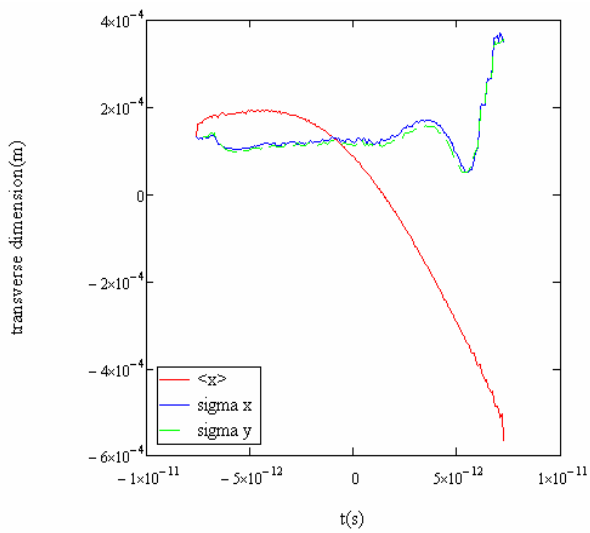

Figure 6: Mean transverse (x) position and transverse (x, y) rms dimensions of the beam in the chicane.

Different runs have been performed by changing the laser waist from 480 μm (B=2 for the flat part of the beam) to 240 μm (B=1 for the flat part of he beam) to obtain a more uniform beam heating. Accordingly, the laser power has been changed (see, eq.(1)) to induce always the same uncorrelated energy spread. Results are shown in Figures 7 and 8.

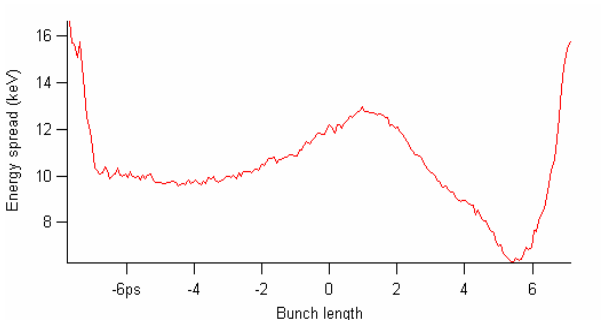

Figure 7: Rms uncorrelated energy spread along the bunch. Laser waist is 240 m (B=1 for the flat part of the beam). Laser peak power is 0.130 MW.

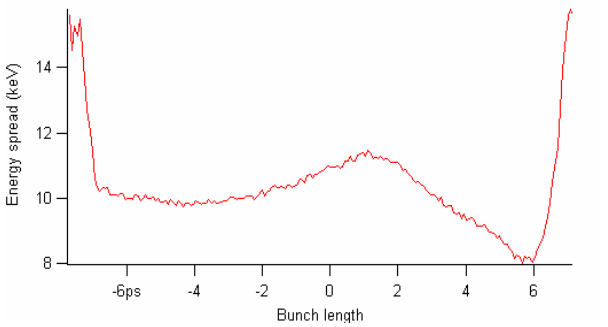

Figure 8: Rms uncorrelated energy spread along the bunch. Laser waist is 480 m (B=2 for the flat part of the beam). Laser peak power is 0.165 MW.

The resulting beam was then propagated through the rest of the linac. The longitudinal phase space at the end of the linac is shown in Figure 9 and in Figure 10, corresponding to Figure 7 and Figure 8, respectively.

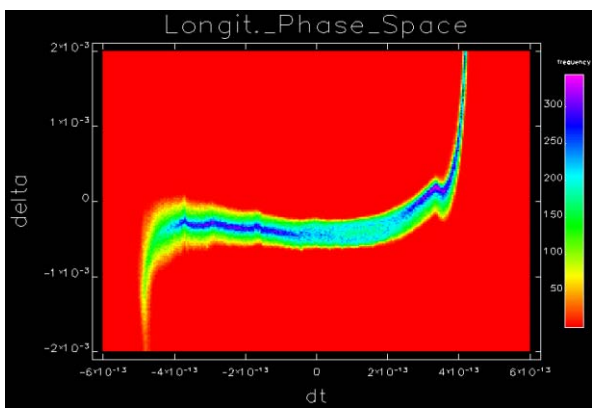

Figure 9: Longitudinal phase space (relative energy spread vs. bunch duration) at the linac end, corresponding to the beam heating in Figure 7.

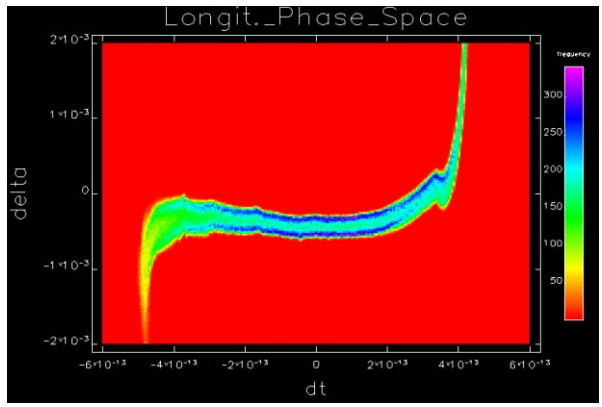

Figure 10: Longitudinal phase space (relative energy spread vs. bunch duration) at the linac end, corresponding to the beam heating in Figure 8.

Simulations predict that an rms uncorrelated energy spread of 10 keV can be induced uniformly over about 60% of the bunch duration with a laser waist of 480 m and a peak power of 0.165 MW. Preliminary calculations indicate that 37 keV energy spread can be reached in the bunch core with a the maximum peak power of 10 MW at a beam energy of 85 MeV.

CONCLUSIONS

The parameters of the laser heater main components (undulator and magnetic chicane) have been explored. Analytical calculations and particle tracking demonstrate that the peak power by the Ti:Sa photo-cathode laser is sufficient for the required beam heating.

[1] FERMI@elettra CDR, to be published.
[2] E.L. Saldin, E.A. Schnaidmiller, M.V. Yurkov, Nuclear Instruments and Methods A 429 (1999) 233.
[3] A.Zolents *et al.*, Fermi Tecnical Note 06/15 (2006).
[4] G.Dattoli, A.Renieri, Laser Handbook Vol.4 (1984).
[5] Z.Huang *et al.*, Phys Rev ST-AB **7** 074401 (2004).
[6] M.Borland, APS LS-287 (2000).

UV PERFORMANCES OF PULSED LASER DEPOSITION GROWN MG PHOTOCATHODES*

L. Cultrera, G. Gatti, F. Tazzioli (INFN/LNF, Frascati (Roma)), C. Ristoscu (INFLPR, Bucharest - Magurele), P. Miglietta, A. Perrone (INFN-Lecce, Lecce)

Abstract

We report a detailed description of the laser cleaning procedure and emission performance measurement on a Pulsed Laser Deposited Mg film. During the tests performed after the end of each cleaning operation we have evidenced an increase of Quantum Efficiency (QE) in time. Then the QE apparently stabilizes at a remarkably higher value. The study of this phenomenon is important because it determines both the working QE value and the lifetime of the cathode. Moreover, the stability of the QE has been revealed for a time scale of several days after each laser cleaning process, in our vacuum conditions.

INTRODUCTION

The electron injectors for the advanced projects of fourth generation X-ray sources, as SASE-FELs [1], and for future linear colliders [2], are mostly based on laser excited photocathodes. Metals have order of femto-second response and they are rugged in handling. Among them, Mg has premium QE, in the order of 10^{-3} at near UV wavelength (266 nm). However, bulk Mg cathodes have shown poor emission uniformity and failures in the high electric fields environment of RF guns. Moreover, the QE value degrades in time even in the UHV vacuum of RF guns.As an alternative, Mg films on copper substrates have been proposed and tested on the basis of their presumed better purity and uniformity [3]. Previous reports on Mg films grown by Pulsed Laser Deposition showed promising results in particular with respect to uniformity of emission, quantum yield, and adhesion to the substrate [4-6].

In order to reach the utmost QE value is necessary to remove the inevitable oxide layer that forms on the film surface. Only two techniques were used to perform such operation: laser cleaning and ionic etching [7]. The laser cleaning operation must be performed with particular care due to the limited thickness of the film and to avoid inducing surface roughness. It was evidenced that the cleaning irradiation may determine a variation of the film surface morphology [8].

The aim of this paper is to describe the film deposition conditions, the laser cleaning procedure and to evidence the performance of Mg films from photoemission point of view.

EXPERIMENTAL

Cathode preparation

The PLD technique is a well-known method for thin films deposition of several materials [9, 10]. The PLD apparatus used to deposit thin films is shown in figure 1. During the deposition the vacuum chamber was filled with pure He at a pressure of 5 Pa to reach the plume confinement regime leading to an increase of the deposition rate [11].

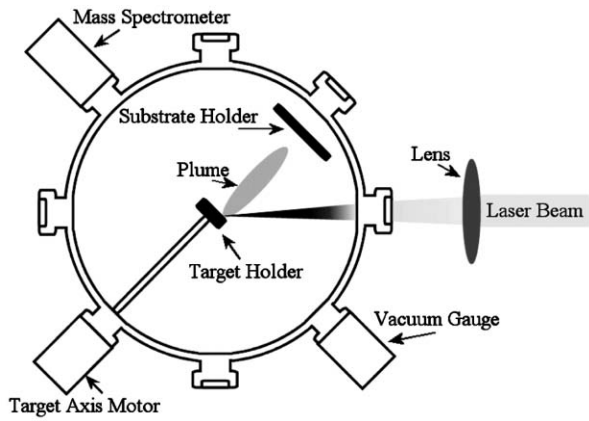

Figure 1: PLD experimental setup.

With the aim to clean the target surface, a pre-irradiation treatment was applied with 5,000 laser pulses. During this laser cleaning, the Cu substrate was shielded from the initial ablated material, which could contain impurities. Several films were prepared to optimize the deposition process. The deposition parameters of the tested sample are shown in table 1.

Table 1: Mg film deposition parameters.

Target	Mg
Substrate	Cu
Target-Substrate distance	3.5 cm
Laser spot size	1.0 mm^2
Base pressure	5 x 10^{-6} Pa
Laser pulses • Cleaning (5 x 10^{-6} Pa) • Deposition (in He at 5 Pa)	 5000 50000
Laser fluence	10 J/cm^2
Film thickness	2.5 μm
Film diameter	12 mm

Vacuum diode cell

The QE measurements were performed in a photodiode cell under UHV condition. The cathode and the anode separated at a distance of 3 mm were placed inside the photodiode cell (fig. 2). The Mg film occupied the cathode position and was electrically grounded. The anode plate was biased with high DC voltages up to 5 kV thus allowing the generation inside the gap of an intense electric field of about 1.7 MVolt/m.

* This work has been partially supported by the EU commission in the sixth framework program, contract no. 011935 EUROFEL and by MIUR, Progetti Strategici, DD 1834. December 4. 2002.

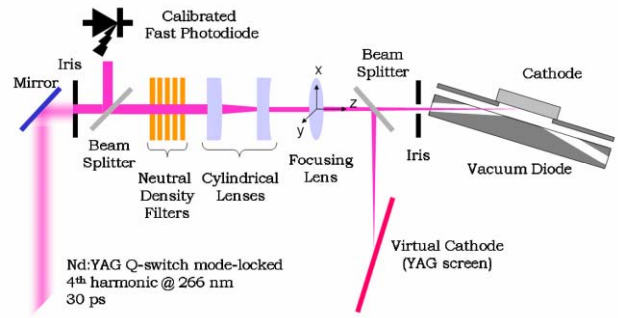

Figure 2: Laser cleaning and QE measurement setup.

In order to illuminate the cathode and for precise alignment of UV laser beam on cathode surface the anode plate was machined with two symmetric holes. They have a diameter of 4 mm and form an angle of 72° with respect to the normal of the cathode surface. This particular geometry was chosen for two main reasons:

- The first was to avoid the use of a metallic grid usually present in such experiments. Our previous experimental results clearly indicated that the light distribution on the cathode surface, in presence of a metallic grid, was affected by diffraction structures and hampered uniform illumination of the cathode surface [6];
- Secondarily, the angle of 72° was chosen in order to perform experiments with the same geometrical configuration used in the last generation of the BNL/SLAC/UCLA 1.6 cells S-Band RF gun [12].

The vacuum chamber in which the photodiode cell was inserted was evacuated at a base pressure of about $2x10^{-7}$ Pa by means of an ionic pump. The quality of the vacuum was controlled by a quadrupole mass spectrometer.

Laser cleaning and QE measurements

Laser cleaning and QE measurements of the Mg films were performed using the UV radiation of the 4th harmonic of a Q-switch, mode-locked Nd:YAG laser (QUANTEL YG-501) able to deliver up to 300 μJoule at 266 nm with a pulse duration of 30 ps. The laser energy measurements were performed by integrating the signal of the calibrated fast photodiode, while the charge measurements were done using a charge integrator.

The laser cleaning procedure was performed by scanning the focused laser beam over an area of about 2.4x2.4 mm^2. The laser beam had a diameter on the cathode surface of about 300 μm and energy of about 25 μJoule per pulse (power density and laser fluence were about 3 GW/cm^2 and 35 mJ/cm^2 per pulse respectively). Such value of the power density was experimentally determined during preliminary tests as being the threshold for the ablation of the oxidized layers. The power density threshold value for the ablation was deduced looking at the vacuum level of the UHV chamber: we observed that once such value was reached, the vacuum level inside the chamber slightly worsened indicating that material ablation was occurring.

The scanning scheme was chosen in such way that laser shots focused over consecutive horizontal path lines slightly overlap in order to make sure that all parts of the surface were exposed to the laser beam. Typically during the laser cleaning the laser repetition rate was set at 5 Hz and the scanning speed of the laser spot was on the order of 10^{-3} m/s.

After each laser cleaning procedure the focusing lens was removed and the laser beam was directed to the central part of the irradiated area of the cathode to measure the QE. In order to perform measurements far from space charge saturation, the laser energy was decreased by means of calibrated neutral density filters.

RESULTS

The first emission measurement was performed before any laser cleaning treatment. It revealed a very poor QE of about $2x10^{-6}$. Just after the first laser cleaning procedure, performed as above described, the QE measured value rose of about 2 orders of magnitude reaching the noticeable value of $5x10^{-4}$, very close to the value reported in literature for bulk pure Mg [13].

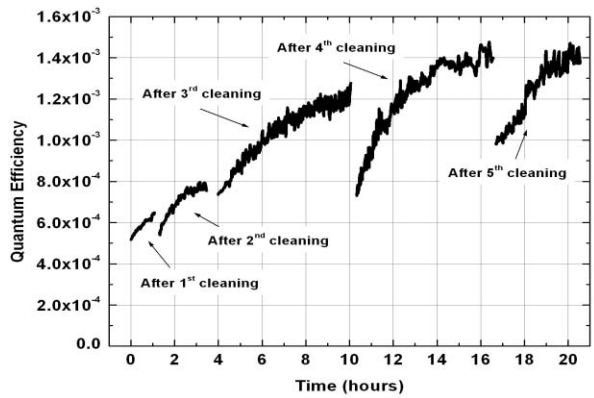

Figure 3: QE measurement vs. time after laser cleaning.

In order to study the stability of emission we performed QE measurements vs. time for several hours (fig. 3). The measurement after the first laser cleaning was performed for about 1.5 hours. We detected a slight increase of the QE value during this time from the initial value (just after the cleaning) of about $5x10^{-4}$ up to $6.5x10^{-4}$. After about 12 hours, we carried out a new laser cleaning of the cathode surface. The QE value was monitored again for about 2.5 hours. After the 2nd cleaning, the measured QE was slightly lower than the last measured value, but also in this case its value increased from $5.5x10^{-4}$ of up to about $8.0x10^{-4}$. About 12 hours later, we executed a 3rd cleaning and measured the QE continuously. We observed again that after an initial decrease just after the laser cleaning (from $8.0x10^{-4}$ to $7.5x10^{-4}$), the QE value increased up to $1.2x10^{-3}$ during the next 6 hours. The 4th cleaning procedure was accomplished about 12 hours before the last QE measurements. In this case, the single raster scheme was performed 5 times. After the laser cleaning we detected a strong decrease of the QE that lowered to an initial value

of $7.5x10^{-4}$. During the next 6.5 hours we continuously measured the QE value, observing a continuous increase up to a value of about $1.4x10^{-3}$. The 5th and final laser cleaning, carried out using a single raster scheme, resulted in an initial QE value of 10^{-3} that rose up to $1.4x10^{-3}$ during next 4 hours. It is evident the strong variation, up to a factor two, during each measurement.

The sample was kept under vacuum at a base pressure of $2x10^{-7}$ Pa during the next two days. After this time we performed new measurements without additional laser cleaning procedure. We observed that the QE value was the same with that measured two days before, i.e. $1.4x10^{-3}$. This value was preserved also after the irradiation of the surface with about 5 μJoule for about 1 hour with a repetition rate of 5 Hz. The aim of the test was to verify the ability of such cathode to maintain its emission performances also during irradiation with laser energy slightly exceeding that required to extract electron bunches of 1 nC charge.

Additionally the QE map of the irradiated area was drawn. In order to perform such measurement the laser energy was lowered to few nJ by means of neutral density filters. The laser was focused on the cathode surface by a 30 cm focal length fused silica lens. The truncated gaussian laser spot was then moved in succession over a grid of 9x9 points on the laser-cleaned area. The average QE on each irradiated area of about 300 μm diameter is evaluated from the slope of emission curves, i.e. collected charge vs. laser energy, far from space charge saturation regime. The 300 μm diameter is the minimum compatible with the sensitivity of our charge detector apparatus to remain below the extractable charge limit. Naturally this entails a limit on the spatial resolution which cannot be less than about twice the value of the laser spot diameter.

The QE map of the sample collected 72 hours after the 5th and last laser cleaning process is reported in figure 4. With the limitations due to the size of the laser spot during such measurements the emission seems to be reasonably uniform inside a circle of about 500 μm of radius centred in the most intense emitting area.

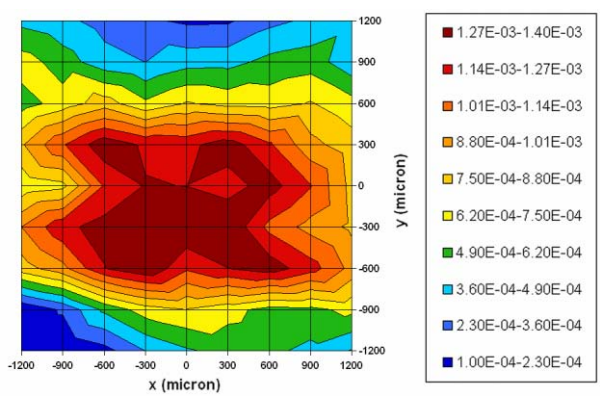

Figure 4: QE map after 5th laser cleaning.

DISCUSSION

QE values for Mg reported by now in literature, either for bulk or film, are scattered in a range within $2.5x10^{-4}$ and $3x10^{-3}$ for an exciting wavelength of 266 nm. The reason of this spread can be the different experimental conditions, as e.g. vacuum base pressure and electric field intensities [14-16].

Theoretical prediction for the QE value for Mg at 266 nm indicates a value of about $5x10^{-4}$. Higher values cannot be predicted assuming a work function of 3.66 eV. A decrease of such value by means of the formation of some electric dipole on the surface due to the gas absorption may be the key to explain such high photoemission performance from this material.

The very gradual laser cleaning procedure described before should remove only the uppermost deeply oxidized layer. It has the typical rock-salt structure of the MgO and was formed by exposing the film surface to air during the time between the deposition procedure and emission characterization, both performed in UHV environment. Ref. 3 reports that successive laser cleaning procedures resulted in an increase of the QE. This is also clearly observed also in our previous [4-6] and present experiments, demonstrating that pure Mg metal surface has been obtained with the removal of surface oxidized layers. Nevertheless, a continuous monitoring of the emission yield of the Mg film during a time interval of several hours after each laser cleaning clearly indicates that some other processes influenced the electron surface emission properties. Few years ago the effects of oxygen adsorption on the quantum yield of Mg films have been reported by Q. Yuan et al. [17]. They showed that a significant increase of QE is achieved by exposing Mg film to controlled fluxes of pure O_2. After an initial increase, strongly dependent on the oxygen dose, the quantum yield deteriorates, pointing to the formation of a thick oxidized layer that delayed the emission of photoelectrons. Similar results were observed in 1935 by R.J. Cashman and W.S. Huxford [18]. Their findings on the lowering of the work function during initial oxidation of the Mg surface were confirmed through numerical computation by E. Schröder et al. [19].

Our experimental situation was quite different from those of the experiments reported in literature. In our case no fluxes of oxygen have been introduced in the vacuum chamber. Our working base pressure was $2.5x10^{-7}$ Pa and the O_2 partial pressure was two orders of magnitude lower than that used in other experiments reported in literature [17, 18]. Partial pressures of residual gases were measured by a quadrupole mass spectrometer. From the residual gas mass spectra we observed that the most abundant chemical species were H_2, H_2O, N_2 and O_2, with partial pressures of $1.9x10^{-7}$ Pa, $1.5x10^{-8}$ Pa, $3x10^{-8}$ Pa and $8x10^{-9}$ Pa, respectively.

According to our readings of partial pressure and to the duration of the QE acquisitions, which, as reported in figure 5, were performed up to a maximum of about 6 hours, we deduced that the Mg surface exposed to O_2, at partial pressure level of $8x10^{-9}$ Pa, led to a surface coverage lower than 1 monolayer. On the contrary, H_2 exposure during the same time, due to higher partial pressure of this chemical species with respect to

molecular oxygen, may give rise to a surface coverage higher than 2-3 monolayers. According to R. J. Cashman and W. S. Huxford [18] who studied the emission properties of Mg surface exposed to H_2 fluxes, we consider that the increase of the quantum yield of our sample is related to the chemisorption of hydrogen in subsurface sites of Mg film, and in a lesser extent of oxygen. This should lead to a decrease of the work function because an electric dipole is formed under those conditions near the surface of the film with orientation that helps photoexcited electrons to escape in vacuum. Such idea is partially confirmed by the findings of P. T. Sprunger and E. W. Plummer [20] who observed a decrease of 0.95 eV of the initial value of the work function after the complete hydrogenation of the Mg(0001) surface due to the formation of a metastable "hydride" phase. They also reported that the activation energy for the chemisorption of H_2 on Mg(0001) surface was of about 0.5 eV and thus at room temperature the formation of this phase should not be observed. PLD films grown at room temperature usually do not present a well defined crystalline structure. XRD spectra (here not showed) reveal that polycrystalline Mg film was formed on laser cleaned areas with slight texture on (002) orientation. Under these conditions, we can expect that the activation energy for chemisorption of H_2 on Mg amorphous surfaces may be lower than that reported for Mg(0001), as also indicated by Nørskov et al. [21].

Tests performed by irradiating the cleaned area with laser pulses (λ=266 nm, τ=30 ps) having 5 μJ of energy show any influence on the QE. This result seems to indicate that the energy required to photo-dissociate the Mg-H bond should be higher than 4.67 eV.

The emission inside the central part of the laser cleaned area within a radius of approximately 500 μm and considering the limitations of our experimental arrangements seems to be uniform within 20%. We found out that the rapid decrease of the efficiency observed for vertical coordinate values close to the extreme of the measured area is just due to a non-perfect alignment of the laser beam inside the *bore* where it has to travel to illuminate the cathode surface. This misalignment does not influence the measurements in the central zone of the scanned area.

Figure 5: Mg film deposited over the backflange of a BNL/SLAC/UCLA 1.6 cells S-Band RF gun.

CONCLUSIONS

We presented the results of laser cleaning effect in terms of Quantum Efficiency, emission uniformity, surface morphology and structure of pulsed laser deposited pure Mg films on copper substrate. Moreover, the influence of the chemisorption of hydrogen, always present as residual gas in ultra high vacuum operating conditions, has been discussed with particular attention with respect to the efficiency and stability of the emission performances of Mg surface. Mg films have been grown in the central part of a backflange suitable to be inserted onto an RF gun and the power tests are in progress (figure 5). This work has been partially supported by the EU commission in the sixth framework program, contract no. 011935 EUROFEL and by MIUR, Progetti Strategici, DD 1834, December 4, 2002.

REFERENCES

[1] C. Pellegrini, *Proc. of EPAC98*, p. 83 (1998)
[2] H. H. Braun et al., *Proc. of PAC01*, p.720 (2001)
[3] T. Srinivasan-Rao et al., *Rev. Sci. Inst.* **62,** p. 2292 (1998)
[4] L. Cultrera et al., *Appl. Surf. Sci.* **248,** p. 397(2005)
[5] A. Perrone et al., *Nucl. Instr. Meth. Phys. Res. A* **554,** p. 220 (2005)
[6] L. Cultrera et al., *Appl. Surf. Sci.* **253,** p. 6531 (2007)
[7] J. F. Schmerge et al., *Proc. of FEL 2006*, p. 732 (2006)
[8] J. Smedley et al., *J. Appl. Phys.* **98,** p. 043111 (2005)
[9] Chrisey D B and Hubler G K 1994 *Pulsed Laser Deposition of Thin Films* (New York, Wiley)
[10] Popescu M *"Pulsed Laser Deposition of Optoelectronic Films"*, (Bucharest, INOE Publishing) A. Pereira et al., *Thin Solid Films* **497,** p. 142 (2006)
[11] D. T. Palmer et al., *Proc. of PAC97*, p. 2687 (1998)
[12] K. L. Jensen et al., *Proc. of FEL 2004*, p. 574 (2004)
[13] X. J. Wang et al., *Nucl. Instr. Meth. Phys. Res. A* **356,** p. 159 (1995)
[14] T. Srinivasan Rao et al., *J. Appl. Phys.* **77,** p. 1275 (1995)
[15] T. Srinivasan Rao et al., *J. Appl. Phys.* **69,** 3291 (1991)
[16] Q. Yuanet al., *J. Vac. Sci. Technol. B* **21,** p. 2830 (2003)
[17] R. J. Cashman and W. S. Huxford, *Phys. Rev.* **48,** p. 734 (1935)
[18] E. Schröder et al., *Phys. Rev. B* **69**, p. 115431 (2004)
[19] P. T. Sprunger and E. W. Plummer, *Chem. Phys. Lett.* **187,** p. 559 (1991)
[20] J. K. et al, *Phys. Rev. Lett.* **46,** p. 257 (1981)

HIGH BRIGHTNESS C-BAND AND X-BAND PHOTOINJECTOR CONCEPTS AND RELATED TECHNOLOGICAL CHALLENGES

M. Ferrario, D. Alesini, V. Fusco, M. Migliorati, L. Palumbo, B. Spataro, INFN-LNF, Frascati, Roma, Italy.
L. Serafini, INFN-Mi, Milano, Italy.
J. B. Rosenzweig, UCLA, Los Angeles, CA, USA.

Abstract

Future light sources based on high gain free electron lasers, require the production, acceleration and transport up to the undulator entrance of high brightness (low emittance, high peak current) electron bunches. Wake fields effects in accelerating sections and in magnetic bunch compressors typically contribute to emittance degradation, hence the photo-injector design and its operation is the leading edge for high quality beam production. The state of the art photoinjector beam brightness can be in principle brought close and above the 10^{15} A/m^2 threshold with C-band and X-band guns and a proper emittance compensation scheme. We discuss in this paper optimized designs of split C-band and X-band photoinjectors and the further technological developments required to reach such an appealing goal.

INTRODUCTION

The optimization of a FEL source is quite a complicated task [1] but the main requirement for the electron beam in order to achieve short wavelength radiation in a reasonable long undulator (30-100 m) is clear: high transverse brightness. Transverse beam brightness is defined hereafter with the approximated [2] expression:

$$B_{\perp} \approx \frac{2I}{\varepsilon_{n,x}\varepsilon_{n,y}}$$

where I is the bunch peak current and ε_n is the bunch transverse normalized emittance. The expected transverse brightness for electron beams driving short wavelength SASE FEL facilities is of the order of $10^{15} - 10^{16}$ A/m^2. Wake fields effects in accelerating sections and in magnetic bunch compressors typically contribute to emittance degradation, hence the photo-injector design and its operation is the leading edge for high quality beam production. In a photoinjector the emitted electrons are rapidly accelerated to relativistic energies, thus partially mitigating the emittance growth due to space charge effects that is the dominant source of emittance degradation in a high brightness photoinjector. One of the key feature that make RF photoinjectors so actractive is that the emittance growth is reduced when operated at high peak field as the one achievable in the RF gun: up to 140 MV/m in a S-band gun. In addition the technique termed "emittance compensation" [3] has been experimentally verified in many laboratories and theoretically well understood [4].

A lot of efforts has been done in the last years at SPRING-8 and SLAC in the context of the high frequency normal conducting linear collider development, in order to achieve high accelerating gradient in C and X-band accelerating structures. Accelerating gradient in multi-cell TW accelerating structures as high as 40 MV/m (C-band) and 100 MV/m (X-band) has been so far achieved with low breakdown rate. In a different context an X-band standing wave 5.5 cells photoinjector has been developed at SLAC as a compact electron source for Thomson backscattering experiments. As reported in [5] a peak field on the cathode surface of 200 MV/m has been achieved.

The decision to adopt L-band superconducting technology for the next International Linear Collider (ILC) has somehow damped the effort towards high frequency structures development. More recently the choice to adopt X-band technology in the framework of the CLIC project [6], which has a less tight temporal time schedule than ILC, has open up again the interest towards X-band high gradient cavity R&D. FEL sources driven by high brightness linacs will certainly take profit from this new effort in the linear collider community, in particular for the possibility to develop high gradient photoinjectors. To this end we discuss in this paper possible designs of high frequency RF photoinjectors based on C-band or X-band technology, able to produce beams with brightness as high as 10^{15} A/m^2 directly from the injector and the related technological developments required to reach such an appealing goal

SCALING APPROACH TO HIGH FREQUENCY PHOTOINJECTORS

We decided to investigate a split photoinjector configuration, consisting in a 1.6 cells standing wave RF gun followed by a booster, because it is a well know scheme in the L and S band projects and also because is a promising design to achieve ultra-high gradients operating at higher frequency: the reduced wall surfaces implies a lower probability for surface defects that may cause RF breakdown. Another possible scheme has been presented in [17]. In addition following the matching condition discussed in [4] a working point very suitable to damp emittance oscillations has been found [7]. As any well optimised design it can be easily scaled [8,9] to any other frequency, gradient or charge design.

As a reference design we have taken the S-band (2856 MHz) SPARC [15] photoinjector. In its ideal configuration the beam consists in a uniform charge distribution inside a cylinder of length L and radius R, and we have scaled its parameters (charge Q, beam sizes

R and L, peak RF field $\hat{E}$ and solenoid field B) to its second (C-band) and fourth (X-band) harmonic frequencies (5.712 GHz and 11.424 GHz respectively) according to the following wavelength scaling laws [8]:

$$Q \propto \lambda_{rf} \ , \ R, L \propto \lambda_{rf} \ , \ \hat{E} \ \propto \lambda_{rf}^{-1} \ , \ \hat{B} \ \propto \lambda_{rf}^{-1}$$

As discussed in [8] both the space charge and RF contributions to the total rms emittance scale with λ_{rf}, in addition since the thermal emittance contribution scale with the beam radius we can expect a similar scaling also for $\varepsilon_{th} \propto \lambda_{rf}$. Hence operation at shorter wavelength results a very convenient choice also for the beam brightness: $B_n \propto \lambda_{rf}^{-2}$ [8].

Tab I: Original and scaled parameters

Freq. [GHz]	Q [nC]	R [mm]	L [ps]	E_{peak} [MV/m]	B [T]
2.856	1	1	10	120	0.275
5.712	0.5	0.5	5	240	0.55
11.424	0.25	0.25	2.5	480	1.1

A direct application of the previous scaling laws leads to the set of new parameters, reported in table I. In addition, to fulfil the scaling approach, also the solenoid length has to be scaled with λ_{rf}, from the original 20 cm long solenoid for the S-band gun design to 10 cm for the C-band case and to 5 cm for the X-band gun case, see figure 1.

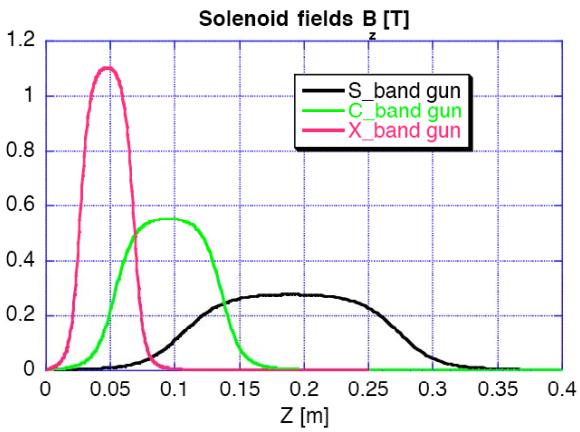

Figure 1: Solenoid fields for the original S-band gun design (black line), the C-band design (green line) and X-band design (red line).

C-BAND PHOTOINJECTOR CASE

HOMDYN simulations for the full C-band injector (1.6 cell RF gun 7. cm long, followed at z = 1 m by 3 C-band travelling wave accelerating structures operating at 40 MV/m accelerating field) show for this case an emittance of 0.49 μm, as reported in figure 2, with a peak current of 92 A, corresponding to a brightness of B_n of 7.7 10^{14} A/m^2, a factor 4 higher than the corresponding S-band design [7]. In this and in the following cases we have assumed a thermal emittance of 0.6 μm/mm for a copper cathode [16].

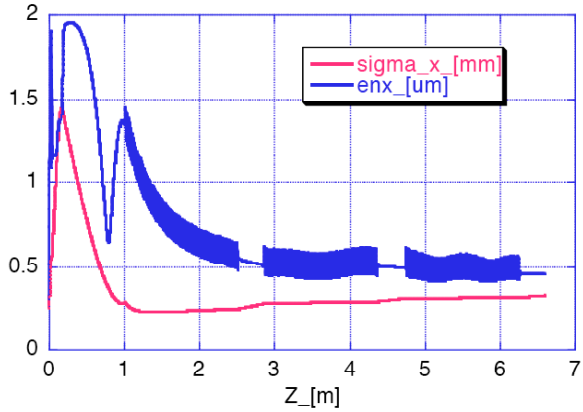

Figure 2: Envelope and rms norm. emittance evolution from the cathode up to the booster exit at 180 MeV for the C-band case.

X-BAND PHOTOINJECTOR CASE

The X-band scaling implies RF and solenoid fields that are too far from the state of the art to be realistic, see Tab. I. A first attempt towards a more realistic design can be done by reducing the solenoid field to 0.575 T and increasing its length, from 5 cm to 10 cm, basically the same solenoid adopted for the C-band case. HOMDYN simulations for the full X-band injector (1.6 cell RF gun, 3.75 cm long, followed at z = 0.6 m by 3 X-band travelling wave accelerating structures of the SLAC type, operating at 56 MV/m accelerating field) show for this optimistic case an emittance of 0.27 μm, as reported in Figure 2, with a peak current of 90 A, corresponding to a brightness of B_n of 2.5 10^{15} A/m^2.

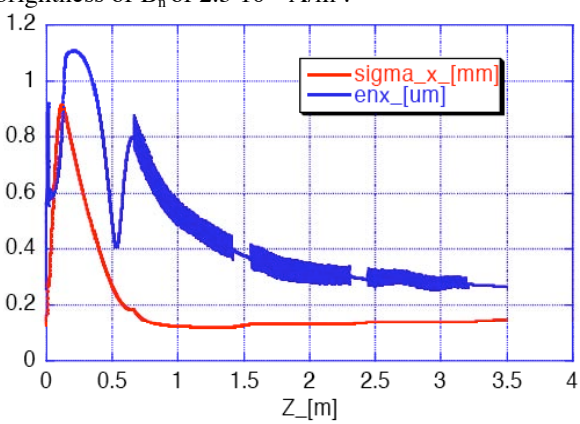

Figure 3: Envelope and rms norm. emittance evolution from the cathode up to the booster exit at 130 MeV for the X-band case.

Again scaling laws can help us to re-optimize the injector parameters in order to obtain a less challenging RF peak field, another important step towards a more realistic design. A reduced gun peak field results in a lower energy gain, hence we have to apply the energy scaling laws derived in [9]:

$$\hat{B} \propto \gamma \ , \ R \propto \gamma^{-2/3} \ , \ L \propto \gamma^{-5/3}$$

Aiming to reduce the peak filed from 480 MV/m to 350 MV/m (reducing the beam energy at the gun exit from 5.5 MeV down to 4.1 MeV) the new parameters computed with the previous equations are reported in table II:

Tab II: Original and scaled parameters

Freq. [MHz]	Q [nC]	R [mm]	L [ps]	E_{peak} [MV/m]	B [T]
11.424	0.25	0.25	2.5	480	0.575
11.424	0.25	0.31	4.2	350	0.420

Envelope and emittance evolution as computed by HOMDYN are reported in figure 4. The final emittance is practically unchanged compared to previous case, resulting 0.28 μm, while the peak current is affected by the lower energy bunch elongation in the drift, resulting 58 A. The corresponding brightness is nevertheless quite high $B_n = 1.5\ 10^{15}$ A/m^2.

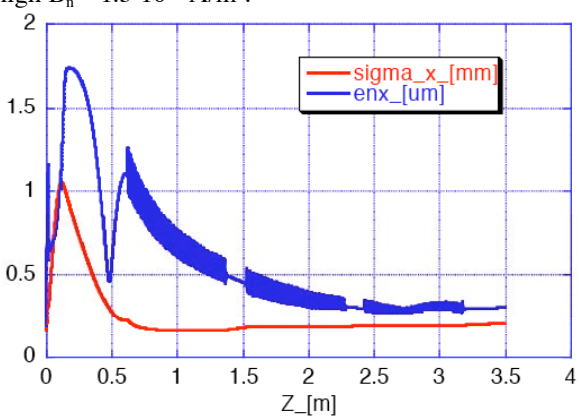

Figure 4: Envelope and rms norm. emittance evolution from the cathode up to the booster exit at 120 MeV for the X-band case with reduced gun peak field .

TECHNOLOGICAL CHALLENGES

In table III are reported for comparison the RF parameters for the S, C and X band guns. As one can see the required peak power from RF source are within the state of the art C and X-band klystron development.

Tab III: RF gun parameters

ν [Ghz]	2.856	5.712	11.424
R_{sh} [MΩ/m]	46	65	92
Q	15335	10843	7668
E_{peak}[MV/m]	120	240	350
P_{RF} [MW]	10	14	10
P_d at 10 Hz [kW/m]	2.6	3.7	2.6
τ [μs]	4	2	1
L_{cav} [cm]	15	7.5	3.75

A serious concern is the compensation scheme to protect the klystron port from RF power reflections since circulators/isolators are not available in C and X-band. A possibility to protect the RF source from reflections is to use a 90 deg hybrid junction as sketched in Fig. 5. The scheme foresees the use of two SW cavities: the gun and a second compensating cavity that can be installed in the injector for acceleration. A first analysis of the sensitivity of such a scheme with respect to the cavity parameters or waveguide electrical length has shown that this solution is not critical. The scheme is commonly implemented in the SLED cavities and has been already and successfully applied to compensate reflections in SW structures for particle accelerators, as illustrated in [10]. It allows to perfectly compensating the "steady state" reflections given by the cavity but it does not allow eliminating the reflected power from discharges or breakdown in one of the two cavities. A second possible scheme is illustrated in Fig. 6. In this case the klystron is coupled to the SW gun through a directional coupler. The power from the source is split in the two waveguide branches: a fraction A(<1) of the input power feed the gun while the fraction (1-A) is dissipated into a load or can feed a matched TW section. In this case, if a discharge occurs in the SW gun the reflected power to the source is, at maximum, a fraction A^2 of the klystron initial output power and can be acceptable if the directional coupler is properly designed. This scheme allows compensating both "steady state" reflected power than that given by a discharge in the SW gun.

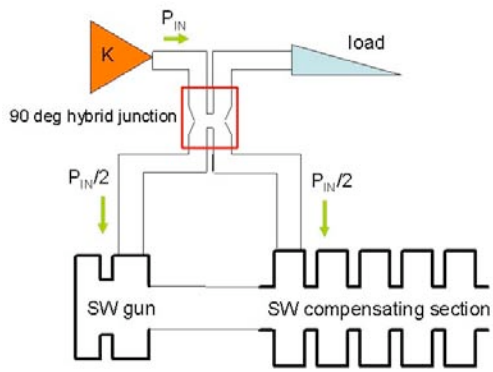

Figure 5: Possible scheme with a 90 deg hybrid junction to protect the klystron from SW gun reflections.

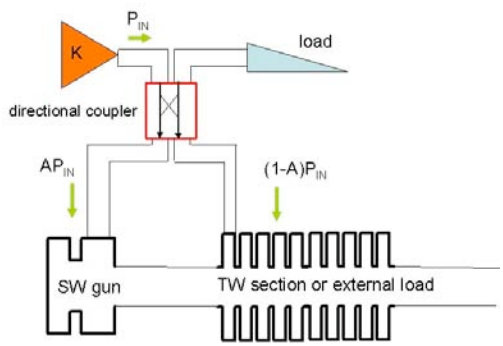

Figure 6: Possible scheme with a directional coupler to protect the klystron from SW gun reflections.

The request of high peak field in the gun cavity is the main challenge at least for the X-band case. It has been

demonstrated that a way to increase the RF fields inside the accelerating structure is the use of Molybdenum for cavity irises [11]. An R&D activity on this direction has been recently started also at INFN-LNF [12] in order to define the best brazing geometry among Mo irises and Cu structure [13]. Electroformed structures [14] are also under study at LNF and a first test of deposition of Mo over Cu in a 4 cells X-band structure has been already successfully done, see figure 6. The lack of X-band power sources at the moment prevents us to perform high power RF tests.

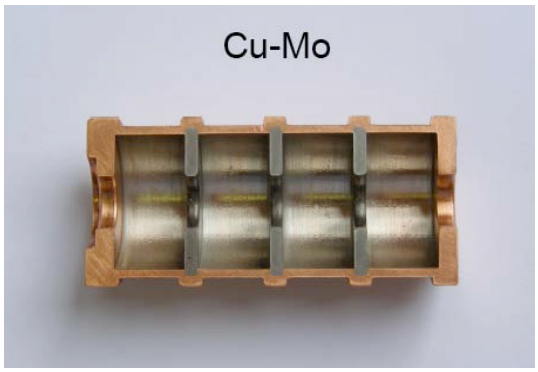

Figure 6: A Mo-Cu electroformed structure produced at INFN-LNF.

REFERENCES

[1] M. Xie, "Design Optimization for an X-ray FEL driven by SLAC linac", Proc. of PAC Conference, 1995.

[2] C. A. Brau, "What brightness means", Proc. of the ICFA workshop on "The physics and applications of high brightness beams", Sardinia, July 2002, World Scientific.

[3] B. E. Carlsten, Nucl. Instrum. Methods A **285**, 313 (1989).

[4] L. Serafini, J. B. Rosenzweig, Phys. Rev. E **55** (1997) 7565.

[5] E. Vlieks et al., "Development of an X-band photoinjector at SLAC", Proc. of LINAC 2002, Korea.

[6] H. Braun et al., "Towards a multi-TeV linear collider", Proc. of APAC 2007, India

[7] M. Ferrario et al., "HOMDYN study for the LCLS RF photoinjector", SLAC-PUB-8400, (2000).

[8] J. B. Rosenzweig and E. Colby, "Charge and Wavelength Scaling of RF Photoinjector Designs", in Proc. of Advanced Accelerator Concepts, AIP Conf. Proc. **335** 724 (1995)

[9] M. Ferrario et al., "Recent Advances and Novel Ideas for High Brightness Electron Beam Production Based on Photo-Injectors", SPARC-BD-03/003

[10] F. Marcellini and D. Alesini, "The RF Deflector for the CTF3 delay loop", Proc of EPAC 2006, Scotland.

[11] T. Ramsvik et al., Phys. Rev. Special Topics - Accelerators And Beams 10, 042001 (2007)

[12] B. Spataro et al., "R&D on X-Band Accelerating Structures at the INFN-LNF", SPARC-RF-06/002

[13] S. Bini et al., "Status report on SALAF technical activity on vacuum brazing on X-band linear accelerating structures", SPARC-RF-07/004

[14] B. Spataro et al., "Electroforming procedures applied to the construction of 11.4 GHz linear accelerating structures", SPARC-RF-07/003

[15] E. Chiadroni et al., these Proceedings

[16] W. Graves et al., "Measurement of thermal emittance for a copper photocathode", Proc. of PAC 2001.

[17] A. Fukasawa et al., "Charge and wavelength scaling of the UCLA/URLS/INFN hybrid photoinjector", Proc. of PAC 2007, New Mexico, USA.

WAKEFIELD INDUCED ENERGY SPREAD IN THE FERMI UNDULATOR

A.A.G. Lutman*, M. Castronovo†, R. Vescovo*, Università degli Studi di Trieste, Trieste, Italy
C. Bonţoiu, P. Craievich‡, L. Rumiz, ELETTRA, Trieste, Italy

Abstract

The FERMI Project aims to achieve very high-brightness photon beam pulses of minimum bandwidth. These goals can be marred by the presence of large wakefields along the undulator small-gap vacuum chamber. Estimations of the induced energy-spread caused by the resistive wall and surface roughness wakefields along the FERMI FEL undulator are presented. The energy spread and losses induced by resistive wall wakefield are determined for three possible transverse geometries of the vacuum chamber, namely circular, rectangular and elliptic cross-section, while the energy spread and losses induced by the surface roughness wakefields are obtained for the circular cross-section case. In this last case in-house surface profile measurements carried on a spare vacuum chamber of ELETTRA are used to provide realistic estimates.

WAKEFIELDS IN THE UNDULATOR VACUUM CHAMBER

In the undulator vacuum chamber the finite conductivity of the metal wall and the roughness of the chamber inner surface wakefields are sources of wakefields. For the FEL effect, the main concern is the longitudinal wake which may impress an energy modulation on the electron bunch and consequently degrade the quality of the FEL radiation. Transverse wakefields are much less disruptive in the undulator and will be neglected.

Resistive Wall Wakefields

The interaction between the electron beam and the metal wall has been evaluated for circular, rectangular and elliptical cross-section vacuum chambers. Regardless of the shape of the cross-section, the chamber is modeled as an infinite pipe with finite conductivity σ, electron relaxation time $\tau > 0$ and infinite wall thickness. The relative longitudinal displacement from the bunch head will be denoted by z. The almost flat-top short bunches which will be used for the FERMI FEL contain very high frequencies components induced by the residual current spikes and thus require, as pointed out by Bane [1], the use of the AC conductivity model. In the following formulas the skin-depth related parameter $\lambda = \sqrt{\frac{Z_0 \sigma |k|}{2}}(i + sign(k))$ will be used, where Z_0 is the intrinsic impedance of the vacuum and k is the wave number.

Circular cross-section: For the circular cross-section, the calculations rely on the formula derived by Chao [2]. Denoting with b the radius of the pipe, the longitudinal coupling impedance is given in SI units by:

$$Z(k) = \frac{Z_0}{4\pi} \frac{1}{b} \frac{2}{\frac{\lambda}{k} - \frac{ikb}{2}} \tag{1}$$

Rectangular cross-section: For the rectangular shape the evaluation relies on the formulas given by Henke and Napoly [3]. Although the theory is elaborated for two conducting infinite parallel plates, we will use it for a rectangular cross-section neglecting the effects of the lateral walls. Denoting with b the half gap between the metal plates, the longitudinal coupling impedance, as given in [4] is in SI units:

$$Z(k) = \frac{Z_0}{4\pi} \int_{-\infty}^{+\infty} \frac{1}{\frac{\lambda}{k} \cosh^2 bx - \frac{ik}{x} \cosh bx \sinh bx} dx \tag{2}$$

Elliptic cross-section: For the elliptic cross-section shape a novel method that holds for AC conductivity and allows one to evaluate the wakes at very short range, has been developed. The fields are obtained by developing a system of solutions to the Maxwell's equations both in the vacuum and in the resistive wall and then imposing the boundary conditions on the wall surface similar to what has been done for the circular case. The longitudinal and transverse wake functions are then calculated using field expansions. Maxwell's equations have been solved in an elliptic cylindrical system of coordinates (u, v, z) (see Fig. 1), taking the source as an ultrarelativistic point charge travelling down the pipe, parallel to its axis, located arbitrarily in (u_1,v_1,0). On the cross-section the interface between the vacuum and the metal wall is the ellipse of equation $u = u_0$. With the observation that, due to causality, any field must vanish for $z > 0$, the Fourier transform of the electric and magnetic longitudinal fields in the vacuum, can be written as:

$$\begin{aligned} \tilde{E}_z &= \sum_{n=0}^{+\infty} A_n \cosh nu \cos nv + \sum_{n=1}^{+\infty} B_n \sinh nu \sin nv \\ c\tilde{B}_z &= \sum_{n=0}^{+\infty} B_n \cosh nu \cos nv - \sum_{n=1}^{+\infty} A_n \sinh nu \sin nv \end{aligned} \tag{3}$$

where A_n and B_n depend on k and are determined by imposing the continuity of the fields $\tilde{E}_z$, $\tilde{B}_z$, $\tilde{E}_v$, $\tilde{B}_v$. In the vacuum, the transverse fields behavior shows a coupling between different modes. In detail the components $\cos nv$,

* DEEI
† Dipartimento di Fisica
‡ paolo.craievich@elettra.trieste.it

$\sin nv$ depend on the $(n-2)$-th, n-th and $(n+2)$-th coefficients. Maxwell's equations in the metal wall, solved by separation of variables, lead to the angular and radial Mathieu functions [5]. For small skin-depth values, the series

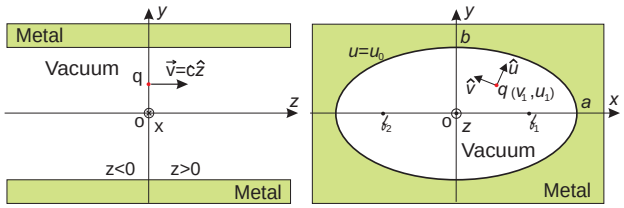

Figure 1: Elliptic cylindrical system of coordinates and the source point charge.

of products of Bessel and Hankel functions for the Mathieu radial functions can be approximated and the boundary conditions yield a tridiagonal infinite linear system for the coefficients A_n and B_n which can be truncated to calculate explicitly the coefficients. Since in the coefficients matrix there is no relation between A_n and B_n, neither between A_{2n} and A_{2n+1} nor between B_{2n} and B_{2n+1}, the whole system can be split up in four independent parts. To solve a truncated tridiagonal subsystem for the first $M+1$ coefficients, the following formula can be used:

$$\begin{cases} X_M = & \dfrac{T^c_M}{C_M} \\ X_n = & \dfrac{T^c_n - z_n X_{n+1}}{C_n} \quad n = 0..M-1 \end{cases} \tag{4}$$

where:

$$\begin{aligned} C_n &= \begin{cases} d_0 & n=0 \\ d_n - \dfrac{s_{n-1}z_{n-1}}{C_{n-1}} & n=1..M \end{cases} \\ D_n &= \dfrac{s_{n-1}}{C_{n-1}} \qquad n=1..M \\ T^c_n &= \begin{cases} t_0 & n=0 \\ t_n - T^c_{n-1}D_n & n=1..M \end{cases} \end{aligned}$$

s_n, d_n, z_n and t_n are yet to be defined for each kind of coefficient, but in the case of the longitudinal wake-function, if the leading charge is on axis, only the A even subsystem is excited and all other coefficients are zero. Denoting with a and b respectively the major and the minor half axis of the cross-section, with $l = \sqrt{a^2 - b^2}$ the half focal length and $h = l\sqrt{\cosh^2 u - \cos^2 v}$ the metric, the following formula for the A even subsystem has been obtained:

$$\begin{aligned} d_n &= -\frac{ikl^2}{\cosh 2nu_0}\left[\frac{\sinh(4n+2)u_0}{8(2n+1)} + \frac{\sinh(4n-2)u_0}{8(2n-1)}\right] + \\ &\quad + \left[\frac{i}{k} + \frac{2ik}{\lambda^2}\right] 2n \sinh 2nu_0 + \\ &\quad + l\cosh u_0 \left[\frac{k}{\lambda}\frac{\cosh 4nu_0}{\cosh 2nu_0} + \frac{\lambda \cosh 2nu_0}{k}\right] \\ s_n &= \frac{ikl^2(1+\delta_{n0})}{8(2n+1)}\frac{\sinh(4n+2)u_0}{\cosh 2(n+1)u_0} \\ z_n &= \frac{ikl^2}{8(2n+1)}\frac{\sinh(4n+2)u_0}{\cosh 2nu_0} \\ t_n &= -\frac{q}{(1+\delta_{n0})\pi\epsilon_0}\frac{\cos 2nv_1 \cosh 2nu_1}{\cosh 2nu_0} \\ n &= 0..M \end{aligned} \tag{5}$$

The Lorentz force due to the leading charge experienced, by a trailing charge q_t travelling down the pipe at the speed of light with coordinates (u, v, z) is:

$$\begin{cases} F_L = q_t E_z \\ \boldsymbol{F}_T = q_t\left[\hat{u}\left(E_u - B_v\right) + \hat{v}\left(E_v + B_u\right)\right] \end{cases} \tag{6}$$

where L denotes longitudinal and T transverse. The longitudinal wake function is obtained by numerically inverse Fourier transforming $\tilde{E}_z$ in (3), while using the relations:

$$\begin{cases} \tilde{E}_v + c\tilde{B}_u = -\frac{i}{hk}\frac{\partial \tilde{E}_z}{\partial v} \\ \tilde{E}_u - c\tilde{B}_v = +\frac{i}{hk}\frac{\partial c\tilde{B}_z}{\partial v} \end{cases} \tag{7}$$

The transverse force is obtained numerically inverting the term:

$$\frac{i}{hk}\left(\hat{u}\frac{c\partial \tilde{B}_z}{\partial v} - \hat{v}\frac{\partial \tilde{E}_z}{\partial v}\right) \tag{8}$$

Next the elliptic cross-section resistive wake function is plotted for several values of the ratio a/b, including the limiting cases $a/b = 1$ and ∞, using the materials specified in Table 1.

Table 1: Conductivity and relaxation time for Al and Cu.

	Aluminium	Copper
$\sigma\ [\Omega^{-1}m^{-1}]$	$4,22 \times 10^7$	$6,45 \times 10^7$
$\tau\ [s]$	$8,00 \times 10^{-15}$	$2,70 \times 10^{-14}$

As shown in Figs. 2 and 3 the peaks of the longitudinal wake functions continuously decrease from the circular case to the parallel plates. The wake functions obtained using copper as material for the vacuum chamber present more oscillations which are due to the higher electron relaxation time.

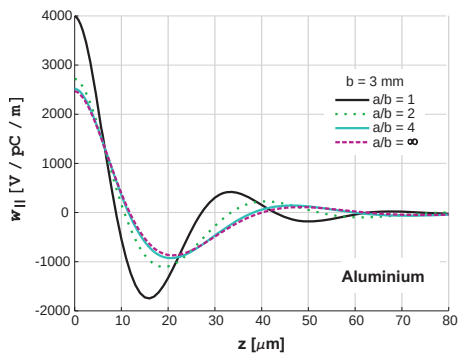

Figure 2: Longitudinal resistive wall wake functions for aluminium made walls and $b = 3$ mm.

Surface Roughness Wakefields

The interaction between the beam and the surface roughness of the undulator vacuum chamber is yet another source of energy spread which could impact FEL process. To a

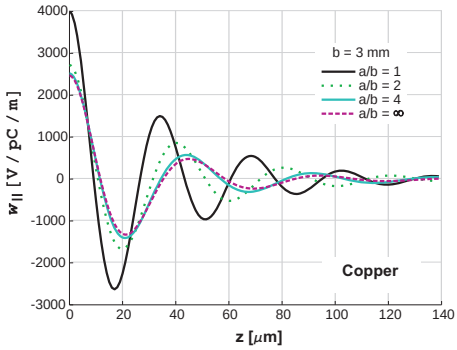

Figure 3: Longitudinal resistive wall wake functions for copper made walls and $b = 3$ mm.

first approximation the surface roughness makes the vacuum chamber behave like a disk-loaded cavity; there will be a continuous change of energy between the beam and what is called a synchronous field mode [6, 7]. Furthermore, if the roughness can be approximated by a collection of bumps whose tangent to the smooth wall is small, there will be one more contribution to the total roughness wakefield coming from their individual impedance, averaged over a certain distribution function [8].

Surface analysis: Several AFM surface scans (see Fig.4) have been carried on a spare vacuum chamber of the ELETTRA storage ring [9] in order to obtain information on the average peak height and periodicity of the roughness.

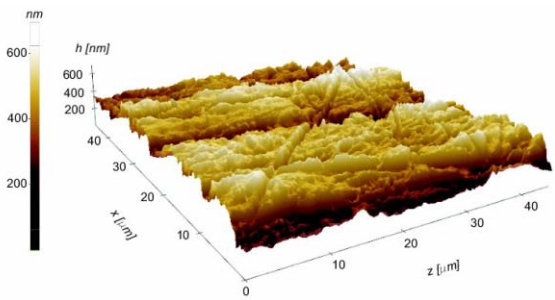

Figure 4: Measured 3D surface profile.

First, it is necessary to distinguish between the long and short range variation of the surface-vacuum boundary. Thus, a longitudinal scan over 120 μm has been filtered (Gaussian filter of 15 μm standard deviation) separating out a low-frequency surface component from a high-frequency component, (see Fig. 5). Fourier transforms of these two components reveal their frequency content $\nu = \frac{c}{\lambda}$ which together with the rms height h_{rms} makes it possible to fit them to a sinusoidal corrugation model. It turns out that the low frequency content can be treated within the resonator model with some corrections due to the very small size of the roughness height [7], while the high frequency component, due to its higher aspect ratio, can be considered within

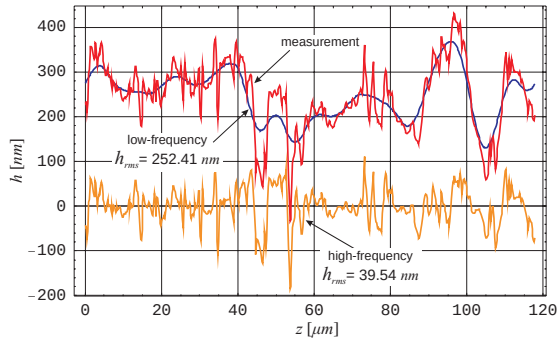

Figure 5: A Gaussian filter is applied to the real surface profile (red) in order to detach its low (blue) and high (orange) frequency components

Table 2: Overview of the corrugation parameters.

Component	λ	h_{rms}	$AR = \lambda/h_{rms}$
low-frequency	30 μm	250 nm	120
high-frequency	10 μm	40 nm	250

the Stupakov's statistical (small-angle) model [8].

Surface wakefield in circular cross-section pipes: Within the modified resonator model proposed by Stupakov [7], the roughness wake function has a cos-like variation of constant amplitude and is defined as:

$$w_{||}(z) = \frac{Z_0 c}{4\pi} \frac{h_{rms}^4 \kappa^6}{64} \cos k_0 z \qquad (9)$$

where $\kappa = 2\pi/\lambda$, b is the vacuum chamber radius and $k_0 = \kappa/2$ is the rough synchronous mode, while the statistical model predicts a damped wake function with a singularity at $z = 0$:

$$w_{||}(z) = \frac{Z_0 c}{4\pi} \frac{h_{rms}^2 \kappa^2}{b} \frac{1}{2\sqrt{\pi}} \frac{\partial}{\partial z} \frac{\cos \frac{1}{2}\kappa z + \sin \frac{1}{2}\kappa z}{\sqrt{\kappa z}} \qquad (10)$$

Using the parameters in Table 2, both wake functions are plotted comparatively for b = 3 mm in Fig. 6.

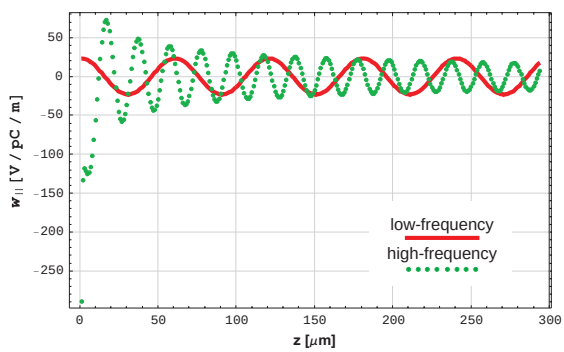

Figure 6: Surface roughness wake functions.

WAKEFIELD INDUCED ENERGY SPREAD

In this section some results concerning the induced energy spread for the medium bunch configuration of FERMI FEL [10] are presented considering contributions from the resistive wall and surface roughness wakefields.

Contribution of the electrical resistivity

Considering only Al for the vacuum chamber walls and AC conductivity, Fig. 7 shows the induced energy spread obtained through convolution between the circular/elliptic ($a/b = 6$)/rectangular (parallel plates) cross-section resistive wake functions and the longitudinal bunch profile mentioned above. Therefore, the rectangular cross-section with rounded lateral sides proposed in the FERMI CDR [10] can be replaced by an elliptic cross-section with $a/b > 6$ without changing the energy spread.

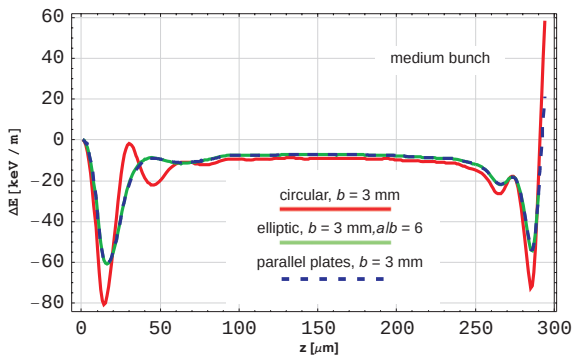

Figure 7: Resistive wall induced energy spread.

Surface roughness contribution

Convoluting separately the wake functions given by (9) and (10) with the medium bunch profile [10] the energy spread is obtained as shown in Fig. 8. As it can be seen, at

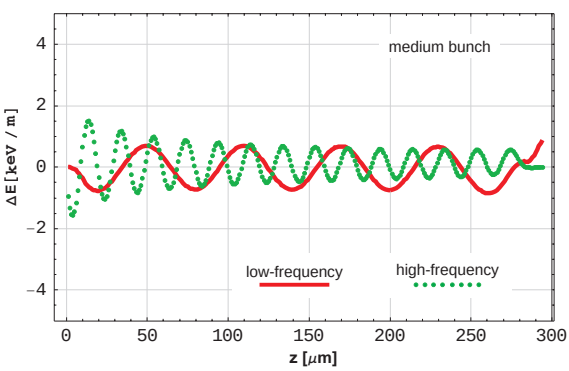

Figure 8: Roughness induced energy spread.

the core of the bunch the contribution of the low-frequency roughness component predominates over the contribution of the high-frequency roughness component both falling in the same range of magnitude.

CONCLUSIONS

Table 3 lists the maximum values of the energy spread in the useful part of the bunch (200 μm for the medium bunch and 350 μm for the long bunch). If the FERMI undulator would have vacuum chamber surface comparable with the one analyzed above, that is for AR = 120. In conclusion, it is recommended for the undulator vacuum chamber to be made of Aluminium, have a rectangular or elliptic cross-section. In what concerns the rectangular cross-section roughness wakefield, calculations are on the way and preliminary results show that the induced energy spread is 35-40 % lower than for the circular cross-section case. As for the surface, when $AR = 120$, the roughness induced energy spread accounts for about 17 % and 12 % of the resistive induced energy spread, respectively for the medium and long bunch.

Table 3: Estimated energy spread for the FERMI FEL undulator.

Source	short bunch	long bunch
Resistive wall	11.71 keV/m	9. 35 keV/m
Surface roughness	1.73 keV/m	1.17 keV/m
Total	13.44 keV/m	10.52 keV/m

REFERENCES

[1] K.L.F. Bane and G. Stupakov, “The Short Range Resistive Wall Wakefields”, SLAC/AP-87, June 1991.

[2] A.W. Chao, “Physics of Collective Beam Instabilities in High Energy Accelerators”, John Wiley & Sons, Inc. 1993.

[3] H.Henke and O.Napoly, “Wake Fields between two Parallel Plates”, CERN/LEP-RF/89-71 CLIC Note 103, 1989.

[4] K.L.F Bane and G. Stupakov, “Resistive Wall Wakefield in the LCLS Undulator Beam Pipe”, SLAC-PUB-10707.

[5] P.M.Morse and H.Feshbach, “Methods of Theoretical Physics”, McGraw-Hill, New York, 1953.

[6] A. Novokhatski and A. Mosnier, “Wakefields of short bunches in canal covered with thin dielectric layer”, PAC 1997, p.1661.

[7] G.V. Stupakov, “Surface roughness impedance”, SLAC-PUB-8743, December, 2000.

[8] G.V. Stupakov, “Impedance of small obstacles and rough surface”, Phys. Rev. ST-AB, Vol.1, 064401 (1998).

[9] A. Gambitta et al., Experience with aluminium vacuum chambers at Elettra, Proceedings of EPAC 2000, Vienna, Austria;

[10] FERMI@Elettra Conceptual Design Report, to be published.

WIDE BAND SEEDING AND WAVELENGTH COMPRESSION

Tsumoru Shintake, RIKEN/SPring-8, 679-5148 Japan

Abstract

The "wavelength compression" has a potentiality to generate seeding signal at the nano-meter wavelength by squeezing optical wavelength of the visible laser beam on a high energy electron beam. Applying energy chirp on the incoming electron beam and overlapping laser beam to produce micro-period energy modulation at optical wavelength, the velocity modulation can be converted into density modulation at shorter wavelength during the bunch compression in a chicane. Using 255 nm 4th harmonic YAG laser as modulation signal, and if we compress bunch length 20 times, we can generate coherent signal below 10 nm. By cascading multiple bunch compressors, higher compression ratio will be obtained. To go X-ray wavelength, we may use HGHG scheme after the wavelength compression. Since compression factor is variable, it becomes tuneable coherent source at X-ray wavelength, which is suitable to seeding the X-ray FELs.

Using femto-second laser at the modulator, it will generate atto-second pulse at short wavelength.

MOTIVATION

SASE-FEL: Self-amplified Spontaneous Emission Free Electron Laser, as it is named, the spontaneous radiation (noise power) is amplified in the long undulator line. If the undulator is long enough, power level reaches to saturation. Since its power level is extremely higher than conventional X-ray sources, even higher than 3rd generation light sources, many new scientific applications are expected with using this source. Also the short pulse feature in femto-sec range is expected to be an important feature for analysing fast chemical and physical reaction of condensed matter.

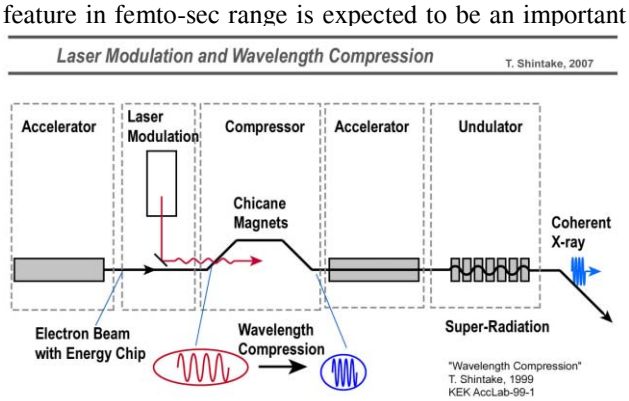

Figure 1: Laser optical modulation and wavelength compression. Applying both the energy chirp at rf wavelength and micro-period energy modulation at optical wavelength using laser beam, the modulation pattern can be compressed into short wavelength during bunch compression, which provides seeding signal to the downstream undulator. By combining with HGHG scheme in the downstream undulator line, an X-ray seeded FEL will be realized.

However, since SASE-FEL process starts from the spontaneous radiation, the resulting saturated radiation power varies shot-by-shot. And most importantly, there are many longitudinal modes, similar to old fashion ruby laser, temporal profile has many spikes, thus longitudinal coherence is quite limited.

If we seed a coherent signal from upstream undulator, the seeding signal will be amplified and saturated. It becomes (1) fully coherent, (2) temporally single-mode, (3) stable energy in pulse-to-pulse and (4) power level controllable. These features are favourable to all kind of scientific applications. Therefore, various proposals have been made on seeding schemes, including HGHG, TUHG,[3,4,5]. G. Lambert reported first observation of amplification of seeded FEL using higher harmonic generation in gas [HHG] at 160 nm in SCSS test accelerator[7].

They are also promising approach to generate coherent radiation at nano-meter wavelength. However they are not wavelength tuneable. In actual machine, a small wavelength shift was observed experimentally at DUV FEL at BNL[6]. However the observed wavelength shift was as low as 1%.

For fully tuneable seeding, the wavelength compression scheme was originally proposed by the author in 1999[1]. As shown in Fig. 2, a modulator, a short undulator was assumed as energy modulator, where a laser beam was introduced from upstream[2]. The velocity modulation is created through $E_t \cdot v_t$ coupling in the undulator. After the undulator, the electron bunch is accelerated at off-crest phase to apply energy chirp, then the bunch length is compressed. After accelerating the beam, the modulated electron beam is fed into undulator to generate coherent radiation. This scheme requires many hardware components, and also spontaneous emission in the upstream undulator cause additional energy spread on the incoming electron beam.

In the previous paper[2], the author proposed a scheme to generate energy modulation at optical wavelength using the focal point laser field. However, the laser beam has to be focused into a very small spot, and the fraction of overlapping the laser beam to the electron beam is fairly small, as a result overall modulation efficiency becomes small.

To overcome this difficulty, the author proposes a new scheme which provides higher coupling efficiency.

#shintake@spring8.or.jp

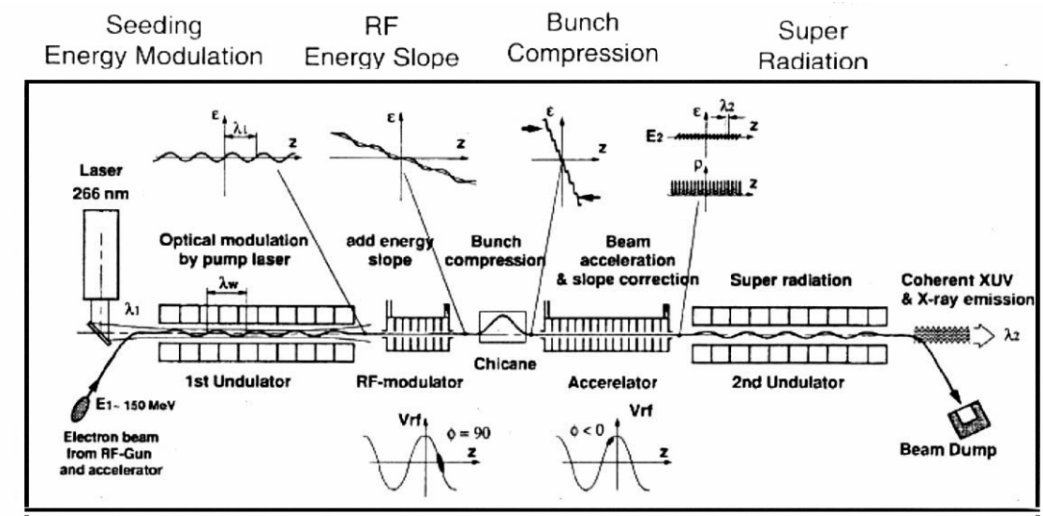

Figure 2: Original wavelength compression scheme[1], which uses independent undulator at upstream as the optical energy modulator, followed by short accelerator to adopt energy chirp. Dispersive section provides two functions of a bunch compression and energy-to-density conversion of optical modulation.

BASIC CONFIGURATION

Figure 1 shows the basic configuration of the new seeding scheme. We apply energy chirp on the incoming electron bunch in the upstream accelerator, and add energy modulation at optical wavelength at the entrance of the chicane, then compress the bunch length through the chicane. At the same time the velocity modulation can be converted into density modulation at short wavelength. The compression factors for the bunch length and the modulation wavelength are exactly same. After accelerating the beam to higher energy, and sending into undulator, the bunch will radiate coherent signal. If the wavelength of undulator radiation is tuned to the compressed modulation wavelength, the undulator will radiate coherent radiation at super radiant mode.

MODULATION PATTERN SMEARING

Electron beam has energy spread, which limits this seeding scheme. The longitudinal diffusion distance during acceleration between point-1 and point-2 is given by[2]

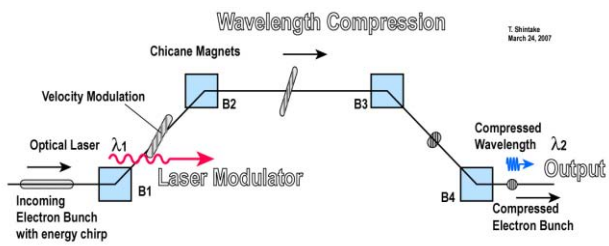

Figure 3: Overlapping laser beam and electron beam with oblique angle at the entrance of the magnetic chicane, the electron beam energy is modulated at optical wavelength. Since the incoming beam has energy chirp, the density modulation pattern is longitudinally compressed into short wavelength together with bunch length being compressed. By cascading multiple chicanes, we obtain high compression ratio, for example 1/10 x 1/10 = 1/100.

$$\Delta z = \frac{\Delta\gamma}{\gamma'}\left(\frac{1}{\beta_1}-\frac{1}{\beta_2}\right)$$
$$\gamma' = eE_z / m_0c^2 \quad , \quad (1)$$
$$\Delta\gamma = eV_{spread} / m_0c^2$$

For example, to accelerate beam up to 8 GeV (β_2 = 1) on 20 MV/m field gradient ($\gamma' = 39.1$), assuming the energy spread 30 eV, which is much higher than the thermionic energy (74 meV,), to make the diffusion distance being lower than 1 nm, we found the threshold energy 14 MeV. If we locate our laser modulator at beam energy higher 14 MeV, we may keep density modulation pattern at 1 nm.

The betatron oscillation of each electron inside the bunch also causes path difference and smearing effect. Average path difference can be estimated by

$$\Delta z_\beta = \frac{2\varepsilon_n}{\pi^2\gamma}\cdot\frac{L}{\langle\beta\rangle} \quad (2),$$

Assuming, $\varepsilon_n = 1\times10^{-6}\,\pi mm\cdot mrad$, L = 300m, β = 30 m, the path difference becomes 2 Å. This is negligibly small for 1 nm modulation.

The space charge effect also contributes to smear out the density modulation. This effect can be estimated by the electron plasma frequency:

$$\omega_p = \gamma^{-3/2}\sqrt{\frac{e\rho_0}{m_e\varepsilon_0}} \quad (3),$$

where ρ_0 is the electron density. For example, assuming beam current 100 A at 50 MeV, β-function 10 m, beam size 0.3 mm, the plasma frequency becomes 25 MHz. After travelling quarter plasma-wavelength, the density modulation becomes zero, i.e., after 3 m travel. It is known that the density modulation will recur again after quarter-wavelength. Within this length, we may accelerate beam to higher energy, where the plasma wavelength

becomes longer, thus we may keep density modulation. If we locate modulator at 500 MeV, the quarter plasma wavelength becomes 100 m. This is long enough to maintain the density modulation.

CHICANE LASER MODULATIOR

Fig. 4 shows interaction of electron beam with laser field. Here we assume the laser beam has Gaussian distribution, its transverse size is w_0. The intensity and field distributions can be expressed as

$$\begin{aligned} I &= I_0 e^{-2x^2/w_0^2}, \\ E &= E_0 e^{-x^2/w_0^2} \end{aligned}, \quad (4)$$

We consider one electron passing the laser beam with slope angle of α. The laser beam polarization is in the plane of the drawing. The energy gain of the electron during the passage is given by the following integration.

$$\begin{aligned} \Delta W &= \int_{-\infty}^{\infty} \mathbf{E}\cdot d\mathbf{s} = \int_{-\infty}^{\infty} E_x \cdot dx \\ &= \int_{-\infty}^{\infty} E_0 \cdot e^{-x^2/w_0^2} \cos(\omega t - kz + \phi) dx \end{aligned}, \quad (5)$$

where ϕ is the phase of laser field. Assuming the electron velocity is close to light velocity, the phase term becomes

$$\begin{aligned} \omega t - kz &= \left(\frac{\omega}{\beta c \cos\alpha} - k \right) \cdot z \\ &= \frac{kz}{2\gamma^2}(1+\gamma^2\alpha^2) = k'z \end{aligned}, \quad (6)$$

where k' is the synchronous wave number. It is corresponding to the wave number of undulator period, and $\gamma\alpha$ is the K-parameter.

$$k_s = \frac{k}{2\gamma^2}(1+\gamma^2\alpha^2), \quad \lambda_s = \lambda_0 \frac{2\gamma^2}{1+\gamma^2\alpha^2}, \quad (7)$$

The energy gain becomes,

$$\Delta W = \sqrt{\pi}\, E_0 w_0 \cos\phi \cdot \exp\left\{ -\left(\frac{k_s l_0}{2} \right)^2 \right\}, \quad (8)$$

Where l_0 is the interaction length of an electron to cross the laser beam: $l_0 = w_0/\alpha$. In order to obtain substantial modulation, the crossing length has to be

Table-1: Small and large angle cases.

Crossing Angle	Small Angle $\alpha = 1/\gamma$	Large Angle $\alpha >> 1/\gamma$
Synchronous Wavelength	$\lambda_s = \gamma^2 \lambda_0$	$\lambda_s = 2\lambda_0/\alpha^2$
Required Laser Size	$w_0 < \frac{\gamma\lambda}{\pi}$	$w_0 < \frac{2\lambda}{\pi\alpha}$
Modulation Energy	$\Delta W = \sqrt{\pi}\, E_0 w_0$	$\Delta W = \sqrt{\pi}\, E_0 w_0$

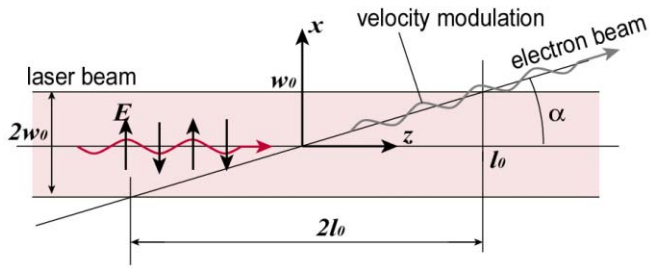

Figure 4: Electron beam passing through laser beam with oblique angle receives energy modulation.

smaller than the synchronous wavelength. From Eq. (8),

$$\frac{k_s l_0}{2} < 1, \quad l_0 < \frac{\lambda_s}{\pi}, \quad (9)$$

In this condition the modulation energy becomes $\Delta W \sim E_0 w_0$. Using Eqs. (7) and (9), we find the condition for the laser waist size,

$$w_0 = \alpha l_0 < \frac{2\lambda_0}{\pi} \frac{\gamma^2\alpha}{1+\gamma^2\alpha^2} \quad (10)$$

Due to the diffraction effect, the laser size expands along its path. If the electron trajectory stays within the laser field longer until the laser spot size becomes larger, the integral energy gain will cancel and become small. Therefore, the electron trajectory has to cross the laser beam with enough angles to make its interaction length smaller than the diffraction angle.

$$\alpha > \frac{\lambda_0}{w_0} \quad (11)$$

Additionally the electron beam size has to be same size or smaller than the laser size

$$\sigma_0 \quad w_0 \quad (12)$$

Table-1 summarizes those conditions for two cases. As seen in the table, for high energy, the required laser size becomes larger, thus easier to focus the laser beam, while it request smaller crossing angle. On the other hand, for lower beam energy, the crossing angle becomes large, but we need to focus laser beam into small size. In practical design of the bunch compressor, to obtain enough R_{56} parameter, the deflection angle becomes much larger than 1/γ. In this case, α>> 1/γ, the synchronous wavelength and laser size and also the energy gain becomes non energy dependent function. Therefore this system has very wide energy bandwidth.

REQUIRED ENERGY CHIRP AND OPTIMUM MODULATION

For the optical modulation the optimum condition is[2],

$$\frac{V_{\mathrm{mod}}}{E_0} = m \cdot \left(k_{\mathrm{mod}} R_{56} \right)^{-1}. \quad (13)$$

Table-2: Example laser modulation system for two difference beam energy.

Target Wavelength	λ_2 (nm)	10
Compression Ratio	m	100:1
Laser Source	λ_1 (nm)	1060
Beam Energy	E (MeV)	50
	γ	100
Crossing Angle	α (mrad)	10
Synchronous Wavelength	λ_s (mm)	10
Interaction Length	L_i(mm)	3
Laser Spot Size	w_0 (μm)	32
Electron Beam Size	(μm)	100 β = 1 m
Laser Power	Watt	100
Field Intensity	E_0 (MV/m)	6
Energy Modulation	ΔW (eV)	200

At this condition, the compressed modulation has the maximum contrast. For example, if we compress bunch length by 100 times at 50 MeV, m = 0.01, with R_{56} = 10 mm, and λ_{mod} = 1064 nm, the required modulation becomes $V_{mod} = 10$ eV . This value can be easily provided by the laser modulation. However, if the energy spread is large, the modulation pattern will be totally smeared out. The energy spread has to be smaller than modulation energy.

There are experimental measurements on energy spread on electron beam from RF guns. Typically, energy spread right after the gun is about 10 keV or higher. This is much larger than the thermal energy spread. This is due to the space charge effect near by the cathode. In the case of the rf photo-cathode gun, the emitted electron beam from the cathode is already bunched, and its has high peak current value ~100 A. When the electron starts from the cathode, image charge on the cathode pulls the electron back and lowers the effective acceleration gradient. This effect varies along its radial position within the beam. Therefore, an electron emitted from the centre of the cathode and from the beam edge feels different field gradient, as a result, it cause energy spread.

On the other hand, in the case of the thermionic DC gun, all electrons gain the same energy, in principle. Only the self-potential gives energy difference, while it is fairly small. At 50 MeV, for 1 nC, 10 psec, the self-potential difference is 12 eV on the electron rest frame. We need further careful discussion on how this potential energy affects on particle motion on the laboratory frame.

DISCUSSIONS

The author has not yet completed quantitative estimation on various effects concerning to the cross-coupling in the bunch compressor, beam divergence, energy spread, photo-emission and CSR effect. Therefore the discussions below are only conceptual.

- The seeded FEL does not require high peak current. If we can lower the peak current, all problem associated with the space charge will be solved.
- Recently, strong OTR radiation was observed at visible wavelength in the LCLS injector at SLAC when the beam was compressed at the first chicane magnets[8]. If the laser on the photo-cathode has intensity modulation, which generates density modulation on the emitted electron beam. When the bunch length is compressed in the chicane, the modulation wavelength was compressed from micron-meter range to visible wavelength, as just we discussed in this paper. Further careful analysis is necessary to proof this hypothesis.

CONCLUSIONS

New optical modulation scheme has been proposed in this paper. If we apply velocity modulation at optical wavelength, and compress it together with bunch length, we may obtain density modulation at shorter wavelength.

Further studies are required on non-linear field in bunch compressor, cross-coupling (R_{15}, R_{16}), non uniform velocity distribution in bunch, energy spread due to radiation excitation, etc.

SCSS test accelerator is currently running at 50 nm with SASE-FEL mode. It will be possible to install a laser modulator in our test accelerator to demonstrate velocity modulation, and demonstrate colour change in OTR radiation, and compress the wavelength by ten times in bunch compression to seed FEL at 50 nm range.

REFERENCES

[1] T. Shintake, “wavelength compression”, KEK Internal Report, AccelLab-99-1.
T. Shintake, "new idesas for future sources", CERN Accelerator School Brunnen 2-9, July 2003.
[2] T. Shintake, “Focal point laser-field as optical seeder”, proc. FEL2006, Berlin, Aug. 2006.
[3] L.-H. Yu, Phys. Rev. A44 (1991) 5178
[4] S. G. Biedron et al., "Modula approach to achieving the next-generation X-ray light source", Nucl. Instrum. Method A475 (2001) pp.401-406
[5] Timur Shaftan and Li Hua Yu, "High-gain harmonic generation free-electron laser with variable wavelength", Phys. Rev. E 71, 046501 (2005)
[6] T. Shaftan et al., "Experimental Demonstration of Wavelength Tuning in High Gain Harmonic Generation Free Electron Laser", Proc. FEL 2004, pp. 282-284, Trieste Italy
[7] Guillaume Lambert, “First Lasing in Seeding Configuration at 160 nm Using High order Harmonic Generated in gas on the FEL of the SCSS Prototype Accelerator”, this conference.
[8] D. Dowell et al., “Commissioning results of the SLAC LCLS gun”, this conference.

FEASIBILITY TEST OF LASER-INDUCED SCHOTTKY-EFFECT-GATED PHOTOCATHODE RF GUN

H. Tomizawa, Accelerator Division, Japan Synchrotron Radiation Research Institute (JASRI/SPring-8), Kouto, Sayo-cho, Sayo-gun, Hyogo 679-5198, Japan
M. Kobayashi, Research & Development Division, Nanophoton Corporation
A-509, Center for Advanced Science and Innovation, Osaka University, Osaka 565-0871, Japan.

Abstract

We propose a laser-induced Schottky-effect-gated photocathode RF gun using Z-polarization of the laser source. This concept of laser-induced Schottky emission can be applied to a photocathode DC gun (even for a polarized electron source). Radial polarized laser propagation modes exist theoretically and were recently generated practically. Focusing a radial polarized beam on the photocathode, the Z-polarization of the laser is generated at the focus point. The generated Z-polarization field can exceed an electrical field of 1 GV/m easily with fundamental wavelength from compact femtosecond Ti:Sa laser systems. According to our calculations (NA=0.15 60-% hollow ratio, inside-out Gaussian beam), the Z-field of 1 GV/m needs 1.3 MW at peak power for the fundamental (790 nm) and 0.32 MW for the second harmonic generation (SHG). In the field of 1 GV/m, the work function of copper cathode reduces ~2 eV. The quantum efficiency is pessimistically estimated to be $\sim 10^{-2}$ % at SHG by the Schottky effect associated with the 1 GV/m. This Schottky effect can be used as a gate of the photo-emission process. We report a feasibility study of this new concept of photocathode.

INTRODUCTION

There are three well-known types of electron guns; the thermionic gun, field emission gun, and photocathode gun. They are widely used for many applications. The future light sources based on linear accelerators such X-ray FEL [1,2,3] and ERL [4] required high brightness electron sources. One of the most promising candidates for such an electron source is a photocathode RF gun.

The photocathode RF gun needs a UV-laser source (~266 nm) for a long-lived metal cathode like copper and even for a higher quantum efficiency (QE) cathode such as Ce_2Te. At SPring-8 in collaboration with Hamamatsu Photonics K.K. a diamond cathode has been developed as the future transparent cathode candidate [5]. The diamond cathode is a robust and high QE cathode. However, it requires a laser wavelength below 197 nm for acceptable QE. For a robust cathode like copper and diamond, we need UV-laser light due to their high work functions. Consequently, the laser system becomes larger and complex. To make the laser source compact, we need to find a cathode with a lower work function and high QE. However, such a high QE NEA-cathode requires an ultra-high vacuum ($< 10^{-8}$Pa) and does not have a long life time.

One solution to make the work function lower is to apply a high field on the cathode. In the field of 1~2 GV/m, the work function of the copper cathode reduces 2~3 eV. To achieve such a high field (~1 GV/m) on the photocathode, the tungsten needle photocathode, the photo-assisted field-emission, was proposed and tested [6]. The dependence of quantum efficiency on a high electric field was investigated using a tungsten needle (radius: ~1μm) photocathode irradiated by the third harmonic generation (THG) of a Nd:YAG laser (353 nm) whose photon energies were lower than the work function of tungsten. The obtained QE of the needle tip is found to be proportional to the >10th power of the electric field over 500 MV/m, and it reached up to 3% at about 800 MV/m. This observed field-enhancement of QE is qualitatively explained with a field-emission process including the Schottky effect and photo excitation. However, such a needle cathode tip became round and broken in the cavity during rf conditioning.

Therefore, we started to investigate with a plane-field emitter assisted by laser radiation field. We have indirect evidence of such a laser field effect through comparison between normal and oblique incidences to the cathode. It is well known that the oblique incidence obtains higher QE than normal incidence. In the oblique incidence, the more intensive the laser illuminating the cathode, the higher a QE we obtain. It cannot be explained only with Brewster's angle. However, we have to think about multi-photon absorption in the case of intensive laser focusing on the cathode. The oblique incidence makes the laser spot elliptically larger on the cathode. However, we can obtain a higher QE. It indicates that the laser field can assist the Schottky effect on the cathode.

Radial polarized laser propagation modes exist theoretically and were recently generated practically. The radial polarization beam is a superposition of π/2 phase-shifted TEM_{01} and TEM_{10} mode in the case of a polarisation direction vertical to each other. Focusing a radial polarized beam on the photocathode, the Z-polarization of the laser is generated at the focus point. The generated Z-polarization can exceed an electrical field of 1 GV/m easily with fundamental wavelength from compact femtosecond laser systems. On the other hand, focusing an azimuth polarized beam on the photocathode results in zero Z-polarization field. Comparing the radial and azimuth polarization with focusing, we conduct a feasibility study of the laser-induced Schottky-effect on the photocathode.

PRINCIPLE OF Z-POLARIZATION

Principle of Z-polarization generation

Focusing a radial polarized beam on the photocathode as shown in Figure 1, the electric field of the laser is generated in the laser propagating direction (Z-direction) at the focus point. The Z-field oscillates with a periodic time of ~2.6 fs at the fundamental Ti:Sa laser (~790 nm). Roughly estimating in the case of a metal cathode, laser radiations (wavelength: λ) enter into the cathode surface with a depth of ~λ/20, and photocathode response is <10 fs. If the Schottky-effect-induced Z-field is large enough, we expected that electrons would make oscillations with the Z-field frequency on the outermost surface of the metal cathode and are extracted with the external electric field of the RF cavity. Note that the perfect back reflection on the cathode with normal incidence cancels out the Z-field generated by laser radiation.

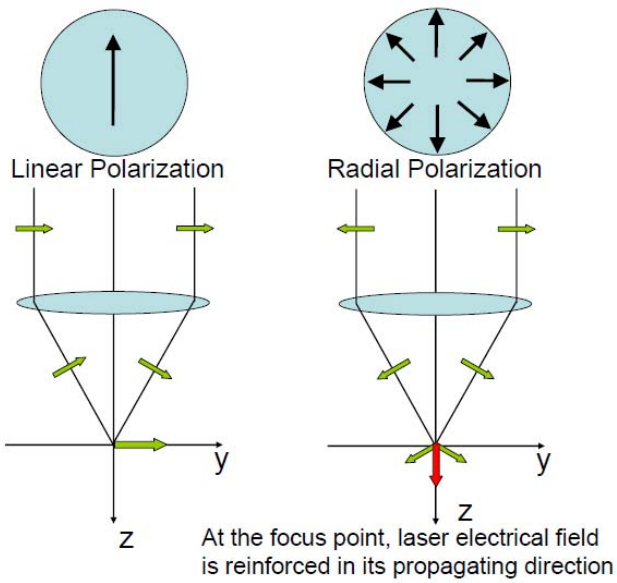

Figure 1: Principle of Z-polarization field on the cathode generated from radial polarization

Reflection ratio of cathode candidates

In order to generate the electrical field in the perpendicular direction on a metal cathode, we have to select a combination of metal cathode material and laser wavelength. Comparison among laser wavelength dependencies of reflectivity with different mirror-finished metal surfaces is shown in Figure 2. Reliable candidates for the combinations are silver with the THG of Yb:fibre laser (~350 nm), copper with the SHG of Ti:Sa laser (~395 nm), and aluminium with the fundamental of Ti:Sa laser (~790 nm). The reflection ratio of the first combination is ~10 %, the second ~30 %, the last ~75%. For the first test run, we chose the second combination with copper illuminated by the Ti:Sa SHG.

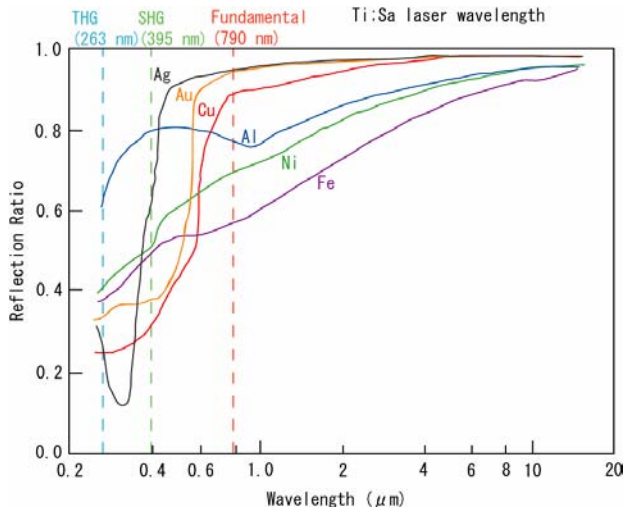

Figure 2: Laser wavelength dependencies of reflection ratio with different mirror-finished metal surfaces

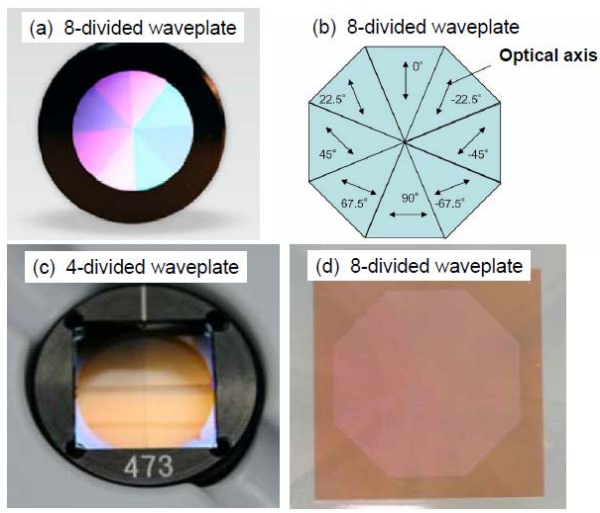

Figure 3: Several divided waveplates manufactured by Nanophoton Corporation: (a), (b) 8-divided waveplate and the direction arrangement of optical axes in each segment, (c) 4-divided waveplate with assembling 4 cuts of waveplate, (d) 8–divided waveplate with growing photonic crystal as a function of waveplate in each segment on single base plate.

Radial polarization beam generator

The radial polarization fundamental mode is generated from a combination of Hermite-Gaussian mode TEM_{01} and TEM_{10} [7]. However, directly lasing with TEM_{01} mode is not practically simple. Therefore, we chose a simple divided waveplate as shown in Figure 3 to generate the radial polarization from a conventional linearly polarized beam. We investigated the divided number dependency of Z-field at the focus point generated with the divided waveplate. The intensity distributions of Z-polarization intensity $|E|^2$ generated with waveplates with different division numbers of are shown in Figure 4. In the case of more than eight divisions, it shows no significant difference from the Z-field intensity generated from ideal radial polarization.

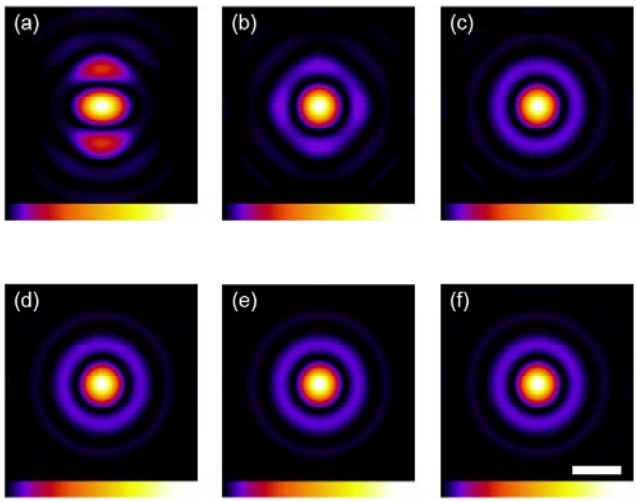

Figure 4: Using divided waveplates, the intensity distribution of Z-polarization intensity $|E|^2$: (a) 2-divided, (b) 4-divided, (c) 8-divided, (d) 16-divided, (e) 32-divided, (f) perfect radial polarization (n: infinity). White scale bar in (f) is 7.5μm @790 nm, NA=0.1 (Flattop).

Z-polarization ratio with divided waveplate

The divided number dependence of the radial polarization ratio to ideal radial polarization is shown in Figure 5 regarding the simulation results of Z-polarization at the focus point compared with analytical under- and over- estimation of the radial polarization ratio at the focus point.

In the case of the 8-divided waveplate, the radial polarization ratio to ideal radial polarization is 95% as with the simulation results of Z-field at the focus point.

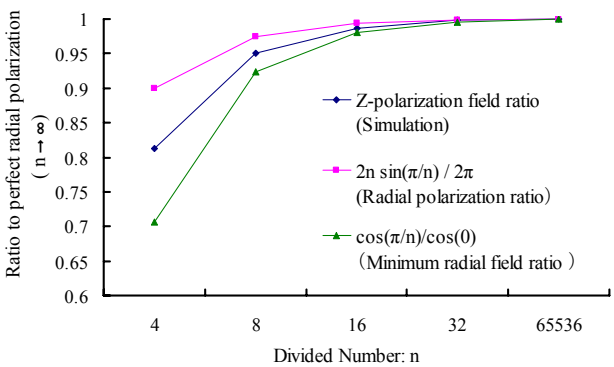

Figure 5: The divided number dependence of radial polarization ratio to ideal radial polarization

Z-polarization electric field dependency of optical characteristics and parameters

To maximize the Z-polarization field, the optical parameters should be optimized. The Z-field is reciprocal proportional to the square of the laser wavelength. This indicates that the SHG can generate a four-time stronger field than the fundamental at the focus point. Utilizing the SHG is totally efficient in Z-field generation, because the SHG conversion efficiency reaches up to 50%. The numerical aperture (NA) is characteristic of the final focusing optics. The Z-polarization field is proportional to NA raised to fourth power. The laser diameter before the final focusing lens should be as large as possible. The focus length should be as short as possible.

To make NA as large as possible, we designed a hollow laser beam generator with an axicon lens pair. The Z-field dependency of the hollow laser beam ratio is shown in Figure 6 in the case of the Gaussian beam incidence to the axicon lens pair. In our feasibility test set-up shown in Figure 7, the diameter of the electron beam is roughly 18 mm. Considering the vacuum duct inner diameter, realistically R0=30 mm and R1=18 mm. In the case of R_{ratio}=R1/R0=60%, the hollow beam makes a 10 times higher Z-field on the photo cathode than Gaussian beam incidence without an axicon lens pair.

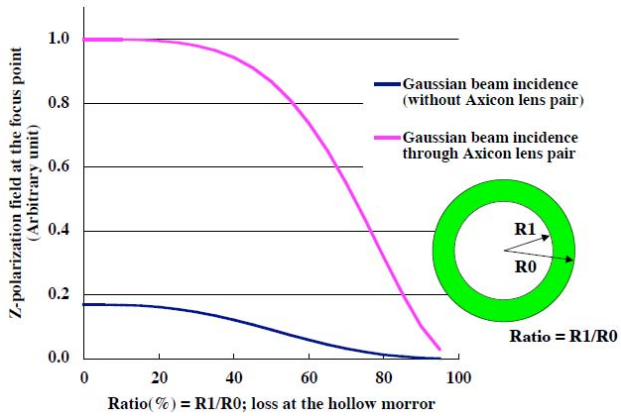

Figure 6: Z-polarization field dependency of hollow laser beam ratio (Gaussian beam incidence to axicon lens pair)

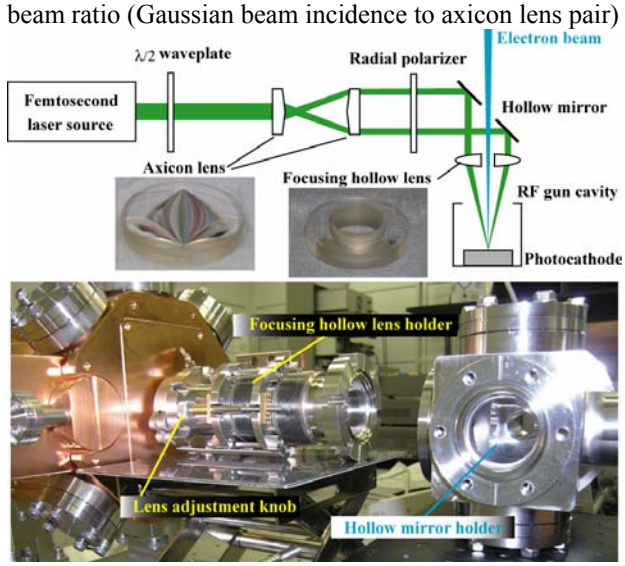

Figure 7: Experiment set-up for Z-polarization RF gun with hollow laser beam incidence optics

TYPE OF LASER INCIDENCE TO CATHODE

It is possible to make several configurations of normal incidence to the cathode. Making NA larger, backward illumination with the transparent cathode can make a short working distance (see (a) in Figure 8). For normal incidence to the conventional reflective cathode, it is necessary to use hollow laser beam incidence as shown

in Figure 7. The hollow inside-out Gaussian laser beam is generated by an axicon lens pair, and then reflected at the hollow mirror for normal incidence and finally focused to the photocathode with a hollow lens in a vacuum. This Schottky effect can be used separately as a gate of the photo-emission process. It is possible to separate the Schottky-gate laser pulse and photo-excitation source as shown in (b) in Figure 8. In the case of a polarized electron source with GaAs, the fundamental is used as a photo-excitation source, the SHG as a gate pulse. However, we have to take into account the time response of the cathode. Several improvements of response time down to 2 ps for GaAs were performed [8]. If the diffusion model is in good agreement in this case, making the cathode even thinner, it is possible to make the response time less than 1ps.

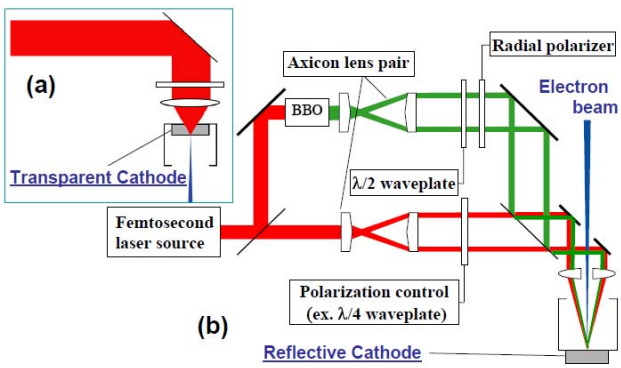

Figure 8: Z-field gun set-ups for different type cathodes

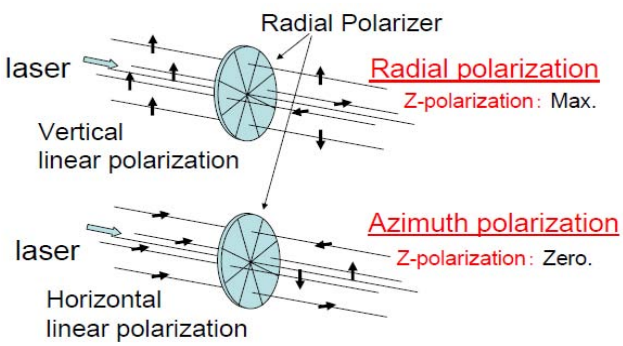

Figure 9: Concept of feasibility test for Schottky effect due to Z-polarization at focus point with the comparison of Z-fields between radial and azimuth polarization

FEASIBILITY TEST PLAN

Up to now, we have only discussed focusing radial polarization to maximize the Z-field on the photocathode. On the other hand, focusing an azimuth polarized beam makes Z-polarization zero. We conducted a feasibility study of the laser-induced Schottky-effect on the photocathode with the comparison between radial and azimuth polarization shown in Figure 9. In this experiment, the linear polarization of the incidence laser switches only from vertical to horizontal. In this method, we can check just the Z-field effect separated from the multi-photon process. Comparing the photo-emission process with these polarizations, we make clear the feasibility of this new concept of photocathode.

SUMMARY AND DISCUSSION

We discussed a new concept of photocathode with Z-polarization and showed the method for its feasibility test. Focusing a radial polarized beam on the photocathode, the Z-polarization of the laser is generated at the focus point. The generated Z-polarization can exceed an electrical field of 1 GV/m easily with the fundamental from compact femtosecond Ti:Sa laser systems. According to our calculations (NA=0.15, 60-% hollow ratio, inside-out Gaussian beam), the Z-field of 1 GV/m needs 1.3 MW at peak power for the fundamental (790 nm) and 0.32 MW for the SHG (395 nm). In the field of 1 GV/m, the work function of the copper cathode reduces ~2 eV.

In our design of the Schottky-effect-gated photocathode, the fundamental is used as a gate pulse and the SHG as a laser source for the photo-excitation with the copper cathode. (In the case of the polarized electron source with GaAs, the circular polarized fundamental wave is used as a photo-excitation source, the SHG as a gate pulse.) The same single laser pulse can also gate its emission by itself. To maintain normal incidence on the cathode, we developed a new type of hollow beam incidence system for cathode illumination with an achromatic axicon lens pair.

In the first feasibility test run, we are preparing a Z-polarizer (8-divided waveplate) for the SHG to generate radial and azimuth polarizations. Comparing the photo-emission process with these polarizations, we make clear the feasibility of this new concept of photocathode.

Using femtosecond laser pulses for photocathode RF guns, a pancake bunch can be created that will evolve automatically into a uniformly filled 3D ellipsoid [9]. This scenario is needed to reduce laser pulse intensity, to avoid damage of the cathode. The Z-polarization RF gun can be fit to this scenario. Next, we will test this scenario to generate a low-emittance beam with our Z-field gun.

REFERENCES

[1] "Linac Coherent Light Source (LCLS) Conceptual Design Report", SLAC-R-593, April 2002.
[2] "TESLA Technical Design Report, PART V, The X-Ray Free Electron Laser", ed. G. Materlik and Th. Tschentscher, March 2001.
[3] J. Rivers, "SCSS X-FEL Conceptual Design Report", RIKEN, May 2005.
[4] I. V. Bazarov, et al. PAC'05, 2005, p. 382.
[5] Japan Patent Application No. 2005-267593.
[6] T. INOUE, et al., JJAP, 41, No. 12, 2002, p. 7402.
[7] S.C. Tidwell, et al., Applied Optics, 29, No. 15, 1990, p. 2234.
[8] K. Aulenbacher, et al., J. Appl. Phys., 92, No. 12, 2002, p. 7536.
[9] M. J. De Loos et al., PAC'99, 1999, p. 3266.

BEAM PROPERTIES FROM S-BAND ENERGY COMPENSATED THERMIONIC RF GUN AND LINAC FOR KU-FEL

Toshiteru Kii, Hideaki Ohgaki, Kai Masuda, Satoshi Sasaki, Takumi Shiiyama, Heishun Zen

Institute of Advanced Energy, Kyoto University, Gokasho, Uji, Kyoto 6110011, Japan

Abstract

Beam properties after the accelerator tube of the KU-FEL system were measured to ensure the potential of the energy compensation technique to compensate for energy degradation in a thermionic RF-gun. Small growth of energy spread and emittance were observed, and its influence to the FEL gain and evolution of output power were estimated. It was found that the influence due to the amplitude modulation was so serious, because the small increase of the energy spread drastically reduces FEL gain. In addition to the amplitude modulation, phase modulation will be required.

INTRODUCTION

An MIR-FEL facility, KU-FEL, has been constructed for application of the energy science[1]. The KU-FEL consists of a thermionic RF gun and a 3-m accelerator tube and an undulator to generate 4-13 μm FEL as shown in fig. 1. As an electron injector, we chose a thermionic RF-gun because of its compactness and an easy-handling feature. However, a serious problem of back-bombardment limits macro-pulse duration up to several micro seconds. Then, we have tested an energy compensation technique[2], which uses an amplitude modulated rf pulse using remotely controllable pulse forming network of the Klystron modulator, to reduce the influence of the back-bombardment, and successfully extracted energy compensated electron beam of 4.0 μsec macro-pulse duration and numerically expected to extract electron beam with constant energy up to 8.0 μsec[3,4]. On the other hand, the amplitude modulated RF pulse will give rise to phase difference between RF-gun and accelerator tube, because timing of RF output from Klystron will be shifted to earlier timing because the velocity of the electrons in the Klystron tube is changed during macro-pulse. Moreover, time-varying beam loading will increase beam emittance due to space charge effect. Therefore, we have studied influence of the beam properties, such as temporal current profile, energy spread and emittance, at the exit of the accelerator tube. We have also studied on a figure-of-merit of average beam current and pulse duration, because higher beam current reduces macro-pulse duration.

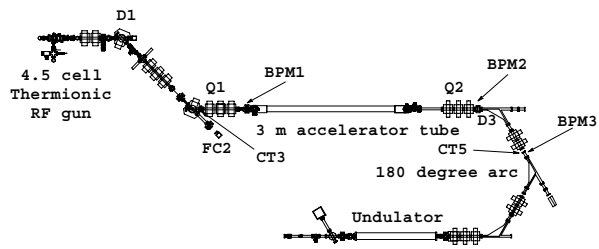

Fig. 1 Arrangement of the KU-FEL.

BEAM PROPERTIES

We have estimated the influence of the energy compensation technique from measurements of beam properties at the entrance and the exit of the accelerator tube. To estimate the influence of the technique clearly, two operational modes were selected. In the first mode, RF pulse of 3 μsec was fed to the RF-gun. Pulse duration after the first bending magnet was about 1.5 μsec. This mode was used to evaluate the beam properties without amplitude modulation. (Mode 1: Non-modulated mode) In the second mode, RF pulse of 7 μsec was fed. Pulse duration after the first bending magnet was about 5.2 μsec. This mode was used to evaluate the effect of the amplitude modulation. (Mode 2: Modulated mode) In these modes, average beam currents were set to around 30 mA, because if the electron beam with higher beam currents and shorter macro pulse duration is used as modulated mode, it is difficult to clear the differences between two modes.

Temporal Current Profile

Temporal profiles of the beam current at the entrance and the exit of the accelerator tube were measured using current transformers (CT3 and CT5 in fig. 1). As shown in figs. 2 and 3, acceleration was performed well in both modes. Although the most of electrons were accelerated in the modulated mode, macro-pulse duration was shortened after acceleration, and beam current was decreased by several percent in the latter part of the macro-pulse as shown in fig 3.

#kii@iae.kyoto-u.ac.jp

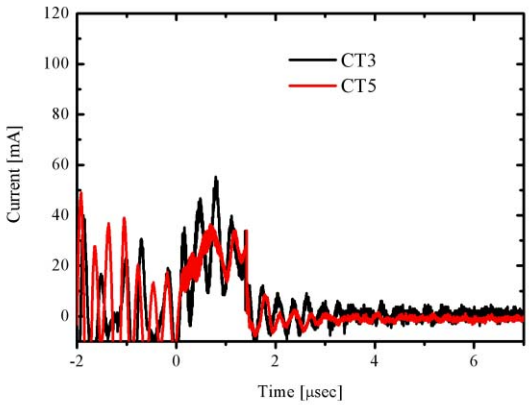

Fig. 2 Temporal profiles of the beam current for non-modulated mode measured at the entrance of the accelerator tube (CT3) and at the exit of the accelerator tube (CT5).

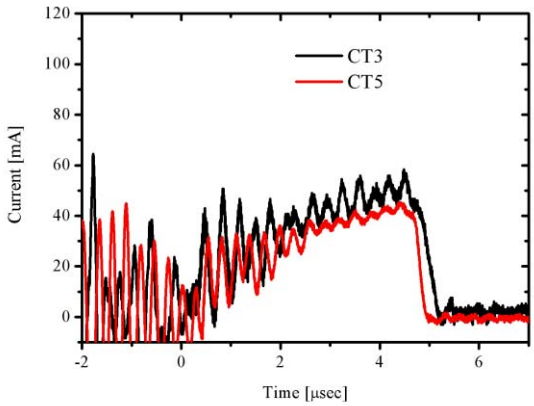

Fig. 3 Temporal profiles of the beam current for modulated mode measured at the entrance of the accelerator tube (CT3) and at the exit of the accelerator tube (CT5).

Energy Spread

Energy spreads were also measured. Before the accelerator, the first bending magnet (D1) and Faraday cup (FC2) were used. After the accelerator, the third bending magnet (D3) and the beam profile monitor (BPM3) was used. As shown in fig. 5, significant growth of the energy spread was observed after acceleration. Absolute value of the energy spread was expanded with modulated RF from 170 keV to 400 keV. It was probable that the phase differences between the stored RF in the gun and the injected RF to the accelerator tube changed the accelerating efficiency in the latter part of the macro-pulse. To estimate the order of the phase difference, phase dependence of the accelerated electron beam energy was measured. Energy difference of 500 keV corresponds to phase difference of about 5 degree around the crest of the phase dependence curve as shown in fig. 6. Therefore, phase difference of several degrees seems to be introduced by the amplitude modulation. FEL gains and power evolutions were also calculated using GENESIS[5] to estimate the influence of the energy spread. In these calculations, bunch length of 1.0 ps, beam energy of 25 MeV, energy spread of 0.5%, transverse emittance of 3.5π mm-mrad were assumed. The FEL power evolutions for electron beam with 0.5% and 1.0% energy spread are shown in fig. 7. As shown in fig. 7, the influence of the modulated RF input is quite serious due to the growth of the energy spread. The result indicates that the FEL gain rapidly decreases in the macro pulse. Phase modulation to the source RF of the Klystron will be effective to reduce expansion of the energy spread. It is important to measure the time evolution of the energy spread, to estimate the FEL power evolution precisely.

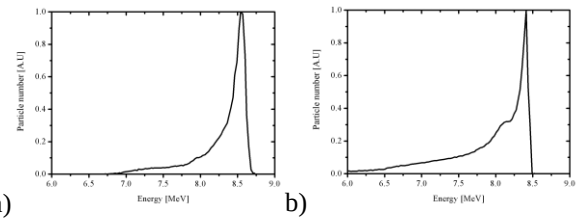

a) b)

Fig. 4 Energy spread before the accelerator tube. a) Non-modulated mode b) Modulated mode

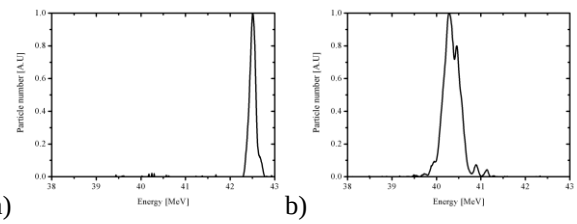

a) b)

Fig. 5 Energy spread after the accelerator tube. a) Non-modulated mode b) Modulated mode

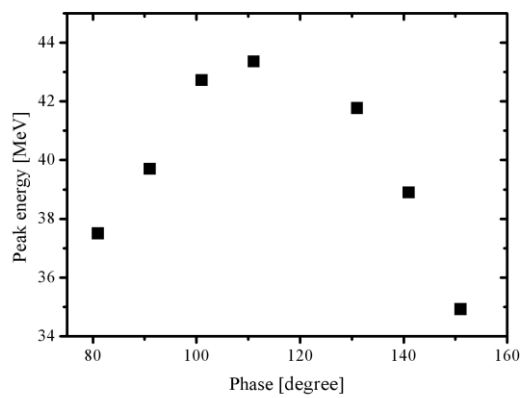

Fig. 6 Phase dependence of the peak energy of the accelerated electron beam.

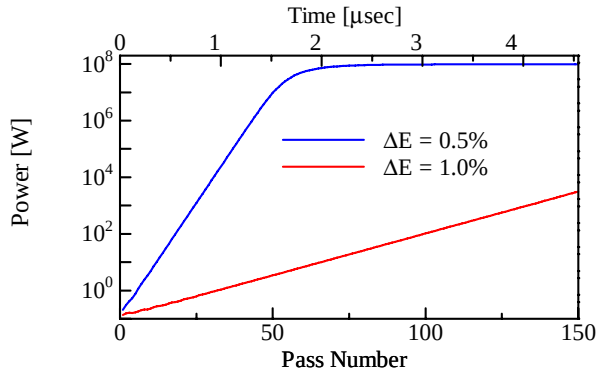

Fig. 7 FEL power evolutions for different energy spread.

Beam Emittance

Beam emittances were also measured using phase space tomography method. Although when we apply the tomography method to the electron beam with energy spreads, estimated emittance will be overestimated[6], in these experimental condition, energy spreads were less than 2.0%, thus the tomography method was effectively worked. Phase space distributions before and after the accelerator were measured using quadrupole magnets (QM1, QM2) and beam profile monitors (BPM1, BPM2). Reconstructed phase space distributions are shown in figs. 8 and 9. As shown in figs. 8 and 9, main components of the electron beams become fuzzy when the modulated RF were used.

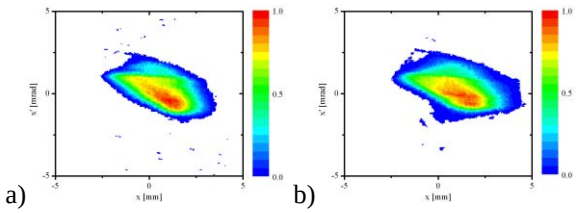

Fig. 8 Phase space distribution in x dimension before the accelerator. a) Non-modulated mode b) Modulated mode.

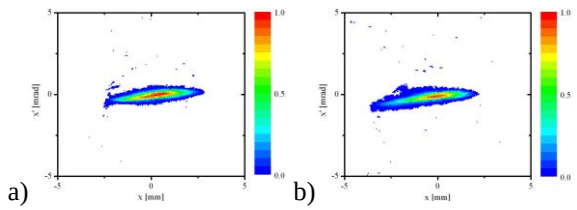

Fig. 9 Phase space distribution in x dimension after the accelerator. a) Non-modulated mode b) Modulated mode.

The evaluated rms emittances after the accelerator were increased by about 40% with modulated RF pulse as shown in table 1. To estimate the influence of the modulation, FEL power evolutions were calculated. As shown in fig. 10, the influence of the emttance growth is small. In these calculations, bunch length of 1.0 ps, beam energy of 25 MeV, energy spread of 0.5 %, transverse emittance of 3.5π and 10.0π mm-mrad were assumed.

Table 1. Evaluated beam emittances at the entrance and the exit of the accelerator tube.

mode	Emittance @ entrance [π mm mrad]	Emittance @ exit [π mm mrad]
1	x : 4.0 , y : 0.9	x : 2.5 , y : 2.5
2	x : 4.5 , y : 1.0	x : 3.3 , y : 3.5

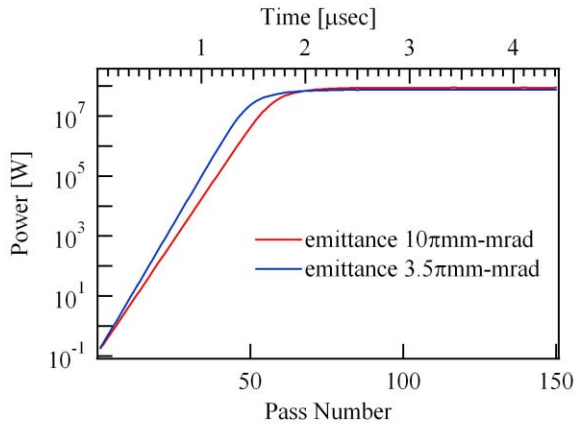

Fig. 10. FEL power evolutions for the electron beam with different emittance.

OPERATION POINT OF THE THERMIONIC RF-GUN

Although the FEL gain becomes larger when extracted beam current is increased, the influence of the back-bombardment becomes larger, and then the macro pulse duration becomes shorter. In case for our RF gun, maximum beam current is about 120 mA, but the pulse duration is limited to less than 500 nsec. On the other hand, if the extracted beam current is limited to 30 mA, the pulse duration is reached up to 5 μsec. To find the better operational point, power evolution of the FEL for various average beam current was estimated. In these calculations, bunch length of 1.0 ps, beam energy of 25 MeV, transverse emittance of 3.5π mm-mrad were assumed. As shown in fig. 11, the FEL gain is sensitive to the average beam current. Therefore, we have tested to increase average beam current. As shown in fig. 12, we successfully extracted electron beam of 50 mA with pulse duration of 3.5 μsec.

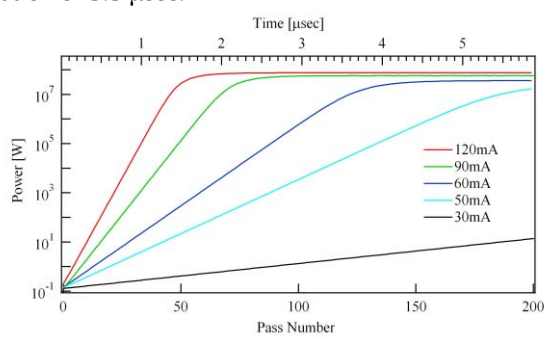

Fig. 11. Estimated FEL power evolutions for various average beam currents using GENESIS.

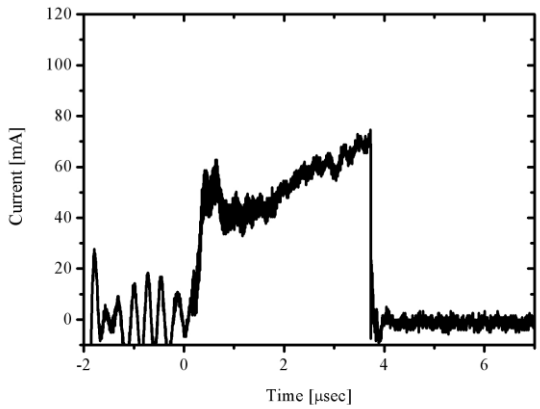

Fig. 12 Temporal profiles of the beam current with 50 mA of average current.

CONCLUSION

Beam property measurements were carried out to evaluate the performance of the energy compensation technique using amplitude modulated RF pulse applied to the thermionic RF gun in KU-FEL system and the influence of the amplitude modulation. It was found that the energy compensation technique was effective for extract the electron beam with longer macro pulse, but the influence to the energy spread was quite serious. To achieve the first lasing of the KU-FEL, an RF phase modulation will be required in addition to the amplitude modulation. The better operational point was also surveyed for higher FEL output. The new operating mode of 50 mA and 3.5 μsec was successfully found.

REFERENCES

[1] T. Yamazaki, et al., Free Electron Laser 2001 (2002), II13-II14.
[2] T. Kii, et al, Proceedings of the 26th International Free Electron Laser conference, (2004) 443-446.
[3] T. Kii, et al., AIP Conference Proceedings Volume 879, SYNCHROTRON RADIATION INSTRUMENTATION: Ninth International Conference on Synchrotron Radiation Instrumentation, (2006) 248-251.
[4] N. Okawachi, et al., Proceedings of International Conference on Free Electron Laser, (2006) 664-667.
[5] S. Reiche, “GENESIS 1.3 User Manual”, (2004).
[6] H. Zen, et al., Proceedings of International Conference on Free Electron Laser, (2006) 668-671.

NUMERICAL EVALUATION OF OSCILLATOR FEL WITH MULTI-BUNCH PHOTO-CATHODE RF-GUN IN KYOTO UNIVERSITY*

Hideaki. Ohgaki#, Toshiteru Kii, Kai Masuda, Satoshi Sasaki, Takumi Shiiyama, Heishun Zen, Institute of Advanced Energy, Kyoto University, Gokasho, Uji, Kyoto 6110011, Japan
Ryunosuke Kuroda, National Institute of Advanced Industrial Science and Technology, Umezono 1-1, Tsukuba, Ibaraki 3058658, Japan
Masao Kuriki, Nobuhiro Terunuma, Junji Urakawa, High Energy Accelerator Research Organization, 1-1, Oho, Tsukuba, Ibaraki, 305-0801, Japan
Yoshio Kamiya, Masakazu Washio, Research Institute for Science and Engineering, RISE, Waseda University, 3-4-1, Okubo, Shinjuku-ku, Tokyo, 169-0072, Japan

Abstract

Numerical evaluations have been performed to install a photo-cathode RF-gun into an oscillator FEL system which has been developed in Kyoto University. The original FEL system was consisted of a 4.5-cell thermionic RF gun with S-band accelerator tube of 3-m to oscillate the mid-infrared FEL. The electron beam properties have been evaluated from an RF-gun to an FEL by using PARMELA and ELEGANT. On the other hand, the FEL parameters have been calculated with GENESIS which takes the optical cavity into account. The evaluated peak current of the electron beam was 10-50 times as high as those with the thermionic RF-gun. Since the oscillator FEL requires a multi-bunch electron beam, evaluation of the round-trip development of the FEL has been also performed by a 100 bunch train beam. The results showed that the FEL gain saturation was achieved within 3 round-trips.

INTRODUCTION

An infrared FEL (4-13 μm) facility for energy science is under construction at the Institute of Advanced Energy, Kyoto University [1]. The electron beam of 40 MeV and peak current of -10 A has been successfully accelerated by a linac system which consists of a 4.5-cell thermionic RF gun, a 'dog-leg' transport system, a 3m s-band linac, and a 180-degree arc bunch compressor [2]. Figure 1 shows the schematic view of the linac system which includes the photo-cathode RF-gun. To reduce the back-bombardment effect in the 4.5-cell RF gun, several attempts have been made, and the macro pulse duration of 5 μs has been achieved [3]. However, there still needs several efforts are needed both to extend the macro pulse duration and to increase the peak current to reach the FEL saturation [4]. Replacing the thermionic RF-gun to a photo-cathode RF-gun is the most promising way to obtain a high peak current electron beam. Therefore, we made a preliminary design study [5] and start to develop a 1.6-cell photo-cathode RF-gun [6]. Recently, the improved design of the

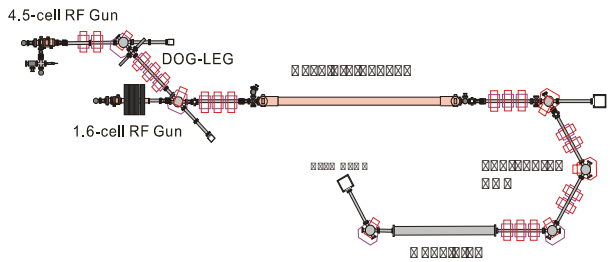

Figure 1: Schematic view of the KU-FEL driver linac.

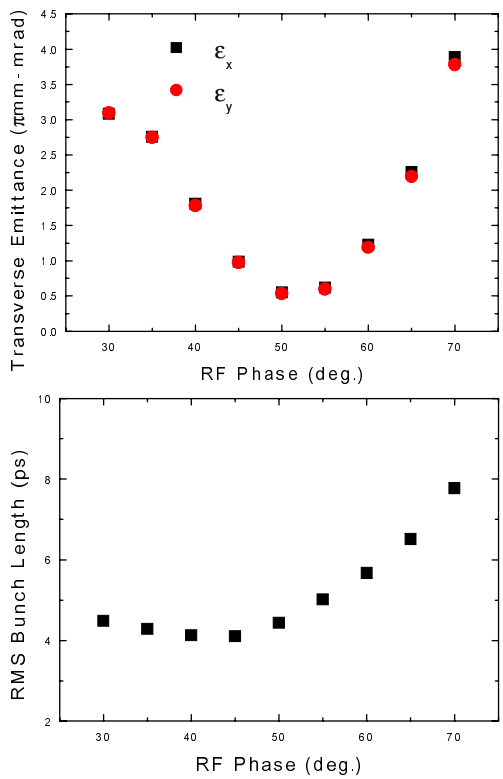

Figure 2: Transverse RMS emittance(a) and energy spread(b) of the electron beam from the gun as a function of the laser injection phase.

*Work supported by Promotion of Collaborative Research Programs in Universities of High Energy Accelerator Research Organization (KEK).
#ohgaki@iae.kyoto-u.ac.jp
+present address: International Center for Elementary Particle Physics, The University of Tokyo, 7-3-1 Hongo, Bunkyo-ku, Tokyo 113-0033, Japan

photo-cathode RF-gun has been installed in the linac in AIST and succeeded to generate 100-bunch electron beam. The beam charge of 1.5 nC/bunch has already been achieved. We are going to install the similar RF-gun system into KU-FEL system. Thus a start-to-end calculation with the photo-cathode RF-gun has been performed. For the electron beam a simulation has been made by PARMELA [7] and ELEGANT [8] from gun to undulator. On the other hand, the FEL parameters have been calculated by using GENESIS [9] which was modified to calculate an optical cavity. Then the FEL gain was compared with the present thermionic RF-gun based system.

1.6-CELL PHOTO-CATHODE RF-GUN

The improved BNL type 1.6-cell photo-cathode RF-gun [10] has succeeded in generation of a high brightness electron beam, about 1 πmm-mrad with 1.5 nC/bunch. A multi-bunch operation also succeeded with a 100 bunch UV drive laser and a Cs_2-Te cathode. This type of photo-cathode RF-gun manufactured in KEK will be installed into KU-FEL system. As is shown in figure 1, the 1.6-cell photo-cathode RF gun will be located at the upstream of the accelerator tube. The RF system will be shared with the existing thermionic RF-gun. Since the thermionic RF-gun operates 2856 MHz bunch train, a large average power FEL will be generated by the thermionic RF-gun. On the other hand, the photo-cathode RF-gun can generate a high peak power FEL but small average power FEL, because the bunch train is depends on the laser frequency of the laser (357 MHz).

The electron beam parameter from the 1.6-cell RF-gun has been evaluated by using PARMELA with the maximum electric field of 50 MV/m at the cathode surface which was given by an acceleration test in AIST. We also assumed that the ratio of the field strength of the half cell and regular cell was 1:1 which was measured with the test gun at KEK. The ratio of the field strength, which can be tuned from 0.8:1 to 1.3:1, and the maximum filed strength should be optimized for its' purpose, because the electric field for the cavity cell largely affects the property of the output beam. The driver laser parameters assumed here was a picosecond UV laser [11], whose beam profile was 0.7 mm at the cathode surface and the pulse duration was 6.0 ps. The Gaussian shapes were also assumed both for the transverse (1 mm cut-off) and for the longitudinal (12 ps cut-off) distribution to simplify the calculation. Figure 2 shows the transverse RMS emittance(a) and energy spread(b) of the electron beam from the RF gun as a function of the laser injection timing. We assumed 1 nC/bunch at the cathode surface in this paper.

It is clear that the transverse RMS emittance of 1 πmm-mrad and energy spread of 2% can be generated at the 45 degree of the laser injection phase at the gun exit. The solenoid field for the emittance compensation [12] which

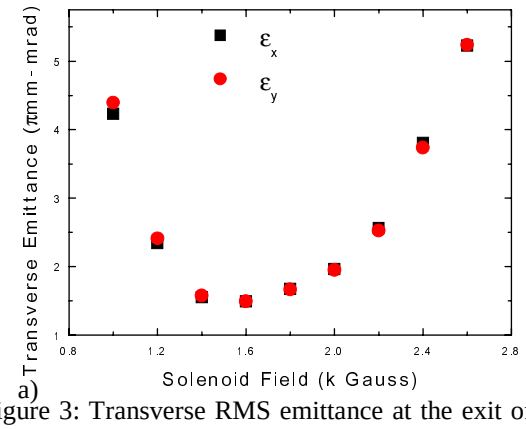

Figure 3: Transverse RMS emittance at the exit of the accelerator tube as a function of the solenoid field.

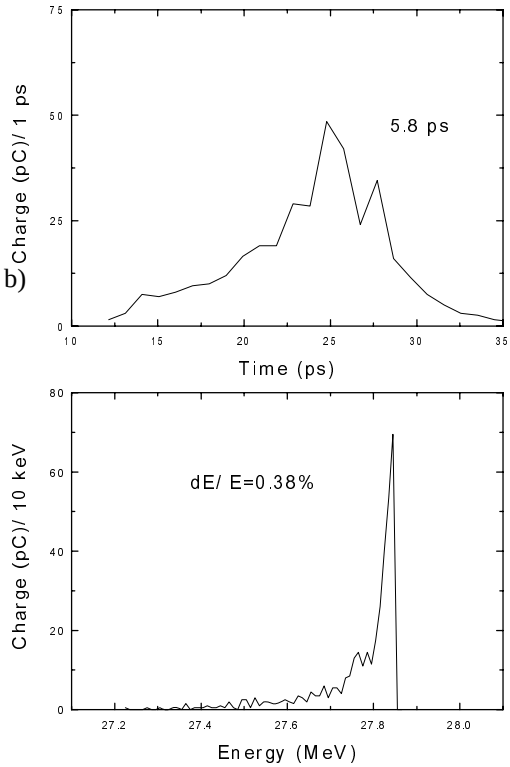

Figure 4: Time distribution (a) and energy distribution (b) at the exit of accelerator tube. The RF phase of the accelerator tube was chosen to 'on crest mode'.

was the same geometric configuration of ref. 13. The field distribution was calculated by using POISSON. As shown in fig.3 the transverse emittance of 1.5 πmm-mrad is obtained from the accelerator tube with the solenoid field of 1600 Gauss. Figure 4 also shows the bunch length(a) and the energy spread(b) of the electron beam from the accelerator tube with the RF-phase of 125 degrees where the smallest energy spread was obtained.

The achromatic 180-degree arc section was tuned both for the matching condition of the undulator parameter and for the bunch compression condition with matrix element, R_{56}, by using ELEGANT. Figure 5 shows the bunch length(a) and the energy spread (b) of the electron beam at the entrance of undulator. As is shown in fig.5 (a) the bunch length successfully reduced below 1 ps, but more than half of the electrons are spread away from the main bunch. This is due to a non-linear relation between phase and energy at the exit of the accelerator tube since the RF phase, 125 degrees, was located at RF crest. We call this operation mode as 'on crest mode'. Thus we also calculated with the RF phase at 132.5 degrees where the relation between phase and energy was close to a linear one. We call this operation mode as 'energy chirp mode'. Figure 6 shows the bunch length (a) and energy spread (b) of the electron beam at the entrance of undulator with RF phase of 132.5 degrees. As the results the bunch length was reduced from 0.8 ps to 0.23 ps and the peak current was increased from 443 A to 2.46 kA.

The expected parameters of the electron beam from 1.6-cell photo-cathode RF-gun were listed in table.1. Consequently, the photo-cathode RF-gun would generate 10-50 times large peak current electron beam to the thermionic RF-gun which generated 40 A peak current of the electron beam [5].

Table 1 Evaluated Electron Beam Parameters

	Thermionic RF gun[5]	Photo-Cathode RF-gun	
		On Crest mode	Energy Chirp mode
Emittance (πmm-mrad)	11.3(H) 10.1(V)	5.02(H) 5.01(V)	4.42(H) 3.03(V)
Energy Spread (%)	0.40	0.054	0.86
Bunch Length (ps)	1.8	0.80	0.23
Peak Current (A)	40.0	443	2,460

OSCILATOR FEL DRIVEN BY 1.6-CELL PHOTO-CATHODE RF-GUN

The FEL gain with the 1.6-cell photo-cathode RF-gun has been calculated by using above evaluated electron beam parameters. The undulator and optical cavity parameters used here are listed in ref. 4. The 1-pass FEL gains with the 'on crest mode' and with the 'energy chirp mode' were calculated as 8.8×10^4% and 7.6×10^7% in 12.1 μm wavelength. On the other hand, the 1-pass FEL gain with the thermionic RF-gun was 38%. The 1-pass gain was extremely enhanced even with the 'on crest mode' because of its' large peak current, more than 400 A. Although a large energy spread in the 'energy chirped mode' a huge peak current, 2.4 kA, brought a huge 1-pass gain.

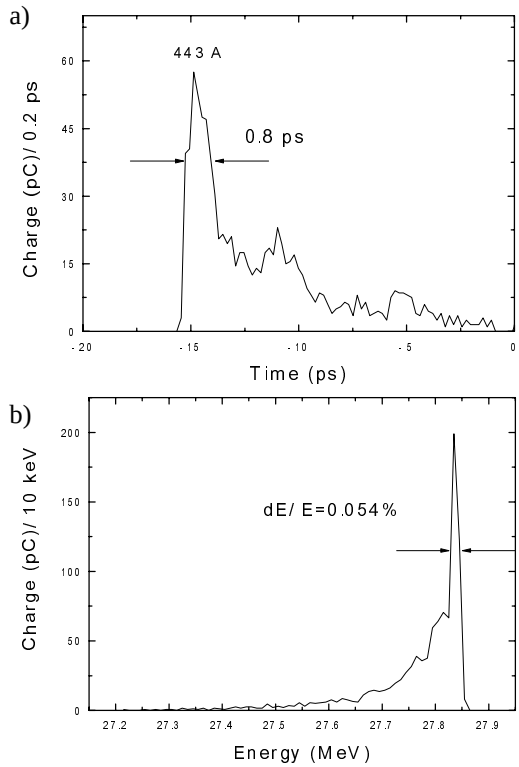

Figure 5: Time distribution (a) and energy distribution (b) at the undulator. The RF phase was 'on crest mode'.

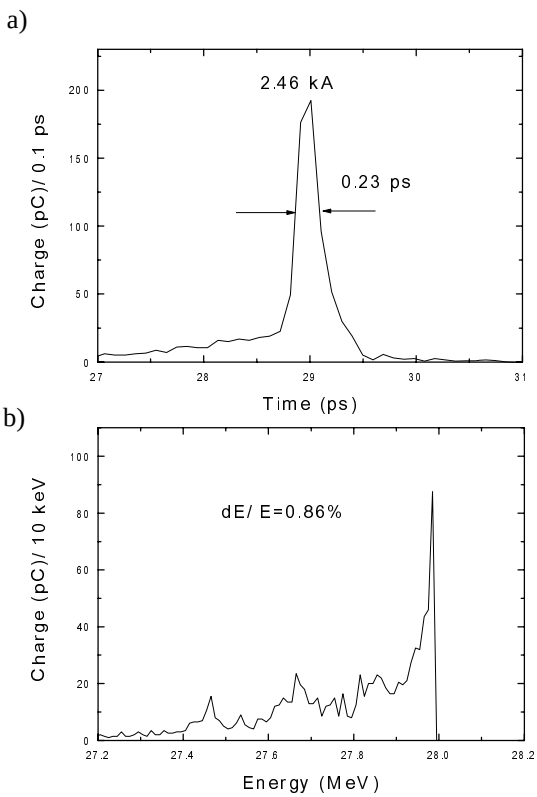

Figure 6: Time distribution (a) and energy distribution (b) at the undulator. The RF phase was 'energy chirped mode'.

To calculate a round-trip development in an oscillator FEL, we modified GENSIS which treated the light propagation in an optical cavity including an optical loss in vacuum duct, mirror surface, and hole coupling [4]. The multi-bunch electron beam, a 100-bunch, has already been achieved by a 100 bunch UV laser system which was based on 357 MHz mode-locker [6]. However, we should note that our cavity length of the undulator is 4.51 m and round-trip frequency is about 33.2 MHz. Therefore about 10 round-trips can be used for the FEL amplification. So we assumed 10-round-trips, about 0.3 μs in macropulse, in this calculation. The round-trip development is shown in fig.7. As is shown in fig.7 FEL saturations are achieved with a few round-trips for both operation modes. The peak output powers were 10 MW with 'on crest mode' and 400 MW with 'energy chirped mode'. The average FEL energies were also calculated as 0.44 mJ/macro-pulse for 'on crest mode' and 4.6 mJ/macro-pulse for 'energy chirped mode'. On the other hand, the saturated output power of 2.4 MW can be obtained after 70 round-trips with the thermionic RF-gun system. The average FEL energy can be calculated as 10 mJ/macro-pulse for 3 μs macropulse length which corresponds to the 100 round-trips. To increase the average energy with a photo-cathode RF-gun, the bunch train should be increased. A 300-bunch train, 1 μs macro-pulse duration, should be the next target for the development of the photo-cathode RF-gun to replace the thermionic RF-gun completely.

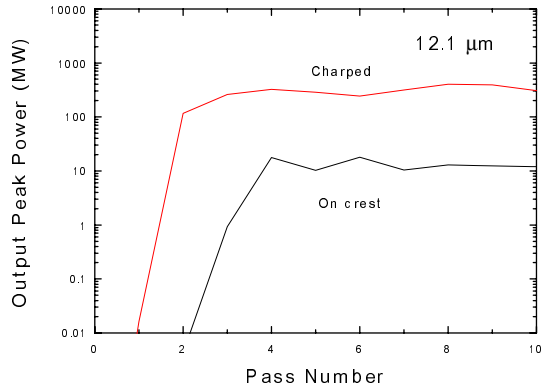

Figure 7: Round-trip development of the FEL output power.

CONCLUSION

An improved BNL type RF-gun, which has already been succeeded in generation of 100 bunch, about 1 πmm-mrad with 1.5 nC/bunch electron beam in AIST-RISE, will be installed in an oscillator FEL system. The FEL system was originally designed with a 4.5-cell thermionic RF gun with a 180-degree arc worked as a bunch compressor to oscillate the mid-infrared FEL in Kyoto University. To evaluate the FEL performance with the photo-cathode RF-gun we made a start-to-end calculation by using PARMELA, ELEGANT and GENESIS which has been improved to take an optical cavity into account.

The evaluated peak current of the electron beam at the undulator was 443 A when the RF phase was tuned to obtain the minimum energy spread, dE/E=0.054%, of the electron beam. When the RF phase was tuned for energy chirped beam, dE/E=0.86%, the peak current of the electron beam was 2.46 kA. Since the thermionic RF-gun generated 40 A electron beam, 10-50 times large peak current was obtained by the photo-cathode RF-gun.

The output power of 12.1 μm FEL, 400 MW, will be saturated within 3 round-trips with the energy chirped beam. On the other hand, the saturated output power of 2.4 MW can be obtained after 70 round-trips with the thermionic RF-gun system. We should note that only 10 round-trips can be used for the FEL amplification when we assumed a 100-bunch electron beam. Therefore, the evaluated average energy of the FEL was 4.6 mJ/macropulse which was smaller than that with a thermionic RF-gun, 10 mJ/macropulse.

Consequently a high brightness electron beam from the photo-cathode RF-gun will generate 100 times high peak power of FEL. However, the average power of FEL with the photo-cathode RF-gun will be smaller than that with thermionic RF-gun when we assume a 100 bunch train for the electron beam. Further developments for generating a longer multi-bunch beam are required to replace a thermionic RF-gun into a photo-cathode RF-gun, completely.

The authors would like to thank Mr. T. Takatomi (KEK) for his help for this work.

REFERENCES

[1] T. Yamazaki, et al., Free Electron Laser2001 (2002), II-13.
[2] H. Zen, et al., in these proceedings.
[3] T. Kii, et al., in these proceedings.
[4] S. Sasaki, et al., in these proceedings.
[5] H. Ohgaki, et al., NIM A528 (2004) 366-370.
[6] K. Hirano, et al., NIM A560 (2006) 233-239.
[7] L. M. Young, James H. Billen, LA-UR-96-1835 (2002).
[8] M. Borland, "User's Manual for elegant", v.15.4.1 (2005).
[9] S. Reiche, "GENESIS 1.3 User Manual", (2004).
[10] Y. Kamiya, et al., Proceedings of the PAC2007 (2007), THPMN040.
[11] F. Sakai, et al., Proceedings of the PAC1999 (1999) 2036.; J. Yang, et al., NIM A491 (2002) 15.
[12] R.E. Carlsten, NIM A285 (1989) 313.
[13] F. Sakai, et al., Jpn. J. Appl. Phys., Vol.41 (2002) 1589.

PRESENT STATUS OF FEL DEVELOPMENT IN KYOTO UNIVERSITY

Satoshi Sasaki, Heishun Zen, Takumi Shiiyama, Toshiteru Kii, Kai Masuda, Hideaki Ohgaki
Institute of Advanced Energy, Kyoto University, Gokasho, Uji, Kyoto, Japan, 611-0011

Abstract

We have constructed an infrared (4-13 μm) FEL facility for advanced energy researches in Kyoto University. The numerical studies on the expected FEL gain, which were based on the experimental measurements both of the undulator and of the electron beam parameters, were carried out. GENESIS code has been modified to simulate an oscillator FEL which took into account the chamber geometry and the mirror including hole coupling. Dependencies on a tilt angle and an offset of the mirror were evaluated by using this modified code, then for the first lasing the mirror parameter was optimized. At the present stage, we have installed the undulator and the mirror cavity. Measurements on spectrum of the spontaneous emission and electron beam characteristics were carried out. The measured spontaneous emission was consistent with the result of the calculation obtained with measured magnetic field of the undulator. Since the evaluated peak current of the electron beam was not enough for the lasing, LaB_6 cathode was ready to use.

INTRODUCTION

We have studied and developed an infrared (4-13 μm) FEL facility (KU-FEL) for advanced energy researches in Kyoto University. The KU-FEL consists of a 4.5-cell thermonic RF gun, 3 m accelerator, beam transport, Halbach-type undulator, and optical cavity. The RF gun and the accelerator operate at 2856 MHz (S-band), and produce electron beams up to 40 MeV.

To optimize the optical cavity, we calculated the FEL gain with the measured magnetic field of the undulator[1]. However, the treatment of the loss in the vacuum chamber and the light output from the cavity was truncated on the assumption of simple Gaussian distributions in transverse direction. On this assumption, the tolerance of the alignment errors of the optical cavity mirrors could not be evaluated. In this study, we carried out calculations of the light propagation taking into account of the duct shape and reflection/transmission of the light at the mirror for optimization of the optical mirrors and evaluation of the misalignment tolerance. For this purpose, we have modified a calculation code, GENESIS1.3[2].

Based on the re-optimized parameters in these calculations, we have installed the optical cavity and undulator in the KU-FEL system. We then observed the spectrum of the spontaneous emission, and compared it with the SRW[3] calculation.

Aiming at a higher peak current, we replaced the tungsten cathode in the RF gun by a LaB_6 cathode. In this paper, the preliminary experimental comparison will be also reported.

FEL GAIN CALCULATION

Calculation Code

We had calculated the FEL gain and round trip development to optimize the optical cavity parametes, by using TDA3D[4], but it didn't take into account the duct shape, reflection on mirror, absorption, and transmission of the mirror. In addition, the detuning parameter can hardly be handled.

To cope with these problems in this study, we modified GENESIS1.3 code taking in the realistic duct shape. We simulated a realistic FEL gain by using the modified code. The duct shape taken in the calculation is shown in Fig.1. The parameters of the electron beam used in the FEL gain calculation were optimized for the measured undulator parameters, and are listed in Table 1. The undulator parameters are listed in Table 2.

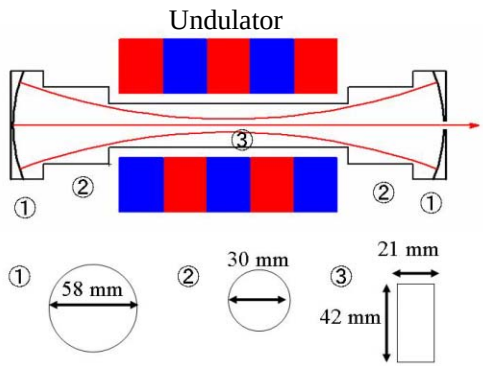

Figure 1: Duct shape

Table 1: Electron beam parameters

Emittance(x)	3.5 πmm-mrad
Emittance(y)	3.5 πmm-mrad
ΔE / E	0.5 %
Beam size(x)	0.6 mm
Beam size(y)	0.4 mm
Twiss parameter α_x	3.6
Twiss parameter α_y	0
Beam energy	25 MeV

Table 2: Parameter of Halbach type undulator

total length	1.6 m
Repetition	40
period	4 cm
gap	25.5 - 45 mm
Maximam magnetic field	0.26 - 0.0045 T
K value	0.99 - 0.17

Set Up of the Optical Cavity

Firstly, the mirror curvatures were designed in the viewpoint of FEL lasing stability as follows. Parameters of the optical cavity were once optimized to obtain the highest FEL gain by using TDA3D with aforementioned truncations, and FEL gain was 87% under the electron beam condition of 25 MeV, while the resultant stability has not been evaluated. By using the modified GENESIS1.3, we calculated FEL gain under the same conditions, and FEL gain was 49%. The reason why FEL gain decreased was due to the diffraction loss.

The stability was then evaluated by using the modified GENESIS1.3 and as the result it was found that the optical cavity was unstable for FEL lasing. The g-parameter was found to be 0.93, We thus re-optimized the parameters of the optical cavity by the use of modified GENESIS1.3, to obtain a g-parameter of ~0.5. As the result, we have selected the curvature of the upper mirror of 3.03 m, the down mirror of 1.87 m, the the rayleigh length of 0.7 m, and beam waist of 1.1 m (see Table 3).

Secondly with the specification of the mirrors, the misalignment tolerance was the evaluated. The results of the mirror offset and tilt dependency are shown in Fig. 2. Here, Dm means down mirror, and Um means upper mirror. X and Y are the direction the mirrors offset and tilt. The FEL gain is seen to decrease ~10% with respect to the ideal alignment when the offset is 0.4 mm or the tilt angle is 400 μrad. In comparison, with the original mirror parameter, the FEL gain is found to decrease by 30%, as shown in Fig.3. The re-optimized parameters are thus found to lead to a much better misalignment tolerance.

Finally, concerning the diameter of mirror hole, we simulated the FEL gains for the diameters of 1, 2 and 3 mmϕ, and the results are summarized in Table 4. As of the numerical treatment of the out-coupling hole, we found that the discontinuity of the optical fields on the edge of the hole results in a numerical problem[5]. So, we rather treated the out-coupling as transpiration. As shown in Table 4, the FEL gain for 3 mmϕ hole is found to be about a half of that for 1 mmϕ. In comparison, the gain decrease for the 2 mmϕ hole is tolerable, and the FEL output is more than two times higher than that for 1 mmϕ. We thus chose the mirror diameter of 2 mmϕ.

The optimized mirrors were then installed in the optical cavity of the KU-FEL. The picture of the mirror is shown in Fig. 4, and the reflectivity is shown in Table 3.

Table 3: Parameters of the optical cavity

Substance	Au coated Cu mirror
Rayleigh range	0.7 m
Beam waist position	1.1 m
infrared reflection	99.04%
down mirror curvature	1872 mm
upper mirror curvature	3030 mm
Cavity length	4.513 m

Table 4: FEL gain dependence on mirror hole diameter

diameter	Gain(%)	Output(MW)	Pass number for saturation
1mmϕ	44	2.0	70
2mmϕ	37	4.9	75
3mmϕ	24	4.8	100

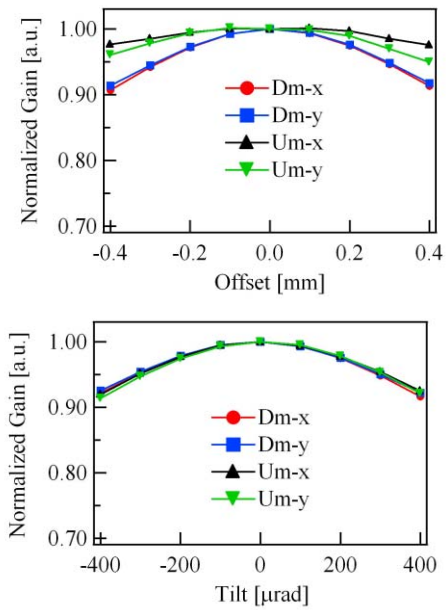

Figure 2: Influence of mirror misalignment of 0.5 g-parameter

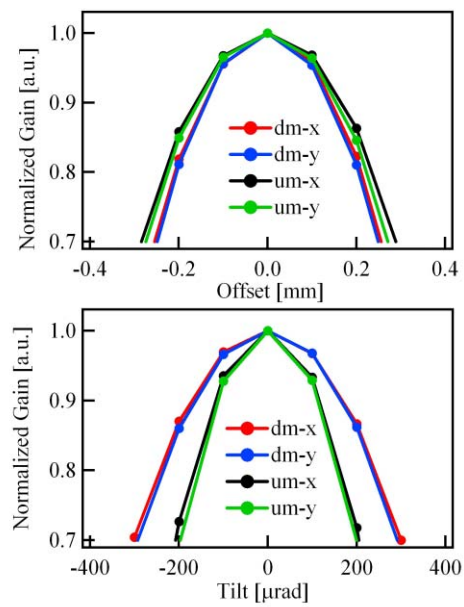

Figure 3: Influence of mirror misalignment of 0.93 g-parameter

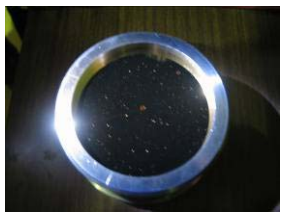

Figure 4: Au coating mirror

The FEL power evolution calculated by modified GENESIS1.3 under electron beam condition of 25 MeV is shown in Fig. 5. For comparison, the preliminary result by the use of TDA3D on same condition is also shown in Fig. 6.

At the present stage, the macro-pulse length of electron beam is about 3 μs in KU-FEL, so it is necessary for electron beam peak current to be 40 A in order to realize FEL lasing.

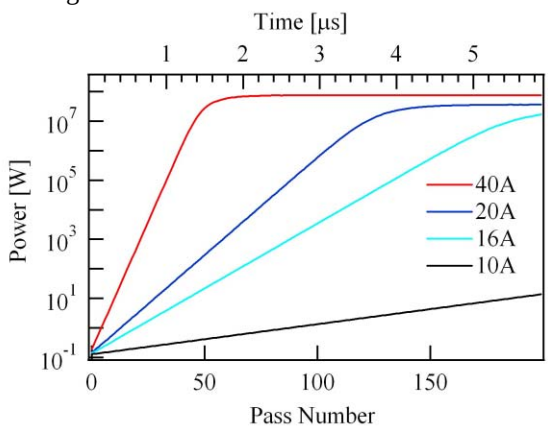

Figure 5: FEL power evolution calculated by GENESIS1.3

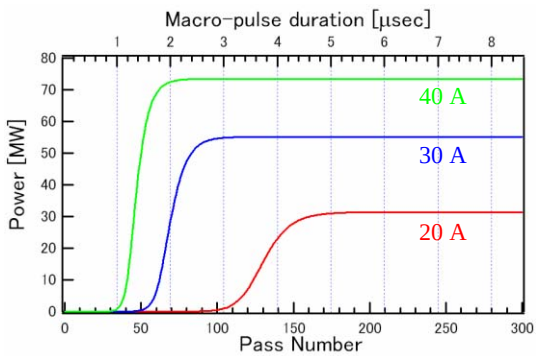

Figure 6: FEL power evolution insufficient on mirror and diffraction losses.

MEASUREMENTS

Measurement of Spontaneous Emission

We measured the spectrum of spontaneous emission using an InSb detector (Judson, J15D12) and a monochromator (Digikrom, DK240). We extract the light from the downstream of the mirror chamber, and then focus it on the entrance of the monochromator by a parabolic mirror. The experimental setup is shown in Fig.7.

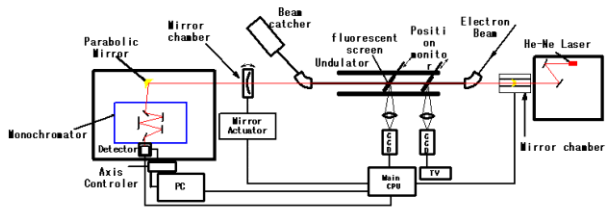

Figure 7: Experimental setup

We observed the spectrum of spontaneous emission, under the condition of the electron beam energy of 29.5 MeV. The electron beam condition is shown in Table 1 except for energy, and the observed spectrum is shown in Fig. 8. The spectrum shows a peak at 9.2 μm, and its FWHM is 270 nm. The undulator parameters are listed in Table 1, and the spectrum calculated by SRW by using these parameters is also shown in Fig. 8 as the dotted line. The observed spectrum shows exactly the same peak wavelength as the calculation, and the FWHM also agrees well with the calculation, considering that the FWHM by the calculation doesn't include resolution of the monochromator, 100 nm.

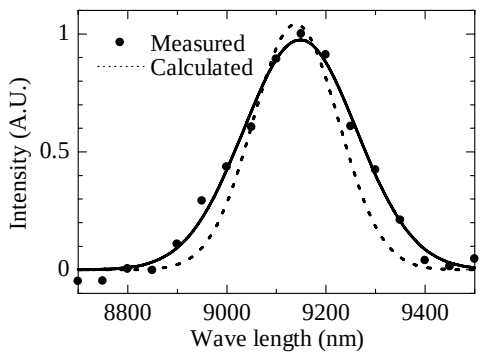

Figure 8: Measured and calculated spectrum of the spontaneous emission

FEL Lasing Experiments

We then started FEL lasing experiments of 11 μm wavelength with an electron beam energy of 26.5 MeV, macro-pulse length of 3 μs, average current of 40 mA. The reasons for the choice of 11 μm are as follows. On one hand, a lower energy electron beam shows in general a higher FEL gain. Furthermore, in the KU-FEL linac, lower energy operation of the RF gun is found to lead to a higher peak current[6]. On the other hand, the InSb detector loses sensitivity rapidly for ~13 μm or longer.

We then carried out experiments aiming at FEL lasing. We succeeded in accumulating the spontaneous emission, but neither FEL amplification nor saturation is observed at this moment.

The peak current of the electron beam of ≥ 7 A is estimated by the bunch length measurement[6]. According to the numerical calculations in the previous chapter, the sum of the diffraction loss and mirror loss exceeds the amplification if an electron beam if 7 A peak current.

Aiming at a higher peak current, we replaced the tungsten cathode in the RF gun by a LaB_6 cathode. An experimental comparison showed that a LaB_6 cathode lead to a higher peak current than a tungsten cathode in an RF gun[7], probably because a LaB_6 cathode is less sensitive to the back-bombardment effect.

Our preliminary test with a LaB_6 cathode when the RF gun operated at 9 MeV, showed that we obtained a 120 mA average current and 2.5 μsec macro-pulse length, which is encouraging compared with 70 mA and 3 μsec by the tungsten cathode.

In the next stage, we will operate the RF gun at 7.5 MeV, which is known as the best operational condition for the optimal peak current at the undulator [6]. Under this operational condition, the peak current by the tungsten cathode was ≥ 7 A. According to the current enhancement by the LaB_6 cathode, we can expect an enhanced peak current of ≥ 12 A. The expected FEL gain is ~5.0%, and the FEL amplification would be ~100.

SUMMARY

We modified the calculation code, GENESIS1.3, to calculate the FEL gain taking into account the duct shape and mirror, while we applied a truncation in the out-coupling treatment for numerical stability. In order to consider mirror out-coupling hole realistically, we must modify the calculation code further.

By using modified GENSIS1.3, we optimized the parameter of the optical cavity, and set up the experimental equipments. For these parameters, we calculated the expected FEL gain. As the result, we found that if the peak current of electron beam is 40 A, and macro-pulse length is 3 μs, 12 μm FEL saturation will be achieved on the electron beam condition of 25MeV.

The spectrum of spontaneous emission was measured. The results agreed well with calculation.

At present, we have not achieved an FEL lasing, mainly due to the limitation of the peak current and macro-pulse duration, i.e. the back-bombardment effect in the RF gun. Against this adverse effect, preliminary tests showed that the use of the LaB_6 cathode would lead to a higher peak current than a dispenser type one. By the LaB_6, 12 A peak current is expected, and the corresponding FEL gain is 5%. Under this condition, we will be able to observe an FEL amplification.

REFERENCES

[1] M.Nakano, et al.," Measurement of the undulator in KU-FEL", in prceedings of FEL conference 2006
[2] S. Reiche, Nucl. Instrum. Methods , A429(1999)243.
[3] O. Chubar, et al., Proc. of EPAC98, p.1177, 1998.
[4] J.S. Wurtele T.M. Tran. Computer Physics Comm., Vol.54, p.263, 1989.
[5] B. Fattz et al., J. Phys. D.: Appl. Phys. 26(1993)1023.
[6] H.Zen, et al., Proc in this conference.
[7] M. Yokoyama et al., Nucl. Instr. and Meth. A 483 (2002) 292.

A TRIODE-TYPE THERMIONIC RF GUN FOR DRASTIC REDUCTION OF BACK-STREAMING ELECTRONS

T. Shiiyama, K. Masuda, H. Zen, S. Sasaki, T. Kii, H. Ohgaki,
Institute of Advanced Energy, Kyoto University, Gokasho, Uji, Kyoto, 611-0011, Japan
K. Kanno, E. Tanabe, AET, INC., 2-7-6 Kurigi, Asaoku, Kawasaki, 215-0033, Japan

Abstract

We have proposed a triode-type thermionic RF gun with an additional small cavity replacing the conventional cathode, which provides the beam extraction phase independent of the main accelerating phase to suppress the back-bombardment effect drastically. In order to compensate the predicted degradation in transverse emittance, a design refinement was carried out by the use of numerical simulations in this study. The results showed that the back-bombardment power can be reduced by more than 80% and the peak current of the output electron beam will be enhanced greatly without emittance degradation. Also the cavity parameters, namely the quality factor and the coupling coefficient of the additional cavity with the RF feed coaxial cable were designed to ensure both the induction of the required cavity voltage and a wide frequency acceptance. The prototype design of the triode-type thermionic RF gun was completed and ready for experiments.

INTRODUCTION

We have used a 4.5-cell thermionic RF gun for the injector of MIR-FEL facility (KU-FEL: Kyoto University Free Electron Laser) at Institute of Advanced Energy, Kyoto University. As is well know thermionic RF guns suffer from the back-bombardment of electrons onto thermionic cathodes, which eventually leads to an output beam energy drop and limitation of the macro pulse duration [1, 2]. This effect is seen significant especially in the 4.5-cell RF gun in the KU-FEL because of its high coupling coefficient β and large number of cells. Some countermeasures were applied so far, such as the use of transverse magnetic fields [3] and the temporal control of the RF input for compensating time-varying beam-loading [4] with limited successes. A longer macro-pulse duration by a new technique against the back-bombardment effect is thus essential for the first FEL lasing.

For this purpose, we have proposed a triode-type thermionic RF gun [5, 6]. An additional small cavity with a thermionic cathode replaces the conventional cathode in the RF gun as schematically shown in Fig.1. An RF field induced at the short gap of the additional small cavity, and both the amplitude and the phase are controlled independently of the main accelerating cavities to minimize the back-bombardment of electrons onto the cathode.

Numerical studies so far have shown that the RF triode concept could reduce the back-bombardment power drastically (80% or higher) while it tends to induce inherent defocusing force at the same time, eventually resulting in an expense of the transverse emittance increase [7].

In this paper, design refinement of a triode-type thermionic cathode was carried out in order to suppress the transverse emittance increase. A wehnelt structure schematically shown in Fig.1 (b) was studied by PIC simulations to compensate the defocusing effect induced by the RF triode.

Also discussed in this paper is the selection of cavity parameters, namely the coupling coefficient β to the additional RF power feed, and the quality factor Q.

A potential feature of the RF triode concept is that the requirement of the RF power into the additional cavity is moderate, thus the cost for the RF system modification is low. For the first experiments we have installed a directional coupler to split the RF power from the existing klystron to feed < 40kW to the additional cavity.

To ensure a sufficient cavity voltage with the limited RF power and also expected resonant frequency shifts due to the beam loading effect and/or the cavity temperature change, the tuning curves were calculated by the use of an equivalent circuit model with the beam loading effect taken into account.

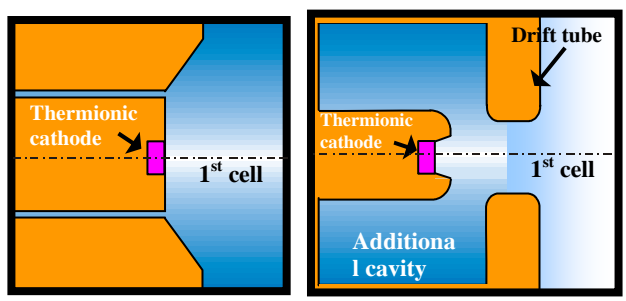

(a) Conventional type (b) Triode type

Figure 1: Schematics of RF cavity structures in the vicinity of the thermionic cathode in (a) a conventional, and (b) a triode-type RF gun.

DESIGN REFINEMENT OF THE ELECTRODE IN A TRIODE-TYPE RF GUN

Numerical Method

Design refinement of a triode-type thermionic cathode was carried out by using a cylindrically 2-dimensional group of codes (KUCODE) [8], which calculates electron dynamics in the RF gun, as follows.

Electric field patterns of cylindrically symmetric standing waves in the 4.5 cells and in the additional small cavity for an RF triode are calculated by a 2-dimensional eigenmode solver (KUEMS). The electric fields are then given with cavity voltages and relative phases as the input parameters, and electron dynamics are calculated by the PIC simulation code (KUBLAI). In this study for simplicity, the back-bombardment effect on the temporal beam-loading variation was neglected, i.e. both the cavity voltages and the cathode current density were assumed to be constant. The KUBLAI code takes into account the space-charge effects by simultaneously solving Maxwell's equations and Lorentz equation.

We used these codes to calculate the beam quality by changing the cathode shape and the relative phase between the main accelerating fields and the additional small cavity fields. From results of simulations, we have evaluated the beam emittance (transverse and longitudinal) and the peak current of the output beam at the exit of 4.5-cell RF gun, as well as the back-bombardment power onto the thermionic cathode.

Design refinement of the cathode by PIC simulations

In this study, the cathode mount position was fixed at -6mm with respect to the cathode position in the original conventional RF gun, according to the numerical results so far from the viewpoints of reducing the back-bombardment power and minimizing the transverse emittance degradation [7]. To further reducing the transverse emittance by compensating the defocusing force induced by the triode system, we adopted a wehnelt structure. Figure 2 shows the electrode geometry and the design parameters in this study, namely the cathode depth d and the wehnelt angle θ.

For every set of d and θ, the optimum RF phase of the additional cavity with respect to the main accelerating cavity of RF gun was searched for the maximum output beam brightness at the exit of RF gun. The other operational parameters were fixed, such as the extraction current density on cathode surface of 80A/cm^2, the cavity voltage in the additional small cavity of 30kV, and the total cavity voltage in the 4.5 main accelerating cavities of 10MV.

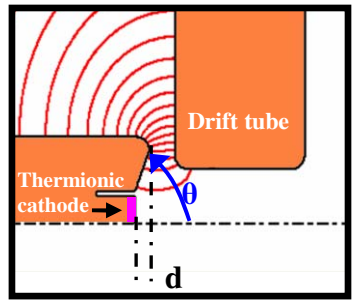

Figure 2: Close-up of a triode-type thermionic cathode with wehnelt structure

As the result, the beam brightness shows maximum at d = 1.6 mm and θ = 40 deg. Figure 3 shows the dependence of the output beam properties on θ for a fixed d = 1.6mm. Only the results with over 80 % reduction of the back-bombardment power are plotted in the figure.

As seen in Figure 3 we can prevent the transverse emittance from increasing, and improve the brightness by 15 times at the wehnelt angle θ of 40 degrees.

Finally, with the optimal d and θ, a minor design modification was then made in practical viewpoints of minimal edge fields and a deep cutoff between the additional cavity and the main cavities, and so on. Table 1 shows the expected electron beam properties by the final design of the refined triode-type thermionic cathode. In comparison with the conventional RF gun, the refined triode-type thermionic RF gun is expected to improve the peak current by 10 times and to reduce the back-bombardment power by ~90 % without degradations of the transverse emittance. The charge in a micro bunch was 77pC.

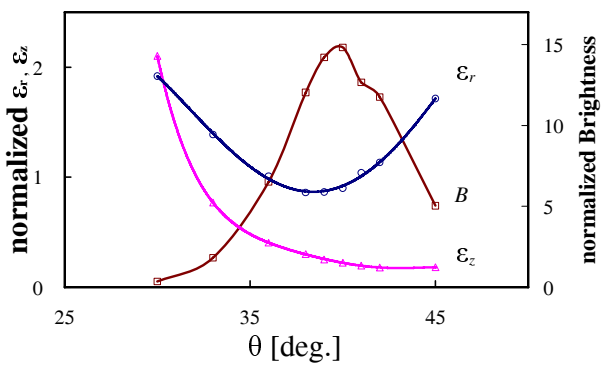

Figure 3: Beam properties by the triode-type cathode at the 4.5-cell RF gun exit as functions of the wehnelt angle θ showing the transverse and longitudinal rms emittances ε_r, ε_z, and the brightness B normalized by those by the conventional RF gun.

Table 1: Comparisons of the back-bombardment power and the output beam properties between the conventional and the refined triode-type thermionic RF gun at the 4.5 cell gun exit.

	Conventional	Triode
P_{back} [kW]	36	3.6
I_{peak} [A]	17	114
ε_r [πmm mrad]	2.5	2.0
ε_z [psec MeV]	0.046	0.012
B [A/(πmm mrad)^2 keV]	0.27	1.6

DESIGN OF CAVITY PARAMETERS

In the additional small cavity for the triode system neither a temperature control nor a frequency tuner is to be installed for simplicity and low cost. Instead, we rather set the coupling coefficient β of the additional cavity with the RF feed coaxial cable at over coupling in order to grade the tuning curve and to ensure a wide frequency acceptance. For this purpose, we will also consider a low unloaded quality factor Q_0 of the additional small cavity. At the same time we have to choose β and Q_0 so that a sufficient RF fields should be induced with the limited RF feed power supplied of < 40 kW_{peak}.

Equivalent circuit model

Frequency tuning curves were calculated by using the equivalent circuit model in Figure 4. The RF power source is represented by a current source I_g, the RF resonant cavity by a resonant circuit with G_c representing the cavity loss, and the beam loading by an admittance Y_b. The external load G_{ex} can be expressed by the coupling coefficient β as $G_{ex}=\beta G_c$.

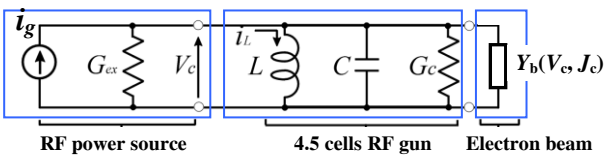

Figure 4: Equivalent circuit model of triode system

In this equivalent circuit shown in Figure 4, the cavity voltage V_c is expressed as formula (1), and I_g is given by the RF input as formula (2).

$$V_c = \frac{I_g}{(G_c + G_b + G_{ex}) + j(B_c + B_b)} \quad (1)$$

$$I_g = \sqrt{8 G_{ex} P_{in}} \quad (2)$$

The RF power P_c consumed by G_c and Y_b i.e. the cavity wall loss and the beam the acceleration, is expressed as follows.

$$P_c = \mathrm{Re}\left[\frac{1}{2}(V_c^* I_g - G_{ex} V_c^* V_c)\right] \quad (3)$$

The reflected RF power P_{ref} is equal to the power subtracted the power consumption P_c from the RF input power P_{in} as formula (4). We thus can calculate the RF power reflection ratio by formula (5).

$$P_{ref} = P_{in} - P_c \quad (4)$$

$$\frac{P_{ref}}{P_{in}} = 1 - \frac{P_c}{P_{in}} = 1 - \frac{4(G_c + G_b)G_{ex}}{(G_c + G_b + G_{ex})^2 + (B_c + B_b)^2} \quad (5)$$

In the formula (5), the beam admittance G_b and B_b are determined by the PIC simulations as functions of the cavity voltage V_c and the cathode surface current density. The cavity admittance G_c and B_c are given by the drive frequency and the cavity parameters, namely the resonant frequency (2856MHz), the shunt impedance (R/Q = 63Ω), and the unloaded quality factor Q_0.

Selection of the coupling coefficient and the quality factor

We used the equivalent circuit model in Fig.4 for calculation of the required RF feed power fed into the additional cavity. From formula (1) and (2), we obtained Fig.5 showing the required RF feed power as a function of the coupling coefficient β for a cathode surface current density of 80 A/cm^2, and a cavity voltage of 30 kV. The unloaded quality factor Q_0 = 4000 was assumed according to the eigenmode calculation for an oxygen-free copper wall.

At a coupling coefficient β of 9.6 the required RF feed power P_{in} is minimum of ~17 kW, which is below the 40 kW limitation of the experimental RF feed system. Taking this margin, we then design a lower Q_0 and/or a higher β for a wide frequency acceptance.

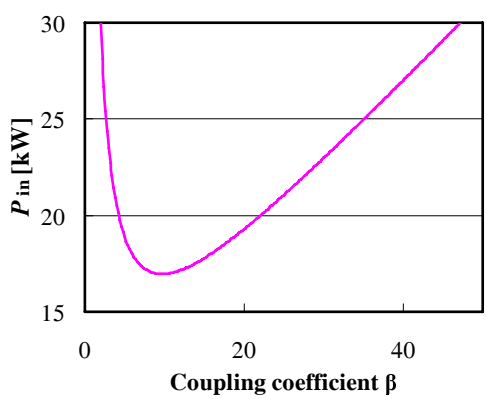

Figure 5: RF input requirement as function of the coupling coefficient β for a cavity voltage of 30kV.

Firstly, we drew tuning curves for various coupling coefficients for Q_0 = 4000 and P_{in} = 40 kW, and thus obtained the Figure 6 showing the frequency acceptance for V_c > 30 kV as a function of β. In Figure 5 and Figure 6, we can see more than 20MHz of frequency acceptance can be ensured by β = 20, and the required RF feed power at resonant frequency is ~20 kW still below the RF feed limitation of 40 kW.

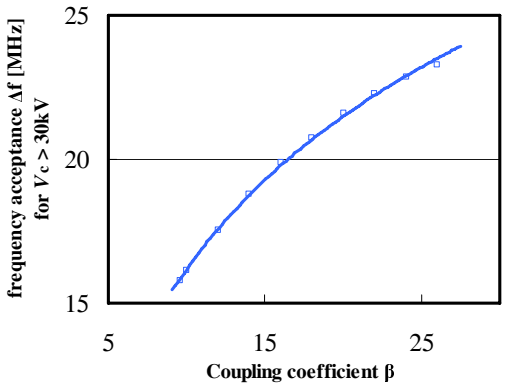

Figure 6: Frequency acceptance Δf for V_c > 30kV, as a function of the coupling coefficient β (P_{in} = 40 kW, Q_0 = 4000)

The red lines in Figure 7 show the calculated tuning curves of the designed additional small cavity (β = 20 and Q_0 = 4000 for oxygen-free copper cavity) with P_{in} = 40 kW. Note that the calculations take the electron beam admittance Y_b into consideration. In Figure 7, the solid lines represent the cavity voltage V_c, the dashed lines the RF power reflection ratio P_{ref}/P_{in}. The black lines in Figure 7 shows those for β = 9.6 and Q_0 = 4000 for comparison.

Secondly we consider a lower Q_0 of ~1000 for a stainless steel (SUS) cavity. The SUS cavity can lower the coupling coefficient β in the same frequency acceptance, so the coupler design is easier than over coupling. The blue lines in Figure 7 show curves for β = 9.6 and Q_0 = 1000. It is found that the SUS cavity can realize the more gentle tuning curves by the lower Q_0. However the frequency acceptance for V_c > 30 kV is found not to be wider, and furthermore the maximum available cavity voltage V_c at resonance is lower.

Thus the additional small cavity for the triode system is to be made of an oxygen-free copper with an over coupling of ~20 with the coaxial RF feed cable.

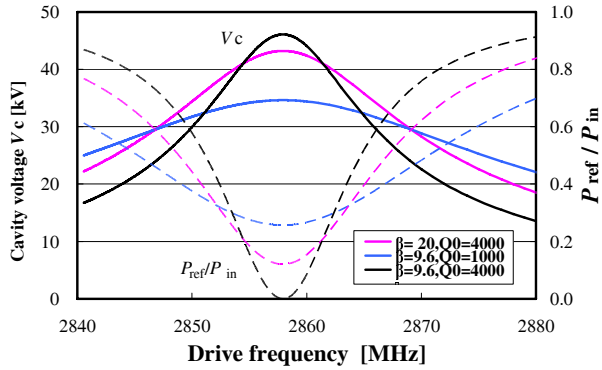

Figure 7: Tuning curves of the additional small cavity, taking the electron beam admittance Y_b into consideration.

SUMMARY

In this study, we evaluated the reduction of the back-bombardment and the output beam properties in a triode-type thermionic RF gun with PIC simulations. With an RF power of ~20 kW fed to the additional small cavity for the triode system, the back-bombardment power is expected to reduce to 3.6 kW from 36 kW in conventional RF gun. Furthermore, the output beam properties at the 4.5-cell RF gun exit, such as the beam emittance and the peak current, are improved as the result of the triode geometry refinement. Especially a great improvement of the peak current is expected because the bunch length of electron beams is to be shortened by using the RF triode system.

We also designed the coupling coefficient β, the shunt impedance *R/Q,* and the quality factor Q_0 to ensure a wide frequency acceptance. Now we are then designing the coupler geometry realize the designed coupling coefficient. We are planning to install a triode-type thermionic cathode based on the designed geometry and parameters for the first experiment this year.

REFERENCES

[1] T. Kii, et al., Nuclear Instruments and Methods in Physics Research A 475 (2001) 588.
[2] K. Masuda, et al., Nuclear Instruments and Methods in Physics Research A 483 (2002) 315.
[3] T. Kii, et al., Proc. 9th Intnl. Conf. Synchrotron Radiation Instrumentation, 2006
[4] T. Kii, et al., Proc of FEl2005 (2006) 584.
[5] E. Tanabe et al., Proc of 27th Linear Accelerator Meeting in Japan, 2002, pp.57 (in Japanese).
[6] K. Kusukame, et al., Proc of the 30th Linear Accelerator Meeting in Japan, 2005
[7] K. Masuda, et al., Proc of FEL2006
[8] K. Masuda, a dissertation of Ph, D. Kyoto University, 1998

NUMERICAL STUDY ON THE OPTIMUM CAVITY VOLTAGE OF RF GUN AND BUNCH COMPRESSION EXPERIMENT IN KU-FEL

H. Zen#, T. Kii, K. Masuda, H. Ohgaki, S. Sasaki, T. Shiiyama,
Institute of Advanced Energy, Kyoto University, Gokasho, Uji, Kyoto, 611-0011

Abstract

High peak current (~40 A) electron beams with the macro-pulse duration of 2-5 μs are required for the lasing of Kyoto University Free Electron Laser (KU-FEL). However, the bunch charge and macro-pulse duration in the facility have a trade-off relationship, and the bunch charge is limited to <30 pC when the macro-pulse duration is ~3 μs. Therefore, the optimization of operational condition of our thermionic rf gun and the bunch compression are necessary to achieve such a high peak current. Optimum field strength of our rf gun was surveyed by numerical simulation. The result indicates that the highest peak current is around 23 A with the average field strength of 24 MV/m. Under the same condition, bunch lengths of electron beams were measured by using a streak camera. The condition of bunch compression was also surveyed in experiment. The measured minimum bunch length was 2.0 ps, which was as short as the temporal resolution of the measurement system. Since the bunch charge was 14 pC, the highest peak current was estimated to be more than 7 A from the experimental result.

INTRODUCTION

A mid-infrared free electron laser facility (3-14 μm) named KU-FEL was constructed for the energy science in Institute of Advanced Energy, Kyoto University [1]. As shown in Fig. 1, the facility consists of an S-band 4.5 cell rf gun with a tungsten dispenser-type thermionic cathode, an energy filtering section (Dog-leg), a S-band accelerator tube (3 m), a bunch compression section (180-deg. arc), an undulator and an optical cavity. Electron beams were successfully accelerated up to 40 MeV [2]. However, due to the back-bombardment effect [3,4], the bunch charge and macro-pulse duration have a trade-off relationship and the bunch charge was limited to smaller than 30 pC with the macro-pulse duration of ~3 μs. Thus the bunch compression is necessary to obtain a peak current of ~40 A, which is required to achieve the FEL saturation [5] in KU-FEL. Another feature of the gun is that the higher average current is available after energy filtering section if the higher electrical fields are induced to its cavities. On the other hand, the nonlinearity of longitudinal phase space distribution, which enlarges a bunch length during a bunch compression, increases if too high electrical fields induced. It means that there is the optimum operational condition of the field strength of rf gun to obtain the highest peak current. In this study, first, the optimum field strength of the gun was surveyed by numerical simulation. Second, the bunch length was measured and the optimum bunch compression condition was determined under the gun condition in experiment. PARMELA [6] was used for particle tracking from the gun to the undulator. And ELEGANT [7] was used to find the achromatic sets of quadrupole magnets of dispersive section in simulation and experiment. And the code was also used to calculate and control the R_{56} of the arc.

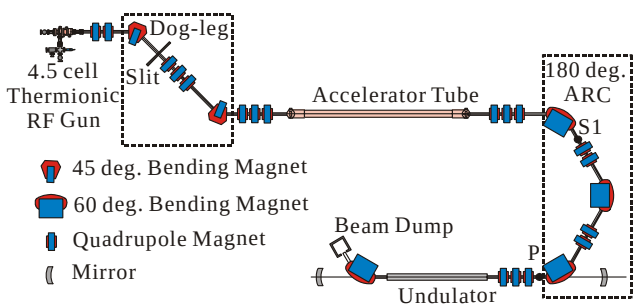

Figure 1: Schematic view of KU-FEL facility.

#heishun@iae.kyoto-u.ac.jp

STUDY ON THE OPTIMUM FIELD STRENGTH OF RF GUN

Dependences of the longitudinal emittance and the average current on the average field strength of the first half cell of the 4.5 cell rf gun were shown in Fig. 2. The field strengths of other 4 cells are about twice higher than that of the first cell. The longitudinal phase space distributions at the entrance of the accelerator tube were shown in Fig. 3. As mentioned in the introduction, the higher average current is available after the energy filtering section if the higher field strength of the cells is induced. As shown in Fig. 2 and 3, however, the nonlinearity of the longitudinal phase space distribution and the corresponding longitudinal emittance rise up if too high electric fields (>25 MV/m) are induced. High bunch charge and low longitudinal emittace are required to obtain high peak current after bunch compression.

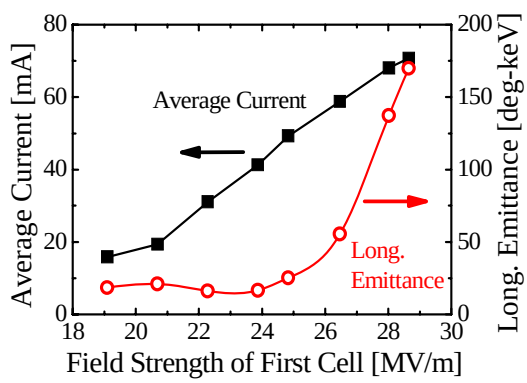

Figure 2: Longitudinal emittance and average current as a function of the field strength of first half cell.

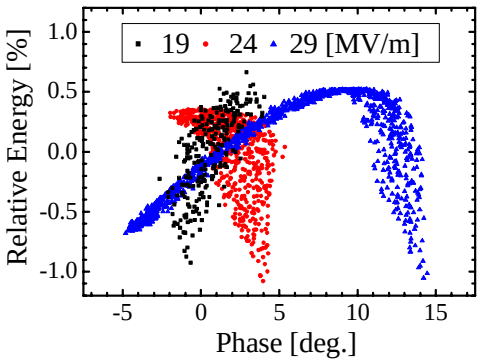

Figure 3: Longitudinal phase space distribution at the entrance of accelerator tube (simulation).

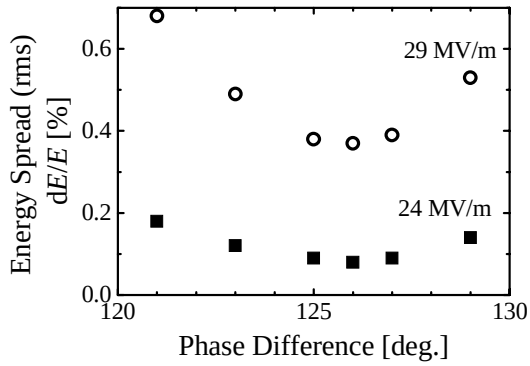

Figure 4: Energy spread as a function of phase difference between the rf gun and the accelerator tube.

There are two candidates of the field strength for the highest peak current. One is around 24 MV/m which have the smallest longitudinal emittance with a medium bunch charge. The other is 29 MV/m which have the highest bunch charge with the largest longitudinal emittance.

Due to the transient energy drop by the back-bombardment effect, in practical experiment, there is a trade-off relationship between the average current and the macro-pulse duration after the energy filter, which means that the macro-pulse duration decreases if the average current increases. Table 1 shows the typical parameters of electron beams that have the highest average currents with the macro-pulse duration of 2.4 μs under the 24 and 29 MV/m conditions. In this numerical study, beam parameters were adjusted to those shown in Table 1.

Table 1: Typical parameters of the electron beam under the 24 and 29 MV/m conditions.

Gun	Field Strength of First Cell [MV/m]	24	29
Gun Exit	Peak Energy [MeV]	7.5	9
	Average Current [mA]	320	320
	Macro-pulse Duration [μs]	3.3	3.3
After Dog-leg	Average Current [mA]	40	70
	Macro-pulse Duration [μs]	2.4	2.4

Bunch Compression

The bunch compression properties under the 24 and 29 MV/m condition were examined by numerical simulation. The energy after the accelerator tube was set to about 25 MeV by adjusting field strength. Under both of the two conditions, the energy spread is minimal when the phase difference between the gun and the tube set to 126 deg. as shown in Fig. 4. An energy chirping is essential for the bunch compression and we gave the energy chirp by selecting the phase difference of 121 deg.

Dependences of the bunch length on R_{56} with energy chirping are shown in Fig. 5. The bunch length was evaluated by the least square fitting of Gaussian distribution to the temporal distribution. The longitudinal phase space distributions under the minimum bunch length condition are shown in Fig. 6, and the temporal

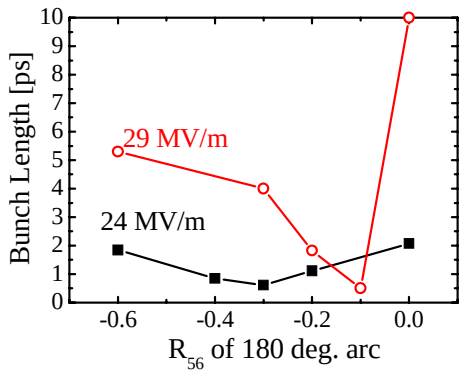

Figure 5: Bunch length as a function of R_{56} of the 180 deg. arc.

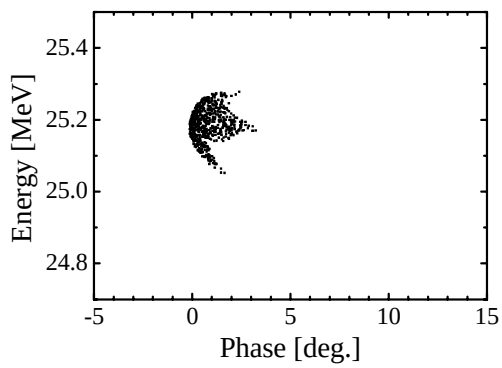

(a) 24 MV/m condition, R_{56} = -0.3.

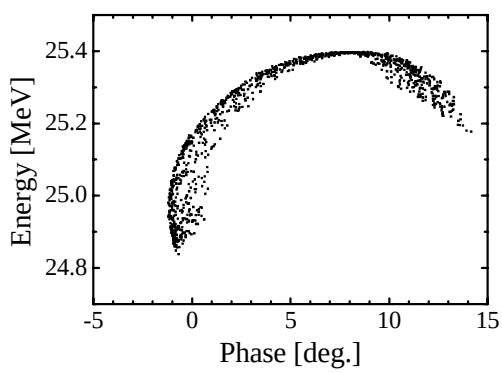

(b) 29 MV/m condition, R_{56} = -0.1.

Figure 6: Longitudinal phase space under the minimum bunch length condition.

profiles are shown in Fig. 7. The peak current was also evaluated by the Gaussian fitting and the results are shown in Table 2. As you can see in Fig. 6 and Fig. 7, all the electrons are bunched well under the 24 MV/m condition, and the electrons are not bunched well under the 29 MV/m condition. Thus the peak current under the 24 MV/m condition was higher than 29 MV/m condition as shown in Table 2, even though the total bunch charge was lower.

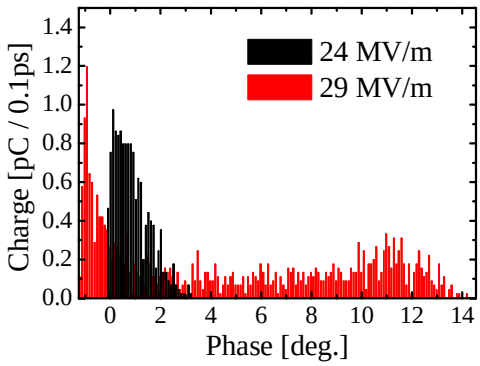

Figure 7: Temporal distributions with the minimum bunch length condition.

Table 2: Results of numerical simulations.

Field Strength of First Cell [MV/m]	24	29
Total Bunch Charge [pC]	14	25
Bunch Length [ps]	0.6	0.5
Peak Current [A]	23	16

BUNCH LENGTH MEASUREMENT AND BUNCH COMPRESSION

The bunch length measurements and the bunch compression were carried out to determine the optimum condition of bunch compression in experiment under the 24 MV/m condition. In experiment, the beam parameters before the accelerator tube were same with ones shown in Table 1. The central energy after the tube was adjusted to 25 MeV, and the phase difference between the gun and the tube was adjusted to the condition that the horizontal beam size at the beam profile monitor S1 in Fig. 1 became minimal.

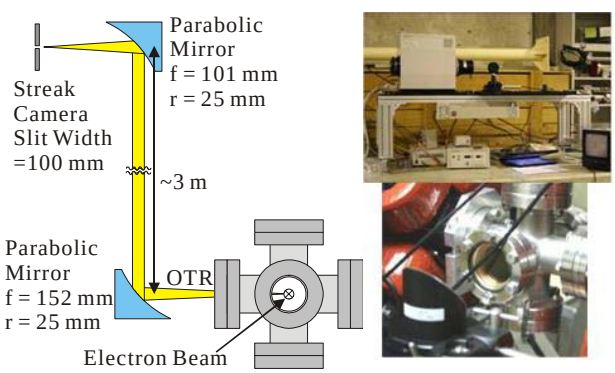

Figure 8: Setup of optics and streak camera.

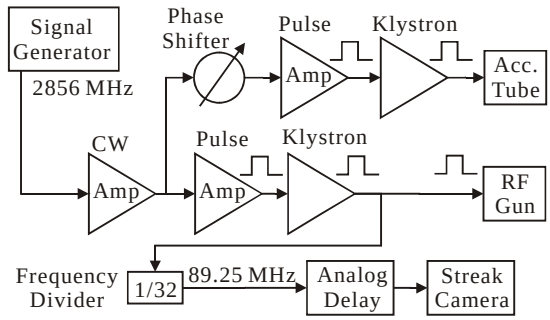

Figure 9: Trigger diagram for the streak camera.

Experimental Setup

A mirror target to generate optical transition radiations (OTRs) from electron beams was inserted at the position P in Fig. 1, and the OTRs were transported to and focused on the entrance slit of a streak camera (HAMAMATSU C6138S) by a pair of parabolic mirrors as shown in Fig. 8. The focusing mirror enables to minimize the deterioration of temporal resolution with the least weakening of the OTR. The slit width of streak camera was limited to over 100 μm due to weak OTRs, and we use 50 ps full scale range. Then, the temporal resolution was around 2.0 ps.

The trigger diagram for the streak camera is shown in Fig. 9. The trigger signal was generated by using a frequency divider (1/32) from rf power fed to the rf gun in order to synchronize the trigger signal with the electron beam.

Result and Discussion

Figure 10 shows the typical result of the bunch length measurement and it was integration of 10 shots. When the temporal profiles were integrated, the mean of each temporal profile were aligned in order to mitigate the deterioration of temporal resolution due to timing jitter (~10 ps) of the trigger signal.

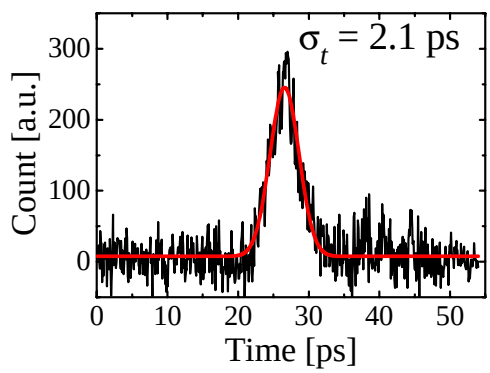

Figure 10: Typical result of the bunch length measurement. This result was integration of 10 shots.

Dependences of measured bunch lengths on R_{56} of 180-deg. arc section were shown in Fig. 11. These results are also integration of 10 shots. The minimum bunch length was around 2.0 ps with R_{56} = -0.3, -0.4. The result was as short as the temporal resolution of this measurement limited by slit width of the streak camera. Therefore, the

actual bunch length must be shorter than 2.0 ps. The peak current of electron beam was measured to be more than 7 A, since the bunch length was shorter than 2.0 ps and the bunch charge was 14 pC. Higher temporal resolution is required to discuss shorter bunch lengths and to shorten the bunch length under 2.0 ps.

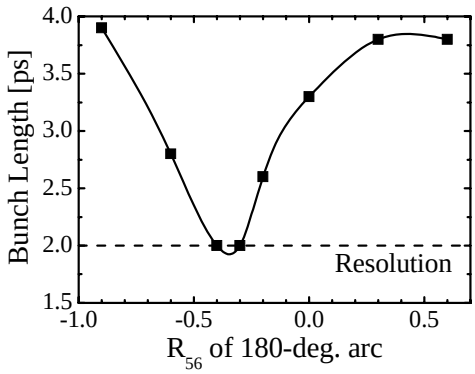

Figure 11: Experimental result of dependences of bunch lengths on R_{56} of 180-deg. arc section.

CONCLUSION

The optimum cavity voltage of our thermionic rf gun was studied by numerical simulation. The result indicated that the field strength of first cell should be around 24 MV/m to obtain high peak current in present setup. The highest peak current was about 23 A under the condition. The bunch length measurement and bunch compression were performed under the optimum condition. The measured minimum bunch length was 2.0 ps when R_{56} was -0.3, -0.4. The minimum bunch length was as short as the temporal resolution of measurement system. Thus the peak current was estimated to be more than 7 A in this experiment. Higher temporal resolution is required to discuss shorter bunch length and to obtain higher peak current. And now, we are preparing a configuration which enables us measurements with higher temporal resolution.

The peak current about 23 A is not enough to achieve FEL saturation [5] in KU-FEL, even if we could shorten the bunch length to 0.6 ps in experiment. To obtain higher peak current, we are now preparing a LaB_6 cathode [8] and a triode-type rf structure [9,10].

REFERENCES

[1] T. Yamazaki, et al., "KU-FEL: A compact and economical S-band linac based FEL for advanced energy science" in Proc. of 23rd Int'l FEL Conf., North-Holland, Amsterdam, (2002), II-13.
[2] H. Ohgaki, et al., NIM, A528, 366-370 (2004).
[3] C. B. McKee, et al., NIM, A 304 (1991) 386.
[4] K. Masuda, et al., NIM A 483 (2002) 315.
[5] M. Nakano, et al., Proc. of FEL 2006, 2006, p656-660.
[6] L. M. Young, James H. Billen, LA-UR-96-1835 (2002)
[7] M. Borland, "User's Manual for elegant", v.15.4.1 (2005).
[8] F. Oda, et al., Proc. of the 26th Linear Accelerator Meeting in Japan, p67-69 (in Japanese).
[9] K. Masuda, et al., Proc. of FEL 2006, (2006), p656-660.
[10] T. Shiiyama, et al., WEPPH026, these proceedings.

DEVELOPMENT OF A COMPACT CHERENKOV FREE-ELECTRON LASER OPERATING IN TERAHERTZ WAVE RANGE

Nozomu Miyabe*,Akira Ikeda,Makoto R.Asakawa,Mitsuhiro Kusaba,Yoshiaki Tsunawaki
Kansai University, 3-3-35 Yamate-cho, Suita, Osaka 562-8680, Japan
Osaka Sangyo University, 3-1-1 Naka-gaito, Daito, Osaka 574-8530, Japan

Abstract

We designed a compact Cherenkov Free-Electron Laser (CFEL) oscillator driven by 50keV electron beam. The resonator, called double-slab resonator, consists of a rectangular waveguide partially filled with two lined parallel silicon slabs, whose dielectric constant ε equals to 11.6 in the terahertz frequency range. The operation frequency ranges from 40GHz to 1THz according to the thickness of the slabs. Numerical calculation predicted 100W-level output at 46GHz by electron beam with 50keV/400mA.

OPERATING FREQUENCY OF THE DOUBLE-SLAB RESONATOR

Our purpose is to develop a CFEL oscillator operating in the terahertz frequency range driven by a low energy electron beam [1]. We examine the operating frequency of the double-slab resonator fed by 50keV electron beam in this section.

Fig.1 shows the schematic view of the double-slab resonator. To simplify the problem, it is assumed that its transverse dimensions are $2(D+d)$ and infinite, where D and d are the vacuum half width and the thickness of the dielectric slab with dielectric constant of ε, respectively.

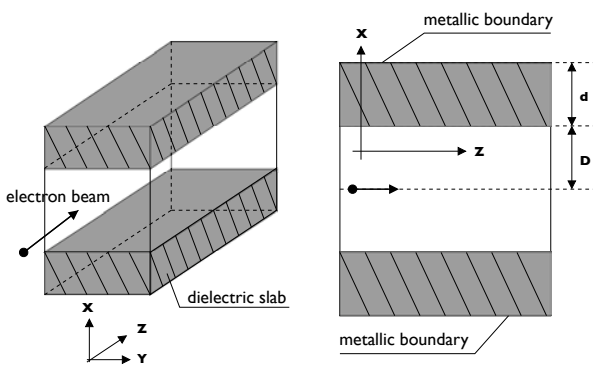

Figure 1: Schematic form of the waveguide partially filled with two lined parallel dielectric slabs with the thickness of d. Electron beam propagates along the Z-axis in the spacing of the slabs with the width of $2D$.

In CFEL oscillator, the radiation is gained by the interaction between the longitudinal electric field E_z and the straightly moving electron [2]. TM modes whose E_z distributes in a symmetrical pattern to the x=0 plane are, therefore, of interest. The electromagnetic field of the symmetric TM mode, in concrete terms TM_1, TM_3, TM_5.., is expressed as following. [3]
In vacuum region: $0 < |x| < D$

$$\begin{aligned}\mathbf{E}(x,z,t) &= E_{z0}\begin{pmatrix}\frac{k_z}{p}\sinh px\\0\\i\cosh px\end{pmatrix}e^{i\theta}\\ \mathbf{H}(x,z,t) &= E_{z0}\begin{pmatrix}0\\\frac{k_0}{p}\sinh px\\0\end{pmatrix}e^{i\theta}\end{aligned} \quad (1)$$

In dielectric region: $D < |x| < D+d$

$$\begin{aligned}\mathbf{E}(x,z,t) &= E_{z0}\begin{pmatrix}\frac{k_z}{\varepsilon p}\left(F\cos\theta' + G\sin\theta'\right)\\0\\-i\frac{q}{\varepsilon p}(F\sin\theta' - G\cos\theta')\end{pmatrix}e^{i\theta}\\ \mathbf{H}(x,z,t) &= E_{z0}\begin{pmatrix}0\\\frac{k_0}{p}\left(F\cos\theta' + G\sin\theta'\right)\\0\end{pmatrix}e^{i\theta}\end{aligned} \quad (2)$$

where E_{z0} is the amplitude of E_z at x=0, k_z and ω are the wavenumber and angular frequency, respectively. The transverse wavenumbers in the vacuum and dielectric regions are defined as $p^2 = k_z^2 - \omega^2/c^2$ and $q^2 = \varepsilon\omega^2/c^2 - k_z^2$, respectively. Here the free-space wavenumber $k_0 = \omega/c$, the longitudinal phase of the radiation field $\theta = k_z z - \omega t$, the transverse phase $\theta' = (x-D)q$, the constants determined by the resonator configuration $F = \sinh pD$, $G = \varepsilon\frac{p}{q}\cosh pD$.

The dispersion relation is given by

$$\varepsilon\frac{p}{q}\cos qd\cosh pD - \sin qd\sinh pD = 0. \quad (3)$$

Fig.2 shows the dispersion curves for TM_1 mode for slabs of silicon (ε=11.6) with thickness d=0.65mm and $30\mu m$. In CFEL, the radiation resonates with electron beam if the phase velocity w/k_z is equals to the electron velocity. Thus the intersections of the curves and the beam mode line $w = \beta_z k_z$ are the resonant points. The resonant frequencies are 46.0GHz and 983 GHz for d=0.65mm and $30\mu m$, respectively. The numerical calculations of the dispersion relations found that the resonant frequency was almost inversely proportional to the thickness d.

On the other hand, the resonant frequency suggests a little dependence on the width of vacuum region D as shown in Fig.3. It decreases only by 3% as the thickness D increases from 0.325mm to 1.3mm.

However, the vacuum width D has a substantial effect on the radiation filed strength of E_z in the vacuum region,

* sa6m051@edu.kansai-u.ac.jp

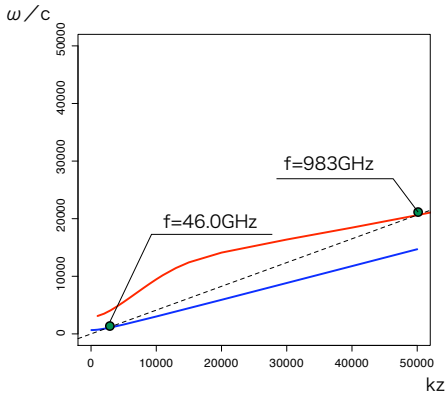

Figure 2: Dispersion curves of the double-slab resonator. Lower and upper curves show the dispersion for d=0.65mm and 30μm, respectively. Dashed line shows the velocity of 50keV.

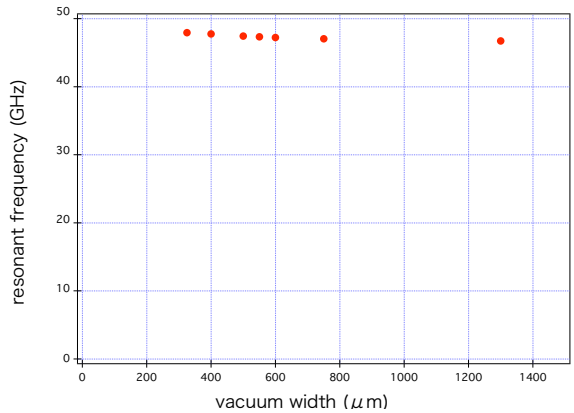

Figure 3: The resonant frequency versus the vacuum width D.

i.e. the interaction region. Fig.4(a) and Fig.4(b) show the E_z distributions at 46.0GHz for D=0.75mm and 0.5mm, respectively. As the width $2D$ decreases from 1.5 mm to 1.0 mm, the E_{z0} increases by a factor of 1.6. To obtain substantial interaction, one should reduce the width of vacuum region D less than $2d$. For higher operating frequency, thus, the beam focusing will be the issue.

NUMERICAL STUDY ON THE CFEL OSCILLATOR AT 46GHZ

In this section, we describe the design of a 46GHz CFEL oscillator for the preliminary experiment. The required resonator configuration, start-up current, the gain and the saturation power were investigated by using the one-dimensional numerical simulation code.

The calculation of CFEL interaction was based on the following equations.

$$\frac{d^2 z_i(t)}{dt^2} = -\frac{e}{\gamma^3 m} E_z(z,t) \tag{4}$$

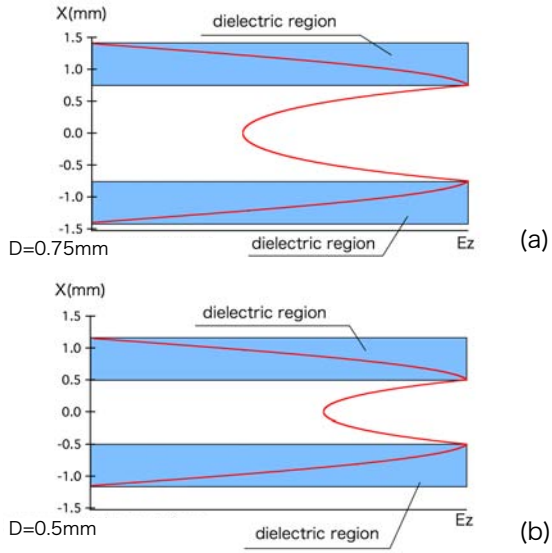

Figure 4: Field distributions for the vacuum width

$$\frac{d\gamma_i(t)}{dt} = -\frac{e}{mc^2} v_{z_i}(t) E_z(z_i,t) \tag{5}$$

where $E_z(z,t) = E_{z0}\cos(\omega t - k_z z_i)$, e is the electron charge, m is the electron rest mass, c is light velocity in the vacuum, and γ is the relativistic factor. The subscript i refers to the quantities of the i-th particle. The power increment for the radiation is related to the decrease in the average electron energy:

$$< \frac{d\gamma}{dt} >= \frac{1}{n} \sum \frac{d\gamma_i}{dt} \tag{6}$$

$$\frac{dP}{dt} = - < \frac{d\gamma}{dt} > \frac{I}{e} mc^2 \tag{7}$$

where n is the number of electron, and I is beam current.

The radiation power inside the resonator is calculated by

$$\begin{aligned} P &= \int_s \mathbf{S} \cdot \mathbf{e}_z dxdy \\ &= A(\omega, k_z) E_{z0}^2 \end{aligned} \tag{8}$$

where,

$$\begin{aligned} A(\omega, k_z) &= \frac{k_z k_0}{4\varepsilon p^2} \left[\varepsilon \left(\frac{e^{2pD} - e^{-2pD}}{2p} - 2D \right) \right. \\ &+ 4 \left[F^2 \left(\frac{\sin 2qd}{4q} + \frac{d}{2} \right) + FG \left(\frac{1 - \cos 2qd}{2q} \right) \right. \\ &+ \left. \left. G^2 \left(\frac{d}{2} - \frac{\sin 2qd}{4q} \right) \right] \right] \end{aligned} \tag{9}$$

From these equations, E_{z0} of the gained radiation was evaluated, and then it is used to calculate the radiation field at the next time step.

To gain the radiation at 46.0GHz, the electron energy should be detuned from the resonant energy of 50keV. The

amount of the detuning was represented with a factor α which means $\gamma = \alpha\gamma_0 : \gamma_0 = 50/511 + 1$. Fig.5 shows the dependence of the small-signal gain on the detuning factor α for the resonator length L=11cm with 400mA electron beam. The meaningful gain is obtained in the range $1.0005 < \alpha < 1.005$, and the gain reaches the maximum at $\alpha = 1.0022$. Because the optimal α is related to the slippage between the radiation and electron, the optimal value changes with the resonator length L.

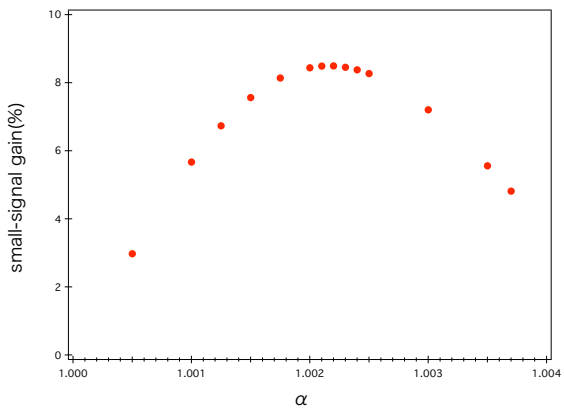

Figure 5: The dependence of the small-signal gain on the detuning factor α for the resonator length L=11cm.

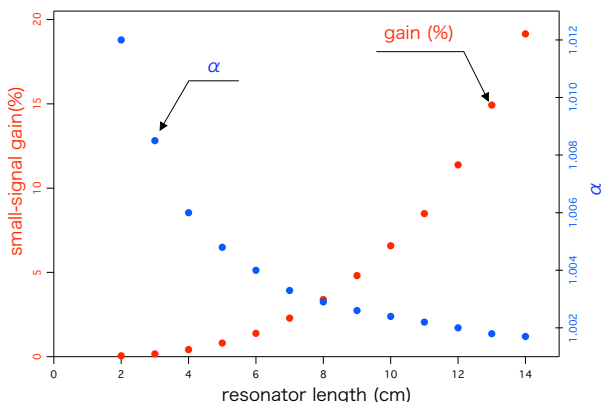

Figure 6: The dependence of the small-signal gain and optimal α on the resonator length.

Red circles in Fig.6 show the dependence of the small-signal gain on the resonator length. Blue circles show the optimal α for each resonator length. The small-signal gain varies as $L^{3.03}$. The optimal α decreases with L: $\alpha - 1$ is inversely proportional to L. We chose L=11cm for practical design because the gain exceeds enough the loss in the resonator, as well as the slabs of this length can be cut from the standard wafer for the semiconductor applications.

Fig.7 shows evolution of the CFEL output power and net gain. The resonator length is 11cm. We assumed the total loss of 5% each round-trip including the dielectric loss of 4% and the extraction efficiency of 1%.

The radiation grows with a net gain of 3.57% until 600 round-trips, then saturates around the 800 round-trips at the saturation power of 97W. In the practical situation, the duty cycle should be limited to 1/1000 to avoid thermal damage. The average power of the practical device will be 100mW level.

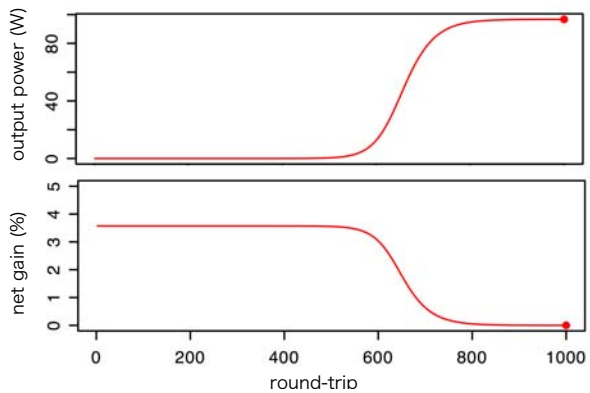

Figure 7: Upper trace shows the output power growth of the electromagnetic wave verses the round-trip. Bottom trace shows the net gain verses the round-trip. The lasing frequency is 46GHz, the resonator length is 11cm. The electron energy is 50keV, and the beam current is 400mA.

CFEL TEST BENCH

To demonstrate 46GHz lasing experiment, we constructed the CFEL device consisting of Spindt-Type Cathode, the silicon double-slab resonator, and superconducting coil. Spindt-Type Cathode can generate 100mA electron beam from emission area of $0.5^2 \times \pi\ mm^2$. Fig.8 shows picture of the silicon double-slab resonator. The slab has the thickness of 0.65mm and the width of 5mm. Superconducting coil produces magnetic flux density up to 5T. This strong field will focus the electron beam.

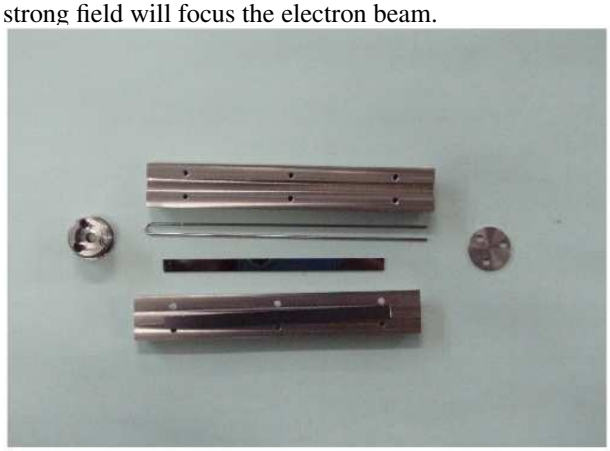

Figure 8: The double-slab resonator

REFERENCES

[1] M.R.Asakawa, K.Nakao, N.Miyabe, M.Kusaba, Y.Tsunawaki, Proceedings of FEL 2006, BESSY,Berlin,Germany, p364.

[2] J.Walsh, B.Johnson, Phys.Rev.Let.Vol.53 (1984) 779.

[3] Wladyslaw Zakowicz, J.Appl.phys.,Vol.55, (1984) 3421.

DEVELOPMENT OF THE LONGITUDINAL PHASE-SPACE MONITOR FOR THE L-BAND ELECTRON LINAC AT ISIR, OSAKA UNIVERSITY*

R. Kato#, S. Kashiwagi, T. Igo, Y. Morio, G. Isoyama
ISIR, Osaka University, Ibaraki, Osaka 567-0047, Japan

Abstract

In order to measure the longitudinal phase-space profile of the high-brightness electron beam, we are developing the measurement system consisted of a profile monitor, a bending magnet and a streak camera. Instead of an optical transition radiation (OTR) monitor as previously considered, a Cherenkov radiator with a hydrophobic silica aerogel is used as a profile monitor. Due to the physical limitation at the installation location, we designed a simple radiator supported with a metallic mirror. The Cherenkov radiator has been designed, and it is in the process of production.

INTRODUCTION

The performance of the self-amplified spontaneous emission free-electron laser (SASE-FEL) strongly depends on beam parameters, such as a longitudinal beam profile, bunch charge, the transverse emittance and an energy profile. A correlation between longitudinal positions of electrons in a bunch and their energies has a crucial effect on the temporal evolution of the optical pulse of SASE. Several types of methods are extensively under study to evaluate the longitudinal phase-space profile of the electron beam [1-4].

A measurement system of the longitudinal phase-space distribution of electrons using the combination of a bending magnet, a profile monitor and a streak camera are currently under development at the Institute of Scientific and Industrial Research (ISIR), Osaka University. In the preliminary experiments using an optical transition radiation (OTR) monitor as the profile monitor, it was confirmed that the monitor had higher momentum resolution rather than the ordinary used momentum analyzer using a slit and a current monitor [5]. However, we could not get the efficient number of photons to obtain the phase-space images since, in addition to low photon yield, the angular distribution of the OTR is too large to concentrate in the electron energy region of 10 – 20 MeV, which is suitable energy for THz-SASE and THz-FEL experiments conducted at this laboratory [6-8]. In order to increase the number of photons, we try to use a Silica aerogel as a profile radiator using example from the results at PITZ [2]. In this report, we introduce the design of the longitudinal phase-space monitor using a Silica aerogel Cherenkov radiator and the system layout.

*Work supported by Japan Society for the Promotion of Science (JSPS), Grant-in-Aid for Scientific Research (C), 18540273, 2006-2007.
#kato@sanken.osaka-u.ac.jp

PROPERTIES OF AEROGEL AND ITS CHERENKOV RADIATION

Aerogel is a low-density light-weight solid material produced by replacing the liquid component in the gel with gas. Silica aerogel, which is a silica-based substance, is the most common type of aerogel and has extremely light weight, extraordinary thermal insulation abilities, etc as a feature. We use a hydrophobic silica aerogel manufactured by Matsushita Electric Works, Ltd. (MEW). They supply several types of aerogel as shown in Table 1. In high energy particle physics, these aerogels are also used as radiators in Cherenkov detectors of the Belle detector system at KEKB.

Table 1. Characteristics of hydrophobic silica aerogels.

Aerogel type	SP-15	SP-30	SP-50
index of refraction	1.015	1.03	1.05
density (g/cm3)	0.06	0.11	0.19

Cherenkov radiation is emitted when a charged particle passes through a medium at a velocity greater than the speed of light in that medium. Cherenkov radiation is emitted in a cone having a subtended angle $2\theta_{\mathrm{CR}}$, which is determined by the average index of refraction in the medium n and the particle velocity β as follows:

$$\cos\theta_{CR} = \frac{1}{\beta n}. \tag{1}$$

Figure 1 shows the emission angle of Cherenkov radiation in the aerogel radiator versus the electron energy. Above the electron energy of 10 MeV, the emission angle is almost constant. However, the angle is too large to gather all rays of light. The number of photons N_{CR} radiated as Cherenkov radiation with wavelengths between λ_1 and λ_2 per a distance d along the path of the electrons is represented as follows:

$$\begin{aligned} N_{CR} &= 2\pi\alpha d\left(\frac{1}{\lambda_1}-\frac{1}{\lambda_2}\right)\left(1-\frac{1}{\beta^2 n^2}\right), \\ &= 2\pi\alpha d\left(\frac{1}{\lambda_1}-\frac{1}{\lambda_2}\right)\sin^2\theta_{CR} \end{aligned} \tag{2}$$

where α is the fine structure constant. Figure 2 shows the number of photons emitted from the aerogel with different indices of refraction. In this case, the wavelength region is assumed to be equal to the sensitivity region of the streak camera (400 ~ 800 nm). The photon yield of Cherenkov

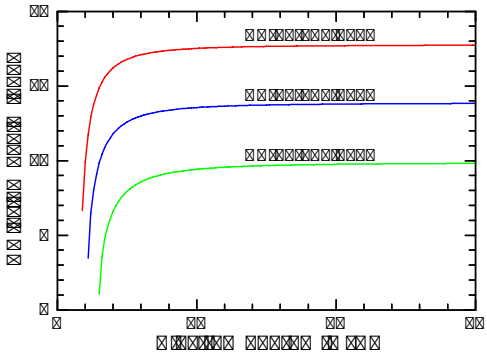

Figure 1: The emission angle of Cherenkov radiation in the aerogels with different indices of refraction.

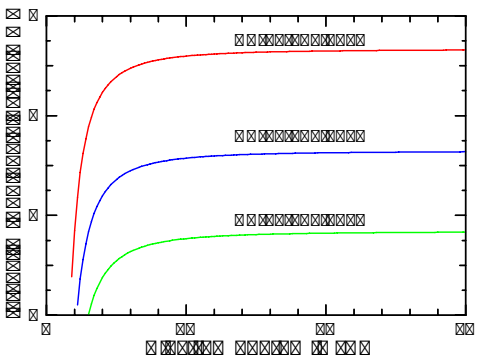

Figure 2: The number of photons as Cherenkov radiation per electron per 1 mm distance emitted from the aerogels with different indices of refraction.

radiation per incident electron in the visible region is larger than that of OTR by two orders of magnitude.

DESIGN OF CHERENKOV RADIATOR

We intend to install the Cherenkov radiator in the beam transport line form the linac to the FEL system as shown in Figure 3. Due to the physical limitation at the installation location, we can not bring a complicated mechanism into a vacuum. We designed a simple radiator supported with a metallic mirror as shown in Figure 4. In this radiator, we use a thin aerogel with a dimension of 45 x 30 mm^2 and a thickness of 1.5 mm manufactured by MEW as a trial. For this thickness, they can produce the aerogels only with the refractive indices of 1.03 (SP-30) and 1.05 (SP-50). Since the aerogels SP-30 are fragile and almost half of them were cracked, we decide to use the aerogels SP-50. Figure 5 shows the example of the manufactured aerogels.

Cherenkov radiation in the aerogel SP-50 is emitted in a cone having a subtended angle of 35.5°. The light is reflected by the metallic mirror into the aerogel again and is refracted by the surface between the aerogel and a vacuum. In order that the direction of the Cherenkov radiation emitted upward in the aerogel may be perpendicular to the horizontal plane in a vacuum, the radiator is attached with a tilt angle of 55.8°. Hereby the effective thickness of the aerogel becomes 2.7 mm.

ESTIMATION OF PHOTON YIELD

A part of the Cherenkov light cone is taken out from the vacuum chamber to the air through a sapphire vacuum window and is transported to the streak camera by mirrors. The light accepted by the first concave mirror is estimated approximately to 10 % of the total radiation. In order to eliminate broadening of the pulse width of light in the air, an interference filter will be used. Assuming that the filter has a wavelength range from 400 nm to 410 nm and that its transmittance is 40 %, the photon yield on the entrance slit of the streak camera is expected to 0.027 photons per electron. The number of electrons in a single bunch accelerated by the L-band linac is typically about 2 x 10^{11}. The net number of photons produced by one bunch is expected to be 5.4 x 10^9 on the slit.

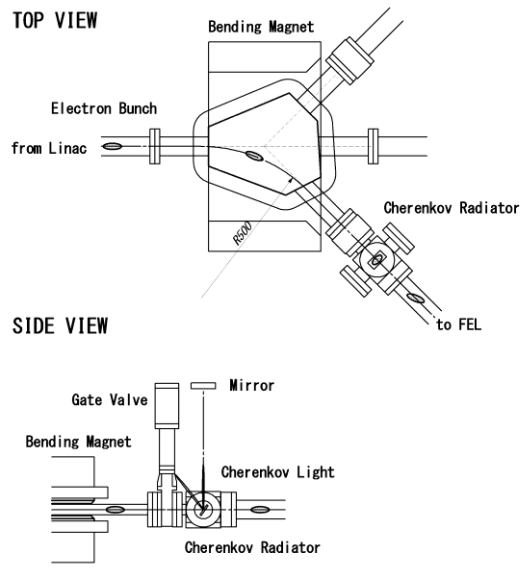

Figure 3: Configuration of the Cherenkov radiator.

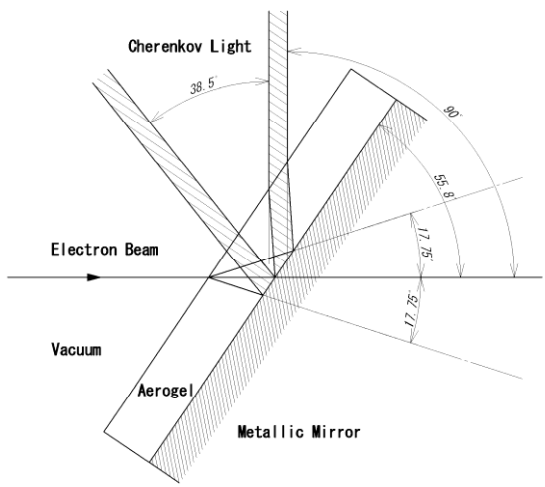

Figure 4: Schematic design of the Cherenkov radiator.

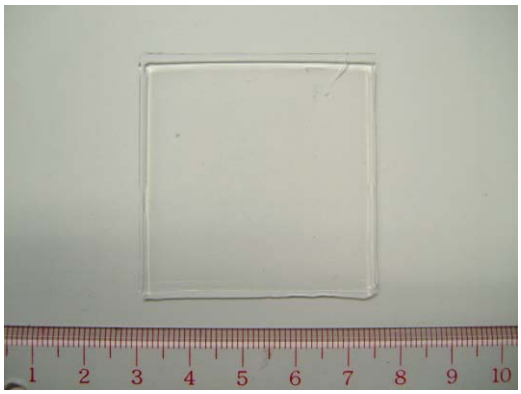

Figure 5: A thin hydrophobic silica aerogel used as a Cherenkov radiator with a thickness of 1.5 mm and the refractive index of 1.05.

In the meanwhile, the view size of a CCD camera used in the streak camera is 10(H) x 9.5(V) mm^2. Since the ratio of the entrance lens of the streak camera is 1/3, an acceptable horizontal width is approximately 30 mm on the entrance slit. If the effective horizontal size of the aerogel without a folder (40 mm) is matched to this size, the aerogel screen size is projected to 30 x 10.5 mm^2 on the entrance slit. If the photons spread on this area uniformly, the density of photon is 1.7 x 10^7 photons / mm^2. This density exceeds the detection limit of the streak camera on the entrance slit, 5,000 photons / mm^2. A streak image of Cherenkov radiation will be obtained using this system.

EVALUATION OF ENERGY RESOLUTION

The Cherenkov radiator is placed at a position 320 mm downstream from the first bending magnet as shown in Figure 3. Since dispersion function η is 0.4 m at the position of the Cherenkov radiator, the energy acceptance of the measurement system and the energy resolution on the radiator are estimated to be 10 % and 0.25 % / mm, respectively. However, the beam image is considered to be broadened due to the thickness of the Aerogel. In order

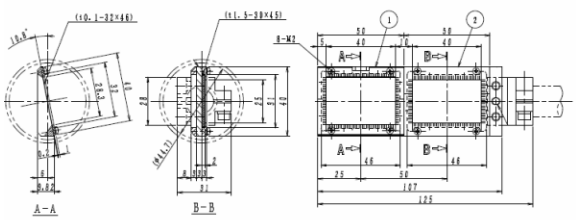

Figure 6: Screen folder mounted with both of a ceramic screen and a Cherenkov radiator. (1) The first screen is a profile monitor with a fluorescence ceramic screen with a thickness of 0.1 mm and it is tilted vertically by an angle of 45° with respect to the bending orbital plane. (2) The second screen is the aerogel radiator and it is tilted of 55.8°.

Figure 7: The drive assembly of the Cherenkov radiator with a two-staged stroke. The first stage is a profile monitor with a fluorescence ceramic screen, and the second stage is the Cherenkov radiator with the aerogel.

to evaluate this broadening, we plan to measure the beam profile with a fluorescence ceramic screen with a thickness of 0.1 mm at the same location. Figures 6 shows a drawing of the screen folder mounted with both of the ceramic screen and the Cherenkov radiator, and Figure 7 shows the photograph of its drive assembly with a two-staged stroke. There is a wire scanner profile monitor at the straight beam line of the L-band linac, and we have already evaluated the broadening of the profile size obtained by the ceramic screen with the wire scanner. Calibrating the broadening of that due to the aerogel with the ceramic screen, the energy resolution will be evaluated precisely.

SUMMARY

In order to measure the longitudinal phase-space profile of the electron beam, we are developing the measurement system consisted of a Cherenkov radiator, a bending magnet and a streak camera. The Cherenkov radiator with an aerogel has been designed, and it is in the process of production.

ACKNOWLEDGEMENTS

The authors express their sincere thanks to Mr. T. Yamamoto for his technical contribution and Mr. S. Suemine for his support of linac operation.

REFERENCES

[1] A. Doria et al., Nucl. Instr. and Meth. in Phys. Res. A 475, (2001) 296.

[2] J. Rönsch et al, “Investigations of the longitudinal beam properties at the photoinjector test facility in Zeuthen”, FEL’06, BESSY, Berlin, Germany, August 2006, p.597, http://www.jacow.org.

[3] H. Loos et al, “Experimental Studies of Temporal Electron Beam Shaping at the DUV-FEL

Accelerator", FEL'05, Stanford, August 2005, p.632, http://www.jacow.org.

[4] S. Zhang et al, "Temporal Characterization of Electron Beam Bunches with a Fast Streak Camera at the JLab FEL Facility", FEL'05, Stanford, August 2005, p.640, http://www.jacow.org.

[5] R. Kato et al, "Longitudinal phase-space measurements of a high-brightness single-bunch beam", FEL'06, BESSY, Berlin, Germany, August 2006, p.676, http://www.jacow.org

[6] R. Kato et al, Nucl. Instr. and Meth. in Phys. Res. A 445 (2000) 164.

[7] R. Kato et al, Nucl. Instr. and Meth. in Phys. Res. A 475 (2001) 334.

[8] R. Kato et al, Nucl. Instr. and Meth. in Phys. Res. A 483 (2002) 46.

DEVELOPMENT OF A PRECISE TIMING SYSTEM FOR THE ISIR L-BAND LINAC AT OSAKA UNIVERSITY

Shigeru Kashiwagi*, Goro Isoyama, Ryukou Kato, Shoji Suemine
ISIR, Osaka University, 8-1 Mihogaoka, Ibaraki, Osaka 567-0047, Japan

Abstract

We are developing a free electron laser (FEL) in the infrared region and also conducting Self-Amplified Spontaneous Emission (SASE) experiment in the same wavelength region using the L-band linear accelerator at the Institute of Scientific and Industrial Research (ISIR), Osaka University. In order to conduct such studies, a stable operation of the linac is critical, so that we have developed a highly precise and flexible timing system for a stable generation of the high intensity electron beam with the energy region of 10-30 MeV. In the timing system, a rubidium atomic clock producing 10 MHz rf signal is used as a time base for a synthesizer which is used as the master oscillator for generating the acceleration frequency of 1.3 GHz. The 1.3 GHz rf signal from the master oscillator is directly counted down to produce the clock signal of the timing system at 27 MHz and the four rf signals for the linac and laser used in the beam experiments. The start signal for the linac is precisely synchronized with the 27 MHz clock signal. To make an arbitrary delayed timing signal, a standard digital delay generator is used to make a gate signal for a GaAs rf switch, which slices out one of the 27 MHz clock pulses to generate the delayed timing signal. Any timing signal can be made at an interval of 37 ns and the timing jitter of the delayed signal is less than 2 ps (rms). We will report the new timing system and its performance in detail.

INTRODUCTION

The L-band electron linear accelerator is used for studies on nanotechnology and beam science as well as for basic studies in the related fields at the Radiation Laboratory of the Institute of Scientific and Industrial Research (ISIR), Osaka University. The L-band linac can produce electron beams of different time structures, like a single-bunch, multi-bunch with 9.1 ns spacing and so on, corresponding to various beam experiments. The high intensity single-bunch beam is the most characteristic beam of this L-band linac and it is very useful for radiation chemistry studies by means of pulse radiolysis

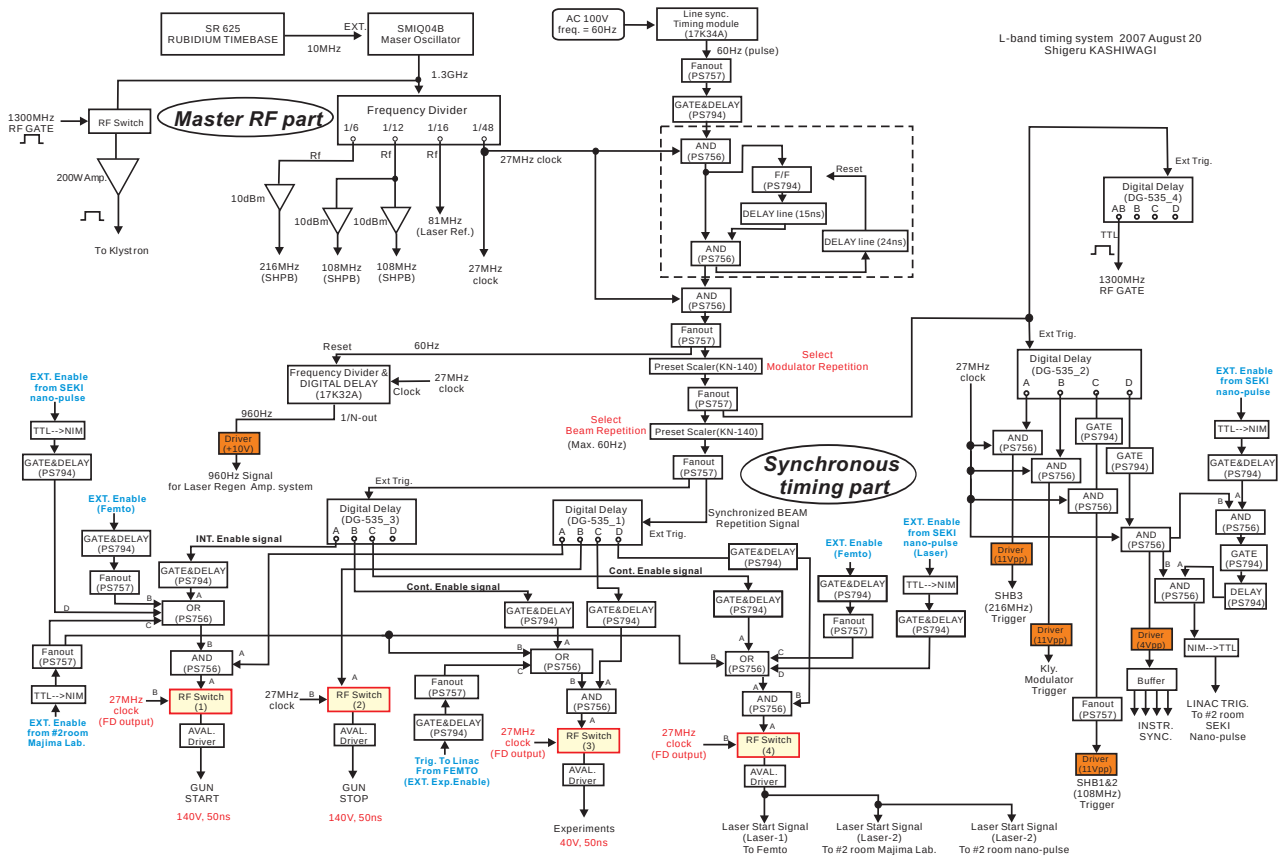

Fig. 1: Block diagram of the new timing system for the L-band linac at ISIR, Osaka University.

*shigeruk@sanken.osaka-u.ac.jp

in the time range down to sub-picoseconds [1,2] and basic study of SASE in the far-infrared region [3,4].

The timing system of the linac plays a very important role in generating a high quality and stable electron beam. The timing jitter between a trigger signal for the electron gun and a reference rf signal of accelerator system directly affects the stability of the electron beam in terms of intensity and energy. Experiments using the L-band linac require synchronized trigger pulse for their data acquisition, and rf signals for laser oscillator. In order to enhance the stability of the linac, we have developed a new highly precise and flexible timing system for the L-band linac at ISIR, Osaka University.

CONFIGURATION OF L-BAND LINAC AND LASER SYSTEM

The fundamental accelerating frequency of the L-band linac at ISIR is 1.3 GHz. The linac has been optimized for generating the high-intensity single-bunch beam. The L-band linac is consisted of a high-current triode electron gun, three stage sub-harmonic bunchers (two operate at 108 MHz, which is a 12th subharmonic of the fundamental frequency and one at 216 MHz, a 6th of 1.3GHz), two fundamental traversing wave bunchers and 3m-long main accelerating structure. The SHB system is used mainly for single-bunch operation. The timing system is required to generate three rf signals for these rf components.

Two grid pulser circuits of the electron gun are used for generating single-bunch and multi-bunch beam. The trigger pulse for the gun grid has to be synchronized with 1.3 GHz rf signals precisely. In single-bunch operation, one trigger pulse for the gun grid with 120V height and 50ns duration is distributed from the timing system at the control room. In multi-bunch operation, two triggers for a start and a stop of pulse are necessary to decide the pulse length of multi-bunch beam in the grid pulser circuit. The trigger pulse for single-bunch and the start trigger of multi-bunch generation are common, and the input trigger pulse for the trigger circuit of the gun is switched by operation mode of the linac.

The laser system for a sub-picosecond pulse radiolysis experiment consists of a CW green laser, a femtosecond Ti:sapphire laser operated at 81 MHz, Nd: YLF laser with a regenerative amplifier operated at 960 Hz, an optical parametric amplifier (OPA) and a pulse generator. Thus, the laser system requires the 81 MHz rf signal and thre960 Hz and 60Hz trigger pulses to the timing system of the linac [1].

Table 1: RF signals and triggers for the L-band linac

RF signal	
1300 MHz	Main accelerating frequency
216 MHz	6th subharmonic buncher
108 MHz	12th subharmonic buncher
81MHz	Laser system (seed resonator)
Clock signal	
27 MHz	Main clock of accelerator
960 MHz	Laser system (Regen Amp)
Trigger pulse	
Electron gun trigger (STARt/ STOP)	
Experimental trigger	
Laser trigger	
Others (kly. modulator, SHB amplifiers)	

NEW SYNCHRONOUS TIMING SYSTEM

To achieve the stable and precise synchronization between RF signals and trigger pulses for the accelerator system, the timing system has been replaced with a new one completely. The new timing system of the linac comprises of a master rf part and a synchronous timing part. It provides four synchronous rf signals and a 27 MHz clock signal as well as various timing signals for operation of the linac and for the experiments. Figure 1 shows a block diagram of new timing system for the L-band linac.

Master RF part

In new timing system, some necessarily harmonic frequencies for the linac operation are produced by dividing a master frequency of 1.3 GHz, because the phase fluctuation of the dividing frequency is much smaller than the multiplied one [5]. The master RF of 1.3 GHz is generated by a frequency synthesizer (Rohde &

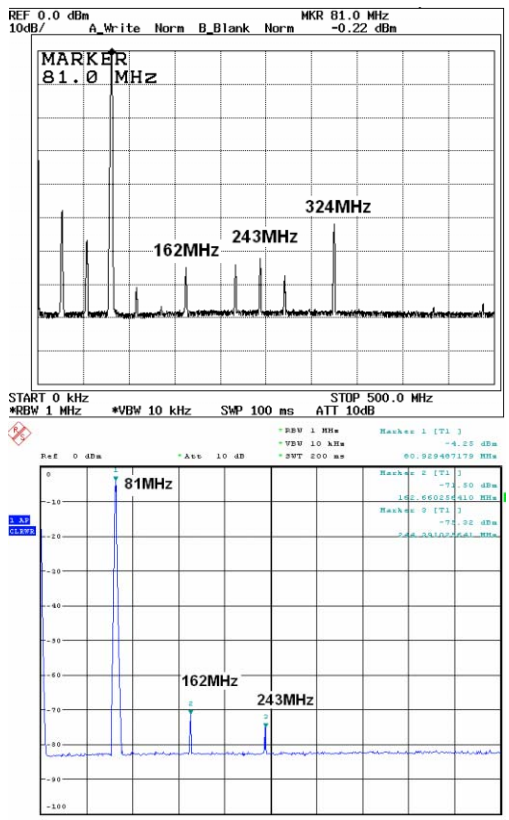

Fig. 2: Frequency spectrum of 81MHz rf signal without band-pass filter (upper) and with crystal narrow-band pass filter (lower).

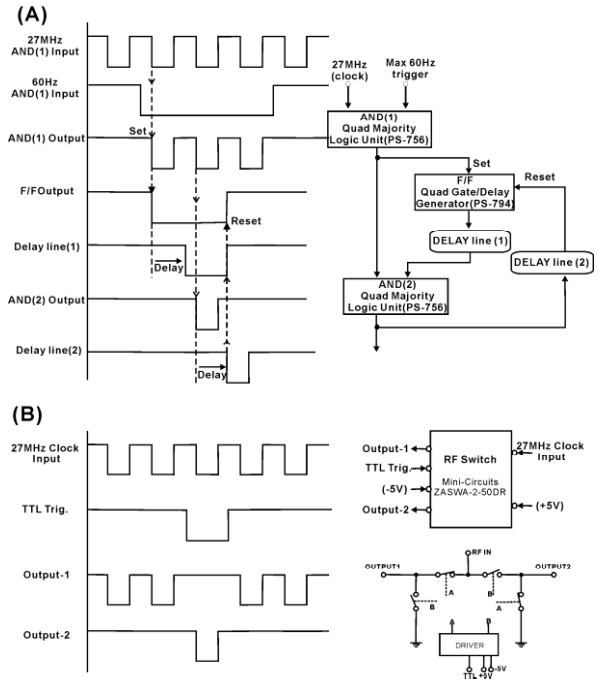

Fig. 3: Timing chart and block diagram of synchronizing system using (A) a logic circuit (Phillips-756) and flip-flop circuit (Phillips-794) and (B) a fast GaAs rf switch.

Schwarz: SMIQ04B) and a rubidium atomic clock producing 10 MHz rf signal is used as an external time base for the frequency synthesizer to realize long term stability. The 1.3 GHz rf signal is directly counted and frequency-divided using a ripple counter circuit to produce rf signals of a 6th and 12th sub-harmonics at 108 MHz and 216 MHz, and a 16th sub-harmonic at 81 MHz together with the NIM-level clock signal of a 48th sub-harmonic signal at 27 MHz. This synchronized 27MHz clock pulses are used as timing step of trigger pulses. The sub-harmonic rf frequencies are amplified to +10dBm level and sent to the SHB main amplifiers and the laser system. The pulse width of 1.3 GHz driving rf pulse for the klystron can be control using a fast rf switch with a synchronized trigger pulse. The width is typically 15 μs in linac operation.

Band-pass filters are introduced at the frequency divider output to suppress the unnecessary higher and lower harmonic frequencies. Figure 2 shows the frequency spectrum of 81 MHz rf signal, which is used as a reference signal for the Ti:Sapphire laser system, without a band-pass filter (upper figure) and with a narrow-band crystal filter (lower figure) at the output of the frequency divider. The generated rf signals are distributed to the laser system or an rf components.

Synchronous timing part

The synchronous timing part was fabricated using commercially available components and devices, such as standard NIM logic modules and digital delay generators, so that it is flexible for future expansion and development. The linac must be operated synchronously with the AC line frequency, which is 60 Hz in the western half of Japan, and the maximum repetition rate of the linac operation is also 60 Hz. In the synchronous timing part, the start signal is produced from the AC line voltage synchronized with the 27 MHz clock signal. Fig. 3(A) shows the timing chart and block diagram of synchronizing system using standard NIM modules and delay lines. The repetition rates of rf pulses and the beam are determined with two preset counter modules, respectively as shown in Fig. 1. The 960 Hz clock for the laser system is generated using synchronous universal counter, which counts the 27 MHz clock pulse and divides the clock frequency by 28212 [6].

To make an arbitrary delayed timing signal, the start signal is sent to standard digital delay generator (Stanford Research Systems: DG535) as the external trigger and it produces preset delayed signals. One of their delayed signals is used for producing a gate signal to slice out one of the 27 MHz clock pulses. Since the gun (start and stop), the experimental and the laser triggers, have to be synchronized with the reference rf signal precisely, we therefore use a fast GaAs RF switch (Mini-Circuits: ZASWA-2-50-DR) to slice out the timing pulses from the 27MHz clock as shown in Fig. 3 (B). The fast RF switch is a passive device, thus the time jitter of the sliced out timing pulse is determined by stability of the 27MHz clock. This is expected the timing jitter to be smaller than a few ps. Any timing signal can be generated at an integer multiple of 37 ns, which is a period of 27 MHz clock. The timing jitter of the delayed pulse does not depend on the delay time by using this delay method. To make other trigger pulses, such as the klystron modulator trigger, the delayed signals are made to be coincident with the 27 MHz clock using a logic module (Phillips-756). The time jitter of the logic module is expected to be about 5 ps.

Avalanche pulser

The avalanche pulser circuit is used to make high voltage pulse with less than a nanosecond rise time at the output part of the timing system. The timing jitter of the arbitrary delayed timing signal for triggering each component is mainly determined by a time jitter of the avalanche pulser. The required avalanche pulser outputs are 140 V for the Gun-start and stop triggers and the 50 V for the Experimental and Laser triggers, respectively. The synchronized timing pulse, which is sliced out by the fast GaAs rf switch, is applied to the avalanche pulser circuit as a trigger. The time jitter of avalanche pulser is strongly dependent on the leading-edge and the voltage of the drive pulse for the avalanche transistor. To get good leading-edge of the drive pulse, a transistor is used as a pre-amplifier with gain 5 (the output voltage: ~3V) and an emitter follower circuit is used for the last pre-amplifying stage of the circuit to provide low output impedance. In this circuit, two transistors are used to provide the drive pulse with good leading-edge for avalanche transistor. The timing jitter of this circuit was smaller than that of

the circuit, which uses only one transistor in emitter ground circuit.

TIMING JITTER MEASUREMENT AND RESULT

The timing jitter measurement have been performed for the produced subharmonic RF signals and the synchronous trigger pulses relative to the master reference RF of 1.3 GHz using the Tektronix Communication Analyzer (Tektronix CSA8000B with 80E03 sampling module). In the measurement, the subharmonic RF signals or the timing pulses are used as a trigger of the oscilloscope. Absolute timing jitters of subharmonic frequencies relative to the 1.3 GHz master reference RF are approximately 1.3-2.0 ps (rms) with bandpass filter and the jitter of 27 MHz clock was 0.96 ps (rms). The timing jitter of the arbitrary delay timing signals sliced out by the fast RF switch from the 27 MHz clock pulses were also measured, and they are approximately 1.1-1.6 ps (rms).

A rise-time (10-90%) of amplified trigger pulse was measured using the sampling module with 20 GHz frequency bandwidth. The measured leading-edge of the 50V trigger pulse with -46 dB attenuator is shown in Fig. 4 (upper) and the rise-time of the 140 and 50 V trigger pulses were 1.86 ns and 0.44 ns, respectively. Absolute timing jitter (rms) of the 140 and 50 V trigger pulses relative to the master RF were 2.7 ps (pk-pk = 16.4 ps) and 1.5 ps (pk-pk = 10.0 ps) in 1 hour measurement, respectively.

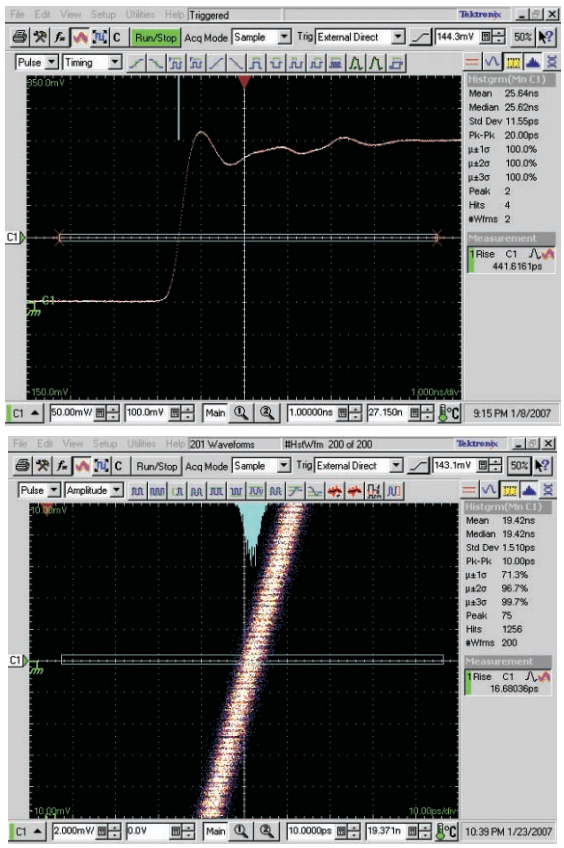

Fig. 4: Measured leading-edge and timing jitter of 50 V trigger pulse. The rise time of one was 0.44 ns and the timing jitter was 1.51 ps (rms) and 10.0 ps (pk-pk) in 1 hour measurement.

SUMMARY

The new highly precise and flexible timing system has been developed for the L-band linac and now it is used in real beam operation. Performance of new timing system exceedingly improved than a former one. In the timing jitter measurement, the jitter of the 50 V trigger pulse relative to the master reference RF was 1.5 ps using new synchronizing technique with the fast GaAs rf switch, before installation of new timing system it was about 7 ps. About other signals such as the subharmonic rf signals, their performances were also improved than before. In the present new timing system, the absolute timing jitter of the arbitrary delayed trigger pulse is mainly determined the stability of the 27 MHz clock pulse. To improve the precision of the 27MHz clock, we are planning to use the limiting amplifier for the 27 MHz clock generation.

ACKNOWLEDGEMENTS

The authors would like to thank Drs. Takao Asaka, Yoshitaka Kawashima and Hirofumi Hanaki of SPring-8 for their help on the fabrication and measurement of the new timing system of the ISIR L-band linac.

REFERENCES

[1] A. Saeki, T. Kozawa, S. Kashiwagi, K. Okamoto, G. Isoyama, Y. Yoshida and S. Tagawa, Nucl. Instr. and Meth. A 546 (2005) 627.

[2] T. Kozawa, Y. Mizutani, K. Yokoyama, S. Okuda, S. Tagawa, Nucl. Instr. and Meth. A 429 (1999) 471.

[3] R. Kato, M. Fujimoto, T. Igo, S. Isaka, T. Onishi, S. Furukawa, S. Okuda, S. Suemine, G. Isoyama, Nucl. Instr. and Meth. A 507 (2003) 409.

[4] R. Kato, R. A. V. Kumar, T. Okita, S. Kondo, T. Igo, T. Konishi, S. Okuda, S. Suemine, G. Isoyama, Nucl. Instr. and Meth. A 445 (2000) 164.

[5] M. Sawamura, E. J. Minehara, R. Nagai, M. Sugimoto, M. Takao, R. Kato, N. Kikuzawa, M. Ohkubo, Nucl. Instr. and Meth. A 358 (1995) ABS 73-74.

[6] H. Suzuki, H. Ego, M. Hara, T. Hori, Y. Kawashima, Y. Ohashi, T. Ohshima, N. Tani, H. Yonehara, Nucl. Instr. and Meth. A 431 (1999) 249.

DEVLOPMENT OF A LOW EMITTANCE DC GUN FOR SMITH-PURCELL BWO FEL

K. Kasamsook#, K. Akiyama ,K. Nanbu, M. Kawai , F. Hinode, T. Muto , T. Tanaka, M. Yasuda, Y. Mori, H. Hama, Laboratory of Nuclear Science, Tohoku University, 1-2-1 Mikamine, Taihaku-ku, Sendai 982-0826, Japan

Abstract

An electron DC gun capable for producing very low emittance beam is now under evaluation of beam qualities at Laboratory of Nuclear Science, Tohoku University. The DC gun employs a high voltage of 50 kV to extract electrons, which is suitable to drive Smith-Purcell backward wave oscillator free electron laser (BWO FEL) [1]. From a result of numerical simulation using a 3-D finite deference time domain (FDTD) method [2], the BWO FEL oscillation at the terahertz wavelength region maybe achieved by using the electron beam with an emittance lower than 1 π mm mrad. Average power is expected to be more than 100 W/mm^2.

In addition to which a very small cathode of LaB_6 single crystal is employed for the gun [3], the geometrical structure is optimized to produce the lower emittance beam. A numerical calculation of the electro-static model for the DC gun to solve equilibrated beam envelope predicts a normalized beam emittance of 0.3 π mm mrad will be possible for the beam current of a couple of hundreds mA. Particularly by applying additional bias voltage between the cathode and the wehnelt, the transverse distribution of electrons is possibly becoming to be an ideal Kapchinskij-Vladimirskij (K-V) beam [4], so that the space charge effect will be minimized.

INTRODUCTION

Smith-Purcell BWO FEL

In order to understand the characteristics of the BWO FEL and the interaction between the DC beam and the evanescent waves supported by a grating, an FDTD simulation has been performed. Nonlinear behavior of the Smith-Purcell radiation was already observed [5]. That was coherent and has been presumed to result from the beam microbunching effect due to interaction with the evanescent modes.

We have chosen a model grating for the simulation as indicated in Fig. 1. The period length λ_g = 400 μm, the groove width W = 200 μm, the groove depth d = 300 μm and the grating full width L = 2 mm, the number of period of 50 are employed, respectively. The sheet DC beam, which has the emittance of 1 π mm mrad for the both directions, is generated by very low horizontal and vertical beta functions of 6.25 cm and 0.4 mm, respectively. Since the evanescent wave is exponentially decreasing as the distance from the grating surface increases, the sheet beam has to travel just above the surface in order to have sufficient overlapping with the evanescent wave (here we have chosen 100 μm).

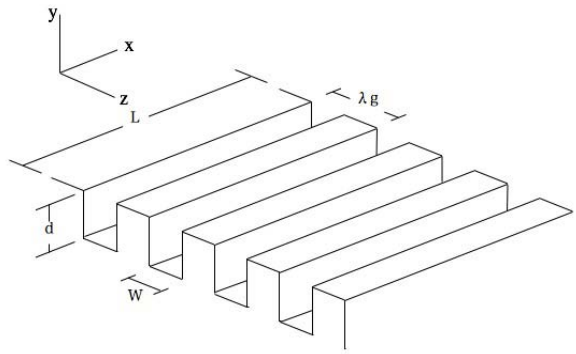

Figure 1: A model grating for FDTD simulations.

The Smith-Purcell BWO FEL is not driven by ponderamotive potential as conventional FELs with wigglers. The microbunching is occurred by the longitudinal electric field (E_z) in the evanescent wave, and the conventional Smith-Purcell radiation becomes coherent. The evanescent mode is much more excited by the bunched beam, so that the gain is yielded.

The FDTD simulation was performed with a DC beam current of 150 mA. To avoid beam brow-up the strong external longitudinal field (B_z ~ 1 T) applied. From the dispersion relation of the evanescent wave [6], the group velocity at the beam frequency negative, so that this is the backward-wave. Time dependent evolutions of radiated power observed at the grating upstream end are shown for two different emittance cases in Fig. 2.

We notice that for the normalized emittance of 1 π mm mrad case, the power increased up to several hundreds W/mm^2 and a damping oscillation was excuted after saturation. Meanwhile a larger normalized emittance case, such as 5 π mm mrad shown in Fig. 2(b), the FEL oscillation was not occurred. The results show the beam emittance is very crucial for the Smith-Purcell BWO FEL.

The frequency spectrum obtained Fourier transform of the power evolution of Fig. 2(a) is shown in Fig. 3. In this grating case, an intense sub-Terahertz radiation may be obtained.

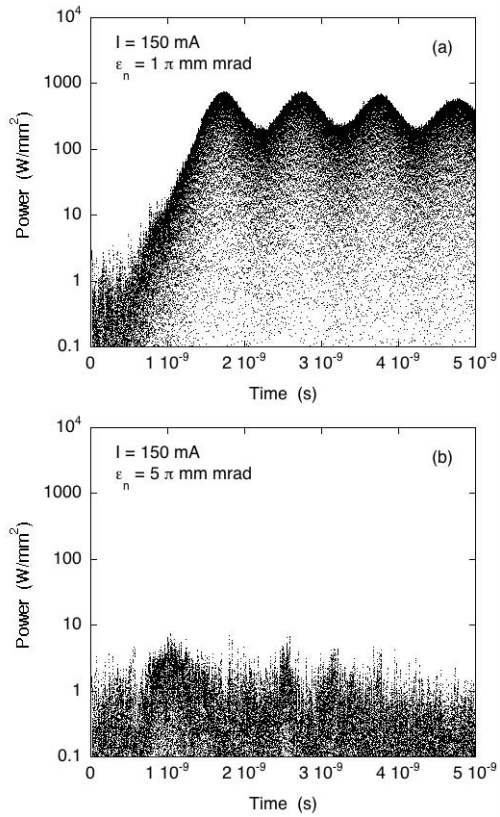

Figure 2: Simulation results of the FDTD Smith-Purcell BWO FEL. (a)The normalized beam emittances are 1 π mm mrad, and (b) 5 π mm mrad, respectively.

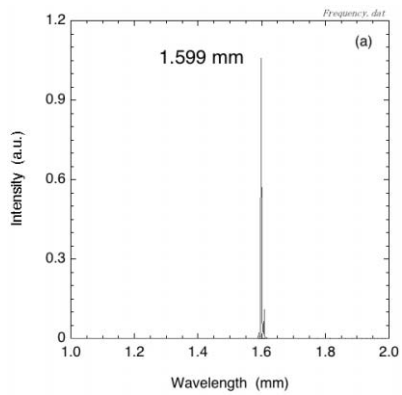

Figure 3: Frequency spectrum of simulated Smith-Purcell BWO FEL (corresponds to Fig. 2(a)).

Low emittance DC gun

The DC gun has been designed with a wehnelt electrode to manipulate electric field arround the cathode. The feasibility study of the gun for the Smith-Purcell BWO FEL has been investigated by the simulation. From the simulation results, we have presumed that the emittance is very sensitive to the equi-potential surface around the cathode. Consequently we found that the equi-potential surface can be manipulated by applying the negative bias between the cathode and the wehnelt electrode. In the simulation, an extremely low emittance less than 1 π mm mrad is achieved [7].

The schematic diagram of DC gun power supply is shown in Fig. 4. The fabrication of the DC gun had been finished and we succeeded to extract the electron beam over 300 mA exceeding our target value [8]. The main design parameters are shown in Table 1. This low emittance DC gun has been studied both experimentally and theoretically. The paper will present the status of the development of the low emittance DC gun.

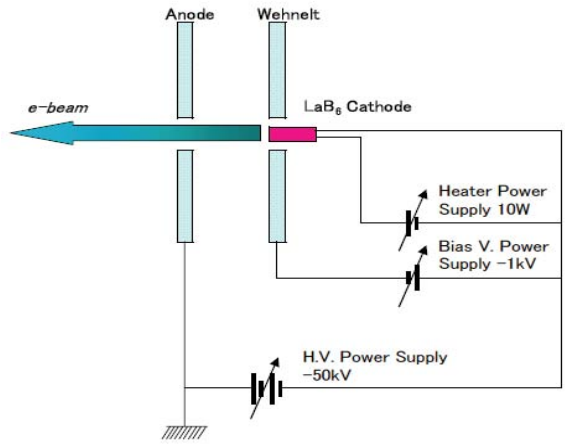

Figure 4: The schematic diagram of DC gun power supply.

Table 1: Design parameters of electron gun.

Beam energy	50 keV (Max.)
Peak current	>300 mA
Pulse width (FWHM)	1-5 μsec
Repetition rate	50 pps
Normalized emittance	< 1 π mm mrad.
Normalized thermal emittance	0.25 π mm mrad* *theoretical
Cathode diameter	1.75 mm.

DC GUN DEVELOPMENT

Beam quality measurements

An experimental set-up for beam size measurements is depicted in Fig. 5. The beam size was measured at downstream of the DC gun by applying the focusing power of the solenoid lens. The main components in this section are solenoid lens, current transformer (CT), the slit and a Faraday plate. The overall beam current was measured by the CT located at the downstream of the solenoid lens. Meanwhile the beam current passing through the slit was measured by the Faraday plate.

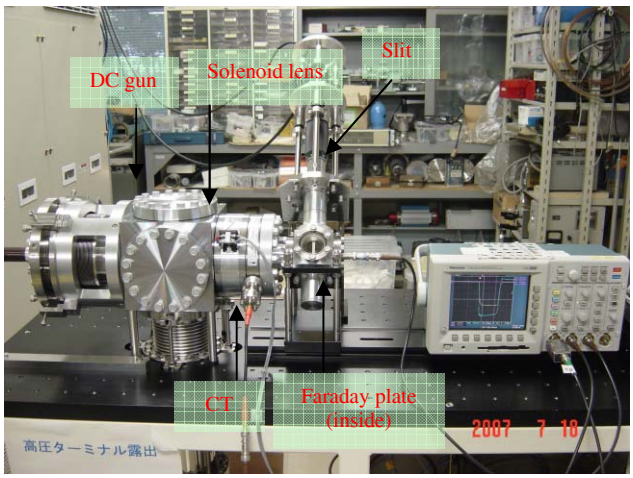

Figure 5: The DC gun configuration for beam size measurement

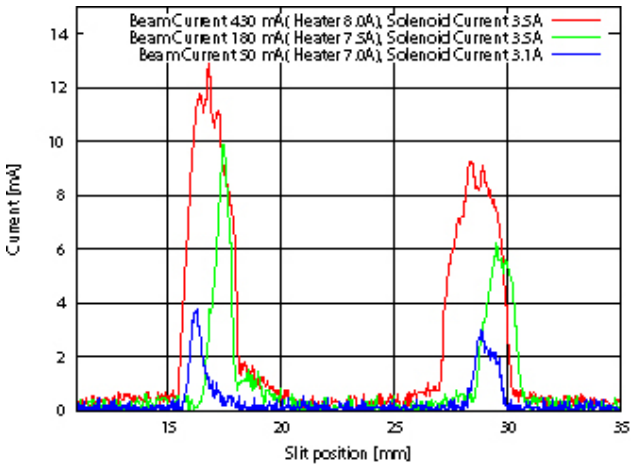

Figure 6: Measured minimum beam size profile at various beam currents.

A slit plate used for the beam size measurement is made of SUS 316L and its thickness is a 50 μm. Two perpendicular slits for X and Y direction with width of 50 ± 2 μm were manufactured by wire cut method, and its width was measured by a high precision microscope. The moving direction of the slit stage is 45-degree between X and Y axes, because only one move can make two axes scans.

The slit plate was mounted on an insertable and rotatable actuator powered by 5-phase stepping motor (Oriental Motor PK545AW-P7.2). This allowed us to align the slits to the beam and insure the proper angle with respect to the beam. Combining the ball bearing spindle (1 mm pitch for one revolution) and the precise stepping motor, the maximum resolution of step is 1/3600 mm. The scanning speed is around 15 second for one beam profile.

The measurement are made as follow; (1)set the slit movable stage to the initial position at first, then using a Faraday plate get the signal of the beam passing through the slit, (2)go to the next stage position, then repeat again until the end position coming. Signals from the CT and the Faraday plate are connected to digital oscilloscope and analyzed by software.

All measurements were performed at various beam currents of 50, 180 and 430 mA that are corresponding to heater current of 7, 7.5 and 8.0 A, respectively. Taking look at the V-I characteristic curve of our DC gun [8], we have chosen 8 A of heater current for an ordinal operating condition. The minimum rms beam size less than 2 mm in both X and Y directions was obtained at the operating condition. The measured beam profiles are shown in Fig. 6. One can notice the shift of a beam position in each case. Possible reasons are alignment errors of the cathode and the solenoid lens. The beam size becomes bigger when the beam current increases and a stronger focusing strength of the solenoid lens is required to confine the beam. It seems the space charge effects play a significant role for the beam size at the higher beam current.

Transverse beam emittance

In the following analysis, we assume an axis-symmetric electron beam confined by a longitudinal magnetic field of solenoid lens. This method is used to deduce a tentative beam emittance of our DC gun. So the measurement can be understood by examining the evolution of the rms beam size in a drift length following a thin lens of focal length *f*. The beam is transported through a solenoid. In this case, the beam matrix transforms at the slit position given by

$$\sigma^1 = R\sigma^0 R^T, \tag{1}$$

where R is the transfer matrix in drift space (L) and solenoid lens (the magnetic strength, Q) represented by

$$R = \begin{pmatrix} 1 & L \\ 0 & 1 \end{pmatrix}\begin{pmatrix} 1 & 0 \\ -Q & 1 \end{pmatrix} = \begin{pmatrix} 1-QL & L \\ -Q & 1 \end{pmatrix}. \tag{2}$$

In this linear analysis, we have explicitly ignored space-charge effect. By applying initial conditions to eq. (1), we can solve the equation for the square of the rms beam size in the term of focal length of the solenoid lens as

$$\sigma_{11}^1 = < x_1^2 > = L^2\sigma_{11}^0 . Q^2 - 2[L\sigma_{11}^0 + L^2\sigma_{12}^0] . Q + L^2\sigma_{22}^0 + 2L\sigma_{12}^0 + \sigma_{11}^0. \tag{3}$$

In this form, we can see that the square of the rms beam size at the end of the drift should depend on the square of the magnetic strength of the solenoid lens. The scan is done by varying the strength of the solenoid lens and measure the beam size at the fixed distance from the lens. In the eq. (3) we can simplify the form as

$$\sigma_{11}^1 = < x_1^2 > = aQ^2 + bQ + c = a\left(Q + \frac{b}{2a}\right)^2 + \frac{4ac - b^2}{4a} \tag{4}$$
$$= a'(Q + b')^2 + c'.$$

The normalized rms emittance is calculated by an equation

$$\varepsilon_{n,rms} = \beta\gamma\sqrt{<x_0^2>.<x'^2_0>-(<x_0.x'_0>)^2} = \frac{\beta\gamma}{2L^2}\sqrt{4a'c'}, \qquad (5)$$

where β is the beam velocity divided by light velocity, γ is the relativistic mass factor, and a', b', c' are coefficients of quadratic function deduced from curve fitting. For solving this problem numerically, an internal MATLAB solver is used [9]. The MATLAB consists of a constrained non-linear least-square fit algorithm based on the Levenberg-Marquardt method. The robustness of the algorithm needs to be assured. Particularly, this algorithm should work for noisy data, such as experimental data.

For the data at the beam current of 430 mA, the emittance is then calculated by fitting the data using the quadratic beam transport equation. The results of fitting are shown in Fig. 7 and Fig. 8. The normalized rms emittances, 2.46 and 2.66 π mm mrad are obtained for the horizontal and the vertical axes, respectively

We calculated the propagation of error by eq. (6). The deduced errors are ± 0.89 and ± 1.05 π mm mrad for the horizontal and vertical normalized rms emittances, respectively.

$$\Delta\varepsilon_{n,rms} = \frac{\beta\gamma}{2L^2}\cdot\sqrt{\left(\frac{c'}{a'}\right)\Delta a'^2+\left(\frac{a'}{c'}\right)\Delta c'^2}. \qquad (6)$$

The same analysis was performed on data taken at 50 and 180 mA of beam currents, respectively. The fits to the data give the normalized rms emittance of 1.14 ± 1.17π mm mrad (horizontal emittance) and 0.82 ± 0.72 π mm mrad (vertical emittance) for 50 mA. For the beam current of 180 mA, the results are 1.84 ± 1.87 and 1.72 ± 1.36 π mm mrad for the horizontal and the vertical normalized rms emittance, respectively. Though these errors seem to be high compared with expected values of normalized rms emittance, anyhow, it seems the current dependence of the emittance exists.

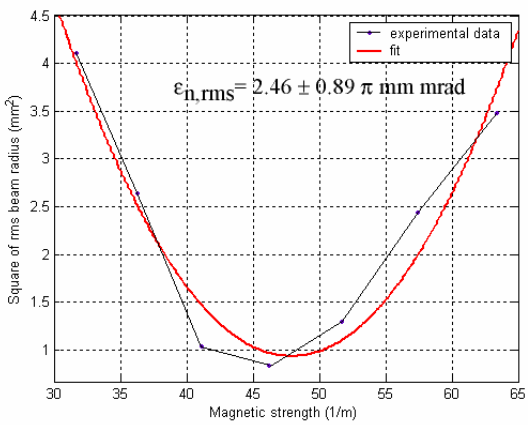

Figure 7: Square of beam radius in the horizontal axis plotted as a function of magnetic strength of solenoid lens.

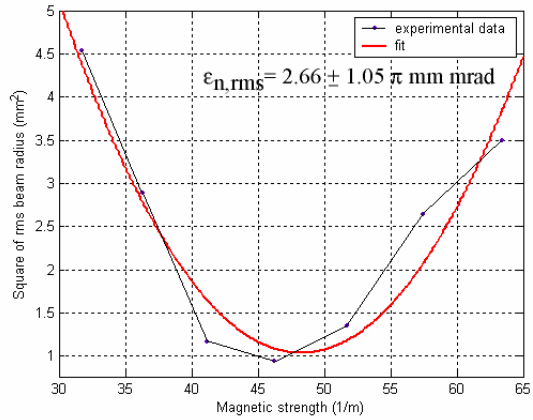

Figure 8: Square of beam radius in the vertical axis plotted as a function of magnetic strength of solenoid lens.

In this linear analysis, we ignore the space charge effects and approximate the effect of solenoid lens by thin lens as well. A rigorous error analysis was not performed in the analysis of the data. We have estimated only the errors result from the uncertainty of the quadratic fit. For this reason, it is highly desired to use the high precision technique instead of the solenoid scanning method to confirm the emittance value.

SUMMARY

We have developed a very low emittance DC gun employing a single crystal of LaB_6 cathode. Preliminary value of the measured normalized emittance was around 2 π mm mrad. Further investigation including manipulation of the equi-potential surface around the cathode by applying the additional bias voltage will be performed.

REFERENCES

[1] V. Kumar and K-J. Kim, Phys. Rev E 73 (2006) 026501.
[2] H. Hama, et al., to be published.
[3] H. Kobayashi et al., Proc. 1992 Linear Accelerator Conf., Ottawa, Canada, August 1992.
[4] I.M. Kapchinsij and V.V. Vladimirskil, Proc. Int. Conf. on High Energy Accelerators p. 274 (CERN, GENEVA, 1959).
[5] J. Urata, M. Goldstein, M.F. Kimmitt, A. Naumov, C. Platt and J. Walsh, Phys. Rev. Lett. 80 (1998) 516
[6] H. L. Andrews et al., Phys. Rev ST Accel. Beam 8, (2005) 050703.
[7] K. Kasamsook et al., Proc. FEL2006, Berlin, Germany (2006) 680.
[8] K. Kasamsook et al., will be appeared in Proc of APAC2007 , Indore, India (2007).
[9] MATLAB, User's Manual, http://www.mathworks.com/access/helpdesk/help/toolbox/curvefit/curvefit.shtml

ZZELECTRON- LINAC BASED FEMTOSECOND THZZZZZ ZRADIATION SOURCE AT PAL*

H. S. Kang†, C. M. Lim, W. W. Lee, B. R. Park, H. G. Kim, S. C. Kim, Y. G. Jung,
M. S. Lee, Y. J. Park, J. Choi, and I. S. Ko
Pohang Accelerator Laboratory, POSTECH, Pohang 790-784, KOREA

Abstract

A 60-MeV electron linac for intense femto-second THz radiation source is under construction at PAL, which is the beamline construction project to be completed by 2008. To get intense femto-second THz radiation up to 3 THz, the electron beam should be compressed down to below 100 fs. The linac will use an S-band photocathode RF-gun as an electron beam source, two S-band accelerating structures to accelerate the beam to 60 MeV, a chicane-type bunch compressor to get femto-second electron bunch, and an optical transition radiation (OTR) target as a radiator. The PARMELA code simulation result shows that the 0.2 nC beam can be compressed down to a few tens of femto-seconds, and the higher charge of 0.5nC to about one hundred femto-seconds. Also, the linac will be able to provide femto-second electron beam for electron pulse radiolysis and compton-scattering experiment for femto-second X-ray.

INTRODUCTION

THz radiation source which can provide rich science and unexplored technology is becoming popular. And, sub pico-second radiation at that wavelength can provide an unprecedented probe for ultra fast dynamics like electronic excitations and magnetic excitations [1]. Pohang Accelerator Laboratory (PAL) is constructing a 60-MeV electron linac for intense femto-second THz radiation source, which is the beamline construction project to be completed by 2008. The radiation wavenumber to provide is 10-100 cm^{-1} (0.3 - 3 THz) and the radiation pulse duration should be shorter than 200 fs.

DESIGN

To achieve this goal, we will make use of relativistic electron beam with the bunch length of shorter than a few hundred femto-seconds. Relativistic particles emit incoherent radiation at all wavelengths, and additional enhanced coherent radiation at wavelengths of the order of the bunch length and longer. The total radiated spectral power from a mono-energetic bunch of N_e electrons at wavelength λ is

$$P(\lambda) = p(\lambda)N_e[1 + (N_e - 1)f(\lambda)], \qquad (1)$$

where $p(\lambda)$ is the spectral radiation power from a single electron and $f(\lambda)$ is a form factor for an azimuthal symmetric bunch, which is the Fourier transform of the actual particle distribution. The first term in the square brackets is the incoherent part of the radiation while the second term corresponds to the coherent radiation which is N_e times the incoherent part assuming $f(\lambda) \approx 1$. The form factor is defined as

$$f(\lambda) = |\int S(x)exp\{i(2\pi x/\lambda)\}dx|^2. \qquad (2)$$

where $S(x)$ is the normalized longitudinal density distribution of electrons in a bunch.

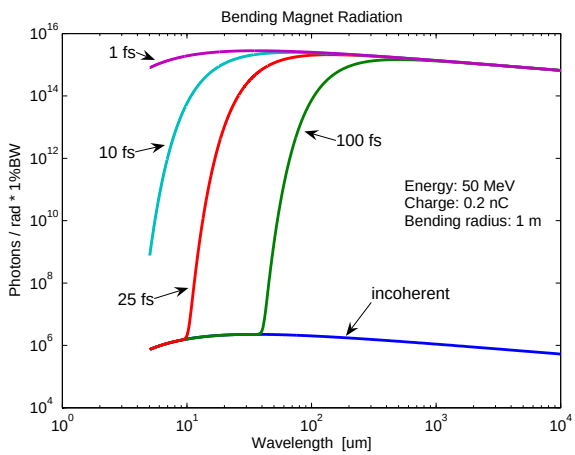

Figure 1: Coherent enhancement of synchrotron radiation from a bending magnet at different bunch lengths in rms.

Figure 1 shows the coherent enhancement of synchrotron radiation from a bending magnet at different bunch lengths in rms. The parameters used for the calculation are an electron beam energy of 50 MeV, a bending radius for synchrotron radiation of 1 m, and the electron bunch charge of 0.2 nC. The photon flux of coherent radiation is much higher than that of the incoherent part, simply N_e times.

From Figure 1, one can find how small the bunch length should be to get coherent THz radiation. Coherent enhancement of radiation is determined by the bunch form factor in Eq. (2). The required bunch length is as short as one tenth of the period of radiation to get the bunch form factor close to 1. For example, to get 10 THz radiation (period = 100 fs), the bunch length should be smaller than 10 fs, which is obviously impossible to get with 0.2 nC charge beam. So, the target bunch length to achieve in this project is about 50 fs with 0.2 nC beam, which can generate coherent THz radiation below 3 THz.

Figure 2 depicts the layout of the electron linac. The linac will use an S-band photocathode RF-gun as an elec-

* Work supported by Korean Ministry of Science and Technology
† hskang@postech.ac.kr

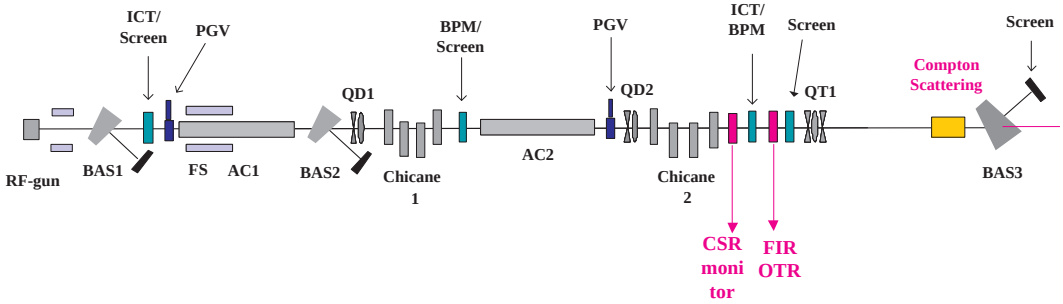

Figure 2: Layout of FIR Linac. (QD: quadrupole doublet, ICT: integrated current transformer, FS: focusing solenoid, AC: accelerating column, QT: quadrupole triplet, OTR: optical transition radiation, BAS: beam energy analyzer, and YAG: YAG screen).

Table 1: Parameters of the Linac

Parameters	Value
Beam energy	60 MeV
Beam Charge	0.2 - 0.5 nC
Beam Emittance	5 mm-mrad
Beam Pulse Repetition rate	60 Hz max.

Table 2: Relation of bunch charge and bunch length

Beam charge	Bunch length after RF-Gun	Bunch length after chicane
0.2 nC	0.5 ps	50 fs
0.5 nC	2 ps	150 fs

tron beam source, two S-band accelerating structures (AC1 and AC2) to accelerate the beam to 60 MeV, a chicane-type bunch compressor to get femto-second electron bunch, and an optical transition radiation (OTR) target as a radiator.

Parameters of the Linac are listed in Table 1. The beam energy is 60 MeV and the beam charge is 0.2 to 0.5 nC. The relation of bunch charge and bunch length is shown in Table 2. The bunch length is designed to be 50 fs with 0.2 nC beam and 150 fs with 0.5 nC. To get short bunch length after bunch compression, the bunch length at the gun is 0.5 ps with 0.2 nC beam, which is the reason why the emittance is relatively high, 5 mm-mrad.

As a wide-band radiation source, optical transition radiation was chosen rather than bending magnet radiation which is difficult to get a good pointing stability of radiation. On the other hand the undulator radiation which is narrow-band is not going to be used at the beginning, but the space is reserved, because the temporal length of the radiation exceeds 1 ps due to the wiggling motion of electron beam in undulator.

Optical transition radiation is generated when an electron crosses the boundary between two different media. Coherent transition radiation energy obtained from N_e electrons is [2]

Table 3: OTR energy vs. bunch charge

Bunch charge [nC]	Radiation energy [μJ]
0.2	3.5
0.5	22
1	88

$$\frac{dW_N}{d\omega} = {N_e}^2 \frac{dW_1}{d\omega} |f(\omega)|^2 \qquad (3)$$

where $\frac{dW_1}{d\omega}$ is the radiation energy generated by single electron, and $f(\omega)$ is the form factor defined in Eq. (2). Table 3 shows the optical transition energy as a function of bunch charge assuming the bunch form factor of 1. A dramatic increase of radiation energy is expected with 1 nC while the radiation bandwidth must be limited because a few tens of femto-second bunch is impossible to get with 1 nC, even with 0.5 nC. So, there should be a compromise between the achievable radiation bandwidth and the radiation energy.

SIMULATION RESULT

The beam dynamics design was carried out by using the PARMELA code. It was designed to be that the beam with 0.2 nC charge can be compressed down to about 30 fs in rms at the position of OTR target by Chicane-2. Figure 3 shows the bunch profile before and after Chicane-2. The rms bunch length is 920 fs before the chicane and 29 fs after the chicane. The parameters of Chicane-2 used in the simulation are: the beam energy is 55 MeV, the bending angle is 10 degrees, and R_{56} is -2.07 cm.

Beam dynamics design was also done for higher charge of 0.5nC. As a result, the bunch length is expected to be about one hundred femto-seconds.

Figure 4 shows the longitudinal bunch profile of electron beam after the 0.2 nC beam is compressed in Chicane-2, which is calculated by using the PARMELA code data. Making use of the longitudinal bunch profile, we can calculate the bunch form factor of the given distribution. Figure 5 depicts the bunch form factor at different bunch charges,

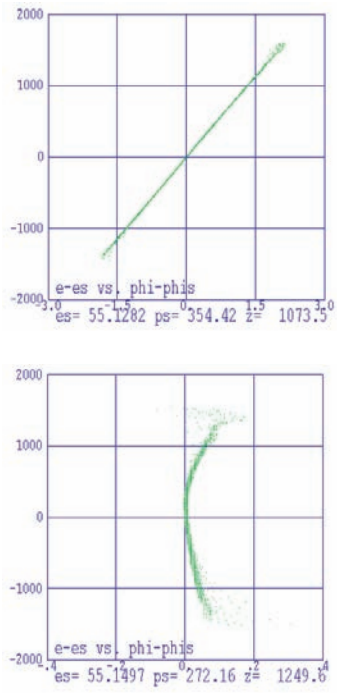

Figure 3: PARMELA simulation result: bunch shape before (a) and after (b) Chicane-2. *es* represents the synchronous particle energy, *phis* the synchronous particle phase. The vertical axis is *e - es* in MeV and the horizontal axis is *phi - phis* in degrees. One degree corresponds to about 1 ps.

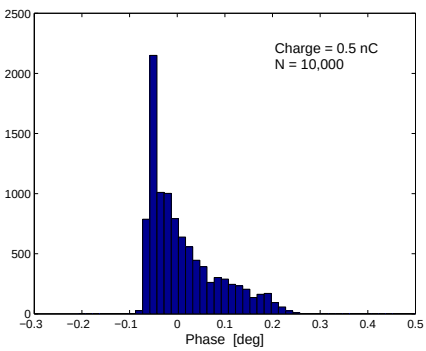

Figure 4: Longitudinal bunch profile of electron beam after the 0.5 nC beam is compressed in Chicane 2

0.2 nC and 0.5 nC, as a function of radiation wavelength. The bunch form factor at 100 μm reaches 0.7 with 0.2 nC beam while it is at most 0.2 with 0.5 nC beam.

In the PARMELA code simulation, the effect of CSR (Coherent Synchrotron Radiation) in the chicane was not included. CSR in the chicane deteriorates the electron beam energy distribution, which causes an increase of emittance and bunch length. The effect of CSR will be checked with other simulation code like ELEGANT.

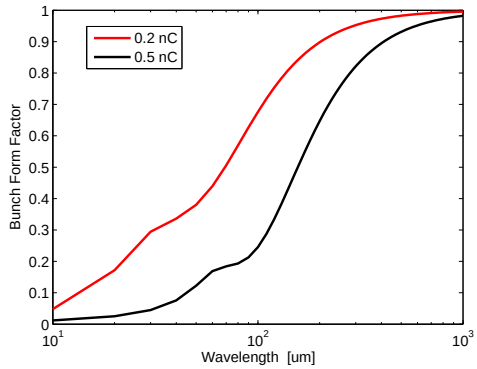

Figure 5: Bunch form factor at different bunch charges, 0.2 nC and 0.5 nC.

Figure 6: Photo of the linac tunnel.

CONSTRUCTION STATUS AND SUMMARY

The construction of the linac is on the way as shown in Fig. 6. The installation will be completed at the end of 2007 and the beam acceleration test will start at the beginning of 2008.

The 60-MeV electron linac was designed to generate intense femto-second THz radiation with the radiation wavenumber of 10-100 cm^{-1} (0.3 - 3 THz) and the radiation pulse duration of shorter than 200 fs. The linac will be able to be used for other applications such as electron pulse radiolysis, X-ray generation by Compton scattering, and SASE-FEL experiments, etc. A space after the chicane 2 is reserved for Compton-Back-Scattering experiment and FEL experiments as shown in Fig. 2.

REFERENCES

[1] DOE-NSF-NIH Workshop on Opportunities in THz Science, February 12-14, (2004).

[2] L. Wartski, et al., Journal of Applied Physics, **46**, 8, 3644 (1975).

STABILIZATION OF A KLYSTRON VOLTAGE AT 100 PPM LEVEL FOR PAL XFEL

J. S. Oh#, J. H. Suh, Y. G. Son, S. D. Jang, S. J. Kwon, PAL/POSTECH, Pohang 790-784, Korea
E. H. Song, Changwon National University, Changwon 641-773, Korea

Abstract

The PAL XFEL needs a stable electron beam. The stable charging of PFN (pulse forming network) of a klystron-modulator is essential to provide the stable acceleration field for an electron beam. For PAL XFEL, stabilization of klystron voltage pulses at 100-PPM level is required. Short-term stability is determined by a minimum resolution of a charging system. Long-term stability is determined by a thermal stability due to the temperature drift. This paper shows details of hardware R&D and test results to achieve the target stability.

INTRODUCTION

PAL XFEL is proposed as a 4th generation light source that is a coherent X-ray free electron laser by utilizing an existing 2.5-GeV linac [1]. Reasonably stable SASE output requests the RF stability of 0.02% rms for both RF phase and amplitude [2]. This is one of technologically challenging issues for PAL XFEL.

The smart modulator driving a klystron RF source for PAL XFEL will use an inverter charging system. Therefore, the stability of RF sources is directly determined by the one of inverter power supplies. In order to stabilize the charging level, we need an ultra fine inverter power supply and a correct feedback signal of the charging voltage. The proper conditioning of feedback signal with a thermally stable probe is necessary to realize an ultra stable charging performance. This paper shows the hardware development and analysis of the charging stability.

INVERTER CHARGING SYSTEM

A traditional klystron-modulator adopts the resonant charging scheme that uses a constant voltage source. A charging scheme that uses a constant current source such as a inverter power supply provides high reliability: a thyratron switch is safely turned off because next charging schedule is digitally controllable, it is fail-safe system under short-circuit condition due to the current limit feature. In addition, it is naturally compact by using a high frequency inverter [3]. These features are well matched to the next generation modulator for PAL XFEL facility. Figure 1 shows the circuit diagram of a modulator adopting an inverter power supply as a PFN charging power supply. Table 1 summarizes the parameters of a modulator that will provide ultra stable pulses to a klystron (model: Toshiba E3712).

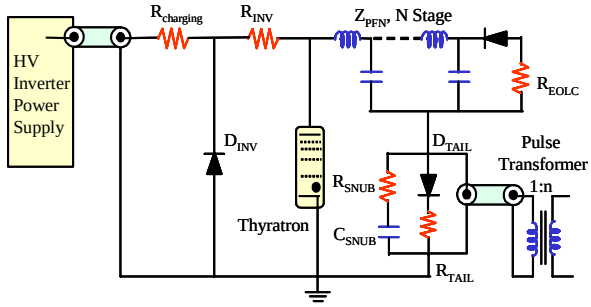

Figure 1: Circuit diagram of a modulator adopting an inverter power as a PFN charging power supply.

Table 1: Modulator specifications

Peak power	160 MW
Peak output voltage	370 kV
Pulse repetition rate	60 Hz
Pulse width	4.7 μs
Pulse energy	750 J
Flat-top width	1.7 μs
Pulse transformer turn ratio	1:17
PFN impedance	2.9 Ω
PFN capacitance	0.8 μF
Main charging inverter	60 kJ/s
Fine charging inverter	2.3 kJ/s
Maximum charging voltage	50 kV

This modulator is to be used for a new facility (fs-THz beamline) of PAL [4], which requires equivalent stability as the one of PAL XFEL. Therefore, this modulator is good test bench for the hardware R&D of the inverter charging system with 100 PPM stability for PAL XFEL.

Figure 2 shows the schematic diagram of the klystron-modulator control including coarse inverters, a fine inverter, a RF driver, a klystron, a thyratron switch of the modulator, a digital inverter controller, a high voltage probe, and a master timing controller (DG535). All the charging inverters are connected to the PFN in parallel. The fine charging inverter has special features that can control the amount of charges per switching cycle to control the regulating ripple of a charging voltage.

Figure 3 shows the timing diagram of a modulator control. The master timing controller provides a charge signal (DG535_A) for inverter power supplies, a thyratron trigger (DG535_B), and a driver trigger for a klystron RF input. The digital inverter controller provides RUN/STOP signals for coarse charging and fine charging.

#jsoh@postech.ac.kr

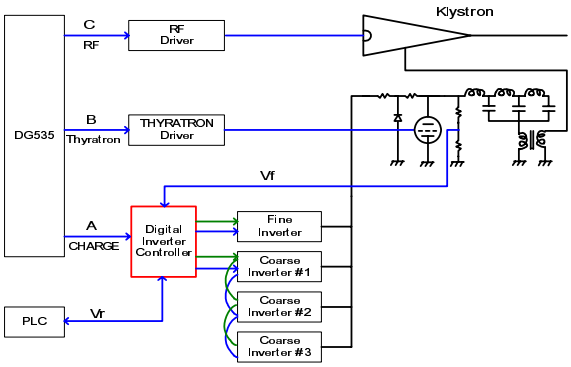

Figure 2: Schematic diagram of the modulator control.

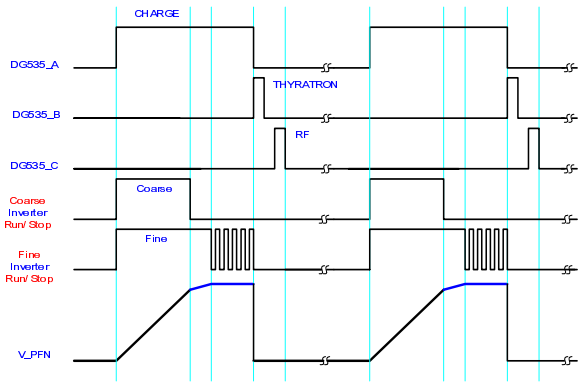

Figure 3: Timing diagram of the modulator control.

The coarse charging level is determined at about 99% of the target charging level. The fine charging unit will charge and regulate the final charging voltage. The increment of the PFN charging voltage per inverter switching cycle, ΔV_{PFN} is given by

$$\Delta V_{PFN} = I_{dc} / (C_{PFN} f_{SW}) = V_{PFN} / (T_C f_{SW}) \quad (1)$$

where I_{dc} is an average charging current, C_{PFN} is a PFN capacitance, T_C is a charging time and f_{SW} is a switching frequency. We have to reduce charging current or increase switching frequency in order to make the charging step small. The charging current has to be large enough to charge the PFN to the target level within the charging time limited by a pulse repetition rate. The switching frequency is also limited to less than 100 kHz due to the switching loss of the solid state devices used in the inverter. Therefore, the PFN charging voltage stability is usually around 0.1% for 100 Hz operating condition. Figure 4 shows typical example of the regulation waveform of a standard inverter, which results 35.6 V fluctuation that is equivalent to 790 PPM at 45 kV with the PFN capacitance of 1.4 μF and a average charging current of 1.8 A.

The charging voltage is not rising smoothly and monotonically but includes high-frequency spikes. The spike is made by the circuit components connected in parallel to the pulse transformer [5]. The noisy spikes have to be removed for the feedback circuit to correctly compare the charging level with a reference level.

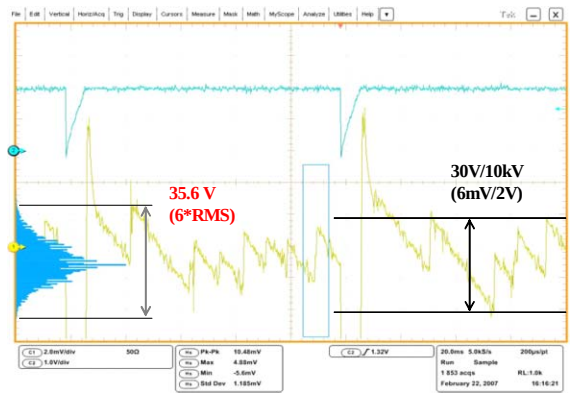

Figure 4: Regulating waveform of PFN voltage at the level of 10 kV with a PFN capacitance of 1.4 μF. The accumulation time for statistical distribution of PFN voltage is 1 hour.

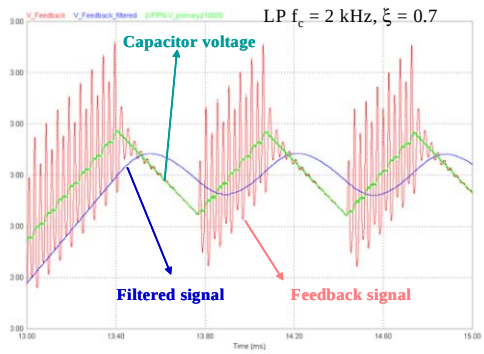

Figure 5: Detail structure of charging regulation.

The conditioning of a feedback signal removes the spiky component by the low-pass filter given by

$$H(s) = \frac{\varpi_o^2}{s^2 + 2\zeta\varpi_o s + \varpi_o^2} \quad (2)$$

where ω_0 is a cut-off frequency and ξ is a damping factor. However it results phase delay of feedback signal. This causes the limitation of fine regulation of the charge level as shown in Figure 5 that shows the detail structure of charging regulation. The signal is filtered with a cut-off frequency of 2 kHz and damping factor of 0.7.

DIGITAL INVERTER CONTROL

In order to overcome the phase correction difficulties of an analog feedback, we adopted a digital controller. The digital controller naturally requires a digital reference command for a charging level of the PFN. This condition is good fit to the upper level control system for the communication. It is also useful to keep a stable reference free from any thermal drift and harmful noise. A DSP-based digital controller is developed for the realization of highly stable inverter charging system. This controller has a high-resolution 18-bit ADC (AD7634) and a high-speed

DSP (TMS320F2811). Optical fibbers are used for the interfaces to the inverters to be free from the noise.

The measured value of the PFN Voltage by the digital controller is checked by the DAC output as shown in Figure 6. The built-in software filter with cut-off frequency of 1 kHz makes the signal delay of 0.45 ms that is close to the rise time of 0.35 ms due to the bandwidth of the feedback system. Therefore, the filter has to be included to reduce the noise but a reasonable bandwidth has to be provided to provide less phase delay of feedback signal.

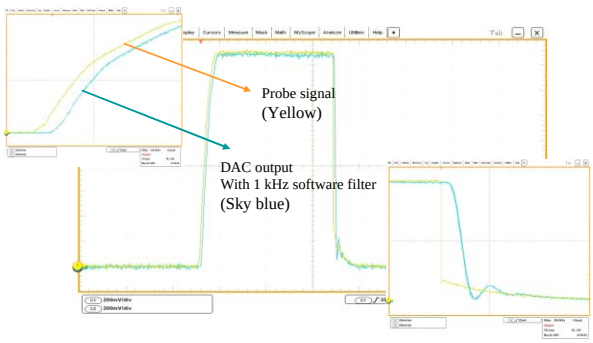

Figure 6: Effect of a digital filter at the charging level of 7.2 kV. The left is fast charging portion of PFN. The right is falling portion at the thyratron switching time.

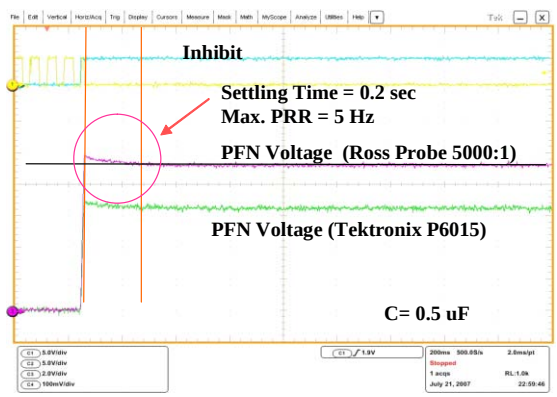

(a)

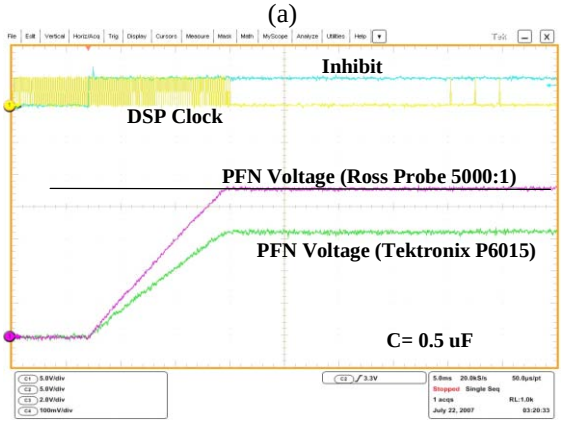

(b)

Figure 7: Digital control of charging overshoot. (a) The charging is done with a digital filter. (b) The charging is done with digital control of a charging pulse rate.

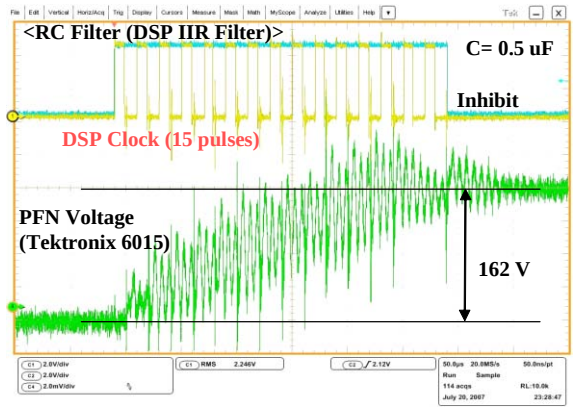

(a)

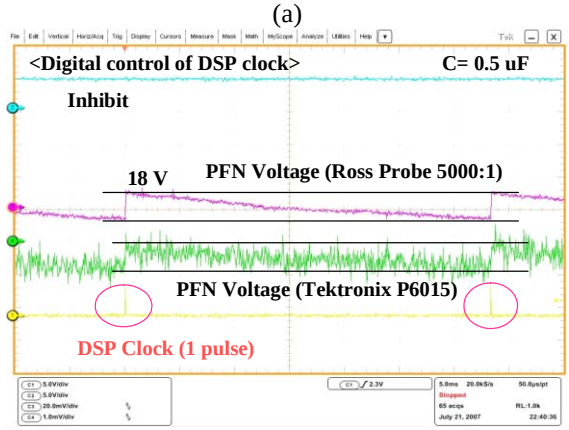

(b)

Figure 8: Digital control of charging regulation. (a) The charging pattern shows multiple current pulses with a digital filter. (b) Digital control of DSP clock permits only one current pulse per each step.

There is also a certain amount of overshoot due to the phase delay of the digital filter as shown in Figure 7-(a). Even a small overshoot, it takes long time to return to the target level within the 100 PPM error, which is enough to limit the pulse repetition rate, for example, 5 Hz in this test. By digitally controlling the pattern of charging pulse rate near the target level, we can charge the PFN smoothly without losing a charging time as shown in Figure 7-(b).

Due to the same reason, the overshoot also makes the regulation poor at the target charging level as shown in Figure 8-(a). There are 15 DSP clocks corresponding to the charging command for an inverter switching in case a digital filter is used. We already know that one charging pulse is enough to recover charging level. Therefore, one charging command is only permitted then next pulses are blocked for a while. After suitable settling time, we can correctly see the charging level that is to be compared with a target level as shown in Figure 8-(b).

Further improvement of the charging regulation is done by reducing the size of a bucket. PWM (pulse width modulation) is a typical method for the bucket size control. After PFN voltage reaches the target level, charging revel is regulated by smaller bucket with PWM mode.

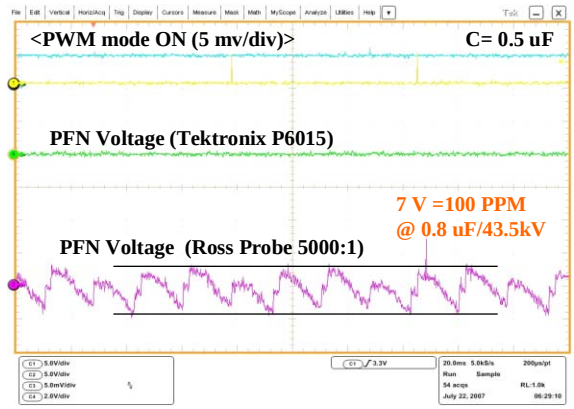

Figure 9: PWM mode and charging regulation.

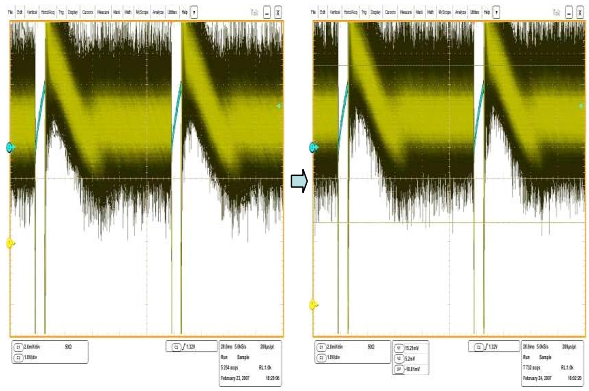

Figure 10: Long-term drift of the PFN charging voltage around 10 kV during 14 hours.

Figure 9 shows the effect of PWM mode on the regulation of charging level. Turning on the PWM mode improves the regulation down to 7 V as shown in Figure 9, which is corresponds to 100 PPM regulation at 45 kV.

PROBING SYSTEM

We need a high voltage probe to measure and feed back the PFN voltage to a controller. A compensated resistive divider is typically used as a high voltage probe. For the stable measurement, the constant division ratio of the probe insensitive to the temperature variation is essential. However the high voltage resistor is temperature sensitive due to the thermal variation of resistance value. Figure 10 shows the mean drift of the charging voltage around 10 kV during 14 hours. It is equivalent to 500 PPM at the 50 kV level. Therefore, we have to use a precision resistor having less temperature coefficient or keep the temperature of the probe body constant by using some temperature control devices such as a Peltier element.

SUMMARY AND DISCUSSION

The charging resolution is determined by the minimum size of charging bucket and the frequency response of a feedback circuit including a probe. The inverter charging system with 100 PPM stability is possible with following considerations. (1) Inverter charging system can meet the short-term stability by choosing both a suitable minimum resolution of a charging system and correct signal conditioning. (2) Long-term stability can be provided by a high precision resistor or a temperature control device of the probe. (3) The residual slow drift can be corrected by adjusting the reference command of the PFN charging voltage in order to provide constant RF amplitude.

REFERENCES

[1] I. S. Ko, “PAL XFEL project,” Proc. FEL2005, Stanford University, USA, 2005
[2] Y. Kim, et al., “Start-To-End Simulation of the PAL XFEL Project,” Proc. FEL2004, Trieste, Italy, 2004
[3] J. S. Oh, et al., “Development and Application of an Inverter Charging Supply to a Pulse Modulator,” the XXI International LINAC Conference, Korea, 2002
[4] H. S. Kang, et al., “Design of Coherent Femto-Second THz Radiation Source using 60 MeV Electron Linac,” Proc. SRI2006, Daegu, Korea, 2006
[5] J. S. Oh, et al., “Analysis of Inverter Charging Waveform for Ultra Stable SCSS Modulator,” Proc. FEL2006, Berlin, Germany, 2006

FOURIER AND NON-FOURIER MODELS FOR PHOTOEMISSION

F. Scarlat, M. Oane, Anca Scarisoreanu, Ecaterina Mitru
National Institute for Laser, Plasma and Radiation Physics - NILPRP, Bucharest, Romania
E-mail of corresponding author: scarlat.f@gmail.com

Abstract

This paper is a theoretical study on the photoemission properties of metallic photocathodes in the high intensity ultrashort laser pulse regime, using Fourier and non Fourier models. First of all the Fourier-model was used. Next an analysis of the electron gas heating phenomenon and how this phenomenon leads to coupled heat equations (two temperature models) was conducted. The authors also tried to show that it is possible to use, in the second approximation, a non-Fourier model instead of two temperature models, using a single temperature hypothesis (the electron gas temperature equals the lattice temperature). The distributions for the thermal fields and photocurrents function of space, time, laser-intensity, incident angle and relaxation time are also represented.

INTRODUCTION

Free electron lasers (FELs) operate over a large portion of the electromagnetic spectrum, i.e.from a μ-wave to the VUV. At the high frequency end of the spectrum, FEL operation is severely limited by a number of factors, among which the transverse beam emittance, which is invers proportional with the square root density current. A high electron density implies not only a high peak current but also a low rms normalized emittance, ε_n. For example, in the case of X-FEL projects, ε_n[mm.mrad] has the values: 1.4 - XFEL [1], 1.2 - LCLS [2] and 0.85 - SCSS [3]. Recent development in the tehnology of photemissive electron sources offer promising advances over the conventional electron injectors [4], [5].

All photo-injector concepts share a drive laser which produces short bunches of photons and a photocathode which converts the photon bunch into short bunches of electrons [6], [7]. Photoemission from photo-cathodes is possible when the work function (or potential barrier, $e\Phi$) of the material is less than the photon energy ($\hbar\omega$) used, by at least: 1 eV if the material is a metal (in this case electrons are extracted from the conduction band) and 2 eV if the material is a semiconductor (electrons are here extracted from the valence band).

A photocathode is characterized by four parameters: quantum efficiency (QE), maximum laser wavelength (λ_m), life time (τ) and its ability to sustain a high electric field (E). For FEL nano-Coulomb pulses in picosecond time are required. The advantages of photoemission are the followings: high peak current density (> 100 A); fast time response (picosecond to femtosecond) and possibility to generate polarized electrons. As drawbaks: the need for very good vacuum, limited lifetime (few month) and very expensive (vacuum systems & laser). Metal cathodes have poor QE but are robust ($\tau \sim$ years).

Alcaline cathodes have good QE but are delicate and they need very good vacuum conditions < 10^{-10} torr. Starting from the above considerations as well as the NUCLEU program [8] for to conduct studies by means of the Nd:YAG laser system with 50 mJ at 1064 nm, 24 mJ at 532 nm, 8 mJ at 355 nm and 4 mJ at 266 nm, this paper represents a start in the metal photocathode studies using Fourier and non Fourier models for photoemission [9].

FOURIER MODELS

Fourier model starting from the basic Fourier heat equation, represented the input of our models [10]

$$\frac{\partial^2 T}{\partial x^2}+\frac{\partial^2 T}{\partial y^2}+\frac{\partial^2 T}{\partial z^2}-\frac{1}{\gamma}\frac{\partial T}{\partial t}=-\frac{Q(x,y,z,t)}{K}, \qquad (1)$$

where K - the thermal conductivity of the sample; γ - the thermal diffusivity of the sample ($\gamma = k/c\cdot\rho$); c -the heat capacity of the sample; ρ - the mass density of the sample. $Q(x, y, z, t)$ represents the heat rate (per volume and time unit) produced by the laser in the solid sample.

Based on Spatial Transform and Laplace Transform, the eigenfunctions from the standard theory and the eigenvalues from the boundary conditions were determined.

So for the proposed device a parallelepiped solid sample with dimensions a, b, and c was considered.
Considering a linear heat transfer (h – heat transfer coefficient) at the sample surface (the "radiation" boundary condition), we have:

$$\left[\frac{\partial K_x}{\partial x}-\frac{h}{K}K_x\right]_{x=-\frac{a}{2}}=0;\left[\frac{\partial K_x}{\partial x}+\frac{h}{K}K_x\right]_{x=\frac{a}{2}}=0, \qquad (2)$$

$$\left[\frac{\partial K_y}{\partial y}+\frac{h}{K}K_y\right]_{y=-\frac{b}{2}}=0;\left[\frac{\partial K_y}{\partial y}+\frac{h}{K}K_y\right]_{y=\frac{b}{2}}=0, \qquad (3)$$

$$\left[\frac{\partial K_z}{\partial z}+\frac{h}{K}K_z\right]_{z=-\frac{c}{2}}=0;\left[\frac{\partial K_z}{\partial z}+\frac{h}{K}K_z\right]_{z=\frac{c}{2}}=0. \qquad (4)$$

The semi-analytical solution to Fourier equation is:

$$\Delta T(x,y,z,t)=\sum_{i=1}^{\infty}\sum_{j=1}^{\infty}\sum_{o=1}^{\infty}a(\alpha_i,\beta_j,\chi_o)\cdot$$

$$\cdot b(\alpha_i,\beta_j,\chi_o,t)K_x(\alpha_i,x)K_y(\beta_j,y)K_z(\chi_o,z), \qquad (5)$$

where we have:

$$a(\alpha_i,\beta_j,\chi_o)=\frac{\alpha I_{ox}}{KC_iC_jC_o}\int_{-\frac{a}{2}}^{+\frac{a}{2}}e^{-\alpha x}K_x(\alpha_i,x)dx\cdot \tag{6}$$

$$\cdot\int_{-\frac{b}{2}}^{+\frac{b}{2}}\int_{-\frac{c}{2}}^{+\frac{c}{2}}e^{-2\left(y^2+z^2\right)/w_{ox}^2}K_y(\beta_j,y)K_z(\chi_0,z)dydz,$$

$$b(\alpha_i,\beta_j,\chi_0,t)=\frac{1}{\alpha_i^2+\beta_j^2+\chi_o^2}\left[1-e^{-\gamma_{ijo}^2t}-\right. \tag{7}$$

$$\left.-\left(1-e^{-\gamma_{ijo}^2(t-t_o)}\right)h(t-t_0),\right.$$

and

$$\gamma_{ijo}^2=\gamma\left(\alpha_i^2+\beta_j^2+\chi_o^2\right). \tag{8}$$

The photocathode employed for the study is 4 mm x 10 mm for a Kerst injector. Using a laser of the intensity (I_{0x}) plotted in Fig.1, by means of equations (5), (6), (7) and (8), some thermal distributions in different situations were plotted.

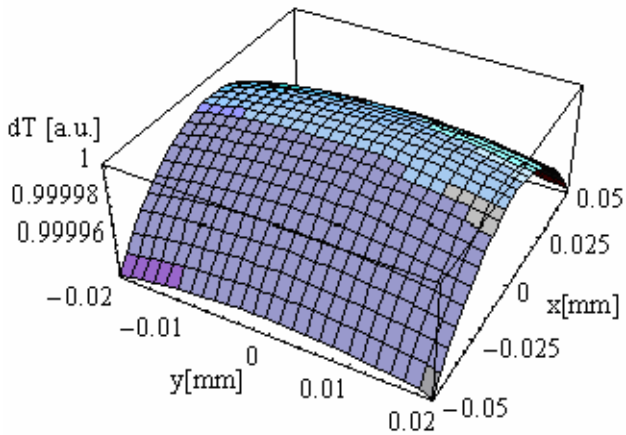

Figure 1: TEM_{00} classical laser field.

Fig. 2 presents the temperature generated by the cathode surface when the incident laser beam acts in TEM_{00} mode

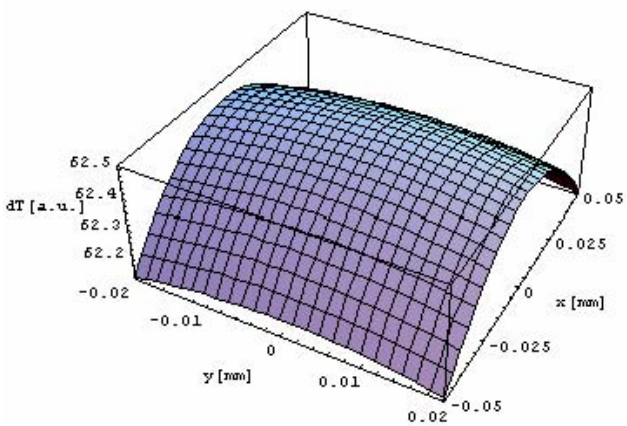

Figure 2: Photocathode temperature.

The thermal fields versus the incident angle of the laser beam are given in Fig.3.

If there is no vacuum than at the margins of the photocathode temperature decreases.

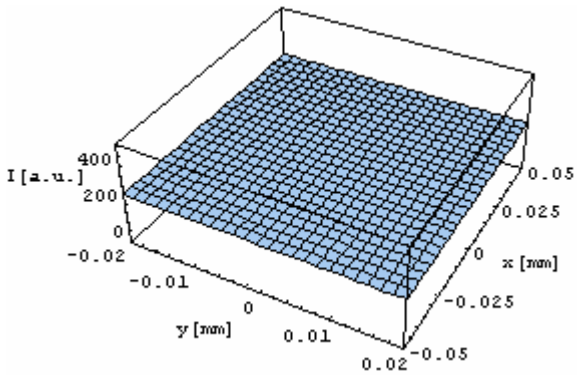

Figure 3: The thermal field produced by a flat laser beam.

The spatial distribution of the thermal field for a given incident angle and a flat laser beam (Fig. 4) when vacuum around the photocathode exists, is presented.

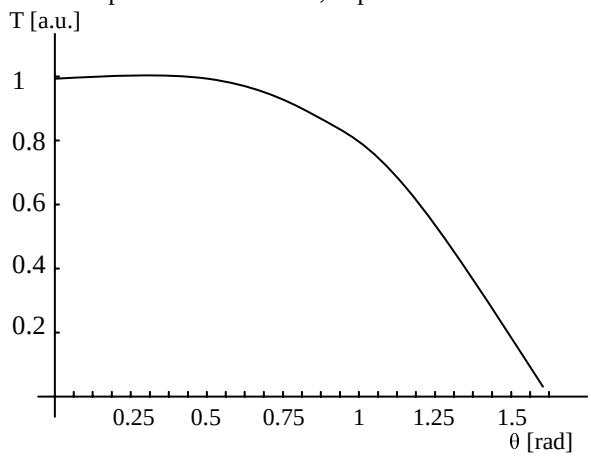

Figure 4: Photocathode temperature vs. the laser incidence angle.

THE NON-FOURIER MODELS

The Fourier model [10] contains several inconsistent implications. The most important is that the model implies an infinite speed of heat propagation.

The non Fourier Models start from the non-Fourier heat conduction equation:

$$\frac{\tau_0}{\alpha}\frac{\partial^2T}{\partial t^2}+\frac{1}{\alpha}\frac{\partial T}{\partial t}=\frac{\partial^2T}{\partial x^2}+\frac{1}{\lambda}\left[Q(x,t)+\tau\frac{\partial Q}{\partial t}\right], \tag{9}$$

where a, λ, τ_0 are thermal diffusivity, thermal conductivity, and relaxation time of the medium.

One of the models is the Anisimov model or the two-temperature model [11]. The coupled differential equations relating the electron temperature T_e to the lattice temperature T_i are given by the equations (10) where g represents the connection between electrons and

lattice; C and K are the heat capacities and thermal conductivity respectively:

$$C_e \frac{\partial}{\partial t} T_e = \frac{\partial}{\partial z}\left[k(T_e, T_i) \frac{\partial}{\partial z} T_e \right] - g(T_e - T_i) + I(z,t),$$

$$C_i \frac{\partial}{\partial t} T_i = g(T_e - T_i). \qquad (10)$$

Instead of the above model, the hyperbolic heat equation was used; assume that: $T_e = T_i$, which is valid when the puls length is comparable to the relaxation time and the electron temperature is higher than the lattice temperature.

Assume a sample with the thickness L with initial temperature distribution $T(x,0) = T_0$. Starting with the time $t = 0$ the front surface of the sample is irradiated by a laser-pulse with the laser pulse of energy intensity:

$$Q(x,t) = \begin{cases} \frac{Q_0}{\Delta x}\left(\frac{t}{t_p}\right)\exp(-t/t_p) & , 0 \le x \le \Delta X, \\ 0 & , \quad \Delta X \le x \le L, \end{cases} \qquad (11)$$

where t_p denotes the time duration of the pulse, Q_0 is the total energy intensity of a single pulse. According to common theory, Δx is corresponding to the skin depth of electromagnetic waves penetrating into the surface of the sample, L is the thickness of the medium.

The boundary conditions are:
$\partial T(0,t)/\partial x = 0$, $\partial T(L,t)/\partial x = 0$ and the initial conditions are: $T(x,0)=T_0$ and $\partial T(x,0)/\partial t = 0$.
Suppose that: $T_e=T_i$, than the solution is the following:

$$T_e(z) = T_0 + [T_e(0)-T_0]\exp(-z/L), \qquad (12)$$

where: $L = n(\hbar k_F/m)\tau$ with: k_F - the Fermi momentum and the factor n given the electron scattering will mimic a random walk – should be on the order of the square root of the ratio of the laser pulse time scale with the scattering time scale, or $n = (1\ ns/0.1\ ps)^{1/2} \approx 100$. τ is the relaxation time. The plot is presented in Fig. 5.

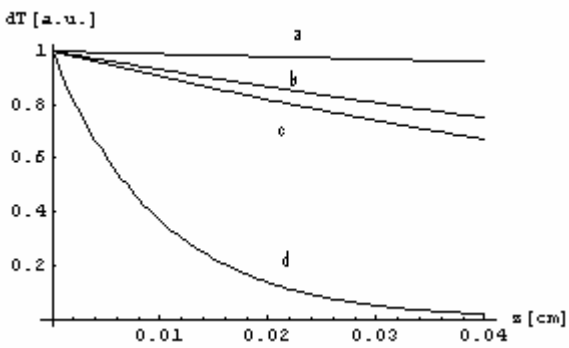

Figure 5: The temperature distribution versus depth in a Non Fourier model: the first curve, which is close to unity, is for the relaxation time 10^{-3} s (a), the others are for 10^{-6} s (b), 10^{-9} s (c) and 10^{-12} s (d).

LIMITS OF THE TWO MODELS

The shorter the relaxation time, the two different models (Fourier and non Fourier) would give the same results. It is obvious that the classical treatment is more powerful than the Quantum Mechanics models for this case of laser-solid interaction. The temperature field depends on the incident angle. The experiments shows that Fourier model is valid up to 10^{-6} s and the non Fourier model is valid up to 10^{-9} s.

Our simulations strongly suggest that all the phenomena are taking place at the sample surface rather than in the volume. Also our simulations prove that the higher the vacuum, the higher the temperature field is. ($A(x,y,z,t)=r_S \cdot \delta(z)$; $\delta(z)$ - Dirac Function).

EXAMPLES

Fig. 6 is a plot of the current densities vs temperature for different photocathodes.

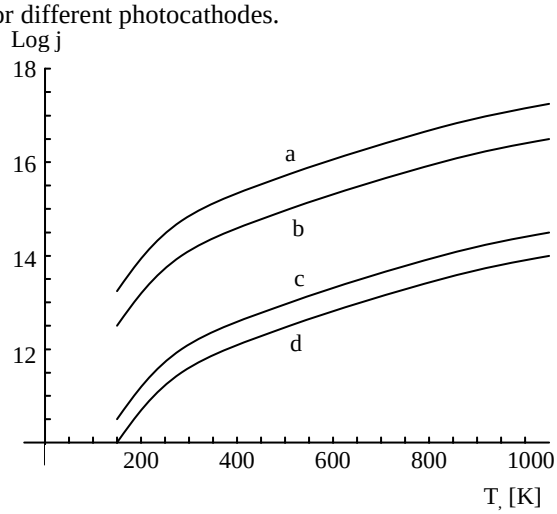

Figure 6: Variation of the current density vs temperature for: bright tungsten (a); lanthanum hexaboride (b), thoriated tungsten (c) and impregnated tungsten (d).

Fig. 7 presents the 3D (Cartesian coordinates) thermal fields for a laser beam heating the FEL photocathode at an angle of $\pi/4$. The laser beam is supposed to act in a Gaussian mode. The exposure time is 10^{-9} s. (Fourier model was used).

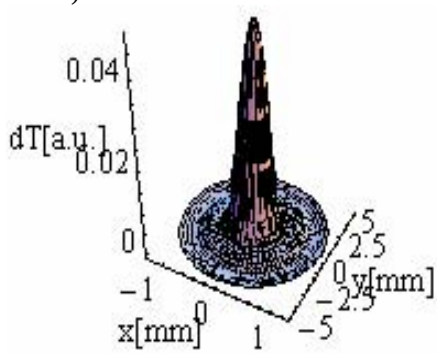

Figure 7: Thermal field for the exposure time of 10^{-9} s.

One can observe the edge effects due to the boundary conditions.

For nano and picoseconds exposure time, Figs. 8 and 9 (radial coordinates versus time) are suggestive. For femtoseconds exposure times the Fourier model breaks - down. In order to overcome the edge effect, it is possible to use the "state of the art" technologies regarding implantations of nano-particle (Au, Al, Ag, Cu, Ni) networks of 100 nm size, at 400 nm distance between them, on the photocathode edges.

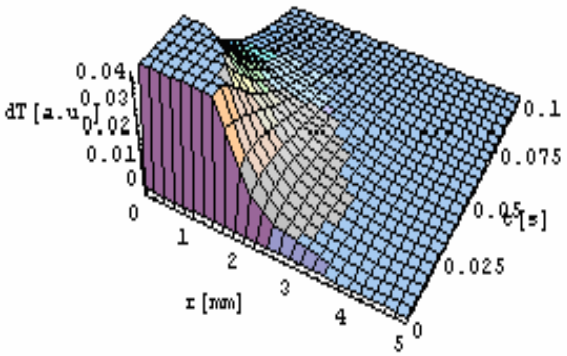

Figure 8: The thermal field for nano-seconds exposure time (radial coordinates versus time).

Table 1

Photocathode Material	Absorption coefficient (cm^{-1})
CsI	40
Au	0.77×10^6
Ag	0.83×10^6
Al	10^6
Cu	$16.6.10^6$
Ni	13.10^6

The big difference between the absorption coefficients (Table 1) of CsI, on one hand, and Al, Au, Ag, Cu, Ni on the other hand, makes our proposal realistic. For example, Fig. 9 presents the thermal field at the surface for a 100 nm diameter Au nano-particle which is at 400 nm depth. One can observe that the peak temperature is increased.

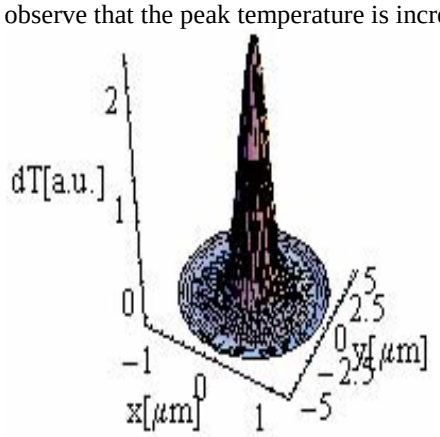

Figure 9: Thermal field at the surface for a 100 nm diameter Au nano-particle.

CONCLUSIONS

First of all Fourier models can offer useful information about the photochatode thermal field, especially when dealing with long a term pulses (μs) and powerful heating sources. In the range of picoseconds one has to take into account non-Fourier models, which imply a finite propagation speed of the thermal waves (in contrast with the Fourier models which involve infinite speed propagation). For non-Fourier models the problem to deal with is the relaxation time. If the heating pulse time is of the order of magnitude (or smaller) than the relaxation time, the differences between the two models are greater. In the range of femto- and atto- seconds one has to deal with a quantum heat transfer model. In fact the non-Fourier models are semi-classical models which take into account the quantum effects via the relaxation time (in an empirical style).

Another conclusion and a suggestion is that nano-particle networks, with a very high absorption coefficient, can improve the photochatode properties.

REFERENCES

[1]. M. Altarelli et al. (Eds.), The European X-Ray Free Electron Laser (XFEL), Technical Design Report, Preprint DESY 2006-097, DESY, Hamburg, 2006, (http://xfel.desy.de)

[2]. J. Arthur et al., Linac Coherent Light Source (LCLS). Conceptual Design Report, SLAC-R593 Stanford 2002 (http://www-ssrl.slac.stanford.edu/lcls/cdr).

[3]. Spring 8 Compact SASE Source (SCSS) X-FEL: Conceptual Design Report, RIEKEN, Japan, May 2005 (http://www-xfel.spring8.or.jp).

[4]. K. L. Jensen, D. W. Feldman, M. Virgo, P. G. O'Shea, "Measurement and analysis of thermal photoemission from a dispenser cathode", Phys. Rev. S.P.- Accelerators and Beams, 6, 083501,2003.

[5]. C. Travier, B. Leblond, M. Bernard, J.N. Kaila, P. Thomas, and P. Georges, Proceedings of the 1995 Particle Accelerator Conference, Vol.2, pp. 945-947, 1995.

[6]. G.R. Neil and L. Merminga, "Technical approaches for high-average-power free-electron lasers", Rev. Mod. Phys, 74, 685 - 699, 2002.

[7]. M. E. Couprie and J. M. Ortega, "Free-electron lasers sources for scientific applications", Analysis 28, pp.725-736, 2000.

[8]. F. Scarlat, M. Oane, A. Scarisoreanu, E. Mitru, "Testing Stand for Experimental Studies on Photocathode Materials", PN06 360503 NILPRP Program, 2006.

[9]. D.W. Tang, N. Arald, "Analytical solution of non-Fourier temperature response in a finite medium under laser-pulse heating", Heat and Mass Transfer 31 (1996) 359, Springer - Verlag, 1996.

[10]. M. Oane, Shyh - Lin Tsao, F. Scarlat, "Temperature field distribution in multi-layered solid media interaction", Optics & Laser Technology, Vol.39, Nr.1, Pg. 179 - 181, February 2007.

[11]. S. I. Anisimov, V.A. Khoklov, "Instabilities in Laser-Matter Interaction", Boca Raton", FL: CRC, 1995.

COHERENCE OF SPACE CHARGE VIBRATION AND PARAMETERS OF ELECTRON GUNS

S. V. Miginsky#, Budker INP, Novosibirsk, Russia

Abstract

Space charge effect always determines the motion of particles in electron guns. Coherence of space charge vibration leads to oscillation of the emittance along a gun or a charge affected beamline. This phenomenon is closely related to a technique known as emittance compensation. It has been considered in the paper. The optimal parameters of guns and the expected emittance of the beam from the optimal ones have been estimated and scaled.

INTRODUCTION

Emittance compensation technique has been mentioned first probably in [1]. It was explained and developed further in [2] and other papers. The two basic effects, caused by the longitudinal nonuniformity of charge density and the transverse one, and their combination in uniform and nonuniform beamlines were considered in [3] - [6], also with accelerating and bunching. The main results of the latter works is that both effects separately or together can be compensated, the charge phase advance through the beamline should be $2n\pi$ (n is integer) and the focusing should be optimal. Then the normalized emittance dilution is well estimated as

$$\varepsilon_n \cong \varepsilon_c x_e \sqrt{\frac{I}{I_0 \beta\gamma}}, \qquad (1)$$

where x_e is the rms size of the beam at the entrance; I is the peak current; $I_0 = 4\pi \cdot mc^2 / Z_0 |e|$, ≈ 17.045 kA for electrons; $\beta = v/c$; $\gamma = 1/\sqrt{1-\beta^2}$; v is the longitudinal velocity; and ε_c is the dimensionless coefficient depended on the type of the beamline.

In this paper we consider electron guns in the same view. We take into account only macroscopic space charge effect and neglect thermal and grid emittance. The main difference between a gun and a beamline is the presence of metallic electrodes near the emitter. Their charge depends on the one of the beam and generates comparable fields, so exclusion of near-cathode electrodes from simulation of beam motion in a gun causes lost of accuracy.

EMITTANCE DILUTION IN GUNS

Phenomena and Basic Scaling

If the emitter is round and the beam is homogeneous and stationary, the gun geometry can be optimized so that the space charge effect doesn't affect the emittance, as in the well known Pierce gun. If the beam is not longitudinally uniform, the transverse phase portraits of its slices differ and their emittances are not zero. Let's consider these phenomena and estimate the total emittance.

Particle motion in the same gun is similar if its voltage and current meet Child-Langmuir law $I \propto U^{3/2}$. In this case the emittance (not normalized!) doesn't depend on the current [5] 4.1. At the same time, the brightness is $I/\varepsilon_n^2 \propto \sqrt{U}$. If all the dimensions of a gun are changed proportionally, its quality factor ε_c preserves while its brightness is $\propto \sqrt{U}/r^2$. Thus, one should find ε_c and the optimal compensation beamline for any gun.

Charge Amplitude and Phase

General equation of small charge vibrations has been derived in [3] (3). It generates a transformation matrix between two arbitrary points of a beamline [5] (2.16). The charge vibration phase is defined in [5] (2.19). Now we can define the differential characteristics of a bunch [5] 4.1, [6]. The local charge phase is

$$\varphi = \arctan\left(\frac{-C'x}{C\sqrt{j}}\right) = \arctan\left(\frac{\dfrac{dx'}{dI} - \dfrac{x'}{x}\dfrac{dx}{dI}}{\left(\dfrac{1}{2I} - \dfrac{1}{x}\dfrac{dx}{dI}\right)\sqrt{j}}\right), \qquad (2)$$

where x is the rms-size of a slice, $j = I/I_0$, C and C' are the transformation matrix elements associated with cos-like trajectories. The quadrant is chosen so that the signs of sinφ and cosφ coincide the ones of the numerator and the denominator respectively. x and x' are considered as functions of the slice current I.

It is also useful to define the relative amplitude of charge vibrations to estimate emittance dilution in a compensation beamline [5] 4.1, [6] (5):

$$a = \sqrt{\left(C'x/\sqrt{j}\right)^2 + C^2}\,. \qquad (3)$$

Then the relative amplitude of a slice is [5] (4.10), [6] (13):

$$A = \sqrt{\left(\frac{2I}{x}\frac{dx}{dI} - 1\right)^2 + \frac{1}{j}\left(2I\left(\frac{dx'}{dI} - \frac{x'}{x}\frac{dx}{dI}\right)\right)^2}\,. \qquad (4)$$

Basic Gun

A simple diode gun has been simulated first. Its geometry is shown in fig. 1. The emitter radius was 5 mm, the distance between the electrodes was 123 mm, while the beam was observed at 200 mm from the cathode. The perveance was very close to the "natural" one, so the optimal current was 2 A at 300 kV. SAM simulation code [7] was used to calculate beam motion in the gun. As usually for emittance compensation, a bunch has been divided by slices, and each slice was considered independently as a steady-state beam. The current density at the cathode was always homogeneous.

#S.V.Miginsky@inp.nsk.su

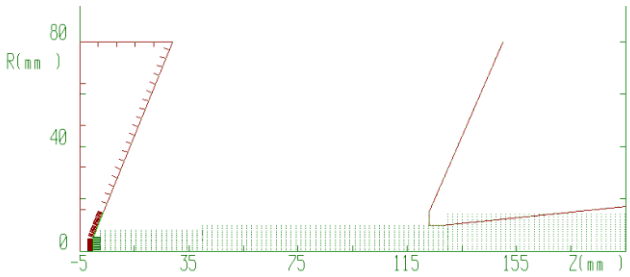

Figure 1: The geometry of the basic gun, red solid lines are electrodes.

The calculated beam parameters depending on the beam current are depicted in fig. 2. They were calculated by the following formulae:

$$x = \sqrt{< x^2 >},$$
$$x' = < xx' > / \sqrt{< x^2 >}, \quad (5)$$
$$\varepsilon = \sqrt{< x^2 >< x'^2 > - < xx' >^2}.$$

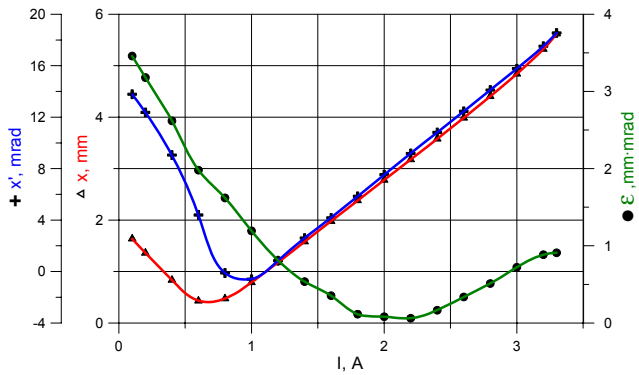

Figure 2: Beam parameters vs. beam current: rms-size, its derivative and emittance.

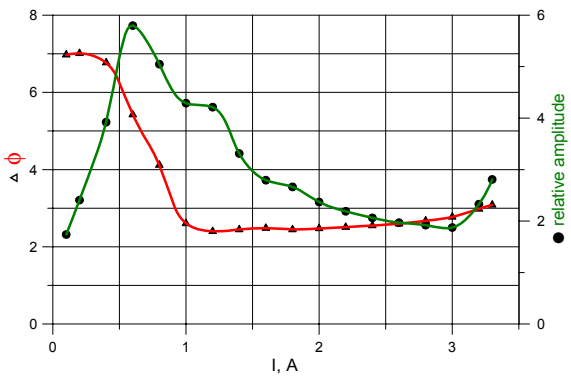

Figure 3: Charge phase and relative amplitude vs. beam current.

The dependencies of the phase and the amplitude on the current for the mentioned gun are shown in fig. 3.It is seen that the phase is almost constant within current limits from 1 to 3 A and its value is $\approx 2.5 \approx 0.8\pi$. Thus, if an ideal uniform beamline (where the phase advance doesn't depend on the amplitude) with the phase advance $\approx 1.2\pi$ is placed after the gun, one should expect the minimal emittance. The following questions are still left: (i) what peak current of a bunch gives the minimum emittance in this system, (ii) which slice should be matched to the compensation beamline, and (iii) what is the optimal phase advance of the latter.

Each slice was considered as a number of particles, representing the motion of the appropriate ring. The longitudinal charge distribution was presumed as Gaussian. An ideal beamline with phase advance φ matched with a slice with the current j_0 and the state x_0 and x_0' has the following produces the following linear transformation:

$$x' \to x' - x \cdot (x_0' / x_0),$$
$$\begin{cases} x \to x_0 + (x - x_0)\cos\varphi + x' x_0 / \sqrt{j}\,\sin\varphi, \\ x' \to x'\cos\varphi - (x / x_0 - 1)\sqrt{j}\,\sin\varphi. \end{cases} \quad (6)$$

Then φ and j_0 were optimized for each peak current value. For example, the minimum for 2.2 A is 1.03 mm·mrad and is situated at $I = 1.043$ A and $\varphi = 3.91 \cong 1.246\pi$. The phase is quite near the predicted value.

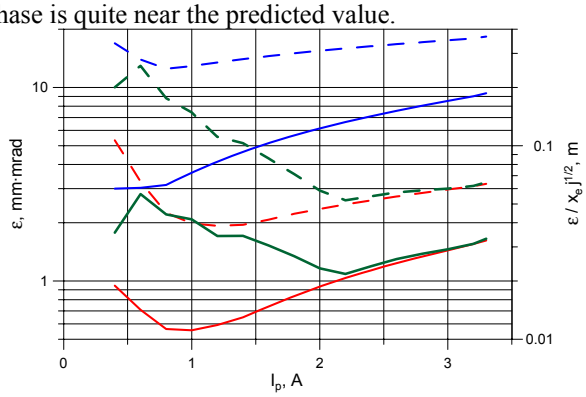

Figure 4: Emittance (solid) and ε_c (dashed) vs. peak current. Blue – no compensation, red – ideal beamline, green – non-uniform beamline.

Plots of the emittance and the quality factor vs. the peak current of a Gaussian bunch with and without the ideal compensation beamline are depicted in fig. 4. One can see that (i) the beamline reduces the emittance six times and (ii) ε_c weakly depends on the peak current. A non-ideal compensation beamline increases the quality factor by ([3]: (5), (15), Table 1)

$$0.037 \frac{x_0}{x_e} A^3 \frac{\varphi}{2\pi} \approx 0.13, \quad (7)$$

where all the parameters belong to the matched slice. Thus, imperfection of the compensation beamline can weaken the compensation significantly.

Consider then a simplest non-uniform beamline that consists of two gaps of different lengths and a thin lens between them. Then the motion of charged rings through it is described by the following equation [3] (12):

$$x'' = \frac{2\tilde{j}}{x}, \quad (8)$$

where $\tilde{j}$ is the current within the ring. The motion is presumed as laminar. Both lengths and the lens strength were optimized. The optimal emittance and ε_c are also placed in fig. 4. It is clear that both beamlines give almost equal results if the peak current is bigger than 2 A.

Other Guns

Seven other guns have been simulated in the same way to investigate the influence of the gun geometry. In five first ones the emitter radius was the same while the length was varied. The electrodes were shaped to make perfect electric field. Additional electrodes were added to the guns "Short 2", "Long 2" and "Long 3" to equalize their perveance to the primary one. The cathode electrode in "Long 3" is planar. The optimal current in all the cases above was ≈ 2 A. The two last guns are similar to first half-cells of 1.3 GHz photo-electron RF guns. The emitter radii in these cases are 2 mm. The results are placed in table 1. The values in parentheses in the second column mean the observation points. The last three columns contain quality factors of non-compensated guns, with ideal lines and with non-uniform lines respectively.

Table 1: Simulated guns parameters

Gun	Length, mm	U, kV	ε_c n/c, m	ε_c ideal, m	ε_c n/u, m
Basic	123 (200)	300	0.3	0.05	0.065
Short	61.5 (100)	150	0.3	0.04	0.05
Short 2	61.5 (100)	300	0.35	0.055	0.15
Long	246 (400)	850	0.43	0.085	0.14
Long 2	246 (400)	300	0.26	0.04	0.065
Long 3	246 (400)	300	0.4	0.07	0.023
RF 1	50 (70)	1000	0.28	0.05	0.02
RF 2	50 (70)	2000	0.28	0.05	0.02

PARAMETERS OF EXISTING GUNS

It is interesting to compare the theoretical parameters above with ones achieved in real guns. One can find them in table 2. Only guns demonstrated record brightness were selected there. The lengths and voltages at the first half-cell of guns were used to calculate ε_c.

Table 2: Existing guns parameters

Gun	Ref.	E_{kin}, MeV	I_p, A	x_e, mm	ε_n, mm·mrad	ε_c, m
LCLS*	[8]	2.0	50	1	0.83	0.034
DESY	[9]	1.05	100	1	2.7	0.06
" *	"	"	43	0.57	1.7	0.10
BNL IV	[10]	1.33	67	0.3	1.4	0.14
"*	"	"	133	"	1.35	0.095
MIT	[11]	0.27	50	0.5	3.5	0.14

* Guns with bunch shaping.

The best ε_c of existing guns are close to ones estimated above, although exceed them. On the one hand, bunch shaping permits to reduce the emittance, as the Gaussian longitudinal distribution was considered in estimations. On the other hand, the rectangular transverse distribution in estimations yields better emittance then the Gaussian one typical for photo-electron guns. Also the temperature of photo-electrons was not taken into account. For example, the emittance of LCLS gun is lower than the temperature limit [9]:

$$\varepsilon_n = x_e \sqrt{\frac{2E_k}{3m_e c^2}} \cong 1\,\text{mm}\cdot\text{mrad}\,. \qquad (9)$$

There could be two explanations: (i) the light spot size was reduced and/or (ii) the temperature of electrons leaving copper cathode is less then of ones from CsTe cathode (0.8 eV by [9]).

CONCLUSIONS

- Appropriate emittance compensation applied to an electron gun always improves emittance by factor 3…15.
- Both effects of the longitudinal nonuniformity of charge density and the transverse one can be compensated well.
- The expected normalized emittance of a well-designed gun with an optimal compensation beamline is

$$\varepsilon_n \approx 0.02...0.07 x_e \sqrt{\frac{I}{I_0 \beta\gamma}} = 0.01...0.035 r_e \sqrt{\frac{I}{I_0 \beta\gamma}}\,, \qquad (10)$$

  where x_e is the rms beam size at the emitter and r_e is the emitter radius.
- Quality factors ε_c of best existing guns approach theoretical limitation. Further improvement is possible with beam shaping.

REFERENCES

[1] B.E.Carlsten. NIM **A 285** (1989) 313.

[2] L.Serafini, J.B.Rosenzweig. Phys. Rev. **E 55** (1997) 7565.

[3] S.V.Miginsky. NIM **A 575** (2007), 234-237.

[4] S.V.Miginsky. Optimal Beamlines for Beams with Space Charge Effect. RuPAC 2006.

[5] S.V.Miginsky. Space charge effect, coherence of charge vibration and emittance. Prepr. BINP #2007-11, Novosibirsk, 2007. http://www.inp.nsk.su/activity/preprints/files/2007_011.pdf

[6] S.V.Miginsky. Electron Guns and Beamlines in the View of Emittance Compensation. APAC'07, Indore, India, Jan 29 - Feb 2 2007.

[7] M.A. Tiunov, B.M. Fomel and V.P. Yakovlev. SAM – an Interactive Code for Evaluation of Electron Guns, Budker INP prepr. 96-11, Novosibirsk, 1996.

[8] http://www-ssrl.slac.stanford.edu/lcls/ http://www-ssrl.slac.stanford.edu/lcls/parameters.html

[9] V. Miltchev, K. Abrahamyan, G. Asova, et al. Transverse Emittance Measurements at the Photo Injector Test Facility at DESY Zeuthen. FEL'04, Trieste, Italy, Aug 29 – Sep 3 2004.

[10] J. Yang, F. Sakai, T. Yanagida, et. al. Experimental Studies of Photocathode RF Gun with Laser Pulse Shaping. EPAC'02, Paris 3-7 June 2002.

[11] W. J. Brown. Low emittance electron beam production and characterization with a 17 GHz photocathode RF gun. Ph. D. thesis. MIT 2001. http://dspace.mit.edu/handle/1721.1/8287

LOW POWER CONSUMING HYBRID BENDING MAGNET AT THE XFEL BEAM DUMP

F. Hellberg, H. Danared, A. Hedqvist, Manne-Siegbahn Laboratory, 10405 Stockholm, Sweden*
W. Decking, B. Krause, A. Petrov, J. Pflüger, M. Schmitz, DESY, 22603 Hamburg, Germany

Abstract

At the end of the European XFEL the electron beam is separated from the photon beam and directed towards the beam dump with a bending magnet. This dipole magnet is designed to bend 10-25 GeV electrons by 1°/m and is 10 meter long in total. By integrating permanent magnet material into a conventional electromagnet, this so-called hybrid magnet with a 1 T bias magnetic field consumes no power at the nominal energy of the XFEL, 17.5 GeV. The magnetic field can be increased or decreased by magnet coils to obtain 1°/m deflection for all energies between 10 and 25 GeV. Here a proposal for such a hybrid configuration is presented together with its characteristics.

INTRODUCTION

In a free electron laser the electrons are bent away from the laser light with electromagnets and stopped in a beam dump situated away from the experimental hall. At the European XFEL the electrons are bent vertically 10° in a 10 m long double bending achromat magnet [1]. Each beam line ends with such a magnet. It is the largest electromagnet of the XFEL and it consumes a significant amount of power. It is therefore desirable to find a way to lower the power consumption of these magnets. This report presents a feasibility study of the use of a permanent magnet/electromagnet hybrid for this purpose [2, 3]. At the nominal energy of the XFEL, 17.5 GeV, the electrons require a magnetic dipole field of 1 T in order to bend 1°/m. Integrating permanent magnet material (PMM) into an electromagnet to produce a 1 T bias field in the pole gap results in a bending magnet that consumes no power at the nominal energy. Magnet coils can then be used to increase or decrease the magnetic field in the pole gap. The aim has been to design a hybrid magnet that uses less power than a conventional electromagnet between 10 and 25 GeV (0.58 and 1.46 T).

A passive safety system must exist in order to prevent the electron beam from reaching the experimental hall in case of component failure. With conventional electromagnets in the bending unit it is necessary to place an additional permanent magnet further down the photon beam line for safety. The advantage of a hybrid magnet is that the bias magnetic field of the permanent magnet also works as an integrated safety system.

*This project was performed within the framework of the Stockholm-Uppsala Centre for Free Electron Laser Research. For more information, please visit: http://www.frielektronlaser.se

MAGNETIC FIELD CALCULATIONS

In a conventional dipole electromagnet the magnetic field is confined in a steel yoke ($\mu_{\rm rel} \approx 1000$) and a small air gap ($\mu_{\rm rel} \approx 1$). If the air gap is increased more current is needed to maintain the field strength (the slope of the magnetization curve dB/dI becomes smaller). Because the permeability of PMM is similar to the permeability of air, the insertion of PMM in the yoke results in lower dB/dI. Despite this it can be favourable to use a hybrid magnet under certain conditions.

Consider a C-shaped dipole electromagnet and assume that the magnitude of the field in the gap is the same as in the yoke. The Maxwell equation important in this case can be presented in integral form by applying Stokes' theorem:

$$\oint \frac{\vec{B}}{\mu\mu_0} \cdot d\vec{l} = \int_S \vec{J} \cdot d\vec{S} = NI, \qquad (1)$$

where I is the current and N the number of turns. For an electromagnet equation 1 can be written as,

$$NI = \frac{B}{\mu_0} l_g + \frac{B}{\mu_s \mu_0} l_s, \qquad (2)$$

where l_g the size of the gap, l_s the average length of the steel yoke, μ_s permeability of steel, and μ_0 is permeability of air. By replacing part of the steel yoke with PMM a bias magnetic field passes through the yoke and the gap. The relationship between B and H in the direction parallel to the easy axis (the main axis of magnetization) of a PMM is linear in a wide range with slope $\mu_p \approx 1$. The magnetization curve can therefore be written as,

$$B_p = \mu_0 \mu_p H_p + B_r, \qquad (3)$$

where B_p is the magnetic field, H_p is the magnetic field intensity, and B_r is the remanent field of the PMM. The magnetic equation for the hybrid magnet can written, similar to equation (1), as

$$NI = \frac{B}{\mu_0} l_g + \frac{B - B_r}{\mu_0 \mu_p} l_p + \frac{B}{\mu_0 \mu_s} l_s, \qquad (4)$$

where l_p is the length of the permanent magnet material along the easy axis. Equations (2) and (4) show that the more PMM is added to increase the bias field the more current needs to go through the coils for a specific correction of the magnetic field. This is illustrated in figure 1 where the ratio of the power consumption of the two types of magnets is plotted as function of beam energy. It is clear that this simple type of hybrid magnet is not a good option for 10-25 GeV electrons.

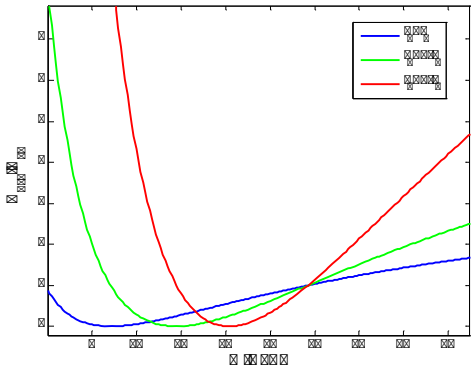

Figure 1: The ratio of the power of a conventional electromagnet and a hybrid magnet with the same geometry as function of beam energy. The hybrid magnet is favoured for ratios lower than 1.

A better alternative is to concentrate the magnetic field with several blocks of PMM. Here an alternative design made of rectangular blocks of PMM is presented, similar to one presented by K. Halbach [4]. The configuration of the blocks is shown figure 2. Calculations were performed

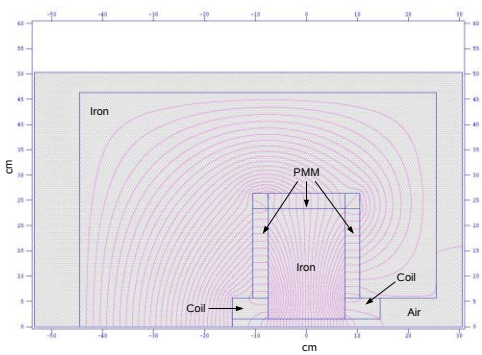

Figure 2: A 2D view of a hybrid dipole made from rectangular blocks of permanent magnets.

using the Pandira program [5] to optimize the magnet with respect to the amount of PMM and dB/dI. Vacomax 225 (Sm_2Co_{17}) with remanent field B_r=1.03 T and H_c=720 kA/m was used as input in Pandira and B as function of H was assumed to be linear in the second quadrant of the magnetization curve. In order to determine the size of the blocks to minimize the amount of PMM a number of geometries were used as input in Pandira. Figure 3 shows the parameters a, c and d that were changed in the simulation. The pole width b was fixed. Results of the calculations are shown in figure 4 and it shows a distinct limit for the minimum amount of PMM for a certain bias field. The second important parameter is the efficiency of the coils of the hybrid magnet. The magnetic field derivative (dB/dI) is approximately constant in the working range of the magnet and was calculated for all configurations. Figure 5 shows the magnetic field strength B at zero current versus dB/dI. To highlight the configurations using a low

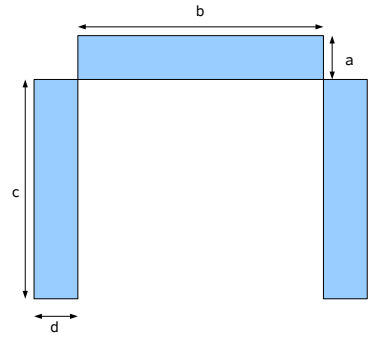

Figure 3: Parameters adjusted in the calculations to optimize the hybrid magnet.

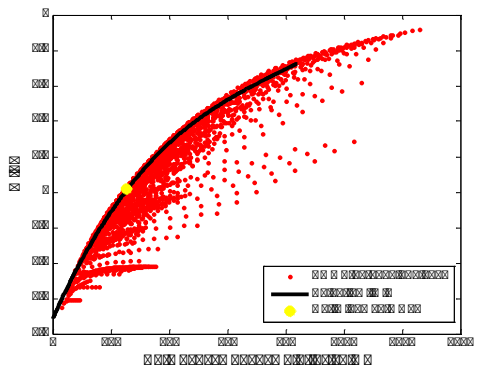

Figure 4: Field strength and mass of PMM per unit length plotted for different hybrid configurations.

amount of PMM the points left of black curve in figure 4 were plotted as black rings in figure 5. From investigating

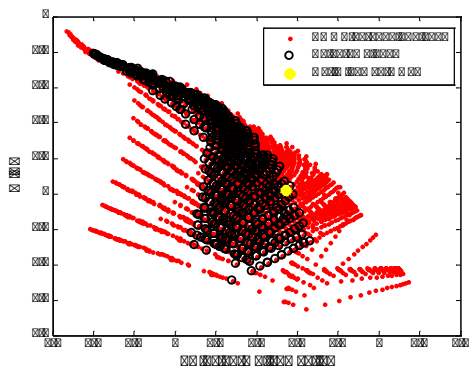

Figure 5: Field strength B and dB/dI for different hybrid configurations.

configurations with bias field close to 1.02 T (17.5 GeV) it is concluded that a possible design is made from blocks with the same thickness as the pole gap (3 cm). Having a,d<3 cm enhances dB/dI, but more of the field from the PMM leaks through the block of PMM instead of passing through the pole gap. This can be compensated for example by increasing c, but results in an increase of the to-

tal amount of PMM. On the other hand a configuration of blocks slightly thicker than 3 cm uses less PMM, but has a lower dB/dI.

Figure 6 shows the characteristics for the optimized hybrid magnet in the interval important for the XFEL bending magnet together with an ideal electromagnet (infinite permeability of iron). The difference in power consumption

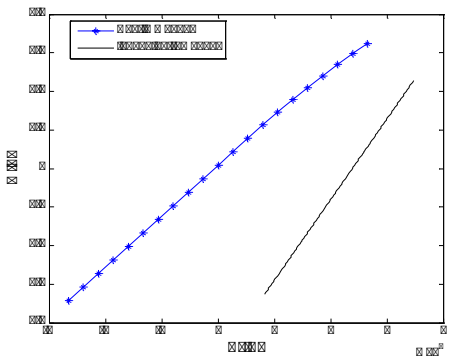

Figure 6: Characteristics for an optimized hybrid magnet and an ideal electromagnet.

between a hybrid magnet and a conventional magnet can be illustrated by plotting the ratio of the power of the hybrid magnet over the power of an electromagnet as function of electron beam energy. Figure 7 shows that this particular hybrid configuration using Vacomax 225 is better than a conventional electromagnet for beam energies larger than 11 GeV.

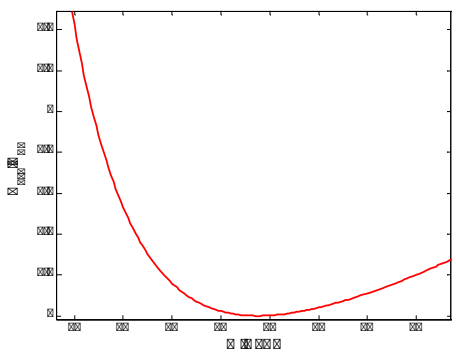

Figure 7: The optimized hybrid magnet compared with a conventional electromagnet. The hybrid magnet is favoured for ratios lower than 1.

SUMMARY

Here a proposal for a permanent magnet/electromagnet hybrid for the XFEL beam dump magnet has been presented. The hybrid magnet has a 1 T bias field and consumes no power at the nominal energy of the XFEL. Magnet coils are used to change the magnetic field when changing the beam energy. The hybrid magnet consumes less power than a conventional electromagnet for electron energies $>$11 GeV. The hybrid magnet can be optimized even further by using permanent magnet material with higher B_r and reducing the bias field in order to make the magnet power efficient between 10 and 25 GeV. The issue whether the hybrid magnet represents a better choice than the conventional electromagnet still needs to be addressed. The hybrid magnet include PMM, is more complicated to manufacture and therefore more expensive than an electromagnet. The higher cost to manufacture the hybrid magnet must be returned by a lower power consumption. Additionally, the hybrid magnet is situated close to the electron beam dump region and is therefore exposed to neutron radiation backscattered from the dump. The permanent magnet material must be able to withstand this [6]. Any loss of bias field due to demagnetization by radiation must be compensated for by the coils and the hybrid will loose its advantage.

If the hybrid magnet can be made cost efficient and radiation resistent it represents an interesting solution for the bending magnet unit as well as the passive safety system of the European XFEL.

REFERENCES

[1] European XFEL Technical design report, edited by M. Altarelli et. al., DESY 2006.

[2] F. Hellberg, "Investigating the possibility of a hybrid magnet design for BV/BW dipole magnets at the XFEL, MSL-06-1, 2006.

[3] F. Hellberg, "Comparison of two hybrid magnet designs", MSL-07-01, 2007.

[4] K. Halbach, J. Appl. Phys. **57**, 1985, p. 3605.

[5] POISSON/SUPERFISH group of codes, Los Alamos National Laboratory.

[6] J. Alderman, P. K. Job, R. C. Martin, C. M. Simmons, G. D. Owen, Nucl. Instr. Meth. in Phys. Res. A **481**, 2002, p. 9-28.

INSTALLATION OF THE OPTICAL REPLICA SYNTHESIZER IN FLASH

G. Angelova, V. Ziemann, Uppsala University, A. Meseck, BESSY
M. Hamberg, P. Salén, P. van der Meulen, M. Larsson, Stockholm University
S. Khan, J. Bödewadt, A. Winter, Universität Hamburg
E. Saldin, H. Schlarb, B. Schmidt, E. Scheidmiller, M. Yurkov, DESY

Abstract

During the shutdown in spring 2007 the optical replica synthesizer, a novel device to diagnose ultra-short electron bunches, is assembled in the FLASH accelerator. We report on the status of the construction work with emphasis on the two electro-magnetic undulators needed for micro-bunching and replica-pulse generation.

INTRODUCTION

Monitoring and tuning the bunch size are essential for the reliable operation of linac-based SASE free-electron lasers such as the FLASH [1], XFEL [2], or LCLS [3]. This need has triggered the development of new diagnostic methods based on a transversely deflecting cavity [4] or electro-optical sampling [5]. The optical replica synthesizer (ORS), a complementary scheme that was introduced in Ref. [6], is similar to an optical klystron FEL seeded by an infrared laser as is shown in Fig. 1. In the modulator the interaction of the laser with the transversely oscillating electrons causes an energy modulation. A small chicane turns this energy modulation into a corresponding density modulation at the wavelength of the light. In a following radiator undulator the micro-bunched beam radiates coherently and the emitted light pulse has the same longitudinal profile as the electron beam. Hence the name optical replica synthesizer. The replica pulse is then extracted from the vacuum pipe by an off-axis mirror and directed to an optical table with optical diagnostics where it will be analyzed by a commercially available second-harmonic generation FROG (frequency resolved optical gating) device, called GRENOUILLE [7].

During the spring shutdown 2007 most components such as the undulators, external laser building, seed laser transport system, and the optical stations were installed and we report on these activities.

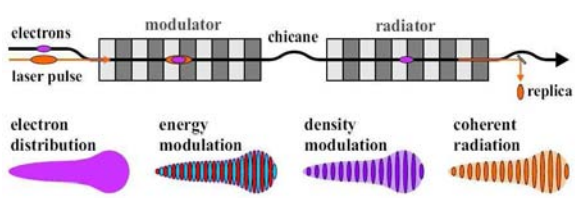

Figure 1: The principle of the optical replica.

UNDULATORS AND CHICANE

The undulators were designed, assembled and tested at Scanditronix Magnet AB, Sweden and were delivered to DESY in March. They have a length of 1450 mm, a width of 454 mm, a height of 817 mm, and weight 480 kg. The gap is 40 mm in order to accommodate the standard 38 mm vacuum pipe without having to break vacuum. The period length is 200 mm with 14 poles and 28 coils connected in 4 separate coil circuits. This allows adjusting the field integrals $I_1 = \int_0^L B(z)dz$ and $I_2 = \int_0^L \int_0^z B(z')dz'dz$ by controlling the end coils in the 1/2, -3/4, +1 pattern. The first and last coil (with 1/4-excitation) have independent supplies and the second and 13th coils are powered in series by another supply. Finally, the ten central coils are connected in series to a fourth power supply. The maximum magnetic field is 0.5 T and nominal field 0.3 T. The undulators can be mounted horizontally or vertically to induce vertical or horizontal beam oscillations, respectively.

Upon arrival at DESY field measurements were performed with a Hall probe and power supply settings were found that zero the field integrals in order to avoid perturbing the electron beam outside the undulator. The individual Hall probe measurements have an accuracy ε of a few Gauss, but the calculation of the first and second field integrals has an accuracy of $\sigma(I_1) = \varepsilon\sqrt{Ldz}$ and $\sigma(I_2) = \varepsilon L\sqrt{Ldz}/\sqrt{3}$ where dz is the distance between consecutive Hall-probe measurements [8]. This allows us to measure the field integrals with an accuracy on the order of 10^{-5} Tm or 10^{-5} Tm^2, respectively, provided we use a small step size of $dz = 2$ mm. We then determined settings of the power supplies for peak fields of 0.1, 0.2,

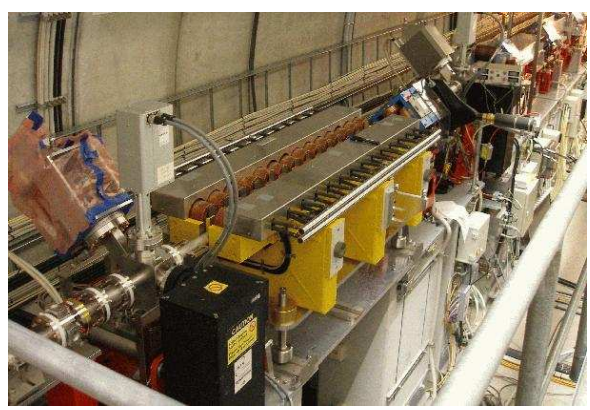

Figure 2: The modulator which causes vertical oscillations.

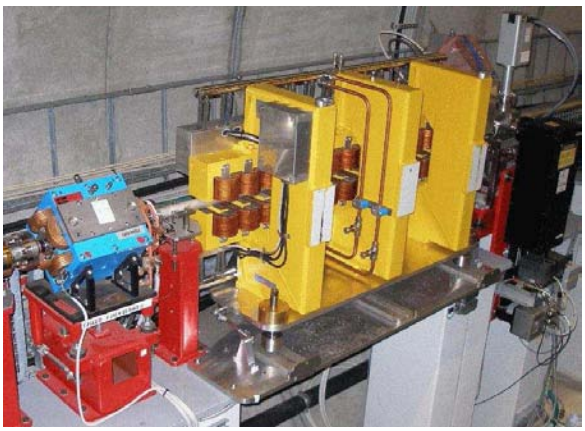

Figure 3: The radiator which causes horizontal oscillations.

0.3, 0.35, 0.4 T for which the field integrals are less than 0.5×10^{-4} Tm and 2×10^{-4} Tm^2. In order to achieve reproducible settings we always cycle the power supplies from zero to the 0.48 T-value, back to zero and then up to the set-value.

After the completed field measurements the undulators were installed in the FLASH beam line after the dog-leg chicane used for momentum collimation. Figure 2 shows the modulator which causes vertical beam oscillations at its final location in the FLASH beam line and Fig. 3 shows the radiator which causes horizontal beam oscillations. This will allow to separate the weak replica pulse from the strong seed laser pulse by polarizers.

The chicane consists of four standard steering dipole magnets which allow a maximum excursion of the beam of 15 mm, thereby producing an R_{56} of 300 μm.

SEED LASER, LASER TRANSPORT AND OPTICAL STATIONS

The seed laser consists of an erbium-fiber oscillator [9], developed at DESY, that can be synchronized to the accelerator-RF. The pulse from the oscillator is frequency-doubled and then fed into a regenerative Ti:Sa amplifier (Clark CPA-2001), based on chirped-pulse amplification and pumped by a Nd:YAG laser. This system, initially prepared at Stockholm University, delivers a pulse output of 0.8 mJ with pulse length of about 170 fs, center frequency 772 nm and 1 kHz repetition rate. The laser will be shipped to DESY in August and then installed in a newly erected 150 m^2 laser building next to the FLASH tunnel. For replica operation the laser stretcher and compressor will be re-tuned to provide about 2 ps pulses and will be synchronized to the beam. The anticipated repetition rate is 5 to 10 Hz. A sketch of the layout along the tunnel is shown in the top of Fig. 4 and a view from above in the lower part of Fig. 4, which shows the 12 m long laser transport system from the laser to the entrance port to the beam vacuum system in the dog-leg chicane. Just before the entrance window a remotely adjustable three-lens telescope will permit adjusting the diameter and the waist position of the laser inside the modulator undulator. The laser transport system was installed and aligned during the recent shutdown.

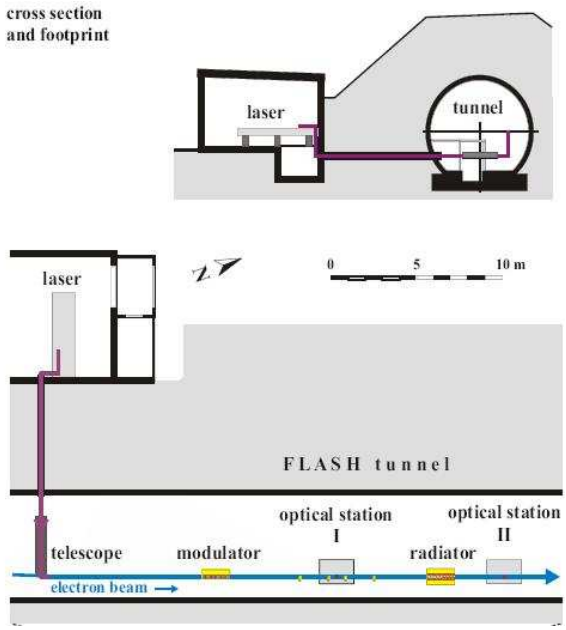

Figure 4: View along the tunnel and top view of the layout of the optical replica synthesizer experiment.

Also indicated in Fig. 4 are two optical stations with optical tables and OTR chambers with a set of different foils that can be viewed by a CCD camera in order to analyze the seed laser or replica pulse and the beam profile. In station I located in the center of the chicane we can image the seed laser, modulator radiation, and the electron beam onto a CCD camera to optimize the spatial overlap of laser and electrons and onto fast photo diodes to optimize the temporal overlap. In station II we will analyze the replica pulse

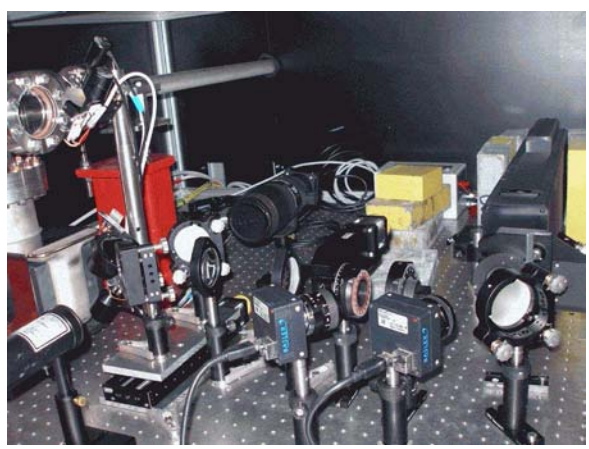

Figure 5: Optical station 2.

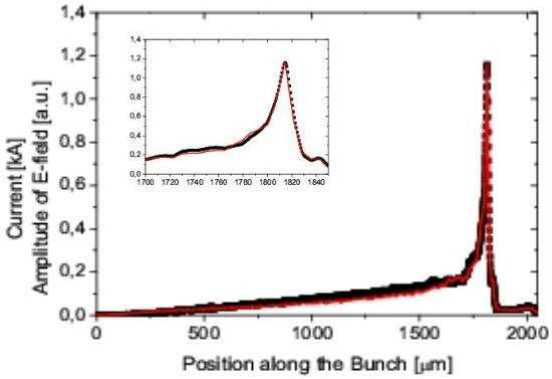

Figure 6: A realistic longitudinal bunch profile (red solid line) and the temporal profile of the emitted replica pulse (black asterisks). The inset figure shows a zoom of the peak region.

generated in the radiator. A picture of optical station II that was installed during the recent shutdown is shown in Fig. 5. At the top of the figure, the beam pipe is visible with the beam moving from right to left. In the top left corner a window from the vacuum tank containing remotely controlled mirrors to extract the replica pulse is visible. The pulse is then vertically deflected by remotely controlled mirrors onto an optical table which contains power meters, fast photo-diodes and the GRENOUILLE [7] that will be used to determine the temporal profile of the replica pulse and thereby the bunch profile. The GRENOUILLE is the black box visible at the right side of Fig. 5.

SIMULATIONS

We perform numerical simulations of the replica process using the Free Electron laser code GENESIS 1.3[10] where the energy modulation in the modulator undulator and the output power from the radiator undulator are calculated. The magnetic chicane is modelled by a transfer matrix. Fig. 6 shows a realistic current profile at the entrance of the modulator determined in start-to-end simulation [11] as the line and the replica pulse as asterisks, both normalized to the same peak value. We observe that the replica pulse faithfully reproduces the initial electron distribution. Simulations, however showed that it is necessary to make the electron beam in the radiator as small and as round as possible in order to achieve the faithful representation, because otherwise diffraction effects of the finite beam size will deteriorate the quality of the reproduction. A slight effect of smearing due to the finite slippage of the electrons with respect to the emitted light is also present, but can easily be de-convoluted, which was, however, not done here.

OUTLOOK

There are 15 shifts alloted for the optical replica synthesizer during September and October when we will start by commissioning the undulators and software to control the beam steering and the beta functions to compensate the weak focusing of the undulators. We then need to verify parasitic operation of the undulators and the chicane during SASE operation. In a second block we will commission the seed laser and optical station I and achieve spatial overlap of laser and electron beam. In a third block of shifts we plan to achieve temporal overlap of seed laser and beam, commission optical station II and eventually record the first FROG traces on the GRENOUILLE.

ACKNOWLEDGMENTS

With pleasure we acknowledge the extensive help of the DESY groups involved in the FLASH installation, as well as the support of the technical groups of the Institut für Experimentalphysik at Hamburg Universität and the help of R. Ruber and M. Johnson, Uppsala University. M. Dohlus, DESY kindly provided beam distributions from start-to-end simulations. This work is supported by the UU-SU-KTH FEL-center.

REFERENCES

[1] V. Ayavazyan, et.al., Eur. Phys. J. D37 (2006) 297.

[2] P. Audebert, et.al., "TESLA XFEL: The first stage of the X-ray laser laboratory - Technical Design Report," DESY 2002-167.

[3] The LCLS Design Study Group, "LCLS Design Study Report," SLAC-R-593, 2002.

[4] M. Hüning, et al., "Observation of femtosecond bunch length using a transverse deflecting structure,"Proceedings of the 2005 FEL conference, 538.

[5] G. Berden, et al., "Electro-Optic Technique with Improved Time Resolution for Real-Time, Nondestructive, Single-Shot Measurements of Femtosecond Electron Bunch Profiles," Phys. Rev. Lett. 93 (2004) 114802.

[6] E. Saldin, E. Schneidmiller, M. Yurkov, "A simple method for the determination of the structure of ultrashort relativistic electron bunches," Nucl. Inst. and Methods A 539 (2005) 499.

[7] R. Trebino, "Frequency Resolved Optical Gating", Kluwer Academic, Boston, 2000.

[8] V. Ziemann, "How accurately can we measure the field integrals of an undulator?" unpublished note, dated 26.3.2007.

[9] A. Winter, et.al., " High-precision laser master oscillators for optical timing distribution systems in future light sources", EPAC 2006, p. 2747.

[10] S. Reiche, Nucl. Inst. and Methods A 429 (1999) 243.

[11] M. Dohlus, FLASH Start-to-end simulations, private communication.

7TH HARMONIC BUNCHER EXPERIMENT AT THE UCLA NEPTUNE LABORATORY

P. Musumeci*, S. Ya. Tochitsky#, R. Tikhoplav*, J. B. Rosenzweig*, C. Joshi#

Abstract

Since typically FEL undulator magnets have period length in the cm range, and the normalized magnetic field strength K is usually close to unity to guarantee a good coupling, a very high energy electron beam is needed to access the UV and x-ray region of the electromagnetic spectrum. One way to reduce the beam energy necessary for short wavelength light sources consists of exploiting the FEL harmonic interaction. An experiment aimed at demonstrating the efficiency of harmonically coupled schemes is proposed for the Neptune Laboratory at UCLA. We plan to inject the 12.4 MeV beam from the split photoinjector in an already available undulator with period = 3.3 cm and K = 1.8. The FEL resonant wavelength with these parameters is 74.2 μm. A copropagating high power 10.6 μm CO2 laser bunches the beam via 7th harmonic FEL/IFEL interaction. Preliminary calculations show that even though the interaction is weakened by the high harmonic number, only 5 -10 MW of laser power are required in order to induce full bunching on the beam in the 10 period long undulator.

INTRODUCTION

Free-electron laser (FEL) amplifiers operating at short wavelengths (<100 nm) are undoubtedly one of the top research fields nowadays because of the new possibilities opened by generation of powerful, short pulses in a range of the electromagnetic spectrum important for material science, biology and chemistry. The lasing wavelength of an FEL depends primarily on the undulator magnet characteristics --period and field amplitude-- and on the electron energy. Since the undulator magnet has typically period lengths in the cm range, and the normalized magnetic field strength *K* is usually close to unity to guarantee an efficient coupling, a very high energy electron beam is needed to access the UV and x-ray region of the electromagnetic spectrum.

One way to reduce the necessary beam energy is to utilize the FEL harmonic interaction[1-5]. The FEL resonance condition, i.e. the condition for efficient energy exchange between the transverse EM wave and the electrons, takes place at electron energies such that the wiggling induced by the laser field has the same frequency as the wiggling induced by the undulator in the electron rest frame. However, a planar undulator resonance can also occur when the laser frequency is a multiple of the undulator wiggling frequency and electrons of a given energy interact with the fundamental radiation frequency and with its higher harmonics[6]. In some cases, when the laser frequency is constrained by the source availability and the energy of the beam is so low that in order to design an FEL at the resonant condition the undulator parameters are unfeasible or the normalized vector potential *K* has to be very small to reduce the magnetic amplitude induced frequency red-shifting, harmonic coupling becomes the only viable solution to ensure a strong interaction.

Even for FEL cascade schemes, one of the factors limiting the frequency multiplication of all cascade schemes is related to the necessity of operating all the stages of the cascade with the same electron beam energy. The change in the resonant wavelength for the different sections must be compensated by variations of the undulator period and *K* parameter. Using the conventional techniques for undulator magnet construction, the span of these variations is limited and harmonic coupling has been considered as a possible solution [7].

Here we propose and discuss an experiment to be carried out at the UCLA Neptune Laboratory to test the efficiency and feasibility of a high order harmonic FEL/IFEL interaction. For this purpose an existing short undulator with a period of 3.3 cm and K = 1.8, for which the resonant wavelength with a 12.4 MeV electron beam is 74.2 μm, will be seeded with a CO2 laser radiation. This will allow to study the microbunching obtained by 7th harmonic FEL/IFEL interaction, since 10.6 x7=74.2μm.

EXPERIMENTAL LAYOUT

Table 1: Parameters for Neptune 7th harmonic interaction experiment

Beam energy	12.4 MeV
Beam energy spread	< 0.2 %
Emittance	5 mm-mrad
Current	100 A
Laser wavelength	10.6 μm
Laser seed Power	10 MW
Laser size (at focus)	650 μm
Undulator period	3.3 cm
Undulator *K*	1.8
Undulator length	33 cm

* UCLA Department of Physics and Astronomy, Los Angeles, CA 90095-1547
# UCLA Department of Electrical Engineering.

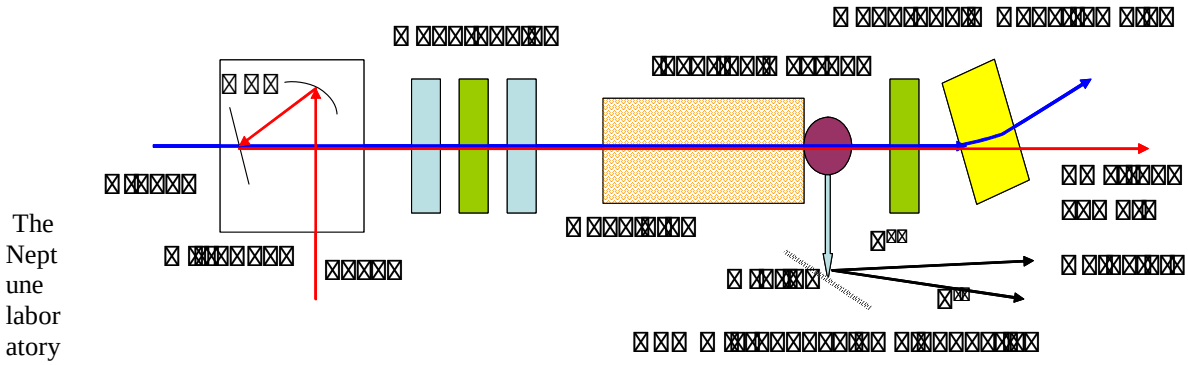

Figure 1: A simplified experimental layout for the 7th harmonic buncher experiment.

hosts a split rf photoinjector capable of producing 10-14 MeV beam with a peak current in excess of 100 A and an emittance as low as 5 mm-mrad.

The CO_2 laser system, which has been reported in detail elsewhere[8], has the capability of producing 1 TW mid-infrared laser pulses. However, the repetition rate at this high power is limited to one shot per few minutes by the main discharge capacitor cooling time. Recently a new high-pressure CO2 laser amplifier was installed which is capable to produce ~1mJ at 1 Hz. By shortening the seed pulses to <100 ps in principle up to 10 MW of drive CO_2 laser power is available to drive the interaction. Such a power level, as will be shown below, is sufficient to bunch the electron beam. At the same time the high pulse repetition rate allows parametric studies of the system which would be otherwise very difficult in a single-shot experiment.

A conceptual design of the experiment is shown in Fig. 1. A laser beam is focused by an off-axis parabolic mirror (F/50 scheme). After the FEL interaction in the undulator the electron beam is sent to a high resolution spectrometer (horizontally focusing quadrupole + bending dipole) to detect the energy modulation imparted by the laser. Electron microbunching at 10.6 μm is observed by measuring the coherent transition radiation spectrum from a foil screen inserted at 25 cm from the exit of the undulator. Because of the background noise due to the high drive laser power, detection of the harmonics is suggested as a way to measure the beam microbunching. A diffraction grating separates the different wavelength content in the beam generated radiation and MCT detectors are placed at the angles corresponding to the 2nd and 3rd harmonic of the CO_2 laser line. The main CO_2 laser beam is sent to a streak camera to enable temporally resolved diagnostic.

FEASIBILITY OF THE 7TH HARMONIC BUNCHING

It can be shown that in planar geometries the coupling between the beam electrons and an electromagnetic wave at a harmonic of the resonant undulator frequency is actually very strong and comparable to the fundamental coupling if the normalized magnetic field amplitude K is larger than 1. The coupling coefficients can be written as:

$$JJ_n = J_{n-1/2}(n\cdot\xi(K)) - J_{n+1/2}(n\cdot\xi(K))$$

for n = 1,3,5,7…where $\xi(K) = K^2/4 + 2K^2$.
Moreover, for a given laser frequency and electron beam energy one has to maintain the resonant condition so the undulator K changes as the square root of the harmonic number. The effective interaction coupling strength is $KJJ_n(K)$.

In Fig. 2, assuming an undulator period of 3.3 cm, we plot the coupling coefficients for different K values and the coupling strengths for the first odd harmonics. The normalized vector potential K to obtain resonance at the fundamental is only 0.1. If the coupling is on the 7th harmonic, K = 1.8 and the effective coupling strength is 2 times higher. This example illustrates the main advantages of choosing an harmonic coupling when designing an undulator/beam interaction.

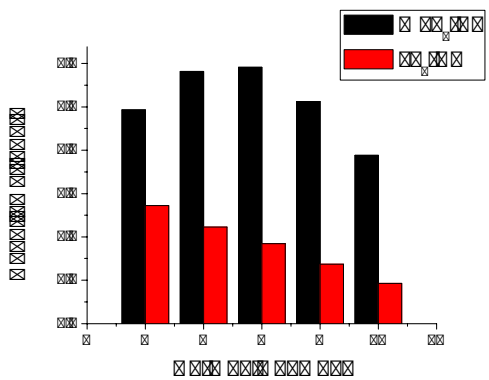

Figure 2: Coupling coefficients and coupling strength.

Fundamental parameters of the interaction like the energy width of the ponderomotive bucket and the synchrotron oscillation frequency depend on the coupling strength. A simple estimate of the power required to bunch the beam

can be obtained requesting that ¼ synchrotron oscillation is obtained during the undulator length. The synchrotron period is given by:

$$z_s = \frac{\lambda_w}{n}\frac{\sqrt{1+K^2/2}}{\sqrt{2KK_rJJ_n}}$$

where $K_r = eE_0\lambda_0/2\pi m_0c^2$ is the normalized electric field associated with the radiation. With the request that along the undulator particles would perform ¼ of synchrotron oscillation i.e.

$$z_s/4 = L_u$$

we can solve for the minimum electric field to achieve microbunching. With the parameters of the short undulator available at Neptune, reported in Table 1, we obtain K_r = 1.2e-4, and E_0= 40 MV/m which corresponds to a laser intensity of I = 0.2 GW/cm^2. The estimate reported here shows that even though the interaction is weakened by the high harmonic number, it is required to use only modest levels of power to induce full bunching on the beam using the 10-periods long undulator.

The amplitude of the ponderomotive bucket in the energy plane is given by:

$$\frac{\delta\gamma}{\gamma} = \sqrt{\frac{2KJJ_nK_r}{1+K^2/2}}$$

which for our parameters is very small (~ 0.5 %) and imposes an important experimental constraint on the quality of the input beam. Thus the energy spread of the electron beam must be well below 0.5 % rms.

Another important constraint in the design is imposed by the amplitude of the beam wiggling oscillations. As shown in Fig.3, the focused CO2 laser beam must cover the entire trajectory of the wiggling electron beam in order to achieve the same acceleration gradient for particles at different distances from the axis. To maintain the required laser intensity level with a spot size of 650 μm at the focus and a relative Rayleigh range of 10 cm, a minimum drive laser power of ~3 MW is required.

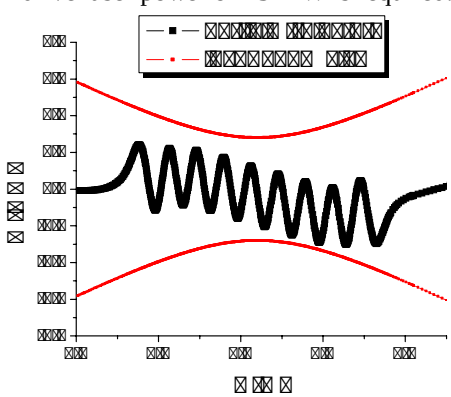

Figure 3: Particle trajectory and laser beam size inside the undulator.

7TH HARMONIC BUNCHER SIMULATIONS

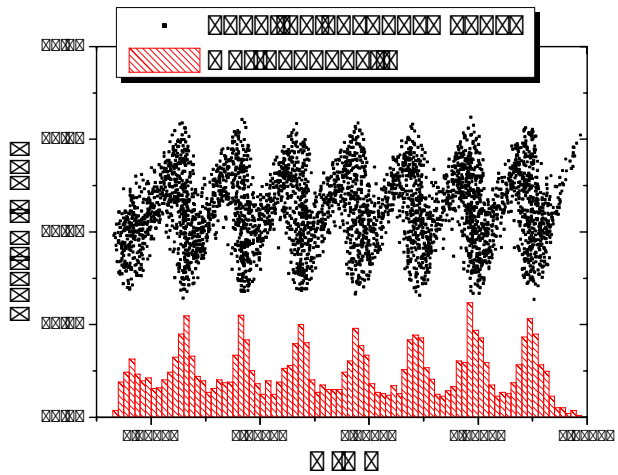

Figure 4: Longitudinal phase space at the undulator exit for 10 MW input CO2 power and initial e-beam energy spread of 0.2 %.

The code GENESIS 1.3 has been used to simulate the three dimensional interaction between the electrons and the laser pulse in the undulator. The code has been recently upgraded to be able to simulate the interaction of the particles with the harmonic of the fundamental field [9]. In Fig. 4 one can see that electrons at the exit of the undulator are fully bunched when a 10 MW CO2 laser is used as a seed.

Along with the goal of first experimental demonstration of the 7th harmonic interaction of a relativistic electron beam and a laser in an undulator, the proposed experiment addresses a couple of other important issues.

For a 0.5 mJ, 100 ps long laser pulse interacting with a 10 ps long electron beam, the energy of the laser available for the electrons to absorb corresponds to 50 μJ of IR power. This energy is the amount required to accelerate a 500 pC beam by 0.1 MeV.

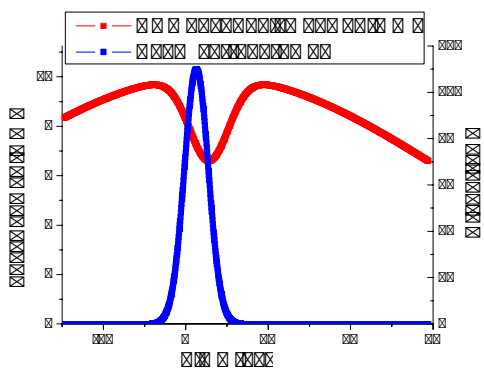

Figure 5: Beam loading in the 7th harmonic IFEL accelerator for a 100 Amp beam current and 12.3 MeV input energy. The beam current longitudinal profile is also shown.

Detuning slightly the input electron beam energy and injecting the beam 100 KeV below resonance, the particles will extract energy from the laser via 7th harmonic interaction. With a temporally resolved diagnostics of the infrared power, one could observe the pump depletion (beam loading) of the laser wave. Up to 30 % of power can be absorbed from the laser as it is shown in the time domain simulation reported in Fig. 5.

Finally, the 10.6 μm buncher running at 1 Hz will allow a detailed study of various microbunching diagnostics [10]. The coherent transition radiation foil has to be located as close as possible to the undulator exit, since the beam debunches quickly due to its low energy and strong longitudinal space charge forces. At 20 cm from the output the bunching factor is still greater than 0.3 and any radiation emitted by the beam (via transition or Cherenkov mechanisms) will be enhanced by the coherent form factor at the bunching wavelength 10.6 μm and the relative harmonics. In Fig. 6 we show the evolution of the bunching coefficients at the 10.6 μm, and its second and third harmonic along the undulator. Because of the strong space charge force and of the low beam energy, debunching quickly takes place after the particles leave the interaction region.

The effect of the finite transverse beam size on the radiation emission is particularly interesting when the emission mechanism has a preferred angular direction as it is the case of a Cherenkov radiator.

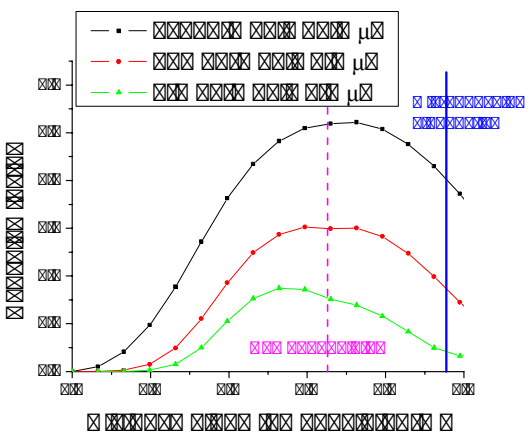

Figure 6: Bunching coefficients at the drive laser frequency and relative harmonics.

CONCLUSIONS

We have proposed and discussed here an experiment to be carried out at the UCLA Neptune Laboratory with the goal to measure the efficiency of a high order harmonic FEL/IFEL coupling. The experiment also addresses important issues like the development of diagnostics for longitudinal microbunching and the beam loading in a vacuum laser accelerator. The implementation costs are very low since most of the hardware is in house (undulator already installed on the beamline after a previous experiment [11]). Some experimental efforts are needed to set up the microbunching diagnostics, however for the relevant wavelengths — harmonics of CO_2 laser frequency — a number of components, optical elements and detectors are already available in the Neptune laboratory.

ACKNOWLEDGEMENTS

This work has been partially supported by DOE grant No. DE-FG03-92ER40727 and DOE grant No. DE-FG03-92ER40693.

REFERENCES

[1] W. B. Colson, G. Dattoli and F. Ciocci, Phys. Rev. A 31, 828 (1985)
[2] H. P. Freund, S. G. Biedron and S. V. Milton, IEEE J. Quantum Electronics. 36, 275 (2000).
[3] Z. Huang and K. J. Kim Phys. Rev. E, 62, 7295 (2000)
[4] P. G. O'Shea et al, Phys. Rev. Lett., 71, 3661 (1993)
[5] B. W. J. McNeil, G. R. M. Robb, M. W. Poole M W Phys. Rev. Lett., 96, 084801 (2006)
[6] P. Musumeci, C. Pellegrini, J. B. Rosenzweig, Phys. Rev. E, 72, 016501 (2005)
[7] L. Giannessi, P. Musumeci, New Journal of Physics, 8, 294, (2006)
[8] S. Y. Tochitsky et al., Opt. Lett. 24, 1717 (1999).
[9] S. Reiche, P. Musumeci and K. Goldhammer, Proceedings of 2007 Particle Accelerator Conference, Albuquerque, NM (2007)
[10] R. Tikhoplav et al., These proceedings.
[11] C. Sung et al. Proceedings of Particle Accelerator Conference 2007, Albuquerque, NM (2007)

The UCSB MM-FEL Injection Locking System *

G. Ramian, S. Takahashi, and M. Sherwin
Dept. of Physics (IQCD and CTST)
University of California, Santa Barbara, CA 93106, USA

Abstract

An Injection locking system has been implemented on the Millimeter Wave Free-Electron Laser (MM-FEL) at the University of California, Santa Barbara (UCSB). It it is based on a commercially available varactor multiplier source and quasi-optical isolator operating at 240 GHz. Lasing on multiple longitudinal modes is shown to collapse to a single repeatable mode by introducing a low power CW signal into the FEL resonator through a silicon-plate coupler. High power and extremely narrow linewidth operation will enable new experimental opportunities such as FEL based pulsed electron paramagnetic resonance spectroscopy.

INTRODUCTION

Injection locking of the UCSB MM-Free-Electron Laser has been demonstrated as shown in Fig. 1. Lasing that normally occurs on a number of longitudinal modes is seen to collapse to a single mode at a single repeatable frequency with less than 1 MHz linewidth. This result is important in demonstrating the suitability of an FEL for applications where extremely narrow linewidth is required.

Linewidth

The UCSB MM-FEL is based on an electrostatic accelerator. As such it does **not** exhibit the picosecond microstructure, characteristic of RF accelerator driven FELs, that Fourier transform limits their linewidth to hundreds of GHz. Instead, a several microsecond quasi-DC macropulse allows sub-MHz width.

The MM-FEL [1, 2] uses a 6.25 meter long resonator which can be described by its Fabry-Perot characteristics. It has a free-spectral range (fsr) of $c/(2L_r)$ = 24 MHz. It has finesse **F** = $\pi/(2\ \mathrm{asin}(1/F))$, where coefficient of finesse $F = 4\sqrt{1-l}\ /(2(1-\sqrt{1-l}\ )-l)$. l is the power loss per pass. Because of its length, the resonator has extremely high $Q = \mathbf{F}N$ where N is the order or simply number of half wavelengths between mirrors. For nominal 25 % loss at 240 GHz, F = 193, **F** = 21.8, Q = 218000. Linewidth is then 240 GHz / Q = 1.1 MHz.

It is important to emphasize that this linewidth is an upper limit, since line-narrowing may take place as in conventional lasers. Line-narrowing can reasonably be expected when lasing is a consequence of stimulated emission and other inhomogeneous broadening effects are correspondingly small.

* Work supported by NSF grants DMR-0321365 and DMR-0520481

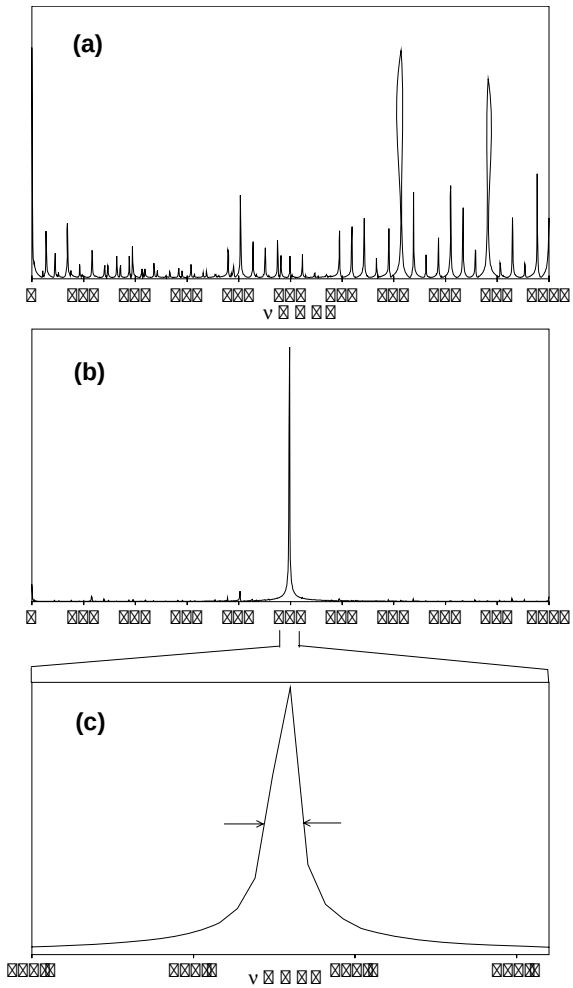

Figure 1: (a) FEL spectrum without injection locking. The spectrum show many longitudinal modes spaced by 25 MHz. (b) FEL spectrum with injection source on. Only single mode lasing with no pulse-to-pulse frequency fluctuation is observed. (c) 1 MHz width is transform limit of sampling window, indicating actual linewidth is much less.

Longitudinal Modes

Another important consequence of the long resonator is the number of longitudinal modes available for lasing. Fig. 2 shows the longitudinal mode structure in relation to the MM-FEL's gain curve. Hundreds of modes would be above threshold and might be expected to lase. However, this doesn't actually happen. Many fewer are seen to lase with only a few growing to dominance. This effect can be understood in terms of the stochastic nature of startup. Startup is from spontaneous emission, essentially noise, so

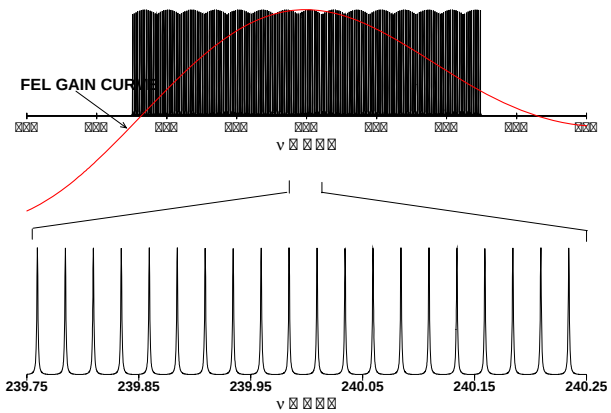

Figure 2: Resonator longitudinal mode structure in relation to gain curve. Hundreds of modes have sufficient gain to lase.

exhibits a fluctuating spectral density distribution. Its basis is "shot-noise" which represents a variance in the statistical distribution of electrons. As these electrons traverse the undulator, they become uncoupled oscillators. The small distributional non-uniformity causes random phase fluctuations that can interfere giving rise to larger amplitude fluctuations than the mere $\sqrt{n}/n$ shot noise variance would suggest. At startup, some modes then appear to enjoy a significant initial advantage over others. The process of stimulated emission then keeps multiplying the advantage. Another form of mode competition can be expected. As the advantaged modes approach saturation, they cause gain for all modes to diminishes. Since loss remains in full effect for all modes, eventually only the few advantaged ones remain above threshold while the rest die. Manifestation of this effect, however, may take longer than the available pulse duration.

Single Mode Lasing

Single mode lasing can occur naturally as has been demonstrated by for example the EA-FEL at the University of Tel Aviv [3]. Lower frequency, a shorter resonator with wider mode spacing, and other parameter differences may explain why this can happen. This clearly doesn't happen with the UCSB MM-FEL so other means of achieving single mode operation were sought. Conventional lasers use intra-cavity etalons. Use of a Fox-Smith coupler was investigated but achieving sufficiently high Q to significantly suppress adjacent 25 MHz spaced modes proved impractical. Further, proposed research with single mode capability requires that each pulse occur on the same frequency and that that frequency be precisely setable. The normal stochastic startup results in about a 0.05 % distribution of the pulse to pulse startup frequency that is unacceptable for many users' experiments.

INJECTION LOCKING

One method of improving this situation is injection-locking or seeding. This has long been used in conventional lasers [4] and is now planned for several VUV/Xray FELs in the form of harmonic injection seeding[5].

Injection locking was partially demonstrated on the original UCSB FEL [7] using a CW molecular laser as the injection source. At that time it was only possible to inject power through a tiny hole coupler which scattered most of the power into high order transverse modes. Since the source was not tunable, the FEL resonator was mechanically tuned with great difficulty. Finally, no spectrometer was available, so locking could only be inferred from a reduction in mode beating and shorter startup time. The current injection locking system overcomes all these problems so is much better suited for users' experiments.

Power Requirement

A fundamental requirement of injection locking is that the power that is finally coupled into the mode that is to lase must exceed the startup power from spontaneous emission by a some margin. The peak spectral density at zero forward angle is [3]

$$\frac{dP}{d\nu} = \frac{4\pi q^2 c\gamma^2 K^2 N n}{\lambda_u^2(1+K^2/2)}$$

where q= electron charge, c = light velocity, γ = Lorentz factor, K = undulator parameter, N = number of periods, $n = \lambda_u I_b/(q\beta_z c)$ = number of electrons radiating per period, and λ_u = undulator period. For the MM-FEL running at 240 GHz, γ = 6.773, K = 0.7071, N = 42, λ_u = 7.14 cm, and β_z = 0.9835. The resulting spectral density is then 1.39 x 10^{-13} Watts/Hz. For a mode-width of 1 MHz, power is 0.139 μWatts, making the estimated 28 μW that is available well exceed the requirement.

Injection System

Fig. 3 is an illustration of the injection locking system. The CW injection source was built by Virginia Diodes Inc. (VDI) [9], consisting of a 15 GHz phase-locked oscillator, doubler, RF amplifier, and three varactor doubler stages, which provides as much as 30 mW power at 240 GHz. The source frequency is tunable within small frequency range by employing a tunable 100 MHz digital synthesizer as a reference for the source's oscillator. This tunability is essential to match the injection source frequency to the FEL's resonator and to precisely set operating frequency for users. A key component is a quasi-optical, Faraday-rotation, isolator developed by Thomas-Keating Ltd. [8] that provides more than 50 dB isolation. Insertion loss is about 6 dB. This is essential to protect the last multiplier stage from the FEL power following startup. Table 1 shows approximate power budget for the injection signal.

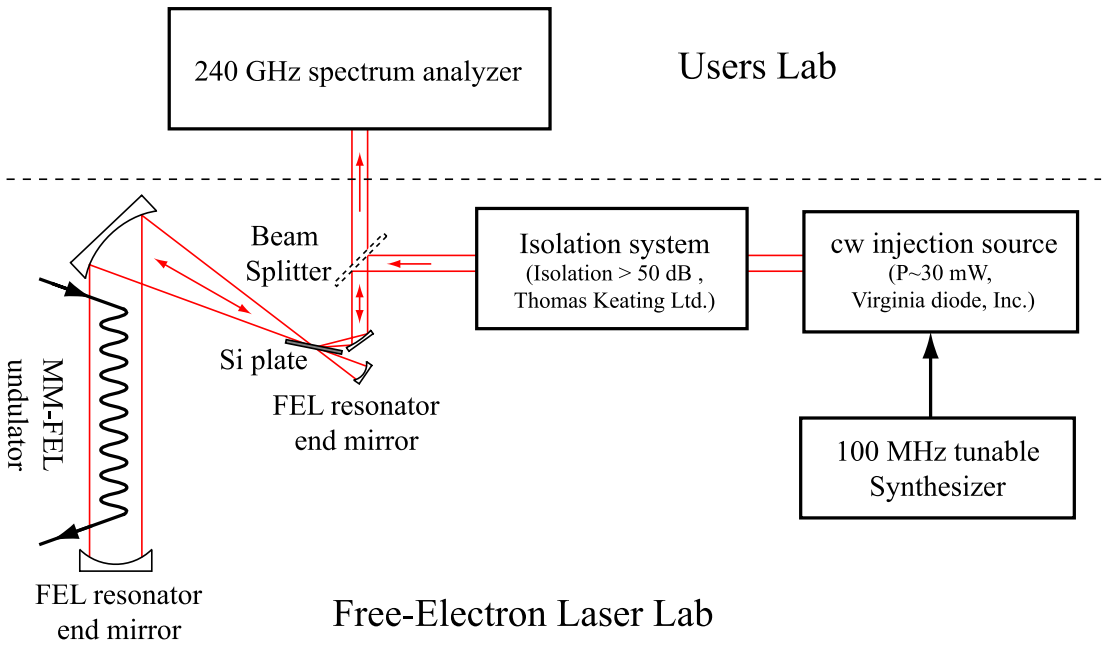

Figure 3: Schematic of the injection locking system for the UCSB MM-FEL. The injection source, the isolator and a tunable 100 MHz synthesizer are located in free-electron laser lab. Output radiation is sent to the users lab through vacuum optical transport system.

Table 1	**Power Budget**
30 mW	VDI Source output
7.5 mW	Isolator output (6 dB insertion loss)
6.9 mW	TPX window (∼92 % transmission)
690 μW	Beam splitter
552 μW	quartz window (∼80 % transmission)
28 μW	silicon plate (5 % coupling)

Optics

When used with injection locking, the FEL's resonator is used in a two arm configuration as shown in Fig. 2. The resonator is a parallel-plate waveguide terminated with cylindrical mirrors. A plano-ellipsoidal mirror couples the main arm to the secondary arm. The lowest order mode has $\cos^2$ intensity distribution in the vertical plane and Gaussian horizontally. Horizontal waists are formed in each arm. Parameters are given in table 2.

Table 2	**Resonator Parameters**
Length	L_r = 6.253 m
Mirror 1	R = 2.970 m
Mirror 2	f_1 = 0.501 m
	f_2 = 3.375 m
Mirror 3	R = 0.0796 m
Waist 1	w = 1.962 cm
Waist 2	w = 3.051 mm

A silicon plate, offset slightly from Brewster' angle, is located at the waist in the short arm and couples injection power in and FEL power out. This allows full coupling to the FEL resonator's fundamental mode. This will also serve as cavity dump coupler when we acquire a suitable doubled-YAG drive laser. The Si plate is rotated to less then Brewster's angle and provides variable coupling to optimize FEL performance. The highly elliptical beam profile, reflected from the silicon plate, is also reflected from a second flat mirror that rotates with the silicon plate to maintain beam alignment. The narrow horizontal dimension diffracts much more rapidly than the large vertical dimension, so a combination of conical and plano-paraboloid mirrors are used to transform the beam to a larger, approximately round, collimated one. A second beam-splitter directs about 90 % of the FEL power to the users lab. Beam transport is through an evacuated, periodic focussing system. Note that 240 GHz does not correspond to any strong atmospheric absorbtion lines so can be transported short distances through air. In fact, both the source and isolator are outside the vacuum system.

Spectrum Analyzer

A spectrum analyzer located in the users' lab measures the FEL's radiation spectrum. It is based on a double heterodyne detection system shown in Fig. 4. The FEL radiation is attenuated and directed to a sub-harmonically pumped mixer driven at 115 GHz by a second digitally controlled VDI multiplier chain as Local Oscillator (LO). The 10 GHz intermediate frequency (IF) signal is then amplified, filtered, and sent to a second mixer for final downconversion to a 1 GHz band centered at 500 MHz. A steep-walled bandpass filter in the 10 GHz IF chain prevents negative frequency artifacts in the final down-conversion. A 2 channel, 8 bit, 5 GS/s digitizer (Tektronix TVS 625A) records both the 500 MHz, and rectified 10 GHz, IF signals.

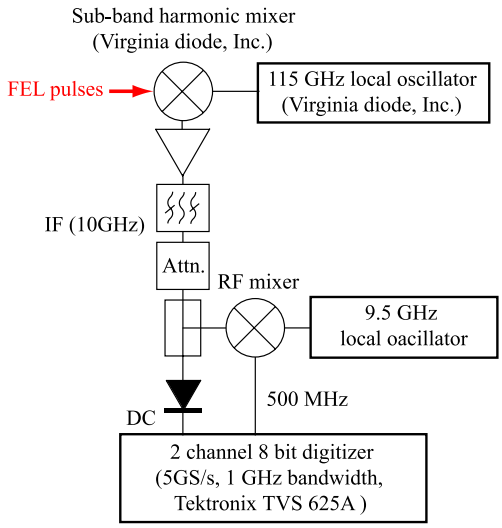

Figure 4: Schematic illustration of the 240 GHz spectrum analyzer.

A Labview program does fast Fourier transform processing for immediate display. A more accurate analysis can be applied to saved data using the Wiener-Khinchin theorem, DFT, and more sophisticated windowing later as needed.

RESULTS

Fig. 1(a) shows the recorded spectrum without injection locking. Many longitudinal modes with 25 MHz spacing are seen. Fig. 1(b) is the spectrum with injection on. The effect is immediate and unequivocal. Lasing is seen to always occur at one frequency on the same longitudinal mode selected by the injection source frequency. The injection locking is observed only when the source frequency matches one of the resonator's longitudinal modes. The linewidth shown in Fig. 1(c) corresponds to the analysis window, indicating an actual linewidth less then 1 MHz as expected.

CONCLUSION

In summary, we have demonstrated injection-locked FEL operation with sub-MHz bandwidth using a tunable solid state source as an injection source. The high-power, tunability, and extremely narrow linewidth of the FEL opens up the possibility for new applications such as a high-power, high-frequency, pulsed EPR spectroscopy. We wish to thank David Enyeart for his support of the injection locking system installation and FEL operation.

REFERENCES

[1] http://sbfel3.ucsb.edu/

[2] G. Ramian,"The New UCSB Free-Electron Lasers," NIM A318, 1992, p. 225

[3] A. Abramovich, et al.,"High Spectral Coherence in Long-Pulse and Continuous Free-Electron Laser: Measurements and Theoretical Limitations," Phys. Rev. Lett., V82, N26, 1999, p. 5257

[4] P. Flamant, R. Menzies, "Mode Selection and Frequency Tuning by Injection in Pulsed TEA-CO2 Lasers," IEEE Journal of Quantum Electronics, QE19, N5, 1983, p. 821

[5] L. Yu., et al.,"High-Gain Harmonic-Generation Free-Electron Laser," Science, V289, 11-Aug-2000, p. 932

[6] J. Jackson, "Classical Electrodynamics," 3rd ed., Wiley (1999), p690

[7] A. Amir, J. Knox-Seith, M. Warden,"Narrow-Bandwidth Operation of a Free-Electron Laser Enforced by Seeding" Phys. Rev. Let., V66, N1, (1991)

[8] Thomas Keating Ltd. Station Mills, West Sussex, RH14 9SH, UK http://www.terahertz.co.uk

[9] Virginia Diodes Inc., 979 Second St. S.E., Suite 309, Charlottesville, VA 22902, USA http://www.virginiadiodes.com

A SUPERCONDUCTING RF PHOTO-INJECTOR FOR OPERATION AT THE ELBE LINEAR ACCELERATOR*

J. Teichert#, A. Arnold, H. Buettig, D. Janssen, M. Justus, U. Lehnert, P. Michel, K. Moeller, P. Murcek, Ch. Schneider, R. Schurig, F. Staufenbiel, R. Xiang, FZD, Dresden, Germany,
J. Stephan, IKS, Dresden, Germany, W.-D. Lehmann, SGE, Pirna, Germany,
T. Kamps, BESSY, Berlin Germany, G. Klemz, I. Will, MBI, Berlin, Germany,
D. Lipka, A. Matheisen, B. v. d. Horst, DESY, Hamburg, Germany
P. vom Stein, ACCEL Instruments, Bergisch Gladbach, Germany
V. Volkov, BINP, Novosibirsk, Russia

Abstract

For the ELBE superconducting linear accelerator at FZD a radiofrequency photoelectron injector with a superconducting cavity (SRF gun) is under development. The SRF gun combines the excellent beam quality which can be delivered by RF photoinjectors with the possibility of continuous wave operation.

The superconducting niobium cavity of the injector consists of 3½ cells and contains a Cs_2Te photocathode which is normal-conducting and cooled by liquid nitrogen. The RF frequency of the cavity is 1.3 GHz. The final electron energy will be about 9.5 MeV and the average electron current will be 1 mA. In the past years the SRF photo injector has been designed and fabricated. Several critical subsystems have been tested. For the cavity, the results of the RF measurements will be shown. An UV driver laser system has been developed which fulfils the different requirements (77 pC @ 13 MHz, 1 nC @ 500 kHz) for the future operation at ELBE. A photo cathode preparation system was developed and installed. The equipment is now in operation and the first series of Cs_2Te photo cathodes have been produced.

INTRODUCTION

In 2004 a R&D program for the development of a superconducting radiofrequency photoelectron injector (SRF gun) was initiated at Forschungszentrum Dresden-Rossendorf (FZD). This project continues the earlier efforts in SRF gun development [1, 2] with the aim to develop a fully operable SRF photo injector for the ELBE superconducting linear accelerator [3].

Compared to the thermionic injector in use, the new SRF gun will reduce the pulse length and the transverse emittance for the standard FEL operation mode with 77 pC bunch charge and 13 MHz pulse repetition rate. Furthermore a second operation mode is now planned at ELBE with a bunch charge of 1 nC and a repetition rate of 500 kHz. Beside the essential beam quality improvement for ELBE, the project should demonstrate the operation of a SRF gun at an accelerator facility for the first time, and the gun will serve as a test bench for R&D studies in this field (beam parameter measurements and optimize operation, long term studies, investigation of photo cathodes, study of emittance compensation methods). For that reason a sophisticated diagnostics beamline has been designed and constructed [4]. In particular, the operation with 2.5 nC bunch charge will be studied which is essentially important for future application of the SRF gun at the BESSY FEL [5]. The Table 1 gives an overview of the SRF gun parameters and planned operation modes.

Table 1: Gun design parameters and expected beam values for the planned operation modes

	ELBE mode	**high charge mode**	**BESSY-FEL**
RF frequency	1.3 GHz		
beam energy	9.5 MeV		
Operation	CW		
drive laser wave length	262 nm		
Photocathode	Cs_2Te		
quantum efficiency	>1 %		>2.5 %
average current	1 mA	0.5 mA	2.5 µA
pulse length	5 ps	15 ps	40 ps
Repetition rate	13 MHz	500 kHz	1 kHz
bunch charge	77 pC	1 nC	2.5 nC
transverse emittance	1 µm	2.5 µm	3 µm[1)]

[1)] flat top laser

An overview of the ELBE accelerator facility is shown in Fig. 1. The heart of the radiation source is a superconducting linac with a thermionic injector and two cryomodules each containing two TESLA-type RF cavities. The accelerator operates in CW, the maximum electron energy is 40 MeV, and the average current is 1 mA. The electron beam is used in two FELs for the generation of infrared radiation, to conduct nuclear physics and radiation physics experiments, and to produce neutrons and positrons.

* We acknowledge the support of the European Community-Research Infrastructure Activity under the FP6 "Structuring the European Research Area" programme (CARE, contract number RII3-CT-2003-506395) and the support of the German Federal Ministry of Education and Research grant 05 ES4BR1/8.
#j.teichert@fz-rossendorf.de

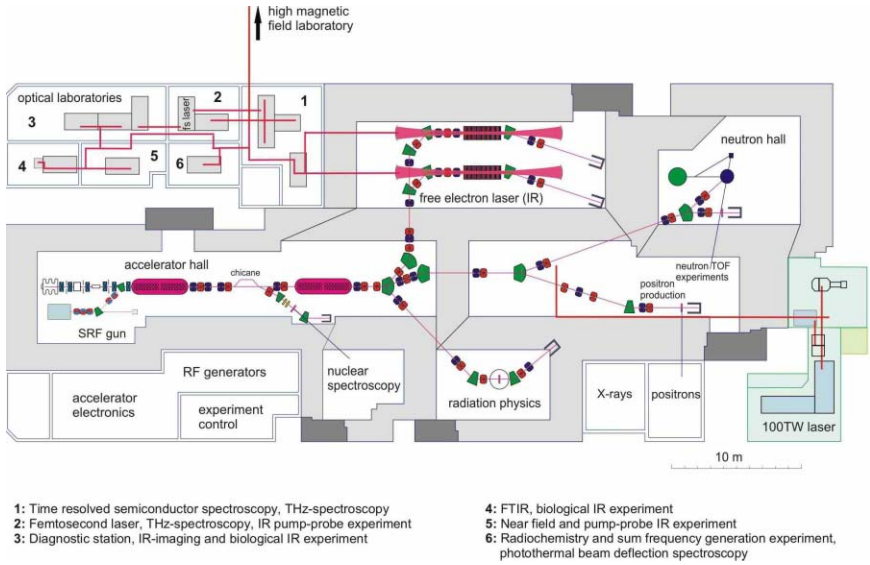

Fig. 1: Layout of the Radiation Source.

The SRF gun project is a collaboration of BESSY, DESY, MBI and FZD. A detailed description of the SRF gun design is given in Ref [6]. We will spend the rest of the paper reporting the progress of the SRF gun construction during the last year and showing the

PHOTOCATHODE PREPARATION

In normal-conducting RF photoinjectors the semiconductor cesium telluride is the preferred photo cathode material. Cs_2Te has a high quantum efficiency for UV light, a long lifetime and requires a moderate vacuum of about 10^{-10} mbar. Due to the good experience in normal-conducting RF photoinjectors, Cs_2Te seems to be the preferred material for SRF photoinjectors too. For a CW electron current of 1 mA and a typical quantum efficiency of 1 %, the UV laser power must be about 1 W. Suitable driver laser systems with such power have been developed [7].

A photocathode preparation system for the deposition of the Cs_2Te layers has been designed and constructed. The equipment is installed in a clean room in order to ensure low particle contamination of the cathodes. Main components are the vacuum chamber for the Cs_2Te deposition, a UV laser system (4 mW @ 262 nm) for online measurements of the quantum efficiency, the exchange and storage system for the photocathodes, and the electronics units for process control. The deposition equipment allows standard deposition technology (Te and Cs in succession) as well as the simultaneous evaporation proposed at CERN [8]. Two quartz monitors measure the deposition rates of Te and Cs separately, and the process computer controls the heating power of the evaporators in order to adjust the stoichiometric ratio of 1:2 between Te and Cs. Although the improvement and optimization is still ongoing, a number of cathodes with quantum efficiencies >4 % have been prepared.

NIOBIUM CAVITY

The 3 ½ cell niobium cavity has been the most critical component. A 3D drawing of this cavity is shown in Fig. 2. After fabrication, the two cavities, one of Nb grade RRR 300 and one of grade RRR 40 (model for technological and RF tests) were warm tuned at FZD and then prepared at DESY (100 µm BCP etching inside, 20 µm etching outside, and 800 °C backing in the UHV oven). After these treatments a second warm tuning was performed.

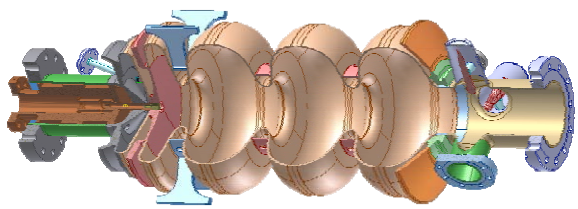

Fig. 2: 3D model of the SRF gun cavity.

Following the tuning, the RRR 300 cavity was moved to DESY for low temperature RF tests. For these measurements the cavity was cleaned by buffered chemical polishing (40µm BCP) and high pressure rinsing (HPR). During the cool down from 4.4 K to 1.6 K the unloaded quality factor was measured at low rf power and the residual surface resistance was determined to R_{res}=3.4 nΩ.

The results of the Q versus E measurements at 1.8 K of the first vertical test measurements are shown in Fig. 7. For comparison, the values are plotted as function of the peak field in the TESLA cells. All together, four vertical tests were carried out. As shown in the figure, field emission started early and the quality factor decreases. Further increasing of rf power results in strong field emission and Q-switches, which are probably caused by

thermal breakdown at activated field emitters. The behaviour of the Q-switches is most likely due to surface pollution. This might be induced by the hardly cleanable choke filter. Because of the narrow cathode feed through between choke filter and gun cell, direct cleaning of the filter cell was not feasible.

Based on this experience, an improved cleaning was realized by the company ACCEL Instruments. A special high pressure rinsing lance was built to enable an additional cleaning of the choke filter beside the established preparation of the cavity cells. Due to technical problems during the cleaning the achieved results of the followed 2nd and 3rd tests are unsatisfactory.

Caused by the shortage of time the 4th preparation and the vertical test had to be the base for further assembly. As in the tests before, the limit in the gradient results from field emission. Beside particle pollution the reason could be a small scratch that we found inside the cavity at the back plane of the half cell. The damage results from a collision between the cavity and the high pressure rinsing lance during the cleaning. So its removal will result in a better performance. Unfortunately there is no time for a 5th vertical test so we have to wait for further tests until the cryostat is completely assembled.

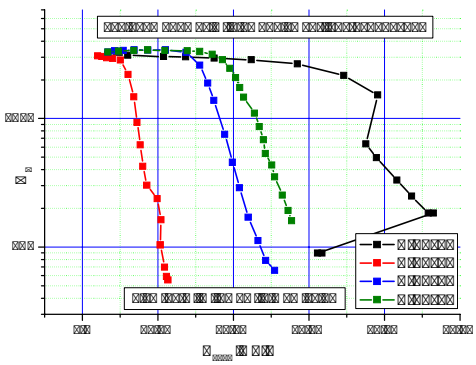

Fig. 3: A comparison of the four vertical test measurements of the SRF gun cavity.

A further indication that the field emission problem limiting the gradient of the cavity is located in the half-cell delivers a comparison of the measurements for the four pass band modes performed in the 4th vertical test. The field distributions of the four modes are shown in Fig. 4. As can be seen, especially the π/4 mode is mainly located in the half-cell. In the results for the four modes shown in Fig. 5, where Q_0 is now plotted versus the peak field in the half-cell, the drop-down of the curves happens at the same field value in the half-cell.

At ACCEL Instruments the helium vessel was welded around the cavity following vacuum leak checks and RF field profile measurements in spring 2007. Then the etching of the cavity was carried out (20 µm BCP, clean water rinsing, drying in class 10 clean room), pick-up and HOM feed-throughs were attached in the clean room, and the cavity was finally cleaned (high pressure rinsing, drying in class 10 clean room, valve assembly, vacuum leak check, filled with clean N_2 gas).

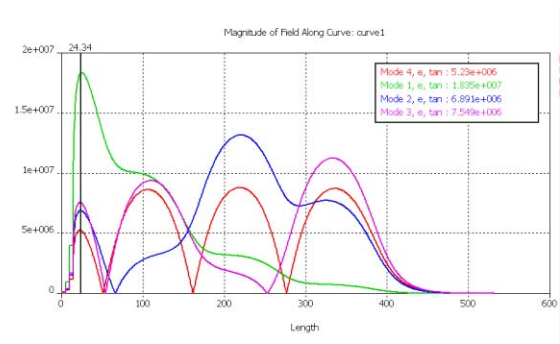

Fig. 4: Field distributions of the four pass band modes.

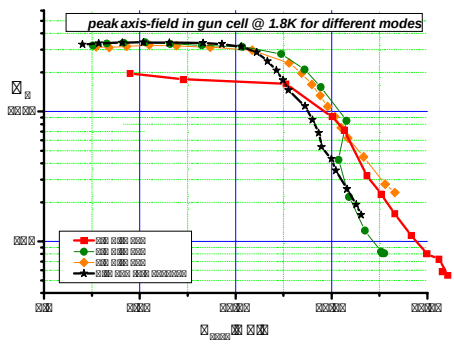

Fig. 5: Measured curves for the four pass band modes. In the graph Q_0 is plotted versus the peak field in the half-cell.

In the class 10 clean room of the FZD the further assembly work was carried out: mounting of cavity tuner parts, assembly of the main power coupler antenna and of the pick-up antenna in the choke filter, temporary insertion of an RF antenna for HOM coupler tuning and adjustment of the choke filter frequency. Finally the beam line parts were mounted at the down-stream side and the complete cathode cooling and support system at the up-stream side of the cavity. Therewith the clean room work was finished and the cavity can now be inserted into the cryostat.

CRYOMODULE

The design of the SRF gun cryostat is presented in Fig. 6. The stainless steel vacuum vessel has a cylindrical shape with 1.3 m length and 0.75 m diameter. The He port and the N_2 port are on top on the right hand side.

From the port the He flows through a heater pot and the two-phase supply tube into the chimney of the He tank. For the cooling of the thermal shield, liquid nitrogen is used. The 70 K shield consists of a cylindrical Al sheet welded to two circular tubes filled with N_2. The liquid N_2 tank is in the upper part of the module. The cavity is passively protected against ambient magnetic fields by means of a µ-metal shield, placed between the 80 K shield and the vacuum vessel.

For a check of all components the cryostat was assembled with exception of the He tank and the cavity in the workshop end of 2006. In May 2007, the final assembly started after delivery of the cavity welted in the

He tank and the following work in the clean room described above. Fig. 7 shows the still open cryostat vessel with the He tank covered with super-isolation.

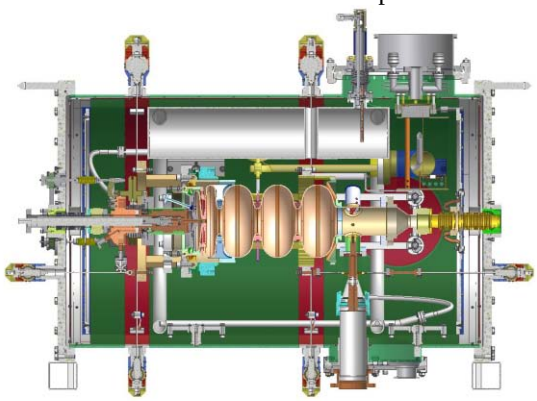

Fig. 6: Design of the SRF gun cryostat.

Fig. 7: Photograph of the vacuum vessel and the He vessel during moving in.

INSTALLATION

During the summer shut-down of ELBE in July 2007, the SRF gun cryostat was installed in the accelerator hall and connected to the He refrigerator. The cool-down was successfully carried out on August 3-4. First measurements with low power RF were performed in order to check the RF installation, the tuning systems and to characterize the cavity. Beside the cryostat, the first part of the diagnostics beamline with the solenoid, the laser input port and a beam dump was installed (see Fig. 8).

SUMMARY AND OUTLOOK

A SRF photo-injector has been installed at the ELBE in summer 2007. The next steps on the way are the commissioning of the high power RF system, and installation of the 500 kHz driver laser. Then the first beam can be produced with the SRF gun. In the following shut-downs of ELBE in autumn and winter, the diagnostics beamline and the cathode transfer system will be installed, which will then allow beam parameter measurements with Cs_2Te photocathodes.

In the future the SRF gun will improve the beam quality for ELBE users (higher bunch charge, lower transverse emittance).

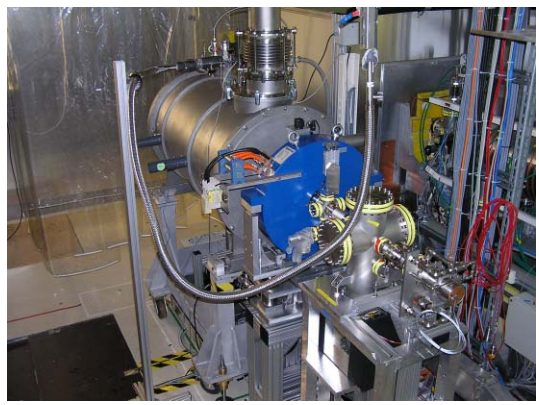

Fig. 8: Photograph of the SRF gun installed in the accelerator hall.

REFERENCES

[1] D. Janssen, et al., “The Development of a Superconducting RF Gun: Status of the Drossel Collaboration”, Proc. of PAC´97, Vancouver, Canada, 1997, p. 2838.

[2] D. Janssen, et al., “First operation of a Superconducting RF-Gun”, Nucl. Instr. and Meth. A 507, 314 (2003).

[3] P. Michel, et al., “The Rossendorf IR-FEL ELBE”, Proc. FEL 2006, Berlin, Germany, p. 488.

[4] T. Kamps, et al.,”Diagnostics Beamline for the SRF Gun Project”, Proc. of FEL´05, Stanford, USA, 2005, p. 530.

[5] “The BESSY Soft X-ray Free Electron Laser”, TDR BESSY March 2004, eds.: D.Krämer, E. Jaeschke, W. Eberhardt, ISBN 3-9809534-0-8, Berlin (2004).

[6] A. Arnold, et al., “Development of a Superconducting Radio Frequency Photo Electron Injektor”, Nucl. Instr. and Meth. A 577, 440 (2007).

[7] I. Will, et al., „Photocathode Laser for the Superconducting Photo Injector at the Forschungszentrum Rossendorf”, Proc. FEL´06, Berlin, Germany, 2006, p. 564.

[8] G. Suberlucq, “Technological Challenges for High Brightness Photo-injectors”, Proc. of EPAC´04, Lucerne, Switzerland, 2004, p. 64.

ELECTRO-OPTIC SPECTRAL DECODING FOR SINGLE-SHOT CHARACTERISATION OF THE COHERENT TRANSITION RADIATION PULSES AT FLASH

V. Arsov, E.-A Knabbe, B. Schmidt, P. Schmüser, B. Steffen, DESY, Hamburg, Germany

Abstract

We report preliminary single-shot electro-optic spectral decoding (EOSD) measurements of coherent transition radiation (CTR) pulses, generated by the electron bunches of the free-electron laser (FLASH) at DESY, Hamburg. The THz radiation is transported through a 20 m long beam-line from the accelerator tunnel to an experimental station outside. The measurements are performed in vacuum with a 0.5 mm ZnTe crystal in crossed-polarizer and near crossed-polarizer detection schemes. Pulses with complex structure and sharp peaks have been detected. The different components have full width at half maximum in the range 400-900 fs.

INTRODUCTION

Intense relativistic electron bunches with a duration less than 100 fs are needed in contemporary light source accelerators, such as the ultraviolet and soft x-ray free-electron laser at Hamburg (FLASH) [1], as well as the future x-ray FELs like the Linac Coherent Light Source at SLAC [2] and the European XFEL [3]. With this there is a growing demand for ultra-fast characterisation of the electron bunches. Some of the leading longitudinal diagnostic techniques with fs abilities are the spectral, the electro-optic (EO), the transverse deflecting cavities and, since recently, the optical replicas [4]. The spectral techniques refer to spectrum measurements of the coherent transition radiation (CTR), diffraction and synchrotron radiation, etc. A Fourier transformation of the measured spectrum has resolved structures with less than 10 fs duration in a single-shot acquisition [5]. In the case of FLASH the single shot CTR spectrometer is situated outside the accelerator tunnel, which is convenient from experimental point of view, but requires knowledge of the transfer function of the beam line. Therefore an independent CTR pulse length measurement, such as an EO technique applied inside the spectrometer can facilitate the interpretation of the CTR spectra.

The EO techniques allow direct characterization of THz fields both in the spectral and in the time-domain. Depending on the analyzer orientation, the measured signal is either linear or quadratic with the THz field [5],[6]. Recently EO signals as short as 55 fs (rms) have been observed, which is a new record in the EO detection of single electron bunches and close to the limit imposed by the properties of the EO material [7].

The temporal profiles of the CTR pulses at FLASH have been measured for the first time by Berden et. al. [8]. Their measurements were carried out in air with ZnTe, using electro-optic spectral decoding (EOSD) in the so called balanced detection scheme. Here we present similar EOSD measurements with ZnTe, but carried out in vacuum, using crossed-polarizer and near crossed-polarizer detection schemes [6].

EXPERIMENTAL SETUP

The CTR electric field temporal profiles are resolved with a spectral decoding electro-optic technique [6], [9]-[11].

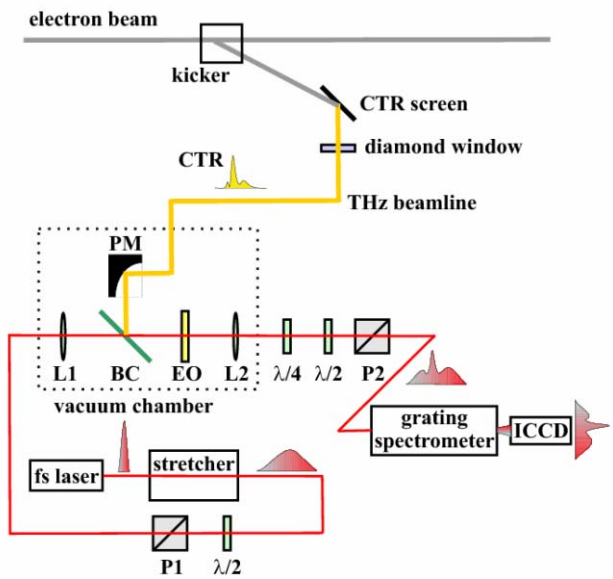

Figure 1: Set-up for electro-optic spectral decoding measurements of coherent transition radiation (CTR). Notations: (l/2), (l/4) – half and quarter wave plates; (P1,2) – polarizers; (L1,2) – lenses; (BC) – indium tin oxide beam combiner; (EO) – 0.5 mm thick ZnTe electro-optic crystal; (PM) – parabolic mirror

A diagram of the experimental setup is shown on Fig. 1. The CTR is generated from single bunches, kicked to an off-axis screen. A diamond window is used to couple the radiation from the ultra high vacuum environment into a 20 m long transfer line, where the pressure is lower than 0.1 mbar. The beam line is equipped with high reflectivity focusing mirrors, designed specially to minimize the diffraction. Special care has been taken to avoid wave guide effects in the pipe by using corrugated bellows. The lowest frequency (ca. 300 GHz) is determined by the diameter of the pipe, which is ca. 200 mm [12]. Outside the accelerator runnel the THz beam line is connected to an evacuated vessel containing several diagnostic experiments, including a single-shot THz grating spectrometer and an EO setup. Alternatively, the radiation

can be coupled out of the vacuum pipe of the transfer line through a single-crystal quartz window for experiments in air. However this is at the expense of suppression of CTR frequencies above 4 THz due to the absorption in quartz and especially by the broad band absorption in air. The CTR radiation is focused on the 0.5 mm thick ZnTe crystal with an off-axis parabolic mirror. The spatial overlap with the probe laser beam is achieved with an indium tin oxide (ITO) beam combiner.

The probe optical pulse is produced by a titanium-sapphire laser (center wavelength 790 nm, bandwidth 36 nm, pulse length 40 fs and repetition rate 1 kHz), synchronized to the 1.3 GHz accelerator frequency. The probe beam is stretched to 7.7 ps in a 40 cm long SF11 glass block (stretcher on Fig. 1). The length of the probe pulse is chosen to be larger than the length of the CTR pulse in order to encompass the whole CTR electric field temporal profile. The chirp of the optical pulse is linear and so is the time-frequency mapping of the corresponding intensity profiles. The probe optical pulse and the THz radiation propagate collinearly in the EO crystal. For ZnTe there is a close match in the group velocities of the THz and the optical pulses. In the ideal case the instantaneous frequency of the probe laser pulse interacts with the same portion of the THz field, thus experiencing a phase retardation in the EO crystal proportional to the local electric field. The specific phase retardation is made apparent by an analysing polarizer P2. Thus the CTR temporal profile is imprinted on the spectrum of the optical pulse and can be resolved with a spectrometer.

The half wave plate preceding the input polarizer P1 (Fig. 1) serves to attenuate the energy of the probe laser pulse below the damaging threshold of the EO crystal (~ 5 mJ)

In the absence of a CTR pulse the transmittance through the polarizer P1 and P2 is minimized. This is the so called acquisition at crossed polarizer. In this arrangement the measured intensity is proportional to the square of the THz electric field. The advantage of this arrangement is the low background in comparison to the balanced detection scheme. The residual birefringence due to mechanical stress in the EO crystal is removed by the quarter wave plate. In the present experiment also measurements at few degrees off-crossed polarizer have been made. The advantage is the higher sensitivity and lower signal to noise ratio at the expense of a slightly higher background [6]. An additional advantage is that the EO signal is linear with the CTR field. The corresponding polarizer arrangement is chosen with the half wave plate in front of P2.

The spectra are resolved with a 0.15 m spectrometer, equipped with a 600 grooves/mm grating. The images are recorded with a 1280x1024 pixel intensified CCD camera (ICCD). The time axis is along the longer side of the sensor. In the other direction the spectra occupy ~ 90 pixels, which is used for binning.

RESULTS AND DISCUSSION

The upper panels of Fig. 2 show the raw CTR signals, measured with 0.5 mm thick ZnTe at different polarization schemes. The leading edge is on the left. The green traces represent the spectral intensities of the probe laser pulse with CTR being blocked (spectrum *A*). These traces are averaged along 20 laser shots. Since the laser pulse is linearly chirped and its duration is known, these traces are also used for time-calibration of the horizontal axis. The blue traces are taken with the presence of the probe laser and CTR radiation (spectrum *B*) and represent a single-shot measurement. At the beginning and the end of each measurement series separate background spectra have been taken without the presence of laser and CTR (spectrum *C*). These traces are not represented on Fig 2, but are used for the signal normalization. The lower panels of Fig. 2 show the normalized electro-optic signals. For the case near crossed polarizer the following relation is used for normalization: $\frac{B-A}{A-C}$, where *A*, *B* and *C* are the above mentioned spectra. For the case of crossed polarizer the normalizing relation is: $\frac{B-A}{D-C}$, where is *D* the laser spectrum taken at few degrees off-cross polarization without the presence of CTR.

The left panel of Fig. 2 represents measurements with 0.5 mm ZnTe in vacuum at crossed polarizer. The measured EO signal has a complex structure. The most pronounced one has a broad base with width 3.3 ps and amplitude 0.4, followed by a sharp peak with normalized amplitude 1.15 and 440 fs width. The rest of the signal is hardly distinguishable from the noise.

The right panel of Fig. 2 shows similar measurements with 0.5 mm ZnTe in vacuum, but with -2° deviation from crossed polarizer. This increases the sensitivity at the expense of slightly increased background. The normalized signal amplitude is also higher. Again a complex CTR structure is observed with two pronounced peaks. The highest peak is 700 fs wide. Its normalized amplitude is 1.6. The preceding lower peak has a normalized amplitude 0.5 and width 900 fs.

The data of Fig. 2 shows the clear difference between the measurements in crossed- and near crossed polarization. In the first case the EO signal is proportional to the square of the CTR electric field. This is the reason for the observed broader step preceding the sharp peak on the left image of Fig. 2. In the case of measurements near crossed polarizer, the EO signal depends linearly on the CTR electric field. As seen from the right image of Fig. 2, there is a negative swing with smaller amplitude at the position, where a broad step in crossed polarizer is observed.

As pointed out by [4] and [8], pulse lengths shorter than $2.4\sqrt{T_0 T_C}$ should be distorted with EOSD measurements. T_0 is the initial length of the laser pulse, which in our case is 40 fs; T_C = 7.7 ps is the length of the chirped laser pulse. For the lower limit of the CTR pulse one obtains 1.3 ps. The measured pulse widths are near

this limit. The choice of the chirped pulse length is a compromise between the possibility to have wide enough time-window and the ability to resolve narrow temporal components. In our case a clear structure in the CTR signal is distinguishable. A distortion free measurement would require temporal decoding set-up [4],[6], [7],[13].

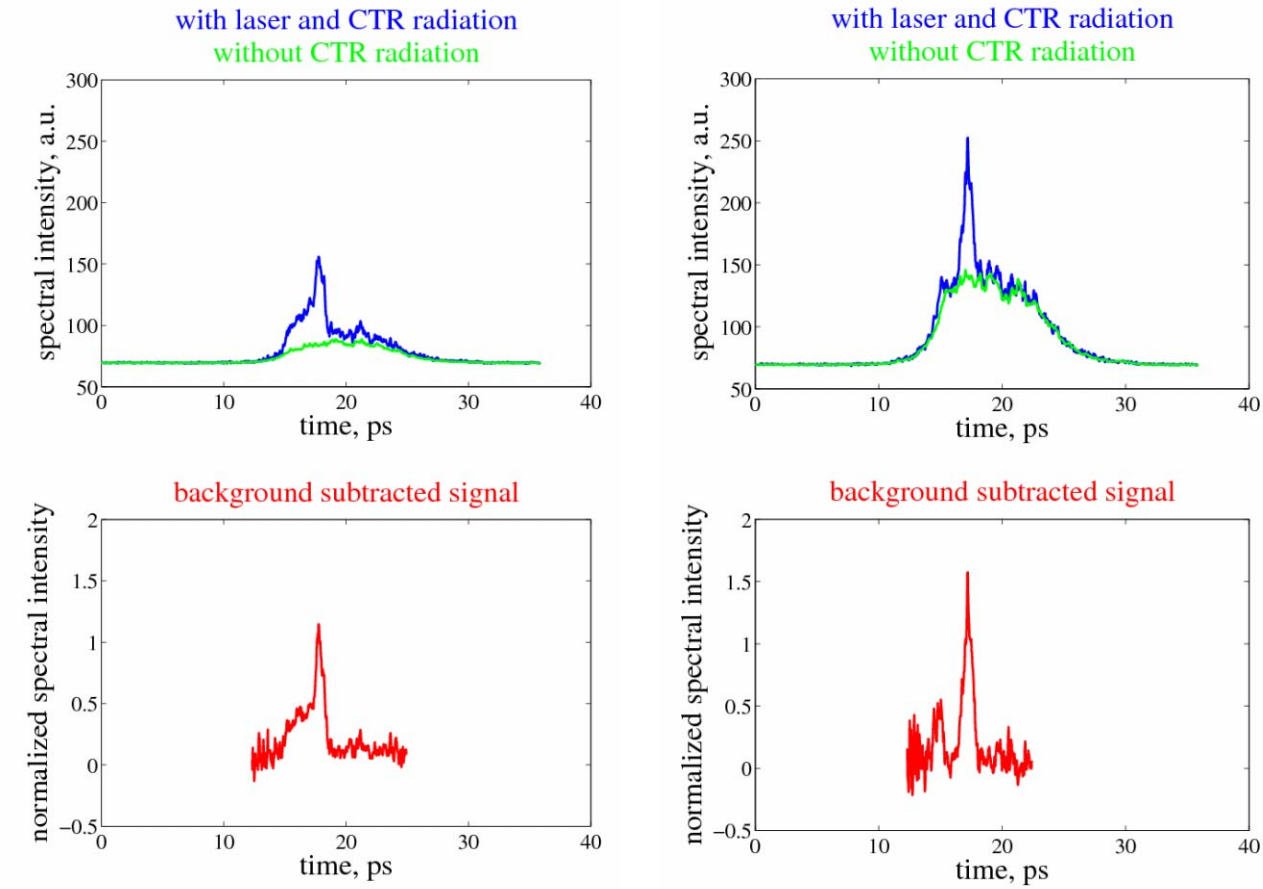

Figure 2: Electro-optic spectral decoding signals of coherent transition radiation (CTR), measured with 0.5 mm ZnTe in vacuum. Upper panels: raw data; the green traces are the laser spectral intensities without CTR radiation; the blue traces are the corresponding intensities with CTR radiation. Lower panels: normalized spectral intensities. The leading edge of the CTR is on the left. Left panel: measurements at crossed polarizer. Right panel: measurements at -2° off- crossed polarizer.

An important result are the sharp and high CTR peaks, despite the lower cut-off frequency (4THz) of ZnTe. Such peaks are familiar from EO measurements of the electron bunch lengths directly in the FLASH tunnel [6],[7],[10]. This demonstrates, that the optics of the THz beam line maintains the amplitude and the phase information in this wavelength range and properly images the electrical field from the CTR screen to the experimental station outside the tunnel. These results are rather preliminary and a more systematic study is necessary with the use of GaP, which has a higher cut-off frequency (11 THz) and better optical properties.

CONCLUSION AND OUTLOOK

A comparison between electro-optic spectral decoding measurements of CTR radiation with crossed polarizer and near crossed polarizer arrangements in ZnTe has been made. In both cases the ability to resolve structure in the CTR signal and sharp peaks is quite promising. Since the THz diagnostics are situated outside the DESY-FLASH tunnel, it is necessary to verify experimentally the transfer function of the THz beam line, which at this point is known through simulation. For this purpose more systematic EO studies with GaP in vacuum with variation of the THz focus are necessary. In addition temporal decoding measurements are foreseen in order to resolve shorter time structures and to avoid a possible signal distortion.

REFERENCES

[1] V. Ayvazyan et al., Eur. Phys J. D **37**, 297 (2006)
[2] http://www-ssrl.slac.stanford.edu/lcls/
[3] http://www.xfel.net
[4] S.P. Jamison et al., Proc. EPAC 2006, Edinburgh, Scotland, p. 915.

[5] H. Delsim-Hashemi et al., Proc. 37th Advanced ICFA Beam Dynamics Workshop on Future Light Sources, FLS 2006, Hamburg, Germany
[6] B. Steffen, PhD Thesis, DESY-Hamburg, Germany, (2007).
[7] G.Berden et al., Phys. Rev.Lett. (2007). (accepted for publication)
[8] G.Berden et al., Proc. EPAC 2006, Edinburgh, Scotland, p. 1058.
[9] I. Wilke et al., Phys. Rev. Lett. **88**, 124801 (2002).
[10] B. Steffen et al., Proc. 27th International Free Electron Laser Conference (FEL 2005), Stanford, USA 2005, p. 549.
[11] G.Berden et al. Proc. 7th European Workshop on Beam Diagnostics and Instrumentation for Particle Accelerators (DIPAC 2005), Lyon, France, 2005. p 69.
[12] S. Casalbuoni et al, TESLA-FEL report 2006-4.
[13] G.Berden et al., Phys.Rev. Lett. **93**, 114802 (2004).

XPS STUDIES OF Cs_2Te PHOTOCATHODES*

S. Lederer†, J.H. Han, and S. Schreiber (DESY, Hamburg, Germany)
A. Vollmer, R. Ovsyannikov, M. Sperling, and H. Duerr (BESSY GmbH, Berlin, Germany)
F. Stephan (DESY, Zeuthen, Germany)
P. Michelato, L. Monaco, C. Pagani, D. Sertore (INFN Milano - LASA, Segrate (MI), Italy)

Abstract

Cesium telluride (Cs_2Te) photocathodes are used as sources for electron beams because of their high quantum efficiency (QE) and their ability to release high peak current electron bunches in a high gradient RF-gun. Starting from a high QE level of about 10 % the quantum efficiency of these cathodes decreases during operation in a photo-injector to below 0.5 %. To understand this behaviour, XPS investigations on the chemical composition were performed at BESSY. In this contribution we compare two fresh cathodes from INFN with one used under normal operation at FLASH and one used at PITZ at a higher than usual RF-gradient of 60 MV/m.

INTRODUCTION

The photocathodes used at FLASH and PITZ are prepared at INFN-LASA (Milano, Italy). The electron emitting film is deposited on polished molybdenum plugs in two steps [1]. First, the plug is coated with 10 nm tellurium. During the following cesium deposition, the quantum efficiency (QE) is monitored, and when maximum QE is reached the Cs evaporation is stopped. During the preparation process the temperature of the plug is kept at 120 °C. The diameter of the Cs_2Te coating is 5 mm. Right after the production of the Cs_2Te cathodes, the QE is about 10 % [2].

During operation in electron guns of accelerators, the QE reduces to below 0.5 %. For a better understanding of the QE degradation, the chemical composition of two new (#90.1 and #42.3) and two used cathodes (#34.6 and #92.1) are investigated by x-ray photoelectron spectroscopy (XPS) at BESSY (Berlin, Germany). In addition, the work function of the cathodes was measured. Cathode #92.1 was used at FLASH under the nominal operation condition for SASE FEL generation for 39 days with a final QE of 0.1 %. Cathode #34.6 was operated at PITZ with accelerating gradients at the cathode of up to 60 MV/m for several days. The QE of this cathode decreased to 2 %.

In this paper first results of the XPS measurements are presented. In the first part an overview in the sense of survey scans is given, followed by a more detailed presentation of precise XPS-studies of the Te 3d levels. In the last part, results of work function determinations are given.

RESULTS AND DISCUSSION

In figure 1, survey scans with photon energies of 900 eV are presented for the two fresh and the two used cathodes. For all spectra, the main peaks correspond to Cs 3d and Te 3d. While for fresh cathodes peaks corresponding to

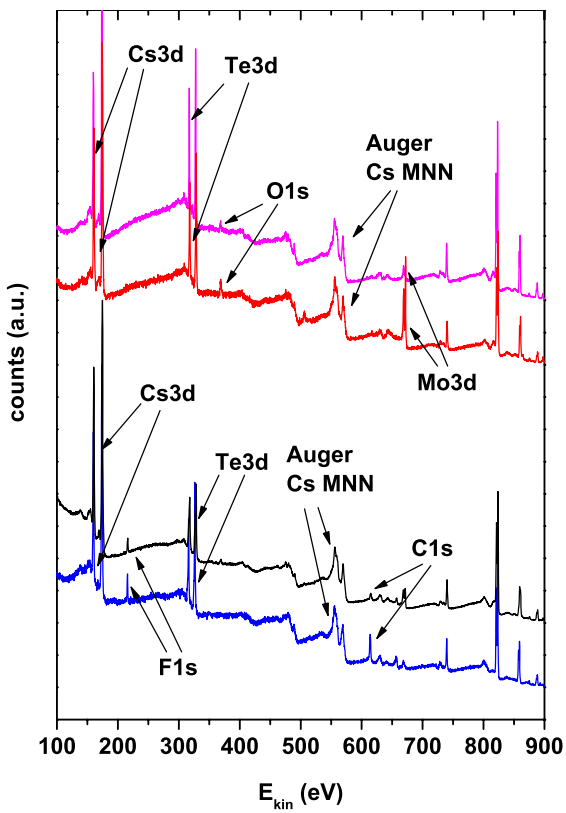

Figure 1: Survey spectra measured at photon energy of 900 eV for fresh cathodes (red: #42.3, magenta: #90.1) and used cathodes (black: #34.6, blue: #92.1)

O 1s are visible, these lines reduce with operation time. We interpret this as a cleaning process during operation caused by the laser pulses (wavelength 262 nm) and the high electrical field at the cathode. Both effects results in

* This work has partly been supported by the European Community, contracts RII3-CT-2004-506008 and 011935, and by the 'Impuls- und Vernetzungsfonds' of the Helmholtz Association, contract VH-FZ-005.

† sven.lederer@desy.de

a local heating up of the photocathode. This is consistent with the effect, known now for several years, that Cs_2Te photocathodes poisoned with oxygen can be rejuvenated by a heating process [3, 4, 5]. A further difference in the spectra is that on used cathodes F 1s and C 1s lines appear. The amounts of both elements are non negligible, be-

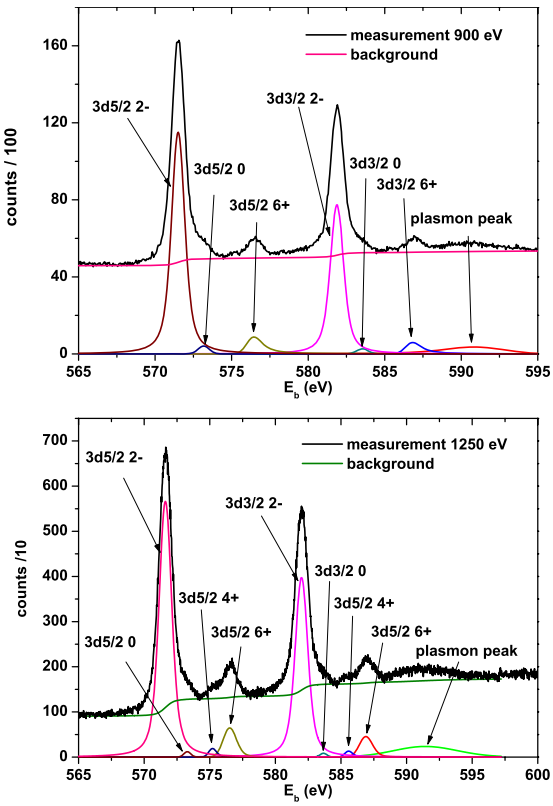

Figure 2: Te 3d lines measured with photon energies of 900 eV (top) and 1250 eV (bottom) at the center of cathode #90.1. In both graphs the measurements as well as the fits to the measurements are presented.

cause of the approximately one order of magnitude smaller photoionization cross sections in comparison to Cs 3d and Te 3d [6]. The origin of this contaminations can be related to some teflon parts inside the beamlines of both facilities right after the gun section.

In figure 2 precise measurements of the Te 3d lines of fresh cathode #90.1 are presented. In this and the following figures, the measured kinetic electron energies (E_{kin}) are converted to the binding energies E_b by the classical formula:

$$E_{kin} = E_{ph} - E_b - \Phi \qquad (1)$$

with E_{ph} being the photon energy and Φ the work function of the analyser. The spectrum on the top of the figure was obtained with an photon energy of 900 eV, the one at the bottom with 1250 eV. For the higher energy the analyzing depth is around 2.5 nm, for the lower 1.5 nm. The dominant peaks in both spectra are assigned to Te^{-2} 3d5/2 with $E_b = 571.6$ eV and Te^{-2} 3d3/2 with $E_b = 581.9$ eV. In coincidence with the oxygen found in the survey scan (figure 1), additional lines caused by chemical shifts are present (Te^{+4} and Te^{+6}) for both spin orbit couplings of the 3d electrons. Also a small amount of metallic tellurium is visible.

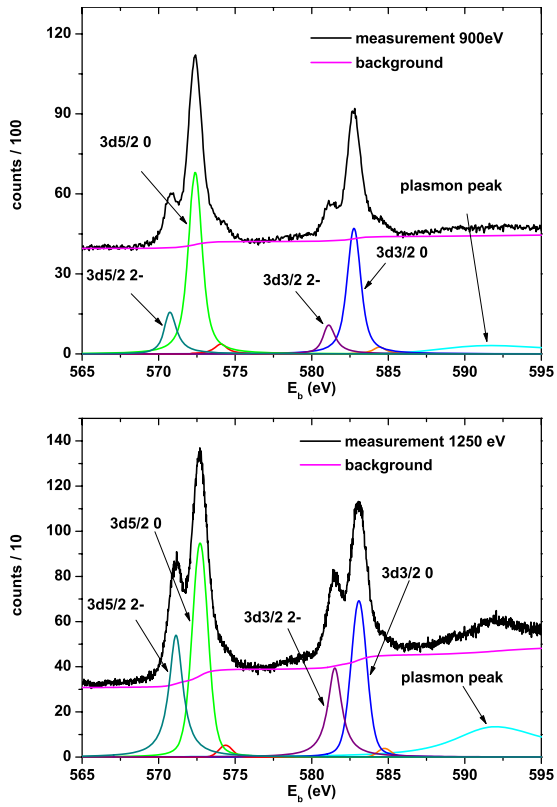

Figure 3: Te 3d lines measured with photon energies of 900 eV (top) and 1250 eV (bottom) at the center of cathode #92.1. In both graphs the measurements as well as the fits to the measurements are presented.

The picture of the Te 3d lines changes dramatically for used cathodes as shown in figure 3. Like for the fresh cathode, measurements were performed in the center of the cathode. Here the dominant peaks for both photon energies are related to the Te^0 3d5/2 and Te^0 3d3/2. For 1250 eV photon energy the amount of Te^{-2} with $E_b = 571.1$ eV for $j = 5/2$ and $E_b = 581.5$ eV for $j = 3/2$ is higher than for the lower energy. Since the analyzing depth is lower for the latter one, the metallic Te states are located close to the surface, while in the bulk region Cs_2Te is still present. The oxidation states Te^{+4} and Te^{+6} disappeared in comparison to the fresh cathodes. This result of being mainly Te^0 on the used cathode we interpret as reason for the reduced QE of this cathode, since a large amount of the cathode changed from Cs_2Te to metallic tellurium. Due to the work function of tellurium of 4.95 eV [7] electron emission caused by the drive laser of the accelerators should be strongly reduced.

As seen in figure 4 (left) [2] cathode #92.1 shows a dark area in the center, which has approximately the same diameter as the laser spot size during operation. This area is sur-

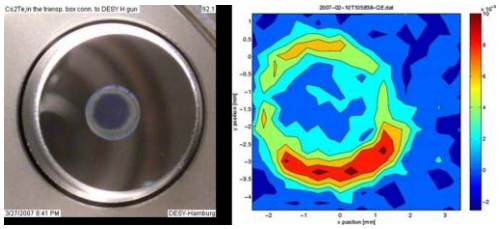

Figure 4: Photograph (left) and QE-map of cathode #92.1.

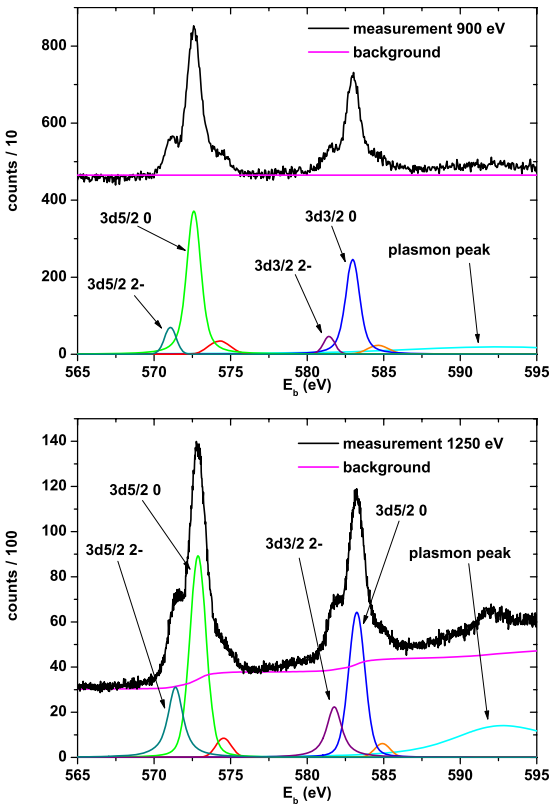

Figure 5: Te 3d lines measured with photon energies of 900 eV (top) and 1250 eV (bottom) at the outer part (for details see text) of cathode #92.1. In both graphs the measurements as well as the fits to the measurements are presented.

rounded by a brighter ring, which also has still some points of higher QE (figure 4 right). Figure 5 shows the measurements of the Te3d lines for 900 eV (top) and 1250 eV (bottom) photon energy together with the fits obtained in the described outer ring. Despite the fact that the laser was most of the time not hitting this area no tellurium oxides can be identified. While the QE of this ring is in some regions higher than in the center of the cathode, the Te 3d spectra measured at both points are comparable. Confirming the observations for the center spot, the main peaks in figure 5 correspond to Te^0 and only small amounts of Te^{-2} with binding energies of $E_b = 571.4$ eV for $j = 5/2$ and $E_b = 581.5$ eV for $j = 3/2$ are found.

In figure 6 secondary electron cut offs are measured with

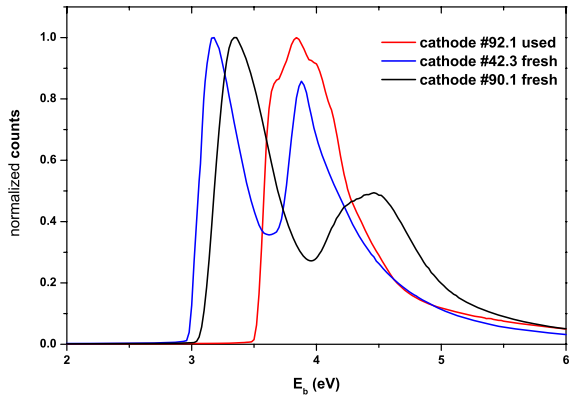

Figure 6: Secondary electron cut offs measured at the center of the two fresh and one used cathode; black curve: #90.1, blue curve: #42.3, red curve: #92.1. For comparison all spectra are normalized to their maximum.

100 eV photon energy for the two new and one used cathode (#92.1). The plot clearly shows that there is a shift of the work function between the fresh cathodes and the used one of about 0.5 eV. Since the lasers at PITZ and FLASH have fixed energies of 4.72 eV, which leads to kinetic energies of 0.55 eV of the emitted electrons, the increase in the work function of 0.5 eV decreases the emission probability of the excited electrons. This results in a strong reduction of the QE (down to 0.1 % for cathode #92.1).

CONCLUSIONS

The chemical composition of Cs_2Te photocathodes has been analyzed by XPS. Both fresh cathodes were contaminated with oxygen, while on the used ones these lines disappear with longer usage in the gun. Survey spectra of the used cathodes clearly showed F and C. The source of these contaminations was identified as teflon parts inside the beamlines at FLASH and PITZ, which will be removed in future.

Precise measurements of the Te 3d levels show, that the main contribution for fresh cathodes originates from Te^{-2}, which corresponds to the expected chemical composition of Cs_2Te. In the case of the used cathode #92.1, the main peaks are related to Te^0 (metallic tellurium). These results are confirmed by comparing the work functions of used and unused cathodes. An increase of about 0.5 eV for used cathodes was obtained, resulting in a reduced QE.

Based on the measurements performed in this work we relate the decreasing of the QE of Cs_2Te photocathodes to a change in the chemical composition. Starting from Cs_2Te after cathode production, metallic tellurium is formed during operation, which leads to the QE degradation.

REFERENCES

[1] D. Sertore et al., "Review of the production process of the TTF and PITZ photocathodes", PAC05, Knoxville, Ten-

nessee, USA, 2005.

[2] http://wwwlasa.mi.infn.it/ttfcathodes/

[3] S.H. Kong, J. Kinross-Wright, D.C. Nguyen, and R.L. Sheffield, J. Appl. Phys. **77**, 6031 (1995).

[4] S.H. Kong, D.C. Nguyen, R.L. Sheffield, and B.A. Sherwood, Nucl. Instrum. Methodes A **358**, 276 (1995).

[5] A. di Bona, F. Sabary, S. Valeri, P. Michelato, D. Sertore, G. Suberlucq, J. Appl. Phys. **80**, 3024 (1996).

[6] J.J. Yeh, and I. Lindau, At. Data Nucl. Data Tables **32**, 1 (1985).

[7] H.B. Michaelson, J. Appl. Phys. **48**, 4729 (1977).

TEST OF A WIRE SCANNER IN THE DIAGNOSTIC SECTION OF PITZ*

Hans-Juergen Grabosch# , Galina Asova##, Juergen Baehr, , Jang Hui Han§, Sergiy Khodyachykh, Sergey Korepanov, Mikhail Krasilnikov, Velizar Miltchev§§, Anne Oppelt§§§ , Bagrat Petrosyan, Martin Sachwitz#, Lazar Staykov, Frank Stephan, DESY, 15738 Zeuthen , Germany.

Abstract

The Photo Injector Test facility at Zeuthen (PITZ) has been established to produce and optimize electron beams of high brilliance. One wire scanner station, developed and used in the undulator section of the FLASH at DESY [1] [2] , has been installed in the diagnostic section of PITZ. Measurements of beam-profile and beam-position were performed to test the usability of such type of wire scanner at PITZ. The test has shown that wire scanners of this type can be well used as complementary measurement device at PITZ. In the final state of the extension of PITZ, two wire scanners are foreseen as standard diagnostic tools for beam-profile and beam-position measurements.

INTRODUCTION

Wire-scanners are important diagnostic tools for particle accelerators in order to tune the beam-line and to measure the beam-profile. Various types of wire-scanners have been developed for different particle accelerators [3][4][5]. In PITZ the beam-electrons will undergo scattering processes when hitting the wire. Once scattered the electron will hit the beam pipe and create a shower of electrons and photons. The shower signal of electrons and gammas can be observed by means of scintillator counters placed nearby the beam pipe. The measured correlation between the wire position and scintillator signal gives information about the beam-position and the beam-profile.

SETUP AND MEASUREMENT

The configuration of PITZ in the year 2005 (PITZ1.5) with the wire scanner station is shown in Figure 1. A wire scanner station consists of two independent scanners for the vertical- and horizontal-direction, respectively. Each scanner is equipped with two tungsten wires of 30 μm diameter in a distance of 10 mm.The whole set up is combined with a scintillation counter. The counter detects secondary particles which are created when the wire interacts with the electron beam. The light of the scintillation counter is read out by wavelength shifter bars and guided via clear fibers to the photomultiplier H6780-4. The gain of the photomultiplier is steered by a reference voltage $v_{ref.}$ and ranges from $10^2 – 10^6$. For this measurement a gain of ~ 500 is mostly used. The photomultiplier signal is read out and digitized by a Tektronics TDS 5104 oscilloscope. Together with the photomultiplier signal the position of the wire is stored and analyzed afterwards. Vertical and horizontal scans provide vertical resp. horizontal measurements of beam-profile and beam-position with μm resolution. The system allows scanning speeds from 5 μm/sec up to 1 m/sec. Absolute position determination in the range of 50 μm is achieved by calibrating the wires. The wire scanner is integrated in the coordinate system of PITZ.

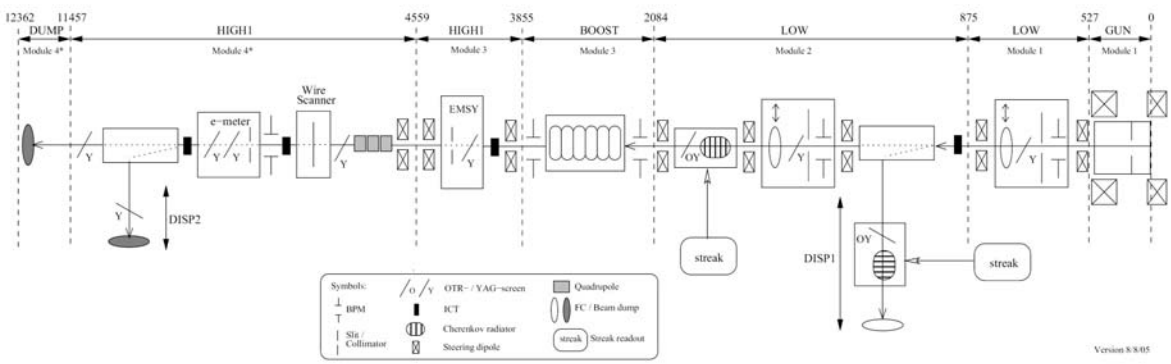

Figure 1: Configuration of PITZ .

* This work has partly been funded by the European Community, contract no.RII3-CT-2004-506008 and 011935 and by the 'Impuls- und Vernetzungsfonds'of the Helmholtz Association, contract no. VH-FZ-005.

hans-juergen.grabosch@desy.de , martin.sachwitz@desy.de

On leave from INRNE, 1784 Sofia, Bulgaria

§ now at DESY , 22603 Hamburg , Germany

§§ now at Hamburg University, 22761 Hamburg, Germany

§§§ now at PSI, 5232 Villingen, Swizerland

Thee parameter settings for this measurement were:

Beam charge	0.5 nC
Beam momentum	12 MeV/c
Bunches/Train	10
Rep.Rate	2 Hz
Focus Point (Screen)	5.74 m from cathode
Wire scanner Position	6.28 m from cathode

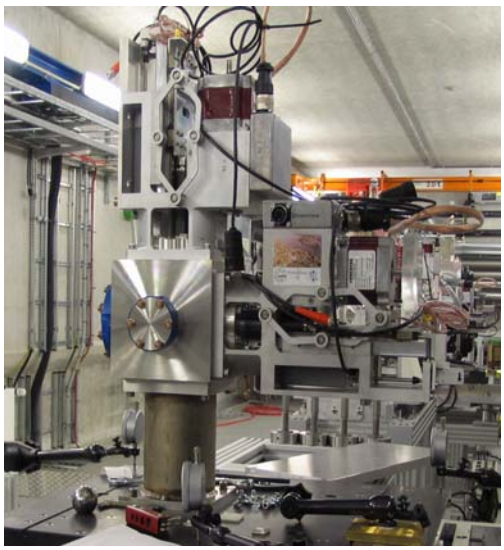

Figure 2: Wire scanner station

Figure 2 shows the wire scanner station mounted at PITZ. The different scanner modules for horizontal- and vertical scans respectively, can be seen.

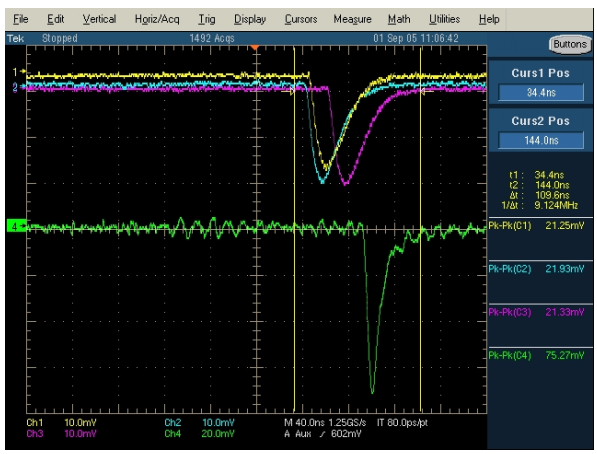

Figure 3: Screen shot of the wire scanner signal

In Figure 3 a typical photomultiplier signal on the oscilloscope (green) is shown together with the signals from the 3 Integrating Current Transformers (ICTs, yellow, blue and magenta), which represent the beam charge before and after the wire scanner. The signal exceeds 0.7 mV when the wire is in the centre of the beam. If the wire is outside the beam a background signal of 0.2 mV is observed. This gives a S/N ration of about 3.5.

RESULTS

To exploit the possibilities of the wire scanner different measurements have been performed. Scans with different step sizes, variation of the gain ($v_{ref.}$ and variation of the beam-size. In Figures 4 and 5 scans of the beam with different step sizes are shown.

The obtained RMS values are X_{RMS} = 1.27 mm and Y_{RMS} = 1.79 mm.

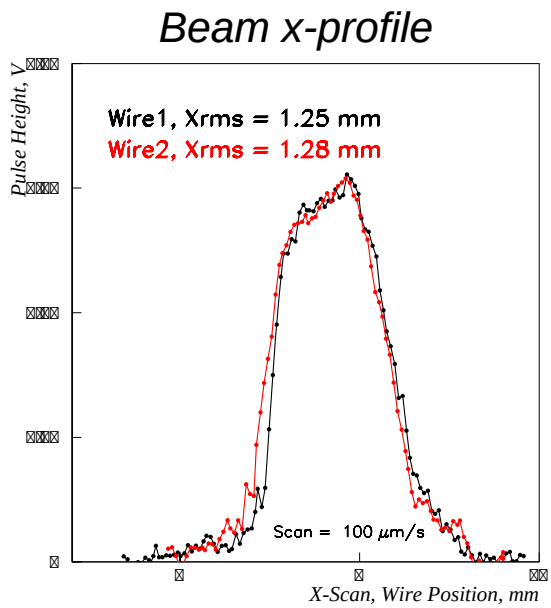

Figure 4: Scan in horizontal direction (the second wire is shifted by 10 mm with respect to the position of the first)

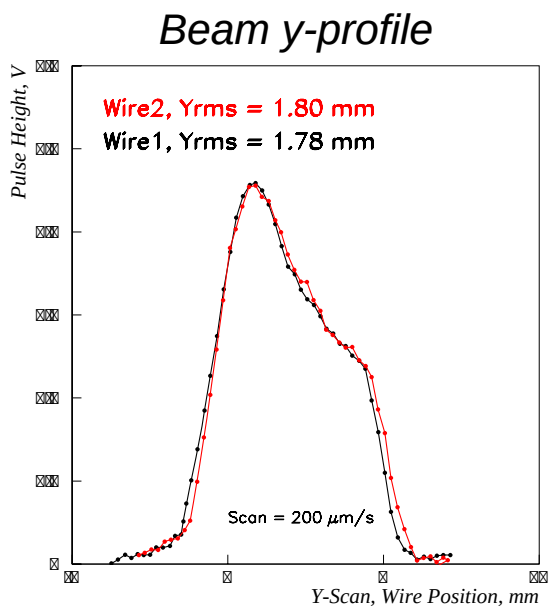

Figure 5: Scan in vertical direction (the second wire is shifted by 10 mm with respect to the position of the first)

The overall measurement error is estimated of about 10 % , the small differencies between the red and black curves in Figure 4 and 5 (wire1 and wire2) may be caused by fluctuations in the electron beam.

To check the capability to measure very small charges with the wire scanner a 50 µm slit [1] was inserted into the beam 199 cm upstream of the wire scanner position. Figure 6 shows this beamlet on a YAG-Screen 54 cm before the wire scanner position.

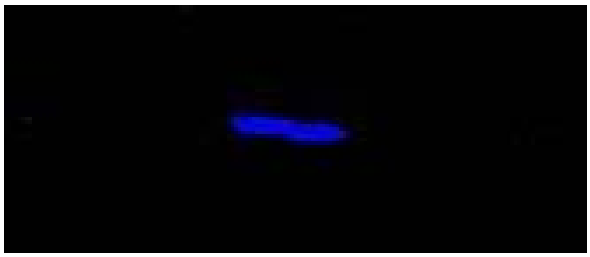

Figure 6: Beamlet from a 50 µm slit

The beamlet was scanned with a step-size of 50 µm/sec in vertical direction. The result of this scan is shown in Figure 7. The beamlet is well resolved. The average RMS value of the measurement is 250 µm, the distance between the wires is measured by 10.10 mm which is 100 µm lager than expected.

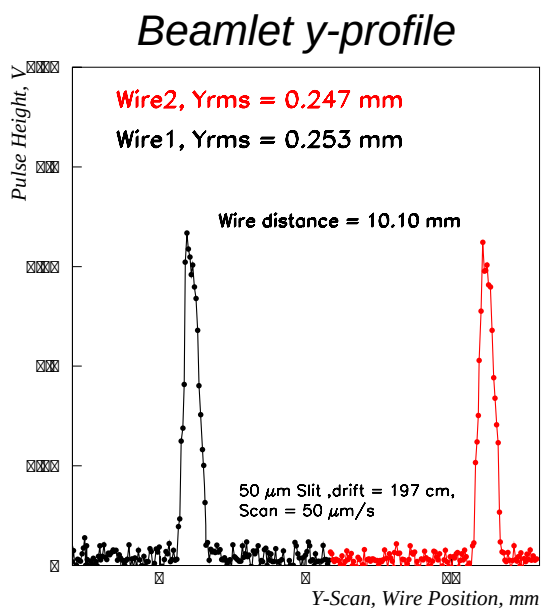

Figure 7: Scan of the beamlet from a 50 µm slit

From simple geometrical considerations one can estimate that the charge of the beamlet must be the order of a few tens of pC.

[1] Tungsten slits are used in PITZ to measure the local divergence

CONCLUSION

Beam-profiles and beam-position could be measured at PITZ with a new type of wire scanner developed for FLASH at DESY. The capability to measure beams of small sizes and charge was also demonstrated. In the final state of the extension of PITZ, two wire scanners are foreseen as standard diagnostic tools for beam-profile and beam-position measurements.

REFERENCES

[1] N.von Bargen, et al., 'Prototyp eines Wirescanners fuer TTF II'
TESLA Collaboration, TESLA 2002-08

[2] P.Castro, et al., ' Wire Scanners in the undulator section of the VUV-FEL at DESY'
Proceedings DIPAC 2005, p. 205.

[3] M.C. Ross, et al., 'Experience with wire scanners at SLC', SLAC-PUB-6014

[4] P. Emma, et al., 'Beam Dispersion Measurements with Wire-Scanners in the SLC Final Focus System', SLAC-PUB-6208

[5] P. Elmfors et al., 'Wire-scanners in low energy accelerators', NIM A 396 (1997) 13-22.

DEVELOPMENT OF A BEAM CURRENT TRANSFORMER FOR THE X-FEL PROJECT IN SPRING-8

Atsushi Higashiya #, Hirokazu Maesaka and Yuji Otake
SPring-8 Joint-project for XFEL/RIKEN, 1-1-1,Kouto, Sayo-cho, ayo-gun, Hyogo JAPAN 679-5148.

Abstract

The SCSS prototype accelerator has been constructed at SPring-8. The output signal of a current transformer (CT) for measuring the electron-beam current in the SCSS prototype accelerator had a few megahertz (MHz) noise emitted from the thyratron of a klystron modulator, a ringing signal caused by the weak field of the electron beam. The long-period undulation of an electrical ground level at the CT monitor output also occurred due to a large electric current generated by the klystron modulator, which flows into ground. As a result, it is difficult to correctly measure the beam current. Therefore, we devised a new CT monitor and the differential circuit from CT monitor in order to improve the problem mentioned above.

The improved points are: (I) We think that the thyratron noise and undulation of the ground level comprise common mode noise. Therefore, these noises were reduced by using a differential detection circuit, and contacting between the ground of the CT case and the outer surface of a CT signal cable. (II) The ringing signal was suppressed by intercalating a dumping resistance material into the space between the case and the ferrite core of the CT monitor. By these developments, the environmental influence to the CT monitor could be suppressed in its output circuit. In an experiment to evaluate the CT monitor, the output waveform of the CT monitor was very clean without any noises as mentioned above.

INTRODUCTION

The X-FEL prototype accelerator (SCSS project) was constructed at SPring-8. SASE (self amplification of spontaneous emission) at a wavelength of about 50 nm and was successfully observed during the last year. The X-FEL project, based on SASE, is currently in progress.[1,2]

In generally, it is important to correctly investigate the beam properties such as the current of an electronic beam. For this reason, in the SCSS prototype accelerator, we use CT monitors.

In commissioning of the prototype accelerator, we found that the CT output signal was influenced by the environment such as noise produced by high-voltage switching in the thyratron of a klystron modulator and occurred due to large electric current flow into the ground, which is also generated by the klystron modulator. Figure1 (a) shows the ringing noise in the CT output. The ringing has a period of about 4 ns (500 MHz). Figure 1 (b) also shows a few megahertz noise emitted from the thyratron. First, in order to eliminate the thyratron noise, we made a contact between the ground of the CT case and the outer surface of the CT signal cables as shown in Fig.1 (d) (indicated by a red circle). As a result of the contact, the noise seemed to be suppressed. However, instead of this noise, a long-period undulation of the electrical ground level (about 220ms) appears as shown in Fig.1 (c). Therefore, it was difficult to correctly determine the beam current (electrons charge amount) due to these problems.

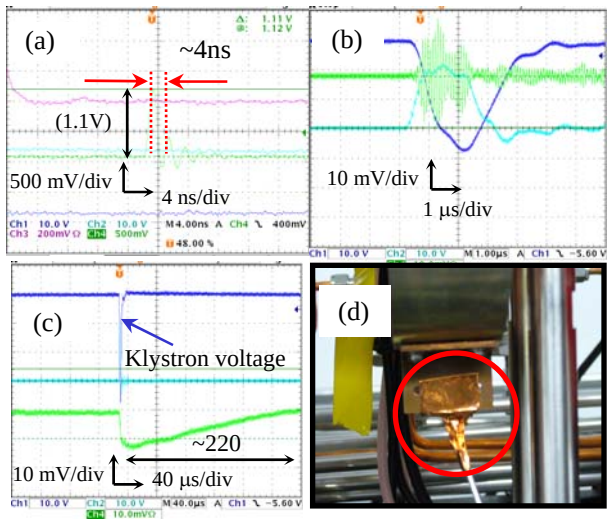

Figure 1: (a) Ringing of the CT output. (b) A few megahertz noise at CT output. (c) Long-period undulation of the electrical ground level at the CT output. (d) Picture of CT at the SCSS prototype accelerator.

In order to improve the problems of the few megahertz noise, the ringing signal and the long-period undulation of the electrical ground level, we devised a differential output-type CT monitor with two output ports and a differential detection circuit to modulate the undulation.

In this paper, we introduce the points of our improvements in the CT used at the prototype accelerator, the detailed configuration of the differential detection circuit, and also demonstrate the clean output waveform without any noises obtained by the differential output-type CT.

codbelo@spring8.or.jp

SYSTEM OF DIFFERENTIAL OUTPUT–TYPE CT MONITOR WITH TWO OUTPUT PORTS

Figure 2 shows a schematic cross-sectional view of the differential output-type CT monitor with two output ports. In this figure, the CT monitor has an amorphous ferrite core with two-one turn coils and two output ports located above and below the core. The upper and lower ports are designed to make opposite signs of the output signals. The amorphous core makes the time response of the CT monitor faster.

As the cause of the ringing signal, we suggested that a

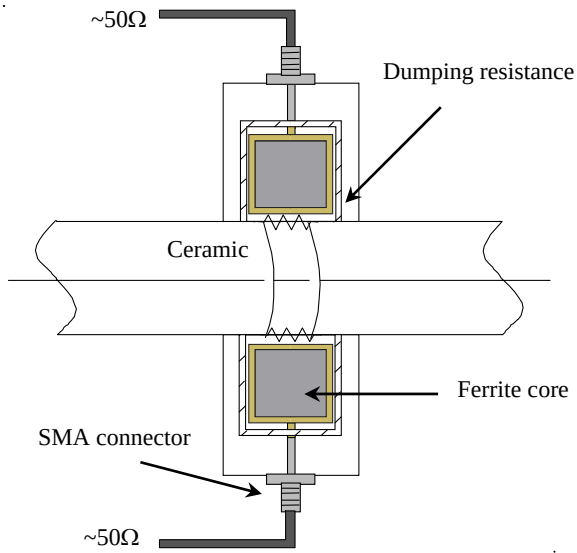

Figure 2: Cross-sectional view of the differential output-type CT monitor.

weak field generated by the electron beam produced ringing. The outer case of the CT monitor could behave as a resonant cavity. To suppress the effect of the wake field, we considered that the damping parameter to the field in the cavity was effective. Therefore, we intercalated the dumping resistance material into the space between the aluminium case and the ferrite core of the CT, shown as the hatched part of Fig. 2. To calculate the resistance at the design stage, a cavity resonant frequency of about 500 MHz was estimated from the case diameter as the cavity, effect of the permeability of the core, and the measured time between the broken red lines, as shown in Fig. 1 (a). The equation of the resonant cavity for an evaluation circuit is represented by

$$L(d^2q/dt^2)+R(dq/dt)+(1/C)q=0, \quad (1)$$

where L, R, q and C are the inductance and the wall resistance of the cavity, the cavity wall current charge induced by the electron beam and the capacitance of the accelerating gap of the cavity, respectively. According to the equation, an adjustment of R was needed to obtain the proper damping effect to suppress the ringing. Namely, it was necessary to fit R to the value of the critical dumping condition of the equation. From a straightforward calculation using this equation and the resonance frequency obtained from Fig. 1 (a), a cavity surface resistivity of more than 3.0 x 10^{-12} $m^2\Omega$ is required to satisfy the condition. Consequently, we achieved this condition by coating a Ni film of 10 μm on the inner surface of the CT case after coating a chrome film of 30 μm. Figure 3 shows the frequency response of the CT monitor having a dumping resistance, which was obtained

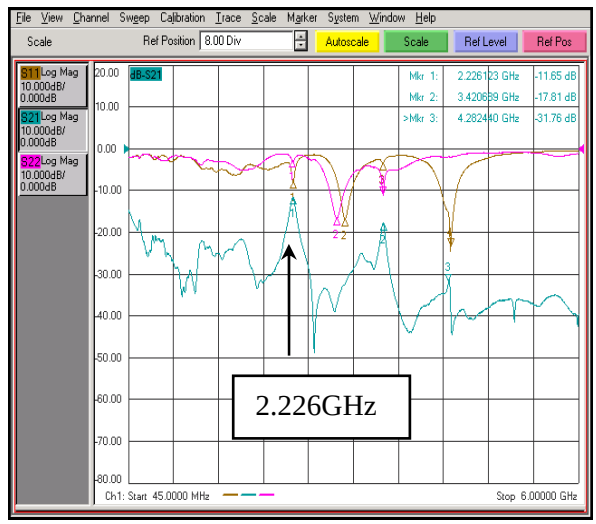

Figure 3: Frequency characteristics of the CT by means of a network analyser.

by a measurement using a network analyzer. A resonant peak at a frequency of 500 MHz existed before coating these films. After the coating, the 500 MHz peak disappears as shown in Fig. 3. However, we can find another resonant peak located at a higher frequency of about 2.2 GHz instead of the 500 MHz peak.

When we thought about the problem of a long-period undulation of the ground level, the undulation was thought to be common mode noise. We then considered how the CT monitor outputs the signal, and devised the following ideas. The devised CT monitor has two output ports at opposite poisons of the case circumference, and the detection circuit is the differential circuit shown in Fig. 4. The two output signals from the CT monitor, indicated as (I) and (II) in Fig. 4, are transmitted to the differential detection circuit by using a 100-ohm differential cable. Then, these signals are terminated by a 100 Ω resistance and imported into the differential circuit. Since the noise of the output waveform is the common mode, the noise components of the wave forms have the same signs, as indicated by the two solid lines of (I) and (II) in Fig. 4. On the other hand, the two necessary signals generated by the electron beam are of the opposite signs, as shown by the dashed lines of (I) and (II) in Fig. 4. Therefore, the common noise of the signals at the circuit input is suppressed when these signals pass through a differential amplifier just in front of an AD converter (ADC), as indicated by the solid line (III) in Fig. 4. In addition, the necessary signal at the converter input makes its voltage double by adding signals (I) and (II), as shown

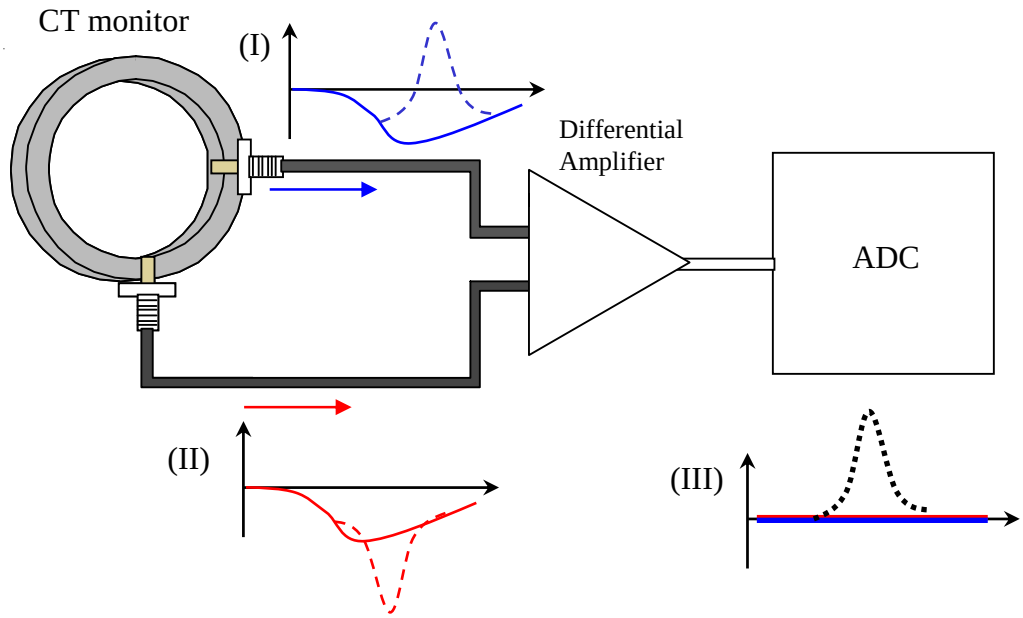

Figure 4: Schematic circuit diagram for the differential reception.

by the dashed line (III). The output signal from the differential amplifier is transferred to the ADC.

DETAILED CONFIGURATION OF DIFFERENTIAL DETECTION CIRCUIT FOR CT MONITOR

Figure 5 shows the detailed configuration of the differential detection circuit for the CT monitor. The differential circuit is composed of a preamplifier, a 100 ohm differential cable, a main amplifier, and a VME ADC module. The output signal from the CT monitor is transferred to the preamplifier. Then and there, the gain adjustment to the amplitude of the CT signal by the

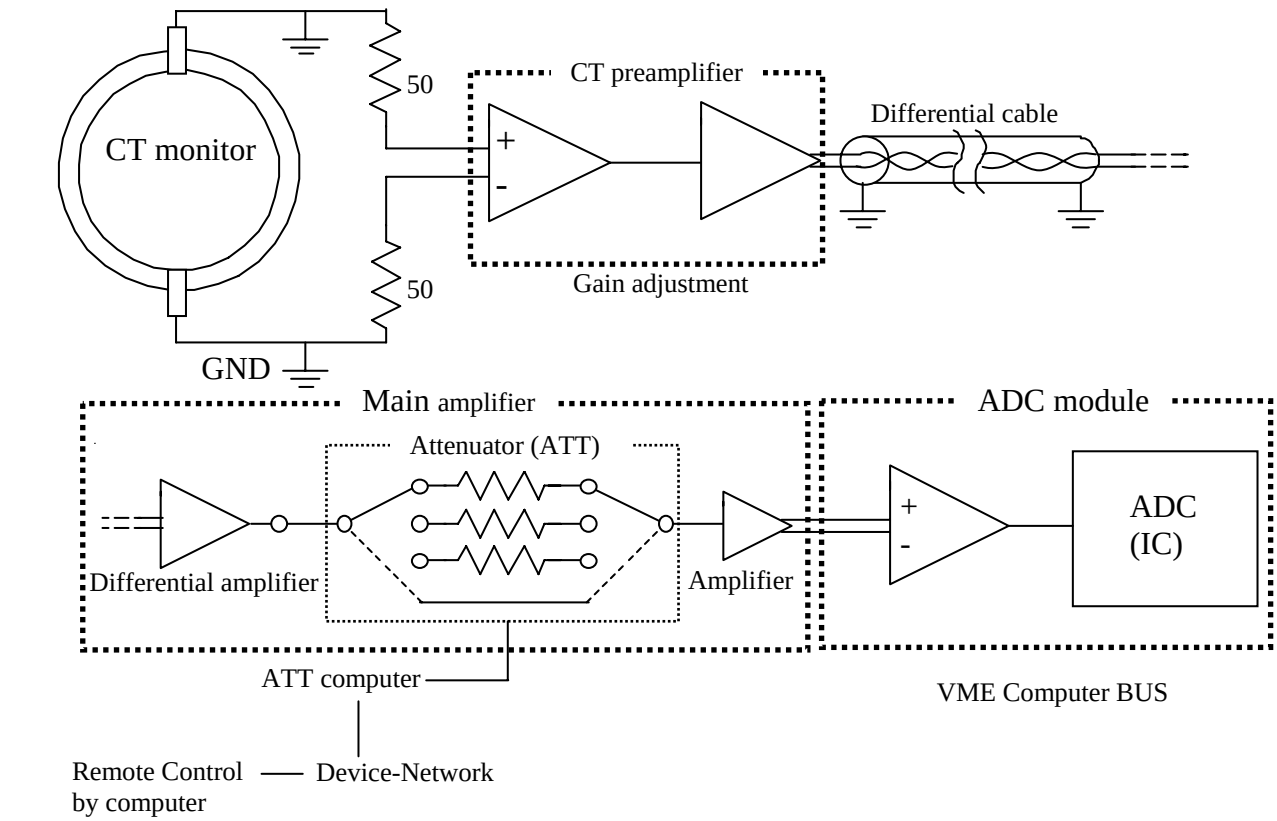

Figure 5: Differential circuit design of CT monitor

preamplifier is done. After then, the signal is transferred to the main amplifier through the differential cable, in which its cable length is about from 10 m to 20 m. The main amplifier includes differential amplifiers and a switching attenuator array. The attenuator array also adjusts the amplitude of an input signal from the CT monitor. The switching of the attenuator is remotely controlled from a computer through the Device-Network. The output signal from the main amplifier is transfer to the VME ADC module that works like an oscilloscope having a differential input, a 12 bits dynamic range, a 238 MHz clock drive circuit. At the present, this differential detection system is under development. However, we believe that a genuine large beam current signal with noise suppressed by the system could be successfully obtained.

TEST OF DIFFERENTIAL OUTPUT-TYPE CT MONITOR

We installed a differential output-type CT monitor to the SCSS prototype accelerator (as shown in Fig. 6 (a)) for a test, and directly measured the output wave forms from the CT monitor, induced by the beam, by using an oscilloscope having a measurement bandwidth from DC to 12 GHz. Figures 6 (b) and (c) show the obtained output wave forms. In these figures, the green, yellow, and red lines are the signal from port 1 and port 2, and their difference (port1-port2), respectively. As shown by the red line, the long-period undulation disappears and the ground level is nearly flat due to the common mode-rejection effect.

SUMMARY

In order to eliminate the ringing signal caused by the weak field of the electron beam, the few MHz noise and the long-period undulation of the ground level at the CT output, we devised a differential output-type CT monitor.

The waveforms obtained by the CT monitor showed clear output signals, which indicated that our improvement could successfully suppress the noise from the environment around the CT monitor. The ringing effect caused by the weak field induced by the electron beam is successfully suppressed by inserting the dumping resistance. Furthermore, the CT monitor time response was fast due to the time response of the amorphous ferrite core with the one-turn coils, and due to the frequency response of the effective permeability of the core up to about 1 GHz. The waveform rise time is less than 200 ps. The obtained signal waveforms had a few structures. At the present time, the reason why the waveform had the structure is not clear. There is some possibility that the true waveforms could have a different shape, and could be hidden due to the limited bandwidth of the oscilloscope. Therefore, we need more accurate measurements using an oscilloscope with higher bandwidth than 12 GHz, or streak camera in order to verify the true waveforms. The differential detection circuit for this CT monitor is still under development, and however, it will be tested within several months. Consequently, we think that it is possible to measure the beam current (the electrons charge amount) more precisely.

ACKNOWLEDGMENT

We thank the members of the SCSS prototype accelerator group for their help with the experiment. For CT monitor production, we are grateful for the effort of Mr. Koji Kase (Toyama corporation, 4-13-16 Hibarigaoka 4-chome, Zama-shi, Kanagawa Prefecture, JAPAN 228-0003).

REFERENCES

[1] SCSS X-FEL R&D Group (http://www-xfel.spring8.or.jp/)
[2] H. Tanaka, et al., Beam Performance of the SCSS Prototype Accelerator, The 3rd Annual Meeting of Particle Accelerator Society of Japan (2006).

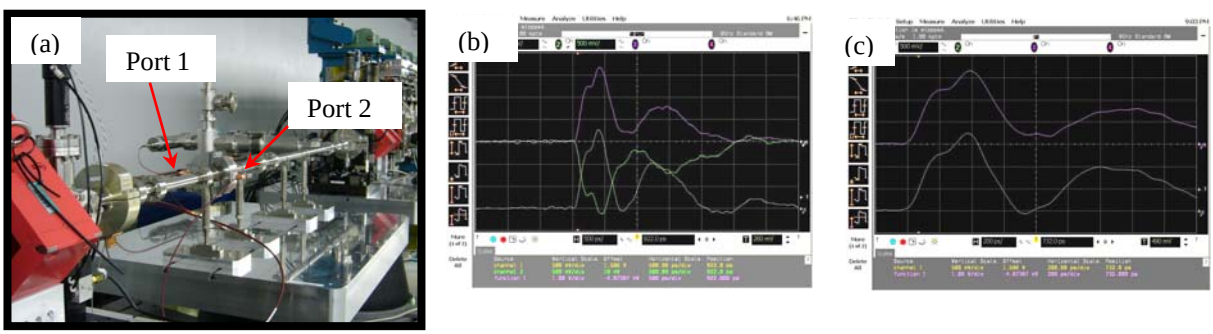

Figure 6: (a) Picture of the CT monitor installed in the SCSS prototype accelerator. (b) Output waveforms induced by the electron beam displayed in the wider time span (500ps/1div). (c) Output waveforms displayed in the narrower time span (200ps/1div.).

IN-SITU UNDULATOR FIELD MEASUREMENT WITH THE SAFALI SYSTEM

Takashi Tanaka, R. Tsusu, T. Nakajima, T. Seike and H. Kitamura
RIKEN SPring-8 Center, Koto 1-1-1, Sayo, Hyogo 679-5148, Japan

Abstract

A new scheme of undulator field measurement has been proposed, which makes it possible to do field mapping inside the vacuum chamber to verify the final magnetic performance of in-vacuum undulators (IVUs) after assembly. Optical laser beams are used in order to measure the positions of the Hall probe during actuation along the longitudinal direction, and dynamic feedback of the position is carried out to ensure a high stability and accuracy of the measurement. A field measurement system based on this concept has been developed at the SPring-8 in order to measure two different types of IVU. Principle of the new measurement scheme and details of the developed system are described together with the results of the field measurement.

INTRODUCTION

Shortening the undulator period is crucial to reducing the electron energy required to get angstrom x-rays in the SR and XFEL facilities and thus the total cost of construction. The in-vacuum undulators (IVUs) have many advantages over out-vacuum devices toward shorter magnetic period and thus have been adopted in a great number of SR facilities all over the world. It should be noted, however, that magnetic measurement after final assembly including the vacuum chamber, i.e., final verification of magnetic performance, is not an easy task. In addition, remeasurement after installation in the accelerator beamline is not trivial. The situation is more severe for cryogenic permanent magnet undulators (CPMUs)[1], an extension of IVUs.

We have recently developed a magnetic measurement system to measure the field inside the vacuum chamber. With optical laser beams introduced into the vacuum chamber, the alignment of the Hall probe positions is dynamically carried out, which ensures a high stability and accuracy of the measurement. This system is called SAFALI for Self-Aligned Field Analyzer with Laser Instrumentation. The SAFALI system has been applied to field measurement of two different undulators. One is an IVU installed in Swiss Light Source in 2001 and had been operated for about 3 years. The other is a CPMU prototype to demonstrate the principle of CPMU. The purpose of the former measurement is to investigate the radiation damage during operation, while that of the latter is to check the variation of the magnetic properties according to the temperature change of magnets. In this paper, details of the SAFALI system are given together with the results of the field measurements.

PRINCIPLE

In the conventional magnetic measurement system, a magnetic sensor such as a Hall probe is placed on a cantilever supported by a 2-axis (x,y) stage mounted on a long actuation table with a high mechanical accuracy, which is usually made of granite. Due to pitching, rolling and yawing of the actuation table, the Hall probe position during actuation can fluctuate. To perform a magnetic measurement with a high accuracy, the positional fluctuation should be kept as low as possible. The positional error of a typical measurement bench is around 30 μm, which corresponds to a field error of 0.02% for an undulator with a magnetic period of 10 mm, and thus enough for magnetic measurement of most undulators. In addition, the measurement result is quite well reproducible: typical deviation of the magnetic measurement in terms of the r.m.s. phase error is usually lower than 0.3 degree. It should be noted, however, that such a Hall-probe scanning method cannot be applied to the field measurement of IVUs as is. We have to modify the actuation method to be adapted to the field measurement of IVUs after assembly.

The most straightforward way is to install a huge vacuum chamber that can accommodate a rigid and robust linear guide with a mechanical accuracy comparable to that of the granite bench, which is not only impractical but also inefficient. Another way is to monitor the position of the Hall probe during actuation along the longitudinal axis and perform a dynamic feedback to ensure that the Hall probe is always in position. In this case, the linear guide does not have to be necessarily rigid or robust: any method of actuation is acceptable unless the positional variation during actuation is too large to be compensated by feedback.

We can consider several methods to measure the Hall probe position. Among them, we decided to use optical laser beams combined with position sensitive detector (PSD) and irises attached to the Hall probe, because they are cost effective compared to other methods. In order to measure the longitudinal position, we can use a commercially available laser scale with a resolution better than $0.1mu$m. Hereinafter, let us call the field measurement method based on this concept "SAFALI", for Self-Aligned Field Analyzer with Laser Instrumentation. We have so far developed two SAFALI systems for measurement of two different IVUs, the details of which will be discussed in the following sections.

SAFALI FOR IVU24

In 2001, an IVU with a magnetic period of 24 mm and magnetic length of 1.5 m (IVU24) has been constructed at the SPring-8 and installed in the storage ring of Swiss

Light Source (SLS) as a collaboration to aim at utilization of angstrom x rays in the medium-sized SR facility. After 3-year operation, IVU24 has been replaced with another IVU and returned to SPring-8. It is important to measure the magnetic field of IVU24 and compare with the initial state, and to check the variation of magnetic performances from the point of view of demagnetization due to electron irradiation during operation.

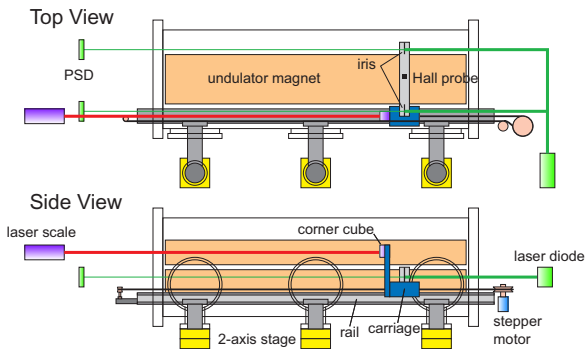

Figure 1: Schematic illustration of the SAFALI system for the CPMU prototype.

Figure 1 shows a schematic illustration of the SAFALI system for IVU24. We have installed a rail and carriage to actuate the Hall probe by means of a tensioned loop wire driven by a stepper motor. The Hall probe cantilever was attached to the carriage together with the cubic mirror to reflect the laser beam of the laser scale to measure the longitudinal position of the Hall probe. In addition, two irises are attached at the both ends of the Hall probe cantilever with a diameter of 2 mm. In order to measure the transverse Hall probe position during actuation, two laser beams were introduced to irradiate the irises and create laser spots at the opposite side. The positions of the laser spot were measured with position sensitive detectors (PSDs), the average of which defines the position of the Hall probe.

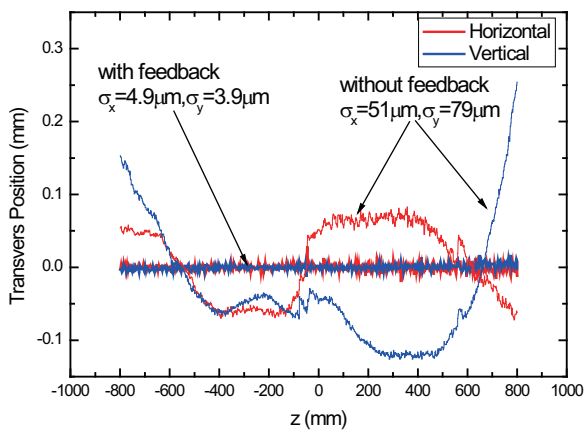

Figure 2: Variation of the Hall probe position with and without feedback.

The feedback of the Hall probe position is done by moving the rail with the three sets of 2-axis stages supporting the rail. Figure 2 shows the variation of the Hall probe position measured with and without the feedback procedure. We can clearly find the effects due to the feedback. The magnetic error due to the positional deviation of 5 μ is just 5×10^{-6} for an undulator with a magnetic period of 10 mm, and smaller for a longer period.

As a field measurement system for undulators, the reproducibility is the most important. We measured the magnetic field distribution of IVU24 four times under the same condition to examine the reproducibility. The results are shown in Fig. 3 in terms of the phase error as a function of the pole number, where we find quite a good agreement between the measurement results.

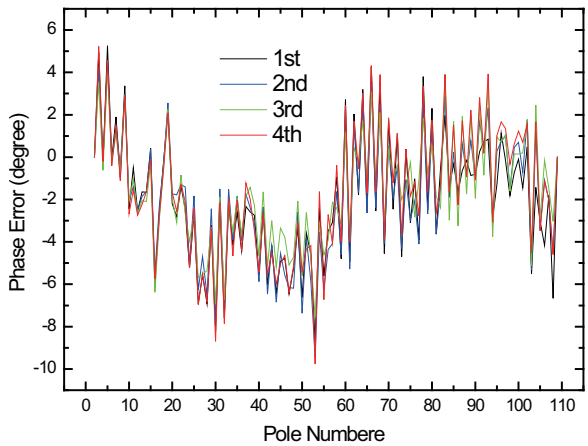

Figure 3: Reproducibility of the field measurement in terms of the phase error distribution.

As described above, the developed SAFALI system has been found to have a performance good and reliable enough to measure the magnetic field of IVU24.

SAFALI FOR CPMU PROTOTYPE

The CPMU is a novel undulator proposed at SPring-8 in 2004 [1]. The permanent magnets in the IVU is cooled down to improve the magnetic property in terms of the remanence and coercivity. The operation temperature will be around 100∼150K where the remanence becomes maximum, and much higher than liquid helium, so the operation will be much more feasible than superconducting undulators composed of NbTi wires. We have constructed a prototype of CPMU with a magnetic length of 600 mm and a magnetic period of 15 mm and made experiments to investigate the feasibility of CPMUs such as the cooling capability, variation of the magnetic gap and tapering during the cooling process [2]. Although promising results have been obtained in these experiments, we have to establish a field measurement technique to be adapted to the CPMUs. So, we have developed a system based on the SAFALI method to measure accurately the magnetic performance at a cryogenic temperature [3].

Figure 4 shows a schematic illustration of the SAFALI system for the CPMU prototype. A pair of O-ring recipro-

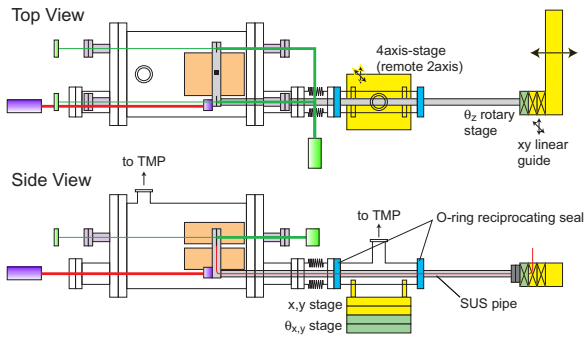

Figure 4: Schematic illustration of the SAFALI system for the CPMU prototype.

cating seals have been installed to insert the SUS tube to fix the cantilever of the Hall probe, which is actuated by means of pushing or pulling the end of the tube. The Hall probe position feedback is performed by the multi-axis stage supporting the vacuum duct including the O-ring seal. The variation of the Hall probe position during actuation was slightly worse than the system for IVU24 described in the preceding section, however, the reproducibility was similar. For details, refer to [3].

RESULTS OF MEASUREMENT

IVU24

We measured the magnetic distribution at the gap values of 6, 8, 10, 14, and 20 mm and compared the magnetic performances with those measured by a conventional method in July 2000, just after the field correction and before installation in the SLS ring. The results are shown in Fig. 5 in terms of the electron trajectory (2nd field integral) and phase error distribution.

We find negligible difference between the two measurements in terms of the electron trajectory, while a small discrepancy in the phase error distribution suggests that the magnetic field distribution has changed slightly. It should be emphasized, however, that the variation is very small and less than 0.5 degree in r.m.s. So we can conclude that no significant demagnetization took place in the IVU24 during operation.

CPMU Prototype

We measured the field distribution of CPMU prototype at different temperatures and found that the peak field became maximum at a temperature of 130 K. During the measurement, the gap was fixed at 5 mm by measuring directly the distance between the top and bottom magnet arrays by means of a laser scan micrometer. From the point of view of field correction, what is important is the phase error variation due to temperature change. Figure 6 shows the magnetic performances measured at room temperature and 130 K in terms of the electron trajectory and phase error. We find negligible difference between the performances at two

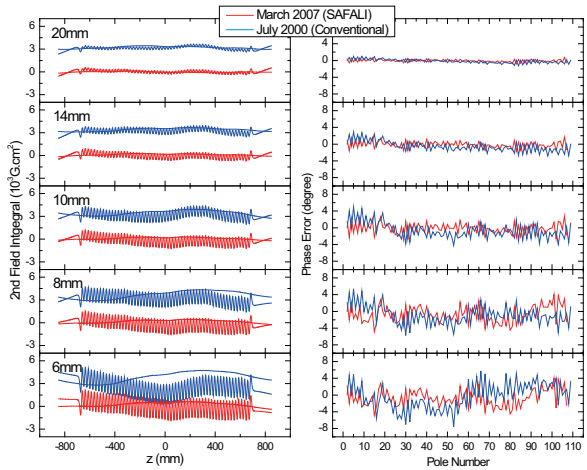

Figure 5: Comparison of magnetic performances of IVU24 between July 2000 and March 2007. Note that measurement in July 2000 was done by a conventional method.

different temperatures, suggesting that cooling the permanent magnets did not induce a large change in the error magnetic components that could affect the undulator performance. This is a very encouraging result toward realization of CPMUs.

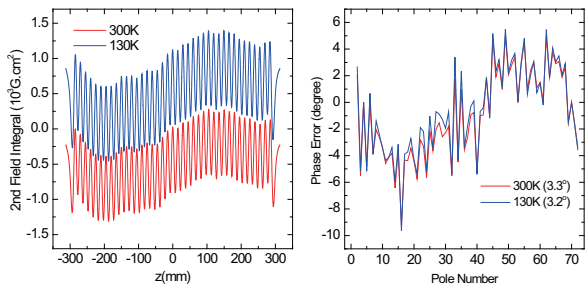

Figure 6: Variation of magnetic performances of CPMU prototype at room temperature and 130 K.

SUMMARY

We have described the SAFALI system as a new scheme of undulator field characterization and its practical application. It should be also stressed that the SAFALI system is portable: the magnetic performance of IVUs can be checked at any time without moving to the laboratory or facility for the field measurement. Such a portability is very important especially in X-ray FEL facilities where a number of undulators will be installed. The SAFALI system can be used not only for the final check after assembly but also to monitor the magnetic performance as the FEL driver. We also note that most undulators nowadays have a C-shaped frame, but not a O-shaped frame, in order to ensure openings for field mapping with Hall probe scanning, whether they are in-vacuum or out-vacuum. This imposes a severe restriction on the undulator design, because C-shape frame

is much less rigid than the O-shape frame. By means of the SAFALI method, the mechanical frame does not have to be C shape from the point of view of field measurement and new undulator designs would be be possible.

REFERENCES

[1] T. Hara, T. Tanaka, H. Kitamura, T. Bizen, T. Seike, T. Kohda, and Y. Matsuura, Phys. Rev. ST-AB 7, 050702 (2004).

[2] T. Tanaka, T. Hara, T. Bizen, T. Seike, R. Tsuru, X. Marechal, H. Hirano, M. Morita, H. Teshima, S. Nariki, N. Sakai, I. Hirabayashi, M. Murakami and H. Kitamura, New J. Phys. 8 287 (2006).

[3] T. Tanaka, R. Tsuru, T. Nakajima and H. Kitamura, J. Synchrotron Rad., 14 416 (2007).

NON-DESTRUCTIVE SINGLE-SHOT 3-D ELECTRON BUNCH MONITOR WITH FEMTOSECOND-TIMING ALL-OPTICAL SYSTEM FOR PUMP & PROBE EXPERIMENTS

H. Tomizawa, H. Hanaki, Accelerator Division, Japan Synchrotron Radiation Research Institute (JASRI/SPring-8), Kouto, Sayo-cho, Sayo-gun, Hyogo 679-5198, Japan
T. Ishikawa, The Institute of Physical and Chemical Research (RIKEN Harima/SPring-8), Kouto, Sayo-cho, Sayo-gun, Hyogo 679-5148, Japan

Abstract

We are developing a non-destructive single-shot 3-D electron bunch monitor based on EO sampling, using the yearlong stable femtosecond laser source developed for the SPring-8 RF gun. The probe laser for spectral decoding EO sampling has been prepared as radial polarized and completely linearly chirped bandwidth (~500nm) supercontinuum generation. The EO-probe element is made of 8 EO-crystals with the assembling of each EO-crystal's optical axes along radial beam axes. The linearly chirped probe laser is longitudinally shifted in 8 transverse sectors for spectral decoding. We are planning to use organic polymer film as a femtosecond resolution EO-probe instead of crystals. This 3-D bunch monitor with spectrograph detects and analyzes the Coulomb field of electron bunches as longitudinally spectral decoding and transversely multi-pole expansion. Our single-shot bunch monitor can characterize the 3-D (both longitudinal (1D) and transverse (2D)) distribution and position of an electron bunch with femtosecond resolution. This non-destructive monitor can be used as an electron energy chirping monitor at a dispersive region for XFEL commissioning. Additionally, the EO-sampled probe laser pulse will be used as a femtosecond-timing signal pulse. This signal pulse is amplified with a NOPA, developing an all-optical timing system.

INTRODUCTION

At the SPring-8 site, construction of the XFEL project [1] has begun under a RIKEN and JASRI joint project. It will enter operation in 2010. For this project, it is necessary to monitor femtosecond electron bunch length for its commissioning. At the moment, the most promising femtosecond electron bunch monitor with an RF deflector, the LOLA cavity [2], is planned to be installed in the 1-GeV energy region of the 8-GeV SPring-8 XFEL linac. However, this monitor requires a few-meters-long cavity structure, and has to measure the bunch length on a fluorescent screen installed a few meters further downstream. The compactness is important in the XFEL project at SPring-8. Therefore, the shorter bunch monitor system is required for bunch length measurement, especially in the 8-GeV region.

In terahertz technology, femtosecond laser pulse duration has been measured utilizing the Pockels effect of ZnTe and so on. This method was the so-called electro-optical sampling (EOS). The variation of the Coulomb field of the electron beam bunch with a duration of less than 1 ps corresponds to terahertz (>10^{12} Hz) in frequency domain. Against this background, this EOS-based bunch monitor has been developed in the accelerator field [3-6]. The advantage of the EOS monitor is that it is non-destructive and has a high resolution of sub-picosecond. To use the laser as a probe allows a timing jitter of femtosecond, and a readout of the monitor head without signal cables. However, the temporal response of inorganic crystals like ZnTe is limited by 110 fs.

There are several types of EOS measurements. One is so-called spectral decoding, that decodes the longitudinal electron bunch structure on the spectrum of the chirped probe laser pulse. One of the others is so-called temporal decoding that is used as conventional pulse measurement with a correlation technique for a femtosecond laser.

The spectral decoding EOS makes possible single-shot measurement with a high repetition rate. Its encoding is simple to perform with a conventional spectrometer. Despite spectral decoding being a convenient method, it is well known that the sensitivity of the signal pulse is reduced because of certain interferences occurring between neighbouring wavelengths. Generally, the temporal resolution R_{res} is given by

$$R_{res} \cong \sqrt{t_0 t_c} \ ,$$

where the Fourier transform limit of the probe laser is t_0, and the probe chirped laser pulse duration is t_c [5-6]. Therefore, it is the tendency for measurement with high precision to use the temporal decoding method, which is superior in resolution. With a broadband (> 400 nm) laser square pulse chirped linearly, for instance, if t_0=2.5 fs, t_c=160 fs, R_{res} is improved around 20 fs.

In our point of view, spectral decoding is simple to encode and useful for measuring more information about the electron bunch. If the three-dimensional charge distribution of the electron bunch is measurable, it is quite useful for many applications. We investigated the bunch-by-bunch measurement possibility of the transverse charge distribution of the electron bunch with spectral decoding. In our strategy, temporal decoding, AO-modulator-based SPIDER [7] (Spectral Phase Interferometry for Direct Electric field Reconstruction) measurement will be used as a precise calibration for our spectral decoding EOS 3-D bunch monitor.

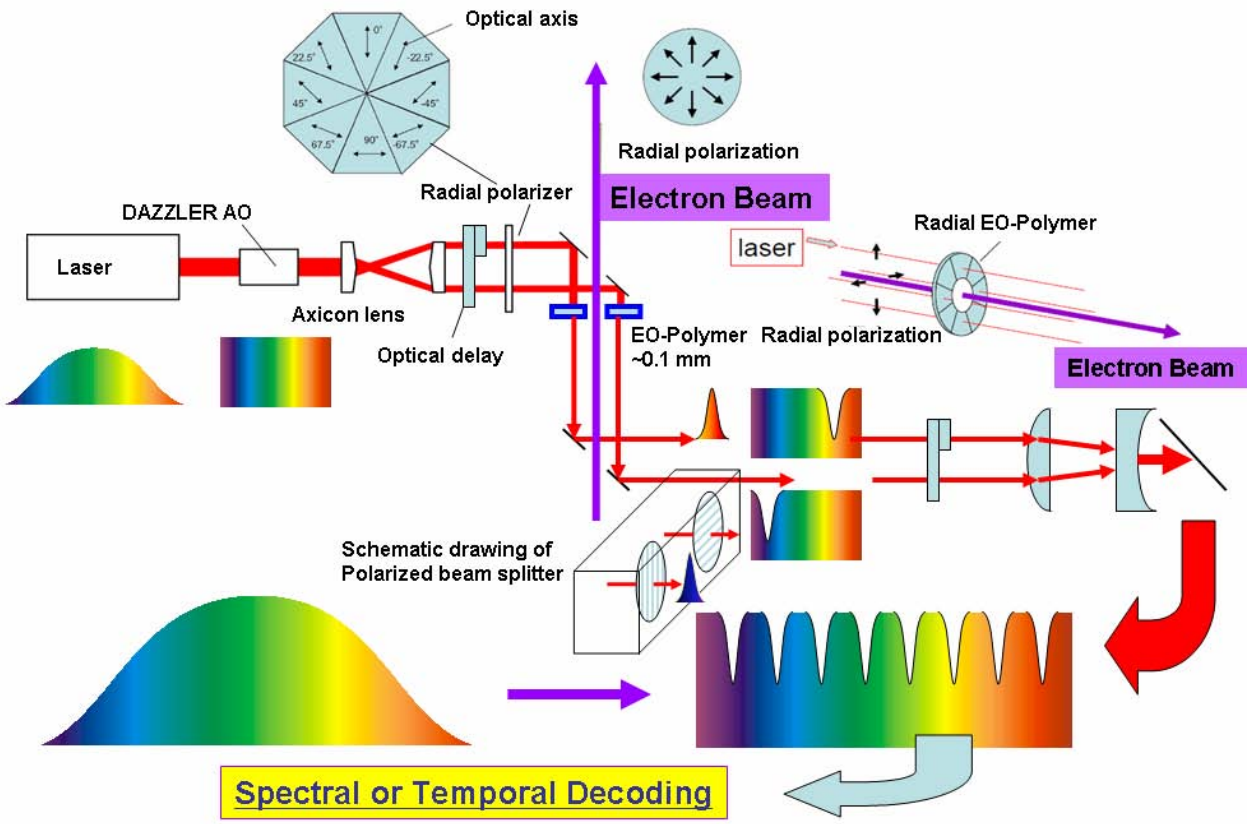

Figure 1: 3-D bunch structure monitor and its probe laser optics:
The probe laser for spectral decoding EOS is prepared as radial polarized and completely linearly chirped bandwidth (~500nm) supercontinuum generation. The EO-probe element is made of 8 EO-crystals (organic films) with the assembling of each EO-crystal's optical axes along radial beam axes. The linearly chirped probe laser is longitudinally sifted in 8 transverse sectors for each spectral decoding to analyze transversely multi-pole expansion.

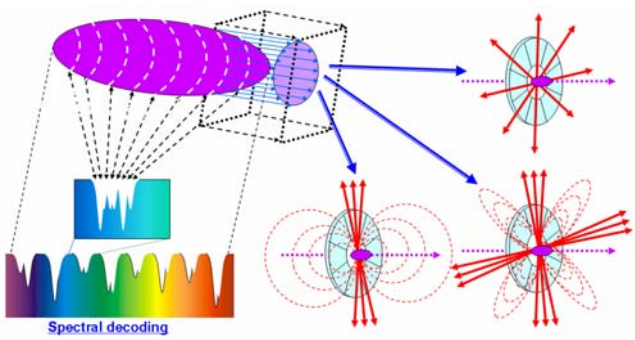

Figure 2: The principle of single-shot EOS-based 3-D bunch monitor: This 3-D bunch monitor with spectrograph detects and analyzes the Coulomb field of electron bunches as longitudinally spectral decoding and transversely multi-pole expansion. In the figure, the Coulomb fields of monopole, dipole, and quadrupole in the bunch slice are shown.

The probe laser will be generated with a photonic crystal, using the yearlong stable femtosecond laser source [8] developed for the SPring-8 RF gun. Recently, the photonic crystal has generated supercontinuum with a broad bandwidth of more than 500 nm. This broadband laser source is linearly chirped and temporally (spectrally at the same time) squared by a broadband AO-modulator (DAZZLER: UWB650-1100; FASTLITE). The squared linear-chirped broadband pulse is radial polarized and converted to a hollow laser pulse with optics we invented [9]. This hollow laser pulse is used as the probe laser for EOS as shown in Figure 1. Using this probe hollow laser pulse, the single-shot 3-D bunch monitor shown in Figure 2 is possible. We propose a single-shot EOS-based 3-D bunch monitor and report the optics for generating a hollow broad-bandwidth laser probe pulse.

CONFIGRATION AND COMPONENTS OF EOS-BASED 3-D BUNCH MONITOR

Radial polarizer for hollow broad-bandwidth laser beam as EOS probe

A radial polarized beam can be generated with 8-divided waveplates [10] as shown in Figure 1. However, the divided type has difficulty being utilized for broad bandwidth (500 nm) supercontinuum. For a broadband source, it is possible to use a radial polarizer based on liquid crystal. In Figure 3, the radial polarization test samples with 90-degree rotation of an additional

polarizer for a white light source are shown, using the radial polarization converter based on liquid crystal.

It is necessary to generate the hollow laser beam for the probe laser, avoiding interaction with the electron beam bunch. The hollow laser beam is generated by an axicon lens pair, and then reflected in and out at the hollow mirrors in a vacuum. The ring width of the hollow probe beam is half of the incident beam radius at the axicon lens pair. The width should be as narrow as possible for accuracy to decode the field of the electron bunch slice.

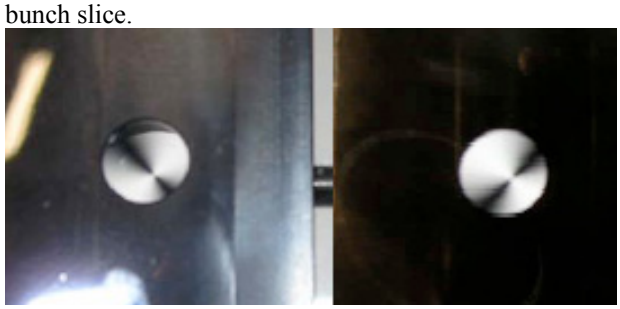

Figure 3: Radial polarization converter (ARCoptix, Switzerland) based on liquid crystal: Comparing the right and left (rotated 90 degrees from each other), it is clear that the converter generates a radial polarization.

Supercontinuum generation and transport

In order to generate supercontinuum (650-1100 nm) with a femtosecond laser oscillator, we selected a photonic crystal. The generated broadband laser has to be transported with optics without distortion in intensity and phase over the spectral range. It is difficult to maintain the whole spectral range, especially for a polarizer. The present status of the optical configuration is shown in Figure 4. At the moment, we have chosen the Glan-Laser Carsite Polarizer limited by the upper limit wavelength of 1000 nm. To maintain the entire supercontinuum spectrum, we are designing a Fresnel-Rohm and apochromatic waveplate.

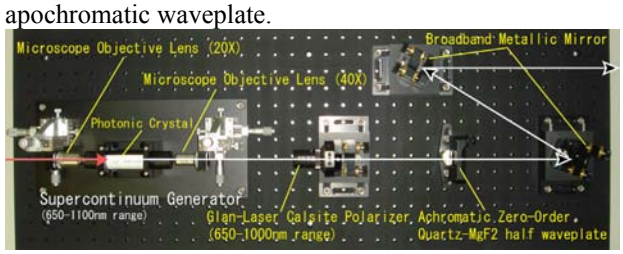

Figure 4: Supercontinuum generator (650-1100 nm) and broadband transport optics

Squared linear-chirped supercontinuum with compensation of transport distortion

The generated broadband laser is distorted in intensity and phase spectra. However, by introducing an AO-moderator, such distortion on intensity and phase spectra can be compensated. We want to prepare the probe laser pulse as a squared linear chirped pulse because it avoids computation to encode the electron-bunch-information-decoded spectra through detection with a spectrometer. Without complex computation to encode, it helps to detect the 3-D bunch structure at a high repetition rate.

We tested spectrum shaping with the AO-modulator DAZZLER, which can compensate optical dispersion up to 4th order in the phase spectrum and gain-narrowing in the intensity spectrum. We installed DAZZLER after the stretcher of the CPA configuration of the Ti: Sapphire terawatt laser. Because of too large a stretching factor of ~19000, it is beyond DAZZLER's capability to compensate GDD (Group Delay Dispersion) in this test. Therefore, we compensated just the gain-narrowing of spectrum for squared pulse generation. Streak spectrographs (streak image in spectrum) are shown in Figures 1 (initial) and 2 (square-shaped). It clearly shows that a square shape is generated successfully.

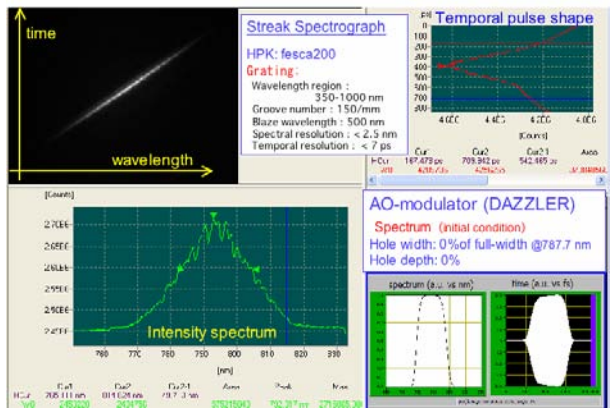

Figure 5: Initial intensity spectrum and chirp of the fundamental of Ti: Sapphire laser (after the stretcher): The linear chirp is measured by monochrometer combined with streak camera (Hamamatsu Photonics K.K.)

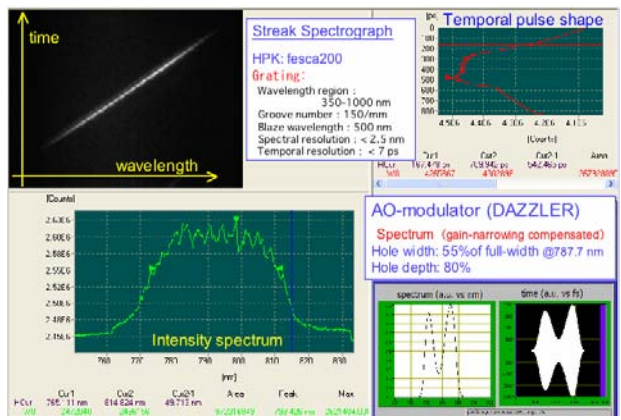

Figure 6: Squared intensity spectrum with a hole made on its spectrum by DAZZLER

EOS BUNCH MONITOR CHAMBER

It is possible to make several configurations of EOS-monitors with different functions and with different boundary conditions (3-D monitor shown in Figure 7, BPM-function shown in Figure 8). Besides, the temporal resolution τ that depends on the distance r between the monitoring probe laser position at the EO element and the charge centre of the electron bunch slice is given by

$$\tau = r/\gamma c ,$$

where the Lorenz factor is γ, and the light speed is c. At the energy region of 8 GeV, with monitoring position r of 1 cm, temporal resolution τ will be 2 fs. The broad bandwidth of 400 nm determines the resolution of 20 fs (already mentioned). At the beginning of the test, the radial EO-probe element will be made of 8 EO-crystals with the assembling of each EO-crystal's optical axes along radial beam axes as shown in Figure 7. We are planning to use organic polymer film [11] for a femtosecond resolution EO-probe instead of inorganic crystals. The existing π-bonding in organic polymer causes a higher response of electrons for Pockels effect than inorganic crystals with only σ-bonding.

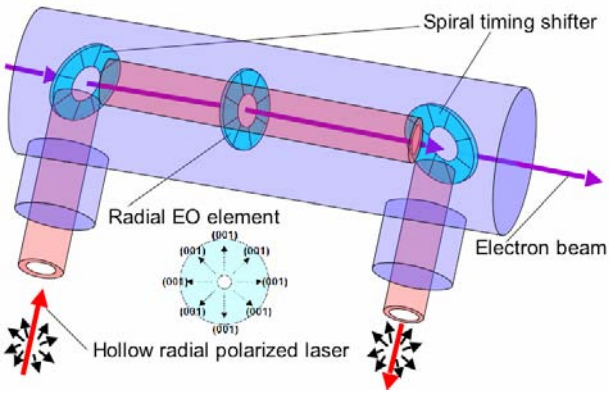

Figure 7: EOS bunch monitor for 3-D electron distribution monitor function: The linearly chirped hollow probe laser is shifted by the spiral timing shifter in 8 transverse sectors for spectral decoding. It has also function of total timing delay of the hollow probe laser, avoiding interaction with the electron beam bunch.

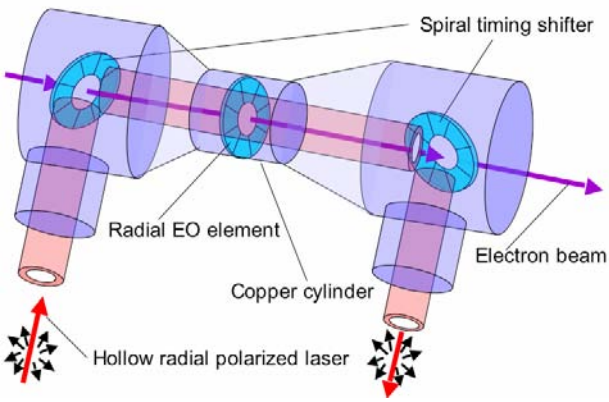

Figure 8: EOS monitor for BPM function: The 3-D monitor EOS chamber shown in Figure 7 is installed between two BPM EOS chambers.

With variation of distance r and boundary condition of a cylindrical metal wall, the combined EOS bunch monitor should be optimized in their geometry. The 3-D monitor function EOS chamber is installed between two BPM function EOS chambers. Analysis of three-dimensional charge distribution requires the charge centre position of the electron bunch slice at the EO element (see Figure 2). A spectrograph encoder detects and analyzes the Coulomb field of the electron bunches as longitudinally spectral decoding and transversely multi-pole expansion. The analysis of transversely multi-pole expansion can be done with the similar manner of a multi-strip-line-electrodes-type BPM [12].

SUMMARY AND DISCUSSION

We discussed a new concept of a 3-D electron bunch monitor based on EOS (spectral decoding), and showed the method for its optical configuration. Our single-shot bunch monitor can characterize the 3-D distribution and position of an electron bunch with femtosecond resolution. This EOS 3-D bunch monitor with spectrograph detects and analyzes the Coulomb field of electron bunches as longitudinally spectral decoding and transversely multi-pole expansion. This non-destructive monitor can be used as an electron energy chirping monitor at a dispersive region for XFEL commissioning.

The probe laser for EOS has been prepared as radial polarized and completely linearly chirped broadband (limited by 350 nm) supercontinuum generation. We are planning to use organic polymer film for a femtosecond resolution EO-probe instead of inorganic one.

At the encoding with the spectrometer the interferences will make resolution worse. Defusing techniques should be applied with the spectrometer.

In addition, we are developing an all-optical system for femtosecond-timing pump & probe experiments. The EO-sampled probe laser pulse will be used as a femtosecond-timing signal pulse. This signal pulse is amplified with a NOPA (noncollinear optical parametric amplifier), using an SHG of Yb fibre laser as a pump laser.

The total design of the EOS-monitoring and all-optical timing system can be improved and simplified with the recent progress of laser technologies.

REFERENCES

[1] J. Rivers, "SCSS X-FEL Conceptual Design Report", RIKEN, May 2005.
[2] R. Akre, et al., Proc. of EPAC 2002, Paris, France, 2002, 1882-1884.
[3] P. Bolton et al., AIP Conf. Proc **648**, 2002, 491.
[4] G. Berden, et al. DIPAC '05, 2005, 69.
[5] Jamison et al. Opt. Lett. **18**, 2003,1710.
[6] I. Wilke et al PRL **88**, 2002, 124801.
[7] C. Iaconis, et al., IEEE J. of Quantum Electron, **35**, 1999, 50.
[8] Tomizawa, et al., Russian Journal of Quantum Electronics, 2007, 697.
[9] Japan Patent Application No. 2007−133046.
[10] H. Tomizawa, et al., "Feasibility test of Laser induced Schottky-effect-gated photocathode RF gun", FEL '07, 2007, to be published.
[11] Hattori T. and Kobayashi T., Chem. Phys. Lett., 113, 1987, 230.
[12] T. Suwada, Jpn. J. Appl. Phys. Vol. 40, 2001, 890.

COHERENT THZ LIGHT SOURCE USING VERY SHORT ELECTRON BUNCHES FROM A THERMIONIC RF GUN

Toshiya Muto#, Takumi Tanaka, Fujio Hinode, Masayuki Kawai, Ken-ichi Nanbu, Kittipong Kasamsook, Kazushi Akiyama, Mafuyu Yasuda, Yoshinosuke Mori, Hiroyuki Hama
Laboratory of Nuclear Science, Tohoku University.

Abstract

We have planned to establish intense terahertz light source using coherent radiation from undulator. In order to emit coherent radiation, it is important to generate very short electron beam with a bunch length around 100fs. Now we have developed an injector to generate such short bunch beam. The injector consists of an Independent Tunable Cells thermionic rf gun (ITC rf gun) and a magnetic bunch compressor. Longitudinal and transverse phase space distribution can be controlled by changing input power of each cells and phase difference between cells in this gun. The compressor can change compression rate R_{56} and 2nd order dispersion effect by 2 sets of quadrupoles and a set of sextupoles, respectively. Test model of ITC rf gun was manufactured and basic parameters were measured. From tracking simulation, it has been turned out the bunch compressor can reduce to bunch length less than 100fs. In this paper, we show overview of the coherent terahertz light source and the detail of the ITC rf gun and the bunch compressor.

INTRODUCTION

Intense coherent radiation at the terahertz region ($\lambda \sim 300\mu m$) will be powerful probe for bio-medical science, solid state physics and other many scientific fields. There was not such intense terahertz light source so far. There are two type of terahertz source, or laser based and accelerator based. We have developed accelerator based terahertz light source using intense coherent radiation [1]. Now a coherent terahertz source using undulator radiation has been planed.

In order to get coherent terahertz light, electron beam with very short bunch length $\sigma_t < 100fs$ must be produced. Therefore an injector, which consists of Independent Tunable Cells rf gun (ITC rf gun) and magnetic bunch compressor, has been developed.

In this paper, the project of undulator coherent terahertz light source and the detail of the ultra short bunch injector are presented.

UNDULATOR COHERENT TERAHERTZ LIGHT SOURCE

A light source consists of an injector, an accelerating structure and an undulator. The schematic design is shown in Fig.1. The injector which consists of the ITC rf gun and magnetic bunch compressor generates electron beam with energy E ~2MeV, normalized emittance $\varepsilon_n < 1\pi$mmmrad and bunch length ~100fs. By the accelerating structure, beam energy goes up to 12 MeV. The ultra short bunch beam is passing through the undulator, then coherent terahertz light is emitted.

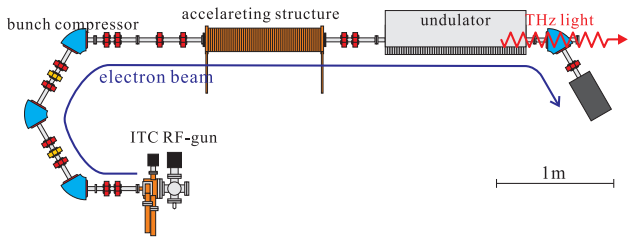

Figure 1: The schematic design of undulator coherent terahertz light source

The parameter of coherent terahertz light source is listed in Table 1.

Table 1: Parameters of coherent terahertz source

Energy ***E***	12MeV
Normalized emittance ε_n	< 1 πmm mrad
Bunch length σ_t	~100fs
Bunch charge I_e	~20pC
Undulator	
period length λ_p	8 cm
# of periods	15
Peak magnetic field B_{ymax}	0.3 T

Calculated terahertz spectrum from the undulator was shown in Fig.2 and Fig.3, where bunch length σ_t=100fs, number of electrons N_e = 1.25 x10^8 electrons /bunch (bunch charge is 20pC).

The fundamental wavelength λ_1 and its harmonics λ_i is

$$\lambda_i = \frac{\lambda_p}{2\gamma^2 i}\left(1+\frac{K^2}{2}+\gamma^2\theta^2\right), \quad (1)$$

where i is harmonic number, K=93.4 B_{ymax}[T] λ_p[m] is the strength parameter, γ is Lorentz factor, θ is the observation angle with respect to the axis[2]. In this case, the fundamental wavelength λ_1 is 257μm. Since bunch length σ_t=100fs ~ 30μm, only the radiation with fundamental wavelength is coherent, so proportional to N^2 ~ 10^{16}. Therefore, compared with the fundamental radiation, higherharmonics is suppressed (See Fig.2 and 3).

#muto@lns.tohoku.ac.jp

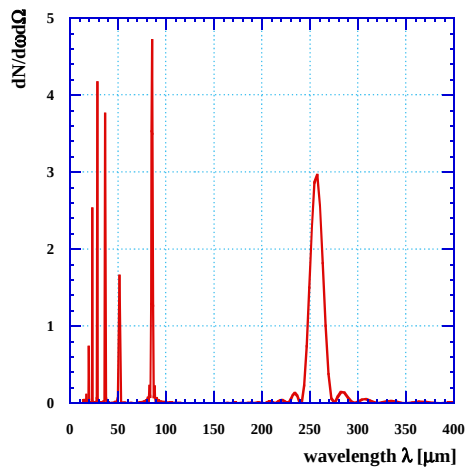

Figure 2: Spectrum of undulator radiation from single electron (θ=0)

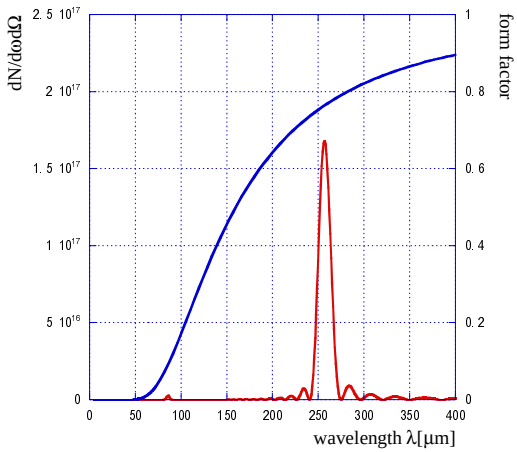

Figure 3: Spectrum of coherent undulator radiation at Ne=1.25x10^8 electrons/bunch, σ_t=100fs, θ=0 (red) and bunch form factor σ_t=100fs(blue)

AN INJECTOR FOR VERY SHORT BUNCH

ITC RF Gun

The ITC rf gun has two cells with a very low coupling, or independent cells as its name indicates. There are two rf input ports at each cells to feed the rf power from a klystron. By changing each input power of two cells and phase difference between cells, longitudinal and transverse phase space distributions at the gun exit can be controlled.

In order to generate low emittance beam with sufficient beam current, the cathode should have small radius and can produce high beam current. Consequently a single crystal LaB_6 cathode with the diameter ϕ1.75mm has been chosen.

By using a self-developed 3-dimensional Finite Difference Time Domain (FDTD) simulation code[3], operating parameters of ITC rf gun was optimized [1]. Table 2 shows optimized operating parameter and generated beam parameter under that condition. Simulation result of longitudinal phase space distribution is shown in Fig.4. The momentum spread Δp/p of the beam from the gun is ranging from maximum momentum P_{max} =1.77MeV/c to almost 0MeV/c. By using momentum slit put on the downstream of the gun, Δp/p will be selected to be less than 2%. From Fig.4, one can see the beam extracted from the gun has bunch length ~ 5ps (full width) within momentum spread Δp/p=2%.

Table 2: Parameters of the rf gun and the extracted beam for simulation

rf gun	
Max electric field of 1st cell E_{1st}	25 MV/m
Max electric field of 2nd cell E_{2nd}	50 MV/m
phase difference between cells	18 deg
current density at cathode(ϕ1.75)	50 A/cm^2
electron beam at the rf gun exit	
maximum momentum P_{max}	1.77 MeV/c
energy spread Δp/p(full width)	2%
normalized emittance ε_n	0.77πmmmrad
Twiss parameter (β,α,γ)	(1.11,1.21,2.22)

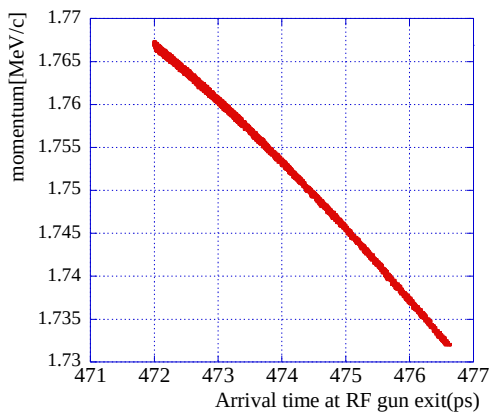

Figure 4: Longitudinal phase space distribution (FDTD simulation)

Magnetic Bunch Compressor

As shown in Fig.4, the relationship between momentum and time (=longitudinal position) is almost linear. Usually an α-magnet is used to bunch compression for a thermionic rf gun injector [4]. For our gun, a bunch compressor with the Triple-Bend-Achromat (TBA) like lattice has been designed. In addition, a set of sextupole magnets is installed in this bunch compressor. Consequently, this bunch compressor has properties 1) By two sets of quadruple magnets between bends, transfer matrix R_{56} can be changed to fit various (Δp/p)/Δt, 2) By a set of sextupoles, 2nd order dispersion function can be

controlled. Especially it is difficult to obtain latter feature for α-magnet.

By the accelerator design code SAD[5], the optics of the bunch compressor is designed and shown in Fig.5.

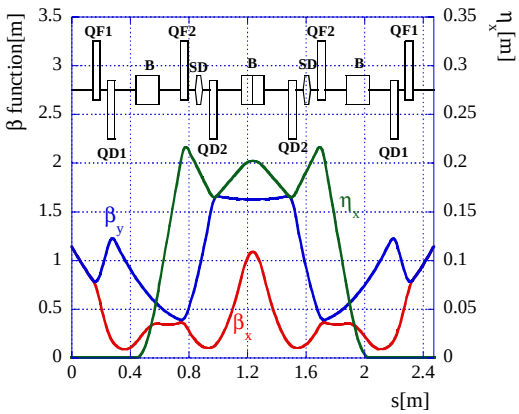

Figure 5: the optics design of bunch compressor

Using the result of FDTD simulation, tracking simulation in the bunch compressor was done by SAD. In this tracking, the space charge effect is not considered. The tracking result of longitudinal phase space distribution with/without sextupoles is shown in Fig.6, 7 respectively. From tracking results, bunch lengths σ_t were obtained 43fs, 38fs respectively. One can also see the 2nd order dependence can be compensated by sextupoles. It was confirmed that this injector can generate very short bunch less than 100fs.

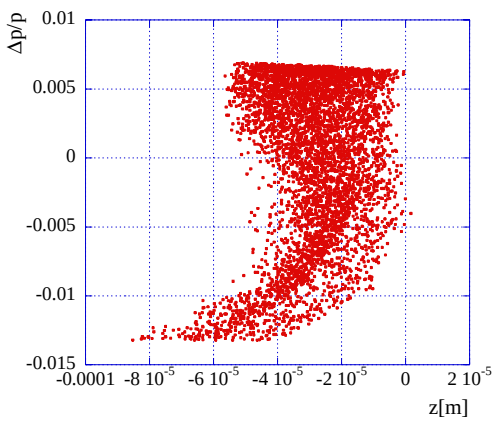

Figure 6: Longitudinal phase space distribution after bunch compressor without sextupole magnets

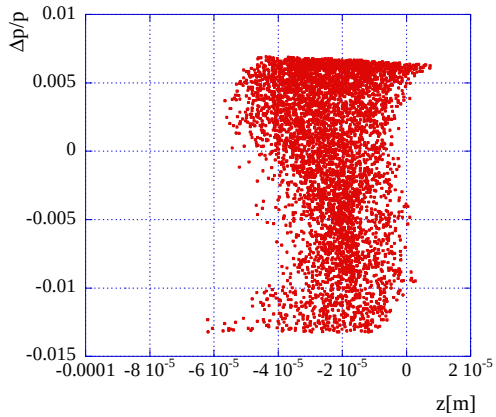

Figure 7: Longitudinal phase space distribution after bunch compressor with sextupole magnet

PERFORMANCE MEASUREMENT OF ITC RF GUN PROTOTYPE

The prototype of ITC RF-gun had been manufactured and basic parameters of rf cavities were measured. Results are shown in Table 3.

Table 3: Cavity parameters of ITC RF-gun prototype

resonant freq.(f_1, f_2)	(2810.81, 2825.36)GHz
coupling(β_1, β_2)	(2.3, 3.4)
Unloaded Q (Q_1, Q_2)	(9984, 9600)
(R/Q_1, R/Q_2)	(117, 129)Ω

As shown in Table 3, resonant frequencies of each cells is different from design frequency 2856MHz. From the 3-dimentional electromagnetic field calculation code Microwave-Studio[6], it was found that this frequency shift is caused by the effect of the coupling port between waveguide and cavity. The amount of shift is consistent with the Microwave-Studio's prediction.

Using a bead perturbation method, electric field distribution along the beam axis was measured. In Fig.8, a measured result is shown. The electric field distribution calculated by SUPERFISH is also shown.

A result of the electric field distribution is consistent with SUPERFISH calculation. R/Qs in Table 3 are calculated using measured data shown in Fig.8. From SUPERFISH, R/Qs are predicted to be 98.2Ω, 114.6Ω respectively and consistent with measurements.

In these measurements for the prototype, we confirmed that basic parameters of the rf gun are consistent with SUPERFISH's prediction except for resonant frequencies. The resonant frequencies can be predicted by 3-D electromagnetic field calculation including rf coupling ports. Now we have designed a modified ITC RF-gun.

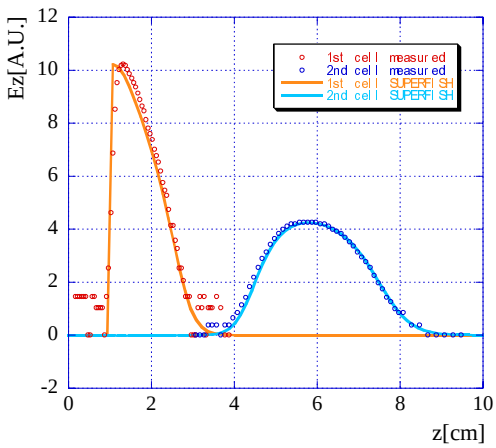

Figure 8: The electric field distribution (circle: results of bead perturbation methods. line: SUPERFISH calculation)

SUMMARY

An intense coherent terahertz light source using undulator radiation has been designed. In order to obtain coherent terahertz radiation, it is important to generate electron beam with very short bunch σ_t < 100fs. To realize such a short electron beam, the injector which consists of the ITC rf gun and the magnetic bunch compressor has been developed. From numerical calculation, it has been turned out that the injector can generate electron beam with very short bunch length σ_t around 50fs. Since it is difficult the beam simulation including space charge effects in low energy region such as the inside of gun, an initial small fluctuation affects results of beam parameters. The design of bunch compressor strongly depends on input beam parameters. We will compare with our simulation code and other commercial codes such as General Particle Tracer (GPT) [7]. At the present, the tracking simulation in the bunch compressor is not included space charge effects. We will investigate whether that space charge effects don't affect to the beam in the bunch compressor.

Additional optimization of the bunch compressor is needed to have wide capability to fit various input beam parameters.

The prototype ITC rf gun has been manufactured and parameters of the cavity also has been measured. From measurements for rf properties, cavity performance can be predicted by using calculation code. We have been designing the modified ITC rf gun.

REFERENCES

[1] H. Hama et al., New Jour. of Phys. 8(2006) 292
[2] Alexander Wu Chao and Maury Tigner, "Handbook of Accelerator Physics and Engineering",World Scientific 1999
[3] H. Hama et al., Nucl. Instr. and Meth. A 528 (2004) 371
[4] H. A. Enge, Rev. Sci. Instrum. 34 (1963) 385; M. Borland,"A High-brightness Termionic Microwave Electron Gun", Ph.D. Thesis, Stanford University, 1991
[5] http://acc-physics.kek.jp/SAD/sad.html
[6] http://www.cst.com/Content/Products/MWS/Overview.aspx
[7] http://www.pulsar.nl/gpt

CHARACTERISTICS OF SMITH-PURCELL RADIATION FROM DIFFERENT PROFILE GRATINGS*

G. Naumenko#, B. Kalinin, G. Saruev, NPI, Tomsk, Russia
D. Karlovets, Yu. Popov, A. Potylitsyn, L. Sukhikh, V. Cha, TPU, Tomsk, Russia

Abstract

To choose the most effective grating the absolute coherent SPR characteristics were measured on the 6.2 MeV electron beam. Gratings with lamellar, triangular and so-called "flat" gratings were studied. It was shown the grating consisted of the conductive strips is more preferable target for SPR generation.

INTRODUCTION

Smith-Purcell radiation (SPR) is widely considered as the spontaneous mechanism for FEL (for example[7]). In recent experiments [1,2], the possibility of creating a monochromatic radiation source of the THz range on the basis of the Smith-Purcell radiation (SPR) has been demonstrated. The SPR from low relativistic electrons is also used in orotrons. For the nonrelativistic electron energies ($E_e \le 100$kev), the approach developed by van den Berg [3,4] ensures a reasonable agreement with experiment [5,6]. In [8] the different models for SPR characteristics calculation were compared for high relativistic electrons. There was shown that the predictions of most models differ by approximately 2 orders of magnitude for the electrons with energy ~20 MeV [9] and by several orders for the electron energies Ee=855 MeV [10]. The available experimental results do not provide an ultimate conclusion on the validity of one of these models.

We distinguish two types of periodic targets, which can be used to generate the SPR: "Volume" gratings (a lamellar grating (Fig. 1) and a grating which consist of a periodic set of conducting strips separated by vacuum gaps) and "Flat" gratings (consisting of separate conducting strips having the thickness essentially smaller than a wavelength).

The coherent Smith-Purcell radiation (CSPR) emitted from the first-type targets with different profile was studied experimentally by several experimental groups ([11, 12]). However, all these works differ in the applied methods. On the other hand, it was shown in works [13, 1] that flat targets are more effective in order to obtain an intensive monochromatic radiation. Therefore, the direct comparison of the measured characteristics of radiation from these targets is difficult. That is why the research of the CSPR characteristics from the targets of different types but under similar conditions is desirable.

* The work was supported by the Ministry of Education and Science of Russian Federation [project no. 2.1.1.889 "Development of Scientific Potential of Higher School (2006-2008)"].
# Naumenko@npi.tpu.ru

MODELS

There are few theoretical models to calculate the SPR characteristics for the different grating profiles. We consider here three models: van den Berg's (vdB) model [3] (applicable for volume gratings), surface current (SC) model [14,15] (the SPR is considered as a radiation generated by the current induced by the field of a particle moving in vacuum close to a perfect conducting periodic surface), and resonant diffraction radiation (RDR) model [16] (for gratings consisting of infinitely thin perfect conducting strips separated by vacuum gaps).

Comparison of models for thin strips grating

We use for calculations the formulas from [8] for the case $\Phi = 0$ [illegible]

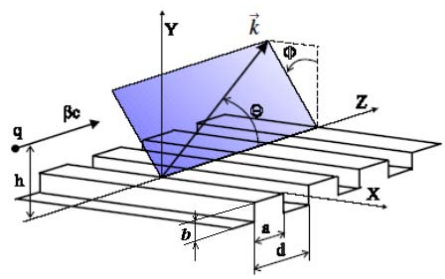

Fig. 1. Scheme of the Smith-Purcell radiation generation

The calculations (Fig. 2) were made for the Lorenz-factor γ = 12 and the grating period d = 8 mm.

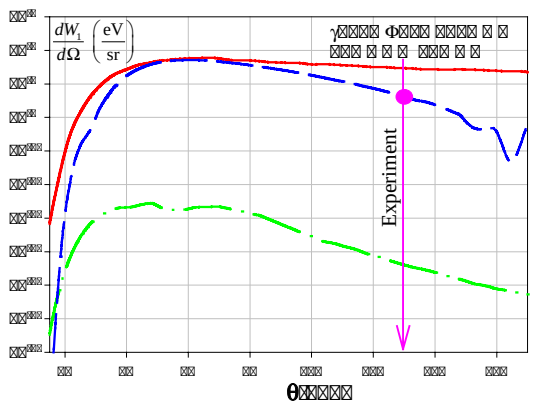

Fig. 2. Angular distribution of the SPR intensity for a flat grating according to the RDR model (red solid line), surface current model (blue a dashed curve) and for van den Berg's model (green dash-dotted line, b/d = 0.001).

We can see from the Fig. 2 a large discrepancy between radiation yields obtained using these three models.

SPR from different type structures

Let us compare the angular distribution of the calculated SPR intensity from different gratings according to the van den Berg's model (Fig. 3): for a volume grating with vacuum gaps and strips 4 mm thick and a for flat grating with $b/d = 0.001$. One may see from the Fig.3 that the intensity of the SPR from a "thick" grating is by 2 orders of magnitude greater.

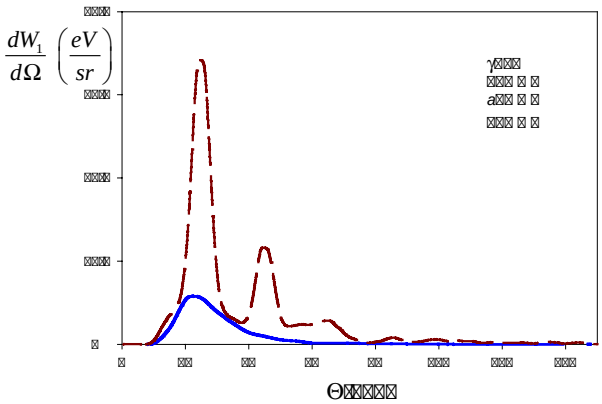

Fig. 3. Angular distribution of the SPR intensity for a flat grating (blue solid line; is multiplied by 10) and for a volume grating (red dashed line).

Coherence

Let's consider the approximation for the case when the size of an electron beam is much smaller than the impact parameter *h*. In this approximation in terms of the Smith-Purcell geometry longitudinal and transverse distributions of electrons in a bunch are factorized, which enables one to extract the longitudinal and transverse geometric form-factors of a bunch in the form of separate factors. In this case only the longitudinal form-factor plays the essential role (see [17]).

The typical dependence of the longitudinal form-factor via the wavelength for the normal (Gauss) distribution of electrons in a bunch is shown in Fig. 4.

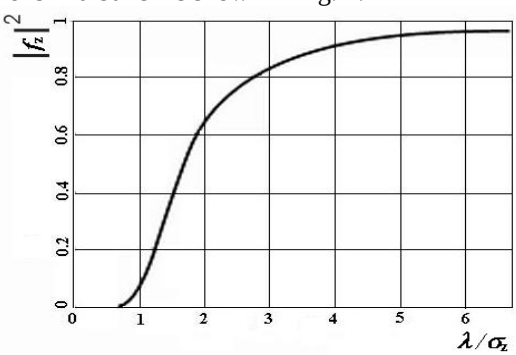

Fig.4 The Dependence of the squared form-factor module on the radiation wavelength for the normal longitudinal distribution of electrons in a bunch with bunch length σ_z.

The registered emission of radiation in the wavelength range $\Delta\lambda$ may be written as:

$$Y(h,\theta,\sigma_z) = N^2 \cdot \int_{\Delta\lambda} \left| f_z\left(\frac{\lambda}{\sigma_z}\right)\right|^2 \cdot \int_{\Omega} \frac{d^2W_{SP}(\lambda,h,\theta)}{d\lambda d\Omega} d\Omega \cdot \varepsilon(\lambda) d\lambda$$

where $W_{sp}(\lambda,h,\theta)$ is the intensity of incoherent SPR, $\varepsilon(\lambda)$ is the spectral efficiency of a detecting system.

EXPERIMENTAL SETUP AND TECHNIQUE

Electron beam

The experiment was carried out on the extracted electron beam of the microtron of the Tomsk Institute for the Nuclear physics.

The scheme of the the experimental zone setup was changed depending on a problem statement (see Figs 5,6). The beam parameters are given in Table 1.

Table 1: Electron beam parameters

Electron energy	6.1 MeV
Macro-pulse duration	≈4 ms
Pulse repetition rate	1 – 8 Hz
Micro-pulse length	≈6mm
Number of electrons per micro-pulse	10^8
Number of micro-pulses per macro-pulse	10^4
Beam size at the microtron output	4×2 mm^2
Emittance: horizontal vertical	$3\cdot10^{-2}$ mm×rad $1.5\cdot10^{-2}$ mm×rad

Detector

To register the radiation within a millimeter wavelength range the authors applied the room-temperature detector operating on the basis of a broadband antenna supplied by a high-frequency diode. The latter was produced at the Institute for Semi-conducting Devices (Tomsk, Russia). The main parameters of the detector for room temperature are:

wavelength range: $\Delta\lambda$ = 3 ~ 20 mm,
sensitivity = 0.3 V/mWatt

Techniques for angular measurements

Cut-off filters cutting passage of the radiation with the wavelengths, exceeding the critical length λ_c, were used.

To compare our data with the theoretical calculations obtained using the classical models we should be sure that the obtained experimental results correspond to the far zone approximation. In paper [18] it was shown that the effect of pre-wave zone may be suppressed while applying the parabolic optics, when a detector is placed in the focus of a parabolic reflector. For this purpose the parabolic reflector with diameter equal to 140 mm and the focal distance equal to 430 mm was used during the experiment.

The scheme for the azimuth angular dependence measurements is presented in Fig. 5

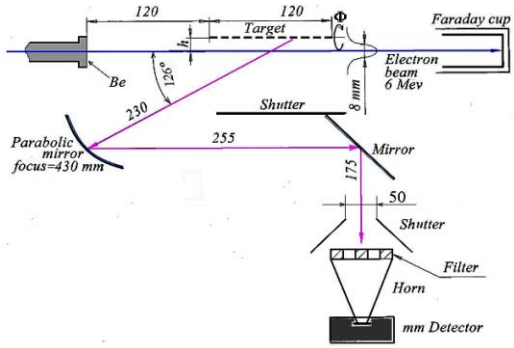

Fig. 5. Experiment scheme for azimuth dependences measurement

The scheme of the of radiation intensity dependences on the polar angle measurements is shown in Fig. 6. Detector together with the parabolic reflector was fixed on a radial rod, which rotated around the target at the angle θ.

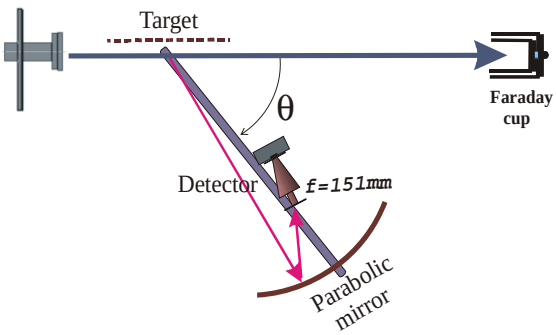

Fig.6. Experimental scheme for the angular dependences measurement

Targets

Table 2. Target parameters (size unit is mm)

1. Flat thin target	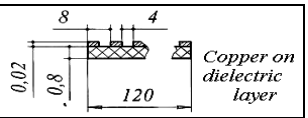
2. Flat volume target	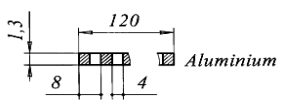
3. Lamellar grating	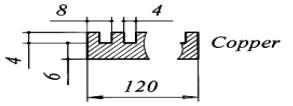
4. Grating with triangular profile	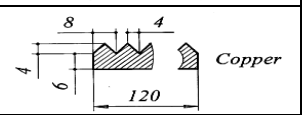

In the experiment the characteristics of the radiation from both volume and flat targets were studied. The parameters of the targets used are given in the Table 2.

EXPERIMENTAL RESULTS

The measurements of the azimuth angular intensity distributions of the CSPR were made with the arrangement presented in Fig. 5 when the value of the polar observation angle was equal to θ = 130°, which corresponds to the wavelength of SP radiation λ = 13.2 mm. Fig. 7 presents the azimuth angular distribution of the CSPR from a flat target 1 with the use of the two cut-off filters having the critical wavelength λ_c=14 mm and λ_c=17.5 mm. The value of Φ = 0 corresponds to the direction in the plane which is perpendicular to the target plane. The measurements with the use of cut-off filters with λ_c < 14 mm give the values which practically coincide with the background.

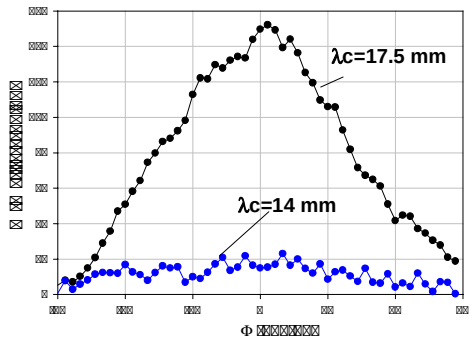

Fig.7. Azimuth CSPR distribution from the target 1 with different cut-off filters.

The absolute azimuth intensity distribution of the CSPR from targets 1, 2, 4 with different profiles for λ_c=17.5 mm is presented in Fig. 8.

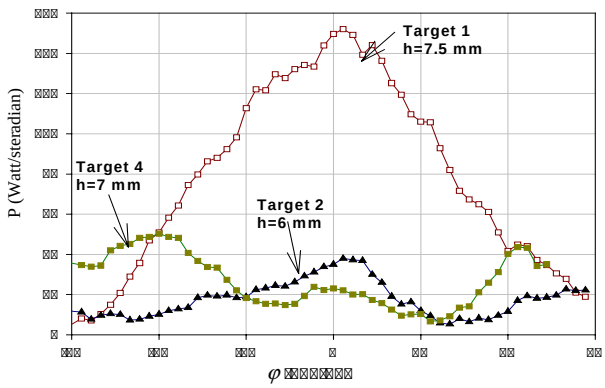

Fig.8. Azimutal CSPR distribution from flat and volume targets for λ_c=17.5mm.

The azimuth intensity distribution of the CSPR with different values of the impact-parameter (Fig. 9) shows the principle influence of the impact-parameter value.

The measurements of the dependences of the CSPR intensity on the value of the polar observation angle were carried out according to the scheme shown in Fig. 6 with the value of the azimuth angle equal to Φ=0.

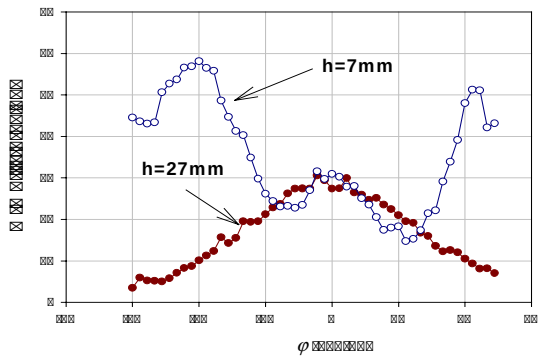

Fig.9. Azimutal CSPR distribution from target 4 for different values of impact-parameter and λc=17.5mm

The radiation cutting off across the wavelength was provided by a cut-off wave-drive with λc=17.5 mm to decrease the background contribution from a RF system of an accelerator. The typical CSPR intensity dependence via the polar observation angle for h=7 mm is shown in Fig. 10.

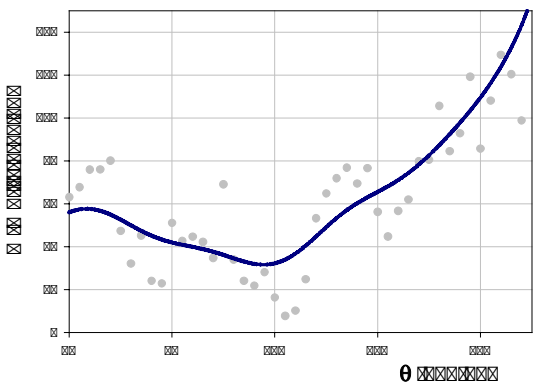

Fig.10. Polar dependence of CSPR from flat target 1

Discussion

Suppression of the pre-wave zone effect by means of wave optics on this experiment enables one to compare the obtained experimental results with the conclusions of the SPR theory in the far zone (Table 3).

Table 3: Target efficiency (experiment)

Target	**CSPR density** $dW/d\Omega$	
	Watt/sr	eV/sr per electron and per period
1. Flat thin target	0.153	$4.8 \cdot 10^{-9}$
2. Flat thick target	0.039	$1.2 \cdot 10^{-9}$
3. Volume target with square profile	0.012	$0.37 \cdot 10^{-9}$
4. Volume target with triangular profile	0.029	$0.9 \cdot 10^{-9}$

On the coherency conditions the CSPR is observed in the range of polar angles exceeding 100° (see Fig.10). The measured azimuth distribution of the targets having a different profile under similar conditions enables us to assert as for the maximum efficiency of flat conducting thin-stripped targets (Table 3).

Comparing the absolute experimental data from Table 3 with the theoretical predictions (Fig. 2) ascertain that the RDR and SC models .

REFERENCES

[1] Yukio Shibata, Shigeru Hasebe, et. al., Phys. Rev. E 57, 1061 (1998).
[2] S.E. Korbly, A. S. Kesar, J.R. Sirigiri, and R. J. Temkin, Phys. Rev. Lett. 94, 054803 (2005).
[3] P.M. van den Berg, J. Opt. Soc. Am. 63, 1588 (1973).
[4] P.M. van den Berg, J. Opt. Soc. Am. 63, 689 (1973).
[5] A. Gover, P. Dvorkis, and U. Elisha, J. Opt. Soc. Am. B 1, 723 (1984).
[6] Y.N. Adischev, A.V. Vukolov, D.V. Karlovets, A. P. Potylitsyn, and G. Kube, Pis'ma Zh. Eksp. Teor. Fiz. 82, 192 (2005) [JETP Lett. 82, 174 (2005)].
[7] H. Backe, W. Lauth, H. Mannweiler, et. al., in NATO Workshop ‘‘Advanced Radiation Sources and Applications’’ (Springer, New York, 2006), pp. 267-282.
[8] D. V. Karlovets* and A. P. Potylitsyn, Phys. Rev. ST AB 9, 080701 (2006)
[9] A.S. Kesar, Phys. Rev. ST Accel. Beams 8, 072801 (2005).
[10] G. Kube, H. Backe, H. Euteneuer, et.al., Phys. Rev. E 65, 056501 (2002).
[11] D. C Nguyen, Nucl. Instrum. Methods Phys. Res., Sect. A 393, 514 (1997).
[12] S.E. Korbly, W.J. Brown, M.A. Shapiro, and R. J. Temkin, in Proceedings of the Particle Accelerator Conference, 2001, Chicago, USA (IEEE, New York, 2001), pp. 2347-2349.
[13] A. Doria, G. P. Gallerano, E. Giovenale, G. Messina, G. Doucas, M. F. Kimmitt, H.L. Andrews, and J. H. Brownell, Nucl. Instrum. Methods Phys. Res., Sect. A 483, 263 (2002).
[14] J. H. Brownell, J. Walsh, and G. Doucas, Phys. Rev. E 57, 1075 (1998).
[15] J. H. Brownell and G. Doucas, Phys. Rev. ST Accel. Beams 8, 091301 (2005).
[16] A. P. Potylitsyn, Nucl. Instrum. Methods Phys. Res., Sect. B 145, 60 (1998).
[17] A. N. Aleinik, A. S. Aryshev, B. N. Kalinin, G. A. Naumenko et.al, JETP Letters, 76, 6, (2002), p. 337.
[18] B. N. Kalinin, G.A. Naumenko, A.P. Potylitsyn, G.A. Saruev,L. G.Sukhikh, and V.A. Cha, JETP Letters, 84, 3, (2006), p. 110.
[19] J.H. Brownell, J. Walsh, G. Doucas, Phys. Rev. E 57 (1998)1075.
[20] A.P. Potylitsyn, Phys. Lett. A 238 (1998) p.112.

GAIN AND COHERENCE ENHANCEMENT OF SASE FEL USING LASER-PREBUNCHED ELECTRONS

Yen-Chieh Huang and Chia-Hsian Chen, Institute of Photonics Technologies, National Tsinghua University, Hsinch 30013, Taiwan
Wai-Keung Lau and Gwo-Huei Luo, National Synchrotron Radiation Research Centre, Hsinchu 30076, Taiwan

Abstract

We conduct a simulation study on the acceleration of periodically loaded electrons in a 6-MeV photocathode electron gun driven by a laser beat wave with a beat frequency of 4.35 THz. The density modulation of the electrons is well preserved during particle acceleration. The periodically bunched electrons are then injected into a single-pass free-electron laser to quickly generate a few tens of kW electron superradiance at 63.5 μm.

INTRODUCTION

It is well known that, if the electron bunch length is significantly shorter than the radiation wavelength, the spectral power of the electron radiation is proportional to the square of the electron current or to the square of the total number of electrons participating in the radiation process. This coherent radiation is dubbed as electron superradiance.

To facilitate the discussion, we briefly describe in the following the theory of electron superradiance based on Gover's formulation [1]. In general, the spectral energy of the radiation from an electron bunch with a bunch length τ_b and an electron number N_b is expressed by the equation

$$(dW/d\omega)_{SR} = N_b^2 (dW/d\omega)_1 M_b^2(\omega), \quad (1)$$

where $(dW/d\omega)_1$ denotes the spectral energy emitted from a single electron with W being the radiation energy and ω being the angular frequency of the radiation, $M_b(\omega)$ is the Fourier transform of the electron pulse-shape function with a unitary peak amplitude. If the radiating electron beam contains N_{pb} such electron bunches repeating at a rate $\omega_{pb}/2\pi$, the total radiated spectral energy becomes

$$(dW/d\omega)_{SR,pb} = N_b^2 N_{pb}^2 (dW/d\omega)_1 M_b^2(\omega) M_{pb}^2(\omega), \quad (2)$$

where

$$M_{pb}^2(\omega) = \frac{\sin^2(N_{pb}\pi\omega/\omega_{pb})}{N_{pb}^2 \sin^2(\pi\omega/\omega_{pb})}, \quad (3)$$

is the coherent sum of the radiation fields from all the micro-bunches and has a unitary peak amplitude at the frequencies $\omega = m\omega_{pb}$ (m = 1, 2, 3…). For a short electron bunch, $M_b^2(\omega)$ is usually a broad-band function. The spectral linewidth of $M_{pb}^2(\omega)$ at $\omega = m\omega_{pb}$ is given by $\sim \omega_{pb}/N_{pb}$, which, for a large number of periodic electron bunches, could be much narrower than the intrinsic spectral linewidth of a radiation device governed by $(dW/d\omega)_1$. Therefore, a self-amplified spontaneous emission (SASE) free-electron laser (FEL) is expected to have enhanced gain and coherence when driven by a periodically bunched electron beam. Since electrons are discrete particles, the term $M_b(\omega)M_{pb}(\omega)$, describing the degree of electron bunching at the frequency ω, is sometimes called the electron bunching factor.

Previously we have proposed the use of a laser beat wave to excite periodic emissions of electrons from the photocathode of an electron accelerator [2]. In this paper, we study a THz single-pass FEL driven by such a laser-beat-wave (Labew) photocathode accelerator. The system configuration of this study is depicted in Fig. 1, consisting of two major components, a RF photocathode gun and a solenoid-derived wiggler. The periodically bunched electrons are excited by a laser beat wave at the cathode, accelerated by a 1.6-cell S-band accelerator, and directly injected into a solenoid-derived wiggler to generate the electron superradiance.

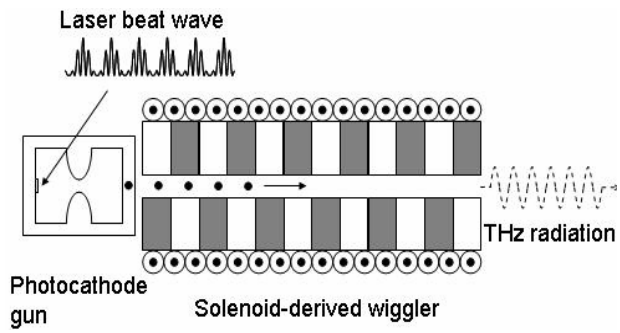

Figure 1: The system configuration for studying a THz superradiance FEL driven by a Labew photocathode gun.

Labew PHOTOCATHODE GUN

In this section, we study the acceleration of periodically bunched electrons in the BNL/UCLA/SLAC 1.6-cell S-band photocathode electron gun [3] by using the space charge tracking code ASTRA [4]. We operate the gun at a peak acceleration gradient of 140 MV/m. The electrons are emitted from the photocathode with a radial distribution within a 0.75-mm rms radius. For the first case in our simulation, we emitted a total of 1-nC electrons uniformly distributed over 10-ps duration. For the second case in our simulation, we equally divided the

1-nC charges into 44 micro-bunches over the same 10 ps duration. The micro-bunch separation is set to be six sigma of the Gaussian bunch length. For both cases, 14080 macro-particles were used in the simulations. The output beam parameters for the two cases are listed in Table 1. Although the essential beam parameters of the macro pulses at the gun exit are nearly identical for both cases, the longitudinal micro-structures of the electrons for the two cases are very different. Figures 2(a) and (b) show a comparison between the longitudinal distributions of the accelerated single electron bunch and the accelerated periodic electron bunches, respectively. The longitudinal distribution of the single-bunch beam remains more or less uniform after acceleration, whereas that of the periodically bunched beam shows redistribution of electrons after acceleration. Although the leading part of the periodically loaded beam retains periodic bunching, the trailing part has no apparent bunching features. The particle redistribution is due to both the space charge field and the acceleration field during the acceleration process.

Table 1. Output beam characteristics for single-bunch acceleration and periodic-bunch acceleration. The two sets of parameters are nearly identical.

	rms beam energy	rms energy spread	rms emittance	rms beam radius
Single-bunch acceleration	6.3 MeV	3.6%	2.8 π-mm-mrad	1.3 mm
Periodic bunch acceleration	6.3 MeV	3.9%	2.6 π-mm-mrad	1.3 mm

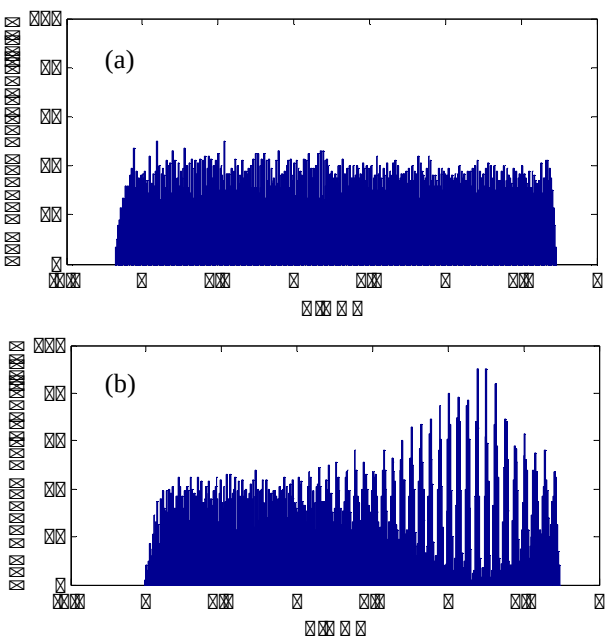

Figure 2: The electron distributions at the exit of the photocathode gun (a) for single-bunch acceleration and (b) for periodic-bunching acceleration.

The degree of electron bunching can be better described from the magnitude of the bunching factor $|M_b(\omega)M_{pb}(\omega)|$. We plot is Figure 3 the values of $|M_b(\omega)M_{pb}(\omega)|$ versus frequency before and after the acceleration of the periodically loaded beam. It is seen in Fig. 3(a) that the periodic bunches are nicely loaded at 4.35 THz at the cathode. In Fig. 3(b), the redistribution of the particles at the gun output causes some frequency broadening and magnitude reduction to the bunching factor. The fundamental frequency of the peak bunching is also shifted from 4.35 THz to 4.72 THz. Nevertheless the bunching factor is slightly reduced from 0.6 to 0.2 at the fundamental bunching frequency. In the next section, we show the importance of this bunching factor when driving a THz superradiance FEL.

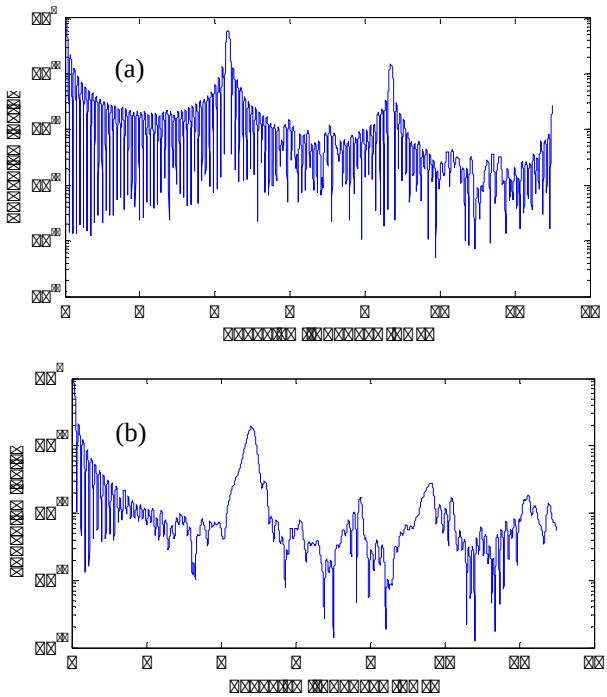

Figure 3: The bunching factor of the periodically loaded electron beam (a) before and (b) after acceleration in the photocathode gun. The space charge field and the acceleration field redistribute the electrons during acceleration and result in frequency broadening and magnitude reduction to the bunching factor.

SUPERRADIANCE FEL

The FEL wiggler in our choice for our simulation is a staggered-array solenoid-derived planar wiggler [5]. Among several advantages of using such a wiggler, the solenoid field is important for confining the low-energy electron beam. The system parameters chosen for our simulation study are: wiggler period = 1.5 cm, peak wiggler field = 7.2 kG., and solenoid field = 7.5 kG. For the 6.3 MeV driving beam, the synchronism wavelength of the FEL radiation is 63.5 μm.

We simulated the FEL power growth as a function of the wiggler length in the computer code GENESIS [6]. We use the Labew-gun beam parameters from ASTRA as

the input beam parameters for the FEL simulation in GENESIS. To see the influence of the initial bunching, we varied the bunching factor when simulating the FEL performance. Figure 4 shows the FEL powers as a function of the wiggler length for initial bunching factors of 0, 10^{-8}, and 2×10^{-2}. To our surprise, the typical exponential growth of the (SASE FEL power is not seen in the range of our simulation study. With the zero bunching factor, the FEL gain is too low to build up the FEL power. However, for a strong initial bunching, the FEL power flats out at a high value almost immediately. This phenomenon suggests a strong superradiance process.

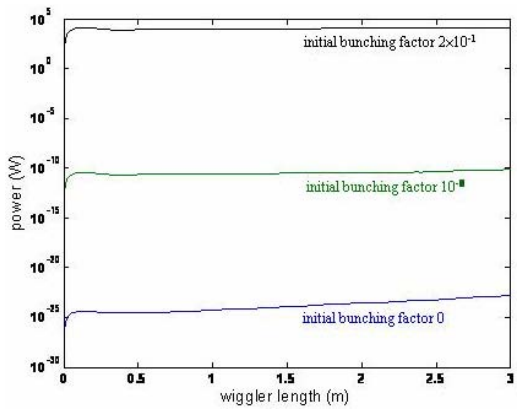

Figure 4: FEL power versus wiggler length with initial bunching factors = 0, 10^{-8}, and 0.2. With the 0.2 bunching factor, the FEL power quickly builds up to tens of kW.

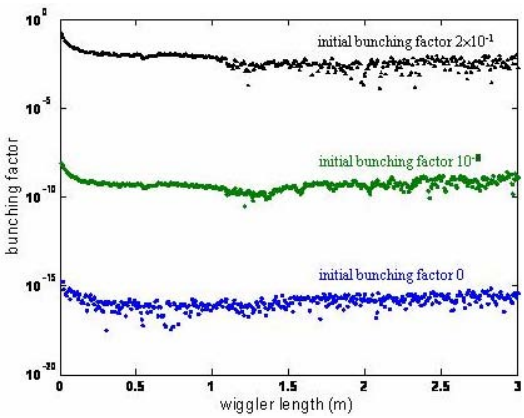

Figure 5: The variation of the bunching factors in the wiggler for the three initial bunching values, 0, 10^{-8}, and 2×10^{-2}. The space charge force in the low-energy beam tends to debunch the electrons.

Figure 5 shows the variation of the electron bunching factors in the wiggler for the three initial bunching values, 0, 10^{-8}, and 2×10^{-2}. It is interesting to see that the bunching factor does not increase over the wiggler length as usually seen in a SASE FEL, but tends to settle to a steady-state value despite of strong initial bunching. For example, the initial bunching factor 0.2 is reduced to about 10^{-3}, although the FEL power quickly reaches a few tens of kW. The steady-state bunching value is a result of the balance between the debunching force from the space charge field and the bunching force from the radiation field. The space-charge induced debunching becomes significant for a low energy beam and is not commonly seen for a short-wavelength SASE FEL. Without initial bunching, it is unlikely for the single-pass THz FEL power to grow to an appreciable value.

CONCLUSIONS

An single-pass FEL driven by laser-prebunched electrons can be a promising radiation source. We simulated the performance of a Labew photocathode gun. With 44 periodic Gaussian bunches loaded at the cathode over 10 ps, the bunching factor of the 6.3-MeV output beam is slightly reduced from an initial value of 0.6 to 0.2 at the fundamental bunching frequency. The debunching is a consequence of the redistribution of electrons under the space charge force and the acceleration force.

By using the beam parameters generated from the gun simulation, we simulated the performance of a single-pass FEL radiating at the fundamental bunching frequency of 4.72 THz. The laser pre-bunched beam promptly generates tens of kW radiation power in the single-pass FEL. This quick generation of the FEL power suggests the potential of implementing an ultra-compact FEL by using the Labew accelerator technology. Our study also shows that it is unlikely to build a single-pass FEL by using such a low-energy driving beam without initial bunching, because the strong space charge force prevents the electrons from forming micro-bunches.

This work is supported in part by National Science Council under Contract NSC 95-2112-M-007 -027 -MY2 and by National Tsinghua University under Code 96N2534E1.

REFERECES

[1] Avi Gover, “Superradiance and stimulated-superradiant emission in prebunched electron-beam radiators. I. Formulation”, Phys. Rev. ST AB, 8, 030701 (2005).

[2] Y. C. Huang, “Laser-beat-wave bunched beam for compact superradiance sources,” International Journal of Modern Physics B, Vol. 21 Issue 3/4, p277-286 (2007).

[3] D. T. Palmer, X. J. Wang, I. Ben-Zvi, R. H. Miller, “Beam dynamics enhancement due to accelerating field symmetrization in the BNL/SLAC/UCLA 1.6 cell S-band photocathode RF gun,” Proceedings of the IEEE Particle Accelerator Conference, Vol. 3, V. 3, p. 2846-2848 (1997).

[4] K. Floettmann, ASTRA User Manual, http://www.desy.de/~mpyflo/Astra_dokumentation/.

[5] Y.C. Huang, H.C. Wang, R.H. Pantell, J. Feinstein, and J. Harris "Performance Characterization of a Far Infrared, Staggered-array Wiggler", Nucl. Instrum. and Methds, A341, 431-435 (1994).

[6] S. Reiche, GENESIS User Manual, http://pbpl.physics.ucla.edu/~reiche/

APPROACHES IN MODELLING A WAVEGUIDE RF-LINAC THz-FEL

Yu. Lurie*, Y. Pinhasi, Ariel University Center of Samaria, Ariel, Israel
M. Tecimer, NHMFL / Florida State University, Tallahassee, FL 32310, USA

Abstract

A widely used approach in describing radiation fields generated by short pulse rf linac FEL oscillators is based on modal expansion of the intracavity fields and solving the wave equation for the amplitudes of the excited transverse cavity eigenmodes, in time and axial dimension. In this time domain approach, mode amplitudes are calculated by adopting the slowly varying envelope approximation (SVEA). The longitudinal propagation number k_z of the carrier wave is usually assumed to represent a group velocity and a wave impedance of the frequencies encompassed within the spectral bandwidth of the optical pulse envelope as it evolves within the interaction region. However, in cases where dispersive effects arising from a waveguided cavity become influential, the space-frequency approach is a straightforward method to tackle the problem without introducing further approximations. One such case is being studied based on a highly slippage dominated short pulse rf-linac FEL operating at long wavelengths.

INTRODUCTION

The aim of this paper is to present numerical design tools for investigating the temporal and spectral characteristics of THz pulses generated by short pulse rf-linac based waveguided FEL oscillators. We demonstrate application of these numerical tools on the design study and parameter optimization of a THz FEL system that is expected to operate over a frequency range between 100-1100 microns [1]. Combination of effects resulting from the use of picoseconds short electron pulses and long radiation wavelengths spread over such a wide spectral range on the one hand and propagation of short radiation pulses in lengthy waveguide resonators (as required in most of the rf-linac driven FELs) on the other hand, necessitate a careful analysis of the interplay between enhanced coherent spontaneous emission (CSE), waveguide dispersion (group velocity dispersion), slippage and cavity desynchronisation effects. In devising the numerical design tool, we adopt space-frequency approach [2, 3] which enables a correct description of these effects but it is time consuming when simulating an oscillator FEL configuration. On the other hand, employing an additional formalism to model the relevant aspects of the problem in an approximated way while creating practical means in terms of cpu usage. The former rigorous formalism is used to validate the application range of the latter in tackling the design problem with a reasonable accuracy and replace it in cases of shortcomings in modelling properly the physics of the above mentioned THz FEL system. The two methods presented in the paper are contemplated for the design study of the planed wide spectral range, long wavelength, short pulse waveguide THz-FEL oscillator.

Sample results are given applying the developed formalisms on a highly slippage dominated FEL regime where submillimeter to millimeter wavelength radiation is generated by a few picoseconds long high peak current electron bunches.

* ylurie@yosh.ac.il

DESCRIPTION OF THE MODELS

Time domain model

The time domain approach presented here and the implemented numerical algorithm is described in details in [4, 5]. Several assumptions are adopted in the model that reduce greatly the computational effort in order to enable an optimization of the system parameters. The longitudinal motion of each macroparticle is tracked whereas the transverse motion is accounted for by the beam envelope equations [4]. The latter includes the influence of 3D beam effects in an averaged manner. The profile of the optical field is defined by the transverse modes that are excited in a parallel plate (PP) waveguide resonator [5, 6]. The evolution of the mode amplitudes is governed by Eq. (1) where, by adopting SVEA and introducing the transformations $z' = z - v_g t$ and $\overline{z} = z - v_z t$, the inhomogeneous wave equation simplifies into:

$$\frac{\partial}{\partial z}u_q(z,z') = j\frac{f_b \mathbf{F} A_{u0}}{2k_{zq}} \cdot \frac{\omega_p^2}{c^2} \times \zeta_q(z,\overline{z})\frac{\chi(z,\overline{z})}{N_{\overline{z}}(z,\overline{z})} \sum_i^{N_{\overline{z}}(z,\overline{z})} e^{-j\theta_{iq}(z,\overline{z})} \quad (1)$$

In (1) $u_q(z,z')$ is the complex envelope of a modulated wave train with carrier frequency ω and axial wavenumber k_{zq} of the excited q'th mode, which satisfy the waveguide dispersion relation. $\theta_{iq}(z,\overline{z})$ is the ponderomotive phase. The longitudinal distribution of the particles is represented by the term $\chi(z,\overline{z}) = N_{\overline{z}}(z,\overline{z})/n_0\pi r_b^2\Lambda$, where $N_{\overline{z}}(z,\overline{z})$ denotes the number of particles within a fraction of the radiation period allowing for a more accurate description of CSE effects when the current profile of the electron bunch varies significantly at the scale of the radiation period [5]. The source term is averaged over the associated subwavelength long beam segment Λ. $\mathbf{F}$ is the filling factor. $\zeta_q(z,\overline{z})$ results from averaging the source term over the transverse gaussian density profile of the electron beam. For the case of a parallel plates (PP) waveguide it can be expressed by

the analytical term:

$$\zeta_q(z,\overline{z}) = \frac{e^{\xi}}{\sqrt{8\kappa}\,\sigma_x(z)} \left\{ e^{\theta^2/4\eta} + e^{\theta^{*2}/4\eta} \right\} \quad (2)$$

with the parameters ξ, κ, η and θ defined in [5]. σ_x and σ_y are the rms transverse dimensions of the beam, determined by solving the beam envelope equations in terms of the longitudinal position z [4].

Due to the waveguide dispersion, slippage effects in short pulse waveguide FELs exhibit differences in comparison to open resonator FELs. The slippage length L_{sp} for the resonant radiation wavelength λ_r is defined as:

$$L_{sp} = N_w \lambda_r \left[1 - \left(k_{\perp q}/\beta_z \gamma_z k_w \right)^2 \right]^{1/2} \quad (3)$$

where N_w and $k_{\perp q}$ are the number of the wiggler periods and the cutoff wavenumber of the q'th transverse mode, respectively.

The boundary conditions for the transverse modes are imposed by the resonator and can be formulated as follows:

$$u_{q''}^{(n+1)}(z=0,t) = \rho^{(1)}\,\rho^{(2)} \times \sum_{q',q} \mathbf{P}^{(1)}_{q''q'}\,\mathbf{P}^{(2)}_{q'q}\,e^{j\Phi_{q''}(\omega)}\,u_q^{(n)}(z=L_w, t-t_r) \quad (4)$$

where $u_q^{(n)}(L_w,t')$ denotes the complex amplitude of the q'th mode at the exit of the interaction region at the pass number n and $t_r = L_c/v_{gr}$ is the cavity round-trip time. $\rho^{(i)}$ signifies reflectivity of the mirrors. $\mathbf{P}^{(i)}_{q''q'}$ describes modes conversion, cavity losses and outcoupling.

The group velocity dispersion effects might influence the dynamics of the FEL amplification process in multiple round-trips. The inclusion of group velocity dispersion into the time domain model requires the solution of the second order wave equation [7]. In the presented model, the quadratic term associated with the group velocity dispersion is omitted in the waveguide dispersion relation as a consequence of SVEA. Instead, the dispersion is allowed for in an approximate manner in the model. Using a Fourier series expansion (FSE), the complex field amplitude $u_q(z,z')$ is expressed, at each pass, at the end of the FEL interaction in terms of longitudinal eigenmodes of the cold cavity with the respective $\omega_l = l \cdot 2\pi/t_r$ and $k_{zq}(\omega_l)$. Each l'th longitudinal mode propagates with the own $k_{zq}(\omega_l)$ over the dispersive feedback section. Prior entering the interaction region,the field amplitudes of the longitudinal modes are summed (FSE^{-1}) to yield the updated $u_q(z=0,t)$ which encompasses the effect of group velocity dispersion over the "drift" section in the preceding round-trip. Subsequently, starting the new round-trip, the procedure is repeated within the interaction region, after carrying out many integration steps in solving the first order wave equation as described in Eq. (1). Although the outlined algorithm makes use of the longitudinal cavity modes in representing the complex field amplitude $u_q(z,z')$, it circumvents to reformulate the wave equation (1) for the amplitudes of the longitudinal modes and spares solving a large number of coupled axial mode equations.

Space-frequency model for FEL oscillators

Assuming a uniform cross-section resonator (usually a waveguide), the total electromagnetic field at every plane z can be expressed in the frequency domain as a sum of a set of transverse (orthogonal) eigenfunctions with profiles $\widetilde{\mathcal{E}}_q(x,y)$ [2, 3]. At the beginning of a round-trip number n, each of the modes is assumed to have an initial amplitude $C_q^{(n)}(0,f)$ and the total field at $z=0$ is given by:

$$\widetilde{\mathbf{E}}^{(n)}(x,y,z=0;f) = \sum_q C_q^{(n)}(0,f)\widetilde{\mathcal{E}}_q(x,y) \quad (5)$$

At the end of the interaction region $z=L_w$, the field is:

$$\widetilde{\mathbf{E}}^{(n)}(x,y,L_w;f) = \sum_q C_q^{(n)}(L_w,f)\widetilde{\mathcal{E}}_q(x,y)e^{+jk_{z_q}(f)L_w} \quad (6)$$

The amplitude of the qth mode excited by the electron beam with current density $\widetilde{\mathbf{J}}^{(n)}(x,y,z;f)$ is given by:

$$C_q^{(n)}(L_w,f) = C_q^{(n)}(0,f) - \frac{1}{2\mathcal{N}_q} \times \int_0^{L_w} \int\int \widetilde{\mathbf{J}}^{(n)}(x,y,z;f)\cdot\widetilde{\mathcal{E}}_q^*(x,y)e^{-jk_{z_q}(f)z}\,dx\,dy\,dz \quad (7)$$

where the normalization of the mode amplitude is made via the complex Poynting vector power $\mathcal{N}_q$ [3]. The spectral density of the energy flow after the interaction with the electron beam at the nth round-trip is:

$$\frac{d\mathcal{W}^{(n)}(L_w)}{df} = \sum_q \left| C_q^{(n)}(L_w,f) \right|^2 \frac{1}{2}\Re\left\{\mathcal{N}_q\right\} \quad (8)$$

After a round-trip in the resonator of length L_c, the field at the entrance of the interaction region is [8]:

$$\widetilde{\mathbf{E}}^{(n+1)}(x,y,z=0;f) = \sum_{q'} C_{q'}^{(n+1)}(0,f)\widetilde{\mathcal{E}}_{q'}(x,y) = = \sum_{q'} \left[\sum_{q''} \rho_{q'q''} C_{q''}^{(n)}(L_w,f) \right] \widetilde{\mathcal{E}}_{q'}(x,y)e^{+jk_{z_{q'}}(f)L_c} \quad (9)$$

where $\rho_{q'q''}$ is a complex coefficient, expressing the intermode field reflectivity of transverse mode q'' to mode q', due to scattering of the resonator mirrors or any other passive elements in the entire feedback loop. Scalar multiplication of both sides of Eq. (9) by $\widetilde{\mathcal{E}}_q^*(x,y)$, results in the initial mode amplitude:

$$C_q^{(n+1)}(0,f) = \sum_{q''} \rho_{qq''} C_{q''}^{(n)}(L_w,f)e^{+jk_{z_q}(f)L_c} \quad (10)$$

which is required in equation (7) to solve the field excited in the consecutive round-trip. In the frequency domain, the

Table 1: Operational parameters of THz-FEL.

PARAMETER	THz FEL
Wavelength:	$\lambda \approx 1100\ \mu$m
Beam energy:	$E_k = 10 \div 13$ MeV
Energy spread:	$\sigma_e(rms) \approx 0.3\%$
Bunch charge:	$Q_b = 135$ pC
Pulse length:	$\sigma_z(rms) = 1.0 \div 3.5$ ps
Repetition rate:	23.6 MHz
Wiggler period:	$\lambda_w = 80$ mm (hybrid.)
Wiggler:	$K(rms) = 0.8 \div 3.9$
Number of periods:	$N_w = 40$
Waveguide:	Rectangular[1] (38×10mm^2) or PP[2] waveguide ($d = 10$mm)
Resonator round-trip length:	$\ell \simeq 6.35$ m

total out-coupled radiation obtained at the oscillator output after N round-trips is composed of a summation of the circulated fields (6) inside the resonator:

$$\widetilde{\mathbf{E}}_{out}(f) = \\ = \sum_q \Upsilon_q \sum_{n=0}^{N} C_q^{(n)}(L_w, f)\widetilde{\mathcal{E}}_q(x,y)e^{+jk_{z_q}(f)L_w} \quad (11)$$

where Υ_q is qth mode field transmission of the out-coupler. The energy spectrum of the electromagnetic radiation obtained at the output after N round-trips is given by:

$$\frac{d\mathcal{W}_{out}(N)}{df} = \sum_q \mathcal{T}_q \left| \sum_{n=0}^{N} C_q^{(n)}(L_w, f) \right|^2 \frac{1}{2}\Re\{\mathcal{N}_q\} \quad (12)$$

where $\mathcal{T}_q = |\Upsilon_q|^2$ is the power transmission coefficient of mode q.

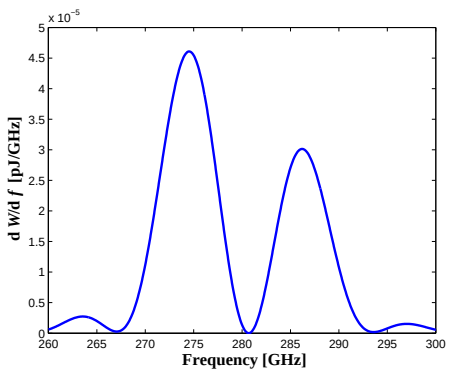

Figure 1: Spontaneous emission spectrum.

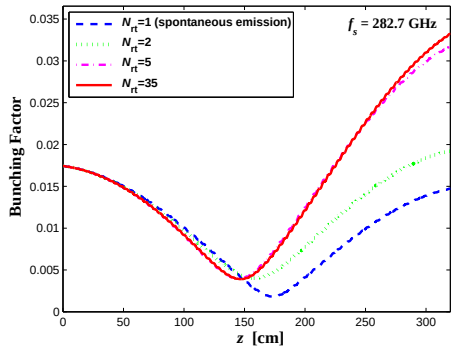

Figure 2: Evolution of the bunching factor along the wiggler for different oscillator round-trips.

SIMULATIONS

To simplify the analysis, single transverse mode TE_{01} is assumed in the simulations. Operational parameters of the system is given in the table 1. Drive electron bunch consists from short $T_b = 7.2$ ps bunches with Gaussian longitudinal distribution and with an energy-phase correlation similar to the ones considered in [9, 10]. Figure 1 demonstrates spectrum of spontaneous emission obtained in the frequency domain by the WB3D code [3, 8]. The simulations were carried out with $N_p = 1000$ macroparticles; the resulted spectrum was then normalized to the number of electrons $N_e = Q_b/(N_p\, e)$ in the simulation (see [11] for details). The power of spontaneous emission is $P_{sp} = W_{tot}^{(sp)}/\tau_{sp} \approx 5.5\ \mu$W, where $W_{tot}^{(sp)} \approx 0.5$ fJ is the total energy flux of spontaneous emission found by integration of the spectrum, and $\tau_{sp} = L_w/v_{z0} - L_w/v_{gr} \approx 0.11$ ns is the slippage time.

The following results relate to FEL oscillator configuration, based on a train of bunches with repetition rate of about 23.6 MHz. Fig. 2 shows evolution of the bunching factor $b(z) = \overline{e^{jw_s t_i(z)}}$ along the wiggler as function of oscillator round-trip number. At the first round-trip, spontaneous emission takes place. At this stage, the intensity of the radiation is rather low and variations in the bunching factor are mainly due to the initial energy-time correlation in the electron bunch. At further round-trips, the emitted field causes additional bunching in the electron beam.

Evolution of the stored intracavity energy during the first round-trips is presented in Fig. 3. Fabry-Perot resonator lineshape is also drawn for the comparison. The *free-spectral range* is $FSR \approx \frac{1}{t_r} \approx 23.6$ MHz, where $t_r = L_c/v_{gr} \approx 42.4$ ns is the round-trip time. The *full-width half-maximum* of the transmission peaks is given by $FWHM = \frac{FSR}{\mathcal{F}} \approx 0.65$ MHz, where $\mathcal{F} = \frac{\pi\sqrt[4]{\mathcal{R}}}{1-\sqrt{\mathcal{R}}} = 36.0$ is the Finesse of the resonator ($\mathcal{R} = |\rho|^2 = 0.84$ is the total round-trip power reflectivity). The oscillator energy buildup is shown in Fig. 4.

[1] Simulations carried out in the time domain model.
[2] Simulations carried out in the space-frequency approach.

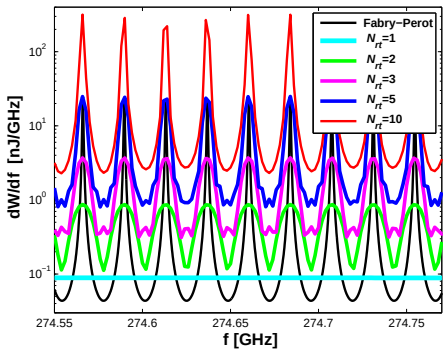

Figure 3: Oscillations build-up at the first round-trips.

Evolution of the radiation build-up process when the bunches with uncorrelated energy spread are injected was considered in the time domain model. Comparison of results of Fig. 4 and 5 reveals significant reduction of optical pulse energy at the last case. The difference is explained by the enhancement of coherent emission due to energy-phase correlation, as described in [10].

CONCLUSIONS

In the paper we presented two approaches for simulating excitation and buildup of FEL radiation in an oscillator configuration. Using the models, a study of a FEL operated at the sub-millimeter wavelengths was carried out. The models consider dispersion effects in the waveguide when a highly slippage radiation pulses are excited by a train of short electron bunches produced by rf-linac.

REFERENCES

[1] M.Tecimer et al., “A design study of a FIR/THz FEL for high magnetic field research”. Proc. of the 28th International FEL Conf., 2006, Berlin, Germany, p. 327.

[2] Y. Pinhasi, V. Shterngartz and A. Gover, Phys. Rev. E **54** (1996) 6774.

[3] Y. Pinhasi, Yu. Lurie, A. Yahalom, Phys. Rev. E **71** (2005) 036503.

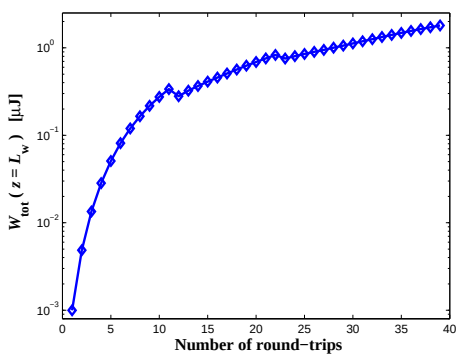

Figure 4: Evolution of the total stored intracavity energy.

[4] G.H.C. van Werkhoven, Dissertation, TU Eindhoven (1995)

[5] M. Tecimer, Dissertation, Tel Aviv University (2004)

[6] L.R. Ellias and J.C. Gallardo, Appl. Phys. B **31** (1983) 229.

[7] N. S. Ginzburg et al., “Dispersion effects in short pulse waveguide FEL”. Proc. of the 28th International FEL Conf., 2006, Berlin, Germany, p. 378.

[8] Y. Pinhasi, Y. Lurie, A. Yahalom, Nucl. Instr. Meth. Phys. Res. A **528** (2004) 62.

[9] A. Doria et al., Phys. Rev. Lett. **80** (1998) 2841.

[10] Yu. Lurie and Y. Pinhasi, Phys. Rev. ST Accel. Beams **10** (2007) 080703.

[11] Y. Pinhasi, Yu. Lurie, Phys. Rev. E **65** (2002) 026501.

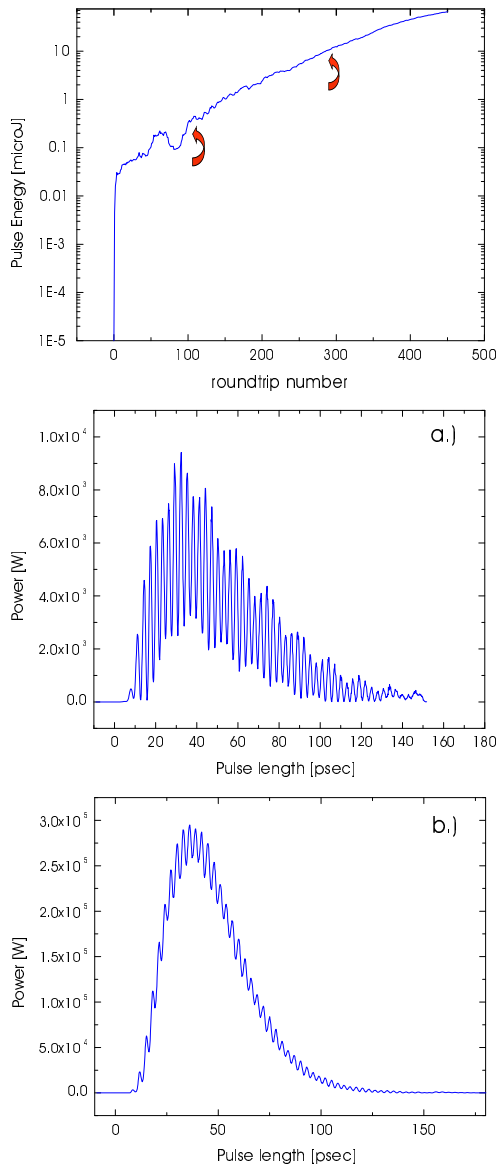

Figure 5: Evolution of the intracavity optical pulse energy with round-trips, and the radiation power shape at small signal gain (a) and at the beginning of the exponential gain (b) regimes, respectively (time domain simulations with an uncorrelated Gaussian beam energy spread).

EXPERIENCE AND PLANS OF THE JLAB FEL FACILITY AS A USER FACILITY*

Michelle D. Shinn#, Thomas Jefferson National Accelerator Facility, 1200 Jefferson ave., Newport News, VA 23606, USA

Abstract

Jefferson Lab's IR Upgrade FEL building was planned from the beginning to be a user facility, and includes an associated 600 m^2 area containing seven laboratories. The high average power capability (multikilowatt-level) in the near-infrared (1-3 microns), and many hundreds of watts at longer wavelengths, along with an ultrafast (~ 1 ps) high PRF (10's MHz) temporal structure makes this laser a unique source for both applied and basic research. In addition to the FEL, we have a dedicated laboratory capable of delivering high power (many tens of watts) of broadband THz light. After commissioning the IR Upgrade, we once again began delivering beam to users in 2005. In this presentation, I will give an overview of the FEL facility and its current performance, lessons learned over the last two years, and a synopsis of current and future experiments.

INTRODUCTION

The Free-electron laser (FEL) User Facility at Jefferson Lab (JLab) saw first light in 1998, and ran as a User Facility from 1999-2001. We then decommissioned our first FEL, the IR Demo, so we could install the IR Upgrade, which had almost an order of magnitude higher output and a larger tuning range. We once again began providing light to users in 2005. Previous reports [1,2] provide details of the uniqueness of the FEL driver accelerator, so this will be touched on only briefly. Along with the capability of the IR Demo to produce high average power, are other unique properties for a laser source (even compared to other FELs) in the mid-IR. To exploit the IR Demo the building that houses it was designed to be a user facility. An earlier report [3] gave some of the details of the facility while it was being built. This paper updates the current status of the facility, including measured values of the laser output, and discusses some of the infrastructure needed to run a user facility efficiently and safely. We then consider some of the interesting applied and basic research which is being done, and conclude with future plans for the facility.

*Work supported by the Commonwealth of Virginia and DOE Contract DE-AC05-06OR23177

#shinn@jlab.org

THE IR UPGRADE FEL

The Electron Accelerator

The driver accelerator of the IR Upgrade FEL uses SRF accelerator technology consisting of a 10 MeV injector (containing a DC photocathode gun driven by a Nd:YLF laser) and a SRF linac (whose total accelerating voltage may be as high as ~ 150 MeV) to produce an electron beam with an average current of ~ 10 mA at a PRF of 74.85 MHz. More than one percent of the electron beam power is converted to outcoupled laser radiation. The beam is then transported back through the linac where it is decelerated and most of the kinetic energy increase due to the linac is converted back into RF power. The use of an energy-recovering linac (ERL) greatly reduces the utility demands and installed RF power and has an added benefit that the waste beam is dumped at an energy below the giant photonuclear resonance threshold, eliminating activation of the beam dump.

This type of FEL was first demonstrated at the Jefferson Lab in the spring of 1999 and, its design and performance has been the subject of a number of papers. [4,5] The FEL is housed in the vault of the user facility [3] and has delivered several thousand hours of laser beam time to users. Given our desire to develop the FEL as an industrial tool, a generous amount of this beam time was delivered to users working on potential industrial applications. [6,7]

The advantage of ERL FELs is the ability to scale the output power to very high levels, many 10's of kW in the IR, without greatly increasing the space required to house it. This is because the FEL output power scales with electron beam power, which can be varied either with electron beam current or energy. Another advantage is the ability to lase at wavelengths that aren't accessible with conventional laser sources and at higher output powers. A disadvantage is that FELs are larger and more complex than conventional laser sources, however, an industrial version could be built which is more compact, and we have already demonstrated high availability (approaching 95% over 80 hours).

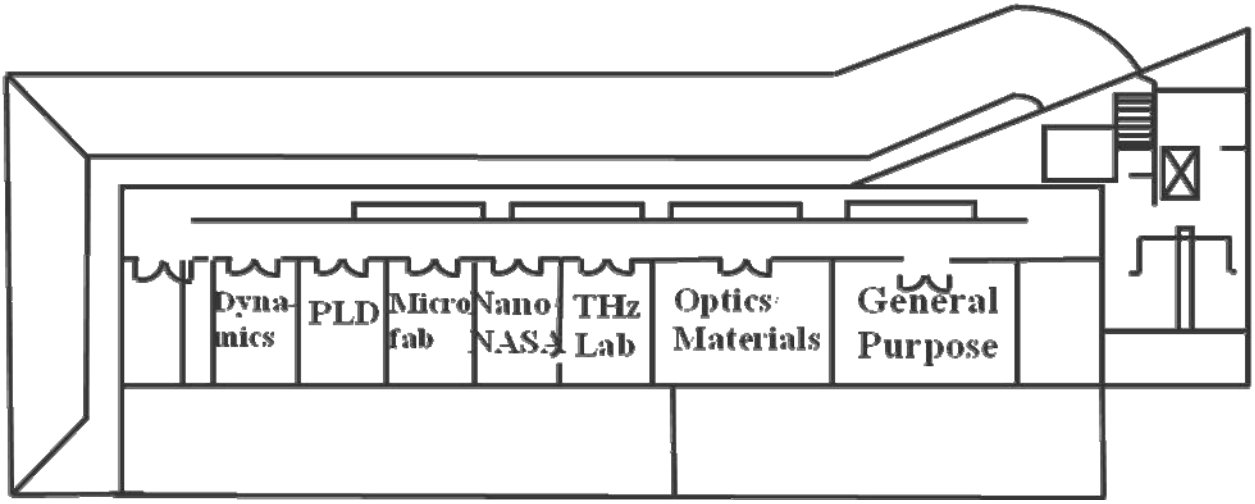

Figure 1 Layout and purpose of user labs in the JLab FEL Facility

The Optical Cavity and Transport

The optical cavity of the FEL is based on a nearly-concentric resonator design of 32.016m length. Mirrors for up to 4 different wavelength regions can be installed in the mirror vessels; operators can switch wavelengths, and be lasing again in about 15 minutes. Some of the design features of the cavity are available in another publication [8].

Currently, the IR Upgrade currently uses a permanent magnet, variable gap wiggler. The highest output at several wavelengths is shown in Table 1. Outcoupling is through a partially reflecting cavity mirror, where it is then collimated and transported upstairs first into the room where the optical diagnostics are located, and then onto the User Labs. (Fig. 1) Diagnosis and beam delivery are simultaneous, only ~0.05% of the laser power is delivered to the diagnostics, giving us the ability to provide realtime information on power, wavelength, and pulselength to our users.

Table 1: IR Upgrade FEL Output Power at several wavelengths.

Wavelength (μm)	**Average Power (kW)**
1.1	2.2
1.6	14.3
2.8	6.7

All mirrors in the cavity and transport are water cooled to minimize thermally-induced surface aberrations that would degrade the wavefront, and shielded to minimize absorption of stray light on the mounting hardware that cause beam steering. Presently, all mirrors in the transport are silicon with protected silver coatings. The choice of metal coatings allows us to transport the wide tuning range of the IR Upgrade without changing mirrors. When lasing on the fundamental, the FEL still produces harmonics with powers in the μW to mW range, which can be used as probes or for alignment purposes. A down side to this choice of coating is the loss of ~ 25% of the laser output to absorption and scatter. The beam is transported in a high vacuum (at ~ 10^{-7} Torr), to avoid absorption by the atmosphere. In order to send beam into any one lab there is a mirror cassette, an assembly containing mirrors on a linear translation stage. Currently, every mirror cassette contains a metal reflector, eventually two more mirrors will be added, each with dielectric coatings for higher reflectivity at a particular wavelength. There is also a home position, where the beam traverses the cassette without intersecting a mirror The mirror cassette diverts the beam into a short line containing an insertable mirror that directs the beam into a water-cooled dump; this serves as a local shutter for the user. When withdrawn, the beam then exits into the lab through a calcium fluoride or fused silica Brewster window.

The THz Beamline

As shown in Fig. 1, there is a THz lab located near the center of the laboratory area. As discussed elsewhere [9,10] we take advantage of the multiparticle coherence of our electron beam to extract broadband radiation in the THz region of the spectrum and transport it into a lab. The lower power (~ 100 W) of the THz beam makes it unnecessary to cool the optics in the beamline. Transport is also in vacuum, with a diamond window placed at a point where the beam is imaged to a waist, and is thus small. From there the beam continues in vacuum, but at a higher pressure (mTorr) than the initial part of the beamline. The beam exits into a hutch within the lab through a second diamond window, where it can travel through evacuated chambers containing the experiment, or in air.

Laser Personnel Safety System (LPSS)

Transport of a beam with such high power requires safety procedures and controls to protect personnel as well as equipment. This was implemented through

PLC-based hardware (with status passed to the controls software) to prevent inadvertent transport of beam into an area that has not been properly interlocked. Several different modes exist. For delivery of the FEL to a lab, either the entire lab can be interlocked (exclusionary mode) or the experiment is enclosed in an interlocked hutch (hutch mode). When a lab's LPSS in made up, a maglock energizes. Entry (when permitted) is by a "smart card" system that allows access only to personnel and users that are aware of the FEL and other hazards in a particular room. Recognizing that for many types of experiments, e.g., pump-probe, alignment is critical and difficult to optimize remotely, we have defined a state of operation known as "alignment mode". In this mode, the accelerator is locked into a state where the laser produces a low duty factor pulsed beam operating at 2 Hz with a pulsewidth of 250 μsec. During this time users can be in what normally be considered an exclusionary lab, or a user can be in the hutch. In the usual mode of operation, known as "laser permit", the lab is "swept", that is, checked to make sure that all personnel are outside the lab before the interlocks are engaged. Failure of an interlock causes the lab to become safe, inserting the local shutter, an intracavity shutter to prevent lasing, and setting the mirror cassette to the home position. However, the accelerator remains on. This allows us to maintain stable operations and more quickly resume lasing after the problem is corrected.

Most labs also have Class 4 laser systems in them, capable of operating without the FEL. To allow FEL beam delivery to one lab, and use of a laser system in another lab, we have a "local laser" mode, whereby the lab must still be swept and the interlocks made up. However, FEL beam delivery is prevented in several ways.

FEL operators and users receive formal training, through documentation and a walk-through by the Laser Systems Supervisor for the FEL. They are then given a test that must be passed before their badge allows them into the lab they will be working in. FEL operators are trained for all labs.

Facility Administration

Formal training of staff and users is just one facet of the administration of a user facility. We have modeled our procedures on those in place at the various synchrotron light sources in the United States; these have an experience based on over two decades of operations. Potential users must submit a request for beam time that is then reviewed externally by a Program Advisory Committee (PAC) and internally for feasibility. If accepted, users must submit two other forms that state what beam conditions and, possibly, changes to the hardware or software that they require, and, an evaluation of any hazards associated with the experiment, *e.g.*, solvents used, or toxic materials produced as a byproduct of exposure to the beam. This latter document is evaluated by the laboratory safety professionals and an experiment cannot proceed without their approval.

APPLICATIONS

Ablative processing of materials

Carbon nanotubes are increasingly utilized in various technologies. Demand for the single-wall variety is such that the price for high-quality material is currently about $500/gm, with pure material priced at over $2K/gm [11]. Current techniques produce about 0.2 gm/hr. [12] In comparison, worldwide demand is of order of thousands of kilograms annually. [13]. Using the IR Demo FEL and delivering an average power of about 300 W onto the target, researchers obtained yields of 1.5 gm/hr, far higher than competing techniques. [14] Work to optimize yield and dimensions have continued using the IR Upgrade FEL delivering about 1 kW of 1.6 μm light into the reactor.

The processing of nonmetallic materials was also studied with the IR Demo FEL. One study [15], showed the benefits of wavelength tunability. In this investigation polyimide (DuPont Kapton HN100) was irradiated at two wavelengths, 3.1 μm (off-resonance) and at 5.8 μm (on-resonance). Processing at the shorter wavelength, where the material was transparent, resulted in blackening of the material, a sign that the polymer has been thermally degraded. Tuning the laser to the longer wavelength resulted in cleanly-drilled holes, indicating the processing was nonthermal. This "cold-cutting" mode exhibited by IR FELs has been noted in earlier studies [16], enabling PLD of polymers.

Surface Processing

Besides ablative processes, thermal (or physiochemical) processes can be employed to perform surface modifications. No material is lost, merely melted and then resolidified, or while quite hot, transformed by oxidation, nitriding, or

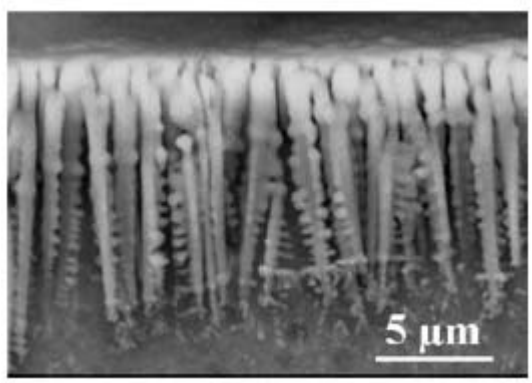

Fig. 2 Formation of dendrites of δ-TiN_x after bursts of FEL irradiation at 3.15 microns. From Ref 19

carburization. An example which is familiar to many is the application of titanium nitride (TiN) on tool bits. This gives the bit a distinctive gold color. TiN is also used to improve the biocompatibility and wear characteristics of replacement joints [17]. In a series of papers, P. Schaaf and coworkers from the University of Göttingen have published the results for the nitriding of Ti metal with the FEL. The FEL was operated at 3 μm, usually in a burst mode (also known as a macropulse). Compared to other types of laser nitrided titanium, the FEL-produced material had a thicker and harder coating [18]. This appears to be due to the formation of oriented (200) dendrites of δ-TiN_x, as shown in Fig. 2. While one might think that this would result in a rough surface, in fact it is fairly smooth. [19]

Medical Applications

With the wavelength and timing flexibility of the IR Upgrade FEL, it is natural to use it in medical applications. One such application is known as selective photothermolysis, the selective heating of tissues with light. By carefully choosing a wavelength in the near infrared, researchers targeted lipid-rich cells and heated them preferentially without heating the surrounding tissue. This study [20] paves the way for a laser treatment of acne, a condition where a sebaceous gland is producing too much lipid. Only the over-active glands, located a few millimeters under the surface of the skin are killed by the absorption of light, leaving the other cells unaffected. This technique also shows promise in the treatment of atherosclerosis, which if left untreated leads to heart disease and stroke.

THz Applications

The spectral region covered by THz radiation, roughly 1 mm to 0.1 mm in wavelength, is absorbed by transitions between electronic states and/or vibrational states in matter. Because these states are specific to a particular molecule, or ion, spectroscopy, either in the time domain, or in the frequency domain can be used for location and identification. This makes the use of the THz region of the spectrum attractive for applications such as medical imaging or hazardous material detection and nondestructive testing. While the list of applications is long, progress from the lab to the field has been hampered by the lack of high average power (several watts) sources. The THz source at JLab, is capable of producing high power, broadband, ultrashort pulsed radiation to evaluate the utility of some of these applications. It was recently used to make full-field video-frame rate images of a moving object [21]. We anticipate exciting results from the research occurring in this lab.

LESSONS LEARNED

While one might think that the user experiments occurring over the last two years were simply a continuation of the IR Demo user runs, with few new lessons to learn, in fact, that wasn't the case. The IR Upgrade was built in part to make it more attractive to users. And, we took the lessons learned from the first several years of operation to improve how we treated beam delivery to the labs, particularly in the use of hutches. By housing experiments in a hutch, the users are in close proximity to their hardware, making interfacing and sample changes far easier. Since the hutch eliminates the need to wear laser safety eyewear while the experiment is underway, we've found that users prefer this mode of operation. The preplanning of an experiment that is necessitated by the proposal and approval process encourages a lot of dialog between the users and members of the facility. This lessens the amount of time lost because the experiment isn't ready, time that is particularly at a premium when the users have come from a distance and have a well-defined period during which their experiment is supposed to run.

Ultimately, when running a user facility, what makes it work is the attitude and aptitude of the staff. The operators of the FEL are also its builders, and thus can respond to requests for unusual modes of machine operation.

CONCLUSIONS

Since the last paper on the JLab FEL User Facility [3], there have been a number of improvements to the facility over and above the upgraded IR FEL. In addition to outlining some of these improvements, I've highlighted some applications and experiments that an ERL-based FEL enables more readily than other lasers. Even then, this is merely a sampling; space does not permit me to discuss all the applications currently envisioned for an IR FEL, much less one that operates in the UV. Indeed, the prevailing view is that the best application for a FEL has yet to be found.

ACKNOWLEDGEMENTS

I'd like to acknowledge my colleagues in the FEL Division at Jefferson Lab, whom I have had the privilege to work with. I would also like to thank our users for sharing their results and enthusiasm for working at our facility

REFERENCES

[1] C. L. Bohn, et al, "Performance of the Accelerator Driver of Jefferson Laboratory's Free-Electron Laser," *Proceedings of the 18th Particle Accelerator Conference (PAC 99)*, New York, NY, March 29-April 2, 1999.

[2] G. R. Neil, *et al*., "Sustained Kilowatt Lasing in a Free-Electron Laser with Same-Cell Energy Recovery," Phys. Rev. Lett. 84 (2000) pp 662-665.
[3] M. D. Shinn, *et al*., "The Jefferson Lab FEL User Facility," in *Laser-Induced Damage in Optical Materials: 1999*, Gregory Exharos, Arthur Guenther, Keith Lewis, M. J. Soileau, Editors, Proceedings of SPIE 3902, (2000) pp. 355-360.
[4] Christopher Behre, Stephen Benson, George Biallas, James Boyce, Christopher Curtis and Others, "First Lasing of the IR Upgrade FEL at Jefferson Lab", Nuclear Instruments & Methods in Physics Research, A528, (2004) pg 19.
[5] G. R. Neil, C. Behre, S. V. Benson, M. Bevins, G. Biallas, J. Boyce, J.Coleman, L.A. Dillon-Townes, D. Douglas, H. F. Dylla, R. Evans, A. Grippo, D. Gruber, J. Gubeli, D. Hardy, C. Hernandez-Garcia, K. Jordan, M. J. Kelley, L. Merminga, J. Mammosser, W. Moore, N. Nishimori, E. Pozdeyev, J. Preble, R. Rimmer, M.Shinn, T. Siggins, C. Tennant, R. Walker, G. P. Williams, and S. Zhang, "The JLab High Power ERL Light Source", Nuclear Instr. & Methods A557 (2006) pg 9.
[6] M. D. Shinn, "High Average Power Free-Electron Lasers - A New Laser Source for Materials Processing," in *High Power Laser Ablation*, Claude A. Phipps, Editor, Proceedings of SPIE 4065, (2000) pp 434-440.
[7] G. R. Neil, "Applications for Energy Recovering Free-Electron Lasers", paper MOZBC03, Proceedings of the 22nd Particle Accelerator Conference (PAC07) Albuquerque, NM, June 25-29 2007.
[8] M. D. Shinn, G. R. Baker, C. P. Behre, S. V. Benson, M. E. Bevins, L. A. Dillon-Townes, H. F. Dylla, E. J. Feldl, J. F. Gubeli, R. D. Lassiter, F. D. Martin, and G. R. Neil "Design of the Jefferson Lab IR Upgrade FEL Optical Cavity," Nuclear Instruments and Methods A507, (2003) pp 196-199.
[9] G.P. Williams, "Far-IR/THz radiation from the Jefferson Lab FEL Energy Recovered Linac", Rev. Sci. Instr. 73 (2002).1461.
[10] G.L. Carr, M.C. Martin, W.R. McKinney, K. Jordan, G.R. Neil and G.P. Williams, "High Power Terahertz Radiation from Relativistic Electrons", Nature 420 (2002) pp 153-156.
[11] See Carbon Nanotechnologies Inc. web site: http://www.cnanotech.com/pages/store/6-0_online_store.html .
[12] M.W. Smith, private communication 2003.
[13] J. Ouellette, "Building the Nanofuture with Carbon Tubes," The Industrial Physicist 8(6) 2002 pp18-21.
[14] P.C. Elkund, B.K. Pradhan, U.J. Kim, Q. Xiong, J.E. Fischer, A.D. Friedman, B.C. Holloway, K. Jordan, and M.W. Smith, "Large-Scale Production of Single-Walled Carbon Nanotubes Using Ultrafast Pulses from a Free Electron Laser," Nanoletters 2, (2002) pp 561-566.
[15] M. Kelley, "Surface processing and micromachining of polyimide driven by a high average power infra-red free electron laser", Mat. Res. Soc. Symp. (2000) pg 617.
[16] D. Bubb et al, "Resonant infrared pulsed-laser deposition of polymer films using a free-electron laser", J. Vac. Sci. Tech A19 2001 pp 2698-2702.
[17] E. Carpene, P. Schaaf, M. Han, K.-P. Lieb and M. Shinn, "Reactive Surface Processing by Irradiation with Excimer Laser, Nd:YAG Laser, Free-Electron Laser and Ti: Sapphire Laser in Nitrogen Atmosphere" Applied Surface Science 186 (2002) pp 195-199.
[18] E. Carpene, M.Shinn, and P. Schaaf, "Synthesis of highly oriented TiNx coatings by free-electron laser processing of titanium in nitrogen gas", Appl. Phys. A247, (2005) pp 307-312.
[19] P.Schaaf, M. Shinn, E. Carpene, and J. Kaspar, "Direct Laser Synthesis of functional coatings by FEL treatments", Proceedings of the Third Intl WLT-Conf on Lasers in Manufacturing, (2005) pg 399.
[20] R. Rox Anderson, William Farinelli, Hans Laubach, Dieter Manstein, Anna N. Yaroslavsky, Joseph Gubeli III, Kevin Jordan, George R. Neil, Michelle Shinn, Walter Chandler, Gwyn P. Williams, Steven V. Benson, David R. Douglas, H.F. Dylla, "Selective photothermolysis of lipid-rich tissues: A free electron laser study", Lasers in Surgery and Medicine 38,(10), pp 913-919
[21] J. Michael Klopf, Matthew Coppinger, Nathan Sustersic, James Kolodzey, and Gwyn P. Williams, "High-Power Terahertz Source Opens the Door for Full-Field Video-Rate Terahertz Imaging", prepared for Nature.

EXPERIMENTAL STUDY OF VOLUME FREE ELECTRON LASER USING A "GRID" PHOTONIC CRYSTAL WITH VARIABLE PERIOD

V.G.Baryshevsky, N.A. Belous, A.A. Gurinovich, V.A. Evdokimov,
P.V. Molchanov *, A.V. Oskin, P.F. Safronov
Research Institute for Nuclear Problems, 11 Bobryiskaya str., 220050, Minsk, Belarus

Abstract

Experimental Study of Volume Free Electron Laser with a "grid" resonator ("grid" photonic crystal) with changing in space parameters are reported.

INTRODUCTION

Generators using radiation from an electron beam in a periodic circuit (traveling wave tubes [1,2], backward wave oscillators, free electron lasers) are now widespread [3].

All the above devices use one-dimensional feedback, which is formed by either two parallel mirrors placed on the both sides of working area or a diffraction grating.

But there are some challenges that restrict applications of such devices: electrical endurance of resonator limits radiation power and current of acceptable electron beam. Conventional waveguide systems are essentially restricted by the requirement for transverse dimensions of resonator, which should not significantly exceed radiation wavelength.

The indicated problems can be overcome by the aid of volume (non-one-dimensional) multi-wave distributed feedback [4–10]. New type of radiation generators using volume multi-wave distributed feedback was called Volume Free Electron Laser (VFEL). Transverse dimensions of VFEL resonator could significantly exceed radiation wavelength. The electron beam and radiation power are distributed over the large volume that is beneficial for electrical endurance of the system.

One of the VFEL types uses a "grid" photonic crystal that is formed by a periodically strained either dielectric or metallic threads, which provides to weaken requirements for beam guiding.

The "grid" structure of dielectric threads was experimentally studied in [11], where it was shown that such "grid" photonic crystals have sufficiently high Q-factor ($10^4 - 10^6$).

Theoretical analysis [12, 13] showed that periodic metal grid does not absorb electromagnetic radiation and the "grid" photonic crystal, made of metal threads, is almost transparent for the electromagnetic waves in the frequency range from GHz to THz. (In this range the skin depth δ is about 1 micron or less for the most of metals (for example, for 10 GHz $\delta_{Cu} = 0.66$ μm, $\delta_{Al} = 0.8$ μm, $\delta_W = 1.16$ μm and so on). Thus, in this frequency range the metallic threads can be considered as perfect conducting.)

* molchanov@inp.minsk.by

Theory of VFEL with spatially variable period was developed in [16, 17]. There it was shown that use of photonic crystal with variable period could provide significant increase in radiation output. It was mentioned that diffraction gratings (photonic crystal) can be used for creation the dynamical wiggler with variable period in the system. This makes possible to develop double-cascaded FEL with variable parameters changing, which efficiency can be significantly higher that of conventional system.

In the present paper experimental study of Volume Free Electron Laser with a "grid" resonator ("grid" photonic crystal) with changing in space parameters are considered.

EXPERIMENTAL SETUP

The "grid" photonic crystal is built from tungsten threads with the diameter 0.1 mm strained inside the rectangular waveguide with the transversal dimensions $a = 35$ mm, $b = 35$ mm and length 300 mm (see Fig.1). A pencil-like electron beam with the diameter 32 mm, energy up to 200 keV and current about 2kA passes through the above structure. The magnetic field guiding the electron beam is $\sim 1.55 - 1.6$ tesla. Period of "grid" photonic crystal is chosen to provide radiation frequency ~ 8.4 GHz. The "grid"

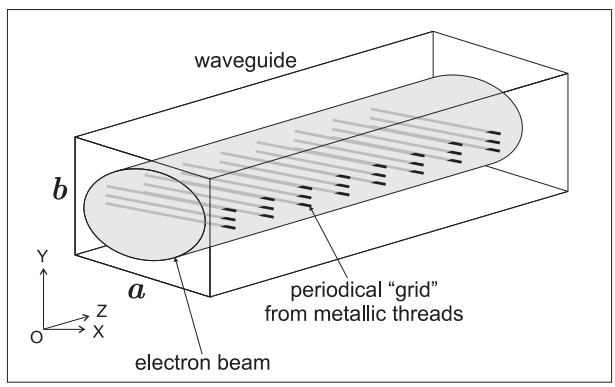

Figure 1: The "grid" diffraction grating placed inside the waveguide

structure is made of separate frames each containing the layer of 1, 3 or 5 parallel threads with the distance between the next threads $d_y = 6$ mm). Frames are joined to get the "grid" structure with the distance d_z between layers.

Frequency range is evaluated by means of tunable waveguide filters, which were tuned in the band 7.8 - 12.4 GHz with passbands 0.25 GHz, 0.5 GHz and 1 GHz. Attenuation of radiation in the suppressed band of this filter

is ~ -25 dB.

Evaluation of "grid" heating by electron beam action provides to expect long-time stability. For example, change of the thread temperature (tungsten threads of 100 μm diameter) due to action of the 250 keV electron beam with diameter 32 mm, current 1 kA and pulse duration 100 nsec can be estimated as $\Delta T < 125°$. Experiments with VFEL with the different "grids" have demonstrated stability of developed photonic crystals to heating caused by electron beam action.

EXPERIMENTAL RESULTS

In the experiments [14] generation in the "grid" VFEL was observed in BWO regime.

The sample oscillogram is shown in Fig.2, where signals marked 1 and 2 are the signals obtained from microwave detectors. Other two curves are the electron gun voltage and electron beam current. Time scale is 80 ns.

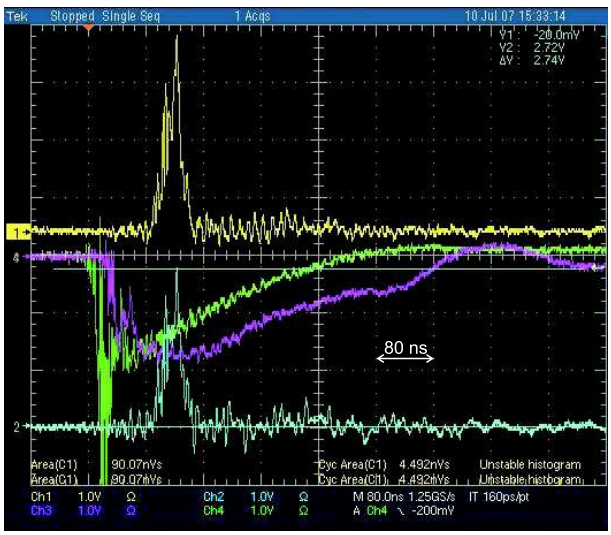

Figure 2: The sample oscillogram

The radiation power is measured for photonic crystal with 4, 6, 10, 12, 14 and 22 frames (period $d_z = 12.5$ mm) each containing five threads distant $d_y = 6$ mm each from other.

The result of these measurements is presented in Fig.3, where the radiation power is normalized to the maximal detected power (10 kiloWatt). Dependence of the generated radiation intensity on the "grid" photonic crystal length is obtained. The solid curve in this figure shows the numerically simulated radiation power, which also normalized. It can be seen from this Figure that for the photonic crystal with more than 14 periods ($\sim 3 \cdot \lambda$) saturation is reached.

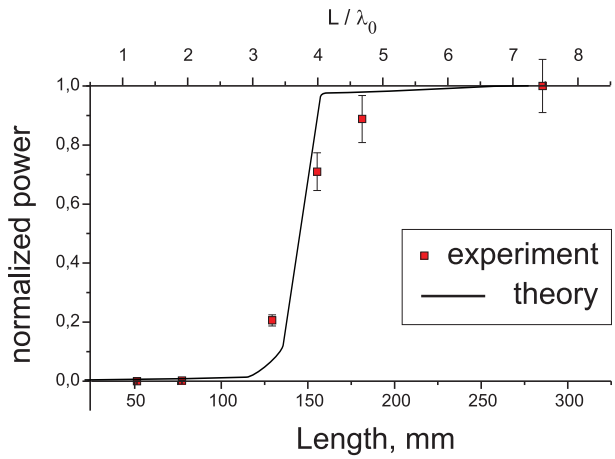

Figure 3: Dependence of the generation intensity on the length of the "grid" photonic crystal with 5 threads in the frame marked with squares and numerically simulated dependence of the wave amplitude on the "grid" photonic crystal length for the electron beam with the energy ~200 keV and current density ~ 2 kA/cm^2

The next experiment uses "grid" resonator made of two photonic crystals with different periods. The "grid" structure is made of separate frames each containing the layer of 5 parallel threads with the distance between the next threads dy=6 mm), 12 frames were joined to get the "grid' photonic crystal with the period 12.5 mm and another 12 frames formed "grid' photonic crystal with the period 10.5 mm . Total resonator length is 300 mm (the same as in the previous experiment). Separate experiments with the first photonic crystal (period 12.5 mm, 12 frames) were done to determine how the electron beam energy reduces after passing it. Period of the second photonic crystal is chosen to provide for the electron beam, which have lost part of its energy for radiation in the first photonic crystal, the same radiation frequency. Distance between two photonic crystals is 25 mm. The typical oscillogram for this experiment is shown in Fig.4.

Two radiation peaks are apparent in this oscillogram. Measurements of radiation frequency gives value close to 8.4 GHz for both peaks. Their intensities are also comparable and detected power is almost twice higher then that for the experiments with "grid" photonic crystal with 5 threads in the frame and fixed period.

Experimental results confirmed conclusion that photonic crystal with variable period could increase radiation output. Experiments are in progress.

Several experiments with Volume Free Electron Laser with the "grid" photonic crystals in millimeter and submillimeter wavelength ranges are in preparation now.

In the experiment with 200 keV electron beam radiation in the range 4-5 mm is expected to be observed. This experiment will be carried out in the Research Institute for Nuclear Problems (INP, Minsk, Belarus) for the "grid" photonic crystal, built from periodically strained tungsten

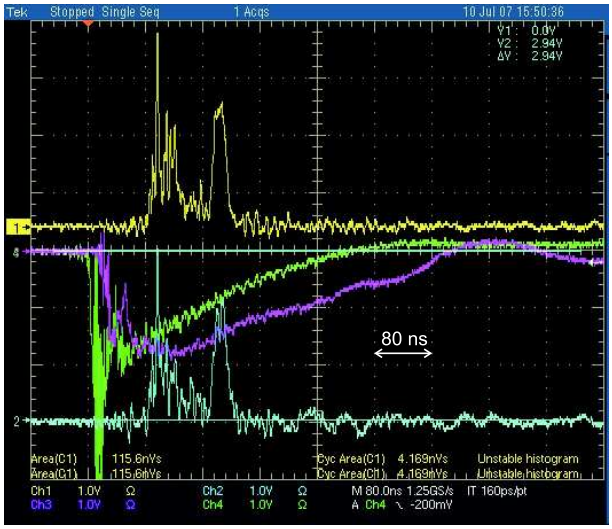

Figure 4: Typical oscillogram for "grid" resonator made of two photonic crystals with different periods

threads in the waveguide.

Joint experiment is being prepared now by INP and Joint Institute for Nuclear Research (JINR, Dubna, Russia) at LINAC-800, where 6 MeV electrons will be used for generation of radiation with mm and mm (150 GHz and 1 THz, respectively).

Realization of VFEL with dynamical wiggler (and conventional wiggler) with spatially varied period is also in our nearest plans.

CONCLUSION

Experimental results confirmed conclusion that photonic crystal with variable period could increase radiation output. Experiments are in progress.

REFERENCES

[1] R.Kompfner, "The traveling wave valve" *Wireless World*, 1946, vol.52, pp.369-372.

[2] R.Pierce, "Theory of the beam-type traveling-wave tube" *Proc. IRE*, 1947, vol.35, pp.111-123.

[3] V.L.Granatstein, R.K.Parker and C.M.Armstrong, "Vacuum electronics at the dawn of the twenty-first century," in *Proceedings of the IEEE*, 1999, vol.87, no.5, pp.702-716 .

[4] V.G.Baryshevsky and I.D.Feranchuk."Parametric beam instability of relativistic charged particles in a crystal", Phys.Lett. A, 102, pp.141-144 (1984).

[5] V.G. Baryshevsky. "Surface parametric radiation of charged particles", Doklady Akademy of Science USSR 299, pp.6-9 (1988).

[6] V.G.Baryshevsky, K.G.Batrakov, I.Ya.Dubovskaya. "Parametric (quasi-Cerenkov) X-ray free electron lasers", J.Phys. D, 24, pp.1250-1257 (1991).

[7] V.G.Baryshevsky, "Volume Free Electron Lasers" *NIM A*, 2000, vol.445, pp.281-282; LANL e-print archive physics/9806039.

[8] V.G.Baryshevsky, K.G.Batrakov, A.A.Gurinovich, I. Ilienko, A. Lobko, V. Moroz, P. Sofronov, and V. Stolyarsky, "First Lasing of Volume FEL (VFEL) at Wavelength Range $\lambda \sim 4 - 6$ mm" *NIM A*, 2002, vol.483, pp.21-24.

[9] V.G.Baryshevsky, K.G.Batrakov, A.A.Gurinovich, I. Ilienko, A. Lobko, V. Moroz, P. Sofronov, and V. Stolyarsky, "Progress of the Volume FEL (VFEL) experiments in millimeter range" *NIM A*, 2003, vol.507, pp.137-140.

[10] V.G.Baryshevsky, K.G.Batrakov, V.Mihalchik, V.P. Peftiev, V.I.Stolyarsky. "A process for generating electromagnetic radiation and volume free electron laser apparatus for carrying out the proces", Eurasian patent EA 004665B1.

[11] V.G.Baryshevsky, K.G.Batrakov, I.Ya.Dubovskaya, et al., "Volume Quasi-Cherenkov FEL in mm-Spectral Range", in Proceedings of FEL 1996, p.II-75, Elsevier Science B.V. (1997).

[12] V.G.Baryshevsky, A.A.Gurinovich, "Electrodynamical properties of a "gri" volume resonator" LANL e-print archive: physics/0409107.

[13] V.G.Baryshevsky, A.A.Gurinovich, "Spontaneous and induced parametric and Smith-Purcell radiation from electrons moving in a photonic crystal built from the metallic threads" *NIM B*, 2006, vol.252, pp.92-101.

[14] V.G. Baryshevsky, K.G. Batrakov, N.A. Belous, A.A. Gurinovich, A.S. Lobko, P.V. Molchanov, P.F. Sofronov, and V.I. Stolyarsky, "First observation of generation in the backward wave oscillator with a "grid" diffraction grating and lasing of the volume FEL with a "grid" volume resonator" LANL e-print archive: physics/0409125.

[15] V.G. Baryshevsky, N.A.Belous, A.A.Gurinovich, A.S.Lobko, P.V.Molchanov, and V.I.Stolyarsky "Experimental study of a volume free electron laser with a "grid" resonator" in *Proceedings of FEL 2006*, BESSY, Berlin, Germany, p331-334, LANL e-print arXiv: physics/0605122.

[16] V.G.Baryshevsky, A.A.Gurinovich. "Generation of radiation in free electron lasers with diffraction gratings (photonic crystal) with the variable spacial period"arXiv: physics/0608068.

[17] V.G.Baryshevsky, A.A.Gurinovich. "Electrodynamical Properties of a Volume Free Electron Laser with a "Grid" Resonator" in Proceedings of FEL 2006, BESSY, Berlin, Germany, pp.335-339 (2006).

RESEARCH HIGHLIGHTS FROM FLASH

R. Treusch and J. Feldhaus, DESY, Hamburg, Germany

Abstract

The Free electron LASer in Hamburg (FLASH) has started regular user operation in summer 2005, providing XUV radiation pulses with pulse energies in the 10–100 μJ range and pulse durations of 10–50 fs. The science programme at FLASH covers a broad range of novel applications including fundamental studies on atoms, ions, molecules and clusters, creation and characterisation of warm dense matter, diffraction imaging of nanoparticles, spectroscopy of bulk solids and surfaces, investigation of surface reactions and spin dynamics, and the development of advanced photon diagnostics and experimental techniques. So far, 16 science projects have been pursued involving approximately 200 scientists from 11 countries. Some of the research highlights were presented in the talk.

Most of the presented results are presently in the publishing process. Hence the reader is kindly referred to the selection of already published research at FLASH as listed below.

SELECTED PUBLICATIONS ON RESEARCH AT FLASH

1. V. Ayvazyan et al.,
First operation of a Free-Electron Laser generating GW power radiation at 32 nm wavelength,
Eur. Phys. J. D, **37**, 297-303 (2006)

2. S. Düsterer et al.,
Spectroscopic characterization of vacuum ultraviolet free electron laser pulses,
Opt. Lett. **31**, 1750-1752 (2006)

3. A.A. Sorokin et al.,
Multi-photon ionization of molecular nitrogen by femtosecond soft x-ray FEL pulses,
J. Phys. B: At. Mol. Opt. Phys. **39**,L299-L304 (2006)

4. H.N. Chapman et al.,
Femtosecond diffractive imaging with a soft-X-ray free-electron laser,
Nature Physics **2**, 839-843 (2006)

5. M. Meyer et al.,
Two-color photoionization in xuv free-electron and visible laser fields,
Phys. Rev. A **74**, 011401(R) (2006)

6. A.A. Sorokin et al.,
Method based on atomic photoionization for spot-size measurement on focused soft x-ray free-electron laser beams,
Appl. Phys. Lett. **89**, 221114 (2006)

7. N. Stojanovic et al.,
Ablation of solids using a femtosecond extreme ultraviolet free electron laser,
Appl. Phys. Lett. **89**, 241909 (2006)

8. A.R.B. de Castro et al.,
Spectroscopy of rare gas clusters using VUV light from a free-electron-laser,
J. Electron Spectrosc. Relat. Phenom. **156158**, 25-29 (2007)

9. M. Kirm et al.,
Time resolved luminescence of solids excited by femtosecond VUV pulses and synchrotron radiation,
phys. stat. sol. (c) **4**, No. 3, 870876 (2007)

10. S. Cunovic et al.,
Time-to-space mapping in a gas medium for the temporal characterization of vacuum-ultraviolet pulses,
Appl. Phys. Lett. **90**, 121112 (2007)

11. P. Radcliffe et al.,
Single-shot characterization of independent femtosecond extreme ultraviolet free electron and infrared laser pulses,
Appl. Phys. Lett. **90**, 131108 (2007)

12. S.P. Hau-Riege et al.,
Damage threshold of inorganic solids under free-electron laser irradiation at 32.5 nm wavelength,
Appl. Phys. Lett. **90**, 173128 (2007)

13. S.P. Hau-Riege et al.,
Subnanometer-Scale Measurements of the Interaction of Ultrafast Soft X-Ray Free-Electron-Laser Pulses with Matter,
Phys. Rev. Lett. **98**, 145502 (2007)

14. S.W. Epp et al.,
Soft x-ray laser spectroscopy on trapped highly charged ions at FLASH,
Phys. Rev. Lett. **98**, 183001 (2007)

15. J. Chalupský et al.,
Characteristics of focused soft X-ray free-electron laser beam determined by ablation of organic molecular solids,
Optics Express **15**, 6036-6043 (2007)

16. A.A. Sorokin et al.,
X-ray-laser interaction with matter and the role of multiphoton ionization: Free-electron-laser studies on neon and helium,
Phys. Rev. A **75**, 051402(R) (2007)

17. M. Nagasono et al.,
Resonant two-photon absorption of extreme ultraviolet FEL radiation in Helium,
Phys. Rev. A **75**, 051406(R) (2007)

18. R. Moshammer et al.,
Few-photon Multiple Ionization of Ne and Ar by Strong Free-Electron-Laser Pulses,
Phys. Rev. Lett. **98**, 203001 (2007)

19. H.B. Pedersen et al.,
Crossed Beams Photodissociation Imaging of HeH^+ with Vacuum Ultraviolet Free Electron Laser Pulses,
Phys. Rev. Lett. **98**, 223202 (2007)

20. W. Ackermann et al.,
Operation of a Free Electron Laser in the Wavelength Range from the Extreme Ultraviolet to the Water Window,
Nature Photonics **1**, 336-342 (2007)

21. A. Föhlisch et al.,
High-brilliance free-electron-laser photoionization of N_2: Ground-state depletion and radiationfield-induced modifications,
Phys. Rev. A **76**, 013411 (2007)

22. H.N. Chapman et al.,
Femtosecond Time-Delay X-ray Holography,
Nature **448**, 676-680 (2007)

MILLIMETER WAVES SENSING BEHIND WALLS - FESEABILITY STUDY WITH FEL RADIATION*

B.Kapilevich, M.Einat, A.Yahalom, M.Kanter, B.Litvak, The Israeli FEL Knowledge Center, the Ariel University Center of Samaria, Ariel, 44837, Israel
A.Gover, Tel Aviv University, Israel

Abstract

Design of through-wall imaging (TWI) system needs the knowledge of constitutive parameters of different building materials. The paper describes the results of measurements of the effective attenuation constant of typical building materials such as concrete bricks, wood, tiles, sand, gypsum, etc. on mm-waves using powerful pulse FEL radiation. Since the Rayleigh criterion for surface roughness cannot be satisfied for majority of measured building materials on mm waves, the increased measured attenuation in comparison with bulky material is taken place. Additional experiments were performed to estimate a role of these effects using quasi-noise mm-wave source and wide-band mm-wave receiver.

INTRODUCTION

The through-wall imaging (TWI) systems provide unique possibility to detect and image objects behind the walls, door and other opaque medium [1, 2]. Basically, through-wall imaging (TWI) systems operate in 1.99 – 10.6 GHz or below 960 MHz [3]. The penetration capability at these frequencies is characterized by rather small attenuation caused by building material as shown in Fig.1 [4]. However, the spatial resolution of TWI systems is degraded when the operating frequency is relatively low. On the other hand, a majority of building materials demonstrate increased losses as the frequency increases. As a result, higher RF power from the source is required for quality TWI process.

The Israeli mm-wave FEL provides unique opportunity to solve the above TWI problem delivering an output power of 100-1000W at 85-105 GHz. But design of TWI system operating on mm-waves needs comprehensive study of constitutive parameters of different building materials that must be measured in real pulse operation FEL conditions. The paper describes the experimental setup assembled for measurements of the effective attenuation constant of typical building materials such as concrete bricks, wood, tiles, sand, gypsum, etc. on mm-waves using powerful FEL radiation. Since the Rayleigh criterion for surface roughness at mm-waves cannot be satisfied for majority of measured materials, the measured attenuation is different in comparison with bulky material.

Additional experiments were performed to estimate a contribution of this effect into the measured attenuation. The special W-band quasi-noise sensor has been designed and assembled to carry out such experiments.

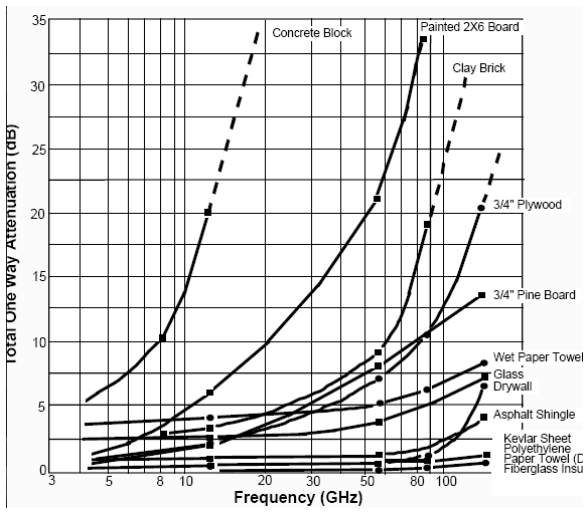

Figure 1: Illustration of penetration capabilities of different building materials as a function of frequency [4].

EXPERIMENTAL SETUP AND CALIBRATION PROCEDURE

The block-diagram of the experimental setup used for measurement of effective attenuation constant is shown in Fig.2. The pulse mm-wave FEL radiation (5-10 μs) propagating in the corrugated wave guide line excites the Tx standard rectangular horn antenna that transforms it to plane wave. This wave partially penetrates though the sample of the tested material and is captured by a similar Rx antenna coupled with the W-band programmable attenuator and DXP-10 detector (Millitech). A similar detector is coupled with the directional couplers providing a total coupling level of -64dB. Both detected signals are independently recorded by the Tektronix digital scope.

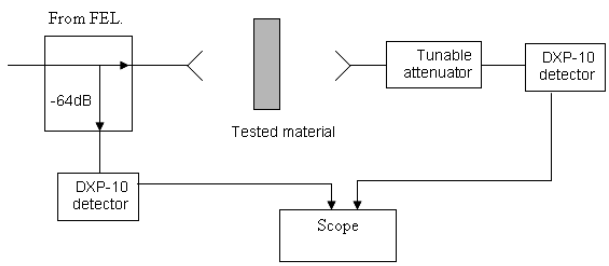

Figure 2: The block-diagram of the experimental setup.

*Work was partly supported by the Israeli Ministry of Science.

Several detectors were preliminary compared in order to choose the two maximally identical units. A general view of the experimental setup is shown in Fig.3.

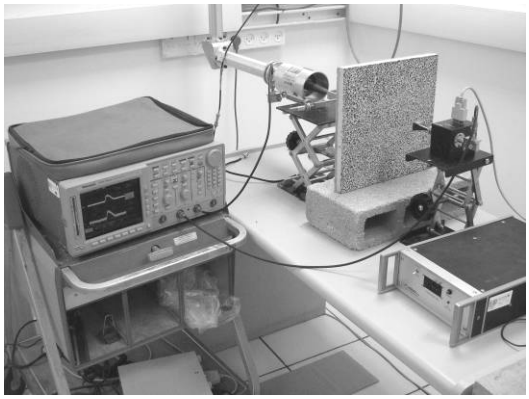

Figure 3: A general view of the experimental setup.

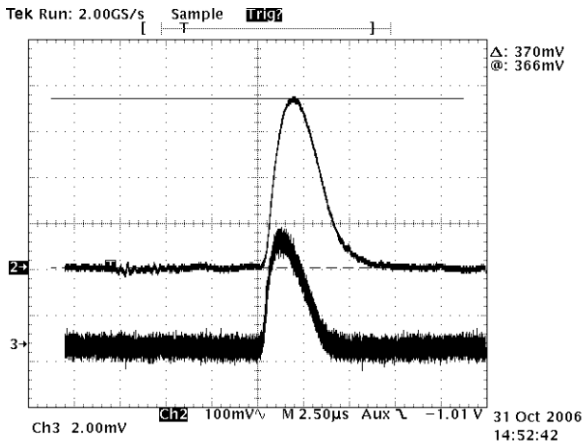

Figure 4: Examples of the detected signals recorded by the digital scope in process of calibration (channel 2 - Rx detector, channel 3 - Tx detector).

Calibration of the setup shown in Fig. 2 was done using free space conditions. Typical detected signals recorded by the digital scope in channel 2 and channel 3 are depicted in Fig. 4 for receiving and transmitting detectors correspondently. Based on this calibration, we have found out that the RF peak power at the FEL output is 150W in the vicinity of 100GHz. When material under test is inserted between Rx and Tx antennas, the detected signal is reduced depending on material transmittance. By adjusting the variable attenuator we can restore the original amplitude of the signal in the Rx channel. The difference of the attenuator readings corresponding to the two situations gives directly the effective attenuation. The only factor that must be taken into account is the variation of the FEL's radiated power from pulse to pulse. However, suitable correction can be easily introduced into the measurements since the Tx detector in channel 3 continuously controls this parameter.

CHARACTERIZATION OF BULDING MATERILAS USING MM-WAVE PULSE RADIATION OF THE FEL

The effective attenuation of various building materials has been measured using mm-wave pulse radiation of the FEL as described in the previous section. Various materials were tested. Some selected results are presented in the Table.1 for cement plate, gypsum board and wood board.

Table 1: Measured effective attenuation of the selected building materials

Type of the material	Effective attenuation [dB]	Comments
one layer of wood board, 2cm	-19	Horizontal polarization
one layer of wood board, 2cm	-20.4	Vertical polarization
two layers of wood board, 4cm	-41.6	Both are in Vertical polarization
one layer of gypsum board, 1.2cm	- 3.5	- - -
one plate of cement tile, 2.5cm	-39.3	Vertical polarization
one plate of cement tile, 2.5cm	-39.5	Horizontal polarization

All samples of materials under test were examined in both orthogonal polarizations – horizontal and vertical. Most of building materials have a texture and demonstrate polarization sensitivity of the measured attenuation. However, the gypsum plate is quite uniform and insensitive to the polarisation of the radiated wave.

CHARACTERIZATION OF BULDING MATERILAS USING MM-WAVE QUASI-NOISE ILLUMINATION

Basically, constitutive parameters of many building materials are characterized using coherent illumination. However, TWI systems operate with UWB signals that leads to uncertainty in estimation of their real penetration capabilities if a frequency domain. The best way to solve this problem is to measure an attenuation applying incoherent (quasi-noise) illumination. We have developed and assembled a wide band mm-wave sensor for experiments with quasi-noise signals schematically depicted in Fig. 5.

The sensor is based on heterodyne circuitry consisting of the receiving antenna connected with the W-band pin-diode modulator that provides 1 KHz pulse modulation of the received signal. Then the signal comes to W-band LNA (gain about 15 dB) and down-converted by mixer with IMPATT LO operating at 94GHz. The IF signal is amplified about 70 dB by IF LNA with 6 GHz bandwidth so that the total double-side bandwidth of the received signal is about 12 GHz. The wideband HP-423A detector, post detector's video-amp and Tektronix Digital Scope are employed for recording the signals propagating through the material under test. Full W-band FARRAN noise generator has been used as the source of incoherent illumination of the container with materials under measurements. The general view of the setup used for quasi-noise characterization of building materials is shown in Fig. 6. W-band FARRAN noise generator is placed beneath container and invisible.

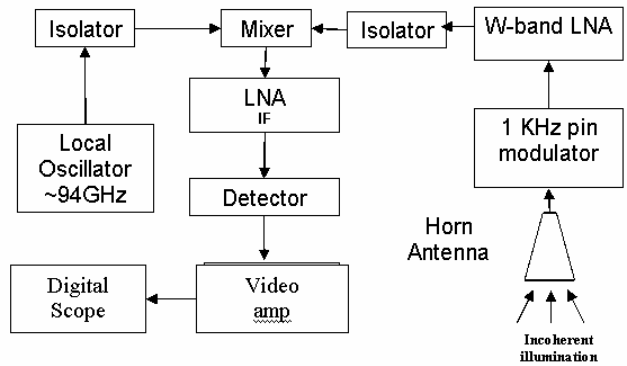

Figure 5: Schematic of the wide band mm-wave sensor.

The setup depicted in Fig.6 was employed for measurement of an attenuation of the sand samples with different thickness. To estimate the role of depolarisation effects the container with sand was rotated and the effective attenuation has been measured for different angular orientations of the sand sample.

Typical measured attenuation as a function of sand's layer thickness is shown in Fig. 7 for the four angular position of container: ooo - 0 deg, xxx – 90 deg, ◊ ◊ ◊ - 180 deg and □□□ – 270 deg. The averaged result is plotted by the solid line.

The same samples of sand have also been tested using coherent illuminations by means of Agilent W-band network analyzer at the frequency 100 GHz. The effective attenuation is depicted in Fig. 8 as a function of the thickness for the four angular position of the container as was done in previous experiments. We observed high variations of the measured attenuation as a function of thickness. It can not explained by properties of bulky material. The most realistic interpretation of such behaviour is interference on boundaries sand-air, surface roughness and possible depolarisation effects.

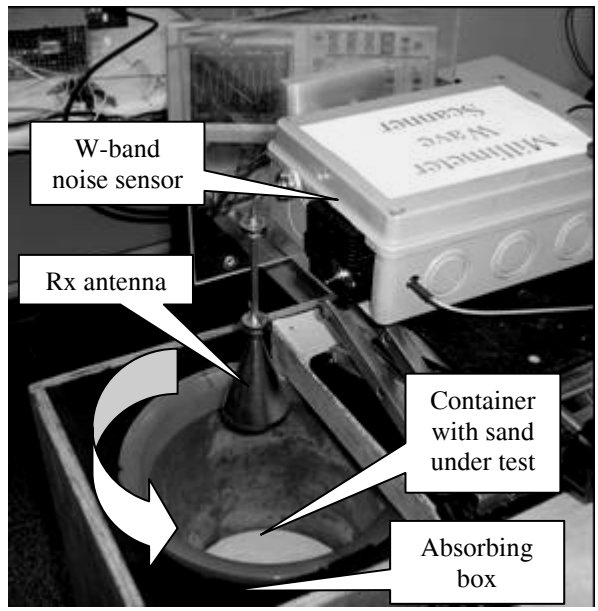

Figure 6: The general view of the setup used for quasi-noise characterization of building materials.

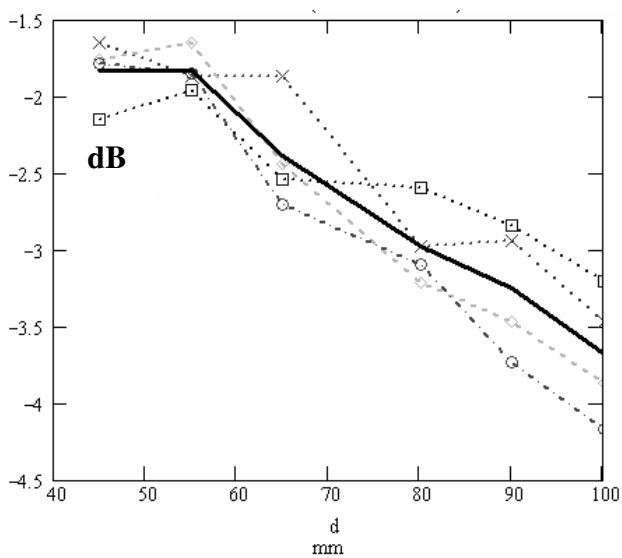

Figure 7: Measured attenuation for quasi-noise illumination in W-band as a function of sand's layer thickness for the four angular position of container: ooo - 0 deg, xxx – 90 deg, ◊ ◊ ◊ - 180 deg and □□□ – 270 deg. The solid line corresponds to the averaged result.

CONCLUSION

The paper has presented the results of measurements of effective attenuation of various building materials using powerful FEL radiation on mm-waves.

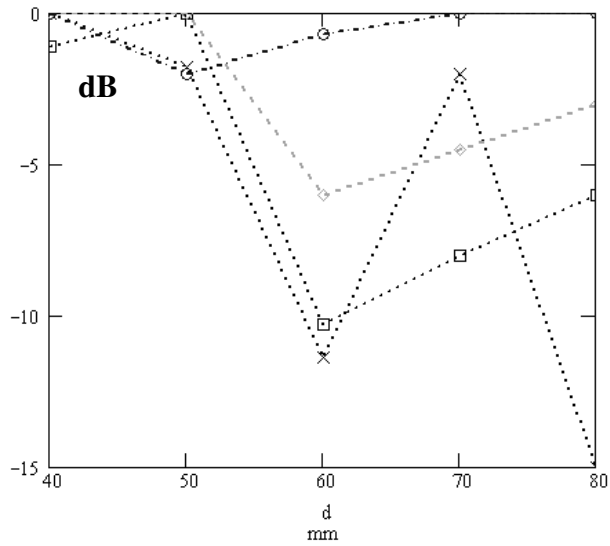

Figure 8: Measured attenuation for coherent illumination at 100 GHz as a function of sand's layer thickness for the four angular position of container: ooo - 0 deg, xxx – 90 deg, ◊ ◊ ◊ - 180 deg and □□□ – 270 deg.

Comparison of the measured losses for coherent and incoherent illuminations has revealed essential differences. The noise-like illumination suppresses interference and depolarization effects due to natural averaging in frequency domain. That can be recommended for characterization of building materials to provide more realistic data needed for design mm-wave TWI systems. The short pulse FEL generating a wide-band spectrum is a good candidate for this purpose.

ACKNOWLEDGEMENTS

Authors would like to thank D.Hardon for his valuable coordinating efforts, M.Harpaz for his assistance in conducting FEL's experiments and A.Konevsky for participating in experiments with the W-band quasi-noise sensor.

REFERENCES

[1] D.D.Ferris Jr. and N.C. Curie, "A Survey of Current Technologies for Through-the-Wall Surveillance (TWS)", Proc. SPIE, 1998, Vol.3577, pp.62-72.

[2] F.Ahmad, M.Amin, and S.Kassam, "Synthetic Aperture Beamformer for Imaging through a Dielectric Wall", IEEE Trans, AES, January 2005, Vol.41, No.1, pp.271-283.

[3] Revision of Part 15 of the Commission's Rules Regarding Ultra-Wideband Transmission Systems, the FCC order of 4-22-2002, www.fcc.gov.

[4] L.M.Frazier, "Radar Surveillance trough Soled Materials", SPIE Photonics East Conference, Boston MA, November 1996, paper 2938-20.

SOURCES OF RADIATION ON ARC-EN-CIEL PROPOSAL

M. E. Couprie, C. Benabderrhamane, C. Bruni, O.Chubar, M. Labat, G. Lambert, A. Loulergue, O. Marcouillé, Synchrotron-SOLEIL, Saint-Aubin, France
L. Giannessi, ENEA, Frascati, Italy.

Abstract

The ARC-EN-CIEL project [1] proposes a panoply of light sources for the scientific community. The choice to base the FEL sources on HGHG (High Gain Harmonic Generation) radiation and their Non Linear Harmonics seeded with the High order Harmonics generated in Gas (HHG) is further confirmed with the successful demonstration experiment of such a scheme at SCSS Prototype Accelerator in Japan [2]. In phase 1 (220 MeV), the radiation extends down to 30 nm, phase 1' (800 MeV) and phase 2 (1 GeV), the radiation reaches 1 nm, with 30-100 fs pulses. The first FEL "LEL1" utilizes in-vacuum undulators of period 26 mm for the modulator, and APPLE-type radiators of period 30 mm, close to the standard SOLEIL insertion devices. The second FEL branch "LEL2" uses in-vacuum planar U18 undulators as radiator. In addition, THz radiation from the magnets of the compression chicanes will be provided and has been calculated using SRW. ARC-EN-CIEL Phase 3 adds ERL loops at 1 GeV and 2 GeV where undulators emit conventional synchrotron radiation above 10 keV from short period in-vacuum undulators and soft X ray using a variable polarisation undulator. An FEL oscillator in the 40-8 nm spectral range is installed in the 1 GeV loop. The HHG seeded "LEL4" uses the electron beam from the 2 GeV loop and further accelerated to 3 GeV for producing coherent light production below 1 nm. Recent calculations and optimisations are presented.

INTRODUCTION

ARC-EN-CIEL (Accelerator-Radiation for Enhanced Coherent Intense Extended Light) aims at providing the user community with coherent femtosecond light pulses covering from UV to soft X ray spectral range in France [2]. It is based on a CW 1.3 GHz superconducting linear accelerator delivering high charge, subpicosecond, low emittance electron bunches at high repetition rate. The completion of ARC-EN-CIEL relies on different phases, according to the electron beam energy, the average current and the light sources available for the users. Phase 1 uses a 1 kHz high charge, short bunch electron beam, reaching an energy of 220 MeV with 3 cryomodules, and a first bunch compressor delivered by a modified Zeuthen RF gun [3], illuminated by a Ti:Sa laser. LEL1 is based on a FEL seeded with HHG with an APPLE-II type undulator as a radiator for adjustable polarisation radiation. Phase 1 (220 MeV, 30 nm) is now extended to 800 MeV (Phase1') with an additional bunch compressor and five cryomodules, and fits in the tunnel of the ALS (Accelerateur Linéaire de Saclay) allowing LEL1 radiation to be extended to shorter wavelengths for users applications. With two additional cryomodules on the Linac leading to 1 GeV (Phase 2), the FEL source "LEL2" will be installed, allowing stronger radiation to be achieved in the 1 nm range. Then, with the installation of an additional high average current gun (AES/JLab type [4]) illuminated by a Ytterbium diode pump fiber laser, two ERL loops at 1 and 2 GeV will be added. On the 1 GeV loop is planned LEL3 and FEL oscillator taking advantage of the mirror development for lithography, and an APPLE-II for subpicosecond radiation synchrotron radiation. On the 2 GeV loop, 6 in vacuum U20 (period of 20 mm) will be installed for hard X ray spontaneous emission. When the 2 GeV beams is not energy recovered but once again accelerated up to 3 GeV, it is sent to "LEL4", an FEL seeded with HHG and using cryogenic undulators. THz radiation is also produced in the bending magnets of the compression chicanes and of the arcs. The general scheme of ARC-EN-CIEL is shown in fig. 1.

Table 1: List of radiation sources on ARC-EN-CIEL. Phase: P. M for Modulator and R for Radiator. SR: Synchrotron Radiation. CSR: Coherent Synchrotron Radiation. BC Bunch Compressor. E: Energy. N: number of periods. Conf: configuration. BL: beam line.

	P	E GeV	Type	M/R, N	Spectral range
FEL radiation					
LEL1 Planar helical branch	1, 1', 2	0.22 - 1	HGHG conf 1-1 1-3 HHG seed	M :U26 200 R : HU30, N2=700	200-1.5 nm
LEL2 Planar branch	2	0.8-1.2	HGHG, conf 1-1 et 1-3 HHG seed	M : U26, N1=500 R : U18 N2=500	10-0.5 nm
LEL4 planar branch	3	3	HGHG conf 1-3and 1-5 HHG seed	M :U35, N1=700 R :U18, N2=1000	2-0.2 nm
LEL3	3	1	FEL oscillator	HU30, N=350	40-8 nm
Spontaneous emission					
VUV BL	3	1	SR	HU30	0.2-4 keV
X BL	3	2	SR	U 20, 100	1-20 keV
THz Radiation					
	1-1' 2, 3		CSR	BC1, 2, arc	0.1-10 THz

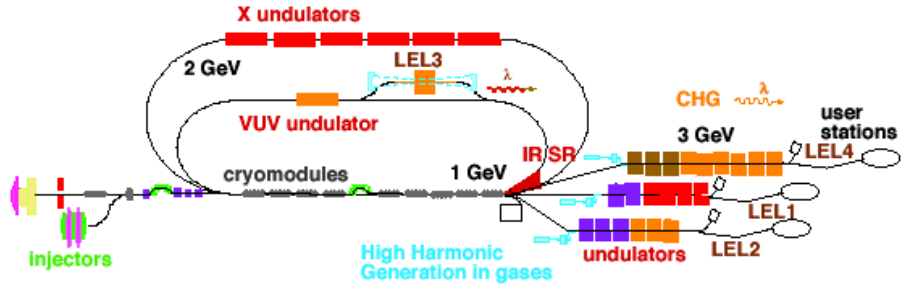

Fig. 1: General scheme of ARC-EN-CIEL, with the different phases and FEL sources

THE CONSTITUTING ELEMENTS

The different parts of the FEL and SR sources are here described, including accelerator parameters, insertion devices, HHG seed for LEL1, LEL2, LEL4 and optics.

The accelerator

A scheme of implementation of Phase1' in the ALS tunnel, showing the different accelerator components, is shown in fig. 2. Another site, the so-called "Mare du Vivier" at Saint-Aubin nearby SOLEIL and Orme des Merisiers, the French third generation synchrotron light source, is considered for Phases 2 and 3. The radiation from a SOLEIL beamline could be coupled to ARC-EN-CIEL radiation.

The beam dynamics has been studied starting from the gun using ASTRA, CSR-Track and TRAFFIC-4 for Phase 1 and 2, and using BETA and BU for Phase 3 [5]. The beam parameters taken for the FEL and radiation simulations are presented in Table 2.

The ERL mode relaxes the constraints with respect to the compression. In such a case, the beam will not go through the second bunch compressor bunch but will travel in a straight vacuum chamber installed at this position. ARC-EN-CIEL Phase 3 aims at achieving high average currents. Typically, 1 mA can be obtained for a repetition rate of 5 MHz. Two regimes depending on the charge level are envisaged, leading to different values of the emittance and peak current as shown in table 2. Higher average currents can be reached in enhancing the repetition rate up to 100 mA.

ARC-EN-CIEL should provide simultaneous electron beams in the accelerators for feeding the light sources for the users: the 1 kHz high peak current for LEL1 and LEL2 should coexist with the high repetition rate (1-100 MHz) recirculated beam in the ERL loops. Such an operation requires the electron beams to be recombined at low energy at the loop entrance and the beams to be separated at the exit of the accelerating structures thanks to kicker magnets.

The operating mode between the different phases relies on the temporal structure illustrated in figure 3.

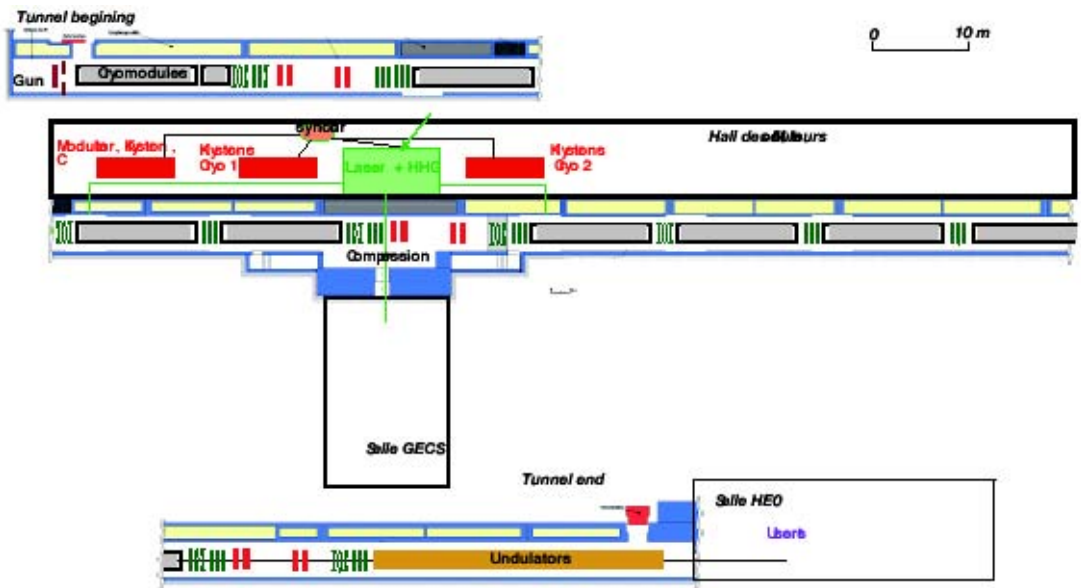

Fig. 2: Possible implementation of ARC-EN-CIEL phase 1' in the tunnel of the former Accelerateur Linéaire de Saclay (Linear Accelerator of Saclay) situated at Orme des Merisiers.

Table 2: ARC-EN-CIEL beam parameters. Total and slice energy spread $\sigma_\gamma/\gamma_{tot}$, and $\sigma_\gamma/\gamma_{slice}$, total and slice beam emittance ε_{tot} and ε_{slice}.

Phase	1	2	3, mode 1	3, mode 2	3
Energy (Gev)	0.2	1	1-2	1-2	3
Rep. rate (kHz)	1-10	1-10	10^3 – 10^5	10^3 – 10^5	1
Charge (nC)	1	1	0.2//1	0.2//1	0.75
ΔT(fs rms)	500-600	200-300	500-600	500-600	200
<I> (μA)	1-10	1-10	10^3-10^5	10^3-10^5	
I_{peak} (kA)	0.8	1.5	0.2	1	
$I_{peak,slice}$(kA)	1	2	1	1	1.5
ε_{tot}(mm mrad)	2.4	1.6	2	6	
ε_{slice} (mm mrad)	1	1.2	1	5	1.2
σ / $_{tot}$ (%rms)	0.1	0.1	0.1	0.2	
σ / $_{slice}$ (%rms)	0.04	0.04	0.04	0.08	0.02

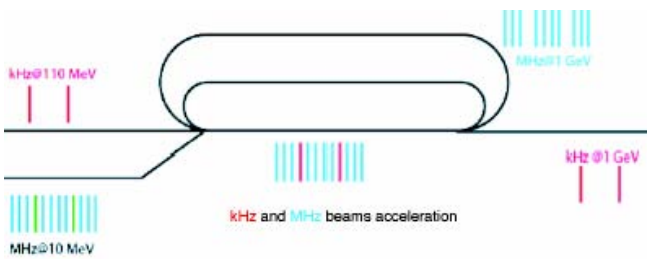

Fig. 3: Simultaneous operation of the electron beams in the different phases of ARC-EN-CIEL.

The undulators

Thanks to the experience on insertion devices acquired at SOLEIL [6], the choice of the undulators tends to select solutions not very different from the ones adopted at SOLEIL. For LEL1, 2, and 4, a conventional HGHG scheme comporting a modulator, a dispersive section and a radiator has been chosen. Different configurations are foreseen, from the 1-1 (modulator and radiator tuned on the seed wavelength), 1-2 (radiator tuned to the second harmonic of the modulator resonant wavelength), 1-3, 1-5 and harmonic cascade (resonant wavelength of the radiator equal to the resonant wavelength of the modulator multiplied by a ratio of integer numbers [7]). The resonant wavelength versus the undulator period has been calculated for different beam energies and the deflection parameter K values in planar and helical configuration. The accessible magnetic field B versus gap for a given undulator period λ_o has been evaluated using the analytical expression for NdFeB of remanent field 1.2T: $B=a\cdot\exp(b\cdot gap/\lambda_o + c\cdot(gap/\lambda_o)^2)$ where the coefficients a, b and c are derived for different cases of undulators types [8]. Further optimisations have been done then specifically with RADIA software [9], as in the example of the APPLE-II HU30. Such an undulator is adopted for the radiator of LEL1 and for the undulator of the FEL oscillator LEL3. At SOLEIL, after the installation of three HU80 on the ring, different APPLE-II types undulators are under construction or to be built, with periods ranging between 60 down to 34 mm. Since the vacuum chamber should be as wide in the horizontal direction and the vacuum constraints are soften with respect to storage ring, a period of 30 mm seems quite reasonable. Further analysis during the TDR phase will investigate the possible use of APPLE-III type undulators [10] and designs of in-vacuum APPLE-II undulators.

Standardization with respect to the different undulators sections of ARC-EN-CIEL and small deviations from the solutions adopted at SOLEIL are aimed. SOLEIL has already built several in vacuum U20 undulators, which type of insertion device has been adopted as the ones for the X ray synchrotron light sources on the 2 GeV loop. Further final adjustments will be made later according to the user requests. The periods for the in-vacuum undulators at SOLEIL range between 20 and 26 mm. An U26 has been chosen as a modulator for LEL1 and LEL2, allowing efficient bunching by the seed for the configuration 1-3 for example. The use of a short period high magnetic field in vacuum undulator allows the total length to be reduced and the system to be more compact. LEL2 aiming at operating even below 1 nm on the non-linear harmonics, the magnetic field has been pushed in this case with a radiator of 18 mm period.

Recent development in cryogenics undulators permit to enhance the peak magnetic field by a factor 1.3 using a specific magnet variety operated at low temperature (typically 140 K). First proposed at SPring-8 [11], real advances have been achieved so far in particular at SPring-8, ESRF [12] and BNL [13]. R&D is launched on this subject at SOLEIL. So far, it has been demonstrated that the shimming can be done at normal temperature and the magnetic field properties remain at low temperature, as far as the girders mechanics is not modified. The cooling of the magnets can be performed either via cryocoolers or nitrogen circulation. The magnetic type allowing the highest magnetic field can not be baked for reaching low vacuum pressure, but this is less limiting on a Linac than on a storage ring. So cryogenic undulators are adopted for LEL2 and LEL4 of ARC-EN-CIEL project.

Table 3 summarizes the characteristics of the undulators considered for the simulations of the light sources. Mainly, simulations have been performed using PERSEO Time Dependent [14] considering a filling factor [15] of 0.1 in order to take into account the transverse overlap between the seed and the electron beam, considering average betatron functions of 2.6 m. The undulators are to be built in 2 meters length segments with a FODO lattice in between two segments. Compared to the values given in Table 3, the length will be slightly

increased for being a multiple of the segment length. After each undulator module will be placed Optical Transition Radiator screens, Beam Position Monitors. These further optimizations (lattice, segmentations) will take place during the TDR phase of the project. Each segment comports four correctors for adjustment of the vertical and horizontal trajectories at its entrance and exit. After checking the magnetic axis, the module effect on the orbit will be measured versus gap and compared with the magnetic measurements. The natural focusing and the one resulting from defects of magnetic fields will be studied thanks to the quadrupoles located between two segments. In a further step, the radiation will be measured versus the electron beam position using a zone plate selecting the spatial distribution at a given energy, such as the DIAGON type measurements performed at SOLEIL [16].

Table 3: Undulators for ARC-EN-CIEL sources, M for Modulator and R for radiator, * for cryogenic undulators. In-vac for in-vacuum.

FEL	Type	λ_o mm	K_{max}	Gap_{min}	Length (m)
LEL1-M	In-vac	26	3.2	3.5	5.2
LEL1-R	Apple-II	30	P:2.16 H:1.5	10 8	21
LEL2-M	In-vac	26	3.2	3.5	13
LEL2-R	In-vac*	18	3.1*	3.7	9
LEL3	Apple-II	30	P:3.36 H:1.5	6 8	10.5
LEL4-M	In-vac *	35	4.8	3.5	24.5
LEL4-R	In-vac *	18	3.1*	3.7	18
VUV	Apple-II	30	P:1.1 H:0.7	15.5	2
X	In-vac	20	1.9	5.5	2x6

Simulations consider a dispersive section compression factor R_{56} of 1.5 µm maximum. The R_{56} can be expressed in terms of magnetic field as: $R_{56} = \frac{L_D}{\gamma^2}\left[1 + \frac{e^2}{L_D m^2 c^2}\int_0^{L_D}\left[\int_0^s B_D(u)du\right]^2 ds\right]$ where L_D is the dispersive section total length, m the mass of the electron, c the speed of light, B_D the magnetic field of the dispersive section and s the longitudinal coordinate. Such a dispersive section can be realised with permanent magnets and modelised with RADIA [9]. In an example, R_{56} ranging between 33 µm at 500 MeV to 6 µm at 1.2 GeV, and 0.9 µm at 3 GeV were found.

HHG seed

The harmonic generation in gas results from the strong non-linear polarisation induced on the rare gases atoms, such as Ar, Xe, Ne and He, by the focused intense electromagnetic field E_{Laser} of a "pump" laser [17]. The radiation spectrum is tunable in the VUV-XUV region by frequency-mixing techniques applied on the pump laser. High order harmonics are linearly polarised sources from 266 nm down to the water window [18, 19, 20], of high temporal [21] and spatial [22] coherence, emitting very short pulses (attosecond pulses in a femtosecond envelope) in a small divergence (1 to 10 mrad), with a relatively high repetition rate (up to few kHz). The High Harmonics generated in Gas cover presently a wide spectral range with already significant intensities, as presented in fig. 4. Presently, in the short wavelength range, one can rely on a 10 fs pulse with peak powers of 10 MW at 30 nm, 1 MW at 10 nm, 1 kW at 4 nm (with further improvement foreseen in the next 3-4 years up to 10 kW) [23].

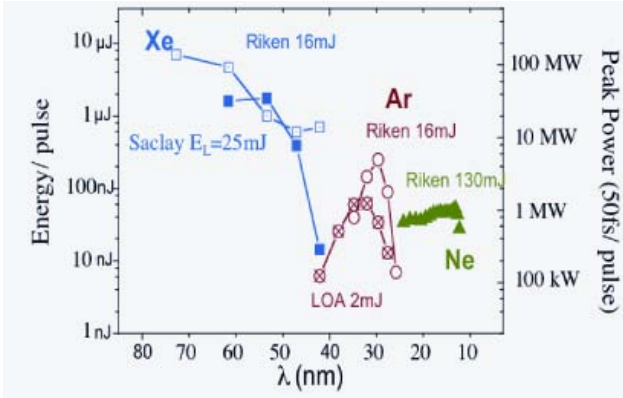

Fig. 4: Peak power and energy per pulse provided by High Harmonics generated in Gas.

Seeding optics and FEL oscillator mirrors

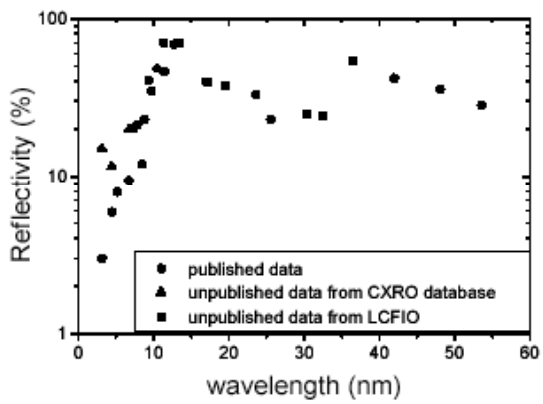

Fig. 5: Normal incidence reflectivity of multilayer mirrors.

The HHG seed can be injected inside the modulator via a set of two spherical mirrors for being able to adjust the focusing inside the undulator, and two periscope mirrors for introducing the light on axis on a dogleg of the accelerator. One can also consider using toroidal and grazing incidence mirrors. For the first, third and fifth harmonics, high reflectivity multilayer mirrors (oxides and fluorides) can be employed. In the VUV, Al metallic and then SiC mirror can be used. In the soft X ray, X ray multilayers are available [24]. In normal incidence, the performances of multilayers around 13 nm benefit from the development carried out for lithography and high

reflectivity has been achieved. Such reflectors, currently developed at Institut d'Optique, will be employed for LEL3 (see fig. 5).

ARC-EN-CIEL SEEDED FEL SOURCES

After comparisons of saturation lengths were performed between PERSEO and GENESIS in the steady state regime, the design, characteristics evaluation of the ARC-EN-CIEL FEL sources has been mainly performed using PERSEO Time Dependent adapted to the ARC-EN-CIEL case. Such a code present the advantage of providing also the radiation on the odd non linear harmonics in the planar undulator case. A Filling factor of 0.1 was applied in the modulator in order to approximate the transverse overlap between the electron and the seed beam. Specific calculations (such as short wavelength case, emittance effects) were also studied with GENESIS1.3 (without the non linear harmonics) [25] coupled to SRW [26]. The GENESIS-SRW combination permits the further propagation of the FEL wavefront to the beamlines and deeper insight on transverse coherence issues. Non linear harmonics in the helical undulator configuration and even harmonics produced on the UVSOR-II FEL seeded with a 1 kHz Ti:Sa laser [27] are under analysis with MEDUSA [28]. Following these studies, one plans to proceed to simulations of even harmonics and non linear harmonics produced in the helical configuration for ARC-EN-CIEL FEL sources.

Power and Spectral range

The spectral range covered by LEL1, LEL2 and LEL4 of ARC-EN-CIEL is shown in fig. 6. In seeded FEL sources, different wavelengths will be provided via various electron beam energies: a kicker will extract the 500 MeV beam after Bunch Compressor 2 for being sent to LEL1 for example, the phase tuning of the LINAC allows the energy to be varied between 0.8 and 1.2 GeV for LEL2 and the 3 GeV will be obtained after the 2 GeV loop after a further injector. A slow adiabatic change of the energy in operating the different beams produced by the two guns will be studied in details in the TDR phase. Fine tuning will result from a simultaneous gap change of the undulators and wavelength modification of the Ti-Sa laser illuminating the gas cell for the HHG production, coupled to a change in the monochromators for allowing the users to scan the energy during the measurements on their samples. Compared to the usual "gap scan" on synchrotron radiation facilities, the coupling with the change of the Ti-Sa laser should be added. At short wavelength, the wavelength of the harmonics produced in gas are very close (they are separated by 0.3 nm at 10 nm), a relatively small change wavelength is required to pass from one to the other. Spectral tuneability performed by means a combined chirp on the laser and the electron beam can also be applied [29].

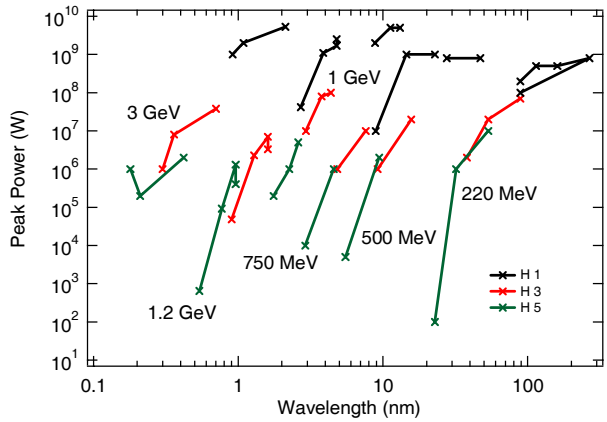

Fig. 6. Spectral range covered by the HHG seeded FEL sources of ARC-EN-CIEL on the fundamental (black), third (red) and fifth (green) harmonics of the radiator.

A closer zoom of the radiation produced by LEL 1 in the short wavelength region for planar and helical configuration is shown in fig. 7. Saturation length depends on the seed wavelength, the number of undulator modules or the dispersive section which can be adjusted.

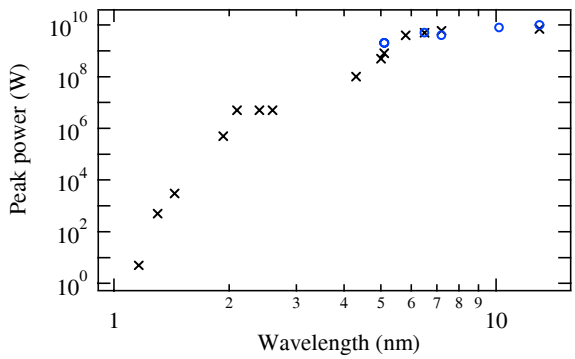

Figure 7: Radiation produced by LEL1 in ARC-EN-CIEL Phase 2. Calculations with 1.5 kA. Seeding power is 30 kW, 50 fs-fwhm, U26 Modulator (100 to 200 periods, depending on seeded wavelength); HU30 Radiator: in (x) planar and (o) helical configuration (400 to 700 periods).

LEL2 allows the spectral range to be extended below 1 nm in the linear polarisation case, as illustrated in fig. 8. Note that in both cases, the calculations were performed with a conservative peak power of 1.5 kA.

LEL4 is more prospective. It allows the spectral range to be extended down to 0.2 nm in the linear polarisation case in configuration 1-5, as illustrated in fig. 9. It exploits the energy enhancement in the loops and the accelerating structures up to 3 GeV and cryogenic undulators technology. The seed ranges between 6.3 and 4 nm, with 30 kW as expected in a near future.

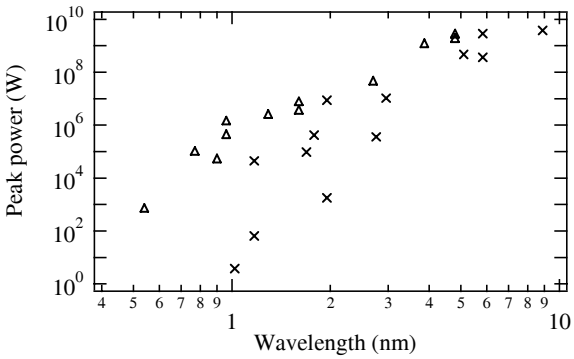

Fig. 8 : Peak power delivered by LEL 2 in ARC-EN-CIEL Phase 2. Seeding power is 50 kW, 50 fs fwhm. Beam parameters of phase 2 with 1.5 kA and (x) E=1 GeV, (Δ) E=1.2 GeV. U26 Modulator (400 to 500 periods), U18 Radiator (400 to 500 periods).

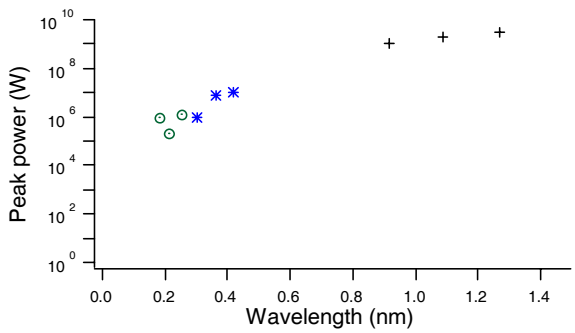

Figure 9: Radiation produced by LEL4 in ARC-EN-CIEL Phase 3. Seeding power is 30 kW, 50 fs-fwhm. U35 Modulator (up to 700 periods), cryogenic U18 radiator (1000 periods).

Longitudinal dynamics, pulse duration and linewidth

Fig. 10 shows the longitudinal dynamics of the FEL radiation followed using evolution diagrams showing the pulse temporal distribution along the progression in the undulators. In the modulator, the seeded fundamental wavelength radiates strongly, with a short, nearly Fourier transformed limited pulse. The non-linear harmonics radiation in contrast are very noisy, wide spectrally and temporally and weak in intensity. The energy modulation of the electrons due to the seed interaction can be seen in phase space, it is transformed into density modulation after the dispersive section. The electrons rotate in phase space when the end of the radiator is reached and some of them escape the separatrix.

At the entrance of the radiator in fig. 10, the radiation first results from the one emitted in the modulator, shifted towards the head of the bunch because of slippage. Then, the emission from the bunched electrons starts and reaches an asymmetric bifurcation, where the light slips along the electron bunch mainly in the forward direction. The electrons situated where the radiation was previously emitted are strongly heated (as seen on phase space analysis) and the radiation starts from the lateral electrons which still have sufficient bunching, exhibiting a thiner pulse duration than the main central pulse. When the heated electrons refresh, the radiation can start again from the center. The behaviour on the harmonics is similar, with a larger number of bifurcation when the harmonic number is higher. The change of slope in the evolution diagram here results the process of saturation of the electrons in the middle of the pulse. The pulse in the modulator appears as a vertical line since slippage here is small with respect to the pulse duration. For this reason the process appears different the one previously observed in the case of a super-radiant regime [30].

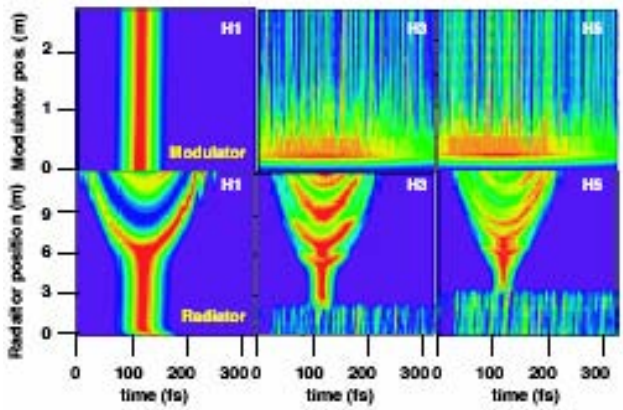

Fig. 10: Evolution of the radiation longitudinal distribution along the position in the modulator (top) and radiator (bottom) for the fundamental (H1), the third (H3) and the fifth harmonic. Case of LEL1, seed at 12.3 nm, 50 fs and 50 kW.

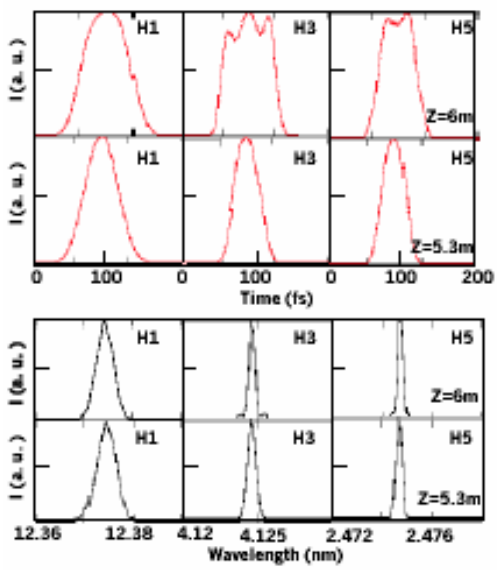

Fig.11 : Temporal and spectral profiles of LEL2 (case of fig. 11) after 6 m in the radiator : H1 : 26 fs rms, 0.014%, 0.38 mJ, H3 : 25 fs, 0.009%, 1.2 µJ, H5 : 20 fs, 0.006%, 30.5 nJ, 2 MW. After 5.1 m in the radiator: H1 : 23 fs fwhm, 0.015%, 0.15 mJ, H3 : 16 fs, 0.0075%, 0.56 µJ, H5 : 14 fs, 0.0054%, 3.7 nJ.

Pulse duration and width decrease along the path in the radiator and start to increase again after saturation. The minimum of pulse duration is reached earlier on the

harmonics than on the fundamental. The FEL pulse duration and spectral width does not vary significantly when the seed pulse is changed from 150 fs to 50 fs.

Tolerances Sensitivity to parameters

The sensitivity to the different parameters (electron beam, seed) has been studied in order to evaluate tolerances. They have been mainly carried out in the case of LEL2, more sensitive than LEL1.

The influence of the emittance has been studied with GENESIS coupled to SRW, and is illustrated in fig. 11. In case of peak current, the peak power drops by one order of mzagnitude from 1.5 kA to 2 kA. Higher peak current permit a more efficient power extraction on the harmonics. An increase of energy spread leads to a significant reduction of the peak power, in particular on the non linear harmonics (from 0.06% to 0.08%, one order of magnitude is lost on H1, more than 1 on H2 and 2 on H5).

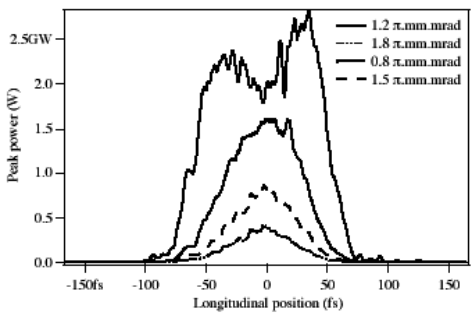

Fig. 11: GENESIS study on the influence of the emittance on the LEL1 on fundamental radiation peak power and pulse duration. LEL1 seeded at 12 nm in the 1-1 configuration.

A change of synchronisation between the seed and the electron bunch leads to a reduction of the saturation length and to a deformation of the pulse shape. At given undulatro length, a tolerance of ±35 fs is found for a 10% change in peak power, while temporal and spectral distribution remain similar.

The maximum of peak power is obtained when the seed wavelength is slightly higher than the undulator resonant one. The influence of the spectral detuning is not symmetrical and becomes much more drastic at short wavelength. Tolerances for 10% peak power change are ±0.025 nm @38 nm, ±0.022 nm (resp. ±0.012nm)@14 nm for a 1-1 (resp. 1-3) configuration.

ARC-EN-CIEL FEL OSCILLATOR SOURCE

The length of the optical resonator is given by the synchronism condition with the electron bunch spacing ($d=c/2f$) with f frequency of the electrons. A 34 m long resonator corresponds to a repetition rate of 4.5 MHz for the 1 GeV loop. In fact, two series of electrons bunches (from the first pass in the 1 GeV loop or from the return pass from the 2 GeV loop in the 1 GeV one) will generate two FELs. For the calculations presented here, a macropulse of 10 ms is considered.

The optical resonator consists of two spherical mirrors with a hole for extraction of the radiation (10 % efficiency assumed for the calculations). For a symmetrical cavity, the waist w_o which minimises the volume of mode along the undulator of length L_{ond} is $w_o = \sqrt{L_{ond}\lambda / 2\pi\sqrt{3}}$ with □ the wavelength. For LEL3 at 10 nm, it is of the order of 100 µm, leading to mirror radius of curvature of 16 m at 10 nm. The corresponding mode divergence $\theta = \frac{\lambda}{\pi w_o}$ is 35 µm at 10 nm. A slight asymmetry of the resonator is better in order to reduce the heat load on the front mirror, so radii of curvature of 16 and 20 m are taken. PERSEO calculations have been carried out for this configuration with the two modes (low and high charge) of operation at 1 GeV. The HU30 undulator allows variable polarisation to be produced. At 1 GeV, the spectral range in circular polarisation on the fundamental covers from 20 to 8.5 nm, with peak power of 120 MW and average power of 90-550 W. In planar polarisation, the spectral range covers from 40 to 10 nm, with peak powers of 50 MW and average power of 200 MW. The absorbed power by the mirrors has been limited to 2 kW, assuming cryogenic cooling as usually done on the SOLEIL beamlines. The use of deformable mirrors is foreseen. Further optimisation of the duty cycle, cavity length and mirror position will be performed during the TDR phase for enhancing the extracted power. Indeed, a longer cavity length allows the mirror to handle a larger laser spot and the power density to be reduced. Pulses are typically 300 fs and 0.5% spectral width. LEL3 is complementary to LEL1, since it provides to the users a source with higher average and lower peak power.

ARC-EN-CIEL SYNCHROTRON RADIATION SOURCES

Radiation from the spontaneous emission undulator sources has been calculated using SRW. The peak brilliance is plotted in fig. 12.

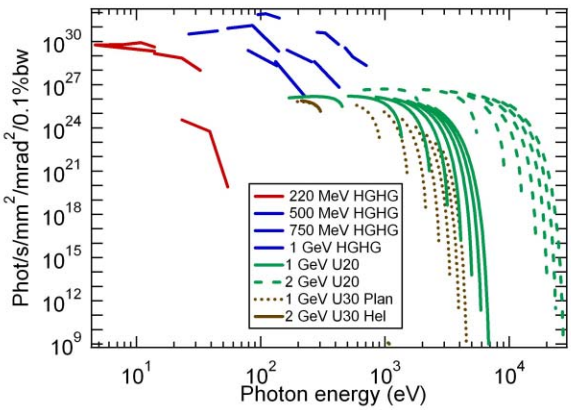

Fig. 12 : Peak Brillance by LEL1 operated at 10 kHz and the spontaneous emission sources for 20 mA in the loops.

ARC-EN-CIEL THZ SOURCES

Figure 13 presents the spectral energy per pulse and the average spectral power of the terahertz emission, calculated for angular apertures of 60 mrad (H) x 40 mrad (V) for three different phases of ARC-EN-CIEL.

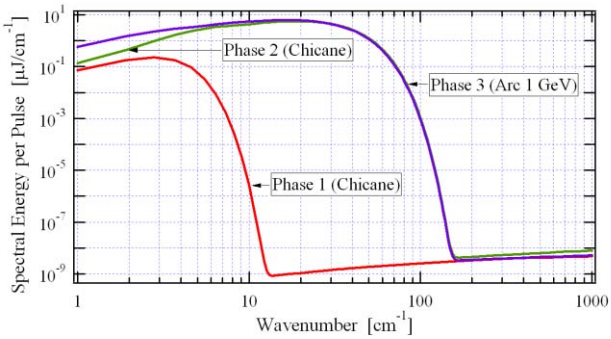

Fig. 13: Pulse energy spectra of terahertz range emission collected by 60 mrad (H) x 40 mrad (V) aperture ports.

REFERENCES

[1] M. E. Couprie et al., "The ARC-EN-CIEL FEL proposal", FEL06, Berlin, Aug 2006, p. 146-149 http://www.jacow.org

[2] G. Lambert et al, "First lasing in seeding configuration at 160 nm using High order Harmonic Generated in gas on the FEL of the SCSS Prototype Accelerator", FEL07, Novosibirsk, Aug 2007, http://www.jacow.org.

[3] J.H. Han et al, "Conditioning and High Power Test of the RF Guns at PITZ", EPAC04, 357

[4] T. Rao et al, "Photoemission Studies on BNL/AES/JLab all Niobium, Superconducting RF Injector", PAC05, 2556.

[5] C. Bruni "ARC-EN-CIEL project electron beam dynamics" these proceedings

[6] C. Benabderrahmane et al, « Commissioning of the First Insertion Devices at SOLEIL » PAC07, Albuquerque, New Mexico, USA, p. 929-931

[7] L. Giannessi, P. Musumeci, *The free-electron laser harmonic cascade*, New Jour. Phys. **8**, 294(2006)

[8] P. Elleaume, J. Chavanne, B. Faatz, "Design Considerations for a 1Å SASE Undulator" Nucl. Instrum. Meth. A **455**, 503 (2000)

[9]http://www.esrf.eu/Accelerators/Groups/InsertionDevices/Software/Radia, P. Elleaume, O. Chubar, J. Chavanne, "Computing 3D Magnetic Field from Insertion Devices", PAC97, 3509-3511 ; O. Chubar, P. Elleaume, J. Chavanne, "A 3D Magnetostatics Computer Code for Insertion devices", SRI97, August 1997, J. Synchrotron Rad. (1998). 5, 481-484

[10] J. Bahrdt, W. Frentrup, A. Gaupp, B. Kuske, A. Meseck, M. Scheer, *Undulators for the BESSY soft-X-Ray FEL*, Proceed. FEL2004, JACoW, 610-613

[10] T. Hara, T. Tanaka, H. Kitamura, J. Bizen, X. Maréchal, T. Seike, "Cryogenic Permanent Magnet Undulators", Phys. Rev. Special Topics Acc. & Beams **7**, 050702 (2004), H. Kitamura, Proceed. Synch. Rad.Inst. 2006, SRI May, Daegu, Korea

[12] C. Kitegi "Development of a cryogenic permanent magnet cryogenic undulator at ESRF", Edimburg, EPAC 06, 3559

[13] T. Tanabe et al., *X-25 Cryo-ready In-vacuum Undulator at the NSLS*, AIP Conference Proceedings **879**, 283 (2007)

[14] http://www.perseo.enea.it/, L. Giannessi, *Overview of PERSEO, a system for simulating FEL dynamics in Matcad*, proceedings of FEL, 91 (2006)

[15] W. Colson P. Elleaume Appl. Phys. B 29, (1982)10

[16] http://www.synchrotron-soleil.fr

[17] P. Salières et al., Adv. At., Mol., *Opt. Phys.* 41, 83 (1999)

[18] Z. Chang et al, Phys. Rev. Lett. **79** (1997), n°16, 2967

[19] Seres, J. *et al. Nature.* **433**, 596 (2005).

[20] E. Gibson *et al. Phys. Rev. Lett.* **92** (03), 3001 (4) (2004).

[21] H. Merdji et al, Phys. Rev. A 74 (2006) 043804

[22] L. Le Déroff et al, Phys. Rev. A**61** (2000), n°19, 43802

[23] H. Merdji, private communication

[24] P. Zeitoun et al, Appl. Phys. B 78, 983 (2004), F. Delmotte, "Applications des sources accordables VUV-X fs combinant accélérateurs et lasers ; slicing à SOLEIL et le projet ARC-EN-CIEL ", Feb. 2004, Orsay

[25] GENESIS, S. Reiche, NIM A 429, (1999) 243

[26] O. Chubar et al, "Numerical Propagation Simulations and Coherence Analysis of SASE Wavefronts" this conference

[27] M. Labat, "Even harmonic production on UVSOR-II storage ring" this conference

[28] H.P. Freund et al., IEEE J. Quantum Electron. 36, 275 (2000).

[39] S. Biedron et al., NIM A475, 401; T. Shaftan, PRE 71, 2005, 046501

[30] R. Bonifacio et al., Phys. Rev. A40, 4467 (1989), L. Giannessi et al., Jour. Appl. Phys. 8, 294 (2006); T. Watanabe et al., Phys. Rev. Lett. 98, 03402 (2007)

STATUS OF THE FEL TEST FACILITY AT MAX-LAB *

Mathias Brandin, Filip Lindau, Nino Cutic, Sara Thorin, Sverker Werin#, MAX-lab, Lund, Sweden
Johannes Bahrdt, Kathrin Goldammer, Michael Abo-Bakr, Dmytro Pugachov, BESSY GmbH, Berlin, Germany
Anne L'Huillier, Lund University, Lund, Sweden

Abstract

An FEL test facility is built on the existing MAX-lab linac system in collaboration between MAX-lab and BESSY. The goal is to study and analyse seeding, harmonic generation, beam compression and diagnostic techniques with the focus of gaining knowledge and experience for the MAX IV FEL and the BESSY FEL projects. The test facility will in the first stage be using the 400 MeV linac beam to generate the third harmonic at 88 nm from a 266 nm Ti:Sapphire seed laser.

The optical klystron is installed and magnetic system, gun and seed laser systems are currently being finalised. Start-to-end simulations have been performed and operation modes for bunch compression defined. The linac and beam transport system is already in operation.

INTRODUCTION

The BESSY FEL project [1] and the MAX IV proposal [2] are both focused on seeded FEL sources as part of the facilities. In the aim of improving the designs a decision was made to build a test facility for harmonic generation at MAX-lab.

By utilising the gun, injector and linac system already available at MAX-lab a test facility for seeded FEL/Harmonic generation could be accomplished by relative low additional funding. Contacts had been taken with BESSY and with the application for the EUROFEL collaboration the project was started. The focus of the activities is to explore ideas of harmonic generation and gain experience with the FEL technology, test diagnostics and working with short pulses.

OVERVIEW OF THE PROJECT

The project is built in one major phase (I) with two improvement phases (phase II: an improved gun system and phase III: HHG seeding). The starting point is the injector built at MAX-lab in the first years of this millennium which was designed to be flexible and also allow accelerator development. A linac system was chosen together with a flexible gun mounting system equipped with a thermionic RF-gun. The source is used for injection into the storage rings (MAX I, II, III) and in the intermediate time this source is one of few available sites for tests of FEL operation at these energies.

An optical klystron system and a seed laser at 266 nm will produce the 3rd and 5th harmonic at 88 and 53 nm respectively using the 400-450 MeV electron beam. The radiator undulator in the optical klystron is not enough for amplification, and thus the activities are focused on harmonic generation. BESSY is providing the undulator and chicane system while MAX-lab is providing the electron beam and the laser system.

The aim is to study several features in the design and operation of this kind of facility. On the electron beam side: bunch compression, electron beam transport (especially with low emittance), beam stability, synchronisation and stability. On the FEL side: Harmonic

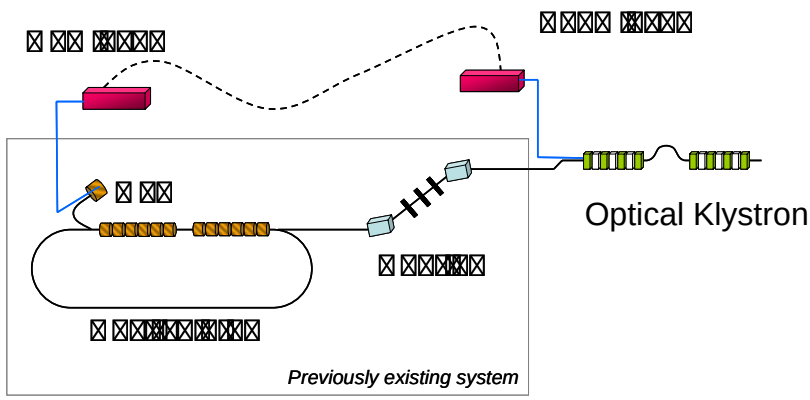

Fig 1. Overview of the accelerator systems and test FEL.

* This work has been partially supported by the EU Commission in the Sixth Framework Program, Contract No. 011935 – EUROFEL and the Swedish Research Council
# sverker.werin@maxlab.lu.se

Generation, laser systems, control of overlap of the optical mode to electron beam focus, modelling, simulations and beam handling.

BASIC LAYOUT & COMPONENTS

The layout out the system is shown in fig 1.

The accelerator system

The accelerator for the FEL test facility utilises the injector system [3] for the storage rings at MAX-lab. These facilities are available during the majority of time as injections are only scheduled for a few instances a day.

The system is built around two 5.2 m long linac structures. These are equipped with SLED cavities [3] and powered by one 35 MW klystron each, thus being able to provide up to 125 MeV each. The electron beam is passed via a recirculation system through the linacs twice and thus reach routinely an energy of 400 MeV. (The design value is 500 MeV.)

The electron source is a RF-gun [4] consisting of ½+½1 cells. The cathode is BaO and is used in two modes. Either as a thermionic source operated at 900 C, mainly aimed for storage ring injection, and in a gated mode with a 5 ns laser to be able to fill bucket-by-bucket into the storage rings. In the latter mode the cathode temperature is reduced just below thermal emission, around 600 C, and the electrons are gated by the laser system.

For the FEL operation the temperature will be reduced further and a more powerful laser system providing 10 ps pulses will generate the electrons.

The electron gun provides 2 MeV and the beam is passed through a magnetic energy filter bending 120 degrees before entering the linac system.

The transport system from the linac to the FEL is the one used for injections into the MAX II storage ring. It consists of mainly a dog-leg moving the beam from the basement up to ground floor level. This dog-leg has proven a good solution for bunch compression.

Table1: Parameters of the undulators and the chicane

Modulator	
Period length	48 mm
Number of periods	30
Minimum gap	10 mm
Maximum K-parameter	4.3
Radiator	
Period length	56 mm
Number of periods	30
Minimum gap	12 mm
Maximum K-parameter	4.3
Chicane	
Number of magnets	4
Type of magnet	H-frame, electromagnet
Gap	15 mm
Maximum field	0.2 T
Distance between magnets	400 mm

The optical klystron

The optical klystron is built around two re-used undulator structures. A pure permanent magnet (PPM) structure has been loaned from the ESRF to be used in the modulator. The radiator will be equipped with the APPLE structure of the BESSY UE56-1. The devices have been re-measured, re-shimmed and equipped with new carriages [5]. The chicane system is a newly constructed system. The parameters are summarized in table 1.

Laser system and transport optics

A combined laser system for the gun and the seeding of the HG-FEL has been purchased from Thales SA. The system comprises a common oscillator system locked to the RF of the accelerators to better than 1 ps and synchronization by optical fibre. The gun laser branch consists of a pulse shaper, amplifier and harmonic generation. The seed laser system is similar, but without the pulse shaper. The layout of the system is shown in fig 2.

The system should deliver 500 μJ in a 10 ps pulse at 266 nm to the RF gun and 100 μJ in a 300 fs pulse at 266 nm to the seeding.

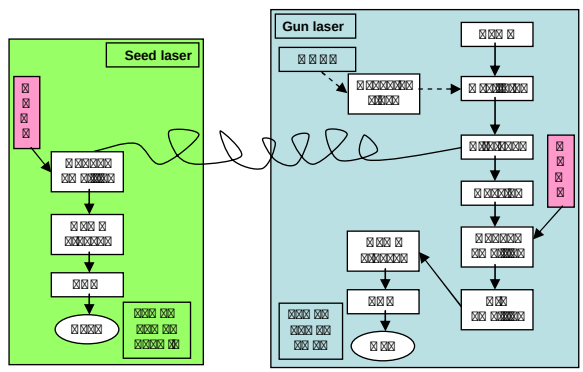

Fig 2. The laser system

Diagnostics

The start up of the system will mainly rely on OTR screens for alignment and beam diagnostics. A calibrated current monitor will be installed, but the response is not in the range of the short pulses accelerated. Beamloss monitors [6] are already installed along the undulators, which will allow a rough estimate of beam position. Energy distribution will be available on a screen at a dispersion point by the beam dump. Alignment of the laser beam to the electron beam will be made by optical methods using the spontaneous emission in the modulator undulator and the laser beam. Temporal overlap between seed laser and electron bunch will be achieved by several techniques: photodiodes for the >ps range, detecting the THz signal from the fraction of the electron bunch interacting with the seed laser [6], detecting increased energy, spread due to seed laser, at the beam dump.

Emittance measurements will be done by quadrupole scans and 1-to-1 imaging of an OTR screen signal. Bunch length measurements will be done both with CTR pulses

measured in a Michelson interferometer [7] and by electro-optical techniques using the seed laser as probe pulse [8].

TARGET PERFORMANCE

The performance of the system in the first phase has been calculated. The basic operation has been established in the injector, but the performance outlined below has not been verified in detail.

final acceleration which increases the final energy spread, but possibly reduces the timing jitter. An achromatic dogleg consisting of two 15 degree bends with 5 quadrupoles in between performs the compression. The dogleg provides an R56 of 5.5 cm which gives maximum compression for an accelerating linac RF phase of 30 deg. This however leads to a very high energy spread (since compression happens after full acceleration). After

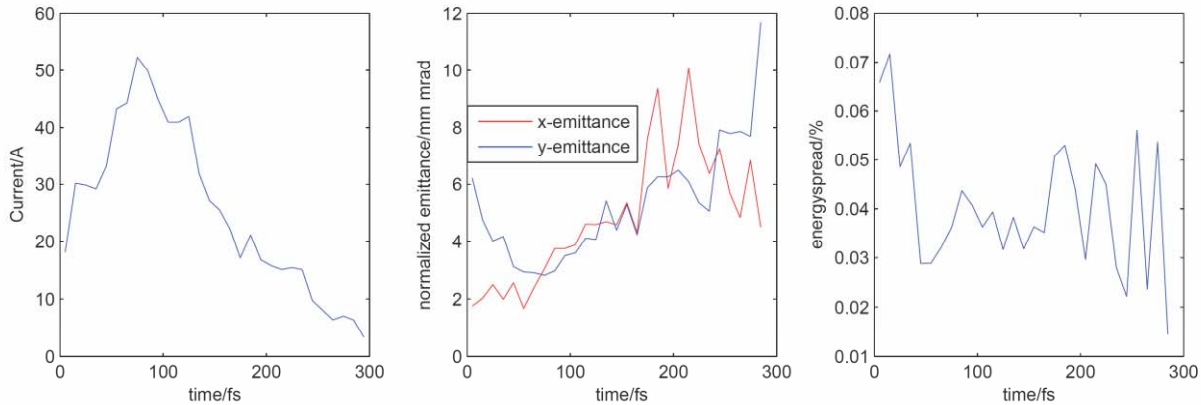

Fig 3. Simulations of the beam performance from the current gun system at the entrance to the optical klystron.

Electron beam

The electron beam is extracted from an RF gun delivering around 2 MeV. In normal thermionic mode there is a strong bunching right at the cathode surface. As the energy is low the space charge effects significantly increase the emittance. By gating at a later phase angle the effect is reduced. For the FEL tests it will be used as a photocathode gated gun. The gun laser will provide a 10 ps pulse which can be tuned to an optimal phase, around 30 degrees, to reduce space charge effects. The gun structure though was not optimised for low emittance operations and thus the extracted charge has to be reducedto ~0.1 nC to meet the demands of FEL tests.

The electrons are then accelerated in the reciruclated linac system to >400 MeV. Compression is done after optimizing the accelerating phase to give maximum peak current while maintaining low emittance and energy spread it was found that 8 deg gives the best electron properties.

The beam has been traced through the system using the codes Parmela [9], ASTRA [10] and elegant [11]. At the entrance of the optical klystron a peak current of 50 A, a normalised emittance around 3.5 mm mRad and an energy spread of 0.04% can be achieved in a time window of 300 fs (fig 3). The total charge in the window defined by the seed laser (time and transverse dimensions) is only 0.01 nC. The pulse has a long tail with lower current which will not interact with the seed laser.

The pulse is stable in tracking and the peak current is matched in time to the lowest emittance and energy spread.

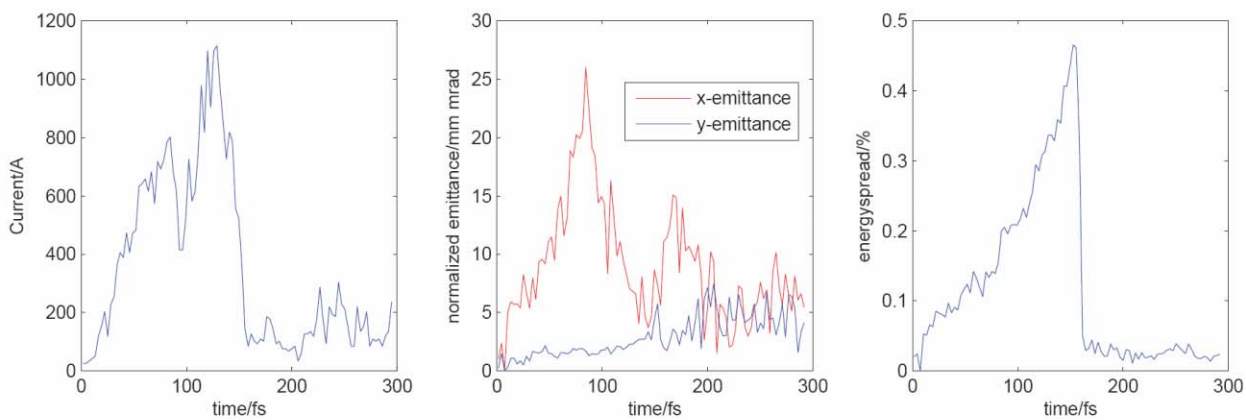

Fig 4. The beam at the optical klystron entrance in improved mode with a new gun. (not optimised results)

Coherent output

The coherent enhancement and the sensitivity to emittance and energy spread have been calculated by a 1D model. In the 300 fs seed-laser-window the power is 0.2 MW (60 nJ) in the third harmonic at 88 nm. The coherent enhancement is $6*10^4$ over the incoherent emission in the window. The total incoherent pulse should have an energy of 6 pJ. A 1D model should in this context be regarded as an "optimum performance".

To increase the power an improved gun structure has been designed.

STATUS

The project is at the moment (summer 2007) developing quickly with the goal of taking the phase 1 into operation in the fall 2007.

Parts in operation

The complete injector and electron beam transport system are in operation. The electron gun is operating in both thermionic mode and in laser gated mode with a long pulse, 5 ns, laser system. The undulator systems are installed and in operation.

Parts installed

The laser systems are being installed/are installed. Laser beam transport and optics will be installed after laser system acceptance tests. The magnetic and vacuum system around the undulators are being installed at the moment. Basic diagnostic systems are currently being installed.

DEVELOPMENT OF THE SYSTEM

The system is planned to be developed in two new phases.

Phase 2 New gun

The second phase contains a new electron gun [12] allowing operation at higher bunch charges while retaining the emittance. This system is an adapted BNL/SLAC type RF gun with an emittance compensating solenoid system [13].

The simulations of the beam performance with the new gun system can be found in fig 4. The current at a maintained emittance is considerably increased allowing for higher output power. The compression of the bunch is trickier in this high charge case and the energy spread tends to increase. In start-to-end simulations it can be seen that the HG-process chooses to operate at a part of the bunch where the current is not the maximum but the energy spread is slightly lower. In the third harmonic at 88 nm a power of 11 MW in < 100 fs is shown and at the 5^{th} harmonic at 53 nm 1.4 MW is shown. The results shown here are not the final optimisations (which await publication).

Phase 3 HHG source

The third phase will use a HHG (High Harmonic Generation) chamber on the seed laser system to seed the FEL process at a lower wavelength down to 100 nm. The drive laser for the seed pulse will be equipped with an additional amplifier and a High Harmonic Generation gas jet chamber. This chamber can provide a tunable seed pulse down to 30 nm range. The electron energy will though limit shortest seeding wavelength in the modulator undulator to around 100 nm.

The gas jet chamber is system is developed and in operation at the Lund Laser Center [14] and an adapted chamber system will be built for the seeding. This part of the project still awaits funding.

REFERENCES

[1] D. Kraemer et al., BESSY TDR, 2004.
[2] MAX IV Conceptual Design report, MAX-lab, 2006.
[3] S. Werin et al., Commissioning of the 500 MeV injector for MAX-lab, proceedings EPAC 2004
[4] B. Anderberg, A. Andersson, M. Demirkan, M. Eriksson, L. Malmgren, S. Werin, The design of a 3GHz thermionic RF-gun and energy filter for MAX-lab, Nucl. Instr. and Meth. A 491 (2002) 307
[5] J. Bahrdt et al., Undulators for a Seeded HGHG-FEL at MAX-lab, EPAC 2006.
[6] J. Bahrdt et al., Status of the undulator system of the seeded HGHG-FEL test bench at MAX-lab, these proceedings.
[7] M. Brandin et al, Measurements and diagnostics on the MAX recirculator, proceedings EPAC 2006
[8] P. J. Phillips et al., Single Shot Longitudinal Bunch Profile Measurements by Temporally Resolved Electro-Optical Detection, proceedings DIPAC07.
[9] PARMELA, K.R. Crandall, J.H. Billen, et al., Los Alamos National Laboratory, USA.
[10] K. Flöttman "ASTRA User Manual", September 18, 2000, www.desy.de/~mpyflo
[11] M. Borland, "Elegant: A flexible SDDS-Compliant Code for Accelerator Simulation", APS LS-287, 2000.
[12] S. Werin, et al., Design of a new preinjector for the MAX recirculator to be use din EUOREL, Proceedings of EPAC 2006, Edinburgh, Scotland
[13] R. Boyce, D.H. Dowell, J. Hodgson, J.F. Schmerge, N. Yu, Design Considerations for the LCLS RF Gun, LCLS TN 04-4 (2004)
[14] A. L'Huillier, F. Krausz, High-Order Harmonic Generation, Handbook of Lasers and Optics (ed. F. Träger), Springer, New York (2007) p. 219

COMPACT RING FEL AS A SOURCE OF HIGH POWER INFRARED RADIATION

O.A. Shevchenko[#], A.N. Matveenko, N.A. Vinokurov,
Budker Institute of Nuclear Physics, 11 Acad. Lavrentyev Prosp., 630090, Novosibirsk, Russia

Abstract

Ring FELs [1] were proposed mainly to improve the quality of radiation of x-ray FELs. Their main advantage is the absence of mirrors. It appears that this advantage is also useful for high power FELs. Another reason to build infrared ring FEL is the proof-of-principle for shorter wavelength FELs. Therefore we considered the scheme of infrared ring FEL which requires ERL with beam energy 50 MeV. Using extensive simulations we developed requirements for electron beam parameters and magnetic system of ring FEL. In spite of rather compact design such FEL may provide more than 10 kW average power.

INTRODUCTION

The further development of FELs towards the region of short wavelengths and high powers is limited by the absence of mirrors with appropriate parameters. There exist different approaches to the solution of this problem. One of them is based on the fact that the beam microbunching which appears in undulator can be partly conserved in the specially designed isochronous bend. Electron outcoupling may be considered as the simplest scheme which utilizes this idea [2-3].

The further evolution of this approach leads to the scheme of the ring FEL which has been proposed in [1]. The lattice of the ring FEL consists of straight undulator sections and isochronous bends which compose a ring. At the bends radiation is lost. The signal between adjacent undulator sections is transferred trough microbunching. Radiation from the last undulator produces energy modulation of the new coming beam inside the first undulator and amplification goes on till saturation. The basic advantage of this scheme is that it has a feedback which is realized without any mirrors.

High power ring FEL implies CW operation mode. Therefore one has to use energy recovery linac (ERL) as a source of electron beams for such FEL. The present state of the art of ERLs allows for producing the beams with required parameters which makes the ring FEL project feasible.

The main problem of the ring FEL which becomes very essential for the short wavelength is that it requires isochronous bends to conserve microbunching. The problem of creating of such bend is discussed in detail in [4]. To demonstrate the feasibility of the ring FEL concept it is desirable to build first the small-scale model for longer wavelength which may be interesting itself as a source of high power infrared radiation.

In this paper we consider the possible design of compact high power infrared ring FEL. We present the possible lattice of the bends, required electron beam parameters and results of simulation of FEL operation.

RING FEL SCHEME AND ELECTRON BEAM PARAMETERS

The schematic layout of the ring FEL is presented in Fig. 1. It includes two undulator sections. One of them plays the role of "modulator" where the energy modulation takes place. The other one may be called "radiator", here the FEL radiation is generated. In the long wavelength case the debunching of the beam is not very severe problem. Therefore one can use 360 degrees bend and additional undulator sections are not required.

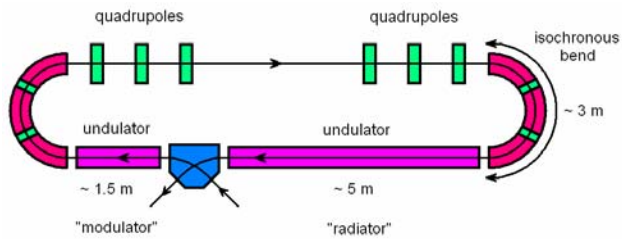

Figure 1. Schematic layout of the ring FEL.

The total 360 degrees bend in the proposed layout is comprised of two 180 degrees isochronous bend sections and a straight section with matching quadrupoles. The lattice of the isochronous bend is presented in Fig 2. It includes three bending magnets with different curvature sign, quadrupoles which are required to focus transversal dispersion and sextupoles which correct the second order aberrations.

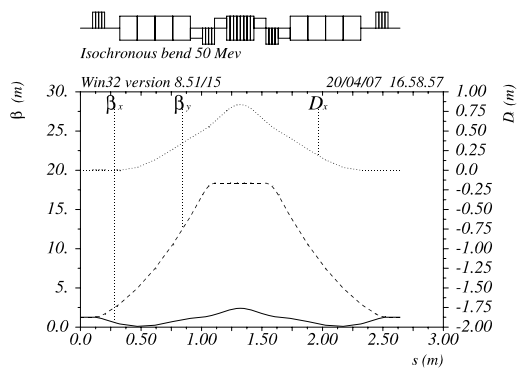

Figure 2. Magnetic lattice of the isochronous bend.

The beam and undulator parameters used in simulations are listed in Table 1.

[#]O.A.Shevchenko@inp.nsk.su

Table 1: Undulator and electron beam parameters

Undulator period, m	0.06
Undulator deflection parameter	1.5
Electron energy, MeV	50
Beam charge, nC	1
Peak current, A	50/100
Relative r.ms. energy spread, %	0.1
Normalized emittance, mm×mrad	5

The beam parameters presented in this table do not make any problems for contemporary accelerators. In principle one can assume shorter bunch length and higher peak current but in this case the wake field created by coherent synchrotron radiation (CSR) significantly reduces electron efficiency.

PARAMETERS OF OPTIMIZATION AND SIMULATION RESULTS

We used different codes to simulate the ring FEL operation. In this paper we present the results of simulations obtained by the code GENESIS [5] which is widely accepted in the FEL community for simulations of conventional FELs. Strictly speaking it was not pure GENESIS simulation as this code is not adapted for the ring FEL lattice. We used GENESIS to simulate amplification of the FEL signal in the undulator sections. The particle tracking in the bends including second-order aberrations and CSR effects was done by external homemade code.

To obtain the best performance of the FEL first of all we optimized the bend lattice. The purpose of this optimization was to achieve the minimal value of beam debunching factor $\left|1-\left\langle e^{i\omega_0\tau_i}\right\rangle\right|$ (here ω_0 is radiation frequency and τ_i - time delay of the *i*-th electron at the exit from the bend). Adjusting the sextupoles it was possible to make debunching less then 4 %.

The other optimization parameters were the lengths of undulator sections which determine the single-pass gain and saturation power. Length of the last undulator section has to be large enough for the radiation power to reach saturation level, but on the other hand increasing of its length leads to the increase of the gain. It worth noting, that the gain does not have to be too large, otherwise the lasing may become unstable. The gain value can be adjusted either by modulator length or by overlap degree between new-coming beam in modulator and illuminating radiation from radiator.

The optimal beam current is limited by CSR effects. Further we present the simulation results for two cases. In the first case the beam current is assumed to be 50 A and CSR effects are tolerable. In the second case of 100 A current the CSR effects become very significant.

50 A peak current case

Setting of the stationary state in the ring FEL for the considered set of parameters requires approximately 50 passes as it is illustrated in Fig 3. Here one can see the dependence of electron efficiency (which is determined as the ratio of radiation energy to electron bunch energy) on the pass number.

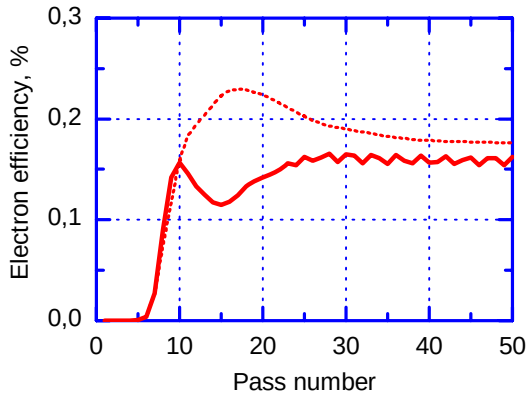

Figure 3. Dependence of the electron efficiency on the pass number in ring FEL for beam current 50 A. Dotted curve corresponds to ideal case without CSR effects.

The dotted curve corresponds to CSR free case. It is seen that CSR effects do not reduce significantly electron efficiency in this case.

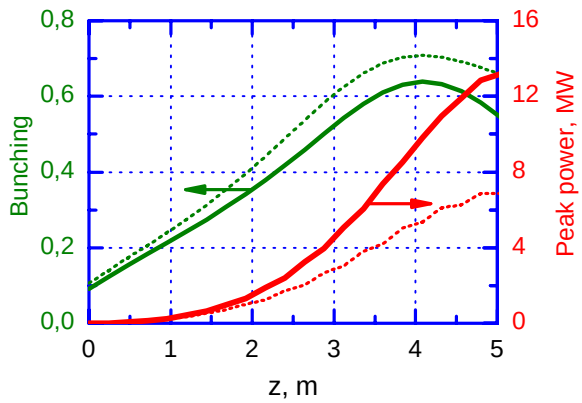

Figure 4. Dependence of the beam bunching factor (green) and peak radiation power (red) on the longitudinal coordinate in the last undulator section (dotted curves – CSR effects are not included).

Dependence of the beam bunching factor and peak radiation power on the longitudinal coordinate in the last undulator section is shown in Fig. 4. Radiation power almost reaches saturation level by the end of undulator (one can probably slightly increase its length yet) and the bunching starts dropping down. It is interesting that the wake created by CSR can increase peak power.

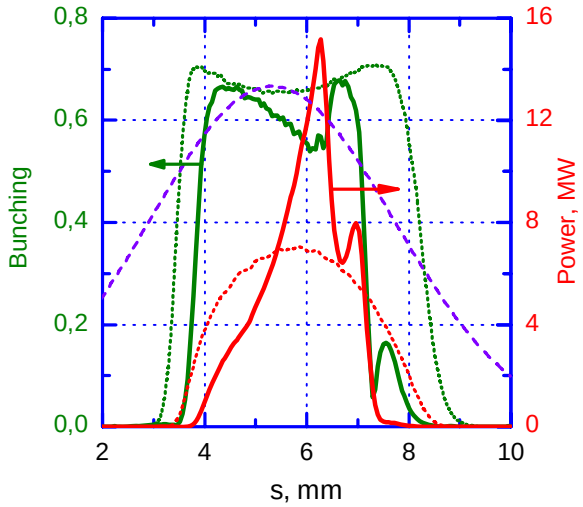

Figure 5. Stationary beam bunching (green) and radiation power (red) distributions at the exit from the last undulator section (dotted curves – CSR effects are not included, dashed violet curve – beam current profile).

The output beam bunching and radiation power distributions corresponding to stationary state are shown in Fig. 5. One can also see here the beam current distribution (dashed violet curve).

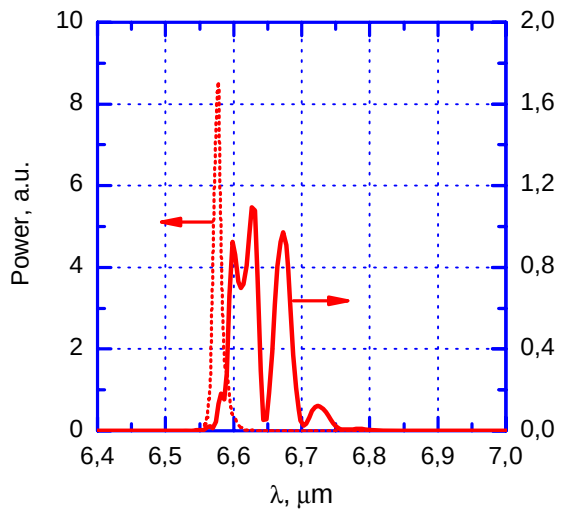

Figure 6. Spectral distribution of the output radiation power (dotted curve – CSR effects are not included).

The output radiation power spectrum is plotted in Fig. 6. From this plot one can see that CSR effects significantly increase the bandwidth.

Table2: Parameters of the output radiation

Wavelength, μm	~ 6.6
Peak power, MW	~ 10
Pulse duration, ps	~ 10
Electron efficiency, %	0.15

Parameters of the output radiation are summarized in Table 2.

100 A peak current case

Increasing the peak current one can increase the radiation peak power but unfortunately in this case the wake field created by CSR effects significantly decreases electron efficiency. This fact is illustrated in Fig. 7-8.

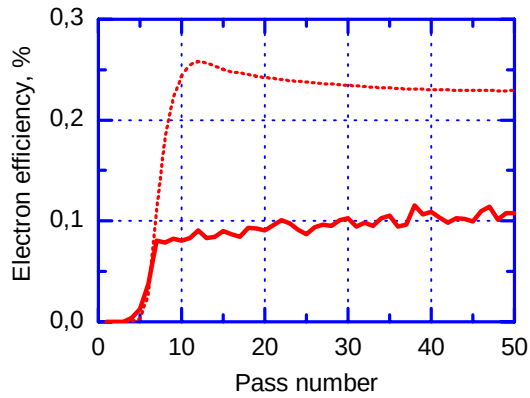

Figure 7. Dependence of the electron efficiency on the pass number in ring FEL for beam current 100 A. Dotted curve corresponds to ideal case without CSR effects.

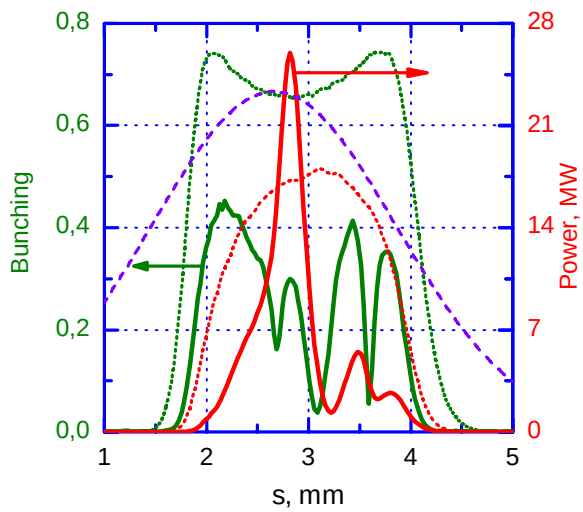

Figure 8. Stationary beam bunching (green) and radiation power (red) distributions at the exit from the last undulator section (dotted curves – CSR effects are not included, dashed violet curve – beam current profile).

One can see from Fig 8. that although the radiation peak power is larger then in CSR free case radiation pulse becomes shorter due to CSR. In this case radiation is formed in the region where the energy chirp created by CSR is small as it is shown in Fig. 9.

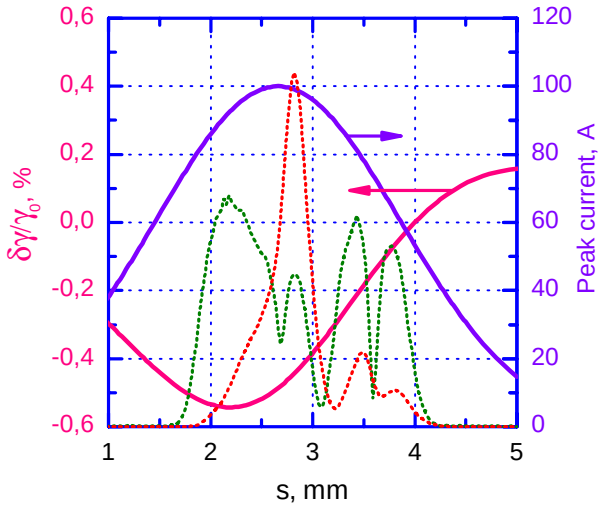

Figure 9. Beam current distribution (violet) and electron energy deviation created by CSR (pink). Dotted curves illustrate the beam bunching (green) and radiation power (red) distributions.

It should be noted that CSR wake field depends on the derivative of the beam current. In our simulations we assumed Gaussian current distribution. In the case of flat-top distribution CSR effects may be smaller.

CONCLUSION

We have shown theoretically the feasibility of the compact high power ring FEL for the infrared region. At that we have considered the problem of beam debunching in the bends and CSR effects. The option to install additional undulator into the free straight section exists. Then all requirements (magnet tolerances, peak current, emittances, etc.) will be even more relaxed. Moreover, the use of this auxiliary undulator may decrease the linewidth.

The next step would be the building of such FEL and demonstrating the feasibility of the ring FEL concept in practice.

REFERENCES

[1] N.A. Vinokurov, O.A. Shevchenko, NIM A528 (2004) 491-496.
[2] N.G.Gavrilov, G.N.Kulipanov, V.N.Litvinenko, I.V.Pinayev, V.M.Popik, I.G.Silvestrov, A.S.Sokolov, P.D.Vobly, and N.A. Vinokurov, IEEE J. Quantum Electron., v.27 (1991), p.2569.
[3] N. A. Vinokurov, NIM A375 (1996) 264.
[4] A.N. Matveenko, O.A. Shevchenko, N.A. Vinokurov, Proc. Of the 2004 FEL Conference, p. 629
[5] S. Reiche, NIM A429, (1999) 243.

RE-COMMISSIONING OF THE FAR-INFRARED FREE ELECTRON LASER FOR STABLE AND HIGH POWER OPERATION AFTER THE RENEWAL OF THE L-BAND LINAC AT ISIR, OSAKA UNIVERSITY

R. Kato, S. Kashiwagi,T. Igo, Y. Morio, G. Isoyama#
Institute of Scientific and Industrial Research, Osaka University, Osaka, Japan

Abstract

The far-infrared FEL at the Institute of Scientific and Industrial Research (ISIR), Osaka University, which was operated in the wavelength region from 32 to 150 μm and was suspended since 1998, is being commissioned for stable and high power operation. The FEL is based on the L-band electron linac constructed in 1978, but it was largely remodelled for higher stability and reproducibility of operation as well as for long pulse operation for FEL. The long pulse mode has been successfully commissioned using a feed forward control system, which can stabilize the amplitude and the phase of the 1.3 GHz RF power in the macropulse within 0.5 % in amplitude and 0.3º in phase. The FEL system is the same as before except for the strong focusing wiggler based on the edge-focussing scheme, which was recently introduced. The FEL experiment is all set up and we are waiting for the next machine time and lasing.

INTRODUCTION

We have been developing a far-infrared FEL since late 1980s based on the 40 MeV, L-band electron linac at the Institute of Scientific and Industrial Research (ISIR), Osaka University. The first lasing was obtained at 32~40 μm in 1994 [1] and since then we progressively modified the FEL system and continued experiment in between to expand the wavelength region toward the longer wavelength side beyond 100 μm. We finally obtained lasing at 150 μm in 1998 [2], which was, at that time, the longest wavelength obtained with FELs based on RF linacs. We could not obtain power saturation because the macropulse duration is 2 μs, though the RF pulse is 4 μs long, due to a long filling time of the acceleration tube of the L-band linac and the number of amplification times is limited to 50 only. The linac was constructed approximately 30 years ago and it was not suitable for stable and high power operation of FEL, so that we suspended the development of the FEL.

In 2002, we had an opportunity to remodel the linac largely for higher stability and reproducibility of operation. We also added a new operation mode for FEL in which the macropulse duration can be extended to 8 μs. I took time to remodel the linac and commission it, but finally the operation mode for FEL is being commissioned and we are resuming the FEL again after the long suspension. We will report the progress and the current status of the re-commissioning of the FEL.

#isoyama@sanken.osaka-u.ac.jp

RENEWED LINAC

The linac is comprised of a thermionic electron gun, a three-stage sub-harmonic buncher system with two 108 MHz RF cavities and a 216 MHz cavity, a pre-buncher, a buncher, and a 3 m long accelerating tube. The last three components are excited by a single klystron of the 1.3 GHz frequency, the maximum peak output power of 30 MW, the pulse duration of up to 8 μs, and the repetition frequency of 60 Hz. The main parameters of the linac are listed in Table 1. A klystron modulator, which provides high voltage pulses to the klystron, has two operation modes; one is the normal mode with the pulse duration of 4 μs and the repetition rate of 60 pps and the other is the long-pulse mode with 8 μs and 30 pps. The operation modes can be changed manually but easily in a short time.

The maximum output power of the klystron is limited to 25 MW in the long pulse mode, so that the maximum beam energy in the multi-bunch mode used for FEL is slightly lower than 40 MeV.

Stability and reproducibility of linac operation are essential for advanced studies with the linac, including FEL and all the possible measures have been taken in the remodelling to reduce fast fluctuations and long-term drifts. Most influential power supply for the stability is the klystron modulator and it is designed and fabricated to reduce pulse-to-pulse fluctuations less than 0.1 %. Voltage ripples on the flat top of the square pulse applied to the klystron should be less than 0.1 % in order to make the amplitude and the phase of the output power from the

Table 1: Main Parameters of the L-Band Linac

Acceleration frequency	1.3 GHz
Sub-harmonic buncher	108 MHz×2, 216MHz×1 λ/4 coaxial resonators
Accelerating structures	Prebuncher×1, Buncher×1, Accelerating tube×1 Travelling wave, 2π/3 mode
Electron gun	Thermionic cathode (EIMAC YU-156), DC 100 kV
Operation modes, peak currents or maximum charge, and pulse durations	Transient: 1.9 A, 8 ns Single bunch: 91 nC, 20 ps Steady: 1.9 A, 4 μs Multi-bunch: 1.9 A, 8 μs
Repetition rate	≤ 60 pps
Klystron	30 MW×1
Total length	10.5 m

klystron constant over the macropulse duration. Figure 1 shows a voltage pulse applied to the klystron with the klystron modulator in the normal mode and a histogram showing the intensity fluctuation in longer than two hours. The undulation of the flat top in the normal mode is measured to be 0.21 % (peak to peak) over the time period of 3.5 μs, which is twice as large as the design goal, but it is much less in the latter third, while the fluctuation of the peak voltage is 0.06 % (two standard deviations) in two hours, which meets the specifications.

Most popular operation modes of the linac are the transient mode used for the pulse radiolysis study in the nanosecond region and the single bunch mode for pulse radiolysis in the sub-picosecond region as well as SASE experiment in the far-infrared region, and hence they are first commissioned to resume the joint-use of the linac.

MULTI-BUNCH MODE FOR FEL

In FEL experiments, the linac is operated in the multi-bunch mode, in which the second 108 MHz and the 216 MHz cavities of the sub-harmonic buncher system are switched on and the 1.3 GHz RF power of 8 μs duration is provided to the accelerating structures so that the multi-bunch beam with time intervals of 9.25 ns between bunches, which is the inverse of 108 MHz is accelerated. In order to make the peak of the energy spectrum of the multi-bunch beam sharp and to make intervals between bunches precisely equal, the amplitude and the phase of the RF power must be constant over the macropulse period. It is said that the amplitude and the phase of the output power from a klystron do not vary in a pulse provided that the flat top of the high voltage pulse applied to the klystron is flat and constant. As the first step for commissioning of the multi-bunch mode for FEL, we began with the steady mode with the macropluse duration of 4 μs, in which the sub-harmonic buncher system is not turned on. Although the condition is met in our case, we could not make the peak of the energy spectrum for the steady mode sharp. We, therefore, measured the amplitude and the phase of the RF pulse from the klystron in the normal mode and found that the amplitude varied by 3.1 % for the most flat part of 2.9 μs and the phase also varied by ~12 degrees in 3.4 μs, both of which are much larger than our expectation of < 1 % in amplitude and < 1 degree in phase.

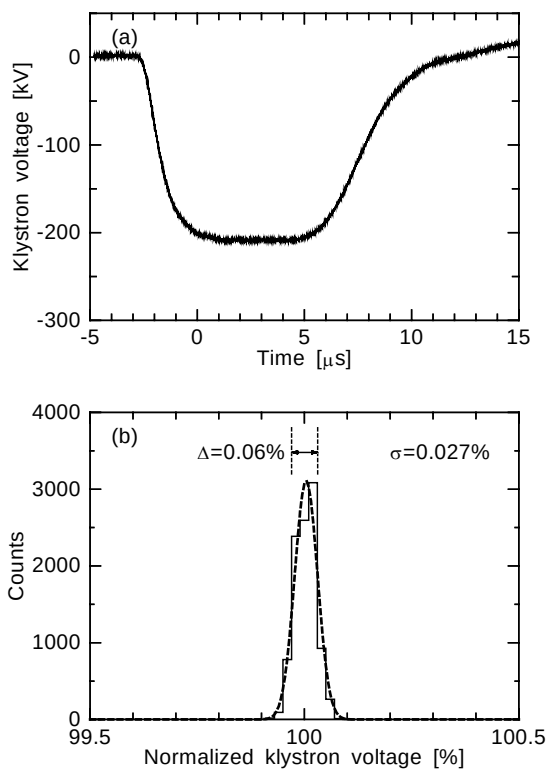

Fig. 1. High voltage pulse provided to the klystron in the normal mode and a histogram showing the peak intensity fluctuation.

Since reproducibility and stability of the high-voltage pulse from the klystron modulator are high and accordingly those of the amplitude and the phase variations of the RF power from the klystron are also high, we have adopted the feed-forward method to compensate for these variations. Figure 2 shows a block diagram of the compensation system for the amplitude and the phase of the 1.3 GHz RF power provided from the klystron to the accelerating structures of the linac. We, for the moment, adopt an analogue phase shifter with PIN diodes for phase control and an I-Q modulator for amplitude control. A part of the RF power is taken at a directional coupler on a waveguide from the klystron to the linac. The amplitude of the RF power is measured with a diode detector and the phase is measured with a phase detector, both of which have sufficiently fast response times, and the output signals are analysed with a digital oscilloscope. A personal computer calculates waveforms to be applied to the phase shifter and the variable attenuator so that both amplitude and phase variations becomes constant and flat over the RF pulse. Among the various components in the RF line, the phase shifter and the AB-class transistor amplifier, which is denoted by 300W amplifier in Fig. 2, have relatively long response times. In order to compensate for the slow response time, we use overdrive technique and the equation

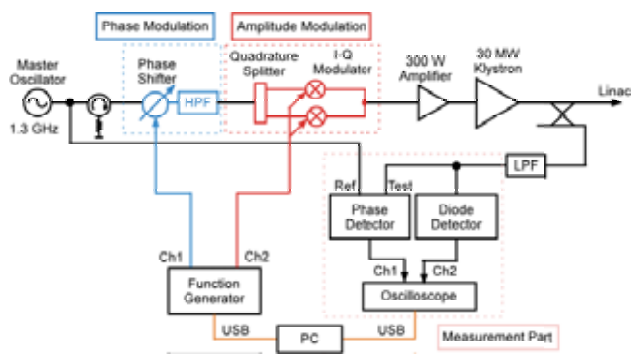

Fig. 2. Block diagram of the compensation system for the amplitude and the phase of the 1.3 GHz RF power from the klystron.

$$V_{in}(t-\Delta t)=V_c(t)+\tau\frac{dV_c(t)}{dt} \qquad (1)$$

is used to calculate the waveform generated with the function generator and applied to the control devices, where V_c is the control voltage for the ideally fast responding system, τ the response time of the system, Δt is the delay time in the control and measurement system, and V_{in} the actual control voltage. The response time and the delay time are measured with the actual system and they are τ = 50 ns and Δt = 540 ns for the amplitude control and τ = 780 ns and Δt = 640 ns for the phase control. Figure 3 shows the amplitude and the phase variations of the 1.3 GHz RF power in the long pulse mode before and after the compensation. The amplitude varies by 14.8 % in 7.4 μs and the phase by 13.5° before the compensation and they are reduced to 0.5 % and 0.3°, respectively, after compensation iteratively made several times.

Another problem we ran up against in the commissioning of the multi-bunch mode is that a correct energy spectrum could not be measured due to a digital current meter used for a Faraday cup in the momentum analyser, which is newly introduced in the upgrade of the linac in place of an old analog current meter, because it does not measure a correct current for an electron beam longer than a microsecond. It took time to find the current meter responsible for it. The long pulse electron beam is accelerated with the corrected RF power and energy spectra are measured with another momentum analyser with a fluorescent plate and a CCD camera. Figure 4

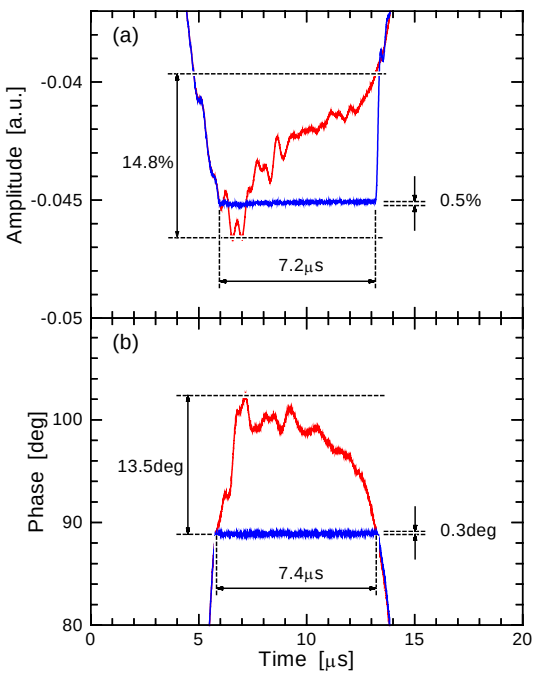

Fig.3. Amplitude and the phase of the 1.3 GHz RF power for the linac before and after the compensation. The panel (a) shows the amplitude and (b) the phase, while the red and the blue lines before and after compensation, respectively.

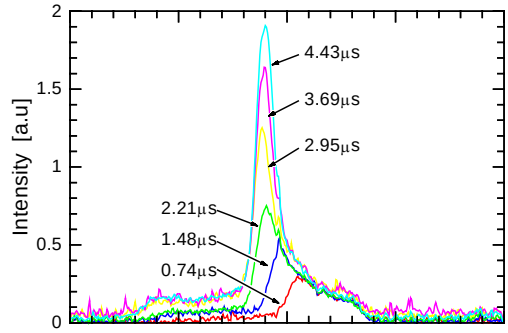

Fig. 4. Energy spectra of electron beams with several time durations in the long pulse mode without the SHB system.

shows energy spectra of electron beams with several different time durations accelerated in the long pulse mode without the SHB system, which we call the steady mode. The filling time of the accelerating tube is approximately 2 μs and energy spectra for the electron beams with pulse durations shorter than it have broader peaks due to the transient effect, while the sharp peaks grow up on the lower energy side in the energy spectra of electron beams longer than the filling time or 2 μs. The electron beam is easily conditioned in the multi-bunch mode with the SHB system being on and thus the multi-bunch mode for FEL is successfully commissioned.

FEL SYSTEM

The infrared FEL system, main parameters of which are listed in Table 2, is the same before the suspension except for the wiggler. The multi-bunch beam accelerated with the L-band linac is transported through the beam transport line consisting of two bending magnets and several quadrupole magnets to the wiggler. We used a conventional planar wiggler, but the magnet arrays were replaced with new ones that can not only wiggle the electron beam but also focus it both horizontally and vertically [3.] Figure 5 shows the magnetic field and the field gradient in the vertical direction measured along the beam axis of the strong focus wiggler at the magnet gap of 3 cm. The period length is 6 cm and the number of periods is 32, which are the same as before. The maximum peak magnetic field is 0.39 T at the minimum gap of 3 cm, which is slightly higher than before because permanent magnet materials advanced in the meanwhile. The FODO structure is adopted for the double focusing so that the electron beam of any energy accelerated with the linac can be focused even at larger wiggler gaps. The wiggler consists of four FODO cells and the cell length is 0.48 m. The focusing and the defocusing units are single wiggler periods with edge angles ±5° and the drift space is four normal wiggler periods. The maximum field gradients are ±3.2 T/m at the gap of 3 cm. The new wiggler was developed and installed for SASE experiments in the far-infrared region being conducted

Table 2: Main Parameters of the Infrared FEL

Wiggler	
Permanent magnet	Ne-Fe-B
Period length	6 cm
Number of periods	32
Magnet gap	12 – 3 cm
Peak magnetic field	0.39 T
K_{rms}-value	0.013 – 1.556
Total length	10.5 m
Focusing type	Strong focus with the edge-focusing scheme
Maximum field gradient	3.2 T
Length of FODO cell	0.48 m
Number of FODO cells	4
Optical resonator	
Type	Concentric resonator with spherical mirrors
Length	5.531 m
Mirrors	
Type	Spherical copper mirrors coated with gold
Curvature radii	3.358 m (upstream), 2.877 m (downstream)
Diameter	8 cm
Rayleigh range	1 m
Output coupling	3ϕ hole at the center of the upstream mirror

with the wiggler, but the FEL gain will be enhanced with it.

The optical resonator is a concentric resonator consisting of two spherical mirrors with different curvature radii. It is 5.531 m long and four optical pulses bounce back and forth in the cavity. The two mirrors are installed asymmetrically to the wiggler due to limitations by the magnets and other components in the FEL beam line and the curvature radii are chosen so that the waist of the stored light is located at the center of the wiggler. The FEL light is taken out through a hole at the center of the upstream mirrors and it is led with mirrors to the measurement room through the evacuated optical transport line, where the low vacuum in the optical transport line is separated with a synthetic diamond window from the high vacuum in the FEL beam line. The FEL light is analysed with a grating monochromator and detected with a Ge:Ga photoconductive detector cooled with liquid helium.

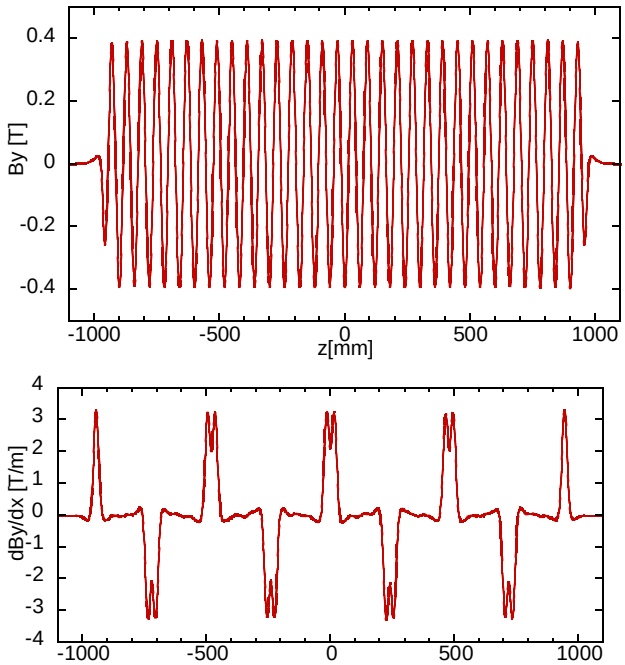

Fig. 5. Magnetic field and the field gradient in the vertical direction measured along the beam axis of the strong focus wiggler at the magnet gap of 3 cm.

SUMMARY

After a long period of suspension, the infrared FEL at ISIR, Osaka University is being commissioned. The linac has been largely remodelled, so that the FEL is expected to operate stably at the saturation power level, which was not possible before. The optical resonator and the measurement system have been aligned, the experiment is all set up, and we are waiting for the machine time for FEL.

REFERENCES

[1] S. Okuda, Y. Honda, N. Kimura, J. Ohkuma, T. Yamamoto, S. Suemine, T. Okada, S. Ishida, T. Yamamoto, S. Takeda, K. Tsumori, and T. Hori, Nucl. Instr. And Meth. A358 (1995) 244.

[2] R. Kato, S. Kondo, T. Igo, T. Okita, T. Konishi, S. Suemine, S. Okuda, and G. Isoyama, Nucl. Instr. And Meth. A445 (2000) 169.

[3] G. Isoyama, R. Kato, S. Kashiwagi, T. Igo, Y. Kon, T. Yamamoto, S. Suemine, "Performance of the Renewed L-band Linac and Recent Progress of Development FEL and SASE at Osaka University, APAC'07, Indore, India, January-February 2007, TUPMA68.